THE UNIVERSITY
of ADELAIDE

Metamorphic and crustal evolution of Australian–Antarctic Proterozoic margins

Naomi M. Tucker

Department of Earth Science
School of Physical Sciences
University of Adelaide

This thesis is submitted in fulfilment of the requirements
for the degree of Doctor of Philosophy

March 2018

Table of contents

Abstract

Regional, long-lived (>>50 Myr), high temperature–ultrahigh temperature (HT–UHT) metamorphism challenges conventional notions on the thermal state of the crust as it requires the sustaining of high energy thermal gradients (>>75 °C/kbar). Regional, long-lived, high thermal gradient metamorphism occurring at continental margins further questions the relationship between continental amalgamation, the mechanisms that promote and maintain elevated heat flow, and thus the tectonic setting(s) of which this metamorphic expression is the hallmark. The Musgrave–Albany–Fraser–Wilkes Orogen (MAFWO) is outstanding in its record of regionally expansive, prolonged, and thermally extreme conditions during the Mesoproterozoic (D_1/M_1: 1345–1260 Ma; D_2/M_2: 1220–1130 Ma). Occurring along the margins of the Australian and East Antarctic Archean–Paleoproterozoic cratons, this system is geographically and geodynamically central to models for the Proterozoic amalgamation of the Australian–Antarctic continent in the Rodinia system. Despite its significance, precise details of the Mesoproterozoic metamorphic evolution of some constituent terranes of the MAFWO are unclear. A metamorphic framework for the orogen in its entirety is also non-existent.

To address this deficiency, this thesis firstly presents an integrated metamorphic, geochronological and geochemical (together "petrochronology"), and isotopic study that characterises the metamorphic and crustal evolution of two key and understudied tectonic regions at opposing ends of the MAFWO. High thermal gradients at mid-crustal levels (6.0–6.5 kbar, 900 °C) prevailed in the east Musgrave Inlier, central Australia (east MAFWO), between ca. 1220–1140 Ma. Despite the protracted record of age data, the excursion to peak UHT metamorphic conditions was transient, and was followed by a slight increase in pressure. It is argued that high thermal gradient conditions occurred in response to magmatic loading and heat advection of coevally-emplaced granite. These new constraints provide insight into local-scale heat sources operating within a regional, mantle-driven thermal system.

The Bunger Hills and Highjump Archipelago, East Antarctica (west MAFWO), are characterised by similarly high thermal gradient conditions to the east MAFWO (5.5–7.1 kbar, 800–960 °C and 6–9 kbar, 850–950 °C, respectively). Metamorphic age data also suggest an extremely long duration of high temperatures (>150 Myr) but peak metamorphism itself is constrained to a comparatively shorter time period (ca. 1220–1180 Ma). In contrast to the east Musgrave Inlier, peak metamorphism was followed by a pressure decrease that is interpreted to reflect the extension of thickened crust.

New isotopic datasets from the Bunger Hills have allowed for re-examination of the pre-existing tectonic setting and thus potential tectonic control(s) on metamorphism. The Bunger Hills is now understood to represent a detached fragment of the Archean Yilgarn Craton that underwent (para)autochthonous crustal reworking during the Paleo–Mesoproterozoic. The tectonic evolution of the Bunger Hills is therefore strongly allied with the west Albany–Fraser Orogen, southwest Australia (also west MAFWO).

In light of these new constraints, the current state of knowledge of regional, long-lived, high thermal gradient metamorphism allied with Proterozoic Australian–East Antarctic continental assembly is reappraised. Mantle-heating is concluded as the overarching thermal driver but the specific mechanism diverges between the two-stage Mesoproterozoic evolution. D_1/M_1 was magmatically juvenile, spatially-confined, controlled by the pre-D_1 tectonic geometry and is reconcilable with a model of extensional accretionary orogenesis. D_2/M_2 was comparatively prolonged (high-T >80 Myr), consistently hot (~150 °C/kbar), and involved voluminous felsic–charnockitic magmatism with a significant mantle source contribution. These features are congruent with mantle lithosphere removal, and specifically lithosphere delamination. Precise details of the tectonic setting within D_1/M_1 and D_2/M_2 and the geodynamic trigger for D_2/M_2 remain unresolved, but the pre-metamorphic geological architecture is a key contributing factor. The ubiquitous metamorphic record of D_2/M_2, occurring across the entire MAFWO, suggests that the converging cratons had assembled prior, with the nature and timing of final amalgamation central to the generation of unusually high heat flow and the longevity of thermally anomalous conditions.

Declaration

I, Naomi Tucker, certify that this work contains no material which has been accepted for the award of any other degree or diploma in my name, in any university or other tertiary institution and, to the best of my knowledge and belief, contains no material previously published or written by another person, except where due reference has been made in the text.

In addition, I certify that no part of this work will, in the future, be used in a submission in my name, for any other degree or diploma in any university or other tertiary institution without the prior approval of the University of Adelaide and where applicable, any partner institution responsible for the joint-award of this degree.

I acknowledge that copyright of published works contained within this thesis resides with the copyright holder(s) of those works.

I also give permission for the digital version of my thesis to be made available on the web, via the University's digital research repository, the Library Search and also through web search engines, unless permission has been granted by the University to restrict access for a period of time.

I acknowledge the support I have received for my research through the provision of an Australian Government Research Training Program Scholarship.

Naomi Tucker Date 01/03/2018

Publications during the course of this thesis

Journal articles

Tucker, N. M., Morrissey, L. M., Payne, J. L. & Szpunar, M. 2018. Genesis of the Archean–Paleoproterozoic Tabletop Domain, Rudall Province, and its endemic relationship to the West Australian Craton. *Australian Journal of Earth Science*, in press, doi: 10.1080/08120099.2018.1479307.

Tucker, N. M., Hand, M., Kelsey, D. E., Taylor, R. J. M., Clark, C. & Payne, J. L. 2018. A tripartite approach to unearthing the duration of high temperature conditions versus peak metamorphism: an example from the Bunger Hills, East Antarctica. *Precambrian Research*, in press.

Bhowany, K., Hand, M., Clark, C., Kelsey, D. E., Reddy, S., Pearce, M., **Tucker, N. M.** & Morrissey, L. J. 2017. Phase equilibria modelling constraints on *P–T* conditions during fluid catalysed conversion of granulite to eclogite in the Bergen Arcs, Norway. *Journal of Metamorphic Geology*, **36**: 315–342, doi: 10.1111/jmg.12294.

Williams, M. A., Kelsey, D. E., Hand, M., Raimondo, T., Morrissey, L. J., **Tucker, N. M.** & Dutch, R. A. 2017. Further evidence for two metamorphic events in the Mawson Continent. *Antarctic Science*, **30**: 44–65, doi: 10.1017/S0954102017000451.

Tucker, N. M., Payne, J. L., Clark, C., Hand, M., Taylor, R. J. M., Kylander-Clark, A. R. C. & Martin, L. 2017. Proterozoic reworking of Archean (Yilgarn) basement in the Bunger Hills, East Antarctica. *Precambrian Research*, **298**: 16–38, doi: 10.1016/j.precamres.2017.05.013.

Tucker, N. M. & Hand, M. 2016. New constraints on metamorphism in the Highjump Archipelago, East Antarctica. *Antarctic Science*, **28**: 487–503, doi: 10.1017/S095410201600033X.

Tucker, N. M., Hand, M., Kelsey, D. E. & Dutch, R. A. 2015. A duality of timescales: Short-lived ultrahigh temperature metamorphism preserving a long-lived monazite growth history in the Grenvillian Musgrave–Albany–Fraser Orogen. *Precambrian Research*, **264**: 204–234, doi: 10.1016/j.precamres.2015.04.015.

Tucker, N. M., Hand, M. and Payne, J. L. 2015. A rift-related origin for regional medium-pressure, high-temperature metamorphism, *Earth and Planetary Science Letters*, **421**: 75–88, doi: 10.1016/j.epsl.2015.04.003.

Conference presentations

Tucker, N. M., Payne, J. L., Clark, C., Hand, M., Taylor, R. J. & Kylander-Clark, A. R. C. Reworking of Archean (Yilgarn) basement during the Proterozoic in the Bunger Hills, east Antarctica [abstract]. In: Australian Earth Sciences Convention (AESC), Abstracts v118 of the 22nd Australian Geological Convention, Adelaide SA, 26–30th June 2016 (ISSN 0729 011 X).

Tucker, N. M., Hand, M. & Payne, J. L. A rift related origin for regional medium-pressure, high-temperature metamorphism: a case study from the Harts Range, central Australia [abstract]. In: Granulites and Granulites 2015, Arebbusch Travel Lodge, Windhoek, Namibia, 26–29th July 2015. Programme and Abstracts.

Tucker, N. M., Hand, M. & Payne, J. L. Regional high-grade metamorphism during rift basin development: implications for burial mechanisms to lower crustal depths [abstract]. In: Fraser, G. L., Forster, M. and McClusky, S. 2014. SGTSG in the Snowies: Program and Abstracts: Biennial Conference of the Specialist Group for Tectonics and Structural Geology.

Acknowledgements

First and foremost, thanks go to my supervisors for their guidance, support and encouragement over these last four years. To Martin, for being a great teacher, for his unwaivering inspiration, and for the opportunity to have embarked on this journey in the first place. For the many field experiences—thank you—I will remember our Antarctic trip with fond memories. Dave, your insight into metamorphic geology has been invaluable. Thanks for all the manuscripts read so reliably and throroughly, and sometimes at very short notice. Justin, your support right throughout, starting well before my PhD, has been much appreciated, and to that I am indebted. Somehow you have managed to teach me a lot about geochemistry, depite me being a 'metamorphic' geologist!

There are countless others who have been involved. Chris and Rich, I am grateful for your assistance and expertise along the way, for the feedback of drafts and the sample preparation. To the staff at Adelaide Microscopy including Ben, Sarah, Aoife, Angus and Ken, thank you for all your help in sample preparation, running the lab, and the countless hours setting up, teaching me (and re-teaching me) the ropes. I could not have done this without you. The Geological Survey of South Australia, the Australian–Antarctic Division and fellow expeditioners at Casey Station in the 2014–2015 summer are sincerely acknowledged for the logistical support to undertake field work in some very remote places. Special thanks go to Billy, our amazing Antarctic field guide. Thanks for your Antarctic expertise, your friendship, and for sharing a tent with me for 5 weeks. To the many journal reviewers who have spent time on the chapters of this thesis, thank you also.

Thank you to the fellow occupants of CERG who have shared this journey at some point or another. Laura, thank you for being a mentor, particularly in the last few years, and for the countless hours shared on field trips and in airports (I have truly lost count), and for my moral support over a hot chocolate.

In retrospect, I would also like to thank Bronwyn, my geology teacher, and subsequently Karin, for introducing me into the world of geology and inspiring me to pursue this path from beginning. Thanks to Rian and the mapping team at the Geological Survey for indulging me in my love of petrography many years ago and for their constant support and interest since.

To my friends, Rosie, Clare and Nicole, thank you just for being, reminding me that there is a life outside PhD. My greatest thanks go to my family, to whom this thesis should be dedicated. Mum, Dad, Bryony, Nan and Pa (and Nigel), there is no way I could have achieved this without you. You have provided tireless support financially, through late night pick-ups from the lab, countless airport drop-offs at ridiculous hours, emotionally...the list is endless. Thank you for your patience, encouragement and for believing in me the whole way.
Finally, thank you to Jonathan, for being interested and for listening to me talk about geology (and "our" thesis) all the time. You are well on your way to writing your own thesis from all our geology conversations!

To anyone else I may have missed, thank you!

Motivation and aims of this thesis

Long-lived (>>50 Myr), high–ultrahigh thermal gradient metamorphism (≥150 ºC/kbar) represents a significant departure from the normal thermal crustal regime for anomalous timescales. Such conditions challenge our understanding of the thermomechanical behaviour of the lithosphere. Nonetheless, examples of long-lived, high–ultrahigh temperature (HT–UHT) metamorphism in the ancient Earth are spatially and temporally widespread (Fig. 1; Brown, 2007; Kelsey, 2008; Kelsey and Hand, 2015, and references therein). Further, an intriguing link in space and time is identified between the generation, and preservation, of regional HT–UHT conditions and the terminal stages of supercontinent assembly (e.g. Brown, 2006; 2007; Clark et al., 2015; Cutts et al., 2013; Santosh et al., 2006; Sizova et al., 2014; Sizova et al., 2010). The existence of long-lived, HT–UHT terranes thus requires thermal energy and a tectonic mechanism to augment crustal temperatures, and in many instances, also generate coeval, regionally-extensive lower crustal melting, that is intrinsically related to continent accretion and/or collision.

The current view suggests that regional, elevated crustal heat flow that is characteristic of long-lived, HT–UHT conditions may be facilitated by two main tectonic endmembers, both of which are allied with continent accretion and collision. In the first instance, anomalous heat flow may be generated by mantle conduction and/or advection in extensional accretionary orogens such as continental back-arc systems (Clark et al., 2011; Currie and Hyndman, 2006; Hyndman et al., 2005; Sizova et al., 2010). Back-arc basins are focussed zones of hot, thinned and mechanically weak lithosphere due to protracted and voluminous magma input, and are thus predisposed to subsequent remobilisation (i.e. shortening and thickening) into continental orogens (Brown, 2010; Chardon et al., 2009; Clark et al., 2011; Collins, 2002; Currie and Hyndman, 2006; Gorczyk et al., 2015; Hyndman et al., 2005; Sizova et al., 2014). An extension on this model is the development of ultra-hot orogens that are also characterised by hot, thin and weak lithosphere with voluminous mafic magmatism and high thermal gradients, but tectonic shortening is accommodated by lithosphere delamination and thus lateral spreading of the orogen, rather than by significant crustal thickening (Chardon et al., 2009; Gorczyk et al., 2015). Secondly, tectonic thickening of crust with above-average heat producing capability may conductively elevate mid–lower crustal temperatures if the exhumation potential is low (Clark et al., 2011; Huerta et al., 1998; Jamieson et al., 1998; Lexa et al., 2011; McLaren et al., 2005; Sandiford and Hand, 1998). Despite the apparent binary tectonic interpretation of regional HT–UHT metamorphic terranes, it is plausible that both advective and conductive mechanisms function together at continental margins to contribute to the generation of high thermal gradient conditions.

The thermal state of the crust is a function of its inherent energy content, its crust–mantle boundary conditions and the way deformation and erosion change the thickness of the crust over time. Thermal perturbations of the crust over time can be probed directly from metamorphic rocks as they preserve a valuable mineralogical and chemical record of their *P–T–t* evolution (e.g. Brown, 2014). This in turn is characteristic of different geodynamic settings and can provide information on the thermal drivers for metamorphism. However, the actual duration of metamorphism that is preserved by the metamorphic rock record may also be influenced more locally by the thermophysical rock properties and rock reactivity, as well as the chemical and physical behaviour of monazite and zircon, in particular at high temperatures (e.g. Harley, 2016; Kelsey and Hand, 2015; Korhonen et al., 2013; Roberts and Finger, 1997; Rubatto et al., 2006; Taylor et al., 2016). Challenges in linking the duration of metamorphism to the *P–T* evolution (so-called "petrochronology") carries through to ambiguities in determining the mechanisms for generation of high temperatures. As the rate of change of crustal temperature with depth is circularly-linked to the geodynamic setting, inferences on the causative mechanisms behind heat transfer can also be investigated by understanding the crustal (isotopic) evolution of

[1]The abbreviation MAFWO (Musgrave–Albany–Fraser–Wilkes Orogen, see also MAFO in Chapters 1–4 of this thesis) collectively refers to geological terranes with a shared Mesoproterozoic magmatic and metamorphic history that is intrinsically and unambiguously linked to the amalgamation of Australia and East Antarctica during the formation of Rodinia.

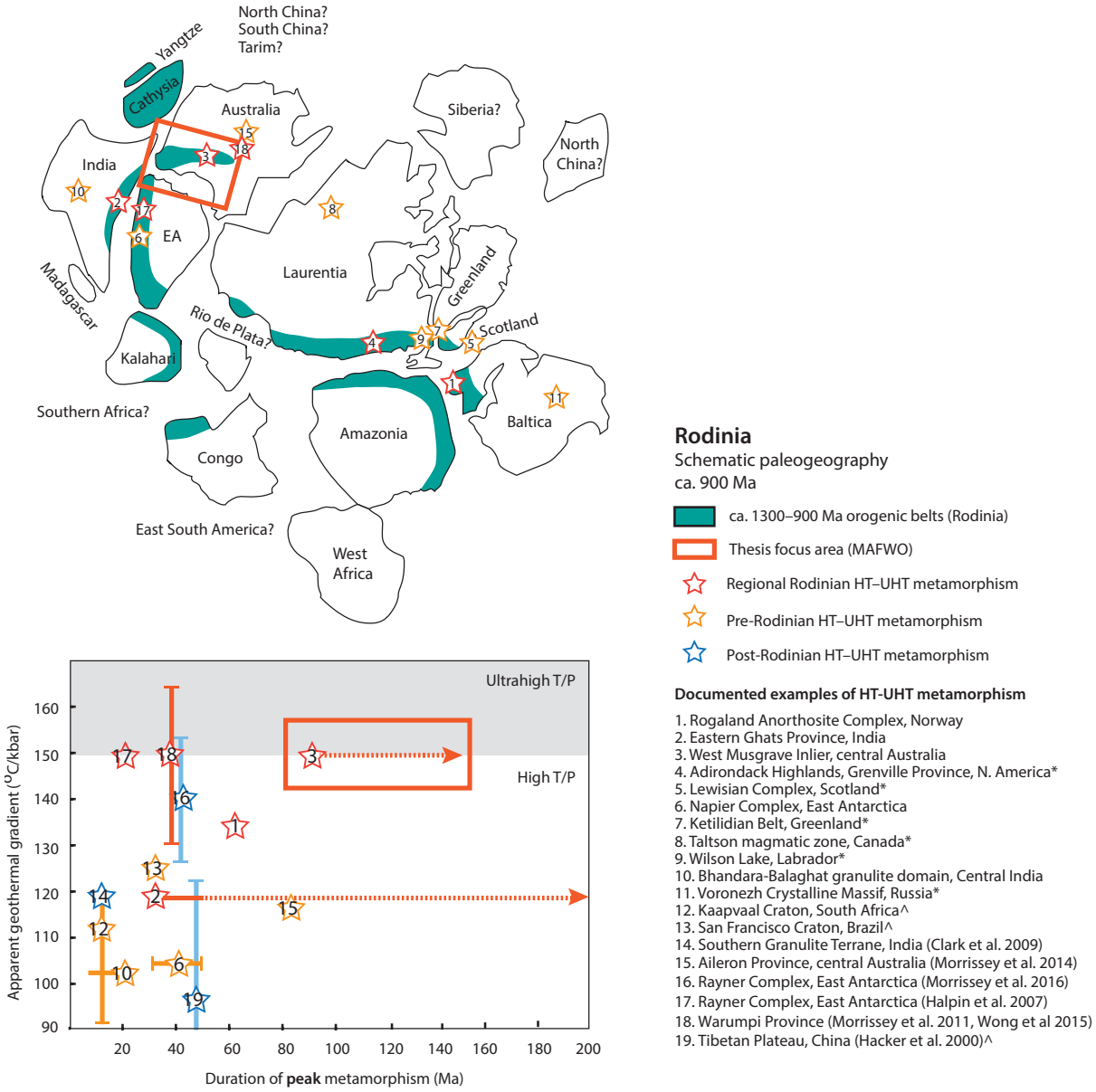

Figure 1. Schematic global paleogeography of Rodinia at ca. 900 Ma. Continental blocks are shown in their approximate relative positions as per the simplified reconstruction visualised in Spencer et al. (2015; based largely on Cawood et al. (2013)), Cawood et al. (2010) and Li et al. (2008)). Rodinian (ca. 1300–900 Ma) collisional belts, indicated in green, are based on Cawood and Pisarevsky (2017), Spencer et al. (2015) and Li et al. (2008). The South China, North China and Tarim cratons, and Siberia are placed northwards of Australia, India and Laurentia. The southern African and eastern South American cratons are considered south of Laurentia. However, their precise positions and orientations are uncertain, and so figure 1 should be used as a visual approximation of the continents and collisional belts only. Documented examples of regional HT–UHT metamorphism during Rodinia, pre-Rodinia and post-Rodinia supercontinent amalgamation are denoted with a star. Examples shown on the map, but not the plot of apparent thermal gradient versus duration of peak metamorphism (as the timescale of peak metamorphism is not documented or is unclear), are indicated with an asterisk. Examples shown on the plot but not geographically (e.g. because they post-date Rodinia) are denoted with an up-arrowhead (^). All example localities are listed by Kelsey and Hand (2015), Kelsey (2008) or Brown (2007), excluding examples where the reference is given on the figure. The focus area of this thesis is defined by the red box. Abbreviation: EA, East Antarctica.

the active tectonics that involve metamorphism.

A remarkable record of protracted, regional HT–UHT metamorphism and coeval, voluminous mafic–felsic magmatism during the Mesoproterozoic (ca. 1330–1140 Ma) is preserved in central and southern Australia, and Wilkes Land, East Antarctica. The Albany–Fraser Orogeny (Stage-1: 1330–1260 Ma, Stage-2: 1225–1140 Ma; Clark et al., 2000; Spaggiari et al., 2015) and concurrent Mount West Orogeny (ca. 1345–1293 Ma) and Musgrave Orogeny (ca. 1220–1140 Ma; Howard et al., 2015) are the major tectono-metamorphic and magmatic events that affected these regions. Mesoproterozoic HT–UHT rocks are presently exposed within the Musgrave Inlier and Albany–Fraser Orogen (all Australia), and the Bunger Hills, Highjump Archipelago and Windmill Islands (all East Antarctica), along the margins of the Australian and Antarctic Archean cratons. These regions share similarities in lithology, the timing of Mesoproterozoic magmatism, deformation and metamorphism, and aspects of their Paleo–Mesoproterozoic crustal evolution that support the existence of a large orogenic belt (herein MAFWO[1], Fig. 2). The MAFWO is keystone in the Proterozoic amalgamation of the North Australian Craton–West Australian Craton with the South Australian Craton–East Antarctic Craton in Rodinia.

Despite general agreement that regionally long-lived, HT–UHT conditions seemingly prevailed within the MAFWO (e.g. ~140–150 °C/kbar, up to 150 Myr in the west Musgrave Inlier; Smithies et al., 2011; Walsh et al., 2015) and were associated with a period of continental amalgamation, precise details of the metamorphic–petrochronologic evolution of several regions of the orogen, including its eastern and western extent, render somewhat equivocal. This is in part a repercussion of remoteness, regions of limited outcrop exposure,

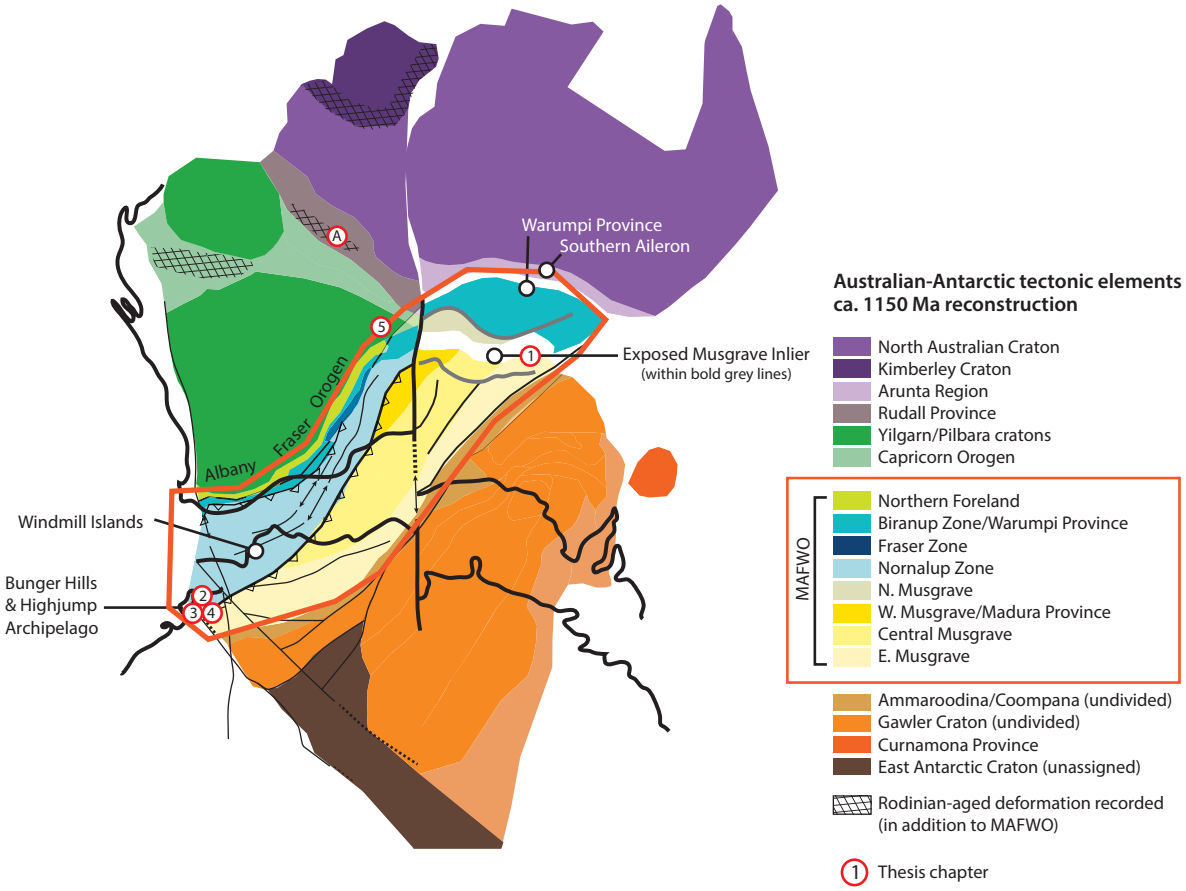

Figure 2. Australian–East Antarctic tectonic elements in Rodinia. Mesoproterozoic (ca. 1260–1130 Ma) configuration and regional geology of Australia and East Antarctica, and ca. 1150 Ma major geological structures are shown (Aitken et al., 2016). The reconstructed Mesoproterozoic architecture of Australia and East Antarctica highlights the former spatial linkage between tectonic elements and geological structures of the Musgrave–Albany–Fraser–Wilkes Orogen (MAFWO). The outline of Australia and East Antarctica are shown in bold. Terranes comprising the MAFWO are enclosed by the red polygon. Additional regions within Australia that record evidence for more localised Rodinian-aged (ca. 1300–900 Ma) deformation, magmatism and amphibolite facies metamorphism are indicated by cross-hatching. The location of terranes investigated in the chapters of this thesis are indicated. Note that Chapter 5 refers to all MAFWO and 'A' refers to the Appendix.

cultural sensitivities, the vast scale of the orogen itself, and varied government jurisdiction that collectively impede consensus on an orogenic-wide metamorphic framework. Variation in metamorphic grade, the spatial and temporal extent of high geothermal gradient metamorphism, and the governing tectonic controls and driving forces for elevated thermal conditions across the orogen are unclear. While the MAFWO is not the largest known example of high-grade deformation (e.g. compare Grenville Orogen, Laurentia, Fig. 1; Rino et al., 2008; Roberts et al., 2015), nor the most magmatically-voluminous (e.g. East African Orogen; Meert, 2003; Stern, 2008), and higher metamorphic temperatures are recorded elsewhere (e.g. >1100 °C, Napier Complex, East Antarctica; Harley and Motoyoshi, 2000; Hokada, 2001), it is the apparent longevity of regionally extreme thermal gradients that is of note. There is considerable scope to provide new and useful constraints on the metamorphic thermal and physical conditions of under-studied regions of the MAFWO. There is significant motivation to investigate the geodynamic impetus for generation of regional, long-lived, high thermal gradient metamorphism along the Proterozoic margins of Australia and Antarctica, and thus the link with continental assembly.

The **central aim** of this thesis is to investigate the time-integrated metamorphic evolution of long-lived, high thermal gradient terranes in central–southwest Australia and East Antarctica to provide information on the thermal characteristics of tectonic events and the geodynamics leading to the Proterozoic (Rodinian) amalgamation of the Australian and East Antarctic cratons. This project focusses on the eastern Musgrave Inlier, central Australia, and the Bunger Hills region, East Antarctica, at opposing ends of the MAFWO. Firstly, this involves quantification of the *P–T* evolution of these regions based on the major silicate mineral record of metamorphic rocks. Secondly, understanding the timescales associated with high geothermal gradient metamorphism involves integrating U–Pb geochronology with trace element geochemical signatures of accessory and major silicate minerals (petrochronology). Thirdly, the crustal evolution of understudied areas of the MAFWO must also be investigated to assist in providing a geodynamic framework in which to better understand the timing of and thermal drivers for metamorphism, and this involves integrating zircon Lu–Hf isotope data with U–Pb geochronology.

The **specific aims** of this thesis are therefore:

1. To investigate the geochronologic and isotopic evolution of under studied areas of the MAFWO to provide a geodynamic framework in which to understand the Mesoproterozoic metamorphic evolution;

2. To place quantitative constraints on the metamorphic architecture through phase equilibria forward modelling to understand the peak conditions, and prograde and retrograde *P–T* paths, associated with high geothermal gradient metamorphism within under studied areas of the MAFWO;

3. To investigate how the age, timescale and rate of high thermal gradient metamorphism can be adequately characterised and interpreted;

4. To determine whether HT–UHT metamorphic terranes comprising the MAFWO exhibit synchronicity—spatially, temporally and thermally;

5. To critically evaluate the available models for the tectonic settings and geodynamic factors that promote long-existing high thermal gradient metamorphic conditions across the MAFWO to ultimately present an integrated framework that characterises the Mesoproterozoic metamorphic features of continental amalgamation in central–southwest Australia and East Antarctica.

The focus of the first aim is the Bunger Hills region, for which the Archean–Mesoproterozoic crustal evolution is poorly known, despite being long considered as a paleogeographic (Aitken et al., 2016; Li et al., 2008; White et al., 2013) and geochronologic (Clark et al., 2000; Fitzsimons, 2000; Sheraton et al., 1995) extension of the Albany–Fraser Orogen. The Bunger Hills region (including the Highjump Archipelago) provides the largest exposure of the East Antarctic Craton that can be directly correlated with Australian tectonic components of the MAFWO and thus offers unique insight into the thermal evolution of the orogen at its westernmost known extent, as well as the unexposed and little-known geology of East Antarctica. The second and third aims are addressed through metamorphic case studies

from the east Musgrave Inlier and Bunger Hills region. Elucidating the metamorphic character of these regions, situated at the orogen ends, is an essential precursor to enabling prior metamorphic studies from other localities across the orogen to be drawn together, compared and contrasted. Accordingly, the final two aims involve the review of petrochronologic, isotopic and geochemical constraints on long-lived, high thermal gradient Mesoproterozoic metamorphism and magmatism from across the orogen.

Chapter Outlines

Chapter 1 constrains the metamorphic evolution of the easternmost exposure of the MAFWO and assesses whether the previously documented extreme thermal and temporal record of UHT metamorphism in the west Musgrave Inlier (Smithies et al., 2011; Walsh et al., 2015) also extends to the east Musgrave Inlier. Utilizing *in situ* monazite geochronology and phase equilibria forward models, this study constrains the *P–T* conditions and timing of metamorphism. In-depth analysis of the microstructural location and major and trace element compositions of garnet, in concert with the trace element composition of monazite, are used to investigate the duration of peak metamorphic conditions, the relative rate of cooling, and the *P–T* path. In doing so, the thermal mechanisms for high thermal gradient metamorphism in the east MAFWO are explored.

Chapter 1 is published as: Tucker, N. M., Hand, M., Kelsey, D. E. & Dutch, R. A. 2015. A duality of timescales: Short-lived ultrahigh temperature metamorphism preserving a long-lived monazite growth history in the Grenvillian Musgrave–Albany–Fraser Orogen. *Precambrian Research*, **264**: 204–234, doi: 10.1016/j.precamres.2015.04.015.

Chapter 2 shifts the focus of this thesis to the westernmost extent of the MAFWO that is exposed in East Antarctica as the Bunger Hills and adjacent Highjump Archipelago. This study specifically addresses the metamorphic evolution of the Highjump Archipelago using legacy thin section samples. *In situ* U–Pb monazite geochronology and quantitative phase equilibria forward models are used to provide new constraints—and the first indication—of a seemingly long duration of high thermal gradient metamorphic conditions in the Highjump Archipelago that are akin to timescales recognised in the Musgrave Inlier, as constrained in Chapter 1. These results pre-empt the development of a more comprehensive metamorphic study on the *P–T* conditions and duration of metamorphism in the Bunger Hills (Chapter 4).

Chapter 2 is published as: Tucker, N. M. & Hand, M. 2016. New constraints on metamorphism in the Highjump Archipelago, East Antarctica. *Antarctic Science*, **28**: 487–503, doi: 10.1017/S095410201600033X.

Chapter 3 presents the first detailed U–Pb, Lu–Hf and oxygen isotope analysis of zircon from igneous and metasedimentary rocks collected from across the Bunger Hills. The age and isotope signature of a previously unrecognised Archean basement, a Paleoproterozoic volcano-sedimentary sequence, Mesoproterozoic igneous intrusive rocks, and their isotopic affinity to other terranes comprising the MAFWO are investigated. This permits inferences to be made on the tectonic model for crustal growth and modification in the Bunger Hills, and more definitively links the Archean–Mesoproterozoic geodynamic relationship of the Bunger Hills to the Albany–Fraser Orogen. This chapter provides an important contextual framework of the Archean–Mesoproterozoic crustal evolution of the Bunger Hills in which to consider the Mesoproterozoic metamorphic evolution of this region.

Chapter 3 is published as: Tucker, N. M., Payne, J. L., Clark, C., Hand, M., Taylor, R. J. M., Kylander-Clark, A. R. C. & Martin, L. 2017. Proterozoic reworking of Archean (Yilgarn) basement in the Bunger Hills, East Antarctica. *Precambrian Research*, **298**: 16–38, doi: 10.1016/j.precamres.2017.05.013.

Chapter 4 applies a three-way approach to deciphering the timescale of overall high-temperature conditions versus peak HT–UHT metamorphism in the Bunger Hills. Previously obtained metamorphic age data (Chapters 2 and 3) elude to a long-lived high thermal gradient regime in the Bunger Hills region. Chapter 4 builds upon these initial findings with new U–Pb zircon and monazite geochronology, trace element chemistry of zircon, monazite and garnet, and phase equilibria forward models, as well as careful interpretation of zircon morphology. The multi-faceted appraisal of metamorphic conditions adopted in this study highlights the differences in age data that can be

gleamed from monazite versus zircon, and the pitfalls of a petrochronology-absent approach to deciphering the timescale of metamorphism in high-grade metamorphic terranes. Together with Chapter 2, this chapter constrains the metamorphic evolution of the westernmost extent of the MAFWO.

Chapter 4 is published as: Tucker, N. M., Hand, M., Kelsey, D. E., Taylor, R. J. M., Clark, C. & Payne, J. L. 2018. A tripartite approach to unearthing the duration of high temperature conditions versus peak metamorphism: an example from the Bunger Hills, East Antarctica. *Precambrian Research*, in press.

Chapter 5 serves as a stand-alone reference for the present state of knowledge regarding the high-temperature Mesoproterozoic evolution of Australian–East Antarctic Proterozoic margins that amalgamated during the assembly of Rodinia. It is a synthesis of all available data, comparing the key features of the metamorphic and magmatic evolution from constituent terranes of the MAFWO, and discusses the geodynamic and tectonic factors that are documented to pre-empt, generate or influence long-lived, high thermal gradient metamorphic conditions along the length of the orogen.

Chapter 5 is written in manuscript-style for submission to *Australian Journal of Earth Science*.

Chapter 6 concludes this thesis by assimilating the key findings presented in the preceding chapters, and outlines directions for future research.

The **Appendix** presents the results of a parallel study undertaken in conjunction with Chapters 1–5 of this thesis. This study investigates the age and origin of basement to the Tabletop Domain of the Rudall Province, northwest Australia, and its geodynamic relationship to the North Australian Craton (NAC) and West Australian Craton (WAC). The Tabletop Domain occurs at the northeast margin of the WAC. Campaign-style sampling across the Tabletop Domain and resultant U–Pb zircon geochronology and Lu–Hf isotope analysis reveal a previously unrecognised Archean–Paleoproterozoic basement. These rocks share age and isotopic similarities with the adjacent Connaughton and Talbot Domains of the Rudall Province, and more broadly, the Capricorn Orogen and Pilbara Craton of the WAC. The comprehensive time-constrained isotopic dataset presented in this chapter is the first of its kind from the Tabletop Domain, and facilitates a more complete evaluation of the Proterozoic crustal evolution of the WAC continental margin with respect to the NAC. The focus of this chapter is not regional, long-lived, high thermal gradient metamorphism, however, it is aligned with Chapters 1–5 in that it too investigates the evolution of Australian continental margins. Further, recent re-evaluation of the metamorphic evolution of the Rudall Province suggests that medium to high-pressure amphibolite facies metamorphism and deformation also occurred during the Meosproterozoic (ca. 1380 Ma and ca. 1285 Ma), at a similar time to metamorphism within the MAFWO, and this has also been suggested to relate to the amalgamation of the WAC and NAC (Anderson, 2015; Maidment, 2017). The reviewers are therefore invited to appraise this chapter in the broader context of this thesis.

The Appendix is published as: Tucker, N. M., Morrissey, L. J., Payne, J. L. & Szpunar, M. Genesis of the Archean–Paleoproterozoic Tabletop Domain, Rudall Province, and its endemic relationship to the West Australian Craton. *Australian Journal of Earth Science*, in press, doi: 10.1080/08120099.2018.1479307.

Chapters 2–5 and the Appendix contain supporting figures and data tables that supplement the discussion within the main text. All supplementary material is presented at the end of each chapter.

REFERENCES

Aitken A. R. A., Betts P. G., Young D. A., Blankenship D. D., Roberts J. L. & Siegert M. J. 2016. The Australo–Antarctic Columbia to Gondwana transition. *Gondwana Research* 29, 136–152.

Anderson J. A. 2015. Metamorphic and isotopic characterisation of Proterozoic belts at the margins of the North and West Australian Cratons. PhD thesis. University of Adelaide, Adelaide.

Brown M. 2006. Duality of thermal regimes is the distinctive characteristic of plate tectonics since the Neoarchean. Geology 34, 961–964.

Brown M. 2007. Metamorphism, plate tectonics, and the supercontinent cycle. *Earth Science Frontiers* 14, 1–18.

Brown M. 2010. Paired metamorphic belts revisited. *Gondwana Research* 18, 46–59.

Brown M. 2014. The contribution of metamorphic petrology to understanding lithosphere evolution and geodynamics. *Geoscience Frontiers* 5, 553–569.

Cawood P. A. & Pisarevsky S. A. 2017. Laurentia-

Baltica-Amazonia relations during Rodinia assembly. *Precambrian Research* 292, 386–397.

Cawood P. A., Strachan R., Cutts K., Kinny P. D., Hand M. & Pisarevsky S. 2010. Neoproterozoic orogeny along the margin of Rodinia: Valhalla orogen, North Atlantic. *Geology* 38, 99–102.

Cawood P. A., Wang Y., Xu Y. & Zhao G. 2013. Locating South China in Rodinia and Gondwana: A fragment of greater India lithosphere? *Geology* 41, 903–906.

Chardon D., Gapais D. & Cagnard F. 2009. Flow of ultra-hot orogens: a view from the Precambrian, clues for the Phanerozoic. *Tectonophysics* 477, 105–118.

Clark, C., Collins, A. S., Timms, N. E., Kinny, P. D., Chetty, T. R. K., & Santosh, M. 2009. SHRIMP U–Pb age constraints on magmatism and high-grade metamorphism in the Salem Block, southern India. *Gondwana Research,* 16, 27–36.

Clark C., Fitzsimons I. C. W., Healy D. & Harley S. L. 2011. How does the continental crust get really hot? *Elements* 7, 235–240.

Clark C., Healy D., Johnson T., Collins A. S., Taylor R. J., Santosh M. & Timms N. E. 2015. Hot orogens and supercontinent amalgamation: a Gondwanan example from southern India. *Gondwana Research* 28, 1310–1328.

Clark D. J., Hensen B. J. & Kinny P. D. 2000. Geochronological constraints for a two-stage history of the Albany–Fraser Orogen, Western Australia. *Precambrian Research* 102, 155–183.

Collins W. J. 2002. Hot orogens, tectonic switching, and creation of continental crust. *Geology* 30, 535–538.

Currie C. A. & Hyndman R. D. 2006. The thermal structure of subduction zone back arcs. *Journal of Geophysical Research: Solid Earth* 111, B08404.

Cutts K. A., Kelsey D. E. & Hand M. 2013. Evidence for late Paleoproterozoic (ca. 1690–1665Ma) high- to ultrahigh-temperature metamorphism in southern Australia: implications for Proterozoic supercontinent models. *Gondwana Research* 23, 617–640.

Fitzsimons I. C. W. 2000. Grenville-age basement provinces in East Antarctica: evidence for three separate collisional orogens. *Geology* 28, 879–882.

Gorczyk W., Smithies H., Korhonen F., Howard H. & Quentin De Gromard R. 2015. Ultra-hot Mesoproterozoic evolution of intracontinental central Australia. *Geoscience Frontiers* 6, 23–37.

Hacker, Bradley R., Edwin Gnos, Lothar Ratschbacher, Marty Grove, Michael McWilliams, Stephen V. Sobolev, Jiang Wan, and Wu Zhenhan. 2000. Hot and dry deep crustal xenoliths from Tibet. *Science* 287: 2463–2466.

Halpin, J. A., Clarke, G. L., White, R. W., & Kelsey, D. E. 2007. Contrasting P–T–t paths for Neoproterozoic metamorphism in MacRobertson and Kemp Lands, east Antarctica. *Journal of Metamorphic Geology*, 25: 683–701.

Harley S. L. 2016. A matter of time: The importance of the duration of UHT metamorphism. *Journal of Mineralogical and Petrological Sciences* 111, 50–72.

Harley S. L. & Motoyoshi Y. 2000. Al zoning in orthopyroxene in a sapphirine quartzite: evidence for >1120 C UHT metamorphism in the Napier Complex, Antarctica, and implications for the entropy of sapphirine. *Contributions to Mineralogy and Petrology* 138, 293–307.

Hokada T. 2001. Feldspar thermometry in ultrahigh-temperature metamorphic rocks: Evidence of crustal metamorphism attaining ~1100 °C in the Archean Napier Complex, East Antarctica. *American Mineralogist* 86, 932–938.

Howard H. M., Smithies R. H., Kirkland C. L., Kelsey D. E., Aitken A., Wingate M. T. D., Quentin De Gromard R., Spaggiari C. V. & Maier W. D. 2015. The burning heart — The Proterozoic geology and geological evolution of the west Musgrave Region, central Australia. *Gondwana Research* 27, 64–94.

Huerta A. D., Royden L. H. & Hodges K. V. 1998. The thermal structure of collisional orogens as a response to accretion, erosion, and radiogenic heating. *Journal of Geophysical Research: Solid Earth* 103, 15287–15302.

Hyndman R. D., Currie C. A. & Mazzotti S. P. 2005. Subduction zone backarcs, mobile belts, and orogenic heat. *GSA Today* 15, 4–10.

Jamieson R. A., Beaumont C., Fullsack P. & Lee B. 1998. Barrovian regional metamorphism: where's the heat? *Geological Society, London, Special Publications* 138, 23–51.

Johansson A. 2014. From Rodinia to Gondwana with the 'SAMBA' model-A distant view from Baltica towards Amazonia and beyond. *Precambrian Research* 244, 226–235.

Kelsey D. E. 2008. On ultrahigh-temperature crustal metamorphism. *Gondwana Research* 13, 1–29.

Kelsey D. E. & Hand M. 2015. On ultrahigh temperature crustal metamorphism: phase equilibria, trace element thermometry, bulk composition, heat sources, timescales and tectonic settings. *Geoscience Frontiers* 6, 311–356.

Korhonen F. J., Clark C., Brown M., Bhattacharya S. & Taylor R. 2013. How long-lived is ultrahigh temperature (UHT) metamorphism? Constraints from zircon and monazite geochronology in the Eastern Ghats orogenic belt, India. *Precambrian Research* 234, 322–350.

Lexa O., Schulmann K., Janoušek V., Štípská P., Guy A. & Racek M. 2011. Heat sources and trigger mechanisms of exhumation of HP granulites in Variscan orogenic root. *Journal of Metamorphic Geology* 29, 79–102.

Li Z. X., Bogdanova S. V., Collins A. S., Davidson A., De Waele B., Ernst R. E., Fitzsimons I. C. W., Fuck R. A., Gladkochub D. P., Jacobs J., Karlstrom K. E., Lu S., Natapov L. M., Pease V., Pisarevsky S. A., Thrane K. & Vernikovsky V. 2008. Assembly, configuration, and break-up history of Rodinia: a synthesis. *Precambrian Research* 160, 179–210.

Maidment D. W. 2017. Geochronology of the Rudall Province, Western Australia: implications for the amalgamation of the West and North Australian Cratons: Geological Survey of Western Australia, Report 161, 95p.

Mclaren S., Sandiford M. & Powell R. 2005. Contrasting styles of Proterozoic crustal evolution: a hot-plate tectonic model for Australian terranes. *Geology* 33, 673–676.

Meert J. G. 2003. A synopsis of events related to the assembly of eastern Gondwana. *Tectonophysics* 362, 1–40.

Mohanty S. 2012. Spatio-temporal evolution of the Satpura Mountain Belt of India: a comparison with the Capricorn Orogen of Western Australia and implication for evolution of the supercontinent Columbia. *Geoscience Frontiers* 3, 241–267.

Morrissey, L., Payne, J. L., Kelsey, D. E., & Hand, M. 2011. Grenvillian-aged reworking in the North Australian Craton, central Australia: constraints from geochronology and modelled phase equilibria. *Precambrian Research,* 191: 141–165.

Morrissey, L. J., Hand, M., Raimondo, T., & Kelsey, D. E. 2014. Long-lived high-T, low-P granulite facies metamorphism in the Arunta Region, central Australia.

Journal of Metamorphic Geology, 32: 25–47.

Morrissey, L. J., Hand, M., Kelsey, D. E., & Wade, B. P. 2016. Cambrian high-temperature reworking of the Rayner–Eastern Ghats terrane: constraints from the northern Prince Charles Mountains region, East Antarctica. *Journal of Petrology*, 57: 53-92.

Rino S., Kon Y., Sato W., Maruyama S., Santosh M. & Zhao D. 2008. The Grenvillian and Pan-African orogens: World's largest orogenies through geologic time, and their implications on the origin of superplume. *Gondwana Research* 14, 51–72.

Roberts M. P. & Finger F. 1997. Do U–Pb zircon ages from granulites reflect peak metamorphic conditions? *Geology* 25, 319–322.

Roberts N. M., Slagstad T. & Viola G. 2015. The structural, metamorphic and magmatic evolution of Mesoproterozoic orogens. *Precambrian Research* 265, 1–9.

Rubatto D., Hermann J. & Buick I. S. 2006. Temperature and bulk composition control on the growth of monazite and zircon during low-pressure anatexis (Mount Stafford, central Australia). *Journal of Petrology* 47, 1973–1996.

Sandiford M. & Hand M. 1998. Australian Proterozoic high-temperature, low-pressure metamorphism in the conductive limit. *Geological Society, London, Special Publications* 138, 109–120.

Santosh M., Sajeev K. & Li J. 2006. Extreme crustal metamorphism during Columbia supercontinent assembly: evidence from North China Craton. *Gondwana Research* 10, 256–266.

Sheraton J. W., Tingey R., Oliver R. & Black L. 1995. Geology of the Bunger Hills–Denman Glacier region, East Antarctica. *AGSO Bulletin*, No. 244, 1–136.

Sizova E., Gerya T. & Brown M. 2014. Contrasting styles of Phanerozoic and Precambrian continental collision. *Gondwana Research* 25, 522–545.

Sizova E., Gerya T., Brown M. & Perchuk L. L. 2010. Subduction styles in the Precambrian: insight from numerical experiments. *Lithos* 116, 209–229.

Smithies R. H., Howard H. M., Evins P. M., Kirkland C. L., Kelsey D. E., Hand M., Wingate M. T. D., Collins A. S. & Belousova E. 2011. High-temperature granite magmatism, crust-mantle interaction and the mesoproterozoic intracontinental evolution of the Musgrave Province, central Australia. *Journal of Petrology* 52, 931–958.

Spaggiari C. V., Kirkland C. L., Smithies R. H., Wingate M. T. D. & Belousova E. A. 2015. Transformation of an Archean craton margin during Proterozoic basin formation and magmatism: the Albany–Fraser Orogen, Western Australia. *Precambrian Research* 266, 440–466.

Spencer C. J., Cawood P. A., Hawkesworth C. J., Prave A. R., Roberts N. M. W., Horstwood M. S. A. & Whitehouse M. J. 2015. Generation and preservation of continental crust in the Grenville Orogeny. *Geoscience Frontiers* 6, 357–372.

Stern R. J. 2008. Neoproterozoic crustal growth: the solid Earth system during a critical episode of Earth history. *Gondwana Research* 14, 33–50.

Taylor R. J., Kirkland C. L. & Clark C. 2016. Accessories after the facts: constraining the timing, duration and conditions of high-temperature metamorphic processes. *Lithos* 264, 239–257.

Walsh A. K., Kelsey D. E., Kirkland C. L., Hand M., Smithies R. H., Clark C. & Howard H. M. 2015. *P–T–*t evolution of a large, long-lived, ultrahigh-temperature Grenvillian belt in central Australia. *Gondwana Research* 28, 531–564.

White L. T., Gibson G. M. & Lister G. S. 2013. A reassessment of paleogeographic reconstructions of eastern Gondwana: bringing geology back into the equation. *Gondwana Research* 24, 984–998.

Wong, B. L., Morrissey, L. J., Hand, M., Fields, C. E., & Kelsey, D. E. 2015. Grenvillian-aged reworking of late Paleoproterozoic crust of the southern North Australian Craton, central Australia: Implications for the assembly of Mesoproterozoic Australia. *Precambrian Research,* 270, 100–123.

Zhao G., Li S., Sun M. & Wilde S. A. 2011. Assembly, accretion, and break-up of the Palaeo–Mesoproterozoic Columbia supercontinent: record in the North China Craton revisited. *International Geology Review* 53, 1331–1356.

Chapter 1

This chapter is published as:

Tucker, N. M., Hand, M., Kelsey, D. E. & Dutch, R. A. 2015. A duality of timescales: Short-lived ultrahigh temperature metamorphism preserving a long-lived monazite growth history in the Grenvillian Musgrave–Albany–Fraser Orogen. *Precambrian Research*, **264**: 204–234, doi: 10.1016/j.precamres.2015.04.015.

Statement of Authorship

Title of paper	A duality of timescales: Short-lived ultrahigh temperature metamorphism preserving a long-lived monazite growth history in the Grenvillian Musgrave–Albany–Fraser Orogen
Pulication status	☒ Published ☐ Accepted for publication ☐ Submitted for publication ☐ Unpublished and unsubmitted work written in manuscript style
Publication details	Tucker, N. M., Hand, M., Kelsey, D. E., & Dutch, R. A. 2015. A duality of timescales: Short-lived ultrahigh temperature metamorphism preserving a long-lived monazite growth history in the Grenvillian Musgrave–Albany–Fraser Orogen. *Precambrian Research*, **264**: 204–234, doi: 10.1016/j.precamres.2015.04.015.

Principal Author

Name of Principal Author	Naomi M. Tucker
Contribution to the paper	Project design; fieldwork; sample selection and preparation; petrology; SEM, EPMA and LA–ICP–MS data collection; all calculations and data processing; critical data interpretation; manuscript design and composition; creation of all figures.
Overall percentage (%)	85
Certification	This paper reports on original research I conducted during the period of my Higher Degree by Research candidature and is not subject to any obligations or contractual agreements with a third party that would constrain its inclusion in this thesis. I am the primary author of this paper.
Signature	Date 04/10/2017

Co-author contributions

By signing the Statement of Authorship, each author certifies that:

i. the candidate's stated contribution to the publication is accurate (as detailed above);
ii. permission is granted for the candidate to include the publication in the thesis; and,
iii. the sum of all co-authors contributions is equal to 100 % less the candidate's stated contribution.

Name of Co-author	Martin Hand
Contribution to the paper	Assistance with project design; fieldwork; data interpretation guidance; manuscript review.
Signature	Date 13/10/2017

Name of Co-author	David E. Kelsey
Contribution to the paper	Assistance with *P–T* modelling; data interpretation guidance; manuscript review.
Signature	Date 05/10/2017

Name of Co-author	Rian A. Dutch
Contribution to the paper	Fieldwork, including logistical support; use of thin section sample; data interpretation guidance; manuscript review
Signature	Date 06/10/2017

A duality of timescales: short-lived ultrahigh temperature metamorphism preserving a long-lived monazite growth history in the Grenvillian Musgrave–Albany–Fraser Orogen

Naomi M. Tucker[a], Martin Hand[a], David E Kelsey[a], Rian A Dutch[b, a]

[a]*Department of Earth Sciences, School of Physical Sciences, The University of Adelaide, Adelaide, South Australia, 5005, Australia*
[b]*Geological Survey of South Australia, Department for State Development. 101 Grenfell Street, Adelaide, South Australia, 5000, Australia*

ABSTRACT

In situ LA–ICP–MS U–Pb monazite geochronology from the eastern Musgrave Inlier, central Australia, suggests that high-*T*, suprasolidus conditions were maintained for >70 Myr during the Grenvillian (ca. 1220–1140 Ma). Calculated phase equilibria modelling constrain peak metamorphic conditions to ~900 °C at 6.0–6.5 kbar. Collectively, the *P–T–t* conditions reflect that high-*T*, low-*P* metamorphism was contemporaneous with similarly thermally extreme metamorphism in the west and central Musgrave Inlier, and therefore that regionally high geothermal gradients (140–150 °C/kbar) prevailed across the entire terrane. However, despite an apparently long-lived history of monazite growth, the results of this study also find evidence for arguably shorter-lived, high-*T* to ultrahigh temperature metamorphism. Conceivably, the preservation of high-*T* major element compositions and relict Y + REE growth profiles in small (<500 μm) garnet grains suggest that the rocks cooled relatively rapidly to sub-diffusive temperatures. At least initially the peak to retrograde *P–T* path was also isobaric, or experienced a slight increase in pressure. Grenvillian-aged metamorphism in the eastern Musgrave Inlier accordingly appears to also record the effects of a transient thermal anomaly. This likely developed in response to magmatic-loading and the advection of heat from syn-metamorphic magmatic rocks of the Pitjantjatjara Supersuite, which were emplaced at mid–lower crustal depths, within a longer-lived system characterised by deep-seated, mantle-driven regional metamorphism.

1. INTRODUCTION

The Musgrave Inlier forms part of the Musgrave–Albany–Fraser Orogen (MAFO) which preserves evidence for Grenvillian-aged (ca. 1300–1100 Ma) tectonism in Australia (Fig. 1; Aitken and Betts, 2008, 2009a; Clark et al., 2000; Wade et al., 2008; Walsh et al., in press). The belt transects central and southern Australia, separating the older Archean–Paleoproterozoic North and West Australian cratons, from the South Australian craton (NAC, WAC and SAC, respectively), and continues into the formerly contiguous Wilkes Land of Antarctica (Aitken and Betts, 2008; Clark et al., 2000; Fitzsimons, 2000; Morrissey et al., 2011; Myers et al., 1996; Wade et al., 2008).

The MAFO is widely interpreted to have formed during the amalgamation of Proterozoic Australia, although the specific mechanism and timing is debated (Betts and Giles, 2006; Betts et al., 2002; Cawood and Korsch, 2008; Clark et al., 2000; Giles et al., 2004; Howard et al., 2015; Kirkland et al., 2011; Myers et al., 1996; Smithies et al., 2011; Smits et al., 2014). Some current models suggest that the NAC, WAC and SAC were largely amalgamated during the early Mesoproterozoic (ca. 1600 Ma), with subsequent rotation and relocation of the SAC along the cratonic margin by 1300 Ma, driving Grenville orogenesis (e.g. Betts and Giles, 2006; Cawood and Korsch, 2008; Giles et al., 2004; Wade et al., 2006). Other studies propose final subduction and craton amalgamation during the Grenvillian (e.g. Myers et al., 1996; Smits et al., 2014) as supported by extensive Grenvillian-aged reworking (ca. 1100 Ma) recorded along the southern margin of the NAC (Morrissey et al., 2011). An alternative view was proposed by Smithies et al. (2011) and Howard et al. (2015) who suggested that following amalgamation of the enclosing older cratons during the Mount West Orogeny (ca. 1290 Ma), much of the Musgrave Orogeny formed during intracratonic, and possibly extensional, processes. Ambiguity surrounding the geodynamic significance of the MAFO arises in part from the thick Neoproterozoic–recent sedimentary basin cover sequences which largely obscure the contact relationship between the orogenic system and enclosing cratons, as well as much of the internal character of the belt (Aitken and Betts, 2008, 2009a,b; Selway et al., 2011; Wade et al., 2008).

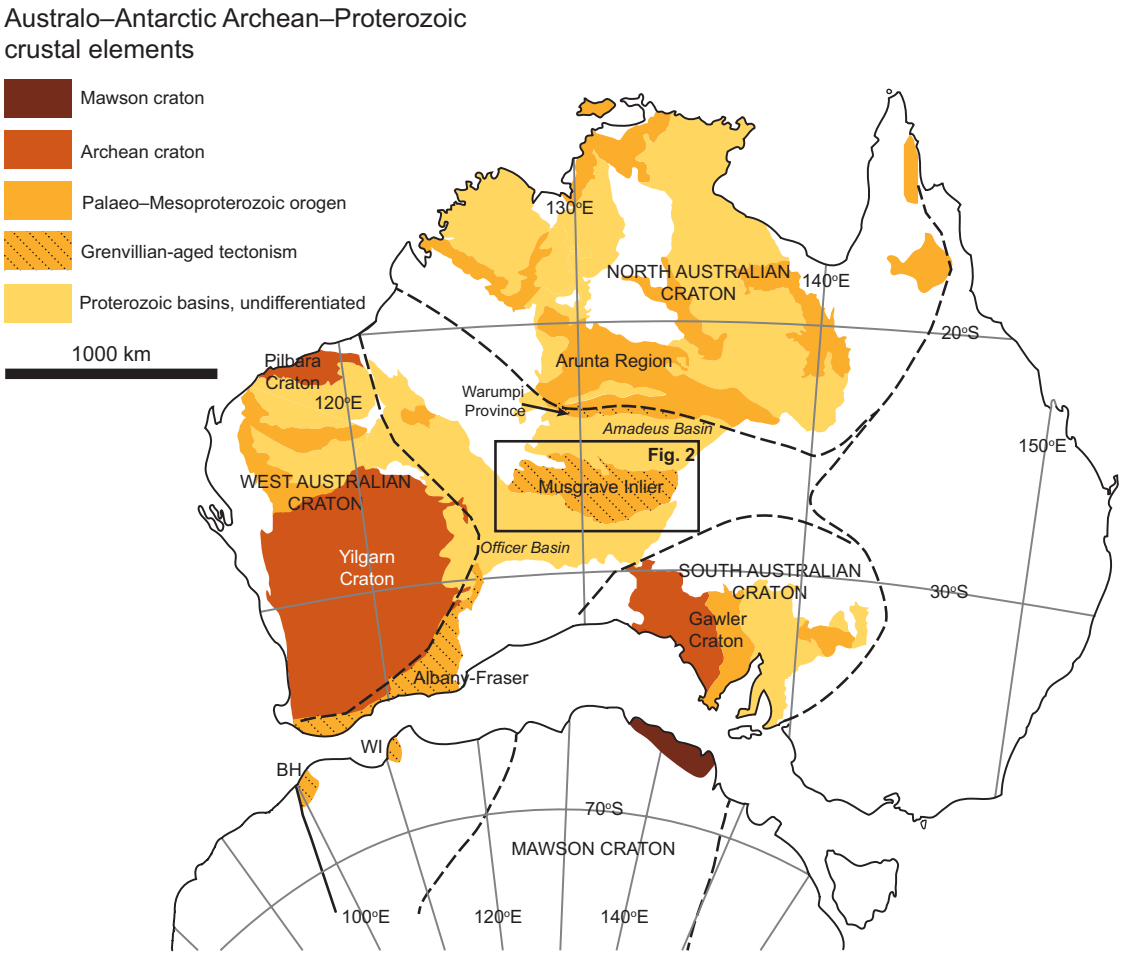

Figure 1. Archean–Proterozoic Australo–Antarctic crustal elements. The location of Australia and Antarctica reflect their relative positions in easternmost Gondwanan reconstructions to highlight their former connectivity. The extent of the North, South and West Australian cratons, and Grenvillian-aged tectonism is shown. The Musgrave Inlier (Fig. 2) is defined by the boxed region. Abbreviations: BH, Bunger Hills; WI, Windmill Islands. Image modified from Kirkland et al. (2011) and Walsh et al. (2015).

In the Musgrave Inlier, Grenvillian-aged tectonism is characterised by regional-scale deformation, continual and voluminous high-*T* magmatism, and high-grade metamorphism dominating the interval ca. 1220–1140 Ma (Camacho and Fanning, 1995; Clarke et al., 1995; Clarke and Powell, 1991; Glikson et al., 1996; Kelly et al., 2006; Maboko et al., 1991; Smithies et al., 2011; Walsh et al., 2014). However, in detail, the high-*T* magmatic record is seemingly punctuated by pulses of felsic magmatism (Howard et al., 2015; Smithies et al., 2015). Recent studies further propose that regional, ultrahigh temperature (UHT; Harley, 1998; Kelsey, 2008; Kelsey and Hand, in press) metamorphism (>900 °C, ~7–8 kbar) characterised by elevated apparent thermal gradients (>125 °C/kbar), prevailed over long periods (>85 Myr) in the western and central parts of the Inlier, suggesting unprecedented timescales for thermally extreme conditions (Smithies et al., 2011; Walsh et al., 2014). Gorczyk et al. (2015) suggested that this high-*T* history may have been located in a back-arc setting associated with ongoing development of the overall convergent system. However, as the vast majority of this preceding work has been undertaken in the west of the Inlier, the metamorphic evolution, and thereby the prevailing tectonic regime, in the central and eastern parts of the Musgrave Inlier remains less understood.

In this contribution, we present the results of *in situ* monazite U–Pb geochronology integrated with mineral chemistry and calculated metamorphic phase diagrams from the eastern Musgrave Inlier, and by extension, the easternmost exposure of the continental-scale MAFO. The findings of this study reflect an apparent duality of timescales recorded within a single orogen. UHT metamorphism in the eastern Musgrave Inlier likely occurred in response to shorter-lived, advective processes at the local scale, within a longer-lived high-*T* system characterised by mantle-driven regional metamorphism during the Grenvillian.

2. GEOLOGICAL SETTING

2.1 Regional setting

The Musgrave Inlier in central Australia is an areally extensive terrane, comprising 200,000 km^2 of exposed Mesoproterozoic–Palaeozoic crystalline basement rocks (Fig. 1; Aitken and Betts, 2009a; Camacho and McDougal, 2000; Kirkland et al., 2013; Smithies et al., 2011; Wade et al., 2008). It is geographically central to the surrounding Archean to Paleoproterozoic NAC, WAC and SAC, and is presently overlain by and structurally juxtaposed against the Neoproterozoic to Paleozoic Amadeus, Officer and Eromanga basins to the north, south-west, and east, respectively (Kirkland et al., 2013; Smithies et al., 2011; Wade et al., 2008). Although Neoproterozoic to Cenozoic cover largely obscures the margins of the Musgrave Inlier, the terrane is expansive, likely continuing beneath the Amadeus and Officer basins (Aitken and Betts, 2008, 2009a,b; Selway et al., 2011).

The Musgrave Inlier is divided into the dominantly amphibolite facies Mulga Park Subdomain and the granulite facies Fregon Subdomain, which are separated by the south-dipping Woodroffe Thrust (Fig. 2; Aitken and Betts, 2009a; Camacho et al., 1997; Camacho and McDougal, 2000; Collerson et al., 1972; Maboko et al., 1991; Wade et al., 2008). The Musgravian Gneiss, termed the Birksgate Complex in the Fregon Subdomain, and the Olia Gneiss in the Mulga Park Subdomain, is the oldest recognised lithology in the eastern Musgrave Inlier (Camacho and Fanning, 1995; Dutch et al., 2013; Edgoose et al., 2004; Wade et al., 2008). The Musgravian Gneiss comprises predominantly felsic orthogneiss, subordinate interlayered mafic units, and rare metapelite, quartzite and calc-silicate, and is interpreted as a volcano-sedimentary sequence (Dutch et al., 2013; Edgoose et al., 2004; Glikson et al., 1996; Wade et al., 2008). The protoliths to these rocks were emplaced or deposited in the interval 1600–1540 Ma (Camacho and Fanning, 1995; Dutch et al., 2013; Edgoose et al., 2004; Gray, 1978). This is interpreted to have occurred within a magmatic arc located outward of the SAC (Aitken and Betts, 2009a; Betts and Giles, 2006; Edgoose et al., 2004; Wade et al., 2006, 2008). In the western parts of the Musgrave Inlier, outcrop consists almost

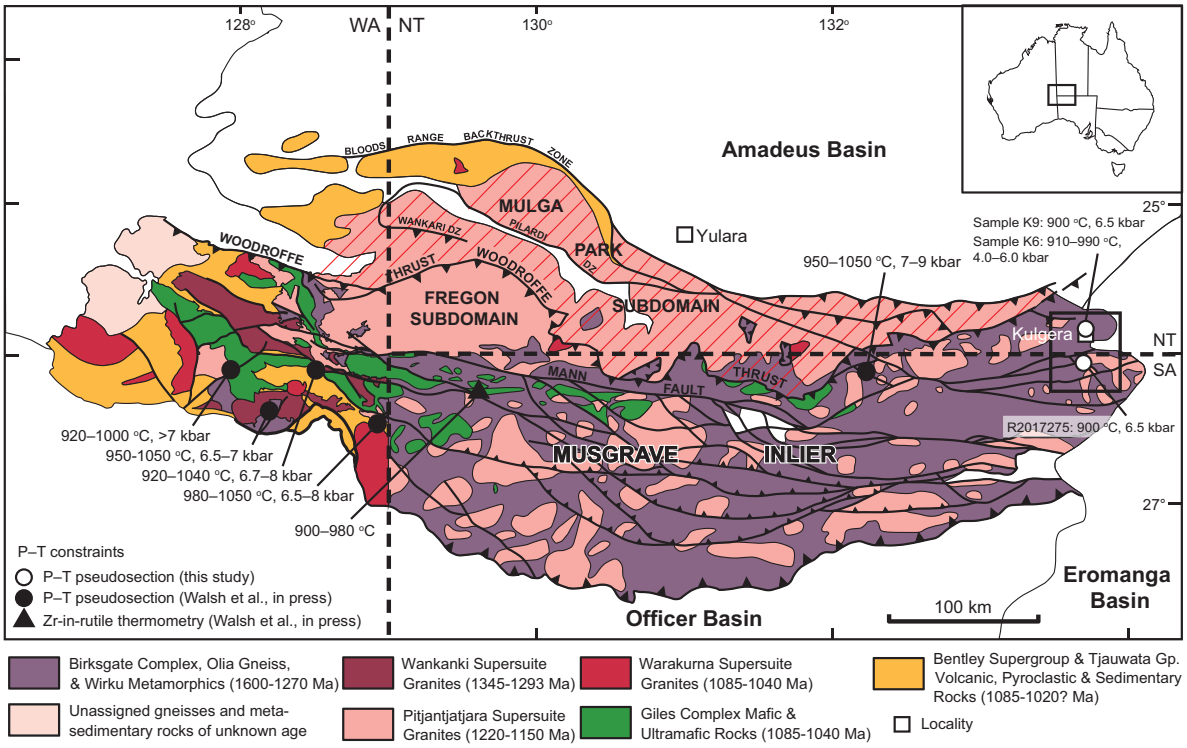

Figure 2. Simplified regional geological map of the Musgrave Inlier. Major Petermann Orogeny-aged shear zones interpreted from aeromagnetic data are shown. The Musgrave Inlier is divided into the amphibolite facies Mulga Park Subdomain and the granulite facies Fregon Subdomain, which are separated by the south-dipping Woodroffe Thrust. The approximate location of the study area in the easternmost Musgrave Inlier is represented by the boxed region (Fig. 3). Pressure–temperature (*P–T*) constraints on Grenvillian granulite facies metamorphism from previous work in the west and central Musgrave Inlier (Walsh et al., 2015), and *P–T* estimates from this study, in the east Musgrave Inlier, are also shown. Figure modified from Dutch et al. (2013). Abbreviations: SA, South Australia; WA, Western Australia; NT, Northern Territory.

entirely of the Fregon Subdomain, however the nature of the basement rocks is more enigmatic, and accordingly the subdivision and classification of lithologies is considerably more detailed (e.g. Howard et al., 2015; Kirkland et al., 2013).

The western Fregon Subdomain was thermally reworked at ca. 1400 Ma and 1345–1293 Ma during the emplacement of the felsic calc-alkaline intrusive Papulankutja Supersuite and by the Mount West Orogeny, respectively (Aitken and Betts, 2009a; Howard et al., 2015; Kirkland et al., 2013; Smithies et al., 2011; Wade et al., 2008). The Mount West Orogeny was characterised by high-grade metamorphism and calc-alkaline magmatism (Wankanki Supersuite), associated with development of a layer-parallel migmatitic fabric and F_1 folding (Aitken and Betts, 2009a; Clarke et al., 1995; Howard et al., 2015; Smithies et al., 2011; White et al., 1999). The broader tectonic significance of this event is not well established. However, deformation was concurrent with the first stage of the Albany–Fraser Orogeny (ca. 1345–1260 Ma) to the south-west of the Musgrave Inlier which suggests a shared tectonic history at this time (Clark et al., 2000). The Mount West Orogeny has been proposed to reflect the final subduction and craton amalgamation of Proterozoic Australia (Aitken and Betts, 2009b; Betts and Giles, 2006; Giles et al., 2004; Kirkland et al., 2013; Smithies et al., 2011). Specifically, it is suggested to have involved the rotation of the SAC from adjacent to the NAC and subsequent collision with the WAC (Giles et al., 2004), possible large-scale northwest-directed thrusting of the SAC over the WAC (Bodorkos and Clark, 2004; Clark et al., 2000; Duebendorfer, 2002), and the intracratonic remelting of a calc-alkaline basement (Smithies et al., 2011).

The Musgrave Orogeny is the most pervasive tectonothermal event to have affected the Musgrave Inlier. Amphibolite–granulite facies metamorphism and intrusion of voluminous A-type felsic magmatic rocks of the Pitjantjatjara Supersuite was widespread and occurred over the interval ca. 1220–1140 Ma (Howard et al., 2015; Smithies et al., 2011; Walsh et al., 2014). Early studies utilising conventional thermobarometry estimate that peak metamorphic conditions ranged from ~650–800 ºC at 5–6 kbar in the east Musgrave Inlier (Camacho and Fanning, 1995) and ~750–850 °C at 5–6 kbar in the west Musgrave Inlier (Glikson et al., 1996), to ~700–800 °C at 9–11 kbar in the Musgrave Ranges (Camacho et al., 1997; Maboko et al., 1991). However, these latter estimates were later found to be the result of thermal resetting during the post-Grenvillian Peterman Orogeny (Gregory et al., 2009; Maboko et al., 1992; Raimondo et al., 2009, 2010; Scrimgeour and Close, 1999; Walsh et al., 2013). Recent work has also identified evidence for UHT metamorphism occurring under conditions >950 ºC at ~7–8 kbar (Smithies et al., 2011; Walsh et al., 2014). Metamorphism was associated with a dominant overprinting gneissic and migmatitic layering and tight to isoclinal F2 folding of variable intensity and orientation (Aitken and Betts, 2008, 2009b; Clarke et al., 1995; Edgoose et al., 2004; Stewart, 1995; Wade et al., 2008). The timing of the Musgrave Orogeny is broadly correlative to the second stage of the Albany–Fraser Orogeny (Clark et al., 2000), and has been proposed to reflect intraplate reworking and anatexis at ca. 1200 Ma (Smithies et al., 2011; Wade et al., 2008). Observed magnetic anomalies trending northeast beneath the Amadeus and Officer basins strengthens support for a connection between the Pitjantjatjara Supersuite granites of the Musgrave Inlier with the contemporaneous Teapot granites of the Warumpi Province to the north, and similarly the Grenville-aged Nornalup Complex granitoid suites of the Albany–Fraser Orogen to the southwest at this time (Aitken and Betts, 2008).

Mafic magmatism in the Musgrave Inlier is restricted to two major events. The ca. 1085–1050 Ma Giles Event involved emplacement of voluminous layered mafic–ultramafic intrusions and the comagmatic Alcurra Dolerite, bimodal volcanism of the Bentley Supergroup, felsic magmatism (Warakurna Supersuite) and rift-related sedimentation (Aitken et al., 2013; Clarke et al., 1995; Edgoose et al., 2004; Evins et al., 2010; Glikson et al., 1996; Howard et al., 2015; Smithies et al., 2015; Sun et al., 1996; Zhao and McCulloch, 1993; Zhao et al., 1994). This event was concurrent with widespread magmatism of the Warakurna Large Igneous Province across western and central Australia and consequently, has been largely interpreted as the result of mantle plume activity, although other mechanisms have not been dismissed (Aitken and Betts, 2009a; Aitken et al., 2013; Evins et al., 2010; Howard et al., 2015; Smithies et al., 2015; Wade et al., 2008; Wingate et al., 2004). The Gairdner and Amata dolerite dykes (c. 800 Ma) dissect much of the

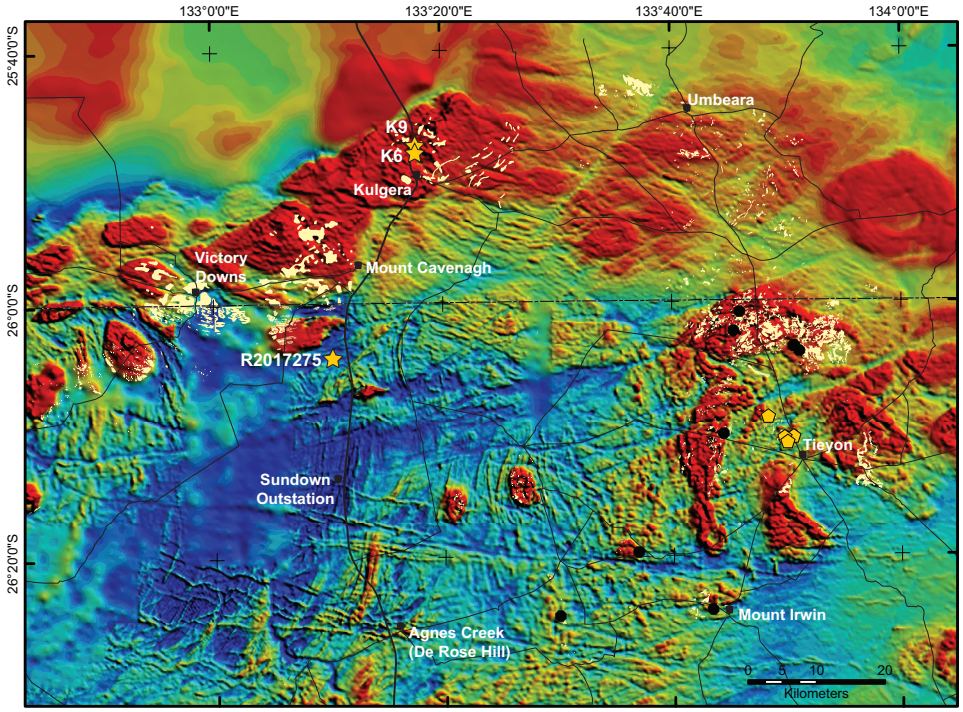

Figure 3. Pseudocolour TMI image of the study area in the eastern Musgrave Inlier. The extensive subsurface distribution of the Pitjantjatjara Supersuite is highlighted by their strong positive magnetic intensity (warmer colours) in the TMI image. Overlain on the TMI image is the outcropping extent (pale yellow polygons) of the Pitjanjatjara Supersuite granite (Dutch et al., 2013; Edgoose et al., 1992, 2002). Locations of Pitjanjatjara Supersuite geochronology (black circles) and the metamorphic ages obtained from orthogneisses of the Birksgate Complex (yellow pentagons) within the Tieyon region, are also shown. The location of samples used in this study—north of Kulgera in the Northern Territory (sample K9 and K6) and south of Kulgera in South Australia (sample R2017275), are indicated (yellow stars).

Musgrave Inlier (Glikson et al., 1996; Wingate et al., 1998; Zhao and McCulloch, 1993; Zhao et al., 1994). Their emplacement was synchronous with inception of the Amadeus and Officer basins (Walter et al., 1995; Zhao et al., 1994), and the proto-Pacific Ocean due to rifting of Australia and Laurentia during the breakup of Rodinia (Aitken and Betts, 2009a; Preiss, 2000; Wade et al., 2008).

Significant reactivation of the Musgrave Inlier occurred during the Petermann Orogeny (ca. 630–530 Ma). The Petermann Orogeny was characterised by an east-trending network of crustal-scale, dextral transpressional shear zones with large vertical offsets (Camacho and McDougal, 2000; Edgoose et al., 2004; Raimondo et al., 2009, 2010; Raimondo et al., 2014; Walsh et al., 2013), and the development of high-pressure granulite facies mylonite, ultramylonite and pseudotachylite zones (Camacho et al., 1995, 1997; Maboko et al., 1992; Scrimgeour and Close, 1999). The Musgrave Inlier was exhumed from mid-crustal levels beneath the broad Neoprotoerozoic Centralian Superbasin and reoriented into the present-day E–W trending structural architecture (Aitken and Betts, 2008, 2009a; Camacho and McDougal, 2000; Flottmann et al., 2004; Hand and Sandiford, 1999; Raimondo et al., 2010; Scrimgeour and Close, 1999; Wade et al., 2008). Sub-eclogite facies metamorphism predominated with peak metamorphic conditions estimated at ~650–750 ºC at 12–14 kbar however, in places, retrograde greenschist–amphibolite facies shear zones overprint the sub-eclogite and mylonite zones (Camacho et al., 1997; Clarke et al., 1995; Maboko et al., 1992; Scrimgeour and Close, 1999; White and Clarke, 1997). The Petermann Orogeny is interpreted to reflect crustal-scale intraplate reworking of the Musgrave Inlier in response to the assembly of Gondwana (Aitken and Betts, 2009a; Camacho and McDougal, 2000; Lambeck and Burgess, 1992; Raimondo et al., 2009, 2010; Sandiford and Hand, 1998b).

2.2 Study area

This study focusses on a region near Kulgera, approximately 230 km south–southwest of Alice Springs, in the easternmost Musgrave Inlier (Figs. 2 and 3). The oldest basement rocks exposed in the

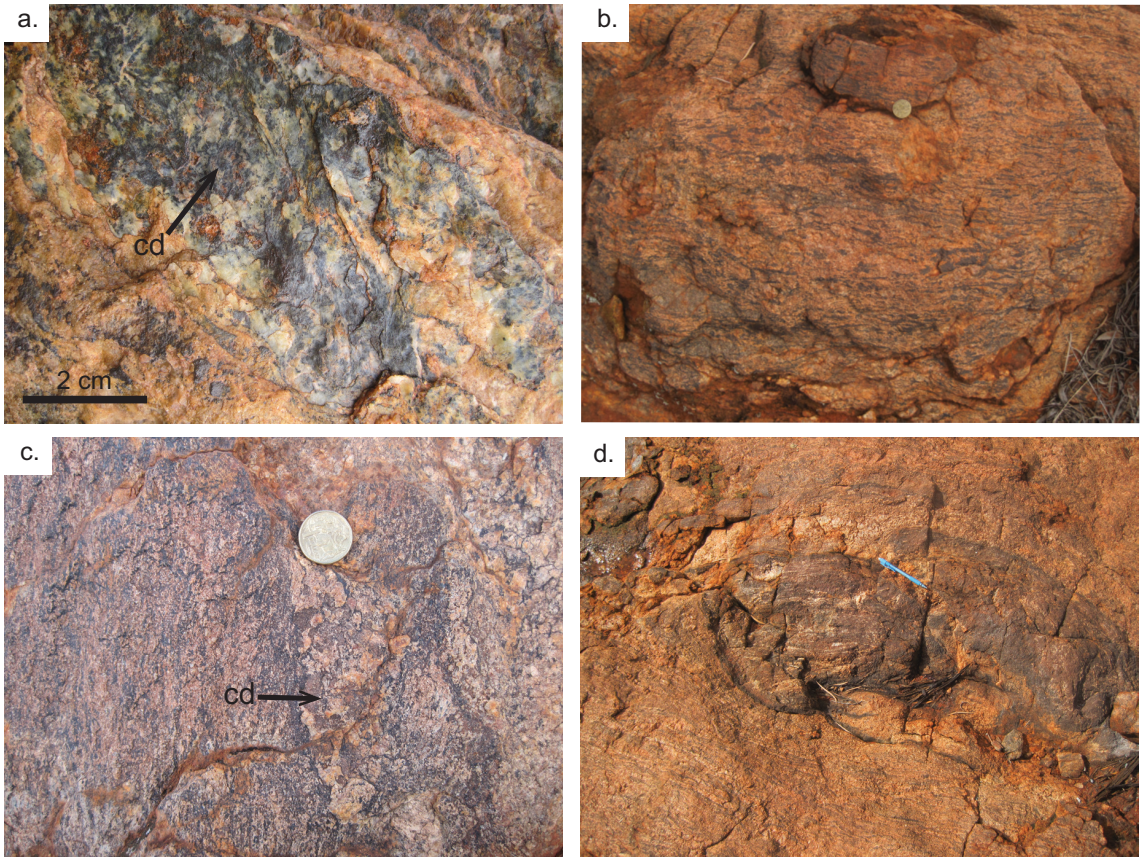

Figure 4. Field photographs of the Kalamurta Gneiss from the study area. The coin shown for scale is approximately 2 cm in diameter. (a) Freshly exposed surface of garnet–cordierite–sillimanite–magnetite ± spinel gneiss near the locality of sample K9 showing the glassy blue appearance of the cordierite; (b) The coarse fabric is defined by alternating domains of predominantly cordierite, weathering brown, and sillimanite, with more quartzofeldspathic layers; (c) Coarse-grained, cordierite-bearing leucosomes (cordierite up to 1.5 cm, indicated by the arrow), and melt lenses, with sub-diffuse boundaries, oriented parallel to the fabric near the location of sample R2017275; (d) An isolate, fine-grained mafic boudin hosted within the Kalamurta Gneiss. Internal layering of the mafic rock is parallel to the external gneissic fabric.

Kulgera region belong to the Birksgate Complex of the Fregon Subdomain (Dutch et al., 2013). They comprise the peraluminous metapelite of the Kalamurta Gneissic Unit intercalated with more quartzofeldspathic, and granitic gneisses (Camacho and Fanning, 1995; Dutch et al., 2013; Edgoose et al., 1993). The terrane is dominated by felsic granitoids and microgranitic dykes of the Pitjantjatjara Supersuite (Fig. 3) and is dissected by Alcurra dolerite of the Giles Complex (Dutch et al., 2013). Approximately 150 km west of the study area, amphibolite facies andalusite-bearing rocks of the Mulga Park Subdomain are separated from the high-grade gneisses of the Fregon Subdomain by the moderately south-dipping (~30º) Woodroffe Thrust which juxtaposed the metamorphically contrasting terranes during the Petermann Orogeny.

The Kalamurta Gneiss crops out immediately north and east of the Kulgera township and less extensively to the south, covering an approximate areal extent of 70 km^2. However, much of this region is obscured by recent sedimentary cover and thus the true extent of the Kalamurta Gneiss is unknown. The lithologies are dominated by strongly foliated cordierite–sillimanite–magnetite ± spinel ± garnet-bearing gneiss (Fig. 4a and b). The occurrence of garnet is localised, and when present, constitutes a volumetrically minor phase (<8 % of the mineral assemblage). The fabric is cross-cut by abundant coarse-grained cordierite-rich leucosomes and weakly foliated to unfoliated microgranite segregations (centimetre-scale) which occur both parallel and discordant to the fabric (Fig. 4c). The pervasive foliation is defined by alternating domains of elongate sillimanite paralleled by cordierite, and locally coarse spinel (up to 8 mm diameter), with comparatively more quartzofeldspathic layers. Lenticular mafic bodies (metre-scale) occur irregularly throughout the Kalamurta Gneiss. Layering within the mafic rocks is parallel to the fabric of the enclosing peraluminous gneiss, and the interface between the

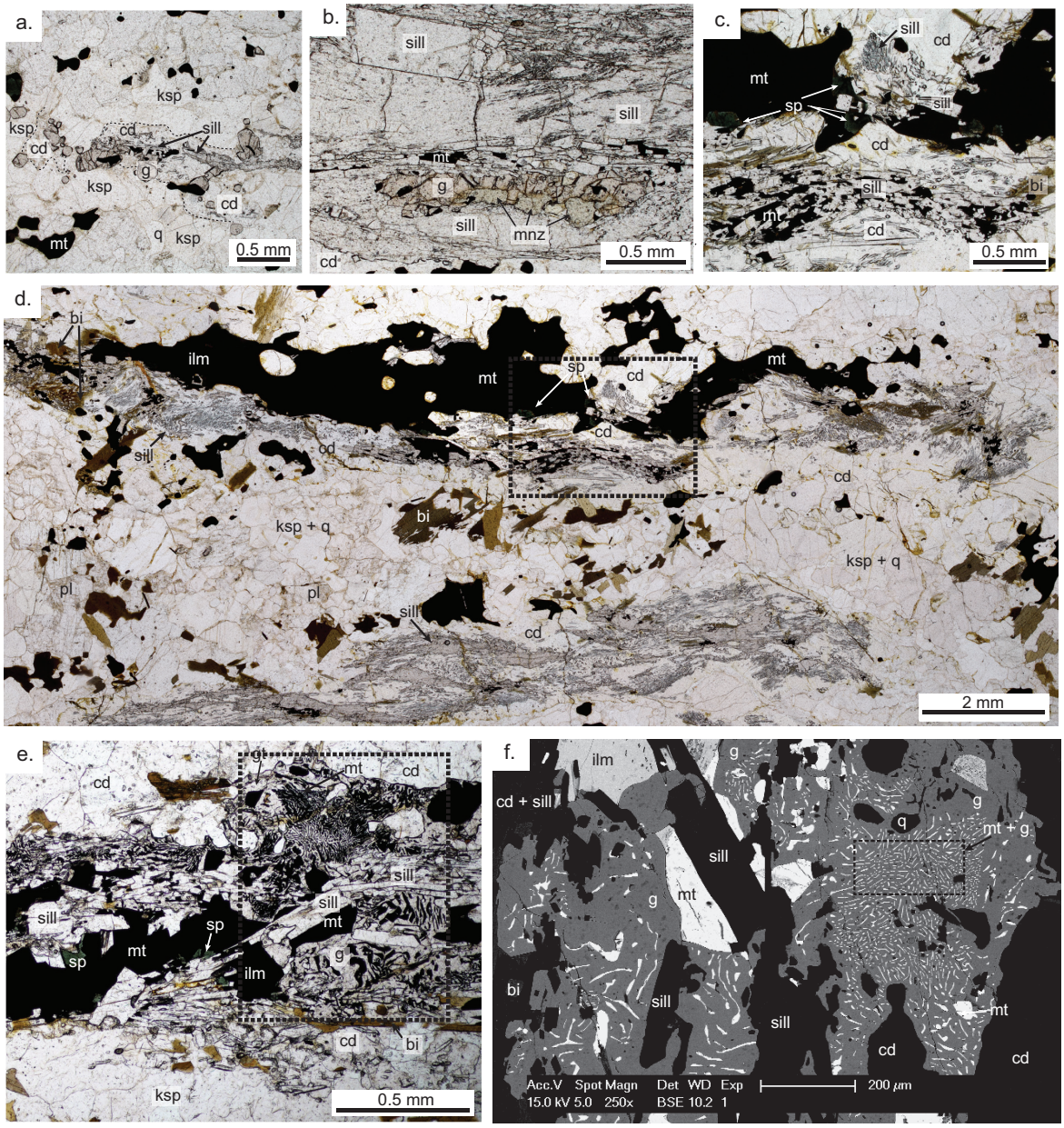

Figure 5. Representative thin section photomicrographs of the Kalamurta Gneiss. Sample K9: (a) Small, rounded–equant garnet grains are often wholly included within K-feldspar and cordierite. These grains are interpreted as reflecting a relict prograde garnet generation. The dashed line outlines the cordierite grain edges; (b) Elongate garnet grains align with sillimanite, hosted in cordierite. Coarse monazite grains are often partially included within garnet; Sample K6: (c) Equant spinel grains (generally <200 μm) always occur in direct contact with magnetite, often at the magnetite grain boundary; (d) The gneissic fabric is defined by alternating domains of cordierite, sillimanite and elongate magnetite (up to 8 mm in some samples), and more quartzofeldspathic layers. The box outlined by the dashed black bold line is magnified in (c) to highlight the textural relationship between spinel and magnetite; Sample R2017275: (e) Within the predominantly cordierite–sillimanite-rich domains, garnet (in sample R2017275 and K9) forms elongate, anhedral grains which often form symplectitic intergrowths with magnetite. The boxed region is magnified in (f) to further highlight this relationship; (f) A back-scatter electron image of fine-grained magnetite–garnet symplectitic intergrowths in sample R2017275. Mineral abbreviations from Holland and Powell (1998).

two lithologies varies with both diffuse and discrete boundaries (Fig. 4d). The fabric, denoted S_1, is largely flat-lying, dipping gently (approximately 20º) to the SSW in the northern localities in the vicinity of Kulgera, and WNW in the south, and is associated with a shallowly south-plunging, SE–SW-trending lineation defined largely by sillimanite and elongate K-feldspar grains. North of Kulgera, isolated S–C style kinematic indicators defined by sillimanite and coarse asymmetric K-feldspar augen wrapped by the fabric, imply a top-to-north relative transport. Elsewhere in the area, the flat-lying fabric is associated with open SSW-trending F_2 folds, and is overprinted by a subvertical S_2 fabric and L_2 intersection lineation.

3. SAMPLE DESCRIPTION AND METAMORPHIC PETROLOGY

Three samples were taken from within the Kalamurta Gneiss for detailed metamorphic analysis and geochronology. Two samples (K9 and K6) are located north and north-east of Kulgera in the Northern Territory, and one sample (R2017275) is located south of Kulgera in South Australia (Fig. 3). Sample location grid references are provided below and refer to datum WGS84 (Zone 53J) and UTM coordinates.

3.1 Sample K9 (53 J 328939 mE 7146568 mN)

This sample contains cordierite, sillimanite, spinel, magnetite, ilmenite, K-feldspar, quartz, minor garnet (<10 %) and plagioclase. Rarely, garnet occurs as equant grains (<500 μm) completely included within coarse-grained K-feldspar (up to 6 mm). These grains are inferred as a relict prograde generation (e.g. Fig. 5a). Garnet is considerably more abundant as coarser, anhedral, elongate poikioblasts (<3 mm) with partial to complete inclusions of magnetite ± spinel, quartz, feldspar, and sillimanite, interpreted to have been stable during peak garnet growth (Fig. 5b). Magnetite also commonly forms extensive fine-grained intergrowths with garnet. The density of magnetite in garnet decreases outward from interior to exterior and the size of the magnetite grains increases. The garnet–magnetite intergrowth is interpreted as a syplectite. Dark-green, equant spinel (<500 μm) only occurs in direct contact with magnetite along magnetite grain boundaries. This textural relationship is suggestive of the prior existence of a magnetite-rich, magnetite–spinel solid solution (referred to herein as magnetite$_{ss}$). Discrete grains of magnetite and ilmenite are commonly in direct contact, with magnetite commonly also hosting both coarse and fine ulvospinel exsolution lamellae. Cordierite is ubiquitous, typically constituting a significant proportion of the rock. Cordierite-rich domains host dense aggregates of aligned, coarse-grained, prismatic (some crystals >5 mm) and acicular sillimanite, elongate ilmenite, magnetite$_{ss}$, and garnet. Sillimanite included partially within garnet also aligns with sillimanite hosted externally in cordierite. The fabric is defined by sub-parallel alternation of the predominantly sillimanite–cordierite layers with more quartzofeldspathic domains. Plagioclase is minor, occurring predominantly as isolated grains (up to 500 μm in size), or late myrmekitic intergrowths with quartz at K-feldspar grain edges. The peak metamorphic mineral assemblage for this sample is interpreted as garnet–cordierite–sillimanite–plagioclase–K-feldspar–quartz–magnetite$_{ss}$–ilmenite–melt, with retrograde garnet growth and the exsolution of spinel from magnetite$_{ss}$.

3.2 Sample K6 (53 J 328867 mE 7145636 mN)

This sample contains cordierite, sillimanite, spinel, magnetite, ilmenite, K-feldspar, quartz, biotite and rare plagioclase. Equant spinel (<200 μm) occurs in direct contact with magnetite, generally along the magnetite grain boundaries (e.g. Fig. 5c and d). Magnetite and ilmenite occur as inclusions within all other matrix minerals, and when in contact with cordierite and sillimanite, are typically elongate (grains up to 8 mm) and aligned with the fabric. Dense aggregates of fine-grained sillimanite are included within elongate cordierite grains (Fig. 5c). Sillimanite also rarely occurs as isolated grains within K-feldspar. Biotite (up to 600 μm in length) is sparsely distributed, commonly within the cordierite–sillimanite domains, and typically in direct contact with opaque minerals, and occurs rarely as inclusions within K-feldspar. Matrix grains are typically oriented oblique to the fabric. A local-scale gneissic fabric is defined by domains of cordierite–sillimanite alternating with more quartzofeldspathic bands (Fig. 5d). The quartzofeldspathic-rich domains are comprised predominantly of anhedral quartz, coarse microcline (up to 6 mm) and minor perthite. The occurrence of plagioclase is largely restricted to minor myrmekitic intergrowths with quartz, and rarely small, subhedral inclusions within K-feldspar. The peak metamorphic mineral assemblage is interpreted as cordierite–sillimanite–magnetite$_{ss}$–ilmenite–K-feldspar–quartz–melt, with the potential localised preservation of prograde biotite. Post-peak mineral development is limited to the exsolution of spinel from magnetitess, potentially retrograde biotite, and the isolated occurrence of plagioclase.

3.3 Sample R2017275 (53 J 317471 mE 7115817 mN)

This sample contains cordierite, sillimanite, K-feldspar, plagioclase, quartz, ilmenite, magnetite, spinel, and minor garnet and biotite. Compared to samples K6 and K9, this sample is considerably more quartzofeldspathic. Garnet is a

volumetrically minor phase (<5 % of the mineral assemblage), and occur as small, equant inclusions (generally <100 μm) hosted in feldspar, and as irregularly-shaped and elongate grains (up to 1 mm in length) within cordierite–sillimanite-rich domains. The latter exhibit extensive retrograde magnetite–garnet symplectitic intergrowths (e.g. Fig. 5e and f). Garnet also rarely forms fine-grained coronae about magnetite and sillimanite. Small spinel grains (<100 μm) are located along the grain edge of magnetite that is commonly aligned with the foliation. Fine to moderately-coarse ulvospinel exsolution lamellae (~5–15 μm) occur within both discrete magnetite grains and symplectitic magnetite. Cordierite is elongate (grains up to 5 mm), and contains abundant inclusions of elongate acicular and prismatic sillimanite, which define the foliation. Minor sillimanite included in large feldspar grains is generally confined to the rim region and is generally not aligned with the external foliation. Coarse, subhedral biotite occurs in direct contact with predominantly magnetite$_{ss}$ and sillimanite. Cordierite–sillimanite domains are aligned subparallel with quartzofeldspathic layers composed of moderately abundant and coarse plagioclase (typically 1–3 mm, locally up to 5 mm), microcline (4–5 mm), quartz, and minor perthite. The peak metamorphic mineral assemblage is interpreted as garnet–sillimanite–cordierite–magnetite$_{ss}$–ilmenite–quartz–plagioclase–K-feldspar–melt, with the post-peak development of biotite and garnet, and the exsolution of spinel from magnetite$_{ss}$.

4. ANALYTICAL METHODS

4.1 Bulk rock and mineral chemistry

4.1.1 Whole-rock geochemistry

Whole-rock geochemical analyses for phase equilibria forward modelling for samples K9 and K6 was undertaken by wavelength dispersive X-ray fluorescence (WD–XRF) spectrometry at the Earth and Environmental Department, Franklin and Marshall College, Lancaster PA, USA. Major elements were analysed on fused disks prepared using a lithium tetraborate flux. Iron content was determined by wet chemistry methods. Whole-rock geochemistry for sample R2017275 was done by ICP–AES and ICP–MS for major and trace elements, respectively, by Australian Laboratory Services, Perth.

4.1.2 Major element chemistry

Mineral compositions and elemental X-ray maps of garnet were obtained using a Cameca SXFive electron microrobe at Adelaide Microscopy, University of Adelaide. A beam current of 20 nA, accelerating voltage of 15 kV and a defocussed beam size of 2 μm were used for all point analyses. Qualitative compositional mapping of garnet for major elements Al, Fe, Mg, Mn, Ca, and Y, was undertaken using a 15 kV accelerating voltage and a beam current of 200 nA on WDS.

4.1.3 LA–ICP–MS garnet trace element chemistry

LA–ICP–MS quantitative trace element analyses of garnet grains in sample K9 were obtained at Adelaide Microscopy, University of Adelaide, using a Resonetics M-50-LR 193 nm excimer laser coupled to an Agilent 7700 cx Quadropole ICP–MS. Garnet grains from all microstructural locations (i.e. inferred prograde, peak and retrograde crystals) were analysed.

Point analyses of elements ^{89}Y, ^{139}La, ^{140}Ce, ^{141}Pr, ^{146}Nd, ^{147}Sm, ^{153}Eu, ^{157}Gd, ^{159}Tb, ^{163}Dy, ^{165}Ho, ^{166}Er, ^{169}Tm, ^{172}Yb and ^{175}Lu, were measured along linear traverses of garnet grains with the following settings: 33 μm spot size, 10 Hz frequency, 7.6 J cm^{-2} fluence, and a total acquisition time of 60 s, inclusive of 30 s of background measurement. Analyses were performed under a He-ablation atmosphere mixed with Ar immediately after the ablation cell. NIST612 was utilised as the external standard and electron microprobe measurements of Al served as an internal standard. NIST610 and in-house garnet standard MON-GT were monitored during all analytical sessions and treated as unknown analyses during data reduction. Instrument drift was corrected for by standard bracketing of unknown analyses and the application of a linear correction using 'Glitter' software (Griffin et al., 2008).

Trace element images of garnet grains were obtained by ablating a grid of parallel rasters across the sample surface. Line spacing for each sample was set to match the diameter of the beam. A laser repetition rate of 10 Hz, a beam diameter of 13 μm and a scan speed of 13 μm was used. Instrument drift and mass bias were corrected for by the application of a linear fit between sets of the standard NIST612 analysed at the start and end of each mapping run. The average background was also subtracted from each raster. Image processing utilised Iolite software developed by

the Melbourne Isotope Group.

4.2 LA–ICP–MS monazite geochronology

Monazite grains were identified in thin section and imaged using a back-scattered electron (BSE) detector on a Phillips XL30 SEM to determine their microstructural location. Elemental mapping of select monazite grains, chosen on the basis of microstructural representation, was also undertaken using a Cameca SXFive electron microprobe to visualise any internal compositional variation. Element maps were obtained using an accelerating voltage of 20 kV and a frequency of 150 nA using WDS for Y, Th, U, Pb and Ce.

In situ monazite geochronology was undertaken using LA–ICP–MS at Adelaide Microscopy, University of Adelaide, following the method of Payne et al. (2008). Analyses were performed using a New Wave 213 nm Nd–YAG laser coupled with an Agilent 7500cs ICP–MS under a He-ablation atmosphere. Ablation was performed with a frequency of 5 Hz. Due to the smaller size of monazite grains in sample R2017275, a 12 µm spot size was used. A spot size of 16 µm was used for samples K9 and K6. The total acquisition time of 100 s for each analysis consisted of 40 s background measurement, inclusive of 10 s of the laser firing with the shutter closed to allow for beam stabilisation, followed by 60 s of sample ablation. Isotopes measured were ^{204}Pb, ^{206}Pb, ^{207}Pb and ^{238}U for dwell times of 10 ms, 15 ms, 30 ms and 15 ms, respectively. Individual spot analyses were targeted on the basis of BSE imagery and qualitative X-ray compositional mapping in an attempt to avoid overlap of individual compositional domains.

Data were corrected for elemental fractionation and mass bias using 'Glitter' software using the primary monazite standard MAdel (TIMS normalisation data: ^{207}Pb/^{206}Pb = 490.0 Ma, ^{206}Pb/^{238}U = 518.4 Ma and ^{207}Pb/^{235}U = 513.1 Ma; Payne et al., 2008, updated with additional TIMS data). An overestimated uncertainty of 1 % was assigned to each MAdel normalisation age for age error calculations on the sample analyses. Throughout the study, the MAdel analyses used as a primary standard yielded weighted mean ages of ^{207}Pb/^{206}Pb = 490.5 ± 5.9 Ma, ^{206}Pb/^{238}U = 518.2 ± 1.5 Ma and ^{207}Pb/^{235}U = 513.0 ± 1.3 Ma (n = 88). Data accuracy was monitored by repeat analysis of the in-house standard 94-222/Bruna NW (ca. 450 Ma; Payne et al., 2008). The weighted average ^{206}Pb/^{238}U age of 94–222/Bruna NW was 454.0 ± 4.1 Ma (n = 42). Instrument drift was also corrected for by standard bracketing of every 10–15 unknown analyses and the application of a linear correction. Due to unresolvable interference of ^{204}Hg on ^{204}Pb, common lead was not corrected for in age calculations; however, analyses were rejected on the basis of appreciable raw ^{204}Pb counts.

Table 1. Whole-rock geochemical analyses

	K6	K9	R2017275
Major elements (wt% oxide)			
SiO_2	53.56	58.05	66.10
TiO_2	0.92	0.83	0.69
Al_2O_3	25.82	22.14	16.15
Fe_2O_3[b]	5.86	4.49	
FeO[b]	4.38	3.82	
Fe_2O_3[a]	10.73	8.74	6.18
MnO	0.20	0.44	0.22
MgO	3.14	2.58	1.71
CaO	0.24	0.66	1.12
Na_2O	0.75	1.27	1.85
K_2O	4.13	4.84	3.83
P_2O_5	0.03	0.06	0.03
LOI	1.25	1.00	0.36
Fe_2O_3[c]	5.79	3.06	2.29
FeO[c]	4.44	5.11	3.50
Trace elements and REE (ppm)			
Rb	147	161	166
Sr	117	195	174
Y	12	21	42
Zr	203	193	320
V	129	90	72
Ni	58	48	19
Cr	128	97	60
Nb	11	8	13
Ga	37	28	22
Cu	1	1	8
Zn	153	98	84
Co	84	57	13
Ba	821	1489	878
La	37	67	56
Ce	87	187	117
U	1	1	2
Th	12	19	24
Sc	17	13	15
Pb	22	43	25

[a] Total iron (FeO + Fe_2O_3) from whole-rock geochemistry.
[b] Iron content determined by wet chemistry.
[c] $_{Actual}$ iron content used for bulk compositions.

4.3 Phase equilibria modelling

P–T pseudosections for samples K9, K6 and R2017275 were calculated using the phase equilibria modelling programme THERMOCALC v. 3.33 (update November 2009, Powell and Holland, 1988) with the

Table 2. Representative electron microprobe mineral analyses

Sample	K9											K6			
Mode	0.06				0.28	0.02	0.28		0.01	0.02	0.01	0.04	0.30	0.003	0.21
Mineral	gt[b]	gt core[c]	gt rim[c]	gt[d]	cd	sp	ksp core	ksp rim	pl	mt	ilm	bi	cd	sp	ksp core
SiO_2	36.15	36.55	36.48	35.95	49.80	0.01	65.28	66.61	61.36	0.01	0.04	34.50	49.57	0.03	67.42
TiO_2	0.04	0.01	0.02	0.11	0.01	0.13	0.00	0.01	0.01	0.01	47.86	1.93	0.01	0.00	0.02
Al_2O_3	21.21	21.35	21.39	21.11	32.09	58.45	19.02	18.56	24.76	0.17	0.00	18.18	32.38	57.48	18.86
Cr_2O_3	0.04	0.02	0.00	0.00	0.00	0.20	0.00	0.00	0.01	0.15	0.00	0.02	0.00	0.16	0.03
FeO	22.74	23.15	23.08	23.11	5.80	26.17	0.03	0.00	0.05	32.22	40.92	18.46	5.73	25.33	0.00
Fe_2O_3	3.63	2.40	2.76	2.56	0.00	2.39	0.00	0.00	0.00	67.23	7.74	0.00	0.00	3.32	0.00
MnO	9.67	9.40	9.35	10.83	0.58	0.80	0.00	0.01	0.01	0.04	2.49	0.06	0.44	1.24	0.00
MgO	5.27	5.84	5.62	4.66	9.74	7.13	0.00	0.02	0.00	0.04	0.36	11.33	9.99	5.56	0.00
ZnO	0.02	0.02	0.00	0.08	0.00	3.69	0.03	0.00	0.00	0.09	0.07	0.04	0.00	6.34	0.00
CaO	1.04	1.00	0.91	0.90	0.01	0.01	0.19	0.14	6.84	0.00	0.00	0.05	0.01	0.00	0.10
Na_2O	0.01	0.02	0.00	0.02	0.08	0.00	3.63	2.12	7.65	0.02	0.00	0.10	0.08	0.10	2.52
K_2O	0.00	0.00	0.00	0.00	0.00	0.00	10.89	13.40	0.16	0.00	0.00	8.63	0.01	0.00	12.09
Cl	0.00	0.00	0.00	0.00	0.01	0.00	0.00	0.01	0.01	0.00	0.00	0.26	0.01	0.00	0.04
F	0.00	0.17	0.00	0.11	0.00	0.00	0.00	0.00	0.00	0.36	0.17	0.27	0.00	0.07	0.00
Total	99.82	99.93	99.62	99.44	98.11	98.98	99.08	100.88	100.86	100.34	99.66	93.85	98.22	99.62	101.08
Oxygens	12	12	12	12	18	4	8	8	8	4	3	11	18	4	8
Si	2.89	2.91	2.91	2.90	5.09	0.00	2.99	3.01	2.71	0.00	0.00	2.66	5.05	0.00	3.02
Ti	0.00	0.00	0.00	0.01	0.00	0.00	0.00	0.00	0.00	0.00	0.92	0.11	0.00	0.00	0.00
Al	2.00	2.00	2.01	2.01	3.86	1.94	1.03	0.99	1.29	0.01	0.00	1.65	3.89	1.92	1.00
Cr	0.00	0.00	0.00	0.00	0.00	0.00	0.00	0.00	0.00	0.00	0.00	0.00	0.00	0.00	0.00
Fe^{3+}	0.22	0.14	0.16	0.15	0.00	0.05	0.00	0.00	0.00	1.94	0.15	0.00	0.00	0.07	0.00
Fe^{2+}	1.52	1.53	1.53	1.54	0.50	0.61	0.00	0.00	0.00	1.04	0.86	1.19	0.49	0.60	0.00
Mn	0.65	0.63	0.63	0.74	0.05	0.02	0.00	0.00	0.00	0.00	0.05	0.00	0.04	0.03	0.00
Mg	0.63	0.69	0.67	0.56	1.48	0.30	0.00	0.00	0.00	0.00	0.01	1.30	1.52	0.24	0.00
Zn	0.00	0.00	0.00	0.00	0.00	0.08	0.00	0.00	0.00	0.00	0.00	0.00	0.00	0.13	0.00
Ca	0.09	0.09	0.08	0.08	0.00	0.00	0.01	0.01	0.32	0.00	0.00	0.00	0.00	0.00	0.00
Na	0.00	0.00	0.00	0.00	0.02	0.00	0.32	0.19	0.65	0.00	0.00	0.01	0.02	0.01	0.22
K	0.00	0.00	0.00	0.00	0.00	0.00	0.64	0.77	0.01	0.00	0.00	0.85	0.00	0.00	0.69
Cl	0.00	0.00	0.00	0.00	0.00	0.00	0.00	0.00	0.00	0.00	0.00	0.03	0.00	0.00	0.00
F	0.00	0.04	0.00	0.03	0.00	0.00	0.00	0.00	0.00	0.04	0.01	0.07	0.00	0.01	0.00
Total Cations	8.00	8.00	8.00	8.00	11.00	3.00	4.98	4.97	4.98	3.00	2.00	7.79	11.00	3.00	4.93
X_{Mg}	0.29	0.31	0.30	0.27	0.75							0.52	0.77		
X_{Al}										0.004					
X_{Fe}	0.71	0.69	0.70	0.73	0.25							0.48	0.24		
X_{alm}	0.53	0.52	0.53	0.53											
X_{py}	0.22	0.24	0.23	0.19											
X_{grs}	0.03	0.03	0.03	0.03											
X_{sps}	0.23	0.21	0.22	0.25											
X_{An}							0.01	0.01	0.33						0.01

Table 2. (continued)

Sample	K6				R2017275									
Mode		0.01	0.04	0.02		0.02		0.07	0.14	0.002	0.16	0.21	0.016	0.02
Mineral	ksp rim	pl	mt	ilm	gt core[c]	gt rim[c]	gt[d]	bi	cd	sp	ksp core	pl	mt	ilm
SiO_2	66.13	60.09	0.01	0.02	36.91	37.25	36.71	37.45	48.05	0.01	63.55	59.98	0.03	0.03
TiO_2	0.03	0.01	0.00	49.68	0.02	0.03	0.01	2.54	0.00	0.03	0.04	0.02	0.03	49.38
Al_2O_3	18.48	25.35	0.22	0.19	21.01	21.30	20.69	15.86	32.59	57.26	17.94	23.34	0.20	0.02
Cr_2O_3	0.00	0.00	0.14	0.00	0.01	0.01	0.03	0.00	0.02	0.18	0.00	0.01	0.27	0.06
FeO	0.04	0.06	32.52	42.50	23.02	23.42	26.45	11.88	6.18	27.73	0.00	0.01	33.22	41.07
Fe_2O_3	0.00	0.00	67.01	3.35	2.31	1.66	1.96	0.00	0.00	2.44	0.00	0.00	66.13	4.59
MnO	0.00	0.00	0.04	2.84	10.63	10.72	9.50	0.18	0.57	2.32	0.00	0.00	0.00	4.09
MgO	0.00	0.00	0.05	0.42	5.12	5.10	3.78	16.65	9.54	3.67	0.00	0.02	0.04	0.04
ZnO	0.00	0.00	0.00	0.00	0.04	0.06	0.09	0.17	0.00	5.98	0.00	0.00	0.05	0.05
CaO	0.02	7.12	0.01	0.01	0.90	0.90	0.80	0.00	0.00	0.00	0.11	5.81	0.00	0.01
Na_2O	1.20	7.42	0.00	0.01	0.01	0.01	0.00	0.10	0.03	0.04	2.35	8.42	0.01	0.02
K_2O	14.65	0.12	0.00	0.00	0.01	0.00	0.00	10.02	0.01	0.00	13.29	0.13	0.00	0.00
Cl	0.00	0.00	0.00	0.00	0.00	0.00	0.00	0.03	0.01	0.01	0.00	0.00	0.00	0.00
F	0.00	0.00	0.39	0.19	0.00	0.05	0.00	4.11	0.00	0.00	0.00	0.00	0.55	0.13
Total	100.56	100.17	100.39	99.22	99.98	100.51	100.02	98.98	97.00	99.66	97.28	97.73	100.54	99.49
Oxygens	8	8	4	3	12	12	12	11	18	4	8	8	4	3
Si	3.01	2.67	0.00	0.00	2.94	2.95	2.96	2.66	4.98	0.00	3.00	2.73	0.00	0.00
Ti	0.00	0.00	0.00	0.96	0.00	0.00	0.00	0.14	0.00	0.00	0.00	0.00	0.00	0.95
Al	0.99	1.33	0.01	0.01	1.97	1.99	1.96	1.33	3.98	1.93	1.00	1.25	0.01	0.00
Cr	0.00	0.00	0.00	0.00	0.00	0.00	0.00	0.00	0.00	0.00	0.00	0.00	0.01	0.00
Fe^{3+}	0.00	0.00	1.94	0.06	0.14	0.10	0.12	0.00	0.00	0.06	0.00	0.00	1.91	0.09
Fe^{2+}	0.00	0.00	1.04	0.89	1.53	1.56	1.78	0.71	0.54	0.66	0.00	0.00	1.07	0.87
Mn	0.00	0.00	0.00	0.06	0.72	0.72	0.65	0.01	0.05	0.06	0.00	0.00	0.00	0.09
Mg	0.00	0.00	0.00	0.02	0.61	0.60	0.45	1.76	1.48	0.16	0.00	0.00	0.00	0.00
Zn	0.00	0.00	0.00	0.00	0.00	0.00	0.01	0.01	0.00	0.13	0.00	0.00	0.00	0.00
Ca	0.00	0.34	0.00	0.00	0.08	0.08	0.07	0.00	0.00	0.00	0.01	0.28	0.00	0.00
Na	0.11	0.64	0.00	0.00	0.00	0.00	0.00	0.01	0.01	0.00	0.21	0.74	0.00	0.00
K	0.85	0.01	0.00	0.00	0.00	0.00	0.00	0.91	0.00	0.00	0.80	0.01	0.00	0.00
Cl	0.00	0.00	0.00	0.00	0.00	0.00	0.00	0.00	0.00	0.00	0.00	0.00	0.00	0.00
F	0.00	0.00	0.05	0.02	0.00	0.01	0.00	0.92	0.00	0.00	0.00	0.00	0.07	0.01
Total Cations	4.97	4.99	3.00	2.00	8.00	8.00	8.00	7.54	11.00	3.00	5.01	5.02	3.00	2.00
X_{Mg}					0.28	0.28	0.20	0.71	0.77					
X_{Al}			0.005										0.005	
X_{Fe}					0.72	0.72	0.80	0.29	0.27					
X_{alm}					0.52	0.53	0.60							
X_{py}					0.21	0.20	0.15							
X_{grs}					0.03	0.03	0.02							
X_{sps}					0.24	0.24	0.22							
X_{An}	0.00	0.34									0.01	0.27		

X_{Mg} (Mg/(Fe^{2+}+Mg)); X_{Al} (Al/(Al+Fe^{3+}+2Ti)); X_{Fe} (Fe/(Fe^{2+} + Mg)); X_{An} (Ca/(Ca+Na+K)).

Mode denotes mineral abundance (as a proportion out of 1).

[a] Relict prograde garnet grain.

[b] Peak metamorphic garnet generation.

[c] Retrograde symplectic garnet.

internally consistent thermodynamic dataset of Holland and Powell (1998). Pseudosections were calculated for the geologically realistic system of MnNCKFMASHTO ($MnO–Na_2O–CaO–K_2O–FeO–MgO–Al_2O_3–SiO_2–H_2O–TiO_2–Fe_2O_3$). The following activity relationships were used: silicate melt (White et al., 2007); cordierite (Holland and Powell, 1998; Mahar et al., 1997); garnet, biotite, and ilmenite (White et al., 2005); orthopyroxene, spinel and magnetite (White et al., 2002); plagioclase and K-feldspar (Holland and Powell, 2003). Whole-rock XRF analyses recalculated to molar oxide percent were used for the preliminary bulk composition of each sample.

The H_2O content was estimated on the basis of abundance and chemical compositions of hydrous minerals in the observed mineral assemblages. The Fe_2O_3 content was evaluated for each sample using an isobaric (P = 5.5 kbar) $T–XFe_2O_3$ ($XFe_2O_3 = Fe_2O_3/(FeO + Fe_2O_3)$) diagram. This allows for assessment of the effect of changing the Fe^{2+}/Fe^{3+} ratio on the phase equilibria over a range of all Fe existing as FeO to all Fe as Fe_2O_3. The *T–X* approach was supplemented by an approximation of the total amount of Fe^{3+} versus Fe^{2+} in the rock estimated by combining the abundance of minerals in thin section—determined from image analysis and a visual estimation from petrography, with the stoichiometrically recast (Droop, 1987) electron microprobe compositions of Fe^{3+}-bearing minerals. This approach indicated that approximately 35%, 37% and 54% of all Fe in samples K9, R2017275 and K6, respectively, was Fe^{3+}. Therefore, in the *T–X* diagrams the composition was chosen so that the Fe_2O_3 content was approximately equal to these constraints. These are the compositions used to generate the respective residual bulk-composition *P–T* pseudosections for each sample. Compositional isopleths and modal proportions were calculated to further constrain the *P–T* conditions.

The observation of leucosomes and microgranite segregations oriented parallel to the gneissic fabric at outcrop scale, as well as a paucity of biotite, suggests that these samples underwent prograde to peak melt generation and loss and accordingly that the rocks preserve a residual peak mineral assemblage (White and Powell, 2002). Estimating the proportion of prograde melt loss and therefore the likely bulk rock composition at prograde to near-peak conditions is often difficult (Kelsey and Hand, 2015), and has not been compositionally accounted for in this study. However, evidence for late melt in the form of leucosomes with sub-diffuse margins cross-cutting the structural fabrics is also suggestive of the potential existence of melt remaining in the rock after the peak temperatures were achieved (Kelsey and

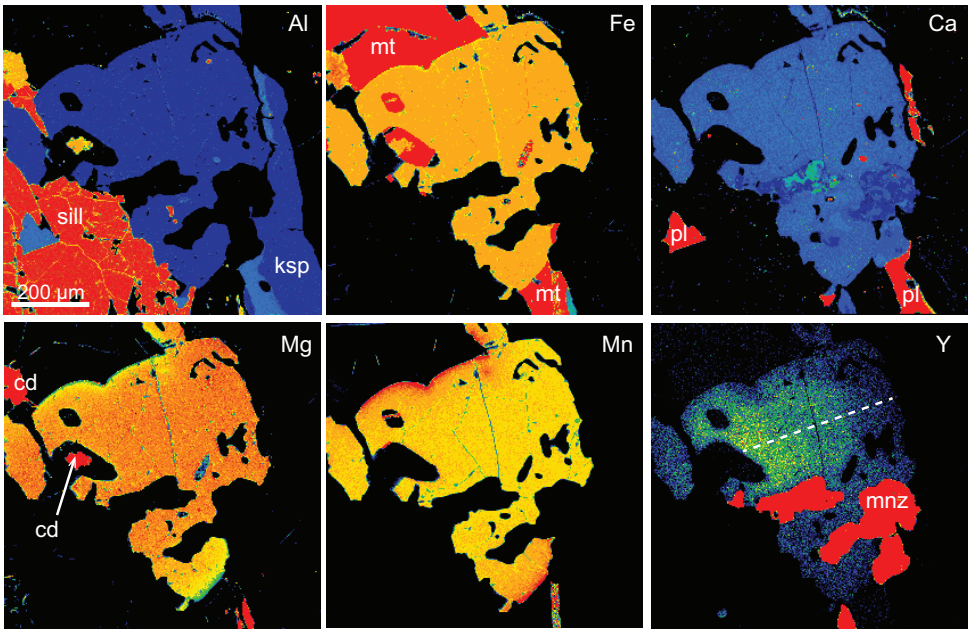

Figure 6. Qualitative electron microprobe elemental X-ray maps for Al, Fe, Ca, Mg, Mn and Y for a garnet grain from sample K9 (crystal g2 in Fig. 8). The colour scale reflects relative concentration, with warmer colours representing higher concentration for that particular element. Coarse-grained monazite is partially hosted within the garnet grain (red in Y map). The position of the transect across this garnet for LA–ICP–MS trace element analyses is indicated by the dashed line in the Y map.

Hand, 2015). Calculated pseudosections based on residual bulk compositions that were formed after the rocks had undergone melt loss, may therefore not be entirely appropriate to model the *P–T* evolution of these mineral assemblages. Partial melting and melt loss in granulite facies rocks has been investigated by a number of studies (e.g. Anderson et al., 2013; Diener et al., 2013; Johnson and Brown, 2004; Korhonen et al., 2010; White and Powell, 2002). In this study, in order to account for the potential existence of melt after peak conditions, and consequently retrograde melt loss or melt crystallisation for these samples, the melt 'reintegration' method of Anderson et al. (2013) was used. This method involves the addition of a nominal amount of leucogranitic melt (derived from the partial melting of aluminous metasedimentary rocks) to the residual bulk composition (Anderson et al., 2013). The Fe^{3+}/Fe^{2+} ratio of the leucogranite composition is maintained as the same as that for the residual bulk composition to avoid changing the oxidation state during the melt reintegration. A calculated $T–M_{melt}$ pseudosection is used to select the appropriate melt-reintegrated bulk composition for each sample within the range $M = 0$ (residual bulk composition) to $M = 1$ (leucogranite composition). The amount of melt chosen to be reintegrated is guided largely by the critical melt loss threshold (i.e. approximately <7 mol% melt addition to the residual bulk composition; Brown, 2010; Brown and Korhonen, 2009; Rosenberg and Handy, 2005; Yakymchuk and Brown, 2014; Yakymchuk et al., 2013). This is assessed by contouring for melt modal abundance in the peak assemblage field. Reintegration of a low proportion of melt is consistent with field observations which reflect a relatively low proportion of leucosomes occurring discordant to the structural fabric and therefore the inferred presence of relatively low amounts of melt retained in these rocks after the thermal maxima. The selected compositions correspond to $M = 0.07$ for sample K9, $M = 0.05$ for sample K6, and $M = 0.06$ for sample R2017275, which are the bulk compositions used to construct their respective melt-reintegrated *P–T* pseudosections.

Recent release of the thermodynamic dataset, ds62 (Holland and Powell, 2011) and re-parameterized *a–x* models, provides an opportunity to compare *P–T* results with those obtained using the existing dataset and *a–x* models. To enable a comparison, a second *P–T* pseudosection was calculated for the residual bulk composition of sample K9. Calculations were done using THERMOCALC v. 3.37 with the internally consistent updated thermodynamic dataset, ds62, of Holland and Powell (2011), for the geologically realistic system of MnNCKFMASHTO ($MnO–Na_2O–CaO–K_2O–FeO–MgO–Al_2O_3–SiO_2–H_2O–TiO_2–Fe_2O_3$). The activity relationships of White et al. (2002) were used for spinel and magnetite; non-Mn-bearing

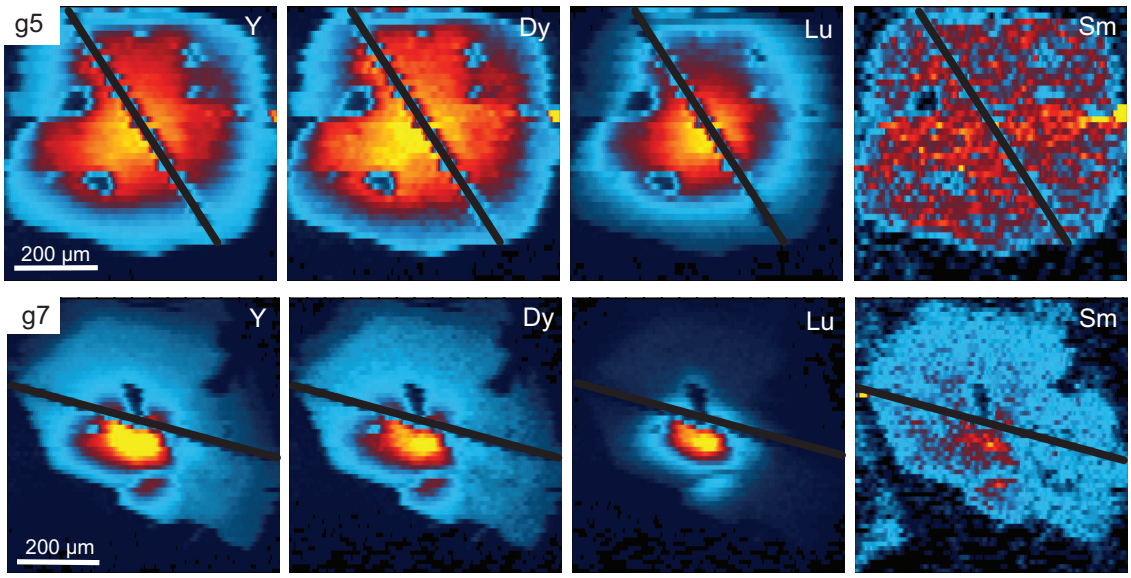

Figure 7. Representative qualitative LA–ICP–MS compositional maps for Y + REE in two peak metamorphic garnet grains from sample K9. The colour scale reflects relative concentration with warmer colours representing higher intensity of signal for the corresponding element. Prograde-style zoning is particularly pronounced for Y, and HREE such as Dy and Lu. Compositional profiles for LREE elements, including Sm, are comparatively flat. The position of the transect across these two garnet grains for LA–ICP–MS quantitative trace element analyses (see Fig. 8) is indicated by the bold black line.

Table 3. LA–ICP–MS trace element analyses (ppm) for garnet from Sample K9

		Element (ppm)													
Analysis	Y	**La**	**Ce**	Pr	Nd	Sm	Eu	Gd	Tb	Dy	Ho	Er	Tm	Yb	Lu
Prograde garnet generation															
Crystal g4															
g4-1 (rim)	1275	0.09	0.30	0.09	1.67	5.32	0.45	26.58	12.24	156.61	46.82	169.59	28.24	203.87	29.08
g4-2	1370	0.12	0.33	0.11	1.61	5.67	0.44	28.24	13.53	169.11	50.49	182.81	30.38	219.65	31.01
g4-3	1384	0.03	0.14	0.06	1.46	5.85	0.43	29.80	13.77	172.37	50.73	184.55	31.08	224.61	31.88
g4-4	1423	0.03	0.19	0.05	1.52	5.77	0.49	30.55	13.96	175.73	52.51	190.93	31.76	232.81	33.53
g4-5	1394	0.09	0.35	0.07	1.23	5.51	0.50	29.30	13.70	172.74	51.60	188.61	31.85	236.89	33.57
g4-6	1265	0.19	0.64	0.09	0.97	4.39	0.38	26.68	12.51	157.44	47.50	174.72	29.36	219.11	31.68
g4-7	1385	0.15	0.55	0.07	1.10	4.82	0.39	27.99	13.21	173.20	52.13	190.34	32.25	242.12	34.84
g4-8	1314	0.11	0.44	0.08	1.24	5.25	0.42	27.06	12.80	162.80	48.84	178.56	30.23	226.84	32.41
g4-9	1314	0.09	0.37	0.08	1.32	5.40	0.43	27.82	12.93	162.69	48.29	180.88	30.13	228.66	32.78
g4-10 (rim)	1408	0.10	0.32	0.06	1.56	6.12	0.51	29.96	13.79	174.01	52.41	191.31	32.41	241.85	35.01
Peak metamorphic garnet generation															
Crystal g2															
g2-1 (core)	2037	0.05	0.21	0.03	0.95	4.46	0.76	39.24	17.33	236.55	83.73	357.47	71.68	634.77	116.17
g2-2	2723	0.22	0.61	0.11	1.89	7.65	0.78	53.18	22.78	310.11	112.28	498.33	101.92	871.32	156.75
g2-3	2424	0.10	0.23	0.07	1.35	7.03	0.70	46.10	20.02	275.01	98.01	434.93	87.85	746.15	131.47
g2-4	2098	0.28	1.16	0.15	1.26	6.04	0.65	41.22	17.89	243.73	84.74	365.97	71.75	605.13	101.25
g2-5	1986	0.15	0.68	0.09	1.38	5.67	0.59	40.43	17.46	235.25	79.86	330.29	62.91	524.13	84.27
g2-6	1958	0.14	0.65	0.13	1.21	6.42	0.74	42.49	18.02	234.33	78.05	306.49	57.40	462.87	73.15
g2-7	1826	0.81	2.22	0.25	3.03	6.02	0.74	42.91	17.53	225.67	70.70	276.44	50.00	395.91	61.35
g2-8	1813	0.22	0.65	0.12	1.94	7.25	0.74	44.15	18.45	230.34	71.38	265.46	46.20	357.69	54.63
g2-9	1521	0.10	0.62	0.11	1.88	6.90	0.67	40.28	16.41	199.33	59.06	208.66	34.22	259.46	38.02
g2-10	1258	0.13	0.54	0.09	1.57	5.58	0.60	35.93	14.21	170.64	48.17	158.91	24.90	177.91	24.05
g2-11	1004	0.11	0.43	0.08	1.10	4.63	0.66	30.58	12.02	140.16	37.18	116.37	16.98	118.69	14.54
g2-12 (rim)	844	0.09	0.36	0.07	0.90	3.64	0.56	26.09	10.47	118.57	31.87	93.43	13.17	87.26	10.07
Crystal g5															
g5-1 (rim)	763	<0.0051	0.13	0.10	1.83	6.01	0.69	29.60	10.72	111.22	28.76	94.50	15.87	124.15	18.46
g5-2	1051	<0.0074	0.14	0.09	2.06	5.74	0.81	33.08	13.08	143.31	40.85	145.35	25.59	204.20	32.50
g5-3	1446	0.04	0.19	0.10	2.45	7.42	0.85	37.65	14.92	186.53	58.95	231.79	43.59	358.92	61.22
g5-4	1930	0.06	0.24	0.12	2.58	7.22	0.79	40.68	17.63	231.72	80.73	349.88	69.05	590.75	106.52
g5-5	2298	0.06	0.33	0.17	2.39	6.97	0.67	41.58	18.55	258.70	96.16	448.66	93.83	831.11	153.52
g5-6	2617	0.05	0.34	0.13	2.49	7.46	0.71	44.96	19.74	287.85	111.58	547.18	119.92	1080.29	205.06
g5-7	2979	0.05	0.30	0.16	2.43	7.63	0.71	47.69	21.25	313.22	125.10	637.54	142.60	1294.07	249.59
g5-8	2756	0.06	0.34	0.14	2.34	6.47	0.64	42.98	19.91	289.97	116.47	585.40	130.52	1170.20	219.78
g5-9	2502	0.06	0.37	0.13	2.33	6.00	0.56	39.73	18.27	267.09	103.56	506.40	110.89	992.25	179.17
g5-10	2255	0.06	0.38	0.15	2.21	6.47	0.67	39.17	17.23	249.18	93.54	441.73	92.73	815.60	143.13
g5-11	2061	0.06	0.37	0.12	1.92	6.26	0.67	37.83	16.83	236.81	85.32	379.45	77.28	677.38	117.04
g5-12	1918	0.05	0.35	0.12	1.91	6.39	0.70	37.36	16.53	228.39	80.07	344.57	67.82	585.97	101.61
g5-13	1625	0.07	0.39	0.11	2.40	6.76	0.69	37.23	15.55	201.72	66.05	271.26	52.06	442.30	74.57
g5-14	973	0.06	0.34	0.14	2.31	6.41	0.71	30.24	11.37	129.82	38.19	142.52	26.53	225.17	35.38
g5-15 (rim)	587	0.08	0.26	0.07	1.14	3.66	0.74	22.36	7.68	81.52	21.65	77.14	13.38	112.28	17.50
Crystal g7															
g7-1 (rim)	196	0.02	0.11	0.09	1.37	4.43	0.64	19.08	4.44	34.98	7.07	20.85	3.01	21.24	2.67
g7-2	228	0.28	0.27	0.08	1.67	5.17	0.77	21.06	5.35	41.25	8.09	22.18	3.39	22.47	2.88
g7-3	286	<0.0089	0.09	0.10	1.77	6.35	0.77	24.97	6.36	49.52	10.10	27.33	3.99	29.22	3.64
g7-4	353	0.05	0.19	0.09	1.81	6.73	0.67	26.89	7.28	57.66	12.37	34.11	5.09	36.79	4.68
g7-5	500	0.04	0.21	0.06	1.61	6.19	0.67	26.57	8.19	73.60	16.85	51.39	8.56	65.65	8.45
g7-6	775	0.04	0.23	0.07	1.73	6.18	0.65	29.27	9.95	107.51	29.73	108.33	19.98	167.93	27.40
g7-7	1312	0.04	0.35	0.14	2.48	7.96	0.81	38.30	14.00	165.78	55.47	241.29	48.55	434.73	83.37
g7-8	1412	0.07	0.25	0.10	2.30	7.66	1.00	37.37	13.79	167.76	60.93	295.63	63.51	595.44	123.27
g7-9	949	0.04	0.24	0.06	1.48	5.70	0.85	27.30	9.37	112.34	41.36	201.93	45.51	442.48	91.82
g7-11	928	0.12	0.34	0.10	1.42	5.99	0.85	28.70	9.69	114.54	39.43	178.70	38.84	368.48	71.58
g7-12	574	0.12	0.26	0.06	1.21	5.35	0.86	25.04	6.97	67.83	21.28	96.57	21.93	227.52	43.73
g7-13	341	0.14	0.34	0.06	0.57	2.92	0.70	15.64	4.55	42.48	12.54	51.52	11.26	110.60	20.13
g7-14	264	0.09	0.36	0.04	0.61	3.39	0.70	16.24	4.24	37.88	9.31	34.44	6.81	60.77	10.05
g7-15	200	0.15	0.33	0.07	0.64	3.18	0.66	15.14	3.82	29.95	6.99	22.73	3.89	31.51	4.57
g7-16	168	0.09	0.37	0.10	1.48	5.35	0.69	19.60	4.54	32.09	5.88	15.18	2.27	16.97	2.22
g7-17	141	0.09	0.35	0.12	1.49	5.09	0.67	17.80	3.95	27.75	4.99	13.24	1.90	12.35	1.74
g7-18 (rim)	99	0.10	0.29	0.08	1.14	3.92	0.71	15.39	3.15	20.31	3.62	8.79	1.22	8.06	0.98

Table 3. (continued)

Analysis	Element (ppm)														
	Y	La	Ce	Pr	Nd	Sm	Eu	Gd	Tb	Dy	Ho	Er	Tm	Yb	Lu
Retrograde garnet generation															
Crystal g6															
g6-1 (rim)	18	0.01	0.06	0.04	0.90	3.01	0.53	6.94	1.15	5.54	0.67	1.49	0.14	0.82	0.08
g6-2	27	0.01	0.07	0.04	0.83	3.80	0.59	8.88	1.61	8.32	1.17	2.22	0.21	0.96	0.13
g6-3	28	0.03	0.10	0.05	0.95	3.68	0.57	9.11	1.42	8.23	1.24	2.44	0.28	1.49	0.16
g6-4	31	0.07	0.37	0.05	0.89	2.61	0.52	7.51	1.37	8.19	1.29	3.13	0.39	2.67	0.37
g6-5	43	0.06	0.22	0.08	1.47	4.43	0.66	10.17	1.82	11.21	1.80	4.04	0.46	2.69	0.32
g6-6	61	0.04	0.23	0.09	1.43	4.59	0.71	11.75	2.25	13.98	2.44	5.79	0.71	4.56	0.54
g6-7	89	0.06	0.23	0.10	1.76	5.07	0.75	13.39	2.70	18.19	3.73	10.20	1.41	8.84	1.23
g6-8	113	0.06	0.27	0.13	2.27	5.27	0.76	14.86	3.05	22.66	4.83	13.84	1.95	12.81	1.80
g6-9	119	0.05	0.33	0.10	2.05	5.71	0.72	14.63	3.24	23.35	5.00	14.55	2.09	13.81	2.06
g6-10	120	0.08	0.25	0.12	2.07	5.91	0.75	14.73	3.35	23.77	5.26	14.90	2.13	14.09	2.08
g6-11	117	0.05	0.26	0.11	2.01	5.50	0.70	15.13	3.31	24.03	5.00	14.37	2.06	14.18	2.01
g6-12	116	0.05	0.26	0.11	1.84	5.70	0.70	14.43	3.16	23.64	5.01	14.00	2.01	13.71	2.00
g6-13	108	0.07	0.39	0.10	1.77	5.40	0.60	12.99	2.88	21.64	4.58	13.03	1.86	12.40	1.80
g6-14	108	0.10	0.44	0.10	1.79	4.81	0.78	13.99	2.89	21.83	4.58	13.30	1.84	12.22	1.85
g6-15	116	0.17	0.53	0.12	1.80	4.95	0.70	13.98	3.06	23.74	4.99	13.99	2.06	13.26	2.03
g6-16	110	0.22	0.60	0.14	1.74	4.99	0.68	14.34	2.97	21.66	4.43	13.23	1.94	12.88	1.95
g6-17	133	0.11	0.45	0.11	1.88	5.58	0.73	16.25	3.45	25.98	5.39	15.51	2.35	14.67	2.18
g6-18	137	0.09	0.40	0.12	2.17	5.77	0.79	16.27	3.54	26.27	5.47	16.10	2.21	15.37	2.23
g6-19	130	0.09	0.35	0.09	1.76	5.45	0.71	15.00	3.39	25.26	5.41	15.73	2.24	15.16	2.23
g6-20 (core)	113	0.09	0.30	0.06	1.36	4.33	0.72	12.68	3.01	22.08	4.56	13.13	1.91	12.62	1.93

phases—silicate melt, muscovite, paragonite, plagioclase and K-feldspar utilised the *a–x* models of White et al. (2014a); and for the Mn-bearing minerals—garnet, orthopyroxene, cordierite, staurolite, chlorite, biotite and ilmenite, the *a–x* models from White et al. (2014b) were used.

5. RESULTS

5.1 Major element mineral chemistry

Whole-rock geochemical data are presented in Table 1. Representative electron microprobe mineral analyses are given in Table 2. The observed trends in major element mineral chemistry are summarised below.

5.1.1 Garnet

Garnet grains are unzoned in X_{alm} ($Fe^{2+}/(Fe^{2+}$ + Mg + Ca + Mn)) and X_{grs} (Ca/(Fe^{2+} + Mg + Ca + Mn)) with ranges of 0.53–0.61 and 0.022–0.031, respectively (Table 2). Core to rim zonation in X_{py} (Mg/(Mg + Fe^{2+} + Ca + Mn)) and X_{sps} (Mn/(Mg + Fe^{2+} + Ca + Mn)) is slight. Garnet core analyses yield values of X_{py} between 0.20–0.22, and X_{sps} between 0.20–0.23; rim analyses range between 0.19–0.23 and 0.17–0.24 for X_{py} and X_{sps}, respectively. The lower X_{py} and higher X_{sps} values from the garnet grain edge correspond to analyses where garnet is in direct contact with Fe–Ti oxide matrix minerals. Similarly, garnet occurring as finer-grained symplectitic intergrowths with magnetite display overall lower X_{py} ranging from 0.15 to 0.18, and slightly elevated X_{sps} to between 0.20 and 0.24, relative to the garnet core analyses. Elemental X-ray mapping of garnet from sample K9 reflect the aforementioned trends (Fig. 6).

5.1.2 Cordierite

Cordierite is magnesian in composition with consistency in X_{Fe} ($Fe^{2+}/(Fe^{2+}$+Mg)) values across all samples, and with no apparent variation in X_{Fe} from core to rim. X_{Fe} values range between 0.25–0.26, 0.24–0.28 and 0.21–0.23 in samples K9, K6 and R2017275, respectively.

5.1.3 Spinel

Spinel has high ZnO contents ranging from 3.37 to 3.74 wt% and corresponding to X_{Zn} (Zn/(Zn + Fe^{2+} + Mg +Mn)) values of 0.070 to 0.078 in sample K9. In sample K6, ZnO content is comparatively higher and more variable with values ranging between 2.43 and 6.67 wt%, equating to X_{Zn} values of 0.061–0.144. ZnO contents in spinel in sample R2017275 is consistently higher than samples K9, with 5.98–6.28 wt% and X_{Zn} values of 0.127–0.134. Spinel grains exhibit minor core to rim zonation in Zn, with lower ZnO contents generally associated with smaller grains, or analyses from nearer the spinel–magnetite grain boundary. X_{Mg} (Mg/(Mg + Zn + Fe^{2+} +Mn) ranges from 0.24 to 0.30 in

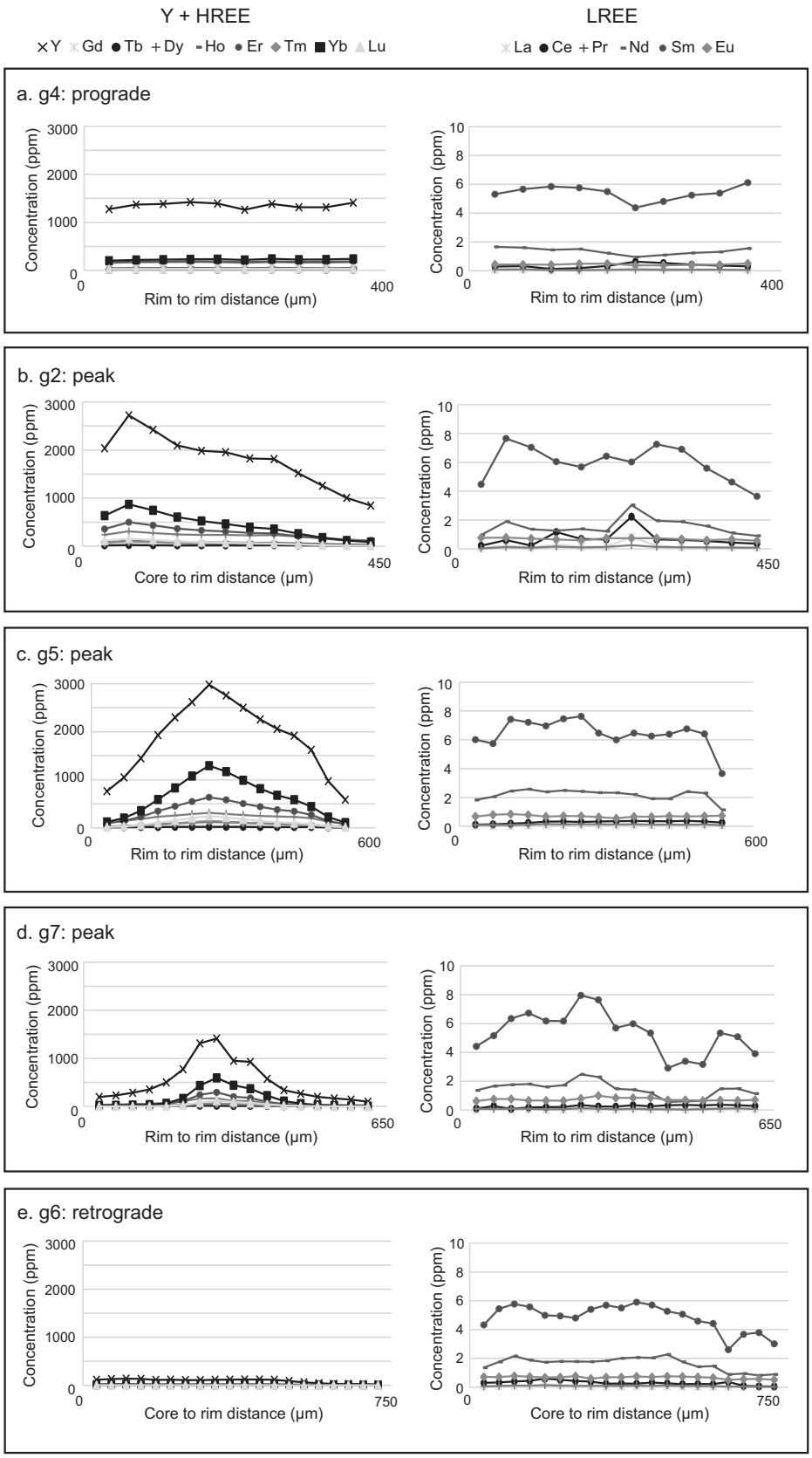

Figure 8. Y + REE zoning patterns measured across garnet grains from sample K9. Garnet grains from all microstructural locations (i.e. inferred prograde, peak and retrograde crystals) were analysed. (a) Prograde garnet generation: Crystal g4; (b–d) Inferred peak metamorphic garnet generation: Crystal g2, g5, g7 (see also Fig. 6 and 7); (e) Retrograde garnet generation: Crystal g6.

Table 4. LA–ICP–MS U–Pb in situ monazite geochronology

										Age (Ma)					
Analysis		$^{207}Pb/^{206}Pb$	1σ	$^{206}Pb/^{238}U$	1σ	$^{207}Pb/^{235}U$	1σ	ρ	Conc.	$^{207}Pb/^{206}Pb$	1σ	$^{206}Pb/^{238}U$	1σ	$^{207}Pb/^{235}U$	1σ
Sample K9															
K9A12A	m	0.07962	0.00134	2.22463	0.04223	0.20274	0.00308	0.80029	100	1188	33	1190	16	1189	13
K9A12B	m	0.07827	0.00133	2.11042	0.04046	0.19564	0.00297	0.79185	100	1154	33	1152	16	1152	13
K9A12C	m	0.07944	0.00118	2.08884	0.03652	0.19079	0.00283	0.84841	102	1183	29	1126	15	1145	12
K9A12D	m	0.08032	0.00144	2.21870	0.04409	0.20044	0.00309	0.77577	101	1205	35	1178	17	1187	14
K9A12E	m	0.07973	0.00144	2.14512	0.04293	0.19522	0.00301	0.77043	101	1190	35	1150	16	1164	14
K9A12F	m	0.07884	0.00122	2.13463	0.03821	0.19645	0.00293	0.83322	100	1168	30	1156	16	1160	12
K9A12G	m	0.08088	0.00163	2.15606	0.04666	0.19342	0.00305	0.72864	102	1219	39	1140	16	1167	15
K9A11A	m	0.08160	0.00145	2.21404	0.04376	0.19688	0.00302	0.77609	102	1236	35	1159	16	1186	14
K9A11B	m	0.07905	0.00137	2.12972	0.04141	0.19549	0.00298	0.78399	101	1173	34	1151	16	1159	13
K9A11C	m	0.07990	0.00131	2.10155	0.03922	0.19085	0.00288	0.80860	102	1194	32	1126	16	1149	13
K9A11D	m	0.07929	0.00139	2.07714	0.04058	0.19008	0.00290	0.78094	102	1179	34	1122	16	1141	13
K9A11E	m	0.07900	0.00143	2.06574	0.04127	0.18972	0.00291	0.76775	102	1172	35	1120	16	1138	14
K9A8A	g*	0.08044	0.00251	2.16894	0.06697	0.19593	0.00352	0.58185	102	1208	60	1153	19	1171	21
K9A8B	g*	0.08087	0.00104	2.19311	0.03447	0.19681	0.00277	0.89547	102	1218	25	1158	15	1179	11
K9A8C	g*	0.08510	0.00163	2.37260	0.04878	0.20232	0.00306	0.73564	104	1318	37	1188	16	1234	15
K9A2A	g	0.08238	0.00192	2.26041	0.05435	0.19910	0.00320	0.66845	103	1255	45	1171	17	1200	17
K9A2B	g	0.08243	0.00164	2.26168	0.04799	0.19909	0.00305	0.72199	103	1256	38	1170	16	1200	15
K9A2C	g	0.08060	0.00148	2.22050	0.04420	0.19989	0.00299	0.75146	101	1212	36	1175	16	1188	14
K9A2D	g	0.07975	0.00161	2.15031	0.04620	0.19566	0.00300	0.71364	101	1191	39	1152	16	1165	15
K9A2E	g	0.08005	0.00156	2.14064	0.04479	0.19404	0.00296	0.72906	102	1198	38	1143	16	1162	14
K9A2F	g	0.08166	0.00157	2.17930	0.04505	0.19364	0.00294	0.73447	103	1238	37	1141	16	1175	14
K9A2G	g	0.07854	0.00193	2.18400	0.05489	0.20178	0.00328	0.64678	99	1161	48	1185	18	1176	18
K9A2H	g	0.08004	0.00153	2.17649	0.04482	0.19733	0.00299	0.73581	101	1198	37	1161	16	1174	14
K9A2I	g	0.08201	0.00147	2.19683	0.04298	0.19437	0.00290	0.76260	103	1246	34	1145	16	1180	14
K9A2J	g	0.08004	0.00158	2.17385	0.04572	0.19708	0.00300	0.72377	101	1198	38	1160	16	1173	15
K9A2K	g	0.07967	0.00146	2.14206	0.04268	0.19509	0.00291	0.74863	101	1189	36	1149	16	1163	14
K9A2L	g	0.07978	0.00151	2.15076	0.04377	0.19562	0.00294	0.73850	101	1192	37	1152	16	1165	14
K9A2M	g	0.07979	0.00153	2.17321	0.04475	0.19765	0.00298	0.73220	101	1192	37	1163	16	1173	14
K9A2N	g	0.07897	0.00136	2.13610	0.04059	0.19628	0.00288	0.77218	100	1172	34	1155	16	1161	13
K9A2O	g	0.08001	0.00154	2.12995	0.04403	0.19318	0.00291	0.72870	102	1197	38	1139	16	1159	14
K9A2P	g	0.08155	0.00199	2.26728	0.05662	0.20175	0.00326	0.64705	101	1235	47	1185	17	1202	18
K9A2Q	g	0.08151	0.00154	2.16786	0.04400	0.19300	0.00289	0.73777	103	1234	37	1138	16	1171	14
K9B1A	m*	0.08030	0.00149	2.20879	0.04475	0.19959	0.00305	0.75426	101	1204	36	1173	16	1184	14
K9B1B	m*	0.07904	0.00157	2.23645	0.04788	0.20533	0.00320	0.72795	99	1173	39	1204	17	1193	15
K9B1C	m*	0.07707	0.00135	2.16657	0.04216	0.20397	0.00308	0.77599	98	1123	34	1197	16	1170	14
K9B2A	m*	0.07880	0.00147	2.16855	0.04431	0.19970	0.00306	0.74991	100	1167	37	1174	16	1171	14
K9B2B	m*	0.08080	0.00154	2.21403	0.04600	0.19882	0.00307	0.74320	101	1217	37	1169	17	1186	15
K9B2C	m*	0.07787	0.00136	2.08476	0.04053	0.19428	0.00293	0.77575	100	1144	34	1145	16	1144	13
K9B2D	m*	0.07955	0.00158	2.16398	0.04617	0.19738	0.00307	0.72900	101	1186	39	1161	17	1170	15
K9B3A	m	0.08353	0.00161	2.20755	0.04562	0.19176	0.00294	0.74190	105	1282	37	1131	16	1183	14
K9B3B	m	0.07858	0.00126	2.05125	0.03718	0.18941	0.00279	0.81266	101	1162	32	1118	15	1133	12
K9B3C	m	0.07683	0.00147	2.01686	0.04159	0.19047	0.00289	0.73580	100	1117	38	1124	16	1121	14
K9B3D	m	0.07939	0.00155	2.06843	0.04326	0.18905	0.00289	0.73093	102	1182	38	1116	16	1138	14
K9B3E	m	0.08123	0.00157	2.10906	0.04372	0.18841	0.00288	0.73739	104	1227	38	1113	16	1152	14
K9B4A	m*	0.07934	0.00094	2.19671	0.03315	0.20091	0.00284	0.93671	100	1181	23	1180	15	1180	11
K9B4B	m*	0.08070	0.00097	2.18135	0.03302	0.19614	0.00277	0.93296	102	1214	23	1155	15	1175	11
K9B4C	m*	0.07902	0.00096	2.14357	0.03276	0.19684	0.00278	0.92411	100	1173	24	1158	15	1163	11
K9B10A	m*	0.08009	0.00175	2.14159	0.04876	0.19403	0.00305	0.69040	102	1199	42	1143	16	1162	16
K9B10B	m*	0.08075	0.00163	2.14101	0.04578	0.19238	0.00296	0.71957	102	1216	39	1134	16	1162	15
K9B10C	m*	0.07853	0.00151	2.07366	0.04276	0.19160	0.00291	0.73654	101	1160	38	1130	16	1140	14
K9B10D	m*	0.08014	0.00152	2.14037	0.04373	0.19381	0.00294	0.74247	102	1200	37	1142	16	1162	14
K9B11A	m*	0.08189	0.00231	2.23019	0.03841	0.20117	0.00291	0.61037	102	1243	54	1182	16	1191	12
K9B11B	m*	0.07976	0.00147	2.18357	0.04368	0.19865	0.00299	0.75243	101	1191	36	1168	16	1176	14
K9B11C	m*	0.09586	0.00199	2.56732	0.05615	0.19432	0.00306	0.72000	113	1545	38	1145	17	1291	16
K9B11D	m*	0.08045	0.00120	2.23019	0.03841	0.20117	0.00291	0.83990	101	1208	29	1182	16	1191	12
K9B11E	m*	0.07867	0.00112	2.13280	0.03579	0.19673	0.00282	0.85421	100	1164	28	1158	15	1160	12
K9B11F	m*	0.07986	0.00133	2.13381	0.03960	0.19389	0.00285	0.79205	102	1194	32	1142	15	1160	13
K9B11G	m*	0.07758	0.00128	2.07411	0.03828	0.19401	0.00284	0.79315	100	1136	32	1143	15	1140	13
K9B11H	m*	0.07898	0.00159	2.17077	0.04639	0.19944	0.00305	0.71561	100	1172	39	1172	16	1172	15
K9B17A	g	0.07821	0.00105	2.12010	0.03395	0.19672	0.00278	0.88250	100	1152	26	1158	15	1155	11
K9B17B	g	0.07837	0.00111	2.06038	0.03413	0.19077	0.00272	0.86074	101	1156	28	1126	15	1136	11
K9B17C	g	0.07947	0.00118	2.12430	0.03631	0.19398	0.00279	0.84147	101	1184	29	1143	15	1157	12
K9B17D	g	0.07852	0.00111	2.07138	0.03431	0.19142	0.00274	0.86418	101	1160	28	1129	15	1139	11

Table 4 (continued)

Analysis		$^{207}Pb/^{206}Pb$	1σ	$^{206}Pb/^{238}U$	1σ	$^{207}Pb/^{235}U$	1σ	ρ	Conc.	Age (Ma) $^{207}Pb/^{206}Pb$	1σ	$^{206}Pb/^{238}U$	1σ	$^{207}Pb/^{235}U$	1σ
K9B17E	g	0.07875	0.00150	2.10284	0.04319	0.19380	0.00294	0.73861	101	1166	37	1142	16	1150	14
K9B17F	g	0.08330	0.00163	2.24090	0.04676	0.19521	0.00299	0.73404	104	1276	38	1150	16	1194	15
K9B17G	g	0.08012	0.00123	2.14140	0.03757	0.19394	0.00282	0.82878	102	1200	30	1143	15	1162	12
K9B17H	g	0.08024	0.00134	2.17313	0.04044	0.19653	0.00291	0.79568	101	1203	33	1157	16	1173	13
K9B17I	g	0.07996	0.00137	2.15710	0.04101	0.19576	0.00292	0.78458	101	1196	33	1153	16	1167	13
K9B17J	g	0.08003	0.00146	2.17328	0.04316	0.19705	0.00298	0.76151	101	1198	35	1159	16	1173	14
K9B17K	g	0.07688	0.00121	2.04820	0.03690	0.19332	0.00284	0.81543	99	1118	31	1139	15	1132	12
K9B17L	g	0.08046	0.00167	2.18318	0.04790	0.19690	0.00308	0.71295	101	1208	40	1159	17	1176	15
K9B17M	g	0.07858	0.00113	2.07108	0.03510	0.19125	0.00277	0.85461	101	1162	28	1128	15	1139	12
K9B17N	g	0.07895	0.00112	2.12239	0.03575	0.19505	0.00283	0.86137	101	1171	28	1149	15	1156	12
K9B17O	g	0.07975	0.00120	2.11046	0.03697	0.19202	0.00282	0.83836	102	1191	29	1132	15	1152	12
K9B17P	g	0.08156	0.00132	2.20208	0.04041	0.19591	0.00292	0.81221	102	1235	31	1153	16	1182	13
K9B17Q	g	0.08079	0.00139	2.23402	0.04288	0.20063	0.00302	0.78423	101	1217	34	1179	16	1192	13
K9B17R	g	0.08123	0.00161	2.20493	0.04713	0.19696	0.00307	0.72922	102	1227	39	1159	17	1183	15
K9B17S	g	0.08005	0.00143	2.14494	0.04239	0.19444	0.00296	0.77030	102	1198	35	1145	16	1163	14
K9B17T	g	0.07853	0.00121	2.17998	0.03834	0.20142	0.00293	0.82711	99	1160	30	1183	16	1175	12
K9B17U	g	0.07650	0.00126	2.11646	0.03907	0.20076	0.00295	0.79600	98	1108	33	1179	16	1154	13
K9B17V	g	0.07969	0.00134	2.18050	0.04073	0.19855	0.00293	0.79002	101	1189	33	1168	16	1175	13
K9B17W	g	0.07904	0.00153	2.16027	0.04467	0.19832	0.00302	0.73643	100	1173	38	1166	16	1168	14
K9B17X	g	0.07726	0.00157	2.11642	0.04553	0.19879	0.00305	0.71320	99	1128	40	1169	16	1154	15
K9B17Y	g	0.07867	0.00150	2.13456	0.04356	0.19690	0.00297	0.73915	100	1164	37	1159	16	1160	14
K9B17Z	g	0.08127	0.00156	2.13042	0.04370	0.19023	0.00288	0.73807	103	1228	37	1123	16	1159	14
K9B17A2	g	0.07980	0.00138	2.10383	0.03990	0.19131	0.00282	0.77723	102	1192	34	1129	15	1150	13
K9B17B2	g	0.08003	0.00161	2.11351	0.04488	0.19162	0.00292	0.71762	102	1198	39	1130	16	1153	15
K9B17C2	g	0.08001	0.00155	2.10350	0.04333	0.19078	0.00288	0.73285	102	1197	38	1126	16	1150	14
K9B17D2	g	0.08040	0.00156	2.11607	0.04363	0.19098	0.00288	0.73139	102	1207	38	1127	16	1154	14
K9B17E2	g	0.07826	0.00133	2.11182	0.03945	0.19583	0.00286	0.78180	100	1153	33	1153	15	1153	13
K9B16A	g*	0.07892	0.00145	2.25293	0.04512	0.20714	0.00314	0.75691	99	1170	36	1214	17	1198	14
K9B16B	g*	0.08041	0.00145	2.25264	0.04453	0.20327	0.00308	0.76651	100	1207	35	1193	16	1198	14
K9B16C	g*	0.07894	0.00124	2.14694	0.03847	0.19734	0.00290	0.82013	100	1171	31	1161	16	1164	12
K9B16D	g*	0.08286	0.00138	2.25906	0.04212	0.19782	0.00294	0.79711	103	1266	32	1164	16	1200	13
Sample K6															
K619A	m	0.07891	0.00088	2.24567	0.03332	0.20650	0.00296	0.96608	99	1170	22	1210	16	1195	10
K619B	m	0.07856	0.00094	2.18694	0.03375	0.20201	0.00293	0.93985	99	1161	24	1186	16	1177	11
K619C	m	0.07951	0.00094	2.21189	0.03383	0.20188	0.00292	0.94569	100	1185	23	1185	16	1185	11
K619D	m	0.07868	0.00092	2.21582	0.03378	0.20437	0.00295	0.94685	99	1164	23	1199	16	1186	11
K61A	m*	0.07785	0.00104	2.13705	0.03507	0.19920	0.00293	0.89631	99	1143	26	1171	16	1161	11
K61B	m*	0.07888	0.00100	2.19126	0.03492	0.20159	0.00294	0.91516	100	1169	25	1184	16	1178	11
K614A	m	0.07589	0.00105	2.11852	0.03543	0.20257	0.00300	0.88554	97	1092	27	1189	16	1155	12
K614B	m	0.07731	0.00108	2.11149	0.03562	0.19817	0.00294	0.87944	99	1129	28	1166	16	1153	12
K614C	m	0.07796	0.00114	2.12755	0.03687	0.19803	0.00296	0.86252	99	1146	29	1165	16	1158	12
K614D	m	0.07879	0.00126	2.14645	0.03940	0.19769	0.00300	0.82673	100	1167	31	1163	16	1164	13
K618A	m	0.07760	0.00091	2.13114	0.03260	0.19926	0.00291	0.95470	99	1137	23	1171	16	1159	11
K618B	m	0.07789	0.00093	2.10780	0.03266	0.19637	0.00287	0.94324	100	1144	24	1156	15	1151	11
K618C	m	0.07993	0.00114	2.16925	0.03714	0.19694	0.00295	0.87489	101	1195	28	1159	16	1171	12
K618D	m	0.07754	0.00101	2.05476	0.03339	0.19229	0.00284	0.90888	100	1135	26	1134	15	1134	11
K618E	m	0.07831	0.00115	2.11972	0.03672	0.19642	0.00293	0.86111	100	1155	29	1156	16	1155	12
K618F	m	0.07786	0.00111	2.12703	0.03628	0.19824	0.00296	0.87540	99	1143	28	1166	16	1158	12
K618G	m	0.07746	0.00103	2.08391	0.03424	0.19521	0.00289	0.90103	99	1133	26	1150	16	1144	11
K618H	m	0.07870	0.00090	2.14251	0.03242	0.19755	0.00287	0.96010	100	1165	23	1162	15	1163	10
K618I	m	0.07865	0.00091	2.15426	0.03285	0.19875	0.00290	0.95687	100	1163	23	1169	16	1166	11
K618J	m	0.07868	0.00091	2.19426	0.03334	0.20238	0.00294	0.95610	99	1164	23	1188	16	1179	11
K68A	m	0.07795	0.00101	2.15425	0.03493	0.20054	0.00296	0.91031	99	1146	26	1178	16	1166	11
K68B	m	0.07818	0.00091	2.12386	0.03238	0.19712	0.00287	0.95499	100	1152	23	1160	15	1157	11
K68C	m	0.07662	0.00102	2.06072	0.03391	0.19518	0.00288	0.89670	99	1111	26	1149	16	1136	11
K68D	m	0.07868	0.00105	2.09210	0.03435	0.19295	0.00285	0.89961	101	1164	26	1137	15	1146	11
K62A	m	0.07754	0.00140	2.08109	0.04085	0.19466	0.00295	0.77205	100	1135	35	1147	16	1143	13
K62B	m	0.08008	0.00107	2.22972	0.03667	0.20205	0.00297	0.89379	100	1199	26	1186	16	1190	12
K62C	m	0.07898	0.00088	2.22302	0.03297	0.20424	0.00292	0.96398	99	1172	22	1198	16	1188	10
K62D	m	0.07890	0.00147	2.13294	0.04331	0.19617	0.00301	0.75566	100	1170	36	1155	16	1160	14
K62E	m	0.07966	0.00089	2.18095	0.03233	0.19868	0.00284	0.96428	101	1189	22	1168	15	1175	10
K62F	m	0.07910	0.00088	2.17999	0.03228	0.19998	0.00286	0.96583	100	1175	22	1175	15	1175	10
K62G	m	0.07981	0.00089	2.16652	0.03217	0.19699	0.00282	0.96409	101	1192	22	1159	15	1170	10
K62H	m	0.08013	0.00089	2.19123	0.03247	0.19844	0.00283	0.96242	101	1200	22	1167	15	1178	10

Table 4 (continued)

Analysis		$^{207}Pb/^{206}Pb$	1σ	$^{206}Pb/^{238}U$	1σ	$^{207}Pb/^{235}U$	1σ	ρ	Conc.	Age (Ma) $^{207}Pb/^{206}Pb$	1σ	$^{206}Pb/^{238}U$	1σ	$^{207}Pb/^{235}U$	1σ
K62I	m	0.07899	0.00089	2.15555	0.03220	0.19802	0.00284	0.96009	100	1172	22	1165	15	1167	10
K62J	m	0.08006	0.00134	2.25701	0.04232	0.20459	0.00307	0.80028	100	1198	33	1200	16	1199	13
K62K	m	0.08045	0.00091	2.24354	0.03343	0.20237	0.00288	0.95509	101	1208	22	1188	15	1195	10
K65A	m	0.08027	0.00142	2.23809	0.04378	0.20235	0.00307	0.77560	100	1204	34	1188	16	1193	14
K65B	m	0.07749	0.00101	2.10604	0.03369	0.19722	0.00284	0.90019	99	1134	26	1160	15	1151	11
K65C	m	0.07890	0.00097	2.25289	0.03485	0.20722	0.00296	0.92342	99	1170	24	1214	16	1198	11
K65D	m	0.08015	0.00105	2.30697	0.03660	0.20888	0.00297	0.89623	99	1201	26	1223	16	1214	11
K65E	m	0.07971	0.00100	2.22806	0.03482	0.20285	0.00290	0.91479	100	1190	25	1191	16	1190	11
K613A	m	0.08043	0.00098	2.27162	0.03475	0.20498	0.00290	0.92484	100	1208	24	1202	16	1204	11
K613B	m	0.08050	0.00097	2.23691	0.03419	0.20166	0.00286	0.92789	101	1209	24	1184	15	1193	11
K613C	m	0.07973	0.00096	2.19399	0.03350	0.19969	0.00284	0.93143	100	1190	24	1174	15	1179	11
K613D	m	0.08006	0.00096	2.20502	0.03370	0.19985	0.00285	0.93309	101	1199	23	1175	15	1183	11
K617A	m	0.08046	0.00098	2.23968	0.03426	0.20202	0.00286	0.92549	101	1208	24	1186	15	1194	11
K617B	m	0.08022	0.00098	2.20761	0.03388	0.19970	0.00283	0.92339	101	1203	24	1174	15	1184	11
K617C	m	0.08066	0.00118	2.17888	0.03725	0.19603	0.00285	0.85041	102	1213	29	1154	15	1174	12
K617D	m	0.07917	0.00133	2.25775	0.04255	0.20695	0.00308	0.78970	99	1176	33	1213	16	1199	13
Sample R2017275															
4_1	m	0.07920	0.00089	0.20599	0.00306	2.24818	0.03411	0.97909	99	1177	22	1207	16	1196	11
4_2	m	0.08099	0.00098	0.20520	0.00307	2.28991	0.03601	0.95139	100	1221	24	1203	16	1209	11
5B_1	m*	0.07680	0.00101	0.19951	0.00301	2.11125	0.03469	0.91820	98	1116	26	1173	16	1153	11
5B_2	m*	0.07928	0.00096	0.20024	0.00302	2.18771	0.03455	0.95499	100	1179	24	1177	16	1177	11
5B_3	m*	0.07813	0.00094	0.19641	0.00295	2.11463	0.03328	0.95435	100	1150	24	1156	16	1154	11
5B_4	m*	0.07885	0.00092	0.19832	0.00299	2.15488	0.03352	0.96922	100	1169	23	1166	16	1167	11
5B_5	m*	0.07819	0.00103	0.19402	0.00296	2.09046	0.03470	0.91909	100	1152	26	1143	16	1146	11
5A_1	m*	0.07709	0.00094	0.19846	0.00300	2.10796	0.03355	0.94977	99	1123	24	1167	16	1151	11
5A_2	m*	0.07906	0.00092	0.20790	0.00314	2.26485	0.03528	0.96959	99	1174	23	1218	17	1201	11
5A_3	m*	0.07869	0.00100	0.19931	0.00304	2.16071	0.03532	0.93308	100	1164	25	1172	16	1169	11
10_1	m	0.07766	0.00093	0.19916	0.00302	2.13092	0.03379	0.95628	99	1138	24	1171	16	1159	11
10_2	m	0.07842	0.00100	0.19518	0.00299	2.10887	0.03466	0.93209	100	1158	25	1149	16	1152	11
16_1	g*	0.07952	0.00097	0.19259	0.00293	2.10960	0.03379	0.94983	101	1185	24	1135	16	1152	11
17_1	m*	0.07951	0.00109	0.19573	0.00307	2.14459	0.03717	0.90497	101	1185	27	1152	17	1163	12
17_2	m*	0.07891	0.00110	0.20138	0.00317	2.18972	0.03835	0.89881	100	1170	27	1183	17	1178	12
17_3	m*	0.07795	0.00095	0.19833	0.00307	2.13019	0.03480	0.94752	99	1146	24	1166	17	1159	11
11_1	m	0.07884	0.00103	0.19902	0.00311	2.16200	0.03669	0.92081	100	1168	26	1170	17	1169	12
11_2	m	0.07922	0.00095	0.20510	0.00318	2.23887	0.03644	0.95260	99	1178	24	1203	17	1193	11
12_1	m	0.07998	0.00116	0.19811	0.00313	2.18340	0.03922	0.87956	101	1197	28	1165	17	1176	13
12_2	m	0.07900	0.00102	0.19723	0.00309	2.14698	0.03639	0.92434	100	1172	25	1160	17	1164	12
2_1	m	0.07960	0.00103	0.20036	0.00315	2.19776	0.03731	0.92609	100	1187	25	1177	17	1180	12
2_2	m	0.07890	0.00107	0.19463	0.00306	2.11605	0.03682	0.90355	101	1170	27	1146	17	1154	12
2_3	m	0.07980	0.00104	0.20545	0.00322	2.25910	0.03859	0.91751	100	1192	26	1205	17	1200	12
21_1	m	0.07974	0.00098	0.19855	0.00310	2.18163	0.03620	0.94095	101	1191	24	1168	17	1175	12
21_2	m	0.07859	0.00105	0.19231	0.00302	2.08262	0.03593	0.91024	101	1162	26	1134	16	1143	12
19_1	m	0.08013	0.00101	0.20053	0.00313	2.21426	0.03717	0.92982	101	1200	25	1178	17	1186	12
19_2	m	0.07978	0.00117	0.19241	0.00306	2.11524	0.03862	0.87105	102	1192	29	1134	17	1154	13
18C_1	m*	0.07886	0.00110	0.19695	0.00312	2.14025	0.03807	0.89059	100	1169	27	1159	17	1162	12
18C_2	m*	0.08057	0.00115	0.19906	0.00317	2.21022	0.03985	0.88325	101	1211	28	1170	17	1184	13
18C_3	m*	0.08018	0.00119	0.19504	0.00310	2.15510	0.03970	0.86281	102	1202	29	1149	17	1167	13
18B_1	m*	0.08011	0.00108	0.20457	0.00323	2.25845	0.03945	0.90391	100	1200	26	1200	17	1199	12

m, monazite located along grain boundaries of matrix minerals (excluding garnet); m*, monazite wholly included in cordierite or feldspar; g, monazite partially included within garnet; g* monazite wholly included within garnet.

samples K9 and K6, and between 0.15 and 0.19 in sample R2017275. Cr_2O_3 content is variable and does not appear to consistently correlate with variation in Zn content with ranges between 0.139 and 0.376 wt%. MnO content ranges between 0.84 and 2.34 wt%.

5.1.4 Magnetite

Magnetite in sample K9 has an Al_2O_3 content of 0.17–0.25 wt% which corresponds to X_{Al} (Al/(Al + Fe^{3+} + 2Ti)) of 0.003–0.006. The TiO_2 content varies between 0.00 and 0.09 wt%. Magnetite in sample K6 has an Al_2O_3 content of 0.19–0.22 wt% (X_{Al} = 0.005) and TiO_2 content of 0.00–0.01 wt%. Magnetite in sample R2017275 has an Al_2O_3 content of 0.18–0.48 wt% (X_{Al} = 0.005 to 0.020) and TiO_2 of 0.01–0.06 wt%. Lower Al_2O_3 contents (<0.19 wt%) in sample K9 and R2017275 correspond to analyses from magnetite occurring as symplectitic intergrowths with garnet, relative to matrix magnetite.

5.1.5 Feldspar

In all samples alkali feldspar is dominantly K-rich and Ca-poor with X_{An} (Ca/(Ca + Na + K)) of 0.00–0.02 and X_{Or} (K/(Ca + Na +K)) of 0.71–0.91. Plagioclase is Na-rich with X_{An} of 0.27–0.34 and X_{Or} of 0.00–0.02. The feldspar grains do not display any core–rim compositional variation.

5.1.6 Biotite

Biotite in sample K6 has moderate TiO_2 and low F contents with TiO_2 ranging from 1.84 to 1.94 wt% and F ranging from 0.22 to 0.31 wt%. X_{Fe} contents range from 0.46 to 0.48. Biotite in sample R2017275 has TiO_2 and F contents of 2.54–3.79 wt% and 3.52–4.24 wt%, respectively, and X_{Fe} ranges between 0.29 and 0.36. There is no apparent systematic compositional variability between biotite in different microstructural settings.

5.1.7 Ilmenite

Ilmenite has a MnO content of 2.30–4.76 wt%, 1.46–2.84 wt% and 2.78–4.09 wt% in samples K9, K6 and R2017275, respectively. Higher values of MnO in samples K9 and R2017275 (>3 wt%) correspond to analyses from ilmenite located in close proximity to garnet.

5.2 Trace element distribution in garnet

Trace element analyses were done by LA–ICP–MS on representative garnet grains from sample K9 (Table 3 and Figs. 7 and 8). Based on their microstructural context, crystals g2, g5 and g7 are inferred as part of the peak metamorphic garnet generation (refer to Section 3). These garnet grains have similar bell-shaped Y + HREE distributions with cores that are moderately to strongly enriched in elements Yb, Er, Dy, Gd, Lu and Y, relative to their rims (Fig. 8). Zonation in yttrium is particularly pronounced, varying ~1500–2000 ppm from core to rim. This trend is reflected by qualitative electron microprobe elemental mapping of yttrium in grain g2 (Fig. 6), and LA–ICP–MS REE mapping of g5 and g7 (Fig. 7). The distribution of LREE in g2 and g7 appear to broadly mirror observed trends for the HREE, albeit at lower absolute concentrations. However, for g5, the LREE distribution is essentially constant across the entire transect.

Crystal g4 is representative of the relict prograde garnet generation. Compared to g2, g5 and g7, garnet grain g4 shows a relatively flat trace element profile in both HREE and LREE although the yttrium concentration is still relatively high (Table 3; Fig. 8). Grain g6 features symplectitic intergrowths with magnetite. As such, g6 is interpreted as peak–retrograde. By contrast to the other analyses, the core to rim profile for this grain shows overall very low concentrations and comparatively flat compositional profiles in all HREE. However, yttrium is very slightly enriched within the core (~120 ppm) relative to the rim (~20 ppm). This trend is also mirrored by elements Er, Gd, Dy and Yb at a lower concentration, showing subtle increases by ~10–15 ppm, within the garnet core (Table 3 and Fig. 8).

5.3 LA–ICP–MS monazite geochronology

In situ monazite LA–ICP–MS was conducted on samples K9, K6 and R2017275 (Table 4 and Fig. 9). Monazite is abundant in all samples, typically occurring along the grain boundaries of cordierite, feldspar, sillimanite, magnetite and, when present, biotite. However, grains are also commonly hosted wholly within cordierite and feldspar, and away from obvious microfractures. In a rare example, in Sample K6, monazite forms a coarse-grained intergrowth (~250 μm) with densely aggregated and elongate sillimanite within the matrix (Fig. 10). In sample K9, monazite is also commonly partially included within garnet.

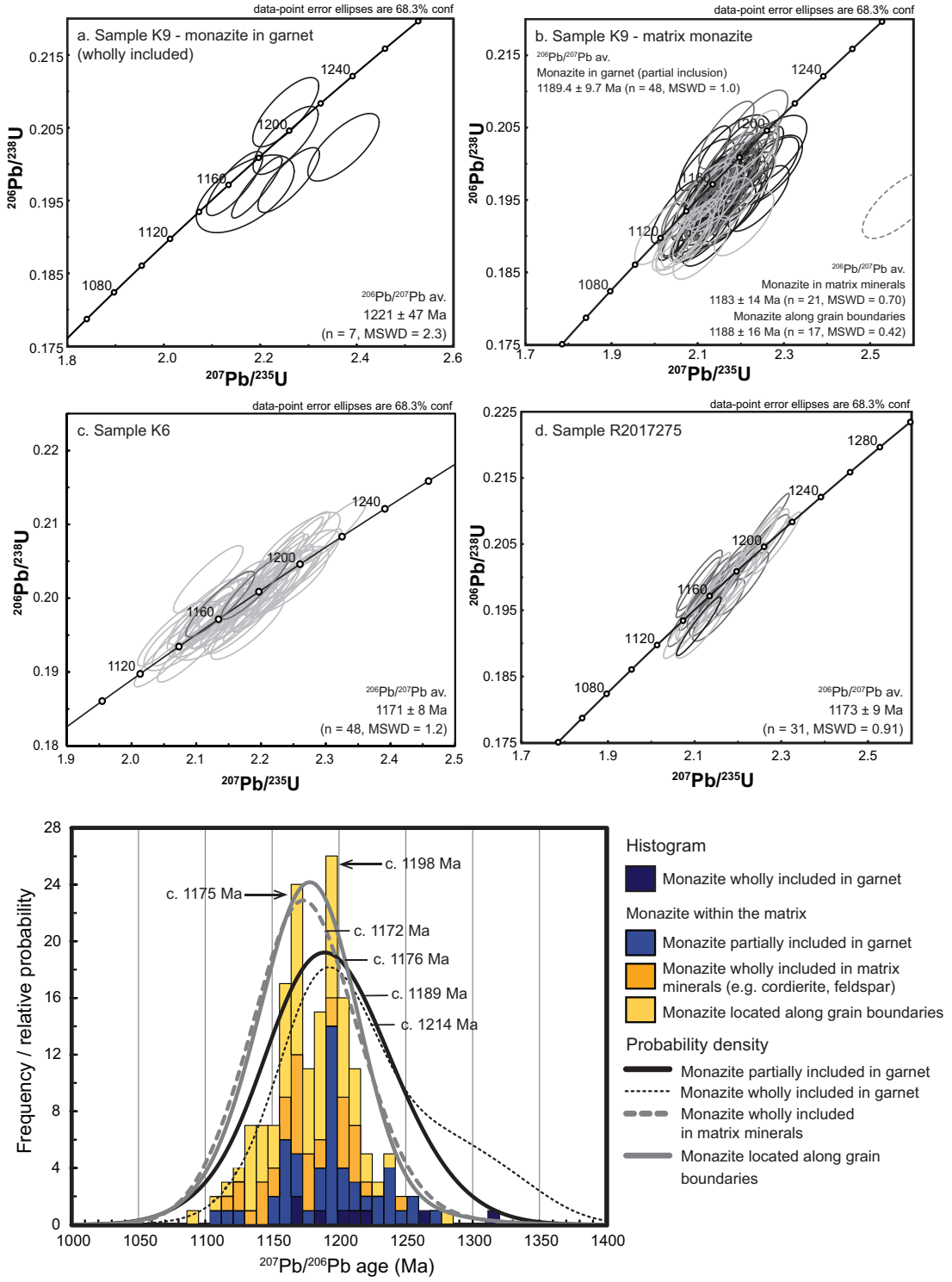

Figure 9. *In situ* LA–ICP–MS monazite U–Pb geochronology. Data are presented on U–Pb concordia diagrams: (a) Sample K9: monazite wholly included within garnet; (b) Sample K9: matrix monazite, inclusive of grains partially included in garnet, wholly included within matrix minerals (cordierite or feldspar), and monazite located along the grain boundaries of matrix minerals. Separate $^{207}Pb/^{206}Pb$ weighted average ages are given for each matrix monazite population for this sample. One discordant analysis (dashed grey ellipse; analysis K9B11C, Table 4) has been excluded from weighted mean calculations and the probability density plot; (c) Sample K6; (d) Sample R2017275. Weighted mean ages given for K6 and R2017275 are for the combined analyses from each sample. Light grey, medium grey and black ellipses represent analyses from monazite located along matrix grain boundaries, monazite wholly hosted within cordierite or feldspar, and monazite in garnet, respectively; (e) Histogram and probability density distribution plot for monazite age data from all microstructural settings, from all three samples. Collectively, the age data define two weak populations at 1198 ± 22 Ma and 1175 ± 6 Ma (approximate age peaks indicated by arrows). The combined weighted mean ages for each microstructural population are listed adjacent their respective probability density distribution.

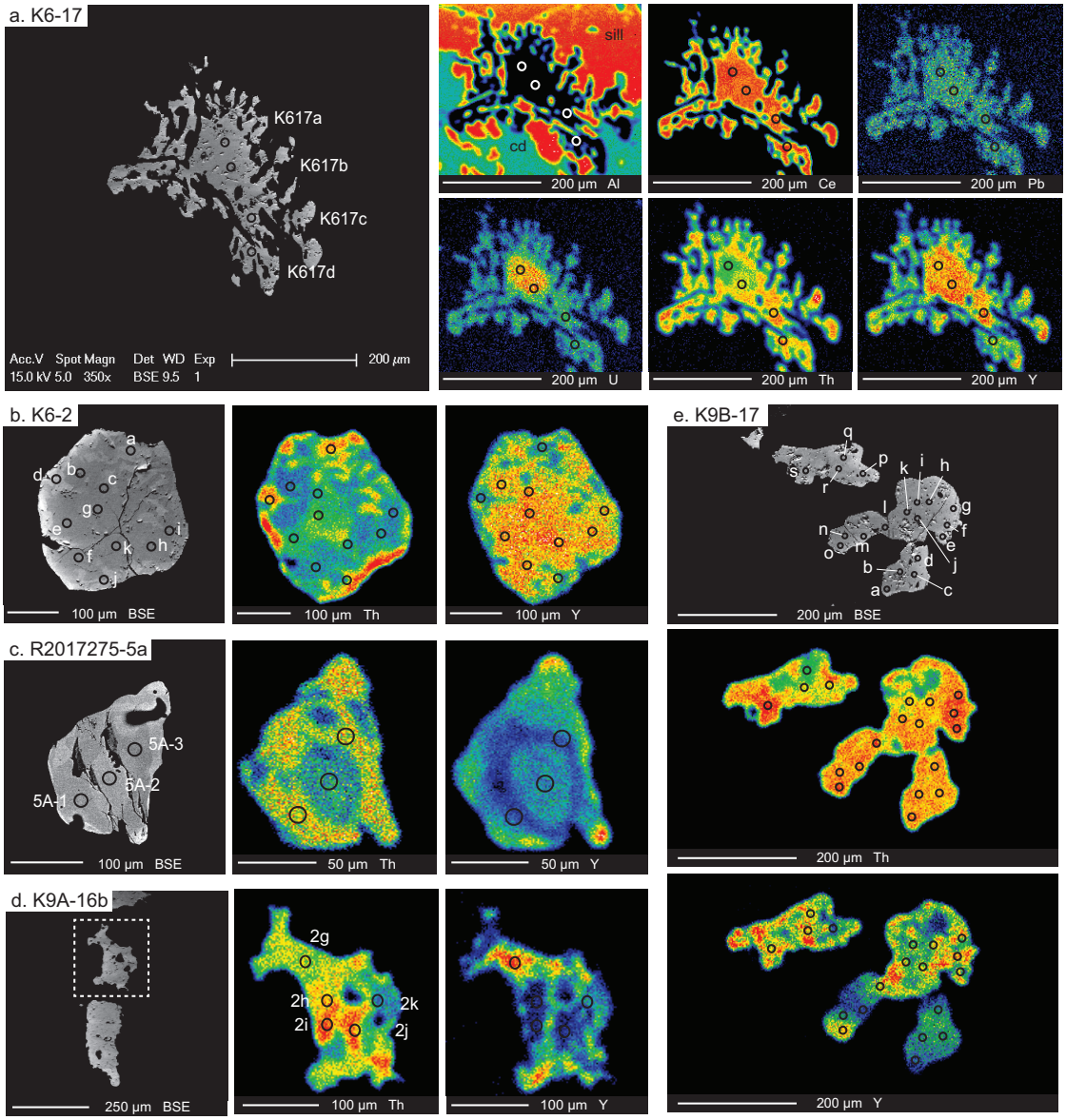

Figure 10. Backscatter electron (BSE) images, and yttrium and thorium X-ray compositional maps of representative monazite grains analysed in this study. A compositional map for Al is also presented in (a) to highlight the textural location of this monazite grain which is intergrown with sillimanite and cordierite in the matrix. The colour scale reflects relative count intensity, with warmer colours representing higher counts. The approximate location of age analysis spots are indicated as open circles (refer to Table 4). Some grains exhibit subtle core–rim zonation however most grains are multidomainal, with indistinct or patchy complex internal zonation which often lack definition in BSE imaging.

Monazite grains have an average size of 60–150 µm, and locally >250 µm. Wholly included grains are generally rounded to subrounded and elongate whereas monazite located along grain boundaries and monazite partially included within garnet are more irregularly shaped. Elongate monazite grains are typically oriented parallel to the foliation. Representative grains were analysed from all microstructural locations.

Compositional variation of monazite as revealed by BSE imaging is not systematic with some grains displaying core and rim type zonation, others with irregular internal variation, and the majority of grains apparently largely unzoned (Fig. 10). However, X-ray elemental mapping for Y, Th, U and Pb reveal that most grains are multidomainal, with complex and indistinct or patchy internal zonation that commonly lack definition in BSE imaging. Where subtle trends are observed in BSE imaging, variations appear to approximate relatively higher-Y chemical zones superimposed on Th and U compositional domains. In other studies, yttrium has primarily been utilised as an independent proxy for identifying different age domains within the monazite grains (e.g. Cubley

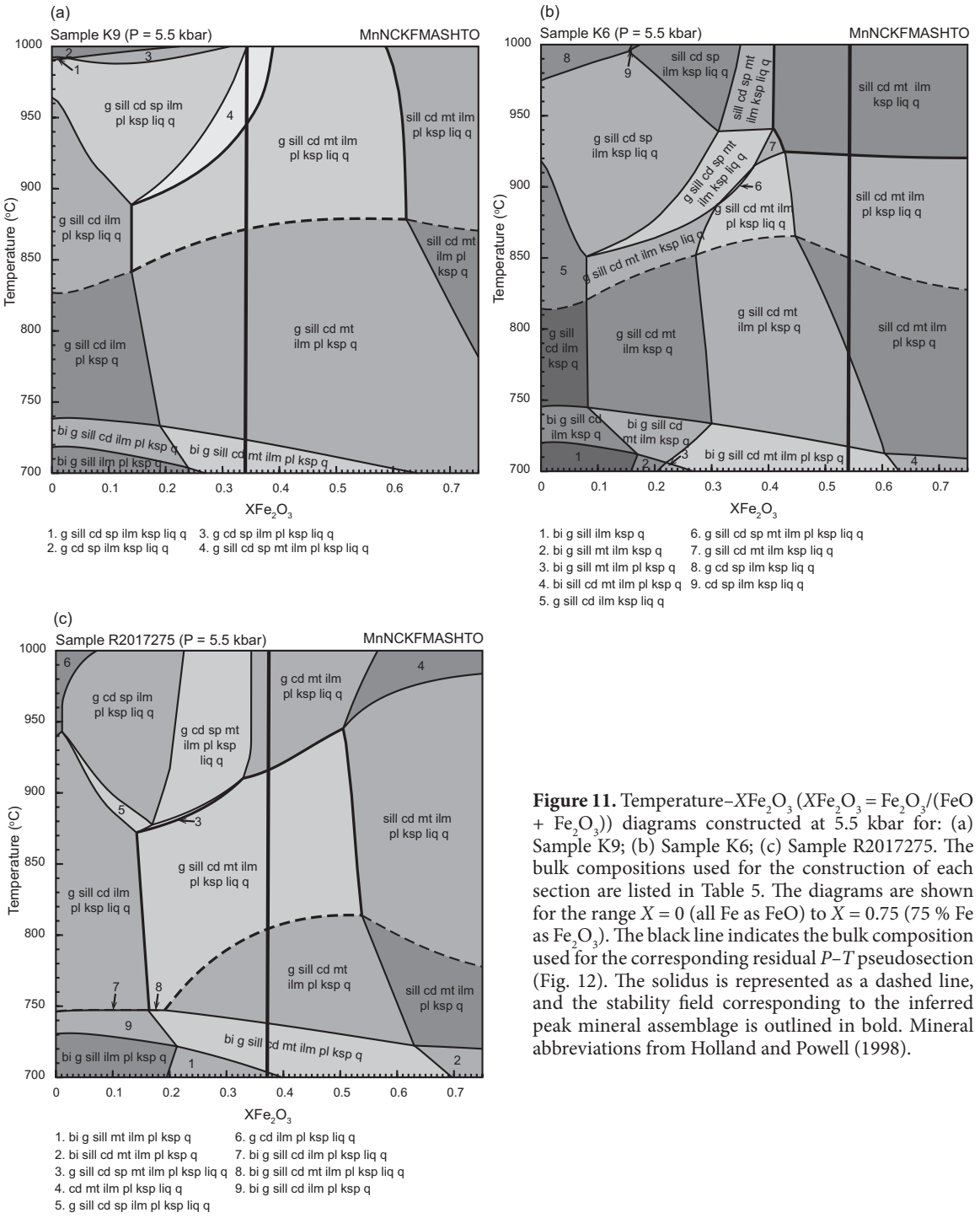

Figure 11. Temperature–XFe_2O_3 ($XFe_2O_3 = Fe_2O_3/(FeO + Fe_2O_3)$) diagrams constructed at 5.5 kbar for: (a) Sample K9; (b) Sample K6; (c) Sample R2017275. The bulk compositions used for the construction of each section are listed in Table 5. The diagrams are shown for the range $X = 0$ (all Fe as FeO) to $X = 0.75$ (75 % Fe as Fe_2O_3). The black line indicates the bulk composition used for the corresponding residual *P–T* pseudosection (Fig. 12). The solidus is represented as a dashed line, and the stability field corresponding to the inferred peak mineral assemblage is outlined in bold. Mineral abbreviations from Holland and Powell (1998).

et al., 2013; Cutts et al., 2013; Mahan et al., 2006; Pyle and Spear, 2003; Reno et al., 2012; Williams et al., 2007). However, the results obtained in this study suggest no apparent systematic relationship between age and internal compositional variability.

As all analyses yield ages older than 1000 Ma, weighted average calculations were made using the $^{207}Pb/^{206}Pb$ age. U–Pb analyses from all samples reveal a broad age spectrum with the majority of data ranging between ca. 1220 and 1135 Ma, and up to ca. 1280 Ma in sample K9 (analysis K9B3A; Table 4). The combined age data suggest two weakly defined populations by the 'unmixing' Isoplot (v. 3.75) algorithm (Ludwig, 2012) at 1198 ± 22 Ma and 1175 ± 6. The two oldest ages—a discordant analysis of ca. 1545 Ma (analysis K9B11C; Table 4), excluded from weighted average age calculations, and a concordant analysis of ca. 1318 Ma (analysis K9A8C; Table 4)—were obtained from monazite hosted wholly in feldspar and garnet, respectively. Collectively, the oldest

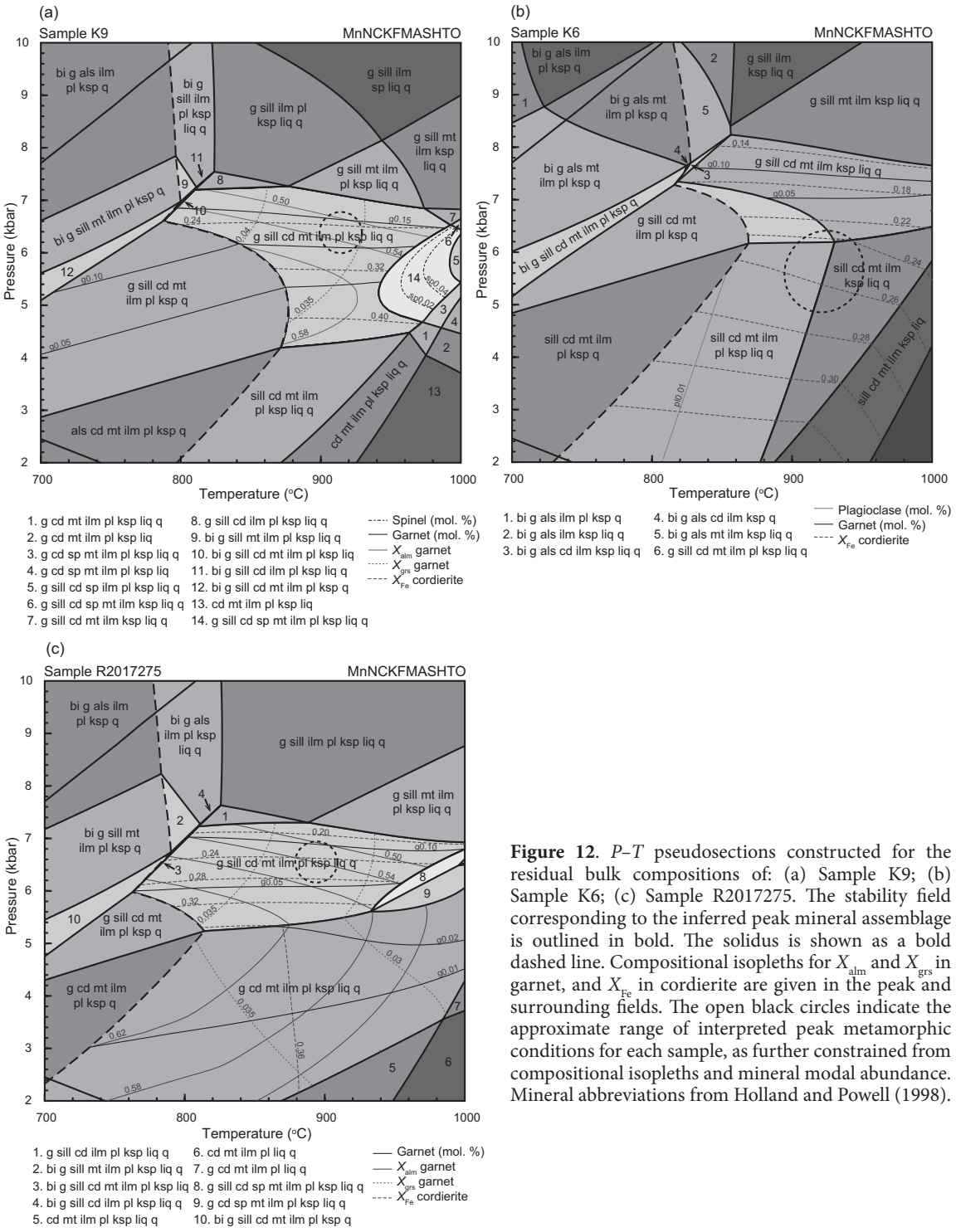

Figure 12. *P–T* pseudosections constructed for the residual bulk compositions of: (a) Sample K9; (b) Sample K6; (c) Sample R2017275. The stability field corresponding to the inferred peak mineral assemblage is outlined in bold. The solidus is shown as a bold dashed line. Compositional isopleths for X_{alm} and X_{grs} in garnet, and X_{Fe} in cordierite are given in the peak and surrounding fields. The open black circles indicate the approximate range of interpreted peak metamorphic conditions for each sample, as further constrained from compositional isopleths and mineral modal abundance. Mineral abbreviations from Holland and Powell (1998).

ages come from monazite hosted completely within garnet, yielding a combined $^{207}Pb/^{206}Pb$ weighted average age of 1214.0 ± 40 Ma (n = 8, MSWD = 2.2; Fig. 9). Matrix monazite, inclusive of grains partially included in garnet, wholly included within feldspar and/or cordierite, and located along grain boundaries, yield combined weighted average ages of 1189.0 ± 9.7 Ma (n = 48, MSWD = 1.0), 1172.2 ± 9.1 Ma (n = 38, MSWD = 0.90) and 1175.6 ± 6.3 Ma (n = 78, MSWD = 1.12), respectively (Fig. 9).

5.3.1 Sample K9

Fifty-five analyses were obtained from nine grains located partially and completely within garnet, and thirty-eight analyses from eight grains located within the foliated matrix (Table 4). Analyses from monazite completely armoured in garnet give a combined $^{207}Pb/^{206}Pb$ weighted average age of 1221 ± 47 Ma (n = 7; MSWD = 2.3). Analyses from matrix monazite partially hosted within garnet, grains wholly included in feldspar

Table 5. Bulk compositions used for phase equilibria modelling (mol. %)

Sample	Figure	Pseudosection	H_2O	SiO_2	Al_2O_3	CaO	MgO	FeO	K_2O	Na_2O	TiO_2	MnO	O
K9 (*X*=0)	11a	T–*X*Fe_2O_3	1.04	65.59	14.74	0.80	4.35	7.43	3.49	1.40	0.70	0.43	0.04
K9 (*X*=1)			0.97	63.32	14.23	0.77	4.19	7.17	3.37	1.34	0.68	0.40	3.55
K6 (*X*=0)	11b	T–*X*Fe_2O_3	1.55	61.28	17.40	0.29	5.36	9.24	3.02	0.83	0.79	0.19	0.05
K6 (*X*=1)			1.48	58.63	16.65	0.28	5.13	8.83	2.88	0.79	0.76	0.18	4.37
R2017275 (*X*=0)	11c	T–*X*Fe_2O_3	1.00	73.53	10.58	1.34	2.84	5.18	2.72	2.00	0.58	0.21	0.03
R2017275 (*X*=1)			0.98	71.72	10.33	1.30	2.76	5.05	2.65	1.95	0.56	0.20	2.50
K9	12a and 13	P–T (residual)	1.01	64.82	14.57	0.79	4.30	7.34	3.45	1.38	0.70	0.42	1.23
K6	12b	P–T (residual)	1.51	59.85	17.00	0.29	5.23	9.02	2.95	0.81	0.77	0.19	2.38
R2017275	12c	P–T (residual)	0.99	72.86	10.49	1.33	2.81	5.13	2.69	1.98	0.57	0.21	0.94
K9 (*M*=0)	14a	T–M_{melt}	1.01	64.82	14.57	0.79	4.30	7.34	3.45	1.38	0.70	0.42	1.23
K9 (*M*=1)			13.12	70.12	8.57	0.82	0.40	1.15	2.42	3.69	0.09	0.04	0.19
K6 (*M*=0)	14b	T–M_{melt}	1.51	59.85	17.00	0.29	5.23	9.02	2.95	0.81	0.77	0.19	2.38
K6 (*M*=1)			13.12	70.12	8.57	0.82	0.40	1.62	2.42	3.69	0.09	0.04	0.43
R2017275 (*M*=0)	14c	T–M_{melt}	0.99	72.86	10.49	1.33	2.81	5.13	2.69	1.98	0.57	0.21	0.94
R2017275 (*M*=1)			13.12	70.12	8.57	0.82	0.40	1.21	2.42	3.69	0.09	0.04	0.22
K9	15a	P–T (melt-reintegrated)	1.85	65.16	14.15	0.79	4.03	6.91	3.38	1.54	0.66	0.39	1.16
K6	15b	P–T (melt-reintegrated)	2.08	60.32	16.57	0.32	4.99	8.65	2.92	0.95	0.74	0.18	2.28
R2017275	15c	P–T (melt-reintegrated)	1.71	72.67	10.37	1.30	2.67	4.89	2.67	2.08	0.54	0.20	0.90

or cordierite, and grains located along grain boundaries, yield respective $^{207}Pb/^{206}Pb$ weighted mean average ages of 1189.4 ± 9.7 Ma (*n* = 48; MSWD = 1.0), 1183 ± 14 Ma (*n* = 21; MSWD = 0.70) and 1188 ± 16 Ma (*n* = 17; MSWD = 0.42). The overall $^{207}Pb/^{206}Pb$ weighted average age for this sample gives a mean of 1190.0 ± 6.9 Ma (*n* = 93, MSWD = 1.07). Analyses are plotted on a U–Pb concordia diagram (Fig. 9a and b).

5.3.2 Sample K6

Forty-six analyses were done on eights grains located along grain boundaries within the foliated matrix, and two analyses, yielding ages of 1143 ± 26 Ma and 1169 ± 25 Ma, from one grain wholly included in matrix minerals (Table 4). The $^{207}Pb/^{206}Pb$ weighted average age for the total sample gives a mean age of 1171 ± 8 Ma (*n* = 48, MSWD = 1.20). The analyses are plotted on a U–Pb concordia diagram (Fig. 9c). In a rare example, monazite is intergrown with elongate sillimanite and cordierite in the matrix (analysis K617, Table 4 and Fig. 10a). This grain displays a comparatively high-Y discrete core and lower-Y rim region. Three analyses of the high-Y core yield ages between ca. 1208 and 1213 Ma, and one spot analysis from the outer domain gives a younger age of ca. 1176 Ma. However, the spindly nature of the low-Y part of the grain intergrown with sillimanite precludes more analyses from this outer region.

5.3.3 Sample R2017275

Thirty analyses were obtained from 10 monazites within the matrix, and one analysis from one grain located wholly within garnet (Table 4). Monazite wholly included within feldspar or cordierite, and grains located along grain boundaries of matrix minerals yield combined weighted average ages of 1166 ± 13 Ma (*n* = 15; MSWD = 1.07) and 1180 ± 13 Ma (*n* = 15; MSWD = 0.69), respectively. The $^{207}Pb/^{206}Pb$ weighted average age for the total sample gives a mean of 1173 ± 8.9 Ma (*n* = 31, MSWD = 0.91). The data are shown on a U–Pb concordia plot (Fig. 9d).

5.4 Pressure–temperature conditions

Pressure–temperature pseudosections were calculated for samples K9, K6 and R2017275. The compositions used for calculating each section are provided in Table 5.

Electron microprobe data indicate that spinel contains up to ~6 wt% ZnO (Table 2). Studies have demonstrated that Zn and Cr may enhance spinel stability such that in reality, spinel is stabilised to lower temperatures and higher pressures (e.g. Nichols et al., 1992; Sengupta et al., 1991; Stoddard, 1979; Tajčmanová et al., 2009b). However, in this study, the absolute *P–T* shift as a result of high Zn cannot be quantified with phase equilibria modelling in the absence of comprehensive models for the thermodynamics of Zn-bearing solid solutions. Electron microprobe data also indicate that biotite contains high concentrations of F and Ti which similarly, at granulite facies conditions, enhances biotite stability to higher temperature (e.g. Peterson et al., 1991; Tajčmanová et al., 2009a). However, the

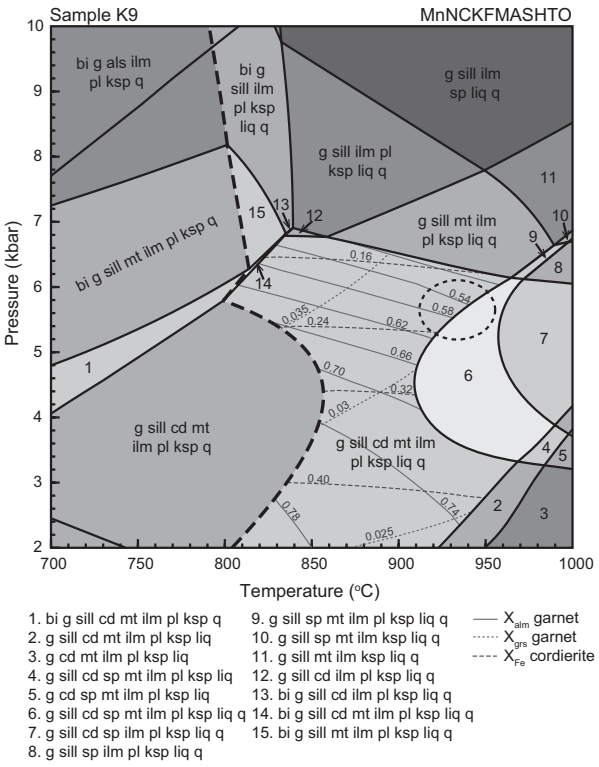

Figure 13. *P–T* pseudosection constructed for the residual bulk composition of sample K9 using the updated thermodynamic dataset, ds62, and re-parameterized *a–x* models. Compositional isopleths for X_{alm} and X_{grs} in garnet, and X_{Fe} in cordierite are given in the peak field. Peak *P–T* conditions (represented by an open black circle) approximate those estimated from the residual bulk composition pseudosection calculated using dataset ds55 and existing *a–x* models, for this sample (Fig. 12a).

absolute temperature effect of fluorine in biotite in specific bulk rock compositions is also currently poorly quantified.

5.4.1 Temperature–XFe$_2$O$_3$ sensitivity analysis

Temperature–XFe$_2$O$_3$ pseudosections were calculated to evaluate the effect of ferric iron (over the range of all Fe as FeO (X = 0) to all Fe as Fe$_2$O$_3$ (X = 1)), on the stability of the preserved peak mineral assemblage and to constrain the ferric iron content of bulk compositions used for *P–T* pseudosection calculations (Fig. 11). Garnet, magnetite and spinel stability are sensitive to variation in the amount of Fe$_2$O$_3$. Garnet occurs in comparatively reduced compositions whereas magnetite stability is favoured by oxidised compositions. The stability of cordierite and biotite is increased slightly to lower temperatures, and the position of the solidus is not significantly affected by variation in Fe$_2$O$_3$. Fe–Ti oxides occur over the entire compositional and temperature range. Ilmenite senso lato is present as the sole Fe–Ti oxide under reduced conditions, with the addition of magnetite at XFe$_2$O$_3$ >0.1–0.2. Increasing XFe$_2$O$_3$ over the interval 0.0 to 0.2 stabilises spinel-bearing assemblages at temperatures >850 °C. However, increasing XFe$_2$O$_3$ >0.4 results in the presence of magnetite at the expense of spinel at this pressure. Microtextural relationships showing spinel grains always directly adjacent to magnetite in all samples suggests that spinel exsolved from a magnetite-rich, magnetite–spinel solid solution upon cooling and thus it is likely that spinel did not form part of the peak mineral assemblage. Therefore, it seems reasonable that the amount of ferric iron in these samples is moderate to allow for the occurrence of magnetite, but not spinel, in the peak mineral assemblage. The selected XFe$_2$O$_3$ values (refer to Section 4.3) from the *T–X* diagram are complemented by constraints on bulk Fe$_2$O$_3$ content provided by combining recalculated electron microprobe mineral composition analyses (Droop, 1987) with the approximate abundance of minerals in each sample (Table 2). In all samples, if the amount of ferric iron was slightly higher or lower than used for the calculation of the *P–T* pseudosection, the peak temperatures would remain very similar due to the relative insensitivity of the boundaries of the peak assemblage field over varied XFe$_2$O$_3$ (Fig. 11).

5.4.2 Residuum bulk composition P–T pseudosections

Pressure–temperature pseudosections for the residuum bulk compositions (i.e. no melt reintegration) of samples K9, K6 and R2017275 calculated using dataset ds55 and the existing *a–x* models, are presented in Fig. 12. The three pseudosections are similar, consistent with the general similarities in petrography and the

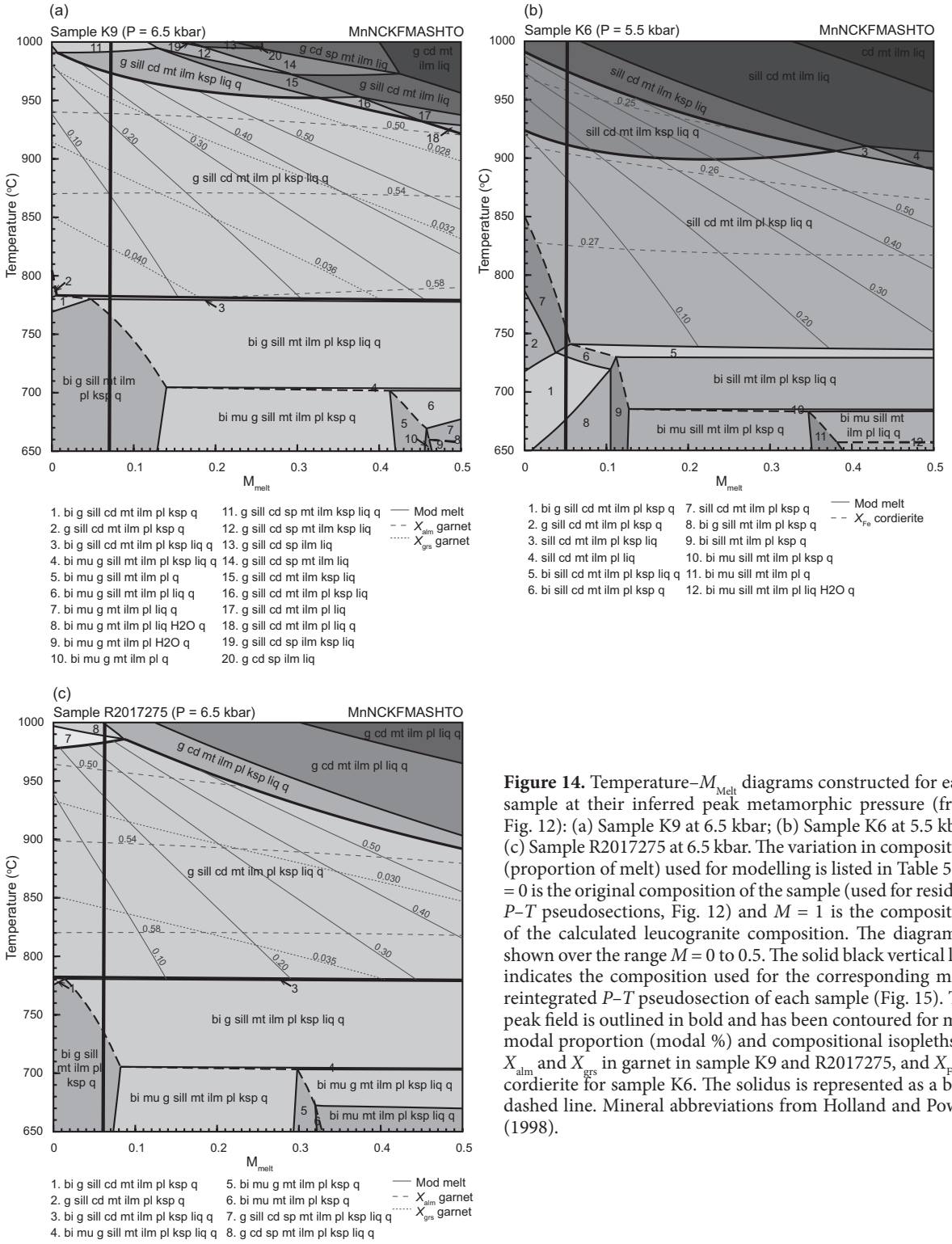

Figure 14. Temperature–M_{Melt} diagrams constructed for each sample at their inferred peak metamorphic pressure (from Fig. 12): (a) Sample K9 at 6.5 kbar; (b) Sample K6 at 5.5 kbar; (c) Sample R2017275 at 6.5 kbar. The variation in composition (proportion of melt) used for modelling is listed in Table 5. M = 0 is the original composition of the sample (used for residual P–T pseudosections, Fig. 12) and M = 1 is the composition of the calculated leucogranite composition. The diagram is shown over the range M = 0 to 0.5. The solid black vertical line indicates the composition used for the corresponding melt-reintegrated P–T pseudosection of each sample (Fig. 15). The peak field is outlined in bold and has been contoured for melt modal proportion (modal %) and compositional isopleths of X_{alm} and X_{grs} in garnet in sample K9 and R2017275, and X_{Fe} in cordierite for sample K6. The solidus is represented as a bold dashed line. Mineral abbreviations from Holland and Powell (1998).

textural relationships observed in each sample. Pseudosections for the three samples show solidus temperatures in excess of approximately 800 °C. The garnet stability field is large, extending above approximately 3 kbar and 5 kbar at 700 °C in samples K9 and K6, respectively. With increasing temperature, garnet is stable at slightly higher pressures. In sample R2017275, garnet is stable across the pseudosection except at the highest temperatures (>900 °C) at low pressure (<4 kbar). In sample K6, the plagioclase stability field is broadly V-shaped and is stable below ~900 °C at pressures less than ~6 kbar. The range of pressures for plagioclase stability widens as temperature decreases.

In sample K9, the interpreted peak metamorphic assemblage of garnet–cordierite–sillimanite–

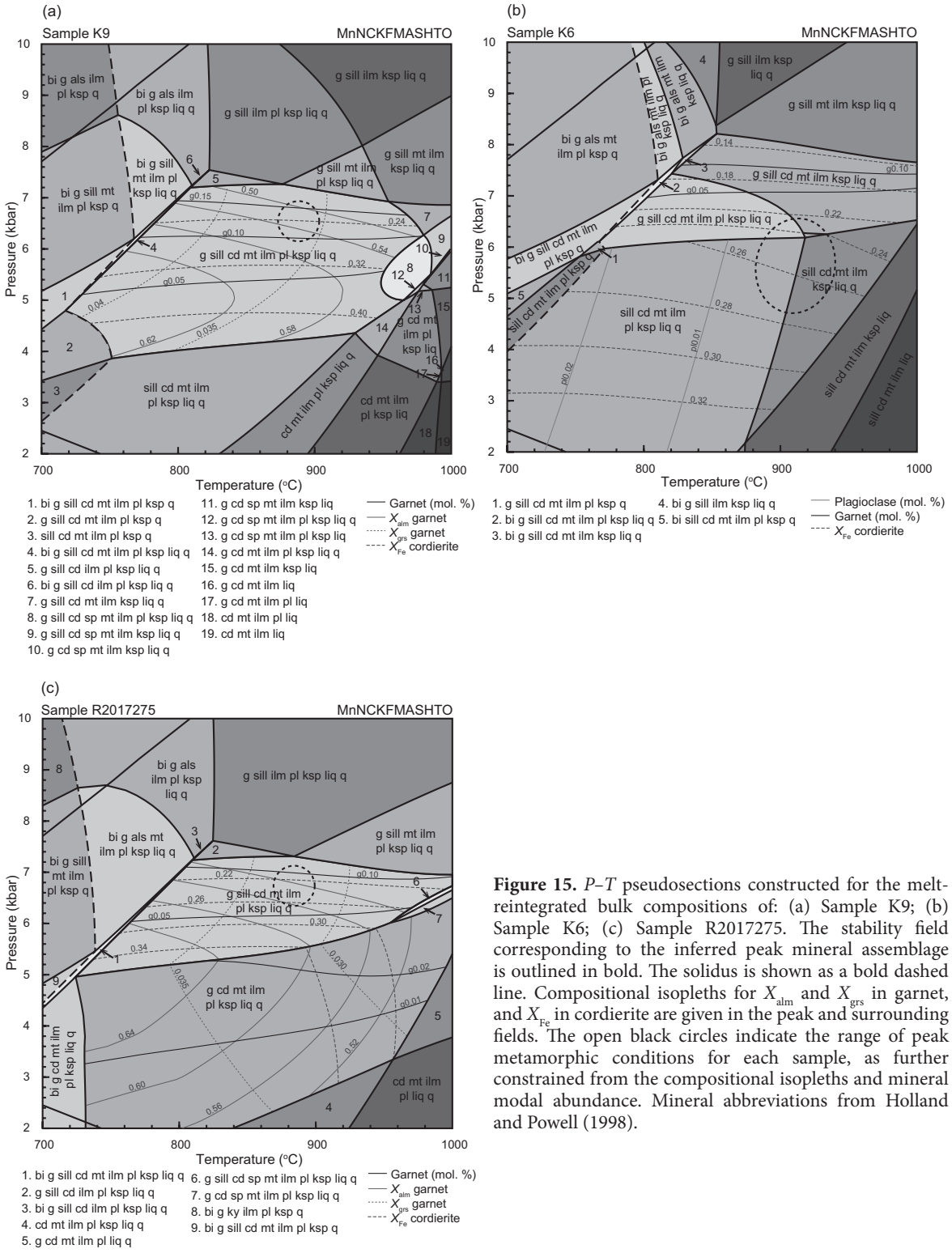

Figure 15. *P–T* pseudosections constructed for the melt-reintegrated bulk compositions of: (a) Sample K9; (b) Sample K6; (c) Sample R2017275. The stability field corresponding to the inferred peak mineral assemblage is outlined in bold. The solidus is shown as a bold dashed line. Compositional isopleths for X_{alm} and X_{grs} in garnet, and X_{Fe} in cordierite are given in the peak and surrounding fields. The open black circles indicate the range of peak metamorphic conditions for each sample, as further constrained from the compositional isopleths and mineral modal abundance. Mineral abbreviations from Holland and Powell (1998).

magneittess–ilmenite–plagioclase–K-feldspar–quartz–silicate melt is stable over a broad *P–T* range between ~4.2–7.4 kbar at 800–980 °C (Fig. 12a). Sample R2017275 has the same inferred peak metamorphic assemblage as sample K9 and is modelled to be stable between ~5.4 and 7.3 kbar at approximately 780–1000 °C (Fig. 12c). In both pseudosections, the peak assemblage field is bound by the solidus and spinel-bearing assemblages to lower and higher temperatures, respectively. Cordierite- and magnetite-absent assemblages occur to higher pressures. The presence of garnet in sample K9, and sillimanite in sample R2017275, constrains the lower pressure limit.

Sample K6 is a garnet-absent metapelite with the inferred peak mineral assemblage cordierite–sillimanite–magnetitess–ilmenite–K-feldspar–

quartz–silicate melt (Fig. 12b). This assemblage is stable in a triangular field. At its widest point at ~6 kbar, this field extends from 930 to 1030 °C, and the temperature range of the stability field narrows and decreases with decreasing pressure. The absence of plagioclase and the abundance of quartz in the peak assemblage of this sample constrain the lower and higher temperature limits of the peak field, respectively. The absence of garnet places an upper pressure constraint of ~6 kbar.

The peak assemblage fields are stable over a wide *P–T* range and do not tightly constrain the peak metamorphic conditions. However, mineral modal abundance, and compositional isopleths of garnet (X_{alm} and X_{grs}) and cordierite (X_{Fe}) can be used to provide additional constraints. Importantly, garnet and cordierite do not show any appreciable major element compositional zonation in these samples. The intersection of X_{Fe} cordierite and X_{alm} garnet compositional isopleths constrain the peak metamorphic conditions to ~900 °C and 6.5 kbar for samples K9 and R2017275. Reasoning for why the measured compositions of the minerals are believed to largely reflect peak *P–T* conditions is provided in the discussion (Section 6.2). A slight discrepancy is observed between the measured and calculated X_{grs} garnet values for all garnet-bearing samples. Electron microprobe data for X_{grs} yield values in the range 0.027–0.031 for sample K9 and 0.022–0.026 for sample R2017275, and calculated isopleths for X_{grs} values in these ranges suggest slightly higher temperatures (i.e. ~980 °C) than that given above. This temperature estimate is inconsistent with the interpretation that spinel is absent from the peak assemblage (refer also to Section 5.3.1). Compositional isopleths for X_{Fe} in cordierite constrain peak conditions to the range ~910–990 °C at ~4.0–6.0 kbar for sample K6.

The *P–T* pseudosection calculated for the residual bulk composition of sample K9 using the updated thermodynamic dataset ds62 and re-parameterized *a–x* models, is presented in Fig. 13 (compare with Fig. 12a). The two pseudosections for the residual bulk composition of sample K9 are similar, however, in Fig. 13, the garnet stability field is expanded significantly to lower pressures, compared with Figure 12a. Consequently, the interpreted peak metamorphic assemblage of garnet–cordierite–sillimanite–magneitte$_{ss}$–ilmenite–plagioclase–K-feldspar–quartz–silicate melt is stabilised over a much broader *P–T* range (~800–960 °C; <6.6 kbar). In Fig. 13, within the peak mineral assemblage field, the composition of cordierite is also predicted to be slightly more Mg-rich, and the composition of garnet as slightly more almandine-rich and grossular-depleted. The location of X_{Fe} cordierite, and X_{alm} and X_{grs} garnet compositional isopleths broadly constrain the peak *P–T* conditions to between ~900 and 930 °C and ~5–6 kbar, which approximate the *P–T* estimates from Figure 12a, for this sample.

5.4.3 Temperature–M_{melt} sensitivity analysis

Calculated *T–*M_{melt} and *P–T* pseudosections for the melt-reintegrated bulk compositions of the three samples are presented in Figs. 14 and 15, respectively. The constructed *T–*M_{melt} pseudosections show that the melt reintegration primarily affects the temperature of the solidus (Fig. 14). Increasing melt abundance (towards *M* = 1) results in a more hydrated composition and thus the position of the solidus is shifted to lower temperature, until the composition becomes water saturated at approximately 650 °C. However, after the integration of <5 % melt, the lower temperature boundary of the peak metamorphic field is instead provided by the biotite-out boundary, and not the solidus, in sample K9 and R2017275 (Fig. 14a and c). The melt sensitivity analysis also shows that for the relatively minor amounts of melt reintegrated (~7 mol%) to account for the potential existence of melt remaining in these rocks after the thermal maxima, although there is a significant shift in the position of the solidus, there is minimal change to the stability of the suprasolidus mineral equilibria. Mainly, the range of stable temperatures of the peak mineral assemblage field is extended and plagioclase becomes stable to slightly higher temperatures at higher pressure (Fig. 15). Contouring for X_{alm} in garnet and X_{Fe} in cordierite in the peak field of each sample also reflects the relative insensitivity of the melt reintegration on the Fe content of the bulk composition (Fig. 14), and therefore results in similar peak *P–T* estimates to those obtained from the residual bulk composition pseudosections (Figs. 12 and 15). Furthermore, Fig. 14 shows that for the reintegration of much higher volumes of melt into the residual bulk composition (i.e. >>7 mol%), the suprasolidus pseudosection topology is likewise not altered to any great degree and that the peak temperatures would remain very similar due to relative insensitivity of the boundaries of the peak mineral fields over varied Mmelt content.

6. DISCUSSION

The aim of this study is to provide greater understanding of the thermal conditions and duration of Grenvillian-aged metamorphism in the eastern Musgrave Inlier. This has been done through integration of *in situ* geochronology and mineral chemistry with calculated pseudosections.

6.1 Duration of high-temperature conditions

The U–Pb monazite geochronology obtained in this study is characterised by a spread of concordant analyses ranging predominantly between ca. 1220 and 1135 Ma (Table 4 and Fig. 9), and extending to ca. 1280 Ma in sample K9. These ages broadly correspond to the timing of the Musgrave Orogeny (ca. 1220–1140 Ma) as established from U–Pb SHRIMP zircon geochronology of the felsic magmatic Pitjantjatjara Supersuite (Howard et al., 2015; Smithies et al., 2011), and existing geochronology from the eastern Musgrave Inlier (Camacho and Fanning, 1995; Dutch et al., 2013). The spread of ages is also akin to constraints from metapelitic rocks in the west Musgrave Inlier which collectively suggest >80 Myr of high-*T* conditions (Walsh et al., 2014). The few analyses obtained in this study that are significantly older than ca. 1280 Ma are possibly relict detrital ages on the basis of U–Pb zircon geochronology from metapelitic rocks in the east Musgrave Inlier (Dutch et al., 2013; L. Jagodinski, personal communication, September 2014).

Determining the precise duration of high-*T* metamorphism is often problematic, in part, owing to difficulties in directly linking geochronology to the *P–T* data (Halpin et al., 2012; Kelly and Harley, 2005; Kelsey and Hand, 2015; Korhonen et al., 2013; Walsh et al., 2014). Collectively, the age data from this study suggest an apparent bimodality with two weakly defined populations at ca. 1198 Ma and ca. 1175 Ma (Fig 9e). Howard et al. (2015) and Smithies et al. (2011) indicate that although felsic magmatism was largely continuous from ca. 1220–1140 Ma, crystallisation ages of the Pitjantjatjara Supersuite granites in the west Musgrave Inlier form at least four distinctive magmatic peaks over this period. Significantly, discrete age peaks are also observed from metamorphic zircon overgrowths in the igneous rocks, consistently offset ~5–10 Myr younger than each distinct magmatic peak (Howard et al., 2015; Smithies et al., 2011). These findings are suggestive of a causal relationship between magmatism and post-intrusion metamorphism of the surrounding country rock. The two largest metamorphic age peaks in the zircon data from the west Musgrave Inlier occur at ca. 1190 Ma and ca. 1170 Ma (Howard et al., 2015; Smithies et al., 2011) which are within error of the two peaks in the age data in this study. Magmatic zircons from Pitjantjatjara Supersuite granitoids in the eastern Musgrave Inlier (Fig. 3) yield slightly younger crystallisation ages than those from the west Musgrave Inlier, with ages ranging between 1136 ± 3 Ma and 1155 ± 14 Ma (Dutch et al., 2013). However, the latter age is also within error of the ca. 1175 Ma population in this study. In contrast to Smithies et al. (2011), U–Pb geochronology of zircon overgrowths from orthogneisses of the Birksgate Complex in the east Musgrave Inlier (Fig. 3) suggest that the onset of metamorphism predated magmatism by ~7 Myr (Dutch et al., 2013), however, the geochronological dataset from this region is considerably smaller than that from the west Musgrave Inlier. It is plausible that shorter–lived thermal pulses of high-*T* metamorphism in the eastern Musgrave Inlier are potentially linked to the regionally synchronous intrusion of the Pitjantjatjara Supersuite granites, providing justification of the observed bimodality in the geochronological data.

Monazite ages from high-grade rocks have typically been argued to reflect the age at which the elevated solidus is approached and crossed during cooling (~700 °C), thereby recording only part of the retrograde rock evolution (Kelsey et al., 2008; Kelsey and Hand, in press; Roberts and Finger, 1997; Vavra and Schaltegger, 1999; Yakymchuk and Brown, 2014). However, experimental work has demonstrated that monazite closure temperatures to Pb diffusion are similar to those observed in zircon (>900 °C; Cherniak, 2010; Cherniak and Watson, 2001; Cherniak et al., 2004), and potentially in excess of 1050 °C (Sajeev et al., 2010). Moreover, under extreme thermal conditions, Stepanov et al. (2012), Yakymchuk and Brown (2014), and Kelsey et al. (2008), predict that monazite can survive to extreme temperatures without complete dissolution into melt. Consequently, monazite may be partially resilient at extreme temperatures, with sluggish Pb diffusion resulting in the partial preservation of growth ages. This may be particularly true for 'dry' systems having previously undergone significant melt loss (e.g. Korhonen et al., 2013;

Walsh et al., 2014), with the age data consequently interpreted to record the protracted and continuous growth and recrystallization of monazite (and zircon) over a temperature range incorporating the entire prograde to retrograde rock evolution at UHT conditions (Korhonen et al., 2013; O'Brien and Miller, 2014; Walsh et al., 2014). In the present case, such an interpretation that monazite ages reflect prograde growth and recrystallization ages rather than cooling ages may explain the large gap between the oldest monazite ages (ca. 1280 Ma) that are not interpreted as detrital ages, and the onset of the Musgrave Orogeny (ca. 1220 Ma). Similarly, monazite growth occurring during cooling and melt crystallisation may also provide justification of age analyses younger than termination of magmatism during the Musgrave Orogeny (ca. 1140 Ma). However, it is also plausible that the observed age array reflects a combination of growth and recrystallization as well as protracted alteration (Pb diffusion) processes if Pb diffusion in monazite at high temperatures (>900 °C) is considered an effective process (e.g. Halpin et al., 2012). Clearly, there are several mechanisms which may explain the widespread distribution of U–Pb age data in this study. Regardless, the overall spread of age data could be used to imply that high-*T*, suprasolidus conditions existed for a long period (>70 Myr) in the eastern Musgrave Inlier, albeit potentially also associated with a pulsed thermal regime.

Compositional mapping of yttrium in peak metamorphic garnet shows the preservation of prograde-style growth zonation (Carlson, 2012; Moore et al., 2013; Pyle and Spear, 1999) with a moderately high-Y core and a relatively low-Y rim (Figs. 6, 7). Several studies have tied the distribution of yttrium in metamorphic garnet to the evolution of accessory phases such as xenotime, monazite, zircon and apatite (e.g. Foster et al., 2000; Gibson et al., 2004; Pyle and Spear, 1999, 2003). However, in the present instance, there is no overall systematic correlation between yttrium distribution in garnet and monazite. The relative yttrium contents of monazite are variable, with grains often displaying complex internal zonation, and no apparent systematic relationship between composition and age. This is not interpreted to be directly related to large-scale changes in the temporal or tectonic conditions. Rather, it is possible that the progressive growth and recrystallization of monazite, and therefore the internal compositional variation, and the large span of ages recorded within both individual grains and overall, is also influenced strongly by microstructural location. Specifically, monazite growth in these rocks may also be controlled by proximity to garnet porphyroblasts and the presence and crystallisation of REE–Th–Y-bearing melt (Catlos, 2013; Hinchey et al., 2007; Kelly et al., 2006, 2012; Reno et al., 2012).

6.2 Evaluation of pressure–temperature conditions

The rocks from the eastern Musgrave Inlier are interpreted to have undergone partial melting and melt loss as suggested by an abundance of leucosomes in outcrop. Therefore, they preserve a relatively anhydrous peak metamorphic mineral assemblage as further substantiated by the low abundance of biotite. In high-grade metasedimentary rocks, melt loss is typically interpreted to occur on the prograde path and melt production to have been complete by peak metamorphic (thermal) conditions (Brown, 2002; Kelsey and Hand, 2015; Powell and Downes, 1990; Sawyer, 2001; White and Powell, 2002). This is supported in this instance by an abundance of leucosomes oriented parallel to structural fabrics. However, estimating the proportion of prograde melt loss and therefore the likely bulk rock composition at prograde to near-peak conditions is often difficult (Kelsey and Hand, 2015) and has not been compositionally accounted for in this study. While it is valid that melt production may be complete by the thermal maxima, this is not necessarily also true for melt loss which may continue during the retrograde *P–T* evolution. The rocks of the eastern Musgrave Inlier preserve evidence for melt loss occurring after the peak of metamorphism in the form of leucosomes with sub-diffuse boundaries that are oriented discordant to the main structural fabric. In this study, the potential existence of some melt remaining in the rock after the thermal peak, is compositionally accounted for using calculated $T–M_{melt}$ pseudosections (Anderson et al., 2013). Approximately 7 mol% melt is reintegrated into the residual bulk composition of each sample. This value corresponds to the melt connectivity threshold at which the melt volume is deemed sufficient to migrate from the rock via an interconnected system of leucosomes (Rosenberg and Handy, 2005). Melt volumes less than ~7 mol% may be partially retained within the rock due to less efficient melt extraction

networks resulting in decreased rock strength and consequently increased deformation rate and heat transfer through advection (e.g. Brown, 2007a; Brown and Korhonen, 2009). The reintegration of a low proportion of melt in this instance is consistent with field observations which reflect a low proportion of discordant leucosomes and therefore the inferred presence of relatively low volumes of melt after the thermal peak. However, it is probable that, at least during the prograde evolution, the rocks experienced several melt extraction events during cyclical periods of melt accumulation and loss, dehydrating the rock and enabling the attainment of HT–UHT conditions (Brown and Korhonen, 2009). Collectively, the calculated residual and melt-reintegrated *P–T* pseudosections (Figs. 12 and 15) can be used to reliably obtain quantitative information regarding the peak to post-peak rock evolution.

In these rocks, the abundance of cordierite, the external Fe–Mg reservoir to garnet, is infinite relative to garnet and the size of the garnet grains are comparatively small. Therefore, there is considerable potential for the garnet to be compositionally reset under high-*T* conditions. Due to the potential for retrograde Fe–Mg exchange between garnet and neighbouring minerals during cooling, Fe–Mg thermometry and compositional isopleths may therefore not reliably record the peak *P–T* conditions in granulite facies rocks (e.g. Fitzsimons and Harley, 1994; Frost and Chacko, 1989; Pattison and Bégin, 1994; Pattison et al., 2003). However, in this instance, even if complete retrograde resetting of garnet is allowed and has occurred, the preserved compositions still reflect that garnet grew at very high temperatures because the location of the relevant isopleths in *P–T* space occur at a high temperature (~900 °C; Figs. 12 and 15). Therefore, the interpretation is effectively unchanged regardless of whether garnet was reset or not; the peak temperature was either ~900 °C or attained even higher temperatures prior to garnet being compositionally reset. It is not possible that the peak temperatures were less than ~900 °C.

The broad *P–T* range of the peak assemblage fields (Figs. 12 and 15) does not tightly constrain the *P–T* conditions. However, calculated mineral compositional isopleths of X_{alm} in garnet and X_{Fe} in cordierite suggest peak metamorphic conditions of ~900 °C at 6.5 kbar in samples K9 and R2017275. Due to the significant abundance of cordierite, and no apparent core–rim compositional variation, the X_{Fe} isopleths are considered a robust pressure constraint. A slight discrepancy exists between calculated and measured X_{grs} garnet compositional isopleths in these samples, suggesting a slightly higher peak temperature estimate (~980 °C). However, a higher temperature is inconsistent with the interpreted absence of spinel from the peak mineral assemblage. Nonetheless, contouring for modal proportions of spinel in sample K9 (Fig 12a) in the mineral assemblage field at this higher temperature indicates that the abundance of spinel is not significant (modal proportion <2 %). The ability of iron to diffuse faster than calcium (Carlson, 2006; Ganguly et al., 1998) may provide one explanation for the observed X_{grs} discrepancy with the garnet indeed having been compositionally reset, and therefore the intersection of X_{Fe} in cordierite and X_{alm} in garnet potentially recording a minimum peak *P–T* estimate. This peak *P–T* estimate for sample K9 is further supported by calculations done using the same bulk composition with the thermodynamic dataset ds62 and re-parameterized *a–x* models, with results of the modelling suggesting similar peak conditions (Fig. 13).

Peak *P–T* constraints on the basis of X_{Fe} cordierite compositional isopleths in sample K6 suggest slightly elevated thermal conditions, relative to samples K9 and R2017275. However, precise *P–T* estimates are not possible since the analysed range of X_{Fe} is broad (~910–990 °C, 4.0–6.0 kbar). The absence of plagioclase and garnet in the inferred peak mineral assemblage of this sample constrains the lower temperature and upper pressure limits, respectively. However, contouring the adjacent fields for modal proportions of plagioclase and garnet indicate that these minerals do not rapidly increase in abundance to lower temperatures and higher pressures, respectively, with 1 mol% plagioclase existing only at ~800 °C, and 2 mol% garnet at ~6.5 kbar. The peak *P–T* estimates for this sample may therefore be slightly more down-temperature and up-pressure than the constraints from petrography and cordierite compositional isopleths alone, being more similar to *P–T* estimates from samples K9 and R2017275. Therefore, assuming a peak *P–T* estimate of ~900 °C at 6.0–6.5 kbar for all three samples, this constraint corresponds to a very elevated apparent crustal thermal gradient of approximately 140–150 °C/kbar, or ~45–55 °C/km (assuming an average crustal density of ~2.7 g/cm^3.

The relative changes in mineral abundance can be used to infer a *P–T* path. Although overall the proportion of garnet in these samples is volumetrically minor, texturally late garnet is predominant, occurring as fine-grained coronae about sillimanite and magnetite, and extensive symplectitic intergrowths with magnetite. This observation is consistent with an increase in garnet abundance along the peak to retrograde *P–T* path. The increase in garnet is also consistent with only minor enrichment of manganese at garnet rims which is commonly indicative of garnet resorption (e.g. Kohn and Spear, 2000). In the calculated *P–T* pseudosections, mineral abundance contours indicate that garnet abundance increases as pressure increases. It is therefore probable that at least initially, the down-temperature peak to retrograde *P–T* path was isobaric, or experienced a slight increase in pressure, to result in the observed slight increase in the abundance of garnet.

6.3 Cooling history

Garnet from samples K9 and R2017275 record high temperature major element compositions in largely unzoned, small grains (generally <500 μm diameter). Therefore, conceivably, the rocks cooled relatively rapidly to sub-diffusive temperatures. This is further substantiated by the preservation of distinctive bell-shaped trace element prograde growth profiles in the peak metamorphic garnet (Fig. 7, 8). Intracrystalline diffusion of Y + REE in garnet is slower than diffusion of the major elements Fe, Mg, Mn and Ca (Caddick et al., 2010; Carlson, 2006, 2012). Nonetheless, original trace element growth zoning is believed to be substantially modified under granulite facies conditions (e.g. Carlson, 2012; Kelly et al., 2011; Moore et al., 2013; Otamendi et al., 2002; Skora et al., 2006). For example, Kelly et al. (2011) report substantial flattening of originally steep Y + REE concentration profiles in garnet from the Taiuyak Gneiss, Labrador, and attribute this to protracted residence (~65 Myr) under very high-grade conditions (~850 °C, 6–9 kbar). These thermal conditions are comparable to the *P–T* estimates from the rocks in this study. However, the size of the unzoned garnet upon which this assertion was made are considerably larger (up to 3 mm diameter) than those from the Kalamurta Gneiss that still retain their originally zoned profiles. Therefore, it is probable that the rocks from the eastern Musgrave Inlier were maintained at HT–UHT conditions for a significantly shorter timescale (i.e. <<65 Myr). However, in the absence of any absolute quantitative constraints on diffusion rates and closure temperatures of REE, precise estimates of the duration of the HT–UHT rock evolution involving garnet growth, and the rate of cooling, cannot be obtained. This notion of rapid cooling is in contrast to the long-lived, slow cooling regime proposed elsewhere in the Musgrave Inlier by previous studies (e.g. Gorczyk et al., 2015; Smithies et al., 2015; Walsh et al., 2014).

Cooling appears to have been associated with a *P–T* path involving increasing garnet abundance, largely evidenced by texturally late garnet (Fig. 5). Cooling may have been achieved following near-isothermal exhumation from mid–lower crustal depths. However, calculated modal isopleths for these samples indicate that near-isothermal decompression would be accompanied by decreasing garnet abundance (Figs. 12 and 15). Further, a decrease in garnet is generally also associated with increasing Mn and decreasing Mg concentrations at garnet rims due to resorption (Kohn and Spear, 2000), and in this instance, only minor, localised increases in Mn at the garnet rim and decrease in Mg are observed. In addition, there is currently no existing data to support the notion that crustal-scale exhumation of granulites occurred within the eastern Musgrave Inlier during the Musgrave Orogeny. Alternatively, rapid cooling may have been achieved by a localised, intense heat source resulting in thermal 'spiking' (an effectively isobaric process) of the surrounding country rock to UHT conditions (~900 °C). If this is the case, then evidence for syn-metamorphic magmatism is required; across the entire Musgrave Inlier, the ca. 1220–1140 Ma Pitjantjatjara Supersuite igneous rocks dominate and preserve a high temperature composition (Dutch et al., 2013; Smithies et al., 2011). Within the Kulgera region in the east Musgrave Inlier, granitoids of the Pitjantjatjara Supersuite comprise the bulk of the outcropping basement geology and have considerable subsurface extent (Fig. 3 and Dutch et al., 2013).

6.4 Regional implications

The east Musgrave Inlier experienced high-grade conditions (~900 °C) at relatively shallow depths (~6.0–6.5 kbar; ~18–22 km). These results are comparable to recent work from the west and central Musgrave Inlier which likewise

demonstrate thermally extreme metamorphism (>900 °C, ~7–8 kbar) and magmatism occurring over apparently long timescales (>85 Myr; Smithies et al., 2011; Walsh et al., 2014). Importantly, although temperature estimates from the western Musgrave Inlier are slightly higher than those from the eastern Musgrave Inlier, the *P–T* conditions collectively suggest that regionally high geothermal gradients (140–150 °C/kbar) prevailed across the entire terrane.

Tectonically, elevated apparent thermal gradients have been associated with high heat producing crust (e.g. Anderson et al., 2013; Sandiford and Hand, 1998a), mantle-driven magmatism (e.g. Guo et al., 2012; Mitchell et al., 2014; Westphal et al., 2003), and significantly thinned lithosphere (Currie and Hyndman, 2006; De Yoreo et al., 1991; Hyndman et al., 2005; Sandiford and Powell, 1986; Sizova et al., 2014; Wickham and Oxburgh, 1985). Elevated radiogenic crustal heat production in thickened crust, in concert with extremely slow erosion rates and crustal preconditioning (i.e. dehydration, partial melting and melt loss) is a possible mechanism for conductively-driven, regional-scale and long-lived (>>10 Myr) high-*T* metamorphism (e.g. Clark et al., 2011; McLaren et al., 1999; Sandiford and Hand, 1998a).

A number of recent studies have also suggested that lithospheric extension may generate high-*T* conditions (Brown, 2006, 2007b; Clark et al., 2011, 2014; Currie and Hyndman, 2006; Hyndman et al., 2005; Sizova et al., 2010, 2014). Specifically, Hyndman et al. (2005) and Currie and Hyndman (2006) propose that modern day continental back-arcs are regions of extended, hot and consequently weak continental lithosphere, often encompassing considerable areal extent. Comprehensive documentation of modern-day Pan-Pacific subduction back-arcs reflects their high temperatures driven by high mantle heat flow and shallow asthenospheric convection (Currie and Hyndman, 2006; Hyndman et al., 2005). Consequently, back-arcs are logical places for high-T orogenic activity and are highly sensitive to changes in the dynamics of the associated subduction margin (Collins, 2002). Renewed continental collision or accretion, or renewed subduction retreat, may result in thickening, or thinning, of the back-arc margin. This notion has been recently explored by 2D forward modelling (Gorczyk et al., 2015; Sizova et al., 2010, 2014) with results attaining temperatures >900 ºC accompanied by thin crust and extensive magmatism. The high-*T* metamorphic conditions generated in the back-arc are expected to last for as long as the heat source remains sufficiently maintained. Although Sizova et al. (2014) and Sizova et al. (2010) predict very short (<10 Myr) timescales, Gorczyk et al. (2015) suggest that UHT conditions may be sustained for up to 70 Myr and that cooling may be significantly retarded if extension, controlled by lithospheric delamination, is spatially confined (e.g. occurring at the join of rigid cratons). If the models encompassed post-extension thickening, then anticlockwise to near-isobaric *P–T* paths would also be expected, with the inversion process also likely accompanied by significant crustal heat production during lateral accretion (Clark et al., 2011). This geodynamic setting for Grenvillian metamorphism in the Musgrave Inlier is supported by Smits et al. (2014) who suggest that a long-lived oceanic arc–backarc system underwent a switch to progressive backarc closure, arc accretion and crustal reworking over the interval ca. 1500–1200 Ma.

Chardon et al. (2009) also note that regions of very weak crust ensuing from voluminous juvenile magmatic input over long timescales (>60 Myr), and associated regional-scale (>600 km width) HT–LP metamorphism, are characteristic of large, hot orogens. Geodynamically, the Musgrave Inlier might therefore also be considered an exceptional example of a large, hot orogen developed through the remobilisation of a pre-existing backarc environment (Howard et al., 2015; Smithies et al., 2011; Smithies et al., 2015; Walsh et al., 2014).

In this study, geochronology in conjunction with *P–T* pseudosections indeed suggests that apparently long-lived, high–thermal gradient conditions prevailed. This was potentially, at least initially, associated with extensional processes. However, the retention of high-*T* major element compositions and Y + REE prograde zoning in small, peak metamorphic garnet grains, eludes more to a shorter-lived thermal event in which the retrograde path was also accompanied by a slight increase in pressure and relatively rapid cooling.

The advection of magma is generally interpreted to result in relatively localised and shorter–lived (<10 Myr) high–*T* metamorphism (e.g. Ague and Baxter, 2007; Brandt et al., 2007; Viete et al., 2013; Westphal et al., 2003). For example, Viete et al. (2013) suggest that metamorphism

of the Barrovian metamorphic series during the Grampian Orogeny, Scotland, was accompanied by episodic, incremental heating that was temporally and spatially associated with voluminous bimodal magmatism at the terrane scale. Further, Brandt et al. (2007) report UHT metamorphism in the Epupa Complex, Namibia, which was attributed to magmatic loading of syn-metamorphic anorthosite that was emplaced structurally above the granulite, with retrograde cooling also linked primarily to cooling of the intrusive body.

The eastern Musgrave Inlier may also preserve evidence for transient metamorphism to ~900 °C linked to episodic, magmatically-driven granite production in the mid–upper crust. An advective heat source is supported by the observation that metamorphism was synchronous with prolonged, regional-scale intrusion of the voluminous magmatic Pitjantjatjara Supersuite at shallow depths (<10 kbar), and at temperatures up to 1000 °C, throughout the interval ca. 1220–1140 Ma (Howard et al., 2015; Smithies et al., 2011). Previous work focussing on the geochemical and isotopic character of the felsic rocks highlight that they contain a significant juvenile mantle component, estimated as much as 85 % (Kirkland et al., 2013; Smithies et al., 2011). Within the Kulgera region, the Pitjantjatjara Supersuite granites could therefore have provided the local heat source for metamorphism, or now-eroded igneous rocks that were previously emplaced above the Kalamurta Gneiss outcrop. Magma ascent and inflation at higher crustal levels, fed by steep conduits, would likely have been accompanied by forceful lateral and downward displacement of the surrounding country rock (e.g. Brown and McClelland, 2000). This process could provide both the heat source for transient UHT metamorphism and account for the interpreted slight up-pressure increase experienced by the host rocks along the retrograde *P–T* path.

7. CONCLUSIONS

This study presents the first in-depth analysis of metamorphic conditions integrated with geochronology in the eastern Musgrave Inlier, which forms the easternmost extension of the MAFO. The rocks of the eastern Musgrave Inlier preserve evidence for high-*T*, low-*P* metamorphism (~900 °C), characterised by elevated thermal gradients, over seemingly prolonged timescales >70 Myr. Importantly, the *P–T–t* conditions collectively reflect that high-*T* metamorphism was contemporaneous with the west Musgrave Inlier, and therefore that regionally high geothermal gradients (140–150 °C/kbar) prevailed across the entire terrane. However, the results of this study also find evidence for arguably shorter–lived HT–UHT metamorphism, within the overall long-lived, high–*T* system. The preservation of high-*T* major element compositions and relict Y + REE growth profiles in small garnet grains suggest that the rocks cooled relatively rapidly to sub-diffusive temperatures. At least initially the peak to retrograde *P–T* path was also isobaric, or experienced a slight increase in pressure. Conceivably, Grenvillian-aged metamorphism in the eastern Musgrave Inlier therefore appears to also record the effects of a transient thermal anomaly. This likely developed in response to magmatic-loading and the advection of heat from syn-metamorphic magmatic rocks of the Pitjantjatjara Supersuite, emplaced at mid–lower crustal depths. The findings of this study provide a unique insight into the local-scale metamorphic processes and mechanisms in a regionally magmatically-driven system.

ACKNOWLEDGEMENTS

The Geological Survey of South Australia are thanked for logistical support in the field and the use of the sample R2017275. B. Wade and A. McFadden, Adelaide Microscopy, are thanked for assistance with analytical equipment. P. Pitra and an anonymous reviewer are thanked for their detailed and contructive reviews. RAD publishes with the permission of the Director, Geological Survey of South Australia. This work was funded by Australian Research Council grant DP120104004 and forms TRaX number 317. NMT acknowledges the support of an Australian Postgraduate Award.

REFERENCES

Ague J. J. & Baxter E. F. 2007. Brief thermal pulses during mountain building recorded by Sr diffusion in apatite and multicomponent diffusion in garnet. *Earth Planetary Science Letters* 261, 500–516.

Aitken A. R. A. & Betts P. G. 2008. High-resolution aeromagnetic data over central Australia assist Grenville-era (1300–1100 Ma) Rodinia reconstructions. *Geophysical Research Letters* 35, L01306.

Aitken A. R. A. & Betts P. G. 2009a. Constraints on the Proterozoic supercontinent cycle from the structural evolution of the south-central Musgrave Province, central Australia. *Precambrian Research* 168, 284–300.

Aitken A. R. A. & Betts P. G. 2009b. Multi-scale integrated structural and aeromagnetic analysis to guide tectonic models: An example from the eastern Musgrave Province, Central Australia. *Tectonophysics* 476, 418–435.

Aitken A. R. A., Smithies R. H., Dentith M. C., Joly A., Evans S. & Howard H. M. 2013. Magmatism-dominated

intracontinental rifting in the Mesoproterozoic: the Ngaanyatjarra Rift, central Australia. *Gondwana Research* 24, 886–901.

Anderson J. A., Kelsey D. E., Hand M. & Collins W. J. 2013. Conductively driven, high-thermal gradient metamorphism in the Anmatjira Range, Arunta region, central Australia. *Journal of Metamorphic Geology* 31, 1003–1026.

Betts P. G. & Giles D. 2006. The 1800–1100 Ma tectonic evolution of Australia. *Precambrian Research* 144, 92–125.

Betts P. G., Giles D., Lister G. S. & Frick L. R. 2002. Evolution of the Australian lithosphere. *Australian Journal of Earth Sciences* 49, 661–695.

Bodorkos S. & Clark D. J. 2004. Evolution of a crustal-scale transpressive shear zone in the Albany–Fraser Orogen, SW Australia: 2. Tectonic history of the Coramup Gneiss and a kinematic framework for Mesoproterozoic collision of the West Australian and Mawson cratons. *Journal of Metamorphic Geology* 22, 713–731.

Brandt S., Will T. M. & Klemd R. 2007. Magmatic loading in the Proterozoic Epupa Complex, NW Namibia, as evidenced by ultrahigh-temperature sapphirine-bearing orthopyroxene–sillimanite–quartz granulites. *Precambrian Research* 153, 143–178.

Brown E. H. & McClelland W. C. 2000. Pluton emplacement by sheeting and vertical ballooning in part of the southeast Coast Plutonic Complex, British Columbia. *Geological Society of America Bulletin* 112, 708–719.

Brown M. 2002. Retrograde processes in migmatites and granulites revisited. *Journal of Metamorphic Geology* 20, 25–40.

Brown M. 2006. Duality of thermal regimes is the distinctive characteristic of plate tectonics since the Neoarchean. *Geology* 34, 961–964.

Brown M. 2007a. Crustal melting and melt extraction, ascent and emplacement in orogens: mechanisms and consequences. *Journal of the Geological Society* 164, 709–730.

Brown M. 2007b. Metamorphism, plate tectonics, and the supercontinent cycle. *Earth Science Frontiers* 14, 1–18.

Brown M. 2010. The spatial and temporal patterning of the deep crust and implications for the process of melt extraction. *Philosophical Transactions of the Royal Society A: Mathematical, Physical and Engineering Sciences* 368, 11–51.

Brown M. & Korhonen F. J. 2009. Some remarks on melting and extreme metamorphism of crustal rocks. *In: Gupta A. K. & Dasgupta S. eds. Physics and Chemistry of the Earth's Interior*, Springer, New York, pp. 67–87.

Caddick M. J., Konopásek J. & Thompson A. B. 2010. Preservation of Garnet Growth Zoning and the Duration of Prograde Metamorphism. *Journal of Petrology* 51, 2327–2347.

Camacho A., Compston W., Mcculloch M. & Mcdoucall I. 1997. Timing and exhumation of eclogite facies shear zones, Musgrave Block, central Australia. *Journal of Metamorphic Geology* 15, 735-751.

Camacho A. & Fanning C. M. 1995. Some isotopic constraints on the evolution of the granulite and upper amphibolite facies terranes in the eastern Musgrave Block, central Australia. *Precambrian Research* 71, 155–181.

Camacho A. & Mcdougal I. 2000. Intracratonic, strike-slip partitioned transpression and the formation and exhumation of eclogite facies rocks: an example from the Musgrave Block, central Australia. *Tectonics* 19, 978–996.

Camacho A., Vernon R. & Fitz Gerald J. 1995. Large volumes of anhydrous pseudotachylyte in the Woodroffe Thrust, eastern Musgrave Ranges, Australia. *Journal of Structural Geology* 17, 371–383.

Carlson W. D. 2006. Rates of Fe, Mg, Mn, and Ca diffusion in garnet. *American Mineralogist* 91, 1–11.

Carlson W. D. 2012. Rates and mechanism of Y, REE, and Cr diffusion in garnet. *American Mineralogist* 97, 1598–1618.

Catlos E. J. 2013. Versatile Monazite: resolving geological records and solving challenges in materials science: Generalizations about monazite: Implications for geochronologic studies. *American Mineralogist* 98, 819–832.

Cawood P. A. & Korsch R. J. 2008. Assembling Australia: Proterozoic building of a continent. *Precambrian Research* 166, 1–35.

Chardon D., Gapais D. & Cagnard F. 2009. Flow of ultra-hot orogens: a view from the Precambrian, clues for the Phanerozoic. *Tectonophysics* 477, 105–118.

Cherniak D. J. 2010. Diffusion in accessory minerals: zircon, titanite, apatite, monazite and xenotime. *Reviews in Mineralogy and Geochemistry* 72, 827–869.

Cherniak D. J. & Watson E. B. 2001. Pb diffusion in zircon. *Chemical Geology* 172, 5–24.

Cherniak D. J., Watson E. B., Grove M. & Harrison T. M. 2004. Pb diffusion in monazite: a combined RBS/SIMS study. *Geochimica et Cosmochimica Acta* 68, 829–840.

Clark C., Fitzsimons I. C. W., Healy D. & Harley S. L. 2011. How does the continental crust get really hot? *Elements* 7, 235–240.

Clark C., Kirkland C. L., Spaggiari C. V., Oorschot C., Wingate M. T. D. & Taylor R. J. 2014. Proterozoic granulite formation driven by mafic magmatism: an example from the Fraser Range Metamorphics, Western Australia. *Precambrian Research* 240, 1–21.

Clark D. J., Hensen B. J. & Kinny P. D. 2000. Geochronological constraints for a two-stage history of the Albany–Fraser Orogen, Western Australia. *Precambrian Research* 102, 155–183.

Clarke G. L., Buick I. S., Glikson A. Y. & Stewart A. J. 1995. Structural and pressure–temperature evolution of host rocks of the Giles Complex, western Musgrave Block, central Australia: evidence for multiple high-pressure events. *AGSO Journal of Australian Geology & Geophysics* 16, 127–146.

Clarke G. L. & Powell R. 1991. Decompressional coronas and symplectites in granulites of the Musgrave Complex, central Australia. *Journal of Metamorphic Geology* 9, 441–450.

Collerson K. D., Oliver R. L. & Rutland R. W. R. 1972. An example of structural and metamorphic relationships in the Musgrave orogenic belt, central Australia. *Journal of the Geological Society of Australia* 18, 379–393.

Collins W. J. 2002. Hot orogens, tectonic switching, and creation of continental crust. *Geology* 30, 535–538.

Cubley J. F., Pattison D. R. M., Tinkham D. K. & Fanning C. M. 2013. U–Pb geochronological constraints on the timing of episodic regional metamorphism and rapid high-*T* exhumation of the Grand Forks complex, British Columbia. *Lithos* 156, 241–267.

Currie C. A. & Hyndman R. D. 2006. The thermal structure of subduction zone back arcs. *Journal of Geophysical Research: Solid Earth* 111, B08404.

Cutts K. A., Kelsey D. E. & Hand M. 2013. Evidence for late Paleoproterozoic (ca 1690–1665Ma) high- to ultrahigh-temperature metamorphism in southern Australia: Implications for Proterozoic supercontinent models. *Gondwana Research* 23, 617–640.

De Yoreo J. J., Lux D. R. & Guidotti C. V. 1991. Thermal modelling in low-pressure/high-temperature metamorphic belts. *Tectonophysics* 188, 209–238.

Diener J. F. A., White R. W., Link K., Dreyer T. S. & Moodley A. 2013. Clockwise, low- metamorphism of the Aus granulite terrain, southern Namibia, during the Mesoproterozoic Namaqua Orogeny. *Precambrian Research* 224, 629–652.

Droop G. T. R. 1987. A general equation for estimating Fe^{3+} concentrations in ferromagnesian silicates and oxides from microprobe analyses, using stoichiometric criteria. *Mineralogical magazine* 51, 431–435.

Duebendorfer E. M. 2002. Regional correlation of Mesoproterozoic structures and deformational events in the Albany–Fraser orogen, Western Australia. *Precambrian Research* 116, 129–154.

Dutch R. A., Werner M. X., Krapf C. B. E. & Rusak T. 2013. Geology of the Tieyon 1:100 000 map sheet (5645), Report Book 2013/00011. Geological Survey of South Australia. Department for Mamufacturing, Innovation, Trade, Resources and Energy, South Australia, Adelaide.

Edgoose C. J., Camacho A. & Wakelin-King G. A. 1992. KULGERA Second Edition (1:250 000 Scale Geological Map). Northern Territory Geological Survey, Alice Springs.

Edgoose C. J., Camacho A., Wakelin-King G. A. & Simons B. A. 1993. Kulgera SG-53 Explanatory Notes, 1250 000 Geological Map Series. Northern Territory Geological Survey, Darwin.

Edgoose C. J., Close D. F., Stewart A. J. & Duncan N. 2002. UMBEARA First Edition (1:100 000 scale geological map). Northern Territory Geological Survey, Alice Springs.

Edgoose C. J., Scrimgeour I. R. & Close D. F. 2004. Geology of the Musgrave Block, Northern Territory. Northern Territory Geological Survey, Report 15.

Evins P. M., Smithies R. H., Howard H. M., Kirkland C. L., Wingate M. T. D. & Bodorkos S. 2010. Devil in the detail; the 1150–1000 Ma magmatic and structural evolution of the Ngaanyatjarra Rift, west Musgrave Province, central Australia. *Precambrian Research* 183, 572–588.

Fitzsimons I. C. W. 2000. Grenville-age basement provinces in East Antarctica: evidence for three separate collisional orogens. *Geology* 28, 879–882.

Fitzsimons I. C. W. & Harley S. L. 1994. The influence of retrograde cation exchange on granulite *P–T* estimates and a convergence technique for the recovery of peak metamorphic conditions. *Journal of Petrology* 35, 543–576.

Flottmann T., Hand M., Close D., Edgoose C. J. & Scrimgeour I. R. 2004. Thrust tectonic styles of the intracratonic Alice Springs and Petermann orogenies, central Australia. In: McClay, K. (Ed.), Thrust Tectonics and Hydrocarbon Systems, vol. 82. *AAPG Mem*., pp. 538–557.

Foster G., Kinny P., Vance D., Prince C. & Harris N. 2000. The significance of monazite U–Th–Pb age data in metamorphic assemblages; a combined study of monazite and garnet chronometry. *Earth and Planetary Science Letters* 181, 327–340.

Frost B. R. & Chacko T. 1989. The granulite uncertainty principle: limitations on thermobarometry in granulites. The *Journal of Geology*, 435–450.

Ganguly J., Cheng W. & Chakraborty S. 1998. Cation diffusion in aluminosilicate garnets: experimental determination in pyrope–almandine diffusion couples. *Contributions to Mineralogy and Petrology* 131, 171–180.

Gibson H. D., Carr S. D., Brown R. L. & Hamilton M. A. 2004. Correlations between chemical and age domains in monazite, and metamorphic reactions involving major pelitic phases: an integration of ID-TIMS and SHRIMP geochronology with Y–Th–U X-ray mapping. *Chemical Geology* 211, 237–260.

Giles D., Betts P. G. & Lister G. S. 2004. 1.8–1.5 Ga links between the North and South Australian cratons and the early–middle Proterozoic configuration of Australia. *Tectonophysics* 380, 27–41.

Glikson A. Y., Stewart A. J., Ballhaus C. G., Clarke G. L., Feeken E. H. J., Leven J. H., Sheraton J. W. & Sun S. S. 1996. Geology of the western Musgrave Block, central Australia, with particular reference to the mafic-ultramafic Giles Complex. *Australian Geological Survey Organisation, Bulletin* 239.

Gorczyk W., Smithies H., Korhonen F. J., Howard H. M. & Quentin De Gromard R. 2015. Ultra-hot Mesoproterozoic evolution of intracontinental central Australia. *Geoscience Frontiers* 6, 23–37.

Gray C. M. 1978. Geochronology of granulite-facies gneisses in the western Musgrave Block, central Australia. *Journal of the Geological Society of Australia* 25, 403–414.

Gregory C. J., Buick I. S., Hermann J. & Rubatto D. 2009. Mineral-scale trace element and U–Th–Pb age constraints on metamorphism and melting during the petermann orogeny (Central Australia). *Journal of Petrology* 50, 251–287.

Griffin W. L., Powell W. J., Pearson N. J. & O'reilly S. Y. 2008. GLITTER: data reduction software for laser ablation ICP–MS. *In: Sylvester P. ed. Laser ablation ICP–MS in the earth sciences: current practices and outstanding issues,* pp. 204–207, Mineralogical Association of Canada, Vancouver, Short Course Series 40.

Guo J. H., Peng P., Chen Y., Jiao S. & Windley B. F. 2012. UHT sapphirine granulite metamorphism at 1.93–1.92 Ga caused by gabbronorite intrusions: Implications for tectonic evolution of the northern margin of the North China Craton. *Precambrian Research* 222–223, 124–142.

Halpin J. A., Daczko N. R., Milan L. A. & Clarke G. L. 2012. Decoding near-concordant U–Pb zircon ages spanning several hundred million years: recrystallisation, metamictisation or diffusion? *Contributions to Mineralogy and Petrology* 163, 67–85.

Hand M. & Sandiford M. 1999. Intraplate deformation in central Australia, the link between subsidence and fault reactivation. *Tectonophysics* 305, 121–140.

Harley S. L. 1998. On the occurrence and characterization of ultrahigh-temperature crustal metamorphism. *In: Treloar P. J. & O'brien P. J. eds. What drives metamorphism and metamorhic relations?,* pp. 81–107, Special Publications. Geological Society, London.

Hinchey A. M., Carr S. D. & Rayner N. 2007. Bulk compositional controls on the preservation of age domains within metamorphic monazite: a case study from quartzite and garnet–cordierite–gedrite gneiss of Thor–Odin dome, Monashee complex, Canadian Cordillera. *Chemical Geology* 240, 85–102.

Holland T. & Powell R. 1998. An internally consistent thermodynamic data set for phases of petrological interest. *Journal of Metamorphic Geology* 16, 309–343.

Holland T. & Powell R. 2003. Activity–composition relations for phases in petrological calculations: an asymmetric multicomponent formulation. *Contributions to Mineralogy and Petrography* 145, 492–501.

Holland, T. & Powell, R. 2011. An improved and extended internally consistent thermodynamic dataset for phases of petrological interest, involving a new equation of state for solids. *Journal of Metamorphic Geology* 29, 333–383.

Howard H. M., Smithies R. H., Kirkland C. L., Kelsey D. E., Aitken A. R. A., Wingate M. T. D., Quentin De Gromard R., Spaggiari C. V. & Maier W. D. 2015. The burning heart — The Proterozoic geology and geological evolution of the west Musgrave Region, central Australia. *Gondwana Research* 27, 64–94.

Hyndman R. D., Currie C. A. & Mazzotti S. P. 2005. Subduction zone backarcs, mobile belts, and orogenic heat. *GSA Today* 15, 4–10.

Johnson T. & Brown M. 2004. Quantitative constraints on metamorphism in the variscides of Southern Brittany—a complementary pseudosection approach. *Journal of Petrology* 45, 1237–1259.

Kelly E. D., Carlson W. D. & Connelly J. N. 2011. Implications of garnet resorption for the Lu–Hf garnet geochronometer: an example from the contact aureole of the Makhavinekh Lake Pluton, Labrador. *Journal of Metamorphic Geology* 29, 901–916.

Kelly N. M., Clarke G. L. & Harley S. L. 2006. Monazite behaviour and age significance in poly-metamorphic high-grade terrains: a case study from the western Musgrave Block, central Australia. *Lithos* 88, 100–134.

Kelly N. M. & Harley S. L. 2005. An integrated microtextural and chemical approach to zircon geochronology: refining the Archaean history of the Napier Complex, east Antarctica. *Contributions to Mineralogy and Petrology* 149, 57–84.

Kelly N. M., Harley S. L. & Möller A. 2012. Complexity in the behavior and recrystallization of monazite during high-T metamorphism and fluid infiltration. *Chemical Geology* 322–323, 192–208.

Kelsey D. E. 2008. On ultrahigh-temperature crustal metamorphism. *Gondwana Research* 13, 1–29.

Kelsey D. E., Clark C. & Hand M. 2008. Thermobarometric modelling of zircon and monazite growth in melt-bearing systems: examples using model metapelitic and metapsammitic granulites. *Journal of Metamorphic Geology* 26, 199–212.

Kelsey D. E. & Hand M. 2015. On ultrahigh temperature crustal metamorphism: phase equilibria, bulk composition, trace element thermometry, heat sources, timescales and tectonic settings. *Geoscience Frontiers* 6, 311–356.

Kirkland C. L., Smithies R. H., Woodhouse A. J., Howard H. M., Wingate M. T. D., Belousova E. A., Cliff J. B., Murphy R. C. & Spaggiari C. V. 2013. Constraints and deception in the isotopic record: the crustal evolution of the west Musgrave Province, central Australia. *Gondwana Research* 23, 759–781.

Kirkland C. L., Spaggiari C. V., Pawley M. J., Wingate M. T. D., Smithies R. H., Howard H. M., Tyler I. M., Belousova E. A. & Poujol M. 2011. On the edge: U–Pb, Lu–Hf, and Sm–Nd data suggests reworking of the Yilgarn craton margin during formation of the Albany-Fraser Orogen. *Precambrian Research* 187, 223–247.

Kohn M. J. & Spear F. 2000. Retrograde net transfer reaction insurance for pressure–temperature estimates. *Geology* 28, 1127–1130.

Korhonen F. J., Clark C., Brown M., Bhattacharya S. & Taylor R. 2013. How long-lived is ultrahigh temperature (UHT) metamorphism? Constraints from zircon and monazite geochronology in the Eastern Ghats orogenic belt, India. *Precambrian Research* 234, 322–350.

Korhonen F. J., Saito S., Brown M. & Siddoway C. S. 2010. Modeling multiple melt loss events in the evolution of an active continental margin. *Lithos* 116, 230–248.

Lambeck K. & Burgess G. 1992. Deep crustal structure of the Musgrave Block, central Australia: results from teleseismic travel-time anomalies. *Australian Journal of Earth Sciences* 39, 1–19.

Ludwig K. R. 2012. User's manual for ISOPLOT 3.75, a geochronological toolkit for Microsoft Excel. *Berkeley Geochronology Centre Special Publication,* pp. 5.

Maboko M. a. H., Mcdougall I., Zeitler P. K. & Williams I. S. 1992. Geochronological evidence for ~530–550 Ma juxtaposition of two Proterozoic metamorphic terranes in the Musgrave Ranges, central Australia. *Australian Journal of Earth Sciences* 39, 457–471.

Maboko M. a. H., Williams I. S. & Compston W. 1991. Zircon U–Pb chronometry of the pressure and temperature history of granulites in the Musgrave Ranges, central Australia. *Journal of Geology* 99, 675–697.

Mahan K. H., Goncalves P., Williams M. L. & Jercinovic M. J. 2006. Dating metamorphic reactions and fluid flow: application to exhumation of high-P granulites in a crustal-scale shear zone, western Canadian Shield. *Journal of Metamorphic Geology* 24, 193–217.

Mahar E. M., Baker J. M., Powell R., Holland T. & Howell N. 1997. The effect of Mn on mineral stability in metapelites. *Journal of Metamorphic Geology* 15, 223–238.

Mclaren S., Sandiford M. & Hand M. 1999. High radiogenic heat–producing granites and metamorphism - an example from the western Mount Isa inlier, Australia. *Geology* 27, 679–682.

Mitchell R. K., Indares A. & Ryan B. 2014. High to ultrahigh temperature contact metamorphism and dry partial melting of the Tasiuyak paragneiss, Northern Labrador. *Journal of Metamorphic Geology* 32, 535–555.

Moore S. J., Carlson W. D. & Hesse M. A. 2013. Origins of yttrium and rare earth element distributions in metamorphic garnet. *Journal of Metamorphic Geology* 31, 663–689.

Morrissey L., Payne J. L., Kelsey D. E. & Hand M. 2011. Grenvillian-aged reworking in the North Australian Craton, central Australia: constraints from geochronology and modelled phase equilibria. *Precambrian Research* 191, 141–165.

Myers J. S., Shaw R. D. & Tyler I. M. 1996. Tectonic evolution of Proterozoic Australia. *Tectonics* 15, 1431–1446.

Nichols G., Berry R. & Green D. 1992. Internally consistent gahnitic spinel-cordierite-garnet equilibria in the FMASHZn system: geothermobarometry and applications. *Contributions to Mineralogy and Petrology* 111, 362–377.

O'Brien T. & Miller E. 2014. Continuous zircon growth during long-lived granulite facies metamorphism: a microtextural, U–Pb, Lu–Hf and trace element study of Caledonian rocks from the Arctic. *Contributions to Mineralogy and Petrology* 168, 1–19.

Otamendi J. E., Jesús D., Douce A. E. P. & Castro A. 2002. Rayleigh fractionation of heavy rare earths and yttrium during metamorphic garnet growth. *Geology* 30, 159–162.

Pattison D. R. M. & Bégin N. J. 1994. Zoning patterns in orthopyroxene and garnet in granulites: implications for geothermometry. *Journal of Metamorphic Geology* 12,

387–410.

Pattison D. R. M., Chacko T., Farquhar J. & Mcfarlane C. 2003. Temperatures of granulite-facies metamorphism: constraints from experimental phase equilibria and thermobarometry corrected for retrograde exchange. *Journal of Petrology* 44, 867–900.

Payne J. L., Hand M., Barovich K. M. & Wade B. P. 2008. Temporal constraints on the timing of high-grade metamorphism in the northern Gawler Craton: implications for assembly of the Australian Proterozoic. *Australian Journal of Earth Sciences* 55, 623–640.

Peterson J. W., Chacko T. & Kuehner S. M. 1991. The effects of fluorine on the vapor-absent melting of phlogopite + quartz; implications for deep-crustal processes. *American Mineralogist* 76, 470–476.

Powell R. & Downes J. 1990. Garnet porphyroblast-bearing leucosomes in metapelites: mechanisms, phase diagrams, and an example from Broken Hill, Australia. High-temperature metamorphism and crustal anatexis, *Springer*, pp. 105–123.

Powell R. & Holland T. 1988. An internally consistent thermodynamic dataset with uncertainties and correlations: 3. Application methods, worked examples and a computer program. *Journal of Metamorphic Geology* 6, 173–204.

Preiss W. V. 2000. The Adelaide Geosyncline of South Australia and its significance in Neoproterozoic continental reconstruction. *Precambrian Research* 100, 21–63.

Pyle J. M. & Spear F. S. 1999. Yttrium zoning in garnet: coupling of major and accessory phases during metamorphic reactions. *Geological Materials Research* 1, 1–49.

Pyle J. M. & Spear F. S. 2003. Four generations of accessory-phase growth in low-pressure migmatites from SW New Hampshire. *American Mineralogist* 88, 338–351.

Raimondo T., Collins A. S., Hand M., Walker-Hallam A., Smithies R. H., Evins P. M. & Howard H. M. 2009. Ediacaran intracontinental channel flow. *Geology* 37, 291–294.

Raimondo T., Collins A. S., Hand M., Walker-Hallam A., Smithies R. H., Evins P. M. & Howard H. M. 2010. The anatomy of a deep intracontinental orogen. *Tectonics* 29, TC4024.

Raimondo T., Hand M. & Collins W. J. 2014. Compressional intracontinental orogens: ancient and modern perspectives. *Earth Science Reviews* 130, 128–153.

Reno B. L., Piccoli P. M., Brown M. & Trouw R. a. J. 2012. In situ monazite (U–Th)–Pb ages from the Southern Brasília Belt, Brazil: constraints on the high-temperature retrograde evolution of HP granulites. *Journal of Metamorphic Geology* 30, 81–112.

Roberts M. P. & Finger F. 1997. Do U–Pb zircon ages from granulites reflect peak metamorphic conditions? *Geology* 25, 319–322.

Rosenberg C. L. & Handy M. R. 2005. Experimental deformation of partially melted granite revisited: implications for the continental crust. *Journal of Metamorphic Geology* 23, 19–28.

Sajeev K., Williams I. S. & Osanai Y. 2010. Sensitive high-resolution ion microprobe U–Pb dating of prograde and retrograde ultrahigh-temperature metamorphism as exemplified by Sri Lankan granulites. *Geology* 38, 971–974.

Sandiford M. & Hand M. 1998a. Australian Proterozoic high-temperature, low-pressure metamorphism in the conductive limit. *Geological Society London, Special Publications* 138, 109–120.

Sandiford M. & Hand M. 1998b. Controls on the locus of intraplate deformation in central Australia. *Earth and Planetary Science Letters* 162, 97–110.

Sandiford M. & Powell R. 1986. Deep crustal metamorphism during continental extension: modern and ancient examples. *Earth and Planetary Science Letters* 79, 151–158.

Sawyer E. W. 2001. Melt segregation in the continental crust: distribution and movement of melt in anatectic rocks. *Journal of Metamorphic Geology* 19, 291–309.

Scrimgeour & Close 1999. Regional high-pressure metamorphism during intracratonic deformation: the Petermann Orogeny, central Australia. *Journal of Metamorphic Geology* 17, 557–572.

Selway K. M., Hand M., Payne J. L., Heinson G. S. & Reid A. 2011. Magnetotelluric constraints on the tectonic setting of Grenville-aged orogenesis in central Australia. *Journal of the Geological Society* 168, 251–264.

Sengupta P., Karmakar S., Dasgupta S. & Fukuoka M. 1991. Petrology of spinel granulites from Araku, Eastern Ghats, India, and a petrogenetic grid for sapphirine-free rocks in the system FMAS. *Journal of Metamorphic Geology* 9, 451–459.

Sizova E., Gerya T. & Brown M. 2014. Contrasting styles of Phanerozoic and Precambrian continental collision. *Gondwana Research* 25, 522–545.

Sizova E., Gerya T., Brown M. & Perchuk L. L. 2010. Subduction styles in the Precambrian: insight from numerical experiments. *Lithos* 116, 209–229.

Skora S., Baumgartner L. P., Mahlen N. J., Johnson C. M., Pilet S. & Hellebrand E. 2006. Diffusion-limited REE uptake by eclogite garnets and its consequences for Lu–Hf and Sm–Nd geochronology. *Contributions to Mineralogy and Petrology* 152, 703–720.

Smithies R. H., Howard H. M., Evins P. M., Kirkland C. L., Kelsey D. E., Hand M., Wingate M. T. D., Collins A. S. & Belousova E. 2011. High-temperature granite magmatism, crust-mantle interaction and the mesoproterozoic intracontinental evolution of the Musgrave Province, central Australia. *Journal of Petrology* 52, 931–958.

Smithies R. H., Kirkland C. L., Korhonen F. J., Aitken A. R. A., Howard H. M., Maier W. D., Wingate M. T. D., Quentin De Gromard R. & Gessner K. 2015. The Mesoproterozoic thermal evolution of the Musgrave Province in central Australia — Plume vs. the geological record. *Gondwana Research* 27, 1419–1429.

Smits R. G., Collins W. J., Hand M., Dutch R. & Payne J. 2014. A Proterozoic Wilson cycle identified by Hf isotopes in central Australia; implications for the assembly of Proterozoic Australia and Rodinia. *Geology* 42, 231–234.

Stepanov A. S., Hermann J., Rubatto D. & Rapp R. P. 2012. Experimental study of monazite/melt partitioning with implications for the REE, Th and U geochemistry of crustal rocks. *Chemical Geology* 300, 200–220.

Stewart A. J. 1995. Resolution of conflicting structures and deformation history of the Mount Aloysius granulite massif, western Musgrave Block, central Australia. *AGSO Journal of Australian Geology and Geophysics* 16, 91–105.

Stoddard E. F. 1979. Zinc-rich hercynite in high-grade metamorphic rocks; a product of the dehydration of staurolite. *American Mineralogist* 64, 736–741.

Sun S. S., Sheraton J. W., Glikson A. Y. & Stewart A. J. 1996. A major magmatic event during 1050–1080 Ma in central Australia, and an emplacement age for the Giles Complex. *AGSO Research Newsletter* 24, 13–15.

Tajčmanová L., Connolly J. a. D. & Cesare B. 2009a. A thermodynamic model for titanium and ferric iron solution in biotite. *Journal of Metamorphic Geology* 27, 153–165.

Tajčmanová L., Konopásek J. & Košler J. 2009b. Distribution of zinc and its role in the stabilization of spinel in high-grade felsic rocks of the Moldanubian domain (Bohemian Massif). *European Journal of Mineralogy* 21, 407-418.

Vavra G. & Schaltegger U. 1999. Post-granulite facies monazite growth and rejuvenation during Permian to Lower Jurassic thermal and fluid events in the Ivrea Zone (Southern Alps). *Contributions to Mineralogy and Petrology* 134, 405–414.

Viete D. R., Oliver G. J., Fraser G. L., Forster M. A. & Lister G. S. 2013. Timing and heat sources for the Barrovian metamorphism, Scotland. *Lithos* 177, 148–163.

Wade B. P., Barovich K. M., Hand M., Scrimgeour I. R. & Close D. F. 2006. Evidence for early Mesoproterozoic arc magmatism in the Musgrave Block, central Australia: implications for Proterozoic crustal growth and tectonic reconstructions of Australia. *Journal of Geology* 114, 43–63.

Wade B. P., Kelsey D. E., Hand M. & Barovich K. M. 2008. The Musgrave Province: stitching north, west and south Australia. *Precambrian Research* 166, 370–386.

Walsh A. K., Kelsey D. E., Kirkland C. L., Hand M., Smithies R. H., Clark C. & Howard H. M. 2014. *P–T–t* evolution of a large, long-lived, ultrahigh-temperature Grenvillian belt in central Australia. *Gondwana Research* http://dx.doi.org/10.1016/j.gr.2014.05.012 (in press).

Walsh A. K., Raimondo T., Kelsey D. E., Hand M., Pfitzner H. L. & Clark C. 2013. Duration of high-pressure metamorphism and cooling during the intraplate Petermann Orogeny. *Gondwana Research* 24, 969–983.

Walter M. R., Veevers J. J., Calver C. R. & Grey K. 1995. Neoproterozoic stratigraphy of the Centralian Superbasin, Australia. *Precambrian Research* 73, 173–195.

Westphal M., Schumacher J. C. & Boschert S. 2003. High-temperature metamorphism and the role of magmatic heat sources at the Rogaland Anorthosite Complex in southwestern Norway. *Journal of Petrology* 44, 1145–1162.

White N., Pomroy N. E. & Powell R. 2005. An in-situ metatexite-diatexite transition in upper amphibolite facies rocks from Broken Hill, Australia. *Journal of Metamorphic Geology* 23, 579–602.

White R. W. & Clarke G. L. 1997. The role of deformation in aiding recrystallization: an example from a high-pressure shear zone, central Australia. *Journal of Petrology* 38, 1307–1329.

White R. W., Clarke G. L. & Nelson D. R. 1999. SHRIMP U-Pb zircon dating of Grenville-age events in the western part of the Musgrave Block, central Australia. *Journal of Metamorphic Geology* 17, 465–481.

White R. W. & Powell R. 2002. Melt loss and the preservation of granulite facies mineral assemblages. *Journal of Metamorphic Geology* 20, 621–632.

White R. W., Powell R. & Clarke G. L. 2002. The interpretation of reaction textures in Fe-rich metapelitic granulites of the Musgrave Block, central Australia: constraints from mineral equilibria calculation in the system K_2O–FeO–MgO–Al_2O_3–SiO_2–H_2O–Ti_2O–Fe_2O_3. *Journal of Metamorphic Geology* 20, 41–55.

White R. W., Powell R. & Holland T. 2007. Progress relating to calculation of partial melting equilibria for metapelites. *Journal of Metamorphic Geology* 25, 511–527.

White R. W., Powell R., Holland T. J. B., Johnson T. E. & Green E. C. R. 2014a. New mineral activity–composition relations for thermodynamic calculations in metapelitic systems. *Journal of Metamorphic Geology* 32, 261–286.

White R. W., Powell R. & Johnson T. E. 2014b. The effect of Mn on mineral stability in metapelites revisited: new a–x relations for manganese-bearing minerals. *Journal of Metamorphic Geology* 32, 809–828.

Wickham S. M. & Oxburgh E. R. 1985. Continental rifts as a setting for regional metamorphism. *Nature* 318, 330–333.

Williams M. L., Jercinovic M. J. & Hetherington C. J. 2007. Microprobe monazite geochronology: Understanding geologic processes by integrating composition and chronology. *Annu. Rev. Earth Planet. Sci.*, pp. 137–175.

Wingate M. T. D., Campbell I. H., Compston W. & Gibson G. M. 1998. Ion microprobe U–Pb ages for Neoproterozoic basaltic magmatism in south-central Australia and implications for the breakup of Rodinia. *Precambrian Research* 87, 135–159.

Wingate M. T. D., Pirajno F. & Morris P. A. 2004. Warakurna large igneous province: a new Mesoproterozoic large igneous province in west-central Australia. *Geology* 32, 105–108.

Yakymchuk C. & Brown M. 2014. Behaviour of zircon and monazite during crustal melting. *Journal of the Geological Society, London* 171, 465–479.

Yakymchuk C., Brown M., Ivanic T. & Korhonen F. 2013. Leucosome distribution in migmatitic paragneisses and orthogneisses: A record of self-organized melt migration and entrapment in a heterogeneous partially-molten crust. *Tectonophysics* 603, 136–154.

Zhao J. & Mcculloch M. T. 1993. Sm–Nd mineral isochron ages of late Proterozoic dyke swarms in Australia: evidence for two distinctive events of mafic magmatism and crustal extension. *Chemical geology* 109, 341–354.

Zhao J., Mcculloch M. T. & Korsch R. J. 1994. Characterisation of a plume-related 800 Ma magmatic event and its implications for basin formation in central-southern Australia. *Earth and Planetary Science Letters* 121, 349–367.

Chapter 2

This chapter is published as:

Tucker, N. M. & Hand, M. 2016. New constraints on metamorphism in the Highjump Archipelago, East Antarctica. *Antarctic Science*, **28**: 487–503, doi: 10.1017/S095410201600033X.

Statement of Authorship

Title of paper	New constraints on metamorphism in the Highjump Archipelago, East Antarctica
Pulication status	☒ Published ☐ Accepted for publication ☐ Submitted for publication ☐ Unpublished and unsubmitted work written in manuscript style
Publication details	Tucker, N. M. & Hand, M. 2016. New constraints on metamorphism in the Highjump Archipelago, East Antarctica. Antarctic Science, **28**: 487–503, doi: 10.1017/S095410201600033X.

Principal Author

Name of Principal Author	Naomi M. Tucker
Contribution to the paper	Project design; sample selection and preparation; petrology; SEM, EPMA and LA–ICP–MS data collection; all calculations and data processing; critical data interpretation; manuscript design and composition; creation of all figures.
Overall percentage (%)	85
Certification	This paper reports on original research I conducted during the period of my Higher Degree by Research candidature and is not subject to any obligations or contractual agreements with a third party that would constrain its inclusion in this thesis. I am the primary author of this paper.
Signature	Date 04/10/2017

Co-author contributions

By signing the Statement of Authorship, each author certifies that:

i. the candidate's stated contribution to the publication is accurate (as detailed above);
ii. permission is granted for the candidate to include the publication in the thesis; and,
iii. the sum of all co-authors contributions is equal to 100 % less the candidate's stated contribution.

Name of Co-author	Martin Hand
Contribution to the paper	Assistance with project design; assistance with sample acquisition; data interpretation guidance; manuscript review.
Signature	Date 13/10/2017

New constraints on metamorphism in the Highjump Archipelago, East Antarctica

Naomi M. Tucker and Martin Hand

Department of Earth Sciences, School of Physical Sciences, The University of Adelaide, Adelaide, South Australia, 5005, Australia

ABSTRACT

The age and conditions of metamorphism in the Highjump Archipelago, East Antarctica, are investigated using samples collected during the 1986 Australian Antarctic expedition to the Bunger Hills–Denman Glacier region. *In situ* U–Pb dating of monazite from three metasedimentary rocks yields ages between ca. 1240–1150 Ma and a weighted mean $^{207}Pb/^{206}Pb$ age of 1183 ± 8 Ma, consistent with previous constraints on the timing of metamorphism in this region and Stage-2 of the Albany–Fraser Orogeny in southwestern Australia. This age is interpreted to date the development of garnet ± sillimanite ± rutile-bearing assemblages that formed at ~850–950 °C and 6–9 kbar. Peak granulite facies metamorphism was followed by decompression, evidenced largely by the partial replacement of garnet by cordierite. These new pressure–temperature determinations suggest that the Highjump Archipelago attained slightly higher temperature and pressure conditions than previously proposed and that the rocks likely experienced a clockwise pressure–temperature evolution.

1. INTRODUCTION

The correlation of Rodinian crustal domains relies upon a thorough knowledge of the tectonothermal history of those vestiges that are preserved in the present day continents. The Bunger Hills and Highjump Archipelago (HJA), together with the Windmill Islands, comprise one of a few outcrops of the East Antarctic Craton in Wilkes Land, east Antarctica, and the only exposure that can be directly correlated with the Musgrave–Albany–Fraser Orogen (MAFO), which is the Australian equivalent in Rodinian supercontinent reconstructions (Fig. 1; Aitken and Betts, 2008; Boger, 2011; Clark et al., 2000; Clarke et al., 1995; Duebendorfer, 2002; Fitzsimons, 2003; Fitzsimons, 2000; Harris, 1995; Nelson et al., 1995). Furthermore, the Bunger Hills and HJA occupy a focal position at the very western periphery of this system.

Intercontinental stitching points are invoked between the MAFO and the Bunger Hills–HJA region on the basis of Gondwanan reconstructions (e.g. White et al. 2013, and references therein) that juxtapose these two continents as well as apparent similarities in the timing of metamorphism, magmatism and deformation. However, the precise configuration of the Australian plate is a source of controversy between the various tectonic reconstructions. Furthermore, the HJA and Bunger Hills are located within a region of disputed overlap between the different suggested fits, and close to a critical piercing point. While the Australian part of the MAFO has been intensely studied (e.g. Clark et al., 2000; Howard et al., 2015; Kirkland et al., 2015; Kirkland et al., 2013; Kirkland et al., 2011; Smithies et al., 2011; Smithies et al., 2015; Smits et al., 2014; Spaggiari et al., 2015; Spaggiari and Tyler, 2014; Tucker et al., 2015; Walsh et al., 2015), prior geological knowledge on the Bunger Hills and HJA is very limited with interpretations based on few reconnaissance geochronological and metamorphic studies.

This study uses *in situ* U–Pb monazite geochronology and quantitative phase equilibria modelling to place new constraints on the metamorphic evolution of the largely undescribed HJA. We utilize thin sections from samples collected during the 1986 Australian Antarctic expedition to the Bunger Hills, Obruchev Hills and Denman Glacier region (Sheraton et al. 1995). The geographical remoteness and thus logistical challenges in accessing the HJA means that legacy samples provide one of the few enduring records of the original rock characteristics. Nevertheless, these samples yield substantial and useful information regarding the timing and pressure–temperature (*P–T*) conditions of metamorphism in the HJA.

2. GEOLOGICAL SETTING

The HJA comprise a narrow belt of small, exposed rocky islands situated north of the Bunger Hills in

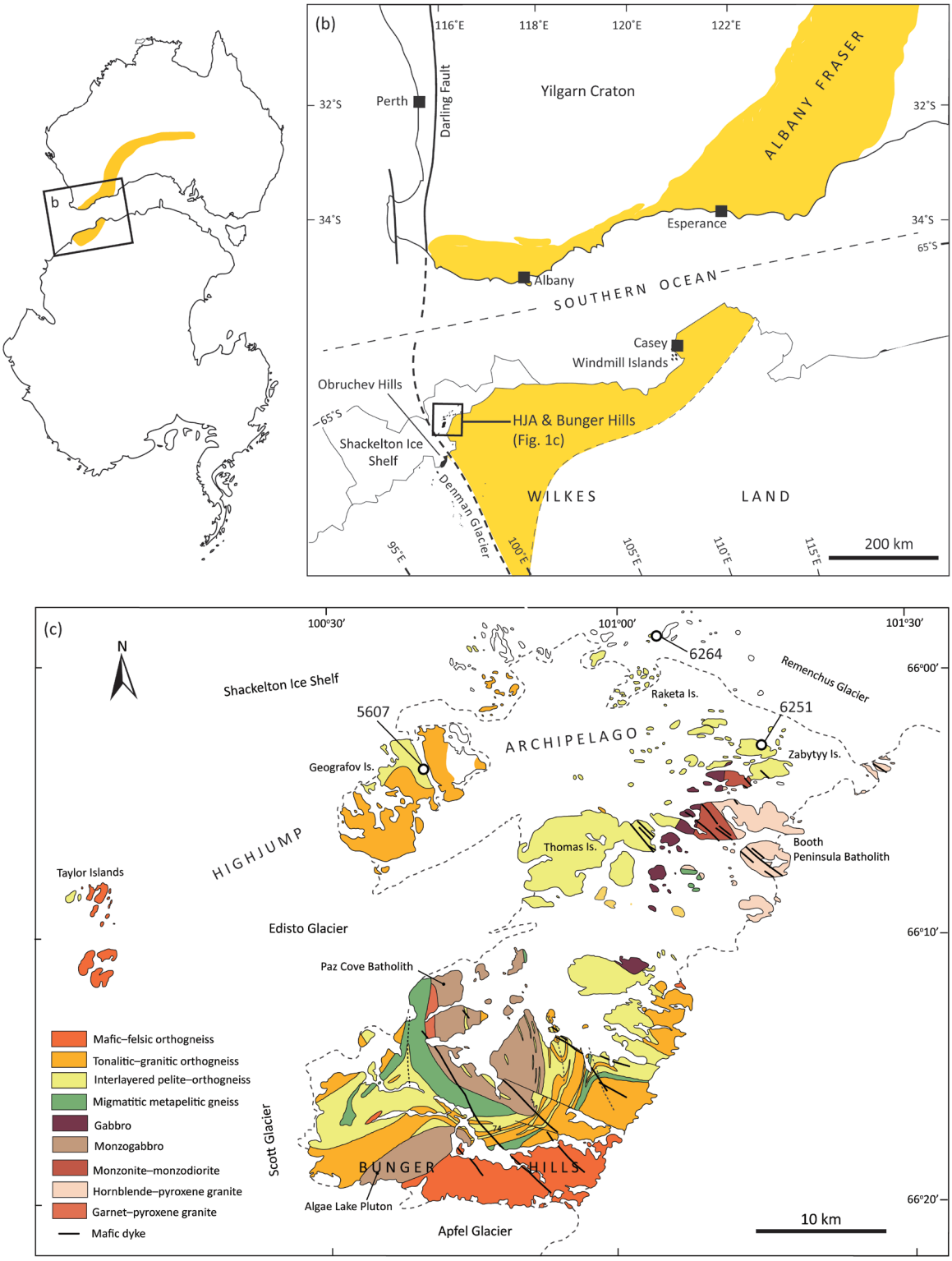

Figure 1. Location of the Bunger Hills and Highjump Archipelago in Wilkes Land, east Antarctica. (a) The approximate location of the Musgrave–Albany–Fraser Orogen in Australia and Antarctica. The position of the two continents reflects their relative positioning in Gondwanan reconstructions; (b) Wilkes Land coastline between Casey and Mirny stations showing the approximate location of the Bunger Hills, Obruchev Hills and Windmill Islands (figure modified from Boger (2011)). The location of (b) is represented by the boxed region on the map of Australia and Antarctica in figure (a); (c) Simplified regional geology of the Bunger Hills and Highjump Archipelago. The location of samples used in this study are indicated (figure modified from Sheraton et al. (1995)).

Table 1. Summary of samples

Sample	UTM (Zone 47D) Easting	Northing	Geographic location	Inferred peak mineralogy	Age (Ma)	Peak *P–T*
8628-6264	593859	2680326	North Raketa Island	g–sill–ilm–ru–pl–ksp–liq–q	1188 ± 12 Ma	> 900 °C, >7 kbar
8628-5607	576132	2671600	Geografov/Currituck Island	g–sill–ilm–ru–pl–liq–q	1161 ± 18 Ma	850–950 °C, 8–10 kbar
8628-6251	601996	2672796	Zabyyty Island	g–cd–ilm–pl–ksp–liq–q	1186 ± 11 Ma	850–950 °C, 5.4–6.6 kbar

Mineral abbreviations from Holland & Powell (1998).

east Antarctica (~100 °E, 66 °S; Fig. 1). The HJA spans ~93 km, varies from 9–23 km in width, and extends north-eastwards from the Taylor Islands to the Southern Ocean. Few studies document this region with previous geological investigations based on only two Antarctic expeditions (1956–57 and 1986), as primarily recorded by Ravich et al. (1968) and Sheraton et al. (1995).

The rocks of the Bunger Hills and HJA consist of predominantly tonalitic–granitic orthogneiss with lesser mafic granulite, interlayered orthogneiss–pelite, and migmatitic garnet–sillimanite–cordierite-bearing metasedimentary rocks (Sheraton et al., 1993, 1995). Sheraton et al. (1992) date the age of the igneous protoliths to felsic orthogneiss from the south-western Bunger Hills and Thomas Island to 1699 ± 15 and 1521 ± 29 Ma, respectively. Tonalitic orthogneiss from the Obruchev Hills, southwest of the Bunger Hills, is dated to the late Archean (ca. 2640 Ma; Sheraton et al., 1992). Within the Bunger Hills, three large intrusive bodies—the Paz Cove batholith, the Algae Lake pluton and the Booth Peninsula batholith, also crop out (Sheraton et al. 1992, 1993, 1995). These voluminous plutonic rocks comprise gabbro, monzogabbro, monzodiorite and granite, and were emplaced between ca. 1170–1150 (Sheraton et al. 1992). Dolerite dykes were emplaced at ca. 1140 Ma, involving at least four chemically distinct suites, and alkaline mafic dykes intruded at ca. 500 Ma (Sheraton et al. 1990).

The definitive structural history of the Bunger Hills–HJA region is debated, however, it is considered to have undergone at least three deformation events (Ding and James, 1991; Harris, 1995; Sheraton et al., 1995, 1993; Stüwe and Wilson, 1990). The earliest recognized event is characterised by a layer-parallel S_1 gneissic fabric (Sheraton et al. 1992) ascribed to crustal extension (Stüwe and Wilson 1990). D_2 is characterised by pervasive, tight to isoclinal and asymmetric F_2 folding (Ding and James 1991, Sheraton et al. 1992) interpreted to reflect compression (Stüwe and Wilson 1990). D_2 structures were reoriented during regional-scale D_3 open and upright folding (Ding and James 1991, Sheraton et al. 1992). The age of emplacement of the major plutonic bodies relative to deformation is the main source of contention. Though generally, intrusion of the Paz Cove batholith and Algae Lake pluton are considered synchronous with the last major stage of deformation (Ding and James 1991, Sheraton et al. 1992). The Booth Peninsula batholith cross cuts D_3 structures and is thus considered to have intruded post-D_3 tectonism (Sheraton et al. 1992). Subsequent, localised formation of shear zones, some coeval with mafic dyke emplacement, is also proposed (Sheraton et al. 1992).

Previous studies utilizing conventional geothermobarometry estimated that peak metamorphic conditions were ~750–800 °C at 5–6 kbar in the Bunger Hills (Stüwe and Powell 1989). Slightly higher pressure conditions were proposed for the HJA (~700–750 °C, 7–9 kbar) consistent with the observation of garnet within

Table 2. Bulk compositions used for phase equilibria modelling

	8628-6264	8628-5607	8628-6251
*Whole rock geochemistry (wt%)**			
SiO_2	85.10	56.30	77.60
TiO_2	0.37	1.54	1.04
Al_2O_3	7.72	23.45	10.23
Fe_2O_3	0.25	3.49	1.30
FeO	1.33	7.79	3.29
MnO	0.02	0.11	0.06
MgO	1.05	3.09	1.84
CaO	0.41	2.07	0.81
Na_2O	0.63	1.00	1.02
K_2O	1.62	0.31	1.57
P_2O_5	0.01	0.05	0.01
LOI	0.84	0.76	0.81
Thermocalc input (mol. %)			
H_2O	0.87	0.75	0.71
SiO_2	89.00	63.30	82.62
Al_2O_3	4.76	15.54	6.42
CaO	0.46	2.49	0.92
MgO	1.64	5.18	2.92
FeO	1.36	10.28	3.97
K_2O	1.08	0.22	1.07
Na_2O	0.64	1.09	1.05
TiO_2	0.29	1.30	0.83
O	0.10	0.15	0.52

*Reproduced from Sheraton *et al.* (1995).

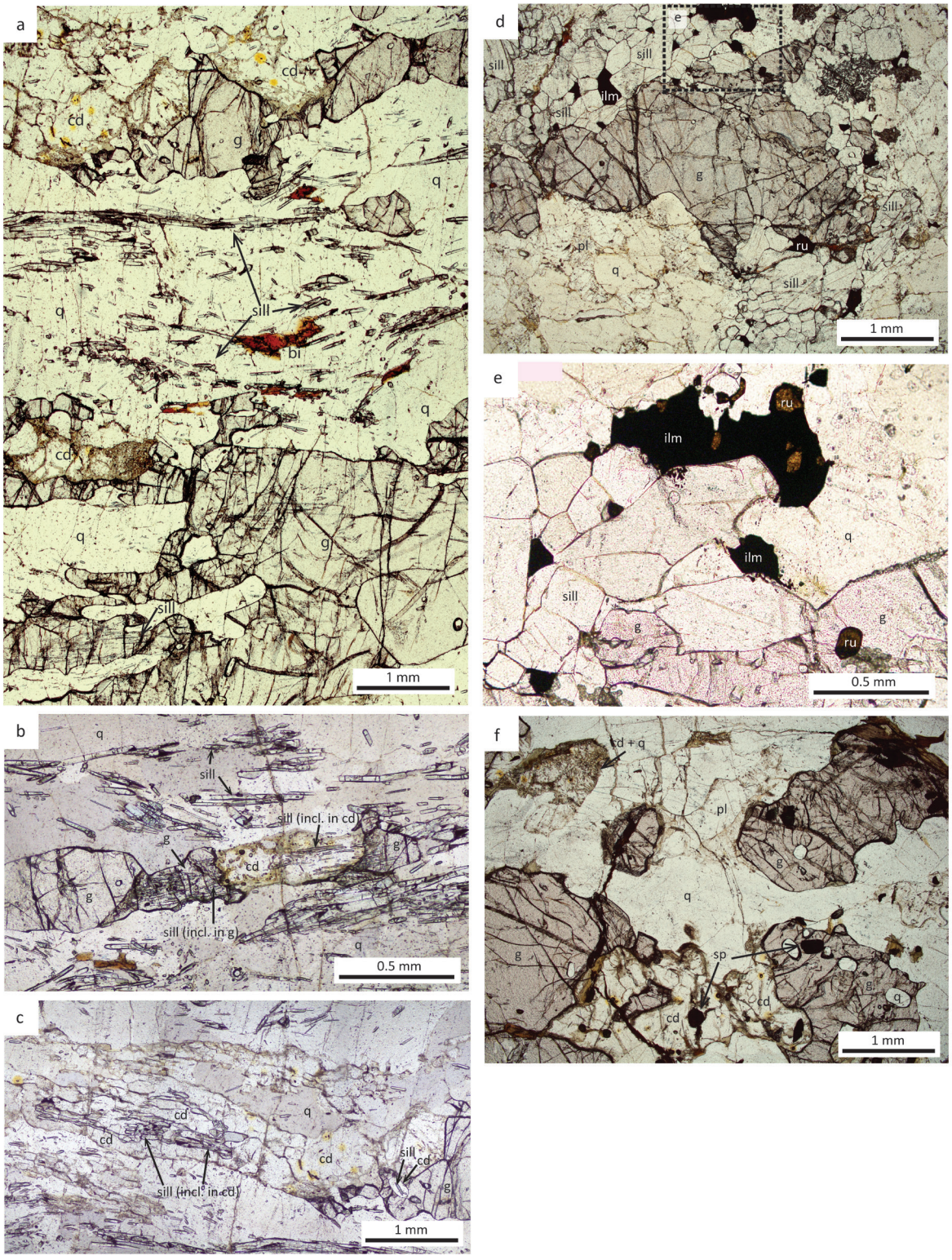

Figure 2. Representative thin section photomicrographs. (a) Sample 6264: coarse, anhedral garnet grains are aligned with acicular sillimanite that defines the foliation. Cordierite grains (with included monazite showing yellow pleochroic halos) exhibit sharp grain boundaries and only occur adjacent to garnet; (b) Sample 6264: anhedral cordierite bridging two garnet grains. Sillimanite is included within garnet and cordierite; (c) Sample 6264: sillimanite completely hosted within cordierite; (d) Sample 5607: coarse grained garnet is surrounded by idoblastic sillimanite, plagioclase and quartz. Ilmenite and rutile occur within the matrix and garnet grain edge; (e) Sample 5607: anhedral ilmenite partially enclosing rutile; (f) Sample 6251: cordierite occurs adjacent to coarse, anhedral garnet and in places, completely surrounds smaller, relict garnet grains. Locally, cordierite occurs as symplectitic intergrowths with quartz. Minor spinel (<200 μm) is included within both the garnet and cordierite. Mineral abbreviations from Holland and Powell (1998).

mafic granulite (Stüwe and Powell 1989, Sheraton et al. 1995). The timing of granulite facies metamorphism in the Bunger Hills is dated at 1190 ± 15 Ma from metamorphic zircon in one sample of tonalitic orthogneiss from Thomas Island (Sheraton et al. 1992) and is suggested to have accompanied D_1 deformation (Stüwe and Powell 1989).

Despite the currently limited geochronological dataset from the Bunger Hills, many studies readily identify parallels between the timing of metamorphism and the emplacement age of Mesoproterozoic intrusive rocks in the Bunger Hills–HJA region with rocks in the Windmill Islands in east Antarctica, and Stage-2 of the Albany–Fraser Orogeny in southwest Australia (e.g. Boger, 2011; Clark et al., 2000; Clarke et al., 1995; Fitzsimons, 2003; Fitzsimons, 2000; Harris, 1995; Sheraton et al., 1993). The Mesoproterozoic Albany–Fraser Orogeny is largely interpreted to record the final stages of assembly between the North and West Australian cratons with the combined South Australian Craton and East Antarctic Craton (Betts and Giles, 2006; Cawood and Korsch, 2008; Clark et al., 2000). Specifically, the Albany–Fraser Orogeny has been characterised by coeval felsic and mafic magmatism and high temperature, high pressure metamorphism pertaining to continental collision between 1345–1260 Ma (Stage-1) followed by intracratonic reactivation involving craton-vergent thrusting, high temperature metamorphism and predominantly felsic magmatism between 1215–1140 Ma (Stage-2; Bodorkos and Clark, 2004; Clark et al., 2000; Kirkland et al., 2011; Nelson et al., 1995). More recently, however, the Albany–Fraser Orogeny has been suggested to have involved oceanic arc accretion onto the West Australian Craton (Spaggiari et al. 2015) and back-arc extensional tectonics (Clark et al. 2014, Spaggiari et al. 2015), rather than simply continental collision and intracratonic orogenesis. Stages 1 and 2 of the Albany–Fraser Orogeny in south-western Australia are also expressed as the Mount West Orogeny (ca. 1345–1293 Ma) and Musgrave Orogeny (ca. 1220–1150 Ma), respectively, in the Musgrave Inlier within central Australia (Howard et al., 2015; Kirkland et al., 2013; Smithies et al., 2011).

3. SAMPLE DESCRIPTIONS

Samples utilized in this study comprise part of a suite of migmatised metasedimentary rocks collected during the 1986 Australian Antarctic research expedition to the Bunger Hills, Obruchev Hills and Denman Glacier region of east Antarctica, and are archived at Geoscience Australia, Canberra. The three samples chosen for this study were collected from north of Raketa Island, Zabytyy Island and Geografov/Currituck Island in the HJA, directly north of the Bunger Hills (Fig. 1, Table 1). These three samples are representative of the metapelitic lithologies that are interlayered with predominantly tonalitic orthogneiss within this region of the HJA. Whole rock geochemical analyses (reproduced from Sheraton et al. 1995; Table 2) show a range from typical pelitic (sample 5607) to more felsic compositions (samples 6264 and 6251) that are more suggestive of impure sandstone–siltstone protoliths and/or sampling of leucocratic-rich domains of a migmatite. Sample names are referred to by their last four digits throughout the text. Sample location grid references are provided in Table 1. The mineralogy, age and peak metamorphic conditions of each sample are also summarised in Table 1.

3.1 Sample 6264 (north Raketa Island)

Sample 6264 contains garnet, sillimanite, quartz, plagioclase, K-feldspar, ilmenite and minor biotite and rutile. Garnet is coarse grained (up to 5 mm in length, ~5 % abundance), is typically elongate, and contains partially to completely enclosed inclusions of sillimanite (Fig. 2a). Included sillimanite crystals are aligned with the external fabric as also defined by aggregates of sillimanite. Cordierite is often located adjacent to and separating garnet grains (e.g. Fig. 2a and b), and exhibits relatively sharp grain boundaries (Fig. 2a). Sometimes small grains of garnet are completely enclosed within the cordierite. Sillimanite is often also wholly included within cordierite occurring adjacent to garnet (e.g. Fig. 2c). Cordierite is never included within garnet. In places, fine-grained (lamellae <50 μm wide) cordierite–quartz symplectitic intergrowths also occur adjacent to garnet. The spatial relationship between garnet, cordierite and sillimanite is suggestive of the increased growth of cordierite following inferred peak growth of garnet and sillimanite. Rare, blocky rutile grains (~1 mm in length) occur in contact with sillimanite and are aligned with the fabric, but do not contain inclusions of sillimanite. Biotite is sparsely distributed and occurs as randomly-oriented, anhedral grains (~200–1000 μm in

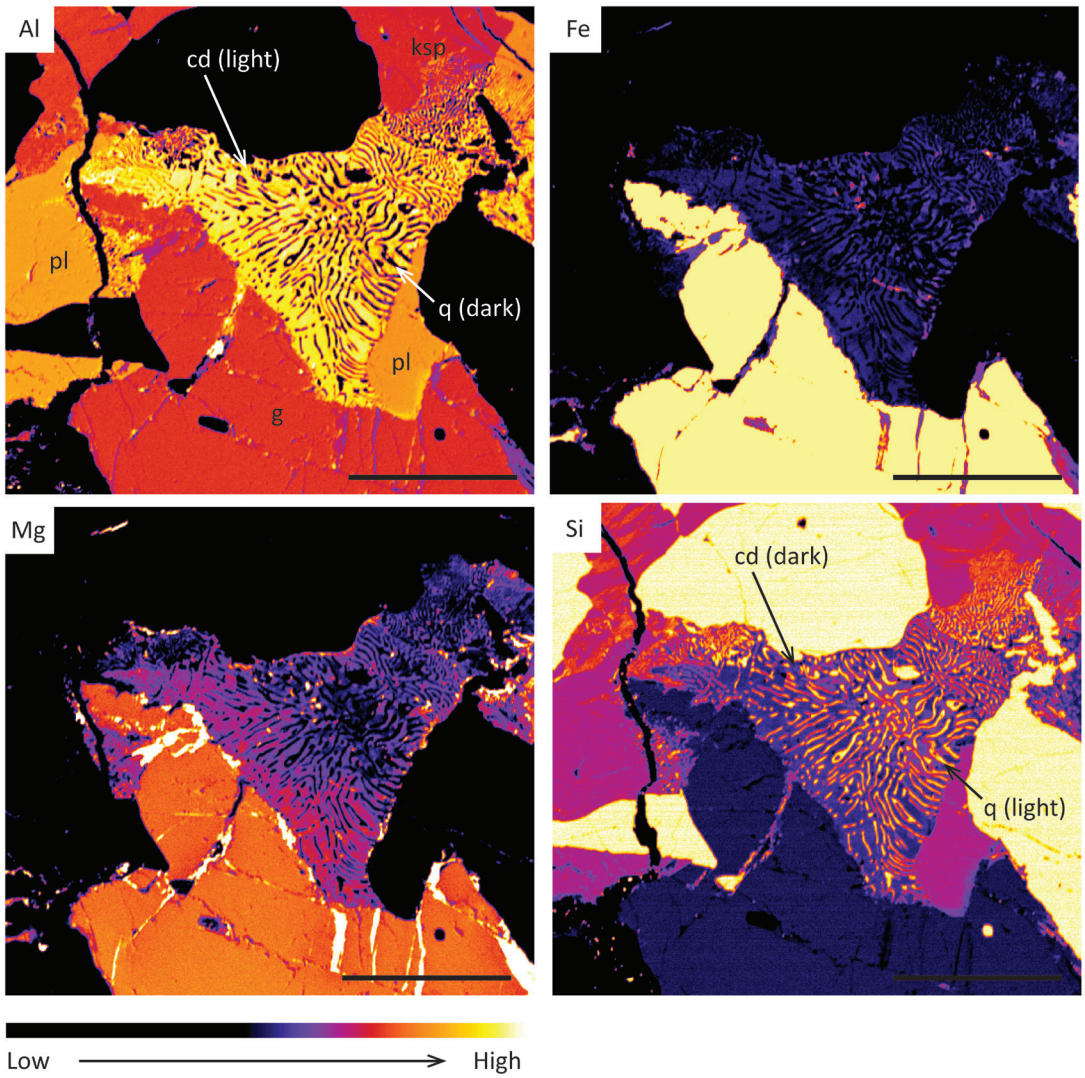

Figure 3. Qualitative compositional maps of aluminium (Al), iron (Fe), magnesium (Mg) and silica (Si) which highlight the symplectitic intergrowth between cordierite and quartz adjacent to garnet in sample 6251. Dark colours represent low elemental abundance; warm colours represent high abundance. The black scale bar represents 1 mm. Mineral abbreviations from Holland and Powell (1998).

length) along quartz–feldspar grain boundaries. The inferred peak mineral assemblage for this sample is garnet–sillimanite–ilmenite–rutile–plagioclase–K-feldspar–melt–quartz, with the post-peak development of cordierite after garnet, and the inferred retrograde growth of biotite.

3.2 Sample 5607 (Geografov Island)

Sample 5607 contains sillimanite, garnet, rutile, ilmenite, quartz, plagioclase and rare biotite. Garnet is abundant (~25 %) as very coarse-grained (up to 1 cm diameter), anhedral poikioblasts which host idioblastic sillimanite, coarse rutile (up to 500 µm), ilmenite and quartz (Fig. 2d). The modal abundance of rutile increases toward the garnet grain edge with many grains only occurring as partial inclusions within the garnet. In general, rutile occurring within garnet is coarser grained than rutile within the matrix (typically <200 µm). Ilmenite is present throughout, but is typically more common external to garnet. Sometimes, ilmenite appears to form partial anhedral overgrowths about rutile (Fig. 2e). Sillimanite is ubiquitous and weakly aligned to define a coarse foliation. Rutile and ilmenite occur in direct contact with sillimanite, but are generally not included within individual sillimanite crystals. Biotite is rare, commonly occurring within fractures in garnet, and is accordingly inferred as being of retrograde origin. The peak metamorphic mineral assemblage for this sample is inferred to be garnet–sillimanite–ilmenite–rutile–plagioclase–melt–quartz.

3.3 Sample 6251 (Zabytyy Island)

Sample 6251 contains garnet, spinel, cordierite, quartz, K-feldspar, plagioclase, and minor biotite, sillimanite and ilmenite. Garnet grains are moderately coarse grained (up to 2 mm diameter, ~5 % abundance) and contain inclusions of minor amounts of dark green spinel (~100–200 μm in size, ~1 % abundance) and rarely sillimanite (up to 250 μm length, <1 % abundance). Spinel grains are also sometimes hosted within cordierite. Commonly, cordierite is anhedral and occurs adjacent to garnet with sharp grain boundaries (Fig. 2f) and/or sometimes as symplectitic intergrowths with quartz (e.g. Fig. 3). Garnet grains are also sometimes wholly included within cordierite (Fig. 2f). Similarly to sample 6264, the observed microstructural relationships between garnet and cordierite are suggestive of the increased growth of cordierite after garnet and that some garnet grains are now potentially partially replaced by cordierite. Minor aggregates of subhedral cordierite grains also occur away from garnet and are aligned with the coarse foliation, and are considered as preserved prograde–peak grains. Plagioclase is moderately abundant, occurring with quartz and minor K-feldspar as the main matrix phases. Biotite is subhedral (grains up to 1 mm in length) with no clear preferred orientation. Grains are sparsely distributed and typically occur adjacent to ilmenite and at the grain boundaries of quartz and feldspar. The inferred peak mineral assemblage for this sample is garnet–cordierite–ilmenite–plagioclase–K-feldspar–melt–quartz. Post-peak mineral development is limited to the occurrence of randomly-oriented biotite, and the additional growth of cordierite after garnet. Spinel and sillimanite are interpreted to be potentially part of the prograde, but not peak, metamorphic mineral assemblage.

4. ANALYTICAL METHODS

4.1 Pressure–temperature conditions

Chemical compositions of minerals from all samples were obtained using a Cameca SX51 electron microprobe at Adelaide Microscopy, the University of Adelaide, using a beam current of 20 nA and an accelerating voltage of 15kV. Elemental X-ray maps of sample 6251 were obtained using the same instrumentation, a 15 kV accelerating voltage and a beam current of 200 nA.

Calculations for *P–T* were done using THERMOCALC v. 3.37 with the internally consistent updated thermodynamic dataset, ds62, of Holland and Powell (2011), for the geologically realistic system of NCKFMASHTO (Na_2O–CaO–K_2O–FeO–MgO–Al_2O_3–SiO_2–H_2O–TiO_2–Fe_2O_3), and using the activity relationships of White et al. (2014). The bulk compositions used for *P–T* pseudosection calculations are based on the whole-rock XRF geochemical analyses (Table 2) of each sample from Sheraton et al. (1995) recalculated to molar oxide percent.

A variety of published methods in metamorphic phase diagram literature are employed to estimate the H_2O content in bulk compositions used in phase equilibria modelling (e.g. Kelsey 2015, and references therein). In this study, the H_2O content for each sample was approximated from the abundance and chemical compositions of hydrous minerals in the observed mineral assemblages.

Table 3. Summary of mineral chemistry

	8628-6264	8628-5607	8628-6251
Garnet core			
X_{alm}	0.54–0.57	0.60–0.65	0.55–0.57
X_{py}	0.40–0.42	0.3–0.35	0.36–0.39
X_{gr}	0.03–0.033	0.039–0.047	0.025–0.038
X_{spss}	0.01–0.015	0.08–0.1	0.02
Garnet rim			
X_{alm}	0.54–0.55	0.60–0.63	0.57–0.63
X_{py}	0.39–0.42	0.3–0.35	0.31–0.37
X_{gr}	0.029–0.033	0.04–0.062	0.029–0.033
X_{spss}	0.01–0.015	0.08–0.1	0.02
Biotite			
X_{Fe}	0.21–0.25	0.22–0.24	0.27–0.38
Al_2O_3 (wt%)	13.41–15.03	15.46–16.01	15.82–16.80
MnO (wt%)	0–0.03	0–0.01	0–0.01
TiO_2 (wt%)	3.12–4.65	4.13–4.76	3.69–4.85
F (wt%)	2.37–2.76	0.57–0.53	0.56–0.96
K–feldspar			
X_{an}	0.0–0.01	-	0–0.01
X_{or}	0.80–0.91	-	0.88–0.92
Plagioclase			
X_{an}	0.38–0.40	0.41–0.50	0.27–0.33
X_{or}	0.01	0.01–0.03	0.01–0.06
Ilmenite			
MnO (wt%)	0	0.06–0.1	0.03–0.65
Cordierite			
X_{Fe}	0.16–0.2	-	0.15–0.18
Spinel			
ZnO (wt%)	-	-	0.97–1.17
X_{gah}	-	-	0.02
X_{sp}	-	-	0.31–0.43
Cr_2O_3 (wt%)	-	-	0.19–1.04
MnO (wt%)	-	-	0.01–0.1

$X_{alm} = Fe^{2+}/(Fe^{2+} + Mg + Ca + Mn)$; $X_{py} = Mg/(Fe^{2+} + Mg + Ca + Mn)$; $X_{gr} = Ca/(Fe^{2+} + Mg + Ca + Mn)$; $X_{spss} = Mn/(Fe^{2+} + Mg + Ca + Mn)$; $X_{Fe} = Fe^{2+}/(Fe^{2+} + Mg)$; $X_{An} = Ca/(Ca + Na + K)$; $X_{Or} = K/(Ca + Na + K)$; $X_{gah} = Zn/(Zn + Mg + Al + Ti)$; $X_{sp} = Mg/(Fe^{2+} + Mg)$.

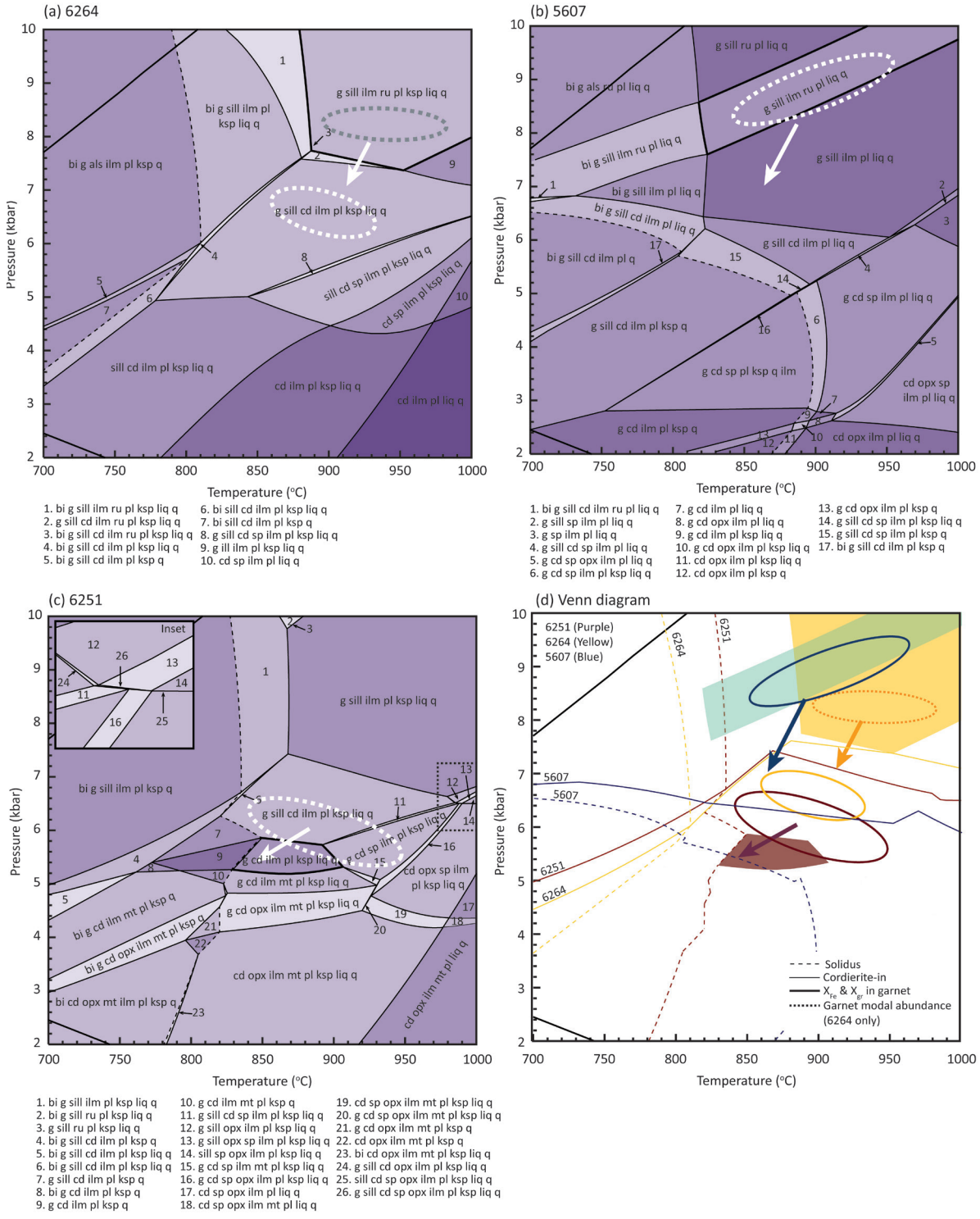

1. bi g sill ilm ru pl ksp liq q
2. g sill cd ilm ru pl ksp liq q
3. bi g sill cd ilm ru pl ksp liq q
4. bi g sill cd ilm pl ksp liq q
5. bi g sill cd ilm pl ksp q
6. bi sill cd ilm pl ksp liq q
7. bi sill cd ilm pl ksp q
8. g sill cd sp ilm pl ksp liq q
9. g ill ilm pl ksp liq q
10. cd sp ilm pl liq q

1. bi g sill cd ilm ru pl liq q
2. g sill sp ilm pl liq q
3. g sp ilm pl liq q
4. g sill cd sp ilm pl liq q
5. g cd sp opx ilm pl liq q
6. g cd sp ilm pl ksp liq q
7. g cd ilm pl liq q
8. g cd opx ilm pl liq q
9. g cd ilm pl ksp liq q
10. g cd opx ilm pl ksp liq q
11. cd opx ilm pl ksp liq q
12. cd opx ilm pl ksp q
13. g cd opx ilm pl ksp q
14. g sill cd sp ilm pl ksp liq q
15. g sill cd sp ilm pl ksp q
17. bi g sill cd ilm pl ksp q

1. bi g sill ilm pl ksp liq q
2. bi g sill ru pl ksp liq q
3. g sill ru pl ksp liq q
4. bi g sill cd ilm pl ksp q
5. bi g sill cd ilm pl ksp liq q
6. bi g sill cd ilm pl ksp liq q
7. g sill cd ilm pl ksp q
8. bi g cd ilm pl ksp q
9. g cd ilm pl ksp q
10. g cd ilm mt pl ksp q
11. g sill cd sp ilm pl ksp liq q
12. g sill opx ilm pl ksp liq q
13. g sill opx sp ilm pl ksp liq q
14. sill sp opx ilm pl ksp liq q
15. g cd sp ilm mt pl ksp liq q
16. g cd sp opx ilm pl ksp liq q
17. cd sp opx ilm pl liq q
18. cd sp opx ilm mt pl liq q
19. cd sp opx ilm mt pl ksp liq q
20. g cd sp opx ilm mt pl ksp liq q
21. g cd opx ilm mt pl ksp q
22. cd opx ilm mt pl ksp q
23. bi cd opx ilm mt pl ksp liq q
24. g sill cd opx ilm pl ksp liq q
25. sill cd sp opx ilm pl ksp liq q
26. g sill cd sp opx ilm pl ksp liq q

Figure 4. *P–T* pseudosections constructed for (a) Sample 6264, (b) Sample 5607 and (c) Sample 6251. Bulk compositions used for the calculation of each pseudosection are provided in Table 2. The solidus is shown as a black dashed line. The stability field of the inferred peak mineral assemblage in each sample is outlined in bold. The approximate range of peak *P–T* conditions on the basis of XFe and Xgr compositional isopleths in garnet and garnet modal abundance is indicated by dashed white circles in (b) and (c). In (a), the peak *P–T* conditions constrained from garnet compositional isopleths are shown as a white dashed circle; *P–T* conditions corresponding to observed garnet modal proportions are represented by the grey dashed circle. White arrows reflect the inferred *P–T* path constrained from microstructural mineral relationships; (d) Summary of *P–T* conditions from all samples. The inferred peak mineral assemblage stability fields corresponding to each sample (shaded regions), *P–T* constraints from garnet compositional isopleths (solid open circles) and modal proportions where different (open dashed circle for sample 6264) are superimposed. Inferred *P–T* paths for each sample are shown. Cordierite-in lines from (a)–(c) are also shown as cordierite is used as a constraint on the *P–T* path. Sample 6264 is represented in yellow, sample 5607 in blue, and sample 6251 in purple. Mineral abbreviations are from Holland and Powell (1998).

The sensitivity of the chosen H_2O content on the phase equilibria—namely the influence of H_2O on the temperature of the solidus, and the range of H_2O contents required to develop the observed peak mineral assemblage, is also evaluated for each sample using a calculated Temperature–M_{H2O} diagram (Supplementary Fig. S1). The Fe_2O_3 content for each sample was selected by an approximation of the abundance and stoichiometrically recast (Droop, 1987) electron microprobe compositions of Fe^{3+}-bearing minerals in each sample. A Temperature–XFe_2O_3 (XFe_2O_3 = Fe_2O_3/ (FeO + Fe_2O_3)) diagram is also presented for each sample in Supplementary Fig. S2. This allows for assessment of the change in stability of the preserved mineral assemblages with variation of the Fe oxidation state from all Fe existing as FeO to all Fe as Fe_2O_3, and a comparison with the selected Fe_2O_3 content estimated from mineral compositions and abundance. The bulk compositions used for *P–T* pseudosection calculations are provided in Table 2. Compositional isopleths and modal proportions of minerals were calculated using software TCInvestigator (version 1; Pearce et al. 2015; Supplementary Fig. S3) to further constrain the *P–T* conditions.

4.2 Laser ablation inductively coupled plasma mass spectrometry monazite geochronology

Monazite grains were imaged using a back-scattered electron (BSE) detector on a Phillips XL30 SEM. *In situ* monazite geochronology was undertaken using Laser Ablation Inductively Coupled Plasma Mass Spectrometry (LA–ICP–MS) at Adelaide Microscopy, the University of Adelaide, following the methods of Payne et al. (2008). U–Pb analyses were acquired using a New Wave 213 nm Nd–YAG laser coupled with an Agilent 7500cs ICP–MS under a He-ablation atmosphere. Analyses involved 40 s of background measurement, including 10 s of the laser firing with the shutter closed to allow for beam stabilisation, followed by 40 s of ablation. Ablation was performed with a frequency of 5 Hz and a spot size of 12 μm. Isotopes ^{204}Pb, ^{206}Pb, ^{207}Pb and ^{238}U were measured for 10 ms, 15 ms, 30 ms and 15 ms, respectively.

The primary monazite standard MAdel (TIMS normalisation data: $^{207}Pb/^{206}Pb$ = 490.0 Ma, $^{206}Pb/^{238}U$ = 518.4 Ma and $^{207}Pb/^{235}U$ = 513.1 Ma; Payne et al. 2008, updated with additional TIMS data) was used to correct for elemental fractionation and mass bias of the monazite data using software 'Glitter' (Griffin et al. 2008). Accuracy was monitored by repeat analysis of the in-house standard 94-222/Bruna NW (ca. 450 Ma, Payne et al. 2008). Over the duration of the study, the MAdel analyses yielded a weighted mean age of $^{207}Pb/^{206}Pb$ = 490.5 ± 9.2 Ma, $^{206}Pb/^{238}U$ = 517.2 ± 3.2 Ma and $^{207}Pb/^{235}U$ = 512.3 ± 2.6 Ma (n = 32), and secondary standard 94-222/Bruna NW yielded weighted mean ages of 207Pb/206Pb = 451 ± 15 Ma, $^{206}Pb/^{238}U$ = 460 ± 12 Ma and $^{207}Pb/^{235}U$ = 459 ± 12 Ma (n = 12). Instrument drift was corrected for by bracketing every 10 unknowns with standard analyses and applying a linear correction. Due to unresolvable interference of ^{204}Hg on ^{204}Pb, a common Pb correction was not applied, however, ^{204}Pb was monitored to assess the common lead of each analysis and analyses were rejected if anomalous ^{204}Pb was observed relative to background levels.

5. RESULTS

5.1 Mineral chemistry

A summary of mineral compositions from all samples is provided in Table 3. Full representative analyses for each mineral are presented in Supplementary Table S1. The chemistry of select minerals is discussed as follows.

Garnet grains from sample 6251 show slight core–rim enrichment in X_{alm} (Fe^{2+}/(Fe^{2+} + Ca + Mg + Mn)), and generally depletion in X_{py} (Mg/(Fe^{2+} + Ca + Mg + Mn)) and X_{gr} (Ca/ (Fe^{2+} + Ca + Mg + Mn)) with values of 0.55–0.57, 0.36–0.39 and 0.025–0.038 obtained from garnet cores and values of 0.57–0.63, 0.31–0.37 and 0.029–0.033 from garnet rims, respectively. Garnet from samples 6264 and 5607 do not exhibit any appreciable core–rim compositional zoning. In sample 6264, X_{alm} ranges between 0.54–0.57, X_{py} between 0.39–0.42, X_{gr} between 0.029–0.033 and X_{spss} (Mn/(Fe^{2+} + Ca + Mg + Mn)) between 0.01–0.015. In sample 5607, X_{alm} ranges between 0.60–0.65, X_{py} between 0.30–0.35, X_{gr} between 0.039–0.062 and Xspss between 0.08–0.1.

Biotite in all samples is magnesian with X_{Fe} (Fe^{2+}/(Fe^{2+} + Mg)) values ranging between 0.21–0.25 in sample 6264, 0.22–0.24 in sample 5607, and 0.27–0.38 in sample 6251. Throughout all samples, TiO_2 values are moderately high and range between 3.12–4.85 wt %. Biotite in samples 5607 and 6251 exhibit relatively low F contents,

Table 4. Laser ablation inductively coupled plasma mass spectrometry U–Pb *in situ* monazite geochronology

Analysis	Location	$^{207}Pb/^{206}Pb$	1σ	$^{206}Pb/^{238}U$	1σ	$^{207}Pb/^{235}U$	1σ	^{204}Pb (cps)	Age (Ma)						
									$^{207}Pb/^{206}Pb$	1σ	$^{206}Pb/^{238}U$	1σ	$^{207}Pb/^{235}U$	1σ	Conc. (%)
Sample 8628-6251															
6251.1.1	g	0.07919	0.00084	0.20115	0.00278	2.19633	0.03051	0	1177	21	1182	15	1180	10	100
6251.1.2	g	0.07892	0.00090	0.20436	0.00285	2.22363	0.03228	5	1170	23	1199	15	1189	10	102
6251.2.1	g	0.07901	0.00084	0.19607	0.00271	2.13577	0.02988	0	1172	21	1154	15	1161	10	98
6251.2.2	g	0.07970	0.00085	0.19442	0.00269	2.13627	0.02990	0	1190	21	1145	15	1161	10	96
6251.2.3	g	0.07924	0.00086	0.19653	0.00272	2.14713	0.03026	0	1178	21	1157	15	1164	10	98
6251.2.4	g	0.07897	0.00086	0.19829	0.00275	2.15897	0.03051	0	1172	21	1166	15	1168	10	100
6251.3.1	m	0.08046	0.00088	0.19387	0.00269	2.15055	0.03047	7	1208	21	1142	15	1165	10	95
6251.3.2	m	0.08009	0.00095	0.19834	0.00278	2.18992	0.03243	1	1199	23	1166	15	1178	10	97
6251.5.1	m	0.08969	0.00122	0.20053	0.00287	2.47959	0.03998	10	1419	26	1178	15	1266	12	83
6251.6.1	g	0.08029	0.00091	0.20864	0.00291	2.30940	0.03345	5	1204	22	1222	16	1215	10	101
6251.6.2	g	0.08331	0.00098	0.21613	0.00303	2.48240	0.03682	11	1276	23	1261	16	1267	11	99
6251.7.1	g	0.08035	0.00096	0.21280	0.00298	2.35717	0.03525	13	1206	23	1244	16	1230	11	103
6251.7.2	g	0.07988	0.00097	0.21338	0.00300	2.34986	0.03540	2	1194	24	1247	16	1228	11	104
6251.7.3	g	0.08178	0.00102	0.20288	0.00286	2.28725	0.03510	13	1240	24	1191	15	1208	11	96
6251.8.1	g	0.07966	0.00086	0.21652	0.00288	2.37691	0.03223	7	1189	21	1264	15	1236	10	106
6251.8.2	g	0.07834	0.00084	0.19398	0.00257	2.09443	0.02822	3	1156	21	1143	14	1147	9	99
6251.11.1	g	0.07969	0.00090	0.19972	0.00264	2.19349	0.03016	0	1189	22	1174	14	1179	10	99
6251.11.2	g	0.07849	0.00088	0.19954	0.00263	2.15856	0.02960	0	1159	22	1173	14	1168	10	101
Sample 8628-6264															
6264.1.1	m	0.07822	0.00086	0.20333	0.00266	2.19225	0.02950	18	1153	22	1193	14	1179	9	104
6264.2.2	m	0.07818	0.00089	0.18190	0.00237	1.96006	0.02680	5	1152	23	1077	13	1102	9	94
6264.3.1	g	0.07639	0.00085	0.17461	0.00225	1.83852	0.02461	9	1105	22	1037	12	1059	9	94
6264.4.1	g	0.07935	0.00089	0.19984	0.00257	2.18558	0.02925	8	1181	22	1175	14	1177	9	99
6264.5.1	m	0.07949	0.00092	0.20882	0.00268	2.28792	0.03105	0	1184	23	1223	14	1209	10	103
6264.7.1	m	0.07912	0.00085	0.20329	0.00272	2.21682	0.03007	9	1175	21	1193	15	1186	9	102
6264.7.2	m	0.07840	0.00085	0.18958	0.00253	2.04835	0.02785	8	1157	21	1119	14	1132	9	97
6264.8.1	m	0.08079	0.00093	0.20170	0.00270	2.24574	0.03156	9	1216	22	1184	14	1196	10	97
6264.8.2	m	0.07863	0.00102	0.21992	0.00298	2.38332	0.03608	0	1163	26	1281	16	1238	11	110
6264.8.3	m	0.07981	0.00096	0.20117	0.00269	2.21289	0.03170	4	1192	23	1182	14	1185	10	99
6264.9.1	m	0.08038	0.00090	0.19802	0.00262	2.19378	0.03014	0	1206	22	1165	14	1179	10	97
6264.9.2	m	0.07917	0.00090	0.18916	0.00249	2.06412	0.02841	2	1177	22	1117	14	1137	9	95
6264.10.1	m	0.07928	0.00089	0.20945	0.00275	2.28850	0.03122	13	1179	22	1226	15	1209	10	104
6264.12.1	m	0.08092	0.00089	0.20606	0.00269	2.29810	0.03097	2	1220	22	1208	14	1212	10	99
6264.12.2	m	0.08034	0.00090	0.19054	0.00248	2.10978	0.02852	7	1205	22	1124	13	1152	9	93
6264.11.1	m	0.08098	0.00091	0.19876	0.00258	2.21826	0.03006	44	1221	22	1169	14	1187	9	96
6264.11.2	m	0.08007	0.00091	0.18722	0.00243	2.06615	0.02812	8	1199	22	1106	13	1138	9	92
Sample 8628-5607															
5607.1.1	g	0.07962	0.00109	0.21197	0.00291	2.32576	0.03646	3	1188	27	1239	15	1220	11	104
5607.1.2	g	0.07792	0.00107	0.20024	0.00274	2.15002	0.03382	1	1145	27	1177	15	1165	11	103
5607.2.1	g	0.07938	0.00098	0.19457	0.00262	2.12833	0.03105	0	1182	24	1146	14	1158	10	97
5607.2.2	g	0.07856	0.00095	0.19466	0.00261	2.10732	0.03044	3	1161	24	1147	14	1151	10	99
5607.3.1	m	0.07896	0.00105	0.19384	0.00263	2.10924	0.03238	0	1171	26	1142	14	1152	11	98
5607.3.2	m	0.07928	0.00115	0.18763	0.00258	2.04997	0.03323	18	1179	28	1109	14	1132	11	94
5607.3.3	m	0.07843	0.00088	0.18895	0.00250	2.04215	0.02814	0	1158	22	1116	14	1130	9	96
5607.3.4	m	0.07880	0.00093	0.18105	0.00241	1.96594	0.02780	0	1167	23	1073	13	1104	10	92
5607.5.1	g	0.07864	0.00135	0.17885	0.00253	1.93823	0.03555	0	1163	34	1061	14	1094	12	91
5607.6.1	g	0.07565	0.00094	0.19374	0.00259	2.01977	0.02954	0	1086	25	1142	14	1122	10	105
5607.6.2	g	0.07715	0.00096	0.19129	0.00255	2.03360	0.02970	4	1125	25	1128	14	1127	10	100
5607.7.1	g	0.10188	0.00163	0.20907	0.00295	2.93501	0.05072	30	1659	29	1224	16	1391	13	74

Abbreviations: g, monazite hosted within garnet; m, matrix monazite.

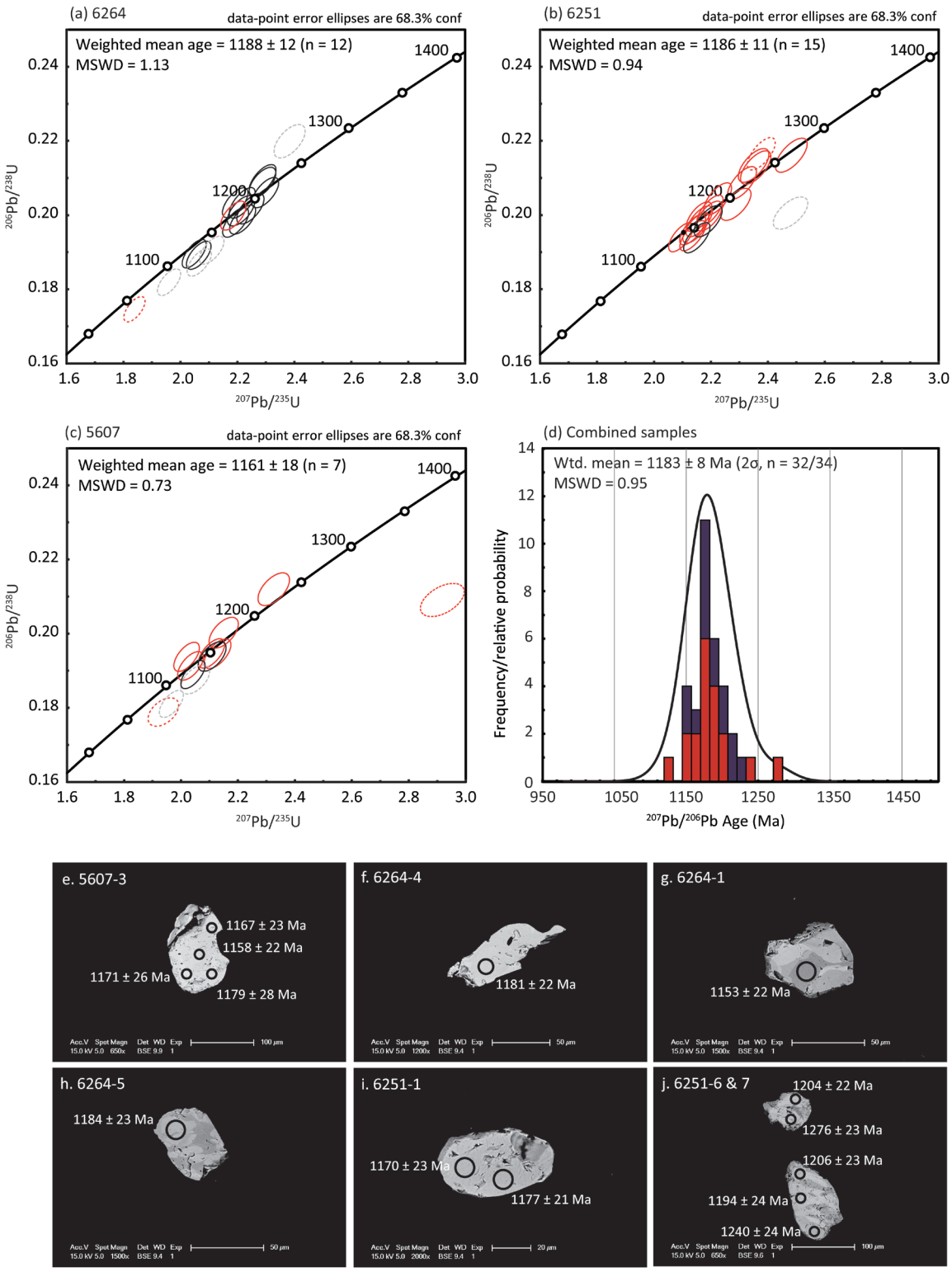

Figure 5. *In situ* LA–ICP–MS monazite U–Pb geochronology. Data are presented on U–Pb concordia diagrams: (a) Sample 6264; (b) Sample 6251; (c) Sample 5607. Red ellipses represent analyses from monazite included within garnet; black ellipses represent analyses from matrix monazite. Red and grey ellipses shown with a dashed outline represent analyses that are >5 % discordant from monazite hosted in garnet and matrix monazite, respectively. Weighted mean $^{207}Pb/^{206}Pb$ ages are given for the combined concordant analyses from each sample; (d) Histogram and probability density distribution plot for monazite age data from all three samples. Analyses from monazite grains included within garnet are shown in red; analyses from monazite included within matrix minerals are shown in blue. Collectively, the age data define a single population which yields a weighted mean $^{207}Pb/^{206}Pb$ age of 1183 ± 8 Ma; (e)–(j) Representative BSE images of analysed monazite grains from all samples. Open black circles represent the approximate location of U–Pb analyses. Corresponding $^{207}Pb/^{206}Pb$ U–Pb ages are shown. Age uncertainties are given at the 1σ level.

between 0.53–0.57 wt % and 0.56–0.96 wt %, respectively; F values range between 2.37–2.76 wt % in sample 6264.

K-feldspar is found in samples 6264 and 6251. K-feldspar is K-rich and Ca-poor with X_{an} (Ca/(Ca + Na + K) of 0–0.01 and X_{or} (K/ Ca + Na + K) of 0.80–0.92 in both samples. Plagioclase is present in all three samples and is Na-rich with X_{an} values between 0.38–0.40, 0.41–0.51 and 0.27–0.33 in samples 6264, 5607 and 6251, respectively. X_{or} values in plagioclase range from 0.01–0.06.

Cordierite occurs in samples 6264 and 6251. Cordierite is magnesian in composition with X_{Fe} values between 0.15–0.20 and no apparent variation in composition between cores or rims.

Ilmenite has a low MnO content in all samples, ranging from 0–0.65 wt %.

Spinel occurs in sample 6251. Spinel contains a moderate amount of ZnO, ranging from 0.97–1.17 wt % and with a X_{gah} (Zn/(Zn + Mg + Al + Ti)) value of 0.02. X_{sp} (Mg/(Fe^{2+} + Mg)) ranges from 0.31–0.43, Cr_2O_3 varies between 0.19–1.04 wt %, and MnO varies between 0.01–0.1 wt %.

5.2 Pressure–temperature conditions

T–$X$$Fe_2O_3$ diagrams used for the determination of ferric iron in the bulk composition of each sample are shown in Fig. S2. Calculated P–T pseudosections for each sample are presented in Fig. 4a–c and are contoured for X_{gr} and X_{Fe} in garnet and modal proportions of relevant phases in Fig. S3. Superimposed pseudosection peak mineral assemblage stability fields for all samples are shown in Fig. 4d for comparison.

In sample 6264 (Fig. 4a), the garnet stability field is broad, extending to pressures above ~5 kbar over the range 700–1000 °C. Decreasing garnet abundance with decreasing pressure is associated with an increase in X_{Fe} in garnet, and consistently low X_{gr} (Fig. S3). Cordierite is present at pressures lower than ~4.5 kbar at 700 °C, and the range of stable pressures increases with temperature. The occurrence of rutile is restricted to pressures higher than ~7 kbar and temperatures >850 °C. The interpreted peak metamorphic assemblage garnet–sillimanite–ilmenite–rutile–plagioclase–K-feldspar–melt–quartz for this sample is stable at >900 °C and >7 kbar. These P–T conditions are in agreement with calculated garnet modal proportions and petrographic observations which suggest approximately 5 % garnet abundance in this sample. However, chemical compositions of X_{Fe} and X_{gr} from unzoned garnet cores suggest P–T conditions of ~850–950 °C at ~6–7 kbar, occurring within the lower pressure field garnet–sillimanite–cordierite–ilmenite–plagioclase–K-feldspar–melt–quartz. This P–T estimate is inconsistent with the presence of rutile and the inferred absence of peak cordierite in this sample. Cordierite is inferred to have grown during post-peak metamorphism at the expense of garnet ± sillimanite (e.g. Fig. 2a and b). This relationship corresponds to a simultaneous increase in the modal proportion of cordierite and a decrease in garnet and sillimanite, and thus suggests that this rock evolved through a broadly decompressional retrograde P–T path (Fig. 4a and S3).

In sample 5607 (Fig. 4b), rutile-bearing assemblages occur at pressures >7 kbar at 700 °C with rutile stability contracting to higher pressures with increasing temperature. Ilmenite is present below 7.5 kbar at 700 °C and occurs at higher pressures with increasing temperature, coexisting with rutile only over a narrow pressure range (~1 kbar). Garnet is present throughout the majority of the pseudosection. The inferred peak mineral assemblage garnet–sillimanite–ilmenite–rutile–plagioclase–melt–quartz for this sample exists over a narrow P–T range extending from ~7.5–8.5 kbar at 850 °C, to >9.5 kbar at 1000 °C. Modal proportions of garnet, and X_{gr} and X_{Fe} compositions from unzoned garnet cores are in agreement with this P–T estimate. In this sample, a lower abundance of rutile is observed within the matrix relative to rutile included within garnet, and anhedral ilmenite overgrowths occur on some rutile grains (e.g. Fig. 2e). This reflects a decreasing modal proportion of rutile and an increase in the abundance of ilmenite following growth of peak metamorphic garnet. Comparison with calculated mineral modal proportions therefore also suggests a decompressional post-peak evolution for this rock.

In sample 6251 (Fig. 4c), garnet exists at pressures >3 kbar at 700 °C and contracts to higher pressures with increasing temperature. Cordierite stability occurs below 7 kbar while sillimanite is restricted to pressures greater than ~5.5–6.5 kbar. Spinel is present at ~900 °C at 5.5 kbar, with the range of stable pressures widening to between ~4–7 kbar

at 1000 °C. The inferred peak mineral assemblage garnet–cordierite–ilmenite–plagioclase–K-feldspar–melt–quartz exists over a small *P–T* range between ~830–900 °C and 5.2–5.8 kbar. However, chemical compositions of X_{Fe} and X_{gr} from garnet suggest that peak conditions were ~850–950 °C and 5.4–6.6 kbar, occurring at a slightly higher pressure than the inferred peak assemblage field, within the garnet–sillimanite–cordierite–ilmenite–plagioclase–K-feldspar–melt–quartz-bearing field or adjacent spinel-bearing, sillimanite–absent field. Calculated modal proportions and estimated abundance of garnet and peak cordierite in this sample are in agreeance with the peak conditions estimated from the garnet compositional isopleths. Similarly to sample 6264, the inferred growth of cordierite after garnet (e.g. Figs. 2f and 3) is suggestive of a broadly decompressional retrograde *P–T* path for this sample. The absence of magnetite in this sample constrains this down-temperature *P–T* path to have tracked along a relatively shallow *P–T* trajectory, above ~5 kbar.

5.3 Monazite U–Pb LA–ICP–MS geochronology

In situ monazite LA–ICP–MS was undertaken on samples 6251, 6264, and 5607 (Table 4, Fig. 5a–d). Monazite is sparse in all samples, and when present, typically occurs within and along the grain boundaries of matrix minerals. Rarely, monazite is partially hosted within garnet. Representative BSE images of analysed monazites are given in Fig. 5e–j. A few grains exhibit indistinct internal core–rim style zonation, however, the majority of grains appear unzoned in BSE imagery. The monazite grains do not show any relationship between their microstructural location and age. Weighted average calculations use the $^{207}Pb/^{206}Pb$ age. Concordia diagrams for each sample and a probability density plot of the combined age data are presented in Fig. 5a–d. Collectively, analyses that are ≤5 % discordant yield a weighted mean age of 1183 ± 8 Ma (n = 32/34, mean square weighted deviation (MSWD) = 0.95).

In sample 6264, 15 analyses were done on nine grains within the matrix and two analyses from two grains hosted within garnet. Grains are ~40–100 µm in size and sub-rounded to elongate in shape. Some grains display subtle, patchy internal zonation visible in BSE imagery. Five analyses that are >5 % discordant are excluded from weighted mean calculations. The remaining 12 analyses range between 1221 ± 22 Ma and 1153 ± 22 Ma and give a $^{207}Pb/^{206}Pb$ weighted average age of 1188 ± 12 Ma (MSWD = 1.13; Fig. 5a).

In sample 6251, 15 analyses were obtained from five grains located partially and completely within garnet, and three analyses from three grains within the foliated matrix. Grains are commonly ~30–100 µm in diameter, sub-rounded, generally unzoned in BSE imagery, and are commonly pitted or cracked. Two analyses that are >5 % discordant (analysis 6251.5.1 and 6251.8.1) and one outlying, older concordant analysis (analysis 6251.6.1, 1276 ± 23 Ma) are excluded from weighted mean calculations. The remaining analyses range between 1240 ± 24 Ma and 1156 ± 21 Ma (n = 15) and yield a $^{207}Pb/^{206}Pb$ weighted mean age of 1186 ± 11 (MSWD = 0.94; Fig. 5b).

In sample 5607, eight analyses were collected from five grains hosted within garnet and four analyses from one grain within the matrix. Grains are ~40–60 µm in size, largely unzoned in BSE imagery, anhedral in shape, and are commonly pitted and fractured. Four analyses that are >5 % discordant (analysis 5607.3.2, 3.4, 5.1 and 7.1) and one anomalously young, concordant analysis (analysis 5607.6.1, 1086 ± 25 Ma) are excluded from weighted mean age calculations. The remaining seven analyses range between 1188 ± 27 Ma and 1125 ± 25 Ma and give a $^{207}Pb/^{206}Pb$ weighted average age of 1161 ± 18 Ma (MSWD = 0.73; Fig. 5c).

6. DISCUSSION

6.1 Age of metamorphism

In situ U–Pb monazite ages obtained in this study range predominantly between ca. 1240–1150 Ma and give a weighted average $^{207}Pb/^{206}Pb$ age of 1183 ± 8 Ma. This mean age is within error of the age of metamorphism previously determined for the Bunger Hills from metamorphic zircon in tonalitic orthogneiss (Sheraton et al. 1992). The timing of metamorphism within this study is also similar to the age of Mesoproterozoic metamorphism and magmatism recorded elsewhere within the MAFO (e.g. Clark et al., 2000; Kirkland et al., 2013; Kirkland et al., 2011; Smithies et al., 2011; Tucker et al., 2015; Walsh et al., 2015). Previous studies have utilized SHRIMP zircon, monazite and rutile geochronology to ascertain that, specifically, the Mesoproterozoic Albany–Fraser Orogeny in south-western Australia was characterised by two discrete thermotectonic pulses at ca. 1345–1260

Ma (Stage-1) and ca. 1214–1140 Ma (Stage-2; Clark et al., 2000; Kirkland et al., 2011; Nelson et al., 1995). Tectonism of a similar age is recorded by felsic gneiss and charnockite (ca. 1380–1180 Ma) from the Windmill Islands in east Antarctica (Post 2000, Zhang et al. 2012). Evidence for widespread felsic magmatism at ca. 1345–1293 Ma (Mount West Orogeny) and ca. 1220–1150 Ma (Musgrave Orogeny) also occurs within the Musgrave Inlier (Howard et al., 2015; Kirkland et al., 2013; Smithies et al., 2011), with the latter also linked with pervasive high temperature to ultra-high temperature metamorphism (Tucker et al. 2015, Walsh et al. 2015).

The Bunger Hills, HJA and Windmill Islands in east Antarctica have been correlated along strike of the Nornalup Complex of the MAFO in Gondwanan tectonic reconstructions (e.g. Clarke et al., 1995; Fitzsimons, 2003; Harris, 1995). Stage-1 tectonism in the Nornalup Complex is recorded by the Malcolm Gneiss (Clark et al. 2000) and the earliest evidence for Recherche Supersuite magmatism (1330 ± 14 Ma; Nelson et al. 1995). The Nornalup Complex is otherwise dominated by Stage-2 tectonism as evidenced by the emplacement of the Esperance Supersuite, amphibolite facies metamorphism of sedimentary rocks from Mount Ragged (1154 ± 15 Ma; Clark et al. 2000) and granulite facies metamorphism of the garnet–cordierite-bearing Salisbury Gneiss (ca. 1215 Ma and ca. 1180 Ma; Clark et al. 2000). Geometric considerations suggest that the Stage-1 tectonothermal events recognised in the Windmill Islands and Nornalup Complex therefore possibly also affected the Bunger Hills and HJA. However, the results from this study and those obtained previously by Sheraton et al. (1992) suggest that the Bunger Hills records only the second stage of the Albany–Fraser Orogeny, with magmatism and metamorphism occurring between ca. 1190–1150 Ma. More geochronological data is required to determine conclusively whether the apparent absence of ca. 1300 Ma tectonism in the Bunger Hills–HJA region is geologically important or if it is merely a reflection of a current paucity in age data.

6.2 New metamorphic constraints for the HJA

The rocks of the HJA experienced intermediate pressure, granulite facies metamorphism (~850–950 °C, 6–9 kbar; Fig. 4d). The highest pressure conditions are recorded by a sample of garnet–sillimanite–rutile-bearing gneiss (sample 5607) from Geografov Island (~850–950 °C, 8–10 kbar). The metamorphic conditions recorded by samples 6264 and 6251 from north of Raketa Island and Zabytyy Island, respectively, are inferred to have occurred at a slightly lower pressure, relative to sample 5607 (Fig. 4d). However, the exact peak metamorphic conditions of these two samples are less assuredly constrained due to some inconsistencies between the calculated *P–T* pseudosections, measured garnet compositions and petrographic observations. The inferred peak mineral assemblage in sample 6264 is stable at *P–T* conditions >900 °C and >7 kbar, with estimated garnet abundance (~5 % abundance) further constraining *P–T* conditions to the lower pressure region of this field (~7–8 kbar). Considering that some garnet grains are potentially now partially replaced by cordierite, this *P–T* estimate is in effect a minimum with peak *P–T* conditions likely occurring at an even higher pressure. Therefore, on the basis of garnet modal proportions, the lower pressure boundary of the inferred peak mineral assemblage field defines the minimum limit on the peak metamorphic conditions. In contrast, measured X_{Fe} and X_{gr} garnet chemical compositions from sample 6264 suggest that peak metamorphic conditions were 850–950 °C and 6–7 kbar, within the adjacent cordierite-present field. Given the relatively small size of garnet grains in this sample (typically 1–5 mm) and the ability of garnet to be compositionally reset under even short-lived granulite facies metamorphism (e.g. Caddick et al., 2010; Spear, 1991), it is probable that these garnets now record a modified composition resulting from diffusion during cooling from slightly higher pressure, peak metamorphic conditions. This interpretation is consistent with the stability of the observed (cordierite-absent) peak mineral assemblage occurring at higher pressure.

In sample 6251, measured X_{Fe} and X_{gr} compositions in garnet suggest that peak metamorphic conditions were ~850–950 °C and 5.4–6.6 kbar. However, these *P–T* conditions correspond to garnet–cordierite–spinel-bearing and/or garnet–sillimanite–cordierite-bearing assemblages. This is inconsistent with the inference that the observed spinel and sillimanite do not form part of the peak mineral assemblage. Spinel is present as a minor phase (~1% abundance) and always occurs as inclusions within garnet or hosted within cordierite that is inferred to have replaced former

peak metamorphic garnet grains. Therefore, spinel is interpreted to have potentially formed part of the prograde mineral assemblage. However as this study does not account for the possibility that the rocks of the HJA underwent melt loss through melt reintegration modelling (e.g. Anderson et al., 2013; Korhonen et al., 2010), the presence or absence of spinel cannot be used reliably to make inferences about the prograde *P–T* path. Furthermore, electron microprobe mineral chemistry indicates that spinel contains a moderate amount of ZnO (0.97–1.17 wt %; Tables 3 and S1). Components such as zinc are known to enhance spinel stability to lower temperatures and higher pressures (e.g. Nichols et al. 1992, Tajčmanová et al. 2009). However, due to the current absence of thermodynamic models for Zn-bearing solid solutions, the phase equilibria modelling approach is limited in that this *P–T* shift cannot be effectively quantified. Thus the presence or absence of spinel cannot be reliably used as a constraint on the *P–T* conditions for this sample.

Although sillimanite is not interpreted to be part of the peak metamorphic assemblage, the calculated abundance of sillimanite is relatively low within the *P–T* region estimated from compositional isopleths (approximately 1–2 % abundance). Therefore, at these conditions, any peak sillimanite would probably not be readily observed in thin section. Sillimanite does occur as rare inclusions within garnet, but not as a noticeable matrix phase. This microstructural relationship is suggestive that sillimanite grew as part of an earlier and probably higher pressure, prograde assemblage and therefore supports the notion that this sample evolved along a broadly clockwise *P–T* evolution. However, as for spinel, the presence of sillimanite cannot be used to definitively constrain the absolute prograde *P–T* trajectory for this sample.

The new *P–T* determinations presented in this study suggest that overall, the HJA attained slightly higher temperature and pressure conditions than previously obtained by Stüwe and Powell (1989). Previous *P–T* estimates constrained using conventional thermobarometry were ~750–800 °C at 5–6 kbar for the Bunger Hills and ~700–750 °C at 7–9 kbar for the HJA (Sheraton et al., 1995; Stüwe and Powell, 1989). The slightly higher pressure conditions proposed for the HJA compared with the Bunger Hills are consistent with the observation of garnet in mafic granulite in the northeastern HJA (Sheraton et al. 1995). However, the previous constraint on peak temperature for the HJA is likely to be unreliable as the garnet utilised for those *P–T* calculations occurred as a coronae about orthopyroxene and was accordingly interpreted to have been of retrograde origin (Sheraton et al. 1995). *P–T* calculations done using conventional thermobarometry rely heavily upon individual, measured mineral compositions, which, as in this example, may not be truly indicative of the compositions that were formed at the peak of metamorphism if the minerals underwent diffusion as is typical at granulite facies.

Stüwe and Powell (1989) initially proposed that rocks of the Bunger Hills underwent an anticlockwise *P–T* evolution. This assertion was made on the basis that relict spinel was commonly surrounded by a cordierite, garnet and/or sillimanite coronae which ostensibly reflected the reaction between a formerly more widespread, low pressure (~800 °C, 4 kbar) spinel–quartz-bearing assemblage to produce a higher pressure, garnet–sillimanite–cordierite-bearing assemblage (~750 °C, 6–7 kbar; Stüwe and Powell, 1989). However, Sheraton et al. (1995) observed in some metapelitic rocks that spinel and quartz commonly formed a stable relationship, often occurring in contact with one another. Although only volumetrically minor (~1 % abundance), Sheraton et al. (1995) also noted the pervasiveness of spinel throughout the metapelitic rocks and thus question the validity of the notion of subsequent overprinting by a high pressure assemblage. Furthermore, the significance of spinel on *P–T* determinations relies heavily on its ZnO content; as the zinc content in spinel is unreported by previous workers, earlier interpretations on the metamorphic evolution made on the basis of the presence of spinel cannot be considered overly robust.

Cordierite is present in samples 6264 and 6251. Typically, cordierite occurs adjacent to and bridges anhedral garnet grains (e.g. Fig. 2a and b), and sometimes completely isolates relict garnet grains (e.g. Fig. 2f). Cordierite occurring near garnet also commonly hosts sillimanite in sample 6264 (e.g. Fig. 2b and c). Sillimanite is also often included within garnet, but garnet never hosts cordierite. The spatial relationship between garnet and cordierite (and sillimanite in sample 6264) therefore suggests that the abundance of cordierite increased following the growth of garnet and sillimanite at the inferred peak metamorphic conditions. Decreasing garnet and sillimanite

modal abundance and increasing cordierite modal abundance occurs along a down–pressure, down–temperature trajectory (e.g. Fig. S3). Furthermore, rare cordierite–quartz symplectites also occur adjacent to garnet (e.g. Fig. 3). Previous studies have ascribed cordierite–quartz symplectites to garnet breakdown and/or the melt assisted breakdown of feldspar in the presence of a Fe–Mg phase (Henry, 1974; Mohan and Windley, 1993; Nandakumar and Harley, 2000); however, the occurrence of these intergrowths typically adjacent to garnet in this instance is suggestive of the former interpretation. In this study, evidence for cordierite growth after garnet in samples 6264 and 6251, and rare growth of ilmenite about rutile therefore suggests that, in contrast to the initial interpretations of Stüwe and Powell (1989), the rocks of the HJA record evidence for a clockwise (decompressional) *P–T* path. The absence of magnetite in sample 6251 further suggests that the trajectory of this down-temperature *P–T* path may have been relatively shallow. This conclusion is supported by another sample of metapelite located north of Raketa Island (sample 86286263) reported by Sheraton et al. (1995) to show garnet partially replaced by orthopyroxene–cordierite–plagioclase symplectites—a microstructural relationship that has been previously ascribed to a decompressional *P–T* evolution (e.g. Brandt et al. 2003, Tong et al. 2014). Sheraton et al. (1995) also report on garnet occurring as symplectitic rims about orthopyroxene in granite from the Paz Cove Batholith and orthogneiss from the northeast HJA (sample 86285979), inferred to have developed as a result of near-isobaric cooling.

Re-examination of the HJA *P–T* conditions in this study suggests that the metamorphic evolution of these rocks is incompatible with the tectonic model proposed initially by Stüwe and Powell (1989) involving extension followed by compressional deformation, although Harris (1995) note that this initial interpretation was also subsequently re-evaluated. If the rocks underwent thickening post extension then an anticlockwise *P–T* path would be expected (e.g. Brown 1993). In contrast, the retrograde evolution of the HJA presented here is characterised by a pressure decrease during cooling from a metamorphic peak that occurred at a high temperature and medium pressure. This scenario appears more consistent with the notion of thinning of over-thickened crust. However, there is also currently little documented structural evidence for extensional thinning in the Bunger Hills and HJA and therefore the drivers for metamorphism and the down-pressure retrograde evolution proposed in this study remain unclear.

A two-stage tectonothermal history has been proposed for the Windmill Islands involving upper amphibolite facies metamorphism (>750 °C, 4 kbar) at ca. 1340–1300 Ma, and subsequently granulite facies metamorphism (~850–900 °C, 5–7 kbar) at ca. 1240–1140 Ma (Post 2000). The latter phase, coincident with Stage-2 of the Albany–Fraser Orogeny and high temperature metamorphism in the HJA, is inferred to have involved a post-peak clockwise *P–T–time* path, interpreted to reflect exhumation and unloading of the terrane following crustal thickening during continental collision (Post 2000). Similarly, peak granulite facies metamorphism (800 °C, >5 kbar) is also recorded by the Salisbury Gneiss in the Nornalup Complex at 1214 ± 8 Ma with zircon rims dating to 1182 ± 13 Ma, suggestive of decompression from peak metamorphic conditions by exhumation along thrust zones (Clark et al. 2000). Although peak metamorphism of the HJA occurred during Stage-2 of the Albany–Fraser Orogeny, the *P–T* conditions attained are also similar to those recorded at ca. 1290 Ma by the Fraser Zone within southwestern Australia (~850 °C and 7–9 kbar; Clark et al. 2014). These rocks are interpreted to reflect the mid-crustal emplacement of mafic magmatism into a back-arc environment followed by near-isobaric cooling at depth (~ 9 kbar, ~27 km depth; Clark et al. 2014). A similar scenario for the HJA would justify the elevated temperatures and medium pressures attained during peak metamorphism but does not necessarily explain the inferred clockwise *P–T* evolution. Geochronological data from the Bunger Hills currently suggests that magmatism also occurred following the main phase of metamorphism (Sheraton et al. 1992).

7. CONCLUSIONS

Legacy thin section samples provide a valuable record of the geological characteristics of rocks of the HJA that are located in a pivotal yet largely inaccessible part of the MAFO. Metasedimentary rocks from the HJA suggest that this region underwent granulite facies metamorphism (~850–950 °C and 6–9 kbar) at ca. 1183 Ma. The inferred growth of cordierite after garnet further suggests that these rocks cooled along a decompressional *P–T* trajectory following peak metamorphic

conditions. The timing of metamorphism determined in this study confirms the age previously constrained for the Bunger Hills–HJA region. However, the new *P–T* determinations suggest that peak metamorphic conditions within the HJA attained slightly higher temperatures and pressures than previously proposed. In contrast to the initial interpretations from reconnaissance *P–T* work, the results of this study also suggest that the rocks evolved along a clockwise rather than anticlockwise *P–T* path.

ACKNOWLEDGEMENTS

This work forms part of Australian Antarctic Science Project 4191. I. Fitzsimons and F. Korhonen are thanked for their thorough and constructive reviews of the manuscript. We gratefully acknowledge Geoscience Australia, and in particular, Chris Carson, for the use of the samples reported in this study. B. Wade and A. McFadden, Adelaide Microscopy, are thanked for their support with analytical instrumentation. NMT acknowledges the support of an Australian Postgraduate Award and Playford Trust PhD Scholarship.

REFERENCES

Aitken A. R. A. & Betts P. G. 2008. High-resolution aeromagnetic data over central Australia assist Grenville-era (1300–1100 Ma) Rodinia reconstructions. *Geophysical Research Letters* 35, 10.1029/2007GL031563.

Anderson J. A., Kelsey D. E., Hand M. & Collins W. J. 2013. Conductively driven, high-thermal gradient metamorphism in the Anmatjira Range, Arunta region, central Australia. *Journal of Metamorphic Geology* 31, 1003–1026.

Betts P. G. & Giles D. 2006. The 1800–1100 Ma tectonic evolution of Australia. *Precambrian Research* 144, 92–125.

Bodorkos S. & Clark D. J. 2004. Evolution of a crustal-scale transpressive shear zone in the Albany–Fraser Orogen, SW Australia: 2. Tectonic history of the Coramup Gneiss and a kinematic framework for Mesoproterozoic collision of the West Australian and Mawson cratons. *Journal of Metamorphic Geology* 22, 713–731.

Boger S. D. 2011. Antarctica—before and after Gondwana. *Gondwana Research* 19, 335–371.

Brandt S., Klemd R. & Okrusch M. 2003. Ultrahigh-Temperature Metamorphism and Multistage Evolution of Garnet–Orthopyroxene Granulites from the Proterozoic Epupa Complex, NW Namibia. *Journal of Petrology* 44, 1121–1144.

Brown M. 1993. *P–T*-t evolution of orogenic belts and the causes of regional metamorphism. *Journal of the Geological Society* 150, 227–241.

Caddick M. J., Konopásek J. & Thompson A. B. 2010. Preservation of Garnet Growth Zoning and the Duration of Prograde Metamorphism. *Journal of Petrology* 51, 2327–2347.

Cawood P. A. & Korsch R. J. 2008. Assembling Australia: Proterozoic building of a continent. *Precambrian Research* 166, 1–35.

Clark C., Kirkland C. L., Spaggiari C. V., Oorschot C., Wingate M. T. D. & Taylor R. J. 2014. Proterozoic granulite formation driven by mafic magmatism: An example from the Fraser Range Metamorphics, Western Australia. *Precambrian Research* 240, 1–21.

Clark D. J., Hensen B. J. & Kinny P. D. 2000. Geochronological constraints for a two-stage history of the Albany–Fraser Orogen, Western Australia. *Precambrian Research* 102, 155–183.

Clarke G. L., Sun S. S. & White R. W. 1995. Grenville-age belts and associated older terranes in Australia and Antarctica. *AGSO Journal of Australian Geology & Geophysics* 16, 25–39.

Ding P. & James P. 1991. Structural evolution of the Bunger Hills area of East Antarctica. *In Thompson, M. R. A., Crame, J. A. & Thompson, J. W., eds. Geological evolution of Antarctica.* Cambridge: Cambridge University Press, 13-18.

Droop G. T. R. 1987. A general equation for estimating Fe^{3+} concentrations in ferromagnesian silicates and oxides from microprobe analyses, using stoichiometric criteria. *Mineralogical magazine* 51, 431–435.

Duebendorfer E. M. 2002. Regional correlation of Mesoproterozoic structures and deformational events in the Albany–Fraser orogen, Western Australia. *Precambrian Research* 116, 129–154.

Fitzsimons I. 2003. Proterozoic basement provinces of southern and southwestern Australia, and their correlation with Antarctica. *Journal of the Geological Society* 206, 93–130.

Fitzsimons I. C. W. 2000. Grenville-age basement provinces in East Antarctica: Evidence for three separate collisional orogens. *Geology* 28, 879–882.

Griffin W. L., Powell W. J., Pearson N. J. & O'reilly S. Y. 2008. GLITTER: data reduction software for laser ablation ICP–MS. *In: Sylvester P. ed. Laser ablation ICP–MS in the earth sciences: current practices and outstanding issues.* Vancouver: Mineralogical Association of Canada, 204–207.

Harris L. B. 1995. Correlations between the Albany, Fraser and Darling mobile belts of Western Australia and Lirnyy to Windmill Islands in the East Antarctic Shield: implications for Proterozoic Gondwanaland reconstructions. *Memoirs - Geological Society of India*, 47–72.

Henry J. 1974. Garnet-cordierite gneisses near the Egersund-Ogna anorthositic intrusion, southwestern Norway. *Lithos* 7, 207–216.

Holland T. J. B. & Powell R. 2011. An improved and extended internally consistent thermodynamic dataset for phases of petrological interest, involving a new equation of state for solids. *Journal of Metamorphic Geology* 29, 333–383.

Howard H. M., Smithies R. H., Kirkland C. L., Kelsey D. E., Aitken A., Wingate M. T. D., Quentin De Gromard R., Spaggiari C. V. & Maier W. D. 2015. The burning heart — The Proterozoic geology and geological evolution of the west Musgrave Region, central Australia. *Gondwana Research* 27, 64–94.

Kirkland C. L., Smithies R. H. & Spaggiari C. V. 2015. Foreign contemporaries – Unravelling disparate isotopic signatures from Mesoproterozoic Central and Western Australia. *Precambrian Research* 265, 218–231.

Kirkland C. L., Smithies R. H., Woodhouse A. J., Howard H. M., Wingate M. T. D., Belousova E. A., Cliff J. B., Murphy R. C. & Spaggiari C. V. 2013. Constraints and deception in the isotopic record: the crustal evolution of the west Musgrave Province, central Australia. *Gondwana*

Research 23, 759–781.

Kirkland C. L., Spaggiari C. V., Pawley M. J., Wingate M. T. D., Smithies R. H., Howard H. M., Tyler I. M., Belousova E. A. & Poujol M. 2011. On the edge: U–Pb, Lu–Hf, and Sm–Nd data suggests reworking of the Yilgarn craton margin during formation of the Albany-Fraser Orogen. *Precambrian Research* 187, 223–247.

Korhonen F. J., Saito S., Brown M. & Siddoway C. S. 2010. Modeling multiple melt loss events in the evolution of an active continental margin. *Lithos* 116, 230–248.

Mohan A. & Windley B. F. 1993. Crustal trajectory of sapphirine-bearing granulites from Ganguvarpatti, South India: evidence for an isothermal decompression path. *Journal of Metamorphic Geology* 11, 867–878.

Nandakumar V. & Harley S. L. 2000. A Reappraisal of the Pressure-Temperature Path of Granulites from the Kerala Khondalite Belt. *Journal of Geology* 108, 687–703.

Nelson D. R., Myers J. S. & Nutman A. P. 1995. Chronology and evolution of the Middle Proterozoic Albany-Fraser Orogen, Western Australia. Australian *Journal of Earth Sciences* 42, 481–495.

Nichols G., Berry R. & Green D. 1992. Internally consistent gahnitic spinel-cordierite-garnet equilibria in the FMASHZn system: geothermobarometry and applications. *Contributions to Mineralogy and Petrology* 111, 362–377.

Payne J. L., Hand M., Barovich K. M. & Wade B. P. 2008. Temporal constraints on the timing of high-grade metamorphism in the northern Gawler Craton: implications for assembly of the Australian Proterozoic. *Australian Journal of Earth Sciences* 55, 623–640.

Pearce M., White A. & Gazley M. 2015. TCInvestigator: automated calculation of mineral mode and composition contours for thermocalc pseudosections. *Journal of Metamorphic Geology* 33, 413–425.

Post N. J. 2000. *Unravelling Gondwana fragments: an integrated structural, isotopic and petrographic investigation of the Windmill Islands, Antarctica.* PhD thesis, University of New South Wales 382 pp. [Unpublished].

Ravich M. G. E., Klimov L. & Solov′ev D. 1968. *The Pre-Cambrian of East Antarctica.* Jerusalem: Israel Program for Scientific Translations, 475 pp.

Sheraton J. W., Black L. P. & Tindle A. G. 1992. Petrogenesis of plutonic rocks in a Proterozoic granulite-facies terrane — the Bunger Hills, East Antarctica. *Chemical Geology* 97, 163–198.

Sheraton J. W., Black L. P., Mcculloch M. T. & Oliver R. L. 1990. Age and origin of a compositionally varied mafic dyke swarm in the Bunger Hills, East Antarctica. *Chemical Geology* 85, 215–246.

Sheraton J. W., Tingey R. J., Black L. P. & Oliver R. L. 1993. Geology of the Bunger Hills area, Antarctica: implications for Gondwana correlations. *Antarctic Science* 5, 85–102.

Sheraton J. W., Tingey R., Oliver R. & Black L. 1995. Geology of the Bunger Hills–Denman Glacier region, East Antarctica. *AGSO Bulletin*, No. 244, 1–136.

Smithies R. H., Howard H. M., Evins P. M., Kirkland C. L., Kelsey D. E., Hand M., Wingate M. T. D., Collins A. S. & Belousova E. 2011. High-temperature granite magmatism, crust-mantle interaction and the mesoproterozoic intracontinental evolution of the Musgrave Province, central Australia. *Journal of Petrology* 52, 931–958.

Smithies R. H., Kirkland C. L., Korhonen F. J., Aitken A. R. A., Howard H. M., Maier W. D., Wingate M. T. D., Quentin De Gromard R. & Gessner K. 2015. The Mesoproterozoic thermal evolution of the Musgrave Province in central Australia — Plume vs. the geological record. *Gondwana Research* 27, 1419–1429.

Smits R. G., Collins W. J., Hand M., Dutch R. & Payne J. 2014. A Proterozoic Wilson cycle identified by Hf isotopes in central Australia; implications for the assembly of Proterozoic Australia and Rodinia. *Geology* 42, 231–234.

Spaggiari C. V. & Tyler I. M. 2014. *Albany-Fraser Orogen seismic and magnetotelluric (MT) workshop 2014: extended abstracts.* Record 2014/6. East Perth: Geological Survey of Western Australia, 182p.

Spaggiari C. V., Kirkland C. L., Smithies R. H., Wingate M. T. D. & Belousova E. A. 2015. Transformation of an Archean craton margin during Proterozoic basin formation and magmatism: the Albany–Fraser Orogen, Western Australia. *Precambrian Research* 266, 440–466.

Spear F. S. 1991. On the interpretation of peak metamorphic temperatures in light of garnet diffusion during cooling. *Journal of Metamorphic Geology* 9, 379–388.

Stüwe K. & Powell R. 1989. Metamorphic evolution of the Bunger Hills, East Antarctica: evidence for substantial post-metamorphic peak compression with minimal cooling in a Proterozoic orogenic event. *Journal of Metamorphic Geology* 7, 449–464.

Stüwe K. & Wilson C. J. L. 1990. Interaction between deformation and charnockite emplacement in the Bunger Hills, East Antarctica. Journal of Structural *Geology* 12, 767–783.

Tajčmanová L., Konopásek J. & Košler J. 2009. Distribution of zinc and its role in the stabilization of spinel in high-grade felsic rocks of the Moldanubian domain (Bohemian Massif). *European Journal of Mineralogy* 21, 407–418.

Tong L. X., Liu X. H., Wang Y. B., & Liang X. R. 2014. Metamorphic *P–T* paths of metapelitic granulites from the Larsemann Hills, East Antarctica. *Lithos* 192, 102–115.

Tucker N. M., Hand M., Kelsey D. E. & Dutch R. A. 2015. A duality of timescales: Short-lived ultrahigh temperature metamorphism preserving a long-lived monazite growth history in the Grenvillian Musgrave–Albany–Fraser Orogen. *Precambrian Research* 264, 204–234.

Walsh A. K., Kelsey D. E., Kirkland C. L., Hand M., Smithies R. H., Clark C. & Howard H. M. 2015. *P–T–t* evolution of a large, long-lived, ultrahigh-temperature Grenvillian belt in central Australia. *Gondwana Research* 28, 531–564.

White L. T., Gibson G. M. & Lister G. S. 2013. A reassessment of paleogeographic reconstructions of eastern Gondwana: bringing geology back into the equation. *Gondwana Research* 24, 984–998.

White R. W., Powell R., Holland T. J. B., Johnson T. E. & Green E. C. R. 2014. New mineral activity–composition relations for thermodynamic calculations in metapelitic systems. *Journal of Metamorphic Geology* 32, 261–286.

Zhang S. H., Zhao Y., Liu X. C., Liu Y. S., Hou K. J., Li C. F., & Ye H. 2012. U–Pb geochronology and geochemistry of the bedrocks and moraine sediments from the Windmill Islands: Implications for Proterozoic evolution of East Antarctica. *Precambrian Research* 206, 52–71.

Supplementary Table 1. Representative mineral analyses

Sample	8628-6264										8628-6251										8628-5607							
Mineral	bi	cd	sill	gt (core)	gt (rim)	ru	ilm	pl	ksp	q	bi	cd	sill	gt (core)	gt (rim)	sp	ilm	pl	ksp	q	bi	sill	gt (core	gt (rim)	ilm	ru	pl	q
SiO_2	38.37	48.39	35.59	38.60	38.89	0.00	0.00	57.29	64.20	98.87	36.55	48.52	36.08	38.46	38.25	0.00	0.00	58.97	63.67	99.49	37.55	36.11	38.32	38.11	0.00	0.00	55.96	99.48
TiO_2	3.77	0.00	0.01	0.03	0.01	99.00	49.83	0.02	0.02	0.05	4.85	0.01	0.03	0.04	0.05	0.01	51.44	0.03	0.03	0.04	4.76	0.06	0.45	0.02	52.43	99.75	0.03	0.08
Al_2O_3	14.81	33.56	62.80	21.92	22.08	0.06	0.01	26.75	19.11	0.08	15.99	33.59	62.29	21.89	21.77	60.34	0.00	25.38	18.83	0.02	15.76	62.82	21.78	21.80	0.02	0.00	27.58	0.03
Cr_2O_3	0.01	0.01	0.00	0.01	0.01	0.04	0.05	0.00	0.01	0.02	0.07	0.00	0.04	0.01	0.01	0.25	0.06	0.00	0.00	0.01	0.11	0.31	0.06	0.06	0.09	0.21	0.00	0.01
FeO	10.50	4.41	1.02	26.93	27.28	0.36	48.08	0.02	0.00	0.02	14.29	4.26	1.57	27.35	30.08	28.19	46.69	0.00	0.00	0.00	10.17	0.27	28.66	29.63	45.29	0.05	0.02	0.00
MnO	0.00	0.01	0.00	0.59	0.60	0.00	0.18	0.00	0.01	0.00	0.00	0.06	0.02	0.88	1.07	0.06	0.21	0.02	0.00	0.00	0.00	0.00	0.37	0.36	0.10	0.00	0.00	0.00
MgO	18.34	11.25	0.02	10.56	10.28	0.00	0.65	0.00	0.00	0.01	14.65	11.40	0.02	10.05	8.22	10.15	0.68	0.00	0.00	0.00	17.96	0.01	9.16	7.95	1.85	0.00	0.00	0.00
ZnO	0.01	0.03	0.00	0.05	0.00	0.00	0.00	0.05	0.01	0.02	0.01	0.00	0.00	0.00	0.00	1.00	0.00	0.00	0.00	0.01	0.04	0.00	0.00	0.10	0.08	0.02	0.03	0.02
CaO	0.00	0.00	0.00	1.10	1.21	0.00	0.00	8.20	0.16	0.00	0.03	0.00	0.00	1.30	1.05	0.00	0.00	6.80	0.07	0.00	0.01	0.00	1.47	1.93	0.00	0.00	9.40	0.00
Na_2O	0.10	0.03	0.01	0.00	0.00	0.00	0.00	7.24	1.89	0.01	0.02	0.01	0.01	0.01	0.00	0.02	0.00	8.05	1.31	0.00	0.11	0.00	0.00	0.00	0.02	0.00	6.68	0.01
K2O	10.39	0.01	0.00	0.01	0.00	0.00	0.00	0.17	14.33	0.01	10.22	0.01	0.00	0.00	0.01	0.00	0.00	0.16	15.23	0.00	9.70	0.00	0.00	0.01	0.00	0.00	0.21	0.01
Cl	0.07	0.01	0.00	0.00	0.00	0.00	0.00	0.00	0.00	0.00	0.10	0.00	0.00	0.00	0.00	0.01	0.00	0.01	0.00	0.00	0.09	0.00	0.00	0.01	0.00	0.00	0.00	0.01
F	2.41	0.00	0.00	0.05	0.01	0.03	0.11	0.00	0.00	0.00	0.64	0.00	0.00	0.00	0.02	0.00	0.10	0.00	0.00	0.00	0.37	0.00	0.00	0.00	0.12	0.02	0.00	0.00
Total	98.78	97.72	99.46	99.85	100.37	99.48	98.92	99.75	99.74	99.06	97.43	97.87	100.06	100.00	100.53	100.02	99.18	99.43	99.14	99.57	96.62	99.58	100.28	99.97	100.00	100.04	99.91	99.64
No. Oxygens	11	18	5	12	12	2	3	8	8	2	11	18	5	12	12	4	3	8	8	2	11	5	12	12	3	2	8	2
Si	2.45	4.91	0.97	2.96	2.97	0.00	0.00	2.56	2.95	1.00	2.38	4.91	0.98	2.95	2.96	0.00	0.00	2.63	2.95	1.00	2.41	0.98	2.95	2.96	0.00	0.00	2.50	1.00
Ti	0.18	0.00	0.00	0.00	0.00	0.99	0.95	0.00	0.00	0.00	0.24	0.00	0.00	0.00	0.00	0.00	0.98	0.00	0.00	0.00	0.23	0.00	0.03	0.00	0.98	1.00	0.00	0.00
Al	1.11	4.01	2.01	1.98	1.98	0.00	0.00	1.41	1.03	0.00	1.23	4.00	1.99	1.98	1.98	1.93	0.00	1.33	1.03	0.00	1.19	2.01	1.98	2.00	0.00	0.00	1.45	0.00
Cr	0.00	0.00	0.00	0.00	0.00	0.00	0.00	0.00	0.00	0.00	0.00	0.00	0.00	0.00	0.00	0.00	0.00	0.00	0.00	0.00	0.01	0.01	0.00	0.00	0.00	0.00	0.00	0.00
Fe^{3+}				0.09	0.08		0.09							0.12	0.09	0.07	0.03						0.07	0.07	0.03			
Fe^{2+}	0.56	0.37	0.02	1.63	1.66	0.00	0.93	0.00	0.00	0.00	0.78	0.36	0.04	1.63	1.86	0.56	0.96	0.00	0.00	0.00	0.54	0.01	1.78	1.85	0.92	0.00	0.00	0.00
Mn^{2+}	0.00	0.00	0.00	0.04	0.04	0.00	0.00	0.00	0.00	0.00	0.00	0.01	0.00	0.06	0.07	0.00	0.00	0.00	0.00	0.00	0.00	0.00	0.02	0.02	0.00	0.00	0.00	0.00
Mg	1.74	1.70	0.00	1.21	1.17	0.00	0.02	0.00	0.00	0.00	1.42	1.72	0.00	1.15	0.95	0.41	0.03	0.00	0.00	0.00	1.72	0.00	1.05	0.92	0.07	0.00	0.00	0.00
Zn	0.00	0.00	0.00	0.00	0.00	0.00	0.00	0.00	0.00	0.00	0.00	0.00	0.00	0.00	0.00	0.02	0.00	0.00	0.00	0.00	0.00	0.00	0.00	0.01	0.00	0.00	0.00	0.00
Ca	0.00	0.00	0.00	0.09	0.10	0.00	0.00	0.39	0.01	0.00	0.00	0.00	0.00	0.11	0.09	0.00	0.00	0.33	0.00	0.00	0.00	0.00	0.12	0.16	0.00	0.00	0.45	0.00
Na	0.01	0.01	0.00	0.00	0.00	0.00	0.00	0.63	0.17	0.00	0.00	0.00	0.00	0.00	0.00	0.00	0.00	0.70	0.12	0.00	0.01	0.00	0.00	0.00	0.00	0.00	0.58	0.00
K	0.85	0.00	0.00	0.00	0.00	0.00	0.00	0.01	0.84	0.00	0.85	0.00	0.00	0.00	0.00	0.00	0.00	0.01	0.90	0.00	0.79	0.00	0.00	0.00	0.00	0.00	0.01	0.00
Cl	0.01	0.00	0.00	0.00	0.00	0.00	0.00	0.00	0.00	0.00	0.01	0.00	0.00	0.00	0.00	0.00	0.00	0.00	0.00	0.00	0.01	0.00	0.00	0.00	0.00	0.00	0.00	0.00
F	0.49	0.00	0.00	0.01	0.00	0.00	0.01	0.00	0.00	0.00	0.13	0.00	0.00	0.00	0.00	0.00	0.01	0.00	0.00	0.00	0.08	0.00	0.00	0.00	0.01	0.00	0.00	0.00
Cations	6.90	11	3	8	8	1	2	5	5	1	6.90	11	3	8	8	3	2	5	5	1	6.90	3	8	8	2	1	5	1
X_{Mg}	0.76	0.82		0.43	0.41						0.65	0.83		0.41	0.34						0.76		0.37	0.33				
X_{alm}				0.55	0.56									0.55	0.63								0.60	0.63				
X_{py}				0.41	0.39									0.39	0.32								0.35	0.31				
X_{sps}				0.01	0.01									0.02	0.02								0.01	0.01				
X_{grs}				0.03	0.03									0.04	0.03								0.04	0.05				
X_{an}								0.38	0.01									0.32	0.00								0.43	
X_{or}								0.01	0.83									0.01	0.88								0.01	

X_{Mg} (Mg/(Fe^{2+} + Mg)); X_{alm} (Fe^{2+}/(Fe^{2+} + Mg + Ca + Mn)); X_{py} (Mg/ (Fe^{2+} + Mg + Ca + Mn)); X_{sps} (Mn/ (Fe^{2+} + Mg + Ca + Mn)); X_{grs} (Ca/(Fe^{2+} + Mg + Ca + Mn)); X_{an} (Ca/Ca + Na + K)); X_{or} (K/(Ca + Na + K)).

Supplementary Figure S1. T–M_{H2O} diagrams for bulk composition determination.
The H_2O content used in the bulk composition for each sample was estimated from the abundance and composition of hydrous minerals in the observed mineral assemblages. The sensitivity of the selected H_2O content on the boundaries of the peak mineral assemblage field to temperature is evaluated for each sample using a calculated T–M_{H2O} diagram (Figures S1a–c, below). The T–M_{H2O} diagrams are presented at the approximate peak pressure of the inferred peak mineral assemblage of each sample (refer to Fig. 4, main text). The T–M_{H2O} diagrams are shown over the range of a near-anhydrous composition (M= 0) to a maximum estimate of the H_2O content as provided by the LOI content (M=1) from whole-rock geochemistry. The inferred peak mineral assemblage stability field of each sample is outlined in bold. The solidus is represented by a dashed line. The selected H_2O content for each sample is represented by the vertical line. Mineral abbreviations refer to Holland and Powell (1998).

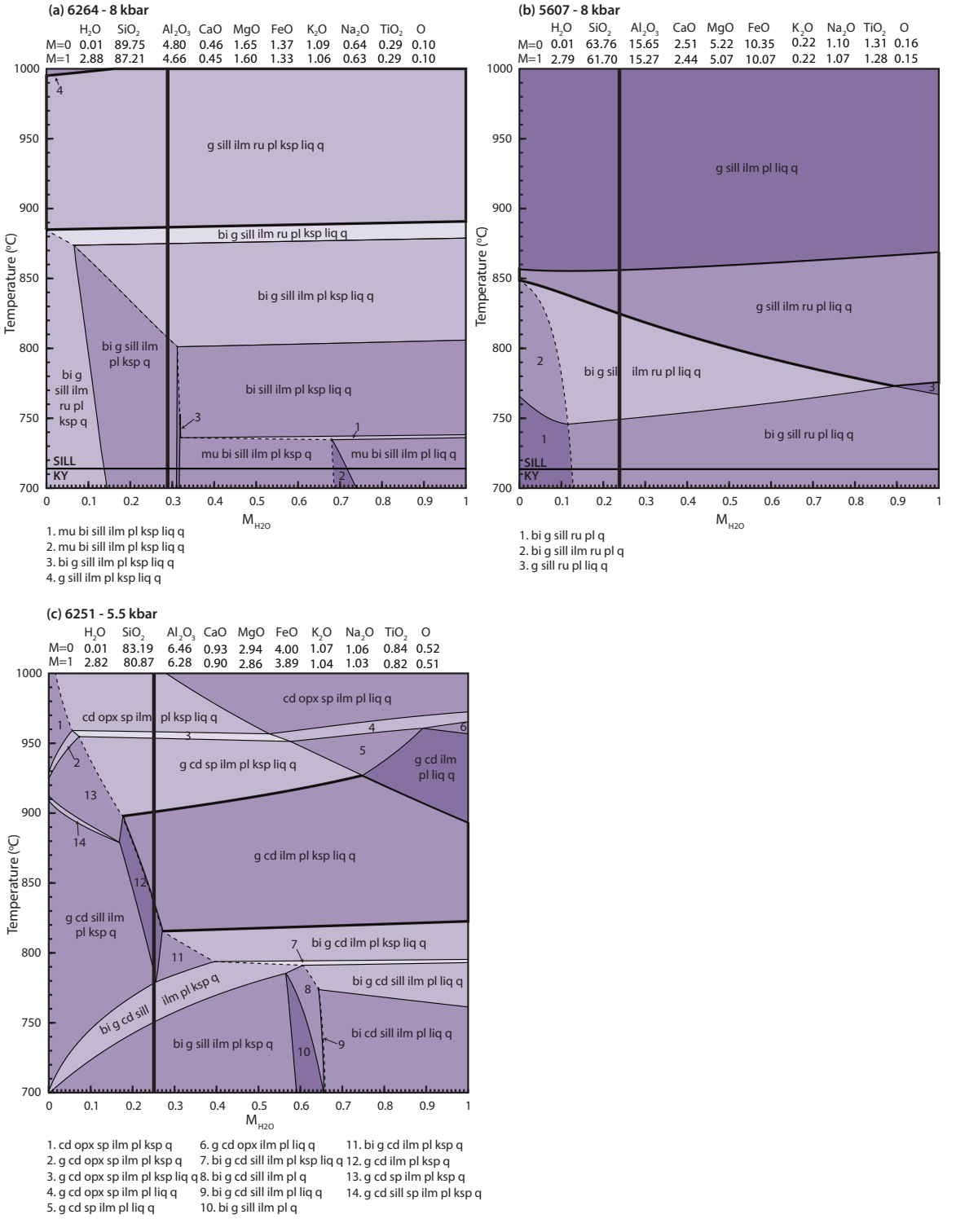

Supplementary Figure S2. Temperature–XFe_2O_3 diagrams for bulk composition determination.
Temperature–XFe_2O_3 (XFe_2O_3 = Fe_2O_3/(FeO + Fe_2O_3)) diagrams constructed for: (a) Sample 6264; (b) Sample 5607; and, (c) Sample 6251. The bulk compositions used for the construction of each pseudosection are given below. The *T*–*X* sections are shown for the range *X*=0 (all Fe as FeO) to *X* = 0.5 (50 % Fe as Fe_2O_3). The bulk composition used for the corresponding *P*–*T* pseudosection for each sample (Fig. 4, main text) is represented by the solid black line. The solidus is represented by a dashed line. Mineral abbreviations from Holland and Powell (1998).

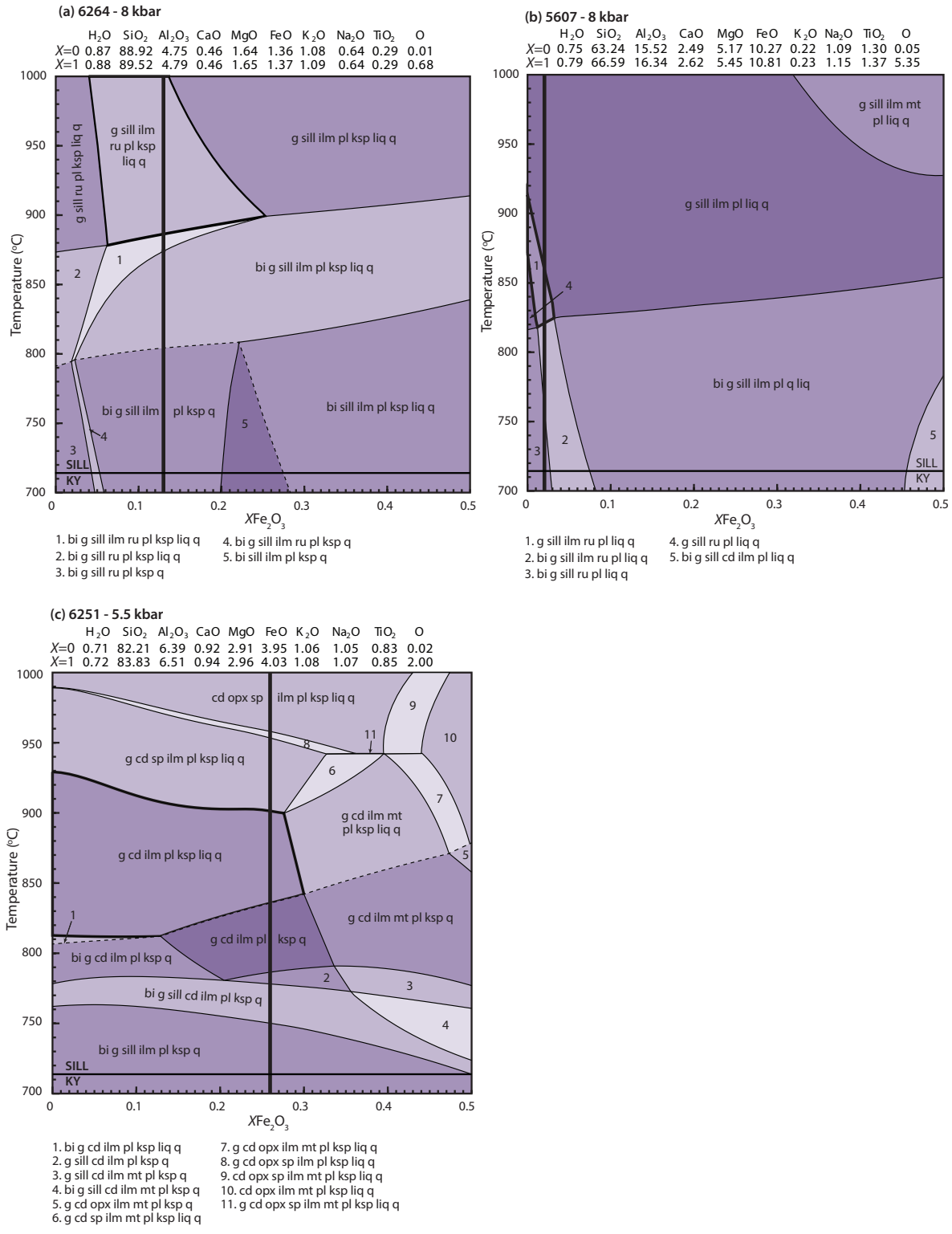

Supplementary Figure S3. TCInvestigator (Pearce et al., 2015) contoured *P–T* pseudosections.
Calculated *P–T* pseudosections are contoured for compositions and modal abundance of relevant phases discussed in the main text. The approximate measured range of compositional isopleths for garnet are indicated by a dashed outline. The inferred peak mineral assemblage stability field is outlined in bold.

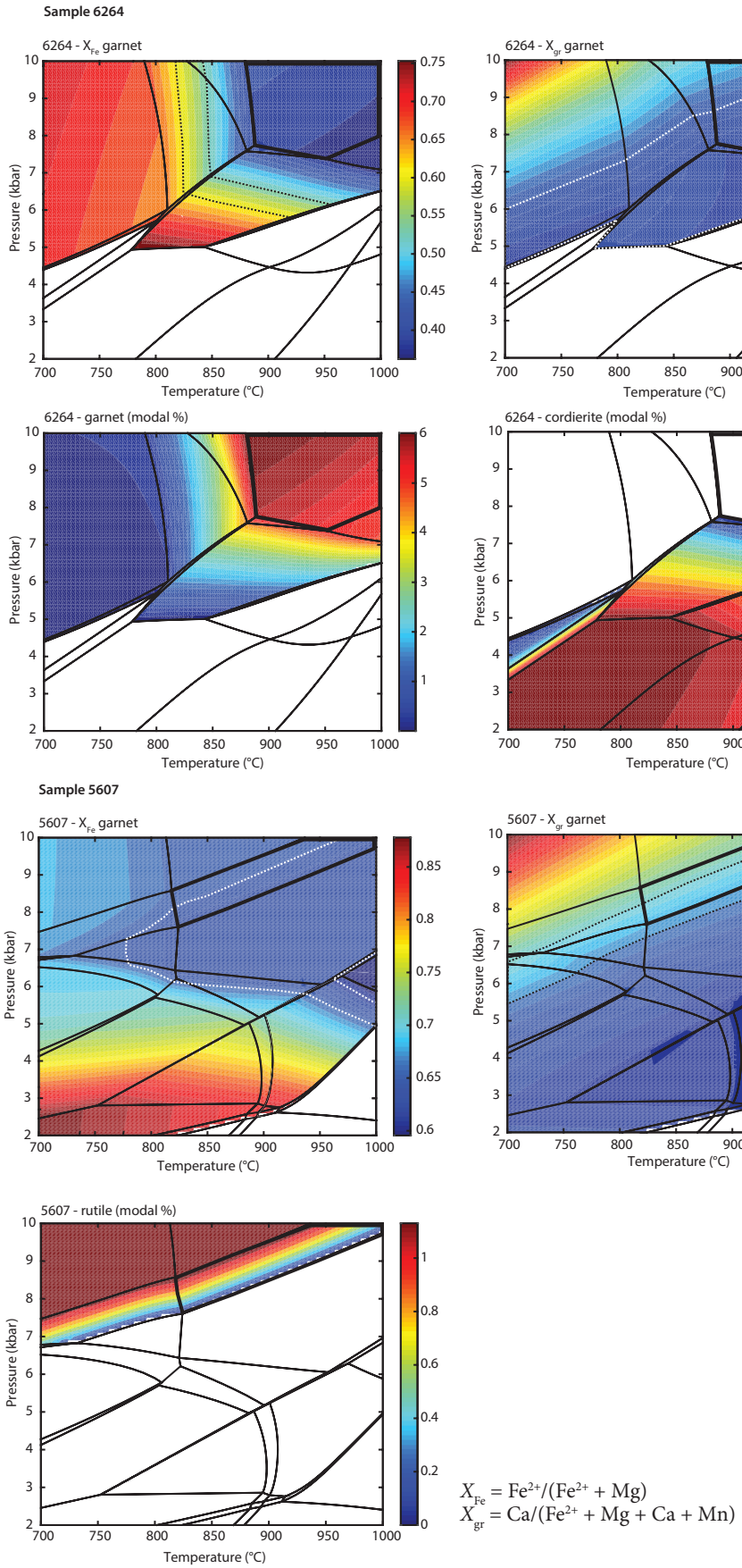

$X_{Fe} = Fe^{2+}/(Fe^{2+} + Mg)$
$X_{gr} = Ca/(Fe^{2+} + Mg + Ca + Mn)$

Supplementary Figure S3. (continued)

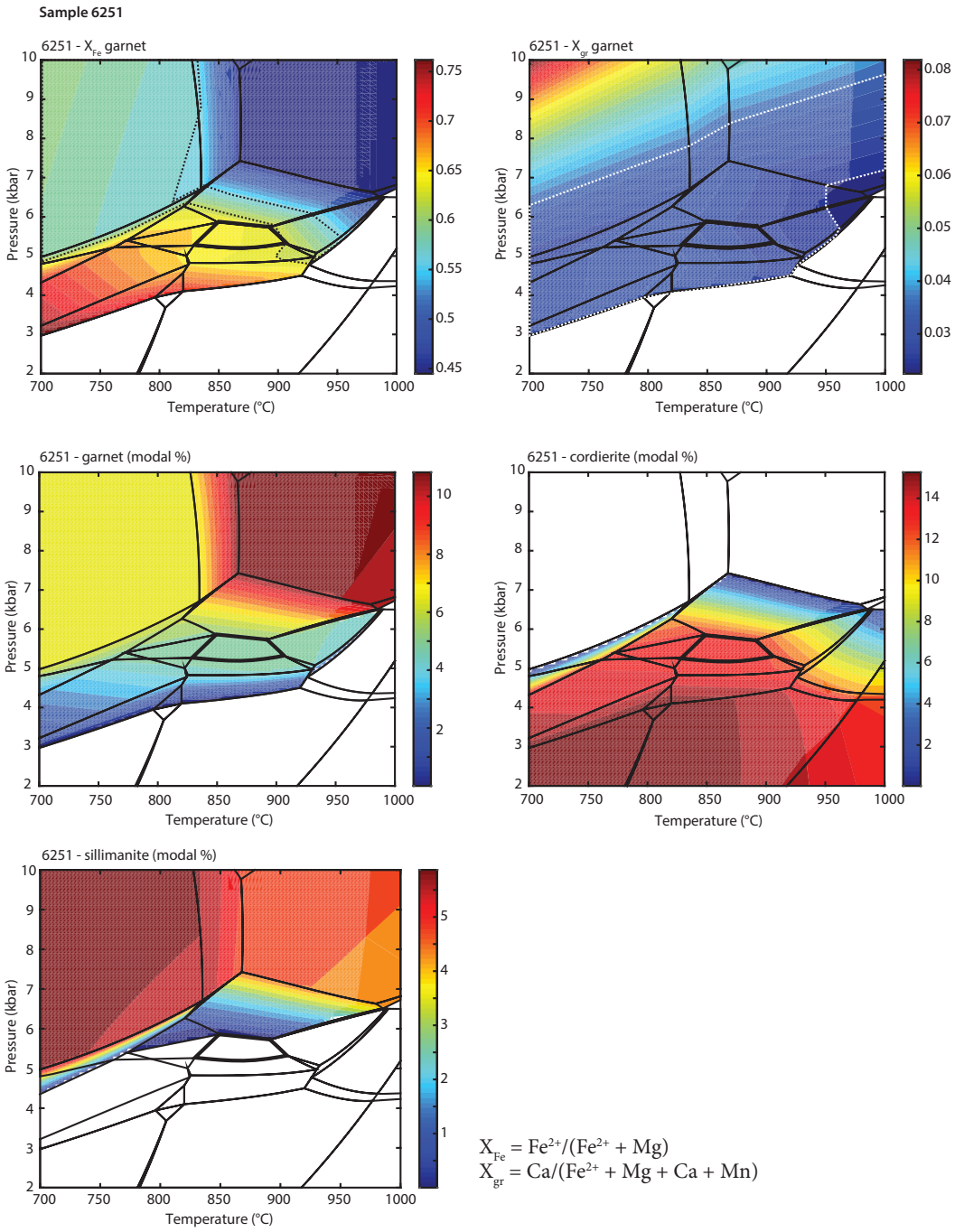

$X_{Fe} = Fe^{2+}/(Fe^{2+} + Mg)$
$X_{gr} = Ca/(Fe^{2+} + Mg + Ca + Mn)$

Chapter 3

This chapter is published as:

Tucker, N. M., Payne, J. L., Clark, C., Hand, M., Taylor, R. J. M., Kylander-Clark, A. R. C. & Martin, L. 2017. Proterozoic reworking of Archean (Yilgarn) basement in the Bunger Hills, East Antarctica. *Precambrian Research*, **298**: 16–38, doi: 10.1016/j.precamres.2017.05.013.

Statement of Authorship

Title of paper	Proterozoic reworking of Archean (Yilgarn) basement in the Bunger Hills, East Antarctica
Pulication status	☒ Published ☐ Accepted for publication ☐ Submitted for publication ☐ Unpublished and unsubmitted work written in manuscript style
Publication details	Tucker, N. M., Payne, J. L., Clark, C., Hand, M., Taylor, R. J. M., Kylander-Clark, A. R. C. & Martin, L. 2017. Proterozoic reworking of Archean (Yilgarn) basement in the Bunger Hills, East Antarctica. *Precambrian Research*, **298**: 16–38, doi: 10.1016/j.precamres.2017.05.013.

Principal Author

Name of Principal Author	Naomi M. Tucker
Contribution to the paper	Project design; fieldwork; sample selection and preparation; LA–ICP–MS data collection; all calculations and data processing; critical data interpretation; manuscript design and composition; creation of all figures.
Overall percentage (%)	80
Certification	This paper reports on original research I conducted during the period of my Higher Degree by Research candidature and is not subject to any obligations or contractual agreements with a third party that would constrain its inclusion in this thesis. I am the primary author of this paper.
Signature	Date 04/10/2017

Co-author contributions

By signing the Statement of Authorship, each author certifies that:
i. the candidate's stated contribution to the publication is accurate (as detailed above);
ii. permission is granted for the candidate to include the publication in the thesis; and,
iii. the sum of all co-authors contributions is equal to 100 % less the candidate's stated contribution.

Name of Co-author	Justin L. Payne
Contribution to the paper	Assistance with LA–ICP–MS data processing; LA–ICP–MS data interpretation guidance; manuscript review.
Signature	Date 04/10/2017

Name of Co-author	Chris Clark
Contribution to the paper	Fieldwork; LA–ICP–MS data interpretation guidance; manuscript review.
Signature	Date 16/01/2017

Name of Co-author	Martin Hand
Contribution to the paper	Fieldwork; data interpretation guidance; manuscript review.
Signature	Date 13/10/2017

Name of Co-author	Richard J. Taylor
Contribution to the paper	Assistance with sample preparation for LA–ICP–MS; sample imaging; data interpretation guidance; manuscript review.
Signature	Date 04/10/2017

Name of Co-author	Andrew R. C. Kylander-Clark
Contribution to the paper	Assistance with LA–ICP–MS data collection; manuscript review.
Signature	Date 04/10/2017

Name of Co-author	Laure Martin
Contribution to the paper	Oxygen isotope data collection using prepared zircon mounts; manuscript review.
Signature	Date 04/10/2017

Proterozoic reworking of Archean (Yilgarn) basement in the Bunger Hills, East Antarctica

Naomi M. Tucker[a], Justin L. Payne[a,b], Chris Clark[c], Martin Hand[a], Richard J. M. Taylor[d], Andrew R. C. Kylander–Clark[e] and Laure Martin[f]

[a]*Department of Earth Sciences, School of Physical Sciences, University of Adelaide, Adelaide, South Australia 5005*

[b]*School of Natural and Built Environments, University of South Australia, Mawson Lakes Campus, South Australia 5095*

[c]*Department of Applied Geology, Curtin University, Perth, Western Australia*

[d]*Department of Earth Sciences, University of Cambridge, Cambridge, CB2 3EQ, UK*

[e]*Department of Earth Science, University of California, Santa Barbara, CA, 93106, USA*

[f]*ARC Centre of Excellence for Core to Crust Fluid Systems and Centre for Microscopy, Characterisation and Analysis, University of Western Australia, Perth, Western Australia 6009*

ABSTRACT

The Bunger Hills in East Antarctica occupy a pivotal location as the westernmost continuation of the Albany–Fraser Orogen in southwestern Australia. Combined U–Pb, Lu–Hf and oxygen isotope data from the Bunger Hills reveal a previously unrecognised Archean basement (ca. 2800–2700 Ma) of Yilgarn Craton affinity. Results also reveal a Paleo–Mesoproterozoic (ca. 1700–1500 Ma) volcano-clastic sequence and late Mesoproterozoic magmatic intrusives (ca. 1260 Ma and 1200 Ma) that were coeval with high-grade metamorphism. Isotopic data reflect the influence of an Archean crustal component in Proterozoic magmatism. Paleoproterozoic magmatism was characterised by voluminous juvenile input and minor recycling of Archean crust. In contrast, Mesoproterozoic magmatism is isotopically evolved, and is interpreted to have been derived largely from reworking of the Paleoproterozoic crust and Archean basement. Strong parallels between the age and isotopic composition of igneous rocks over time from the Bunger Hills and Albany–Fraser Orogen in southwest Australia suggest that the Paleo–Mesoproterozoic tectonic evolution of these two elements of the orogen is linked. Specifically, the Bunger Hills are interpreted to represent the Paleo–Mesoproterozoic (para)autochthonous modification of a reworked fragment of the Archean Yilgarn Craton that was extended during the late Paleoproterozoic.

1. INTRODUCTION

Zircon isotope signatures form part of the method that allows one to distinguish magmatic events and the source of magmas (e.g. Archibald et al., 2016; Belousova et al., 2006, 2010; Kemp et al., 2006; Taylor et al., 2015). Distinction between magmatic events that represent refertilisation of the crust by the addition of new juvenile material versus those that involve crustal recycling is important to understand the crustal growth history of any given geologic terrane. This is of particular importance in reconstructing the crustal evolution of continental margins which may represent sites of *in situ* crustal reorganisation as well as crustal growth by magmatism and exotic terrane accretion (Cochrane et al., 2014; Hawkesworth and Kemp, 2006a,b; Kirkland et al., 2015a, 2011).

The Albany–Fraser Orogen in southwestern Australia provides one example of the transformation of an Archean craton margin that occurred during the Proterozoic (Kirkland et al., 2015a, 2011; Spaggiari et al., 2015). The Albany–Fraser Orogen, together with the Musgrave Inlier[1] in central Australia, and the Bunger Hills and Windmill Islands in East Antarctica, is broadly interpreted as the product of Rodinian amalgamation of the Archean North and West Australian cratons (NAC and WAC, respectively), with the South Australian Craton (SAC) and East Antarctic Craton (EAC; e.g. Betts and Giles, 2006; Cawood and Korsch, 2008; Giles et al., 2004). Geochronological and isotopic data have been used to suggest that, specifically, the Albany–Fraser Orogen records evidence for autochthonous (*in situ*) crustal reworking by

[1]Musgrave Province, herein referred to as Musgrave Inlier. The Musgrave Inlier is enclosed by the younger Neoproterozoic–Palaeozoic sedimentary basins of the Amadeus, Officer, Canning and Eromanga Basins.

extension of the southern Yilgarn Craton margin during the Paleoproterozoic (Kirkland et al., 2015a; Spaggiari et al., 2015), the emplacement of juvenile magmatism during extension (Kirkland et al., 2015a; Kirkland et al., 2011), the subsequent generation of isotopically evolved magmas during the Mesoproterozoic (Kirkland et al., 2011), and allochthonous, active margin processes such as accretion of an exotic oceanic arc (Spaggiari et al., 2015). Isotopic data from the Musgrave Inlier and Albany–Fraser Orogen have also been used to suggest that while these two tectonic elements have long been considered part of the same geologic system due to similarities in their timing of Mesoproterozoic magmatism and metamorphism (e.g. Fitzsimons, 2003), their pre-Mesoproterozoic crustal evolution involved reworking of isotopically disparate basement rocks (Kirkland et al., 2015a).

Our understanding of the crustal evolution of the Albany–Fraser Orogen and Musgrave Inlier has recently advanced. However, the Antarctic elements of the orogen, and in particular the Bunger Hills, remain comparatively elusive. We accordingly present new U–Pb geochronology and the first Lu–Hf and oxygen isotope data for detrital and igneous zircon from the Bunger Hills. U–Pb geochronology is used to constrain the timing of magmatism, sedimentary protolith deposition and metamorphism. Lu–Hf and oxygen isotope data are used to trace the extent of intracrustal recycling through time. We integrate our data with existing data from the Albany–Fraser Orogen, Musgrave Inlier, Windmill Islands, Yilgarn Craton and correlated offshore microcontinents (e.g. Gulden Draak Knoll) to provide a synopsis of the crustal evolution of the Bunger Hills. Isotopic data reveal the dominant role of a Paleoproterozoic

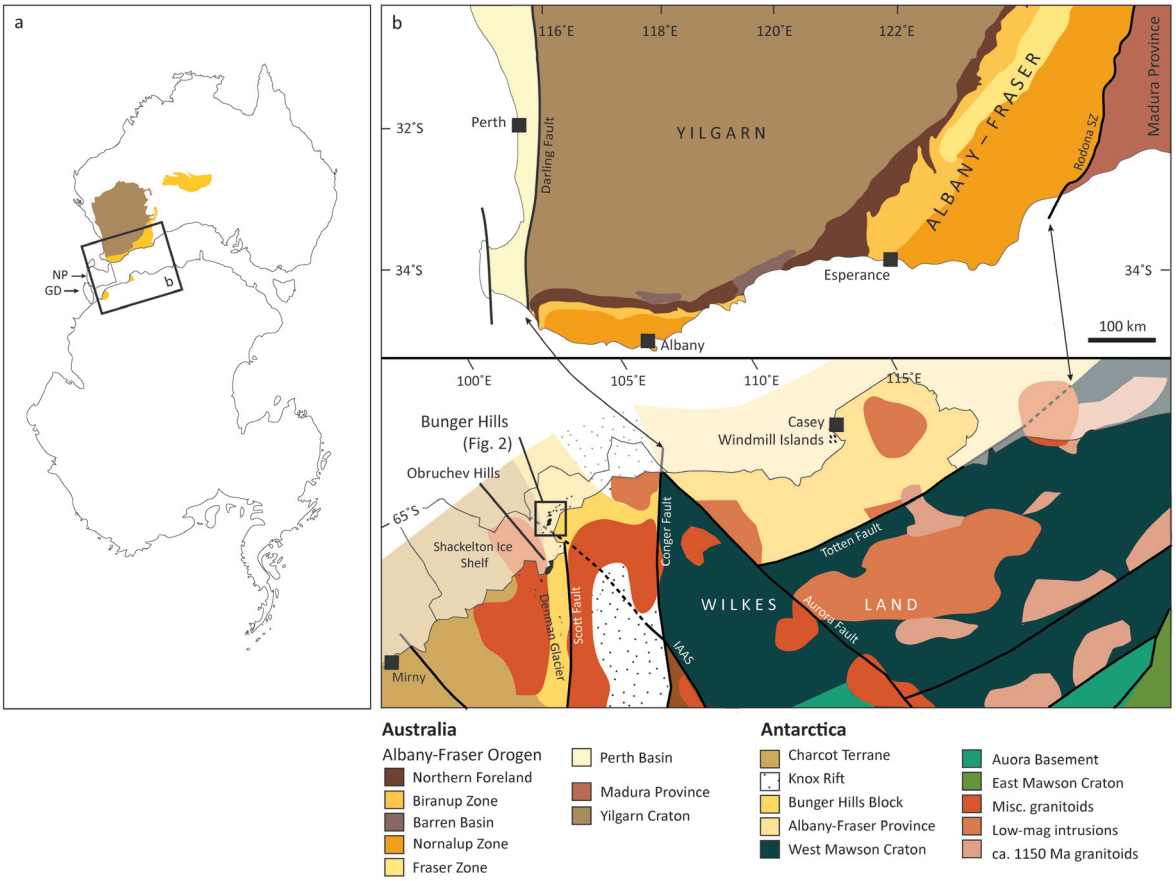

Figure 1. Simplified schematic of Australo–Antarctic palaeogeography and tectonic elements. (a) The relative location of Australia and Antarctica reflect their approximate positions in Gondwanan reconstructions to highlight their former connectivity. The Musgrave Inlier in central Australia, the Albany–Fraser Orogen in southwest Australia, and the Bunger Hills and Windmills Islands in East Antarctica are shown in yellow. The Yilgarn Craton is represented in brown. The location of the Gulden Draak Knoll (GD) and Naturaliste Plateau (NP) are shown according to the Gondwanan tectonic reconstruction (ca. 136 Ma) of Gibbons et al. (2012) (in Gardner et al. (2015)). The boxed region is expanded in (b); (b) Grid references refer to the present-day positioning of Australia and Antarctica. Areas of outcrop in Antarctica are shaded black. The location of the Bunger Hills (enlarged in Fig. 2) is indicated. Geological boundaries and structures are adapted from Tucker et al. (2015), Maritati et al. (2016), Aitken et al. (2014), Boger (2011), Spaggiari et al. (2009) and the 1:2 500 000 interpreted bedrock geology of Western Australia (Geological Survey of Western Australia, 2015). Intercontinental piercing points of Aitken et al. (2014) between the Darling–Conger Fault and Rodona–Totten Fault are indicated.

crustal source, and Archean basement of Yilgarn Craton affinity, in the origin of Mesoproterozoic magmas. We propose that the crustal evolution of the Bunger Hills is allied with the Albany–Fraser Orogen.

2. GEOLOGICAL SETTING

The Bunger Hills are an ice-free region of low hills and deep glacial lakes covering ~400 km2 along the coast of Wilkes Land, East Antarctica (located at approximately 100°E, 66°S), and separated from the Southern Ocean by the Shackleton Ice Shelf (Fig. 1). Collectively, the Bunger Hills, surrounding rocky islands of the Highjump Archipelago, and the Obruchev Hills to the southwest, provide good exposure (~1500 km2) of the Precambrian EAC in a region where there is otherwise limited outcrop.

The Bunger Hills are situated in the Bunger Hills Block that is bounded by the Scott Fault and Knox Rift to the east and characterised by a series of aligned, high magnetic intensity

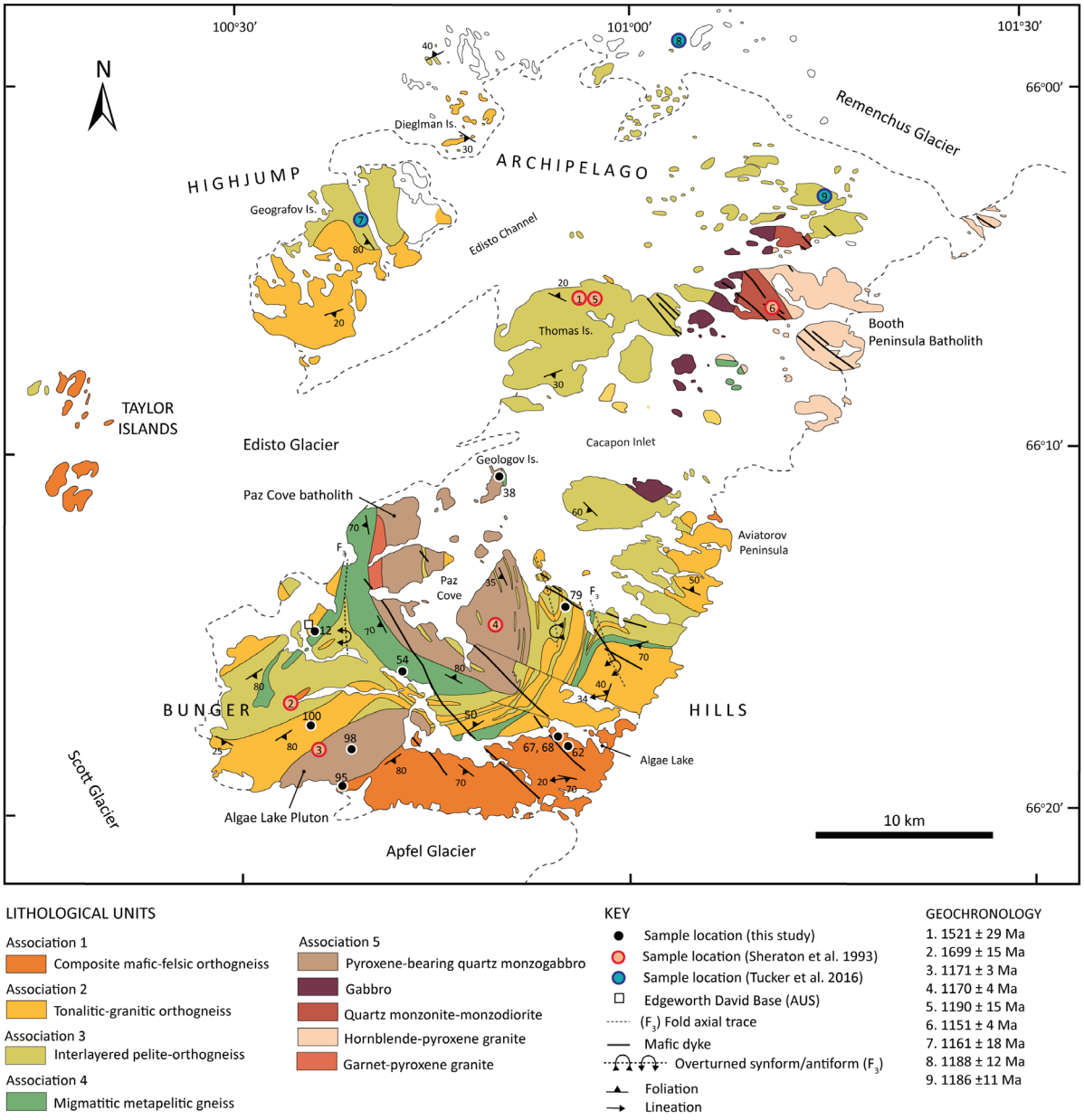

Figure 2. Simplified regional geological map of the Bunger Hills, surrounding islands of the Highjump Archipelago and the Taylor Islands (figure modified after Sheraton et al. (1995) and Stüwe and Wilson (1990)). The Highjump Archipelago is inclusive of outcrop north of Geologov Island in the Cacapon Inlet. The location of samples from this study are indicated as black filled circles. Geochronological sample locations from Sheraton et al. (1992) and Tucker and Hand (2016) are denoted as numbered, pink and blue circles, respectively, and the corresponding age is quoted in the legend. Representative structural data from Sheraton et al. (1995) are shown.

anomalies (Fig. 1b; Aitken et al., 2014; Maritati et al., 2016). Aitken et al. (2014) delineate intercontinental correlations between the Wilkes Land coast and southwest Australia from major geophysical lineaments including the Bunger Hills Block and Yallingup Shelf (offshore western Australia), the Darling–Conger Fault and the Rodona–Totten Fault (Fig. 1b). The Bunger Hills Block is inferred intersected by the Indo–Australo–Antarctic Suture (Aitken et al., 2014) that continues offshore, between the interpreted reconstructed location of the submarine Gulden Draak Knoll and Naturaliste Plateau (Fig. 1a; Gardner et al., 2015; Gibbons et al., 2012; Halpin et al., 2008). Protoliths to basement gneisses from the Gulden Draak Knoll and Naturaliste Plateau share similarities in age and isotopic affinity to the Mesoproterozoic crust of the Albany–Fraser Orogen, Bunger Hills and Windmill Islands and are interpreted as microcontinental fragments of the orogen that were rifted during the Cretaceous breakup of Australia and Antarctica (Gardner et al., 2015; Halpin et al., 2008).

The following description of the Bunger Hills geology is compiled from our own field observations, and previously published work. Rocks of the Bunger Hills can be subdivided into five major lithological units (Fig. 2). The southeastern Bunger Hills are dominated by composite mafic–felsic orthogneiss that ranges in composition from metatonalite to metadolerite (Association 1). To the northwest, the orthogneiss is increasingly tonalitic–granitic in composition and interlayered with metasedimentary rocks (Association 2). Reconnaissance U–Pb zircon geochronology on Y-depleted, I-type granodioritic orthogneiss from the southwest Bunger Hills, and tonalitic orthogneiss from Thomas Island to the north (inferred equivalent to Association 2) date the emplacement age of the igneous protoliths as 1699 ± 15 Ma and 1521 ± 29 Ma, respectively (Sheraton et al., 1992, 1995, 1993). Tonalitic orthogneiss from the nearby Obruchev Hills yielded a U–Pb zircon age of 2641 ± 15 Ma (Sheraton et al., 1992, 1993).

The central Bunger Hills are characterised by a finely interlayered sequence (centimetre–metre scale) of predominantly garnet–cordierite ± sillimanite gneiss and orthopyroxene-bearing tonalitic orthogneiss, with minor psammitic gneiss, mafic gneiss, garnet ± biotite granitic gneiss, and rare calc-silicate (collectively Association 3). The regular layer-parallel distribution of interpreted sedimentary precursors to the garnet–cordierite–sillimanite gneiss, psammitic gneiss and calc-sillicate, with the igneous rocks, is suggestive that the entire package is a volcano-clastic basin-style fill sequence (i.e. simultaneous emplacement of magmas and deposition of sediments during extension). Farther northwards, the interlayered orthogneiss–pelitic gneiss sequence transitions into a monotonous migmatitic garnet–cordierite ± sillimanite ± orthopyroxene ± spinel-bearing gneiss, with minor interlayered psammite gneiss and quartzite (collectively Association 4). Rocky islands to the north of the Bunger Hills comprise a similar lithological association (Sheraton et al., 1995, 1993; Tucker and Hand, 2016).

Several large orthopyroxene-bearing intrusive bodies (up to 10 km diameter) also crop out in the Bunger Hills area (Association 5) with compositions ranging from granite to gabbro, and geochemical and isotopic data suggestive of derivation from an enriched mantle source (Sheraton et al., 1992, 1995; Stüwe and Wilson, 1990). U–Pb zircon geochronology gives ages of 1171 ± 3 Ma and 1170 ± 4 Ma for the Algae Lake Pluton and Paz Cove Batholith, respectively (Sheraton et al., 1992). A quartz monzodiorite from the Booth Peninsula yielded a slightly younger age of 1151 ± 4 Ma (Sheraton et al., 1992). The region is dissected by abundant dolerite–basalt dykes comprising at least four chemically distinct suites that intruded at ca. ≥1140 Ma and ca. 500 Ma (Sheraton et al., 1990, 1993).

The region has experienced at least three major phases of deformation (Ding and James, 1991; Sheraton et al., 1995, 1993; Stüwe and Wilson, 1990; and this study). The earliest tectonic fabric is defined by a pervasive, gentle to moderate SW–NW-dipping composite S_1–S_2 gneissic fabric. The S2 fabric forms the axial planar foliation to F_2 folds. F_2 folds are tight to isoclinal, reclined to recumbent in orientation and have shallow, generally SSW-dipping axial planes. Stüwe and Wilson (1990) attribute the layer-parallel S_1 fabric to flattening from crustal extension and D_2 structures to a major shortening event. Subsequent deformation (D_3) produced open, upright meso–macroscale, generally SSE-trending F_3 folds with steep SW-dipping axial planes and shallow south plunges that locally reorient the earlier fabrics. Variation in the structural trend of F_3 folds (F_2 folds of Stüwe and Wilson (1990)) was suggested by previous

Table 1. Summary of samples

	Location (Zone 47D)						
Sample	Geographic position	Easting	Northing	Lithological description	Mineralogy	Association	Protolith
BH12	Edgeworth David	572349	2650858	bi–opx-bearing tonalitic gneiss	bi + opx + pl + q + ilm ± mt	2	Igneous
BH38	Geologov Island	582703	2658995	Migmatitic enderbite	opx + hbl + pl + q + ilm + mt + ap ± Ksp ± bi	5	Igneous
BH54	Central Bunger Hills	577940	2648390	g–cd–opx–sp gneiss	g + sp + mt + ilm + cd + bi + q + pl + Ksp	4	Sedimentary
BH62	SE Bunger Hills	584098	2644099	g–cd–opx ± sa gneiss	g + opx + sp + cd + bi + perth ± sa ± Ksp ± pl	1	Sedimentary
BH67	SE Bunger Hills	582248	2644753	opx-tonalitic–granodioritic orthogneiss	opx + Ksp + pl + perth + q + ilm ± cpx ± mt	1	Igneous
BH68	SE Bunger Hills	582248	2644753	opx-dioritic orthogneiss	opx + cpx + pl + perth + q + ilm ± Ksp ± mt	1	Igneous
BH79	NE Bunger Hills	586592	2652074	opx-tonalitic orthogneiss	opx + pl + q ± Ksp ± ilm ± mt	3	Igneous
BH95	SW Bunger Hills	573418	2642853	g–cd–sp–opx gneiss	g + opx + bi + sp + cd + ilm + q ± pl	1	Sedimentary
BH98	SW Bunger Hills	572934	2644706	migmatitic enderbite	opx + hbl + pl + q + ilm + mt + ap ± Ksp ± bi	5	Igneous
BH100	SW Bunger Hills	571911	2645966	bi–opx-tonalitic–granitic orthogneiss	bi + opx + pl + q + Ksp + ilm ± cpx ± ap	2	Igneous

Mineral abbreviations: g, garnet; cd, cordierite; opx, orthopyroxene; sill, sillimanite; bi, biotite; pl, plagioclase; q, quartz; Ksp, K-feldspar; ilm, ilmenite; mt, magnetite; hbl, hornblende; sa, sapphirine; sp, spinel; ap, apatite; cpx, clinopyroxene.

studies to result from late-D_3 emplacement of both the Algae Lake Pluton and Paz Cove Batholith (Ding and James, 1991; Sheraton et al., 1992, 1995, 1993). The Booth Peninsula Batholith on east Thomas Island crosscuts D_3 structures of Sheraton et al. (1993). The intense, steeply SW–NW-dipping S_3 fabric (axial planar to F_3 folds) is primarily preserved in the northeast Bunger Hills. Elsewhere, F_2 folds are often sheared by steep S_3 shear fabrics, and F_2–F_3 fold interference patterns are also locally observed. Sheraton et al. (1993) has interpreted the present-day regional structure of the Bunger Hills to primarily reflect D_3 deformation. Previous studies also postulated localised D_4 brittle deformation characterised by multiple generations of retrograde shear zones, pseudotachylite and mylonitic fabrics (Ding and James, 1991; Sheraton et al., 1995, 1993; Stüwe and Wilson, 1990).

Metamorphic zircon from orthogneiss on Thomas Island and monazite from three samples of garnet ± sillimanite ± rutile-bearing gneiss in the northern Highjump Archipelago (Fig. 2) suggest that peak metamorphism occurred between ca. 1190–1180 Ma (Sheraton et al., 1993; Tucker and Hand, 2016). Early *P–T* calculations utilizing conventional thermobarometry estimated that peak metamorphism in the Bunger Hills and Highjump Archipelago attained granulite facies conditions (Bunger Hills: ~750–800 °C, 5–6 kbar, Highjump Archipelago: ~ 700–750 °C, 7–9 kbar; Sheraton et al., 1993; Stüwe and Powell, 1989) and potentially involved an anticlockwise *P–T* path (Stüwe and Powell, 1989). Stüwe and Powell (1989) and Sheraton et al. (1993) postulate that metamorphism accompanied D_1 deformation. Recent re-evaluation of the peak metamorphic conditions of the Highjump Archipelago using forward phase equilibria modelling suggests that the rocks experienced higher temperature conditions (850–950 °C, 6–9 kbar) than previously proposed (Tucker and Hand, 2016). In contrast to Stüwe and Powell (1989) and Sheraton et al. (1993), Tucker and Hand (2016) also propose that metamorphism occurred during D_3 deformation and was accompanied by a clockwise *P–T* path inferred to reflect cooling during thinning of over-thickened crust.

The timing of metamorphism in the Bunger Hills correlates with metamorphism recorded in the Windmill Islands at ca. 1210–1180 Ma (Zhang et al., 2012), the Warumpi Province (Wong et al.,

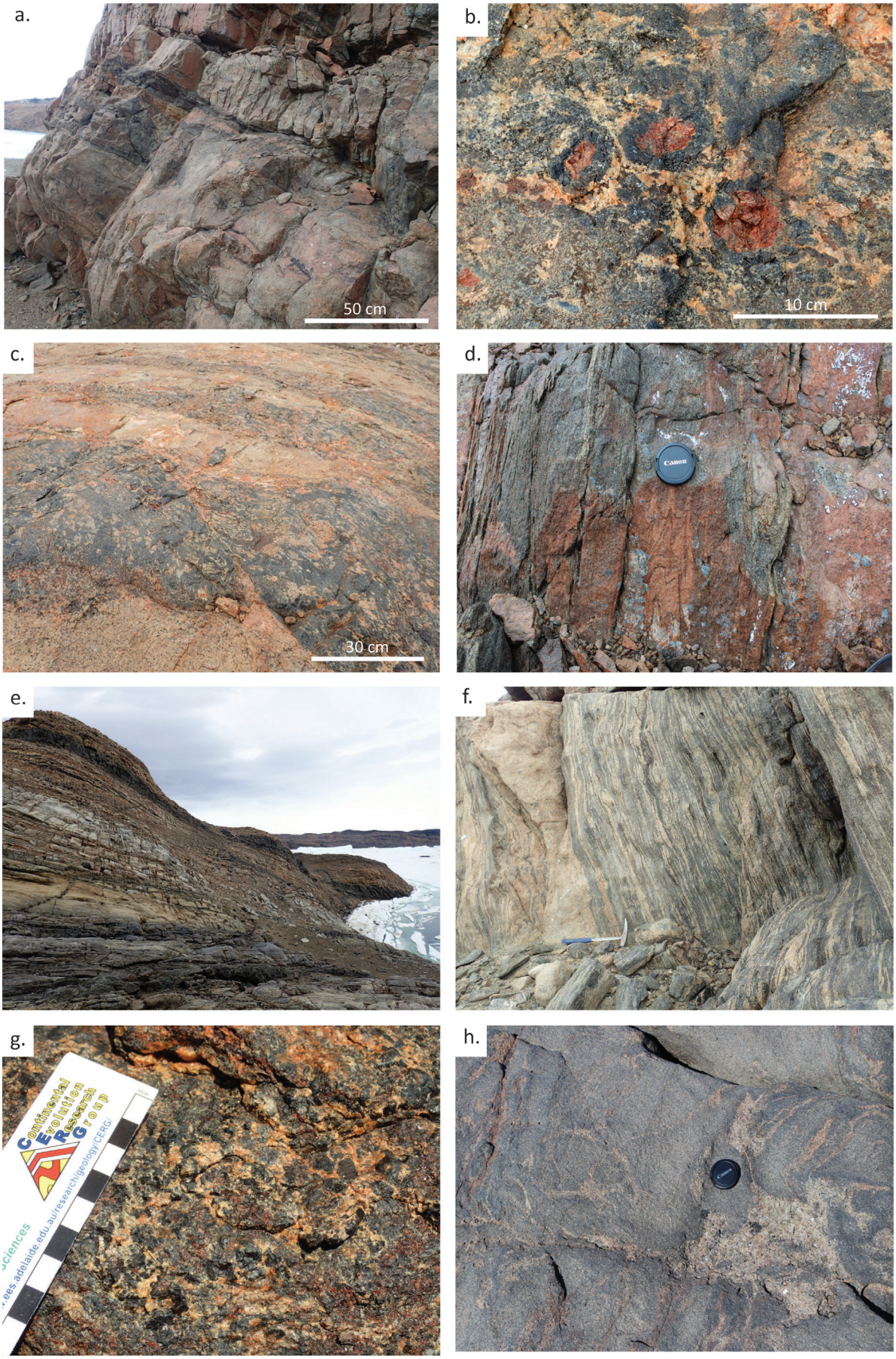
a.
50 cm
b.
10 cm
c.
30 cm
d.
e.
f.
g.
h.

Figure 3. (facing page) Field photographs of sampled lithologies from the Bunger Hills. (a) Composite tonalitic–doleritic orthogneiss from the location of BH67 and BH68; (b) Relict garnet grains surrounded by thick, blue–purple cordierite and black orthopyroxene coronae, and cordierite–orthopyroxene symplectitic intergrowths from the location of sample BH62. Coarse-grained orthopyroxene-bearing leucosomes parallel and crosscut the moderately NNW-dipping fabric at this locality. In some instances, garnet is near-completely replaced by cordierite and orthopyroxene. The garnet prophyroblasts are surrounded by a matrix of cordierite, orthopyroxene, plagioclase, biotite and rarely sapphirine; (c) Outcrop appearance of metasedimentary enclave within tonalitic orthogneiss in the southeastern Bunger Hills from the location of BH62. The rocks are heterogeneous at mesoscale with alternating domains (up to 2 m thick) of Mg-rich pelitic gneiss and K-feldspar–orthopyroxene-bearing leucosomes; (d) Biotite-rich tonalitic–granitic orthogneiss from the location of BH100; (e) Typical appearance of the interlayered orthogneiss–pelitic gneiss unit (Association 3). Pelitic–psammitic gneiss and minor calc-silicate are systematically distributed between igneous lithology's on centimetre- to meter-scale; (f) Characteristic appearance of the monotonous pelitic gneiss that predominates in the central–northern Bunger Hills (Association 4). This photograph shows stromatic K-feldspar-rich leucosomes occurring layer-parallel (on a centimetre-scale) with pelitic gneiss characterised by the typical assemblage garnet–cordierite ± sillimanite ± orthopyroxene ± spinel; (g) Within lower D_3 strain zones of the pelitic gneiss unit, orthopyroxene-bearing leucosomes cross cut the NNW-dipping fabric near the location of BH54; (h) Typical outcrop appearance of late enderbite from the Paz Cove Batholith and Algae Lake Pluton. Photograph taken from near the location of BH38 on Geologov Island, showing orthopyroxene ± hornblende-bearing melt segregations that cross cut a weakly defined fabric.

2015), the Musgrave Orogeny in central Australia (ca. 1225–1135 Ma; Kirkland et al., 2013b; Smithies et al., 2011; Tucker et al., 2015; Walsh et al., 2015) and equivalent-aged deformation during Stage-2 of the Albany–Fraser Orogeny in Western Australia (ca. 1225–1140 Ma; Clark et al., 2000; Kirkland et al., 2011; Spaggiari et al., 2015). Geochronological similarities have accordingly fuelled suggestions that these regions were along-strike equivalents within a single orogenic system during the Mesoproterozoic (e.g. Clark et al., 2000; Fitzsimons, 2003, 2000). The Windmill Islands, along strike of the Bunger Hills, also preserve a history of metamorphism and deformation at ca. 1340–1310 Ma, which correlates with Stage-1 of the Albany–Fraser Orogeny (ca. 1330–1260 Ma; Clark et al., 2014, 2000; Kirkland et al., 2011; Spaggiari et al., 2015). Stage-1 aged deformation is not presently recorded within the Bunger Hills. Stage-1 was triggered by oceanic arc accretion onto the margin of the Albany–Fraser Orogen by ca. 1330 Ma (Spaggiari et al., 2015; Spaggiari and Smithies, 2015) and involved crustal thickening followed by extension—within either a back-arc setting (Clark et al., 2014; Kirkland et al., 2011; Morrissey et al., 2017; Smithies et al., 2013), by relaxation and delamination of the lower crust and/or orogenic collapse resulting in magmatism in a mid–deep crustal hot zone (Smithies et al., 2015; Spaggiari and Smithies, 2015). Stage-2 tectonism is considered to have been largely associated with extensional processes following juxtaposition of the WAC and SAC–EAC (e.g. Morrissey et al., 2017; Tucker and Hand, 2016). Both stages were accompanied by voluminuous, high temperature magmatism and metamorphism (Bodorkos and Clark, 2004; Clark et al., 2014, 2000; Kirkland et al., 2011; Nelson et al., 1995).

3. SAMPLE SELECTION AND DESCRIPTION

Ten representative samples were taken from all major lithological units within the Bunger Hills for U–Pb geochronology, and Lu–Hf and oxygen isotope analysis (Fig. 2). A summary of all sample lithologies, mineral assemblages and sampling localities is given in Table 1. Samples are discussed below in accordance to their lithological subdivisions.

3.1 Association 1: composite mafic–felsic orthogneiss

Two samples of orthogneiss (sample BH67 and BH68) were collected from the southeast Bunger Hills (Fig 3a). These samples are representative of the two dominant compositional end-members of igneous composite gneiss: orthopyroxene-bearing tonalitic–granodioritic gneiss and quartz-rich dolerite gneiss, respectively. The tonalitic–granodioritic gneiss is volumetrically dominant (comprising up to 90 % of the outcrop) and intrudes the dolerite gneiss. Sample BH67 is composed of orthopyroxene ± clinopyroxene (grains 0.5–1 mm, collectively ~20 % abundance), K-feldspar (10 %), perthite (20 %), quartz (25 %), plagioclase (20 %) and ilmenite ± magnetite (5 %). Sample BH68 is mineralogically equivalent but contains a higher proportion of pyroxene (up to 25 %), significantly more plagioclase (up to 30–35 %) and lesser K-feldspar (5 %). The rocks are characterised by a moderate NW–SE-striking and SW-dipping S_1–S_2 fabric defined by the alignment of pyroxene. Minor orthopyroxene ± hornblende leucosomes are present that are both concordant and discordant with the S1–S2 fabric.

Locally, the composite gneiss contains metre-scale (10–100's of meters) metasedimentary enclaves and screens. Sample BH62 was taken from a metapelitic lens within tonalitic gneiss, proximal to samples BH67 and BH68, and contains orthopyroxene (25 %), spinel (5 %), cordierite (30 %), biotite (10 %), garnet (20 %), minor plagioclase (5 %) and perthite (<5 %), and rare sapphirine (<5 %). Coarse garnet grains (up to 3 cm diameter) appear to have been partially to completely replaced by cordierite and orthopyroxene coronae, and orthopyroxene–cordierite ± spinel symplectitic intergrowths (Fig 3b). The overall outcrop is characterised by alternating layer-parallel cordierite–garnet–orthopyroxene-rich, and K-feldspar–quartz-rich domains (Fig 3c). Coarse orthopyroxene-bearing leucosomes (orthopyroxene up to 2 cm) are prevalent largely within the Mg-rich domains and occur both parallel and discordant to the moderately SW-dipping fabric. This outcrop extends over >200 m, however the true size and nature of the contact with the surrounding orthogneiss is largely ambiguous due to moraine cover.

Sample BH95 was taken from cordierite–orthopyroxene ± spinel ± garnet-bearing gneiss interlayered with orthopyroxene-bearing tonalitic gneiss in the southern Bunger Hills. This sample contains orthopyroxene (10 %), biotite (15 %), spinel (5 %), garnet (25 %), cordierite (~20 %), quartz (20 %), and minor plagioclase (5–10 %) and ilmenite (<2 %). The S_1–S_2 fabric is defined by elongate orthopyroxene, garnet and biotite grains, and dips moderately to the NW.

3.2 Association 2: tonalitic–granitic orthogneiss

Sample BH12 is a migmatitic orthopyroxene–biotite-bearing tonalitic gneiss consisting of abundant and coarse biotite (8 %), orthopyroxene (15 %), plagioclase (up to 45 %), quartz (20–25 %), minor K-feldspar (5 %) and ilmenite (2 %). The tonalitic gneiss is interlayered with pelitic gneiss (on meter-scale) immediately to the northeast of the sampled locality. In places, the tonalitic gneiss appears to also intrude into the layers of pelitic gneiss. The outcrop is characterised by a gentle–moderate SW-dipping composite S_1–S_2 fabric, and mesoscale open, upright F_3 folds that plunge shallowly SSW, verge WNW, and are sheared locally by a steeply WNW-dipping S_3 fabric. This sample contains orthopyroxene-bearing veinlets (centimetre–metre scale) that are transposed into the foliation.

Sample BH100 is a tonalitic–granodioritic gneiss (Fig. 3d) consisting of abundant biotite (grains up to 1 mm length, 20–25 % abundance), orthopyroxene (grains up to 1 mm, 10 % abundance), plagioclase (30–35 %), quartz (20 %), K-feldspar (10 %), minor clinopyroxene (5 %) and apatite (2–3 %). The biotite-bearing gneiss contains stromatic orthopyroxene-bearing leucosomes and encloses boudins of mafic gneiss with a fabric parallel to that externally in the surrounding gneiss. This sequence is interlayered on a meter-scale with garnet–sillimanite-bearing gneiss. The fabric is defined by strong alignment of biotite and dips steeply to the SE.

3.3 Association 3: interlayered orthogneiss–pelitic gneiss

One sample was taken from the interlayered orthogneiss–pelitic gneiss that defines Association 3 (Fig. 3e). Sample BH79 is an orthopyroxene-bearing tonalitic gneiss containing orthopyroxene (20–25 %), plagioclase (30 %), quartz (30–35 %), minor K-feldspar (<10 %), and ilmenite (2 %) and is from the NE Bunger Hills near Paz Cove. Orthogneiss at this locality is volumetrically dominant, comprising up to 80 % of the outcrop. In the northeast Bunger Hills the sequence records pervasive D_3 deformation resulting in meso-macroscale recumbent-style F_3 folds reoriented to lie in the plane of an intense SW–NW-dipping S_3 fabric, and plunge to the SW.

3.4 Association 4: garnet–cordierite ± sillimanite ± orthopyroxene ± spinel-bearing gneiss

Sample BH54 was selected from the extensive metapelitic gneiss that predominates in the central–northwest Bunger Hills. At outcrop-scale, the rocks from this unit contain an intense, moderate to steeply dipping composite gneissic S_1–S_2 fabric defined by the alternating Mg-rich domains and quartz–K-feldspar ± plagioclase-rich segregations (Fig. 3f). Sample BH54 is a migmatitic garnet–cordierite–magnetite ± spinel-bearing gneiss (Fig. 3g) and contains coarse-grained garnet (grains up to 1 cm, 20 %), spinel (<3 %), cordierite (15 %), biotite (10 %), quartz (25 %), plagioclase (15 %), K-feldspar (10 %), and ilmenite and magnetite (~5 %). This rock is representative of lower D_3 strain zones within the pelitic gneiss unit, and preserves

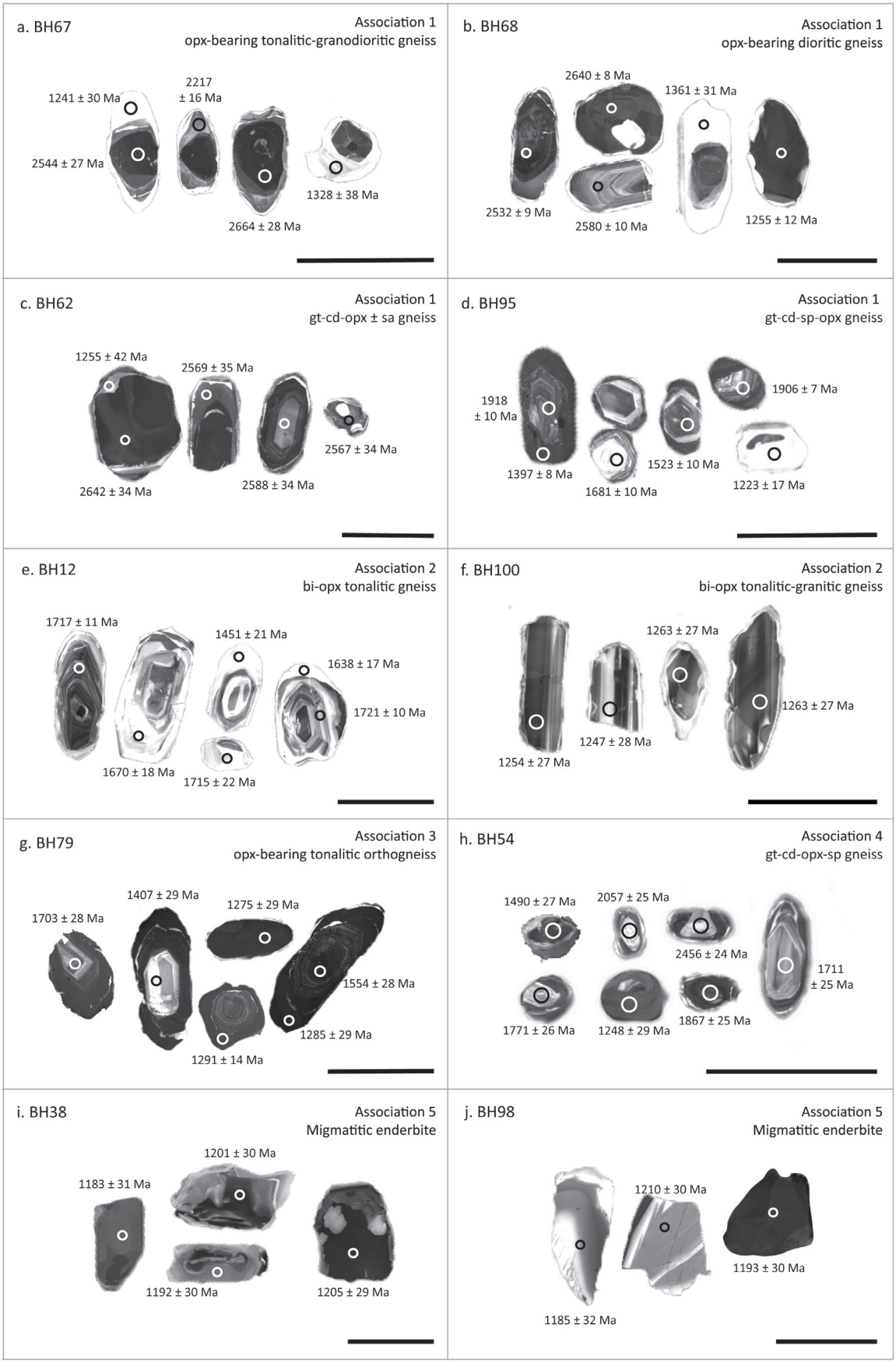

Figure 4. Cathodoluminescence (CL) images of representative zircon grains from the Bunger Hills. The approximate location of U–Pb analysis spots (20 μm in diameter) and the corresponding $^{207}Pb/^{206}Pb$ ages with 2σ error are shown for each grain: (a) BH67; (b) BH68; (c) BH62; (d) BH95; (e) BH12; (f) BH100; (g) BH79; (h) BH54; (i) BH38; (j) BH98. Lu–Hf and oxygen isotope analyses were done on the same sites as for U–Pb analyses, and within the same CL zone (using a 40–60 μm and 10–15 μm spot size, respectively). The black scale bar represents 250 μm.

the thermal peak of metamorphism in which K-feldspar-rich leucosomes containing coarse orthopyroxene (up to 2 cm diameter) cross cut the steeply-dipping NNE fabric at this locality.

3.5 Association 5: late D_3 gabbroic–granitic plutonic rocks

Sample BH38 was collected from migmatitic enderbite of the Paz Cove Batholith near the contact with metasedimentary gneiss on Geologov Island (Fig. 3h). This sample consists of orthopyroxene (10 %), hornblende (10 %), plagioclase (20–25 %), quartz (30–35 %), minor K-feldspar (10–15 %), ilmenite ± magnetite (2–3 %), apatite (<2 %), and biotite (<2 %), and is compositionally heterogeneous at the meso-scale with hornblende–biotite-rich and orthopyroxene-rich domains. The rocks at this locality are characterised by a weak, gently WSW-dipping fabric. In contrast, the metasedimentary gneiss contains a strongly defined, moderately WSW-dipping fabric which parallels the axial plane of upright F_3 folds, and is locally truncated by the enderbite. Sample BH38 contains stromatic orthopyroxene-bearing leucosomes that cross cut the gently WSW-dipping fabric at a low angle (Fig. 3h). Towards the edge of the intrusive body, numerous discontinuous schlieren of quartzite and metasedimentary rocks (up to 10 m thick and 300 m in length) are interleaved with the enderbite. Sample BH98 was obtained from the Algae Lake Pluton and is mineralogically and petrographically equivalent to sample BH38, although is comparatively unfoliated.

4. ANALYTICAL METHODS

4.1 Sample preparation

Zircon grains were separated by SelFrag electrostatic disaggregation from crushed rock samples, and a combination of hand panning, magnetic separation and methylene iodide heavy-liquid separation techniques. Approximately 200 zircon grains per sample were handpicked and mounted in epoxy resin. Cathodoluminescence (CL) imagery was obtained using a Tescan MIRA3 Field Emission SEM housed at the John de Laeter Centre, Curtin University, Perth.

4.2 Laser–ablation split–stream U–Pb zircon geochronology

U–Pb zircon geochronology and trace element analyses were conducted by Laser–Ablation Split–Stream (LASS) Inductively Coupled Plasma–Mass Spectrometry (ICP–MS) at the University of California, Santa Barbara (UCSB). Analytical procedures follow those detailed by Kylander-Clark et al. (2013). Analyses were carried out using a Photon Machines Excite argon-fluoride excimer laser (193 nm) equipped with a two-volume 'HelEx' ablation cell, and attached to two mass spectrometers. U–Pb analyses were measured using a Nu Plasma multi-collector–ICP–MS fitted with Faraday detectors and $10^{11}\Omega$ amplifiers, and four low-mass ion counters. Each analysis involved simultaneous measurement on masses ^{238}U, ^{232}Th, ^{208}Pb, ^{207}Pb, ^{206}Pb and $^{204}(Pb+Hg)$. The lanthanides, yttrium, titanium and hafnium were measured simultaneously to U–Pb analyses using an Agilent 7700S quadrupole ICP–MS. Zircon grains were ablated with a frequency of 4 Hz, intensity of ~2 J cm^{-2} and a spot size of 20 μm. The analysis time was approximately 35 s, inclusive of two cleaning shots followed by 15 s of background acquisition and 20 s ablation.

Data were corrected for mass bias, elemental fractionation and instrument drift based on the measured isotopic ratios of the primary zircon reference material GJ-1 (TIMS normalisation data: $^{207}Pb/^{206}Pb$ = 608.3 Ma, $^{206}Pb/^{238}U$ = 600.7 Ma, $^{207}Pb/^{235}U$ = 602.2 Ma; Jackson et al. (2004)). Throughout the study, the GJ-1 analyses yielded a $^{206}Pb/^{238}U$ weighted mean age of 600.4 ± 0.6 (n = 131). To monitor data accuracy, secondary reference standards Mud Tank, 91500 and Plesovice were analysed concurrently by standard–sample bracketing every eight unknown analyses. Repeat analyses of Mud Tank, 91500 and Plesovice during the analytical session gave weighted mean ages of $^{206}Pb/^{238}U$ = 731.5 ± 2.2 [14] (n = 42, MSWD = 1.03), $^{207}Pb/^{206}Pb$ = 1062.8 ± 2 [19] Ma (n = 125, MSWD = 0.98) and $^{206}Pb/^{238}U$ = 342.0 ± 0.7 [6] (n = 45, MSWD = 0.64), respectively, consistent with published values for these standards (Black and Gulson, 1978; Slama et al., 2008; Wiedenbeck et al., 1995).

Reduction of age data, including corrections for baseline, instrumental drift, mass bias and down-hole fractionation were carried out using Iolite (version 3) developed by the Melbourne Isotope Group. Details of the data reduction methodology are outlined in Paton et al. (2011). Age data were plotted using Isoplot v. 4.15 (Ludwig, 2012). Ages were not corrected for common Pb,

however, analyses were rejected on the basis of elevated levels of ^{204}Pb relative to background concentrations. Trace element analyses were utilised to filter the U–Pb dataset for inclusions and zoning in the reference materials and unknowns.

The quoted analytical uncertainties on individual analyses include contributions from the external reproducibility of the primary reference standard GJ-1 (approximately 2 %), and are given at the 2σ level, unless stated otherwise. Uncertainties quoted with weighted mean and upper intercept calculations for pooled analyses are given at the 95 % confidence level. Calculations for each weighted mean and upper intercept age also quote an additional uncertainty value that incorporates the systematic uncertainty of the facility indicated by the long-term external reproducibility of the secondary reference material 91500. These are 0.90 % and 0.92 % for $^{207}Pb/^{206}Pb$ and $^{206}Pb/^{238}U$, respectively (n = 220, 1 SD). The in-run, analytical uncertainty is first represented in age calculations; the propagated uncertainty which incorporates the long-term external reproducibility of the secondary standards is enclosed in square brackets (e.g. ± [10]), where necessary.

4.3 Lu–Hf isotope analysis

Lu–Hf isotope analyses were undertaken using the same instrumentation as for U–Pb geochronology. Lu–Hf analysis spots were placed on top of U–Pb spot localities, within the same CL zone. Analytical methods for zircon Hf isotopic determination by LA–MC–ICP–MS are also detailed in Kylander-Clark et al. (2013). A typical analysis consisted of two cleaning shots to remove surface contamination followed by approximately 35 s of background and 30 s ablation and involved measurement on masses ^{171}Yb, ^{173}Yb, ^{175}Lu, ^{176}Hf (+ Lu + Yb), ^{177}Hf, ^{178}Hf, ^{179}Hf and ^{180}Hf. Analyses were carried out using a beam diameter of 40 µm, a 12 Hz repetition rate and an intensity of ~2 J/cm^2 for all samples excluding samples BH67, BH68, BH12 and BH100 for which a spot size of 65 µm and a repetition rate of 10 Hz were utilized.

Data were normalised by an exponential mass bias correction using a stable $^{179}Hf/^{177}Hf$ ratio of 0.7325. Isobaric interferences of ^{176}Hf by Yb and Lu were corrected using the methods of Woodhead et al. (2004) with direct measurement of $^{171}Yb/^{173}Yb$ fractionation, using the $^{171}Yb/^{173}Yb$ isotopic values of 1.130172 (Segal et al., 2003). Assuming the same mass bias behaviour as Yb, a correction for Lu isobaric interference on ^{176}Hf used a $^{176}Lu/^{175}Lu$ ratio of 0.02655 (Vervoort et al., 2004). Data were processed using Iolite software.

Instrument performance and stability were monitored by analysis of zircon standards Mud Tank, Plesovice, 91500 and GJ-1. The average $^{176}Hf/^{177}Hf$ value for Mud Tank for the analytical session was 0.282516 ± 0.000009 (2σ, n = 80) which is within uncertainty of the published value of 0.282507 ± 0.000006 (Woodhead and Hergt, 2005). The mean $^{176}Hf/^{177}Hf$ value for Plesovice analyses was 0.282487 ± 0.000013 (2σ, n = 33) and for 91500 analyses was 0.282321 ± 0.000015 (2σ, n = 48) which are likewise within uncertainty of their respective published values of 0.282482 ± 0.000013 (Slama et al., 2008) and 0.282306 ± 0.000008 (Woodhead and Hergt, 2005). The average $^{176}Hf/^{177}Hf$ value for GJ-1 during the session was 0.282034 ± 0.000017 (2σ, n = 21). This value is slightly higher than the uncertainty on the published mean value of 0.282000 ± 0.000005 (Morel et al., 2008). To some extent, this may be a result of the smaller sample size of GJ-1 over the analytical period, relative to the other standards.

Depleted mantle crustal model ages ($T_{DM\ crustal}$) and epsilon hafnium values ($\varepsilon_{Hf}(t)$) were calculated following the methods of Griffin et al. (2002). An average crustal composition of $^{176}Lu/^{177}Hf$ = 0.015 (Griffin et al., 2002), chondritic uniform reservoir (CHUR) values of Bouvier et al. (2008) and a ^{176}Lu decay constant of 1.865 x 10^{-11} yr^{-1} (Scherer et al., 2001) were used.

4.4 Ion microprobe oxygen isotope analysis in zircon

Oxygen isotope ratios ($^{18}O/^{16}O$) in zircon were determined using a Cameca IMS 1280 multi-collector ion microprobe hosted by the Centre for Microscopy, Characterisation and Analysis, University of Western Australia. The samples were carefully cleaned with detergent, distilled water and ethanol in an ultrasonic bath and coated with gold (30 nm in thickness) prior to SIMS analyses. Analyses were performed within the same CL zones on grains used for U–Pb and Lu–Hf analyses.

Oxygen secondary ions are sputtered from the sample by bombarding its surface with a 10 kV, Gaussian Cs^+ beam with intensity of 3 nA and

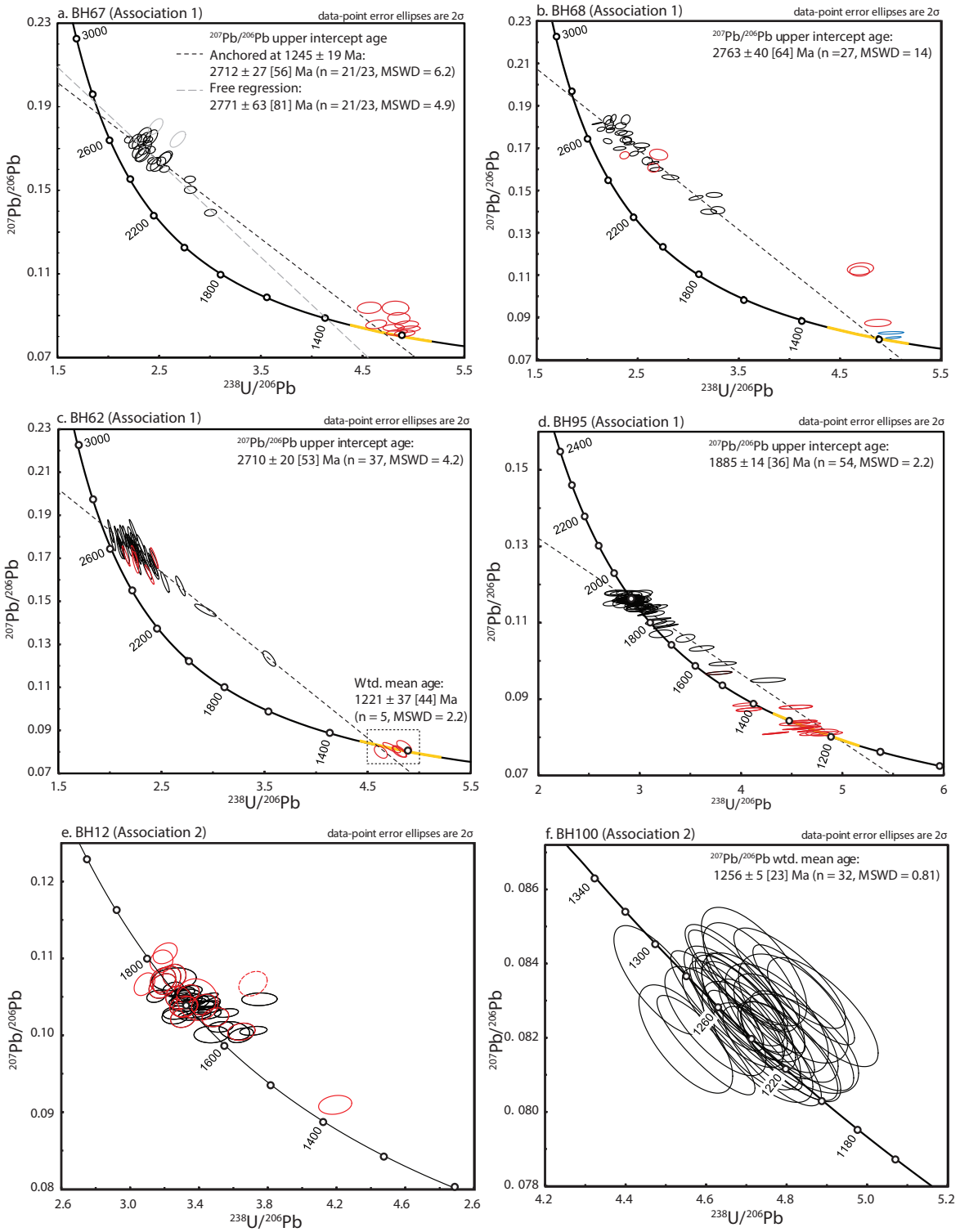

Figure 5. Tera–Wasserburg Concordia diagrams of zircon U–Pb geochronology for samples from lithological associations 1 and 2: (a) BH67; (b) BH68; (c) BH62; (d) BH95; (e) BH12; (f) BH100. For sample BH12, analyses that are >10 % discordant are shown as dashed ellipses. Due to the majority of analyses being >10% discordant from samples BH67, BH68 and BH62, these analyses are not differentiated from those between +10 % and -10 % discordance for these samples. Black ellipses represent analyses from oscillatory-zoned zircon cores; red ellipses represent analyses from zircon rims; blue ellipses reflect analyses from dark, unzoned grains. $^{207}Pb/^{206}Pb$ upper intercept ages are calculated using zircon core analyses only. In (a) both a free regression and regression anchored to the metamorphic population (using a lower intercept of 1245 ± 19 Ma) are shown and calculated. The two grey ellipses shown in (a) are excluded from upper intercept calculations as they appear to exist on a different Pb-loss trajectory to the main population. A $^{207}Pb/^{206}Pb$ weighted mean age is given for sample BH100. The period of known Mesoproterozoic metamorphism and magmatism in the Musgrave Inlier (ca. 1345–1293 Ma and ca. 1220–1150 Ma; Howard et al., 2015) and Albany–Fraser Orogen (ca. 1330–1280 Ma and 1225–1160 Ma; Clark et al., 2000; Spaggiari et al., 2015; Spaggiari and Tyler, 2014) is highlighted on the concordia curve in yellow in (a)–(d). However, note that the time interval between Stages 1 and 2 of the Albany–Fraser Orogeny (ca. 1280–1225 Ma) and equivalent Mount West Orogeny and Musgrave Orogeny (ca. 1293–1225 Ma) is not distinguished.

Table 2. Summary of zircon isotopic data

	U–Pb Age Data (Ma)				Isotope Data	
Sample	Inheritance	Max. dep.	Crystallisation	Metamorphism	εHf (2σ)*	$\delta^{18}O$ (‰, 2σ)*
BH12	-	-	ca. 1750–1650[1]	-	−2.2 ± 0.6	6.75 ± 0.29
BH38	-	-	1200 ± 6[2]	-	−10.8 ± 0.5	8.67 ± 0.09
BH54	Neoarchean to Paleoproterozoic	1490 ± 27	-	1255 ± 42[2]	-	-
BH62	Neoarchean	-		1221 ± 37[2]	3.0 ± 0.6	4.77 ± 0.11
BH67	-	-	2712 ± 27[3]	1245 ± 19[2]	1.7 ± 0.8	5.80 ± 0.45
BH68	-	-	2763 ± 40[3]		−1.5 ± 0.7	-
BH79	-	-	1666 ± 49[3]		−1.7 ± 0.6	7.39 ± 0.08
BH95	Paleoproterozoic	-		ca. 1300–1200[1]	2.3 ± 0.6	4.47 ± 0.36
BH98	-	-	1203 ± 5[2]		−9.7 ± 0.4	8.59 ± 0.08
BH100	-	-	1256 ± 5[2]		−6.9 ± 0.6	8.09 ± 0.07

*Reported as mean isotope value of the main age population.
Method of age calculation: [1] Individual zircon ages; [2] weighted mean $^{207}Pb/^{206}Pb$ age; [3] upper intercept $^{207}Pb/^{206}Pb$ age.

total impact energy of 20 keV. This primary beam is rastered over a 10 x 10 µm area at the surface of the sample. Secondary ions are admitted in the double focusing mass spectrometer within a 110 µm entrance slit and are focused in the centre of a 4000 µm field aperture (x 130 magnification). They are energy filtered using a 40 eV band pass with a 5 eV gap toward the high-energy side. ^{16}O and ^{18}O are collected simultaneously in Faraday cup detectors fitted with 10^{10} Ω (L'2) and 10^{11} Ω (H'2) resistors, respectively, and operating at a mass resolution of ~2430. The magnetic field was regulated using NMR control.

Each analysis includes a pre-sputtering over a 15 x 15 µm area during 30 s and the automatic centering of the secondary ions in the field aperture, contrast aperture and entrance slit. Each analysis then consists of 20 four-second cycles, which give an average internal precision of ~0.16‰ (2 SE). The analytical session was monitored in terms of drift and precision using at least two bracketing standards (Temora II; 8.2 ‰; Black et al. (2004)) every six sample analyses. Instrumental mass fractionation was corrected using Temora II following the procedure described in Kita et al. (2009). The spot-to-spot reproducibility was 0.3–0.4 ‰ (2 SD) on Temora II during the analytical session. Penglai zircon, which was analysed as a secondary standard, returned average $\delta^{18}O$ values of 5.2 ± 0.3 ‰ (2 SD) and 5.3 ± 0.3 ‰ (2 SD), which are similar to the published value for this standard (5.31 ± 0.1‰, Li et al., 2010).

Uncertainty on each $\delta^{18}O$ spot has been calculated by propagating the errors on instrumental mass fractionation determination, which include the standard deviation of the mean oxygen isotope ratio measured on the primary standard during the session, and internal error on each sample data point. Data are presented as raw $^{18}O/^{16}O$ ratios and corrected $\delta^{18}O$ quoted with respect to Vienna standard mean ocean water (VSMOW).

5. RESULTS

5.1 U–Pb zircon geochronology

Representative CL imagery of zircon from all samples are shown in Fig. 4. U–Pb zircon data are presented in Appendix A. The majority of individual analyses yield ages >1500 Ma, in which case, the $^{207}Pb/^{206}Pb$ age is considered the most geologically valid age (Spencer et al., 2015). Furthermore, some samples exhibit evidence for recent Pb loss (e.g. sample BH100) and thus the $^{207}Pb/^{206}Pb$ age is also considered the most robust estimate. Therefore, for consistency across all samples, the $^{207}Pb/^{206}Pb$ age is quoted for all individual analyses as well as for upper intercept and weighted mean calculations. Weighted mean calculations and probability density plots utilize analyses between +10 % and -10 % discordance only, unless stated otherwise. Concordia diagrams and $^{207}Pb/^{206}Pb$ age spectra are shown in Figs. 5 and 6. Samples are subdivided and discussed below in accordance to their inferred lithological subdivisions. A summary of U–Pb isotopic results is presented in Table 2.

5.1.1 Association 1

5.1.1.1 Sample BH67: tonalitic–granodioritic orthogneiss

Zircon from this sample are sub-rounded to elongate, brown–colourless and 40–250 µm in size with width to length aspect ratios of 1:1 to 1:3. CL images reveal predominantly dark to weakly luminescent, oscillatory-zoned cores with thin,

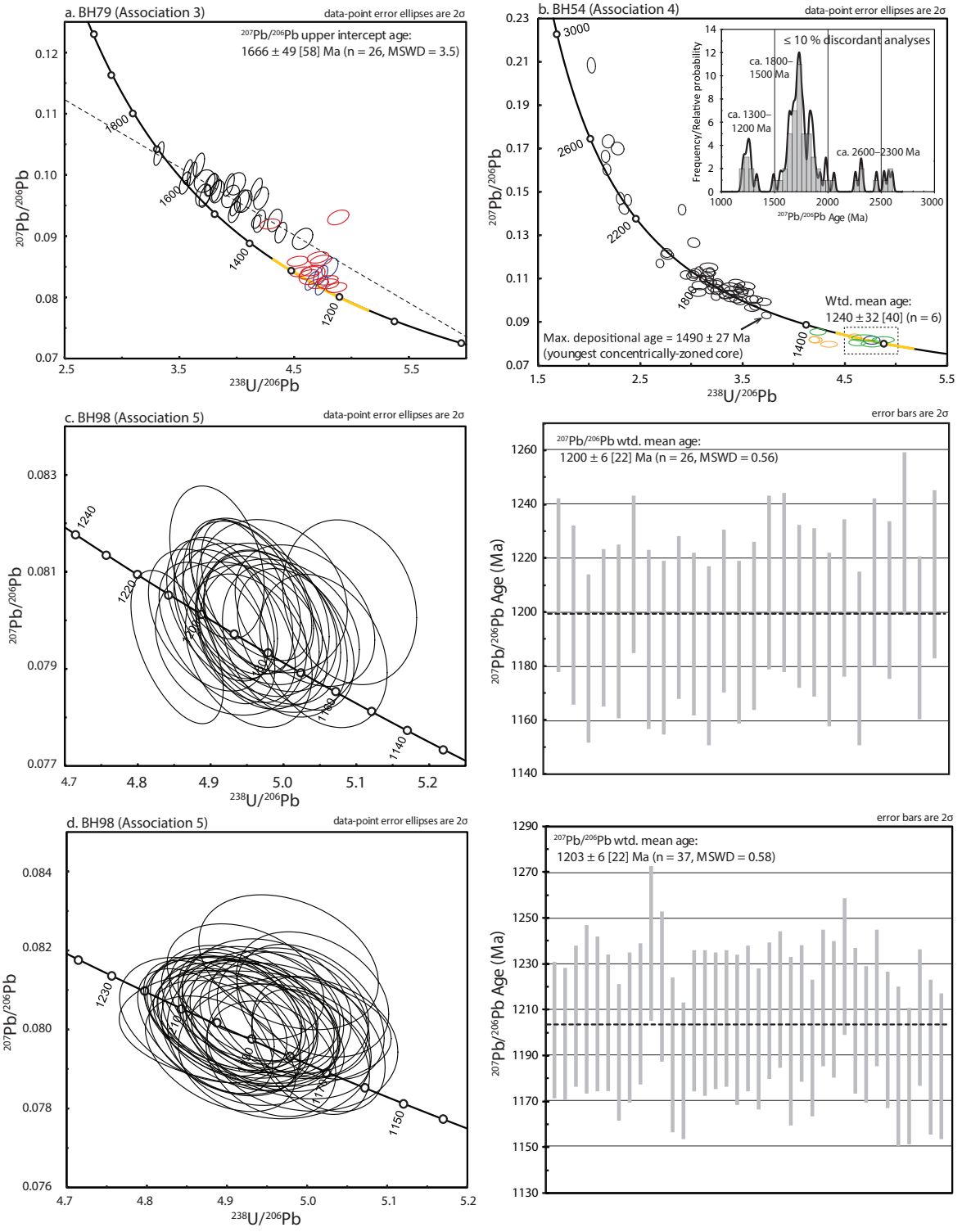

Figure 6. Tera–Wasserburg Concordia diagrams of zircon U–Pb geochronology for samples from lithological associations 3, 4 and 5: (a) BH79; (b) BH54; (c) BH38; (d) BH98. Analyses from oscillatory-zoned zircon cores are represented as dark ellipses; analyses from dark, unzoned grains are shown in blue. Zircon rim analyses from sample BH79 are shown in red; analyses from dark zircon rims and weakly luminescent rims in sample BH54 are shown in green and yellow, respectively. The $^{207}Pb/^{206}Pb$ upper intercept age for sample BH79 is calculated using zircon core analyses only. A probability density plot of all detrital zircon data from sample BH54 is shown. The $^{207}Pb/^{206}Pb$ weighted mean age of the youngest concordant (metamorphic) population in sample BH54 is 1240 ± 32 Ma ($n = 6$). The maximum depositional age of sample BH54 is 1490 ± 27 Ma as shown by the youngest concordant analysis from an oscillatory-zoned zircon core. $^{207}Pb/^{206}Pb$ weighted mean plots and ages are shown for samples BH38 and BH98 from the Paz Cove Batholith and Algae Lake Pluton, respectively. The period of known Mesoproterozoic metamorphism and magmatism in the Musgrave Inlier (ca. 1345–1293 Ma and ca. 1220–1150 Ma; Howard et al., 2015) and Albany–Fraser Orogen (ca. 1330–1280 Ma and 1225–1160 Ma; Clark et al., 2000; Spaggiari et al., 2015; Spaggiari and Tyler, 2014) is highlighted on the concordia curve in yellow in (a)–(d). However, note that the time interval between Stages 1 and 2 of the Albany–Fraser Orogeny (ca. 1280–1225 Ma) and equivalent Mount West Orogeny and Musgrave Orogeny (ca. 1293–1225 Ma) is not distinguished.

luminescent overgrowths (Fig. 4a). Twenty-three analyses were obtained from zircon cores, and nine analyses from zircon rims for this sample (Fig. 5a). The majority of analyses from oscillatory-zoned cores are discordant and are interpreted to record ages affected by ancient Pb loss (i.e. Pb loss attributed to metamorphism/resetting). These data points yield an upper intercept age of 2771 ± 63 [81] Ma (n = 21/23, MSWD = 4.9). However, the lower intercept of the free regression is 1386 ± 120 Ma, inconsistent with the timing of metamorphism recorded by zircon rims from this sample, and other lithologically and geographically-related samples (i.e. BH62 and BH68). Two rim analyses are concordant, yielding ages of 1241 ± 30 Ma and 1248 ± 26 Ma, and a weighted mean age of 1245 ± 19 [30] Ma. Anchored to a lower intercept of 1245 ± 19 Ma, the core analyses yield an upper intercept age of 2712 ± 27 [56] Ma (n = 21/23, MSWD = 6.2). This result is not precise enough to constrain the crystallisation age of the magmatic precursor, but nevertheless reveals a ca. 2800–2700 Ma magmatic event.

5.1.1.2 Sample BH68: quartz-rich dioritic orthogneiss

Zircon from this sample are typically sub-rounded to elongate, brown–colourless and approximately 100–400 µm in size. CL imagery reveals predominantly dark, oscillatory-zoned cores surrounded by thin to moderately thick, luminescent rims (Fig. 4b). Twenty-seven analyses were obtained from oscillatory-zoned cores, two analyses from dark, unzoned grains, and six analyses from zircon rims (Fig. 5b). Analyses from oscillatory-zoned zircon cores form a discordant array, and collectively, yield an upper intercept age of 2763 ± 40 [64] Ma (n = 27, MSWD = 14). Similarly to sample BH67, this age is suggestive of a ca. 2800–2700 Ma magmatic event. Two analyses from dark, unzoned grains yield dates of 1199 ± 11 Ma and 1255 ± 12 Ma. The rim analyses yield variable dates, ranging between 2687 ± 17 Ma and 1361 ± 31 Ma, however, are also discordant.

5.1.1.3 BH62: garnet–cordierite–orthopyroxene ± sapphirine gneiss

Zircon from this sample are subhedral and rounded to elongate in shape, brown, and 50–350 µm in size with aspect ratios of 1:1 to 1:3. CL imagery reveals generally dark to weakly luminescent, oscillatory-zoned cores surrounded by narrow, weakly luminescent to luminescent overgrowths on some grains (Fig. 4c). Thirty-seven analyses were done on zircon cores and 10 analyses on zircon rims from this sample (Fig. 5c). The data reveal a relatively coherent, linear spread of analyses with the oscillatory-zoned cores yielding an upper intercept age of 2710 ± 20 [53] Ma (n = 37, MSWD = 4.2). Most data cluster near the upper intercept and come from both cores and rims. Five rim analyses yield concordant data at the lower intercept, with a weighted mean age of 1221 ± 37 [44] Ma (n = 5, MSWD = 2.2).

5.1.1.4 Sample BH95: garnet–cordierite–spinel–orthopyroxene gneiss

Zircon in this sample are sub-rounded to elongate with rounded crystal faces, brown–colourless and 75–250 µm in size with width to length aspect ratios of 1:1 to 1:3. CL imagery reveals weakly luminescent to bright, oscillatory-zoned cores and generally thin, dark overgrowths (Fig. 4d). Few grains exhibit luminescent rims. Fifty-four analyses were done on oscillatory-zoned cores and 12 analyses on zircon rims for this sample (Fig. 5d). The core analyses form a concordant population at ca. 1900–1800 Ma and a discordant array of dates to ca. 1520 Ma. Collectively, these core analyses yield an upper intercept age of 1886 ± 14 [36] Ma (n = 54, MSWD = 2.2). The majority of rim analyses define a spread of concordant ages between ca. 1300–1200 Ma (n = 10). Two concordant rim analyses yield ages older than the main population at 1397 ± 8 Ma and 1368 ± 8 Ma. Generally, Th/U ratios distinguish rim analyses (<0.1) from the zircon cores, excluding two analyses—BH95-74 (1223 ± 17 Ma) and BH95-79 (1217 ± 11 Ma)—which come from a thick, luminescent rim and dark rim, respectively, and yield Th/U values of 1.01 and 1.26.

5.1.2 Association 2.

5.1.2.1 Sample BH12: tonalitic orthogneiss

Zircon from this sample are sub-rounded with ovoid to elongate shapes and sub-rounded crystal face terminations. Grains are brown–colourless, 100–500 µm in size and exhibit width to length aspect ratios between 1:1 and 1:4. CL imaging reveals generally dark to weakly luminescent, zoned cores. Some grains exhibit moderately thick, luminescent overgrowths (Fig. 4e). Thirty-two analyses were obtained from oscillatory-zoned

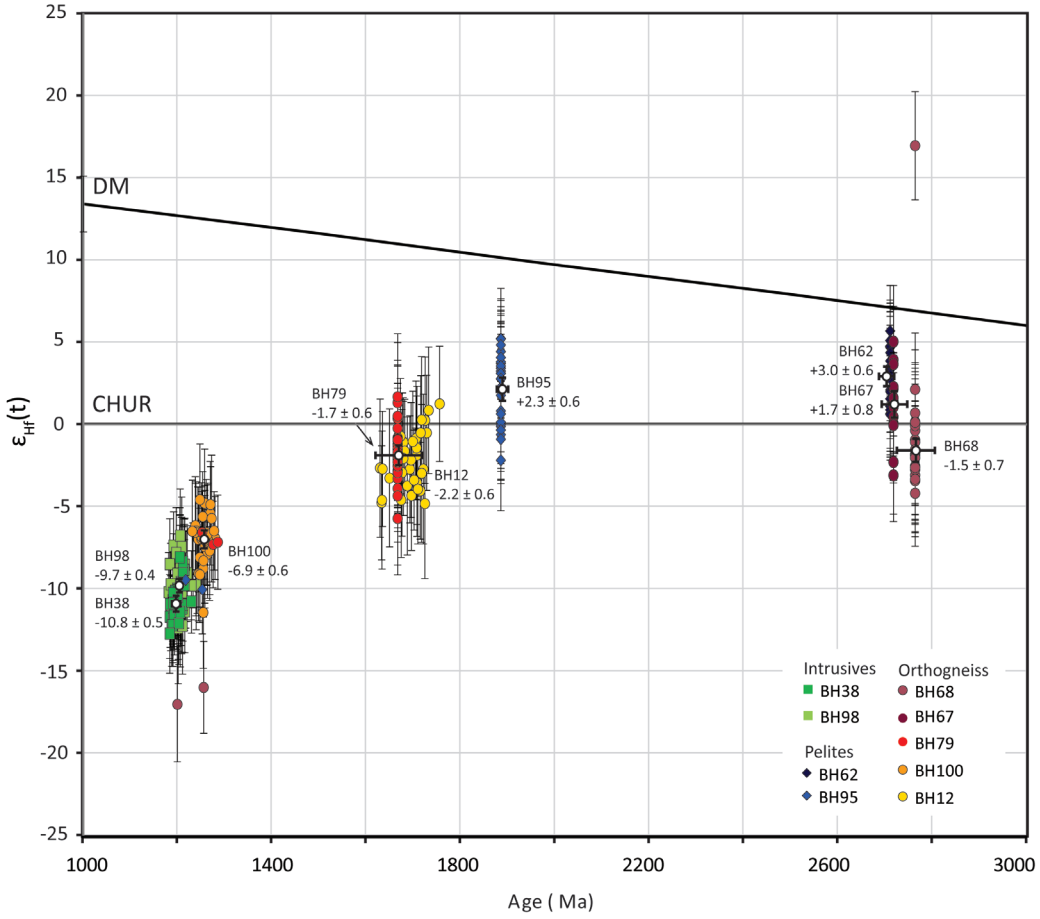

Figure 7. Lu–Hf isotope results from the Bunger Hills. Deviations of Hf ($^{176}Hf/^{177}Hf$) isotopic composition from the chondrite uniform reservoir (CHUR) standard are expressed in epsilon units, $\varepsilon_{Hf}(t)$. Data from orthogneiss samples are presented as circles in shades of red–yellow; metapelitic samples are presented as blue diamonds; late intrusive (migmatitic enderbite) samples are shown as green squares. Uncertainties on $\varepsilon_{Hf}(t)$ values are shown with error bars (2σ) for individual data points. For samples showing Pb-loss (i.e. samples BH67, BH68, BH62, BH95, BH79; Figs. 5 & 6) $\varepsilon_{Hf}(t)$ analyses are plotted at the respective calculated $^{207}Pb/^{206}Pb$ upper intercept age for the corresponding sample. All other analyses are plotted at their apparent $^{207}Pb/^{206}Pb$ ages. Weighted mean $\varepsilon_{Hf}(t)$ values for all samples are also shown as filled, white circles. Weighted mean $\varepsilon_{Hf}(t)$ values are plotted at either the $^{207}Pb/^{206}Pb$ ages upper intercept or weighted average age of the corresponding sample.

zircon cores, and 18 analyses from zircon rims (Fig. 5e). Core and rim analyses predominantly define a spread of ages between ca. 1750–1650 Ma. The rim analyses, on average, are slightly older than the zircon cores but are typically still within uncertainty of the ages obtained from the core analyses. One rim analysis occurs at ca. 1450 Ma and is from a luminescent overgrowth exhibiting ghosted oscillatory zoning (Fig. 4e). This date is accordingly interpreted to reflect the effects of progressive recrystallization of the magmatic core and associated Pb loss.

5.1.2.2 Sample BH100: tonalitic–granitic orthogneiss

Zircon from this sample are generally elongate and tabular in shape with sub-rounded crystal face terminations. Grains are light brown–colourless, 150–800 µm in length and have aspect ratios between 1:1 and 1:4. CL imagery show zircon grains display typical magmatic oscillatory zoning. Some grains exhibit narrow, luminescent rims (Fig. 4f). Thirty-one analyses were obtained from zircon cores for this sample (Fig. 5f). The data yield a weighted mean age of 1256 ± 5 [23] Ma (n = 31, MSWD = 0.82). The $^{206}Pb/^{238}U$ age is on average, younger than the corresponding $^{207}Pb/^{206}Pb$ age for individual analyses and is accordingly interpreted as a result of minor, recent Pb loss.

5.1.3 Association 3

5.1.3.1 Sample BH79: tonalitic orthogneiss

Zircon from this sample are sub-rounded to elongate with blocky to sub-rounded crystal face terminations. Grains are brown in colour,

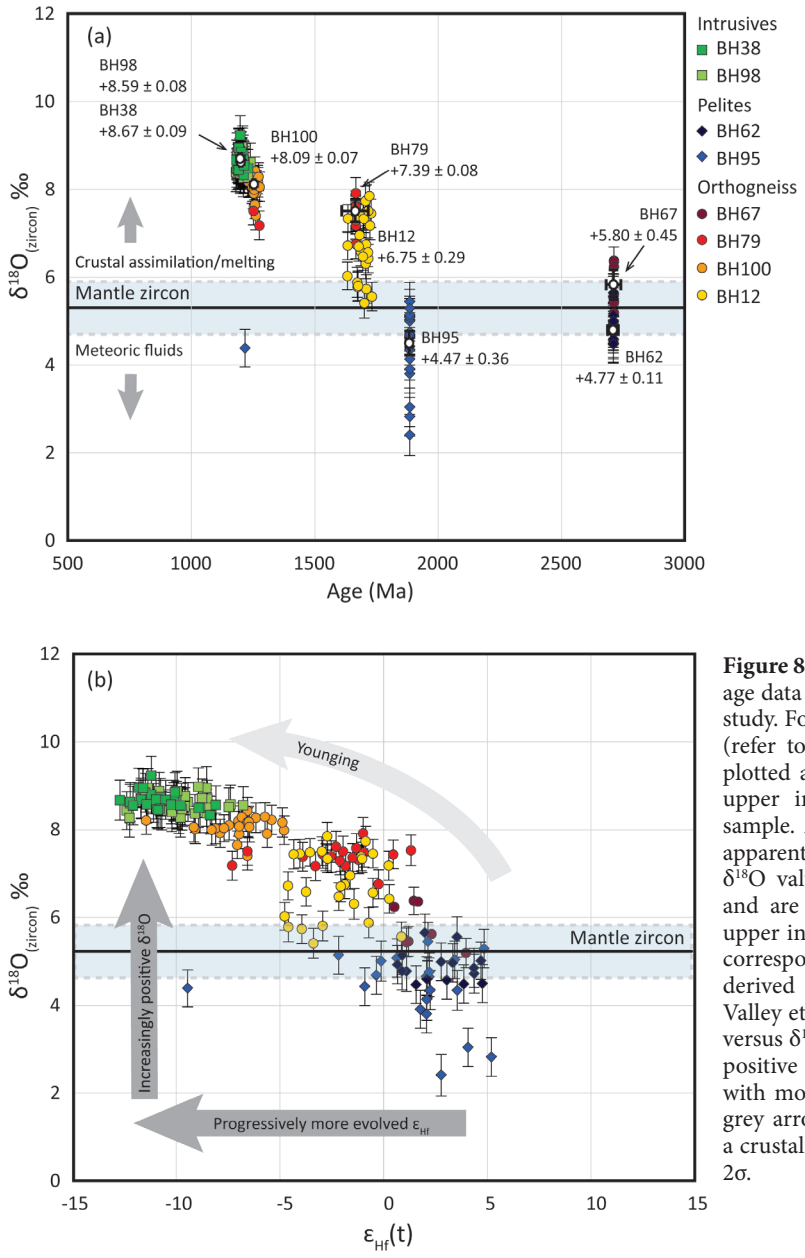

Figure 8. Oxygen isotope data. (a) Plot of U–Pb age data versus $\delta^{18}O$ for zircon analysed in this study. For samples showing evidence of Pb-loss (refer to section 5.2), individual analyses are plotted at the respective calculated $^{207}Pb/^{206}Pb$ upper intercept age for that corresponding sample. All other analyses are plotted at their apparent $^{207}Pb/^{206}Pb$ ages. Weighted mean $\delta^{18}O$ values are shown as filled, white circles and are plotted at either the $^{207}Pb/^{206}Pb$ ages upper intercept or weighted average age of the corresponding sample. The range of mantle derived $\delta^{18}O$(zircon) values (5.3 ± 0.6 ‰; Valley et al 1998) is indicated; (b) Plot of $\varepsilon_{Hf}(t)$ versus $\delta^{18}O$ values. Younger zircon reveal more positive (heavier) $\delta^{18}O$ values, and correlate with more evolved $\varepsilon_{Hf}(t)$ values (annotated by grey arrows), having likely been derived from a crustal source. Error bars on $\delta^{18}O$(zircon) are 2σ.

100–400 µm in size, and have 1:2 to 1:4 aspect ratios. CL imagery of grains reveal predominantly dark, oscillatory zoned cores, and moderately thick luminescent and dark overgrowths (Fig. 4g). Twenty-six analyses were obtained from oscillatory-zoned zircon cores, four analyses from dark, unzoned grains, and 13 analyses from zircon rims (Fig. 6a). Core analyses show a spread of apparent ages between ca. 1700–1400 Ma. The oldest analysis yields a concordant age of 1703 ± 28 Ma. Collectively, these analyses yield an upper intercept age of 1666 ± 49 [58] Ma (*n* = 26, MSWD = 3.5). The upper intercept age is considered to hold geological significance as it coincides with a concordant age and a number of near-concordant analyses. The lower intercept age of ca. 960 Ma is considerably younger than the age of metamorphism constrained by zircon rims from this sample. Assuming the ca. 1700 Ma zircon in this sample represent newly crystallised material (i.e. not detrital grains), this lower intercept age is interpreted to reflect at least two, superimposed Pb-loss events. These events may include partial Pb-loss of ca. 1700 Ma zircon at ca. 1300–1250 Ma, corresponding to the age of zircon rim growth and, subsequently, recent Pb-loss. Dark, unzoned grains yield three equivalent dates of 1252 ± 30 Ma, 1275 ± 29 Ma and 1285 ± 30 Ma, and one older analysis of 1317 ± 30 Ma. Rim analyses from this sample mostly define a near-concordant population at ca. 1300–1250 Ma with few older, discordant analyses. Analyses from rims and

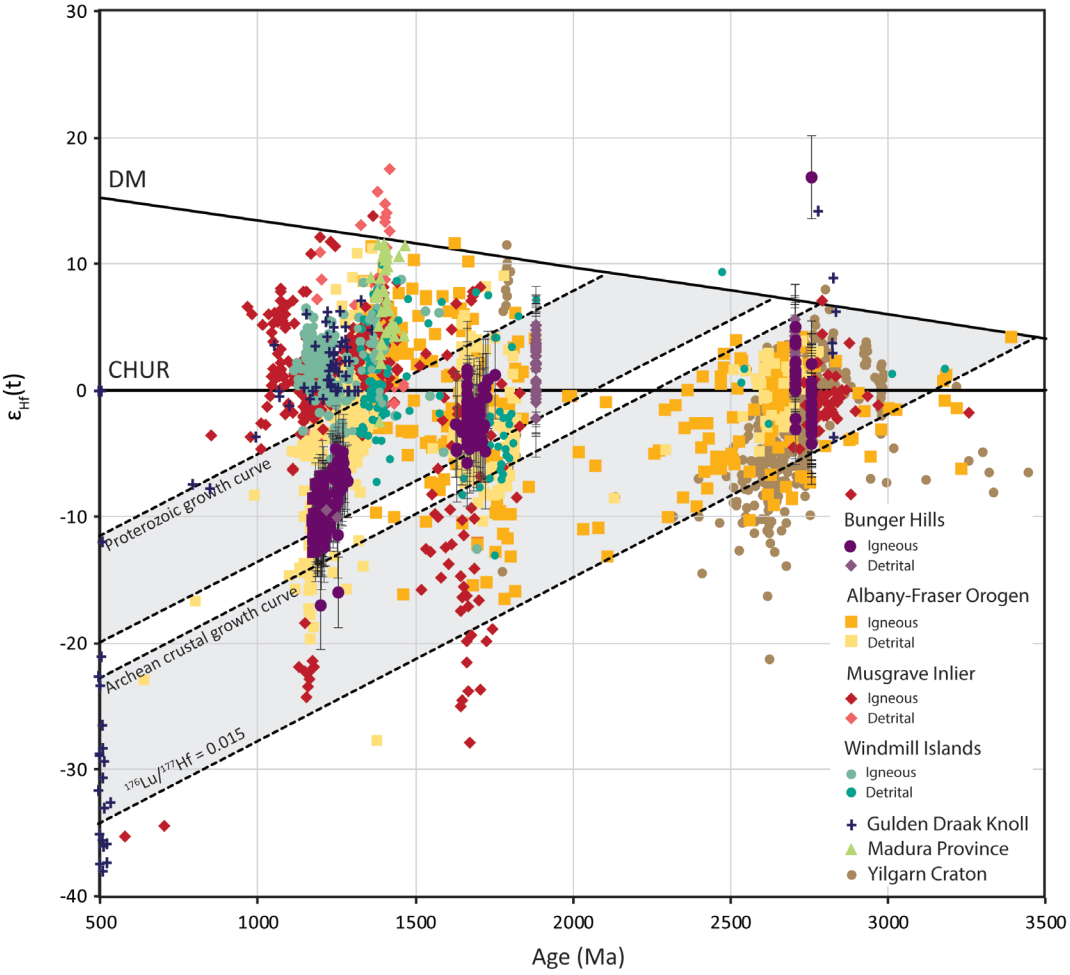

Figure 9. Lu–Hf isotope results from the Bunger Hills (this study, Fig. 7) plotted against existing data (see also Appendix E) from the Albany–Fraser Orogen and Musgrave Inlier (Kirkland et al., 2015a, 2013b, 2011, 2014; Smithies et al., 2011; Smits et al., 2014, and references therein; Spaggiari et al., 2015), the Madura Province (Kirkland et al., 2015a), the Yilgarn Craton (Ivanic et al., 2012; Kirkland et al., 2015b; Wyche et al., 2012), the Windmill Islands (Morrissey et al., 2017; Zhang et al., 2012), and the Gulden Draak Knoll (Gardner et al., 2015). The Albany–Fraser Orogen dataset is inclusive of analyses from the Northern Foreland, Biranup Zone, Nornalup Zone, Fraser Zone, Barren Basin, Arid Basin, and Esperance and Recherche Supersuites. Data from the Bunger Hills show 2σ uncertainties on the $\varepsilon_{Hf}(t)$ values. Crustal growth curves using a bulk crust value of $^{176}Lu/^{177}Hf$ = 0.015 (Griffin et al., 2002) are drawn through the Archean and Paleoproterozoic-aged zircon populations from this study. Abbreviations: CHUR, Chondritic uniform reservoir; DM, depleted mantle.

metamorphic cores (Th/U typically <0.12) overall give lower Th/U ratios compared to the inherited cores (Th/U = 0.10–0.72; Appendix A).

5.1.4 Association 4

5.1.4.1 Sample BH54: garnet–cordierite–orthopyroxene gneiss

Zircon from this sample are rounded and elongate with sub-rounded crystal faces, light brown–colourless and 50–200 µm in size with aspect ratios of 1:1 to 1:3. CL imagery shows weakly luminescent to dark concentric zoned cores often overgrown by moderately-thick, dark rims (Fig. 4h). Fifty-four analyses were obtained from oscillatory zircon cores, nine analyses from zircon rims and one analysis from a dark, unzoned grain (Fig. 6b). Analyses from oscillatory zoned cores range between 2894 ± 22 Ma and 1490 ± 27 Ma, with subpopulations at ca. 2600–2400 Ma, ca. 2300 Ma, ca. 2000 Ma and ca. 1800–1500 Ma. The youngest concordant analysis from an oscillatory-zoned core (1490 ± 27 Ma) provides the maximum depositional age for this sample. Rim analyses occur between ca. 1330 Ma–1190 Ma. The zircon rims are homogeneous and featureless in CL imagery, equivalent in age to overgrowths on igneous and detrital zircon in other analysed samples, and are interpreted to have formed in situ during metamorphism (i.e. are not of detrital origin). One analysis obtained from a dark, unzoned grain yields an age of 1229 ± 36 Ma. Analyses from six of the zircon rims and the dark, unzoned grain define a discrete population

that gives a weighted mean age of 1255 ± 42 [48] Ma (n = 7, MSWD = 9.9). There is no apparent difference in the Th/U ratio with values ranging between 0.04–2.82 for zircon rims and unzoned grains, and 0.02–1.72 for oscillatory-zoned cores.

5.1.5 Association 5

5.1.5.1 Sample BH38: migmatitic enderbite

Zircon from this sample are anhedral and blocky to elongate with sub-rounded crystal faces. There is minor fracturing of intact grains and a moderate amount of fragmented zircon. Zircon grains are typically light brown–colourless and 100–500 µm in size. The internal morphology of the zircon is chaotic with dark to weakly luminescent oscillatory-zoned cores that are commonly partially recrystallised and resorbed (Fig. 4i). A small number of grains show weak sector zoning and rarely, moderately thick, luminescent rims. The internal morphology of the zircon is interpreted to reflect the crystallisation of primary, igneous zircon during emplacement of the enderbite followed by recrystallization and resorption during migmatisation. Twenty-six analyses were obtained from this sample yielding one population with a weighted mean age of 1200 ± 6 [22] Ma (n = 26, MSWD = 0.56; Fig. 6c). Analyses from overgrowths that resorb the zoned cores, and the cores themselves, are equivalent in age.

5.1.5.2 Sample BH98: migmatitic enderbite

Zircon isolated from this sample are anhedral, fragmented and have blocky crystal faces. Grains are yellow brown–brown in colour and 100–400 µm in size. CL imagery reveals dark grains and moderately to strongly luminescent grains, both exhibiting diffuse internal zoning (Fig. 4j). Thirty-seven analyses were obtained from this sample, yielding a weighted mean age of 1203 ± 5 [22] Ma (n = 37, MSWD = 0.58; Fig. 6d).

5.2 Lu–Hf and oxygen isotope analysis

Lu–Hf isotope analysis was undertaken on five orthogneiss, two pelitic gneiss and two late intrusive samples (Appendix B; Table 2). These samples are representative of all lithological units in the Bunger Hills excluding the massive pelitic gneiss unit (Association 4, refer to Section 3.4). Analyses were not obtained from sample BH54 due to the relatively small size and complex internal zonation of the zircon grains. Oxygen isotope analyses were done on all samples except BH68 and BH54, and on the same zircon grains used for U–Pb geochronology and Hf isotope measurements (Appendix C; Table 2). Lu–Hf data are presented as $\varepsilon_{Hf}(t)$ versus U–Pb age data in Fig. 7. Oxygen isotope data are presented as $\delta^{18}O$ (zircon) ‰ VSMOW ratios versus U–Pb age data (Fig. 8a) and $\varepsilon_{Hf}(t)$ values (Fig. 8b). Uncertainties on Lu–Hf and oxygen isotope data are quoted at the 2σ level.

A number of samples analysed in this study yield zircon that have been variably affected by Pb-loss, which is common of high-grade metamorphic terranes. As U–Pb and Lu–Hf systems in zircon are decoupled, variable Pb-loss processes typically result in a spread in apparent $^{207}Pb/^{206}Pb$ ages, but the Hf isotope composition will remain unaffected (e.g. Guitreau and Blichert-Toft, 2014; Halpin et al., 2012). Therefore, Pb-loss in zircon can be identified by horizontal trends in initial $^{176}Hf/^{177}Hf$ versus $^{207}Pb/^{206}Pb$ age (Appendix D). If initial $^{176}Hf/^{177}Hf$ is converted to $\varepsilon_{Hf}(t)$, this relationship leads to positive correlation between $\varepsilon_{Hf}(t)$ and the apparent $^{207}Pb/^{206}Pb$ ages (e.g. BH67, Appendix D). However, such trends are an artefact of Pb-loss and are not indicative of the actual crustal evolution. U–Pb discordance in zircon is also reported to result in depletion of original ^{18}O values (e.g. Booth et al., 2005). Accordingly, for samples with zircon significantly affected by ancient Pb loss such that a Pb-loss discord was calculated (Figs. 5 and 6; samples BH67, BH68, BH62, BH79 and BH95), zircon $\varepsilon_{Hf}(t)$ and $\delta^{18}O$ (zircon) data are plotted at the U–Pb upper intercept age rather than the apparent $^{207}Pb/^{206}Pb$ ages of individual zircon grains (Figs. 7 and 8). A plot of zircon $\varepsilon_{Hf}(t)$ versus apparent $^{207}Pb/^{206}Pb$ ages for each sample is also presented in Appendix D for comparison with Figs. 7 and 8.

Further, an important consideration in many isotopic studies of granitoid formation and crustal evolution is the mixing of melts and/or material derived from various crustal and/or mantle sources. A range of $\varepsilon_{Hf}(t)$ values returned from a single sample or intrusive can be interpreted to represent such mixing. The data collected in this study often show large ranges of $\varepsilon_{Hf}(t)$ within individual samples (e.g. sample BH67: $\varepsilon_{Hf}(t)$ = +5.1 to -3.0) that could be readily interpreted to represent mixing of material from different sources. However, the measured $^{176}Hf/^{177}Hf$ ratios

have relatively large uncertainties compared to many published studies and hence it is also plausible that the observed spread in $\varepsilon_{Hf}(t)$ values actually represents analytical uncertainty as opposed to real geological variation. To assess both possibilities and avoid over-interpretation of the data, calculated weighted mean $\varepsilon_{Hf}(t)$ values are also quoted in addition to the observed range of $\varepsilon_{Hf}(t)$. Calculated weighted mean $\varepsilon_{Hf}(t)$ values are plotted at either the weighted average $^{207}Pb/^{206}Pb$ age or upper intercept $^{207}Pb/^{206}Pb$ age for samples of igneous origin as well as metasedimentary samples BH62 and BH95 (Fig. 7). If the weighted mean returns a MSWD and probability value indicative of a single population in the data (e.g. Spencer et al., 2015), the mean is used as the best estimate of isotopic composition of the sample for comparison with other samples and regions. In some instances, this approach also provides improved constraints on the likely source components that may be involved in the formation of the igneous host rocks. Hf isotope data from this study are compared with existing data from the Musgrave Inlier, Albany–Fraser Orogen, Yilgarn Craton, Madura Province, Windmill Islands and Gulden Draak microcontinent in Fig. 9. The regional dataset shown in Fig. 9 is compiled in Appendix E.

5.2.1 Association 1

Zircon from the mafic–felsic orthogneiss and associated pelitic gneiss reveal a moderately juvenile signature. $\varepsilon_{Hf}(t)$ values range between +5.1 ± 3.4 and -3.0 ± 2.8 for sample BH67 (2712 ± 27 Ma), and give a weighted mean of +1.7 ± 0.8 (*n* = 14/15, MSWD = 1.3). Zircon cores from sample BH67 yield $\delta^{18}O$ values between +5.19 ± 0.34 ‰ and +6.38 ± 0.34 ‰ with a weighted mean value of +5.80 ± 0.45 ‰ (*n* = 7).

Twenty-four analyses were obtained from sample BH68 (2763 ± 40 Ma). Analyses from oscillatory-zoned zircon cores (*n* = 22) yield $\varepsilon_{Hf}(t)$ values between +2.1 ± 3.4 and -4.2 ± 3.2, with one anomalously juvenile analysis ($\varepsilon_{Hf}(t)$ = +17.0 ± 3.3, also excluded from weighted mean calculations), and give a weighted mean value of -1.5 + 0.7 (*n* = 21/22, MSWD = 0.90). Two analyses from dark, unzoned grains dated at 1199 ± 11 Ma and 1255 ± 12 Ma, give significantly more evolved signatures of -17.0 ± 3.5 and -16.0 ± 2.8, respectively, and are plotted at their apparent $^{207}Pb/^{206}Pb$ age. These two values fall on a crustal growth curve with $^{176}Lu/^{177}Hf$ = 0.015 projected from the isotopic composition of the Archean zircon core population for this sample. This suggests that new metamorphic zircon formed from a near-homogenized anatectic melt during the Mesoproterozoic with Hf composition sourced from the Archean zircon (Halpin et al., 2013).

Twenty analyses from sample BH62 (2710 ± 20 Ma) yield $\varepsilon_{Hf}(t)$ values between +5.7 ± 2.8 and +0.6 ± 2.8 and give a weighted mean of +3.0 ± 0.6 (*n* = 20, MSWD = 1.5). Zircon cores from sample BH62 have $\delta^{18}O$ values between +4.48 ± 0.44 ‰ and +5.65 ± 0.43 ‰ with a weighted mean value of +4.77 ± 0.11 ‰ (*n* = 14/16).

Thirty-four analyses were obtained from sample BH95 (1885 ± 12 Ma). Analyses from oscillatory-zoned zircon cores yield $\varepsilon_{Hf}(t)$ values that range between +5.2 ± 2.3 and -2.2 ± 3.1 and give a weighted mean of +2.3 ± 0.6 (*n* = 31/32, MSWD = 1.6). Two analyses from zircon rims with ages of 1217 ± 11 Ma and 1252 ± 9 Ma, give $\varepsilon_{Hf}(t)$ values of -9.5 ± 2.9 and -10.0 ± 2.7, respectively, and are plotted at their apparent $^{207}Pb/^{206}Pb$ ages. The spread in the Hf isotopic composition of the Paleoproterozoic zircon population (Appendix B) makes it difficult to distinguish whether the Mesoproterozoic zircon rims reflect isotopic resetting of the older detrital zircon, or represent new zircon growth (e.g. Halpin et al., 2013). Zircon cores from sample BH95 yield $\delta^{18}O$ values between +2.41 ± 0.47 ‰ and +5.45 ± 0.44 ‰ with a weighted mean value of +4.47 ± 0.36 ‰ (*n* = 18/19). One dark rim from BH95 yielded a $\delta^{18}O$ value of 4.39 ± 0.42 ‰ (analysis BH95-79).

5.2.2 Association 2

Twenty-nine analyses from sample BH100 (1256 ± 5 Ma) yield $\varepsilon_{Hf}(t)$ values that range between -4.6 ± 3.4 and -11.4 ± 3.4 with a weighted mean $\varepsilon_{Hf}(t)$ of -6.9 ± 0.6 (*n* = 29, MSWD = 0.90). Zircon from sample BH100 yield $\delta^{18}O$ values between +7.40 ± 0.32 ‰ and +8.43 ± 0.31 ‰ with a weighted mean of +8.09 ± 0.07 ‰ (*n* = 23/24).

Thirty-two analyses from oscillatory-zoned cores in sample BH12 (ca. 1750–1650 Ma) give $\varepsilon_{Hf}(t)$ values between +1.3 ± 3.5 and -4.8 ± 4.6 and yield a weighted mean $\varepsilon_{Hf}(t)$ of -2.2 ± 0.6 (*n* = 32, MSWD = 0.91). Zircon from sample BH12 have $\delta^{18}O$ values between +5.41 ± 0.34 ‰ and + 7.85 ± 0.31 ‰ with a weighted mean value of +6.75 ±

0.29 ‰ (n = 27).

5.2.3 Association 3

Thirty analyses were obtained from sample BH79 (1666 ± 49 Ma). Twenty-six analyses from oscillatory-zoned zircon cores yield $\varepsilon_{Hf}(t)$ values between +1.3 ± 4.2 and -6.3 ± 3.3 and are plotted at their collective upper intercept age, and give a weighted mean $\varepsilon_{Hf}(t)$ value of -1.7 ± 0.6 (n = 26, MSWD = 0.9), using the upper intercept age as t. Oscillatory-zoned zircon cores give $\delta^{18}O$ values between +6.76 ± 0.33 ‰ and +7.92 ± 0.36 ‰ with a weighted mean value of +7.39 ± 0.08 (n = 17/19). Four analyses from dark, unzoned grains (1317 Ma, 1285 Ma, 1275 Ma and 1252 Ma) that are younger than the main age population from this sample, are equivalent in $\varepsilon_{Hf}(t)$, yield a weighted mean $\varepsilon_{Hf}(t)$ value of -6.9 ± 1.4, and are plotted at their respective $^{207}Pb/^{206}Pb$ ages (Fig. 7). Two of these unzoned zircon cores yielded $\delta^{18}O$ values of +7.36 ± 0.32 ‰ (1317 Ma, analysis BH79-38) and +7.48 ± 0.33 ‰ (1285 Ma, analysis BH79-45). The Hf-isotopic composition of the dark, unzoned grains sit on a crustal growth curve (with slope represented by an average crustal evolution, $^{176}Lu/^{177}Hf$ = 0.015) projected from the older, oscillatory-zoned zircon population. The unzoned grains are inferred to represent metamorphic zircon growth from an anatectic melt with a Hf-isotopic composition derived from the >1500 Ma grains (Halpin et al., 2013).

5.2.4 Association 5

Thirty-seven analyses from sample BH98 (1203 ± 5 Ma) yield $\varepsilon_{Hf}(t)$ values that range between -12.4 ± 3.4 and -6.8 ± 2.8, and a weighted mean of -9.7 ± 0.4 (n = 37, MSWD = 0.98). Zircon from sample BH98 have a similar range of $\delta^{18}O$ with values between +8.27 ± 0.43 ‰ and +8.97 ± 0.44 ‰ and a weighted mean +8.59 ± 0.08 ‰ (n = 33).

Twenty-six analyses from sample BH38 (1200 ± 6 Ma) yield $\varepsilon_{Hf}(t)$ values that range between -12.7 ± 2.4 and -8.1 ± 3.0 Ma, and give a weighted mean of -10.8 ± 0.5 (n = 26, MSWD = 0.84). Zircon from sample BH38 yield $\delta^{18}O$ ratios between +8.33 ± 0.43 ‰ and +9.23 ± 0.44 ‰ with a weighted mean value of +8.67 ± 0.09 ‰ (n = 26). The range of negative $\varepsilon_{Hf}(t)$ values and positive $\delta^{18}O$ values highlights the highly evolved nature of these two samples.

6. DISCUSSION

6.1 Geological architecture

On the basis of field relations and new U–Pb geochronology, the sample set can be divided into three main groups: (1) Archean "basement" samples from the southeastern Bunger Hills (comprising Association 1); (2) a Paleo–Mesoproterozoic volcano-clastic sequence comprising an interlayered orthogneiss–pelitic gneiss package (Associations 2 and 3, and sample BH95) and a pelitic gneiss-dominated succession (Association 4); and (3) late intrusive samples of Mesoproterozoic age (Association 5).

6.1.1 Nature of the Archean basement

Zircon populations from composite mafic–felsic orthogneiss in the southeastern Bunger Hills (samples BH67 and BH68) are dominated by Archean grains that suggest a ca. 2800–2700 Ma magmatic event. Zircon grains of a similar age were analysed from garnet–cordierite–orthopyroxene gneiss (sample BH62) obtained from within the mafic–felsic association. The intensity of metamorphism and deformation means that the original nature of the mafic–felsic association is unclear. However, close correspondence in age and morphology of zircon grains between the orthogneiss samples (BH67 and BH68) and those from the pelitic gneiss (BH62) suggest that the protoliths to these rocks may have been created at a similar time, for example, within an extensional basin with volcano-clastic sedimentation. The Archean ages obtained in this study are significantly older than previous estimates of the inferred emplacement age of the protolith to gneissic basement dated at 1699 ± 15 Ma by Sheraton et al. (1992).

Zircon from these three samples yield $\varepsilon_{Hf}(t)$ values between predominantly -5 and +8, highlighting the role of mantle-derived magmas in their origin. Furthermore, zircon from sample BH67 yield a mean $\delta^{18}O$ value of +5.80 ± 0.45 ‰ which is similar to $\delta^{18}O$ values from primitive mantle-derived magmas ($\delta^{18}O$ = 5.3 ± 0.6 ‰; Valley, 2003). Oxygen isotope values for the detrital zircon grains from sample BH62 range between +4.48 ± 0.44 and +5.65 ± 0.43, consistent with the source being the Archean igneous rocks represented by BH67 and BH68. Both the age and Hf isotope signature of the Archean Bunger Hills basement are broadly comparable to magmatic

rocks of the Yilgarn Craton (Fig. 9; Cassidy et al., 2006; Griffin et al., 2004; Ivanic et al., 2012; Kirkland et al., 2015b; Mole et al., 2012; Wyche et al., 2012) and ca. 3000–2600 Ma gneisses, granites and fault-bound packages of metasedimentary rocks of the Northern Foreland that represent the reworking of the Yilgarn Craton margin during the Albany–Fraser Orogeny (Kirkland et al., 2015a, 2011; Spaggiari et al., 2009; Spaggiari et al., 2014). However, a direct correlation cannot be made with the individual terranes of the Yilgarn Craton due to spread in the age and Hf-isotopic composition of the dataset. The Archean Bunger Hills zircon also partially overlap in Hf–age space with detrital zircon from the Biranup Zone of the Albany–Fraser Orogen (Spaggiari et al., 2015), inferred sourced from the Yilgarn Craton, and the Indulkana Suite of the West Musgrave Inlier (Smits et al., 2014).

6.1.2 Proterozoic cover sequence to the Archean basement

6.1.2.1 Mid-Paleoproterozoic (ca. 1900 Ma) metasedimentary rocks

U–Pb geochronology from sample BH95 reveal a main population at ca. 1900–1800 Ma and a spread of dates along a discordant array to ca. 1520 Ma (Fig. 5d). One interpretation, is that analyses occurring along the discordant array record the effects of ancient Pb-loss from an original ca. 1900 Ma population. Accordingly, zircon $\varepsilon_{Hf}(t)$ and $\delta^{18}O$ (zircon) data from the main population from this sample are plotted at their calculated U–Pb upper intercept age (refer to Section 5.2). However, sample BH95 could also record a spread of near-concordant detrital ages that are unaffected by Pb-loss and form multiple discrete populations between ca. 1900–1800 Ma, or younger. The observed spread in the Hf and oxygen isotope values for the 1900–1800 Ma population (Figs. 7 and 8, Appendix B and C) supports the latter interpretation of a more diverse provenance than a single ca. 1900 Ma protolith. In this case however, populations are indistinguishable in age given the uncertainties on individual analyses. Regardless of the interpretation, a source is required to explain the dominance of ca. 1900–1800 Ma ages, and zircon of relatively juvenile affinity (weighted mean $\varepsilon_{Hf}(t) = +2.3 \pm 0.6$) and approximately mantle-like $\delta^{18}O$ values (mean $\delta^{18}O = +4.48 \pm 0.36$ ‰).

A dominant age population for a metasedimentary rock is suggestive of local zircon derivation. However, while juvenile magmatism at ca. 1950–1900 Ma is considered globally significant (Condie et al., 2009), magmatism correlating to this age and isotopic signature is not currently recognised, or not presently exposed, within the Bunger Hills nor surrounding outcrop in East Antarctica. Within Australia, sources for detrital zircon components spanning ca. 2550–1850 Ma are also comparatively rare and are not recognised within the Albany–Fraser Orogen. Nonetheless detrital zircon from the Aileron Province of the

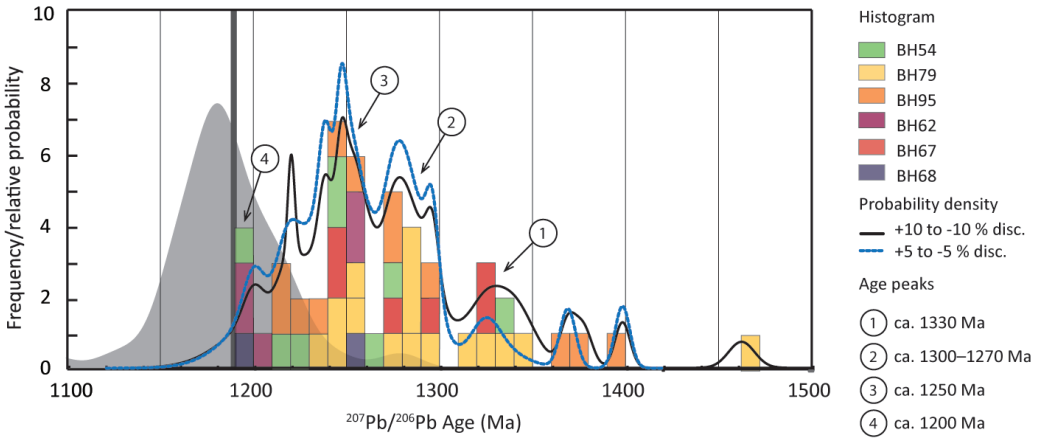

Figure 10. Histogram and probability density plot of U–Pb zircon data from inferred metamorphic zircon core and rim analyses with $^{207}Pb/^{206}Pb$ ages <1500 Ma. Data that are < 10 % discordant define a broad spread of ages between ca. 1460 Ma and ca. 1190 Ma with age peaks at ca. 1330 Ma, ca. 1300–1270 Ma, ca. 1250 Ma and ca. 1200 Ma (numbered 1–4). A probability density distribution of age data is also shown for <5 % discordant analyses. The age of metamorphism in the Highjump Archipelago constrained by Sheraton et al. (1993) and Tucker and Hand (2016) is overlain on the data from this study as a solid grey vertical line and probability density plot (shaded grey), respectively.

NAC and the Pine Creek Orogen have recorded ca. 1920 Ma ages (Hollis et al., 2014) and oxygen isotopes and Hf model ages from the Mugrave Inlier, Rudall Province and Capricorn Orogen in central Australia have also suggested a major crust formation event at ca. 1950–1900 Ma (Kirkland et al., 2013a, b). No igneous rocks of this age have been dated in these terranes, however, 1914 ± 8 Ma orthogneiss basement has been recorded in the northern Gawler Craton (Jagodzinski et al., 2013; Reid et al., 2014). These new data were used to evoke a geodynamic and spatial connection between the Gawler Craton and central and western Australian terranes at this time (Reid et al., 2014). Therefore, detrital zircon of ca. 1900 Ma age in the Bunger Hills could have been derived from igneous rocks comprising a potentially extensive, although completely obscured and/or destroyed, Paleoproterozoic basement component within central and western Australia or Antarctica.

6.1.2.2 Late Paleoproterozoic (ca. 1700 Ma) volcano-clastic sequence

Zircon from orthopyroxene-bearing tonalitic orthogneiss in the west Bunger Hills (sample BH12), and tonalitic orthogneiss interlayered with metasedimentary rocks in the northeast Bunger Hills (sample BH79) yield respective $^{207}Pb/^{206}Pb$ ages of ca. 1750–1650 Ma and 1666 ± 49 [58] Ma (2σ). These ages are within uncertainty of an emplacement age of 1699 ± 15 Ma determined previously for a sample of granodioritic orthogneiss in the central Bunger Hills (Sheraton et al., 1992). Results of U–Pb geochronology from these samples, in conjunction with previous work, thus suggest that the tonalitic–granitic orthogneiss and interlayered orthogneiss–pelitic gneiss unit form a Paleoproterozoic volcano-clastic cover sequence to an Archean basement.

Paleoproterozoic magmatism of ca. 1700 Ma age is not recognised in the southern Yilgarn Craton (e.g. Cassidy et al., 2006; Mole et al., 2012). However, the Northern Foreland, and the Biranup and eastern Nornalup Zones of the Albany–Fraser Orogen (Fig. 1) record the episodic emplacement of granitic and gabbroic magmas between ca. 1810–1625 Ma (Kirkland et al., 2011, 2014). Furthermore, the Hf-isotopic signature of the Biranup Zone spans the range $\varepsilon_{Hf}(t)$ = -10 to +8 (Fig. 9; Kirkland et al., 2011, 2014), which encompass the isotopic range of samples BH12 and BH79 ($\varepsilon_{Hf}(t)$ = -6 to +2).

Previously, average crustal isotopic growth curves ($^{176}Lu/^{177}Hf$ = 0.015) have been utilised to propose that the Biranup Zone formed on the Yilgarn Craton margin with Paleoproterozoic juvenile magmatic input increasingly incorporated over time (Kirkland et al., 2015a). In this study, Hf isotope data from samples BH12 and BH79 span a range of Hfinitial and $\varepsilon_{Hf}(t)$ values that are significantly more juvenile than could be solely represented by reworking of crust of Yilgarn affinity and/or Bunger Hills Archean basement composition (Fig. 9). However, zircon $\delta^{18}O$ values deviate to a slightly higher range than represented by zircon in equilibrium with the mantle, and therefore indicate that these grains were crystallised from at least a partially, crustal-derived melt (Hawkesworth and Kemp, 2006b; Kemp et al., 2006). As with the Biranup Zone, the samples analysed here are thus also consistent with mixing of a new juvenile source at ca. 1700 Ma, as well as a recycled Archean basement component.

6.1.2.3 Post-1490 Ma sedimentary cover

Detrital zircon from a sample of garnet–cordierite–orthopyroxene-bearing gneiss from the extensive pelitic gneiss unit in the central Bunger Hills (sample BH54) are sourced predominantly from Neoarchean to Paleoproterozoic (ca. 2600–2200 Ma), late Paleoproterozoic (ca. 2000 Ma), and late Paleoproterozoic to Mesoproterozoic rocks (ca. 1800–1500 Ma; Fig. 6d). The maximum depositional age of the protolith to this metasedimentary rock is 1490 ± 27 Ma (2σ) based on the age of the youngest concordant analysis from an oscillatory-zoned zircon core. However, there is limited constraint on the minimum depositional age, other than intrusion of migmatitic enderbite of the Paz Cove batholith at ca. 1200 Ma (i.e. sample BH38) that is observed interlayered with and hosting enclaves of this pelitic gneiss on Geologov Island (Fig. 2, see also Section 3.5).

The abundance of ca. 1800–1600 Ma zircon detritus and the close proximity of these rocks to similarly-aged igneous rocks from the Bunger Hills and Biranup Zone of the Albany–Fraser Orogen, indicate that these regions were the most likely sources. A period of magmatic quiescence is noted between ca. 1600–1455 Ma in the Albany–Fraser Orogen (Kirkland et al., 2011; Spaggiari et al., 2015; and this study) implying provenance of rare zircon grains of this age in sample BH54 from unrecognised or destroyed basement terranes

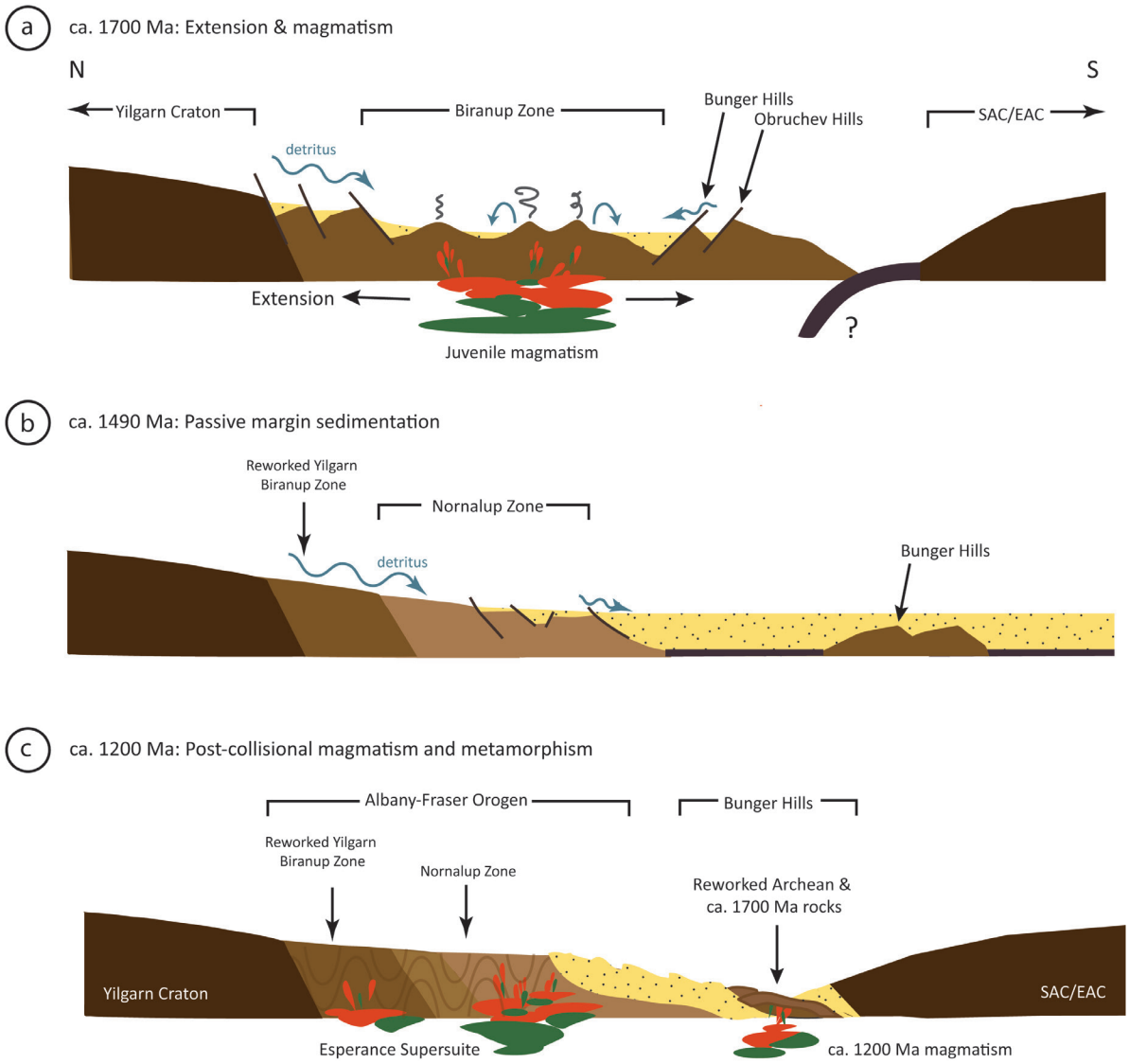

Figure 11. A simplified three-stage model proposed for the Paleo–Mesoproterozoic tectonic evolution of the Bunger Hills relative to the Albany–Fraser Orogen. Model is modified from Kirkland et al. (2011) and Spaggiari et al. (2015), but does not consider development of the Loongana oceanic-arc at ca. 1410 Ma. The tectonic reconstructions shown reflect an approximate N–S cross section through the Albany–Fraser Orogen and Bunger Hills. (a) Extension of the southern margin of the Yilgarn Craton resulted in a horst–graben-style architecture, exposing the Bunger Hills as a basement high. Magmatism with a relatively juvenile isotopic signature accompanied extension in the Biranup Zone of the Albany–Fraser Orogen (ca. 1815–1600 Ma) and Bunger Hills region (ca. 1700 Ma). Extension facilitated basin formation with detritus sourced from erosion of the exposed Yilgarn Craton hinterland, rifted Archean basement highs, coeval magmatic rocks of the Biranup Zone and/or Bunger Hills, and potentially external sources. The subduction margin is shown proximal to the Bunger Hills in (a), however, it's true location (e.g. proximal of or further outboard of the craton margin) at this time remains unclear; (b) Transition to a passive margin basin by ca. 1490 Ma and deposition of the protolith to the Bunger Hills pelitic gneiss (Association 4). Minimal Archean age component within the detrital zircon spectra from metasedimentary rocks from the Bunger Hills suggests that protolith deposition occurred some distance from the craton margin, and/or that the topography of the Yilgarn Craton and any reworked remnants of Archean crust was relatively subdued at this time; (c) Following collision of the SAC/EAC with the WAC, isotopically evolved magmatic rocks were emplaced in the Bunger Hills at ca. 1200 Ma. Magmatism in the Bunger Hills was coeval with intrusion of the Esperance Supersuite in the Nornalup Zone and high-grade metamorphism.

within the Bunger Hills. This is supported by one sample of granodioritic orthogneiss on Thomas Island that was dated by Sheraton et al. (1992) at 1521 ± 29 Ma. Alternatively, Paleoproterozoic detritus in sample BH54 could have been derived from sources much further afield of the Bunger Hills and Albany–Fraser Orogen, such as the north and west Gawler Craton, that was intruded by igneous rocks during the Kimban Orogeny (ca. 1750–1690 Ma), post-Kimban granitoids, and the mafic–felsic Hiltaba Suite (ca. 1595–1560 Ma; Hand et al., 2007; Howard et al., 2011; Payne et al., 2008; Reid et al., 2014; Swain et al., 2005). The Coompana Province located east of the Madura Province also records magmatism at ca. 1610 Ma and ca. 1500 Ma (Dutch et al., 2015; Spaggiari

and Smithies, 2015). Minor age components recognised between ca. 2200–1800 Ma may also imply provenance from distal sources such as the Gawler Craton or equivalent aged rocks in the Adelie Craton of East Antarctica (Payne et al., 2009), the Aileron Province of the North Australian Craton, and potentially the Capricorn Orogen located along the northern margin of the Yilgarn Craton, recording major phases of orogenesis at 2215–2145 Ma and 2005–1950 Ma which relate to the assembly of the WAC (Johnson et al., 2011; Occhipinti et al., 2004; Sheppard et al., 2004). Subsidiary Neoarchean ages from this sample match known magmatism within the Yilgarn Craton (e.g. Cassidy et al., 2006).

6.2 Late Mesoproterozoic magmatism in the Bunger Hills

Magmatic crystallisation of biotite-rich tonalitic–granitic gneiss in the central Bunger Hills (sample BH100) is dated at 1256 ± 5 [23] Ma. The Hf-isotopic compositions of these zircon grains encompass one main population with $\varepsilon_{Hf}(t)$ values of -11 to -5 (weighted mean $\varepsilon_{Hf}(t) = -6.9 \pm 0.6$). The timing of magmatism does not correlate with emplacement of the Recherche Supersuite (ca. 1330–1280 Ma) nor emplacement of the Esperance Supersuite (ca. 1198–1135 Ma) during Stages 1 and 2 of the Albany–Fraser Orogeny in southwestern Australia (Clark et al., 2000; Kirkland et al., 2011, 2014) . However, the Hf-isotopic range of this sample does overlap with the isotopic composition of the Recherche Supersuite granites (Kirkland et al., 2011, 2014). This event might therefore reflect the delayed magmatic expression of Stage-1 tectonism as recorded in the Bunger Hills.

Migmatitic enderbite sampled from the Paz Cove Batholith and Algae Lake Pluton yield indistinguishable emplacement ages of 1200 ± 6 [22] Ma and 1203 ± 5 [22] Ma, respectively. Previous work has dated both these intrusive bodies to ca. 1170 Ma (Sheraton et al., 1992). This large age discrepancy could be attributed to differences in analytical methodology, or a result of differences in sampling locality. The latter is supported by field observations which show that the intrusive bodies are lithologically heterogeneous at outcrop scale (over 10–100's meters) with the different lithological domains locally exhibiting cross-cutting and intrusive relationships. This suggests that both the Paz Cove Batholith and Algae Lake Pluton consist of a cluster of multiple, smaller intrusions of varied mineralogy, and potentially age and isotopic composition. Late magmatism in the Bunger Hills may therefore have occurred over a significantly longer timescale than previously thought, between at least ca. 1200–1170 Ma. This explanation is also proposed to justify observed differences in emplacement ages obtained by Zhang et al. (2012; 1205 ± 13 Ma and 1196 ± 8 Ma) and Post (2000; 1163 ± 7 Ma) for the Ardery Charnockite in the Windmill Islands (Blight and Oliver, 1977; Zhang et al., 2012). The timing of magmatism as constrained by this study and Sheraton et al. (1992) coincides with Stage-2 of the Albany–Fraser Orogeny, and the Musgrave Orogeny in central Australia associated with the voluminous intrusion of the Pitjanjatjara Supersuite (ca. 1220–1140 Ma; Clark et al., 2000; Smithies et al., 2011). Similarly to sample BH100, Lu–Hf isotope data from samples BH38 and BH98 show that the parental magma was isotopically evolved with $\varepsilon_{Hf}(t)$ values between -13 and -6 (weighted mean $\varepsilon_{Hf}(t) = -10.8 \pm 0.5$ and -9.7 ± 0.4, respectively). This result is consistent with previous isotopic work with results revealing low $\varepsilon_{Nd}(t)$ ($\varepsilon_{Nd}(t) = -9.4$; Sheraton et al., 1992). Significant deviation of $\delta^{18}O$ from mantle-like values for samples BH38, BH98 and BH100 (mean $\delta^{18}O = +8.67 \pm 0.09$ ‰, $+8.59 \pm 0.08$ ‰ and $+8.09 \pm 0.07$ ‰, respectively) further validates that these magmas were likely the result of mantle interaction with significant assimilation of supracrustal materials.

In Fig. 9, crustal growth curves using a bulk crust value $^{176}Lu/^{177}Hf = 0.015$ are drawn through the Archean and Paleoproterozoic-aged zircon populations from this study. If the bulk of the Bunger Hills Proterozoic crust was formed from predominantly reworking of locally-sourced Archean material ($T_{DM(crustal)}$ = 2.7–3.4 Ga), one would expect the Paleoproterozoic and Mesoproterozoic datasets to fall within the Archean growth curve. However, only two of the most evolved analyses from the Mesoproterozoic population fall along this trend (Fig. 9). These analyses are from unzoned zircon from sample BH68, and are inferred of metamorphic origin (refer also to Section 5.2.1). These zircon grains likely formed by in situ reworking (melting) of an Archean upper crustal source pertaining to the isotopic composition of samples BH62, BH67 and BH68 and/or a more juvenile Archean lower crustal component, in the presence of

a well-mixed anatectic melt (Halpin et al., 2013). The bulk of the Bunger Hills Proterozoic analyses spread towards a less evolved isotopic composition, and fall within the Paleoproterozoic growth curve (Fig. 9). The Mesoproterozoic crust could therefore have formed from: (1) reworking of an Archean source (similar to exposed crust in the Bunger Hills region) with the addition of juvenile melts, and/or (2) isotopic reworking of Bunger Hills Paleoproterozoic igneous and/or metasedimentary rocks ($T_{DM(crustal)}$ = 2.1–2.6 Ga), with little or no additions from a depleted mantle (juvenile) source.

The covariant $\varepsilon_{Hf}(t)$ versus $\delta^{18}O$ array presented in Fig. 8b further highlights that the parental magmas to the Bunger Hills igneous rocks were increasingly contaminated by assimilation of sedimentary-derived materials and/or intracrustal recycling through the Archean to Mesoproterozoic. This is reflected by an increasingly evolved Hf-isotopic signature and more positive (i.e. heavier) $\delta^{18}O$ values exhibited by progressively younger zircon.

Despite their generally evolved isotopic character, the Mesoproterozoic Esperance and Recherche granitoids within the Albany–Fraser Orogen are interpreted to have involved juvenile input to account for isotopic signatures that are too juvenile to be produced by the reworking of a Biranup–Yilgarn crustal source alone (Kirkland et al., 2015a; Smithies et al., 2015). Sheraton et al. (1992) note significant compositional variation of Mesoproterozoic intrusives from the Bunger Hills, and particularly the heterogeneity of rocks from the Booth Peninsula which include a significant proportion of gabbro (see also Fig. 2). Therefore, we cannot exclude the possibility that Mesoproterozoic magmatism in the Bunger Hills also incorporated a juvenile component which may have, in part, diluted the Hf signature of any reworked Archean crustal and/or Proterozoic component towards less evolved isotopic values. Yet the most radiogenic data still remain within the confines of the Paleoproterozoic crustal growth curve, suggesting that any additional juvenile input into the magma in which these zircon grains grew was likely minimal. The isotopic signature of these rocks is overall more evolved than similarly-aged granitoids from the Windmill Islands, Albany–Fraser Orogen and Musgrave Inlier (Fig. 9), which further suggests a reduced juvenile and/or increased crustal component relative to these regions.

6.3 Mesoproterozoic metamorphism

Granulite facies metamorphism in the Highjump Archipelago is reported by Sheraton et al., (1993) and Tucker and Hand (2016) to have occurred at 1190 ± 15 Ma and 1183 ± 8 Ma, respectively. The timing of metamorphism in the Bunger Hills, as constrained by this study, appears more complex. U–Pb data from dark to weakly luminescent, unzoned grains—grains interpreted to be of metamorphic origin, and unzoned zircon rims on oscillatory-zoned cores, that yield $^{207}Pb/^{206}Pb$ ages <1500 Ma, define a broad spread of ages extending from ca. 1460 Ma to ca. 1190 Ma (Fig. 10). The broad age range observed for the metamorphic age data within each sample, and overall, likely reflects a complex range of metamorphic processes (e.g. presence or absence of melt, recrystallization, temperature) and bulk rock composition controls facilitating zircon growth. The spread in ages may also reflect: (1) zircon growth over a single and protracted, although unlikely, period spanning >200 Myr; (2) zircon growth during multiple, discrete pulses of metamorphism occurring between ca. 1460–1190 Ma; (3) zircon growth and subsequent partial isotopic disturbance and resetting of the zircon age population(s); (4) or possible recycling of metamorphic zircon from their original protolith. The dataset is asymmetrically skewed towards late Mesoproterozoic ages, with majority of data occurring over the interval ca. 1300–1270 Ma and at ca. 1250 Ma, with less distinct age peaks at ca. 1330 Ma and ca. 1200 Ma (Fig. 10). The ca. 1330 Ma and ca. 1300–1270 Ma age peaks fit well with the approximate timing of Stage-1 of the Albany–Fraser Orogeny (Clark et al., 2014, 2000; Spaggiari et al., 2014). The ca. 1200 Ma and ca. 1250 Ma peaks observed in the histogram of pooled age data also coincide with the timing of two episodes of Mesoproterozoic magmatism in the Bunger Hills as determined by this study. The ca. 1200 Ma ages also correlate with Stage-2 of the Albany–Fraser Orogeny; the ca. 1250 Ma metamorphic age does not coincide with either of the currently recognised phases of the Albany–Fraser Orogeny and could potentially be recording minor effects of Pb-loss on Stage-1 overgrowths. However, since this metamorphic age correlates strongly with a period of magmatism in the Bunger Hills it is more likely recording either the delayed metamorphic response of Stage-1, the early onset of Stage-2, or a third and previously unrecognised event between Stages 1 and 2.

6.4 A regional Paleo–Mesoproterozoic tectonic model for the Bunger Hills

Changes in the isotopic composition of igneous rocks over time can be used as a geochemical tracer for the tectono-magmatic evolution of developing orogens (e.g. Kemp et al., 2009; Payne et al., 2016; Smits et al., 2014). Recent isotopic and geochemical work has shown that the Albany–Fraser Orogen in southwestern Australia is the result of largely authochonous modification of the Archean Yilgarn Craton margin with the periodic addition of juvenile material during the Paleoproterozoic–Mesoproterozoic (Kirkland et al., 2011, 2015b; Spaggiari et al., 2015; Spaggiari and Tyler, 2014). The Hf isotope–time profile from the Bunger Hills is likewise suggestive of partial recycling of an Archean basement source diluted by significant generation of new crust at ca. 1700 Ma that was in turn, reworked during the Mesoproterozoic (ca. 1330–1150 Ma) with potentially further mantle and Archean crustal input at this time. Given the parallels between the age and isotopic composition of rocks in the Bunger Hills with those from the Albany–Fraser Orogen and the pre-Gondwanan breakup spatial proximity, it seems likely that the Paleo–Mesoproterozoic tectonic evolution of these two regions is analogous. This crustal evolution history contrasts strongly with that of the Musgrave Inlier in central Australia which exhibits a significantly more juvenile isotopic trajectory, and is believed to have been strongly influenced by reworking of a Madura Province crustal source, potentially derived from a ca. 1900 Ma juvenile component, and juvenile magmatism at ca. 1600–1550 Ma (Kirkland et al., 2015a, 2013b).

Previous models for the Paleoproterozoic tectonic evolution of the Albany–Fraser Orogen favour west-dipping subduction of the SAC–East Antarctic Craton (EAC) beneath the WAC along the southeast Yilgarn Craton margin (e.g. Fig. 11; Kirkland et al., 2011). Within this overall convergent setting, extension is used to account for a period of prolonged juvenile magmatism and coeval basin formation recorded by the Biranup Zone between ca. 1815–1600 Ma (Kirkland et al., 2011; Spaggiari et al., 2015). On the basis of subduction-like geochemistry and increasingly juvenile isotopic signature over time, Kirkland et al. (2011) specifically propose backarc extension linked to the retreat of an active subduction margin by ca. 1710 Ma. In contrast, Spaggiari et al. (2015) suggest continental rifting, or alternatively, that the active subduction margin was not proximal to the Albany–Fraser Orogen at this time due to maturity of the basin sediments and a lack of exotic detritus, and further geochemical analysis of intrusive rocks that show a lack of subduction-like features (Smithies et al., 2015). The subduction margin is proposed to have been as far outboard of the Albany–Fraser Orogen as the Madura Province or Coompana Province (Smithies et al., 2015; Spaggiari et al., 2015). The ca. 1700 Ma rocks of the Bunger Hills are likewise ascribed to (para)autochthonous and extensional processes occurring proximal to the Archean Bunger Hills and/or Yilgarn Craton margin (Fig. 11a). Due to a paucity of geochemical data on the samples analysed in this study, discrimination of the specific tectonic environment, and specifically, the position of the subduction margin relative to the Bunger Hills is not possible. However, interestingly, Sheraton et al. (1995) infer that protoliths to a sample of tonalite and granodiorite emplaced at 1699 ± 15 Ma and 1521 ± 29 Ma, respectively, were derived by the melting of subducted, hydrated oceanic crust (i.e. a feldspar-poor, mafic source) owing to their high Sr content and the absence of a Sr anomaly. Negative Nb anomalies in plutonic rocks from the Algae Lake Pluton, Paz Cove Batholith and Booth Peninsula Batholith are likewise ascribed to the partial melting of subducted oceanic crust (Sheraton et al., 1992, 1995)

Similarly to the Biranup and Nornalup zones, extension was likely accompanied by the rapid uplift of syn-magmatic rocks, isolating the Bunger Hills and Obruchev Hills as Archean basement highs, and providing the bulk of detritus to the evolving rift or extensional basin with volcanoclastic sedimentation (Fig. 11a). The Paleoproterozoic addition of juvenile material was sufficient that it diluted, but did not entirely mask, the isotopic signal of the incorporated Archean crustal component into the melts generated during extension (Fig. 9).

Provenance studies from the Albany–Fraser Orogen suggest that a period of relative tectonic quiescence occurred from ca. 1600 Ma until at least ca. 1455 Ma with transition to a passive margin and the formation of the marginal Arid Basin (Fig. 11b; Spaggiari et al., 2015). Deposition of protoliths to the extensive metapelitic unit within in the Bunger Hills is likewise interpreted

to have occurred post ca. 1700 Ma magmatism but prior to Stage-1 tectonism in the Albany–Fraser Orogen. Sediment was derived locally from ca. 1815–1600 Ma magmatic rocks of the Biranup Zone or Nornalup Zone and/or Bunger Hills, Yilgarn crustal sources, and potentially sources further afield such as the western Gawler Craton and Capricorn Orogen. The minimal Archean age component in the Bunger Hills metasedimentary rocks (e.g. Fig. 6d) suggests insignificant input from the adjacent WAC during basin formation, in turn, suggesting that deposition potentially occurred either some distance from the craton margin, and/or that the topography of the Yilgarn Craton and any rifted remnants of Archean crust was relatively subdued at this time. Deposition within the Bunger Hills region continued until at least ca. 1490 Ma.

Smits et al. (2014) utilize an inverted U-shaped array of zircon Hf-isotopic compositions versus age with increasingly evolved signature over time to suggest that the Musgrave Inlier and Albany–Fraser Orogen underwent a period of backarc closure and progressive crustal thickening during the Mesoproterozoic (ca. 1500–1200 Ma). Continental collision between the combined WAC–NAC and SAC–EAC culminated by ca. 1300 during Stage-1 of the Albany–Fraser Orogeny, followed by intracratonic reactivation at ca. 1200 Ma (Clark et al., 2014, 2000). In contrast to this simple continental collision model, Spaggiari et al. (2015) propose that Stage-1 involved accretion of the exotic Loongana oceanic arc, renewed backarc extension during subduction roll-back, and that the suture zone with the SAC–EAC actually occurred much further to the east within the Madura and/or Coompana provinces. The Loongana oceanic arc is not incorporated into the tectonic model presented in Fig. 11c, but the suture with the SAC–EAC is considered to occur south of the Bunger Hills region. Crystallisation of Mesoproterozoic magmatic protoliths within the Bunger Hills occurred at ca. 1260 Ma and between ca. 1200 Ma (this study) to ca. 1150 Ma (Sheraton et al., 1992), the latter consistent with timing of emplacement of the Esperance Supersuite (ca. 1198–1135 Ma). These igneous rocks display an evolved isotopic signature signifying greater crustal component within melts produced post lithospheric thickening.

7. CONCLUSIONS

This study presents the first comprehensive integrated zircon U–Pb geochronology and Hf and oxygen isotope analysis of rocks of the Bunger Hills. Isotopic results indicate that the Bunger Hills records the progressive recycling of Archean basement (ca. 2800–2700 Ma) of Yilgarn Craton affinity with the generation of voluminous, juvenile magmatism at ca. 1700 Ma. This new crust was in turn reworked during the Mesoproterozoic (ca. 1300–1150 Ma) with the addition of further mantle and Archean crustal components at this time. Strong parallels can be drawn between the isotope–time profile of the Bunger Hills with that from the Albany–Fraser Orogen. In relation to the Albany–Fraser Orogen, the Bunger Hills are considered to represent a remnant fragment of Archean Yilgarn basement that was extended and reworked between ca. 1815–1600 Ma. Similarly to the Biranup Zone, emplacement of the ca. 1700 Ma juvenile magmatic rocks in the Bunger Hills was most likely also associated with extensional processes, which was followed by transition to a passive marginal ocean basin at ca. 1490 Ma. Crystallisation of crustally-derived Mesoproterozoic magmatic protoliths occurred at ca. 1260 Ma and ca. 1200 Ma, the latter synchronous with Stage-2 of the Albany–Fraser Orogeny, and was accompanied by high-grade metamorphism. This evidence confirms earlier hypotheses that these two regions shared a similar tectonic evolution, recording largely (para) autochthonous reworking of the southern Yilgarn Craton margin during the Proterozoic.

ACKNOWLEDGEMENTS

Logistical and financial support for field work in Antarctica was provided by the Australian Antarctic Division. We also gratefully acknowledge the logistical support of fellow expeditioners at Casey Station, and the crew of Kenn Borek Air, during the 2014–2015 summer season. In particular, Kimerly (Billy) Wallace is thanked for her invaluable assistance in the field. Chris Kirkland is thanked for his comments on an earlier version of the dataset. Analytical work was funded by an Australian Research Council DECRA fellowship (DE120103067). We thank reviewers Catherine Spaggiari, Jacqueline Halpin and John Goodge for their constructive comments and suggestions on earlier versions of this manuscript. NMT acknowledges the support of an Australian Government Research Training Program Scholarship (formerly Australian Postgraduate Award) and Playford Trust PhD Scholarship. This work forms part of Australian Antarctic Science Project 4191.

REFERENCES

Aitken A. R. A., Young D. A., Ferraccioli F., Betts P. G., Greenbaum J. S., Richter T. G., Roberts J. L., Blankenship

D. D. & Siegert M. J. 2014. The subglacial geology of Wilkes Land, East Antarctica. *Geophysical Research Letters* 41, 2390–2400.

Archibald D. B., Collins A. S., Foden J. D., Payne J. L., Holden P., Razakamanana T., De Waele B., Thomas R. J. & Pitfield P. E. J. 2016. Genesis of the Tonian Imorona–Itsindro magmatic suite in central Madagascar: insights from U–Pb, oxygen and hafnium isotopes in zircon. *Precambrian Research* 281, 312–337.

Belousova E. A., Griffin W. L. & O'reilly S. Y. 2006. Zircon crystal morphology, trace element signatures and Hf isotope composition as a tool for petrogenetic modelling: examples from eastern Australian granitoids. *Journal of Petrology* 47, 329–353.

Belousova E. A., Kostitsyn Y. A., Griffin W. L., Begg G. C., O'reilly S. Y. & Pearson N. J. 2010. The growth of the continental crust: constraints from zircon Hf-isotope data. *Lithos* 119, 457–466.

Betts P. G. & Giles D. 2006. The 1800–1100 Ma tectonic evolution of Australia. *Precambrian Research* 144, 92–125.

Black L. P. & Gulson B. L. 1978. The age of the Mud Tank carbonatite, Strangways Range, Northern Territory. *BMR Journal of Australian Geology and Geophysics* 3, 227–232.

Black L. P., Kamo S. L., Allen C. M., Davis D. W., Aleinikoff J. N., Valley J. W., Mundil R., Campbell I. H., Korsch R. J., Williams I. S. & Foudoulis C. 2004. Improved $^{206}Pb/^{238}U$ microprobe geochronology by the monitoring of a trace-element-related matrix effect; SHRIMP, ID–TIMS, ELA–ICP–MS and oxygen isotope documentation for a series of zircon standards. *Chemical Geology* 205, 115–140.

Blight D. & Oliver R. 1977. The metamorphic geology of the Windmill Islands, Antarctica: a preliminary account. *Journal of the Geological Society of Australia* 24, 239–262.

Bodorkos S. & Clark D. J. 2004. Evolution of a crustal-scale transpressive shear zone in the Albany–Fraser Orogen, SW Australia: 2. Tectonic history of the Coramup Gneiss and a kinematic framework for Mesoproterozoic collision of the West Australian and Mawson cratons. *Journal of Metamorphic Geology* 22, 713–731.

Boger S. D. 2011. Antarctica—before and after Gondwana. *Gondwana Research* 19, 335–371.

Booth A. L., Kolodny Y., Chamberlain C. P., Mcwilliams M., Schmitt A. K. & Wooden J. 2005. Oxygen isotopic composition and U-Pb discordance in zircon. *Geochimica et Cosmochimica Acta* 69, 4895–4905.

Bouvier A., Vervoort J. D. & Patchett P. J. 2008. The Lu–Hf and Sm–Nd isotopic composition of CHUR: constraints from unequilibrated chondrites and implications for the bulk composition of terrestrial planets. *Earth and Planetary Science Letters* 273, 48–57.

Cassidy K. F., Champion D. C., Krapez B., Barley M. E., Brown S. J. A., Blewett R. S., Groenwald P. B. & Tyler I. M. 2006. A revised geological framework for the Yilgarn Craton, Western Australia. Geological Survey of Western Australia, Record 2006/8, 8p.

Cawood P. A. & Korsch R. J. 2008. Assembling Australia: Proterozoic building of a continent. *Precambrian Research* 166, 1–35.

Clark C., Kirkland C. L., Spaggiari C. V., Oorschot C., Wingate M. T. D. & Taylor R. J. 2014. Proterozoic granulite formation driven by mafic magmatism: An example from the Fraser Range Metamorphics, Western Australia. *Precambrian Research* 240, 1–21.

Clark D. J., Hensen B. J. & Kinny P. D. 2000. Geochronological constraints for a two-stage history of the Albany–Fraser Orogen, Western Australia. *Precambrian Research* 102, 155–183.

Cochrane R., Spikings R., Gerdes A., Winkler W., Ulianov A., Mora A. & Chiaradia M. 2014. Distinguishing between in-situ and accretionary growth of continents along active margins. *Lithos* 202, 382–394.

Condie K. C., Belousova E., Griffin W. L. & Sircombe K. N. 2009. Granitoid events in space and time: Constraints from igneous and detrital zircon age spectra. *Gondwana Research* 15, 228–242.

Ding P. & James P. 1991. Structural evolution of the Bunger Hills area of East Antarctica. Geological Evolution of Antarctica. Cambridge University Press, Cambridge, pp. 13–18.

Dutch R. A., Pawley M. J. & Wise T. W. 2015. What lies beneath the western Gawler Craton? 13GA-EG1E Seismic and Magnetotelluric Workshop 2015, Report Book 2015/00029. Department of State Development, South Australia, Adelaide.

Fitzsimons I. 2003. Proterozoic basement provinces of southern and southwestern Australia, and their correlation with Antarctica. *Journal of the Geological Society, London* 206, 93–130.

Fitzsimons I. C. W. 2000. Grenville-age basement provinces in East Antarctica: evidence for three separate collisional orogens. *Geology* 28, 879–882.

Gardner R. L., Dazko N. R., Halpin J. A. & Whittaker J. M. 2015. Discovery of a microcontinent (Gulden Draak Knoll) offshore Western Australia: implications for East Gondwana reconstructions. *Gondwana Research* 28, 1019–1031.

Gibbons A. D., Barckhausen U., Den Boggard P., Hoernle K., Werner R., Whittaker J. M. & Muller R. D. 2012. Constraining the Jurassic extent of Greater India: tectonic evolution of the West Australian margin. *Geochemistry, Geophysics, Geosystems* 13, 1–25.

Giles D., Betts P. G. & Lister G. S. 2004. 1.8–1.5 Ga links between the North and South Australian cratons and the early–middle Proterozoic configuration of Australia. *Tectonophysics* 380, 27–41.

Griffin W. L., Belousova E., Shee S. R., Pearson N. J. & O'reilly S. Y. 2004. Archean crustal evolution in the northern Yilgarn Craton: U-Pb and Hf-isotope evidence from detrital zircons. *Precambrian Research* 131, 231–282.

Griffin W. L., Wang X., Jackson S. E., Pearson N. J., O'reilly S. Y., Xu X. & Zhou X. 2002. Zircon chemistry and magma mixing, SE China: in-situ analysis of Hf isotopes, Tonglu and Pingtan igneous complexes. *Lithos* 61, 237–269.

Guitreau M. & Blichert-Toft J. 2014. Implications of discordant U-Pb ages on Hf isotope studies of detrital zircons. *Chemical Geology* 385, 17–25.

Halpin J. A., Crawford A. J., Direen N. G., Coffin M. F., Forbed C. J. & Borissova I. 2008. Naturaliste Plateau, offshore Western Australia: a submarine window into Gondwana assembly and breakup. *Geology* 36, 807–810.

Halpin J. A., Daczko N. R., Clarke G. L. & Murray K. R. 2013. Basin analysis in polymetamorphic terranes: an example from east Antarctica. *Precambrian Research* 231, 78–97.

Halpin J. A., Daczko N. R., Milan L. A. & Clarke G. L. 2012. Decoding near-concordant U–Pb zircon ages spanning several hundred million years: recrystallisation, metamictisation or diffusion? *Contributions to Mineralogy*

and Petrology 163, 67–85.

Hand M., Reid A. & Jagodzinski L. 2007. Tectonic Framework and Evolution of the Gawler Craton, Southern Australia. *Economic Geology* 102, 1377–1395.

Hawkesworth C. & Kemp A. 2006a. Evolution of the continental crust. *Nature* 443, 811–817.

Hawkesworth C. & Kemp A. 2006b. Using hafnium and oxygen isotopes in zircons to unravel the record of crustal evolution. *Chemical Geology* 226, 144–162.

Hollis J. A., Carson C. J., Glass L. M., Kositcin N., Scherstén A., Worden K. E., Armstrong R. A., Yaxley G. M. & Kemp A. I. S. 2014. Detrital zircon U–Pb–Hf and O isotope character of the Cahill Formation and Nourlangie Schist, Pine Creek Orogen: implications for the tectonic correlation and evolution of the North Australian Craton. *Precambrian Research* 246, 35–53.

Howard H. M., Smithies R. H., Kirkland C. L., Kelsey D. E., Aitken A., Wingate M. T. D., Quentin De Gromard R., Spaggiari C. V. & Maier W. D. 2015. The burning heart — The Proterozoic geology and geological evolution of the west Musgrave Region, central Australia. *Gondwana Research* 27, 64–94.

Howard K. E., Hand M., Barovich K. M., Payne J. L., Cutts K. A. & Belousova E. A. 2011. U–Pb zircon, zircon Hf and whole-rock Sm–Nd isotopic constraints on the evolution of Paleoproterozoic rocks in the northern Gawler Craton. *Australian Journal of Earth Sciences* 58, 615–638.

Ivanic T. J., Van Kranendonk M. J., Kirkland C. L., Wyche S., Wingate M. T. D. & Belousova E. A. 2012. Zircon Lu–Hf isotopes and granite geochemistry of the Murchison Domain of the Yilgarn Craton: Evidence for reworking of Eoarchean crust during Meso-Neoarchean plume-driven magmatism. *Lithos* 148, 112–127.

Jackson S. E., Pearson N. J., Griffin W. L. & Belousova E. A. 2004. The application of laser ablation-inductively coupled plasma-mass spectrometry to in situ U–Pb zircon geochronology. *Chemical Geology* 211, 47–69.

Jagodzinski E. A., Reid A. J. & Dutch R. 2013. Zircon and monazite geochronology via SHRIMP and LA-ICPMS for the northern Gawler Craton, from 2009 GOMA Drilling, Report Book, 2013/00013. Department for Manufacturing, Innovation, Trade, Resources and Energy, South Australia, Adelaide.

Johnson S. P., Sheppard S., Wingate M. T. D., Kirkland C. L. & Belousova E. A. 2011. Temporal and hafnium isotopic evolution of the Glenburgh Terrane basement: an exotic crustal fragment in the Capricorn Orogen: Geological Survey of Western Australia, Report 110, 27p.

Kemp A., Hawkesworth C., Collins W., Gray C. & Blevin P. 2009. Isotopic evidence for rapid continental growth in an extensional accretionary orogen: the Tasmanides, eastern Australia. *Earth and Planetary Science Letters* 284, 455–466.

Kemp A., Hawkesworth C., Paterson B. & Kinny P. 2006. Episodic growth of the Gondwana supercontinent from hafnium and oxygen isotopes in zircon. *Nature* 439, 580–583.

Kirkland C. L., Johnson S. P., Smithies R. H., Hollis J. A., Wingate M. T. D., Tyler I. M., Hickman A. H., Cliff J. B., Tessalina S., Belousova E. A. & Murphy R. C. 2013a. Not-so-suspect terrane: constraints on the crustal evolution of the Rudall Province. *Precambrian Research* 235, 131–149.

Kirkland C. L., Smithies R. H. & Spaggiari C. V. 2015a. Foreign contemporaries – Unravelling disparate isotopic signatures from Mesoproterozoic Central and Western Australia. *Precambrian Research* 265, 218–231.

Kirkland C. L., Smithies R. H., Woodhouse A. J., Howard H. M., Wingate M. T. D., Belousova E. A., Cliff J. B., Murphy R. C. & Spaggiari C. V. 2013b. Constraints and deception in the isotopic record: the crustal evolution of the west Musgrave Province, central Australia. *Gondwana Research* 23, 759–781.

Kirkland C. L., Spaggiari C. V., Pawley M. J., Wingate M. T. D., Smithies R. H., Howard H. M., Tyler I. M., Belousova E. A. & Poujol M. 2011. On the edge: U–Pb, Lu–Hf, and Sm–Nd data suggests reworking of the Yilgarn craton margin during formation of the Albany-Fraser Orogen. *Precambrian Research* 187, 223–247.

Kirkland C. L., Spaggiari C. V., Smithies R. H. & Wingate M. T. D. 2014. Cryptic progeny of craton margins: geochronology and isotope geology of the Albany-Fraser Orogen, with implications for evolution of the Tropicana Zone. *In: Spaggiari C. V. & Tyler I. M. eds. Albany-Fraser Orogen seismic and magnetotelluric (MT) workshop 2014: extended abstracts* pp. 81–92. Geological Survey of Western Australia, Record 2014/6.

Kirkland C. L., Spaggiari C. V., Smithies R. H., Wingate M. T. D., Belousova E. A., Gréau Y., Sweetapple M. T., Watkins R., Tessalina S. & Creaser R. 2015b. The affinity of Archean crust on the Yilgarn—Albany–Fraser Orogen boundary: implications for gold mineralisation in the Tropicana Zone. *Precambrian Research* 266, 260–281.

Kita N. T., Ushikubo T., Fu B. & Valley J. W. 2009. High precision SIMS oxygen isotope analysis and the effect of sample topography. *Chemical Geology* 264, 43–57.

Kylander-Clark A. R., Hacker B. R. & Cottle J. M. 2013. Laser-ablation split-stream ICP petrochronology. *Chemical Geology* 345, 99–112.

Li X. H., Long W. G., Li Q. L., Liu Y., Zheng Y. F., Yang Y. H., Chamberlain K. R., Wan D. F., Guo C. H., Wang X. C. & Tao H. 2010. Penglai zircon megacrysts: a potential new working reference material for microbeam determination of Hf–O isotopes and U–Pb age. *Geostandards and Geoanalytical Research* 34, 117-134.

Ludwig K. R. 2012. User's manual for ISOPLOT 3.75, a geochronological toolkit for Microsoft Excel. Berkeley Geochronology Centre Special Publication 5.

Maritati A., Aitken A. R. A., Young D. A., Roberts J. L., Blankenship D. D. & Siegert M. J. 2016. The tectonic development and erosion of the Knox Subglacial Sedimentary Basin, East Antarctica. *Geophysical Research Letters* 43, 2016GL071063.

Mole D. R., Fiorentini M. L., Thebaud N., Mccuaig T. C., Cassidy K. F., Kirkland C. L., Wingate M. T. D., Romano S. S., Doublier M. P. & Belousova E. A. 2012. Spatio-temporal constraints on lithospheric development in the southwest–central Yilgarn Craton, Western Australia. *Australian Journal of Earth Sciences* 59, 625–656.

Morel M., Nebel O., Nebel-Jacobsen Y., Miller J. & Vroon P. 2008. Hafnium isotope characterization of the GJ-1 zircon reference material by solution and laser-ablation MC-ICPMS. *Chemical Geology* 255, 231–235.

Morrissey L. J., Payne J. L., Hand M., Clark C., Taylor R., Kirkland C. L. & Kylander-Clark A. 2017. Linking the Windmill Islands, east Antarctica and the Albany–Fraser Orogen: Insights from U–Pb zircon geochronology and Hf isotopes. *Precambrian Research* 293, 131–149.

Nelson D. R., Myers J. S. & Nutman A. P. 1995. Chronology and evolution of the Middle Proterozoic Albany-Fraser Orogen, Western Australia. *Australian Journal of Earth Sciences* 42, 481–495.

Occhipinti S. A., Sheppard S., Passchier C., Tyler I. M. & Nelson D. R. 2004. Palaeoproterozoic crustal accretion and collision in the southern Capricorn Orogen: the Glenburgh Orogeny. *Precambrian Research* 128, 237–255.

Paton C., Hellstrom J., Paul B., Woodhead J. & Hergt J. 2011. Iolite: Freeware for the visualisation and processing of mass spectrometric data. *Journal of Analytical Atomic Spectrometry* 26, 2508–2518.

Payne J. L., Hand M., Barovich K. M., Reid A. & Evans D. a. D. 2009. Correlations and reconstruction models for the 2500-1500 Ma evolution of the Mawson Continent. *In: Reddy S. M., Evans D. a. S. & Collins A. S. eds. Palaeoproterozoic Supercontinents and Global Evolution* pp. 319–355, Geological Society of London.

Payne J. L., Hand M., Barovich K. M. & Wade B. P. 2008. Temporal constraints on the timing of high-grade metamorphism in the northern Gawler Craton: implications for assembly of the Australian Proterozoic. *Australian Journal of Earth Sciences* 55, 623–640.

Payne J. L., Mcinerney D. J., Barovich K. M., Kirkland C. L., Pearson N. J. & Hand M. 2016. Strengths and limitations of zircon Lu-Hf and O isotopes in modelling crustal growth. *Lithos* 248, 175-192.

Reid A. J., Jagodzinski E. A., Armit R. J., Dutch R. A., Kirkland C. L., Betts P. G. & Schaefer B. F. 2014. U-Pb and Hf isotopic evidence for Neoarchean and Paleoproterozoic basement in the buried northern Gawler Craton, South Australia. *Precambrian Research* 250, 127–142.

Scherer E., Münker C. & Mezger K. 2001. Calibration of the Lutetium-Hafnium Clock. *Science* 293, 683–687.

Segal I., Halicz L. & Platzner I. T. 2003. Accurate isotope ratio measurements of ytterbium by multiple collection inductively coupled plasma mass spectrometry applying erbium and hafnium in an improved double external normalization procedure. *Journal of Analytical Atomic Spectrometry* 18, 1217–1223.

Sheppard S., Occhipinti S. A. & Tyler I. M. 2004. A 2005–1970 Ma Andean-type batholith in the southern Gascoyne Complex, Western Australia. *Precambrian Research* 128, 257–277.

Sheraton J. W., Black L. P., Mcculloch M. T. & Oliver R. L. 1990. Age and origin of a compositionally varied mafic dyke swarm in the Bunger Hills, East Antarctica. *Chemical Geology* 85, 215–246.

Sheraton J. W., Black L. P. & Tindle A. G. 1992. Petrogenesis of plutonic rocks in a Proterozoic granulite-facies terrane — the Bunger Hills, East Antarctica. *Chemical Geology* 97, 163–198.

Sheraton J. W., Tingey R., Oliver R. & Black L. 1995. Geology of the Bunger Hills–Denman Glacier region, East Antarctica. *AGSO Bulletin*, No. 244, 1–136.

Sheraton J. W., Tingey R. J., Black L. P. & Oliver R. L. 1993. Geology of the Bunger Hills area, Antarctica: implications for Gondwana correlations. *Antarctic Science* 5, 85–102.

Slama J., Kosler J., Condon D. J., Crowley J. L., Gerdes A., Hanchar J. M., Horstwood M. S. A., Morris G. A., Nasdala L., Norberg N., Schaltegger U., Schoene N., Tubrett M. N. & Whitehouse M. J. 2008. Plesovice zircon - a new natural reference material for U–Pb and Hf isotopic microanalysis. *Chemical Geology* 249, 1–35.

Smithies H. R., Spaggiari C. V., Kirkland C. L., Howard H. & Maier W. D. 2013. Petrogenesis of gabbros of the Mesoproterozoic Fraser Zone: constraints on the tectonic evolution of the Albany-Fraser Orogen. Geological Survey of Western Australia, Record 2013/5, 29p.

Smithies R. H., Howard H. M., Evins P. M., Kirkland C. L., Kelsey D. E., Hand M., Wingate M. T. D., Collins A. S. & Belousova E. 2011. High-temperature granite magmatism, crust-mantle interaction and the mesoproterozoic intracontinental evolution of the Musgrave Province, central Australia. *Journal of Petrology* 52, 931–958.

Smithies R. H., Spaggiari C. V. & Kirkland C. L. 2015. Building the crust of the Albany-Fraser Orogen: constraints from granite geochemistry. Geological Survey of Western Australia, Report 150, 49p.

Smits R. G., Collins W. J., Hand M., Dutch R. & Payne J. 2014. A Proterozoic Wilson cycle identified by Hf isotopes in central Australia; implications for the assembly of Proterozoic Australia and Rodinia. *Geology* 42, 231–234.

Spaggiari C. V., Bodorkos S., Barquero-Molino M., Tyler I. M. & Wingate M. T. D. 2009. Interpreted bedrock geology of the South Yilgarn and central Albany-Fraser Orogen, Western Australia: Geological Survey of Western Australia, Record 2009/10, 84p.

Spaggiari C. V., Kirkland C. L., Smithies R. H., Occhipinti S. A. & Wingate M. T. D. 2014. Geological framework of the Albany-Fraser Orogen. *In: Spaggiari C. V. & Tyler I. M. 2014. Albany-Fraser Orogen seismic and magnetotelluric (MT) workshop 2014: extended abstracts* pp. 44–59. Geological Survey of Western Australia, Record 2014/6.

Spaggiari C. V., Kirkland C. L., Smithies R. H., Wingate M. T. D. & Belousova E. A. 2015. Transformation of an Archean craton margin during Proterozoic basin formation and magmatism: The Albany–Fraser Orogen, Western Australia. *Precambrian Research* 266, 440–466.

Spaggiari C. V. & Smithies R. H. 2015. Eucla basement stratigraphic drilling results release workshop: extended abstracts: Geological Survey of Western Australia, Record 2015/10, 70p.

Spaggiari C. V. & Tyler I. M. 2014. Albany-Fraser Orogen seismic and magnetotelluric (MT) workshop 2014: extended abstracts: Geological Survey of Western Australia, Record 2014/6. 165p.

Spencer C. J., Kirkland C. L. & Taylor R. J. M. 2015. Strategies towards statistically robust interpretations of in situ U–Pb zircon geochronology. *Geoscience Frontiers* http://dx.doi.org/10.1016/j.gsf.2015.11.006.

Stüwe K. & Powell R. 1989. Metamorphic evolution of the Bunger Hills, East Antarctica: evidence for substantial post-metamorphic peak compression with minimal cooling in a Proterozoic orogenic event. *Journal of Metamorphic Geology* 7, 449–464.

Stüwe K. & Wilson C. J. L. 1990. Interaction between deformation and charnockite emplacement in the Bunger Hills, East Antarctica. *Journal of Structural Geology* 12, 767–783.

Swain G., Woodhouse A., Hand M., Barovich K., Schwarz M. & Fanning C. M. 2005. Provenance and tectonic development of the late Archaean Gawler Craton, Australia; U–Pb zircon, geochemical and Sm–Nd isotopic implications. *Precambrian Research* 141, 106–136.

Taylor R. J. M., Clark C., Johnson T. E., Santosh M. & Collins A. S. 2015. Unravelling the complexities in high-grade rocks using multiple techniques: the Achankovil Zone of southern India. *Contributions to Mineralogy and Petrology* 169, 51.

Tucker N. M. & Hand M. 2016. New constraints on metamorphism in the Highjump Archipelago, East Antarctica. *Antarctic Science* 28, 487–503.

Tucker N. M., Hand M., Kelsey D. E. & Dutch R. A. 2015. A duality of timescales: Short-lived ultrahigh temperature metamorphism preserving a long-lived monazite growth

history in the Grenvillian Musgrave–Albany–Fraser Orogen. *Precambrian Research* 264, 204–234.

Valley J. W. 2003. Oxygen Isotopes in Zircon. *Reviews in Mineralogy and Geochemistry* 53, 343–385.

Vervoort J. D., Patchett P. J., Söderlund U. & Baker M. 2004. Isotopic composition of Yb and the determination of Lu concentrations and Lu/Hf ratios by isotope dilution using MC-ICPMS. *Geochemistry, Geophysics, Geosystems* 5, Q11002, doi: 10.1029/2004GC000721.

Walsh A. K., Kelsey D. E., Kirkland C. L., Hand M., Smithies R. H., Clark C. & Howard H. M. 2015. *P–T*–t evolution of a large, long-lived, ultrahigh-temperature Grenvillian belt in central Australia. *Gondwana Research* 28, 531–564.

Wiedenbeck M., Alle P., Corfu F., Griffin W., Meier M., Oberli F., Quadt A. V., Roddick J. & Spiegel W. 1995. Three natural zircon standards for U-Th-Pb, Lu-Hf, trace element and REE analyses. *Geostandards Newsletter* 19, 1–23.

Wong B. L., Morrissey L. J., Hand M., Fields C. E. & Kelsey D. E. 2015. Grenvillian-aged reworking of late Paleoproterozoic crust of the southern North Australian Craton, central Australia: Implications for the assembly of Mesoproterozoic Australia. *Precambrian Research* 270, 100–123.

Woodhead J., Hergt J., Shelley M., Eggins S. & Kemp R. 2004. Zircon Hf-isotope analysis with an excimer laser, depth profiling, ablation of complex geometries, and concomitant age estimation. *Chemical Geology* 209, 121–135.

Woodhead J. D. & Hergt J. M. 2005. A preliminary appraisal of seven natural zircon reference materials for in-situ Hf-isotope determination. *Geostandards and Geoanalytical Research* 29, 183–195.

Wyche S., Kirkland C. L., Riganti A., Pawley M. J., Belousova E. & Wingate M. T. D. 2012. Isotopic constraints on stratigraphy in the central and eastern Yilgarn Craton, Western Australia. *Australian Journal of Earth Sciences* 59, 657–670.

Zhang S., Zhao Y., Liu X., Liu Y., Hou K., Li C. & Ye H. 2012. U–Pb geochronology and geochemistry of the bedrocks and moraine sediments from the Windmill Islands: implications for Proterozoic evolution of East Antarctica. *Precambrian Research* 206–207, 52-71.

Appendix A. U–Pb zircon geochronology

Analysis	Location	^{238}U (ppm)	^{232}Th (ppm)	^{232}Th/^{238}U	204/206	^{207}Pb/^{235}U	2σ	^{206}Pb/^{238}U	2σ	^{207}Pb/^{206}Pb	2σ	Rho	Age (Ma)						
													^{207}Pb/^{235}U	2σ	^{206}Pb/^{238}U	2σ	^{207}Pb/^{206}Pb	2σ	Conc. (%)
Sample BH12																			
BH12-1	c	320	159.3	0.52	9.97E-04	4.13000	0.08000	0.29070	0.00570	0.10299	0.00063	0.95081	1659	16	1645	29	1678	11	98
BH12-2	c	70.3	65.41	0.95	4.20E-03	4.35400	0.08800	0.30620	0.00630	0.10316	0.00071	0.94320	1702	17	1721	31	1681	13	102
BH12-3	c	60.5	49.71	0.85	5.02E-03	4.34900	0.08500	0.30730	0.00580	0.10266	0.00081	0.91623	1701	16	1727	28	1672	14	103
BH12-5	c	282.1	226.7	0.82	1.08E-03	4.36300	0.09100	0.30270	0.00630	0.10458	0.00047	0.97674	1704	17	1704	31	1707	8	100
BH12-6	c	166.2	151.6	0.94	1.87E-03	4.19400	0.08300	0.29630	0.00630	0.10271	0.00043	0.98175	1672	16	1672	31	1674	8	100
BH12-8	c	1352	769	0.59	2.98E-04	3.86000	0.08900	0.26700	0.00600	0.10461	0.00067	0.96075	1604	19	1525	31	1707	12	89
BH12-9	c	103.8	58.21	0.58	3.12E-03	3.99000	0.10000	0.28850	0.00690	0.10032	0.00090	0.93396	1630	22	1633	35	1629	17	100
BH12-10	c	389	217.5	0.57	9.74E-04	4.56000	0.15000	0.30780	0.01000	0.10740	0.00120	0.94167	1739	27	1729	49	1755	20	99
BH12-12	c	148.2	127.9	0.88	2.04E-03	4.27900	0.06500	0.29710	0.00490	0.10448	0.00043	0.96958	1689	12	1677	24	1705	8	98
BH12-13	c	132.5	91.9	0.71	2.36E-03	3.96700	0.06600	0.28410	0.00480	0.10139	0.00056	0.94586	1627	14	1612	24	1649	10	98
BH12-14	c	151.1	133.3	0.91	2.04E-03	4.34500	0.09000	0.30000	0.00590	0.10501	0.00053	0.97008	1701	17	1691	29	1714	9	99
BH12-15	c	188.6	180.7	0.99	1.69E-03	4.13100	0.05700	0.28960	0.00460	0.10344	0.00041	0.97408	1660	11	1639	23	1687	7	97
BH12-16	c	225.1	221.1	1.01	1.41E-03	4.19400	0.08200	0.29080	0.00550	0.10455	0.00055	0.96313	1672	16	1645	27	1706	10	96
BH12-17	c	200.6	205	1.03	1.61E-03	4.37000	0.08500	0.30040	0.00560	0.10538	0.00054	0.96469	1706	16	1693	28	1721	10	98
BH12-18	c	230	118.2	0.51	1.38E-03	4.17800	0.07500	0.29120	0.00530	0.10394	0.00041	0.97628	1669	15	1647	27	1696	7	97
BH12-19	c	88.7	59.8	0.69	3.88E-03	3.79700	0.05900	0.27490	0.00450	0.10049	0.00078	0.88293	1591	12	1565	23	1632	14	96
BH12-20	c	64.11	44.8	0.71	4.81E-03	4.25100	0.06300	0.29520	0.00470	0.10429	0.00067	0.91511	1683	12	1667	23	1701	12	98
BH12-21	c	137.9	117	0.86	2.31E-03	4.38500	0.06800	0.30330	0.00500	0.10470	0.00046	0.96412	1709	13	1707	25	1709	8	100
BH12-22	c	148.4	246.2	1.68	2.05E-03	4.32800	0.09200	0.30190	0.00640	0.10377	0.00056	0.96769	1697	17	1700	32	1692	10	100
BH12-23	c	173	206	1.23	1.80E-03	4.37800	0.08000	0.29970	0.00560	0.10578	0.00056	0.95921	1707	15	1689	28	1728	10	98
BH12-24	c	72.8	50.4	0.69	4.17E-03	4.51600	0.06500	0.30840	0.00460	0.10602	0.00071	0.89619	1733	12	1732	23	1732	12	100
BH12-25	c	170	119.6	0.71	2.01E-03	3.74400	0.06300	0.26950	0.00470	0.10054	0.00047	0.96341	1580	14	1538	24	1634	9	94
BH12-27	c	331	530	1.61	1.01E-03	4.21500	0.08900	0.29690	0.00680	0.10280	0.00045	0.98349	1675	18	1675	34	1675	8	100
BH12-28	c	276	361.7	1.33	1.11E-03	4.44800	0.06300	0.30540	0.00480	0.10555	0.00036	0.97929	1721	12	1718	24	1724	6	100
BH12-29	c	88.1	86.35	0.98	3.35E-03	4.41600	0.07000	0.30290	0.00510	0.10559	0.00057	0.94723	1715	13	1705	25	1724	10	99
BH12-30	c	89	86.7	0.99	3.72E-03	3.86000	0.09400	0.27780	0.00560	0.10052	0.00096	0.92502	1603	20	1580	29	1633	18	97
BH12-31	c	221.2	140.9	0.64	1.39E-03	4.17700	0.07100	0.29060	0.00530	0.10410	0.00034	0.98528	1669	14	1644	27	1698	6	97
BH12-32	c	165.4	133	0.80	1.74E-03	4.61400	0.06400	0.31800	0.00450	0.10517	0.00064	0.90587	1751	12	1780	22	1717	11	104
BH12-33	c	432	373	0.87	7.35E-04	4.20600	0.04800	0.29010	0.00400	0.10506	0.00043	0.96471	1675	9.3	1642	20	1715	8	96
BH12-34	c	112.4	166.3	1.48	2.74E-03	4.18100	0.04900	0.29160	0.00370	0.10389	0.00046	0.93724	1670	9.5	1650	19	1695	8	97
BH12-35	c	133.7	113.6	0.84	2.37E-03	3.99900	0.06100	0.28140	0.00450	0.10297	0.00046	0.96021	1633	12	1598	23	1678	8	95
BH12-36	c	58.6	55.7	0.95	4.95E-03	4.40900	0.05300	0.30390	0.00410	0.10517	0.00061	0.90295	1714	10	1710	20	1717	11	100
BH12r-1	r*	30.86	18.6	0.61	7.87E-03	4.61500	0.10000	0.31190	0.00650	0.10730	0.00150	0.78438	1751	19	1750	32	1752	26	100
BH12r-2	r*	39.84	21.73	0.56	5.96E-03	4.33800	0.09300	0.30270	0.00600	0.10425	0.00110	0.87208	1700	18	1704	30	1700	19	100
BH12r-3	r*	54.9	41.93	0.79	4.92E-03	4.76600	0.09100	0.31490	0.00540	0.10985	0.00120	0.82355	1778	16	1765	27	1796	19	98
BH12r-4	r*	46	31.76	0.71	6.69E-03	3.00300	0.06000	0.23890	0.00450	0.09124	0.00100	0.84215	1408	15	1381	23	1451	21	95
BH12r-5	r*	52.5	29.29	0.58	4.45E-03	4.27900	0.08100	0.30300	0.00540	0.10256	0.00100	0.86092	1689	16	1706	27	1670	18	102
BH12r-6	r*	55.9	39.2	0.72	4.42E-03	4.57700	0.09100	0.30760	0.00520	0.10782	0.00120	0.82891	1745	16	1729	26	1762	20	98
BH12r-7	r*	19.99	13.03	0.66	1.25E-02	4.27000	0.16000	0.29550	0.00860	0.10470	0.00220	0.82967	1687	30	1669	43	1707	39	98
BH12r-8	r*	61.8	43.25	0.72	4.32E-03	3.81200	0.07100	0.27470	0.00490	0.10078	0.00091	0.87823	1595	15	1564	25	1638	17	95

Appendix A. (continued)

Analysis	Location	^{238}U (ppm)	^{232}Th (ppm)	^{232}Th/^{238}U	204/206	^{207}Pb/^{235}U	2σ	^{206}Pb/^{238}U	2σ	^{207}Pb/^{206}Pb	2σ	Rho	Age (Ma) ^{207}Pb/^{235}U	2σ	^{206}Pb/^{238}U	2σ	^{207}Pb/^{206}Pb	2σ	Conc. (%)
BH12r-9	r*	40.02	40.23	1.04	6.94E-03	4.77900	0.08400	0.31280	0.00560	0.11048	0.00110	0.84265	1781	15	1754	27	1807	18	97
BH12r-11	r*	67	39.92	0.62	3.78E-03	4.42500	0.09700	0.30550	0.00560	0.10510	0.00120	0.85382	1716	18	1718	28	1715	22	100
BH12r-12	r*	48.9	28.58	0.60	4.95E-03	4.32000	0.08000	0.30170	0.00540	0.10390	0.00110	0.83150	1697	15	1699	27	1694	19	100
BH12r-13	r*	75.5	52.3	0.71	3.39E-03	4.37000	0.06800	0.30020	0.00470	0.10562	0.00094	0.83746	1706	13	1692	23	1725	16	98
BH12r-14	r*	45.3	41.6	0.95	7.31E-03	3.97400	0.07600	0.26970	0.00490	0.10680	0.00130	0.78810	1629	15	1539	25	1744	23	88
BH12r-15	r*	59.4	53.2	0.93	4.27E-03	4.64800	0.09400	0.31400	0.00590	0.10730	0.00130	0.80957	1757	17	1760	29	1753	21	100
BH12r-16	r*	74	46.2	0.64	3.65E-03	4.05100	0.07700	0.28660	0.00520	0.10267	0.00100	0.86354	1644	15	1624	26	1672	18	97
BH12r-17	r*	82.6	65.6	0.82	3.03E-03	4.78600	0.07600	0.32500	0.00520	0.10682	0.00120	0.75168	1782	13	1814	25	1745	20	104
BH12r-18	r*	38.63	27.14	0.73	6.07E-03	4.61700	0.09500	0.31420	0.00640	0.10650	0.00130	0.82230	1752	17	1761	31	1740	22	101
BH12r-19	r*	65.73	40.7	0.64	3.94E-03	4.19800	0.07300	0.29230	0.00490	0.10423	0.00110	0.80963	1673	14	1653	25	1700	19	97
Sample BH38																			
BH38-1	c	121.4	227.6	1.93	3.22E-03	2.24400	0.05400	0.20230	0.00270	0.08056	0.00130	0.77343	1195	17	1188	15	1210	32	98
BH38-2	c	89.7	153.3	1.75	4.32E-03	2.23200	0.05800	0.20270	0.00280	0.08012	0.00130	0.83966	1191	18	1190	15	1199	33	99
BH38-3	c	122	195.5	1.65	3.03E-03	2.20900	0.05500	0.20190	0.00290	0.07944	0.00130	0.78075	1184	17	1186	16	1183	31	100
BH38-4	c	477.9	181.9	0.39	7.89E-04	2.25200	0.05400	0.20420	0.00280	0.07989	0.00120	0.81719	1197	17	1198	15	1194	29	100
BH38-5	c	118	209.6	1.82	3.20E-03	2.21400	0.05300	0.20140	0.00280	0.07985	0.00130	0.75311	1185	17	1183	15	1193	32	99
BH38-6	c	93.3	146.8	1.61	4.10E-03	2.23900	0.05700	0.20170	0.00280	0.08057	0.00130	0.82125	1193	18	1184	15	1214	29	98
BH38-8	c	72.2	119.5	1.69	5.33E-03	2.19900	0.05800	0.20020	0.00360	0.07975	0.00130	0.79415	1180	18	1176	19	1190	33	99
BH38-10	c	110.2	194.1	1.80	3.42E-03	2.19300	0.05300	0.19990	0.00280	0.07963	0.00130	0.75883	1178	17	1175	15	1187	32	99
BH38-11	c	299	484.8	1.65	1.30E-03	2.21300	0.05400	0.20070	0.00300	0.08005	0.00120	0.81446	1185	17	1179	16	1198	30	98
BH38-12	c	142.5	159.1	1.13	2.63E-03	2.23900	0.05500	0.20370	0.00270	0.07980	0.00120	0.84917	1193	17	1195	14	1192	30	100
BH38-13	c	124.2	133.8	1.08	2.91E-03	2.25600	0.05400	0.20600	0.00220	0.07952	0.00130	0.82098	1198	17	1207	12	1184	33	102
BH38-14	c	517	147.3	0.29	7.27E-04	2.19500	0.05500	0.19880	0.00310	0.08015	0.00120	0.82775	1179	18	1169	16	1201	30	97
BH38-16	c	214.8	176.2	0.83	1.80E-03	2.18700	0.05100	0.19930	0.00260	0.07968	0.00120	0.80071	1177	16	1171	14	1189	30	98
BH38-17	c	105	197.8	1.92	3.59E-03	2.20800	0.05700	0.20060	0.00310	0.07994	0.00130	0.80311	1183	18	1178	16	1195	31	99
BH38-18	c	88.8	140.3	1.61	4.36E-03	2.22600	0.05700	0.20060	0.00340	0.08061	0.00130	0.78672	1189	18	1178	18	1211	32	97
BH38-19	c	72.6	126.2	1.77	5.44E-03	2.17600	0.05400	0.19640	0.00290	0.08060	0.00140	0.72615	1173	17	1156	16	1211	33	95
BH38-20	c	377	747	2.02	1.03E-03	2.22800	0.05700	0.20170	0.00320	0.08022	0.00120	0.84069	1189	18	1184	17	1202	30	98
BH38-21	c	160.1	294.4	1.87	2.39E-03	2.21800	0.05400	0.20110	0.00300	0.08012	0.00130	0.75994	1186	17	1181	16	1200	31	98
BH38-22	c	128.4	158	1.25	2.85E-03	2.22700	0.05700	0.20290	0.00350	0.07972	0.00130	0.77772	1189	18	1191	19	1190	32	100
BH38-23	c	688	1597	2.36	5.53E-04	2.24800	0.05100	0.20320	0.00240	0.08034	0.00120	0.80441	1196	16	1192	13	1205	29	99
BH38-24	c	116.1	202.9	1.78	3.23E-03	2.16400	0.05300	0.19780	0.00280	0.07947	0.00130	0.76815	1169	17	1163	15	1183	32	98
BH38-26	c	221.6	446.3	2.05	1.82E-03	2.24100	0.05200	0.20200	0.00210	0.08057	0.00130	0.80040	1194	16	1186	11	1211	31	98
BH38-27	c	683	1743	2.60	5.56E-04	2.25000	0.05200	0.20350	0.00250	0.08031	0.00120	0.81322	1197	16	1194	14	1205	29	99
BH38-28	c	143.8	249.4	1.77	2.76E-03	2.28000	0.05000	0.20370	0.00220	0.08133	0.00130	0.72212	1206	16	1195	12	1229	30	97
BH38-30	c	209.8	550.6	2.68	1.86E-03	2.21000	0.05500	0.20120	0.00300	0.07975	0.00120	0.82903	1184	17	1182	16	1191	30	99
BH38-31	c	183.6	202.1	1.12	2.14E-03	2.24300	0.05600	0.20180	0.00280	0.08070	0.00120	0.85842	1194	17	1185	15	1214	31	98
Sample BH54																			
BH54-1	c†	63.41	176.3	2.82	5.36E-03	2.36300	0.05500	0.20980	0.00290	0.08140	0.00150	0.61114	1231	17	1227	15	1229	36	100
BH54-2	c	461	45	0.10	6.33E-04	3.44000	0.06200	0.26770	0.00270	0.09309	0.00130	0.63687	1514	14	1529	14	1490	27	103
BH54-3	c	682	22.5	0.03	3.17E-04	6.72600	0.12000	0.34350	0.00360	0.14210	0.00200	0.61517	2076	16	1903	17	2253	25	84

Appendix A. (continued)

Analysis	Location	^{238}U (ppm)	^{232}Th (ppm)	^{232}Th/^{238}U	204/206	^{207}Pb/^{235}U	2σ	^{206}Pb/^{238}U	2σ	^{207}Pb/^{206}Pb	2σ	Rho	Age (Ma)						
													^{207}Pb/^{235}U	2σ	^{206}Pb/^{238}U	2σ	^{207}Pb/^{206}Pb	2σ	Conc. (%)
BH54-6	c	77	76.2	1.01	2.28E-03	8.79000	0.19000	0.43320	0.00600	0.14760	0.00230	0.69517	2316	19	2320	27	2318	27	100
BH54-8	c	279	114	0.40	9.67E-04	3.70500	0.07600	0.27590	0.00320	0.09772	0.00150	0.67183	1572	16	1571	16	1581	28	99
BH54-9	c	810	216	0.27	2.70E-04	5.99400	0.11000	0.37100	0.00430	0.11804	0.00160	0.67557	1975	16	2034	20	1927	25	106
BH54-10	c	912.9	560.3	0.63	2.73E-04	4.90100	0.08900	0.31360	0.00320	0.11416	0.00160	0.64074	1802	15	1758	16	1867	25	94
BH54-14	c	359	135	0.38	8.28E-04	4.01600	0.07500	0.28070	0.00320	0.10509	0.00150	0.64583	1637	15	1595	16	1716	26	93
BH54-17	c	1306	31.3	0.02	2.35E-04	3.83400	0.06700	0.27660	0.00260	0.10137	0.00140	0.61791	1600	14	1574	13	1649	26	95
BH54-18	c	736	88.2	0.12	3.73E-04	4.18000	0.07300	0.28760	0.00280	0.10597	0.00150	0.58643	1670	14	1630	14	1731	25	94
BH54-19	c	514	98	0.19	5.41E-04	4.33300	0.08000	0.30870	0.00330	0.10232	0.00140	0.67879	1700	15	1734	16	1667	26	104
BH54-21	c	483	64.7	0.13	5.75E-04	4.22300	0.07400	0.28900	0.00290	0.10645	0.00150	0.59485	1679	14	1637	15	1739	25	94
BH54-22	c	375.6	271.9	0.74	6.61E-04	4.54400	0.08000	0.31440	0.00320	0.10517	0.00140	0.65948	1739	15	1762	16	1717	25	103
BH54-24	r^	229	35.49	0.16	1.36E-03	2.68600	0.04900	0.23781	0.00230	0.08198	0.00120	0.60099	1325	14	1375	12	1245	29	110
BH54-25	c	1223	942	0.78	2.11E-04	5.09300	0.09100	0.32500	0.00340	0.11378	0.00160	0.61777	1835	15	1814	16	1861	25	98
BH54-27	c	427	199.5	0.48	5.71E-04	4.25400	0.07800	0.30100	0.00370	0.10262	0.00140	0.66813	1684	15	1696	18	1672	26	101
BH54-28	r^	131.6	6.7	0.05	2.61E-03	2.49000	0.04700	0.21730	0.00240	0.08325	0.00120	0.64875	1269	14	1268	13	1275	29	99
BH54-30	c	118.6	76.5	0.66	1.58E-03	8.48000	0.17000	0.41970	0.00500	0.14659	0.00210	0.70886	2283	18	2259	23	2306	25	98
BH54-33	c	357	113.9	0.32	5.14E-04	10.93000	0.28000	0.45670	0.01000	0.17474	0.00250	0.82989	2516	24	2425	44	2604	24	93
BH54-34	c	456	65.9	0.15	5.72E-04	4.38100	0.08800	0.30120	0.00420	0.10587	0.00150	0.70901	1708	16	1697	21	1729	26	98
BH54-35	r†	231.7	144.9	0.64	1.49E-03	2.40300	0.05100	0.21630	0.00310	0.08073	0.00120	0.71487	1243	15	1262	16	1214	29	104
BH54-36	c	532	18.15	0.03	5.13E-04	3.95600	0.08100	0.28740	0.00430	0.10005	0.00140	0.73003	1625	17	1629	21	1625	26	100
BH54-37	r^	200.9	80.5	0.40	1.66E-03	2.67800	0.05300	0.23720	0.00300	0.08215	0.00120	0.67570	1322	15	1372	16	1249	29	110
BH54-38	c	474	255	0.55	4.65E-04	6.04000	0.15000	0.36160	0.00680	0.12127	0.00170	0.82853	1981	21	1989	32	1975	25	101
BH54-39	c	578	120.5	0.21	4.21E-04	10.29000	0.28000	0.43830	0.00980	0.17122	0.00240	0.85788	2460	25	2343	44	2570	23	91
BH54-42	c	416.8	33.5	0.08	6.51E-04	4.50300	0.11000	0.30880	0.00570	0.10609	0.00150	0.81784	1731	21	1735	28	1733	26	100
BH54-43	c	132.6	84.7	0.65	1.82E-03	4.67500	0.10000	0.31320	0.00450	0.10839	0.00160	0.72573	1762	18	1756	22	1772	28	99
BH54-44	r†	262.4	128.4	0.50	1.38E-03	2.31500	0.05500	0.20980	0.00370	0.08008	0.00120	0.77676	1216	17	1227	19	1199	29	102
BH54-45	c	1042	1220	1.18	2.38E-04	4.90300	0.11000	0.31490	0.00510	0.11301	0.00150	0.81114	1802	18	1765	25	1848	25	95
BH54-46	c	584	275	0.48	3.27E-04	10.62000	0.23000	0.46220	0.00730	0.16697	0.00230	0.77289	2490	20	2449	32	2527	23	97
BH54-47	c	519.7	96	0.17	5.19E-04	4.33800	0.11000	0.29580	0.00610	0.10638	0.00150	0.83133	1700	22	1670	30	1738	26	96
BH54-49	r^	155.1	241.2	1.58	2.06E-03	2.53100	0.05200	0.23000	0.00350	0.07995	0.00110	0.74266	1281	15	1334	18	1196	28	112
BH54-50	c	888	49.8	0.06	3.63E-04	4.31500	0.11000	0.29010	0.00540	0.10832	0.00160	0.81995	1696	21	1642	27	1771	28	93
BH54-51	c	99.5	80	0.82	2.34E-03	4.78600	0.12000	0.32450	0.00620	0.10712	0.00160	0.80431	1782	21	1811	30	1751	28	103
BH54-52	c	503	333.2	0.67	6.22E-04	5.10600	0.11000	0.33060	0.00490	0.11226	0.00150	0.79118	1837	18	1841	24	1836	25	100
BH54-54	c	395.2	261.2	0.67	4.46E-04	8.38000	0.20000	0.42690	0.00710	0.14254	0.00200	0.81794	2273	21	2291	32	2258	24	101
BH54-55	c	255	105	0.33	1.07E-03	4.19600	0.10000	0.29530	0.00550	0.10331	0.00140	0.82368	1672	20	1668	28	1684	26	99
BH54-56	c	389	34.45	0.09	6.24E-04	5.77600	0.13000	0.33050	0.00530	0.12699	0.00180	0.77967	1942	20	1841	25	2057	25	90
BH54-57	c	167	130	0.76	1.36E-03	4.42900	0.09800	0.30710	0.00510	0.10481	0.00150	0.76276	1717	18	1726	25	1711	26	101
BH54-58	c	337	316	0.95	7.00E-04	4.65600	0.11000	0.32550	0.00630	0.10372	0.00150	0.79125	1759	20	1816	31	1692	26	107
BH54-59	c	446	415	0.93	5.37E-04	4.58300	0.10000	0.30900	0.00530	0.10767	0.00150	0.76981	1745	19	1735	26	1760	25	99
BH54-60	c	291	76.9	0.27	7.86E-04	5.10800	0.11000	0.32860	0.00490	0.11279	0.00160	0.75497	1837	18	1831	24	1845	26	99
BH54-61	c	636	190	0.30	4.22E-04	4.23000	0.11000	0.29300	0.00620	0.10465	0.00150	0.83464	1679	20	1656	31	1708	26	97
BH54-62	c	742	26.9	0.04	3.84E-04	3.83200	0.09300	0.27650	0.00520	0.10056	0.00140	0.82036	1599	20	1573	26	1634	25	96

Appendix A. (continued)

Analysis	Location	^{238}U (ppm)	^{232}Th (ppm)	^{232}Th/^{238}U	204/206	^{207}Pb/^{235}U	2σ	^{206}Pb/^{238}U	2σ	^{207}Pb/^{206}Pb	2σ	Rho	Age (Ma) ^{207}Pb/^{235}U	2σ	^{206}Pb/^{238}U	2σ	^{207}Pb/^{206}Pb	2σ	Conc. (%)
BH54-63	c	479	156.1	0.33	5.40E-04	4.57500	0.08900	0.30660	0.00380	0.10828	0.00150	0.70539	1745	16	1724	19	1771	26	97
BH54-64	c	440.3	42.9	0.10	4.68E-04	6.09300	0.13000	0.36220	0.00550	0.12209	0.00170	0.75918	1989	19	1992	26	1987	25	100
BH54-66	r†	313.1	70.3	0.23	1.24E-03	2.31200	0.05200	0.20500	0.00370	0.08211	0.00120	0.76124	1216	16	1202	20	1248	29	96
BH54-67	r†	336.5	95	0.29	1.06E-03	2.43000	0.06300	0.21310	0.00450	0.08292	0.00120	0.82985	1251	19	1245	24	1267	27	98
BH54-68	c	334	423	1.28	7.42E-04	5.09000	0.11000	0.33230	0.00480	0.11126	0.00150	0.79112	1834	18	1849	23	1820	25	102
BH54-69	c	421	119	0.29	6.11E-04	4.77100	0.12000	0.31680	0.00540	0.10942	0.00160	0.82727	1779	20	1774	26	1790	26	99
BH54-70	c	683	241.8	0.36	3.63E-04	4.85300	0.11000	0.31670	0.00510	0.11128	0.00150	0.81011	1793	19	1773	25	1820	25	97
BH54-72	c	619	63	0.10	4.72E-04	4.16300	0.11000	0.28280	0.00570	0.10681	0.00150	0.85172	1666	21	1605	29	1746	25	92
BH54-74	c	385.7	668	1.71	7.41E-04	4.11900	0.08800	0.29540	0.00460	0.10124	0.00140	0.76303	1658	17	1668	23	1647	26	101
BH54-76	r†	250.8	192.1	0.77	1.42E-03	2.78200	0.05800	0.23590	0.00360	0.08567	0.00120	0.74073	1350	16	1365	19	1331	27	103
BH54-78	c	412	452.5	1.12	6.36E-04	4.03100	0.08600	0.29060	0.00430	0.10061	0.00140	0.76102	1640	17	1645	21	1635	26	101
BH54-79	c	437.3	148.5	0.34	3.66E-04	14.21000	0.32000	0.49380	0.00800	0.20856	0.00290	0.78974	2763	21	2587	35	2894	22	89
BH54-80	c	181.9	114.8	0.65	1.54E-03	5.01000	0.14000	0.31510	0.00710	0.11566	0.00170	0.85170	1820	23	1765	35	1890	27	93
BH54-81	c	841.7	45.18	0.05	3.58E-04	4.12900	0.08900	0.28610	0.00440	0.10480	0.00140	0.78836	1660	17	1622	22	1711	25	95
BH54-82	c	624	199.8	0.33	4.62E-04	4.09800	0.09100	0.28700	0.00470	0.10350	0.00140	0.79516	1653	18	1626	23	1688	25	96
BH54-84	c	221.7	187.9	0.87	1.04E-03	5.22900	0.11000	0.33910	0.00500	0.11170	0.00160	0.73307	1857	18	1882	24	1827	26	103
BH54-85	c	107.7	132.1	1.25	1.50E-03	10.17000	0.21000	0.45940	0.00670	0.16004	0.00220	0.74732	2450	19	2437	29	2456	24	99
BH54-86	c	147	40.8	0.28	1.77E-03	4.22600	0.10000	0.29840	0.00550	0.10250	0.00150	0.78586	1678	20	1683	27	1669	28	101
BH54-87	c	647	15.3	0.02	4.21E-04	3.69200	0.07900	0.26930	0.00410	0.09918	0.00140	0.75267	1569	17	1537	21	1608	26	96
BH54-88	c	508.6	17.1	0.03	5.43E-04	3.70900	0.08100	0.27850	0.00430	0.09624	0.00130	0.79015	1573	18	1584	22	1552	26	102
Sample BH62																			
BH62-1	c	302.6	162.3	0.55	6.85E-04	12.17000	0.43000	0.49360	0.00590	0.17882	0.00370	0.92902	2617	33	2586	26	2642	34	98
BH62-2	r^	90.1	2.02	0.02	5.61E-03	2.34300	0.08500	0.20600	0.00250	0.08242	0.00180	0.78751	1225	26	1208	14	1255	42	96
BH62-4	c	141.4	155.6	1.12	1.92E-03	8.64000	0.32000	0.39440	0.00520	0.15915	0.00330	0.95055	2300	33	2143	24	2447	35	88
BH62-5	r^	280.7	162.3	0.59	1.81E-03	2.30200	0.08100	0.20810	0.00240	0.08038	0.00170	0.78253	1213	25	1219	13	1206	41	101
BH62-7	c	114.1	34.11	0.30	1.86E-03	11.50000	0.41000	0.47630	0.00620	0.17525	0.00360	0.89957	2564	33	2511	27	2608	35	96
BH62-9	c	385.4	85.3	0.22	9.87E-04	4.79700	0.17000	0.28200	0.00400	0.12393	0.00260	0.89574	1784	31	1601	20	2013	37	80
BH62-10	c	988	300.6	0.31	2.51E-04	9.61000	0.34000	0.41590	0.00510	0.16830	0.00340	0.96622	2400	29	2242	23	2541	34	88
BH62-12	c	339	80.4	0.24	8.61E-04	8.07000	0.30000	0.37250	0.00530	0.15754	0.00320	0.95598	2238	33	2046	22	2429	35	84
BH62-14	r^	301.6	29.19	0.10	7.73E-04	10.31800	0.36000	0.44490	0.00520	0.16871	0.00340	0.89876	2464	33	2372	23	2545	34	93
BH62-16	c	904	64.4	0.07	2.65E-04	11.21000	0.40000	0.45260	0.00620	0.18051	0.00370	0.95071	2540	34	2406	27	2658	34	91
BH62-17	r*	488.9	29.76	0.06	5.19E-04	9.39000	0.35000	0.41930	0.00630	0.16307	0.00330	0.97662	2377	34	2257	29	2488	34	91
BH62-19	c	778	80.1	0.10	2.85E-04	10.62000	0.38000	0.44430	0.00540	0.17367	0.00360	0.96748	2493	39	2370	24	2593	34	91
BH62-22	c	249.8	65.22	0.27	8.80E-04	11.70000	0.41000	0.47480	0.00610	0.17937	0.00360	0.96754	2580	34	2504	27	2647	33	95
BH62-27	c	636	462.4	0.74	3.49E-04	10.52000	0.39000	0.44060	0.00710	0.17416	0.00350	0.97877	2480	35	2353	32	2598	34	91
BH62-28	c	432.1	276.5	0.65	5.13E-04	10.79000	0.40000	0.45020	0.00720	0.17495	0.00350	0.98540	2505	34	2396	32	2606	33	92
BH62-33	c	590	319.5	0.55	4.78E-04	6.87000	0.30000	0.34170	0.00990	0.14641	0.00290	0.98346	2094	44	1895	49	2304	35	82
BH62-34	r^	125.1	1.58	0.03	3.68E-03	2.38800	0.08700	0.21130	0.00310	0.08229	0.00170	0.92769	1238	26	1236	16	1252	40	99
BH62-36	c	445.9	255	0.58	4.99E-04	10.66000	0.84000	0.45190	0.03300	0.17107	0.00350	0.93390	2494	64	2404	160	2568	34	94
BH62-37	c	586	385.2	0.67	4.13E-04	9.47800	0.36000	0.41240	0.00590	0.16734	0.00340	0.97927	2385	34	2226	27	2531	34	88
BH62-40	r^	392.9	107.4	0.28	5.67E-04	10.16000	0.36000	0.44060	0.00530	0.16743	0.00340	0.97219	2449	33	2353	24	2532	34	93

Appendix A. (continued)

Analysis	Location	^{238}U (ppm)	^{232}Th (ppm)	^{232}Th/^{238}U	204/206	^{207}Pb/^{235}U	2σ	^{206}Pb/^{238}U	2σ	^{207}Pb/^{206}Pb	2σ	Rho	Age (Ma) ^{207}Pb/^{235}U	2σ	^{206}Pb/^{238U}	2σ	^{207}Pb/^{206}Pb	2σ	Conc. (%)
BH62-41	c	1335	99.8	0.08	1.80E-04	10.85700	0.38000	0.45030	0.00520	0.17441	0.00350	0.98743	2511	33	2397	23	2600	34	92
BH62-46	r^	410	108.5	0.27	1.14E-03	2.29200	0.08000	0.20780	0.00230	0.07996	0.00160	0.88107	1210	25	1217	12	1196	40	102
BH62-47	c	1085	569.9	0.54	1.79E-04	11.68000	0.42000	0.46960	0.00620	0.18027	0.00360	0.98293	2579	33	2482	27	2655	33	93
BH62-49	c	476.3	169.6	0.36	5.04E-04	9.34000	0.34000	0.41110	0.00600	0.16532	0.00330	0.96396	2372	33	2220	27	2511	34	88
BH62-50	r^	150.4	81.7	0.56	2.83E-03	2.38100	0.08500	0.21610	0.00240	0.07994	0.00170	0.68570	1237	25	1261	13	1195	42	106
BH62-51	c	793	250.2	0.32	2.88E-04	9.65000	0.35000	0.41210	0.00590	0.16959	0.00340	0.97851	2401	33	2224	27	2554	34	87
BH62-54	c	632	225.7	0.37	2.98E-04	12.53900	0.44000	0.49800	0.00580	0.18253	0.00370	0.97519	2645	33	2605	25	2676	33	97
BH62-56	c	969	344	0.36	2.15E-04	10.55000	0.39000	0.43420	0.00670	0.17622	0.00360	0.97748	2484	34	2325	30	2618	34	89
BH62-57	c	729	415	0.59	2.80E-04	10.79500	0.38000	0.44570	0.00530	0.17543	0.00360	0.86745	2505	33	2376	24	2610	34	91
BH62-59	r†	823	224.6	0.28	2.76E-04	9.64500	0.34000	0.41110	0.00520	0.16969	0.00340	0.97276	2401	33	2220	24	2555	34	87
BH62-61	c	397	160	0.41	5.12E-04	11.00000	0.40000	0.45240	0.00680	0.17579	0.00360	0.97323	2523	34	2406	30	2614	34	92
BH62-65	c	475.7	134.8	0.29	4.03E-04	11.51000	0.41000	0.46420	0.00560	0.17875	0.00360	0.97016	2565	33	2458	25	2641	34	93
BH62-66	c	1009	83.6	0.08	2.02E-04	11.32000	0.42000	0.44850	0.00680	0.18276	0.00370	0.98658	2550	34	2388	30	2678	33	89
BH62-67	c	574.8	205.2	0.36	3.65E-04	9.98000	0.35000	0.42340	0.00490	0.17011	0.00340	0.97556	2433	33	2276	22	2559	34	89
BH62-70	r^	289.9	192	0.66	7.14E-04	10.93000	0.40000	0.46350	0.00670	0.17095	0.00350	0.98035	2516	34	2455	30	2567	34	96
BH62-71	c	552.5	247	0.46	3.49E-04	11.13000	0.40000	0.45810	0.00570	0.17569	0.00360	0.95427	2534	33	2431	25	2613	34	93
BH62-73	c	757	604	0.82	2.62E-04	11.12000	0.41000	0.45570	0.00730	0.17746	0.00360	0.98155	2533	34	2420	32	2629	34	92
BH62-74	c	765	313.1	0.42	2.60E-04	10.25000	0.37000	0.43330	0.00550	0.17141	0.00350	0.97515	2458	33	2320	25	2571	34	90
BH62-76	c	1048	99.6	0.10	2.01E-04	10.92000	0.39000	0.44720	0.00610	0.17756	0.00360	0.97724	2516	33	2383	24	2630	34	91
BH62-78	r^	191.3	149.4	0.80	1.01E-03	10.50000	0.38000	0.44570	0.00570	0.17116	0.00350	0.95501	2479	34	2376	26	2569	35	92
BH62-80	c	609	403	0.68	2.93E-04	11.53000	0.41000	0.47630	0.00640	0.17570	0.00350	0.98735	2567	33	2511	28	2613	34	96
BH62-83	c	884	371	0.43	2.23E-04	10.45900	0.37000	0.44040	0.00520	0.17292	0.00350	0.97897	2476	32	2352	23	2586	34	91
BH62-85	c	563.3	349.9	0.63	3.96E-04	9.62000	0.36000	0.42320	0.00660	0.16520	0.00340	0.96174	2399	34	2275	30	2510	35	91
BH62-87	c	748	391.2	0.53	2.60E-04	9.98000	0.37000	0.42810	0.00650	0.16985	0.00340	0.99051	2432	35	2296	29	2556	34	90
BH62-88	c	1087	737.6	0.69	1.62E-04	11.96000	0.42000	0.48230	0.00580	0.18056	0.00360	0.98685	2601	33	2537	25	2658	33	95
BH62-90	c	123.6	31.22	0.26	1.46E-03	11.05000	0.40000	0.46420	0.00640	0.17309	0.00360	0.92612	2527	34	2458	28	2588	34	95
BH62-92	c	218.3	67.3	0.31	8.06E-04	11.39000	0.40000	0.47300	0.00590	0.17462	0.00350	0.94923	2555	33	2496	26	2604	29	96
BH62-95	c	337.5	154.5	0.46	6.49E-04	10.57800	0.37000	0.44520	0.00540	0.17203	0.00350	0.95538	2487	33	2374	24	2577	34	92
Sample BH67																			
BH67-1	c	995	365.4	0.38	3.34E-04	10.09000	0.20000	0.40540	0.00950	0.18123	0.00310	0.69908	2443	18	2193	44	2664	28	82
BH67-3	c	157.1	374.6	2.43	1.77E-03	9.95000	0.19000	0.42350	0.00940	0.17002	0.00280	0.69139	2430	17	2276	43	2558	27	89
BH67-4	c	138.5	223	1.63	2.24E-03	8.92000	0.17000	0.39130	0.00930	0.16532	0.00280	0.70782	2330	18	2129	43	2511	29	85
BH67-10	c	940	203.5	0.21	3.44E-04	8.96100	0.17000	0.37260	0.00860	0.17360	0.00310	0.65517	2334	17	2042	40	2593	30	79
BH67-21	c	114.6	233.5	2.04	2.05E-03	9.90000	0.19000	0.42950	0.01000	0.16730	0.00270	0.72729	2425	17	2303	45	2531	27	91
BH67-23	c	173.8	262.9	1.52	1.66E-03	9.00000	0.20000	0.40170	0.00990	0.16330	0.00280	0.73695	2342	24	2177	46	2490	29	87
BH67-24	c	683.7	267.7	0.39	3.84E-04	8.92800	0.17000	0.39250	0.00870	0.16590	0.00270	0.69778	2330	18	2134	41	2517	27	85
BH67-25	c	173.3	621.3	3.62	1.37E-03	9.83000	0.20000	0.42710	0.01000	0.16723	0.00270	0.73627	2418	19	2292	46	2530	27	91
BH67-26	c	186	576.5	3.17	1.29E-03	10.11000	0.21000	0.43460	0.01000	0.16867	0.00270	0.73717	2444	19	2326	47	2544	27	91
BH67-27	c	172	292.5	1.74	1.43E-03	9.16000	0.18000	0.40870	0.00960	0.16176	0.00260	0.73611	2354	18	2209	44	2474	27	89
BH67-30	c	753	160.3	0.22	3.31E-04	10.00000	0.20000	0.41410	0.00980	0.17442	0.00310	0.68050	2438	19	2233	45	2600	29	86
BH67-31	c	174.9	450.3	2.67	1.29E-03	10.56000	0.20000	0.44150	0.01000	0.17290	0.00280	0.71037	2487	19	2357	46	2586	27	91

Appendix A. (continued)

Analysis	Location	^{238}U (ppm)	^{232}Th (ppm)	^{232}Th/^{238}U	204/206	^{207}Pb/^{235}U	2σ	^{206}Pb/^{238}U	2σ	^{207}Pb/^{206}Pb	2σ	Rho	Age (Ma) ^{207}Pb/^{235}U	2σ	^{206}Pb/^{238}U	2σ	^{207}Pb/^{206}Pb	2σ	Conc. (%)
BH67-32	c	136	335.9	2.56	1.73E-03	10.35000	0.22000	0.43350	0.01100	0.17194	0.00280	0.76989	2465	20	2321	48	2577	27	90
BH67-34	c	1121	438.8	0.41	2.14E-04	10.22000	0.19000	0.42540	0.00930	0.17332	0.00280	0.69209	2454	18	2285	42	2590	27	88
BH67-37	c	574	130.5	0.23	4.04E-04	10.34000	0.22000	0.42470	0.01000	0.17535	0.00280	0.75066	2465	20	2281	47	2609	27	87
BH67r-1	r*	44.89	262.5	6.05	8.45E-03	2.41600	0.05500	0.20810	0.00370	0.08400	0.00130	0.73483	1247	16	1218	20	1291	31	94
BH67r-2	r*	23.81	85.6	3.72	1.60E-02	2.67600	0.09800	0.20730	0.00460	0.09360	0.00270	0.61617	1320	27	1214	24	1495	56	81
BH67r-3	r*	25.18	69.4	2.85	1.51E-02	2.52000	0.07800	0.20590	0.00380	0.08890	0.00220	0.60066	1277	22	1207	20	1399	47	86
BH67r-4	c	124.1	158.1	1.32	1.97E-03	7.38000	0.14000	0.35630	0.00610	0.14992	0.00140	0.87102	2157	17	1965	29	2345	16	84
BH67r-5	r*	34.16	239.4	7.24	1.05E-02	2.55400	0.05700	0.21580	0.00390	0.08570	0.00170	0.53455	1287	16	1259	21	1328	38	95
BH67r-6	c	90.4	196.6	2.25	2.61E-03	6.39100	0.11000	0.33280	0.00530	0.13919	0.00130	0.84390	2031	15	1852	25	2217	16	84
BH67r-7	r*	43.85	31.15	0.73	8.72E-03	2.28800	0.04600	0.20350	0.00340	0.08190	0.00130	0.64214	1208	14	1194	18	1241	30	96
BH67r-8	r*	41.21	170.7	4.28	9.23E-03	2.32500	0.04700	0.20180	0.00370	0.08340	0.00120	0.72549	1219	14	1185	20	1278	29	93
BH67r-10	r*	31.3	76.07	2.51	1.12E-02	2.33700	0.04300	0.20670	0.00360	0.08217	0.00110	0.72190	1223	13	1211	19	1248	26	97
BH67r-11	r*	32.72	233.1	7.36	1.17E-02	2.39300	0.05600	0.20270	0.00390	0.08560	0.00150	0.67823	1240	17	1190	21	1327	33	90
BH67r-12	r*	27.84	77.9	2.89	1.36E-02	2.83100	0.08400	0.21900	0.00460	0.09380	0.00220	0.61894	1363	22	1276	24	1500	44	85
BH67r-13	c	151.9	392.1	2.67	1.50E-03	10.91500	0.17000	0.45440	0.00700	0.17417	0.00130	0.88396	2516	14	2415	31	2598	13	93
BH67r-14	c	132.6	365.6	2.85	1.45E-03	9.29600	0.15000	0.41080	0.00640	0.16410	0.00130	0.87579	2367	15	2218	29	2498	13	89
BH67r-15	c	1103	920	0.86	3.25E-04	10.05400	0.16000	0.41840	0.00660	0.17379	0.00120	0.90508	2440	15	2253	30	2594	12	87
BH67r-16	c	136.7	332.9	2.51	1.38E-03	8.65300	0.14000	0.39170	0.00610	0.16024	0.00130	0.87012	2302	15	2131	28	2458	13	87
BH67r-17	c	165.8	280	1.74	1.32E-03	7.63700	0.13000	0.35690	0.00560	0.15537	0.00130	0.87226	2189	15	1967	27	2406	15	82
BH67r-18	c	203.2	274.6	1.39	9.47E-04	9.66500	0.16000	0.41390	0.00640	0.16950	0.00140	0.86907	2403	15	2233	29	2553	14	87
Sample BH68																			
BH68-4	c	199.2	167.9	0.85	1.00E-03	11.54000	0.16000	0.46800	0.00690	0.17858	0.00082	0.95032	2567	13	2474	31	2640	8	94
BH68-6	c	471.8	211.6	0.45	4.65E-04	10.06000	0.20000	0.41970	0.00820	0.17350	0.00110	0.94841	2439	19	2259	38	2591	11	87
BH68-7	c	475	187.2	0.40	4.79E-04	10.67000	0.20000	0.42890	0.00820	0.18010	0.00120	0.93825	2494	17	2300	37	2654	11	87
BH68-8	c	369	143.4	0.39	6.50E-04	10.46000	0.21000	0.42820	0.00900	0.17655	0.00098	0.96454	2475	19	2297	41	2620	9	88
BH68-9	c	616	357	0.58	4.54E-04	8.46000	0.13000	0.37700	0.00670	0.16266	0.00067	0.97953	2281	14	2061	32	2483	7	83
BH68-10	c	1079	759	0.71	4.28E-04	6.25000	0.13000	0.30690	0.00610	0.14753	0.00093	0.95297	2011	18	1725	30	2317	11	74
BH68-11	c	404	131.7	0.33	5.49E-04	11.03000	0.16000	0.44850	0.00690	0.17800	0.00100	0.93102	2525	13	2388	31	2634	9	91
BH68-15	c	632	912	1.47	6.57E-04	11.23000	0.11000	0.44300	0.00460	0.18420	0.00160	0.63080	2545	10	2364	21	2691	14	88
BH68-16	c	285.1	83.11	0.30	9.13E-04	9.17900	0.10000	0.39390	0.00470	0.16936	0.00076	0.92668	2356	10	2141	22	2551	8	84
BH68-17	c†	506.2	106.7	0.21	9.42E-04	2.19300	0.02200	0.19860	0.00250	0.08009	0.00043	0.91174	1179	7	1168	13	1199	11	97
BH68-20	c	49.2	56.2	1.17	6.16E-03	7.62000	0.20000	0.35410	0.00860	0.15617	0.00093	0.97520	2185	24	1953	41	2414	10	81
BH68-21	c	200.1	122.1	0.63	1.12E-03	10.08000	0.21000	0.43080	0.00940	0.16990	0.00070	0.98240	2441	19	2308	42	2557	7	90
BH68-23	c	447	259.4	0.59	4.43E-04	11.93000	0.21000	0.47660	0.00950	0.18159	0.00045	0.99899	2597	17	2511	42	2667	4	94
BH68-24	c†	592.2	340.5	0.59	9.16E-04	2.26600	0.04400	0.19950	0.00410	0.08242	0.00049	0.95733	1201	14	1173	22	1255	12	93
BH68-25	c	1073	109.9	0.11	2.71E-04	6.55000	0.10000	0.32480	0.00600	0.14638	0.00088	0.95415	2052	14	1813	29	2304	10	79
BH68-26	c	357	176.4	0.51	8.06E-04	9.82000	0.16000	0.41370	0.00720	0.17239	0.00065	0.97711	2417	15	2231	33	2581	6	86
BH68-27	c	349	168.6	0.50	9.36E-04	8.20000	0.16000	0.37220	0.00740	0.15985	0.00076	0.97104	2252	18	2039	35	2454	8	83
BH68-28	c	475.6	106.3	0.23	4.80E-04	9.98000	0.18000	0.41740	0.00640	0.17420	0.00130	0.91252	2432	17	2248	29	2598	12	87
BH68-29	c	271	191.5	0.73	7.72E-04	11.09000	0.18000	0.44750	0.00740	0.17914	0.00086	0.95724	2529	15	2391	37	2645	8	90
BH68-30	c	414.5	236.7	0.58	5.77E-04	9.36000	0.12000	0.40590	0.00580	0.16749	0.00094	0.91992	2373	12	2196	26	2532	9	87

Appendix A. (continued)

Analysis	Location	^{238}U (ppm)	^{232}Th (ppm)	^{232}Th/^{238}U	204/206	^{207}Pb/^{235}U	2σ	^{206}Pb/^{238}U	2σ	^{207}Pb/^{206}Pb	2σ	Rho	Age (Ma)						
													^{207}Pb/^{235}U	2σ	^{206}Pb/^{238U}	2σ	^{207}Pb/^{206}Pb	2σ	Conc. (%)
BH68-31	c	565.4	316.8	0.58	4.32E-04	9.30000	0.24000	0.39400	0.01000	0.17119	0.00090	0.97904	2365	28	2140	48	2569	9	83
BH68-32	c	341	169.4	0.51	9.30E-04	6.01000	0.13000	0.31200	0.00630	0.13980	0.00100	0.94379	1976	19	1750	31	2224	13	79
BH68-33	c	153	83.9	0.56	1.34E-03	10.84000	0.20000	0.45400	0.00720	0.17230	0.00100	0.95391	2508	17	2412	32	2580	10	93
BH68-34	c	486.7	65.65	0.14	6.29E-04	10.23000	0.24000	0.41980	0.01000	0.17673	0.00093	0.97534	2454	22	2258	45	2622	9	86
BH68r-5	c	66.9	62.5	0.96	3.48E-03	11.25000	0.19000	0.45070	0.00680	0.18080	0.00190	0.78967	2544	16	2398	30	2659	17	90
BH68r-6	r*	48.66	27.48	0.58	4.92E-03	8.33000	0.17000	0.37620	0.00670	0.16010	0.00170	0.85418	2267	18	2058	31	2457	17	84
BH68r-7	c	104.1	57.38	0.57	2.36E-03	8.70000	0.16000	0.38530	0.00620	0.16380	0.00150	0.86725	2307	16	2101	29	2494	16	84
BH68r-8	r*	34.12	72.2	2.18	1.32E-02	3.27200	0.07800	0.21270	0.00360	0.11140	0.00190	0.69874	1474	19	1243	19	1821	32	68
BH68r-12	r*	23.03	43.2	1.93	1.83E-02	3.29900	0.09300	0.21230	0.00480	0.11260	0.00230	0.69712	1480	22	1241	25	1839	38	67
BH68r-13	c	106.2	80.9	0.78	2.67E-03	5.87900	0.12000	0.30350	0.00520	0.14060	0.00140	0.87361	1958	17	1709	25	2235	17	76
BH68r-15	c	58.77	64.6	1.13	4.08E-03	11.47000	0.18000	0.45420	0.00720	0.18320	0.00170	0.82698	2562	15	2414	32	2682	15	90
BH68r-16	r*	16.51	25.22	1.56	2.23E-02	2.45900	0.06400	0.20480	0.00450	0.08710	0.00140	0.78849	1259	19	1201	24	1361	31	88
BH68r-17	r*	173.9	92	0.55	1.22E-03	9.68600	0.16000	0.42200	0.00670	0.16650	0.00140	0.86599	2405	15	2270	30	2523	14	90
BH68r-18	r*	49.64	51.79	1.08	6.17E-03	8.49000	0.27000	0.36920	0.01000	0.16670	0.00210	0.92080	2283	29	2025	48	2524	21	80
BH68r-20	c	808	560	0.71	2.31E-04	10.61500	0.17000	0.42000	0.00640	0.18370	0.00190	0.78206	2490	15	2260	29	2687	17	84
Sample BH79																			
BH79-1	c	703.7	181.6	0.26	6.67E-04	3.59900	0.04700	0.26520	0.00290	0.09865	0.00150	0.20629	1549	11	1516	15	1599	28	95
BH79-4	c	1109	356.3	0.33	4.81E-04	3.15300	0.04900	0.23780	0.00300	0.09711	0.00150	0.41335	1445	12	1375	16	1569	29	88
BH79-5	c	243	95.8	0.40	1.74E-03	4.30700	0.05200	0.30190	0.00330	0.10439	0.00160	0.11490	1694	9.9	1700	16	1703	28	100
BH79-7	c	664	149.6	0.23	6.69E-04	3.82600	0.05200	0.27310	0.00300	0.10205	0.00160	0.19951	1598	11	1556	15	1662	28	94
BH79-8	c†	975	59	0.06	5.95E-04	2.38500	0.03000	0.21120	0.00200	0.08226	0.00130	0.00779	1238	9.1	1235	11	1252	30	99
BH79-9	c	904.5	237.4	0.26	5.78E-04	3.24900	0.05200	0.24630	0.00330	0.09634	0.00150	0.45060	1469	12	1419	17	1554	28	91
BH79-11	c	354.1	74.84	0.21	1.42E-03	3.26000	0.04400	0.25180	0.00270	0.09422	0.00140	0.26381	1471	10	1447	14	1512	29	96
BH79-12	c	487	147.3	0.29	9.97E-04	3.52000	0.04400	0.26200	0.00240	0.09775	0.00150	0.02045	1531	9.9	1500	12	1581	29	95
BH79-14	c	364	84.5	0.23	1.26E-03	3.83400	0.04800	0.27760	0.00270	0.10006	0.00160	0.01788	1600	10	1579	13	1625	29	97
BH79-16	c	873	244.4	0.28	5.85E-04	3.26800	0.05000	0.24770	0.00320	0.09547	0.00150	0.38988	1473	12	1427	17	1537	29	93
BH79-17	c	492	111	0.23	9.85E-04	3.67600	0.08200	0.26940	0.00540	0.09864	0.00150	0.74713	1565	18	1537	27	1598	28	96
BH79-18	c	1523	234.1	0.16	3.84E-04	2.70200	0.04800	0.21890	0.00350	0.08913	0.00140	0.57124	1328	13	1276	18	1407	29	91
BH79-20	c	777	152.5	0.20	6.67E-04	3.05600	0.03000	0.24020	0.00190	0.09179	0.00140	0.47451	1422	7.6	1388	9.9	1463	29	95
BH79-21	c	721	160.1	0.23	6.66E-04	3.59300	0.05600	0.26510	0.00370	0.09799	0.00150	0.46750	1547	12	1516	19	1586	28	96
BH79-23	c	1403	330	0.24	3.85E-04	2.95000	0.04700	0.23120	0.00280	0.09212	0.00150	0.35078	1395	12	1341	15	1470	31	91
BH79-24	c	647	174.1	0.27	7.82E-04	3.37700	0.05900	0.25390	0.00410	0.09645	0.00150	0.57445	1498	14	1458	21	1557	29	94
BH79-26	c	176.1	67.36	0.39	2.58E-03	3.58100	0.04800	0.26910	0.00310	0.09632	0.00150	0.22620	1545	11	1536	16	1554	29	99
BH79-27	c	857	205.6	0.25	5.69E-04	3.45500	0.04200	0.25480	0.00250	0.09815	0.00150	0.04394	1517	9.5	1463	13	1589	29	92
BH79-28	c	154.9	87.47	0.58	2.89E-03	3.89100	0.04900	0.28070	0.00270	0.10034	0.00160	0.01304	1611	10	1595	13	1630	29	98
BH79-31	c	805	216.2	0.27	6.38E-04	3.40700	0.06300	0.25080	0.00420	0.09894	0.00150	0.63379	1505	15	1442	22	1604	29	90
BH79-32	c	755	142.6	0.19	6.91E-04	3.04000	0.04600	0.23860	0.00250	0.09258	0.00150	0.24043	1417	11	1379	13	1479	30	93
BH79-34	c	500	128.5	0.26	9.50E-04	3.50800	0.05600	0.26170	0.00350	0.09779	0.00150	0.46468	1529	13	1499	18	1582	29	95
BH79-37	c	791	203.2	0.27	4.98E-04	3.84300	0.05100	0.28250	0.00320	0.09897	0.00150	0.24853	1602	11	1604	16	1605	28	100
BH79-38	c†	1774	60.86	0.04	3.05E-04	2.43200	0.03600	0.20800	0.00250	0.08506	0.00130	0.36534	1252	11	1218	13	1317	30	92
BH79-39	c	75.7	31.94	0.44	5.73E-03	3.60400	0.06200	0.27040	0.00390	0.09738	0.00150	0.53744	1550	14	1543	20	1574	30	98

Appendix A. (continued)

Analysis	Location	^{238}U (ppm)	^{232}Th (ppm)	^{232}Th/^{238}U	204/206	^{207}Pb/^{235}U	2σ	^{206}Pb/^{238}U	2σ	^{207}Pb/^{206}Pb	2σ	Rho	Age (Ma) ^{207}Pb/^{235}U	2σ	^{206}Pb/^{238}U	2σ	^{207}Pb/^{206}Pb	2σ	Conc. (%)
BH79-41	c†	1149	70.8	0.07	4.54E-04	2.45100	0.02800	0.21510	0.00220	0.08324	0.00130	0.03763	1260	9.3	1256	12	1275	29	99
BH79-43	c	1209	118.7	0.11	4.35E-04	2.85100	0.04000	0.22840	0.00220	0.09112	0.00140	0.19817	1369	11	1326	12	1449	29	92
BH79-44	c	628	156.1	0.27	7.45E-04	3.28700	0.03600	0.25130	0.00230	0.09512	0.00140	0.06439	1478	8.5	1445	12	1532	31	94
BH79-45	c†	1236	62.7	0.05	4.52E-04	2.43800	0.03300	0.21160	0.00230	0.08368	0.00130	0.20395	1254	9.7	1237	12	1285	30	96
BH79-46	c	1478	955	0.71	3.23E-04	3.23300	0.03900	0.24020	0.00250	0.09739	0.00150	0.06620	1465	9.2	1387	13	1574	29	88
BH79r-1	r†	1095	77.6	0.07	3.26E-04	2.40700	0.03600	0.21240	0.00330	0.08195	0.00065	0.86536	1245	11	1242	18	1244	15	100
BH79r-3	r†	2054	64.76	0.03	1.75E-04	2.53500	0.04100	0.21260	0.00350	0.08631	0.00076	0.85456	1282	12	1242	18	1345	17	92
BH79r-6	r†	1503	58.42	0.04	2.47E-04	2.50000	0.03900	0.21530	0.00340	0.08392	0.00062	0.88929	1272	11	1257	18	1291	14	97
BH79r-7	r†	74	52.5	0.73	4.91E-03	2.47900	0.05200	0.21500	0.00430	0.08370	0.00130	0.71363	1266	15	1255	23	1285	29	98
BH79r-9	r†	1635	76.4	0.05	2.20E-04	2.54600	0.04000	0.21950	0.00370	0.08388	0.00065	0.88910	1285	11	1279	19	1290	15	99
BH79r-10	r†	1075	52.9	0.05	3.50E-04	2.49600	0.03600	0.21630	0.00330	0.08348	0.00063	0.87217	1271	11	1262	18	1280	15	99
BH79r-11	r†	798	43.62	0.06	4.59E-04	2.36300	0.03700	0.20860	0.00320	0.08194	0.00066	0.86516	1231	11	1222	17	1244	16	98
BH79r-12	r†	2008	210.9	0.11	1.68E-04	2.96000	0.04800	0.23350	0.00390	0.09171	0.00067	0.90191	1397	12	1353	20	1461	14	93
BH79r-13	r†	1896	42.5	0.02	1.85E-04	2.61600	0.04200	0.22100	0.00360	0.08537	0.00066	0.88584	1305	12	1287	19	1324	15	97
BH79r-15	r†	1249	79.75	0.07	2.89E-04	2.50700	0.03800	0.21150	0.00340	0.08591	0.00071	0.86158	1274	11	1237	18	1336	16	93
BH79r-16	r†	2204	138.3	0.06	1.93E-04	2.62800	0.04000	0.20490	0.00320	0.09329	0.00099	0.76345	1308	11	1201	17	1493	20	80
BH79r-17	r*	1470	66.34	0.05	2.60E-04	2.38300	0.03600	0.20890	0.00330	0.08260	0.00063	0.87912	1237	11	1223	18	1260	15	97
BH79r-20	r†	1056	38.89	0.04	3.38E-04	2.31000	0.03400	0.20550	0.00310	0.08137	0.00065	0.85660	1215	10	1205	17	1230	16	98
Sample BH95																			
BH95-2	c	247.3	182.1	0.73	5.55E-03	5.03200	0.09400	0.31980	0.00690	0.11422	0.00053	0.98369	1824	16	1789	34	1867	8	96
BH95-3	c	103.7	74.3	0.73	1.28E-02	5.07300	0.09100	0.32380	0.00700	0.11390	0.00061	0.98048	1831	15	1808	34	1862	10	97
BH95-4	c	139.9	95.2	0.69	8.62E-03	5.57900	0.09800	0.34770	0.00750	0.11633	0.00042	0.99900	1913	15	1924	36	1900	6	101
BH95-5	r†	1171	5.5	0.00	1.65E-03	2.40700	0.04400	0.21350	0.00470	0.08165	0.00027	0.99900	1245	13	1247	25	1237	6	101
BH95-6	c	360.9	479	1.36	3.70E-03	4.93300	0.09500	0.31370	0.00700	0.11467	0.00054	0.98507	1808	16	1759	34	1875	9	94
BH95-7	r†	1120	62.2	0.05	1.67E-03	2.51800	0.06000	0.21710	0.00550	0.08413	0.00029	0.99204	1277	17	1267	29	1295	7	98
BH95-8	c	143.2	118.2	0.85	9.55E-03	4.23100	0.08500	0.28970	0.00640	0.10630	0.00083	0.93583	1680	17	1640	32	1736	14	94
BH95-9	c	108.2	75.3	0.72	1.07E-02	5.17700	0.09600	0.32900	0.00740	0.11452	0.00063	0.98241	1849	16	1834	36	1872	10	98
BH95-10	c	103.1	75.3	0.75	1.09E-02	5.38500	0.11000	0.33690	0.00790	0.11623	0.00051	0.98944	1882	17	1871	38	1899	8	99
BH95-11	c	1050	581	0.57	1.34E-03	3.53100	0.09200	0.26450	0.00740	0.09679	0.00035	0.99357	1533	21	1513	38	1563	7	97
BH95-13	c	186.2	190.7	1.06	5.61E-03	5.49800	0.09400	0.34160	0.00710	0.11678	0.00043	0.99900	1900	15	1894	34	1907	7	99
BH95-17	r†	1742	3.9	0.00	8.27E-04	2.57500	0.05400	0.23040	0.00560	0.08092	0.00015	0.99900	1293	15	1336	29	1219	4	110
BH95-23	c	206.7	164.5	0.83	4.50E-03	5.44000	0.16000	0.33980	0.00980	0.11664	0.00079	0.97315	1891	25	1885	47	1905	12	99
BH95-24	r†	1573	33.8	0.02	8.85E-04	2.66900	0.07500	0.22020	0.00650	0.08773	0.00042	0.98740	1319	21	1282	35	1376	9	93
BH95-27	c	100.7	89.6	0.93	8.20E-03	5.55000	0.16000	0.34750	0.01000	0.11537	0.00064	0.98145	1907	24	1922	49	1886	10	102
BH95-28	c	126.4	94.43	0.78	6.67E-03	5.43000	0.14000	0.34050	0.00920	0.11552	0.00065	0.97837	1889	22	1889	44	1888	10	100
BH95-29	c	199.6	113.6	0.59	4.19E-03	5.33800	0.13000	0.33600	0.00930	0.11490	0.00045	0.99900	1874	20	1867	45	1878	7	99
BH95-32	c	347.1	353.8	1.07	2.20E-03	5.44000	0.13000	0.34000	0.01000	0.11621	0.00052	0.99900	1896	26	1886	49	1899	8	99
BH95-34	c	145.4	125.1	0.91	5.17E-03	5.30900	0.13000	0.33740	0.00880	0.11395	0.00059	0.98100	1869	20	1873	42	1863	9	101
BH95-37	c	206.9	152.7	0.78	3.34E-03	5.81000	0.15000	0.36610	0.01000	0.11480	0.00057	0.98411	1947	22	2010	48	1877	9	107
BH95-38	c	297.1	136.7	0.48	2.66E-03	5.06200	0.11000	0.32390	0.00800	0.11327	0.00051	0.98932	1829	19	1808	39	1852	8	98
BH95-39	c	147.6	91.8	0.65	5.21E-03	4.94000	0.13000	0.31880	0.00900	0.11225	0.00062	0.98194	1807	22	1783	44	1836	10	97

Appendix A. (continued)

Analysis	Location	^{238}U (ppm)	^{232}Th (ppm)	^{232}Th/^{238}U	204/206	^{207}Pb/^{235}U	2σ	^{206}Pb/^{238}U	2σ	^{207}Pb/^{206}Pb	2σ	Rho	Age (Ma) ^{207}Pb/^{235}U	2σ	^{206}Pb/^{238}U	2σ	^{207}Pb/^{206}Pb	2σ	Conc. (%)
BH95-41	c	126.9	79.5	0.66	6.73E-03	3.94300	0.09900	0.27690	0.00760	0.10311	0.00058	0.98101	1622	20	1575	38	1681	10	94
BH95-42	r†	1652	3.61	0.00	6.79E-04	2.44900	0.05300	0.21540	0.00550	0.08227	0.00039	0.99338	1257	16	1257	29	1252	9	100
BH95-43	c	407	139.7	0.36	2.15E-03	3.58500	0.09800	0.26190	0.00750	0.09901	0.00042	0.98959	1545	22	1499	38	1605	8	93
BH95-45	c	93.5	79.9	0.90	7.12E-03	5.43000	0.15000	0.34090	0.00900	0.11517	0.00082	0.96627	1889	23	1891	43	1882	13	100
BH95-46	c	150.3	110.4	0.77	4.60E-03	5.34000	0.17000	0.33400	0.01100	0.11639	0.00061	0.98748	1874	28	1857	54	1901	9	98
BH95-47	c	705	350.4	0.52	1.34E-03	3.06900	0.09700	0.23440	0.00770	0.09474	0.00050	0.98733	1424	24	1357	40	1523	10	89
BH95-48	c	123.7	117.2	0.99	5.01E-03	5.61000	0.15000	0.35300	0.00980	0.11510	0.00110	0.93919	1917	22	1948	47	1881	16	104
BH95-49	c	145.7	178.5	1.29	4.58E-03	5.16700	0.12000	0.32850	0.00820	0.11409	0.00057	0.98108	1846	19	1830	40	1865	9	98
BH95-52	c	152	105.9	0.74	4.48E-03	4.80200	0.12000	0.31630	0.00850	0.11022	0.00053	0.98543	1784	20	1771	42	1803	9	98
BH95-56	c	212.4	128.3	0.64	2.80E-03	5.58000	0.14000	0.34730	0.01000	0.11650	0.00056	0.99350	1912	22	1921	48	1903	9	101
BH95-57	c	125.6	78.7	0.66	4.56E-03	5.51000	0.17000	0.34560	0.01100	0.11570	0.00058	0.98769	1899	27	1912	54	1891	9	101
BH95-58	c	324.2	185.3	0.61	1.81E-03	5.56000	0.16000	0.34560	0.01100	0.11666	0.00046	0.99900	1908	25	1913	50	1906	7	100
BH95-60	c	157.9	95.7	0.64	3.89E-03	5.03500	0.11000	0.32490	0.00830	0.11257	0.00043	0.99900	1824	19	1813	40	1841	7	98
BH95-61	c	99.3	56.8	0.61	6.18E-03	5.48000	0.25000	0.34200	0.01500	0.11680	0.00100	0.98246	1894	40	1894	72	1908	15	99
BH95-62	c	408.8	653	1.68	1.36E-03	5.60000	0.14000	0.34780	0.00940	0.11658	0.00047	0.99101	1916	21	1924	45	1904	7	101
BH95-64	c	355.7	294.7	0.87	1.65E-03	5.41000	0.18000	0.33390	0.01200	0.11813	0.00082	0.98283	1885	28	1856	56	1928	12	96
BH95-65	c	179	121.2	0.71	3.17E-03	5.54000	0.21000	0.34500	0.01300	0.11703	0.00073	0.98640	1904	32	1908	61	1911	11	100
BH95-66	c	288.6	174.5	0.64	1.87E-03	5.70200	0.12000	0.35610	0.00850	0.11620	0.00043	0.99431	1931	18	1963	40	1899	7	103
BH95-67	c	276.3	369	1.38	1.97E-03	5.52000	0.17000	0.34600	0.01200	0.11654	0.00046	0.99900	1902	26	1914	59	1904	7	101
BH95-68	r†	710	4.69	0.01	1.12E-03	2.95000	0.06900	0.24520	0.00620	0.08735	0.00038	0.98704	1394	18	1413	32	1368	8	103
BH95-69	c	167.1	128.5	0.81	3.23E-03	5.37000	0.13000	0.33890	0.00900	0.11487	0.00062	0.98163	1879	20	1881	43	1878	10	100
BH95-70	c	175.4	155.3	0.92	3.05E-03	5.50000	0.14000	0.34450	0.00960	0.11597	0.00052	0.98993	1899	22	1907	46	1895	8	101
BH95-71	c	134.9	87.97	0.68	4.31E-03	4.66900	0.11000	0.30860	0.00820	0.10935	0.00056	0.98630	1761	20	1734	40	1789	9	97
BH95-72	c	202.4	163.1	0.85	2.73E-03	5.51000	0.27000	0.34000	0.01600	0.11786	0.00073	0.99250	1898	41	1886	74	1924	11	98
BH95-73	c	403	260.8	0.68	1.44E-03	4.79000	0.13000	0.31310	0.00910	0.11088	0.00034	0.99900	1782	22	1755	45	1814	6	97
BH95-74	r*	106.6	102.8	1.01	7.98E-03	2.33400	0.06100	0.20830	0.00570	0.08109	0.00070	0.94896	1222	19	1220	31	1223	17	100
BH95-75	c	192.4	166.7	0.90	2.68E-03	5.54000	0.16000	0.34270	0.01000	0.11758	0.00076	0.97527	1906	25	1899	48	1919	12	99
BH95-77	c	213.5	223.9	1.10	2.36E-03	5.27000	0.15000	0.33640	0.00990	0.11322	0.00061	0.98323	1864	24	1869	48	1852	10	101
BH95-78	c	227	125.9	0.58	2.29E-03	5.32000	0.14000	0.33390	0.00930	0.11527	0.00054	0.98664	1871	22	1857	45	1886	9	98
BH95-79	r†	181.6	222.3	1.28	4.66E-03	2.30400	0.05500	0.20640	0.00540	0.08083	0.00045	0.97939	1213	17	1209	29	1217	11	99
BH95-80	c	174.8	115.2	0.69	2.83E-03	5.58000	0.15000	0.34680	0.01100	0.11700	0.00065	0.99900	1912	24	1918	52	1911	10	100
BH95-83	c	155	170.3	1.15	3.11E-03	5.28000	0.14000	0.33550	0.01000	0.11379	0.00050	0.99464	1865	23	1864	49	1861	8	100
BH95-86	r†	1167	2.64	0.00	6.40E-04	2.48800	0.06600	0.21630	0.00610	0.08318	0.00038	0.98792	1268	19	1262	32	1273	9	99
BH95-87	c	128.6	151.1	1.21	3.88E-03	5.23000	0.15000	0.33180	0.01000	0.11421	0.00070	0.97950	1855	24	1846	49	1867	11	99
BH95-88	c	60.4	24.73	0.43	8.03E-03	5.30000	0.17000	0.33730	0.01100	0.11379	0.00080	0.97651	1866	27	1872	54	1860	13	101
BH95-90	c	229.8	227	1.01	4.67E-03	5.81000	0.23000	0.35800	0.01400	0.11708	0.00049	0.99442	1945	34	1972	66	1912	7	103
BH95-91	c	99.8	67.7	0.70	1.86E-03	4.60000	0.13000	0.31150	0.00920	0.10716	0.00082	0.96590	1748	24	1747	45	1751	14	100
BH95-93	c	413.1	314.1	0.78	5.04E-03	5.81400	0.13000	0.35770	0.00890	0.11762	0.00045	0.99256	1948	19	1971	42	1920	7	103
BH95-94	c	249	134.3	0.56	1.05E-03	5.87000	0.19000	0.36150	0.01200	0.11747	0.00063	0.98693	1955	29	1988	57	1918	10	104
BH95-95	r†	942	4.72	0.00	1.70E-03	3.02300	0.06700	0.24750	0.00610	0.08869	0.00037	0.98971	1413	17	1426	31	1397	8	102
BH95-96	c	151	112	0.75	6.59E-04	4.61200	0.12000	0.30680	0.00930	0.10981	0.00045	0.99900	1754	24	1724	46	1796	8	96

Appendix A. (continued)

Analysis	Location	^{238}U (ppm)	^{232}Th (ppm)	^{232}Th/^{238}U	204/206	^{207}Pb/^{235}U	2σ	^{206}Pb/^{238}U	2σ	^{207}Pb/^{206}Pb	2σ	Rho	Age (Ma) ^{207}Pb/^{235}U	2σ	^{206}Pb/^{238}U	2σ	^{207}Pb/^{206}Pb	2σ	Conc. (%)
BH95-97	r†	1500	7	0.00	3.30E-03	2.48700	0.06100	0.21920	0.00600	0.08204	0.00023	0.99900	1268	18	1278	32	1246	6	103
BH95-98	r†	1239	5.2	0.00	4.56E-04	2.54400	0.06400	0.22080	0.00600	0.08346	0.00041	0.98532	1284	18	1286	32	1280	10	100
BH95-99	c	94.7	73.4	0.81	5.72E-04	5.65000	0.15000	0.35330	0.01000	0.11592	0.00057	0.98596	1922	23	1949	49	1896	10	103
Sample BH98																			
BH98-1	c	837	1435	1.76	4.69E-04	2.24700	0.05700	0.20360	0.00310	0.08017	0.00120	0.84310	1195	18	1194	16	1201	30	99
BH98-2	c	384.6	284.9	0.76	1.02E-03	2.23400	0.07600	0.20260	0.00570	0.08009	0.00120	0.90082	1190	26	1189	31	1199	29	99
BH98-3	c	424	598	1.44	9.23E-04	2.23800	0.05500	0.20200	0.00320	0.08041	0.00130	0.76228	1193	17	1186	17	1207	31	98
BH98-4	c	52.6	125.3	2.44	7.37E-03	2.24100	0.06200	0.20210	0.00360	0.08059	0.00150	0.74702	1193	19	1186	19	1210	37	98
BH98-5	c	64.1	151	2.41	6.24E-03	2.21500	0.06000	0.19980	0.00300	0.08047	0.00140	0.80709	1185	19	1174	16	1208	34	97
BH98-6	c	315.4	262.4	0.85	1.28E-03	2.22300	0.05800	0.20110	0.00350	0.08030	0.00120	0.83719	1188	18	1181	19	1204	30	98
BH98-7	c	303.5	195	0.66	1.34E-03	2.21100	0.06100	0.20130	0.00370	0.07977	0.00120	0.86049	1184	19	1182	20	1191	30	99
BH98-8	c	54.1	124.4	2.35	7.28E-03	2.24200	0.06500	0.20300	0.00380	0.08023	0.00140	0.81669	1193	20	1191	21	1202	33	99
BH98-9	c	418.9	515.8	1.26	9.61E-04	2.22300	0.05600	0.20070	0.00310	0.08045	0.00130	0.78650	1188	18	1183	15	1208	31	98
BH98-10	c	45.5	101.2	2.27	9.01E-03	2.26200	0.06500	0.20090	0.00370	0.08176	0.00140	0.82358	1199	20	1180	20	1239	34	95
BH98-11	c	53.8	127.9	2.43	7.69E-03	2.22600	0.05700	0.19970	0.00310	0.08096	0.00130	0.80356	1189	18	1174	16	1220	33	96
BH98-12	c	62.5	148	2.42	6.42E-03	2.19700	0.06100	0.20020	0.00390	0.07976	0.00140	0.77864	1179	19	1176	21	1190	34	99
BH98-13	c	292.2	238.7	0.83	1.38E-03	2.23600	0.05800	0.20440	0.00320	0.07946	0.00120	0.84940	1192	18	1199	17	1183	30	101
BH98-14	c	596	542	0.93	6.85E-04	2.25300	0.06400	0.20340	0.00400	0.08035	0.00120	0.86875	1197	21	1193	22	1205	31	99
BH98-15	c	85.4	197	2.35	4.68E-03	2.27000	0.06300	0.20530	0.00360	0.08031	0.00130	0.83806	1202	20	1204	20	1204	32	100
BH98-16	c	373.8	455.3	1.24	1.07E-03	2.25100	0.05700	0.20360	0.00330	0.08032	0.00120	0.82926	1196	18	1194	18	1205	30	99
BH98-17	c	462.4	542.6	1.19	8.56E-04	2.26800	0.05600	0.20500	0.00280	0.08038	0.00120	0.85003	1202	17	1202	15	1206	30	100
BH98-18	c	53.46	130.1	2.48	7.51E-03	2.24400	0.05700	0.20340	0.00330	0.08020	0.00140	0.73246	1194	18	1193	18	1201	33	99
BH98-19	c	78.6	190.5	2.47	5.41E-03	2.22800	0.05600	0.20090	0.00330	0.08040	0.00130	0.77523	1189	18	1180	18	1206	32	98
BH98-20	c	305	299	1.01	1.35E-03	2.22500	0.05800	0.20210	0.00330	0.08000	0.00120	0.84711	1188	18	1186	17	1197	31	99
BH98-21	c	413.4	386	0.95	9.57E-04	2.26100	0.05800	0.20400	0.00330	0.08052	0.00120	0.84058	1200	18	1197	17	1209	30	99
BH98-22	c	756	1199	1.62	5.48E-04	2.26100	0.05400	0.20360	0.00280	0.08072	0.00120	0.81980	1200	17	1194	15	1214	30	98
BH98-23	c	50.4	122.1	2.47	7.97E-03	2.23200	0.06100	0.20270	0.00360	0.08003	0.00150	0.73246	1190	19	1189	19	1196	37	99
BH98-24	c	462.9	590.3	1.30	8.49E-04	2.25700	0.06000	0.20380	0.00360	0.08047	0.00120	0.84793	1198	19	1195	20	1208	30	99
BH98-25	c	313.7	237.7	0.77	1.27E-03	2.24500	0.05700	0.20420	0.00320	0.07986	0.00120	0.83496	1195	18	1198	17	1193	30	100
BH98-26	c	596	812.8	1.39	6.94E-04	2.24800	0.05700	0.20230	0.00330	0.08073	0.00120	0.83177	1196	18	1188	18	1215	30	98
BH98-27	c	528.9	605	1.16	7.55E-04	2.25600	0.05300	0.20340	0.00260	0.08054	0.00120	0.82137	1198	17	1194	14	1210	30	99
BH98-28	c	759.1	1303	1.74	5.46E-04	2.27300	0.05700	0.20310	0.00330	0.08131	0.00120	0.82837	1203	18	1192	18	1229	30	97
BH98-29	c	67.3	161.1	2.44	5.90E-03	2.26100	0.06000	0.20520	0.00290	0.08038	0.00130	0.85641	1200	19	1203	16	1205	32	100
BH98-30	c	366.6	255.7	0.71	1.10E-03	2.24100	0.06300	0.20320	0.00380	0.08010	0.00120	0.87079	1193	20	1192	20	1199	30	99
BH98-31	c	576	680	1.20	6.97E-04	2.26100	0.05800	0.20340	0.00330	0.08075	0.00120	0.84148	1200	18	1193	17	1215	30	98
BH98-32	c	305.9	306.6	1.02	1.38E-03	2.23900	0.05200	0.20330	0.00250	0.07999	0.00120	0.81504	1193	16	1193	14	1197	30	100
BH98-33	c	47.7	119.5	2.55	8.62E-03	2.20700	0.06100	0.20160	0.00400	0.07957	0.00140	0.77320	1182	19	1184	22	1185	35	100
BH98-34	c	271.7	271	1.01	1.52E-03	2.20400	0.05000	0.20180	0.00270	0.07935	0.00120	0.76593	1182	16	1185	14	1181	30	100
BH98-35	c	331.5	323.9	0.99	1.27E-03	2.23800	0.05900	0.20230	0.00330	0.08040	0.00120	0.85844	1192	19	1187	18	1206	30	98
BH98-36	c	62.5	149.4	2.43	6.56E-03	2.18800	0.05600	0.19940	0.00270	0.07971	0.00140	0.76455	1177	18	1172	14	1189	34	99
BH98-37	c	92.02	213.6	2.35	4.47E-03	2.18700	0.05200	0.19980	0.00240	0.07953	0.00130	0.77455	1177	17	1174	13	1185	32	99

Appendix A. (continued)

Analysis	Location	^{238}U (ppm)	^{232}Th (ppm)	^{232}Th/^{238}U	204/206	^{207}Pb/^{235}U	2σ	^{206}Pb/^{238}U	2σ	^{207}Pb/^{206}Pb	2σ	Rho	Age (Ma) ^{207}Pb/^{235}U	2σ	^{206}Pb/^{238}U	2σ	^{207}Pb/^{206}Pb	2σ	Conc. (%)
Sample BH100																			
BH100-2	c	160.2	88.4	0.56	2.57E-03	2.41500	0.08100	0.21200	0.00470	0.08252	0.00120	0.94474	1247	24	1240	25	1257	28	99
BH100-3	c	534	438.6	0.83	7.82E-04	2.44100	0.07900	0.21220	0.00440	0.08323	0.00120	0.94587	1255	23	1241	23	1277	30	97
BH100-4	c	276.5	111.9	0.41	1.54E-03	2.43600	0.07900	0.21350	0.00440	0.08275	0.00110	0.97235	1253	23	1248	24	1263	27	99
BH100-5	c	341.3	274	0.81	1.26E-03	2.56300	0.08400	0.22300	0.00460	0.08342	0.00120	0.95607	1290	24	1298	24	1279	27	101
BH100-6	c	273.8	88	0.33	1.51E-03	2.41500	0.08100	0.21170	0.00450	0.08269	0.00110	0.98172	1247	24	1238	24	1262	26	98
BH100-7	c	195	69.9	0.37	2.15E-03	2.36700	0.07600	0.21090	0.00450	0.08167	0.00110	0.95227	1232	23	1233	24	1237	27	100
BH100-9	c	94.5	26.3	0.28	4.45E-03	2.35800	0.08000	0.20840	0.00460	0.08238	0.00120	0.95215	1230	24	1220	25	1254	29	97
BH100-11	c	379.1	297	0.79	1.10E-03	2.35300	0.07700	0.20990	0.00440	0.08172	0.00110	0.96877	1228	23	1228	23	1239	27	99
BH100-15	c	282	180.3	0.65	1.52E-03	2.33800	0.07600	0.20820	0.00440	0.08193	0.00110	0.96294	1224	23	1219	23	1244	27	98
BH100-16	c	279	183.8	0.67	1.49E-03	2.47800	0.08100	0.21980	0.00460	0.08222	0.00120	0.94538	1266	24	1281	24	1250	27	102
BH100-17	c	129.4	51.27	0.40	3.25E-03	2.39500	0.07900	0.21220	0.00450	0.08221	0.00120	0.94688	1241	24	1241	24	1250	28	99
BH100-18	c	281.8	193	0.69	1.43E-03	2.44600	0.08300	0.21740	0.00470	0.08196	0.00110	0.98058	1256	24	1268	25	1244	27	102
BH100-19	c	299.2	164.7	0.56	1.46E-03	2.38700	0.07800	0.21180	0.00430	0.08207	0.00110	0.98002	1239	23	1238	23	1247	26	99
BH100-20	c	497.1	379.7	0.78	8.47E-04	2.43300	0.07900	0.21380	0.00440	0.08276	0.00110	0.97360	1252	23	1249	23	1263	27	99
BH100-21	c	164.4	64.85	0.40	2.61E-03	2.41400	0.07900	0.21250	0.00430	0.08263	0.00120	0.95855	1247	23	1242	23	1260	28	99
BH100-22	c	329	225.1	0.70	1.30E-03	2.44800	0.08100	0.21410	0.00470	0.08299	0.00110	0.96443	1257	24	1251	25	1269	27	99
BH100-24	c	305.6	172.2	0.57	1.34E-03	2.43300	0.08100	0.21430	0.00470	0.08249	0.00110	0.96661	1252	24	1251	25	1257	27	100
BH100-25	c	405	295.5	0.74	1.12E-03	2.38100	0.07700	0.21050	0.00430	0.08208	0.00110	0.97146	1237	23	1231	23	1247	27	99
BH100-26	c	648	430.3	0.68	7.18E-04	2.32600	0.08200	0.20450	0.00470	0.08238	0.00120	0.96198	1220	25	1199	25	1254	28	96
BH100-27	c	341.1	108	0.28	1.23E-03	2.32900	0.07700	0.20670	0.00450	0.08168	0.00110	0.96257	1221	24	1211	24	1238	27	98
BH100-28	c	401.9	152.1	0.39	1.08E-03	2.33400	0.07600	0.20790	0.00440	0.08140	0.00110	0.96177	1222	23	1217	23	1231	26	99
BH100-29	c	134.9	62.1	0.47	3.23E-03	2.37700	0.07900	0.20940	0.00460	0.08232	0.00120	0.94142	1236	24	1225	24	1253	28	98
BH100-30	c	293	134.3	0.47	1.48E-03	2.36400	0.08000	0.20760	0.00480	0.08248	0.00120	0.93817	1231	24	1216	26	1257	27	97
BH100-31	c	151	79	0.51	2.81E-03	2.45300	0.08400	0.21630	0.00480	0.08208	0.00120	0.95494	1258	24	1262	26	1247	28	101
BH100-32	c	584	606	1.06	7.34E-04	2.36200	0.07900	0.20650	0.00440	0.08274	0.00110	0.97937	1231	24	1210	24	1263	26	96
BH100-34	c	274.1	132.9	0.50	1.56E-03	2.46700	0.08000	0.21610	0.00440	0.08251	0.00110	0.97568	1262	24	1261	23	1257	27	100
BH100-35	c	573	347	0.62	7.63E-04	2.39200	0.08400	0.20800	0.00490	0.08294	0.00110	0.97445	1240	25	1218	26	1268	27	96
BH100-36	c	432	330.4	0.78	9.67E-04	2.42800	0.08000	0.21300	0.00450	0.08238	0.00110	0.97232	1251	24	1245	24	1254	27	99
BH100-37	c	242	88.29	0.37	1.85E-03	2.45600	0.08300	0.21370	0.00460	0.08302	0.00110	0.98280	1259	24	1248	24	1270	27	98
BH100-38	c	427	301.6	0.73	1.00E-03	2.46500	0.08200	0.21410	0.00460	0.08312	0.00110	0.97457	1262	24	1250	25	1272	27	98
BH100-39	c	124.6	67.1	0.55	3.25E-03	2.44600	0.08600	0.21190	0.00480	0.08335	0.00130	0.94549	1256	25	1239	26	1277	30	97

Microstructural location classification: c, oscillatory-zoned core; r*, luminescent rim; r†, dark rim; r^, weakly luminescent rim.
Additional classifications for metasedimentary samples: c†, dark unzoned grain; c^, weakly luminescent unzoned grain.

Appendix B. Lu-Hf isotope analyses

Spot ID	$^{176}Hf/^{177}Hf$	2 S.E.	$^{176}Lu/^{177}Hf$	$^{176}Yb/^{177}Hf$	$Hf_{initial}$	$\varepsilon_{Hf}(t)$	2σ	$T_{DM(crustal)}$ (Ga)	Age (Ma)*
Sample BH12									
BH12-1	0.281725	0.000077	0.001207	0.0575	0.281687	-1.07	2.70	2.42	1678
BH12-2	0.281700	0.000090	0.000962	0.0451	0.281669	-1.62	3.15	2.45	1681
BH12-3	0.281740	0.000100	0.001242	0.05937	0.281701	-0.71	3.50	2.39	1672
BH12-5	0.281620	0.000093	0.000664	0.0274	0.281599	-3.54	3.26	2.59	1707
BH12-6	0.281630	0.000100	0.001248	0.0545	0.281590	-4.59	3.50	2.63	1674
BH12-8	0.281710	0.000120	0.001998	0.0917	0.281645	-1.87	4.20	2.49	1707
BH12-9	0.281700	0.000120	0.000848	0.0381	0.281674	-2.65	4.20	2.48	1629
BH12-10	0.281740	0.000100	0.001129	0.0529	0.281702	1.26	3.50	2.34	1755
BH12-12	0.281700	0.000100	0.000767	0.0353	0.281675	-0.86	3.50	2.43	1705
BH12-13	0.281690	0.000120	0.001476	0.0655	0.281644	-3.26	4.20	2.53	1649
BH12-14	0.281630	0.000084	0.001546	0.0676	0.281580	-4.04	2.94	2.63	1714
BH12-15	0.281640	0.000120	0.001063	0.04856	0.281606	-3.74	4.20	2.59	1687
BH12-16	0.281702	0.000090	0.001345	0.06416	0.281659	-1.42	3.15	2.46	1706
BH12-17	0.281660	0.000130	0.001453	0.0681	0.281613	-2.72	4.55	2.55	1721
BH12-18	0.281624	0.000095	0.001258	0.0533	0.281584	-4.33	3.33	2.63	1696
BH12-19	0.281634	0.000099	0.000701	0.03124	0.281612	-4.77	3.47	2.61	1632
BH12-20	0.281657	0.000087	0.001563	0.0593	0.281607	-3.39	3.05	2.58	1701
BH12-21	0.281652	0.000095	0.002042	0.075	0.281586	-3.94	3.33	2.62	1709
BH12-22	0.281671	0.000093	0.001242	0.0533	0.281631	-2.72	3.26	2.53	1692
BH12-23	0.281700	0.000100	0.000906	0.04165	0.281670	-0.51	3.50	2.42	1728
BH12-24	0.281740	0.000110	0.001028	0.04564	0.281706	0.86	3.85	2.34	1732
BH12-25	0.281680	0.000100	0.000349	0.0162	0.281669	-2.70	3.50	2.48	1634
BH12-27	0.281670	0.000110	0.001066	0.04937	0.281636	-2.93	3.85	2.53	1675
BH12-28	0.281620	0.000130	0.002090	0.0745	0.281552	-4.81	4.55	2.68	1724
BH12-29	0.281720	0.000110	0.000788	0.03792	0.281694	0.25	3.85	2.37	1724
BH12-30	0.281640	0.000120	0.000765	0.03472	0.281616	-4.60	4.20	2.60	1633
BH12-31	0.281694	0.000087	0.000602	0.02664	0.281675	-1.03	3.05	2.43	1698
BH12-32	0.281740	0.000110	0.001248	0.05457	0.281699	0.27	3.85	2.37	1717
BH12-33	0.281705	0.000099	0.000816	0.04091	0.281678	-0.51	3.47	2.41	1715
BH12-34	0.281670	0.000100	0.000767	0.03578	0.281645	-2.16	3.50	2.50	1695
BH12-35	0.281686	0.000099	0.000862	0.0429	0.281659	-2.07	3.47	2.48	1678
BH12-36	0.281630	0.000120	0.000679	0.0324	0.281608	-2.97	4.20	2.56	1717
Sample BH38									
BH38-1	0.281712	0.000076	0.000419	0.01924	0.281702	-11.19	2.66	2.67	1210
BH38-2	0.281752	0.000083	0.000367	0.0167	0.281744	-9.98	2.91	2.59	1199
BH38-3	0.281715	0.000073	0.000417	0.01827	0.281706	-11.69	2.56	2.68	1183
BH38-4	0.281752	0.000081	0.000402	0.01771	0.281743	-10.11	2.84	2.59	1194
BH38-5	0.281710	0.000069	0.000366	0.01617	0.281702	-11.60	2.42	2.68	1193
BH38-6	0.281774	0.000079	0.000338	0.0157	0.281766	-8.84	2.77	2.53	1214
BH38-8	0.281706	0.000073	0.000346	0.0156	0.281698	-11.80	2.56	2.69	1190
BH38-10	0.281697	0.000071	0.000381	0.01676	0.281688	-12.21	2.49	2.72	1187
BH38-11	0.281723	0.000071	0.000579	0.0258	0.281710	-11.20	2.49	2.66	1198
BH38-12	0.281716	0.000060	0.000583	0.0291	0.281703	-11.59	2.10	2.68	1192
BH38-13	0.281750	0.000075	0.001044	0.0516	0.281727	-10.92	2.63	2.64	1184
BH38-14	0.281749	0.000073	0.000360	0.01624	0.281741	-10.05	2.56	2.60	1201
BH38-16	0.281694	0.000072	0.000301	0.01376	0.281687	-12.21	2.52	2.72	1189
BH38-17	0.281738	0.000065	0.000599	0.0266	0.281725	-10.75	2.28	2.63	1195
BH38-18	0.281773	0.000077	0.000306	0.01354	0.281766	-8.92	2.70	2.53	1211
BH38-19	0.281716	0.000063	0.000342	0.01468	0.281708	-10.97	2.21	2.66	1211
BH38-20	0.281709	0.000072	0.001166	0.0613	0.281683	-12.08	2.52	2.72	1202
BH38-21	0.281738	0.000070	0.000433	0.0191	0.281728	-10.51	2.45	2.62	1200
BH38-22	0.281762	0.000075	0.000880	0.0428	0.281742	-10.24	2.63	2.60	1190
BH38-23	0.281745	0.000095	0.002017	0.1062	0.281699	-11.42	3.33	2.68	1205
BH38-24	0.281684	0.000069	0.000314	0.01422	0.281677	-12.71	2.42	2.74	1183
BH38-26	0.281795	0.000075	0.000579	0.02568	0.281782	-8.36	2.63	2.50	1211
BH38-27	0.281837	0.000086	0.001902	0.0973	0.281794	-8.08	3.01	2.48	1205
BH38-28	0.281712	0.000055	0.000419	0.01938	0.281702	-10.77	1.93	2.66	1229
BH38-30	0.281739	0.000075	0.000672	0.0305	0.281724	-10.87	2.63	2.64	1191
BH38-31	0.281749	0.000079	0.000398	0.01773	0.281740	-9.78	2.77	2.59	1214
Sample BH62									
BH62-1	0.281166	0.000087	0.000453	0.02121	0.281142	3.53	3.05	2.96	2710
BH62-7	0.281097	0.000088	0.000443	0.01893	0.281074	1.10	3.08	3.10	2710
BH62-9	0.281227	0.000079	0.000469	0.0206	0.281203	5.68	2.77	2.83	2710
BH62-16	0.281191	0.000075	0.000268	0.01161	0.281177	4.77	2.63	2.88	2710
BH62-33	0.281104	0.000081	0.000814	0.03698	0.281062	0.66	2.84	3.13	2710
BH62-47	0.281184	0.000065	0.000906	0.0414	0.28	3.34	2.28	2.97	2710

Appendix B. (continued)

Spot ID	$^{176}Hf/^{177}Hf$	2 S.E.	$^{176}Lu/^{177}Hf$	$^{176}Yb/^{177}Hf$	$Hf_{initial}$	$\varepsilon_{Hf}(t)$	2σ	$T_{DM(crustal)}$ (Ga)	Age (Ma)*
BH62-49	0.281115	0.000091	0.000538	0.02344	0.281087	1.56	3.19	3.07	2710
BH62-51	0.281193	0.000072	0.000349	0.01606	0.281175	4.69	2.52	2.89	2710
BH62-56	0.281110	0.000067	0.000803	0.03634	0.281068	0.90	2.35	3.11	2710
BH62-61	0.281194	0.000086	0.000543	0.02383	0.281166	4.37	3.01	2.91	2710
BH62-65	0.281225	0.000081	0.000942	0.04054	0.281176	4.73	2.84	2.89	2710
BH62-67	0.281189	0.000072	0.000451	0.0204	0.281166	4.36	2.52	2.91	2710
BH62-71	0.281118	0.000078	0.000961	0.04324	0.281068	0.89	2.73	3.11	2710
BH62-73	0.281165	0.000080	0.000700	0.03152	0.281129	3.04	2.80	2.99	2710
BH62-74	0.281141	0.000085	0.000747	0.03324	0.281102	2.10	2.98	3.04	2710
BH62-80	0.281146	0.000070	0.000904	0.042	0.281099	1.99	2.45	3.05	2710
BH62-87	0.281099	0.000079	0.000748	0.03412	0.281060	0.61	2.77	3.13	2710
BH62-88	0.281256	0.000085	0.002013	0.0913	0.281152	3.86	2.98	2.94	2710
BH62-92	0.281180	0.000093	0.001138	0.04877	0.281121	2.77	3.26	3.00	2710
BH62-95	0.281245	0.000096	0.001128	0.0505	0.281187	5.10	3.36	2.86	2710
Sample BH67									
BH67-1	0.281010	0.000080	0.001027	0.04034	0.280957	-3.03	2.8	3.34	2712
BH67-3	0.281110	0.000110	0.000528	0.02711	0.281083	1.45	3.85	3.08	2712
BH67-4	0.281092	0.000087	0.000320	0.01567	0.281075	1.19	3.045	3.10	2712
BH67-10	0.281187	0.000087	0.000645	0.02924	0.281154	3.97	3.045	2.93	2712
BH67-21	0.281109	0.000093	0.000394	0.01905	0.281089	1.66	3.255	3.07	2712
BH67-23	0.281064	0.000088	0.000365	0.01615	0.281045	0.11	3.08	3.16	2712
BH67-24	0.281210	0.000097	0.000494	0.0241	0.281184	5.07	3.395	2.87	2712
BH67-25	0.281126	0.000082	0.000424	0.02167	0.281104	2.21	2.87	3.04	2712
BH67-26	0.281113	0.000095	0.000480	0.02357	0.281088	1.65	3.325	3.07	2712
BH67-27	0.281180	0.000100	0.000653	0.02989	0.281146	3.71	3.5	2.95	2712
BH67-30	0.281121	0.000094	0.000924	0.04674	0.281073	1.11	3.29	3.10	2712
BH67-31	0.281080	0.000110	0.000455	0.02182	0.281056	0.52	3.85	3.14	2712
BH67-32	0.281070	0.000100	0.000533	0.02585	0.281042	0.02	3.5	3.17	2712
BH67-34	0.281131	0.000060	0.000466	0.02237	0.281107	2.31	2.1	3.03	2712
BH67-37	0.281019	0.000090	0.000765	0.03457	0.280979	-2.22	3.15	3.30	2712
Sample BH68									
BH68-4	0.280999	0.000090	0.000324	0.01483	0.280982	-0.94	3.15	3.26	2763
BH68-6	0.280978	0.000097	0.001251	0.0539	0.280912	-3.43	3.40	3.41	2763
BH68-7	0.281111	0.000098	0.000812	0.03731	0.281068	2.13	3.43	3.08	2763
BH68-8	0.281047	0.000096	0.000694	0.02896	0.281010	0.07	3.36	3.20	2763
BH68-9	0.280980	0.000100	0.001101	0.03912	0.280922	-3.08	3.50	3.39	2763
BH68-10	0.281025	0.000081	0.000515	0.02212	0.280998	-0.37	2.84	3.23	2763
BH68-11	0.281060	0.000100	0.000889	0.03733	0.281013	0.17	3.50	3.20	2763
BH68-15	0.281060	0.000110	0.001552	0.0762	0.280978	-1.08	3.85	3.27	2763
BH68-16	0.281032	0.000085	0.001417	0.0582	0.280957	-1.82	2.98	3.31	2763
BH68-17	0.281560	0.000100	0.000657	0.02687	0.281545	-17.02	3.50	3.02	1199
BH68-20	0.280993	0.000092	0.001936	0.0747	0.280891	-4.18	3.22	3.45	2763
BH68-21	0.280989	0.000099	0.000718	0.03169	0.280951	-2.03	3.47	3.33	2763
BH68-23	0.281026	0.000086	0.001341	0.0569	0.280955	-1.89	3.01	3.32	2763
BH68-24	0.281551	0.000080	0.000527	0.02354	0.281539	-15.99	2.80	3.00	1255
BH68-25	0.281001	0.000093	0.001203	0.05043	0.280937	-2.52	3.26	3.35	2763
BH68-26	0.280970	0.000093	0.000734	0.02713	0.280931	-2.74	3.26	3.37	2763
BH68-27	0.280988	0.000091	0.001384	0.0475	0.280915	-3.32	3.19	3.40	2763
BH68-28	0.281060	0.000110	0.001024	0.0446	0.281006	-0.08	3.85	3.21	2763
BH68-29	0.281060	0.000110	0.000608	0.02591	0.281028	0.70	3.85	3.17	2763
BH68-30	0.280978	0.000098	0.000505	0.01997	0.280951	-2.03	3.43	3.33	2763
BH68-31	0.281035	0.000088	0.000441	0.0207	0.281012	0.12	3.08	3.20	2763
BH68-32	0.281539	0.000094	0.001030	0.0394	0.281485	16.95	3.29	2.20	2763
BH68-33	0.280953	0.000092	0.000348	0.01355	0.280935	-2.62	3.22	3.36	2763
BH68-34	0.281000	0.000130	0.000660	0.02957	0.280965	-1.53	4.55	3.30	2763
Sample BH79									
BH79-1	0.281690	0.000100	0.001386	0.06131	0.281646	-2.78	3.50	2.51	1666
BH79-4	0.281770	0.000088	0.001020	0.0441	0.281738	0.47	3.08	2.32	1666
BH79-5	0.281703	0.000089	0.000664	0.0289	0.281682	-1.51	3.12	2.44	1666
BH79-7	0.281766	0.000093	0.000985	0.03876	0.281735	0.37	3.26	2.32	1666
BH79-8	0.281808	0.000071	0.000062	0.003634	0.281807	-6.56	2.49	2.42	1252
BH79-9	0.281820	0.000120	0.001847	0.0855	0.281762	1.32	4.20	2.26	1666
BH79-11	0.281693	0.000089	0.000740	0.03081	0.281670	-1.95	3.12	2.46	1666
BH79-12	0.281665	0.000092	0.001045	0.0436	0.281632	-3.29	3.22	2.54	1666
BH79-14	0.281723	0.000081	0.001024	0.04296	0.281691	-1.20	2.84	2.42	1666
BH79-16	0.281730	0.000100	0.001056	0.0451	0.281697	-0.99	3.50	2.40	1666
BH79-17	0.281716	0.000085	0.000903	0.03777	0.281688	-1.32	2.98	2.42	1666
BH79-18	0.281587	0.000098	0.000744	0.0356	0.281564	-5.72	3.43	2.69	1666

Appendix B. (continued)

Spot ID	$^{176}Hf/^{177}Hf$	2 S.E.	$^{176}Lu/^{177}Hf$	$^{176}Yb/^{177}Hf$	$Hf_{initial}$	$\varepsilon_{Hf}(t)$	2σ	$T_{DM(crustal)}$ (Ga)	Age (Ma)*
BH79-20	0.281680	0.000068	0.001200	0.0461	0.281642	-2.93	2.38	2.52	1666
BH79-21	0.281726	0.000067	0.001676	0.0713	0.281673	-1.83	2.35	2.46	1666
BH79-23	0.281692	0.000084	0.001222	0.0514	0.281653	-2.53	2.94	2.50	1666
BH79-24	0.281769	0.000097	0.000953	0.04207	0.281739	0.51	3.40	2.31	1666
BH79-26	0.281679	0.000094	0.000432	0.02029	0.281665	-2.10	3.29	2.47	1666
BH79-27	0.281645	0.000093	0.000960	0.04067	0.281615	-3.90	3.26	2.58	1666
BH79-28	0.281630	0.000120	0.000882	0.0437	0.281602	-4.35	4.20	2.61	1666
BH79-31	0.281734	0.000077	0.001031	0.0449	0.281701	-0.82	2.70	2.39	1666
BH79-32	0.281689	0.000076	0.000914	0.0349	0.281660	-2.29	2.66	2.48	1666
BH79-34	0.281760	0.000110	0.001335	0.05269	0.281718	-0.24	3.85	2.36	1666
BH79-37	0.281721	0.000097	0.001214	0.05224	0.281683	-1.49	3.40	2.43	1666
BH79-38	0.281776	0.000094	0.000122	0.00698	0.281773	-6.26	3.29	2.45	1317
BH79-39	0.281717	0.000090	0.000598	0.02936	0.281698	-0.94	3.15	2.40	1666
BH79-41	0.281778	0.000075	0.000296	0.01487	0.281771	-7.30	2.63	2.48	1275
BH79-43	0.281733	0.000089	0.001069	0.04616	0.281699	-0.90	3.12	2.40	1666
BH79-44	0.281741	0.000059	0.001360	0.05715	0.281698	-0.94	2.07	2.40	1666
BH79-45	0.281771	0.000082	0.000108	0.00643	0.281768	-7.16	2.87	2.48	1285
BH79-46	0.281738	0.000096	0.001937	0.077	0.281677	-1.70	3.36	2.45	1666
Sample BH95									
BH95-2	0.281698	0.000077	0.001588	0.0706	0.281641	2.07	2.70	2.39	1885
BH95-3	0.281727	0.000082	0.001467	0.05936	0.281675	3.26	2.87	2.32	1885
BH95-6	0.281706	0.000079	0.001815	0.0904	0.281641	2.07	2.77	2.39	1885
BH95-8	0.281686	0.000072	0.001245	0.0578	0.281641	2.08	2.52	2.39	1885
BH95-9	0.281694	0.000073	0.001383	0.0595	0.281645	2.19	2.56	2.38	1885
BH95-11	0.281818	0.000066	0.002460	0.1001	0.281730	5.23	2.31	2.20	1885
BH95-27	0.281716	0.000081	0.001021	0.04494	0.281679	3.43	2.84	2.31	1885
BH95-28	0.281621	0.000078	0.001163	0.05	0.281579	-0.12	2.73	2.52	1885
BH95-32	0.281638	0.000076	0.001548	0.0725	0.281583	-0.01	2.66	2.52	1885
BH95-34	0.281651	0.000071	0.001264	0.05389	0.281606	0.82	2.49	2.47	1885
BH95-37	0.281751	0.000091	0.001782	0.0822	0.281687	3.71	3.19	2.29	1885
BH95-38	0.281789	0.000088	0.001675	0.0716	0.281729	5.20	3.08	2.20	1885
BH95-39	0.281748	0.000083	0.001617	0.075	0.281690	3.81	2.91	2.29	1885
BH95-42	0.281745	0.000077	0.001556	0.0649	0.281708	-10.04	2.70	2.63	1252
BH95-43	0.281728	0.000072	0.001364	0.0607	0.281679	3.42	2.52	2.31	1885
BH95-45	0.281601	0.000077	0.000997	0.0437	0.281565	-0.62	2.70	2.55	1885
BH95-46	0.281697	0.000078	0.001020	0.04535	0.281661	2.76	2.73	2.35	1885
BH95-47	0.281770	0.000110	0.002787	0.1319	0.281670	3.11	3.85	2.33	1885
BH95-56	0.281692	0.000072	0.001316	0.0567	0.281645	2.21	2.52	2.38	1885
BH95-57	0.281695	0.000088	0.001366	0.05947	0.281646	2.25	3.08	2.38	1885
BH95-60	0.281753	0.000078	0.001271	0.054	0.281708	4.43	2.73	2.25	1885
BH95-69	0.281754	0.000073	0.001586	0.0706	0.28	4.06	2.56	2.27	1885
BH95-70	0.281644	0.000072	0.001602	0.07296	0.281587	0.14	2.52	2.51	1885
BH95-71	0.281676	0.000067	0.001214	0.05083	0.281633	1.77	2.35	2.41	1885
BH95-73	0.281768	0.000075	0.002380	0.0985	0.281683	3.55	2.63	2.30	1885
BH95-78	0.281722	0.000063	0.001450	0.0668	0.281670	3.10	2.21	2.33	1885
BH95-79	0.281774	0.000084	0.001164	0.0568	0.281747	-9.45	2.94	2.57	1217
BH95-83	0.281655	0.000082	0.001509	0.0677	0.281601	0.65	2.87	2.48	1885
BH95-87	0.281644	0.000093	0.001985	0.0945	0.281573	-0.35	3.26	2.54	1885
BH95-88	0.281677	0.000078	0.000955	0.04315	0.281643	2.13	2.73	2.39	1885
BH95-99	0.281552	0.000088	0.000849	0.0382	0.281522	-2.17	3.08	2.65	1885
BH95-91	0.281763	0.000080	0.001231	0.05901	0.281719	4.84	2.80	2.22	1885
BH95-94	0.281731	0.000090	0.001955	0.0888	0.281661	2.78	3.15	2.35	1885
BH95-96	0.281594	0.000071	0.001026	0.04631	0.281557	-0.91	2.49	2.57	1885
Sample BH98									
BH98-1	0.281711	0.000097	0.001590	0.0776	0.281675	-12.37	3.40	2.74	1201
BH98-2	0.281754	0.000078	0.000630	0.02839	0.281740	-10.12	2.73	2.60	1199
BH98-3	0.281748	0.000082	0.000746	0.0351	0.281731	-10.25	2.87	2.61	1207
BH98-4	0.281692	0.000084	0.000845	0.04285	0.281673	-12.25	2.94	2.74	1210
BH98-5	0.281804	0.000083	0.001110	0.0557	0.281779	-8.54	2.91	2.51	1208
BH98-6	0.281765	0.000062	0.000396	0.01765	0.281756	-9.43	2.17	2.56	1204
BH98-7	0.281831	0.000059	0.000387	0.01713	0.281822	-7.37	2.07	2.43	1191
BH98-8	0.281739	0.000072	0.000914	0.04615	0.281718	-10.81	2.52	2.64	1202
BH98-9	0.281727	0.000074	0.001217	0.05836	0.281699	-11.35	2.59	2.68	1208
BH98-10	0.281739	0.000078	0.000607	0.03116	0.281725	-9.74	2.73	2.61	1239
BH98-11	0.281777	0.000083	0.000897	0.04678	0.281756	-9.06	2.91	2.55	1220
BH98-12	0.281736	0.000073	0.000788	0.0407	0.281718	-11.09	2.56	2.65	1190
BH98-13	0.281805	0.000079	0.000407	0.0184	0.281796	-8.49	2.77	2.49	1183
BH98-14	0.281800	0.000081	0.000575	0.02776	0.281787	-8.31	2.84	2.49	1205
BH98-15	0.281789	0.000080	0.000827	0.04311	0.281770	-8.93	2.80	2.53	1204

Appendix B. (continued)

Spot ID	$^{176}Hf/^{177}Hf$	2 S.E.	$^{176}Lu/^{177}Hf$	$^{176}Yb/^{177}Hf$	$Hf_{initial}$	$\varepsilon_{Hf}(t)$	2σ	$T_{DM(crustal)}$ (Ga)	Age (Ma)*
BH98-16	0.281846	0.000081	0.000682	0.0317	0.281830	-6.77	2.84	2.40	1205
BH98-17	0.281780	0.000100	0.001733	0.08035	0.281741	-9.93	3.50	2.59	1206
BH98-18	0.281713	0.000074	0.000832	0.04345	0.281694	-11.69	2.59	2.70	1201
BH98-19	0.281771	0.000073	0.000875	0.04624	0.281751	-9.56	2.56	2.57	1206
BH98-20	0.281761	0.000067	0.000562	0.02473	0.281748	-9.86	2.35	2.58	1197
BH98-21	0.281745	0.000063	0.000620	0.02736	0.281731	-10.20	2.21	2.61	1209
BH98-22	0.281799	0.000079	0.001039	0.05086	0.281775	-8.52	2.77	2.51	1214
BH98-23	0.281766	0.000074	0.000863	0.04463	0.281747	-9.95	2.59	2.59	1196
BH98-24	0.281832	0.000087	0.001003	0.04473	0.281809	-7.45	3.05	2.44	1208
BH98-25	0.281757	0.000056	0.000395	0.01735	0.281748	-9.96	1.96	2.58	1193
BH98-26	0.281797	0.000081	0.000988	0.0462	0.281774	-8.53	2.84	2.51	1215
BH98-27	0.281764	0.000073	0.000828	0.03855	0.281745	-9.68	2.56	2.58	1210
BH98-28	0.281748	0.000060	0.000773	0.03849	0.281730	-9.79	2.10	2.60	1229
BH98-29	0.281796	0.000092	0.000934	0.04894	0.281775	-8.74	3.22	2.52	1205
BH98-30	0.281777	0.000069	0.000353	0.01598	0.281769	-9.08	2.42	2.54	1199
BH98-31	0.281719	0.000072	0.001069	0.05184	0.281695	-11.36	2.52	2.69	1215
BH98-32	0.281819	0.000079	0.000558	0.02546	0.281806	-7.81	2.77	2.46	1197
BH98-33	0.281731	0.000065	0.000916	0.04584	0.281711	-11.48	2.28	2.67	1185
BH98-34	0.281760	0.000069	0.000492	0.02171	0.281749	-10.21	2.42	2.59	1181
BH98-35	0.281761	0.000069	0.000466	0.02089	0.281750	-9.58	2.42	2.57	1206
BH98-36	0.281747	0.000071	0.000753	0.03824	0.281730	-10.69	2.49	2.63	1189
BH98-37	0.281793	0.000071	0.001474	0.0745	0.281760	-9.72	2.49	2.56	1185
Sample BH100									
BH100-2	0.281816	0.000081	0.000551	0.02684	0.281803	-6.56	2.84	2.43	1257
BH100-4	0.281781	0.000077	0.000805	0.03784	0.281762	-7.88	2.70	2.51	1263
BH100-5	0.281801	0.000072	0.000900	0.0421	0.281779	-6.90	2.52	2.46	1279
BH100-7	0.281838	0.000085	0.000464	0.02135	0.281827	-6.15	2.98	2.39	1237
BH100-9	0.281753	0.000081	0.000430	0.0202	0.281743	-8.76	2.84	2.56	1254
BH100-11	0.281839	0.000085	0.000918	0.0482	0.281818	-6.46	2.98	2.41	1239
BH100-15	0.281823	0.000091	0.001014	0.0499	0.281799	-7.00	3.19	2.44	1244
BH100-16	0.281822	0.000090	0.001085	0.0547	0.281796	-6.95	3.15	2.45	1250
BH100-17	0.281810	0.000094	0.000428	0.02044	0.281800	-6.83	3.29	2.44	1250
BH100-18	0.281762	0.000082	0.000919	0.0453	0.281740	-9.08	2.87	2.57	1244
BH100-19	0.281784	0.000086	0.000761	0.0374	0.281766	-8.10	3.01	2.51	1247
BH100-20	0.281826	0.000097	0.001598	0.0796	0.281788	-6.96	3.40	2.46	1263
BH100-21	0.281814	0.000092	0.000547	0.02449	0.281801	-6.56	3.22	2.43	1260
BH100-22	0.281853	0.000090	0.001035	0.0513	0.281828	-5.40	3.15	2.36	1269
BH100-24	0.281877	0.000094	0.001015	0.0501	0.281853	-4.79	3.29	2.32	1257
BH100-25	0.281899	0.000097	0.001436	0.06817	0.281865	-4.58	3.40	2.30	1247
BH100-26	0.281681	0.000097	0.000571	0.0295	0.281667	-11.43	3.40	2.72	1254
BH100-27	0.281849	0.000084	0.001422	0.0686	0.281816	-6.55	2.94	2.41	1238
BH100-28	0.281849	0.000089	0.001188	0.0509	0.281821	-6.50	3.12	2.40	1231
BH100-29	0.281842	0.000078	0.000404	0.01752	0.281832	-5.61	2.73	2.37	1253
BH100-30	0.281794	0.000098	0.000668	0.0326	0.281778	-7.44	3.43	2.48	1257
BH100-31	0.281747	0.000083	0.000435	0.01998	0.281737	-9.14	2.91	2.58	1247
BH100-32	0.281828	0.000087	0.001390	0.0711	0.281795	-6.72	3.05	2.44	1263
BH100-34	0.281801	0.000078	0.000502	0.024	0.281789	-7.05	2.73	2.46	1257
BH100-35	0.281800	0.000086	0.001492	0.0728	0.281764	-7.69	3.01	2.50	1268
BH100-36	0.281781	0.000098	0.001050	0.0514	0.281756	-8.28	3.43	2.53	1254
BH100-37	0.281857	0.000066	0.000602	0.0259	0.281843	-4.87	2.31	2.33	1270
BH100-38	0.281860	0.000110	0.001783	0.093	0.281817	-5.72	3.85	2.39	1272
BH100-39	0.281814	0.000068	0.000881	0.0414	0.281793	-6.47	2.38	2.44	1277

*Age εHf data points are plotted against in Figures 8 and 9 in the main text.

Appendix C. Oxygen Isotope Data

		$^{18}O/^{16}O$ Data			
Analysis	Age (Ma)	Uncorrected $^{18}O/^{16}O$	SE in %	$\delta^{18}O$ (‰)	2σ
Sample BH12					
O-RT-NT1-12@1	1678	0.00201856	0.00775334	7.39	0.32
O-RT-NT1-12@2	1681	0.00201770	0.00707873	6.96	0.32
O-RT-NT1-12@3	1672	0.00201558	0.00978351	5.88	0.34
O-RT-NT1-12@5	1707	0.00201874	0.00659505	7.48	0.31
O-RT-NT1-12@6	1674	0.00201537	0.00845739	5.78	0.33
O-RT-NT1-12@8	1707	0.00201727	0.00788548	6.75	0.32
O-RT-NT1-12@12	1705	0.00201924	0.00959576	7.74	0.34
O-RT-NT1-12@14	1714	0.00201868	0.00800562	7.45	0.32
O-RT-NT1-12@15	1687	0.00201693	0.00811034	6.58	0.32
O-RT-NT1-12@16	1706	0.00201643	0.00996172	6.31	0.35
O-RT-NT1-12@17	1721	0.00201946	0.00686072	7.85	0.31
O-RT-NT1-12@18	1696	0.00201864	0.00875579	7.44	0.33
O-RT-NT1-12@19	1632	0.00201586	0.00706335	6.03	0.31
O-RT-NT1-12@20	1701	0.00201462	0.00928865	5.41	0.34
O-RT-NT1-12@21	1709	0.00201526	0.00804262	5.74	0.32
O-RT-NT1-12@23	1728	0.00201866	0.00801807	7.45	0.32
O-RT-NT1-12@24	1732	0.00201492	0.00840344	5.56	0.33
O-RT-NT1-12@25	1634	0.00201842	0.00703840	7.34	0.31
O-RT-NT1-12@27	1675	0.00201541	0.00916292	5.80	0.34
O-RT-NT1-12@29	1724	0.00201811	0.00867908	7.18	0.33
O-RT-NT1-12@30	1633	0.00201719	0.00753743	6.72	0.32
O-RT-NT1-12@31	1698	0.00201841	0.00712432	7.33	0.32
O-RT-NT1-12@32	1717	0.00201658	0.00789899	6.42	0.32
O-RT-NT1-12@33	1715	0.00201686	0.00850663	6.57	0.33
O-RT-NT1-12@34	1695	0.00201668	0.00696874	6.47	0.31
O-RT-NT1-12@35	1678	0.00201714	0.00970263	6.70	0.34
O-RT-NT1-12@36	1717	0.00201876	0.00832147	7.51	0.33
Sample BH38					
O-RT-NT2-38@1	1210	0.00202239	0.00831787	8.80	0.44
O-RT-NT2-38@2	1199	0.00202213	0.00595885	8.67	0.43
O-RT-NT2-38@3	1183	0.00202217	0.00799322	8.69	0.44
O-RT-NT2-38@4	1194	0.00202214	0.00904490	8.67	0.45
O-RT-NT2-38@5	1193	0.00202270	0.00766064	8.94	0.44
O-RT-NT2-38@6	1214	0.00202183	0.02014657	8.51	0.58
O-RT-NT2-38@8	1190	0.00202274	0.00740725	8.96	0.44
O-RT-NT2-38@10	1187	0.00202200	0.00797293	8.59	0.44
O-RT-NT2-38@11	1198	0.00202329	0.00806594	9.23	0.44
O-RT-NT2-38@12	1192	0.00202273	0.00639064	8.95	0.43
O-RT-NT2-38@13	1184	0.00202214	0.00748525	8.49	0.44
O-RT-NT2-38@14	1201	0.00202253	0.00892971	8.85	0.45
O-RT-NT2-38@16	1189	0.00202243	0.00815517	8.63	0.44
O-RT-NT2-38@17	1195	0.00202265	0.00533372	8.74	0.42
O-RT-NT2-38@18	1211	0.00202216	0.00763314	8.49	0.44
O-RT-NT2-38@19	1211	0.00202255	0.00786799	8.68	0.44
O-RT-NT2-38@20	1202	0.00202229	0.00764121	8.55	0.44
O-RT-NT2-38@21	1200	0.00202254	0.00818656	8.68	0.44
O-RT-NT2-38@22	1190	0.00202233	0.00763437	8.57	0.44
O-RT-NT2-38@23	1205	0.00202237	0.00701083	8.58	0.43
O-RT-NT2-38@24	1183	0.00202254	0.00980542	8.67	0.46
O-RT-NT2-38@26	1211	0.00202186	0.00635937	8.33	0.43
O-RT-NT2-38@27	1205	0.00202234	0.00719091	8.56	0.43
O-RT-NT2-38@28	1229	0.00202218	0.00680220	8.48	0.43
O-RT-NT2-38@30	1191	0.00202211	0.00528214	8.45	0.42
O-RT-NT2-38@31	1214	0.00202233	0.00661614	8.55	0.43
Sample BH62					
O-RT-NT2-62@1	2710	0.00201594	0.01065862	5.56	0.46
O-RT-NT2-62@7	2710	0.00201437	0.00983088	4.77	0.45
O-RT-NT2-62@16	2710	0.00201382	0.00746223	4.50	0.44
O-RT-NT2-62@33	2710	0.00201469	0.00713813	4.93	0.43
O-RT-NT2-62@47	2710	0.00201479	0.00746506	4.96	0.44
O-RT-NT2-62@49	2710	0.00201380	0.00654849	4.47	0.43
O-RT-NT2-62@51	2710	0.00201490	0.00582365	5.02	0.43
O-RT-NT2-62@56	2710	0.00201516	0.00847978	5.14	0.44
O-RT-NT2-62@61	2710	0.00201430	0.00902886	4.72	0.45
O-RT-NT2-62@67	2710	0.00201459	0.00849181	4.85	0.44

Appendix C. (continued)

		$^{18}O/^{16}O$ Data			
Analysis	Age (Ma)	Uncorrected $^{18}O/^{16}O$	SE in %	$\delta^{18}O$ (‰)	2σ
O-RT-NT2-62@71	2710	0.00201445	0.00735912	4.78	0.43
O-RT-NT2-62@73	2710	0.00201405	0.00742980	4.58	0.43
O-RT-NT2-62@74	2710	0.00201409	0.00620002	4.60	0.43
O-RT-NT2-62@80	2710	0.00201621	0.00634718	5.65	0.43
O-RT-NT2-62@88	2710	0.00201388	0.00791898	4.48	0.44
O-RT-NT2-62@92	2710	0.00201491	0.00660942	4.99	0.43
Sample BH67					
O-RT-NT1-67@3	2712	0.00201630	0.00938541	6.38	0.34
O-RT-NT1-67@4	2712	0.00201444	0.00662489	5.45	0.31
O-RT-NT1-67@10	2712	0.00201390	0.00959430	5.19	0.34
O-RT-NT1-67@21	2712	0.00201625	0.00871291	6.36	0.33
O-RT-NT1-67@30	2712	0.00201438	0.00848741	5.43	0.33
O-RT-NT1-67@31	2712	0.00201600	0.00839025	6.24	0.33
O-RT-NT1-67@34	2712	0.00201477	0.00690578	5.62	0.31
Sample BH79					
O-RT-NT1-79@4	1666	0.00201837	0.00584317	7.37	0.30
O-RT-NT1-79@5	1666	0.00201850	0.00815380	7.44	0.33
O-RT-NT1-79@9	1666	0.00201865	0.00771401	7.51	0.32
O-RT-NT1-79@11	1666	0.00201867	0.01011549	7.53	0.35
O-RT-NT1-79@12	1666	0.00201862	0.00978882	7.50	0.34
O-RT-NT1-79@14	1666	0.00201795	0.00838264	7.17	0.33
O-RT-NT1-79@16	1666	0.00201823	0.00680021	7.31	0.31
O-RT-NT1-79@17	1666	0.00201942	0.01076355	7.92	0.36
O-RT-NT1-79@18	1666	0.00201875	0.00786513	7.58	0.32
O-RT-NT1-79@21r	1666	0.00201844	0.00711421	7.44	0.32
O-RT-NT1-79@23	1666	0.00201796	0.00597387	7.18	0.31
O-RT-NT1-79@24	1666	0.00201838	0.01098213	7.39	0.36
O-RT-NT1-79@27	1666	0.00201816	0.00692800	7.29	0.31
O-RT-NT1-79@28	1666	0.00201836	0.00836438	7.38	0.33
O-RT-NT1-79@34	1666	0.00201880	0.01052979	7.61	0.35
O-RT-NT1-79@37	1666	0.00201708	0.00891505	6.76	0.33
O-RT-NT1-79@38	1317	0.00201829	0.00732642	7.36	0.32
O-RT-NT1-79@43	1666	0.00201791	0.00867823	7.18	0.33
O-RT-NT1-79@45	1285	0.00201851	0.00810578	7.48	0.33
Sample BH95					
O-RT-NT2-95@2	1885	0.00201439	0.00899546	4.66	0.45
O-RT-NT2-95@6	1885	0.00201266	0.00731514	3.80	0.43
O-RT-NT2-95@8	1885	0.00201332	0.01219564	4.13	0.48
O-RT-NT2-95@9	1885	0.00201434	0.00840020	4.64	0.44
O-RT-NT2-95@27	1885	0.00201512	0.00622367	5.03	0.43
O-RT-NT2-95@28	1885	0.00201504	0.01013700	5.00	0.46
O-RT-NT2-95@38	1885	0.00201067	0.00787157	2.82	0.44
O-RT-NT2-95@56	1885	0.00201452	0.00775627	4.75	0.44
O-RT-NT2-95@57	1885	0.00201370	0.00876605	4.34	0.44
O-RT-NT2-95@69	1885	0.00201110	0.00814641	3.04	0.44
O-RT-NT2-95@71	1885	0.00201284	0.00676334	3.91	0.43
O-RT-NT2-95@73	1885	0.00201370	0.00944368	4.34	0.45
O-RT-NT2-95@79	1217	0.00201378	0.00548886	4.39	0.42
O-RT-NT2-95@83	1885	0.00201515	0.00797425	5.08	0.44
O-RT-NT2-95@87	1885	0.00201436	0.00723080	4.68	0.43
O-RT-NT2-95@88	1885	0.00201588	0.00779399	5.45	0.44
O-RT-NT2-95@99	1885	0.00201525	0.00628178	5.14	0.43
O-RT-NT2-95@91	1885	0.00201556	0.00785731	5.29	0.44
O-RT-NT2-95@94	1885	0.00200978	0.01168026	2.41	0.47
O-RT-NT2-95@96	1885	0.00201382	0.00626014	4.42	0.43
Sample BH98					
O-RT-NT2-98@1	1201	0.00202163	0.00653728	8.44	0.43
O-RT-NT2-98@2	1199	0.00202203	0.00794687	8.64	0.44
O-RT-NT2-98@4	1210	0.00202129	0.00682533	8.27	0.43
O-RT-NT2-98@5	1208	0.00202266	0.01345703	8.95	0.49
O-RT-NT2-98@6	1204	0.00202203	0.00900443	8.63	0.45
O-RT-NT2-98@7	1191	0.00202192	0.00843514	8.58	0.44
O-RT-NT2-98@8	1202	0.00202254	0.00606645	8.88	0.43
O-RT-NT2-98@9	1208	0.00202267	0.00848978	8.95	0.44
O-RT-NT2-98@10	1239	0.00202202	0.00675105	8.62	0.43
O-RT-NT2-98@12	1190	0.00202200	0.00787013	8.61	0.44

Appendix C. (continued)

		$^{18}O/^{16}O$ Data			
Analysis	Age (Ma)	Uncorrected $^{18}O/^{16}O$	SE in %	$\delta^{18}O$ (‰)	2σ
O-RT-NT2-98@13	1183	0.00202218	0.00615874	8.69	0.43
O-RT-NT2-98@15	1204	0.00202273	0.00727179	8.97	0.44
O-RT-NT2-98@16	1205	0.00202220	0.00629688	8.55	0.43
O-RT-NT2-98@17	1206	0.00202200	0.00752113	8.45	0.44
O-RT-NT2-98@18	1201	0.00202253	0.00937296	8.72	0.45
O-RT-NT2-98@19	1206	0.00202262	0.00490275	8.76	0.42
O-RT-NT2-98@20	1197	0.00202182	0.00893001	8.36	0.45
O-RT-NT2-98@21	1209	0.00202206	0.00736612	8.47	0.44
O-RT-NT2-98@22	1214	0.00202187	0.00969997	8.38	0.45
O-RT-NT2-98@23	1196	0.00202287	0.00878429	8.88	0.45
O-RT-NT2-98@24	1208	0.00202216	0.00768707	8.52	0.44
O-RT-NT2-98@25	1193	0.00202208	0.00680511	8.47	0.43
O-RT-NT2-98@26	1215	0.00202213	0.00565390	8.50	0.43
O-RT-NT2-98@27	1210	0.00202211	0.00579316	8.49	0.43
O-RT-NT2-98@28	1229	0.00202166	0.00804653	8.27	0.44
O-RT-NT2-98@29	1205	0.00202256	0.00744309	8.71	0.44
O-RT-NT2-98@30	1199	0.00202187	0.00670421	8.37	0.43
O-RT-NT2-98@31	1215	0.00202236	0.00803539	8.61	0.44
O-RT-NT2-98@33	1185	0.00202283	0.00783140	8.84	0.44
O-RT-NT2-98@34	1181	0.00202195	0.00917817	8.40	0.45
O-RT-NT2-98@35	1206	0.00202222	0.00651793	8.53	0.43
O-RT-NT2-98@36	1189	0.00202202	0.00690646	8.43	0.43
O-RT-NT2-98@37	1185	0.00202210	0.01208919	8.47	0.48
Sample BH100					
O-RT-NT1-100@2	1257	0.00202058	0.00621537	8.43	0.31
O-RT-NT1-100@4	1263	0.00201957	0.00752876	7.92	0.32
O-RT-NT1-100@7	1237	0.00202026	0.00918077	8.27	0.34
O-RT-NT1-100@15	1244	0.00202010	0.00990691	8.20	0.35
O-RT-NT1-100@16	1250	0.00201949	0.00878855	7.90	0.33
O-RT-NT1-100@17	1250	0.00202027	0.00801882	8.28	0.32
O-RT-NT1-100@18	1244	0.00201972	0.00838315	8.01	0.33
O-RT-NT1-100@19	1247	0.00201975	0.01035804	8.03	0.35
O-RT-NT1-100@20	1263	0.00201984	0.01038358	8.07	0.35
O-RT-NT1-100@21	1260	0.00201849	0.00741963	7.40	0.32
O-RT-NT1-100@22	1269	0.00202013	0.00843418	8.22	0.33
O-RT-NT1-100@24	1257	0.00201965	0.00784591	7.99	0.32
O-RT-NT1-100@26	1254	0.00202009	0.00664540	8.21	0.31
O-RT-NT1-100@27	1238	0.00202001	0.00845241	8.17	0.33
O-RT-NT1-100@28	1231	0.00202002	0.01128817	8.17	0.36
O-RT-NT1-100@29	1253	0.00201948	0.00622938	7.91	0.31
O-RT-NT1-100@30	1257	0.00201986	0.00947241	8.10	0.34
O-RT-NT1-100@31	1247	0.00201977	0.00859537	8.05	0.33
O-RT-NT1-100@34	1257	0.00201895	0.00739375	7.65	0.32
O-RT-NT1-100@35	1268	0.00201971	0.00584994	8.03	0.31
O-RT-NT1-100@36	1254	0.00201964	0.01042804	7.99	0.35
O-RT-NT1-100@37	1270	0.00201998	0.00911500	8.16	0.34
O-RT-NT1-100@38	1272	0.00202024	0.00765002	8.29	0.32
O-RT-NT1-100@39	1277	0.00201978	0.00917072	8.06	0.34

Appendix D. $^{176}Hf/^{177}Hf$ (initial) versus age and $\varepsilon_{Hf}(t)$ versus age plots for samples exhibiting evidence for ancient Pb loss (i.e. by metamorphism/resetting). $\varepsilon_{Hf}(t)$ data plotted at apparent $^{207}Pb/^{206}Pb$ ages are shown as grey datapoints; $\varepsilon_{Hf}(t)$ data plotted at the corresponding $^{207}Pb/^{206}Pb$ upper intercept for that sample are shown in black.

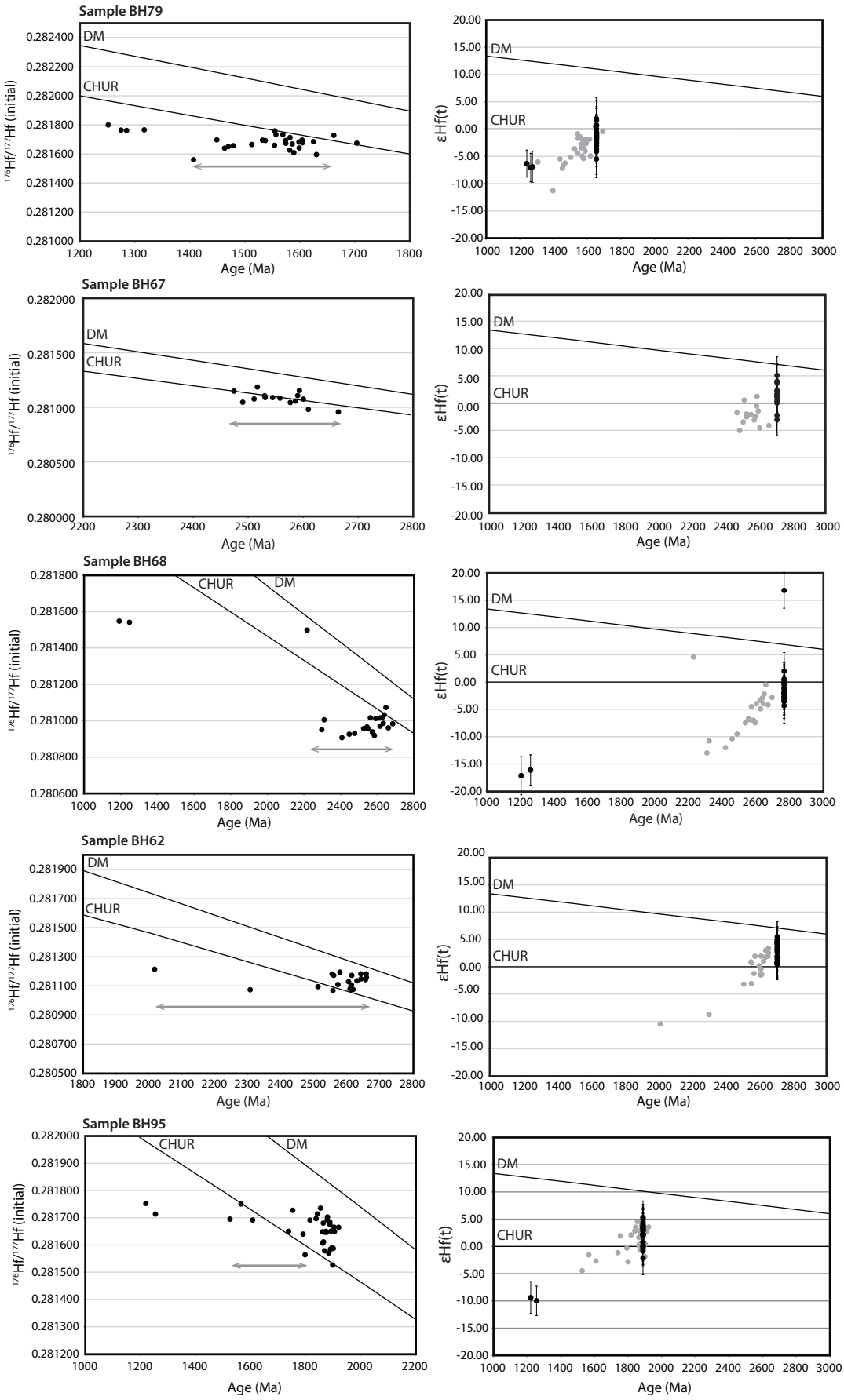

Appendix D. (continued)

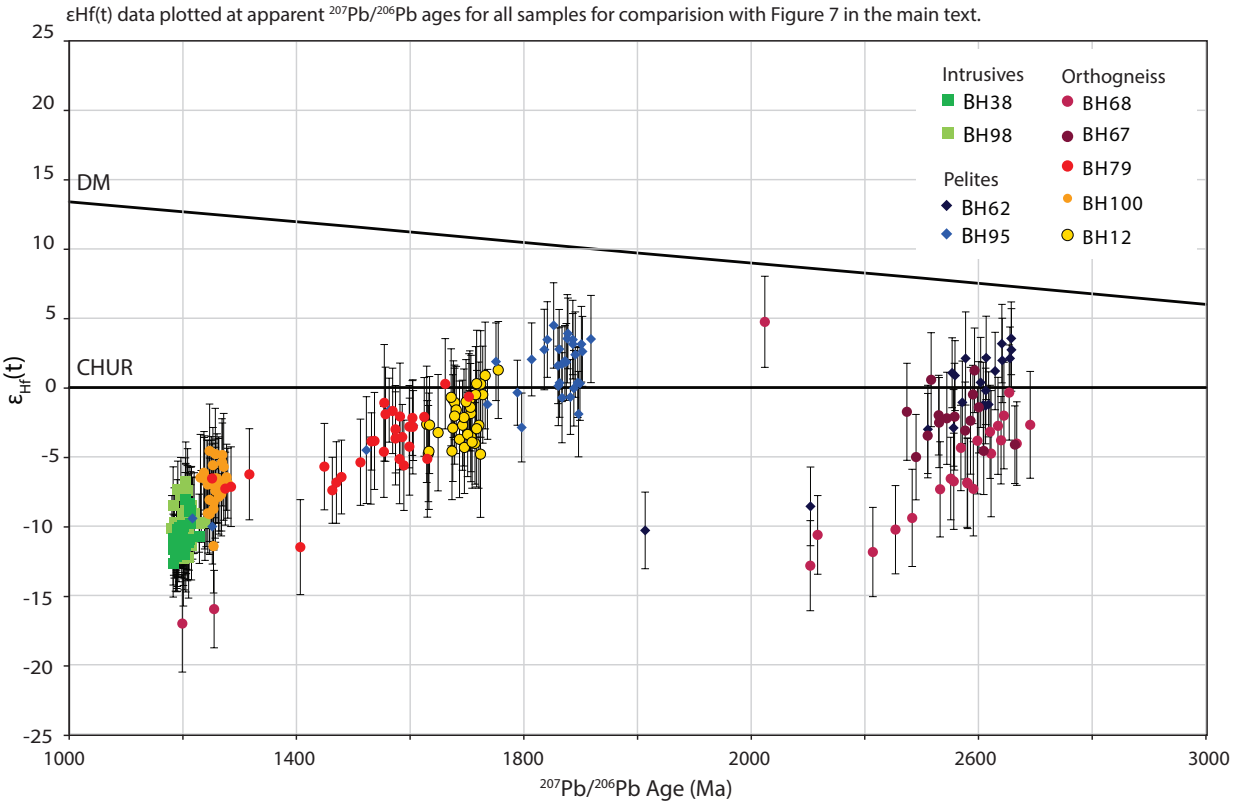

Appendix E. Lu–Hf zircon data compilation for the Bunger Hills, Albany–Fraser Orogen and surrounding regions

Appendix E comprises >3000 zircon Lu–Hf isotopic data compiled from published datasets. Data are from terranes comprising the Musgrave–Albany–Fraser–Wilkes Orogen, and surrounding tectonic regions. Compiled data are plotted in Figure 9 of the main text for comparison with the Bunger Hills isotopic data from this study.

As the data are previously published, and the size of the compiled dataset is large, the individual data points are not listed below. However, the bibliographic sources of all published data are attributed, and the dataset is readily accessible for download: doi.org/10.1016/j.precamres.2017.05.013.

Tectonic region	Protolith	Data source*
Bunger Hills	Igneous Sedimentary	This study
Albany–Fraser Orogen	Igneous Sedimentary	Kirkland et al., (2015a) Kirkland et al., (2015b) Spaggiari et al., (2015) Kirkland et al., (2011) Geological Survey of Western Australia report books as referenced in Smits et al., (2014) supplementary tables
Musgrave Inlier	Igneous Sedimentary	Kirkland et al., (2015a) Kirkland et al., (2013b) Dutch et al., (2013) Smits et al., (2014, and references therein supplementary tables)
Windmill Islands	Igneous Sedimentary	Zhang et al., (2012) Morrissey et al., (2017)
Gulden Draak Knoll	Igneous	Gardner et al., (2015)
Madura Province	Igneous	Kirkland et al., (2015a)
Yilgarn Craton	Igneous	Ivanic et al., (2013) Wyche et al., (2012)

*Reference according to the main text.

Chapter 4

This chapter is published as:

Tucker, N. M., Hand, M., Kelsey, D. E., Taylor, R. J. M., Clark, C. & Payne, J. L. 2018. A tripartite approach to unearthing the duration of high temperature conditions versus peak metamorphism: an example from the Bunger Hills, East Antarctica. *Precambrian Research*, in press.

Statement of Authorship

Title of paper	A tripartite approach to unearthing the duration of high temperature conditions versus peak metamorphism: an example from the Bunger Hills, East Antarctica.
Pulication status	☒ Published ☐ Accepted for publication ☐ Submitted for publication ☐ Unpublished and unsubmitted work written in manuscript style
Publication details	Tucker, N. M., Hand, M., Kelsey, D. E., Taylor, R. J. M., Clark, C. & Payne, J. L. 2018. A tripartite approach to unearthing the duration of high temperature conditions versus peak metamorphism: an example from the Bunger Hills, East Antarctica." *Precambrian Research*, in press.

Principal Author

Name of Principal Author	Naomi M. Tucker
Contribution to the paper	Project design; fieldwork; sample selection and preparation; petrography; LA–ICP–MS, SEM and EPMA data collection; *P–T* modelling; all calculations and data processing; critical data interpretation; manuscript design and composition; creation of all figures.
Overall percentage (%)	85
Certification	This paper reports on original research I conducted during the period of my Higher Degree by Research candidature and is not subject to any obligations or contractual agreements with a third party that would constrain its inclusion in this thesis. I am the primary author of this paper.
Signature	Date 04/10/2017

Co-author contributions

By signing the Statement of Authorship, each author certifies that:

i. the candidate's stated contribution to the publication is accurate (as detailed above);
ii. permission is granted for the candidate to include the publication in the thesis; and,
iii. the sum of all co-authors contributions is equal to 100 % less the candidate's stated contribution.

Name of Co-author	Martin Hand
Contribution to the paper	Fieldwork assistance; data interpretation guidance; manuscript review.
Signature	Date 13/10/2017

Name of Co-author	David E. Kelsey
Contribution to the paper	*P–T* data interpretation guidance; manuscript review.
Signature	Date 05/10/2017

Name of Co-author	Richard J. Taylor
Contribution to the paper	Assistance with sample preparation for zircon LA–ICP–MS; sample (zircon) imaging; data interpretation guidance; manuscript review.
Signature	Date 04/10/2017

Name of Co-author	Chris Clark
Contribution to the paper	Fieldwork assistance; zircon LA–ICP–MS data interpretation guidance; manuscript review.
Signature	Date 16/01/2017

Name of Co-author	Justin L. Payne
Contribution to the paper	LA–ICP–MS data interpretation guidance; manuscript review.
Signature	Date 04/10/2017

A tripartite approach to unearthing the duration of high temperature conditions versus peak metamorphism: an example from the Bunger Hills, East Antarctica

Naomi M. Tucker[a], Martin Hand[a], David E. Kelsey[a,b], Richard Taylor[c], Chris Clark[d] and Justin L. Payne[e,a]

[a]*Department of Earth Science, School of Physical Sciences, The University of Adelaide, Adelaide, South Australia, 5005, Australia*

[b]*Adelaide Microscopy, The University of Adelaide, Adelaide, South Australia, 5005, Australia*

[c]*Department of Earth Sciences, University of Cambridge, Cambridge CB2 3EQ, UK*

[d]*Department of Applied Geology, Curtin University, Perth, Western Australia, Australia*

[e]*School of Natural and Built Environments, University of South Australia, Mawson Lakes Campus, South Australia 5095, Australia*

ABSTRACT

We present LA–ICP–MS U–Pb monazite and zircon geochronology, trace element chemistry and phase equilibria forward modelling to constrain the *P–T–t* evolution of the Bunger Hills, East Antarctica. Metasedimentary rocks in the Bunger Hills record evidence for a protracted metamorphic history during the Mesoproterozoic. Taken in isolation, zircon and monazite ages suggest an extremely long duration of high-temperature conditions (ca. 200 Myr). Calculated *P–T* models indicate metamorphism involved medium pressures of 5.5–7.1 kbar and high to ultrahigh temperatures of 800–960 °C, and that the *P–T* path likely tracked along a down-pressure to isobaric cooling trajectory. Integrating trace element data from zircon, monazite and garnet indicates that, despite the spread in U–Pb ages, peak metamorphism essentially occurred over the interval ca. 1220–1180 Ma. The age and conditions of Mesoproterozoic metamorphism are consistent with the high-grade metamorphic evolution proposed previously for Stage-2 of the Albany–Fraser Orogeny in southwestern Australia. The *P–T–t* conditions are interpreted to reflect extension, potentially associated with unloading and exhumation of a collisional orogen following Stage-1 of the Albany–Fraser Orogeny. This is the first study to integrate geochronology, trace element chemistry and *P–T* modelling to constrain the metamorphic evolution of the Bunger Hills and to interpret these constraints within the context of the now separate terranes of the Musgrave–Albany–Fraser Orogen. The three-way approach adopted in this study demonstrates that zircon and monazite may grow and modify through a number of processes. An integrated petrochronologic approach is therefore essential for investigations on high-grade terranes.

1. INTRODUCTION

The occurrence of ostensibly long-lived, regional, high to ultrahigh temperature metamorphism is widely documented (Korhonen et al., 2013; Morrissey et al., 2014; Tucker et al., 2015; Walsh et al., 2015; Zhang et al., 2015). Long-lived high-temperature metamorphism is of interest in that it provides evidence that the mid–lower crust is capable of attaining, and sustaining, extreme thermal conditions. Linking the timing, duration and pressure–temperature (*P–T*) evolution of granulite facies terranes is therefore critical to our understanding of the geodynamic mechanisms that prevail to drive such thermal perturbation of the crust.

The common observation in high-temperature metamorphic terranes that monazite and zircon yield an extended record of age data owes to the complex behaviour of these minerals at suprasolidus conditions. Controls on the growth of zircon and monazite include, but are not limited to, the *P–T–t* path (Kelsey and Powell, 2011; Kelsey et al., 2008), closure temperature to diffusion (Cherniak, 2010; Halpin et al., 2012; Rubatto et al., 2001), solubility (Kelsey et al., 2008; Stepanov et al., 2012), bulk chemistry (Fitzsimons et al., 2005; Rubatto et al., 2006), the growth and breakdown of trace phases and rock forming minerals (Bingen and van Breemen, 1998; Degeling et al., 2001; Hoskin and Black, 2000; Kohn et al., 2015; Kohn and Malloy, 2004; Rubatto, 2002; Yakymchuk, 2017), and the open-system behaviour of partial

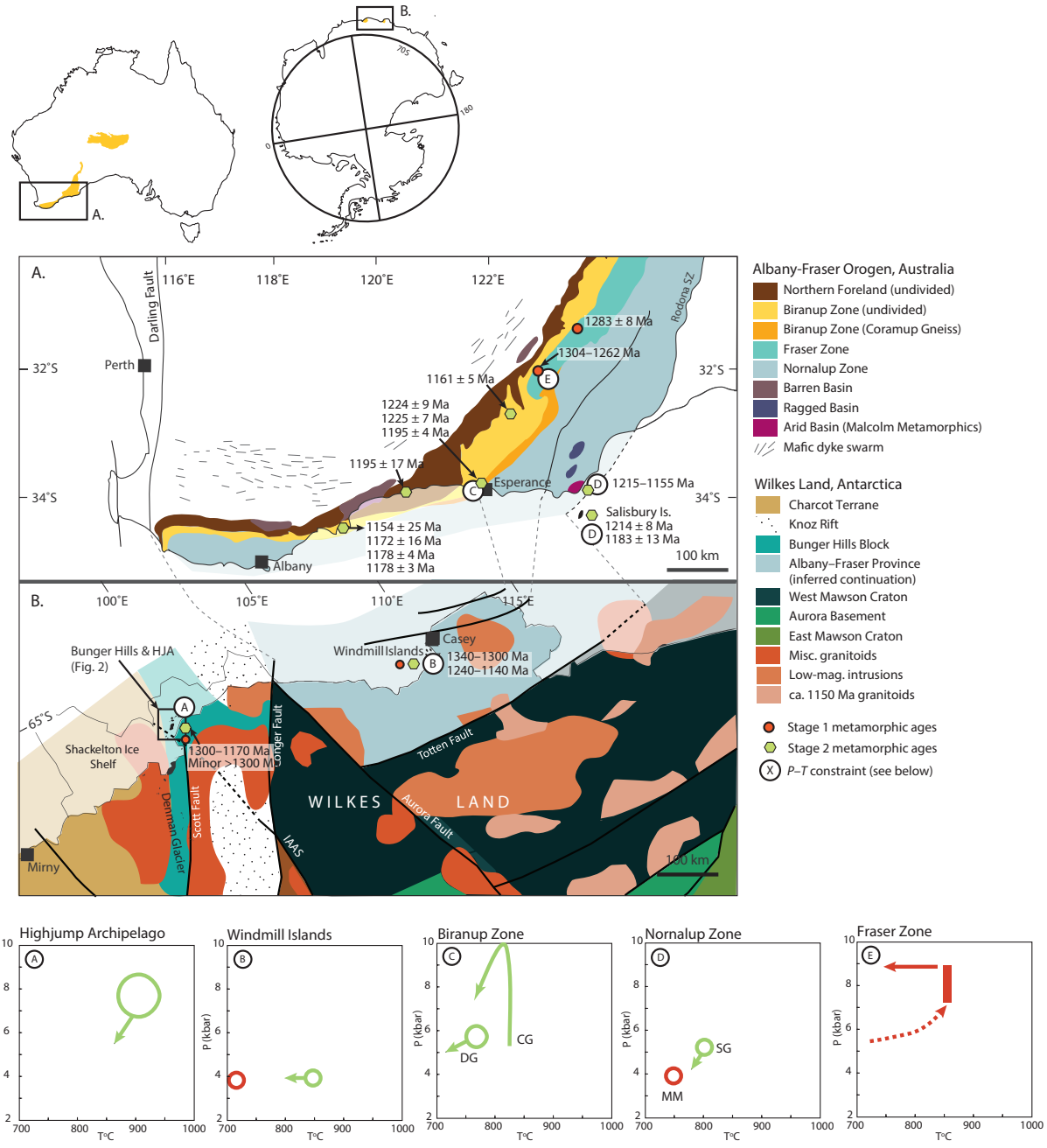

Figure 1. Simplified regional geology of (A) the Albany–Fraser Orogen, southwest Australia, and (B) Wikes Land, East Antarctica and summarised P–T constraints for the Mesoproterozoic Albany–Fraser Orogeny in these regions. The location of (A) and (B) are indicated by boxed regions on Australia and Antarctica that are illustrated at the top of the figure. Grid references refer to the present-day geographic location of Australia and Antarctica. The Gondwanan intercontinental piercing points of Aitken et al. (2014) are shown as dashed lines. The location of the Bunger Hills (enlarged in Fig. 2) is indicated in (B). Geological boundaries and structures are adapted from Tucker et al. (2017), Maritati et al. (2016), Aitken et al. (2014), Boger (2011), Spaggiari et al. (2009) and the 1:2 500 000 interpreted bedrock geology of Western Australia (Geological Survey of Western Australia, 2015). The location of existing interpreted metamorphic ages pertaining to the Albany Fraser Orogeny (Geological Survey of Western Australia online database, GeoVIEW.WA: <https://geoview.dmp.wa.gov.au/GeoViews/?Viewer=GeoVIEW>, and additional references in Table 1) are indicated as red (Stage-1) and green (Stage-2) filled symbols, and the corresponding ages are given. Localities with documented *P–T* constraints on metamorphism are indicated by white, lettered circles and illustrated at the bottom of the figure (see also Table 1). In plots of pressure versus temperature, red and green symbols represent Stage-1 and Stage-2 Albany–Fraser Orogeny constraints, respectively. Abbreviations: DG, Dalyup Gneiss; CG, Coramup Gneiss; MM, Malcolm Metamorphics; SG, Salisbury Gneiss; HJA, Highjump Archipelago.

melting, melt crystallisation, melt loss and fluid infiltration (Carson et al., 2002; Harlov et al., 2011; Hokada and Harley, 2004; Watt et al., 1996; Williams, 2001; Williams et al., 1996; Yakymchuk, 2017; Yakymchuk and Brown, 2014). The careful quantification and interpretation of age data from granulite facies rocks, and the relationship of these ages to the *P–T* path experienced by the rock (e.g. heating, cooling, exhumation, melt interaction) is thus contentious and has been the subject of much discussion (e.g. Harley et al., 2007, and references therein; Johnson et al., 2015; Roberts and Finger, 1997; Taylor et al., 2016; Tucker et al., 2015). In reality, the analysis of high-grade terranes is fraught with the constant challenge of deciphering what is the "true" duration of peak metamorphism.

Anomalously long-lived, high to ultrahigh-temperature conditions appear to have prevailed throughout central and southern Australia and East Antarctica during the Mesoproterozoic. Existing zircon and monazite age data suggest that anatectic conditions were sustained for >80 Myr (e.g. Tucker et al., 2015; Walsh et al., 2015). The spatial footprint of regionally extreme Mesoproterozoic metamorphism is exceptional, extending over 2000 km along the margins of the Archean Australian and East Antarctic cratons within the Musgrave Inlier, Albany–Fraser Orogen, Windmill Islands, Highjump Archipelago and Bunger Hills (Clark et al., 2014; Gorczyk et al., 2015; Morrissey et al., 2017a; Smithies et al., 2011; Tucker and Hand, 2016; Tucker et al., 2015, 2017; Walsh et al., 2015), collectively termed in this instance as the Musgrave–Albany–Fraser Orogen (MAFO). These high-grade terranes are also the Australian–Antarctic record of Rodinian supercontinent amalgamation. Despite this intriguing correlation between the generation of thermally extreme metamorphism and continental assembly, the true duration of the peak of metamorphism versus generation of overall high-temperature conditions is currently not well understood. The concept of a long-lived, spatially-extreme, high-temperature regime also challenges conventional notions on the thermal stability of the crust, the causative mechanisms and the prevailing geodynamic regime.

The Bunger Hills are the least studied element of the MAFO but hold an important place at its western periphery. Reconnaissance metamorphic work (Stüwe and Powell, 1989) and recent U–Pb geochronology on metamorphic zircon obtained from orthogneiss and metasedimentary rocks in the Bunger Hills reflect that high temperature conditions were potentially maintained for up to ca. 150 Myr (Tucker et al., 2017). The focus of this study is the Bunger Hills, and primarily its relationship to the Albany–Fraser Orogen, Highjump Archipelago and Windmill Islands. We adopt a three-way approach that integrates: (1) monazite and zircon geochronology; (2) the trace element compositions of garnet, zircon and monazite; and, (3) calculated phase equilibria forward models, to evaluate the duration and *P–T* conditions of peak metamorphism. The results of this study provide a metamorphic framework in which to evaluate the geodynamic setting for high thermal gradient regimes associated with the Proterozoic amalgamation of Australia and Antarctica.

2. GEOLOGICAL FRAMEWORK

2.1 Regional setting

Rodinian and Gondwanan paleogeographic reconstructions (e.g. Aitken et al., 2016; Li et al., 2008; White et al., 2013, and references therein), geophysical interpretations (Aitken et al., 2014; Maritati et al., 2016), and recent geochronological and isotopic work (Tucker et al., 2017) place the Bunger Hills, in East Antarctica, as the former, westernmost vestige of the Albany–Fraser Orogen. The Bunger Hills are presently located on the Wilkes Land coastline, East Antarctica (~100 °E, 66 °S; Fig. 1), in a region characterised by high magnetic intensity geophysical anomalies (Bunger Hills Block; Aitken et al., 2014).

The Bunger Hills and Albany–Fraser Orogen share similar histories, recording evidence for Paleo–early Mesoproterozoic autochthonous reworking of the Yilgarn Craton margin (Kirkland et al., 2015, 2011b; Spaggiari et al., 2015; Tucker et al., 2017). In contrast, the proposed crustal evolution of the Windmill Islands, situated 400 km east of the Bunger Hills, diverges from the Bunger Hills, and is more strongly linked to the Mesoproterozoic modification of the eastern margin of the orogen (Morrissey et al., 2017b). Furthermore, the pre-Mesoproterozoic crustal histories of the Bunger Hills, Windmill Islands and Albany–Fraser Orogen are all unrelated to the Musgrave Inlier in central Australia (Kirkland et al., 2015; Smits et al., 2014; Wade et al., 2006), despite being considered part of the same orogenic system.

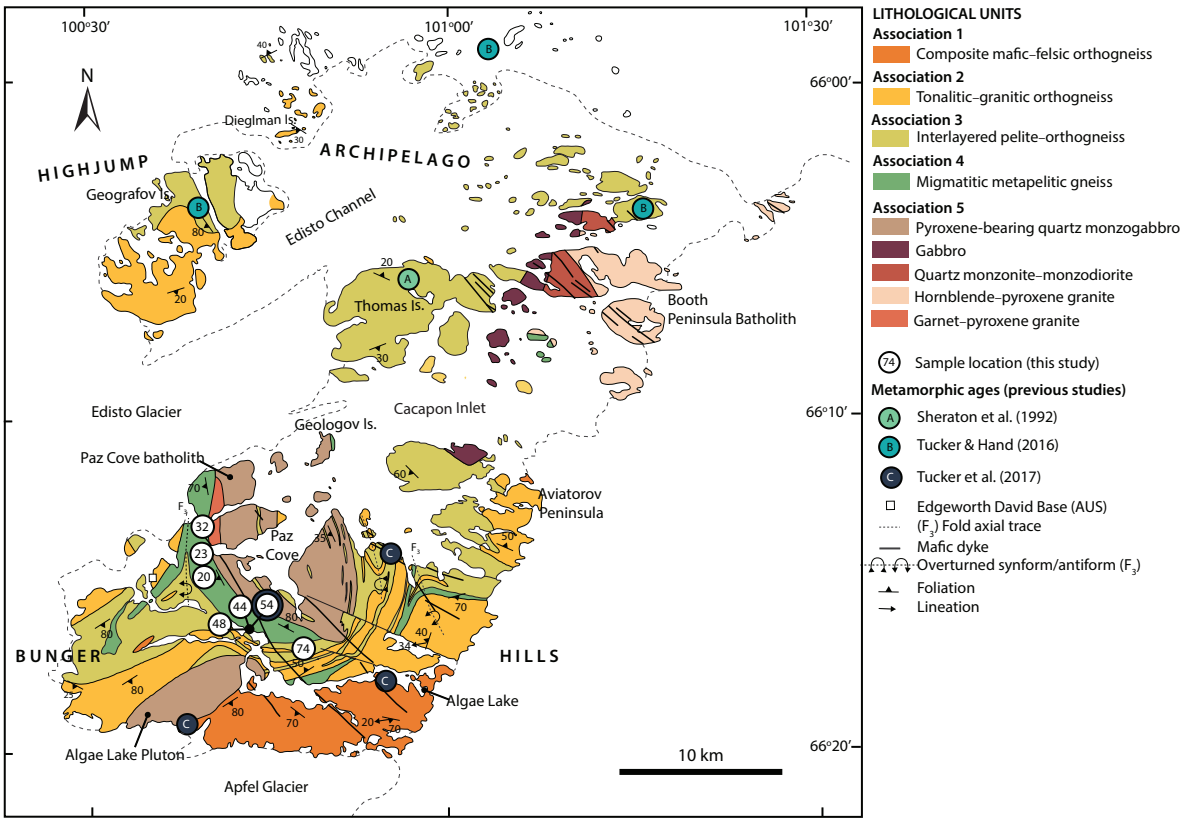

Figure 2. Simplified geology of the Bunger Hills and Highjump Archipelago. Figure modified from Sheraton et al. (1995), Stüwe and Wilson (1990) and Tucker et al. (2017). The location of samples from this study are indicated as white, numbered circles. The location of samples yielding metamorphic zircon and monazite ages from Sheraton et al. (1992), Tucker and Hand (2016) and Tucker et al. (2017), and representative structural data from Sheraton et al. (1995) are also shown.

Exposures in the Bunger Hills and the Highjump Archipelago that is located immediately to the north, are divided into five lithological associations (Fig. 2; Sheraton et al., 1995; Tucker et al., 2017). The southeast Bunger Hills are composed of Archean mafic–felsic orthogneiss with age and isotopic affinity to the Yilgarn Craton (Tucker et al., 2017). The Archean basement is considered to represent a now detached, reworked fragment of the Yilgarn Craton margin (Tucker et al., 2017) that underwent extension between ca. 1815–1600 Ma (Kirkland et al., 2015, 2011b; Spaggiari et al., 2015) in response to far-field subduction retreat and/or continental rifting (Kirkland et al., 2011b; Smithies et al., 2015; Spaggiari et al., 2015). The central region of the Bunger Hills and majority of the islands comprising the Highjump Archipelago are composed of tonalitic–granitic orthogneiss interlayered with metasedimentary gneiss (e.g. Fig. 3a; Sheraton et al., 1995; Tucker et al., 2017). Igneous protoliths to tonalite orthogneiss in the central Bunger Hills are inferred to have been emplaced at ca. 1700 Ma (Sheraton et al., 1993; Tucker et al., 2017) into a volcano–sedimentary basin that developed during extension of the craton margin (Tucker et al., 2017). Sheraton et al. (1992) also dated one sample of granodiorite orthogneiss from the central Bunger Hills at 1521 ± 29 Ma and proposed that the protolith to this rock was the product of melting of subducted oceanic crust. The northern Bunger Hills are dominated by a thick sequence of migmatitic garnet–cordierite ± sillimanite ± orthopyroxene ± spinel ± magnetite-bearing gneiss (e.g. Fig. 3b; Tucker et al., 2017). Sedimentary protoliths to this unit are inferred to have been deposited in a passive margin setting post ca. 1700 Ma magmatism but prior to Stage-1 tectonism of the Albany–Fraser Orogeny, with a probable maximum depositional age of ca. 1490 Ma (Tucker et al., 2017). Isotopically-evolved magmas were emplaced at ca. 1260 Ma, ca. 1200–1170 Ma and ca. 1150 Ma (Sheraton et al., 1995; Tucker et al., 2017).

2.2 Regional Mesoproterozoic tectono–metamorphic evolution

The Bunger Hills, Highjump Archipelago, Windmill Islands and Albany–Fraser Orogen experienced high-temperature deformation and metamorphism during the Albany–Fraser Orogeny (Stage-1: 1330–1260 Ma, Stage-2: 1225–1140 Ma; Table 1, and references therein). Tectono-metamorphic events of equivalent age

Table 1. The distribution and character of Mesoproterozoic metamorphism in the Albany–Fraser Orogen and Wilkes Land

Region	Age (Ma)*	Deformation	Peak P–T	P–T path	Interpretation	References
Northern Foreland (Munglinup Gneiss)	1195 ± 17	Macroscale folding, localised shearing and boudinage (late).	Amphibolite–granulite	-	-	Bodorkos and Wingate (2008b), Spaggiari *et al.* (2009) and Spaggiari *et al.* (2014)
Fraser Zone	ca. 1305–1290	Gneissic–migmatitic fabrics. Subsequent localised, dextral shearing.	7–9 kbar, 850 °C	Isobaric (9 kbar)	Contact metamorphism from mafic–felsic magmatism. Mid–lower crustal hot zone in a back-arc or rift. Subsequent cooling at depth.	Clark *et al.*, (1999), Wingate and Bodorkos (2007), De Waele and Pisarevsky (2008), Spaggiari *et al.* (2009), Kirkland *et al.* (2011a), Clark *et al.* (2014), Kirkland *et al.* (2014b) and Spaggiari *et al.* (2014)
Biranup Zone (Coramup Gneiss)	ca. 1300	Layer-parallel gneissosity. Subsequent shear zone development, tight asymmetric folding and NW-directed thrusting.	5–7 kbar, 800-850 °C**	Anticlockwise (through 10 kbar and 800–850 °C) to 7–8 kbar, 700–800 °C**	Extension, subsequent burial and recrystallization.	Beeson *et al.* (1988), Black *et al.* (1992), Nelson (1995), Bodorkos and Clark, (2004a; b), Bodorkos and Wingate, (2008a; b; c; d; e), Barquero-Molina (2009), Spaggiari *et al.* (2009), Kirkland *et al.* (2011b) Kirkland *et al.* (2011c), Kirkland *et al.* (2014a) and Spaggiari *et al.* (2014)
Biranup Zone (Dalyup Gneiss)	ca. 1225–1150	Gneissic fabric development. Repeat open–isoclinal, recumbent–upright folding (oblique compression) and NE–NW trending boudinage. Ductile shearing (late).	5–6 kbar, 750–850 °C	Down-pressure	Alternating extension and folding (NNW-directed compression). Exhumation along shear zones (late, decompression).	
Barren Basin	1205 ± 10	-	7–12 kbar, 560–675 °C	-	Contact metamorphism (Gnowangerup–Fraser Dyke Suite).	Wetherley (1998) and (Dawson *et al.*, 2003)
West Nornalup Zone (near Albany)	1314 ± 5 1304 ± 3	Layer-parallel gneissic fabrics and recumbent folding.	Amphibolite–granulite (?)	-	-	(Clark, 1995), Love, (1999), Duebendorfer (2002) and Spaggiari *et al.* (2009)
Arid Basin (Malcolm Metamorphics)	ca. 1330–1304	Layer parallel gneissosity Subsequent isoclinal folding and open–tight folding (NW-directed compression)	4 kbar, 750 °C	-	-	Clark *et al.* (2000), Fitzsimons and Buchan (2005), Spaggiari *et al.* (2009) and Adams (2012)
	ca. 1215–1140	NE-trending ductile thrusting and strike-slip reactivation	-	-	-	
Salisbury Gneiss	ca. 1214–1183	Gneissic fabric development and isoclinal folding. Subsequent NW–SE open folding and shear development.	> 5 kbar, 800 °C	Down-pressure	High-temperature exhumation along ductile thrusts.	Clark *et al.* (2000)
Ragged Basin	> 1154 ± 15	NW–SE and NE–SW open folding. Layer-parallel shearing.	4–5 kbar, 550 °C	-	Crustal thickening (due to over thrusting of Salisbury Gneiss).	Clark *et al.* (2000), Spaggiari *et al.* (2009) and Spaggiari *et al.* (2014)
Windmill Islands	ca. 1340–1300	Development of horizontal fabrics, isoclinal folding.	3.7–4.2 kbar, 710–740 °C	-	Extension, possible back-arc (?)	Paul *et al.* (1995), Post (2000), Morrissey (2016) and Morrissey *et al.* (2017)
	ca. 1240–1140	Upright–inclined isoclinal folding, open–tight (SE-plunging) folding, partial melting.	4 kbar, >850 °C	Down-pressure to isobaric	Contact metamorphism	
Bunger Hills & Highjump Archipelago	ca. 1300–1170 Minor >1300	Layer parallel gneissic fabric transposed by tight–isoclinal mesoscale folding. Subsequent regional, open, upright NW–SE folding. Localised shear zone development.	5.5–7.1 kbar, 800–960 °C (HJA) 6–9 kbar, 850-950 °C (BH)	Down-pressure to isobaric	Extension of thickened crust	Stüwe and Powell (1989), Sheraton *et al.* (1995), Tucker and Hand (2016), Tucker *et al.* (2017), and this study.

*Interpreted metamorphic ages (i.e. does not include Mesoproterozoic igneous crystallisation ages); **interpreted by Spaggiari *et al.* (2009) to reflect Stage-2 metamorphism.

are recognized in the Warumpi Province and Musgrave Inlier in central Australia (Kirkland et al., 2013; Morrissey et al., 2011; Smithies et al., 2011; Tucker et al., 2015; Walsh et al., 2015; Wong et al., 2015), and within the Pinjarra Orogen, Capricorn Orogen and Rudall Province that are situated along the margins of the WAC (e.g. Korhonen et al., 2017; Maidment, 2017), but are not discussed below.

The spatial distribution of Stage-1 deformation and metamorphism is patchy, and seemingly restricted to the eastern and south-eastern rock units and localities, that is, within the Windmill Islands, and the Nornalup and Fraser Zones, of the Albany–Fraser Orogen (Table 1, Fig. 1). Stage-1 involved development of layer-parallel fabrics and subsequent NW-directed, compressive–transpressive deformation. The Nornalup Zone and Windmill Islands were metamorphosed under low-pressure, amphibolite facies conditions (Clark et al., 2000; Fitzsimons and Buchan, 2005; Morrissey et al., 2017b; Paul et al., 1995; Post, 2000; Spaggiari et al., 2009). Metasedimentary rocks in the Fraser Zone attained slightly higher pressures and temperatures (7–9 kbar, 850 °C; Clark et al., 2014, 1999). Metamorphism was accompanied by voluminous mafic and granitic magmatism of the Recherche Supersuite (ca. 1330–1280 Ma; Clark et al., 2000; Kirkland et al., 2011b; Smithies et al., 2015; Spaggiari and Tyler, 2014), Fraser Zone gabbro (ca. 1305-1290 Ma; Clark et al., 1999; De Waele and Pisarevsky, 2008; Smithies et al., 2013), and felsic protoliths to the Clark Peninsula orthogneiss (ca. 1315 Ma) in the Windmill Islands (Morrissey et al., 2017b; Zhang et al., 2012). Stage-1 metamorphism is specifically proposed to have occurred during extension, possibly in a back-arc setting (Clark et al., 2014; Kirkland et al., 2011b; Morrissey et al., 2017a, b; Smithies et al., 2013) and/or associated with a lower crustal hot zone that formed from orogenic collapse of previously thickened crust (Spaggiari et al., 2015; Spaggiari and Smithies, 2015). Crustal thickening occurred as a result of soft collision of the exotic Loongana Arc onto the margin of the Albany–Fraser Orogen by ca. 1330 Ma (Kirkland et al., 2017; Smithies et al., 2015; Spaggiari and Smithies, 2015). A broad decrease in the age of Stage-1 magmatism from east (Nornalup Zone) to west (Fraser Zone) of the orogen is interpreted to reflect the westward delamination of the lower crust and migration of this hot zone (Smithies et al., 2015).

Stage-2 of the Albany–Fraser Orogeny occurred post rafting of the South Australian Craton–East Antarctic Craton (SAC–EAC) onto the West Australian Craton (WAC). Stage-2 was regional, increased in deformational intensity towards the core of the orogen, and involved NW-directed compression translating into open–isoclinal folding and north-directed thrusting (Table 1, and references therein). Metamorphism was comparatively long-lived, characterised by medium-pressure, high-temperature conditions, and slightly down-pressure to isobaric cooling is inferred to have followed the metamorphic peak (Beeson et al., 1988; Clark et al., 2000; Dawson et al., 2003; Morrissey et al., 2017a; Nelson et al., 1995; Paul et al., 1995; Post, 2000; Post et al., 1997; Spaggiari et al., 2009; Stüwe and Powell, 1989; Tucker and Hand, 2016). Stage-2 deformation was associated with emplacement of the voluminous Esperance Supersuite in the Albany–Fraser Orogen (ca. 1200–1125 Ma; Clark et al., 2000; Kirkland et al., 2011b; Smithies et al., 2015; Spaggiari and Tyler, 2014), the Ardery Charnockite and Ford Granite (ca. 1200–1160 Ma) and more juvenile felsic intrusives (ca. 1250–1215 Ma) in the Windmill Islands (Morrissey et al., 2017b; Zhang et al., 2012), and isotopically-evolved magmas in the Bunger Hills (ca. 1200–1170 Ma, ca. 1150 Ma; Sheraton et al., 1992; Tucker et al., 2017). The geodynamic setting of high temperature conditions has been variably interpreted (Table 1). Models include post-collisional extension of over-thickened crust (Post, 2000; Tucker and Hand, 2016), high temperature exhumation along thrust systems (Clark et al., 2000), and contact metamorphism from coevally-emplaced felsic magmas (Morrissey et al., 2017a) or mafic dykes (Dawson et al., 2003).

The Nornalup and Biranup zones cooled quickly from granulite facies conditions (~800 °C) to 365 ± 35 ºC by 1175–1159 Ma (Scibiorski et al., 2015). Scibiorski et al. (2015) interpret the rapidity of cooling and overlap of the ca. 1175–1159 Ma age range with documented constraints on the age of peak granulite facies metamorphism elsewhere in the orogen (see Table 1) to reflect syn–late orogenic cooling via a fast, tectonically-driven mechanism for exhumation (e.g. thrusting or shearing). Passive, isostasy-driven exhumation was proposed for after 1159 Ma (Scibiorski et al., 2015).

3. SAMPLE SELECTION AND DESCRIPTION

Seven samples of pelitic gneiss were selected to investigate the age and conditions of metamorphism in the Bunger Hills (Table 2, Fig. 2). Representative field photographs and photomicrographs are shown in Figs. 3 and 4, respectively. Three samples—BH32, BH54 and BH74—are used for phase equilibria forward modelling. These samples are mineralogically, microtexturally and structurally representative of the majority of pelitic gneiss that dominates the central–northwest region of the Bunger Hills (e.g. Figs. 3a and b). These three samples were also utilized for metamorphic zircon U–Pb geochronology, and garnet and zircon trace element chemistry. All samples were used for monazite U–Pb geochronology and trace element analysis. Cathodoluminescence (CL) imagery of zircon and back-scatter electron (BSE) imagery of monazite from each sample are shown in Fig. 5 and are representative of the varying internal morphology of the analysed grains.

3.1 Structure of the Bunger Hills

The oldest preserved fabric in the central–northwest Bunger Hills is a shallowly SW–NW-dipping gneissic fabric defined by K-feldspar-rich leucosomes that alternate with Mg–Fe–Al-rich melanosome, and within the melanosome, by the alignment of sillimanite–biotite ± garnet ± cordierite ± magnetite aggregates (Fig. 3b). This fabric is denoted a composite S_1–S_2 fabric and is comprised of a S_1 fabric that is near-completely transposed into co-planar S_2 and locally folded into tight to isoclinal, reclined to recumbent F_2 folds (e.g. Fig. 3c). The S_1–S_2 composite fabric was steeply-reoriented by regional open, upright, meso-macroscale F_3 folds that trend approximately ESE, have steep SW-dipping axial planes and shallow south plunges. Steep S_3 fabrics locally shear F_2 folds and in places F_2–F_3 interference patterns are observed. Coarse-grained orthopyroxene-bearing (Fig. 3d) and cordierite-bearing leucosomes (Fig. 3e) overprint reoriented S_1–S_2 fabrics (by D_3 deformation) and mesoscale F_3 folds in the migmatitic pelitic gneiss. Locally, garnet-bearing leucosomes and pegmatites also occur parallel to steeply-dipping F_3 axial planes and within the hinges of F_3 folds.

3.2 Metamorphic petrography and zircon/monazite morphology

3.2.1 Sample BH20

Sample BH20 is taken from the central Bunger Hills (Fig. 2) and contains biotite, garnet, cordierite, sillimanite, magnetite, ilmenite, K-feldspar, plagioclase and quartz. This sample is characterised by a strong S_1–S_2 foliation defined by the alignment of garnet, sillimanite, cordierite, biotite and magnetite, and the interlayering of these aluminium-rich domains with quartz–K-feldspar-rich layers (Fig. 3b). The aluminous layers are inferred to represent the residual portion of the rock; the quartzofeldspathic layers are interpreted as K-feldspar-rich leucosomes and therefore evidence for partial melting. The foliation at this locality dips moderately (~30–60 º) to the southwest and parallels the axial planes of inferred F_2 isoclinal folds (Fig. 3c). In places, the leucosomes overprint discontinuous horizons of the aluminium-rich domains.

Garnet grains (200–1500 μm) are anhedral to elongate and contain abundant inclusions of fibrous sillimanite (Fig. 4a). Sillimanite included within garnet does not appear to systematically align with the fabric external to garnet grains, and is denoted sillimanite$_1$ (generation 1). Garnet also contains lesser inclusions of cordierite, opaque minerals and rarely biotite. Sillimanite external to garnet is coarse-grained (up to 800 μm in length), prolific (comprising ~18 % of the sample), commonly occurs as dense aggregates, and is denoted as sillimanite$_2$ (generation 2; Fig. 4a). Sillimanite$_2$ grains occur within, and include, cordierite, magnetite and ilmenite. Cordierite is moderately coarse-grained (up to 500 μm) and nearly always in contact with dense aggregates of sillimanite and garnet. Biotite typically occurs as sub-aligned grains at the edges of garnet–cordierite–sillimanite$_2$ aggregates and as randomly-oriented grains at the boundaries of K-feldspar and quartz.

The peak mineral assemblage for this sample is interpreted as garnet–cordierite–sillimanite$_2$–magnetite–ilmenite–K-feldspar–plagioclase–melt–quartz. Sillimanite$_1$ is interpreted to form part of the prograde *P–T* evolution. The origin of biotite is less clear however the predominantly random orientation of grains and their location at the edges of matrix phases suggests that most biotite is retrograde.

Table 2. Summary of samples

Sample	Location (Zone 47D)		Lithological description	Peak assemblage^	Peak P–T
	Easting	Northing			
BH20	575915	2651034	g–cd–sill–bi–mt gneiss	g–cd–sill–mt–ilm–ksp–pl–liq–q	
BH23	575940	2651087	g–cd–bi–mt–sp gneiss	bi–g–cd–ilm–ksp–liq–q	
BH32	575287	2655333	g–cd–sill gneiss	g–cd–sill–ilm–ksp–pl–liq–q	5.9–7.0 kbar, 810-950 °C
BH44	578054	2648372	g–cd–mt–sp gneiss, opx-leucosomes	g–cd–sp–ilm–ksp–pl–liq–q	
BH48	577940	2648390	g–cd–mt–sp gneiss, opx-leucosomes	g–cd–sp–ilm–ksp–pl–liq–q	
BH54	577940	2648390	g–cd–mt–sp ± sill gneiss	g–cd–mt–ilm–ksp–pl–liq–q	6.5–7.2 kbar, 840–960 °C
BH74	580151	2646770	g–cd–sill gneiss	g–sill–cd –ilm–ksp–pl–liq–q	5.4–6.6 kbar, 800-920 °C

^Mineral abbreviations from Holland and Powell (1998)

Monazite grains are 100–150 μm in size and generally subrounded–rounded. Backscatter electron (BSE) imagery reveal that some grains exhibit low BSE response (dark) rounded–anhedral cores and high BSE response outer domains (e.g. BH20-M14 and 16; Fig. 5). Some grains exhibit complex patchy internal textures with randomly-distributed regions of both low and high BSE intensity that are also common to other samples.

3.2.2 Sample BH23

Sample BH23 is located approximately 60 meters NNE of sample BH20, near the contact between migmatitic pelitic gneiss and charnockite that comprises the Paz Cove Batholith (Fig. 2). This outcrop preserves a strong S_1–S_2 composite fabric and evidence for macroscale F_2 folding. Magnesian-rich parts of the outcrop contain coarse-grained, orthopyroxene–K-feldspar-bearing leucosome segregations that broadly align with the foliation (Fig. 3f). Minor amounts of heterogeneously-distributed orthopyroxene also occur in the melanosome within these regions. Aluminium-rich parts of this outcrop lack orthopyroxene. Sample BH23 is representative of an orthopyroxene-absent region of the outcrop and contains biotite, garnet, cordierite, ilmenite, K-feldspar, quartz and minor spinel and sillimanite.

Large garnet porphyroblasts (~500–2000 μm in diameter) contain inclusions of biotite, cordierite, feldspar and quartz. Some garnet cores contain discrete aggregates of acicular sillimanite (Fig. 4b). Fine-grained sillimanite is also included within the cores of a few large cordierite grains (Fig. 4b). Sillimanite does not occur external to garnet or cordierite. The foliation is defined by elongation of predominantly garnet and cordierite, and sillimanite included within these two phases. Small (~100–200 μm), rounded spinel grains are exclusively included within the cores of some cordierite grains. Biotite is moderately abundant (~15 % abundance), very coarse-grained (up to 1 mm), and commonly occurs within the matrix (i.e. is not included within garnet), although the majority of biotite grains are not systematically aligned with the foliation. The remainder of the sample comprises abundant K-feldspar and quartz.

The peak mineral assemblage for this sample is interpreted to be biotite–garnet–cordierite–ilmenite–K-feldspar–melt–quartz with spinel and sillimanite forming part of the prograde assemblage. Although biotite grains are commonly randomly oriented, biotite is considered part of the peak assemblage due to its coarse grain size.

Monazite grains are typically 50–150 μm in size, anhedral, and occur as partial inclusions within garnet, and along grain boundaries of biotite, cordierite and feldspar within the matrix. Monazite show largely uniform BSE response with no obvious zoning (e.g. BH23-11; Fig. 5).

3.2.3 Sample BH32

Sample BH32 comes from the northwest Bunger Hills (Fig. 2) and contains biotite, garnet, cordierite, sillimanite, ilmenite, K-feldspar, plagioclase, quartz, minor magnetite and rare spinel. The outcrop appearance of BH32 is very similar to BH20. The strong S_1–S_2 fabric at this locality dips moderately to steeply towards the WSW. The fabric is defined by systematically alternating layers of feldspar–quartz ± biotite and more aluminous layers of garnet–sillimanite–ilmenite ± biotite ± cordierite (Fig. 3g). A prominent lineation defined by the alignment of sillimanite also plunges to the WSW. Similarly to sample BH20, the quartzofeldspathic layers are interpreted as K-feldspar-rich leucosomes.

Garnet grains (200–1000 μm, Fig. 3g) occur largely as subhedral porphyroblasts to slightly elongate in shape and include fine-grained

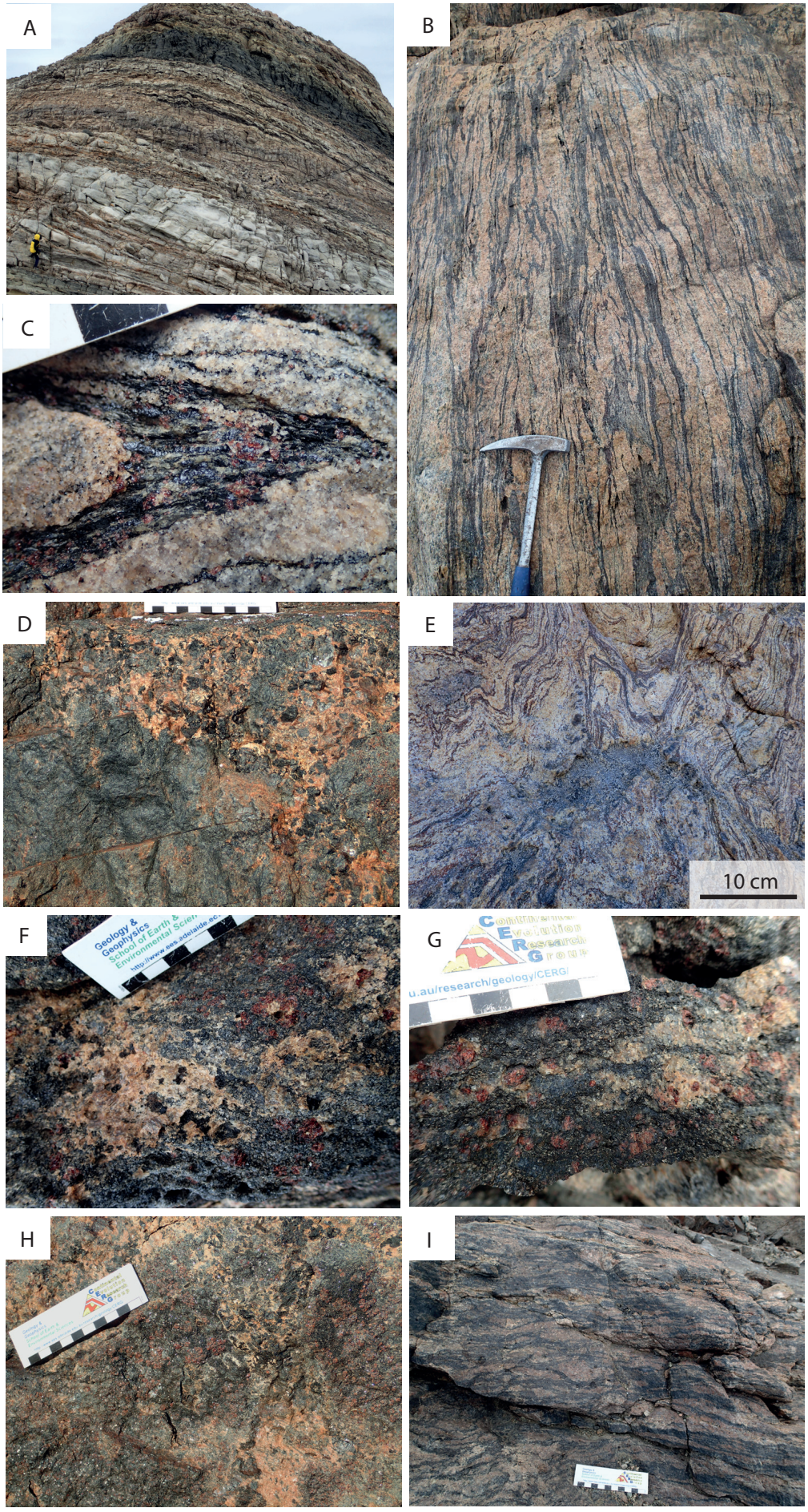
A
B
C
D
E
10 cm
F
G
H
I

Figure 3. **(previous page)** Field photographs of key rock relationships and sampled lithologies from the Bunger Hills. (a) Outcrop appearance of the interlayered othogneiss–pelite gneiss in the northeast Bunger Hills, near the location of BH74; (b) Typical outcrop appearance of the migmatitic pelite gneiss characterised by the assemblage garnet-cordierite ± sillimanite ± orthopyroxene ± spinel in the central Bunger Hills. Photo taken near the location of sample BH20. Aluminium-rich melanosome alternates with stromatic, K-feldspar-rich leucosomes. In places, the K-feldspar leucosomes overprint the strongly-defined S_1–S_2 fabric, isolating the pelite as enclaves; (c) The S_2 fabric is axial planar to F_2, defined by the alignment of sillimanite–biotite ± cordierite ± garnet ± magnetite in this image within the hinge of a tight, recumbent F_2 fold; (d) Coarse-grained orthopyroxene-bearing leucosomes overprinting pelite gneiss near the location of BH44, BH48 and BH54; (e) Coarse-grained cordierite-bearing leucosomes (centred) overprinting the steeply-dipping S_1–S_2 fabric (reoriented by D_3) and inferred mesoscale F_3 folds in aluminous, migmatitic pelite gneiss near the location of BH32; (f) Dark blue–grey, coarse-grained garnet–cordierite–biotite-rich melanosome with a discordant, coarse K-feldspar–orthopyroxene-bearing leuco-segregation from the location of BH23. The distribution of orthopyroxene is heterogeneous within the melanosome, external to the leucosome; (g) Coarse-grained garnet–cordierite ± sillimanite gneiss from the location of BH32; (h) Outcrop appearance near the location of BH44, BH48 and BH54 showing dark regions of coarse-grained garnet–cordierite ± sillimanite ± spinel ± magnetite and overprinting orthopyroxene-bearing leucosomes; (i) Sample BH74, taken from a garnet ± cordierite ± sillimanite gneiss. Graduations on the scale bar, where shown, are 1 cm.

sillimanite (denoted sillimanite$_1$), biotite, quartz and ilmenite (Fig. 4c). Elongate, coarser-grained sillimanite (up to 1 mm in length) is abundant within the matrix, sometimes wraps about garnet, and is denoted as sillimanite$_2$ (Fig. 4c). Cordierite (grains up to 500 μm) is a minor phase and near-always occurs adjacent to garnet and sillimanite. Biotite typically occurs as small inclusions within garnet and as relatively coarse (100–700 μm), weakly aligned grains at the boundaries of feldspar, garnet and sillimanite.

The peak mineral assemblage for sample BH32 is interpreted to be garnet–cordierite–sillimanite–ilmenite–K-feldspar–plagioclase–quartz–melt. Sillimanite$_1$ and minor biotite included within garnet are considered to form part of the prograde mineral assemblage. It is difficult to assign the matrix biotite to the peak or retrograde assemblage. However, the sub-aligned nature of the grains suggests that biotite may have developed late in the peak *P–T* evolution.

Monazite grains are 50–250 μm, rounded to anhedral in shape, and occur largely within the matrix along the boundaries of biotite, cordierite and feldspar (Fig. 5). Grains exhibit a varied BSE response. The majority of monazite have anhedral cores with a low BSE response that are mantled by one or more anhedral, outer domains with progressively higher BSE response (e.g. BH32-M10 and BH32-M15; Fig. 5). Some grains have a uniform BSE response with no to patchy internal zonation (e.g. BH32-20; Fig. 5).

Zircon are typically 75–100 μm with few grains up to 200 μm. Grains are subrounded to elongate with subrounded crystal faces and aspect ratios of 1:1 to 1:2. Five main CL responses are observed and are discussed below in order of relative age (Fig. 5). Strongly oscillatory-zoned cores typically yield a low CL response and are interpreted as inherited grains. These strongly-zoned cores also rarely contain small, luminescent centres. In many instances, the strongly-zoned cores appear near-completely to entirely overprinted by dark CL domains that exhibit relic, weak ghosted-zoning, sector zoning and/or convoluted internal textures. Rarely, the dark cores are mantled by a thin, irregularly-shaped, strongly-luminescent rim. These strongly-luminescent rims are homogeneous or exhibit weak internal features. Majority of dark cores (with or without strongly-luminescent rims) are surrounded by a weakly-luminescent rim that is featureless to sector-zoned in appearance. In a number of instances, weakly-luminescent rims appear to truncate the dark cores and their internal features, giving them sharp edges. Some weakly-luminescent rims are gradational from and/or show indistinct separation from the dark cores and/or strongly-luminescent rims. Very rarely, the weakly luminescent rims are surrounded by a narrow to moderately-wide, homogeneous overgrowths with low CL response. These dark overgrowths clearly truncate internal features of the inner CL domains with distinct separation and making the inner zones appear with sharp edges.

3.2.4 Samples BH44 and BH48

Samples BH44 and BH48 are from the same location (Fig. 2), are mineralogically and texturally equivalent, and contain biotite, garnet, cordierite, spinel, magnetite, ilmenite, K-feldspar, plagioclase and quartz. The strong S_1–S_2 foliation at this locality dips near-vertically to the NNE–SSW. Coarse-grained orthopyroxene–K-feldspar ± magnetite-bearing leucosomes are abundant, although heterogeneously distributed, and generally overprint this foliation (Figs. 3d and h). The orthopyroxene leucosomes vary in size from centimetre-scale veinlets to segregations that

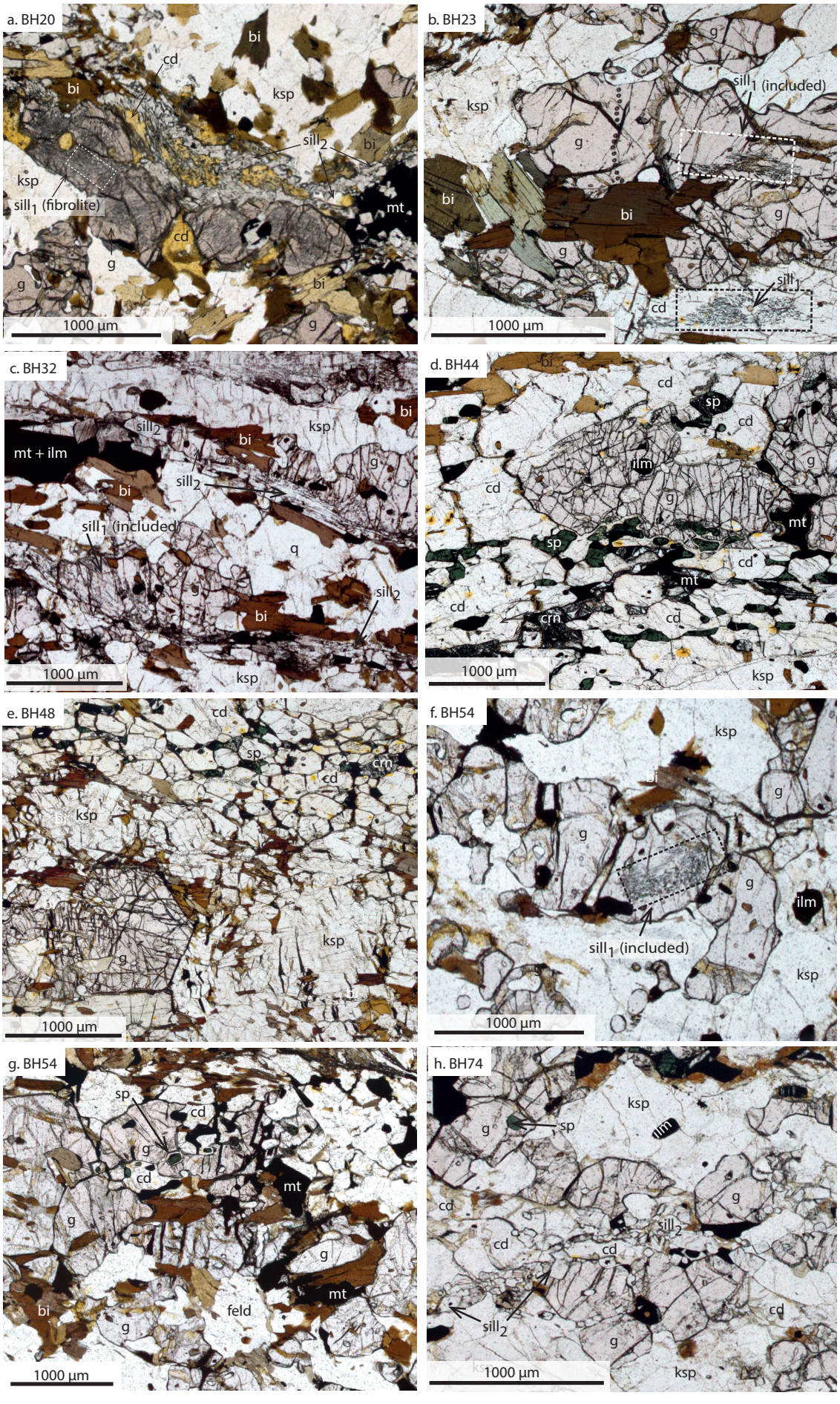
a. BH20
bi
cd
bi
ksp
sill2
bi
ksp
sill1 (fibrolite)
mt
cd
g
g
bi
g
1000 µm
b. BH23
g
sill1 (included)
ksp
g
bi
bi
g
g
sill1
cd
1000 µm
c. BH32
bi
sill2
ksp
mt + ilm
bi
g
sill2
bi
sill1 (included)
q
g
sill2
bi
1000 µm
ksp
d. BH44
bi
cd
sp
cd
ilm
g
cd
g
mt
sp
cd
mt
cd
crn
cd
1000 µm
ksp
e. BH48
cd
sp
crn
cd
bi
ksp
ksp
g
1000 µm
f. BH54
ksp
bi
g
g
g
ilm
sill1 (included)
ksp
1000 µm
g. BH54
sp
cd
g
cd
mt
g
g
mt
bi
feld
g
1000 µm
h. BH74
ksp
g
sp
ilm
cd
g
sill2
cd
cd
cd
sill2
g
ksp
1000 µm

Figure 4. **(previous page)** Representative thin section photomicrographs of pelite gneiss from the Bunger Hills. (a) BH20: alignment of garnet, sillimanite, cordierite, biotite and magnetite. Garnet contains dense fibrous aggregates of sillimanite; (b) BH23. Coarse garnet porphyroblasts contain acicular sillimanite in places. Cordierite grains also rarely contain aggregates of acicular sillimanite; (c) BH32. Fabric is defined by alternating layer of quartz-K-feldspar-plagioclase with aluminous layers of sillimanite, garnet, cordierite, biotite and magnetite + ilmenite. Biotite is typically included within garnet and occurs as anhedral grains at grain boundaries of feldspar, garnet and sillimanite; (d) BH44. Coarse garnet surrounded by cordierite, magnetite and spinel. Spinel is shown at the grain boundaries of cordierite grains and where adjacent to garnet, is separated by cordierite; (e) BH48. Equant garnet porphyroblast surrounded by cordierite-dominated matrix. Spinel is included within the cordierite, and at the cordierite grain boundaries. Biotite is anhedral and randomly oriented at the grain boundaries of feldspar, garnet and corderite; (f) BH54. Dense aggregates of acicular sillimanite include the cores of some subhedral garnet grains. Sillimanite does not occur external to garnet; (g) BH54. Coarse-grained, anhedral to elongate garnet contains inclusions of magnetite, ilmenite, quartz, feldspar, spinel and cordierite and is surrounded by coarse biotite; (h) BH74. Small, subhedral to rounded garnet grains are surrounded by fine-grained sillimanite, minor cordierite, K-feldspar and quartz. Spinel is rarely included in garnet.

isolate the pelite gneiss as enclaves.

These samples are characterised by semi-continuous, alternating layers of spinel–cordierite ± magnetite and quartz–feldspar–biotite (Figs. 4d and e). Garnet is present throughout the sample. Garnet is subhedral, large (1–5 mm), porphyroblastic to elongate, and contains inclusions of quartz, feldspar, ilmenite, biotite and spinel. Elongate garnet, spinel and cordierite grains define the foliation. Where garnet is situated at the interface of the spinel–cordierite ± magnetite-rich layers and quartz–feldspar–biotite layers, spinel occurs as abundant, coarse-grained partial inclusions within the garnet rims. However, spinel occurring near the garnet rims are systematically separated from garnet by thin coronae of cordierite (e.g. Fig. 4d). Spinel grains hosted within garnet cores generally occur in direct contact with garnet. Minor corundum and magnetite are rarely observed adjacent to spinel. The quartz–feldspar–biotite layers are dominated by K-feldspar and plagioclase.

The peak mineral assemblage for these samples is interpreted to be garnet–cordierite–spinel–ilmenite–K-feldspar–plagioclase–melt–quartz. Biotite is considered to form part of the post-peak mineral assemblage due to the randomly-oriented and anhedral nature of the grains that predominantly occur at the grain boundaries of inferred peak minerals.

Monazite grains are 50–200 μm, anhedral–elongate and commonly microfractured or pitted. Grains appear to be located exclusively within the matrix and occur along the boundaries of spinel, cordierite, feldspar and quartz. Monazite grains typically exhibit simple zoning with low BSE response cores mantled by thin to moderately-thick zones of higher BSE response (e.g. BH48-17, BH48-22, BH44-7; Fig. 5). Some grains show core regions with convoluted internal textures and randomly-distributed zones of both low and high BSE intensity (e.g. BH44-2 and BH44-7; Fig. 5).

3.2.5 Sample BH54

Sample BH54 comes from the same outcrop as sample BH48 but is taken from a meter-wide, aluminous layer of garnet–cordierite ± sillimanite-bearing gneiss. This sample contains biotite, garnet, cordierite, spinel, magnetite, ilmenite, K-feldspar, plagioclase, quartz and rare sillimanite. Similarly to samples BH44 and BH48, the strong S_1–S_2 fabric at this outcrop is defined by layers of garnet–spinel–cordierite ± magnetite that alternate with layers of quartz–feldspar ± biotite. Orthopyroxene-bearing leucosomes are not present within this part of the outcrop. Immediately north of the sampled locality (approximately 200 m), a sillimanite-rich variation of BH54 is folded into open, upright, mesoscale F_3 folds that are overprinted by orthopyroxene-absent, K-feldspar-rich leucosomes.

Garnet occurs in two microstructural settings. In the first instance, garnet occurs as subhedral porphyroblasts (<1 mm) with a relatively low abundance of inclusions of other phases, and largely within quartz–feldspar dominated layers. Rarely, these garnet also host small aggregates of acicular sillimanite (Fig. 4f). Garnet commonly also occurs as coarser, anhedral to elongate (varies in size from 800 μm to 2 mm) grains that are aligned within the foliation. These coarse, elongate garnet grains contain a higher abundance of inclusions of matrix phases such as quartz, biotite, coarse magnetite and ilmenite, minor cordierite and spinel. Sillimanite is only very rarely included within these elongate garnet grains. Sillimanite, where included in garnet, is broadly aligned with the external foliation as defined by alignment of elongate garnet grains, spinel, magnetite and cordierite. Spinel occurs as small (< 200 μm), rounded inclusions within

elongate garnet cores, coarser-grained inclusions at elongate garnet rims (200–600 μm), within cordierite and along cordierite grain boundaries. Similar to sample BH44, spinel occurring within garnet rim regions are separated from garnet by thin cordierite coronae (<100 μm, e.g. Fig. 4g). Spinel grains included in garnet cores also rarely exhibit cordierite coronae but there are instances of spinel occurring in direct contact with garnet. Cordierite is moderately coarse grained (100–500 μm) and abundant. Magnetite and ilmenite (grains up to 1 mm length) occur throughout this sample and are included within all phases except sillimanite. Biotite occurs as inclusions within garnet as well as anhedral grains along garnet, feldspar and cordierite grain edges. Quartz and perthite grains are large (up to 6 mm) with smaller recrystallised quartz grains at their grain boundaries.

The peak mineral assemblage for sample BH54 is interpreted to be garnet–cordierite–magnetite–ilmenite–plagioclase–K-feldspar–quartz–melt. Sillimanite, spinel and biotite are considered to form part of the prograde assemblage. Matrix biotite and minor cordierite (forming coronae about spinel) are considered to form part of the post-peak mineral assemblage. The elongate, anhedral nature of many garnet grains that have a moderately-high density of inclusions of other inferred peak minerals suggests that these garnet grew late during peak metamorphism.

Monazite grains are 75–300 μm, anhedral–rounded and often occur along grain boundaries within the cordierite-bearing matrix. Few grains are included within garnet, but are not isolated from microfractures within the garnet. Monazite grains commonly show patchy, indistinct internal textures with no clear pattern to the distribution of zones with light and dark BSE response (e.g. BH54-15, BH54-24, BH54-4; Fig. 5). Sometimes grains broadly exhibit simple internal zoning with the core yielding the lowest BSE response.

Zircon are typically 50–150 μm with few grains up to 200 μm. Grains are subrounded to elongate with subrounded crystal faces and aspect ratios of 1:1 to 1:2.5. Zircon in this sample exhibit similar internal morphology to sample BH32 (Fig. 5). The majority of grains yield dark cores that appear unzoned to weakly-ghost zoned, sector zoned and/or exhibit convoluted and indistinct internal textures. These dark cores appear to near-completely overprint more strongly oscillatory-zoned cores that are rarely preserved. Commonly the dark cores are mantled by thin luminescent rims. The luminescent rims are generally irregular in shape and are homogeneous or exhibit weak, indistinct internal textures. The majority of dark cores (with or without luminescent rims) are surrounded by featureless to sector-zoned, weakly-luminescent rims. In some instances, the weakly-luminescent rims appear to cross cut the dark cores, truncating their internal features. In other instances, the weakly-luminescent rims appear to have gradational contacts with the dark cores and/or luminescent rims. Rarely, entire grains exhibit the same CL response as the weakly-luminescent rims (i.e. do not surround dark cores). The weakly-luminescent rims and whole grains with a similar CL response are surrounded by a narrow to moderately-wide, dark, homogeneous overgrowth that truncates internal features of the inner domains and gives the inner domains an equant appearance with sharp edges.

3.2.6 Sample BH74

Sample BH74 comes from a five-meter wide metasedimentary raft (Fig. 3i) within orthopyroxene-bearing gneiss in the interlayered orthogneiss–pelite unit (i.e. Fig. 3a) in the central Bunger Hills. This sample contains garnet, cordierite, sillimanite, ilmenite, K-feldspar, plagioclase, quartz and rare magnetite and spinel, and is considerably more quartzofeldspathic than the other analysed samples. The foliation at this locality is defined by alternating layers of garnet–sillimanite–cordierite with layers of quartz ± feldspar.

Garnet grains are small (typically 500–800 μm), subrounded–anhedral porphyroblasts and contain minor amounts of quartz, ilmenite, magnetite, fine-grained sillimanite and rare spinel (Fig. 4h). Spinel included in garnet is volumetrically minor (<1 % abundance), rounded, < 200 μm and commonly occurs in direct contact with garnet (i.e. without cordierite coronae). Rare spinel is also included within cordierite and sillimanite. Sillimanite external to garnet is moderately-abundant, coarse-grained (up to 1 mm length), consistently elongate and in places wraps garnet where it also occurs in direct contact with ilmenite and cordierite. The remainder of the sample is comprised largely of coarse quartz and K-feldspar (some grains up to 9 mm) and lesser plagioclase. The peak mineral assemblage for this sample is

interpreted to be garnet–sillimanite–cordierite–ilmenite–K-feldspar–plagioclase–melt–quartz.

Monazite grains are 50–300 μm and subrounded. BSE imagery typically show grains with broad zoning in which low BSE response cores are surrounded by one or multiple anhedral zones of progressively higher BSE response (e.g. BH74-M3 and BH74-5; Fig. 5). Some grains exhibit convoluted internal textures with incoherent distribution of anhedral, low and high BSE response zones (e.g. BH74-M13; Fig. 5).

Zircon are typically 75–150 μm, and rarely up to 250 μm. Grains are subrounded and elongate with subrounded crystal faces and have aspect ratios of 1:1 to 1:2.5. Zircon in sample BH74 exhibit the same internal morphology as samples BH32 and BH54 but the relationship between domains with different CL responses is more clearly and consistently defined (Fig. 5). A small number of grains exhibit strongly oscillatory-zoned cores with a low CL response, and are interpreted as inherited grains. The strongly-zoned cores rarely contain luminescent, anhedral centres. The majority of grains in this sample exhibit dark cores with ghosted, broad simple zoning and/or indistinct and convoluted internal textures. These dark cores appear to be near-completely overprinting the strongly-zoned (inherited) cores and mimic the shape of the original grain. The dark cores are typically mantled by thin, irregularly-shaped, strongly-luminescent rims. The strongly-luminescent rims are homogeneous or exhibit incoherent, faint internal textures. Most of the strongly-luminescent rims are in turn surrounded by a weakly-luminescent rim. The weakly-luminescent rims are homogeneous and featureless or contain broad simple zoning or sector zoning. The contact between the weakly-luminescent rim and the inner strongly-luminescent rim (or directly the dark core where absent) varies from grain to grain and appears both sharp and gradational. Where the contact is distinct, the weakly-luminescent rims appear to truncate the internal textures of the inner CL domains, and give the inner domains equant appearance with sharp edges. The weakly luminescent rims themselves typically have a rounded morphology irrespective of the size of the grain and can be up to 150 μm thick. Rarely, entire grains have a weakly-luminescent CL response and are featureless to weakly sector zoned. The weakly-luminescent rims and grains are commonly surrounded by a narrow to moderately-wide, dark, homogeneous overgrowth. These dark overgrowths clearly truncate the inner CL domains and their internal features.

4. ANALYTICAL METHODS

4.1 Zircon geochronology and trace element chemistry

Zircon grains were separated from crushed rock samples by hand panning, magnetic separation and using heavy-liquid techniques. Zircon grains were handpicked, mounted in epoxy resin and imaged using a CL detector on a Tescan MIRA3 Field Emission scanning electron microscope at Curtin University, Perth.

U–Pb isotopic analyses and trace element analyses (lanthanides, yttrium, titanium and hafnium) on zircon from samples BH54, BH32 and BH74 were obtained by Laser–Ablation Split–Stream (LASS) Inductively Coupled Plasma–Mass Spectrometry (ICP–MS) at the University of California, Santa Barbara. Analytical parameters utilized are documented in Tucker et al. (2017). Analytical methods follow those of (Kylander-Clark et al., 2013). Zircon inferred of metamorphic origin based on internal morphology (versus inferred inherited zircon, see Tucker et al., (2017)) were targeted to provide constraints on the timing of metamorphism. Data reduction was done using Iolite (v. 3.1), developed by the Melbourne Isotope Group (Paton et al., 2011). Age data were plotted using Isoplot v. 4.15 (Ludwig, 2012). REE data were normalized to the CI chondrite vales of McDonough and Sun (1995), denoted with subscript N. Europium anomalies are quoted as Eu_N/Eu_N^* values ($Eu_N/Eu_N^* = Eu_N/0.5*(Sm_N + Gd_N)$).

4.2 Monazite geochronology and trace element chemistry

Monazite were analysed *in situ*, in thin section, for all samples excluding BH20, in an attempt to link the timing of major silicate mineral growth to the crystallisation of monazite. Monazite grains were also analysed on grain separates mounted in epoxy for samples BH20, BH32, BH54 and BH74 due to the relatively low abundance of monazite in thin sections of these samples. Monazite grains were imaged using a BSE detector on a Phillips XL30 SEM at Adelaide Microscopy, the University of Adelaide, to ascertain their microstructural

location and internal compositional variation.

LA–ICP–MS analyses were obtained at Adelaide Microscopy using an ASI Resolution M-50 193 nm excimer laser under a He-ablation atmosphere, connected to an Agilent 7700s ICP–MS. Isotopes measured for geochronology were ^{202}Hg, ^{204}Pb, ^{206}Pb, ^{207}Pb, ^{208}Pb, ^{232}Th and ^{238}U. Yttrium, silica, phosphorous, calcium and select lanthanides (^{139}La, ^{140}Ce, ^{141}Pr, ^{146}Nd, ^{147}Sm and ^{157}Gd) were measured concurrently to U–Pb analyses. The acquisition time was 60 s for each analysis comprising two pre-ablation cleaning pulses to remove surficial contamination, 30 s of background measurement, and 30 s of sample ablation. Ablation was performed with a frequency of 5 Hz, a 13 µm spot size and a fluence of ~2 J/cm^2 on unknown analyses.

Data reduction was done using Iolite (v. 3.1). Mass bias and elemental fractionation on U–Pb analyses were corrected using the measured isotopic ratios of the primary monazite reference material MAdel (TIMS normalisation data: ^{207}Pb/^{206}Pa = 491.0 ± 2.7 Ma, ^{206}Pb/^{238}U = 518.4 ± 1.0 Ma and ^{207}Pb/^{235}U = 513.1 ± 0.2 Ma; updated from Payne et al. (2008) with additional TIMS data). Throughout the study, MAdel yielded weighted mean ages of ^{207}Pb/^{20}6Pb = 473.4 ± 5.5 Ma, ^{206}Pb/^{238}U = 518.3 ± 0.9 Ma and ^{207}Pb/^{235}U = 512.2 ± 1.1 Ma (n = 94). The accuracy of the corrected data was monitored by analysis of in-house standards 94-222/Bruna NW (450.2 ± 3.4 Ma; Payne, 2008) and MtGt (ca. 325 Ma). The weighted average ^{206}Pb/^{238}U age of 94-222/Bruna NW and MtGt was 453.3 ± 1.0 Ma (MSWD = 1.0, n = 58/61) and 319.8 ± 1.2 Ma (MSWD = 0.77, n = 30/33), respectively. NIST610 glass was utilized as the external standard for major and trace element analysis of monazite and cerium was used as the internal standard. Elemental analyses were also utilised to filter the U–Pb dataset for unknown contamination and zoning in the reference materials and unknowns. Instrument drift was rectified by standard–sample bracketing every 15 unknown analyses.

The quoted analytical uncertainties on individual analyses are given at the 2σ level, and include contributions from the external reproducibility of the primary reference standard MAdel for the measured ratios, propagated in quadrature. Age data were plotted using Isoplot v. 4.15 (Ludwig, 2012). Analyses (also zircon age data, above) that occur outside 2σ uncertainty of concordia are denoted 'discordant' (see also Spencer et al., 2015). Traditionally, the ^{207}Pb/^{206}Pb age has been considered the most geologically valid age for zircon older than ca. 1200 Ma and/or zircon having undergone recent Pb-loss. Spencer et al. (2015) recently proposed an older cutoff (ca. 1500 Ma) due to greater imprecision and larger uncertainties on the ^{207}Pb/^{206}Pb age than the ^{206}Pb/^{238}U age for zircon <1500 Ma. All data within this study fall in this cross over interval. Accordingly, where age data are discussed, only concordant analyses are referred to, unless stated otherwise. The ^{206}Pb/^{238}U age is primarily quoted for all individual analyses, however ^{207}Pb/^{206}Pb age data are also presented as necessary for comparison.

4.3 LA–ICP–MS garnet trace element chemistry

Quantitative rare earth element analyses of garnet from samples BH32, BH54 and BH74 were done using the same instrumentation as for LA–ICP–MS monazite geochronology. Elements ^{89}Y, ^{139}La, ^{140}Ce, ^{141}Pr, ^{146}Nd, ^{147}Sm, ^{153}Eu, ^{157}Gd, ^{159}Tb, ^{163}Dy, ^{165}Ho, ^{166}Er, ^{169}Tm, ^{172}Yb and ^{175}Lu were measured along linear traverses from rim to rim through the cores of representative garnet grains. A 30 µm spot size, frequency of 5 Hz, and fluence of 3.5 J/cm^2 were used for unknown analyses and analysis of secondary standards BHVO and NIST610 glass. A 67 µm spot size was used for analysis of the primary standard NIST612 glass. The total acquisition time was 90 s, inclusive of five pre-ablation cleaning pulses, 30 s of background measurement and 60 s of ablation. Electron microprobe measurements of Ca served as an internal standard. Instrument drift was corrected for by standard bracketing of every 15 unknown analyses. Data processing was done using Iolite software (v. 3.1). REE data were normalized to the CI chondrite vales of McDonough and Sun (1995). Europium anomalies are quoted as Eu_N/Eu_N^* values ($Eu_N/Eu_N^* = Eu_N/0.5*(Sm_N + Gd_N)$).

4.4 Phase equilibrium forward modelling

Whole rock geochemical analyses for phase equilibria forward modelling were undertaken by Wavelength Dispersive X-ray Fluorescence (XRF) spectrometry at the Department of Earth and Environment, Franklin and Marshall College, USA. Major element analyses of minerals and qualitative elemental X-ray maps of garnet were obtained using a Cameca SXFive electron

microprobe at the University of Adelaide. A beam current of 20 nA, accelerating voltage of 15 kV and a defocussed beam size of 5 μm were used for all point analyses. Compositional mapping of garnet for major elements Fe, Mg, Mn and Ca was undertaken using a 15 kV accelerating voltage and a beam current of 150 nA. Data calibration and reduction was carried out in Probe for EPMA, distributed by Probe Software Inc.

P–T models were calculated for samples BH32, BH54 and BH74 using THERMOCALC v. 3.37 with the internally consistent updated thermodynamic dataset ds62 (Holland and Powell, 2011), for the geologically realistic system NCKFMASHTO (Na_2O–CaO–K_2O–FeO–MgO–Al_2O_3–SiO_2–H_2O–TiO_2–Fe_2O_3), and using the activity composition relationships of White et al. (2014). Mineral reaction microstructures were not observed in these rocks (except minor development of cordierite coronae around spinel in sample BH54), and as such the samples are considered homogeneous on a thin section scale. The bulk compositions used for *P–T* calculations are therefore based on whole-rock XRF geochemical analyses (Table 3) recalculated to molar oxide percent.

The H_2O content of each sample was based on the abundance of hydrous phases (i.e. cordierite and biotite) in the observed mineral assemblages, and a known, conservative estimate of the H_2O content of these minerals in granulites (e.g. Rigby and Droop, 2011). The sensitivity of the selected H_2Ocontent on the peak temperature for each sample was evaluated using an isobaric Temperature–M_{H2O}model (Appendix A). *T*–M_{H2O} models (also *T*–M_o models in Appendix A, discussed below) were calculated at the approximate peak pressure of the inferred peak mineral assemblage field for each sample. The *T*–M_{H2O} models reflect the changes in topology of the phase equilibria and position of the solidus over a range of H_2O contents from a 'dry' composition (M = 0) to the maximum H_2O content (M = 1) as proxied by the LOI value from whole rock geochemistry.

The Fe oxidation state on the stability of preserved mineral assemblages in each sample was assessed using calculated *T*–M_o and Pressure–M_o models (M_o = Fe_2O_3/ (FeO + Fe_2O_3); Appendix A) over the compositional range M_o = 0 (i.e. reduced) to M_o = 0.75 (i.e. oxidised). A Fe_2O_3 content was chosen so that the inferred peak mineral assemblage field was intersected on the *T*–M_o and *P*–M_o diagram. The selected Fe_2O_3 content was also guided by an estimation of Fe^{3+} in ferric iron-bearing minerals in thin section and their stoichiometrically-recast (Droop, 1987) electron microprobe compositions. This approach indicated that approximately 20 %, 45 % and 15 % Fe in samples BH32, BH54 and BH74, respectively, was Fe^{3+}.

Mineral compositional isopleths and modal abundances were calculated for the forward models using TCInvestigator (v. 2.0; Pearce et al., 2015; Appendix A) to further constrain the peak *P–T* conditions.

5. RESULTS

5.1 Major element mineral chemistry

Major element mineral chemistry is presented for samples BH32, BH54 and BH74 which were used for phase equilibrium forward modelling. Mineral chemistry is summarised in Table 4 and representative electron microprobe mineral analyses are given in Appendix B.

5.1.1 Garnet

Garnet in all samples are dominantly almandine–pyrope with core X_{alm} (Fe^{2+}/(Fe^{2+} + Ca + Mg + Mn)) values of 0.54–0.62 and X_{py} (Mg/(Fe^{2+} + Ca + Mg + Mn)) values of 0.30–0.43. Sample BH54 shows slight enrichment in X_{alm} to values of 0.57–0.60 and depletion in X_{py} to values of 0.37–0.40, in garnet rim analyses. All other samples are unzoned in X_{alm} and X_{py} with values between 0.58–0.62 and 0.29–0.33 from garnet rims, respectively. Garnets are unzoned in grossular and spessartine in all samples, with X_{grs} (Ca/(Fe^{2+} + Ca + Mg + Mn)) and X_{spss} (Mn/(Fe^{2+} + Ca + Mg + Mn)) values of 0.02–0.04 and 0.01–0.05, respectively.

5.1.2 Cordierite

Table 3. Whole rock geochemistry

	BH32	BH54	BH74
Major elements (wt%)			
SiO_2	61.86	60.99	65.06
TiO_2	1.04	1.61	0.89
Al_2O_3	18.10	15.69	17.19
Fe_2O_3	9.44	12.63	8.62
MnO	0.19	0.16	0.38
MgO	3.16	4.66	2.57
CaO	0.65	0.43	0.83
Na_2O	1.37	1.31	1.45
K_2O	4.00	2.38	2.88
P_2O_5	0.04	0.03	0.05
LOI	1.14	1.46	1.00

Cordierite is magnesian with X_{Mg} (Mg/(Fe^{2+} + Mg)) values ranging between 0.80–0.89. The cores and rims of cordierite grains, and cordierite forming coronae about spinel in garnet (sample BH54) yield equivalent X_{Mg} values.

5.1.3 Spinel

Spinel contains high proportions of zinc. ZnO contents range between 2.20–3.53 wt% in samples BH32 and BH54, and are higher in in sample BH74 (7.61–7.77 wt%). Cr_2O_3 contents are variable, ranging between 0.34–1.29 wt%. MnO varies between 0.01–0.31 wt%.

5.1.4 Magnetite

Magnetite has Al_2O_3 contents of 0.19–0.36 wt% which corresponds to X_{Al} (Al/(Al + Fe^{3+} + 2Ti)) of 0.004–0.007. The TiO_2 content ranges between 0–0.32 wt%.

5.1.5 Feldspar

K-feldspar is present in all samples and yields X_{Or} (K/(Ca + Na + K)) values of 0.72–0.92 and X_{An} (Ca/ (Ca + Na + K)) values of 0–0.04. Plagioclase grains in sample BH32 and BH74 yield X_{An} of 0.27–0.30. Plagioclase in sample BH54 occurs predominantly as perthite and is less calcic, with X_{An} of 0.02–0.13.

5.1.6 Biotite

Biotite is titanium-rich and magnesian with TiO_2 contents of 3.75–5.69 wt% and X_{Mg} values of 0.72–0.79. Fluorine contents are consistently elevated across all samples with values of 1.05–1.55 wt%.

5.1.7 Ilmenite

Imenite has low MnO content in all samples, ranging between 0.08–0.58 wt%.

5.2 Zircon geochronology

U–Pb zircon age data are presented in Appendix C and Fig. 6. Zircon interpreted to have formed *in situ* during metamorphism (i.e. are not inherited grains) are reported on in this study to constrain the timing of metamorphism. U–Pb data obtained from sample BH54 are presented in Tucker et al. (2017) but the inferred metamorphic ages are summarised with samples BH32 and BH74 for completeness. In this study, we adopt the terminology 'overgrowth' for zircon rims with a CL response that are unequivolcally representative of new zircon growth; the term 'rim' is used to designate recrystallization and zircon rims with inferred mixed origin (refer to Section 6.1).

5.2.1 Sample BH32

Twenty-four analyses were done on sample BH32 inclusive of nine analyses from dark cores, two analyses from strongly-luminescent rims, nine analyses from weakly-luminescent rims and whole

Table 4. Summary of mineral chemistry

	BH32	BH54	BH74
Garnet core			
X_{alm}	0.58–0.592	0.544–0.587	0.583–0.620
X_{py}	0.328–0.340	0.381–0.427	0.301–0.338
X_{grs}	0.025–0.027	0.015–0.016	0.028–0.039
X_{spss}	0.053–0.055	0.013–0.016	0.047–0.053
Garnet rim			
X_{alm}	0.587–0.601	0.571–0.601	0.592–0.619
X_{py}	0.315–0.323	0.370–0.401	0.293–0.327
X_{grs}	0.025–0.031	0.015	0.031–0.037
X_{spss}	0.055–0.062	0.013–0.017	0.048–0.052
Biotite			
X_{Mg}	0.72–0.77	0.74–0.79	–
Al_2O_3 (wt %)	14.950–15.611	15.02–15.46	–
MnO (wt %)	0.006–0.046	0–0.022	–
TiO_2 (wt %)	4.12–4.67	3.75–5.69	–
F (wt%)	1.05–1.22	1.20–1.55	–
K-feldspar			
X_{An}	0.003–0.012	0.000	0–0.04
X_{Or}	0.723–0.88	0.86–0.92	0.74–0.89
Plagioclase			
X_{An}	0.28–0.30	0.02–0.13	0.27-0.30
X_{Or}	0.010	0–0.01	0.010
Ilmenite			
MnO (wt%)	0.57–0.58	0.08–0.12	0.40–0.43
TiO_2 (wt %)	46.72–47.50	49.02–49.60	49.78–49.95
Cordierite			
X_{Mg}	0.82–0.86	0.88–0.89	0.80–0.83
Spinel			
ZnO (wt %)	3.46–3.53	2.20–2.78	7.61–7.77
X_{gah}	0.031–0.032	0.021–0.023	0.065–0.067
X_{sp}	0.330	0.45–0.49	0.35–0.36
Cr_2O_3 (wt %)	0.34–0.36	0.72–1.29	0.90–0.96
MnO (wt%)	0.28–0.31	0.01–0.04	0.09–0.16
Magnetite			
Al_2O_3 (wt %)	0.217–0.263	0.19–0.25	0.26–0.30
X_{Al}	0.005–0.006	0.004–0.006	0.006–0.007
TiO_2 (wt %)	0.004–0.005	0.14–0.32	0.010–0.014

Unless indicated by the units (wt%), proportions are atomic/molecular.
X_{alm} = Fe^{2+}/(Fe^{2+} + Mg + Ca + Mn);
X_{py} = Mg/(Fe^{2+} + Mg + Ca + Mn)
X_{gr} = Ca/(Fe^{2+} + Mg + Ca + Mn)
X_{spss} = Mn/(Fe^{2+} + Mg + Ca + Mn)
X_{Mg} = Mg/(Fe^{2+} + Mg)
X_{An} = Ca/(Ca + Na + K)
X_{Or} = K/(Ca + Na + K)
X_{gah} = Zn/(Zn + Mg + Al + Ti)
X_{sp} = Mg/(Fe2+ + Mg)
X_{Al} = Al/(Al + Fe^{3+} + 2Ti)

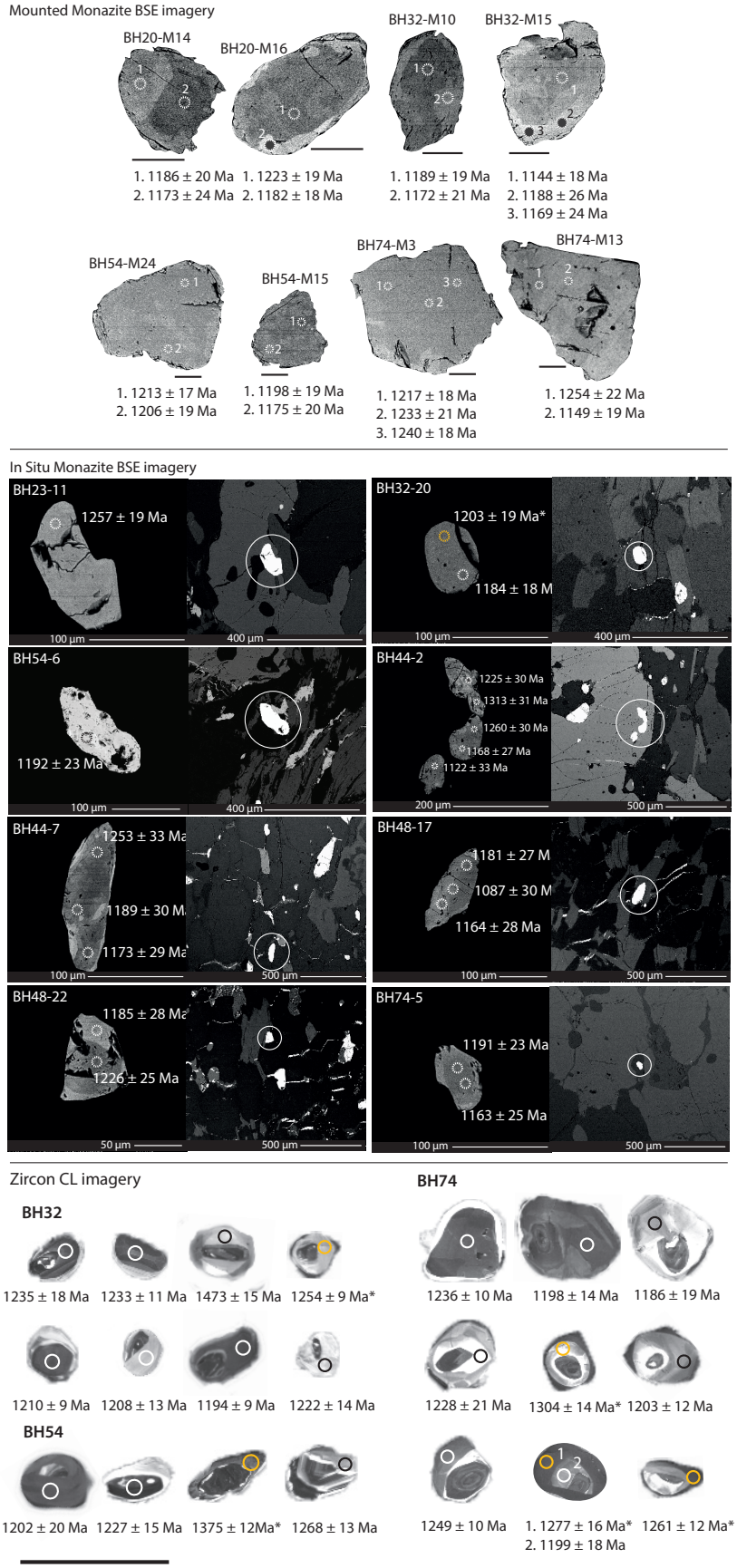

Figure 5. Zircon and monazite morphology. Representative backscatter electron images of analysed monazite grains (mounted grains and in situ grains within thin section), and cathodoluminescence imagery of zircon. The approximate location of U–Pb analysis spots are indicated by white (concordant analyses) and yellow (discordant analyses) open circles and the corresponding $^{206}Pb/^{238}U$ ages are shown. Uncertainties on age data are given at the 2σ level. The solid black scale bar shown for mounted monazite and zircon imagery represents 100 μm.

grains, and four analyses from dark overgrowths (Fig. 6a, Appendix C). Fourteen analyses were discordant. Five concordant analyses from dark cores gave ages between 1235 ± 18 Ma and 1195 ± 10 and at 1310 ± 11 Ma. One concordant analysis from a strongly-luminescent rim yielded an age of 1222 ± 14 Ma. Two concordant analyses were obtained from a zircon rim and whole grain with a weakly-luminescent CL response and weak sector zoning, yielding both the youngest (1182 ± 6 Ma) and oldest (1473 ± 15 Ma) ages from this sample, respectively. Two concordant analyses obtained from homogeneous, dark overgrowths gave equivalent ages of 1192 ± 13 Ma and 1194 ± 9 Ma. Overall, the age of zircon cores, rims and overgrowths in this sample are statistically indistinguishable.

5.2.2 Sample BH54

Ten analyses were done on sample BH54, inclusive of one analysis from a dark core, five analyses from weakly-luminescent rims, and four analyses from dark overgrowths (Fig. 6b, Appendix C). Four analyses, all from weakly-luminescent rims, were discordant. The dark zircon core yielded a concordant age of 1227 ± 15 Ma. One concordant analysis from a weakly-luminescent rim gave an age of 1268 ± 13 Ma. Four concordant analyses from dark overgrowths gave ages of 1201 ± 20 Ma, 1227 ± 19 Ma, 1245 ± 24 Ma and 1365 ± 19 Ma and are statistically indistinguishable in age from the concordant dark core and weakly-luminescent rim analyses.

5.2.3 Sample BH74

Fifty-seven analyses were done on sample BH74, inclusive of 18 analyses from dark cores, eight analyses from strongly-luminescent zircon rims, 27 analyses from weakly-luminescent rims, and three analyses from dark overgrowths (Fig. 6c, Appendix C). Twenty-six analyses were discordant. Fourteen concordant analyses obtained from the dark cores gave ages between 1269 ± 17 Ma and 1193 ± 14 Ma, but range predominantly between ca. 1245–1230 Ma. Three concordant analyses from the strongly-luminescent rims gave variable ages of 1199 ± 11 Ma, 1232 ± 11 Ma and 1414 ± 17 Ma. Fourteen concordant analyses from weakly-luminescent rims range between 1249 ± 10 Ma and 1186 ±19 Ma with two older ages of 1286 ± 20 Ma and 1295 ±15 Ma, however, the majority of analyses occur between ca. 1220–1200 Ma. All three analyses obtained from dark overgrowths that cross cut inner CL zones were discordant. One of these analyses is near-concordant (-1 % discordant) and dates to 1184 ± 25 Ma. Collectively, concordant analyses from sample BH74 define two age peaks at ca. 1230 Ma and ca. 1200 Ma. Dark cores largely comprise the older age peak. The weakly-luminescent zircon rims and dark overgrowths predominantly comprise the younger age peak. Overlap of uncertainties on individual analyses does not permit weighted mean age calculations of these age peaks.

5.3 Trace element distribution in zircon

Zircon trace element data are given in Appendix C. Chondrite-normalised zircon REE plots and plots of select trace elements versus age are shown in Appendix D.

5.3.1 Sample BH32

Zircon from sample BH32 show flat to slightly positive M–HREE patterns. Excluding one anomalously HREE enriched analysis, analyses from the strongly-luminescent and weakly-luminescent zircon rims exhibit the flattest M–HREE patterns corresponding to the lowest Yb_N/Gd_N values of 0.41–1.28 and Yb_N values of 50.3–146. Analyses from dark overgrowths yield a range of Yb_N/Gd_N values (Yb_N/Gd_N = 1.0–2.4, 8.76) and Yb_N (133.5–349.7, 1695.7). Dark cores exhibit the most variable M–HREE patterns with Yb_N/Gd_N of 0.6–13.5 and Yb_N 50.3–4229.8 (but typically Yb_N <500). Overall the majority of all data from this sample yield Yb_N/Gd_N values that cluster at 1.0 for ages <1250 Ma (Appendix D). The yttrium (Y) content is generally low for all analyses (typically <725 ppm) and weakly-luminescent rims appear to yield consistently the lowest values. Broadly, the Eu_N/Eu_N* anomaly appears slightly more pronounced for zircon rims relative to cores, however there is also no clear separation with Eu_N/Eu_N* for all analyses ranging between 0.04–0.15. Titanium (Ti) values range between 6–23 ppm and Th/U between 0.02–1.7.

5.3.2 Sample BH54

Zircon from sample BH54 yield a flat to slightly positive M–HREE pattern. One analysis from a dark, unzoned grain gave Yb_N/Gd_N of 1.4 and Yb_N of 117.4. Analyses from weakly-luminescent zircon rims yield variable Yb_N/Gd_N values of 0.55–

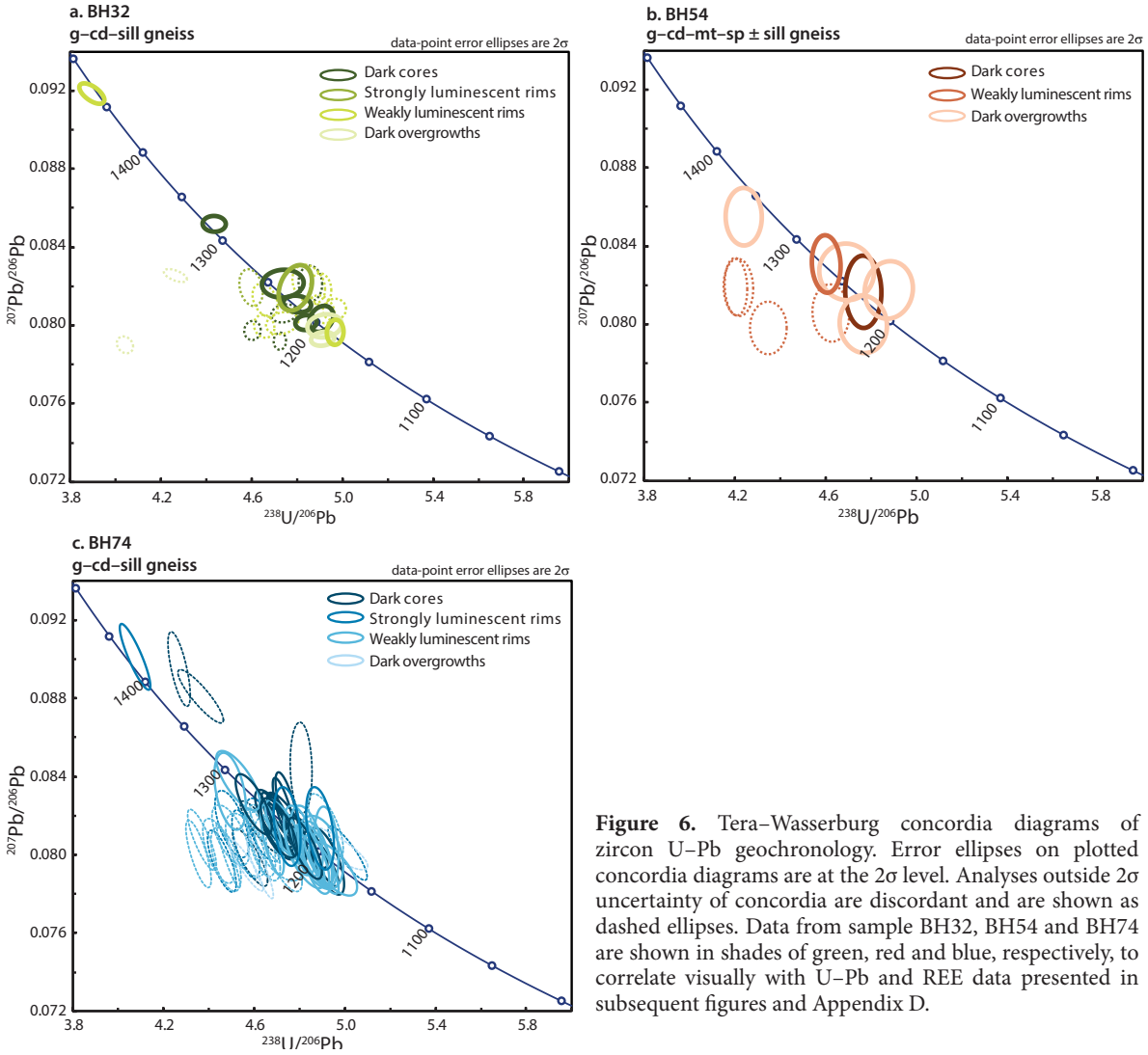

Figure 6. Tera–Wasserburg concordia diagrams of zircon U–Pb geochronology. Error ellipses on plotted concordia diagrams are at the 2σ level. Analyses outside 2σ uncertainty of concordia are discordant and are shown as dashed ellipses. Data from sample BH32, BH54 and BH74 are shown in shades of green, red and blue, respectively, to correlate visually with U–Pb and REE data presented in subsequent figures and Appendix D.

85.7 and Yb_N of 21.3–1292. Dark overgrowths yield Yb_N/Gd_N values of 1.91–12.36 and Yb_N of 50.3–496.9. Y content and Eu_N/Eu_N* values are variable, ranging between 30–793 ppm and 0.07–0.37, respectively, for the weakly-luminescent zircon rims and dark overgrowths. The dark core yielded a Y content of 189 ppm and Eu_N/Eu_N* of 0.03. Ti values range between 4.7–10.4 ppm. Th/U values range between 0.16–1.58 with the dark core yielding the most elevated value of 2.82. The data collectively show a broad decrease in Y content and Eu_N/Eu_N*, and increase in Ti content, with decreasing age, but the trace element content of zircon with different CL responses is not distinguishable (Appendix D).

5.3.3 Sample BH74

Zircon from sample BH74 show two distinct M–HREE patterns. Analyses from dark cores yield largely steep M–HREE patterns corresponding to Yb_N/Gd_N values of 3.7–42.7. Two analyses from dark cores yield flatter M–HREE patterns than the main population with Yb_N/Gd_N values of 0.78 and 0.82. Analyses from weakly-luminescent zircon rims display overall flat M–HREE patterns (Yb_N/Gd_N = 0.68–2.7, 5.3 and 10.8) relative to analyses from the dark cores. Dark overgrowths yield consistently low Yb_N/Gd_N values (Yb_N/Gd_N = 0.41–0.95) corresponding to flat M–HREE patterns. The M–HREE patterns of strongly-luminescent rims are more variable than the other CL responses with Yb_N/Gd_N values ranging between 0.65–1.51 and more elevated values at 6.9, 13.1 and 19.4. The zircon rims and dark overgrowths exhibit a more pronounced negative Eu anomaly (Eu_N/Eu_N* = 0.03–0.27, typically <0.1) than the dark cores (Eu_N/Eu_N* = 0.08–0.41, typically >0.15). The existence of two zircon populations in the trace element data for sample BH74, and a correlation between their age and trace element content, is further highlighted in Appendix D. The dark cores

typically yield concordant ages ca. 1245–1230 Ma and show elevated HREE (Yb_N = >400) and Y content (~590–2500 ppm, excluding three outlying analyses) compared with weakly-luminescent rims and dark overgrowths. Weakly-luminescent rims and dark overgrowths yield ages typically between ca. 1220–1200 Ma and are depleted in HREE (Yb_N generally <100) and Y (71–180 ppm). Ti content ranges between 3.5–19.5 ppm and broadly increases with decreasing age, but the two zircon populations are not clearly separated. A similar trend is observed for Th/U with dark cores typically yielding the lowest values (Th/U typically 0.01–0.17) and a broad shift towards higher values (typically Th/U >0.7) for weakly-luminescent rims. Dark overgrowths yield consistently low Th/U (0.01–0.08). Strongly-luminescent rims are variable in Y, Ti and Th/U content.

5.4 Monazite geochronology

U–Pb monazite age data are presented in Appendix C and Fig. 7. Analyses were performed on core and inferred recrystallized zone textures with a low and high BSE response, respectively (refer to Section 3.1). Overall, the age of low BSE monazite cores and high BSE response recrystallised zones are statistically indistinguishable. However, in some instances within individual grains, recrystallised outer domains do exhibit younger ages relative to the lower BSE response core of the same grain. Age data overall show a broad spread of analyses between predominantly ca. 1280–1100 Ma, and slight positive skew. The spread of ages within individual samples and their uncertainties does not allow for statistically valid weighted mean age calculations except for sample BH23.

5.4.1 Sample BH20

Twenty-six analyses were collected from 20 mounted monazite grains. All analyses are concordant and range between 1245 ± 26 Ma and 1157 ± 18 Ma.

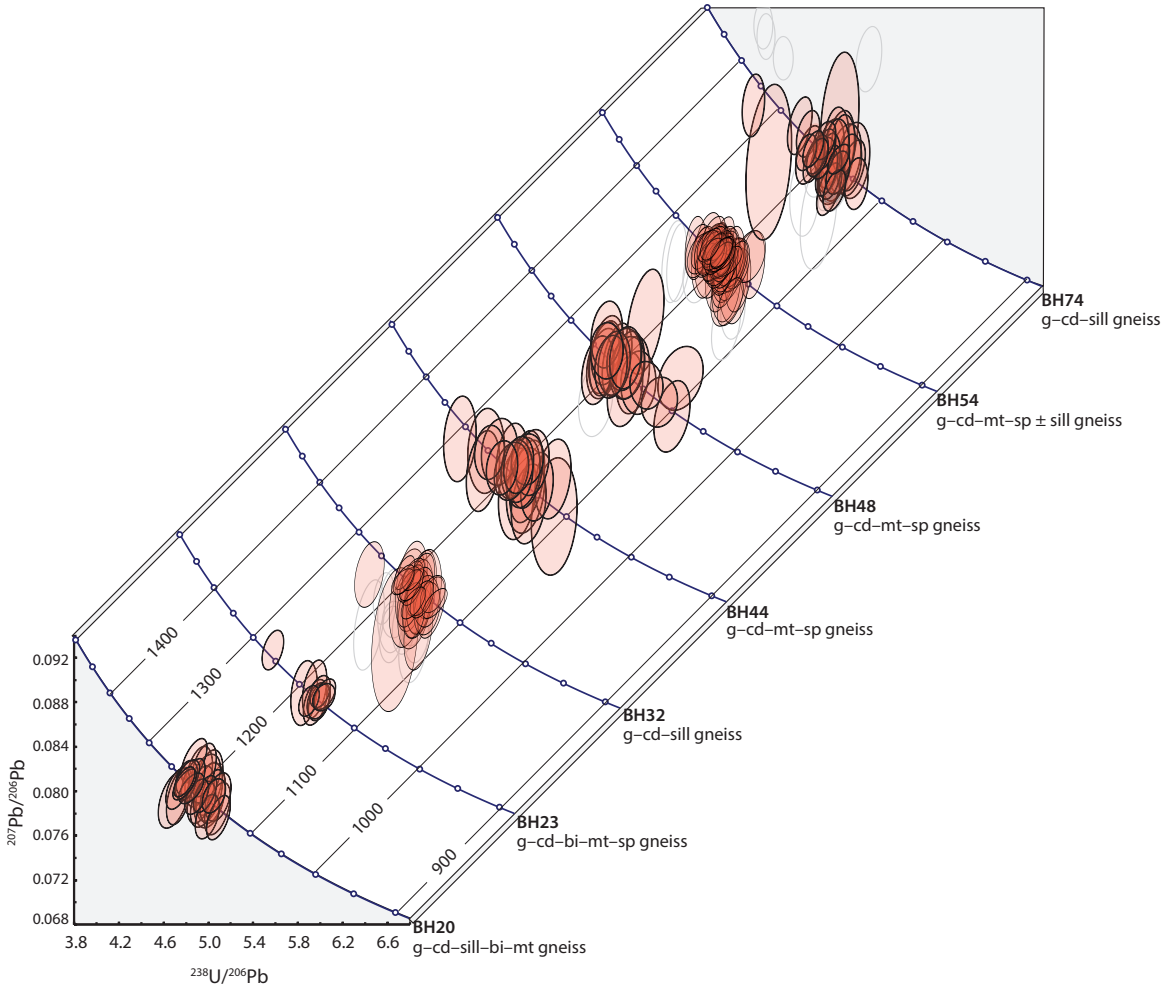

Figure 7. Stacked Tera–Wasserburg concordia diagrams of monazite U–Pb geochronology. Error ellipses are plotted at the 2σ level. Analyses outside 2σ uncertainty of concordia are discordant and are shown in grey. Concordant analyses are shaded to illustrate the ages with highest density of analyses.

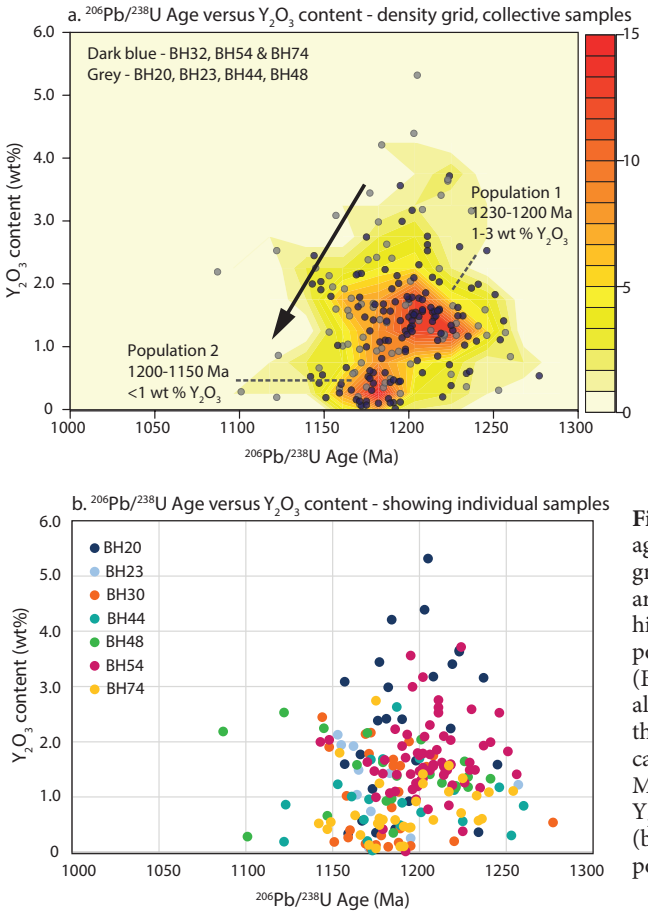

Figure 8. Monazite trace element chemistry. (a) $^{206}Pb/^{238}U$ age (Ma) versus Y_2O_3 (wt %) content shown as a density grid (concordant data, all samples). Individual data points are overlain on the density grid. Red shading represents high abundance; cream represents low abundance. Data points from the three samples used for zircon geochronology (BH32, BH54 and BH74) are shown in dark blue; data from all other samples are shown in grey. The density plots indicate that the Y_2O_3 content is approximately bimodal (monazite ca. 1230–1200 Ma = 1–3 wt% Y_2O_3; monazite ca. 1200–1150 Ma, <1 wt % Y_2O_3) and therefore there is a broad decrease in Y_2O_3 content with decreasing age as indicated by the arrow; (b) $^{206}Pb/^{238}U$ age (Ma) versus Y_2O_3 (wt %) content with data points separated by sample.

5.4.2 Sample BH23

Ten analyses were collected *in situ* from seven monazite grains. All analyses except one come from matrix monazite located at the grain boundaries of biotite, cordierite and feldspar. One grain is wholly included within garnet although the monazite grain itself is microfractured (grain BH23-14). All analyses are concordant and cluster predominantly between 1195 ± 22 Ma and 1153 ± 16 Ma, with one older analysis at 1257 ± 19 Ma. The main age population yields a weighted average $^{206}Pb/^{238}U$ age of 1167 ± 10 Ma (MSWD = 2.1, n = 9).

5.4.3 Sample BH32

Twelve analyses were collected from eight grains *in situ*, and 25 analyses were collected from 13 mounted monazite grains. Monazite in thin section occur exclusively within the matrix. Grains typically occur along grain boundaries of biotite, cordierite and feldspar but sometimes are also wholly included within these phases. Nine grains are discordant. The remaining concordant analyses range between 1220 ± 40 Ma and 1144 ± 18 Ma, with one older analysis at 1277 ± 28 Ma.

5.4.4 Sample BH44

Twenty-one analyses were collected *in situ* from six grains. Analysed grains occur along grain boundaries of spinel, cordierite, feldspar and quartz. Two grains are located wholly included within garnet, however are not isolated from the matrix due to micro fractures. Twenty-one analyses are concordant and form a spread of ages between 1260 ± 30 Ma and 1122 ± 33 Ma, with one slightly older analysis at 1313 ± 31 Ma.

5.4.5 Sample BH48

Twenty-three analyses were collected *in situ* from 10 grains. All grains were located along grain boundaries of cordierite, feldspar and opaque minerals within the matrix. One analysis is discordant. Concordant analyses yield ages ranging between 1241 ± 27 Ma and 1087 ± 30 Ma.

5.4.6 Sample BH54

Twenty-one analyses from eight grains were

collected *in situ*, and 54 analyses were collected from 26 mounted monazite grains. Monazite analysed in thin section are located along grain boundaries of, or hosted within, cordierite and feldspar, and rarely as inclusions within garnet, although are not isolate from microfractures within the garnet. Six analyses are discordant. Concordant analyses range from 1256 ± 19 Ma to 1143 ± 18 Ma.

5.4.7 Sample BH74

Sixteen analyses were collected from eight grains *in situ*, and 28 analyses were collected from 13 mounted monazite grains. All monazite analysed in thin section are located within the cordierite-bearing matrix, typically along or hosted within cordierite and feldspar. One grain was located adjacent to garnet (grain BH74-10). Eight analyses are discordant. The remaining concordant analyses yield ages predominantly between 1254 ± 22 and 1142 ± 17 Ma, with two older analyses at 1364 ± 24 Ma and 1324 ± 46 Ma.

5.5 Trace element distribution in monazite

Monazite trace element data are given in Appendix C. Collectively, all samples reveal a strongly positive relationship between the yttrium content (Y_2O_3 wt%) and age of the monazite (Fig. 8a). Analyses yielding ages between ca. 1230–1200 Ma yield the highest Y_2O_3 values (~1–3 wt%) and yttrium content decreases with decreasing age. Monazite with ages ca. 1200–1150 Ma exhibit Y_2O_3 <1 wt%. Using yttrium as a proxy for M–HREE abundance therefore indicates overall M–HREE depletion in younger monazite relative to older grains. When the monazite age data are viewed by individual samples (Fig. 8b) a clear decrease in Y_2O_3 content is only present for sample BH74 with the remaining samples showing an increased number of low Y analyses at younger ages (<1200 Ma) but no statistically definable decrease.

5.6 Trace element distribution in garnet

Analysed garnet from samples BH32, BH54 and BH74 appear to occur in two microstructural contexts (Section 3.1). Moderately coarse-grained, subhedral porphyroblasts (typically <800 μm) that contain few inclusions are denoted as Type-1 garnet. Coarse-grained (up to 2 mm), anhedral to elongate grains that contain a greater density of inclusions of inferred peak matrix minerals are described for BH54, and are classified as Type-2 garnet. Chondrite-normalised REE plots and REE + Y core–rim profiles are shown for representative garnet grains in Appendix D. A complete data table for garnet trace element analyses can be found in Appendix E.

5.6.1 Sample BH32

Type-1 garnet cores and rims from sample BH32 exhibit near flat to positive M–HREE slope (Yb_N/Gd_N = 1.08–1.49 for garnet 1, 1.90–3.19 for garnet 2). Analysed grains in this sample are unzoned from core to rim in REE + Y. However, Y (and HREE) contents are consistently elevated and comparable to the HREE-enriched cores of Type-1 garnet in samples BH54 and BH74. Y content ranges between 258–449 ppm in garnet 1 and 504–790 ppm in garnet 2. Europium anomalies yield Eu/Eu* values of 0.03 to 0.1.

5.6.2 Sample BH54

Type-1 garnet and Type-2 garnet were analysed from sample BH54. Two distinct garnet HREE patterns are evident. Type-1 garnet displays strong enrichment in Y and HREE within their cores (Y = 500 ppm) relative to their rims (Y = 150–230 ppm). Garnet core analyses yield Yb_N/Gd_N values of 4.97–12.8, corresponding to steep positive M–HREE slope on chondrite-normalised plots. Garnet rim analyses are depleted in HREE + Y relative to the garnet cores with Yb_N/Gd_N values of 2.35–7.67, and overall have flatter M–HREE slope. There is more variation in the Eu anomaly for the cores compared to the rims with Eu/Eu* values of 0.12–0.23 and 0.12–0.17, respectively.

Type-2 garnet are depleted and unzoned in HREE + Y, and display an approximately flat to negative M–HREE slope on chondrite-normalised plots (Yb_N/Gd_N = 0.20–0.88). The Eu anomaly is variable with Eu/Eu* of 0.09–0.29. The concentration of yttrium and HREE within Type-2 garnet is lower than the concentration of these elements within the rim region of Type-1, zoned garnets within the same sample.

5.6.3 Sample BH74

Type-1 garnet cores show positive M–HREE slope with Yb_N/Gd_N = 1.76–4.85. The rims yield slightly flatter M–HREE patterns than the cores with Yb_N/Gd_N = 1.17–3.35. The Eu anomaly

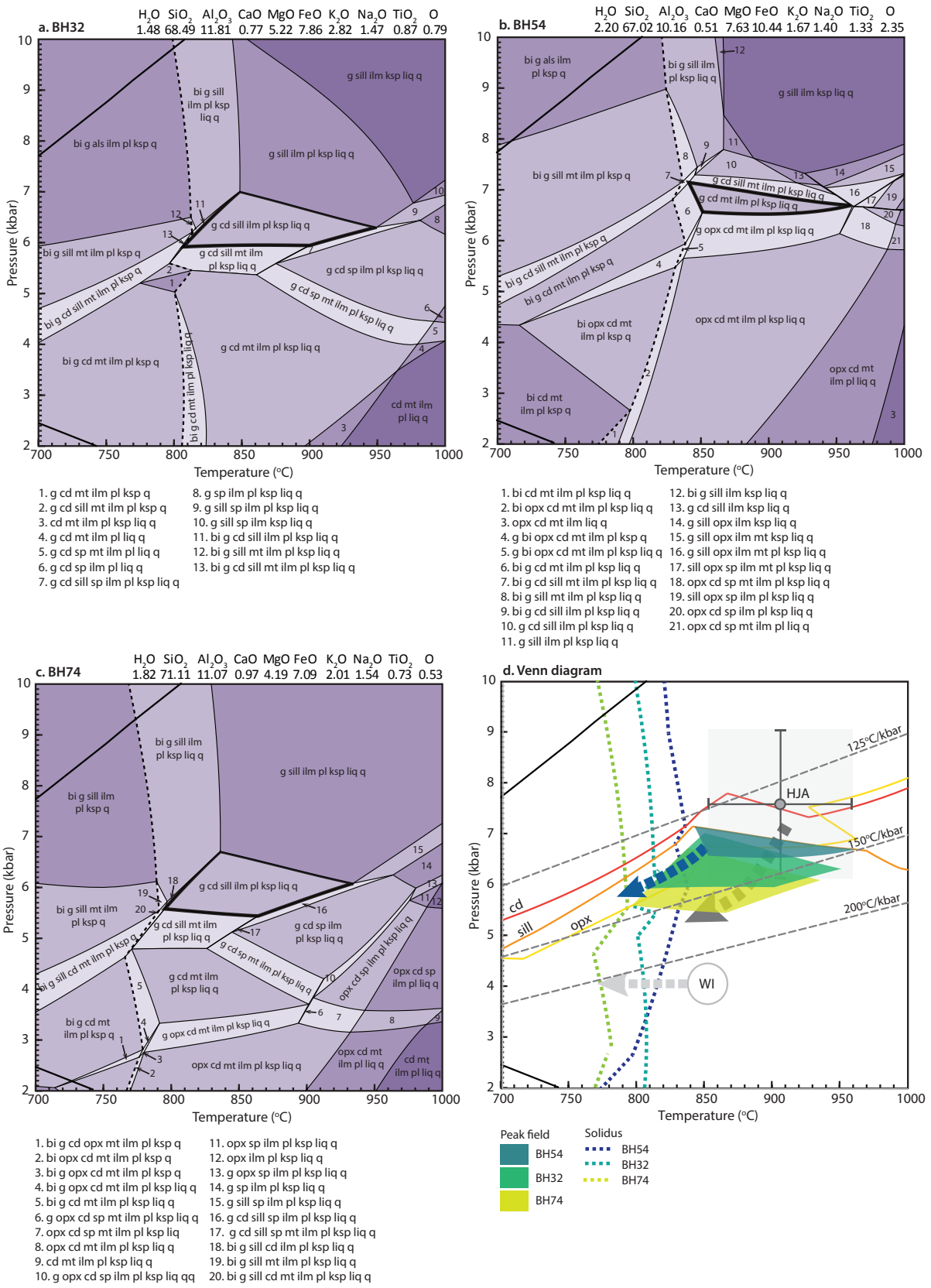

1. g cd mt ilm pl ksp q
2. g cd sill mt ilm pl ksp q
3. cd mt ilm pl ksp liq q
4. g cd mt ilm pl liq q
5. g cd sp mt ilm pl liq q
6. g cd sp ilm pl liq q
7. g cd sill sp ilm pl ksp liq q
8. g sp ilm pl ksp liq q
9. g sill sp ilm pl ksp liq q
10. g sill sp ilm ksp liq q
11. bi g cd sill ilm pl ksp liq q
12. bi g sill mt ilm pl ksp liq q
13. bi g cd sill mt ilm pl ksp liq q

1. bi cd mt ilm pl ksp liq q
2. bi opx cd mt ilm pl ksp liq q
3. opx cd mt ilm liq q
4. g bi opx cd mt ilm pl ksp q
5. g bi opx cd mt ilm pl ksp liq q
6. bi g cd mt ilm pl ksp liq q
7. bi g cd sill mt ilm pl ksp liq q
8. bi g sill mt ilm pl ksp liq q
9. bi g cd sill ilm pl ksp liq q
10. g cd sill ilm pl ksp liq q
11. g sill ilm pl ksp liq q
12. bi g sill ilm ksp liq q
13. g cd sill ilm ksp liq q
14. g sill opx ilm ksp liq q
15. g sill opx ilm mt ksp liq q
16. g sill opx ilm mt pl ksp liq q
17. sill opx sp ilm mt pl ksp liq q
18. opx cd sp mt ilm pl ksp liq q
19. sill opx sp ilm pl ksp liq q
20. opx cd sp ilm pl ksp liq q
21. opx cd sp mt ilm pl liq q

1. bi g cd opx mt ilm pl ksp q
2. bi opx cd mt ilm pl ksp q
3. bi g opx cd mt ilm pl ksp q
4. bi g opx cd mt ilm pl ksp liq q
5. bi g cd mt ilm pl ksp liq q
6. g opx cd sp mt ilm pl ksp liq q
7. opx cd sp mt ilm pl ksp liq
8. opx cd mt ilm pl ksp liq q
9. cd mt ilm pl ksp liq q
10. g opx cd sp ilm pl ksp liq qq
11. opx sp ilm pl ksp liq q
12. opx ilm pl ksp liq q
13. g opx sp ilm pl ksp liq q
14. g sp ilm pl ksp liq q
15. g sill sp ilm pl ksp liq q
16. g cd sill sp ilm pl ksp liq q
17. g cd sill sp mt ilm pl ksp liq q
18. bi g sill cd ilm pl ksp liq q
19. bi g sill mt ilm pl ksp liq q
20. bi g sill cd mt ilm pl ksp liq q

Figure 9. Pressure–temperature (*P–T*) models for (a) BH32, (b) BH54, and (c) BH74. Bulk compositions used for the calculation of each pseudosection are provided at the top of each section. The solidus is indicated as a dashed line. The stability field of the inferred peak mineral assemblage in each sample is outlined in bold; (d) Venn diagram depicting the stability field of interpreted peak metamorphic assemblages for each sample. The inferred peak mineral assemblage stability fields corresponding to each sample are shaded and the position of the solidus is represented by a dashed line. The inferred *P–T* path (in blue), and lines reflecting cordierite, sillimanite and orthopyroxene stability from sample BH54 are indicated as these minerals provide constraint on the post-peak *P–T* trajectory (see Section 6.1). Apparent thermal gradients and approximate *P–T* constraints from the Windmill Islands (WI; Morrissey *et al.*, 2017a) and Highjump Archipelago (HJA; Tucker and Hand, 2016) are overlain. Mineral abbreviations after Holland and Powell (1998).

is approximately equivalent for cores and rims with Eu/Eu* values of 0.12–0.16. Zonation in Y is pronounced with strongly enriched cores (Y = 236–446 ppm), relative to the rims (Y = 121–331 ppm). The observed core–rim bell-shaped distribution in Y concentration is also replicated in HREEs such as Yb, Er, Dy, Gd and Lu.

5.7 Pressure–temperature conditions

In this study, phase equilibria forward modelling is used to constrain the general conditions of peak metamorphism in the Bunger Hills. The results provide a *P–T* framework for the metamorphic conditions experienced by the Paleo–Mesoproterozoic cover to an Archean basement. The modelled rocks are considered to have undergone partial melting and melt loss and accordingly preserve a residual, comparatively anhydrous bulk composition relative to their protolith. The open-system behaviour of melt loss means that the effective (equilibrium) bulk rock composition evolves as a function of prograde melting and melt drainage. A number of studies have engaged in melt re-integration modelling to account for this change in bulk chemistry and therefore to obtain quantitative information on the prograde *P–T* path (e.g. Bartoli, 2017, and references therein). Melt reintegration was not incorporated into the forward modelling of rocks in this study due to a lack of preservation of their inferred prograde mineral assemblages, and uncertainty surrounding the amount of melt, number of melt reintegration steps, and the *P–T* conditions at which to reintegrate melt. Therefore, the modelled residual bulk compositions are appropriate to obtain information about the peak and retrograde *P–T* evolution, assuming that the last melt loss event was at or prior to the rock reaching peak conditions. The *P–T* models cannot however, be used to make specific, quantitative interpretations about the prograde *P–T* history.

Spinel occurs as a minor phase (~1 % abundance) in samples BH32 and BH74, and in slightly higher abundance in sample BH54 (<4 % abundance). Spinel in the modelled samples contains moderate to high amounts of zinc (Zn) and chromium (Cr) (Table 4). Zn and Cr are known to increase the stability of spinel at lower temperatures and higher pressures (e.g. Nichols et al., 1992; Tajčmanová et al., 2009), but the absolute down-temperature, up-pressure shift is not quantified. Zn and Cr are also not incorporated into the *a–x* model for spinel, and therefore spinel cannot be accurately modelled as part of the stable assemblage. For simplicity, spinel has not been considered part of the peak mineral assemblages of the modelled samples in this study with the caveat that peak conditions could actually occur at higher temperature in the calculated spinel-bearing field regardless of its high Zn or Cr contents. A further caveat is that analysed biotite contains appreciable fluorine (Table 4) that expands its stability to higher temperatures (e.g. Sankar et al., 2005) than those calculated in the forward phase equilibria models. Therefore in reality, since biotite defines the lower-temperature boundary of the inferred peak mineral field for all modelled samples, the minimum constraint on the peak metamorphic conditions probably occurs at slightly higher temperatures.

Calculated *P–T* models are presented in Fig. 9. Regions of the *P–T* models corresponding to the measured modal abundance of inferred peak minerals and electron microprobe compositions of garnet and cordierite in each sample are summarised in Appendix A to further constrain the peak metamorphic conditions.

5.7.1 Sample BH32

The interpreted peak mineral assemblage for sample BH32 is garnet–cordierite–sillimanite–ilmenite–K-feldspar–plagioclase–quartz–melt. This assemblage is calculated to occur at 5.9–7.0 kbar and 810–950 °C (Fig. 9a). The calculated solidus is located at 800–810 °C. Spinel is present at >860 °C at 5.4 kbar and the range of stable pressures increases with increasing temperature. The exclusion of spinel from the inferred peak mineral assemblage therefore constrains the upper temperature boundary of the peak field. Biotite is stable below 810–850 °C (pressure-dependant). It is unclear from mineral textural relationships whether biotite conclusively formed part of the peak or post-peak assemblage. Due to its occurrence largely at the boundaries of inferred peak minerals, the growth of biotite was presumably late and biotite is accordingly excluded from the peak mineral assemblage. Therefore peak conditions are inferred to have occurred at temperatures >810–850 °C. However, some matrix biotite is coarse and sub-aligned with the foliation which suggests that some biotite may have formed part of the peak assemblage. We can therefore not discount that the adjacent, narrow, biotite-bearing field (to lower temperature) represents the

peak field. The upper pressure constraint on the peak field is based on the presence of cordierite. Magnetite is present in very minor abundance in this sample, but it is not interpreted to form part of the peak metamorphic mineral assemblage. Magnetite is predicted to be stable at pressures <5.5–6.0 kbar, thereby defining the lower pressure limit of the peak field. However, if the bulk Fe_2O_3 versus FeO content is adjusted moderately to a more reduced or oxidised composition, magnetite stability will contract or expand to lower or higher pressures accordingly (Appendix A). Therefore, the position of the magnetite line does not provide a robust, independent constraint on the *P–T* field. The presence of sillimanite in this sample, and its predicted stability above 5.2–6.1 kbar over the temperature range of the peak field, is considered as a more reliable lower pressure constraint. Compositional contours corresponding to the composition of garnet and cordierite cores determined by electron microprobe data (Table 4, Appendix B) are modelled to overlap in the upper temperature realm of the peak assemblage field (6.0–6.7 kbar, 860–950 °C; Appendix A). Modal proportions of peak minerals place less conclusive constraints on the peak *P–T* conditions, but generally overlap in greatest abundance towards the higher-temperature and lower-pressure bounds of the peak field.

5.7.2 Sample BH54

The interpreted peak mineral assemblage for sample BH54 is garnet–cordierite–magnetite–ilmenite–plagioclase–K-feldspar–quartz–melt. This assemblage corresponds to a narrow field over 6.5–7.2 kbar and 840–960 ºC (Fig. 9b). The calculated solidus is located at 790–830 °C. The $T–M_o$ and $P–M_o$ models for sample BH54 reveals that the stability of this peak assemblage is favoured under moderately oxidised conditions (Appendix A). If the amount of ferric iron in the bulk composition for sample BH54 was slightly higher or lower than the chosen value (M_o = 0.45), the range of peak pressures would narrow, but would remain very similar. In contrast, the range of peak temperatures contracts with decreasing ferric iron content at the expense of increasing sillimanite stability, and expands under more oxidised conditions over the range M_o = 0.37–0.54. At M_o >0.54, the peak assemblage is not observed (i.e. is restricted to pressures higher than represented by the $T–M_o$) due to increased stability of orthopyroxene. In the calculated *P–T* model, sillimanite is stable at pressures higher than ~7 kbar (at T >850 ºC) and therefore constrains the upper pressure limit of the peak field to pressures <7 kbar. Biotite typically occurs within the matrix as anhedral grains at the grain boundaries of peak minerals (see also Section 3.5, e.g. Fig. 4f and g). Biotite is thus considered texturally late and is not interpreted to form part of the peak assemblage. The calculated presence of biotite at temperatures <870–800 ºC therefore forms the lower temperature constraint on peak conditions. At lower pressures and higher temperatures, orthopyroxene is stabilised and garnet is absent. The absence of orthopyroxene in this sample constrains the peak pressures to >6.5 kbar (at >850 ºC) and the presence of garnet to temperatures <960 ºC. Modelled modal proportions of the inferred peak minerals corresponding to their abundances in thin section occur within the peak field. In contrast, compositional contours for cordierite occur to a slightly higher pressure than the inferred peak field, within the adjacent magnetite-absent field. Garnet compositional contours for X_{alm} and X_{grs} occur predominantly to lower pressure and temperature than the peak field, and overlap marginally between ~5.0–6.4 kbar and ~700–800 ºC.

5.7.3 Sample BH74

The interpreted peak mineral assemblage for sample BH74 is garnet–sillimanite–cordierite–ilmenite–K-feldspar–plagioclase–melt–quartz. The field corresponding to this mineral assemblage occurs between 5.4–6.6 kbar and 800–935 °C (Fig. 9c). The calculated solidus is located at 770–790 °C. The topology of the modelled pseudosection for BH74 is very similar to BH32 and the location of their peak fields marginally overlap. In contrast to BH32, orthopyroxene is stable at 2 kbar at 700 ºC and the range of stable pressures expands with increasing temperature to its widest point at 950 ºC (2–5.7 kbar). The upper pressure limit of the peak field is constrained by the modelled absence

Figure 10. **(facing page)** Zircon–garnet partitioning profiles for M–HREE from samples BH32, BH54 and BH74. Traditional (averaged) D_{REE}(zircon–garnet) plots are presented on the left; D_{REE}(zircon–garnet) data for individual zircon analyses are presented on the array plot of Taylor et al. (2017) on the right. The experimental data of Taylor et al. (2015) and D_{REE}(zircon–garnet) data for detrital zircon for each corresponding sample are overlain on the array plots for visual comparison with the metamorphic zircon data from this study.

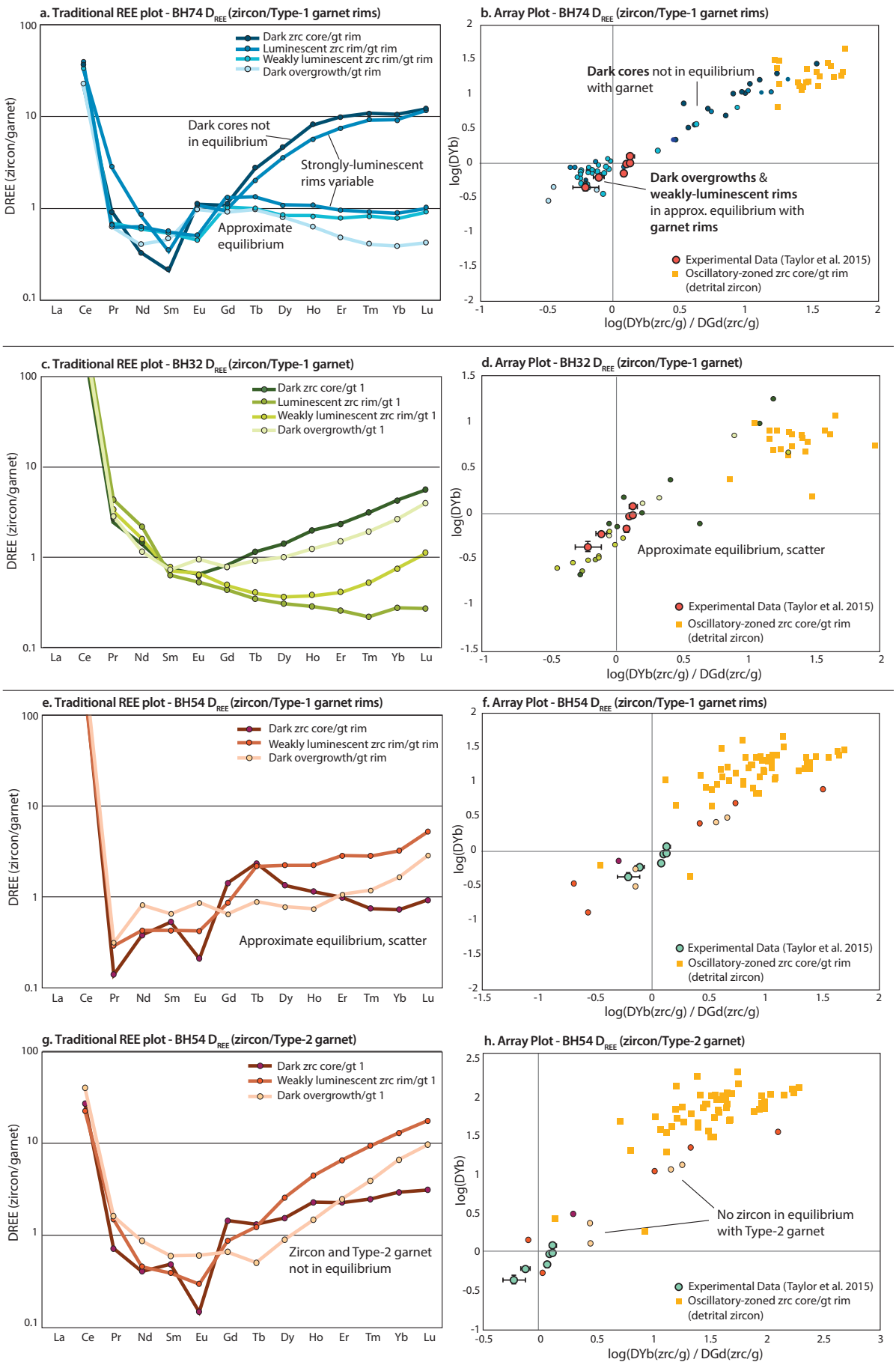
a. Traditional REE plot - BH74 D_{REE} (zircon/Type-1 garnet rims)
DREE (zircon/garnet)
Dark zrc core/gt rim
Luminescent zrc rim/gt rim
Weakly luminescent zrc rim/gt rim
Dark overgrowth/gt rim
Dark cores not in equilibrium
Strongly-luminescent rims variable
Approximate equilibrium
La Ce Pr Nd Sm Eu Gd Tb Dy Ho Er Tm Yb Lu
b. Array Plot - BH74 D_{REE} (zircon/Type-1 garnet rims)
log(DYb)
log(DYb(zrc/g) / DGd(zrc/g)
Dark cores not in equilibrium with garnet
Dark overgrowths & weakly-luminescent rims in approx. equilibrium with garnet rims
Experimental Data (Taylor et al. 2015)
Oscillatory-zoned zrc core/gt rim (detrital zircon)
c. Traditional REE plot - BH32 D_{REE} (zircon/Type-1 garnet)
Dark zrc core/gt 1
Luminescent zrc rim/gt 1
Weakly luminescent zrc rim/gt 1
Dark overgrowth/gt 1
d. Array Plot - BH32 D_{REE} (zircon/Type-1 garnet)
Approximate equilibrium, scatter
e. Traditional REE plot - BH54 D_{REE} (zircon/Type-1 garnet rims)
Approximate equilibrium, scatter
f. Array Plot - BH54 D_{REE} (zircon/Type-1 garnet rims)
g. Traditional REE plot - BH54 D_{REE} (zircon/Type-2 garnet)
Zircon and Type-2 garnet not in equilibrium
h. Array Plot - BH54 D_{REE} (zircon/Type-2 garnet)
No zircon in equilibrium with Type-2 garnet

of cordierite at pressures >6 kbar. At pressures lower than the peak field, magnetite is stable and sillimanite is absent. Magnetite is rarely observed in this sample, and is not considered to be a part of the peak mineral assemblage. Similarly to sample BH32, altering the ferric iron content adjusts the *P–T* range over which magnetite is present (Appendix A) and therefore the modelled occurrence of sillimanite is taken as a more robust lower pressure constraint than magnetite on the peak pressure. The lower temperature boundary of the peak field is constrained by the presence of biotite at temperatures <830–770 °C. The exclusion of magnetite and spinel from the peak mineral assemblage but the presence of sillimanite constrains the upper temperature boundary to temperatures <935 °C at 6.0 kbar. Modelled contours for X_{alm} and X_{grs} corresponding to the composition of the garnet cores and X_{Fe} from cordierite cores, overlap within the peak field at 6.1–6.5 kbar 820–870 °C. Modelled and estimated mineral modes for the inferred peak minerals in thin section overlap within the lower pressure realm of the peak field.

6. DISCUSSION

6.1 Interpretation of metamorphic zircon textures and zircon ages

At high temperature, metamorphic zircon primarily form via solid-state recrystallization of pre-existing (protolith) zircon, or by new zircon growth due to partial melting and melt crystallisation (Hoskin and Black, 2000; Rubatto, 2017). Internal zircon morphology as visualised in CL and the uniformity of these internal features from grain to grain suggest that the dark zircon cores and strongly-luminescent zircon rims analysed in this study are consistent with solid-state recrystallization of inherited grains (Corfu et al., 2003; Hoskin and Black, 2000; Rubatto, 2017; Taylor et al., 2016; Vonlanthen et al., 2012). The dark cores are featureless and/or exhibit indistinct relict primary oscillatory zoning (i.e. ghosted-zoning), convoluted internal structures, and appear to retain their original grain morphology. The strongly-luminescent rims that commonly surround these dark cores have irregular shape and a general lack of regular growth textures. In contrast, evidence for new zircon growth is provided by dark overgrowths as well as many weakly-luminescent rims, which are homogeneous or exhibit consistent internal textures such as sector zoning, clear truncation of the internal features of inner CL zones, and a distinct textural change from the inner CL zones (i.e. dark cores and strongly-luminescent rims). Although many weakly-luminescent rims exhibit features typical of new zircon growth, few grains do exhibit more convoluted internal textures and gradational contacts with inner CL zones that may also be indicative of minor recrystallization.

Partial recrystallization may result in incomplete resetting of U–Pb ages, producing an apparent spread in age data and large uncertainties on individual analyses (e.g. Hoskin and Black, 2000, and references therein). The ghosted-zoning visible in some dark zircon cores in this study provide direct evidence that some inherited zircon grains were incompletely (and variably) recrystallised, and explains the observed scatter in U–Pb zircon age data. Therefore, significance is not given to the age of individual zircon analyses but rather to the overall trends. Zircon age data from sample BH74 provide the clearest trends. Concordant analyses from dark cores yield ages >ca. 1195 Ma and are predominantly ca. 1245–1230 Ma. In contrast, weakly-luminescent zircon rims and dark overgrowths that surround these dark cores typically yield younger, concordant ages between ca. 1220–1200 Ma as illustrated in Appendix D.

6.2 Relationship between zircon and garnet

Chondrite-normalised zircon REE arrays and select trace element concentrations plotted against age (Appendix D) reflect a prominent shift in the trace element signature recorded by zircon in sample BH74. D_{REE}(zircon–garnet) patterns in Fig. 10 further highlight differences in REE partitioning of the metamorphic zircon with garnet in this sample and provide an indication of the equilibrium coexistence (or lack thereof) of these two phases. For type-1 garnet grains (across all samples), zircon–garnet rim partitioning is only considered (i.e. not zircon–garnet cores). Type-1 garnet grains exhibit prograde-style growth zoning in REE + Y with HREE-enriched cores and HREE-depleted rims (e.g. Carlson, 2012). The garnet cores are not in chemical and textural equilibrium with the surrounding matrix and are effectively isolated from the reacting, melt-bearing system during peak metamorphism.

Dark zircon cores from BH74 (typically ca. 1245–1230 Ma) are enriched in HREE + Y (Appendix D) and exhibit steep, concave $D_{M–HREE}$(zircon–

garnet) patterns (Fig. 10a). In contrast, weakly-luminescent zircon rims and dark overgrowths (typically ca. 1220–1200 Ma) from this sample are depleted in HREE + Y (Appendix D) and reveal approximately flat $D_{M–HREE}$(zircon–garnet) profiles relative to the dark cores (Fig. 10a). Garnet strongly sequesters M–HREE which results in REE-depletion of stably-coexisting minerals. Many studies consequently interpret the REE enrichment of zircon and monazite to reflect their crystallisation in a garnet-absent environment (e.g. Foster et al., 2000; Hokada and Harley, 2004; Rubatto, 2002; Stearns et al., 2013). The steep $D_{M–HREE}$(zircon–garnet) patterns of the dark cores in sample BH74 are >>1, suggesting that these zircon and type-1 garnet rims did not form in equilibrium. The traditional REE partioning plot is refined into the array plot of Taylor et al. (2017) in Fig. 10b which more accurately conveys that the dark cores in fact record the relic trace element composition of pre-existing, inherited zircon that underwent varied degrees of recrystallization. The experimental data of Taylor et al. (2015) are shown on the array plot to provide a visual framework against which the dataset from this study can be compared for equilibrium co-existence with garnet. Trace element data are also overlain for detrital zircon from this sample. Data corresponding to the dark zircon cores are clearly offset from the experimental array but track towards it from the detrital zircon population that have little to no systematic variation. This trend reflects variable and gradual recrystallization over a range of chemical environments and temperatures.

Conversely, the relatively flat D_{M-HREE}(zircon–garnet rim) patterns for the weakly-luminescent zircon rims and zircon overgrowths, approaching unity, suggests that these zircon grew in approximate equilibrium with the progressively HREE-depleted type-1 garnet rims, and under high temperature conditions (e.g. Rubatto, 2002; Taylor et al., 2015). Equilibration between garnet rims and these zircon is illustrated clearly on the array plot which shows a very close match between the position of the experimental data and data from the weakly-luminescent rims and dark overgrowths. This relationship suggests that growth of the HREE + Y enriched garnet cores must have occurred > ca. 1220 Ma, prior to the crystallisation of HREE-depleted weakly-luminescent zircon rims and dark overgrowths (1220–1200 Ma) that grew in equilibrium with the HREE-depleted garnet rims.

Zircon from samples BH32 and BH54 do not exhibit obvious depletion in HREE + Y by ca. 1230 Ma as for sample BH74. However, zircon yielding ages <1230 Ma from these two samples do exhibit generally low Y and Yb/Gd, comparable to similarly aged zircon from BH74 (Appendix D). When compared with zoned type-1 garnet from these samples all zircon from BH32 and BH54 return variable but, on average, flat to slightly positive $D_{M–HREE}$(zircon–garnet) patterns consistent with overall chemical equilibrium between zircon and the garnet rims (Fig. 10). Data from sample BH32 shown on the array plot (Fig. 10d) exhibit a broadly similar trend to BH74 in which the data (from predominantly dark cores) track from the detrital zircon population onto the experimental array. Scatter in the metamorphic zircon data that occurs as a linear trend approximately parallel to the experimental data for both BH32 and BH54 (Figs. 10d and f), may reflect the gradational process of solid-state recrystallization, local-scale chemical re-equilibration with garnet-bearing volumes within the rock, or could also be an effect of the garnet composition used for the experimental data not being identical to the garnet in BH32 and BH54.

HREE-depleted, unzoned garnet was also analysed in sample BH54 (i.e. Type-2 garnet). $D_{M–HREE}$(zircon–garnet) patterns exhibit a steep, positive slope that directly contrasts to the partitioning pattern from type-1 garnet in the same sample (Fig. 10g). This trend reflects the preferential incorporation of HREE into zircon relative to type-2 garnet. The array plot further highlights that zircon and type-2 garnet do not reflect equilibrium partitioning with a clear offset of metamorphic zircon data from the experimental array (Fig. 10h). As garnet is a more dominant sink for HREE than zircon, the zircon must have grown prior to the HREE-depleted, unzoned garnet. The unzoned garnet is significantly more depleted in HREE than both the zoned garnet cores in BH54 (and equivalent HREE-enriched grains in BH74 and BH32) and the HREE-depleted rims on those zoned garnets. The unzoned garnet is also aligned with the fabric and contains inclusions of other minerals interpreted to comprise part of the peak metamorphic mineral assemblage, suggesting that this garnet probably formed during peak metamorphism but was texturally late. This evidence argues for continued garnet growth in a HREE-depleted environment, after zircon crystallisation ceased at ca. 1180 Ma.

6.3 Relationship between monazite and garnet

A quasi-systematic relationship is observed between the yttrium content and age of monazite in this study whereby, typically, the oldest ages (ca. 1230 Ma) yield the highest yttrium contents and concentration decreases with decreasing age (Fig. 8). Fig. 8a illustrates that, when all samples are plotted together, monazite analyses with ages of ca. 1230–1200 Ma are generally characterised by Y_2O_3 contents of 1–3 wt%, and monazite with ages ca. 1200–1170 Ma have Y_2O_3 <1 wt%. The observed trend reflects an overall reduction in the "effective" REE reservoir available to monazite over time within the pelite gneiss.

On the assumption that REE are not being lost from the rock via significant melt loss (e.g. Yakymchuk and Brown, 2014), then decreasing REE availability could reflect one or a combination of two main scenarios. Firstly, the yttrium, and by inference M–HREE, depletion in monazite may reflect the coexistence and/or progressive increase in the modal proportion of strongly (M–HREE + Y)-partitioning minerals such as garnet, zircon or xenotime which exert a more dominant control on these elements than monazite (e.g. Bea et al., 1994). For example, the crystallisation of monazite may have occurred during or after garnet nucleation. This scenario is supported by overlap between the monazite age data and interpreted timing of garnet growth and zircon crystallisation (Section 6.1). Secondly, depleting REE content with age in monazite may reflect the progressive exhaustion of the overall bulk rock REE budget as monazite crystallises, assuming the whole rock as the equilibration volume. The progressive depletion of M–HREE + Y in the equilibrium volume of the studied rocks is well demonstrated by $D_{M–HREE}$(zircon–garnet) relationships (Fig. 10) that suggest that HREE-enriched garnet cores grew prior to ca. 1230 Ma, followed by HREE-depleted garnet rim growth, and further HREE-depleted, unzoned garnet growth < ca. 1180 Ma. Although collectively the monazite data show declining Y_2O_3 content over time (Fig. 8a), when visualising the data by individual samples (Fig. 8b), a clear decrease in Y_2O_3 content is only obvious for sample BH74, although the remaining samples do show an increased number of analyses with low Y_2O_3 at younger ages. This observation may also indicate a strong dependence of the monazite chemistry on the textural location of the grain (i.e. local equilibrium), crystallisation in equilibrium with crystallising melt at grain boundaries, or that younger monazite (with ages <1200 Ma) with atypical high Y_2O_3 contents are a result of minor Pb-loss post-crystallisation.

6.4 Relationship between zircon and monazite and the absolute timing of peak metamorphism

The monazite and zircon analysed in this study reveal a protracted spread of ages (Fig. 11, Appendix C). This spread of ages is more complex than previously reported by Sheraton et al. (1993), Tucker and Hand (2016) and Tucker et al. (2017), with collective metamorphic age data from the Bunger Hills and Highjump Archipelago now documented to span ca. 200 Myr (Fig. 11). Furthermore, the zircon age data are bimodal and in general, are older than the bulk of the monazite ages. The youngest zircon age peak aligns with the main monazite age peak. These observations are consistent with other high-grade metamorphic terranes in which monazite and zircon commonly yield an extended record of age data, and zircon typically yield older ages than monazite (Clark et al., 2014; Kelsey et al., 2008; Taylor et al., 2016, and references therein; Williams et al., 1996).

Simplistically, the age data reflect long-lasting, high-temperature conditions, but do not necessarily reflect that the duration of peak metamorphism itself was long-lived. As previously discussed (Section 6.1), zircon ages likely reflect solid-state recrystallization and subsequent new zircon growth. The monazite age data could be interpreted variably in the context of the *P–T* path. Typically, monazite has been regarded as susceptible to partial dissolution–re-precipitation in the presence of melt. Monazite ages have therefore largely been interpreted to reflect cooling on approach to the solidus during final melt crystallisation (Hermann and Rubatto, 2003; Kelsey et al., 2008; Roberts and Finger, 1997; Vavra et al., 1996; Williams et al., 1996; Yakymchuk and Brown, 2014). However, increasing evidence suggests that monazite, as well as zircon, also commonly preserve prograde growth ages (e.g. Johnson et al., 2015; Rubatto et al., 2001). This may be related to the high closure temperature of both zircon and monazite (>900 °C) to Pb diffusion (Cherniak, 2010). Alternatively, prograde ages may be preserved due to the unreactivity of zircon and monazite in 'dry' systems because of the absence of fluids or preconditioning by polymetamorphism

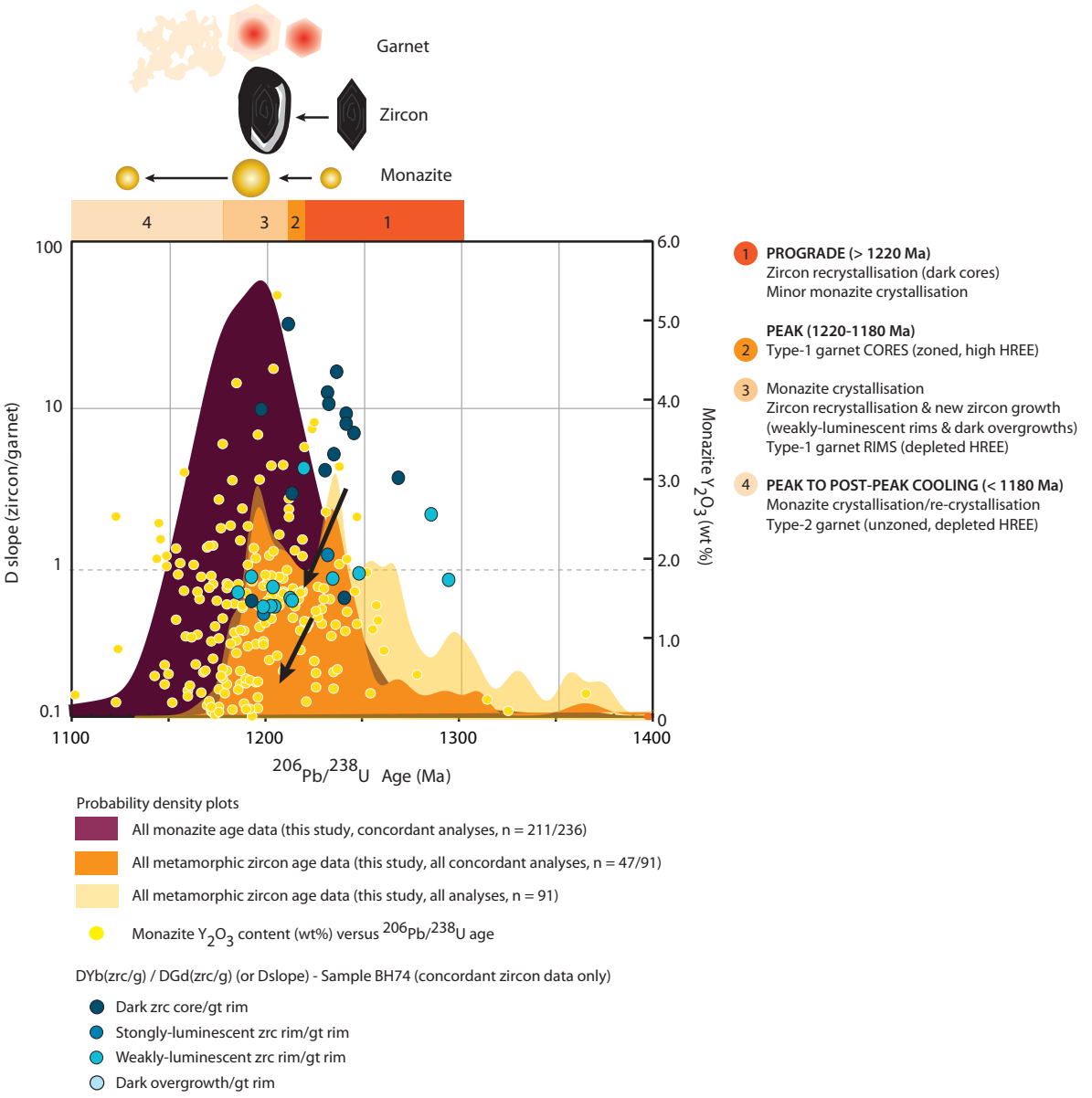

Figure 11. Illustrated summary of age and trace element data and interpretation. Metamorphic zircon age data from this study (n = 91) are shown as a probability density curve in shades of orange (concordant data in solid colour; discordant data is transparent). Concordant monazite age data from this study (n = 211/236) are presented as a probability density curve in purple. D_{REE} (zircon–type 1 garnet rim) data for individual zircon from sample BH74 plotted against their corresponding $^{206}Pb/^{238}U$ age (concordant analyses only) are overlain as solid blue circles. Monazite Y_2O_3 content (wt%) versus $^{206}Pb/^{238}U$ age for concordant analyses (all samples) are shown as solid yellow circles. The overall trend in the D_{REE} (zircon–garnet) data for BH74 and the monazite data with decreasing age (see also Fig. 8 and Appendix D) is indicated by the arrows. The age and trace element data can be divided into four phases of mineral growth and modification as illustrated along the top and to the right of the figure.

(e.g. Korhonen et al., 2013; Morrissey et al., 2016; Walsh et al., 2015). Zircon is more likely to preserve older ages than monazite because of difference in their chemical and physical growth behaviour including non-linear growth rates as controlled by temperature (Kelsey et al., 2008), melt volume (Yakymchuk and Brown, 2014), and differences in saturation of Zr and LREE with respect to temperature and the position of the solidus (Yakymchuk and Brown, 2014). Difference in zircon and monazite ages may also indicate that the peak of metamorphism exceeded monazite stability to dissolution and Pb diffusion (Cherniak, 2010; Kelsey et al., 2008; Stepanov et al., 2012; Yakymchuk and Brown, 2014), that the terrane cooled relatively slowly (Kelsey et al., 2008), or that there were variations in the host rock or mineral reactions that resulted in accessory mineral growth (Taylor et al., 2016). U–Pb age data from granulites likely reflect a combination of these prograde, peak and retrograde processes.

The relationship between the trace element geochemistry of zircon, monazite and garnet

in this study, and the relationship of garnet to the *P–T* evolution, demonstrate a more cryptic interpretation than can be determined from the age data alone. The age data are accordingly interpreted to reflect: (1) metamorphic zircon formed by solid-state recrystallization of inherited grains and minor prograde monazite growth in a relatively HREE-enriched, garnet-absent environment prior to 1230 Ma; (2) zircon, garnet and monazite cogenesis at the peak of metamorphism in a melt-bearing, progressively HREE-depleted environment (ca. 1220–1180 Ma); (3) continued garnet growth late-syn to post zircon crystallisation in a HREE-depleted environment; and, (4) monazite crystallisation and/or recrystallization during protracted cooling ca. 1180–1100 Ma as the *P–T* path tracks approximately isobarically towards the solidus. The interpretation of the zircon and monazite ages, relationship to garnet, and the timing of metamorphism is summarised in Fig. 11.

6.5 *P–T* evolution

Pseudosection modelling predicts that the three samples of garnet–cordierite ± sillimanite gneiss have peak *P–T* stability fields over the range 5.5–7.1 kbar and 800–960 °C. We assume that all three modelled rocks record a *P–T–t* evolution that relates to the same metamorphic event as the sampled regions are not structurally juxtaposed. The analysed samples contain a strong gneissic S_1–S_2 fabric. The *P–T* estimates therefore likely relate to development of the S_1–S_2 fabric (i.e. associated with D_1–D_2) which the inferred peak metamorphic minerals define. The S_1–S_2 fabrics are commonly steeply-reoriented by F_3 folding. D_3 is interpreted to have occurred at high temperature as evidenced by orthopyroxene- and cordierite-bearing melts that cross cut reoriented S_1–S_2 fabrics, and leucosomes that sometimes align axial planar to F_3. Orthopyroxene-bearing and cordierite-bearing leucosomes that overprint the reoriented S_1–S_2 fabrics (by D_3) provide evidence that the rocks continued to undergo partial melting as pervasive strain declined.

Fig. 9d presents a comparison of the calculated peak metamorphic conditions in the Bunger Hills, Highjump Archipelago and Windmill Islands. The calculated *P–T* conditions occur at a slightly lower pressure (i.e. higher apparent thermal gradient) than those from the Highjump Archipelago that is situated immediately north of the Bunger Hills where garnet ± sillimanite ± rutile assemblages formed at 6–9 kbar and 850–950 °C (Tucker and Hand, 2016). The Bunger Hills rocks formed under a slightly lower thermal regime than equivalent aged metamorphism in the Windmill Islands where M_2 peak conditions attained >850 °C and ~4 kbar (Morrissey et al., 2017a). The Highjump Archipelago and Windmill Islands record evidence for post-peak, decompressive and isobaric cooling, respectively (Morrissey et al., 2017a; Tucker and Hand, 2016). Three lines of evidence from sample BH54 likewise constrain the Bunger Hills post-peak *P–T* path along an isobaric to slightly down-pressure trajectory. Zircon–garnet partitioning from sample BH54 suggests that a generation of HREE-depleted garnet grew post zircon crystallisation. The HREE-depleted garnet in this sample appears texturally late as, although it is coarse-grained and elongate with the fabric, it contains many inclusions of other peak phases. Therefore, the peak to post-peak *P–T* path must have involved steady or increasing garnet abundance. The absence of inferred peak sillimanite and orthopyroxene in sample BH54 further constrains the post-peak *P–T* path to have tracked slightly down-pressure, between 6.5–7.2 kbar at 850 °C to 4.4–4.8 kbar at 700 °C. Cordierite-bearing and orthopyroxene-bearing leucosomes broadly support that cooling and crystallisation of these melts occurred at low pressures and high temperatures. However, as these melts are inferred late in the metamorphic evolution (i.e. syn–late D_3, and the absolute timing is unconstrained), it is unclear what mineral assemblage they existed in equilibrium with as the *P–T* models are interpreted to relate to S_1–S_2.

6.6 Mechanisms for high-*T* metamorphism in a regional context

The Bunger Hills are interpreted to have once comprised the western part of the Albany–Fraser Orogen (Tucker et al., 2017). *P–T–t* results from the Bunger Hills therefore allow several conclusions to be drawn in the wider context of the Albany–Fraser Orogen. Firstly, the age of high temperature metamorphism in the Bunger Hills correlates with Stage-2 of the Albany–Fraser Orogeny. Secondly, the Bunger Hills and thus the westernmost part of the orogen was largely metamorphically unresponsive to Stage-1 deformation and metamorphism, or Stage-1 features were essentially overprinted. Thirdly, the peak metamorphic conditions recorded in the Bunger Hills are equivalent to regional, sustained

high-temperature conditions elsewhere across the orogen, and reflect a similar down-pressure *P–T* evolution following peak conditions. An explanation is required for the lack of preservation of Stage-1 metamorphism in the Bunger Hills as well as a mechanism for the long-lived, hot thermal regime and down-pressure *P–T* path that was experienced during Stage-2 by the western Albany–Fraser Orogen.

As alluded to by previous studies, the patchy, spatial nature of Stage-1 deformation and metamorphism is likely linked to tectonic control. Stage-1 is considered to have occurred following collision of the Loongana oceanic arc with the eastern Albany–Fraser Orogen and the subsequent generation of a back-arc and/or west-ward migrating mid–lower crustal hot zone (Morrissey et al., 2017b; Smithies et al., 2015; Spaggiari et al., 2015). It is therefore logical that Stage-1 is predominantly recorded within the eastern regions of the orogen such as the Windmill Islands, eastern Nornalup Zone and Fraser Zone, and not within the Bunger Hills. It is possible that evidence for Stage-1 in some regions but not others may also reflect rock unreactivity controlled by bulk chemical composition and the unavailability of fluids or melt (e.g. Morrissey et al., 2016; Phillips et al., 2007). It is possible that Stage-1 metamorphism occurred in a comparatively dry system relative to Stage-2 that appears to have been melt-bearing (Morrissey et al., 2017a; Tucker and Hand, 2016, and this study).

The heat source for Stage-2 metamorphism in the Albany–Fraser Orogen and now separated terranes is not well understood. Field observations suggest that at least late Stage-2 involved a fold and thrust architecture and exhumation (Table 1, references therein). Rapid cooling syn (Stage-2) orogenesis is also interpreted to have been facilitated by NW-directed thrusting (Scibiorski et al., 2015). Tucker and Hand (2016) investigated Stage-2 metamorphism using phase equilibria forward modelling and proposed that the peak of Stage-2 metamorphism was possibly related to extension of over-thickened crust. Alternatively, Morrissey et al. (2017a) interpret that the Stage-2 event seen by the Windmill Islands was mostly thermal, relating to the voluminous emplacement of charnockite although earlier studies also initially propose exhumation and unloading of the terrane following crustal thickening (Post, 2000; Post et al., 1997).

Magmatism in the Bunger Hills occurred at 1256 ± 5 Ma, ca. 1200–1170 Ma and 1151 ± 4 Ma resulting in emplacement of protoliths to an unnamed tonalite orthogneiss, the Paz Cove Batholith and Algae Lake Pluton, and the Booth Peninsula Batholith, respectively (Sheraton et al., 1992; Tucker et al., 2017). The main phase of magmatism (ca. 1200–1170 Ma) was coeval with inferred peak metamorphism (ca. 1220–1180 Ma, this study). However, field observations and phase equilibria modelling do not identify a spatial relationship between these igneous intrusives and variation in metamorphic grade of the surrounding pelite gneiss. Therefore, unlike the Windmill Islands, metamorphism and felsic magmatism in the Bunger Hills are inferred to be coeval but not necessarily causal. It is possible that heat for metamorphism was provided in part by mafic magmatism at lower crustal depths evidenced directly from gabbro and diorite that crop out on the Booth Peninsula (Fig. 2), and Hf-isotope signatures from felsic intrusives dating to ca. 1200–1170 Ma that suggest some juvenile component (Tucker et al., 2017). But overall, the medium-pressure, high to ultrahigh temperature conditions, isobaric to down-pressure *P–T* path and long-lived thermal regime experienced by the Bunger Hills is reflective of a more regional mechanism.

Kelsey and Hand (2015) and Clark et al. (2011) summarise that granulites reflecting long-lived, high temperature conditions and near-isothermal decompression and exhumation can form in a number of tectonic settings. Typically however, these terranes are often a function of the amount and distribution of radiogenic elements during crustal thickening combined with sufficiently slow erosion rates and crustal preconditioning. Stage-2 metamorphism in the Bunger Hills was likely associated with collapse of a compressional orogen following arc accretion and northwest-directed crustal thickening during Stage-1 of the Albany–Fraser Orogeny. The age data from this study suggest that although peak metamorphism only occurred over ca. 1220–1180 Ma, the terrane probably experienced high thermal conditions over a much longer timeframe to facilitate minor prograde monazite crystallisation, monazite crystallisation during cooling and zircon recrystallization. This evidence is suggestive of a slowly-exhuming extensional system with relatively slow post-peak cooling. The proposed isobaric to slightly down-pressure *P–T* path from

P–T modelling is also consistent with cooling at depth within a broadly extensional tectonic regime. While exhumation of the terrane is consistent with several previous interpretations on Stage-2 deformation from field observations and metamorphic studies (see above), this notion of slow cooling contrasts with recent interpretations that suggest rapid syn-orogenic cooling occurred along thrust zones (Scibiorski et al., 2016). Field observations indicate that the Bunger Hills do not record evidence for thrusting during peak metamorphism. It is possible that the metamorphosed Bunger Hills rocks thus reflect a more ductile regime and is the more slowly-exhumed core of the orogen from mid-crustal depths (~18 km) compared with the upper-crust and orogenic margins that underwent comparatively brittle deformation. Slight differences in the metamorphic conditions experienced at the same time by the Bunger Hills and adjacent Highjump Archipelago may suggest that these regions today represent an obliquely exposed portion of the crust where the adjacent Highjump Archipelago attained slightly higher pressures (6–9 kbar) at lower crustal depths and was therefore more deeply exhumed.

7. CONCLUSIONS

Extreme spreads in age data are a repercussion of granulite facies conditions that pose serious challenges for interpreting the true duration of peak metamorphism. The resultant spread in ages may be erroneously interpreted as reflecting a single, long-lived event when, in reality, a number of processes may be responsible for the growth and modification of zircon and monazite. Zircon and monazite U–Pb geochronology alone suggest that the Bunger Hills in East Antarctica experienced long-lived (ca. 200 Myr), high-temperature conditions during the Mesoproterozoic (ca. 1300–1100 Ma). Forward phase equilibria modelling of garnet–cordierite ± sillimanite gneiss estimate that peak metamorphism attained high to ultrahigh temperatures (5.5–7.1 kbar, 800–960 °C). Integrating zircon, monazite and garnet trace element chemistry reveals a more covert meaning to the U–Pb ages that are interpreted to reflect: (1) solid-state recrystallization of inherited zircon and minor prograde monazite growth in the absence of garnet >ca. 1230 Ma; (2) the stable-coexistence of zircon, garnet and monazite at the peak of metamorphism between ca. 1220–1180 Ma; (3) continued garnet growth in a HREE-depleted environment post zircon crystallisation; and, (4) monazite crystallisation during cooling <ca. 1180 Ma along an approximately isobaric *P–T* path. The results of this study reveal that the duration of high-temperature conditions in the Bunger Hills was very long-lived, but peak metamorphism itself was comparatively shorter. This study more definitively extends the spatial footprint of Stage-2 of the Albany–Fraser Orogeny into East Antarctica. It seems likely that the long duration of high thermal gradients was facilitated by regional extension, potentially due to collapse of over-thickened crust and that the Bunger Hills reflect the more slowly-exhumed core of the Albany–Fraser Orogen.

ACKNOWLEDGEMENTS

Logistical and financial support for field work in Antarctica was provided by the Australian Antarctic Division. We acknowledge the logistical support of fellow expeditioners at Casey station, the crew of Kenn Borek Air, and invaluable field assistance from Kimberly (Billy) Wallace during the 2014–2015 Antarctic field season. S. Gilbert and B. Wade, Adelaide Microscopy, and A. Kylander-Clark, University of California Santa Barbara, are thanked for assistance with analytical work. S. Mertzmann, Franklin and Marshall College, is thanked for geochemical analyses. An anonymous reviewer is thanked for their constructive comments and feedback on the manuscript. Analytical work was in part funded by an Australian Research Council DECRA fellowship (DE12010367) awarded to CC. NMT acknowledges the support of an Australian Government Research Training Program Scholarship (formerly Australian Postgraduate Award), University of Adelaide Supplementary Scholarship and Playford Trust PhD scholarship. This work forms part of Australian Antarctic Science Project 4191.

REFERENCES

Adams M. 2012. Structural and geochronological evolution of the Malcolm Gneiss, Nornalup Zone, Albany-Fraser Orogen, Western Australia: Geological Survey of Western Australia, Record 2012/4, 132p.

Aitken A. R. A., Betts P. G., Young D. A., Blankenship D. D., Roberts J. L. & Siegert M. J. 2016. The Australo-Antarctic Columbia to Gondwana transition. *Gondwana Research* 29, 136–152.

Aitken A. R. A., Young D. A., Ferraccioli F., Betts P. G., Greenbaum J. S., Richter T. G., Roberts J. L., Blankenship D. D. & Siegert M. J. 2014. The subglacial geology of Wilkes Land, East Antarctica. *Geophysical Research Letters* 41, 2390–2400.

Barquero-Molina M. 2009. Kinematics of bidirectional extension and coeval NW-directed contraction in orthogneisses of the Biranup Complex, Albany–Fraser Orogen, southwestern Australia. PhD thesis. The University of Texas, Austin.

Bartoli O. 2017. Phase equilibria modelling of residual migmatites and granulites: an evaluation of the melt-reintegration approach. *Journal of Metamorphic Geology*, **35**, 919–942.

Bea F., Pereira M. & Stroh A. 1994. Mineral/leucosome

trace-element partitioning in a peraluminous migmatite (a laser ablation–ICP–MS study). *Chemical Geology* 117, 291–312.

Beeson J., Delor C. P. & Harris L. B. 1988. A structural and metamorphic traverse across the Albany Mobile Belt, Western Australia. *Precambrian Research* 40, 117–136.

Bingen B. & Van Breemen O. 1998. U–Pb monazite ages in amphibolite-to granulite-facies orthogneiss reflect hydrous mineral breakdown reactions: Sveconorwegian Province of SW Norway. *Contributions to Mineralogy and Petrology* 132, 336–353.

Black L. P., Harris L. B. & Delor C. P. 1992. Reworking of Archaean and early Proterozoic components during a progressive, middle Proterozoic tectonothermal event in the Albany Mobile Belt, Western Australia. *Precambrian Research* 59, 95–123.

Bodorkos S. & Clark D. J. 2004a. Evolution of a crustal-scale transpressive shear zone in the Albany–Fraser Orogen, SW Australia: 1. *P–T* conditions of Mesoproterozoic metamorphism in the Coramup Gneiss. *Journal of Metamorphic Geology* 22, 691–711.

Bodorkos S. & Clark D. J. 2004b. Evolution of a crustal-scale transpressive shear zone in the Albany–Fraser Orogen, SW Australia: 2. Tectonic history of the Coramup Gneiss and a kinematic framework for Mesoproterozoic collision of the West Australian and Mawson cratons. *Journal of Metamorphic Geology* 22, 713–731.

Bodorkos S. & Wingate M. 2008a. 184119: monzogranitic gneiss, Point Henry; Geochronology Record 699: Geological Survey of Western Australia, 4p.

Bodorkos S. & Wingate M. 2008b. 184128: leucocratic tonalitic gneiss, Powell Point; Geochronology Record 705: Geological Survey of Western Australia, 4p.

Bodorkos S. & Wingate M. 2008c. 184307: pegmatitic granodiorite, Point Henry Geochronology Record 706: Geological Survey of Western Australia, 4p.

Bodorkos S. & Wingate M. 2008d. 184310: leucocratic granodiorite, Fisheries Bay headland; Geochronology Record 707: Geological Survey of Western Australia, 4p.

Bodorkos S. & Wingate M. 2008e. 184312: granodioritic gneiss, Short Beach headland; Geochronology Record 709: Geological Survey of Western Australia, 4p.

Boger S. D. 2011. Antarctica—before and after Gondwana. *Gondwana Research* 19, 335–371.

Carlson W. D. 2012. Rates and mechanism of Y, REE, and Cr diffusion in garnet. *American Mineralogist* 97, 1598–1618.

Carson C. J., Ague J. J., Grove M., Coath C. D. & Harrison T. M. 2002. U–Pb isotopic behaviour of zircon during upper-amphibolite facies fluid infiltration in the Napier Complex, east Antarctica. *Earth and Planetary Science Letters* 199, 287–310.

Cherniak D. 2010. Diffusion in accessory minerals: zircon, titanite, apatite, monazite and xenotime. *Reviews in Mineralogy and Geochemistry* 72, 827–869.

Clark C., Fitzsimons I. C. W., Healy D. & Harley S. L. 2011. How does the continental crust get really hot? *Elements* 7, 235–240.

Clark C., Kirkland C. L., Spaggiari C. V., Oorschot C., Wingate M. T. D. & Taylor R. J. 2014. Proterozoic granulite formation driven by mafic magmatism: An example from the Fraser Range Metamorphics, Western Australia. *Precambrian Research* 240, 1–21.

Clark D. J., Hensen B. J. & Kinny P. D. 2000. Geochronological constraints for a two-stage history of the Albany–Fraser Orogen, Western Australia. *Precambrian Research* 102, 155–183.

Clark D. J., Kinny P. D., Post N. J. & Hensen B. J. 1999. Relationships between magmatism, metamorphism and deformation in the Fraser Complex, Western Australia: Constraints from new SHRIMP U–Pb zircon geochronology. *Australian Journal of Earth Sciences* 46, 923–932.

Clark W. C. 1995. Granite petrogenesis, metamorphism and geochronology of the western Albany-Fraser Orogen, Albany, Western Australia. BSc. (Honours) Thesis. Curtin University of Technology, Perth.

Corfu F., Hanchar J. M., Hoskin P. W. & Kinny P. 2003. Atlas of zircon textures. Reviews in mineralogy and geochemistry 53, 469–500.

Dawson G. C., Krapež B., Fletcher I. R., Mcnaughton N. J. & Rasmussen B. 2003. 1.2 Ga thermal metamorphism in the Albany–Fraser Orogen of Western Australia: consequence of collision or regional heating by dyke swarms? *Journal of the Geological Society* 160, 29–37.

De Waele B. & Pisarevsky S. 2008. Geochronology, paleomagnetism and magnetic fabric of metamorphic rocks in the northeast Fraser Belt, Western Australia. *Australian Journal of Earth Sciences* 55, 605–621.

Degeling H., Eggins S. & Ellis D. 2001. Zr budgets for metamorphic reactions, and the formation of zircon from garnet breakdown. *Mineralogical Magazine* 65, 749–758.

Droop G. T. R. 1987. A general equation for estimating Fe3+ concentrations in ferromagnesian silicates and oxides from microprobe analyses, using stoichiometric criteria. *Mineralogical magazine* 51, 431–435.

Duebendorfer E. M. 2002. Regional correlation of Mesoproterozoic structures and deformational events in the Albany–Fraser orogen, Western Australia. *Precambrian Research* 116, 129–154.

Fitzsimons I., Kinny P., Wetherley S. & Hollingsworth D. 2005. Bulk chemical control on metamorphic monazite growth in pelitic schists and implications for U–Pb age data. *Journal of Metamorphic Geology* 23, 261–277.

Fitzsimons I. C. W. & Buchan C. 2005. Geology of the western Albany-Fraser Orogen, Western Australia - a field guide: Western Australia Geological Survey, Record 2005/11, 32p.

Foster G., Kinny P., Vance D., Prince C. & Harris N. 2000. The significance of monazite U–Th–Pb age data in metamorphic assemblages; a combined study of monazite and garnet chronometry. *Earth and Planetary Science Letters* 181, 327–340.

Gorczyk W., Smithies H., Korhonen F., Howard H. & Quentin De Gromard R. 2015. Ultra-hot Mesoproterozoic evolution of intracontinental central Australia. *Geoscience Frontiers* 6, 23–37.

Halpin J. A., Daczko N. R., Milan L. A. & Clarke G. L. 2012. Decoding near-concordant U–Pb zircon ages spanning several hundred million years: recrystallisation, metamictisation or diffusion? *Contributions to Mineralogy and Petrology* 163, 67–85.

Harley S. L., Kelly N. M. & Möller A. 2007. Zircon behaviour and the thermal histories of mountain chains. *Elements* 3, 25–30.

Harlov D. E., Wirth R. & Hetherington C. J. 2011. Fluid-mediated partial alteration in monazite: The role of coupled dissolution-reprecipitation in element redistribution and mass transfer. *Contributions to Mineralogy and Petrology* 162, 329–348.

Hermann J. & Rubatto D. 2003. Relating zircon and monazite domains to garnet growth zones: age and duration of

granulite facies metamorphism in the Val Malenco lower crust. *Journal of Metamorphic Geology* 21, 833–852.

Hokada T. & Harley S. L. 2004. Zircon growth in UHT leucosome: constraints from zircon-garnet rare earth elements (REE) relations in Napier Complex, East Antarctica. *Journal of Mineralogical and Petrological Sciences* 99, 180–190.

Holland T. & Powell R. 1998. An internally consistent thermodynamic data set for phases of petrological interest. *Journal of Metamorphic Geology* 16, 309–343.

Hoskin P. & Black L. 2000. Metamorphic zircon formation by solid-state recrystallization of protolith igneous zircon. *Journal of metamorphic Geology* 18, 423–439.

Johnson T. E., Clark C., Taylor R. J., Santosh M. & Collins A. S. 2015. Prograde and retrograde growth of monazite in migmatites: An example from the Nagercoil Block, southern India. *Geoscience Frontiers* 6, 373–387.

Kelsey D. & Powell R. 2011. Progress in linking accessory mineral growth and breakdown to major mineral evolution in metamorphic rocks: a thermodynamic approach in the Na_2O–CaO–K_2O–FeO–MgO–Al_2O_3–SiO_2–H_2O–TiO_2–ZrO_2 system. *Journal of Metamorphic Geology* 29, 151–166.

Kelsey D. E., Clark C. & Hand M. 2008. Thermobarometric modelling of zircon and monazite growth in melt-bearing systems: examples using model metapelitic and metapsammitic granulites. *Journal of Metamorphic Geology* 26, 199–212.

Kelsey D. E. & Hand M. 2015. On ultrahigh temperature crustal metamorphism: Phase equilibria, trace element thermometry, bulk composition, heat sources, timescales and tectonic settings. *Geoscience Frontiers* 6, 311–356.

Kirkland C., Smithies R., Spaggiari C., Wingate M., De Gromard R. Q., Clark C., Gardiner N. & Belousova E. 2017. Proterozoic crustal evolution of the Eucla basement, Australia: Implications for destruction of oceanic crust during emergence of Nuna. *Lithos* 278, 427–444.

Kirkland C., Wingate M. & Spaggiari C. 2011a. 194718: mafic granulite, American Granulite Quarry; Geochronology Record 993: Geological Survey of Western Australia, 7p.

Kirkland C. L., Smithies R. H. & Spaggiari C. V. 2015. Foreign contemporaries – Unravelling disparate isotopic signatures from Mesoproterozoic Central and Western Australia. *Precambrian Research* 265, 218–231.

Kirkland C. L., Smithies R. H., Woodhouse A. J., Howard H. M., Wingate M. T. D., Belousova E. A., Cliff J. B., Murphy R. C. & Spaggiari C. V. 2013. Constraints and deception in the isotopic record; The crustal evolution of the west Musgrave Province, central Australia. *Gondwana Research* 23, 759–781.

Kirkland C. L., Spaggiari C. V., Pawley M. J., Wingate M. T. D., Smithies R. H., Howard H. M., Tyler I. M., Belousova E. A. & Poujol M. 2011b. On the edge: U–Pb, Lu–Hf, and Sm–Nd data suggests reworking of the Yilgarn craton margin during formation of the Albany–Fraser Orogen. *Precambrian Research* 187, 223–247.

Kirkland C. L., Spaggiari C. V., Smithies R. H. & Wingate M. T. D. 2014a. Cryptic progeny of craton margins: geochronology and isotope geology of the Albany–Fraser Orogen, with implications for evolution of the Tropicana Zone. *In: Spaggiari C. V. & Tyler I. M. (eds.) Albany–Fraser Orogen seismic and magnetotelluric (MT) workshop 2014: extended abstracts.* Geological Survey of Western Australia, Record 2014/6, pp. 81–92.

Kirkland C. L., Wingate M. T. D. & Spaggiari C. V. 2011c. 194705: metasyenogranite, Cowalinya Pool; Geochronology Record 988: Geological Survey of Western Australia, 4p.

Kirkland C. L., Wingate M. T. D. & Spaggiari C. V. 2014b. 194740: psammitic gneiss, Harris Lake; Geochronology Record 1217: Geological Survey of Western Australia, 7p.

Kohn M. J., Corrie S. L. & Markley C. 2015. The fall and rise of metamorphic zircon. *American Mineralogist* 100, 897–908.

Kohn M. J. & Malloy M. A. 2004. Formation of monazite via prograde metamorphic reactions among common silicates: implications for age determinations. *Geochimica et Cosmochimica Acta* 68, 101–113.

Korhonen F. J., Johnson, S., Wingate, M., Kirkland, C., Fletcher, I., Dunkley, D., Roberts, M., Sheppard, S., Muhling, J. & Rasmussen, B. 2017. Radiogenic heating and craton-margin plate stresses as drivers for intraplate orogeny. *Journal of Metamorphic Geology* 35, 631–661.

Korhonen F. J., Clark C., Brown M., Bhattacharya S. & Taylor R. 2013. How long-lived is ultrahigh temperature (UHT) metamorphism? Constraints from zircon and monazite geochronology in the Eastern Ghats orogenic belt, India. *Precambrian Research* 234, 322–350.

Kylander-Clark A. R., Hacker B. R. & Cottle J. M. 2013. Laser-ablation split-stream ICP petrochronology. Chemical Geology 345, 99–112.

Li Z. X., Bogdanova S. V., Collins A. S., Davidson A., De Waele B., Ernst R. E., Fitzsimons I. C. W., Fuck R. A., Gladkochub D. P., Jacobs J., Karlstrom K. E., Lu S., Natapov L. M., Pease V., Pisarevsky S. A., Thrane K. & Vernikovsky V. 2008. Assembly, configuration, and break-up history of Rodinia: A synthesis. *Precambrian Research* 160, 179–210.

Love G. J. 1999. A study of wall-rock contamination in a tonalitic gneiss from King Point, near Albany, Western Australia. BSc. (Honours) Thesis. Curtin University of Technology, Perth.

Ludwig K. R. 2012. User's manual for ISOPLOT 3.75, a geochronological toolkit for Microsoft Excel. Berkeley Geochronology Centre Special Publication 5.

Maidment, D. W. 2017. Geochronology of the Rudall Province, Western Australia: implications for the amalgamation of the West and North Australian Cratons: Geological Survey of Western Australia, Report 161, 95p.

Maritati A., Aitken A. R. A., Young D. A., Roberts J. L., Blankenship D. D. & Siegert M. J. 2016. The tectonic development and erosion of the Knox Subglacial Sedimentary Basin, East Antarctica. *Geophysical Research Letters* 43, 10,728–10,737.

Mcdonough W. F. & Sun S. S. 1995. The composition of the Earth. *Chemical geology* 120, 223–253.

Morrissey L., Payne J. L., Kelsey D. E. & Hand M. 2011. Grenvillian-aged reworking in the North Australian Craton, central Australia: constraints from geochronology and modelled phase equilibria. *Precambrian Research* 191, 141–165.

Morrissey L. J. 2016. Characterising the *P*–*T*–t histories and effects of melt loss in high thermal gradient terranes. PhD Thesis. The University of Adelaide, Adelaide.

Morrissey L. J., Hand M. & Kelsey D. E. 2017a. A curious case of agreement between conventional thermobarometry and phase equilibria modelling in granulites: new constraints on *P*–*T* estimates in the Antarctica segment of the Musgrave–Albany–Fraser–Wilkes Orogen. *Journal of Metamorphic Geology* 35, 1023–1050.

Morrissey L. J., Hand M., Kelsey D. E. & Wade B. P. 2016. Cambrian High-temperature Reworking of the Rayner–

Eastern Ghats Terrane: Constraints from the Northern Prince Charles Mountains Region, East Antarctica. *Journal of Petrology* 57, 53–92.

Morrissey L. J., Hand M., Raimondo T. & Kelsey D. E. 2014. Long-lived high-T, low-P granulite facies metamorphism in the Arunta region, central Australia. *Journal of Metamorphic Geology* 32, 25–47.

Morrissey L. J., Payne J. L., Hand M., Clark C., Taylor R., Kirkland C. L. & Kylander-Clark A. 2017b. Linking the Windmill Islands, east Antarctica and the Albany–Fraser Orogen: Insights from U–Pb zircon geochronology and Hf isotopes. *Precambrian Research* 293, 131–149.

Nelson D. R. 1995. 83676A: hornblende syenogranite gneiss, Mount Andrew, in. Compilation of geochronology data, 1994: Geological Survey of Western Australia, Record 1995/3, p. 49–52.

Nelson D. R., Myers J. S. & Nutman A. P. 1995. Chronology and evolution of the Middle Proterozoic Albany-Fraser Orogen, Western Australia. *Australian Journal of Earth Sciences* 42, 481–495.

Nichols G., Berry R. & Green D. 1992. Internally consistent gahnitic spinel-cordierite-garnet equilibria in the FMASHZn system: geothermobarometry and applications. Contributions to Mineralogy and Petrology 111, 362–377.

Paton C., Hellstrom J., Paul B., Woodhead J. & Hergt J. 2011. Iolite: Freeware for the visualisation and processing of mass spectrometric data. *Journal of Analytical Atomic Spectrometry* 26, 2508–2518.

Paul E., Stüwe K., Teasdale J. & Worley B. 1995. Structural and metamorphic geology of the Windmill Islands, east Antarctica: field evidence for repeated tectonothermal activity. *Australian Journal of Earth Sciences* 42, 453–469.

Payne J. L. 2008. Palaeo- to Mesoproterozoic evolution of the Gawler Craton, Australia: gechronological, geochemical and isotopic constraints. PhD Thesis. The University of Adelaide, Adelaide.

Pearce M., White A. & Gazley M. 2015. TCInvestigator: automated calculation of mineral mode and composition contours for thermocalc pseudosections. *Journal of Metamorphic Geology* 33, 413–425.

Phillips G., White R. & Wilson C. 2007. On the roles of deformation and fluid during rejuvenation of a polymetamorphic terrane: inferences on the geodynamic evolution of the Ruker Province, East Antarctica. *Journal of Metamorphic Geology* 25, 855–871.

Post N. J. 2000. Unravelling Gondwana fragments: an integrated structural, isotopic and petrographic investigation of the Windmill Islands, Antarctica. PhD Thesis. University of New South Wales, Sydney.

Post N. J., Hensen B. J. & Kinny P. D. 1997. Two metamorphic episodes during a 1340-1180 Ma convergent tectonic event in the Windmill Islands, East Antarctica. *In: Ricci C. A. (ed.) The Antarctic Region: Geological Evolution and Processes,* Terra Antarctica, Siena, 157–161.

Rigby M. & Droop G. 2011. Fluid-absent melting versus CO_2 streaming during the formation of pelitic granulites: A review of insights from the cordierite fluid monitor. *Geological Society of America Memoirs* 207, 39–60.

Roberts M. P. & Finger F. 1997. Do U–Pb zircon ages from granulites reflect peak metamorphic conditions? *Geology* 25, 319–322.

Rubatto D. 2002. Zircon trace element geochemistry: partitioning with garnet and the link between U–Pb ages and metamorphism. *Chemical geology* 184, 123–138.

Rubatto D. 2017. Zircon: the metamorphic mineral. *Reviews in mineralogy and geochemistry* 83, 261–295.

Rubatto D., Hermann J. & Buick I. S. 2006. Temperature and bulk composition control on the growth of monazite and zircon during low-pressure anatexis (Mount Stafford, central Australia). *Journal of Petrology* 47, 1973–1996.

Rubatto D., Williams I. S. & Buick I. S. 2001. Zircon and monazite response to prograde metamorphism in the Reynolds Range, central Australia. *Contributions to Mineralogy and Petrology* 140, 458–468.

Sankar B., Kaushik D. & Fukuoka M. 2005. Fluorine content of biotite in granulite-grade metapelitic assemblages and its implications for the Eastern Ghats granulites. *European Journal of Mineralogy* 17, 665–674.

Scibiorski, E., Tohver, E., & Jourdan, F. 2015. Rapid cooling and exhumation in the western part of the Mesoproterozoic Albany-Fraser Orogen, Western Australia. Precambrian Research, 265, 232–248.

Sheraton J. W., Black L. P. & Tindle A. G. 1992. Petrogenesis of plutonic rocks in a Proterozoic granulite-facies terrane — the Bunger Hills, East Antarctica. *Chemical Geology* 97, 163–198.

Sheraton J. W., Tingey R., Oliver R. & Black L. 1995. Geology of the Bunger Hills–Denman Glacier region, East Antarctica. *AGSO Bulletin*, No. 244, 1–136.

Sheraton J. W., Tingey R. J., Black L. P. & Oliver R. L. 1993. Geology of the Bunger Hills area, Antarctica: implications for Gondwana correlations. *Antarctic Science* 5, 85–102.

Smithies H. R., Spaggiari C. V., Kirkland C. L., Howard H. & Maier W. D. 2013. Petrogenesis of gabbros of the Mesoproterozoic Fraser Zone: constraints on the tectonic evolution of the Albany-Fraser Orogen. Geological Survey of Western Australia, Record 2013/5, p. 29.

Smithies R. H., Howard H. M., Evins P. M., Kirkland C. L., Kelsey D. E., Hand M., Wingate M. T. D., Collins A. S. & Belousova E. 2011. High-temperature granite magmatism, crust-mantle interaction and the mesoproterozoic intracontinental evolution of the Musgrave Province, central Australia. *Journal of Petrology* 52, 931–958.

Smithies R. H., Spaggiari C. V. & Kirkland C. L. 2015. Building the crust of the Albany-Fraser Orogen: constraints from granite geochemistry. Geological Survey of Western Australia, Report 150, 49p.

Smits R. G., Collins W. J., Hand M., Dutch R. & Payne J. 2014. A Proterozoic Wilson cycle identified by Hf isotopes in central Australia; implications for the assembly of Proterozoic Australia and Rodinia. *Geology* 42, 231–234.

Spaggiari C. V., Bodorkos S., Barquero-Molino M., Tyler I. M. & Wingate M. T. D. 2009. Interpreted bedrock geology of the South Yilgarn and central Albany-Fraser Orogen, Western Australia: Geological Survey of Western Australia, Record 2009/10, 84p.

Spaggiari C. V., Kirkland C. L., Smithies R. H., Occhipinti S. A. & Wingate M. T. D. 2014. Geological framework of the Albany-Fraser Orogen. in Albany-Fraser Orogen seismic and magnetotelluric (MT) workshop 2014: extended abstracts: Geological Survey of Western Australia, Record 2014/6. p. 44–59.

Spaggiari C. V., Kirkland C. L., Smithies R. H., Wingate M. T. D. & Belousova E. A. 2015. Transformation of an Archean craton margin during Proterozoic basin formation and magmatism: The Albany–Fraser Orogen, Western Australia. Precambrian Research 266, 440–466.

Spaggiari C. V. & Smithies R. H. 2015. Eucla basement stratigraphic drilling results release workshop: extended abstracts: Geological Survey of Western Australia, Record 2015/10, 70p.

Spaggiari C. V. & Tyler I. M. 2014. Albany-Fraser Orogen seismic and magnetotelluric (MT) workshop 2014: extended abstracts: Geological Survey of Western Australia, Record 2014/6. 165p.

Spencer C. J., Kirkland C. L. & Taylor R. J. M. 2015. Strategies towards statistically robust interpretations of in situ U–Pb zircon geochronology. *Geoscience Frontiers* 7, 581–589.

Stearns M. A., Hacker B. R., Ratschbacher L., Lee J., Cottle J. M. & Kylander-Clark A. 2013. Synchronous Oligocene–Miocene metamorphism of the Pamir and the north Himalaya driven by plate-scale dynamics. *Geology* 41, 1071–1074.

Stepanov A. S., Hermann J., Rubatto D. & Rapp R. P. 2012. Experimental study of monazite/melt partitioning with implications for the REE, Th and U geochemistry of crustal rocks. *Chemical Geology* 300, 200–220.

Stüwe K. & Powell R. 1989. Metamorphic evolution of the Bunger Hills, East Antarctica: evidence for substantial post-metamorphic peak compression with minimal cooling in a Proterozoic orogenic event. *Journal of Metamorphic Geology* 7, 449–464.

Stüwe K. & Wilson C. J. L. 1990. Interaction between deformation and charnockite emplacement in the Bunger Hills, East Antarctica. *Journal of Structural Geology* 12, 767–783.

Tajčmanová L., Konopásek J. & Košler J. 2009. Distribution of zinc and its role in the stabilization of spinel in high-grade felsic rocks of the Moldanubian domain (Bohemian Massif). *European Journal of Mineralogy* 21, 407–418.

Taylor R., Harley S., Hinton R., Elphick S., Clark C. & Kelly N. 2015. Experimental determination of REE partition coefficients between zircon, garnet and melt: a key to understanding high-T crustal processes. *Journal of Metamorphic Geology* 33, 231–248.

Taylor R. J., Kirkland C. L. & Clark C. 2016. Accessories after the facts: Constraining the timing, duration and conditions of high-temperature metamorphic processes. *Lithos* 264, 239–257.

Taylor R. J. M., Clark C., Harley S. L., Kylander-Clark A. R. C., Hacker B. R. & Kinny P. D. 2017. Interpreting granulite facies events through rare earth element partitioning arrays. *Journal of Metamorphic Geology* 35, 759–775.

Tucker N. M. & Hand M. 2016. New constraints on metamorphism in the Highjump Archipelago, East Antarctica. *Antarctic Science* 28, 487–503.

Tucker N. M., Hand M., Kelsey D. E. & Dutch R. A. 2015. A duality of timescales: Short-lived ultrahigh temperature metamorphism preserving a long-lived monazite growth history in the Grenvillian Musgrave–Albany–Fraser Orogen. *Precambrian Research* 264, 204–234.

Tucker N. M., Payne J. L., Clark C., Hand M., Taylor R. J., Kylander-Clark A. R. C. & Martin L. 2017. Reworking of Archean (Yilgarn) basement in the Bunger Hills, East Antarctica. *Precambrian Research* 298, 16–38.

Vavra G., Gebauer D., Schmid R. & Compston W. 1996. Multiple zircon growth and recrystallization during polyphase Late Carboniferous to Triassic metamorphism in granulites of the Ivrea Zone (Southern Alps): an ion microprobe (SHRIMP) study. *Contributions to Mineralogy and Petrology* 122, 337–358.

Vonlanthen P., Gerald J. D. F., Rubatto D. & Hermann J. 2012. Recrystallization rims in zircon (Valle d'Arbedo, Switzerland): An integrated cathodoluminescence, LA-ICP-MS, SHRIMP, and TEM study. *American Mineralogist* 97, 369–377.

Wade B. P., Barovich K. M., Hand M., Scrimgeour I. R. & Close D. F. 2006. Evidence for Early Mesoproterozoic Arc Magmatism in the Musgrave Block, central Australia: Implications for Proterozoic Crustal Growth and Tectonic Reconstructions of Australia. *Journal of Geology* 114, 43–63.

Walsh A. K., Kelsey D. E., Kirkland C. L., Hand M., Smithies R. H., Clark C. & Howard H. M. 2015. *P–T*–t evolution of a large, long-lived, ultrahigh-temperature Grenvillian belt in central Australia. *Gondwana Research* 28, 531–564.

Watt G., Burns I. & Graham G. 1996. Chemical characteristics of migmatites: accessory phase distribution and evidence for fast melt segregation rates. *Contributions to Mineralogy and Petrology* 125, 100–111.

Wetherley S. 1998. Tectonic evolution of the Mount Barren Group, Albany–Fraser Province, Western Australia. PhD Thesis. University of Western Australia, Perth.

White L. T., Gibson G. M. & Lister G. S. 2013. A reassessment of paleogeographic reconstructions of eastern Gondwana: Bringing geology back into the equation. *Gondwana Research* 24, 984–998.

Williams I. 2001. Response of detrital zircon and monazite, and their U–Pb isotopic systems, to regional metamorphism and host-rock partial melting, Cooma Complex, southeastern Australia. *Australian Journal of Earth Sciences* 48, 557–580.

Williams I. S., Buick I. S. & Cartwright I. 1996. An extended episode of early Mesoproterozoic metamorphic fluid flow in the Reynolds Range, central Australia. *Journal of Metamorphic Geology* 14, 29–47.

Wingate M. & Bodorkos S. 2007. 177910: Metamorphosed quartz sandstone, Peters Dam, Geochronology Record 660. Geological Survey of Western Australia.

Wong B. L., Morrissey L. J., Hand M., Fields C. E. & Kelsey D. E. 2015. Grenvillian-aged reworking of late Paleoproterozoic crust of the southern North Australian Craton, central Australia: Implications for the assembly of Mesoproterozoic Australia. *Precambrian Research* 270, 100–123.

Yakymchuk C. 2017. Behaviour of apatite during partial melting of metapelites and consequences for prograde suprasolidus monazite growth. *Lithos* 274, 412–426.

Yakymchuk C. & Brown M. 2014. Behaviour of zircon and monazite during crustal melting. *Journal of the Geological Society, London* 171, 465–479.

Zhang S., Zhao Y., Liu X., Liu Y., Hou K., Li C. & Ye H. 2012. U–Pb geochronology and geochemistry of the bedrocks and moraine sediments from the Windmill Islands: Implications for Proterozoic evolution of East Antarctica. *Precambrian Research* 206–207, 52–71.

Zhang Z., Xiang H., Dong X., Ding H. & He Z. 2015. Long-lived high-temperature granulite-facies metamorphism in the Eastern Himalayan orogen, south Tibet. *Lithos* 212, 1–15.

Appendix A. Sensitivity analyses for forward phase equilibria modelling

Figure 1. Temperature–M_o (M_o = Fe_2O_3/ (FeO + Fe_2O_3)) models for (a) BH54, (b) BH32, and (c) BH74. T–M_o models are shown over the compositional range M = 0 (i.e. reduced) to M = 0.75 (i.e. relatively oxidised). Models were calculated at pressures that intersect the inferred peak mineral assemblage field on corresponding P–T models (main text). The solidus is shown as a dashed line. The stability field of the inferred peak mineral assemblage in each sample is outlined in bold. The bulk composition chosen for each sample intersects the inferred peak mineral assemblage field and is indicated by a bold vertical line. Mineral abbreviations after Holland and Powell (1998).

Bulk compositions used for modelling (Figs. 1-3)

			H_2O	SiO_2	Al_2O_3	CaO	MgO	FeO	K_2O	Na_2O	TiO_2	O
BH32	T-MH_2O	M = 0	0.04	69.49	11.98	0.78	5.29	7.98	2.87	1.49	0.88	0.80
		M = 1	4.10	66.67	11.49	0.75	5.08	7.65	2.75	1.43	0.84	0.77
	P-Mo	M = 0	1.47	67.95	11.72	0.76	5.18	7.80	2.80	1.46	0.86	0.01
		M = 1	1.52	70.68	12.19	0.80	5.38	8.12	2.92	1.52	0.89	4.02
	T-Mo	M = 0	1.47	67.95	11.72	0.76	5.18	7.80	2.80	1.46	0.86	0.01
		M = 1	1.52	70.68	12.19	0.80	5.38	8.12	2.92	1.52	0.89	4.02
BH54	T-MH_2O	M = 0	0.04	68.50	10.38	0.52	7.80	10.67	1.70	1.43	1.36	2.40
		M = 1	5.19	64.97	9.85	0.49	7.40	10.12	1.62	1.35	1.29	2.28
	P-Mo	M = 0	2.15	65.48	9.93	0.49	7.46	10.20	1.63	1.36	1.30	0.01
		M = 1	2.26	68.96	10.45	0.52	7.86	10.74	1.72	1.44	1.37	5.32
	T-Mo	M = 0	2.15	65.48	9.93	0.49	7.46	10.20	1.63	1.36	1.30	0.01
		M = 1	2.26	68.96	10.45	0.52	7.86	10.74	1.72	1.44	1.37	5.32
BH74	T-MH_2O	M = 0	0.04	72.41	11.27	0.99	4.26	7.22	2.04	1.56	0.74	0.54
		M = 1	3.58	69.84	10.87	0.95	4.11	6.96	1.97	1.51	0.72	0.52
	P-Mo	M = 0	1.81	70.76	11.02	0.97	4.17	7.05	2.00	1.53	0.73	0.04
		M = 1	1.88	73.30	11.41	1.00	4.32	7.31	2.07	1.58	0.75	3.62
	T-Mo	M = 0	1.81	70.76	11.02	0.97	4.17	7.05	2.00	1.53	0.73	0.04
		M = 1	1.88	73.30	11.41	1.00	4.32	7.31	2.07	1.58	0.75	3.62

Mineral assemblages in (a)

1. bi g sill ilm pl q
2. bi g sill mt ilm pl ksp liq q
3. bi g cd sill ilm pl ksp liq q
4. bi g cd sill mt ilm pl ksp liq q
5. bi g cd mt ilm pl ksp liq q
6. bi g opx cd mt ilm pl ksp q
7. bi g sill opx cd mt ilm pl ksp q
8. bi sill opx cd mt ilm pl ksp q
9. bi opx cd mt ilm pl ksp q
10. bi opx cd mt ilm pl ksp liq q
11. g sill ilm pl ksp liq q
12. g sill opx cd mt ilm pl ksp liq q
13. g opx sill mt ilm pl ksp liq q
14. g opx sill mt ilm ksp liq q
15. g opx sill ilm ksp liq q
16. g sill cd mt ilm ksp liq q
17. g sill opx cd ilm ksp liq q
18. g opx sill sp ilm ksp liq q
19. g opx sill sp ilm pl ksp liq q
20. opx sill sp ilm pl ksp liq q
21. opx sill sp mt ilm pl ksp liq q
22. bi g cd mt ilm pl ksp q
23. bi g opx cd mt ilm pl ksp liq q

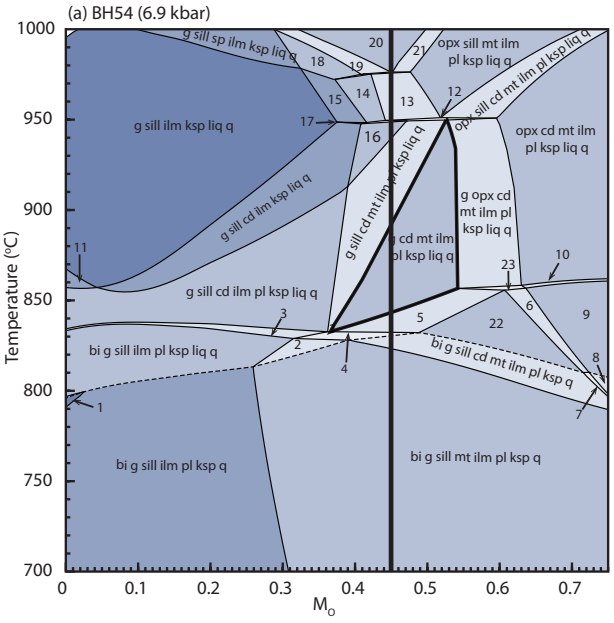

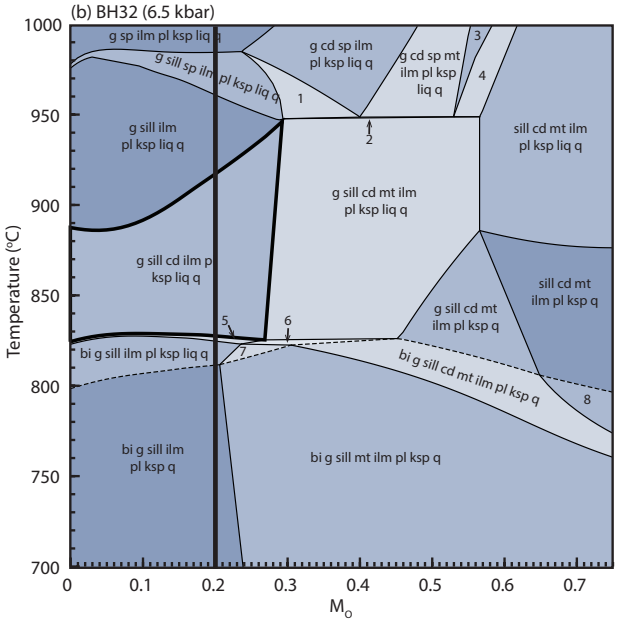

1. g sill cd sp ilm pl ksp liq q
2. g sill cd sp mt ilm pl ksp liq q
3. cd sp mt ilm pl ksp liq q
4. sill cd sp mt ilm pl ksp liq q
5. bi g sill cd ilm pl ksp liq q
6. bi g sill cd mt ilm pl ksp liq q
7. bi g sill mt ilm pl ksp liq q
8. bi sill cd mt ilm pl ksp q

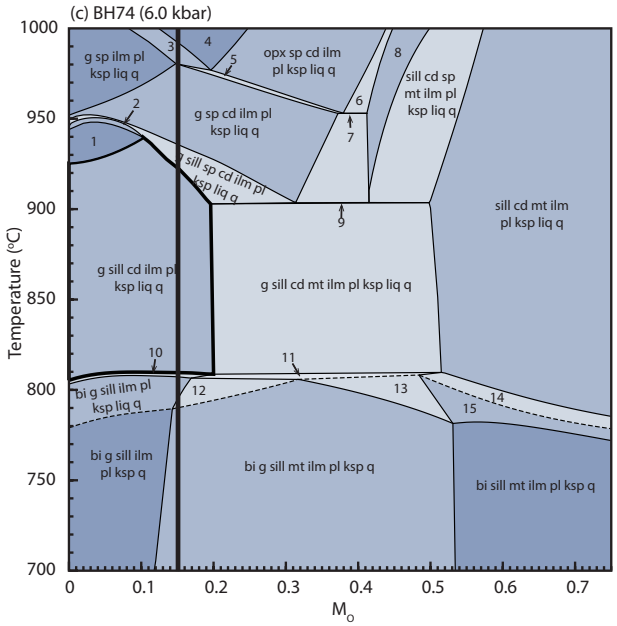

1. g sill ilm pl ksp liq q
2. g sill sp ilm pl ksp liq q
3. g opx sp ilm pl ksp liq q
4. opx sp ilm pl ksp liq q
5. g opx sp cd ilm pl ksp liq q
6. opx sp cd mt ilm pl ksp liq q
7. g opx sp cd mt ilm pl ksp liq q
8. sp cd mt ilm pl ksp liq q
9. g sill cd sp mt ilm pl ksp liq q
10. bi g sill cd ilm pl ksp liq q
11. bi g sill cd mt ilm pl ksp liq q
12. bi g sill mt ilm pl ksp liq q
13. bi g sill d mt ilm pl ksp q
14. bi sill cd mt ilm pl ksp liq q
15. bi sill cd mt ilm pl ksp q

Appendix A. (continued)
Figure 2. Pressure–M_o (M_o = Fe_2O_3/ (FeO + Fe_2O_3)) models for (a) BH54, (b) BH32, and (c) BH74. P–M_o models are shown over the compositional range M = 0 (i.e. reduced) to M = 0.75 (i.e. relatively oxidised). Models were calculated at temperatures that intersect the inferred peak mineral assemblage field on corresponding P–T models (main text). The stability field of the inferred peak mineral assemblage in each sample is outlined in bold. The bulk composition chosen for each sample intersects the inferred peak mineral assemblage field and is indicated by a bold vertical line. Mineral abbreviations after Holland and Powell (1998).

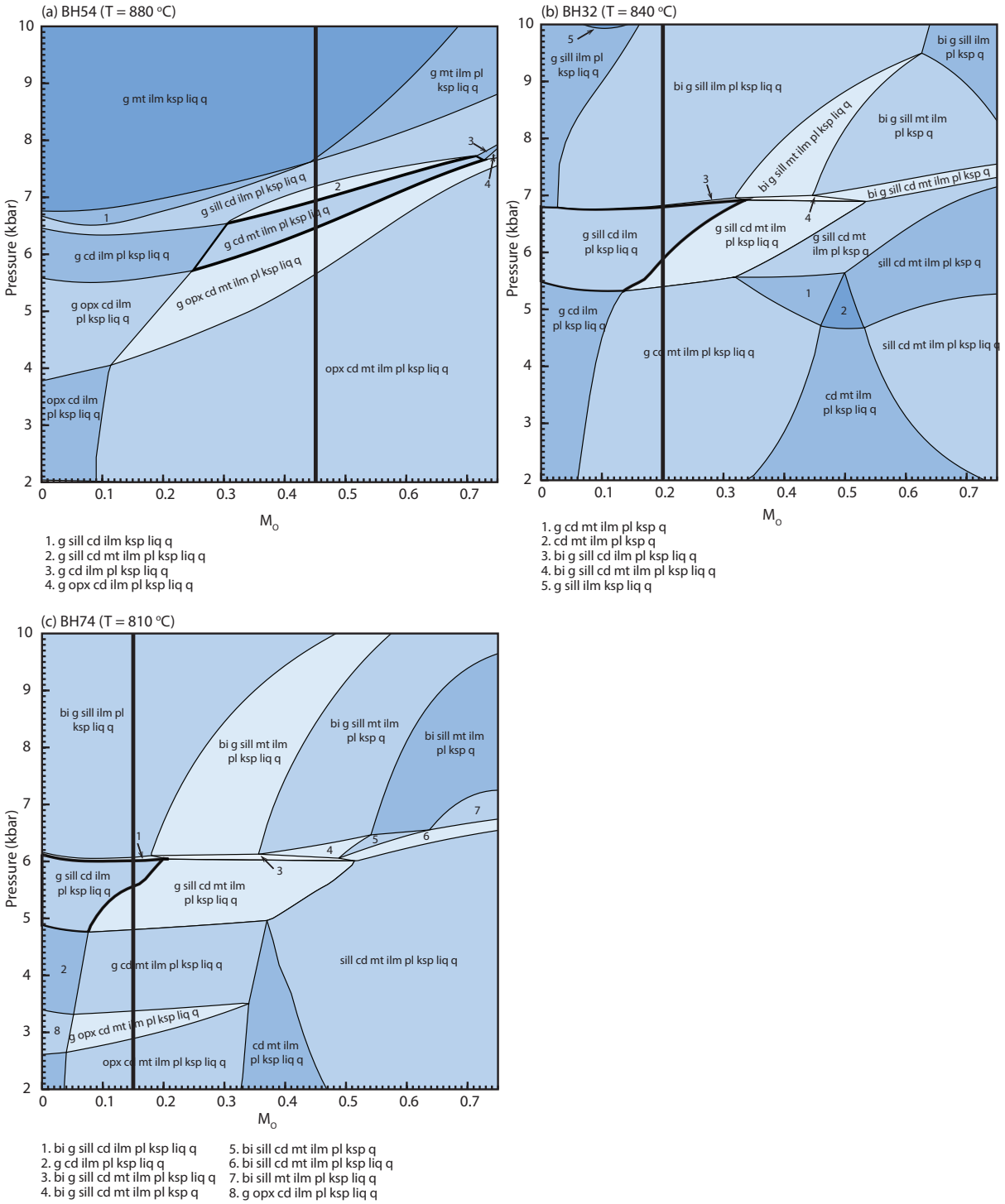

Appendix A. (continued)
Figure 3. Temperature–M_{H2O} models for (a) BH54, (b) BH32, and (c) BH74. T–M_{H2O} models are shown over the range of H_2O contents from a 'dry' composition (M = 0) to the maximum H_2O content (M = 1) as proxied by the LOI value in whole rock geochemistry. Models were calculated at pressures that intersect the inferred peak mineral assemblage field on corresponding P–T models (main text). The solidus is shown as a dashed line. The stability field of the inferred peak mineral assemblage in each sample is outlined in bold. The bulk composition chosen for each sample intersects the inferred peak mineral assemblage field and is indicated by a bold vertical line. Mineral abbreviations after Holland and Powell (1998).

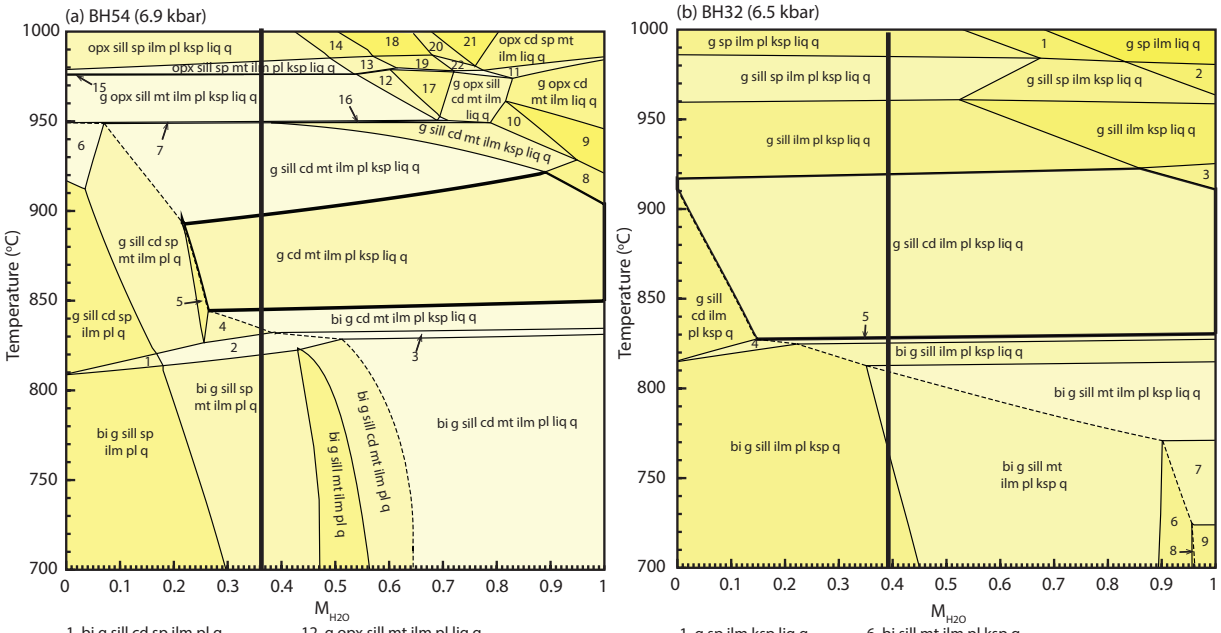

1. bi g sill cd sp ilm pl q
2. bi g sill cd sp mt ilm pl q
3. bi g sill cd mt ilm pl ksp liq q
4. bi g cd sp mt ilm pl q
5. g cd sp mt ilm pl q
6. g sill opx cd sp mt ilm pl q
7. g sill opx cd mt ilm pl ksp liq q
8. g cd mt ilm ksp liq q
9. g cd mt ilm liq q
10. g cd sill mt ilm liq q
11. g opx cd mt ilm ksp liq q
12. g opx sill mt ilm pl liq q
13. opx sill sp mt ilm pl liq q
14. opx sill sp ilm pl liq q
15. g opx sill sp mt ilm pl ksp liq q
16. g sill opx cd mt ilm ksp liq q
17. g opx sill mt ilm liq q
18. opx sill sp ilm liq q
19. opx sill sp mt ilm liq q
20. opx sill cd sp ilm liq q
21. opx cd sp ilm liq q
22. opx cd sp mt ilm liq q

1. g sp ilm ksp liq q
2. g sill sp ilm liq q
3. g sill cd ilm ksp liq q
4. bi g sill cd ilm pl ksp q
5. bi g sill cd ilm pl ksp liq q
6. bi sill mt ilm pl ksp q
7. bi sill mt ilm pl ksp liq q
8. bi sill ilm pl ksp q
9. bi sill ilm pl ksp liq q

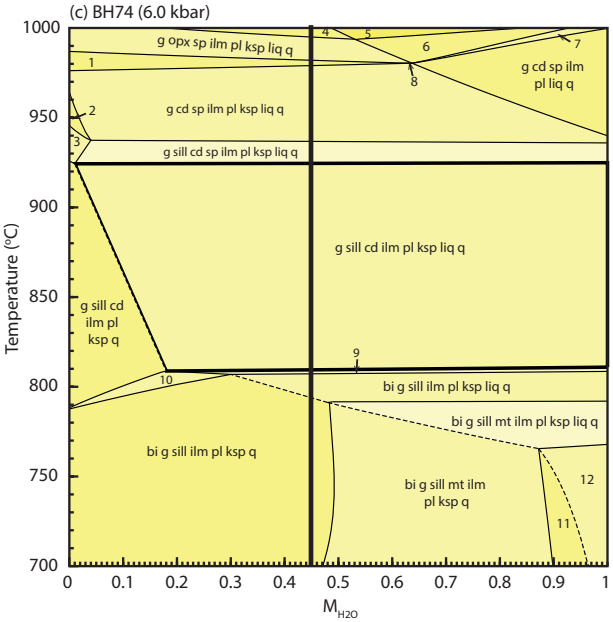

1. g sp ilm pl ksp liq q
2. g cd sp ilm pl ksp q
3. g sill cd sp ilm pl ksp q
4. opx sp ilm pl ksp liq q
5. opx sp ilm pl liq q
6. g opx sp ilm pl liq q
7. g opx cd sp ilm pl liq q
8. g cd opx sp ilm pl ksp liq q
9. bi g sill cd ilm pl ksp liq q
10. bi g sill cd ilm pl ksp q
11. bi g sill mt ilm pl q
12. bi g sill mt ilm pl liq q

Appendix A. (continued)

Figure 4. Pressure–Temperature models for BH32, BH54 and BH74. Bulk compositions are given with Figure 9 in the main text. Regions corresponding to the measured modal abundance of inferred peak minerals (left) and electron microprobe compositions (right) of garnet cores (X_{alm} & X_{gr}, light red) and cordierite (X_{Fe}, dark red) are overlain. Approximate measured modal proportions of the inferred peak metamorphic minerals for each sample are provided in the table below. Cordierite and garnet compositions are provided in Table 4 (main text). The field corresponding to the inferred peak mineral assemblage of each sample is outlined in bold (refer to main text).

	Inferred peak metamorphic minerals							
Sample	**g**	**mt**	**ilm**	**pl**	**ksp**	**q**	**cd**	**sill**
BH32	17–19%		2–3%	3–6%	28–31	22–25	7–9%	7%
BH54	16–19%	2%	4–5%	3–5%	19–22%	27%	19–22%	
BH74	14–18%		2–5%	8–12%	24%	30%	6%	6%

Approximate measured modal proportions of inferred peak metamorphic minerals (normalized to 100%).

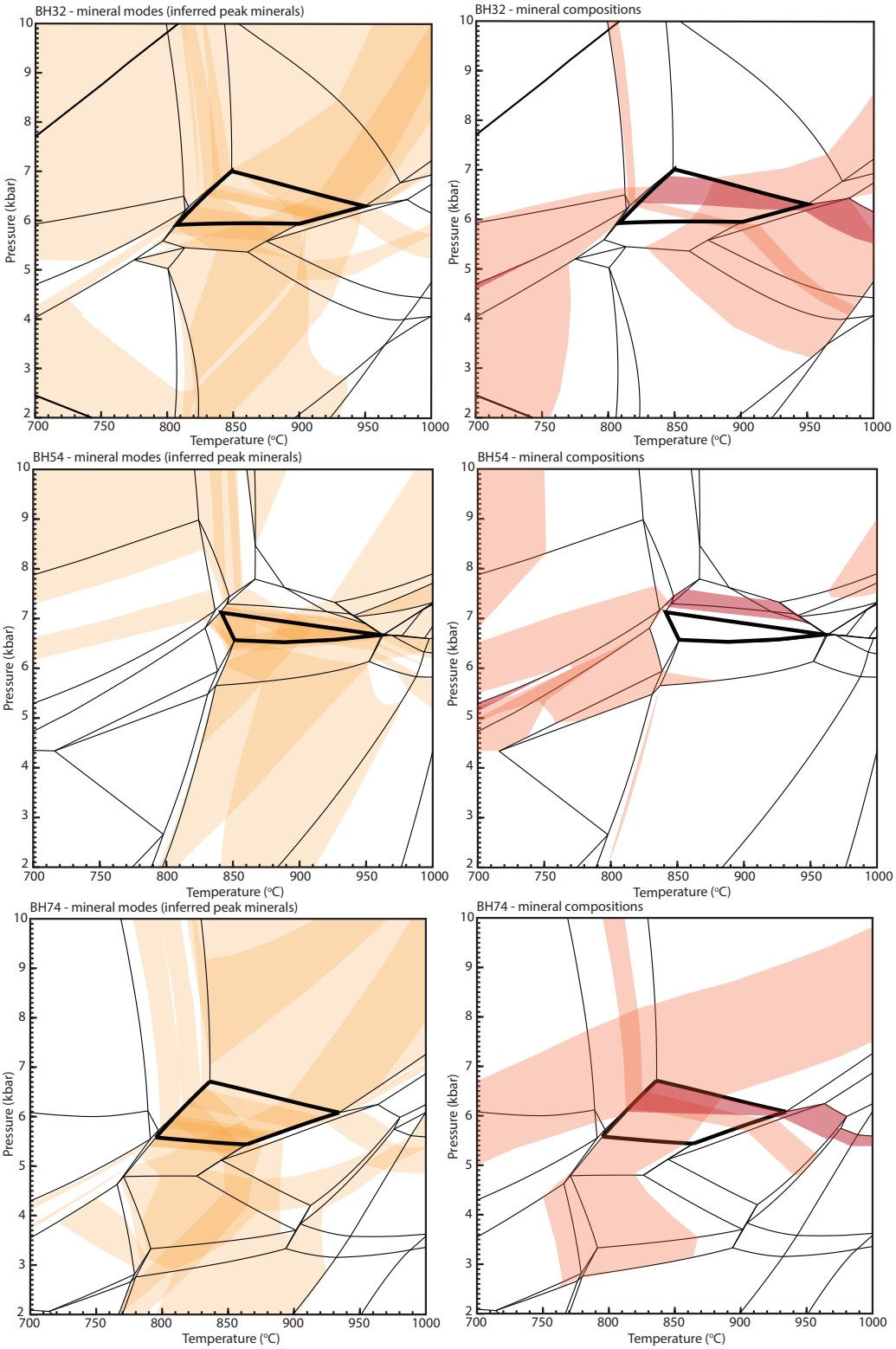

Appendix B. Representative mineral chemistry for samples used for forward phase equilibria modelling

Sample	BH32									BH54									BH74						
Mineral	bi	cd	ksp	pl	gt core	gt rim	ilm	mt	sp	bi	cd	ksp	pl	gt core	gt rim	ilm	mt	sp	cd	ksp	gt core	gt rim	sp	mt	ilm
SiO_2	37.11	48.49	65.80	61.58	38.01	37.89	0.04	0.01	0.03	36.88	49.16	65.49	65.62	38.42	38.39	0.02	0.00	0.01	48.76	64.54	38.46	38.02	0.05	0.10	0.13
TiO_2	4.12	0.01	0.02	0.00	0.02	0.00	47.28	0.00	0.04	4.54	0.00	0.04	0.04	0.00	0.02	48.76	0.14	0.00	0.01	0.05	0.03	0.03	0.00	0.01	49.19
Al_2O_3	15.43	32.56	17.86	23.77	21.32	21.07	0.03	0.22	56.71	15.25	33.10	18.05	21.98	21.74	21.29	0.05	0.25	59.40	33.39	19.69	21.63	20.74	58.08	0.26	0.10
Cr_2O_3	0.01	0.00	0.00	0.00	0.00	0.00	0.03	0.33	0.35	0.08	0.00	0.01	0.01	0.01	0.02	0.02	0.41	1.25	0.00	0.00	0.00	0.00	0.90	0.63	0.07
FeO	11.16	4.35	0.00	0.05	27.91	29.14	49.74	92.03	29.21	10.69	2.67	0.00	0.02	28.58	28.63	48.86	91.65	24.93	4.12	0.00	28.77	27.71	25.22	90.58	47.73
MnO	0.02	0.12	0.00	0.00	2.43	2.65	0.58	0.00	0.28	0.00	0.00	0.00	0.01	0.73	0.61	0.08	0.00	0.04	0.09	0.00	2.39	2.22	0.16	0.00	0.39
MgO	16.95	11.22	0.00	0.04	8.57	8.00	0.88	0.03	7.02	17.24	12.46	0.00	0.00	9.82	10.10	0.98	0.04	10.83	11.03	0.00	8.01	7.64	7.24	0.06	0.37
ZnO	0.01	0.00	0.02	0.03	0.00	0.00	0.00	0.00	3.38	0.00	0.00	0.00	0.02	0.00	0.01	0.00	0.00	2.60	0.00	0.00	0.03	0.00	7.75	0.00	0.00
CaO	0.01	0.01	0.06	5.97	0.94	0.89	0.00	0.00	0.00	0.01	0.00	0.00	2.78	0.57	0.54	0.00	0.00	0.00	0.00	0.73	1.00	1.06	0.01	0.00	0.02
Na_2O	0.09	0.04	1.35	8.49	0.01	0.00	0.00	0.02	0.13	0.03	0.01	0.79	10.26	0.00	0.00	0.00	0.02	0.10	0.04	2.54	0.00	0.39	0.02	0.05	0.03
K_2O	9.46	0.01	14.30	0.08	0.00	0.00	0.00	0.00	0.00	9.56	0.00	14.84	0.11	0.00	0.00	0.00	0.00	0.00	0.00	12.82	0.00	0.02	0.00	0.01	0.00
Cl	0.09	0.00	0.00	0.00	0.01	0.01	0.00	0.00	0.00	0.15	0.00	0.01	0.00	0.00	0.00	0.00	0.00	0.00	0.00	0.00	0.00	0.05	0.00	0.00	0.01
F	1.17	0.00	0.00	0.00	0.00	0.01	0.19	0.35	0.02	1.39	0.00	0.00	0.00	0.00	0.00	0.15	0.30	0.00	0.00	0.00	0.02	0.06	0.00	0.27	0.15
Total	95.12	96.81	99.41	100.00	99.22	99.66	98.68	92.83	97.15	95.19	97.41	99.22	100.86	99.88	99.62	98.86	92.69	99.15	97.43	100.37	100.32	97.93	99.43	91.86	98.12
No. Oxygens	11	18	8	8	12	12	3	4	4	11	18	8	8	12	12	3	4	4	18	8	12	12	4	4	3
Si	2.71	4.99	3.03	2.74	2.97	2.97	0.00	0.00	0.00	2.69	4.98	3.03	2.87	2.96	2.96	0.00	0.00	0.00	4.97	2.94	2.98	3.02	0.00	0.00	0.00
Ti	0.23	0.00	0.00	0.00	0.00	0.00	0.90	0.00	0.00	0.25	0.00	0.00	0.00	0.00	0.00	0.93	0.00	0.00	0.00	0.00	0.00	0.00	0.00	0.00	0.95
Al	1.33	3.95	0.97	1.25	1.96	1.94	0.00	0.01	1.91	1.31	3.95	0.98	1.13	1.97	1.94	0.00	0.01	1.91	4.01	1.06	1.98	1.94	1.92	0.01	0.00
Cr	0.00	0.00	0.00	0.00	0.00	0.00	0.00	0.01	0.01	0.00	0.00	0.00	0.00	0.00	0.00	0.00	0.01	0.03	0.00	0.00	0.00	0.00	0.02	0.02	0.00
Fe^{3+}					0.09	0.12	0.18	1.94	0.09					0.10	0.13	0.13	1.93	0.07			0.05	0.06	0.06	1.93	0.09
Fe^{2+}	0.68	0.37	0.00	0.00	1.73	1.78	0.87	1.04	0.61	0.65	0.23	0.00	0.00	1.74	1.72	0.90	1.03	0.50	0.35	0.00	1.82	1.77	0.53	1.03	0.94
Mn^{2+}	0.00	0.01	0.00	0.00	0.16	0.18	0.01	0.00	0.01	0.00	0.00	0.00	0.00	0.05	0.04	0.00	0.00	0.00	0.01	0.00	0.16	0.15	0.00	0.00	0.01
Mg	1.85	1.72	0.00	0.00	1.00	0.93	0.03	0.00	0.30	1.88	1.88	0.00	0.00	1.13	1.16	0.04	0.00	0.44	1.68	0.00	0.93	0.90	0.30	0.00	0.01
Zn	0.00	0.00	0.00	0.00	0.00	0.00	0.00	0.00	0.07	0.00	0.00	0.00	0.00	0.00	0.00	0.00	0.00	0.05	0.00	0.00	0.00	0.00	0.16	0.00	0.00
Ca	0.00	0.00	0.00	0.28	0.08	0.07	0.00	0.00	0.00	0.00	0.00	0.00	0.13	0.05	0.04	0.00	0.00	0.00	0.00	0.04	0.08	0.09	0.00	0.00	0.00
Na	0.01	0.01	0.12	0.73	0.00	0.00	0.00	0.00	0.01	0.00	0.00	0.07	0.87	0.00	0.00	0.00	0.00	0.01	0.01	0.22	0.00	0.06	0.00	0.00	0.00
K	0.88	0.00	0.84	0.00	0.00	0.00	0.00	0.00	0.00	0.89	0.00	0.87	0.01	0.00	0.00	0.00	0.00	0.00	0.00	0.75	0.00	0.00	0.00	0.00	0.00
Cl	0.01	0.00	0.00	0.00	0.00	0.00	0.00	0.00	0.00	0.02	0.00	0.00	0.00	0.00	0.00	0.00	0.00	0.00	0.00	0.00	0.00	0.01	0.00	0.00	0.00
F	0.27	0.00	0.00	0.00	0.00	0.00	0.02	0.04	0.00	0.32	0.00	0.00	0.00	0.00	0.00	0.01	0.04	0.00	0.00	0.00	0.00	0.01	0.00	0.03	0.01
Cations	8	11	5	5	8	8	2	3	3	8	11	5	5	8	8	2	3	3	11	5	8	8	3	3	2

Appendix C. Zircon LASS–ICP–MS U–Pb geochronology

Analysis	Internal morphology	^{238}U (ppm)	^{232}Th (ppm)	^{232}Th/^{238}U	^{207}Pb/^{235}U	2σ	^{206}Pb/^{238}U	2σ	^{207}Pb/^{206}Pb	2σ	Rho	Age (Ma) ^{207}Pb/^{235}U	2σ	^{206}Pb/^{238}U	2σ	^{207}Pb/^{206}Pb	2σ	Conc. (%)**
Sample BH32																		
BH32-01	Rim (weakly-luminescent)	249	73.34	0.302114804	2.333	0.029	0.2112	0.0026	0.08013	0.00046	0.89237	1222	9	1235	14	1200	11	103
BH32-02	Core (dark, weak internal features)	418	269	0.633312223	2.311	0.015	0.21165	0.001	0.07927	0.00036	0.71458	1216	5	1238	5	1179	9	105
BH32-03	Core (dark, weak internal features)	313.5	108.9	0.357653791	2.388	0.019	0.2172	0.0014	0.07982	0.0004	0.77742	1239	6	1267	8	1192	10	106
BH32-10	Core (dark, weak internal features)	188.7	156.2	0.838926174	2.331	0.03	0.2058	0.0018	0.08216	0.00074	0.71520	1222	9	1207	10	1249	18	97
BH32-12	Rim (weakly-luminescent)	211.5	114.2	0.554323725	2.368	0.025	0.2148	0.0017	0.07992	0.00048	0.82595	1233	8	1254	9	1195	12	105
BH32-16	Overgrowth (dark)	650	14.59	0.022522523	2.226	0.019	0.2035	0.0017	0.07932	0.00029	0.90650	1189	6	1194	9	1180	7	101
BH32-17	Rim (strongly-luminescent)	84.3	142.5	1.738223536	2.357	0.034	0.2086	0.0026	0.08192	0.00096	0.62879	1229	10	1222	14	1243	23	98
BH32-19	Rim (weakly-luminescent)	74.9	110.9	1.523925632	2.333	0.041	0.2061	0.0025	0.08206	0.00082	0.83530	1222	13	1208	13	1247	20	97
BH32-22	Rim (weakly-luminescent)	115.8	129.5	1.152073733	2.301	0.027	0.2039	0.0016	0.08179	0.00067	0.71765	1212	8	1196	9	1240	16	96
BH32-24	Core (dark, weak internal features)	406	164.8	0.418060201	2.33	0.028	0.2083	0.0022	0.08111	0.00036	0.93074	1221	9	1220	12	1224	9	100
BH32-26	Core (dark, weak internal features)	461	124.7	0.278086763	2.649	0.027	0.2254	0.0021	0.08518	0.00033	0.92501	1314	8	1310	11	1321	8	99
BH32-28	Core (weakly-luminescent)	152.9	165	1.109877913	2.211	0.019	0.2013	0.0012	0.07969	0.00052	0.65203	1184	6	1182	6	1189	13	99
BH32-33	Rim (strongly-luminescent)	93.2	163.5	1.814882033	2.457	0.036	0.2175	0.002	0.08194	0.00077	0.78279	1259	10	1268	10	1243	18	102
BH32-37	Core (weakly-luminescent)	114.9	119.6	1.069518717	2.258	0.022	0.2038	0.0018	0.08037	0.00055	0.73271	1199	7	1195	10	1206	13	99
BH32-41	Rim (weakly-luminescent)	103.5	141.3	1.405876564	2.405	0.036	0.2146	0.0021	0.08129	0.00069	0.845770	1244	11	1253	11	1228	17	102
BH32-45	Overgrowth (dark)	427	30.9	0.073746313	2.695	0.025	0.2474	0.0018	0.07892	0.00035	0.88395	1327	7	1425	9	1170	9	122
BH32-47	Core (weakly-luminescent)	156.2	181.8	1.199040767	2.27	0.03	0.2037	0.0019	0.08068	0.00058	0.85171	1203	9	1195	10	1213	14	98
BH32-48	Core (weakly-luminescent)	132.2	138.9	1.076426265	2.244	0.022	0.2014	0.0017	0.08069	0.00045	0.82331	1195	7	1183	9	1214	11	97
BH32-51	Overgrowth (dark)	526	123.3	0.240384615	2.242	0.029	0.2032	0.0025	0.07997	0.00048	0.88806	1194	9	1192	13	1196	12	100
BH32-55	Core (dark, weak internal features)	278	112.7	0.418235048	2.284	0.019	0.2066	0.0016	0.08013	0.0003	0.89377	1207	6	1210	9	1200	7	101
BH32-56	Core (dark, weak internal features)	284.3	202.8	0.732600733	2.343	0.024	0.2108	0.0021	0.08086	0.00038	0.89217	1225	7	1233	11	1218	9	101
BH32-60	Core (dark, weak internal features)	380.7	234.4	0.632111252	2.392	0.041	0.2111	0.0034	0.08216	0.00058	0.91168	1240	12	1235	18	1249	14	99
BH32-62	Rim (weakly-luminescent)	193.4	75.8	0.4	3.252	0.048	0.2567	0.0029	0.09153	0.00044	0.96667	1469	11	1473	15	1458	9	101
BH32-71	Overgrowth (dark)	1541	35.8	0.021978022	2.669	0.032	0.2345	0.0023	0.08265	0.00027	0.97486	1320	9	1358	12	1261	6	108
Sample BH54																		
BH54-01	Core (dark, weak internal features)	63.41	176.3	2.817695125	2.363	0.055	0.2098	0.0029	0.0814	0.0015	0.61114	1231	17	1227	15	1229	36	100
BH54-24	Rim (weakly-luminescent)	229	35.49	0.157480315	2.686	0.049	0.23781	0.0023	0.08198	0.0012	0.60099	1325	14	1375	12	1245	29	110
BH54-28	Rim (weakly-luminescent)	131.6	6.7	0.0456621	2.49	0.047	0.2173	0.0024	0.08325	0.0012	0.64875	1269	14	1268	13	1275	29	99
BH54-35	Rim (weakly-luminescent)	231.7	144.9	0.636537237	2.403	0.051	0.2163	0.0031	0.08073	0.0012	0.71487	1243	15	1262	16	1214	29	104
BH54-37	Rim (weakly-luminescent)	200.9	80.5	0.396825397	2.678	0.053	0.2372	0.003	0.08215	0.0012	0.67570	1322	15	1372	16	1249	29	110
BH54-44	Overgrowth (dark)	262.4	128.4	0.498007968	2.315	0.055	0.2098	0.0037	0.08008	0.0012	0.77676	1216	17	1227	19	1199	29	102
BH54-49	Rim (weakly-luminescent)	155.1	241.2	1.584032948	2.531	0.052	0.23	0.0035	0.07995	0.0011	0.74266	1281	15	1334	18	1196	28	112
BH54-66	Overgrowth (dark)	313.1	70.3	0.228832952	2.312	0.052	0.205	0.0037	0.08211	0.0012	0.76124	1216	16	1202	20	1248	29	96
BH54-67	Overgrowth (dark)	336.5	95	0.288101412	2.43	0.063	0.2131	0.0045	0.08292	0.0012	0.82985	1251	19	1245	24	1267	27	98
BH54-76	Overgrowth (dark)	250.8	192.1	0.769822941	2.782	0.058	0.2359	0.0036	0.08567	0.0012	0.74073	1350	16	1365	19	1331	27	103

Appendix C. Zircon geochronology (continued)

Analysis	Internal morphology	^{238}U (ppm)	^{232}Th (ppm)	^{232}Th/^{238}U	^{207}Pb/^{235}U	2σ	^{206}Pb/^{238}U	2σ	^{207}Pb/^{206}Pb	2σ	Rho	Age (Ma) ^{207}Pb/^{235}U	2σ	^{206}Pb/^{238}U	2σ	^{207}Pb/^{206}Pb	2σ	Conc. (%)**
Sample BH74																		
BH74-01	Core (dark, weak internal features)	523	20.49	0.03917782	2.396	0.06	0.2107	0.0019	0.0825	0.00072	0.88055	1241	18	1232	10	1257	17	98
BH74-02	Rim (strongly-luminescent)	115.5	109.1	0.944588745	2.367	0.06	0.2107	0.0021	0.0813	0.00086	0.65641	1233	18	1232	11	1228	21	100
BH74-03	Rim (strongly-luminescent)	69.3	188.6	2.721500722	2.295	0.062	0.2045	0.0021	0.08106	0.00099	0.69915	1210	19	1199	11	1222	24	98
BH74-05	Core (dark, weak internal features)	414	13.68	0.033043478	2.89	0.072	0.2342	0.0022	0.08895	0.00077	0.86918	1379	19	1357	11	1403	16	97
BH74-06	Rim (weakly-luminescent)	265.6	84.5	0.31814759	2.381	0.06	0.2137	0.0019	0.08057	0.0007	0.85378	1237	18	1249	10	1211	17	103
BH74-07	Core (dark, weak internal features)	151.8	158	1.040843215	2.422	0.06	0.208	0.0017	0.08406	0.00086	0.43027	1249	18	1218	9	1294	20	94
BH74-08	Core (dark, weak internal features)	494	34.07	0.068967611	2.396	0.06	0.2113	0.0019	0.08187	0.00068	0.91345	1241	18	1236	10	1242	16	99
BH74-09	Rim (weakly-luminescent)	152.5	143.2	0.939016393	2.255	0.056	0.2033	0.0018	0.08021	0.00082	0.57547	1198	18	1193	10	1202	20	99
BH74-15	Rim (weakly-luminescent)	125.8	164.6	1.308426073	2.387	0.065	0.2152	0.0026	0.08027	0.00081	0.85857	1238	20	1256	14	1203	20	104
BH74-19	Core (dark, weak internal features)	548	20.44	0.03729927	2.247	0.059	0.2042	0.0026	0.0797	0.00067	0.96473	1196	19	1198	14	1190	16	101
BH74-20	Rim (weakly-luminescent)	143.3	203.7	1.421493371	2.484	0.068	0.2224	0.0033	0.08117	0.00079	0.89664	1267	20	1294	17	1225	19	106
BH74-21	Overgrowth (dark)	1090	82.2	0.075412844	2.363	0.06	0.2161	0.0022	0.0793	0.00065	0.96123	1231	18	1261	12	1180	16	107
BH74-25	Core (dark, weak internal features)	431	17.06	0.039582367	2.783	0.085	0.2291	0.0043	0.08822	0.00079	0.98176	1350	23	1329	23	1387	17	96
BH74-26	Rim (strongly-luminescent)	262.2	158.2	0.603356217	2.464	0.064	0.2243	0.0026	0.07961	0.00071	0.90836	1261	19	1304	14	1187	18	110
BH74-28	Core (dark, weak internal features)	267.3	35.11	0.131350542	2.407	0.067	0.2132	0.0032	0.08182	0.00077	0.93488	1244	20	1246	17	1241	18	100
BH74-31	Rim (weakly-luminescent)	170.5	119.6	0.701466276	2.369	0.066	0.2113	0.0031	0.08124	0.00077	0.93043	1233	20	1235	16	1227	19	101
BH74-32	Rim (weakly-luminescent)	187.6	181.3	0.96641791	2.458	0.064	0.2229	0.0021	0.07983	0.00077	0.97012	1260	19	1297	11	1192	19	109
BH74-34	Rim (weakly-luminescent)	137.4	135.1	0.983260553	2.304	0.06	0.207	0.0025	0.08076	0.00086	0.77865	1213	18	1213	14	1215	21	100
BH74-35	Rim (weakly-luminescent)	206.8	117.8	0.569632495	2.269	0.062	0.2055	0.0029	0.08012	0.00079	0.8968	1202	19	1204	16	1200	20	100
BH74-36	Core (dark, weak internal features)	394.6	19.95	0.050557527	2.377	0.061	0.2115	0.0023	0.0816	0.00069	0.93976	1235	18	1237	12	1236	17	100
BH74-37	Core (dark, weak internal features)	948	33.8	0.035654008	2.302	0.062	0.2068	0.003	0.08081	0.00068	0.962	1213	19	1212	16	1217	17	100
BH74-38	Rim (strongly-luminescent)	278.7	127.3	0.456763545	2.415	0.065	0.2155	0.0029	0.08142	0.00079	0.88796	1247	19	1258	15	1231	19	102
BH74-39	Rim (weakly-luminescent)	369	85.7	0.232249322	2.267	0.059	0.2056	0.0024	0.08017	0.00073	0.91587	1202	19	1205	13	1201	18	100
BH74-41	Core (dark, weak internal features)	572	14.55	0.025437063	2.383	0.064	0.2126	0.003	0.0817	0.00067	0.92464	1237	19	1242	16	1238	16	100
BH74-43	Rim (weakly-luminescent)	146.4	157.8	1.077868852	2.351	0.074	0.2123	0.004	0.08081	0.00096	0.89932	1227	22	1241	21	1216	24	102
BH74-44	Rim (weakly-luminescent)	371.6	22.1	0.059472551	2.548	0.067	0.2288	0.0027	0.08118	0.0007	0.93988	1286	19	1328	14	1226	17	108
BH74-47	Rim (strongly-luminescent)	144.1	153.8	1.067314365	2.433	0.064	0.2191	0.0024	0.08096	0.00079	0.86088	1252	19	1277	13	1220	19	105
BH74-48	Rim (weakly-luminescent)	141.1	174.3	1.235294118	2.488	0.067	0.225	0.0029	0.08051	0.00079	0.87636	1268	19	1308	15	1209	19	108
BH74-49	Rim (weakly-luminescent)	188.9	128.6	0.680783483	2.259	0.06	0.2051	0.0023	0.08021	0.00081	0.80407	1199	19	1203	12	1202	20	100
BH74-51	Rim (weakly-luminescent)	109.1	148.2	1.358386801	2.555	0.069	0.2225	0.0028	0.08353	0.00093	0.76453	1288	20	1295	15	1281	22	101
BH74-54	Rim (weakly-luminescent)	148.2	154.3	1.041160594	2.403	0.064	0.2159	0.0024	0.08088	0.00085	0.82105	1243	19	1260	13	1218	21	103
BH74-57	Rim (weakly-luminescent)	180.3	105.9	0.587354409	2.21	0.064	0.2021	0.0035	0.0792	0.00076	0.93366	1184	20	1186	19	1177	19	101
BH74-59	Rim (weakly-luminescent)	154.9	82.6	0.533247256	2.32	0.06	0.2083	0.0024	0.08083	0.00084	0.80077	1220	20	1220	13	1217	21	100
BH74-61	Core (dark, weak internal features)	585	24.41	0.041726496	2.396	0.063	0.2126	0.0026	0.0815	0.00069	0.9595	1241	19	1242	14	1234	17	101
BH74-63	Core (dark, weak internal features)	613	23.48	0.038303426	2.352	0.062	0.2104	0.0028	0.08085	0.00067	0.96794	1228	19	1231	15	1218	16	101
BH74-65	Rim (weakly-luminescent)	152.9	167.2	1.09352518	2.284	0.062	0.2034	0.0026	0.0812	0.00079	0.89054	1207	19	1193	14	1226	19	97
BH74-67	Overgrowth (dark)	1771	16.29	0.009198193	2.234	0.075	0.2016	0.0047	0.08016	0.0007	0.98256	1191	23	1184	25	1201	17	99
BH74-68	Rim (weakly-luminescent)	166.8	137	0.821342926	2.282	0.063	0.2073	0.003	0.07973	0.00076	0.91974	1206	20	1214	16	1190	19	102
BH74-69	Rim (dark, weak internal features)	276.7	47.91	0.173147814	2.403	0.066	0.2182	0.003	0.07969	0.00071	0.94885	1243	20	1272	16	1189	18	107
BH74-70	Rim (strongly-luminescent)	136.1	217	1.594415871	2.498	0.069	0.2221	0.003	0.08145	0.00085	0.87361	1271	20	1293	16	1232	21	105

Appendix C. Zircon geochronology (continued)

Analysis	Internal morphology	^{238}U (ppm)	^{232}Th (ppm)	^{232}Th/^{238}U	^{207}Pb/^{235}U	2σ	^{206}Pb/^{238}U	2σ	^{207}Pb/^{206}Pb	2σ	Rho	Age (Ma) ^{207}Pb/^{235}U	2σ	^{206}Pb/^{238}U	2σ	^{207}Pb/^{206}Pb	2σ	Conc. (%)**
BH74-71	Core (dark, weak internal features)	658.3	6.72	0.010208112	2.378	0.065	0.2108	0.0031	0.08195	0.00071	0.95655	1236	20	1233	16	1244	17	99
BH74-72	Rim (strongly-luminescent)	352.1	50	0.142005112	3.049	0.085	0.2453	0.0033	0.09016	0.00078	0.96596	1419	21	1414	17	1429	17	99
BH74-73	Core (dark, weak internal features)	192.7	122.4	0.635184224	2.233	0.062	0.2032	0.0026	0.07971	0.0008	0.89119	1191	19	1193	14	1189	20	100
BH74-75	Core (dark, weak internal features)	361.4	30	0.083010515	2.478	0.068	0.2175	0.0031	0.08295	0.00077	0.92947	1265	20	1269	17	1268	18	100
BH74-76	Rim (weakly-luminescent)	141.1	126.1	0.893692417	2.552	0.076	0.2208	0.0038	0.0841	0.00083	0.94128	1286	22	1286	20	1294	19	99
BH74-77	Core (dark, weak internal features)	593	30	0.050590219	2.423	0.07	0.2159	0.0035	0.08146	0.0007	0.97529	1249	21	1260	19	1232	17	102
BH74-78	Rim (weakly-luminescent)	179.7	129.2	0.718976071	2.457	0.063	0.2234	0.0027	0.07991	0.00076	0.84861	1259	19	1300	14	1194	19	109
BH74-79	Rim (weakly-luminescent)	191.3	133.6	0.698379509	2.534	0.067	0.2296	0.0024	0.08026	0.00075	0.90657	1282	19	1332	13	1203	18	111
BH74-80	Rim (weakly-luminescent)	172	167.6	0.974418605	2.322	0.064	0.2113	0.0029	0.07988	0.00077	0.90777	1219	20	1236	15	1194	19	104
BH74-81	Overgrowth (dark)	1077	34.7	0.032219127	2.401	0.064	0.2191	0.003	0.07953	0.00065	0.97643	1243	19	1277	16	1185	16	108
BH74-82	Rim (weakly-luminescent)	160.5	156.9	0.977570093	2.259	0.067	0.2044	0.0034	0.07993	0.001	0.80737	1199	21	1199	18	1195	25	100
BH74-83	Core (dark, weak internal features)	309	21.34	0.069061489	2.296	0.061	0.2072	0.0026	0.08034	0.00074	0.92472	1211	19	1214	14	1205	18	101
BH74-84	Rim (weakly-luminescent)	130.9	142.9	1.091673033	2.403	0.061	0.2152	0.0025	0.08064	0.00084	0.98575	1243	18	1257	13	1212	21	104
BH74-86	Rim (weakly-luminescent)	133.2	198.5	1.49024024	2.432	0.07	0.2191	0.0035	0.08017	0.0009	0.88599	1252	21	1277	19	1201	22	106
BH74-87	Rim (weakly-luminescent)	162.8	121.4	0.745700246	2.239	0.06	0.2042	0.0026	0.07936	0.0007	0.94337	1193	19	1198	14	1181	17	101
BH74-89	Rim (strongly-luminescent)	533.2	17.93	0.033627157	2.203	0.06	0.1995	0.0028	0.07973	0.00067	0.96764	1182	19	1172	15	1190	17	98
BH74-90	Core (dark, weak internal features)	109.9	116.8	1.062784349	2.384	0.063	0.2124	0.0029	0.08101	0.00076	0.91204	1238	19	1241	16	1221	18	102

**Concordance value calculated by (^{206}Pb/^{238}U Age)/(^{207}Pb/^{206}Pb Age) x 100.

Analyses denoted in blue text in the table occur outside 2σ uncertainty of concordia.

Appendix C. Zircon trace element analyses

	Element concentration (ppm)																																	
Analysis	Ti	2σ	Y	2σ	Nb	2σ	La	2σ	Ce	2σ	Pr	2σ	Nd	2σ	Sm	2σ	Eu	2σ	Gd	2σ	Tb	2σ	Dy	2σ	Ho	2σ	Er	2σ	Tm	2σ	Yb	2σ	Lu	2σ	Hf	2σ
Sample BH32																																				
BH32-01	10.2	5.4	155	11	1.73	0.49	b.d.l.		19.7	1.5	0.12	0.09	2.4	1.5	5.3	1.5	0.45	0.29	18.5	3.4	3.0	0.5	23.1	3.2	4.9	0.7	13.0	1.6	1.8	0.3	12.5	2.1	1.8	0.4	12110	800
BH32-02	13.2	2.8	725	94	3.53	0.37	b.d.l.		15.9	2.6	0.14	0.08	3.08	0.96	11.6	2.4	0.48	0.12	54.5	9.7	13.3	2.2	100.0	15.0	22.0	2.7	58.2	7.8	7.9	1.1	56.7	7.3	8.2	0.8	12610	910
BH32-03	8.8	3.3	160	10	5.21	0.59	b.d.l.		11.1	0.9	0.04	0.05	1.01	0.6	2.11	0.69	0.08	0.08	7.6	1.4	2.0	0.4	19.1	1.2	4.7	0.6	18.4	1.3	3.2	0.7	29.5	2.3	4.5	0.4	12920	640
BH32-10	12.1	5.7	191	12	1.3	0.74	b.d.l.		18.6	1.5	0.11	0.06	2.7	1	9.6	2.5	0.72	0.32	29.1	3.4	4.4	0.8	30.6	3.6	5.9	1.1	21.2	4.6	2.3	1.1	27.0	11.0	4.6	2.6	12350	740
BH32-12	13.7	3.0	177	12	1.71	0.64	b.d.l.		19.6	1.4	0.29	0.43	2.22	0.68	6.3	1.4	0.50	0.11	19.1	2.5	4.3	0.7	26.8	2.4	5.5	0.5	18.0	2.1	2.3	0.4	19.8	2.8	3.2	0.9	13850	890
BH32-16	8.1	3.2	262	12	1.96	0.35	b.d.l.		17.2	1.5	0.03	0.03	1.65	0.44	5.66	0.79	0.32	0.11	26.7	4.5	5.5	0.7	38.0	4.6	7.7	1.4	20.7	3.6	2.6	0.6	21.5	3.5	2.8	0.8	11800	2000
BH32-17	15.4	7.1	127	19	0.71	0.63	b.d.l.		20.8	3.5	0.10	0.03	3.3	2	5.6	2.2	0.23	0.38	18.6	2.5	2.9	0.5	19.0	3.8	3.7	0.8	11.6	3.0	1.2	0.4	11.9	2.9	1.5	0.9	12000	1100
BH32-19	10.9	6.5	153	14	1.17	0.28	b.d.l.		19.3	1.3	0.06	0.03	1.96	0.68	8.2	1.9	0.27	0.18	19.9	4.2	3.1	1.0	23.1	4.5	4.5	1.2	11.4	2.1	1.7	0.5	11.2	0.8	1.8	0.2	13100	1400
BH32-22	11.0	2.6	126	9	1.24	0.87	b.d.l.		17.9	2.4	0.06	0.04	1.73	0.5	6.5	1.5	0.20	0.19	17.7	1.7	3.2	0.7	17.9	2.5	3.9	0.9	10.6	1.7	1.7	0.3	12.0	1.8	1.8	0.5	12700	710
BH32-24	6.7	2.3	633	37	3.69	0.74	b.d.l.		14.3	1.7	0.06	0.03	1.45	0.85	6	1.4	0.25	0.14	37.7	4.7	10.8	1.5	86.8	8.1	22.6	1.6	62.2	6.3	10.9	1.8	88.0	14.0	18.9	5.0	13150	710
BH32-26	10.6	3.1	1143	87	3.69	0.69	b.d.l.		12.1	1.4	b.d.l.		2.23	0.5	6.2	1.2	0.45	0.14	33.5	4.6	11.1	1.4	119.0	11.0	40.9	3.4	155.4	9.7	40.0	4.5	367.0	37.0	81.6	7.3	13050	660
BH32-28	10.4	5.0	137	10	1.36	0.36	b.d.l.		18.0	1.2	0.15	0.04	2.63	0.67	10.1	1.9	0.65	0.21	28.3	3.8	4.4	0.5	23.0	2.9	3.7	0.3	8.8	1.2	1.6	0.3	9.3	1.2	1.2	0.3	12180	750
BH32-33	12.4	4.6	126	9	1.32	0.28	b.d.l.		22.6	1.6	0.19	0.08	2.42	0.68	6.4	1.5	0.43	0.14	17.3	2.3	3.1	0.6	20.9	2.0	4.5	0.7	10.2	2.2	1.5	0.5	8.8	1.2	1.3	0.3	12130	910
BH32-37	8.0	4.3	96	7	1.13	0.23	b.d.l.		16.8	1.5	0.15	0.06	2.21	0.49	6.1	1.1	0.23	0.08	16.6	2.6	2.3	0.5	12.9	3.2	2.9	0.4	8.4	1.8	1.2	0.4	8.1	1.6	1.2	0.3	11810	600
BH32-41	12.8	2.9	169	12	1.35	0.36	b.d.l.		23.1	2.7	0.07	0.04	2.8	1	6	1.6	0.57	0.24	18.6	3.9	3.5	0.6	26.2	3.2	5.6	0.7	13.7	2.8	1.8	0.5	16.7	2.3	2.9	0.8	13190	650
BH32-45	23.0	15.0	490	30	1.47	0.34	b.d.l.		14.1	1.4	0.16	0.08	1.11	0.46	4.4	1.1	0.59	0.26	29.3	3.3	7.3	0.8	59.0	4.7	16.6	1.3	54.0	6.0	8.2	1.0	56.3	5.6	12.6	0.9	12740	690
BH32-47	9.4	2.5	229	18	1.38	0.29	b.d.l.		23.6	2.1	0.09	0.05	2.73	0.57	8.8	1.6	0.58	0.16	28.9	4.1	5.1	0.5	37.1	4.8	8.7	0.8	22.0	2.3	2.8	0.4	23.5	2.4	3.5	0.6	12010	690
BH32-48	8.1	3.3	126	17	1.19	0.48	b.d.l.		20.3	1.1	0.09	0.05	1.78	0.53	7.5	1.6	0.57	0.28	24.8	2.1	3.9	0.3	21.9	3.2	4.3	0.9	12.3	2.7	1.2	0.2	10.7	2.6	1.9	0.6	12020	780
BH32-51	9.4	5.4	327	22	1.55	0.65	b.d.l.		23.2	3.1	0.12	0.06	1.9	1	9.4	1.4	0.69	0.28	34.3	8.0	7.2	1.0	47.1	4.3	11.9	0.9	37.3	4.3	5.8	1.2	49.3	4.7	10.1	0.8	12900	1400
BH32-55	6.7	3.1	387	35	2.47	0.59	b.d.l.		13.0	1.4	0.06	0.03	1.04	0.42	5.9	1.4	0.29	0.10	27.0	3.9	6.7	0.6	55.4	6.8	13.6	1.5	35.7	6.2	5.0	1.1	38.5	7.4	6.2	2.0	12300	1200
BH32-56	8.3	3.4	451	17	2.97	0.64	b.d.l.		14.5	1.8	0.10	0.04	1.53	0.53	8.5	1.9	0.34	0.15	36.3	5.0	10.0	1.1	63.9	6.7	13.6	1.3	35.3	5.3	4.4	0.9	29.4	4.9	4.0	0.5	11860	540
BH32-60	11.7	2.8	3060	360	9.49	0.66	b.d.l.		19.7	1.0	0.12	0.07	2.06	0.9	7.56	0.7	0.69	0.23	48.9	6.2	21.3	3.9	279.0	12.0	111.0	13.0	426.0	25.0	81.4	4.5	681.0	82.0	113.0	14.0	10900	1000
BH32-62	8.8	3.0	366	28	1.88	0.74	b.d.l.		14.4	1.2	0.07	0.05	1.45	0.4	3.4	1.1	0.19	0.12	9.5	2.3	2.4	0.5	28.2	3.6	11.9	1.4	59.3	5.5	16.2	1.6	172.0	14.0	40.6	3.5	12330	950
BH32-71	5.7	1.9	1055	55	3.05	0.57	b.d.l.		18.1	1.1	0.08	0.04	1.36	0.49	8.1	1.2	0.77	0.22	38.5	1.7	11.3	0.9	116.7	8.5	35.8	1.5	145.2	5.8	30.1	1.7	273.0	12.0	57.8	3.2	12840	580
Sample BH54																																				
BH54-01	10	4.4	189	20	1.24	0.37	b.d.l.		11.9	1.8	0.056	0.05	0.99	0.48	4.07	0.78	0.109	0.091	17.1	4.2	3.26	0.61	25.5	4	6.89	0.36	18.7	3.5	2.83	0.95	18.9	5	2.77	0.8	11050	940
BH54-24	6.5	2.6	71.7	6.6	0.71	0.37	b.d.l.		18.4	1.7	0.186	0.081	1.99	0.74	5.8	2.1	0.43	0.14	9.3	1.6	1.09	0.2	10.5	1.7	2.57	0.69	8.3	2.1	1.71	0.33	14.4	2	2.81	0.47	12050	840
BH54-28	7.3	4.3	35	18	0.75	0.4	b.d.l.		18.7	2.1	0.062	0.036	2.53	0.54	5.5	2.8	0.37	0.28	5.2	1.9	0.64	0.3	5.3	2.1	1.27	0.74	5.5	4.6	0.92	0.66	8.1	7.4	2	2	12300	1200
BH54-35	4.7	3	226	45	1.3	0.58	b.d.l.		12.8	1.5	0.083	0.049	1.6	0.65	5	0.79	0.32	0.21	8.7	2.3	1.77	0.52	21.1	3.6	7.02	0.88	32.1	6.9	7.5	2.3	69	25	12.5	4.9	12120	630
BH54-37	5.5	3.3	249	20	1.15	0.26	b.d.l.		21.1	2	0.173	0.084	2.36	0.64	3.76	0.86	0.68	0.24	8	1.7	1.48	0.35	22.3	4.2	6.9	1.1	35.3	6.3	7.8	1.5	80	16	17	4.1	12060	630
BH54-44	4.9	1.9	636	39	0.81	0.31	b.d.l.		0.45	0.18	0.03	0.034	0.021	0.049	0.26	0.3	0.122	0.073	3	1.3	1.49	0.42	39.1	9.1	18.1	3.5	102	21	23.5	4.7	208	44	43.1	8.5	10600	2200
BH54-49	5.8	2.5	793	95	1.18	0.42	0	0.0002	2.1	0.53	0.082	0.065	0.26	0.17	0.71	0.36	0.16	0.18	11.1	3.2	4.98	0.56	77.9	5.1	26.5	2.8	100.7	7.4	19	2.1	131.2	5.7	21.8	0.63	12380	570
BH54-66	7.5	5.2	30	4.7	0.47	0.26	b.d.l.		17.07	0.47	0.191	0.084	2.2	0.46	4.05	0.79	0.3	0.14	5.8	2	0.7	0.29	5	1.5	0.81	0.25	2.5	1.2	0.41	0.2	3.43	0.78	0.82	0.29	12250	560
BH54-67	6.1	2	496	29	1.6	0.46	b.d.l.		5.04	0.67	0.102	0.052	0.37	0.24	1.69	0.78	0.202	0.087	11.6	2.6	4.25	0.55	59.3	3.2	16.5	1.3	52.7	3.5	9.27	0.82	66.3	3.3	11	1.1	12590	780
BH54-76	9.4	3.6	144.8	7.9	1.44	0.42	b.d.l.		24.8	2.8	0.177	0.091	2.69	0.38	9.7	1.5	0.31	0.12	20	4.5	3.83	0.61	31.2	4.2	5.01	0.49	11.4	1.7	1.53	0.22	8.9	2	1.48	0.45	12580	980

Appendix C. Zircon trace element analyses (continued)

	Element concentration (ppm)																																	
Analysis	Ti	2σ	Y	2σ	Nb	2σ	La	2σ	Ce	2σ	Pr	2σ	Nd	2σ	Sm	2σ	Eu	2σ	Gd	2σ	Tb	2σ	Dy	2σ	Ho	2σ	Er	2σ	Tm	2σ	Yb	2σ	Lu	2σ	Hf	2σ
Sample BH74																																				
BH74-01	7.6	5.7	1810	140	2.76	0.48	b.d.l.		6.43	0.79	0.079	0.059	1.16	0.53	2.95	0.88	0.85	0.18	25	3.9	15.3	1.3	191	13	66.3	5.2	216	12	42.6	4.4	321	42	47.6	4.5	13370	910
BH74-02	11.2	3.5	139.4	8.2	0.81	0.3	0.01	0.0003	8.6	1.1	0.098	0.056	1.62	0.48	3.19	0.61	0.18	0.068	14.3	2.3	3.51	0.39	20	2.5	4.63	0.46	13.3	2.3	2.21	0.37	17.5	2.5	2.71	0.5	12420	880
BH74-03	19.5	6.1	191	14	1.01	0.3	b.d.l.		12.1	0.84	0.112	0.049	3.03	0.83	6.2	1.3	0.3	0.11	32.7	4.9	6.21	0.67	32.4	2.6	6.63	0.86	16.6	2.2	2.34	0.29	17.1	1.9	3	0.48	12300	710
BH74-05	14	2.7	1433	77	2.36	0.58	b.d.l.		4.7	1.1	0.16	0.1	1.33	0.45	1.74	0.76	0.76	0.34	15.4	3.1	7.9	1	107.1	8.8	49.9	7.1	200	13	39	2.1	324	32	52.9	3.3	13800	1100
BH74-06	15.4	5.1	162.4	7.2	0.76	0.28	b.d.l.		7.61	0.69	0.085	0.044	1.99	0.37	4.9	0.75	0.29	0.16	17.3	2.7	4.27	0.59	26.4	2.9	5.76	0.88	14.8	1	2.83	0.26	16.2	2.4	2.32	0.69	13300	1100
BH74-07	15.1	4.2	155	12	0.64	0.35	b.d.l.		10.05	0.31	0.234	0.084	2.91	0.68	8	2.1	0.31	0.11	22.4	4.2	4.24	0.66	24.8	1.6	5.3	1	13.2	2.2	2.44	0.67	15.1	2	2.59	0.43	13690	500
BH74-08	7.5	4.3	1037	89	2.97	0.69	b.d.l.		6.39	0.71	0.04	0.028	0.82	0.51	1.89	0.56	0.55	0.2	23.4	4.4	11.2	1.6	100	16	33.8	2.1	93	15	15.7	2.8	123	8.8	16.6	2.8	14200	1000
BH74-09	15.4	4.8	136	11	0.89	0.41	b.d.l.		10.56	0.75	0.053	0.035	2.64	0.71	4.95	0.88	0.36	0.15	19.7	2.8	3.92	0.74	22	3.7	4.3	0.59	12.3	1.6	2.3	0.44	17.6	2.4	2.49	0.5	13300	1000
BH74-15	13.7	5.6	159	10	0.58	0.29	b.d.l.		10.2	1.1	0.082	0.046	2.91	0.79	6.5	1.2	0.33	0.12	21.7	3.3	4.45	0.56	24.1	2.6	5.61	0.69	14.5	2.1	2.86	0.45	21.1	2.3	3.42	0.37	11990	800
BH74-19	11.6	3	1570	100	2.48	0.71	b.d.l.		4.2	0.72	0.086	0.088	0.97	0.32	2.24	0.71	0.64	0.18	20.7	3.7	12.3	1.7	146.5	8.4	53.4	3.9	175.1	9.3	31.1	2.8	208	22	32.6	1.6	13800	1100
BH74-20	15.2	4.2	136.6	8.5	0.99	0.29	b.d.l.		11.8	1.8	0.34	0.11	3.5	1.2	6.5	1.5	0.36	0.16	23.3	2.9	4.93	0.81	22.8	3.1	4.2	1.3	12.6	2.4	1.72	0.42	13.5	2.2	2.13	0.5	13540	900
BH74-21	12.9	3.7	74.6	7.3	0.48	0.24	b.d.l.		7.11	0.79	0.109	0.074	1.18	0.42	3.03	0.75	0.21	0.11	10.7	1.5	2.3	0.48	10.7	2.2	2.54	0.57	5.64	0.64	1.01	0.27	8.2	1.4	1.33	0.31	13220	630
BH74-25	6.3	4.4	1210	100	1.59	0.38	b.d.l.		4.54	0.67	0.072	0.064	0.89	0.56	1.55	0.51	0.64	0.16	15.5	2.3	9.8	1.1	112.6	8.4	41.7	3.9	150	13	27.2	2	207	18	34.4	3.6	13300	1200
BH74-26	14	3.4	189	16	0.7	0.23	b.d.l.		12.2	1.8	0.142	0.092	3.39	0.64	7.4	1.6	0.39	0.14	27.7	3.2	5.88	0.72	33.7	4.2	6.24	0.68	18.4	3	2.92	0.51	20.8	1.8	3.27	0.53	13030	680
BH74-28	8.5	3.7	618	35	1.91	0.42	b.d.l.		6.94	0.7	0.064	0.036	0.89	0.54	1.94	0.72	0.41	0.13	13.7	2.3	6.55	0.67	62	3.4	20.3	1.3	75.4	5.2	12.4	1.1	98	6.6	16.6	1.5	12200	790
BH74-31	11.3	5.9	116.6	7.1	0.68	0.26	b.d.l.		9.88	0.89	0.115	0.067	2.91	0.84	5.47	0.77	0.31	0.17	16.3	2.2	3.55	0.71	18.9	3.5	3.71	0.64	11.3	1.8	1.6	0.3	14.2	2.9	2.34	0.37	12600	1000
BH74-32	9.3	4.2	147.3	8.3	0.92	0.28	b.d.l.		10.35	0.95	0.128	0.061	2.69	0.63	6.4	1	0.3	0.072	20	3	4.3	0.83	23	4.2	5.43	0.67	14.9	2.7	2.29	0.17	14.1	1.4	2.47	0.38	12770	520
BH74-34	6.6	5.6	81.4	5.8	0.79	0.32	b.d.l.		10.8	2.4	0.076	0.05	1.97	0.49	3.8	1.5	0.27	0.19	13.4	2.1	2.56	0.53	13.6	2	2.1	0.45	9	1.4	1.14	0.4	8.8	1.7	1.24	0.37	12410	890
BH74-35	14.4	9.2	147	16	0.88	0.29	b.d.l.		10	1.6	0.108	0.058	3.8	1.1	5.7	1.4	0.21	0.15	19.7	2.6	3.96	0.47	23.8	4.5	4.68	0.6	13.3	1.3	1.95	0.47	15.2	1.8	2.31	0.61	13150	940
BH74-36	7.2	2.8	2490	140	2.64	0.45	b.d.l.		5.74	0.86	0.181	0.078	1.22	0.35	2.37	0.67	1.03	0.16	23	2.7	13.3	1.5	193	22	77.4	6.3	362	23	59.8	5.6	399	29	71.4	5.2	12400	750
BH74-37	8	5.8	2500	160	3.06	0.5	b.d.l.		12.7	3.2	1.68	0.61	10.5	4.8	2.7	0.94	1.15	0.49	16.1	2.5	11.1	1.3	178.1	8.8	78	2.8	379	22	67.7	4	556	27	104.2	4.7	15150	950
BH74-38	10.3	4.9	636	53	1.16	0.32	b.d.l.		17.2	2	1.55	0.28	10.7	1.9	6.2	1	0.97	0.28	19.9	2.8	5.87	0.64	59.8	8.1	21.6	3.2	89.8	7.9	17.5	2.1	111	17	21.1	2.9	12940	810
BH74-39	8.4	4.1	185	15	0.79	0.31	b.d.l.		9.2	1.4	0.21	0.19	3.21	0.75	7.2	2.1	0.26	0.12	26.8	4.4	5.47	0.46	29.5	3	5.66	0.59	16.4	2.1	2.67	0.49	15.6	2.4	2.25	0.63	13250	700
BH74-41	7.5	3.5	1986	79	2.26	0.45	b.d.l.		3.57	0.74	0.107	0.065	0.89	0.41	2.13	0.38	0.87	0.17	22.5	2.4	14.15	0.98	179.4	6.5	66	3.7	234	16	36.3	2.2	213	12	33	2.6	12800	720
BH74-43	7.7	7.6	136	15	0.61	0.24	0	0.00019	9.52	0.92	0.105	0.083	2.6	1.1	6	2.1	0.29	0.15	20.4	4.4	3.99	0.48	22.1	3.4	4.84	0.77	12.5	2	1.94	0.62	11.8	3.2	2.09	0.56	11850	700
BH74-44	4.4	3.1	934	70	1.22	0.39	b.d.l.		4.89	0.75	0.055	0.035	0.97	0.58	1.35	0.56	0.5	0.24	14.4	2.5	7.89	0.68	95.9	7	31	1.7	119	10	19.2	1.2	126.3	8.3	23.3	1.4	13000	710
BH74-47	17.2	4.5	154	13	1.14	0.38	b.d.l.		9.43	0.87	0.133	0.069	2.22	0.64	5.07	0.91	0.34	0.15	16.1	2.6	3.94	0.57	26.3	2.3	5.07	0.38	13.6	1.5	1.91	0.38	13.2	1.9	1.93	0.35	12200	450
BH74-48	14.4	4.1	101.3	8.8	0.8	0.2	b.d.l.		10.1	1.1	0.122	0.034	2.04	0.99	4.9	1.6	0.24	0.13	15	2.3	2.69	0.48	15.9	1.7	3.23	0.7	9.7	1.6	1.2	0.21	9.8	1.7	1.3	0.21	12500	670
BH74-49	13.1	2.8	111.9	6.4	0.65	0.29	b.d.l.		13.7	8.1	0.31	0.29	2.01	0.95	5.3	1.2	0.17	0.11	17.3	3	2.76	0.51	18.8	3.5	3.37	0.48	8.7	1.7	1.53	0.29	10.1	2	1.52	0.39	13140	920
BH74-51	14.8	3.9	70.8	4.5	0.85	0.36	b.d.l.		9.1	1.1	0.045	0.027	1.77	0.67	2.06	0.6	0.23	0.16	8.3	1.2	1.88	0.41	11.1	1.3	2.09	0.3	6.1	1.3	1	0.23	7.1	1.3	0.94	0.2	13130	520
BH74-54	15.2	3.2	180	10	1.07	0.27	b.d.l.		9.61	0.66	0.096	0.052	2.51	0.81	7.2	1.1	0.41	0.13	24.1	3.3	4.76	0.46	31.1	2.1	6.31	0.64	14.6	1.9	2.65	0.42	16.3	2	3.26	0.34	12920	670
BH74-57	12.6	4.9	184	16	0.82	0.22	b.d.l.		9.43	0.85	0.094	0.058	2.43	0.86	6.2	1.3	0.32	0.13	21.7	2	4.3	0.68	28.3	3.2	5.39	0.7	15.8	1.8	2.29	0.49	15.4	1.6	2.88	0.64	13070	990
BH74-59	12	5.3	479	24	0.78	0.21	b.d.l.		7.47	0.93	0.182	0.045	3.1	0.88	4.38	0.72	0.43	0.12	17	2.6	5.54	0.64	54.2	5.9	15.1	1.2	47.8	4.8	9.5	1.2	72.9	7.5	14.2	1.7	13060	890
BH74-61	13.1	4.6	1557	80	2.66	0.5	b.d.l.		5.06	0.65	0.067	0.039	1.51	0.49	2.89	0.79	0.7	0.23	24.6	3.1	12.27	0.98	148	10	48.7	2.7	171	13	30.6	1.5	201	15	32.3	3	13350	900
BH74-63	3.5	2.7	599	39	1.57	0.26	0.01	0.00014	4.87	0.71	0.02	0.028	0.6	0.3	2.17	0.67	0.45	0.14	17.3	2.4	6.84	0.62	67.1	3.4	18	1.2	59.6	4.4	10.2	1.2	72.1	6.2	11.6	1.2	13380	700
BH74-65	14.4	4.1	151	12	0.8	0.22	b.d.l.		11.5	1.3	0.203	0.084	3	1.1	6.8	1.2	0.37	0.14	21.8	1.9	3.84	0.35	24.5	2.7	4.99	0.5	12.6	1.7	2.02	0.31	14.4	2.1	2.27	0.32	12300	1200
BH74-67	9.4	3.3	167	14	0.68	0.13	b.d.l.		4.4	1	0.096	0.028	2.5	0.96	7.5	1.3	1.33	0.41	24.6	5.7	6	0.9	33.2	3.2	4.68	0.69	10.2	1.3	1.25	0.45	8.9	1.8	1.37	0.4	14330	550
BH74-68	12.5	5.7	100.8	9	0.97	0.23	b.d.l.		10.13	0.77	0.078	0.035	2.71	0.65	4.5	1.3	0.27	0.13	15.5	1.8	2.74	0.42	17.3	1.7	2.74	0.29	7.58	0.95	1.39	0.27	9.8	1.3	1.51	0.29	12680	680
BH74-69	5.3	1.8	317	17	1.44	0.45	b.d.l.		7.26	0.6	0.15	0.1	0.82	0.41	2.43	0.7	0.34	0.11	14.9	2.1	4.59	0.42	39.2	4.5	10.72	0.95	35	3.4	5.8	0.76	43.2	3.7	6.97	0.89	12900	680
BH74-70	10.9	4.6	225	11	0.67	0.26	b.d.l.		11.1	1	0.154	0.034	5.4	3.1	9	1.7	0.39	0.18	35.2	3	6.77	0.54	37.6	2.6	6.93	0.55	17.6	1.4	2.71	0.39	17.1	1.5	2.98	0.47	12300	730

Appendix C. Zircon trace element analyses (continued)

	Element concentration (ppm)																															
Analysis	Ti	2σ	Y	2σ	Nb	2σ	La	2σ	Ce	2σ	Pr	2σ	Nd	2σ	Sm	2σ	Eu	2σ	Gd	2σ	Tb	2σ	Dy	2σ	Ho	2σ	Er	2σ	Tm	2σ	Yb	2σ	Lu	2σ	Hf	2σ
BH74-71	9	4.6	2100	160	2.91	0.7	b.d.l.		3.53	0.49	0.041	0.044	0.68	0.43	1.88	0.71	0.98	0.25	25.6	3.1	13.5	1.8	189	16	62.6	7.2	227	22	44.6	5.6	279	25	46.1	5.5	13740	920
BH74-72	8.1	3.9	691	56	1.51	0.51	b.d.l.		5.9	1.3	0.163	0.078	1.39	0.49	2.75	0.95	0.38	0.13	13.6	2.9	5.03	0.54	56.9	5.4	21.2	1.5	95.5	6.3	24.7	2.4	213	14	42.7	2	12520	670
BH74-73	12	3.1	105.9	4.3	1.12	0.42	b.d.l.		10	1.2	0.113	0.055	2.76	0.76	5.87	0.93	0.286	0.092	17.8	2.3	2.85	0.53	19.5	2.5	3.08	0.66	8.3	1.6	1.6	0.28	11.2	2.2	1.88	0.5	12640	560
BH74-75	5.8	2.8	637	95	1.57	0.57	b.d.l.		6.7	1.4	0.26	0.17	2.4	1.8	2.28	0.64	0.41	0.17	17.4	2	6.82	0.95	75.4	7.6	20.3	2.7	67	12	10.2	1.7	65.1	7.6	10.8	2.1	12440	700
BH74-76	11.3	4	162	25	0.81	0.38	b.d.l.		7.8	0.57	0.067	0.05	2.01	0.69	3.99	0.57	0.24	0.13	13.6	1.8	2.87	0.56	21.1	3	5.35	0.82	17.7	2.6	3.8	0.77	30	7.1	6.2	1.6	11560	700
BH74-77	4.9	3.6	1386	96	2.51	0.48	b.d.l.		6.5	1.1	0.016	0.016	1.3	1.1	4.8	1.1	1.4	0.31	41.3	4	16.2	1.6	175.3	5.8	45.9	3.1	143	10	22.1	2.1	143.6	7	22.5	1.2	13730	690
BH74-78	10.9	6.1	167	13	0.82	0.39	b.d.l.		9.6	1.3	0.148	0.087	3.94	0.81	8.1	1	0.36	0.16	25.7	4.6	4.59	0.68	27.5	4	5.88	0.85	14.6	2.1	2.66	0.5	17.1	2.6	2.93	0.56	13090	600
BH74-79	11.6	4	147.3	7	0.58	0.15	b.d.l.		8.96	0.63	0.441	0.071	4.94	0.89	7.1	1.4	0.38	0.1	22.7	3.9	4.14	0.52	24.7	2.7	4.74	0.46	12.7	1.4	2.13	0.53	12.4	1.4	2.52	0.31	12700	600
BH74-80	8.6	4.6	175.5	8	0.69	0.35	0.01	0.00018	9.73	0.9	0.109	0.036	3.94	0.99	8	1.1	0.26	0.11	24.4	2.8	4.31	0.46	27.4	4.2	5.9	0.58	18.9	2.3	2.92	0.44	22.7	3.7	3.88	0.67	11700	1100
BH74-81	9.6	3.6	99.1	8.7	0.77	0.3	b.d.l.		6.37	0.98	0.183	0.056	2.3	0.83	4.82	0.44	0.32	0.14	17.2	2.9	3	0.39	21.5	1.4	3.24	0.43	8.37	0.77	0.96	0.2	5.7	1.3	0.84	0.31	14000	490
BH74-82	12.1	7.4	161	14	0.8	0.35	0.01	0.00022	10.5	1.4	0.042	0.035	4.08	0.75	8.6	1.9	0.19	0.17	25.4	2.2	4.6	1.4	25.6	4.6	4.2	1.1	11.5	2.9	1.9	0.35	14.7	4.4	2.39	0.64	10900	2800
BH74-83	8	2.5	370	16	1.01	0.3	b.d.l.		5.12	0.91	0.049	0.031	0.56	0.51	1.56	0.56	0.27	0.13	14.6	1.8	4.81	0.8	47.2	3.3	12.07	0.82	37.2	2.2	5.93	0.67	43.6	6.3	7.35	0.66	13100	1100
BH74-84	13.2	5.4	127.5	7.2	0.99	0.54	b.d.l.		9.47	0.74	0.17	0.1	3.7	1.1	5.83	0.69	0.41	0.21	22.5	3.5	4.1	0.83	24.4	2.4	4.61	0.61	12.2	1.7	2.29	0.52	15.9	1.6	2.45	0.31	12520	530
BH74-86	10.5	2.9	170	7.5	0.65	0.33	b.d.l.		10.1	1.3	0.19	0.11	3.7	1.2	7.2	1.9	0.147	0.079	23.4	2.7	4.07	0.5	24.3	2.7	4.8	0.48	17.5	3.5	2.84	0.33	18.4	2.5	3.43	0.69	13180	510
BH74-87	9.7	2.8	85	4.4	0.86	0.21	b.d.l.		9.1	0.97	0.081	0.025	2.5	1	4.3	1.2	0.22	0.13	13	2.2	2.31	0.47	15.6	2	2.85	0.47	8.7	1.3	1.32	0.27	7.8	1.3	1.11	0.26	11930	730
BH74-89	5.6	2.6	1640	130	2.23	0.61	0.01	0.00016	3.2	0.4	0.019	0.021	0.62	0.36	2.46	0.68	0.72	0.14	20.8	2.9	12.51	0.89	176	15	49.9	4.5	186	13	30.4	2.6	221	17	34	1.9	13510	390
BH74-90	15.3	4.4	180	13	0.95	0.35	0	0.0003	8.77	0.8	0.133	0.069	3.38	0.85	6	1.5	0.34	0.34	23.9	2.9	4.76	0.39	32.3	2.3	6.16	0.59	16.9	2	2.1	0.28	15.7	1.9	2.2	0.36	12590	550

Appendix C. Monazite geochronology and trace element analyses

Analysis	Textural location	$^{207}Pb/^{235}U$	2σ	$^{206}Pb/^{238}U$	2σ	$^{207}Pb/^{206}Pb$	2σ	Rho	Age (Ma) $^{207}Pb/^{235}U$	2σ	$^{206}Pb/^{238}U$	2σ	$^{207}Pb/^{206}Pb$	2σ	Conc.** (%)	Element oxide concentration (wt %) SiO_2	P_2O_5	CaO	Y_2O_3	La_2O_3	Ce_2O_3	Pr_2O_3	Nd_2O_3	Sm_2O_3	Gd_2O_3	Total PbO	ThO_2	UO_2
Sample BH44																												
BH44-1-1	m	2.26900	0.07300	0.20490	0.00520	0.08080	0.00150	0.59342	1201	22	1201	28	1207	38	100	1.27	27.75	0.73	0.73	14.61	28.66	3.05	11.61	1.67	0.88	0.47	8.32	0.26
BH44-1-2	m	2.23500	0.06900	0.19920	0.00460	0.08140	0.00100	0.67476	1190	21	1171	25	1225	24	96	1.13	28.23	0.94	0.96	14.87	28.88	3.03	11.49	1.86	1.26	0.44	6.31	0.59
BH44-1-3	m	2.20800	0.07500	0.19750	0.00480	0.08130	0.00160	0.52144	1185	24	1161	26	1216	39	95	1.16	28.02	0.49	1.01	15.10	29.50	3.13	11.99	1.84	1.06	0.34	6.21	0.15
BH44-2-2	g	2.36900	0.08900	0.20940	0.00570	0.08250	0.00190	0.61931	1228	27	1225	30	1240	46	99	1.97	26.86	0.65	0.56	14.59	29.06	3.11	11.86	1.38	0.59	0.48	8.78	0.12
BH44-2-3	g	2.59300	0.11000	0.22600	0.00600	0.08340	0.00240	0.47758	1298	32	1313	31	1268	59	104	2.56	25.54	0.35	0.23	13.81	28.00	3.02	11.62	1.08	0.32	0.68	12.73	0.06
BH44-2-4	g	2.39300	0.09200	0.21600	0.00560	0.08030	0.00210	0.39926	1236	28	1260	30	1202	51	105	0.95	28.14	0.40	0.84	14.48	29.36	3.22	12.62	1.92	1.08	0.35	6.54	0.10
BH44-2-5	g	2.12000	0.08400	0.19870	0.00500	0.07740	0.00220	0.39484	1150	27	1168	27	1119	58	104	0.94	28.13	0.37	0.59	14.96	29.85	3.18	12.41	1.86	0.99	0.34	6.31	0.07
BH44-2-6	g	2.00000	0.12000	0.19020	0.00600	0.07700	0.00380	0.36979	1104	39	1122	33	1060	100	106	1.31	27.59	0.33	0.19	14.64	30.70	3.26	12.64	1.57	0.65	0.33	6.74	0.04
BH44-4-1	m	2.18100	0.07900	0.19920	0.00500	0.07970	0.00220	0.26937	1174	26	1170	27	1164	55	101	0.77	28.23	0.19	0.20	15.59	30.59	3.27	12.69	1.66	0.71	0.31	5.70	0.09
BH44-4-2	m	2.31800	0.07300	0.20850	0.00490	0.08040	0.00120	0.62927	1216	22	1220	26	1200	28	102	0.80	28.57	0.85	1.12	14.55	28.70	3.02	11.77	1.94	1.24	0.42	6.65	0.37
BH44-4-3	m	2.41300	0.07600	0.21340	0.00490	0.08160	0.00110	0.64052	1245	22	1246	26	1238	25	101	0.94	28.65	1.01	1.18	14.86	29.17	3.04	11.67	1.99	1.34	0.41	5.22	0.54
BH44-4-4	m	2.25600	0.06800	0.20230	0.00440	0.08050	0.00110	0.54024	1197	21	1187	24	1202	26	99	0.72	29.14	1.10	2.63	14.58	28.43	2.93	10.96	1.83	1.34	0.40	5.32	0.63
BH44-5-1	g	2.24800	0.08000	0.20290	0.00470	0.08000	0.00150	0.59585	1193	25	1190	25	1184	39	101	0.76	28.62	0.91	0.89	14.42	28.94	3.05	12.05	1.86	1.06	0.39	6.89	0.17
BH44-5-2	g	2.29300	0.08500	0.20470	0.00480	0.08110	0.00180	0.43179	1206	26	1200	26	1207	45	99	0.62	28.96	0.90	1.70	14.10	28.58	3.07	11.97	2.07	1.40	0.35	6.14	0.15
BH44-5-3	g	2.21900	0.07900	0.20070	0.00490	0.07990	0.00180	0.47957	1183	25	1179	26	1179	44	100	0.73	28.75	0.74	1.69	14.56	28.86	3.00	11.70	1.96	1.42	0.34	6.09	0.17
BH44-5-4	g	2.13200	0.07500	0.19590	0.00450	0.07840	0.00160	0.46121	1158	23	1153	24	1163	43	99	0.49	28.91	0.58	1.23	14.61	29.32	3.13	12.20	2.02	1.32	0.31	5.72	0.16
BH44-6-1	m	2.21400	0.08200	0.19950	0.00470	0.07960	0.00180	0.38995	1181	25	1172	25	1171	44	100	0.76	28.61	0.55	1.68	14.44	29.03	3.08	12.09	1.97	1.34	0.32	6.01	0.13
BH44-6-2	m	2.09100	0.07900	0.19050	0.00470	0.07920	0.00200	0.37014	1142	26	1123	25	1165	52	96	1.43	27.46	0.55	0.86	14.18	28.40	3.05	12.15	1.70	1.02	0.45	8.62	0.12
BH44-7-1	m	2.43200	0.11000	0.21470	0.00610	0.08190	0.00240	0.55398	1250	33	1253	33	1230	61	102	3.24	24.88	0.51	0.31	12.65	27.73	3.00	12.36	1.40	0.59	0.66	12.59	0.09
BH44-7-3	m	2.18900	0.10000	0.20280	0.00560	0.07660	0.00250	0.40645	1171	33	1189	30	1085	66	110	1.39	27.54	0.63	0.49	13.76	28.99	3.19	12.73	1.67	0.80	0.40	8.33	0.08
BH44-7-4	m	2.16500	0.09400	0.19980	0.00550	0.07850	0.00250	0.44112	1162	30	1173	29	1135	62	103	5.63	20.98	0.33	0.03	9.98	23.85	2.77	11.77	1.02	0.23	1.17	22.10	0.15
Sample BH48																												
BH48-2-1	m	2.32500	0.07900	0.21000	0.00530	0.08100	0.00160	0.44707	1219	25	1228	28	1208	40	102	0.57	29.07	1.18	1.37	14.60	28.70	2.95	11.34	1.81	1.14	0.37	6.73	0.18
BH48-2-2	m	2.28400	0.07900	0.20710	0.00500	0.07980	0.00150	0.57336	1207	24	1213	27	1190	38	102	0.24	29.55	0.96	1.26	15.09	30.24	3.07	11.67	1.82	1.07	0.27	4.55	0.20
BH48-10-1	m	2.33500	0.07700	0.20940	0.00510	0.08010	0.00180	0.37649	1220	23	1228	28	1201	44	102	0.03	29.77	1.33	1.18	14.72	28.84	2.98	11.21	1.74	1.05	0.37	6.60	0.18
BH48-10-2	m	2.38500	0.08100	0.20870	0.00490	0.08250	0.00160	0.52775	1235	25	1221	26	1246	37	98	0.10	30.05	1.73	1.17	15.55	29.19	2.91	10.66	1.65	0.99	0.30	5.52	0.18
BH48-10-3	m	2.26900	0.08800	0.21320	0.00570	0.07740	0.00190	0.48282	1200	27	1245	30	1127	51	110	1.72	27.80	1.34	1.22	14.73	28.68	2.92	11.07	1.73	1.00	0.41	7.19	0.19
BH48-11-1	m	2.34200	0.07700	0.20840	0.00500	0.08130	0.00160	0.44009	1222	23	1219	27	1216	39	100	0.44	29.41	1.63	1.20	14.44	28.36	2.90	11.01	1.79	1.04	0.41	7.18	0.18
BH48-11-2	m	2.34300	0.08100	0.20870	0.00510	0.08150	0.00140	0.67850	1222	24	1221	27	1222	35	100	0.40	29.62	1.28	1.20	15.25	30.28	3.08	11.69	1.83	1.08	0.25	3.87	0.19
BH48-11-3	m	2.21900	0.07400	0.20080	0.00470	0.08000	0.00150	0.46239	1184	23	1179	25	1184	38	100	0.00	29.98	1.48	1.63	14.21	28.65	2.92	11.29	1.83	1.11	0.37	6.32	0.22
BH48-11-4	m	2.24700	0.07500	0.20170	0.00470	0.08060	0.00150	0.56028	1195	23	1184	25	1199	36	99	0.28	29.24	1.04	0.97	13.54	28.94	3.13	12.45	1.92	1.00	0.39	6.91	0.20
BH48-15-2	m	1.94200	0.06800	0.18640	0.00450	0.07560	0.00170	0.35644	1092	23	1101	24	1065	46	103	1.06	28.10	0.67	0.28	13.85	30.34	3.29	12.88	1.82	0.77	0.34	6.44	0.15
BH48-15-3	m	2.25800	0.09600	0.19490	0.00510	0.08370	0.00290	0.17383	1192	30	1147	28	1257	69	91	8.90	19.92	1.48	0.66	14.64	30.51	3.15	12.30	1.80	0.87	0.29	5.32	0.18
BH48-16-1	m	2.25000	0.07700	0.20230	0.00500	0.08080	0.00150	0.58265	1196	25	1187	27	1218	34	97	-0.03	29.77	1.01	1.38	15.25	29.54	2.92	11.14	1.76	1.05	0.34	5.64	0.23
BH48-13-1	m	2.17700	0.08200	0.19920	0.00480	0.07910	0.00200	0.39804	1170	26	1170	26	1154	50	101	0.54	29.31	1.27	2.16	13.98	28.22	2.96	11.55	1.84	1.17	0.36	6.54	0.12
BH48-13-2	m	2.01600	0.06500	0.19030	0.00470	0.07740	0.00120	0.67737	1119	22	1122	26	1126	30	100	0.17	30.08	1.84	2.53	13.89	27.45	2.84	10.86	1.78	1.11	0.42	6.45	0.59
BH48-13-3	m	2.27700	0.07200	0.20480	0.00450	0.08040	0.00120	0.27429	1203	22	1201	24	1204	31	100	-0.02	30.23	1.68	2.04	14.53	27.90	2.94	11.03	1.88	1.27	0.37	5.82	0.33
BH48-17-1	m	2.21700	0.07500	0.20120	0.00510	0.08000	0.00150	0.56077	1184	24	1181	27	1191	37	99	0.99	28.67	1.15	0.93	14.71	29.80	3.11	11.90	1.80	0.95	0.31	5.49	0.20
BH48-17-2	m	2.00100	0.07200	0.18380	0.00550	0.08040	0.00170	0.60274	1114	25	1087	30	1199	41	91	0.38	29.47	1.10	2.19	14.48	28.78	2.95	11.37	1.86	1.12	0.33	5.58	0.41
BH48-17-3	m	2.13800	0.08000	0.19730	0.00490	0.07880	0.00170	0.61738	1158	26	1164	28	1161	41	100	0.30	29.25	0.94	1.58	13.36	28.90	3.09	12.16	1.96	1.10	0.36	6.85	0.15
BH48-22-1	m	2.17100	0.08000	0.20190	0.00520	0.07820	0.00200	0.42232	1168	25	1185	28	1132	49	105	0.83	28.45	1.21	0.35	11.93	28.75	3.22	13.21	2.07	0.91	0.47	8.44	0.16
BH48-22-2	m	2.33200	0.07900	0.20960	0.00470	0.08080	0.00170	0.35381	1219	24	1226	25	1203	40	102	0.43	29.49	1.33	1.65	14.46	28.85	2.99	11.60	1.92	1.21	0.33	5.53	0.22

Appendix C. Monazite geochronology and trace element analyses (continued)

Analysis	Textural location	$^{207}Pb/^{235}U$	2σ	$^{206}Pb/^{238}U$	2σ	$^{207}Pb/^{206}Pb$	2σ	Rho	Age (Ma) $^{207}Pb/^{235}U$	2σ	$^{206}Pb/^{238}U$	2σ	$^{207}Pb/^{206}Pb$	2σ	Conc.** (%)	Element oxide concentration (wt %) SiO_2	P_2O_5	CaO	Y_2O_3	La_2O_3	Ce_2O_3	Pr_2O_3	Nd_2O_3	Sm_2O_3	Gd_2O_3	Total PbO	ThO_2	UO_2
BH48-23-1	m	2.28000	0.07800	0.20590	0.00490	0.08050	0.00150	0.53793	1203	24	1206	26	1196	38	101	-0.05	29.91	1.56	1.41	13.67	28.50	2.85	11.04	1.81	1.13	0.42	7.54	0.21
BH48-23-3	m	2.33200	0.07800	0.21230	0.00520	0.08000	0.00160	0.44592	1219	24	1241	27	1187	39	105	0.05	29.72	0.88	1.33	14.94	29.55	3.15	12.20	2.04	1.23	0.29	4.41	0.20
BH48-24-1	m	2.10100	0.06900	0.19450	0.00450	0.07840	0.00110	0.73522	1149	23	1145	25	1149	27	100	0.63	29.24	1.17	2.25	14.30	28.98	2.93	11.34	1.84	1.14	0.35	5.40	0.43
Sample BH23																												
BH23-14-1	g	2.14300	0.03900	0.19790	0.00310	0.07840	0.00170	0.46176	1161	12	1164	17	1154	43	101	0.81	28.62	1.04	1.04	14.06	29.02	2.99	11.55	1.93	1.18	0.40	7.11	0.25
BH23-13-1	m	2.14900	0.04100	0.19820	0.00320	0.07880	0.00170	0.54738	1163	13	1165	17	1157	44	101	0.84	28.79	1.12	1.49	15.36	29.33	2.89	10.65	1.58	0.94	0.36	6.36	0.30
BH23-13-2	m	2.19200	0.05800	0.19950	0.00350	0.07940	0.00250	0.29393	1175	19	1172	19	1162	62	101	0.63	28.47	0.71	0.74	13.81	28.91	3.01	11.69	2.10	1.15	0.42	8.14	0.21
BH23-11-3	g (edge)	2.47200	0.04500	0.21540	0.00360	0.08350	0.00190	0.49492	1261	13	1257	19	1270	44	99	0.15	29.42	0.94	1.22	14.41	29.00	3.01	11.79	1.94	1.25	0.35	6.29	0.22
BH23-8-1	m	2.15700	0.04500	0.19930	0.00340	0.07880	0.00200	0.36530	1165	15	1171	18	1157	51	101	0.70	28.47	0.63	0.08	14.74	30.94	3.22	12.37	1.54	0.40	0.34	6.41	0.16
BH23-7-1	g (edge)	2.18400	0.03400	0.20150	0.00300	0.07880	0.00170	0.55054	1176	11	1183	16	1158	42	102	1.08	28.43	1.22	1.43	14.66	28.93	2.88	10.59	1.58	0.91	0.42	7.57	0.30
BH23-4-1	m	2.13700	0.03600	0.19630	0.00310	0.07884	0.00150	0.69446	1159	12	1155	17	1162	39	99	0.66	29.27	1.57	1.95	14.46	28.13	2.84	10.55	1.90	1.22	0.41	6.57	0.48
BH23-4-2	m	2.14100	0.03200	0.19600	0.00300	0.07930	0.00160	0.55873	1161	10	1153	16	1174	40	98	0.81	29.05	1.43	2.13	14.43	28.21	2.80	10.48	1.94	1.30	0.41	6.49	0.53
BH23-4-3	m	2.16500	0.03600	0.19760	0.00290	0.07960	0.00170	0.54168	1168	11	1162	15	1179	41	99	0.32	29.50	1.30	1.92	14.54	28.55	2.83	10.56	1.90	1.22	0.41	6.45	0.52
BH23-1-1	m	2.22400	0.07000	0.20330	0.00400	0.07940	0.00270	0.36892	1182	22	1195	22	1151	69	104	1.85	26.77	0.35	0.25	13.57	30.37	3.20	12.50	1.44	0.52	0.46	8.64	0.09
Sample BH54																												
BH54-U1-2	m	2.41500	0.07300	0.21520	0.00360	0.08240	0.00200	0.35087	1246	22	1256	19	1245	45	101	0.67	28.81	0.78	1.41	14.98	28.12	2.96	12.27	2.01	1.45	0.31	6.16	0.07
BH54-U1-3	m	2.34200	0.07200	0.21480	0.00460	0.08000	0.00170	0.52481	1221	22	1253	24	1188	42	105	0.78	28.51	0.64	0.88	15.20	28.50	3.02	12.52	2.01	1.24	0.31	6.34	0.06
BH54-U1-4	m	2.25100	0.08400	0.20440	0.00390	0.08070	0.00250	0.35916	1194	25	1198	21	1193	60	100	1.03	28.14	0.51	0.96	14.74	28.80	3.09	12.77	1.89	1.15	0.31	6.55	0.05
BH54-U1-5	m	2.45800	0.08600	0.22250	0.00430	0.08060	0.00250	0.23050	1254	25	1294	23	1210	59	107	1.08	27.85	0.34	0.57	14.48	28.95	3.14	13.03	1.90	0.99	0.35	7.28	0.04
BH54-U1-6	m	2.10400	0.06800	0.20080	0.00360	0.07650	0.00190	0.40844	1149	23	1179	19	1102	49	107	1.36	27.41	0.22	0.04	14.29	30.01	3.43	14.39	1.04	0.24	0.34	7.18	0.06
BH54-6-2	m	2.18900	0.08000	0.20330	0.00440	0.07820	0.00250	0.32031	1172	26	1192	23	1132	63	105	1.40	27.42	0.24	0.01	15.81	30.81	3.28	12.75	0.80	0.15	0.33	6.95	0.05
BH54-7-1	m	2.25100	0.08500	0.20600	0.00430	0.08030	0.00280	0.25945	1194	27	1206	23	1163	71	104	0.89	28.27	0.12	1.77	14.83	28.66	3.06	12.67	2.14	1.61	0.27	5.69	0.03
BH54-14-1	m	2.25400	0.05800	0.20380	0.00320	0.08010	0.00130	0.47662	1198	18	1195	17	1190	33	100	0.29	29.35	0.85	1.42	14.76	28.19	3.03	12.73	2.13	1.40	0.30	5.34	0.21
BH54-14-2	m	2.24200	0.05400	0.20460	0.00340	0.07960	0.00120	0.48592	1195	17	1200	18	1180	30	102	0.47	29.27	1.36	1.76	14.27	27.12	2.83	11.43	2.01	1.40	0.40	7.46	0.23
BH54-14-3	m	2.25000	0.06000	0.20550	0.00320	0.07930	0.00140	0.45521	1194	19	1205	17	1169	36	103	0.92	28.09	0.43	0.78	14.38	28.49	3.10	12.86	1.93	1.13	0.36	7.43	0.11
BH54-14-4	m	2.15300	0.06300	0.19900	0.00360	0.07860	0.00190	0.26453	1163	20	1170	19	1143	48	102	0.88	28.46	0.58	1.63	14.50	27.56	2.99	12.80	2.26	1.54	0.31	6.39	0.09
BH54-14-5	m	2.28700	0.05400	0.20520	0.00310	0.08071	0.00110	0.62463	1207.2	17	1203	17	1209	27	100	0.23	29.75	1.51	1.49	14.65	27.28	2.89	12.10	2.14	1.42	0.34	5.94	0.27
BH54-14-6	m	2.49400	0.09100	0.22440	0.00460	0.08090	0.00250	0.23739	1264	26	1304	24	1197	62	109	1.14	27.67	0.25	0.54	14.14	28.68	3.15	13.34	1.89	1.05	0.36	7.74	0.03
BH54-14-7	m	2.23700	0.06600	0.20200	0.00320	0.08010	0.00180	0.29088	1190	21	1186	17	1191	46	100	0.68	28.95	0.89	2.23	14.48	27.36	2.90	12.00	2.09	1.64	0.31	6.38	0.09
BH54-14-8	m	2.30700	0.08000	0.20940	0.00480	0.08100	0.00230	0.46771	1219	25	1225	25	1205	53	102	1.13	27.59	0.16	0.38	14.24	28.60	3.19	13.47	1.94	0.97	0.37	7.92	0.04
BH54-14-9	m	2.16200	0.08900	0.20080	0.00420	0.07800	0.00260	0.40513	1161	28	1179	22	1110	68	106	1.09	27.73	0.29	0.42	14.32	28.44	3.17	13.40	1.96	1.02	0.36	7.76	0.04
BH54-8-1	g	2.31900	0.06100	0.20750	0.00330	0.08100	0.00140	0.39421	1216	18	1215	17	1216	34	100	1.28	28.25	1.46	1.47	14.44	26.92	2.83	11.36	1.57	1.05	0.45	8.73	0.19
BH54-9-1	g	2.28700	0.05600	0.20570	0.00300	0.08050	0.00110	0.54415	1207	17	1206	16	1204	28	100	0.53	29.47	1.34	2.30	14.84	27.63	2.90	11.57	1.82	1.45	0.32	5.57	0.26
BH54-9-2	g	2.33700	0.08300	0.21170	0.00420	0.07980	0.00220	0.40663	1218	25	1237	22	1178	56	105	0.97	28.54	0.70	1.93	14.92	27.94	3.01	12.44	1.94	1.45	0.29	5.81	0.04
BH54-10-2	m	2.23800	0.05700	0.20070	0.00320	0.08050	0.00150	0.32077	1193	17	1179	17	1204	35	98	1.04	28.26	0.79	1.42	14.78	27.87	2.96	12.01	1.78	1.14	0.39	7.35	0.20
BH54-12-1	g	2.13800	0.06800	0.19410	0.00340	0.07960	0.00200	0.27623	1157	22	1143	18	1172	51	98	0.63	28.96	0.96	2.00	14.25	27.20	2.93	12.27	1.96	1.44	0.35	6.97	0.09
BH54-M1-1	Mount	2.26900	0.03400	0.20510	0.00350	0.08040	0.00110	0.45919	1201	11	1202	19	1199	28	100	0.57	29.14	1.13	1.79	15.19	27.48	2.89	11.51	1.85	1.37	0.35	6.53	0.22
BH54-M1-2	Mount	2.26500	0.03700	0.20450	0.00340	0.08030	0.00120	0.52673	1202	11	1199	18	1196	30	100	0.64	29.04	1.24	1.80	14.49	26.87	2.91	11.77	1.91	1.40	0.39	7.32	0.24
BH54-M1-3	Mount	2.27200	0.04900	0.20330	0.00390	0.08100	0.00140	0.57798	1201	15	1192	21	1211	35	98	0.70	28.77	0.92	1.71	14.95	26.90	2.87	11.88	1.95	1.55	0.36	7.30	0.13
BH54-M2-1	Mount	2.32100	0.03900	0.20680	0.00360	0.08170	0.00150	0.30440	1217	12	1211	19	1226	36	99	0.10	30.03	1.41	2.76	14.61	26.66	2.85	11.51	1.93	1.52	0.32	6.14	0.17
BH54-M2-2	Mount	2.32200	0.05200	0.20720	0.00390	0.08140	0.00190	0.33748	1218	17	1214	21	1220	44	100	0.37	29.41	1.16	1.55	15.06	27.79	2.93	11.70	2.05	1.63	0.29	5.98	0.07
BH54-M3-1	Mount	2.28700	0.02700	0.20480	0.00340	0.08090	0.00100	0.49488	1207.5	8.4	1201	18	1212	24	99	0.14	29.64	0.93	1.31	15.46	28.54	3.05	12.25	2.10	1.59	0.26	4.51	0.23
BH54-M3-2	Mount	2.23500	0.04100	0.20350	0.00370	0.07930	0.00150	0.41915	1190	13	1193	20	1172	36	102	0.81	28.77	0.79	2.13	14.61	27.78	3.01	12.17	1.96	1.41	0.30	6.12	0.13

Appendix C. Monazite geochronology and trace element analyses (continued)

Analysis	Textural location	$^{207}Pb/^{235}U$	2σ	$^{206}Pb/^{238}U$	2σ	$^{207}Pb/^{206}Pb$	2σ	Rho	Age (Ma) $^{207}Pb/^{235}U$	2σ	$^{206}Pb/^{238}U$	2σ	$^{207}Pb/^{206}Pb$	2σ	Conc.** (%)	Element oxide concentration (wt %) SiO_2	P_2O_5	CaO	Y_2O_3	La_2O_3	Ce_2O_3	Pr_2O_3	Nd_2O_3	Sm_2O_3	Gd_2O_3	Total PbO	ThO_2	UO_2
BH54-M4-1	Mount	2.29800	0.04000	0.20770	0.00380	0.08030	0.00130	0.47733	1210	12	1216	21	1197	33	102	0.38	29.31	1.02	1.49	15.10	28.12	2.93	11.75	1.96	1.49	0.32	5.95	0.19
BH54-M4-2	Mount	2.25700	0.03700	0.20610	0.00350	0.07960	0.00110	0.57985	1199	11	1208	18	1181	28	102	1.15	28.24	1.70	1.56	13.61	24.83	2.59	10.74	1.85	1.45	0.58	11.46	0.25
BH54-M5-1	Mount	2.32700	0.03200	0.20750	0.00350	0.08128	0.00099	0.56507	1219.3	9.7	1215	19	1223	24	99	0.15	29.74	1.64	1.56	14.28	26.63	2.82	11.34	1.98	1.50	0.41	7.68	0.26
BH54-M5-2	Mount	2.32800	0.03200	0.20810	0.00350	0.08120	0.00100	0.52878	1219.8	9.8	1218	18	1220	25	100	0.24	29.53	1.63	1.58	14.83	26.20	2.65	10.78	1.81	1.40	0.47	8.60	0.27
BH54-M5-3	Mount	2.28800	0.03100	0.20510	0.00330	0.08104	0.00089	0.54871	1207.5	9.7	1202	17	1218	22	99	0.49	29.30	1.89	1.54	13.59	25.51	2.76	11.20	1.99	1.47	0.50	9.49	0.27
BH54-M6-1	Mount	2.37100	0.03900	0.20810	0.00360	0.08280	0.00130	0.54423	1234	12	1218	19	1256	30	97	0.67	29.07	1.24	2.03	14.46	26.57	2.86	11.93	2.06	1.63	0.35	6.99	0.14
BH54-M7-1	Mount	2.29600	0.04100	0.20790	0.00380	0.08020	0.00130	0.50705	1209	12	1217	20	1199	31	102	0.47	29.04	0.41	0.85	15.48	30.40	3.26	13.19	2.02	1.23	0.19	3.24	0.23
BH54-M7-2	Mount	2.23600	0.03400	0.20220	0.00380	0.08010	0.00097	0.67987	1191	11	1187	20	1195	24	99	-0.02	29.94	0.43	1.41	15.78	30.95	3.30	13.15	2.30	1.63	0.13	0.53	0.47
BH54-M7-3	Mount	2.29100	0.03300	0.20510	0.00340	0.08105	0.00098	0.61742	1208	10	1202	18	1222	23	98	-0.01	30.01	0.56	1.33	16.73	30.48	3.28	12.75	2.20	1.64	0.11	0.51	0.40
BH54-M7-4	Mount	2.31700	0.04300	0.20460	0.00350	0.08230	0.00160	0.31593	1215	13	1200	18	1239	38	97	0.34	29.34	1.13	1.47	14.86	27.47	2.91	11.71	2.07	1.64	0.34	6.62	0.11
BH54-M8-1	Mount	2.37300	0.06400	0.21020	0.00430	0.08110	0.00200	0.35352	1230	19	1229	23	1218	53	101	0.68	28.90	0.98	1.62	14.97	27.61	2.94	11.90	1.92	1.48	0.32	6.59	0.06
BH54-M8-2	Mount	2.16900	0.07200	0.20220	0.00550	0.07800	0.00290	0.25497	1166	23	1186	29	1110	73	107	1.06	27.99	0.33	1.10	15.09	28.56	3.04	12.22	2.03	1.45	0.32	6.78	0.04
BH54-M9-1	Mount	2.34600	0.03800	0.20910	0.00380	0.08110	0.00110	0.61755	1225	12	1226	19	1218	26	101	0.89	28.46	1.37	1.26	13.85	26.07	2.80	11.10	2.02	1.60	0.50	9.91	0.15
BH54-M9-2	Mount	2.35900	0.05000	0.21130	0.00350	0.08050	0.00140	0.48553	1228	15	1235	19	1203	37	103	0.77	28.50	1.20	1.17	14.01	26.32	2.79	11.19	2.06	1.65	0.48	9.76	0.11
BH54-M10-1	Mount	2.30900	0.04000	0.20670	0.00350	0.08100	0.00140	0.42274	1213	12	1211	19	1211	34	100	0.44	29.51	1.29	2.62	14.23	27.04	2.89	11.75	1.85	1.38	0.33	6.52	0.16
BH54-M10-2	Mount	2.16900	0.05700	0.19510	0.00440	0.08030	0.00180	0.52985	1169	18	1148	24	1194	44	96	0.93	28.59	0.93	2.04	14.43	27.20	2.94	11.94	1.92	1.44	0.34	7.21	0.10
BH54-M111-1	Mount	2.31200	0.05400	0.20650	0.00340	0.08150	0.00200	0.21349	1215	17	1210	18	1214	48	100	0.39	29.27	0.87	1.86	15.23	27.84	2.93	11.63	2.04	1.60	0.29	5.99	0.06
BH54-M111-2	Mount	2.39700	0.05900	0.21430	0.00430	0.08070	0.00180	0.41411	1238	18	1251	23	1206	47	104	0.43	29.24	0.92	1.83	14.91	27.94	2.95	11.71	2.04	1.63	0.30	6.03	0.07
BH54-M111-3	Mount	2.33200	0.03900	0.21070	0.00370	0.08010	0.00120	0.57854	1221	12	1232	20	1194	28	103	0.32	29.57	1.64	1.49	14.85	26.73	2.77	11.21	1.87	1.40	0.41	7.49	0.25
BH54-M111-4	Mount	2.22500	0.05800	0.20280	0.00490	0.07900	0.00180	0.54797	1187	18	1190	26	1163	47	102	0.61	29.07	0.93	1.92	14.93	27.80	2.92	11.92	2.05	1.55	0.28	5.91	0.10
BH54-M12-1	Mount	2.30100	0.03700	0.20730	0.00340	0.08020	0.00110	0.54599	1211	11	1214	18	1194	27	102	0.43	29.40	1.45	1.40	14.84	27.66	2.87	11.50	1.83	1.26	0.37	6.77	0.22
BH54-M113-1	Mount	2.21800	0.05100	0.20090	0.00390	0.07970	0.00180	0.41650	1185	16	1180	21	1178	43	100	0.66	28.84	0.73	1.67	15.20	27.90	2.93	11.93	2.13	1.54	0.30	6.02	0.15
BH54-M113-2	Mount	2.38400	0.04400	0.21240	0.00370	0.08130	0.00140	0.40569	1236	13	1241	19	1218	35	102	0.38	29.28	0.99	1.99	14.55	27.12	2.92	11.56	2.23	1.85	0.34	6.65	0.13
BH54-M113-3	Mount	2.20100	0.05100	0.20400	0.00370	0.07790	0.00180	0.34865	1178	16	1196	20	1127	45	106	0.74	28.59	0.71	1.14	14.33	28.15	3.03	12.59	2.19	1.51	0.32	6.63	0.08
BH54-M113-4	Mount	2.20400	0.05600	0.19980	0.00400	0.07960	0.00180	0.48208	1178	18	1174	21	1176	43	100	0.84	28.52	0.68	1.47	14.80	27.86	2.96	12.26	2.15	1.53	0.31	6.54	0.07
BH54-M14-1	Mount	2.27800	0.04100	0.20500	0.00340	0.08030	0.00140	0.37391	1207	12	1202	18	1197	35	100	0.50	29.47	1.17	3.17	14.17	26.61	2.82	11.70	2.06	1.68	0.31	6.19	0.15
BH54-M14-2	Mount	2.33600	0.03800	0.21030	0.00340	0.08020	0.00120	0.46558	1222	12	1230	18	1194	30	103	0.32	29.64	1.21	2.59	14.71	26.91	2.88	11.64	2.02	1.64	0.32	5.88	0.24
BH54-M15-1	Mount	2.19900	0.04400	0.20010	0.00370	0.07950	0.00170	0.23853	1179	14	1175	20	1173	44	100	0.88	28.21	0.45	1.00	14.38	28.18	3.07	12.74	2.15	1.38	0.35	7.08	0.13
BH54-M15-2	Mount	2.27700	0.03800	0.20420	0.00350	0.08020	0.00100	0.63174	1203	12	1198	19	1196	26	100	0.50	29.08	1.19	1.25	14.81	27.48	2.86	11.69	1.88	1.28	0.38	7.41	0.20
BH54-M16-1	Mount	2.35700	0.03500	0.20910	0.00330	0.08077	0.00095	0.55162	1228	11	1224	18	1218	25	100	0.25	29.92	1.32	3.72	13.79	26.26	2.83	11.46	2.14	1.68	0.34	6.04	0.24
BH54-M17-2	Mount	2.36300	0.04100	0.21010	0.00360	0.08140	0.00110	0.64825	1232	13	1229	19	1224	27	100	0.44	29.32	1.23	1.49	15.28	27.78	2.90	11.42	1.90	1.29	0.34	6.37	0.22
BH54-M17-3	Mount	2.29300	0.03700	0.20620	0.00350	0.08020	0.00110	0.58643	1208	11	1208	19	1200	25	101	0.66	29.01	1.49	1.59	14.09	27.01	2.82	11.14	1.85	1.31	0.43	8.34	0.25
BH54-M18-1	Mount	2.28200	0.03000	0.20530	0.00350	0.07996	0.00094	0.62302	1207.2	8.9	1203	19	1194	22	101	0.43	29.39	1.56	2.10	13.77	26.05	2.81	11.42	2.05	1.52	0.43	8.22	0.27
BH54-M19-1	Mount	2.08800	0.06900	0.20330	0.00440	0.07510	0.00260	0.25877	1142	24	1192	24	1028	71	116	1.24	27.57	0.38	0.41	13.22	28.08	3.27	14.17	2.11	1.06	0.36	8.10	0.03
BH54-M19-2	Mount	2.26900	0.04800	0.20660	0.00350	0.07940	0.00150	0.48895	1200	15	1211	19	1177	39	103	0.53	29.19	1.12	2.53	14.10	26.87	2.81	11.35	2.04	1.67	0.37	7.27	0.16
BH54-M19-3	Mount	2.33800	0.05000	0.20740	0.00390	0.08130	0.00130	0.57361	1221	15	1214	21	1224	34	99	0.55	29.06	0.94	2.10	14.49	27.47	2.91	11.57	2.02	1.62	0.34	6.82	0.11
BH54-M20-1	Mount	2.20800	0.05800	0.20160	0.00410	0.07900	0.00210	0.24487	1180	18	1183	22	1158	56	102	0.79	28.41	0.42	1.07	14.53	28.70	3.11	12.96	2.10	1.31	0.29	6.25	0.06
BH54-M21-1	Mount	2.30500	0.05000	0.20800	0.00330	0.08020	0.00180	0.28479	1215	15	1218	18	1191	44	102	0.90	28.63	0.64	1.60	15.39	28.82	3.08	12.16	2.02	1.48	0.26	4.84	0.17
BH54-M22-1	Mount	2.26300	0.04600	0.20390	0.00320	0.08050	0.00170	0.23249	1198	14	1196	17	1195	42	100	0.14	29.77	1.24	2.99	13.82	26.53	2.78	11.34	2.00	1.62	0.36	7.27	0.14
BH54-M23-1	Mount	2.25600	0.04100	0.20450	0.00340	0.07960	0.00120	0.52814	1197	13	1199	18	1178	31	102	0.60	28.95	0.61	1.19	16.61	29.66	3.02	11.71	1.71	1.11	0.24	4.41	0.18
BH54-M24-1	Mount	2.12900	0.04300	0.20180	0.00380	0.07650	0.00170	0.27961	1156	14	1184	21	1094	44	108	0.81	28.31	0.57	0.91	14.28	27.95	3.09	12.62	2.16	1.37	0.35	7.47	0.11
BH54-M24-2	Mount	2.31000	0.03000	0.20590	0.00360	0.08100	0.00100	0.46858	1214.1	9.4	1206	19	1219	26	99	0.85	28.65	1.08	1.48	14.96	27.83	2.85	11.32	1.74	1.20	0.39	7.44	0.22
BH54-M24-3	Mount	2.33600	0.04000	0.20710	0.00330	0.08150	0.00120	0.55727	1221	12	1213	17	1226	28	99	0.73	28.89	1.22	1.62	14.77	27.39	2.87	11.36	1.86	1.32	0.39	7.34	0.24
BH54-M25-1	Mount	2.32100	0.03900	0.20820	0.00350	0.08050	0.00100	0.62131	1219	12	1219	19	1207	27	101	0.52	29.02	1.23	1.21	14.39	27.32	2.89	11.68	1.95	1.34	0.41	7.82	0.23

Appendix C. Monazite geochronology and trace element analyses (continued)

Analysis	Textural location	$^{207}Pb/^{235}U$	2σ	$^{206}Pb/^{238}U$	2σ	$^{207}Pb/^{206}Pb$	2σ	Rho	Age (Ma) $^{207}Pb/^{235}U$	2σ	Age (Ma) $^{206}Pb/^{238}U$	2σ	Age (Ma) $^{207}Pb/^{206}Pb$	2σ	Conc.** (%)	Element oxide concentration (wt %) SiO_2	P_2O_5	CaO	Y_2O_3	La_2O_3	Ce_2O_3	Pr_2O_3	Nd_2O_3	Sm_2O_3	Gd_2O_3	Total PbO	ThO_2	UO_2
BH54-M26-1	Mount	2.28900	0.03600	0.20480	0.00340	0.08090	0.00120	0.43660	1207	11	1201	18	1210	30	99	0.34	29.33	1.15	1.29	15.75	28.03	2.84	11.00	1.84	1.28	0.35	6.58	0.22
BH54-M27-1	Mount	2.29400	0.04000	0.20380	0.00340	0.08100	0.00130	0.49193	1208	12	1195	18	1216	31	98	0.41	29.69	1.33	3.56	13.96	26.29	2.79	11.18	2.04	1.72	0.33	6.53	0.17
BH54-M27-2	Mount	2.38000	0.04800	0.21340	0.00420	0.08110	0.00140	0.56339	1238	15	1246	22	1223	33	102	0.31	29.61	1.52	2.53	13.73	26.14	2.79	11.36	2.00	1.55	0.40	7.91	0.15
Sample BH20																												
BH20-M1-1	Mount	2.17400	0.03800	0.19820	0.00330	0.07940	0.00120	0.57736	1171	12	1166	18	1174	29	99	0.74	28.85	1.04	1.77	13.64	27.66	3.01	12.16	2.23	1.64	0.33	6.73	0.19
BH20-M1-2	Mount	2.10400	0.03900	0.19660	0.00330	0.07760	0.00150	0.30132	1148	13	1157	18	1123	38	103	0.97	28.45	0.84	1.60	12.73	27.93	3.13	13.11	2.38	1.75	0.32	6.63	0.16
BH20-M2-2	Mount	2.28200	0.06000	0.20360	0.00410	0.08100	0.00200	0.33747	1202	19	1194	22	1207	51	99	0.93	28.38	1.05	0.93	12.62	27.51	3.09	12.88	2.46	1.77	0.36	7.96	0.05
BH20-M3-1	Mount	2.32900	0.03100	0.20900	0.00330	0.08070	0.00094	0.57745	1220.1	9.6	1223	18	1209	23	101	0.39	29.63	1.02	3.63	13.81	27.22	2.86	11.23	2.21	1.92	0.34	5.26	0.48
BH20-M4-1	Mount	2.34000	0.04300	0.21160	0.00380	0.07970	0.00120	0.46312	1223	13	1237	20	1188	32	104	0.43	29.72	1.25	3.16	14.04	27.53	2.87	11.67	2.17	1.69	0.28	4.94	0.25
BH20-M4-3	Mount	2.13000	0.04700	0.19700	0.00360	0.07870	0.00180	0.28763	1156	15	1159	19	1147	46	101	0.86	28.45	0.67	0.34	12.89	30.25	3.38	13.94	2.43	1.21	0.24	5.23	0.09
BH20-M5-1	Mount	2.20200	0.05800	0.19980	0.00380	0.07950	0.00210	0.32866	1177	18	1176	21	1169	54	101	0.61	29.20	1.03	2.38	13.56	27.46	3.02	12.58	2.33	1.71	0.26	5.78	0.07
BH20-M5-2	Mount	2.15500	0.04800	0.19670	0.00360	0.07930	0.00160	0.41171	1164	15	1157	19	1164	42	99	0.74	29.34	1.32	3.09	14.11	27.21	2.86	11.63	2.12	1.61	0.26	5.63	0.09
BH20-M6-1	Mount	2.24000	0.03700	0.20440	0.00360	0.07880	0.00110	0.55392	1192	12	1198	19	1168	28	103	0.67	28.93	1.03	1.66	13.81	27.53	3.01	12.60	2.17	1.51	0.33	6.54	0.21
BH20-M8-1	Mount	2.34200	0.04000	0.20530	0.00390	0.08290	0.00150	0.42243	1223	12	1203	21	1262	34	95	0.01	31.01	2.12	4.39	13.89	26.82	2.75	10.91	2.06	1.70	0.20	3.98	0.13
BH20-M8-2	Mount	2.14800	0.04400	0.20050	0.00350	0.07730	0.00140	0.40097	1162	14	1177	19	1121	39	105	0.53	29.59	1.00	3.44	13.61	28.29	2.98	12.15	2.22	1.67	0.21	4.18	0.13
BH20-M8-3	Mount	2.29500	0.04000	0.20560	0.00360	0.08050	0.00140	0.37826	1209	12	1205	19	1203	34	100	0.08	31.02	2.17	5.32	12.94	25.78	2.74	11.00	2.16	1.84	0.23	4.55	0.15
BH20-M10-1	Mount	2.27800	0.05100	0.20180	0.00370	0.08190	0.00190	0.32201	1202	16	1184	20	1226	46	97	0.35	30.16	1.64	4.21	13.54	26.26	2.82	11.34	2.09	1.74	0.26	5.50	0.09
BH20-M12-1	Mount	2.22900	0.05500	0.20290	0.00400	0.07910	0.00190	0.31009	1186	18	1190	21	1169	48	102	0.54	29.39	1.05	2.41	14.26	28.25	2.98	11.91	2.27	1.73	0.23	4.87	0.12
BH20-M13-1	Mount	2.32500	0.03800	0.20760	0.00360	0.08090	0.00110	0.57479	1218	11	1218	20	1212	26	100	0.48	29.11	0.73	2.24	14.03	27.89	3.00	12.16	2.23	1.64	0.31	5.97	0.22
BH20-M14-1	Mount	2.19500	0.04700	0.20200	0.00370	0.07850	0.00150	0.43960	1177	15	1186	20	1146	39	103	1.46	27.31	0.74	0.42	10.59	27.05	3.28	14.88	2.61	1.31	0.45	9.76	0.12
BH20-M14-2	Mount	2.19200	0.06800	0.19970	0.00450	0.07910	0.00220	0.41779	1173	21	1173	24	1149	57	102	0.81	28.66	0.95	1.15	13.19	28.19	3.14	13.01	2.45	1.60	0.30	6.49	0.07
BH20-M15-1	Mount	2.32800	0.06000	0.21320	0.00500	0.07860	0.00180	0.44653	1220	19	1245	26	1155	47	108	0.79	28.64	0.90	1.59	12.74	27.72	3.07	13.04	2.37	1.61	0.32	7.13	0.08
BH20-M15-2	Mount	2.22800	0.06300	0.20010	0.00420	0.08040	0.00230	0.30649	1185	20	1175	23	1177	58	100	1.56	26.92	0.68	0.36	11.07	26.60	3.10	13.47	2.34	1.17	0.53	12.15	0.05
BH20-M16-1	Mount	2.32100	0.03200	0.20890	0.00370	0.08023	0.00087	0.63265	1217.7	9.7	1223	19	1199	21	102	0.35	29.69	1.12	3.66	13.72	26.84	2.82	11.28	2.20	1.87	0.35	5.66	0.46
BH20-M16-3	Mount	2.21300	0.03500	0.20130	0.00340	0.07940	0.00120	0.46807	1185	11	1182	18	1175	30	101	0.49	29.44	1.04	2.99	13.88	27.27	2.89	12.13	2.23	1.66	0.29	5.45	0.24
BH20-M18-2	Mount	2.17700	0.05100	0.19860	0.00360	0.07910	0.00180	0.30566	1170	16	1167	20	1155	48	101	1.65	27.23	1.11	0.57	10.04	25.99	3.21	14.71	2.65	1.46	0.48	10.82	0.09
BH20-M19-1	Mount	2.25000	0.05300	0.20120	0.00440	0.08070	0.00170	0.53425	1193	17	1181	24	1198	42	99	1.03	28.70	1.25	2.42	12.94	26.76	2.97	12.27	2.23	1.76	0.33	7.26	0.08
BH20-M20-1	Mount	2.28200	0.03500	0.20630	0.00380	0.07990	0.00098	0.67211	1207	11	1208	20	1193	23	101	0.76	29.07	1.55	3.18	13.10	25.28	2.68	10.85	2.01	1.64	0.47	9.03	0.38
BH20-M20-2	Mount	2.31400	0.05500	0.21100	0.00410	0.07920	0.00190	0.27539	1213	17	1234	22	1156	50	107	3.24	24.42	0.92	0.36	8.88	23.00	2.86	13.17	2.30	1.18	0.84	18.75	0.09
BH20-M21-1	Mount	2.32400	0.04500	0.20820	0.00350	0.08040	0.00140	0.51694	1218	14	1219	19	1206	35	101	0.38	29.87	1.40	3.41	13.83	27.33	2.86	11.41	2.10	1.64	0.27	5.32	0.19
Sample BH32																												
BH32-21-1	m	2.13600	0.06400	0.20220	0.00360	0.07870	0.00160	0.48352	1158	20	1186	19	1150	42	103	1.65	27.16	0.81	1.00	10.50	26.27	3.16	14.54	2.46	1.49	0.49	10.38	0.09
BH32-20-1	m	2.14900	0.05900	0.20170	0.00340	0.07970	0.00160	0.37847	1163	19	1184	18	1176	39	101	1.19	27.72	0.73	0.81	10.75	26.84	3.21	14.80	2.56	1.58	0.46	9.25	0.10
BH32-20-2	m	2.14800	0.06300	0.20520	0.00360	0.07860	0.00180	0.40198	1161	21	1203	19	1144	45	105	1.48	27.33	0.88	0.72	10.26	26.67	3.23	14.79	2.27	1.16	0.50	10.65	0.07
BH32-18-1	m	2.08600	0.08000	0.20010	0.00420	0.07870	0.00270	0.19265	1138	26	1175	22	1124	71	105	4.32	24.83	0.89	0.13	13.44	31.22	3.49	14.97	2.05	0.72	0.18	3.70	0.05
BH32-17-1	m	2.06800	0.07900	0.20170	0.00440	0.07640	0.00250	0.24063	1135	25	1184	24	1098	68	108	5.30	23.57	0.84	0.13	12.60	30.90	3.50	15.43	1.96	0.63	0.22	4.87	0.04
BH32-16-1	m	2.29800	0.09200	0.21930	0.00540	0.07960	0.00310	0.15166	1206	29	1277	29	1149	81	111	1.58	27.14	0.81	0.10	10.82	27.52	3.34	15.32	1.85	0.55	0.48	10.45	0.03
BH32-16-2	m	2.17800	0.06500	0.21020	0.00380	0.07810	0.00170	0.42069	1171	21	1230	20	1139	45	108	1.37	27.51	0.86	0.19	10.75	27.93	3.37	15.01	2.25	0.84	0.45	9.41	0.07
BH32-13-1	m	2.20600	0.05300	0.20920	0.00360	0.07966	0.00098	0.68341	1182	17	1224	19	1184	24	103	0.64	29.13	1.30	1.47	14.54	27.87	2.84	11.86	2.00	1.51	0.38	6.06	0.40
BH32-11-1	m	2.24500	0.09500	0.20960	0.00480	0.08050	0.00280	0.38377	1186	30	1226	26	1179	72	104	9.13	19.39	0.62	0.17	14.40	32.75	3.48	14.49	2.09	0.75	0.13	2.56	0.05
BH32-1-1	m	2.09500	0.07500	0.20040	0.00390	0.07850	0.00240	0.31929	1142	25	1177	21	1149	56	102	1.90	27.40	0.67	0.14	13.29	31.12	3.47	15.08	1.98	0.63	0.20	4.07	0.05
BH32-1-2	m	2.30300	0.06000	0.21310	0.00350	0.08070	0.00140	0.42218	1211	18	1245	19	1205	35	103	1.27	28.27	1.34	1.69	13.28	27.26	2.86	12.21	1.92	1.23	0.43	8.04	0.20
BH32-1-3	m	2.15000	0.15000	0.20890	0.00740	0.07730	0.00500	0.22910	1156	48	1220	40	1040	140	117	22.22	4.51	0.79	0.20	13.53	32.38	3.58	15.32	1.98	0.64	0.26	4.53	0.05

Appendix C. Monazite geochronology and trace element analyses (continued)

Analysis	Textural location	$^{207}Pb/^{235}U$	2σ	$^{206}Pb/^{238}U$	2σ	$^{207}Pb/^{206}Pb$	2σ	Rho	Age (Ma) $^{207}Pb/^{235}U$	2σ	$^{206}Pb/^{238}U$	2σ	$^{207}Pb/^{206}Pb$	2σ	Conc.** (%)	Element oxide concentration (wt %) SiO_2	P_2O_5	CaO	Y_2O_3	La_2O_3	Ce_2O_3	Pr_2O_3	Nd_2O_3	Sm_2O_3	Gd_2O_3	Total PbO	ThO_2	UO_2
BH32-M2-2	Mount	2.17200	0.05100	0.19940	0.00380	0.07900	0.00170	0.46120	1169	16	1171	20	1156	43	101	0.89	28.73	1.18	1.78	14.07	27.73	2.90	11.60	1.99	1.40	0.34	7.27	0.11
BH32-M2-3	Mount	2.09000	0.05400	0.19550	0.00380	0.07810	0.00190	0.20026	1144	18	1151	21	1128	49	102	1.37	27.93	1.13	0.19	13.84	28.77	3.11	12.85	2.13	0.94	0.34	7.33	0.08
BH32-M2-4	Mount	2.22500	0.04300	0.20240	0.00350	0.07990	0.00150	0.38460	1186	14	1188	19	1182	37	101	0.80	28.86	1.27	1.09	14.30	27.87	2.96	12.24	2.17	1.45	0.31	6.59	0.11
BH32-M3-1	Mount	2.26600	0.03300	0.20580	0.00350	0.08019	0.00089	0.71290	1201	10	1208	20	1197	22	101	1.16	28.60	1.60	1.75	14.62	26.98	2.74	10.90	1.84	1.39	0.42	7.66	0.33
BH32-M3-2	Mount	2.18900	0.05700	0.19950	0.00420	0.07990	0.00220	0.25596	1174	18	1172	23	1175	55	100	0.82	29.01	1.40	2.16	14.39	27.32	2.83	11.40	1.84	1.25	0.34	7.15	0.09
BH32-M4-2	Mount	2.24200	0.03300	0.20190	0.00330	0.08061	0.00099	0.56003	1193	10	1185	18	1210	25	98	0.70	29.06	1.28	1.68	14.34	27.76	2.89	11.56	2.10	1.68	0.36	6.17	0.42
BH32-M5-2	Mount	2.19600	0.05600	0.20270	0.00420	0.07900	0.00220	0.21324	1179	19	1189	23	1159	58	103	1.07	27.95	0.99	0.43	12.02	27.51	3.13	13.14	2.36	1.46	0.43	9.43	0.08
BH32-M5-3	Mount	2.15100	0.07900	0.20150	0.00490	0.07820	0.00290	0.29009	1169	26	1182	26	1144	74	103	2.15	26.17	1.00	0.10	10.73	25.77	3.09	13.48	1.87	0.64	0.64	14.32	0.03
BH32-M5-4	Mount	2.10400	0.05600	0.19700	0.00370	0.07800	0.00200	0.44479	1149	19	1159	20	1127	50	103	1.21	27.76	1.08	0.27	12.14	27.55	3.07	12.96	2.17	1.15	0.46	10.11	0.06
BH32-M5-5	Mount	2.16200	0.07600	0.19690	0.00400	0.07950	0.00250	0.44053	1164	24	1158	22	1163	62	100	0.79	28.46	0.81	1.02	13.14	28.04	3.05	13.01	2.16	1.42	0.35	7.69	0.06
BH32-M5-6	Mount	2.12500	0.06000	0.19730	0.00370	0.07840	0.00190	0.53378	1152	19	1160	20	1137	48	102	1.22	27.67	0.95	0.40	11.83	27.36	3.08	13.00	2.27	1.40	0.47	10.28	0.07
BH32-M6-2	Mount	2.43400	0.07600	0.21930	0.00520	0.08110	0.00240	0.43179	1250	22	1277	28	1207	58	106	1.77	26.93	0.71	0.54	11.29	27.82	3.23	14.33	1.85	0.67	0.46	10.34	0.05
BH32-M7-1	Mount	2.23400	0.03800	0.20350	0.00360	0.08020	0.00120	0.56532	1190	12	1194	19	1193	29	100	0.75	29.20	1.31	2.01	14.21	28.43	2.97	11.92	2.09	1.43	0.28	5.21	0.21
BH32-M7-2	Mount	2.20400	0.09800	0.20390	0.00570	0.07960	0.00360	0.25753	1170	31	1195	30	1130	90	106	1.69	27.19	0.87	0.12	11.79	28.35	3.37	14.56	1.81	0.57	0.41	9.24	0.02
BH32-M9-1	Mount	2.26700	0.02900	0.20540	0.00320	0.08052	0.00090	0.56581	1202.5	9.3	1204	17	1209	23	100	0.38	29.64	1.66	1.55	15.39	27.56	2.75	10.68	1.87	1.55	0.37	6.24	0.38
BH32-M10-1	Mount	2.22300	0.03500	0.20270	0.00360	0.08020	0.00100	0.64147	1187	11	1189	19	1196	25	99	0.33	29.64	1.79	1.57	14.28	26.85	2.71	10.96	1.98	1.66	0.43	7.36	0.44
BH32-M10-2	Mount	2.16000	0.07600	0.19960	0.00400	0.07910	0.00270	0.29243	1161	25	1172	21	1143	68	103	1.88	26.64	0.72	0.06	11.38	27.95	3.25	13.96	1.80	0.51	0.51	11.30	0.03
BH32-M11-2	Mount	2.14600	0.03600	0.19880	0.00340	0.07870	0.00120	0.46871	1162	12	1169	18	1168	29	100	0.83	29.08	1.46	2.14	13.96	27.54	2.87	11.52	2.02	1.54	0.34	6.44	0.26
BH32-M12-1	Mount	2.15400	0.07000	0.20060	0.00410	0.07870	0.00250	0.32017	1161	23	1178	22	1135	62	104	0.89	28.61	1.39	0.31	14.12	28.28	3.00	12.27	2.01	1.12	0.35	7.60	0.06
BH32-M13-1	Mount	2.11700	0.04100	0.19500	0.00350	0.07940	0.00130	0.57391	1152	13	1148	19	1172	33	98	0.63	29.19	1.33	1.91	14.53	27.90	2.84	11.18	1.98	1.40	0.33	6.61	0.16
BH32-M13-2	Mount	2.28300	0.03100	0.20520	0.00310	0.08110	0.00100	0.42344	1205.8	9.6	1203	17	1221	26	99	0.27	29.61	1.18	1.51	16.13	28.44	2.87	10.79	1.91	1.55	0.31	5.06	0.37
BH32-M14-1	Mount	2.17000	0.03100	0.20190	0.00360	0.07880	0.00100	0.58760	1170.4	9.8	1185	19	1160	25	102	0.78	29.07	1.35	1.57	14.24	28.28	2.94	11.94	2.08	1.53	0.32	5.57	0.32
BH32-M15-1	Mount	2.08700	0.02800	0.19430	0.00340	0.07885	0.00087	0.62151	1143.6	9.1	1144	18	1164	22	98	0.30	29.99	1.53	2.45	14.86	28.02	2.92	11.32	2.11	1.48	0.31	4.12	0.59
BH32-M15-2	Mount	2.21900	0.08900	0.20260	0.00480	0.08050	0.00330	0.22468	1181	29	1188	26	1175	82	101	2.16	26.46	0.93	0.17	11.43	27.24	3.14	13.86	1.90	0.75	0.52	11.42	0.02
BH32-M15-3	Mount	2.16600	0.07800	0.19900	0.00440	0.07940	0.00290	0.18890	1162	25	1169	24	1148	76	102	1.55	27.24	0.97	0.16	11.30	27.36	3.26	14.30	1.96	0.69	0.49	10.71	0.03
Sample BH74																												
BH74-2-1	m	2.33300	0.06500	0.19020	0.00340	0.08750	0.00180	0.36829	1222	20	1122	18	1364	41	82	2.09	27.41	1.35	1.12	13.65	27.90	2.87	12.35	2.23	1.75	0.33	6.84	0.11
BH74-2-2	m	2.15500	0.06000	0.19620	0.00350	0.07890	0.00170	0.41441	1169	18	1154	19	1155	43	100	0.54	29.44	1.74	1.80	13.14	27.06	2.86	12.23	1.91	1.54	0.36	7.27	0.11
BH74-11-1	m	2.22300	0.06600	0.19830	0.00340	0.08000	0.00170	0.45016	1185	21	1166	19	1182	43	99	0.24	29.28	1.29	0.31	14.10	28.02	2.94	12.43	2.10	1.33	0.36	7.50	0.08
BH74-11-2	m	2.23500	0.05900	0.20360	0.00350	0.07880	0.00160	0.28412	1190	19	1194	19	1152	41	104	0.48	29.02	1.31	0.44	14.02	27.73	2.87	12.44	2.13	1.43	0.37	7.67	0.09
BH74-1-1	m	2.29000	0.14000	0.19960	0.00560	0.08250	0.00500	0.19497	1186	46	1171	30	1130	130	104	0.64	28.34	0.58	0.13	13.65	29.14	3.14	13.48	1.69	0.70	0.38	8.13	0.01
BH74-10-1	g (edge)	2.89200	0.06900	0.23050	0.00350	0.08960	0.00120	0.63218	1379	18	1337	18	1413	25	95	0.52	29.10	1.08	1.45	14.47	28.73	2.93	11.90	1.65	1.02	0.38	6.51	0.26
BH74-10-2	g (edge)	2.73300	0.06600	0.22260	0.00360	0.08820	0.00110	0.66982	1336	18	1295	19	1382	23	94	0.50	29.25	1.18	1.78	14.39	28.41	2.91	11.67	1.80	1.22	0.38	6.16	0.34
BH74-10-3	g (edge)	2.94000	0.07200	0.23180	0.00370	0.09130	0.00120	0.64257	1391	19	1344	20	1448	25	93	0.48	29.15	0.99	1.70	14.59	28.61	2.88	11.67	1.77	1.15	0.39	6.33	0.30
BH74-10-4	g (edge)	2.75600	0.08200	0.23580	0.00460	0.08410	0.00190	0.45007	1343	21	1364	24	1280	45	107	1.24	27.42	0.61	0.30	11.63	28.13	3.30	14.49	1.35	0.48	0.49	10.48	0.08
BH74-9-1	m	2.51000	0.18000	0.22840	0.00870	0.07840	0.00530	0.27050	1255	54	1324	46	1090	150	121	0.67	28.43	0.71	0.09	13.80	29.50	3.14	13.40	1.68	0.67	0.36	7.54	0.01
BH74-9-2	m	2.14500	0.08100	0.19480	0.00460	0.07970	0.00250	0.41998	1158	26	1147	25	1176	59	98	1.22	27.52	0.76	0.42	12.13	27.10	2.99	13.52	2.00	1.08	0.50	10.72	0.05
BH74-9-3	m	2.24100	0.06500	0.20050	0.00360	0.08110	0.00170	0.50246	1194	21	1177	19	1210	41	97	3.97	25.59	1.76	1.25	13.85	28.17	2.92	12.10	2.01	1.38	0.34	6.51	0.15
BH74-5-1	m	2.18200	0.07100	0.19780	0.00470	0.08010	0.00210	0.40104	1173	23	1163	25	1184	53	98	0.65	29.00	1.25	0.67	14.29	28.60	3.01	12.73	2.02	1.21	0.29	6.17	0.08
BH74-5-2	m	2.25400	0.06600	0.20310	0.00430	0.08090	0.00200	0.28670	1196	20	1191	23	1202	49	99	0.70	28.88	1.24	0.47	14.18	28.93	3.02	12.66	1.97	1.12	0.32	6.42	0.09
BH74-4-1	m	2.07800	0.05400	0.19380	0.00320	0.07800	0.00140	0.42714	1140	18	1142	17	1137	34	100	0.42	29.00	1.03	0.52	14.20	28.38	2.91	12.21	2.24	1.60	0.33	7.02	0.13

Appendix C. Monazite geochronology and trace element analyses (continued)

Analysis	Textural location	$^{207}Pb/^{235}U$	2σ	$^{206}Pb/^{238}U$	2σ	$^{207}Pb/^{206}Pb$	2σ	Rho	Age (Ma) $^{207}Pb/^{235}U$	2σ	$^{206}Pb/^{238}U$	2σ	$^{207}Pb/^{206}Pb$	2σ	Conc.** (%)	Element oxide concentration (wt %) SiO_2	P_2O_5	CaO	Y_2O_3	La_2O_3	Ce_2O_3	Pr_2O_3	Nd_2O_3	Sm_2O_3	Gd_2O_3	Total PbO	ThO_2	UO_2
BH74-3-1	m	2.26000	0.07300	0.20080	0.00370	0.08190	0.00210	0.39325	1196	23	1179	20	1224	49	96	5.17	23.70	1.26	0.59	13.87	28.38	2.90	12.37	2.03	1.34	0.37	7.91	0.10
BH74-M1-1	Mount	2.20400	0.05300	0.20290	0.00340	0.07920	0.00190	0.29646	1179	17	1191	18	1158	48	103	0.88	28.14	0.81	0.11	11.60	28.90	3.40	14.54	2.10	0.71	0.40	8.33	0.09
BH74-M1-2	Mount	2.18500	0.05900	0.20270	0.00410	0.07910	0.00190	0.51199	1174	19	1189	22	1153	49	103	0.83	28.28	1.05	0.11	11.51	28.39	3.35	14.28	2.08	0.71	0.43	8.91	0.09
BH74-M2-1	Mount	2.30200	0.03900	0.20920	0.00340	0.08050	0.00140	0.30148	1211	12	1224	18	1198	35	102	0.32	29.87	2.04	0.71	14.11	28.24	2.92	11.77	2.24	1.52	0.30	5.83	0.12
BH74-M2-2	Mount	2.30400	0.03900	0.20790	0.00350	0.08110	0.00130	0.45854	1212	12	1217	19	1215	32	100	0.10	30.16	1.93	1.57	13.62	28.08	2.85	11.36	2.20	1.78	0.32	5.81	0.22
BH74-M2-3	Mount	2.25700	0.05500	0.20830	0.00410	0.07880	0.00160	0.55547	1195	17	1219	22	1153	41	106	0.57	28.87	0.82	0.73	14.39	29.23	3.01	12.31	2.26	1.65	0.28	5.79	0.09
BH74-M2-4	Mount	2.16600	0.04600	0.20330	0.00380	0.07750	0.00190	0.21454	1167	15	1195	21	1121	47	107	0.15	29.28	0.82	0.45	14.62	29.24	3.08	12.18	2.29	1.55	0.29	6.00	0.06
BH74-M3-1	Mount	2.29500	0.04100	0.20780	0.00340	0.08080	0.00130	0.48140	1213	13	1217	18	1212	31	100	0.39	29.79	2.26	1.10	13.43	27.12	2.84	11.27	2.16	1.64	0.38	7.49	0.14
BH74-M3-2	Mount	2.36000	0.04400	0.21100	0.00390	0.08180	0.00150	0.38590	1229	13	1233	21	1235	36	100	0.32	29.83	2.24	1.03	13.66	27.09	2.82	11.18	2.13	1.60	0.39	7.58	0.13
BH74-M3-3	Mount	2.35700	0.04200	0.21210	0.00340	0.08090	0.00120	0.53035	1228	13	1240	18	1211	30	102	0.24	29.81	2.04	1.09	13.52	27.31	2.83	11.19	2.17	1.63	0.38	7.66	0.14
BH74-M4-1	Mount	2.15000	0.11000	0.20800	0.00580	0.07520	0.00380	0.18017	1163	36	1217	31	1050	100	116	2.01	26.18	0.59	0.09	10.95	26.76	3.14	13.72	1.75	0.64	0.62	13.52	0.02
BH74-M4-3	Mount	2.14200	0.04000	0.20140	0.00340	0.07730	0.00140	0.38798	1160	13	1182	18	1122	37	105	0.58	28.92	0.90	0.97	14.15	28.84	3.08	12.19	2.30	1.70	0.29	5.93	0.14
BH74-M5-1	Mount	2.16600	0.03700	0.20400	0.00340	0.07770	0.00130	0.44368	1170	12	1197	18	1135	33	105	0.32	29.26	1.28	0.59	14.33	28.19	2.89	11.68	2.20	1.65	0.35	7.11	0.14
BH74-M6-2	Mount	2.22000	0.04400	0.20430	0.00340	0.07910	0.00160	0.28548	1185	14	1198	18	1159	41	103	0.51	29.08	1.04	0.92	14.09	28.63	3.03	12.37	2.32	1.68	0.30	5.90	0.12
BH74-M7-1	Mount	2.33800	0.05900	0.21110	0.00430	0.08070	0.00210	0.32094	1220	18	1234	23	1194	50	103	0.39	29.58	1.94	0.57	13.87	27.98	2.94	11.76	2.12	1.36	0.35	7.03	0.09
BH74-M7-2	Mount	2.27100	0.04300	0.20580	0.00370	0.08020	0.00140	0.46849	1203	14	1208	20	1197	34	101	0.48	29.53	2.01	0.59	13.91	27.99	2.96	11.64	2.13	1.35	0.34	6.96	0.09
BH74-M7-3	Mount	2.39800	0.05200	0.21150	0.00380	0.08200	0.00160	0.46498	1239	16	1236	20	1240	38	100	0.22	29.71	1.85	0.61	13.77	28.06	2.91	11.75	2.12	1.37	0.35	7.17	0.09
BH74-M8-1	Mount	2.28500	0.04100	0.20500	0.00340	0.08090	0.00140	0.42615	1206	13	1202	18	1209	33	99	0.20	29.94	1.96	1.42	13.58	27.56	2.86	11.33	2.18	1.71	0.35	6.73	0.18
BH74-M8-2	Mount	2.33500	0.03700	0.20940	0.00330	0.08070	0.00120	0.45915	1221	11	1225	18	1212	28	101	0.23	29.86	1.83	1.34	13.61	28.39	2.82	11.20	2.18	1.69	0.33	6.34	0.18
BH74-M8-3	Mount	2.30800	0.04200	0.20510	0.00340	0.08140	0.00120	0.51796	1213	13	1202	18	1223	30	98	0.09	30.16	2.06	1.24	13.79	27.59	2.87	11.57	2.19	1.68	0.32	6.27	0.17
BH74-M9-1	Mount	2.17200	0.04400	0.20010	0.00350	0.07870	0.00140	0.45024	1172	14	1176	19	1159	36	101	0.41	29.04	1.09	0.52	14.17	28.60	2.96	11.87	2.19	1.65	0.34	7.02	0.13
BH74-M9-2	Mount	2.16800	0.03500	0.20210	0.00330	0.07770	0.00140	0.34241	1169	11	1186	18	1127	35	105	0.45	29.10	1.26	0.59	14.18	28.28	2.94	11.80	2.24	1.66	0.34	7.02	0.14
BH74-M10-1	Mount	2.20400	0.03100	0.19990	0.00320	0.07979	0.00093	0.60547	1181.1	9.9	1175	17	1186	23	99	0.20	30.24	1.89	2.75	13.78	27.24	2.81	11.04	2.16	1.87	0.31	5.38	0.32
BH74-M11-1	Mount	2.14400	0.04000	0.20040	0.00330	0.07770	0.00150	0.23268	1161	13	1177	18	1131	38	104	0.38	28.98	0.99	0.49	14.06	28.43	2.91	12.07	2.25	1.65	0.35	7.31	0.13
BH74-M11-2	Mount	2.15300	0.04200	0.20030	0.00350	0.07800	0.00150	0.34284	1166	13	1177	19	1133	39	104	0.43	29.15	1.33	0.62	14.04	28.07	2.88	11.84	2.25	1.75	0.35	7.14	0.15
BH74-M11-3	Mount	2.21500	0.08400	0.20020	0.00490	0.08030	0.00310	0.17977	1177	27	1175	26	1186	82	99	0.97	27.97	0.51	0.07	14.29	29.63	3.19	12.84	1.81	0.77	0.34	7.59	0.03
BH74-M12-1	Mount	2.25800	0.09500	0.21360	0.00490	0.07710	0.00280	0.40927	1193	28	1247	26	1079	75	116	1.86	26.51	0.79	0.13	12.34	26.68	2.94	12.49	1.70	0.74	0.59	13.21	0.03
BH74-M13-1	Mount	2.45700	0.05900	0.21480	0.00410	0.08310	0.00200	0.30535	1256	17	1254	22	1252	47	100	0.22	29.90	1.76	1.11	14.42	28.55	2.94	11.57	2.06	1.49	0.27	5.62	0.08
BH74-M13-2	Mount	2.13100	0.04900	0.19520	0.00360	0.07920	0.00180	0.23799	1156	16	1149	19	1160	46	99	0.56	28.79	0.82	0.55	14.45	28.90	3.09	12.50	2.07	1.48	0.30	6.39	0.09

*Textural location: m, matrix; g, within garnet.

**Concordance value calculated by ($^{206}Pb/^{238}U$ Age)/($^{207}Pb/^{206}Pb$ Age) x 100.

Analyses denoted in blue text in the table occur outside 2σ uncertainty of concordia.

Appendix C. Trace element data from strongly oscillatory-zoned zircon cores (detrital grains), presented for comparison with metamorphic zircon in Fig. 10 in the main text

		Element concentration (ppm)																															
Analysis	Internal morphology*	Ti	2σ	Y	2σ	Nb	2σ	Ce	2σ	Pr	2σ	Nd	2σ	Sm	2σ	Eu	2σ	Gd	2σ	Tb	2σ	Dy	2σ	Ho	2σ	Er	2σ	Tm	2σ	Yb	2σ	Lu	2σ	Hf	2σ
Sample BH32																																			
BH32-4	Zoned core	8.6	6.5	980	100	5.41	0.76	3.4	0.6	0.02	0.03	1.17	0.95	0.64	0.51	0.14	0.09	6.9	1.2	4.1	0.5	63.0	12.0	29.8	2.2	193.0	11.0	52.0	1.9	599.0	41.0	129.0	10.0	12600	1400
BH32-40	Zoned core	10.4	3.5	944	75	2.15	0.38	12.5	1.2	0.21	0.09	2.4	1.5	2.4	1.1	0.68	0.33	17.8	3.7	4.7	0.4	56.9	4.9	29.8	1.7	163.0	13.0	49.0	3.0	544.0	32.0	130.0	11.0	14800	1300
BH32-36	Zoned core	8.4	2.3	940	120	3.9	1	8.3	1.6	0.52	0.12	2.93	0.71	2.31	0.68	0.85	0.21	8.5	1.7	3.7	0.3	54.2	4.5	29.7	4.5	159.0	16.0	48.0	5.6	505.0	64.0	111.0	13.0	12900	1500
BH32-7	Zoned core	8.1	4.4	1207	82	2.58	0.29	16.0	4.4	0.09	0.14	0.4	0.46	2.6	1.3	0.52	0.24	14.9	3.8	6.0	1.2	84.2	9.1	36.7	3.0	222.0	13.0	56.6	3.7	640.0	42.0	130.0	12.0	12270	890
BH32-49	Zoned core	11.1	3.1	987	66	3.5	1	20.7	6.4	3.08	0.81	23.5	7.9	6.1	2	1.10	0.28	11.0	2.8	4.1	0.4	67.0	4.0	31.0	2.6	186.0	14.0	50.1	3.2	590.0	37.0	139.0	12.0	13490	610
BH32-43	Zoned core	10.4	3.4	1040	100	3.19	0.91	6.4	1.2	0.01	0.03	0.93	0.6	3.8	1.4	0.47	0.19	21.5	6.3	6.7	0.9	94.7	6.8	38.1	3.1	194.0	17.0	54.1	6.0	658.0	46.0	156.0	20.0	13650	750
BH32-57	Zoned core	430.0	200.0	769	41	2.53	0.83	5.6	1.2	0.55	0.19	2.6	0.88	3.2	1.4	0.48	0.15	8.4	1.8	2.8	0.5	55.3	4.6	23.7	2.1	116.0	8.0	32.3	2.0	353.0	27.0	77.6	4.6	12900	1100
BH32-32	Zoned core	7.2	3.7	1079	47	1.82	0.52	6.3	1.1	0.19	0.07	1.52	0.46	2.53	0.5	0.44	0.18	9.8	2.6	4.6	0.6	74.8	7.8	36.3	2.2	180.2	9.4	47.4	2.4	443.0	30.0	98.6	6.0	12560	470
BH32-18	Zoned core	10.4	6.1	1551	90	3.01	0.67	3.6	0.5	0.02	0.03	0.75	0.42	1.83	0.54	0.24	0.13	13.2	1.4	6.7	0.8	109.0	13.0	51.0	3.7	260.0	25.0	58.4	4.2	599.0	51.0	122.9	9.8	12650	970
BH32-66	Zoned core	12.1	6.2	1039	55	3.76	0.89	3.8	1.4	0.12	0.14	0.51	0.26	1.28	0.76	0.34	0.15	12.4	2.5	4.8	0.9	70.0	7.6	30.8	2.3	155.0	21.0	42.0	2.3	407.0	43.0	94.7	7.9	12790	740
BH32-53	Zoned core	8.9	3.1	729	62	2.73	0.29	1.4	0.4	0.02	0.03	0.23	0.19	0.63	0.44	0.12	0.07	2.4	1.4	2.1	0.4	43.2	3.1	21.7	1.9	130.1	8.0	35.0	2.1	459.0	49.0	105.5	8.0	12760	970
BH32-67	Zoned core	9.2	3.4	1010	58	3.66	0.4	17.1	2.7	0.56	0.12	4.2	1	3.1	0.63	0.78	0.23	10.1	1.9	3.9	0.8	66.0	11.0	30.3	1.1	172.4	9.6	46.7	2.8	547.0	24.0	125.6	4.7	12900	410
BH32-59	Zoned core	12.1	5.5	1088	61	2.7	1	23.4	5.7	1.95	0.62	10.8	2.4	8.9	2.9	2.35	0.76	19.3	5.3	5.9	0.9	72.5	4.2	35.2	3.2	194.5	9.5	58.8	3.0	673.0	40.0	173.0	12.0	12990	410
BH32-9	Zoned core	13.0	5.5	757	45	1.37	0.45	4.8	1.8	0.22	0.11	2.39	0.53	1.45	0.78	0.35	0.16	6.9	2.4	2.8	0.3	50.8	6.4	21.3	1.5	138.8	6.5	31.3	3.7	392.0	36.0	80.5	6.1	12800	1000
BH32-21	Zoned core	12.5	4.0	1142	50	1.18	0.38	4.6	1.0	0.17	0.05	2.25	0.58	2.8	1.7	1.84	0.34	8.3	1.6	4.5	0.5	78.4	6.5	39.5	1.9	219.0	11.0	58.8	2.5	661.0	56.0	135.8	8.1	13180	920
BH32-54	Zoned core	7.4	2.4	966	43	2.08	0.31	7.2	0.7	0.11	0.08	0.65	0.32	2.1	1.1	0.33	0.15	11.1	3.5	4.8	0.6	75.1	7.7	35.3	3.3	153.0	10.0	36.7	1.3	411.0	20.0	92.5	6.2	12700	1300
BH32-65	Zoned core	2.6	2.1	1263	44	2.2	0.92	5.2	1.0	0.52	0.12	3.72	0.42	2.4	1.2	0.88	0.20	10.1	2.2	4.5	1.0	80.0	2.4	41.5	2.7	252.6	5.1	78.6	5.1	967.0	24.0	224.8	6.8	14200	530
BH32-34	Zoned core	10.2	3.5	2230	120	12.6	1.4	58.8	4.0	0.35	0.16	3.1	1.2	7.93	0.9	0.85	0.29	34.0	2.4	11.9	1.1	145.8	7.7	75.5	3.8	348.0	16.0	89.4	2.9	804.0	33.0	185.0	14.0	11700	730
BH32-77	Zoned core	9.4	4.6	237	21	2.06	0.6	6.6	5.4	0.18	0.18	0.86	0.44	1.8	1	0.25	0.14	2.0	1.0	0.8	0.2	10.8	2.1	6.0	1.0	36.8	3.2	10.6	1.5	127.0	18.0	31.6	2.7	10600	660
BH32-20	Zoned core	8.7	4.1	693	55	3.82	0.57	13.8	0.8	0.04	0.02	1.02	0.58	2.35	0.91	0.19	0.14	12.6	2.3	4.2	0.8	54.6	5.2	22.8	2.8	105.8	6.1	21.3	1.8	194.0	12.0	40.0	2.4	11160	690
Sample BH54																																			
BH54-2	Zoned core	7.9	2.2	1012	35	0.97	0.47	2.7	0.2	0.02	0.02	0.5	0.23	0.91	0.25	0.38	0.12	8.4	1.5	4.4	0.6	76.4	6.5	32.4	2.3	156.0	12.0	42.0	4.7	403.0	53.0	87.0	11.0	13220	580
BH54-87	Zoned core	7.2	3.0	926	65	1.44	0.44	1.7	0.8	0.08	0.04	0.71	0.31	0.56	0.23	0.16	0.10	6.6	1.9	3.4	0.5	56.4	5.6	28.6	2.7	186.0	14.0	55.8	4.9	637.0	52.0	128.0	8.0	13180	820
BH54-8	Zoned core	8.1	3.3	660	100	0.76	0.38	4.8	0.9	0.10	0.10	1.01	0.32	1.61	0.55	0.19	0.17	11.1	1.6	3.1	0.6	56.9	8.3	22.8	3.2	132.0	23.0	29.2	4.6	296.0	31.0	59.5	7.3	11780	880
BH54-62	Zoned core	6.8	2.8	1219	93	1.84	0.33	9.1	1.1	0.63	0.10	3.01	0.97	2.93	0.65	0.91	0.31	10.1	1.6	5.0	0.6	93.0	11.0	40.1	4.3	209.0	16.0	57.1	4.7	607.0	55.0	130.2	7.6	13900	1000
BH54-17	Zoned core	10.0	3.6	1217	87	1.16	0.3	3.9	1.1	0.89	0.46	2.84	0.83	2.7	1	0.59	0.25	7.7	1.3	3.5	0.5	68.3	3.4	37.0	2.7	222.0	18.0	63.2	3.9	717.0	34.0	147.7	7.2	14420	950
BH54-88	Zoned core	6.2	3.7	1123	34	1.1	0.32	1.1	0.3	0.02	0.02	0.33	0.19	0.52	0.4	0.22	0.12	7.0	1.3	3.7	0.5	73.5	4.4	37.1	2.6	220.6	8.9	65.3	2.9	750.0	37.0	150.8	8.6	12580	460
BH54-14	Zoned core	6.7	2.9	970	85	1.38	0.37	18.8	1.6	0.12	0.08	0.8	0.32	2.76	0.58	0.58	0.19	17.4	1.9	6.2	0.8	85.1	5.0	31.4	2.1	150.0	10.0	34.6	1.9	368.0	20.0	75.7	5.3	11760	710
BH54-72	Zoned core	6.8	3.3	1340	120	3.09	0.29	6.1	1.2	0.16	0.09	1.29	0.54	4.3	1.1	0.68	0.34	18.5	2.3	8.3	0.7	124.7	8.8	46.0	4.9	210.0	17.0	47.6	2.9	459.0	32.0	84.1	5.3	12010	790
BH54-81	Zoned core	8.3	3.0	1094	70	1.13	0.25	4.0	0.7	0.10	0.05	0.83	0.37	1.82	0.57	0.44	0.12	11.9	1.5	4.8	0.8	84.0	4.6	32.0	2.8	193.0	17.0	50.8	4.0	594.0	43.0	121.0	12.0	14200	1100
BH54-82	Zoned core	7.0	2.0	1404	95	2.97	0.6	12.9	1.7	0.25	0.11	3.4	1.8	2.56	0.54	0.46	0.14	21.4	1.7	8.4	0.8	119.0	11.0	45.0	3.4	218.0	19.0	51.6	5.6	524.0	17.0	103.4	4.2	12480	670
BH54-36	Zoned core	7.9	1.9	897	64	1.22	0.18	2.6	0.6	0.11	0.04	0.57	0.41	0.55	0.32	0.30	0.15	7.6	1.3	3.8	0.7	69.3	6.9	29.1	2.5	145.6	8.9	38.1	2.4	409.0	25.0	85.3	4.8	12410	760
BH54-18	Zoned core	5.8	4.0	859	57	1.51	0.39	10.5	1.8	1.03	0.27	3.26	0.53	3	1.7	0.69	0.32	9.5	0.9	4.1	0.6	66.4	6.3	26.5	2.0	147.7	8.8	40.1	3.2	475.0	39.0	102.3	7.7	12080	900
BH54-21	Zoned core	6.0	3.3	953	54	0.89	0.4	4.3	0.5	0.09	0.06	0.41	0.22	1.28	0.58	0.26	0.15	9.1	1.4	4.0	0.5	65.9	4.7	29.1	1.8	168.0	11.0	45.0	2.3	487.0	22.0	99.2	5.5	12630	890
BH54-50	Zoned core	6.6	1.9	995	66	1.9	1.1	5.8	1.3	0.28	0.12	1.34	0.34	2.08	0.85	0.50	0.11	11.0	3.3	5.1	0.6	80.0	14.0	30.1	2.5	133.0	15.0	29.7	2.4	287.0	13.0	56.7	4.4	13700	1300
BH54-78	Zoned core	17.5	5.3	1456	83	1.72	0.32	45.4	2.4	0.22	0.08	6	1.1	11.7	1.2	6.63	0.91	54.5	5.9	15.3	0.9	152.0	14.0	47.5	3.6	193.0	15.0	35.5	3.5	319.0	17.0	57.1	3.8	10530	430
BH54-61	Zoned core	6.7	2.4	1570	150	1.98	0.67	12.5	1.5	0.12	0.06	2.41	0.65	6.5	1.7	0.76	0.45	25.8	4.0	8.7	1.8	138.0	12.0	53.9	4.4	257.0	19.0	58.2	4.5	594.0	49.0	126.1	6.1	11430	860
BH54-55	Zoned core	5.9	2.2	493	80	1.32	0.34	8.8	2.5	0.10	0.05	0.94	0.45	2.6	1.2	0.83	0.25	15.8	3.9	4.9	1.0	54.3	9.0	16.1	3.4	64.0	13.0	13.0	3.4	116.0	25.0	21.9	5.0	12760	740
BH54-74	Zoned core	16.3	4.6	1410	190	1.91	0.45	67.1	8.3	1.14	0.34	17.7	5.6	28.1	6.2	10.60	2.50	98.0	20.0	20.2	3.2	176.0	25.0	45.9	6.2	179.0	23.0	33.9	2.9	281.0	25.0	53.8	5.0	11510	360
BH54-47	Zoned core	7.6	4.5	1450	160	2.3	0.42	9.7	1.2	0.40	0.09	2.38	0.68	7.3	2.8	0.38	0.10	26.0	7.7	8.6	2.0	116.0	19.0	50.5	7.3	236.0	23.0	55.2	4.5	536.0	42.0	117.0	12.0	11520	870

Appendix C. Detrital zircon trace element data (continued)

		Element concentration (ppm)																													
Analysis	Internal morphology*	Ti	2σ	Y	2σ	Nb	2σ	Ce	2σ	Pr	2σ	Nd	2σ	Sm	2σ	Eu	2σ	Gd	2σ	Tb	2σ	Dy	2σ	Ho	2σ	Er	2σ	Tm	2σ	Yb	2σ	Lu	2σ	Hf	2σ
BH54-86	Zoned core	10.5	2.8	769	57	1.34	0.52	59.8	3.9	0.13	0.06	4.56	0.87	5.3	1.3	1.96	0.28	26.2	3.2	6.9	0.4	77.1	4.9	24.7	1.9	117.3	9.9	26.1	2.1	272.0	29.0	54.1	4.1	7900	530
BH54-27	Zoned core	7.6	2.7	922	71	2.34	0.88	29.7	2.7	0.17	0.08	1.81	0.54	5.1	1.4	2.69	0.51	29.3	4.1	7.7	0.8	91.0	8.1	30.6	3.0	130.0	14.0	26.1	2.5	240.0	19.0	51.2	5.9	11680	890
BH54-34	Zoned core	8.9	3.0	3440	210	2.11	0.57	3.0	1.3	0.24	0.21	1.47	0.6	3.6	1.1	0.33	0.14	37.9	2.6	16.5	1.2	273.0	18.0	116.8	5.8	563.0	31.0	131.2	7.2	1180.0	65.0	248.0	13.0	12510	690
BH54-63	Zoned core	7.1	2.7	1430	100	1.13	0.32	11.9	1.3	0.31	0.08	3.32	0.85	7.3	1.4	0.77	0.13	28.9	2.0	9.7	0.6	131.8	7.5	48.2	3.7	223.0	10.0	48.8	1.9	467.0	32.0	96.4	5.6	11350	590
BH54-57	Zoned core	4.3	3.1	449	37	0.59	0.19	24.3	1.4	0.24	0.09	4.9	1.3	12.6	2.5	4.73	0.97	33.9	4.0	6.6	1.0	54.1	7.2	16.5	1.6	67.5	5.8	13.7	1.4	120.0	10.0	22.2	1.8	9840	520
BH54-19	Zoned core	6.5	2.1	757	68	3.93	0.8	21.6	4.3	0.95	0.54	4.4	2.8	2.8	1.1	1.12	0.57	8.7	1.9	3.3	0.5	56.9	2.5	23.8	2.0	133.6	9.0	36.1	3.7	375.0	21.0	79.7	6.1	11470	710
BH54-42	Zoned core	3.9	1.4	963	97	1.16	0.41	6.8	1.4	0.20	0.15	0.73	0.35	1.65	0.72	0.24	0.10	7.6	1.7	2.9	0.4	66.1	7.9	31.7	2.7	192.0	17.0	54.2	3.7	598.0	38.0	129.5	9.8	11650	900
BH54-59	Zoned core	10.3	2.9	1550	110	6.4	1.5	42.5	5.0	0.15	0.07	2.28	0.68	6.4	1.6	1.25	0.13	26.3	4.5	9.4	1.0	125.0	11.0	50.2	4.2	249.0	18.0	54.7	4.0	533.0	26.0	118.8	9.5	11190	680
BH54-43	Zoned core	6.1	2.1	1811	99	1.43	0.33	7.5	0.6	0.15	0.06	2.48	0.7	8.43	0.79	0.92	0.16	32.7	3.2	12.2	1.2	159.0	13.0	61.0	2.4	285.0	15.0	62.1	3.8	590.0	38.0	116.2	6.1	9950	370
BH54-10	Zoned core	11.0	4.0	1660	81	6.6	0.55	25.7	2.6	0.33	0.13	3.13	0.89	6.4	1.3	0.44	0.14	30.5	3.9	10.4	0.9	141.0	12.0	55.0	4.1	264.0	27.0	62.7	5.1	604.0	70.0	129.0	16.0	10600	1000
BH54-22	Zoned core	7.7	2.7	1290	95	4.3	1.1	40.9	4.2	0.82	0.76	2.6	1.4	4.6	0.73	1.03	0.22	22.9	2.4	6.9	0.7	99.7	8.5	42.3	3.9	209.0	18.0	51.6	5.4	524.0	32.0	103.3	7.7	11020	780
BH54-45	Zoned core	17.7	5.2	3650	290	15.8	1.7	93.5	6.3	0.60	0.22	6.01	0.95	21.3	3.5	1.97	0.43	75.5	8.8	25.2	2.0	329.0	11.0	121.4	8.1	551.0	23.0	114.3	6.4	1031.0	67.0	197.0	14.0	10490	680
BH54-80	Zoned core	4.6	3.2	801	99	1.09	0.39	7.4	0.7	0.19	0.14	2.97	0.93	5.8	1.6	0.22	0.17	27.6	3.9	7.8	0.9	94.7	8.8	27.6	3.2	108.0	12.0	23.6	2.1	201.0	17.0	35.8	4.1	10810	420
BH54-70	Zoned core	7.1	2.7	598	31	0.92	0.23	49.3	4.6	1.96	0.30	12.8	2.3	7.8	2.1	2.10	0.48	19.1	3.7	4.7	0.3	56.8	3.5	19.3	1.8	97.2	8.9	24.7	1.9	266.0	19.0	57.0	4.0	10280	670
BH54-69	Zoned core	4.5	2.3	645	47	2.26	0.38	14.9	2.4	0.21	0.07	2.71	0.5	3.11	0.97	0.39	0.19	12.4	1.8	4.0	0.6	51.2	5.0	19.5	1.3	96.9	8.9	22.3	3.2	210.0	28.0	42.0	4.5	12480	820
BH54-51	Zoned core	5.4	3.4	37	5	0.78	0.29	11.4	1.2	0.09	0.08	0.64	0.33	1.9	1.2	0.61	0.28	2.4	0.8	0.6	0.3	4.1	0.8	1.4	0.3	4.8	1.2	1.0	0.3	11.3	2.8	2.6	0.6	9990	570
BH54-25	Zoned core	23.5	3.1	2860	170	15.3	1.4	134.6	7.6	3.07	0.52	19	2.2	27.1	3.5	13.27	0.88	88.7	6.1	23.2	1.9	293.0	14.0	97.7	5.1	422.0	27.0	88.8	6.5	790.0	45.0	162.0	12.0	9630	640
BH54-58	Zoned core	10.6	6.3	1230	160	2.06	0.72	57.6	9.0	0.23	0.12	3.27	0.76	9.6	1.6	2.46	0.66	29.0	5.3	7.5	0.9	102.0	10.0	36.7	3.2	163.0	18.0	36.0	3.2	348.0	29.0	76.1	2.9	11090	620
BH54-60	Zoned core	10.2	4.2	1750	100	2.23	0.67	6.2	1.1	0.04	0.05	1.06	0.75	3.7	1.2	0.80	0.26	25.6	3.6	10.2	1.2	142.0	8.2	59.1	4.3	287.0	18.0	67.3	4.1	638.0	32.0	130.5	8.0	12800	690
BH54-52	Zoned core	11.5	6.2	1570	100	3.51	0.95	88.0	12.0	11.10	1.70	71	14	55.6	8.5	4.61	0.67	41.3	3.8	10.6	1.0	126.3	8.4	53.1	3.5	251.0	15.0	59.2	3.1	601.0	36.0	124.6	8.5	10980	620
BH54-56	Zoned core	8.3	3.4	1048	70	0.96	0.3	7.3	0.9	0.10	0.06	0.85	0.29	3.04	0.79	0.47	0.19	16.7	3.1	5.9	0.6	87.8	5.3	34.7	3.1	176.0	13.0	41.0	2.8	413.0	28.0	88.5	6.0	12650	650
BH54-68	Zoned core	9.5	3.2	1302	83	2.57	0.48	64.1	5.9	0.40	0.11	6.05	0.89	11.4	2.1	4.12	0.64	45.5	4.8	11.5	0.9	138.0	10.0	46.2	3.7	202.0	18.0	41.9	3.0	401.0	17.0	77.6	4.4	10600	550
BH54-84	Zoned core	6.9	2.3	1476	96	5.77	0.81	47.3	3.3	0.08	0.05	1.56	0.35	4.13	0.71	1.37	0.26	27.9	3.3	9.9	1.0	123.5	5.2	48.5	3.7	232.0	13.0	51.1	2.1	464.0	22.0	89.0	3.7	11080	790
BH54-3	Zoned core	9.9	5.3	271	51	0.48	0.17	1.3	0.5	0.18	0.15	0.3	0.21	2.19	0.72	0.18	0.08	21.5	2.6	6.9	1.0	51.0	6.3	7.2	1.1	14.7	3.8	1.8	0.8	16.4	8.9	2.9	1.8	12840	790
BH54-38	Zoned core	6.8	3.9	1207	35	4.65	0.62	26.8	1.5	0.22	0.19	1.1	0.41	2.58	0.86	0.17	0.09	18.4	2.1	6.9	1.2	92.7	6.8	40.0	2.4	183.0	18.0	42.1	3.6	386.0	48.0	76.1	4.8	10590	510
BH54-64	Zoned core	5.6	3.3	2360	120	1.28	0.35	1.4	0.2	0.03	0.03	0.73	0.29	3.7	1	0.23	0.10	26.7	2.9	12.5	1.0	194.0	15.0	72.4	4.3	370.0	17.0	83.9	5.2	841.0	56.0	157.7	8.9	13200	1000
BH54-9	Zoned core	7.0	2.2	820	39	4.5	1.1	18.8	3.5	0.82	0.23	3.9	1.2	5.4	1.2	0.42	0.24	16.2	2.4	5.3	0.8	70.9	6.1	26.8	1.5	129.0	3.8	30.7	2.9	312.0	14.0	58.3	3.7	10280	520
BH54-30	Zoned core	7.3	3.9	1110	100	1.2	0.21	3.1	0.4	0.35	0.12	3.79	0.79	6.9	1.2	0.51	0.28	33.9	3.0	10.2	0.8	119.6	8.6	39.4	2.1	167.0	15.0	34.7	2.8	307.0	17.0	60.2	4.8	9460	730
BH54-54	Zoned core	10.5	1.9	1690	100	2.74	0.46	17.6	1.3	0.16	0.08	2.09	0.57	11.7	2.3	0.55	0.19	42.6	7.7	12.1	1.3	135.0	16.0	56.6	8.5	253.0	20.0	48.2	2.5	427.0	38.0	80.3	5.0	11780	690
BH54-6	Zoned core	14.9	9.0	805	37	2.58	0.72	26.9	3.0	0.08	0.08	1.09	0.36	3.1	1	0.84	0.30	17.4	3.3	5.4	1.0	73.0	11.0	27.1	2.6	120.0	15.0	23.7	3.6	239.0	21.0	48.8	4.4	10110	750
BH54-39	Zoned core	10.0	4.0	442	61	2.06	0.95	27.7	3.7	2.29	0.75	8.6	4.1	7.6	1.8	1.13	0.28	9.9	2.9	3.0	0.6	36.9	4.0	13.6	2.8	67.0	12.0	17.3	1.7	177.0	16.0	34.9	4.6	12640	720
BH54-33	Zoned core	9.8	3.6	1460	120	4.7	1.1	9.4	2.2	0.06	0.04	0.88	0.21	2.5	1.1	0.41	0.11	26.7	4.0	8.4	1.1	121.0	13.0	49.6	3.7	214.0	12.0	42.1	3.2	411.0	20.0	77.7	4.0	10800	1400
BH54-85	Zoned core	6.8	4.1	919	99	1.1	0.36	21.3	1.9	0.27	0.10	5.5	1.1	6.8	1.5	2.83	0.52	34.0	6.2	8.9	1.2	93.0	11.0	32.5	3.8	134.0	16.0	26.9	3.9	219.0	25.0	41.0	5.2	7960	660
BH54-46	Zoned core	13.6	4.2	459	36	0.97	0.21	28.8	2.7	0.09	0.06	0.7	0.25	2.4	0.37	0.83	0.15	9.4	1.3	3.0	0.5	37.5	4.2	14.6	1.4	68.0	7.5	16.3	1.3	179.0	13.0	39.9	2.6	11420	490
BH54-79	Zoned core	16.6	7.4	1540	160	5.08	0.86	32.5	2.4	0.12	0.06	0.99	0.44	2.7	1.2	1.60	0.33	22.7	6.4	8.9	1.0	120.0	13.0	48.4	4.5	248.0	22.0	61.3	4.0	626.0	25.0	134.9	8.8	11090	650

Appendix C. Detrital zircon trace element data (continued)

		Element concentration (ppm)																															
Analysis	Internal morphology*	Ti	2σ	Y	2σ	Nb	2σ	Ce	2σ	Pr	2σ	Nd	2σ	Sm	2σ	Eu	2σ	Gd	2σ	Tb	2σ	Dy	2σ	Ho	2σ	Er	2σ	Tm	2σ	Yb	2σ	Lu	2σ	Hf	2σ
Sample BH74																																			
BH74-62	Zoned core	6.2	2.6	1008	68	1.67	0.3	3.6	0.7	0.07	0.04	0.8	0.48	0.84	0.37	0.37	0.12	9.1	1.6	5.8	0.5	83.3	6.1	29.5	2.5	128.6	9.6	30.6	2.3	250.0	22.0	47.5	3.6	13080	560
BH74-27	Zoned core	12.4	2.5	819	56	2.06	0.72	5.6	2.6	0.15	0.12	0.59	0.42	1.26	0.65	0.37	0.15	11.6	2.7	5.6	0.7	67.2	4.2	28.8	1.9	143.0	13.0	32.9	2.4	293.0	24.0	53.3	5.2	12670	500
BH74-45	Zoned core	b.d.l.		882	72	1.56	0.35	4.5	0.8	0.04	0.04	0.25	0.21	1.01	0.31	0.56	0.16	8.6	2.3	5.2	1.1	68.8	8.2	27.3	1.5	130.8	7.3	27.0	1.5	229.0	10.0	44.0	2.0	13120	580
BH74-17	Zoned core	9.3	6.2	860	110	1.47	0.51	7.4	2.0	0.27	0.07	1.61	0.7	0.92	0.53	0.40	0.21	9.8	1.5	4.4	0.5	64.7	8.1	27.1	3.7	118.0	16.0	27.0	4.8	255.0	43.0	46.2	6.5	13160	980
BH74-4	Zoned core	6.9	2.6	1780	180	2.36	0.6	3.6	0.8	0.09	0.11	1.02	0.62	0.72	0.49	0.59	0.19	11.6	2.0	7.6	0.7	120.0	15.0	59.0	4.9	274.0	23.0	60.1	5.5	516.0	43.0	88.1	6.1	12940	970
BH74-55	Zoned core	7.9	2.7	1217	39	1.32	0.37	2.6	0.2	0.00	0.01	0.24	0.19	0.63	0.37	0.27	0.09	7.4	1.4	4.8	0.4	87.4	7.7	39.3	2.4	179.0	10.0	39.9	2.9	346.0	17.0	63.9	3.8	12720	580
BH74-53	Zoned core	8.6	5.1	1483	52	3.64	0.82	25.5	2.3	0.11	0.11	2.39	0.9	4.1	1.5	1.24	0.36	26.9	2.9	9.6	1.4	125.8	7.8	45.8	4.0	214.0	14.0	51.4	3.1	471.0	34.0	96.6	8.9	9170	510
BH74-13	Zoned core	8.2	2.8	2120	180	2.39	0.95	5.5	0.8	0.14	0.05	1.54	0.87	0.69	0.49	0.43	0.18	13.2	3.1	9.3	1.2	150.0	15.0	68.0	8.9	290.0	21.0	64.6	3.5	559.0	38.0	93.6	6.6	12650	950
BH74-56	Zoned core	6.2	5.1	1205	85	1.48	0.27	3.4	1.2	0.03	0.02	0.34	0.37	0.63	0.36	0.40	0.13	7.6	1.6	4.6	0.6	83.4	4.9	38.2	3.0	205.0	11.0	47.7	3.9	416.0	26.0	76.8	5.4	12040	610
BH74-64	Zoned core	7.5	3.8	1203	81	2.82	0.71	8.8	1.0	0.06	0.04	0.54	0.24	1.28	0.52	0.68	0.23	11.9	2.7	6.4	0.7	95.3	7.7	39.2	2.6	181.4	7.6	47.0	3.1	413.0	24.0	80.7	4.1	11250	670
BH74-33	Zoned core	9.0	4.0	1033	50	1.46	0.32	4.1	1.8	0.26	0.28	1.9	1.8	0.49	0.35	0.20	0.11	7.0	2.0	4.2	0.6	72.0	6.6	34.7	3.8	200.0	16.0	40.9	3.7	371.0	46.0	77.8	8.3	12900	1900
BH74-23	Zoned core	12.5	4.8	1310	130	2.85	0.98	33.1	4.2	1.91	0.40	12	2.5	4.9	1.7	1.60	0.29	15.6	3.0	7.7	0.8	97.5	8.3	42.3	4.2	217.0	20.0	56.1	5.0	460.0	41.0	88.0	6.4	12860	860
BH74-14	Zoned core	18.8	4.8	609	51	2.09	0.61	16.0	3.2	1.29	0.28	8.6	1.2	1.6	0.67	1.03	0.43	7.4	2.9	3.4	0.6	39.2	3.4	19.1	1.0	98.0	10.0	26.0	1.7	263.0	29.0	52.3	3.7	13040	730
BH74-88	Zoned core	7.5	4.0	2123	66	3.39	0.29	2.5	0.3	0.01	0.02	0.91	0.79	1.76	0.52	0.57	0.30	16.0	3.5	8.7	1.6	162.0	12.0	71.8	9.5	386.0	23.0	91.7	9.3	908.0	56.0	177.0	14.0	12600	1000
BH74-52	Zoned core	9.8	3.8	772	59	6.7	1.7	52.9	5.1	0.16	0.14	1.32	0.66	1.71	0.5	0.37	0.21	9.7	2.5	3.9	0.6	50.0	5.9	24.0	2.5	129.0	10.0	35.6	2.2	357.0	26.0	89.0	3.8	11010	800
BH74-42	Zoned core	13.1	3.6	2010	220	7	1.2	11.6	1.3	0.06	0.05	2.34	0.77	5.7	1.3	0.79	0.25	37.4	4.3	14.1	1.5	181.0	14.0	74.6	5.9	369.0	24.0	70.4	4.1	624.0	39.0	125.7	8.0	11300	650
BH74-16	Zoned core	9.7	4.5	894	62	3.98	0.33	11.2	1.5	0.11	0.07	0.84	0.41	1.6	0.59	0.36	0.22	15.2	2.3	6.5	1.1	71.4	4.9	30.5	4.7	125.8	9.3	30.0	4.1	279.0	38.0	54.8	6.0	11760	740
BH74-92	Zoned core	10.5	3.4	1644	85	4.5	0.83	22.1	1.3	0.14	0.05	3.4	1.2	5.4	1.3	0.85	0.28	33.4	2.9	11.4	0.7	149.1	8.5	56.8	3.0	288.0	21.0	62.8	3.6	607.0	35.0	119.5	5.9	10050	340
BH74-30	Zoned core	13.7	5.4	857	57	4.8	1.1	13.7	2.0	1.23	0.23	8.3	2.1	3.12	0.86	0.80	0.15	10.0	1.7	4.6	0.6	62.9	6.7	27.7	0.8	159.0	13.0	33.5	2.1	300.0	35.0	61.8	4.7	12880	890
BH74-24	Zoned core	8.8	3.5	780	72	3.75	0.96	5.5	0.9	0.30	0.18	1.89	0.86	1.43	0.4	0.22	0.07	10.2	1.9	4.0	0.7	58.2	3.1	26.2	2.0	137.0	10.0	33.4	3.5	295.0	29.0	59.7	6.5	15500	1400
BH74-50	Zoned core	7.0	2.3	367	29	2.68	0.57	12.0	1.8	0.05	0.04	0.64	0.51	1.17	0.68	0.28	0.10	7.2	1.1	2.3	0.4	29.8	3.3	11.7	1.6	56.9	3.7	13.2	1.9	127.0	14.0	25.1	1.9	11080	900

*All analysed zircon are strongly oscillatory zoned cores.

Appendix D. Zircon and garnet trace element chemistry
Figure 1. Chondrite-normalised zircon and garnet REE plots.
Zircon (left) and garnet (centre and right) from samples BH32, BH54 and BH74. Analyses from sample BH32, BH54 and BH74 are shown in shades of green, red and blue, respectively. On zircon REE plots, zircon trace element analyses corresponding to concordant age data are shown as solid lines; discordant analyses are shown as dashed lines. On garnet REE plots, the position of M–HREE patterns from type-2 garnet in sample BH54 are indicated on the type-1 garnet plots; the position of type-1 garnet BH54 is indicated on the plot of type-2 BH54 garnet, to highlight the shift in REE concentrations.

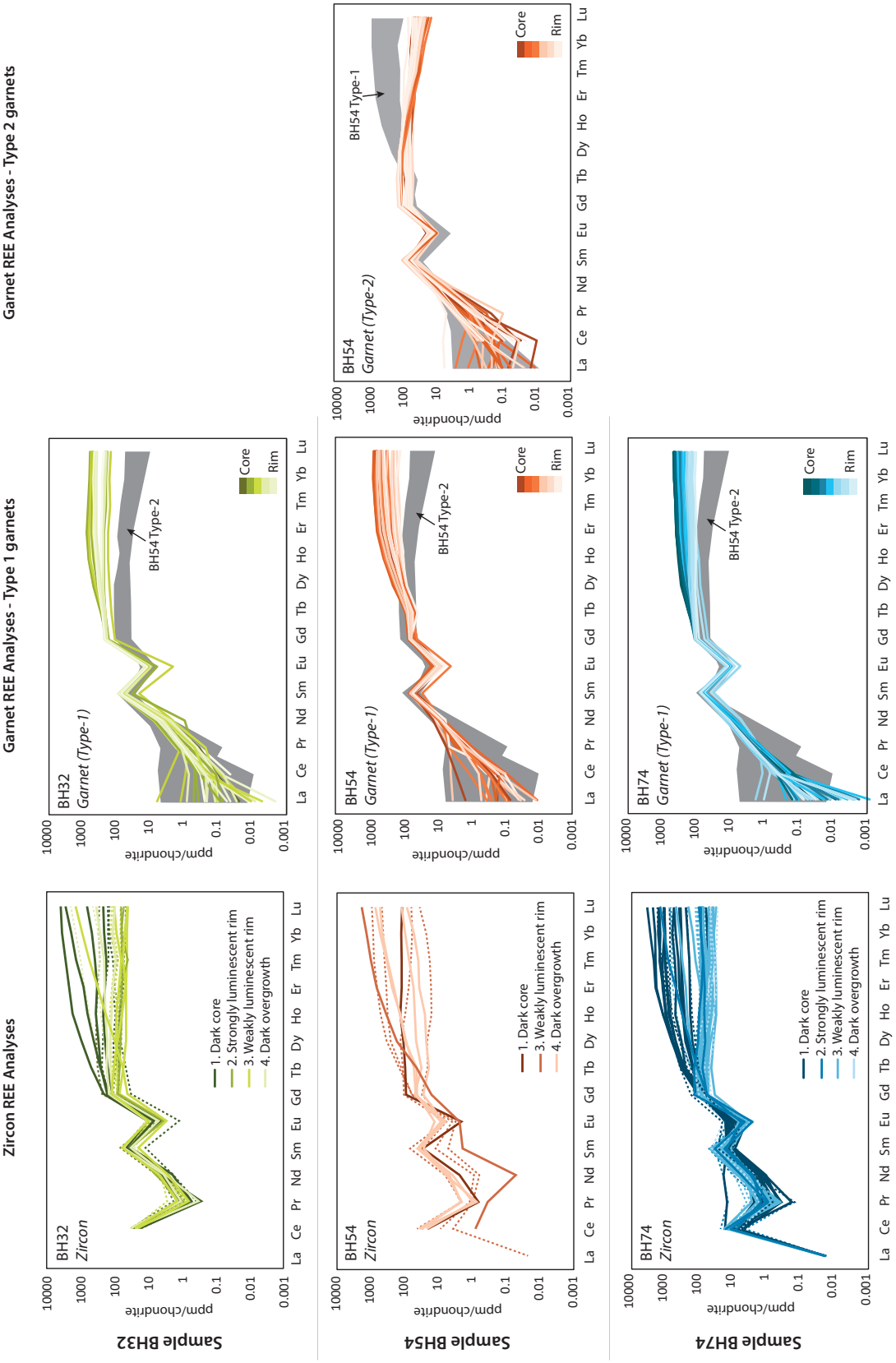

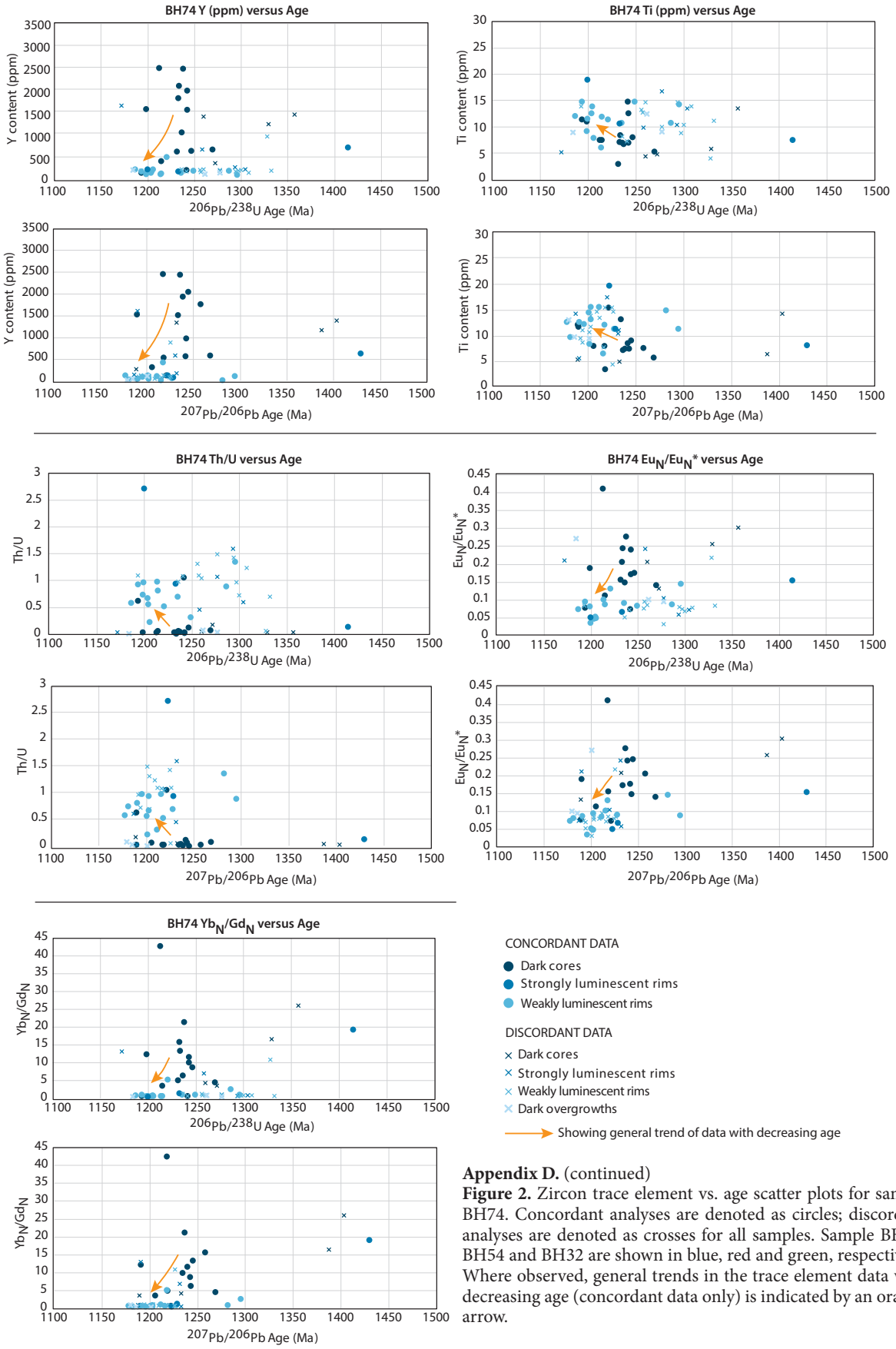

Appendix D. (continued)
Figure 2. Zircon trace element vs. age scatter plots for sample BH74. Concordant analyses are denoted as circles; discordant analyses are denoted as crosses for all samples. Sample BH74, BH54 and BH32 are shown in blue, red and green, respectively. Where observed, general trends in the trace element data with decreasing age (concordant data only) is indicated by an orange arrow.

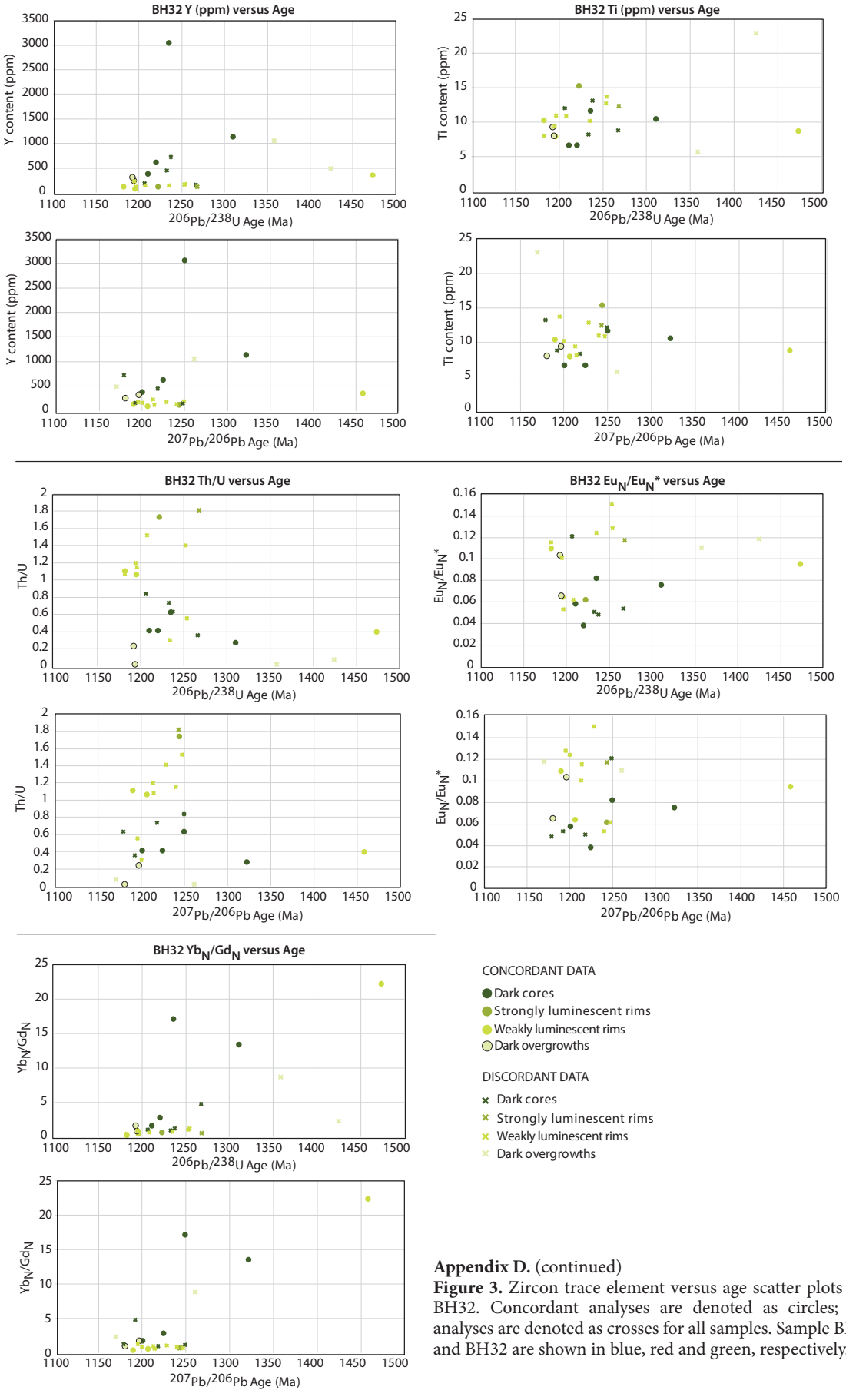

Appendix D. (continued)
Figure 3. Zircon trace element versus age scatter plots for sample BH32. Concordant analyses are denoted as circles; discordant analyses are denoted as crosses for all samples. Sample BH74, BH54 and BH32 are shown in blue, red and green, respectively.

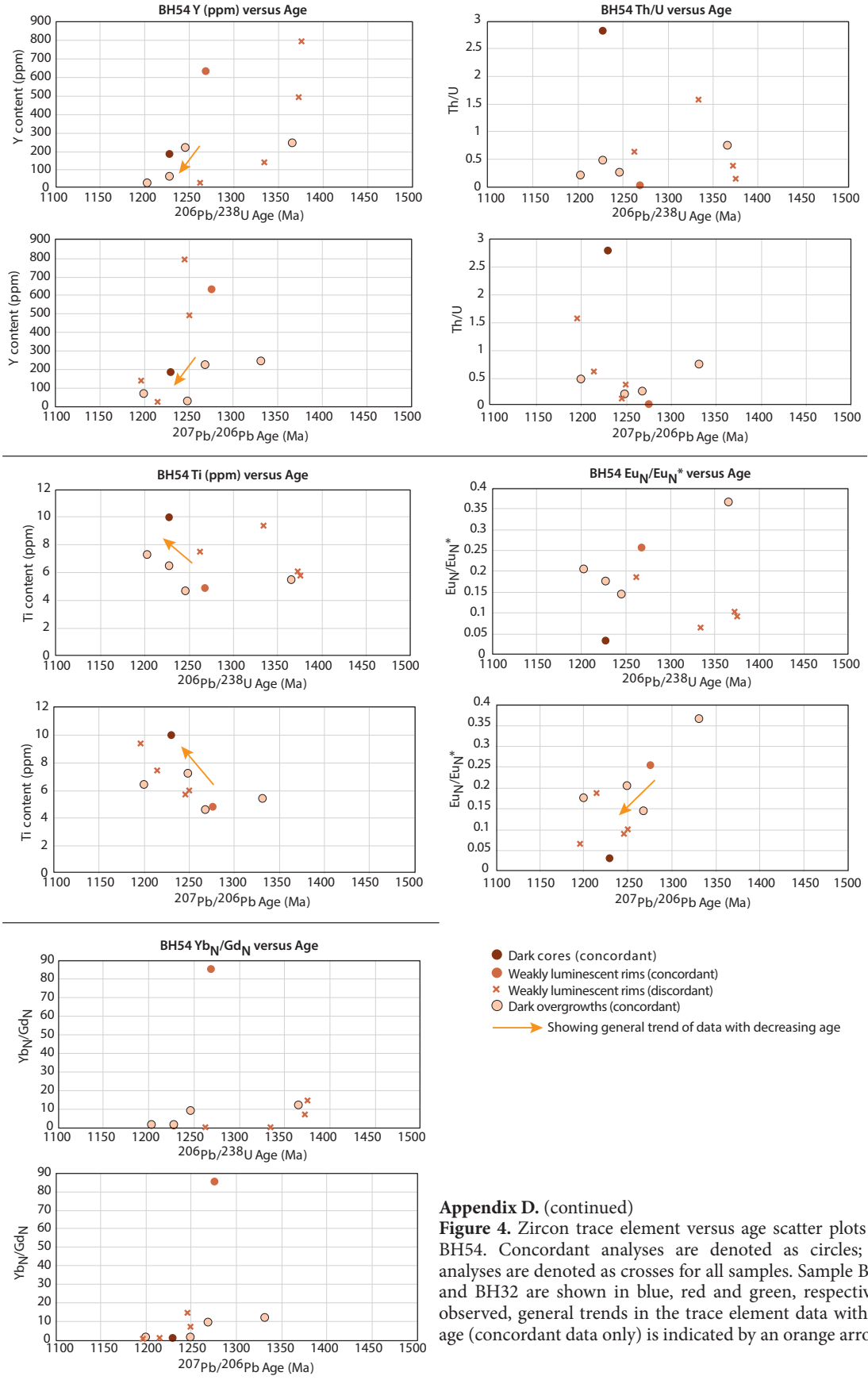

Appendix D. (continued)
Figure 4. Zircon trace element versus age scatter plots for sample BH54. Concordant analyses are denoted as circles; discordant analyses are denoted as crosses for all samples. Sample BH74, BH54 and BH32 are shown in blue, red and green, respectively. Where observed, general trends in the trace element data with decreasing age (concordant data only) is indicated by an orange arrow.

Appendix D. (continued)
Figure 5. Representative garnet REE + Y zoning proles.
Garnet grains shown for each sample correspond with garnet analyses presented as chondrite-normalised M-HREE plots in Figure 1 of this appendix.

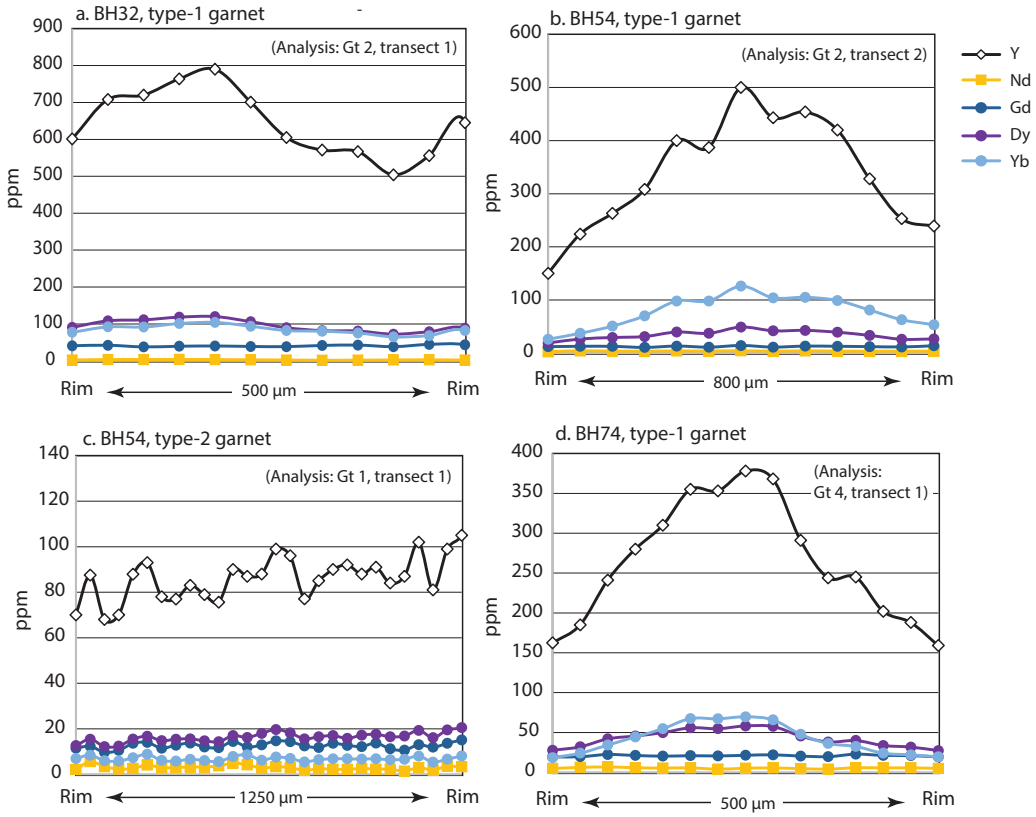

Appendix E. Garnet trace element chemistry

	Elemental concentration (ppm)																													
Analysis	Y	2σ	La	2σ	Ce	2σ	Pr	2σ	Nd	2σ	Sm	2σ	Eu	2σ	Gd	2σ	Tb	2σ	Dy	2σ	Ho	2σ	Er	2σ	Tm	2σ	Yb	2σ	Lu	2σ
Sample BH54																														
Garnet 1, transect 1 (Type-2 garnet)																														
BH54_Gt1-1.d	70.00	32.00	0.00	0.00	0.01	0.03	0.05	0.08	2.09	0.31	5.40	1.60	0.62	0.55	11.50	5.00	1.90	1.50	12.60	6.00	2.70	1.40	8.50	4.20	1.11	0.52	6.90	3.30	1.16	0.45
BH54_Gt1-2.d	87.50	9.60	1.27	0.94	3.60	2.70	0.44	0.27	5.60	1.90	9.40	1.20	0.79	0.15	12.30	1.50	2.32	0.36	15.40	1.70	3.49	0.48	9.60	1.20	1.32	0.17	8.40	1.30	1.19	0.18
BH54_Gt1-3.d	68.00	14.00	0.00	0.00	0.08	0.05	0.11	0.04	3.38	0.93	7.20	1.70	0.48	0.12	9.70	2.20	1.65	0.31	12.20	2.60	2.64	0.47	7.30	1.50	0.99	0.19	6.00	1.40	0.84	0.22
BH54_Gt1-4.d	70.00	13.00	0.04	0.03	0.13	0.10	0.05	0.04	2.30	0.76	5.70	1.20	0.48	0.16	10.50	2.40	1.81	0.42	12.40	2.30	2.61	0.39	7.50	1.40	1.00	0.17	5.80	1.10	0.91	0.15
BH54_Gt1-5.d	87.90	9.10	0.00	0.00	0.09	0.05	0.00	0.00	2.57	0.64	7.20	1.80	0.79	0.11	13.60	2.10	2.24	0.47	15.50	2.30	3.31	0.27	9.70	1.90	1.31	0.29	7.30	1.30	0.94	0.17
BH54_Gt1-6.d	93.00	19.00	0.10	0.07	0.23	0.12	0.11	0.07	4.10	1.10	10.80	2.00	0.69	0.32	14.00	2.50	2.59	0.49	16.70	4.30	3.42	0.66	10.40	1.20	1.30	0.42	8.80	2.00	1.07	0.15
BH54_Gt1-7.d	78.00	13.00	0.00	0.00	0.08	0.05	0.09	0.03	2.87	0.71	8.70	1.50	0.71	0.21	11.50	1.90	2.25	0.34	14.80	2.60	2.92	0.51	7.50	1.60	0.94	0.22	6.10	1.30	0.85	0.14
BH54_Gt1-8.d	77.00	14.00	0.00	0.00	0.10	0.07	0.07	0.03	2.99	0.44	8.50	1.50	0.56	0.23	12.80	2.40	2.04	0.44	15.40	3.20	2.88	0.62	6.50	1.60	1.03	0.32	5.80	1.50	0.70	0.19
BH54_Gt1-9.d	83.00	12.00	0.00	0.01	0.08	0.06	0.10	0.04	3.20	0.54	10.30	2.10	0.80	0.14	13.70	2.10	2.10	0.29	15.60	2.10	2.98	0.39	8.00	1.30	1.08	0.16	6.60	1.10	0.92	0.17
BH54_Gt1-10.d	78.90	9.50	0.00	0.00	0.06	0.02	0.09	0.04	3.21	0.59	9.70	1.50	0.59	0.11	12.00	1.40	2.01	0.24	14.70	1.90	2.83	0.35	8.20	1.10	0.96	0.12	6.03	0.60	0.94	0.14
BH54_Gt1-11.d	75.60	8.50	0.00	0.00	0.06	0.04	0.13	0.07	3.71	0.97	7.07	0.88	0.58	0.17	11.70	2.00	2.09	0.40	14.30	1.90	2.79	0.35	8.10	1.50	1.10	0.15	5.60	1.00	0.94	0.18
BH54_Gt1-12.d	90.00	11.00	0.03	0.02	0.12	0.04	0.13	0.04	4.90	1.10	8.60	1.50	0.76	0.11	14.40	2.30	2.56	0.43	17.00	2.00	3.55	0.43	10.00	1.50	1.26	0.17	7.80	1.20	1.05	0.24
BH54_Gt1-13.d	87.00	61.00	0.00	0.00	0.02	0.04	0.10	0.07	4.20	2.60	9.80	6.50	1.03	0.81	12.00	9.70	2.30	1.90	16.20	9.70	3.00	2.00	9.40	5.90	1.40	1.20	8.60	8.10	1.08	0.71
BH54_Gt1-14.d	88.00	12.00	0.03	0.06	0.15	0.16	0.05	0.04	2.75	0.84	7.50	2.70	0.74	0.13	12.90	1.00	2.25	0.52	18.00	3.90	3.08	0.40	8.90	1.40	1.18	0.41	6.20	2.10	0.96	0.14
BH54_Gt1-15.d	99.00	11.00	0.00	0.00	0.06	0.03	0.04	0.02	3.32	0.47	9.50	1.60	0.88	0.16	14.70	1.90	2.59	0.30	19.70	2.30	3.61	0.42	9.80	1.40	1.20	0.14	7.60	1.10	0.90	0.14
BH54_Gt1-16.d	96.00	14.00	0.00	0.01	0.01	0.01	0.05	0.03	2.95	0.73	9.30	1.50	0.79	0.22	14.30	2.30	2.88	0.50	18.20	2.80	3.79	0.60	9.60	1.40	1.25	0.23	7.00	1.10	0.93	0.11
BH54_Gt1-17.d	77.10	9.20	0.02	0.01	0.02	0.01	0.02	0.01	1.74	0.42	8.30	1.30	0.67	0.13	12.50	1.60	2.18	0.28	15.60	2.50	2.80	0.30	7.60	1.00	0.98	0.14	5.47	0.59	0.85	0.14
BH54_Gt1-18.d	85.00	12.00	0.11	0.07	0.44	0.35	0.08	0.06	2.43	0.84	8.40	1.20	0.74	0.17	11.80	2.20	2.47	0.38	16.50	2.40	3.02	0.36	8.20	1.40	1.14	0.23	6.44	0.97	0.89	0.19
BH54_Gt1-19.d	90.00	13.00	0.05	0.06	0.08	0.07	0.03	0.02	2.21	0.40	9.40	1.50	0.78	0.17	13.60	2.50	2.49	0.35	17.00	2.60	3.05	0.39	8.50	1.40	1.15	0.19	6.80	1.20	0.85	0.14
BH54_Gt1-20.d	92.00	13.00	0.06	0.08	0.08	0.12	0.09	0.09	2.18	0.66	8.50	1.70	0.93	0.15	12.70	2.80	2.43	0.53	15.80	2.90	4.05	0.71	9.70	2.70	1.37	0.42	6.80	1.60	0.86	0.24
BH54_Gt1-21.d	88.00	16.00	0.01	0.02	0.13	0.07	0.06	0.03	2.54	0.49	9.70	2.00	0.81	0.23	12.20	2.80	2.52	0.50	17.20	3.30	3.48	0.67	8.70	1.60	1.21	0.24	6.70	1.50	0.93	0.20
BH54_Gt1-22.d	91.00	10.00	0.26	0.28	0.33	0.31	0.09	0.04	2.28	0.38	10.24	0.97	0.84	0.13	13.70	1.70	2.32	0.28	17.60	2.20	3.56	0.48	9.40	1.20	1.15	0.12	6.82	0.86	0.94	0.12
BH54_Gt1-23.d	84.00	16.00	0.60	1.10	1.00	1.90	0.08	0.11	2.24	0.78	8.00	2.50	0.67	0.24	11.20	3.20	2.38	0.45	16.50	3.00	3.56	0.68	10.20	2.30	1.20	0.33	6.40	1.50	0.92	0.32
BH54_Gt1-24.d	87.00	16.00	0.05	0.05	0.13	0.12	0.01	0.01	1.42	0.63	7.90	1.50	0.65	0.22	10.60	2.10	2.16	0.46	16.80	3.40	3.62	0.65	9.50	2.00	1.24	0.21	6.60	1.30	0.78	0.14
BH54_Gt1-25.d	102.00	13.00	0.03	0.02	0.14	0.05	0.07	0.04	2.94	0.60	10.10	1.80	0.74	0.17	13.00	1.60	2.44	0.31	19.30	2.40	3.95	0.53	10.40	1.40	1.47	0.27	8.00	1.20	1.10	0.25
BH54_Gt1-26.d	81.00	14.00	0.01	0.01	0.02	0.02	0.05	0.02	1.86	0.34	7.10	1.70	0.64	0.13	11.90	1.70	2.17	0.34	16.10	3.30	3.45	0.69	8.30	1.30	1.09	0.19	5.37	0.70	0.74	0.20
BH54_Gt1-27.d	99.00	26.00	0.00	0.00	0.05	0.04	0.06	0.04	3.60	1.70	8.80	2.10	0.64	0.20	13.60	3.20	2.60	0.73	19.50	4.40	3.90	1.00	9.80	2.30	1.28	0.29	6.70	1.40	0.90	0.25
BH54_Gt1-28.d	105.00	17.00	0.00	0.00	0.03	0.03	0.07	0.05	3.35	0.78	9.60	2.30	0.69	0.17	15.10	2.80	2.52	0.50	20.50	4.20	4.26	0.79	12.40	2.00	1.49	0.31	8.10	1.60	1.14	0.23
BH54_Gt1-29.d	121.10	2.80	0.00	0.00	0.08	0.00	0.22	0.09	5.00	2.20	10.80	2.20	0.80	0.15	16.30	2.80	2.73	0.74	23.70	4.20	5.27	0.72	14.40	2.20	2.14	0.08	10.01	0.46	1.61	0.37
BH54_Gt1-31.d	84.00	14.00	0.00	0.00	0.28	0.10	0.22	0.07	6.00	1.20	9.50	2.30	0.95	0.16	12.30	2.40	2.22	0.35	17.20	2.80	3.80	0.74	10.80	1.90	1.33	0.21	6.70	1.00	1.01	0.20
BH54_Gt1-32.d	74.00	14.00	0.00	0.00	0.19	0.07	0.21	0.08	5.20	1.30	8.20	1.70	0.69	0.17	10.30	1.90	1.94	0.36	14.20	2.60	3.11	0.56	8.70	2.10	0.94	0.20	5.80	1.20	0.87	0.17
Garnet 2, transect 2 (Type-1 garnet)																														
BH54_Gt2-16.d	150.00	150.00	0.00	0.00	0.06	0.06	0.40	0.40	2.60	2.60	7.70	7.70	0.52	0.52	12.00	12.00	1.40	1.40	19.00	19.00	6.00	6.00	19.00	19.00	3.80	3.80	26.00	26.00	3.00	3.00
BH54_Gt2-17.d	224.00	20.00	0.01	0.01	0.16	0.04	0.15	0.03	4.24	0.65	7.90	1.10	0.44	0.07	12.70	1.60	2.46	0.23	26.40	2.50	8.29	0.76	31.10	3.00	5.28	0.55	37.20	3.30	5.14	0.52
BH54_Gt2-18.d	263.00	34.00	0.01	0.02	0.18	0.08	0.20	0.09	3.61	0.91	9.10	1.30	0.59	0.16	12.60	3.50	2.40	0.40	29.20	3.10	9.60	1.20	40.70	5.20	6.90	1.10	50.70	6.30	7.30	1.00
BH54_Gt2-19.d	308.00	75.00	0.06	0.06	0.34	0.16	0.11	0.06	3.60	1.70	7.70	2.10	0.50	0.16	10.60	3.00	2.46	0.62	31.10	7.60	13.20	3.40	55.00	13.00	10.00	2.30	70.00	17.00	11.20	2.60
BH54_Gt2-20.d	400.00	50.00	0.02	0.01	0.19	0.06	0.16	0.04	3.97	0.66	8.60	1.20	0.63	0.12	13.10	2.00	2.87	0.37	39.60	5.30	16.50	2.00	74.30	9.20	13.30	1.70	98.00	12.00	15.70	1.90
BH54_Gt2-21.d	387.00	36.00	0.02	0.01	0.15	0.04	0.12	0.03	3.67	0.56	6.93	0.83	0.51	0.08	11.10	1.30	2.60	0.24	37.10	3.70	16.60	1.60	73.50	6.50	13.40	1.30	98.00	9.20	15.30	1.30
BH54_Gt2-22.d	500.00	100.00	0.04	0.04	0.08	0.05	0.21	0.14	4.35	0.98	8.80	2.80	0.69	0.21	14.20	3.10	3.13	0.63	49.00	10.00	20.70	4.10	97.00	20.00	17.40	4.00	126.00	26.00	18.80	4.20
BH54_Gt2-23.d	443.00	74.00	0.00	0.00	0.12	0.05	0.13	0.04	3.44	0.75	7.50	1.50	0.49	0.13	11.20	1.70	2.74	0.37	41.90	6.40	18.40	3.10	84.00	14.00	14.60	2.50	104.00	17.00	14.80	2.50
BH54_Gt2-24.d	454.00	70.00	0.02	0.02	0.18	0.08	0.16	0.05	4.15	0.95	8.80	1.90	0.52	0.12	13.10	2.70	2.85	0.60	42.70	7.30	19.10	3.20	82.00	13.00	15.10	2.30	105.00	15.00	15.10	2.50
BH54_Gt2-25.d	420.00	61.00	0.00	0.00	0.09	0.03	0.14	0.04	3.60	0.52	9.30	1.30	0.60	0.11	12.70	1.50	2.85	0.37	39.20	5.00	17.10	2.00	76.70	9.50	13.90	1.80	99.00	11.00	14.90	1.90
BH54_Gt2-26.d	328.00	43.00	0.00	0.00	0.06	0.03	0.14	0.04	3.47	0.51	8.40	1.50	0.56	0.14	12.10	2.10	2.41	0.30	33.20	4.50	13.30	1.80	60.00	7.70	11.30	1.60	81.00	11.00	12.60	1.60

Appendix E. Garnet trace element chemistry (continued)

	Elemental concentration (ppm)																											
Analysis	Y	2σ	La	2σ	Ce	2σ	Pr	2σ	Nd	2σ	Sm	2σ	Eu	2σ	Gd	2σ	Tb	2σ	Dy	2σ	Ho	2σ	Er	2σ	Tm	2σ	Yb	2σ	Lu	2σ
BH54_Gt2-27.d	253.00	25.00	0.11	0.07	0.36	0.15	0.17	0.04	3.57	0.47	7.66	0.85	0.45	0.07	11.50	1.20	2.11	0.19	26.00	2.60	10.20	1.10	45.40	4.50	8.21	0.72	62.80	6.50	9.81	0.87
BH54_Gt2-28.d	239.00	32.00	0.01	0.02	0.09	0.05	0.10	0.06	3.53	0.66	8.23	0.79	0.55	0.27	13.70	2.50	2.58	0.48	26.50	3.00	9.40	1.00	38.30	5.10	7.10	1.00	53.30	9.30	8.50	1.40
Sample BH32																														
Garnet 1, transect 1 (Type-1 garnet)																														
BH32_Gt1-1.d	420.00	25.00	0.00	0.00	0.03	0.01	0.03	0.01	1.49	0.16	9.95	0.79	0.66	0.07	45.20	2.90	9.27	0.59	70.10	4.00	15.52	0.94	45.30	2.70	6.40	0.40	40.50	2.50	5.70	0.34
BH32_Gt1-2.d	414.00	29.00	0.00	0.00	0.05	0.01	0.04	0.01	1.59	0.21	10.38	0.99	0.66	0.08	44.00	3.30	8.96	0.63	69.10	5.00	15.00	1.10	43.80	3.00	6.45	0.53	39.10	2.70	5.58	0.47
BH32_Gt1-3.d	393.00	26.00	0.02	0.01	0.08	0.02	0.05	0.01	1.44	0.19	10.08	0.80	0.69	0.07	43.30	3.30	8.65	0.58	66.60	4.60	14.18	0.90	41.40	2.80	5.97	0.39	37.90	2.60	5.24	0.38
BH32_Gt1-4.d	397.00	29.00	0.00	0.00	0.05	0.02	0.05	0.02	1.70	0.21	10.27	0.81	0.66	0.08	42.80	3.30	8.98	0.70	68.20	5.30	14.70	1.10	43.30	3.50	6.32	0.52	39.50	3.30	5.18	0.43
BH32_Gt1-5.d	376.00	26.00	0.09	0.03	0.29	0.06	0.06	0.01	1.39	0.23	9.40	0.82	0.57	0.08	40.10	2.90	8.42	0.62	63.80	4.50	13.92	0.96	41.70	2.90	5.78	0.42	36.80	2.80	4.95	0.35
BH32_Gt1-6.d	362.00	27.00	0.31	0.08	0.59	0.11	0.07	0.02	1.14	0.21	7.90	0.73	0.54	0.08	36.50	3.00	8.06	0.67	62.70	5.10	13.60	1.10	39.70	2.90	5.59	0.43	35.10	2.90	4.87	0.42
BH32_Gt1-7.d	387.00	23.00	0.01	0.00	0.07	0.02	0.03	0.01	1.32	0.17	9.46	0.73	0.63	0.08	41.20	2.90	8.61	0.58	65.50	3.90	14.51	0.89	42.70	2.70	6.06	0.39	37.70	2.30	5.25	0.35
BH32_Gt1-8.d	258.00	51.00	1.51	0.69	1.77	0.56	0.12	0.09	1.02	0.54	3.20	1.80	0.12	0.06	22.20	4.10	5.20	1.30	40.00	7.20	9.70	1.70	28.70	6.10	3.91	0.79	26.80	5.40	3.70	1.00
BH32_Gt1-9.d	343.00	25.00	0.13	0.03	0.31	0.08	0.05	0.02	0.45	0.15	5.17	0.73	0.36	0.06	35.10	2.90	7.95	0.63	58.30	4.60	12.84	0.89	37.80	3.10	5.27	0.39	34.10	2.70	4.58	0.36
BH32_Gt1-10.d	394.00	28.00	0.03	0.01	0.08	0.02	0.02	0.01	1.07	0.17	9.05	0.71	0.59	0.08	40.20	2.50	8.61	0.61	67.00	4.90	14.60	1.00	43.50	3.20	5.95	0.44	37.80	2.80	5.21	0.37
BH32_Gt1-11.d	383.00	25.00	0.01	0.01	0.04	0.01	0.04	0.01	1.31	0.20	9.48	0.84	0.59	0.07	40.30	2.70	8.57	0.62	65.30	4.50	14.30	1.00	41.70	2.90	5.91	0.41	37.10	2.60	5.14	0.38
BH32_Gt1-12.d	411.00	25.00	0.01	0.01	0.07	0.02	0.04	0.01	1.19	0.17	8.74	0.67	0.59	0.06	42.90	2.60	9.26	0.58	69.10	4.30	15.12	0.92	44.10	2.60	6.19	0.37	38.50	2.20	5.24	0.33
BH32_Gt1-13.d	373.00	18.00	0.03	0.01	0.11	0.03	0.05	0.01	1.35	0.16	7.77	0.60	0.62	0.06	37.10	2.10	8.00	0.45	61.60	3.30	13.60	0.69	39.60	1.90	5.69	0.30	35.60	1.80	4.93	0.26
BH32_Gt1-14.d	448.00	34.00	0.05	0.02	0.12	0.02	0.05	0.01	1.60	0.22	10.07	0.89	0.69	0.08	45.70	3.60	9.46	0.69	72.70	5.50	15.90	1.30	45.90	3.50	6.58	0.51	42.10	3.20	5.71	0.50
BH32_Gt1-15.d	449.00	34.00	0.06	0.02	0.20	0.05	0.12	0.02	2.56	0.26	11.40	1.00	0.76	0.08	45.20	3.60	9.41	0.71	73.30	5.70	16.00	1.30	46.30	3.50	6.71	0.52	43.90	3.80	5.89	0.46
Garnet 2, transect 1 (Type-1 garnet)																														
BH32_Gt1-16.d	601.00	41.00	0.00	0.00	0.10	0.02	0.09	0.02	2.27	0.22	11.64	0.91	0.67	0.06	40.90	2.80	9.30	0.62	90.60	6.30	25.10	1.70	83.80	5.60	12.22	0.89	77.40	5.30	11.26	0.77
BH32_Gt1-17.d	708.00	48.00	0.00	0.00	0.14	0.03	0.17	0.03	3.60	0.38	13.00	1.00	0.76	0.08	42.30	3.10	10.18	0.73	108.40	7.70	32.10	2.20	105.60	7.20	15.10	1.10	92.00	6.60	13.35	0.93
BH32_Gt1-18.d	720.00	41.00	0.00	0.00	0.17	0.02	0.14	0.02	3.61	0.32	12.60	0.81	0.73	0.07	37.80	2.30	9.90	0.59	111.10	6.80	34.10	1.90	111.20	6.30	15.14	0.83	91.70	5.30	13.60	0.77
BH32_Gt1-19.d	764.00	48.00	0.00	0.00	0.16	0.03	0.16	0.02	3.77	0.36	13.28	0.96	0.71	0.08	39.60	2.60	10.37	0.70	118.40	7.70	36.30	2.30	120.50	7.70	16.40	1.00	101.10	6.40	14.63	0.90
BH32_Gt1-20.d	790.00	45.00	0.02	0.01	0.22	0.07	0.15	0.03	3.40	0.42	12.70	1.10	0.70	0.07	40.30	2.30	10.44	0.61	120.00	6.60	37.50	2.20	126.40	7.20	17.50	1.00	104.10	5.90	15.17	0.85
BH32_Gt1-21.d	701.00	43.00	0.00	0.00	0.11	0.03	0.11	0.02	2.86	0.33	11.61	0.92	0.65	0.07	39.00	2.80	9.54	0.63	106.10	6.40	33.00	2.00	109.70	6.40	15.42	0.91	93.70	5.50	14.02	0.89
BH32_Gt1-22.d	605.00	35.00	0.02	0.01	0.07	0.02	0.07	0.01	2.28	0.26	10.52	0.65	0.71	0.06	38.50	2.30	8.73	0.52	89.80	5.30	26.40	1.50	90.20	5.10	13.42	0.82	82.20	4.50	12.48	0.75
BH32_Gt1-23.d	571.00	29.00	0.05	0.01	0.15	0.02	0.05	0.01	1.67	0.17	10.43	0.72	0.72	0.07	41.70	2.20	9.07	0.46	81.90	4.30	23.00	1.20	80.40	4.10	12.27	0.63	80.20	4.10	12.02	0.63
BH32_Gt1-24.d	567.00	38.00	0.05	0.02	0.14	0.02	0.09	0.02	1.91	0.22	11.70	1.00	0.75	0.08	42.70	3.00	9.03	0.62	80.80	5.30	22.20	1.50	76.90	5.10	11.37	0.75	75.60	5.30	11.27	0.75
BH32_Gt1-25.d	504.00	43.00	0.21	0.04	0.45	0.06	0.12	0.02	2.41	0.25	11.00	1.00	0.71	0.08	38.50	3.10	8.24	0.72	72.30	6.20	19.40	1.70	65.00	5.50	9.93	0.84	65.00	5.70	9.47	0.84
BH32_Gt1-26.d	556.00	35.00	0.01	0.01	0.15	0.02	0.10	0.02	2.83	0.23	12.96	0.97	0.84	0.07	44.60	2.70	9.32	0.56	78.90	4.70	20.90	1.40	69.60	4.40	10.57	0.65	68.60	4.10	9.86	0.60
BH32_Gt1-27.d	645.00	41.00	0.06	0.01	0.22	0.03	0.10	0.02	2.15	0.24	10.75	0.88	0.72	0.07	43.50	2.90	9.98	0.66	88.20	5.70	23.60	1.60	78.80	5.30	12.25	0.79	82.20	5.50	11.68	0.74
Sample BH74																														
Garnet 1, transect 1 (Type-1 garnet)																														
BH74_Gt1-1.d	267.00	15.00	0.01	0.01	0.27	0.04	0.21	0.03	4.96	0.40	9.91	0.72	0.64	0.07	19.70	1.20	4.71	0.30	43.90	2.80	10.86	0.65	35.50	2.10	5.69	0.35	41.90	2.80	6.33	0.40
BH74_Gt1-2.d	331.00	22.00	0.02	0.01	0.23	0.03	0.23	0.03	5.05	0.40	9.64	0.63	0.57	0.06	20.30	1.50	5.17	0.36	53.50	3.60	13.92	0.95	48.50	3.30	7.71	0.50	55.10	3.50	8.76	0.57
BH74_Gt1-3.d	399.00	25.00	0.00	0.00	0.22	0.03	0.22	0.03	6.07	0.50	10.94	0.86	0.66	0.07	20.00	1.50	6.01	0.42	62.90	4.20	17.40	1.10	60.50	3.70	9.68	0.61	69.10	4.50	10.69	0.68
BH74_Gt1-4.d	409.00	24.00	0.01	0.01	0.18	0.02	0.18	0.03	5.01	0.41	9.53	0.65	0.59	0.06	18.80	1.30	5.73	0.34	63.10	3.70	17.90	1.10	61.90	3.70	10.13	0.63	71.80	4.40	11.26	0.70
BH74_Gt1-5.d	402.00	26.00	0.00	0.00	0.11	0.02	0.13	0.02	4.42	0.37	9.00	0.68	0.58	0.05	18.60	1.30	5.52	0.38	61.20	4.00	17.60	1.10	62.10	4.00	10.24	0.70	72.80	5.00	11.28	0.72
BH74_Gt1-6.d	395.00	24.00	0.00	0.00	0.10	0.02	0.15	0.02	4.17	0.40	9.53	0.74	0.55	0.06	18.10	1.20	5.51	0.35	60.80	3.60	17.30	1.00	61.50	3.70	9.99	0.61	70.70	4.30	11.31	0.73
BH74_Gt1-7.d	367.00	22.00	0.00	0.00	0.13	0.02	0.15	0.02	4.67	0.42	9.40	0.74	0.55	0.07	17.90	1.20	5.20	0.31	57.10	3.40	16.33	0.99	56.40	3.30	9.20	0.52	65.10	4.00	10.37	0.68
BH74_Gt1-8.d	367.00	26.00	0.00	0.00	0.20	0.03	0.24	0.03	5.70	0.49	10.35	0.87	0.62	0.07	19.10	1.40	5.47	0.37	58.90	4.20	16.00	1.10	55.90	4.00	8.89	0.68	63.80	4.50	9.84	0.70
BH74_Gt1-9.d	309.00	22.00	0.01	0.01	0.21	0.03	0.23	0.03	5.44	0.43	10.42	0.82	0.67	0.07	20.40	1.70	5.30	0.39	49.70	3.50	12.98	0.90	43.90	3.00	7.11	0.51	51.50	3.70	8.02	0.58
BH74_Gt1-10.d	150.00	20.00	0.25	0.05	0.43	0.06	0.13	0.02	2.34	0.32	5.76	0.80	0.42	0.07	11.50	1.60	2.76	0.37	24.30	3.20	5.55	0.74	19.40	2.60	2.99	0.40	22.50	3.00	3.51	0.47

Appendix E. Garnet trace element chemistry (continued)

	Elemental concentration (ppm)																													
Analysis	Y	2σ	La	2σ	Ce	2σ	Pr	2σ	Nd	2σ	Sm	2σ	Eu	2σ	Gd	2σ	Tb	2σ	Dy	2σ	Ho	2σ	Er	2σ	Tm	2σ	Yb	2σ	Lu	2σ
Garnet 2, transect 1 (Type-1 garnet)																														
BH74_Gt1-11.d	166.00	11.00	0.01	0.01	0.16	0.03	0.14	0.02	3.92	0.36	8.52	0.76	0.54	0.07	17.00	1.30	3.82	0.28	28.10	1.90	5.88	0.44	17.40	1.20	2.87	0.25	20.90	1.50	2.89	0.23
BH74_Gt1-12.d	209.00	14.00	0.00	0.00	0.18	0.03	0.19	0.03	4.70	0.43	10.16	0.81	0.64	0.07	20.50	1.60	4.64	0.32	35.80	2.40	7.68	0.53	23.00	1.60	3.66	0.24	26.90	1.60	3.77	0.26
BH74_Gt1-13.d	232.00	17.00	0.00	0.00	0.18	0.03	0.17	0.03	4.66	0.39	10.06	0.82	0.62	0.06	20.20	1.50	4.86	0.37	39.60	3.00	8.64	0.63	26.40	1.90	4.29	0.33	31.00	2.40	4.65	0.37
BH74_Gt1-14.d	276.00	17.00	0.00	0.00	0.14	0.02	0.17	0.02	4.74	0.44	10.36	0.75	0.64	0.06	21.10	1.20	5.30	0.34	46.10	3.00	11.20	0.75	36.10	2.20	6.04	0.42	41.40	2.50	6.67	0.43
BH74_Gt1-15.d	288.00	18.00	0.00	0.00	0.11	0.02	0.13	0.03	4.19	0.40	9.69	0.83	0.55	0.05	20.30	1.40	4.99	0.33	46.50	3.00	12.11	0.74	43.00	2.80	6.81	0.44	48.50	3.00	8.06	0.50
BH74_Gt1-16.d	282.00	17.00	0.00	0.00	0.11	0.02	0.12	0.02	3.44	0.30	8.66	0.65	0.57	0.06	19.10	1.30	4.93	0.35	45.40	2.90	12.18	0.75	43.70	2.90	7.22	0.51	50.20	3.20	8.15	0.52
BH74_Gt1-17.d	304.00	21.00	0.01	0.01	0.20	0.03	0.20	0.03	4.43	0.38	10.31	0.94	0.67	0.08	19.90	1.40	5.28	0.41	47.20	3.20	12.79	0.88	44.50	3.20	7.31	0.54	51.60	3.50	8.47	0.58
BH74_Gt1-18.d	258.00	16.00	0.03	0.02	0.19	0.04	0.13	0.02	3.47	0.36	8.48	0.60	0.63	0.07	17.20	0.97	4.21	0.26	40.30	2.50	10.84	0.71	38.20	2.70	6.24	0.41	44.90	2.70	7.13	0.44
BH74_Gt1-19.d	236.00	15.00	0.06	0.04	0.26	0.10	0.13	0.03	3.28	0.33	8.13	0.68	0.53	0.07	16.90	1.10	4.08	0.28	36.00	2.10	9.80	0.65	34.60	2.20	5.70	0.40	41.00	2.50	6.64	0.46
BH74_Gt1-20.d	121.00	23.00	0.45	0.07	0.71	0.09	0.14	0.02	2.23	0.37	4.63	0.93	0.29	0.06	9.40	1.90	2.12	0.43	19.10	3.70	4.72	0.93	17.20	3.40	2.75	0.55	21.00	4.20	3.35	0.67
BH74_Gt1-21.d	201.00	12.00	0.03	0.01	0.26	0.03	0.22	0.03	4.93	0.43	9.80	0.71	0.58	0.06	18.20	1.10	3.94	0.23	33.20	2.10	7.85	0.52	26.00	1.60	4.22	0.28	31.30	2.10	5.09	0.33
BH74_Gt1-22.d	169.00	12.00	0.02	0.01	0.18	0.03	0.18	0.02	4.31	0.40	8.96	0.79	0.61	0.07	17.00	1.40	3.53	0.25	27.30	2.00	6.06	0.44	19.40	1.40	3.25	0.24	24.10	1.70	3.65	0.26
Garnet 3, transect 1 (Type-1 garnet)																														
BH74_Gt1-23.d	202.00	15.00	0.00	0.00	0.17	0.03	0.15	0.03	4.10	0.34	9.09	0.77	0.71	0.09	19.40	1.80	4.20	0.31	32.90	2.40	7.43	0.57	23.50	1.70	3.64	0.25	28.30	1.90	4.19	0.32
BH74_Gt1-24.d	251.00	17.00	0.00	0.00	0.20	0.03	0.20	0.03	5.14	0.47	10.61	0.81	0.67	0.08	20.60	1.60	4.79	0.32	41.60	2.90	9.76	0.69	30.90	2.10	5.12	0.35	35.80	2.50	5.66	0.37
BH74_Gt1-25.d	291.00	20.00	0.00	0.00	0.17	0.03	0.20	0.03	5.34	0.54	10.04	0.82	0.67	0.06	19.50	1.40	5.10	0.38	46.70	3.20	11.37	0.78	36.90	2.50	6.10	0.42	43.30	3.00	6.72	0.47
BH74_Gt1-26.d	381.00	25.00	0.00	0.00	0.18	0.03	0.21	0.03	4.99	0.44	10.19	0.81	0.69	0.08	18.90	1.50	5.78	0.43	59.40	4.00	16.30	1.10	54.60	3.50	8.81	0.61	62.90	4.20	10.07	0.74
BH74_Gt1-27.d	398.00	23.00	0.00	0.00	0.15	0.03	0.20	0.03	4.84	0.34	9.41	0.66	0.64	0.06	17.30	1.20	5.69	0.34	62.40	3.80	16.96	0.98	59.10	3.50	9.46	0.57	65.80	3.70	10.39	0.62
BH74_Gt1-28.d	405.00	21.00	0.00	0.00	0.17	0.03	0.17	0.02	4.66	0.29	9.31	0.58	0.61	0.06	17.10	1.00	5.58	0.30	61.90	3.20	17.27	0.88	59.60	3.00	9.60	0.51	67.10	3.50	10.54	0.57
BH74_Gt1-29.d	431.00	25.00	0.01	0.00	0.17	0.03	0.20	0.03	5.26	0.41	10.37	0.77	0.66	0.07	18.60	1.20	6.03	0.39	65.90	3.80	18.20	1.10	63.50	3.70	10.02	0.57	72.60	4.30	11.12	0.66
BH74_Gt1-30.d	404.00	23.00	0.01	0.01	0.14	0.02	0.16	0.02	4.59	0.36	8.90	0.59	0.58	0.06	17.60	1.10	5.62	0.34	62.00	3.60	16.95	0.99	58.80	3.30	9.67	0.61	68.20	4.20	10.45	0.62
BH74_Gt1-31.d	446.00	24.00	0.00	0.00	0.19	0.03	0.20	0.02	5.46	0.40	10.80	0.72	0.64	0.06	20.00	1.20	6.27	0.37	68.50	3.70	18.49	0.94	64.30	3.40	10.39	0.56	74.40	4.10	11.57	0.62
BH74_Gt1-32.d	377.00	20.00	0.00	0.00	0.18	0.02	0.18	0.02	5.04	0.36	9.60	0.69	0.60	0.06	19.10	1.20	5.59	0.33	59.20	3.20	15.93	0.91	54.30	3.10	8.69	0.45	61.50	3.30	9.69	0.54
BH74_Gt1-33.d	332.00	22.00	0.03	0.01	0.34	0.05	0.22	0.03	4.67	0.49	9.98	0.87	0.64	0.07	19.70	1.40	5.45	0.41	53.90	4.10	13.90	1.00	46.70	3.30	7.69	0.56	55.40	4.20	8.25	0.55
BH74_Gt1-34.d	295.00	16.00	0.00	0.00	0.16	0.03	0.19	0.02	4.95	0.44	9.94	0.70	0.60	0.07	20.80	1.30	5.16	0.32	48.40	2.60	12.17	0.69	39.70	2.20	6.37	0.36	45.30	2.60	7.05	0.40
BH74_Gt1-35.d	249.00	14.00	0.00	0.00	0.29	0.03	0.26	0.03	6.07	0.43	11.31	0.77	0.75	0.07	20.50	1.30	5.04	0.29	42.00	2.40	9.69	0.57	30.60	1.70	5.06	0.30	35.20	1.90	5.35	0.30
BH74_Gt1-36.d	190.00	11.00	0.00	0.00	0.26	0.03	0.22	0.03	5.08	0.40	10.80	0.86	0.74	0.07	19.50	1.20	4.19	0.25	33.20	2.00	7.14	0.41	21.60	1.30	3.31	0.20	24.80	1.60	3.56	0.24
Garnet 4, transect 1 (Type-1 garnet)																														
BH74_Gt2-1.d	162.30	9.50	0.00	0.00	0.21	0.04	0.21	0.03	4.90	0.42	11.03	0.86	0.72	0.10	19.40	1.30	3.80	0.26	27.70	1.70	5.56	0.38	16.40	1.10	2.61	0.18	18.40	1.10	2.56	0.16
BH74_Gt2-2.d	185.00	10.00	0.01	0.01	0.33	0.04	0.25	0.03	6.19	0.49	10.95	0.77	0.68	0.07	19.60	1.30	4.11	0.28	32.00	1.90	6.81	0.43	20.30	1.20	3.24	0.21	24.00	1.50	3.31	0.21
BH74_Gt2-3.d	241.00	15.00	0.01	0.01	0.36	0.05	0.28	0.04	6.79	0.52	11.95	0.89	0.77	0.09	22.40	1.60	4.97	0.34	42.00	2.80	9.38	0.57	30.00	2.00	4.80	0.32	34.20	2.30	5.06	0.31
BH74_Gt2-4.d	280.00	17.00	0.00	0.00	0.26	0.03	0.27	0.04	5.83	0.42	11.08	0.91	0.69	0.06	21.20	1.50	5.19	0.33	45.60	3.00	11.51	0.70	38.20	2.30	6.20	0.39	44.40	2.80	6.91	0.47
BH74_Gt2-5.d	310.00	18.00	0.02	0.01	0.20	0.03	0.20	0.03	5.34	0.41	10.26	0.66	0.61	0.07	20.30	1.30	5.20	0.32	49.80	3.00	13.53	0.75	47.60	2.70	7.63	0.45	54.70	3.30	8.91	0.51
BH74_Gt2-6.d	355.00	21.00	0.03	0.01	0.25	0.03	0.20	0.02	5.64	0.43	11.26	0.79	0.67	0.08	20.90	1.40	5.39	0.32	55.90	3.30	16.20	1.00	57.60	3.60	9.54	0.57	67.50	4.20	11.01	0.68
BH74_Gt2-7.d	353.00	20.00	0.00	0.00	0.09	0.02	0.13	0.02	4.00	0.37	10.38	0.76	0.64	0.07	20.60	1.40	5.28	0.31	54.80	3.20	16.07	0.95	58.10	3.30	9.57	0.62	67.20	4.20	11.32	0.73
BH74_Gt2-8.d	378.00	24.00	0.00	0.00	0.16	0.03	0.18	0.03	5.19	0.42	11.05	0.82	0.67	0.08	21.40	1.50	5.48	0.37	58.20	3.70	16.90	1.10	61.10	3.90	9.96	0.66	69.70	4.20	11.49	0.74
BH74_Gt2-9.d	368.00	22.00	0.04	0.01	0.29	0.04	0.23	0.03	5.56	0.49	11.15	0.88	0.68	0.07	22.00	1.50	5.79	0.40	57.60	3.70	16.10	1.00	56.30	3.40	9.23	0.63	65.90	4.30	10.70	0.69
BH74_Gt2-10.d	291.00	18.00	0.00	0.00	0.20	0.03	0.18	0.02	4.66	0.37	10.35	0.70	0.69	0.07	20.40	1.50	4.89	0.32	45.50	3.00	12.03	0.80	40.80	2.50	6.61	0.42	47.70	3.10	7.33	0.46
BH74_Gt2-11.d	244.00	13.00	0.00	0.00	0.11	0.02	0.12	0.02	4.06	0.34	9.95	0.65	0.63	0.06	19.70	1.10	4.34	0.26	38.10	2.00	9.35	0.53	30.20	1.70	4.95	0.29	36.20	2.00	5.51	0.32
BH74_Gt2-12.d	245.00	14.00	0.00	0.00	0.23	0.03	0.24	0.03	5.79	0.47	11.74	0.85	0.79	0.07	22.80	1.30	4.91	0.29	39.90	2.30	8.71	0.48	27.60	1.60	4.58	0.29	32.50	1.90	4.64	0.25
BH74_Gt2-13.d	202.00	12.00	0.00	0.00	0.26	0.03	0.26	0.03	5.57	0.42	11.41	0.87	0.69	0.07	21.30	1.40	4.45	0.29	33.70	2.20	7.26	0.46	21.70	1.40	3.39	0.23	24.00	1.50	3.45	0.22
BH74_Gt2-14.d	188.00	14.00	0.01	0.01	0.30	0.05	0.21	0.03	5.67	0.51	11.14	0.86	0.66	0.09	21.00	1.70	4.27	0.28	31.70	2.20	6.64	0.48	20.30	1.60	2.97	0.21	22.00	1.80	3.18	0.24
BH74_Gt2-15.d	159.00	11.00	0.02	0.01	0.26	0.04	0.21	0.03	4.96	0.43	11.16	0.91	0.64	0.06	19.30	1.50	3.91	0.28	27.30	1.80	5.47	0.36	16.60	1.10	2.64	0.20	19.50	1.40	2.80	0.22

Chapter 5

This chapter is written as a review article for submission to *Australian Journal of Earth Science*

Statement of Authorship

Title of paper	Towards a synthesis of the Mesoproterozoic evolution of reworked Australian–Antarctic convergent margins
Pulication status	☐ Published ☐ Accepted for publication ☐ Submitted for publication ☒ Unpublished and unsubmitted work written in manuscript style
Publication details	Unpublished and unsubmitted work, written in manuscript style of *Australian Journal of Earth Science.*

Principal Author

Name of Principal Author	Naomi M. Tucker
Contribution to the paper	Project design; regional data collation; data interpretation; manuscript design and composition; creation of all figures, tables and datasets.
Overall percentage (%)	85
Certification	This paper reports on original research I conducted during the period of my Higher Degree by Research candidature and is not subject to any obligations or contractual agreements with a third party that would constrain its inclusion in this thesis. I am the primary author of this paper.
Signature	Date 20/02/2018

Co-author contributions

By signing the Statement of Authorship, each author certifies that:
i. the candidate's stated contribution to the publication is accurate (as detailed above);
ii. permission is granted for the candidate to include the publication in the thesis; and,
iii. the sum of all co-authors contributions is equal to 100 % less the candidate's stated contribution.

Name of Co-author	Laura J. Morrissey
Contribution to the paper	Discussions on project design, manuscript composition and assistance with data interpretation; manuscript review.
Signature	Date 20/02/2018

Name of Co-author	Martin Hand
Contribution to the paper	Discussions on project design, manuscript composition and assistance with data interpretation; manuscript review.
Signature	Date 20/02/2018

Name of Co-author	David E. Kelsey
Contribution to the paper	Discussions/assistance with data interpretation; manuscript review.
Signature	Date 20/02/2018

Name of Co-author	Justin L. Payne
Contribution to the paper	Discussions/assistance with data interpretation; manuscript review.
Signature	Date 20/02/2018

Towards a synthesis of the high-temperature Mesoproterozoic evolution of reworked Australian–Antarctic convergent margins

ABSTRACT

The Mesoproterozoic assembly of Australia and East Antarctica is recorded by terranes that formed along the reworked margins of Archean cratons. Together, these terranes comprise the Musgrave–Albany–Fraser–Wilkes Orogen (MAFWO), and they preserve an orogen-wide record of regional and sustained high thermal gradients, voluminous mantle and crustal melting, and little metamorphic evidence for crustal thickening. These primary observations challenge conventional views on the thermal behaviour of the crust and a simplistic model of continental collision. This review summarises the spatial, temporal and thermal features of Mesoproterozoic metamorphism and magmatism within the MAFWO to provide clarity on the likely driving forces for thermally-extreme crustal behaviour within the context of continental amalgamation. The MAFWO records a two-stage magmatic and metamorphic history with D_1/M_1 at ca. 1340–1260 Ma and D_2/M_2 at ca. 1220–1130 Ma. High heat flow for long duration in thin crust suggests that the MAFWO is overall an inherently mantle-driven thermal system, but the thermal driver and tectonic setting for each stage of its evolution is interpreted to have varied. D_1/M_1 was localised to the central MAFWO in regions of highly-extended, juvenile crust, and involved bimodal mafic and calc-alkaline felsic magmatism, variably high-temperature metamorphism, the development of quasi-horizontal fabrics and was associated with basin formation. D_1/M_1 appears consistent with extensional accretionary orogenesis and was ultimately controlled by the pre-D_1 tectonic geometry of the MAFWO. However, the specific mechanism for extension and the timing of extension relative to arc accretion remains unclear with two viable models—delamination and orogenic collapse, and back-arc extension—currently proposed. D_2/M_2 was pervasive and involved long-lived and remarkably consistent high–ultrahigh thermal gradient metamorphism (~150 °C/kbar) in thin and extending crust. Metamorphism was accompanied by voluminous, high-temperature, near-exclusively felsic–charnockitic magmatism with a significant mantle source contribution. These characteristics suggest that D_2/M_2 was the response to mantle lithosphere removal by delamination or convective erosion of the lithosphere by asthenosphere mantle flow. However, the geodynamic trigger and therefore the specific mechanism for lithosphere removal remains unclear. This is largely due to uncertainties in the timing and nature of final craton amalgamation that occurred prior to D_2/M_2 and was therefore central to the longevity of unusually high thermal conditions.

1. INTRODUCTION

The majority of the global Mesoproterozoic geological record relates to events along convergent margins (e.g. Roberts et al., 2015) as they are zones of focused metamorphism, magmatism and deformation. Marginal terranes to the Archean–Paleoproterozoic Australian and East Antarctic cratons are interpreted to record evidence for the Mesoproterozoic amalgamation of components of Australia and East Antarctica (Fig. 1; Aitken et al., 2016; Li et al., 2008; Pisarevsky et al., 2003). At face value, this system—herein Musgrave–Albany–Fraser–Wilkes Orogen (MAFWO)—has all the hallmarks of a collisional orogen in that thick, old cratonic nuclei are juxtaposed by a series of juvenile, reworked and metamorphosed terranes (Beaumont et al., 2010; Jamieson and Beaumont, 2013). Yet high to ultrahigh thermal gradient metamorphism and voluminous, felsic, high-temperature magmatism persisted over long timescales within the MAFWO (e.g. Smithies et al., 2011; Walsh et al., 2015), contradicting the archetypal view of continental collision that involves Barrovian thermal regimes (England and Thompson, 1984) and anatectic melting of existing continental crust (Douce and McCarthy, 1998). Granulite facies metamorphism is not an uncommon consequence of collision or accretion with many ancient and modern examples globally (e.g. Clark et al., 2015; Drüppel et al., 2013; Kelsey and Hand, 2015; Santosh et al., 2009). However, within the MAFWO, it is the longevity of regionally extreme thermal gradients that is noteworthy, with a two-phase tectono-metamorphic and magmatic evolution documented between ca. 1345–1260 Ma and ca. 1220–1130 Ma. The duration of ultrahigh temperature (UHT) conditions in the west

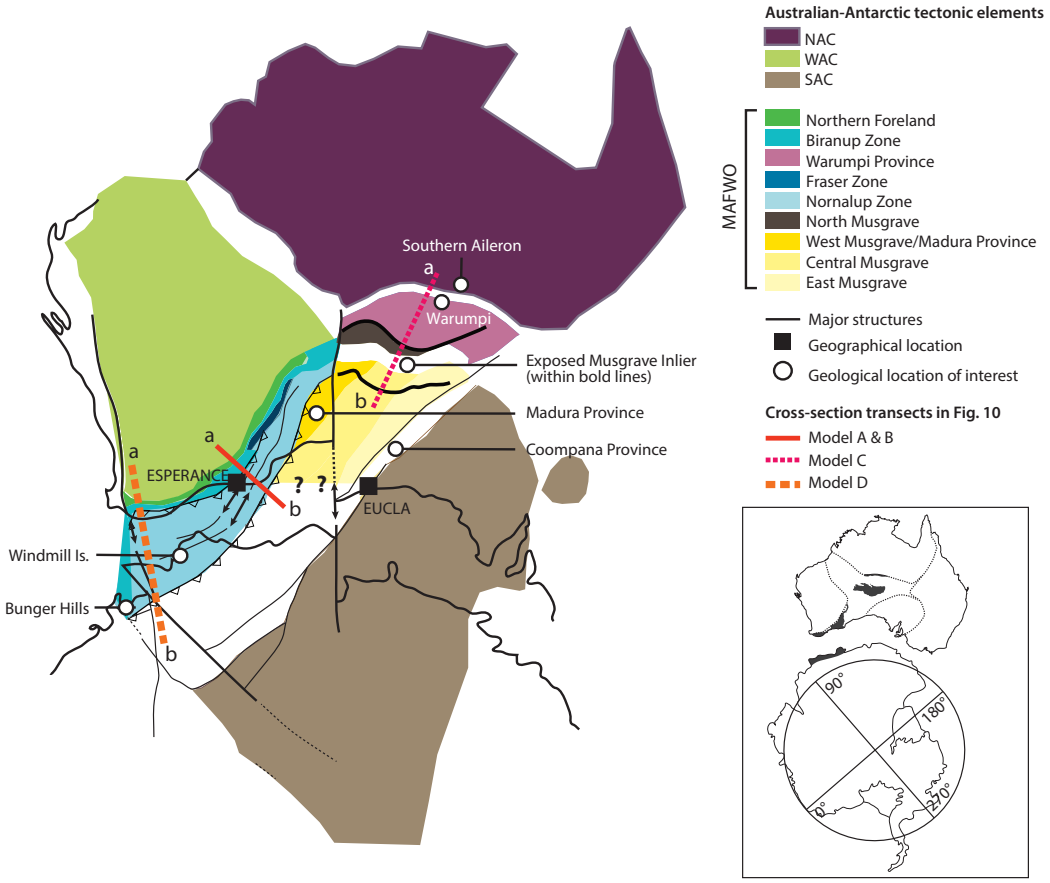

Figure 1. Mesoproterozoic (ca. 1260–1130 Ma) configuration and regional geology of Australia and East Antarctica (after Aitken et al., 2016). Major geological structures (at ca. 1150 Ma) interpreted from magnetic intensity and gravity anomaly data are overlain (also Aitken et al., 2016). The reconstructed Mesoproterozoic architecture highlights the former spatial linkage between tectonic elements and geological structures of the Musgrave–Albany–Fraser–Wilkes Orogen (MAFWO). Correction for offset along major structures aligns the Musgrave Inlier with the north-east Albany–Fraser Orogen, and the Bunger Hills with the west Albany–Fraser Orogen. The present-day exposure of tectonic elements of the MAFWO are shown in the inset. Cross section transects corresponding to the approximate location of the tectonic models presented in Fig. 8 are indicated.

Musgrave Inlier appear to have been unusually long-lasting (e.g. >80 Myr, possibly up to 150 Myr; Walsh et al., 2015), second globally in duration to metamorphism in the Eastern Ghats (ca. 1130–930 Ma; Kelsey and Hand, 2015; Korhonen et al., 2013). The geographical extent of the orogen is also vast, spanning approximately 2000 km.

Regionally long-lived, high thermal gradient metamorphism and magmatism approaching ultra-high temperatures in the MAFWO pushes the limit of the normal conductive ability of the crust (~100 °C/kbar, assuming normal crustal heat production: <1.5–2.0 μWm^{-3}, and normal mantle heat flow: ~30 mW^{-2}; Kelsey and Hand, 2015). The generation of such conditions thus requires an additional thermal driver through mantle heat advection/conduction and/or (very) elevated radiogenic crustal heat production (Clark et al., 2011). Heat advection is common in (extension-dominated) accretionary orogens through the generation of hot, thin and rheologically weak lithosphere and shallow convection in back-arc basins, and their subsequent closure during convergence and crustal thickening (Clark et al., 2011; Collins, 2002; Currie and Hyndman, 2006; Hyndman et al., 2005; Sizova et al., 2010). Where the existing crust is sufficiently thin, weak and warm, shortening may result in sagduction, gravitational dripping or delamination of the lithosphere rather than crustal thickening. This process forms ultra-hot orogens that are great in areal expanse, lack topography and are characterised by a long duration of mantle heating that is self-propagating (Chardon et al., 2009; Gorczyk et al., 2015; Harley, 2016; Perchuk et al., 2016). Collisional orogens are commonly superimposed on otherwise extensional accretionary orogens. The interiors of large, hot (collisional) orogens can also provide a conducive environment to augment crustal temperatures. In this scenario, elevated levels of heat producing elements may strongly enhance conductive heating

in the mid–lower crust following significant tectonic thickening (e.g. Tibetan-style), if the crust is incubated at depth over an extended period (e.g. 60 Myr; Beaumont et al., 2010; Clark et al., 2011) because the rate of erosion or exhumation is slow (Bea, 2012; Chamberlain and Sonder, 1990; Clark et al., 2011; Huerta et al., 1998; Sandiford et al., 2002). Further, regional high temperatures may ensue during post-collision extensional relaxation of the over-thickened crust (Beaumont et al., 2006; England and Thompson, 1984; Jamieson et al., 2002; Sandiford et al., 1998). However, where requirements for elevated (>>3.5 $\mu W\ m^{-3}$) upper crustal heat production, slow erosion rates (<0.05 mm/yr), and great lateral expanse of the collisional orogen are not satisfied (Kelsey and Hand, 2015, and references therein), additional, mantle-derived advective heat sources are also required. Broadly, the relationship between regional, high thermal gradient metamorphism and convergent deformation might therefore be considered indicative of: (1) an extensional regime during or leading up to intial amalgamation; or (2) a response of crustal thickening post the terminal stage of amalgamation. However, heating mechanisms are often difficult to distinguish and are poorly quantified, and a number of mechanisms for the generation of regional, long-lived, high thermal gradients may operate in concert.

Attempts to understand the formation or style of orogens commonly use the degree of crustal thickening, distribution of strain, crustal temperature and topography as classifiers (e.g. Chardon et al., 2009; Jamieson and Beaumont, 2013). Using such approaches, the Musgrave Inlier and Albany–Fraser Orogen, that comprise the majority of the MAFWO, are classified as ultra-hot and mixed (i.e. an accretionary–large hot orogen hybrid) orogens, respectively (Roberts et al., 2015). However, this broad characterisation is based on geographical extent, and temperature and does not provide specific information on the metamorphic features (and variation) of the orogen nor the likely thermal drivers. It also fails to accommodate the complex and disparate, but seemingly synchronous, metamorphic and magmatic conditions reflected within individual tectonic elements of the broader system. As the MAFWO has recently seen a rapid expansion of geological knowledge for the inaccessible regions of East Antarctica (in part of this thesis) and the south-eastern margin of the Albany–Fraser system (e.g. Morrissey et al., 2017b; Tucker et al., 2018, 2017b), a review of the Mesoproterozoic geology of the orogen, its thermal drivers and tectonic setting is timely. This is particularly the case as recent models proposed for the metamorphic and crustal evolution of the MAFWO are commonly restricted in the breadth of information that is integrated in their creation (e.g. only considered at the terrane-scale or for a specific time frame).

The primary focus of this review is the compilation and integration of the metamorphic record across the entire MAFWO. However, the pre-Mesoroterozoic crustal evolution, and geochemical and geochronological features of syn-metamophic magmatism are also considered, as this allows for a holistic consideration of the available data to better elucidate the metamorphic evolution of the system. As such, it is the first review that integrates metamorphic and magmatic data from across the MAFWO to assess: (1) the spatial and temporal extent of individual events within the orogen; (2) secular changes in the thermal character of the crust; and, (3) the relationship between magmatism and metamorphism within the orogen. This information is combined to re-evaluate existing tectonic models for the MAFWO and discuss the likely thermal drivers for regional, long-lived, high thermal gradients.

2. A NOTE ON TERMINOLOGY

Throughout this review, the abbreviation MAFWO is used to collectively refer to all geological terranes with a shared high-temperature, Mesoproterozoic magmatic and metamorphic history that are central to the amalgamation of components of Australia and East Antarctica during the assembly of Rodinia (ca. 1300–900 Ma; Aitken et al., 2016; Li et al., 2008; Pisarevsky et al., 2003). The MAFWO can accordingly be subdivided into Australian and Antarctic components (Section 3, Fig. 1). The terminology west, central and east MAFWO is adopted to collectively discuss the Mesoproterozoic D_1/M_1 and D_2/M_2 magmatic and metamorphic features of different parts of the MAFWO (Table 1, Fig. 2).

As stated previously, the MAFWO records evidence for a two-stage Mesoproterozoic tectono-metamorphic and magmatic evolution involving intense deformation, amphibolite–granulite facies crustal reworking and emplacement of voluminous mafic and felsic intrusives. However, different tectonic regions of the MAFWO are

Table 1. Defined nomenclature and time periods of MAFWO orogenesis, by tectonic region*

This study	Southern NAC	Musgrave Inlier	Albany–Fraser Orogen	Windmill Islands	Bunger Hills region
D_1/M_1 1345–1260 Ma		*Mt. West Orogeny* 1345–1293 Ma	*Stage-1 AFO* 1330–1260 Ma	*D_1/M_1* 1320–1300 Ma	
D_2/M_2 1220–1130 Ma	*Teapot Event* 1160–1130 Ma	*Musgrave Orogeny* 1220–1140 Ma	*Stage-2 AFO* 1225–1140 Ma	*D_2/M_2* 1200–1160 Ma	Stage-2 AFO equiv. 1220–1150 Ma
Reference	Black and Shaw (1995) Claoue-Long and Hoatson (2005) Morrissey *et al.* (2011) Wong *et al.* (2015)	Howard *et al.* (2015) Smithies *et al.* (2015)	Spaggiari *et al.* (2015) Spaggiari *et al.* (2014)	Morrissey *et al.* (2017a) Post (2000)	Sheraton *et al.* (1992) Tucker *et al.* (2018) Tucker *et al.* (2017)

*Time-periods are approximate and encompass the age of magmatism and metamorphism. Abbreviation: AFO, Albany–Fraser Orogeny.

documented to have experienced metamorphism and magmatism at slightly different times, and the terminology of such events is region-specific (Table 2). To account for the differences in age and nomenclature, the terminology adopted here is D_1/M_1 and D_2/M_2, to refer collectively to metamorphism and magmatism that occurred orogen-wide between the approximate time periods ca. 1345–1260 Ma and ca. 1220–1130 Ma, respectively. The nomenclature D_1 and D_2 are used to refer overall to the period of orogenesis; M_1 and M_2 specifically refer to the associated metamorphism.

Specific details of the Mesoproterozoic ca. 1090–1040 Ma Giles Event (Warakurna Large Igneous Province; Evins et al., 2010) that affected much of central and western Australia are not covered in this review as this event post-dates D_2/M_2 and is accordingly outside the immediate scope of this study. However, it is important to note, that the geodynamic interpretation of D_2/M_2 in the Musgrave Inlier is likely to be an important precursor for the Giles Event (Smithies et al., 2015a), and this is discussed (Section 9.3). Further, this review does not discuss syn- to post-D_2/M_2 dolerite dyke emplacement in the Albany–Fraser Orogen, Bunger Hills and Windmill Islands.

3. TECTONIC SUBDIVISIONS OF THE MAFWO

The Australian components of the MAFWO have historically been considered to comprise the Musgrave Inlier and Albany–Fraser Orogen. The Musgrave Inlier is exposed in central Australia and separates the North and South Australian cratons (NAC and SAC, respectively; Fig. 1). The Mesoproterozoic–Neoproterozoic rocks that comprise the Musgrave Inlier are surrounded by younger, Neoproterozoic–Paleozoic basins. These basins conceal the contact relationships between rocks in the Musgrave Inlier, Albany–Fraser Orogen, NAC and SAC. However, recent metamorphic work suggests that D_2/M_2 tectonism within the Musgrave Inlier extends into the the Warumpi Province and southern Aileron Province along the southern edge of the NAC (Morrissey et al., 2011; Wong et al., 2015). A geodynamic connection between these two regions is also interpreted from geophysical surveys (Selway et al., 2009) and evidence for contemporaneous Mesoproterozoic granite magmatism (e.g. Nelson et al., 1989; Sun et al., 1995; Wong et al., 2015). A reappraisal of the metamorphic evolution of Proterozoic Australian continental margins therefore also warrants inclusion of the southern NAC.

The Paleoproterozoic–Mesoproterozoic Albany–Fraser Orogen extends ~1200 km along the southern and south-eastern margin of the Archean Yilgarn Craton (West Australian Craton, WAC; Fig. 1). Magnetic anomalies imaged beneath the Officer Basin that separates the uncovered Musgrave basement from the northern Albany–Fraser Orogen suggest a continuation of Mesoproterozoic magmatic rocks between these two regions and therefore that their true geographical extent is much greater than their current exposure (Aitken and Betts, 2008). The Madura and Coompana Provinces are located east of the Albany–Fraser Orogen and are separated by crustal-scale shear zones. However, both domains are entirely concealed by Paleozoic sedimentary rocks. Seismic transects suggest that the SAC margin lies beneath the Coompana Province (Dutch et al., 2015b). Recent stratigraphic and mineral exploration drilling into geophysical magnetic and/or gravity highs find evidence for Mesoproterozoic mafic–intermediate intrusive rocks in these regions (Kirkland et al., 2017; Spaggiari and Smithies, 2015; Wise et al., 2015). These rocks have an interpreted early

Table 2. Tectonic subdivisions of the MAFWO

	West MAFWO	Central MAFWO	East MAFWO
Australia	**West Albany–Fraser Orogen***	**East Albany–Fraser Orogen**	**Central and east Musgrave Inlier**
	▪ Northern Foreland	▪ East Biranup Zone (minor)	**Southern NAC**
	▪ West Biranup Zone	▪ Fraser Zone	▪ Warumpi Province
	▪ West Nornalup Zone (minor)	▪ East Nornalup Zone	▪ Southern Aileron Province
		Madura Province	
		Coompana Province	
		West Musgrave Inlier	
East Antarctica	**West Wilkes Land**	**East Wilkes Land**	
	▪ Bunger Hills	▪ Windmill Islands	
	▪ Highjump Archipelago		

*Approximately west of Esperance township (see Figs. 1 and 3)

Mesoproterozoic geodynamic connection with the east Nornalup Zone, and conceivably also with the west Musgrave Inlier (refer to Section 4; Aitken et al., 2016; Dutch et al., 2017; Kirkland et al., 2017; Spaggiari et al., 2015; Spaggiari and Smithies, 2015) and therefore their Mesoproterozoic evolution is also considered in this review.

The Windmill Islands, the Bunger Hills and the Highjump Archipelago are located on the coast of Wilkes Land, East Antarctica, and provide the only exposure of the Precambrian East Antarctic Craton that can be directly linked to the MAFWO (Fig. 1; Fitzsimons, 2003; Morrissey et al., 2017b; Tucker et al., 2017). The Windmill Islands include approximately 400 km^2 of exposed outcrop on peninsulas and islands in the vicinity of the Australian Antarctic Casey Station (located at approximately 111°E, 66°S). The Bunger Hills and Highjump Archipelago crop out over a similar size area and are located approximately 400 km west of the Windmill Islands, within the geophysically-defined Bunger Hills Block that is characterised by a series of aligned, high-intensity magnetic anomalies (Aitken et al., 2014).

Magnetic intensity and gravity anomaly data reflect a continuity of major geophysical features from southwest Australia into East Antarctica (Aitken et al., 2016; Aitken et al., 2014). The reconstructed (original) Mesoproterozoic configuration of Wilkes Land to southwest Australia accounts for significant offset along these geological structures. The Windmill Islands are reconciled with the east Nornalup Zone in the east Albany–Fraser Orogen, and the Bunger Hills with the west Albany–Fraser Orogen, as the westernmost exposure of the MAFWO (Fig. 1; Aitken et al., 2016). Geographic correlations between the Australian and Antarctic components of the orogen mean that the Windmill Islands and Bunger Hills can provide additional data for Mesoproterozoic tectonic models of the central and west MAFWO, respectively.

4. PRE-D_1/M_1 GEOLOGICAL ARCHITECTURE

The pre-D_1/M_1 regional geology and crustal evolution of Australian and Antarctic components of the MAFWO prior to Mesoproterozoic orogenesis has been investigated in numerous studies (e.g. Howard et al., 2015; Kirkland et al., 2015a, 2013b, 2011; Morrissey et al., 2017b; Scrimgeour et al., 2005; Smithies et al., 2015b; Spaggiari et al., 2009, 2015; Spaggiari and Tyler, 2014; Tucker et al., 2017) and is therefore only briefly summarised here (also Fig. 2). MAFWO tectonic components are grouped and discussed below based upon similarities in their pre-D_1/M_1 crustal evolution.

4.1 West Albany–Fraser Orogen and Bunger Hills

The pre-D_1/M_1 crustal evolution of the west Albany–Fraser Orogen and the Bunger Hills is similar in that both regions record evidence for Paleoproterozoic to early Mesoproterozoic autochthonous reworking of the Yilgarn Craton margin (Kirkland et al., 2015a, 2011; Smithies et al., 2015b; Spaggiari et al., 2015; Spaggiari and Tyler, 2014; Tucker et al., 2017). Within the Albany–Fraser Orogen, the Northern Foreland and the Tropicana Zone represent the reworked margin of the Archean Yilgarn Craton that was thrust north-westwards over non-reworked Yilgarn crust (Kirkland et al., 2015b; Occhipinti et al., 2017; Spaggiari et al., 2009; Spaggiari and Tyler, 2014). Archean mafic–felsic orthogneiss and interlayered paragneiss with age and isotopic affinity to the Yilgarn Craton also crop out in the southeast of the Bunger Hills, and are interpreted to represent a rifted fragment of the Yilgarn Craton (during ca. 1815–1600 Ma extension; Tucker et al., 2017).

From NW to SE, away from the Yigarn Craton margin, the Albany–Fraser Orogen is comprised of the fault-bound Biranup, Fraser and Nornalup Zones, and remnants of three major basin systems (Barren, Arid and Ragged basins; Spaggiari et al., 2014, 2015; Spaggiari and Tyler, 2014). These regions record a broad south-eastwards transition to progressively younger tectonism, increasingly extended crust, and decreasing isotopic influence from the Yilgarn Craton. Protoliths to voluminous mafic–felsic orthogneiss in the Biranup and Nornalup Zones were emplaced during Paleoproterozoic extension and reworking of the Yilgarn Craton margin (three main phases: 1815–1800 Ma, 1780–1760 Ma, 1710–1650 Ma; Kirkland et al., 2011; Smithies et al., 2015b; Spaggiari et al., 2015). Extension was accompanied by significant mantle magmatism (Smithies et al., 2015b) and coeval, widespread sedimentation within a series of sub-basins (all Barren Basin) across the south and south-eastern Yilgarn Craton (Spaggiari et al., 2015). Similarly, the Bunger Hills records the emplacement and deposition of Paleoproterozoic protoliths to felsic–intermediate orthogneiss, minor mafic gneiss and interlayered metasedimentary rocks within a volcano-sedimentary basin (Sheraton et al., 1992; Tucker et al., 2017). Paleoproterozoic sediment deposition was cyclically-linked with the emplacement, crystallisation and erosion of Paleoproterozoic magmatic rocks that released the bulk of detritus into the evolving basin (Spaggiari et al., 2015). Kirkland et al. (2011) initially suggested that Paleoproterozoic extension occurred within a back-arc that formed as a result of a retreating subduction margin by ca. 1710 Ma on the basis of subduction-like geochemistry and increasingly juvenile isotope signatures of the Paleoproterozoic igneous rocks over time. However, Smithies et al. (2015b) subsequently reinterpreted the geochemistry of the intrusive rocks as not having a subduction-related petrogenesis. Spaggiari et al. (2015) also noted the maturity of the Barren Basin sediments and a lack of detritus exotic to the Yilgarn Craton. In light of these more recent findings, Paleoproterozoic extension is now considered to have occurred in a continental rift, or that the active subduction margin was far-field of the Albany–Fraser Orogen, possibly as distal as the present day Madura or Coompana Provinces (Smithies et al., 2015b; Spaggiari et al., 2015).

Protoliths to a thick sequence of migmatitic pelitic gneiss in the Bunger Hills were deposited during the Mesoproterozoic, with a probable maximum depositional age of ca. 1490 Ma (Tucker et al., 2017). Detritus is inferred sourced primarily from the Paleoproterozoic igneous rocks of the Biranup Zone and/or Bunger Hills, with a minor contribution from Archean (Yilgarn) basement (Tucker et al., 2017). Deposition was approximately synchronous with passive margin sedimentation in the central MAFWO (see Arid Basin, below).

4.2 East Albany–Fraser Orogen, Windmill Islands, Madura and Coompana Provinces

The east Albany–Fraser Orogen, Windmill Islands, Madura Province and Coompana Province have pre-D_1/M_1 geological histories that involved reworking of comparatively young, highly extended and juvenile crust (Kirkland et al., 2017; Morrissey et al., 2017b; Spaggiari et al., 2015; Spaggiari and Smithies, 2015; Zhang et al., 2012). A regionally extensive basin system (Arid Basin) formed between ca. 1600–1305 Ma and involved the deposition of sedimentary protoliths to the Malcolm Metamorphics (east Nornalup Zone), Gwynne Creek Gneiss (between the Fraser Zone and Biranup Zone), Snowys Dam Formation (Fraser Zone), and paragneiss from the west Nornalup Zone near Whalehead Rock, Albany (Adams, 2012; Love, 1999; Spaggiari et al., 2015; Spaggiari and Tyler, 2014). Arid Basin detritus is dominated by isotopically-juvenile ca. 1425–1375 Ma zircon derived from the ca. 1410 Ma Loongana Oceanic Arc, Madura Province, which was located near the east margin of the Albany–Fraser Orogen at this time (Spaggiari et al., 2015; Spaggiari and Smithies, 2015). Early Arid Basin sedimentation is inferred to have occurred in a passive margin setting, distal to the Yilgarn Craton, due to a paucity of Archean detritus (Spaggiari et al., 2015). Within this passive margin setting, a fore-arc basin is specifically invoked for deposition of protoliths to the Malcolm Metamorphics (Spaggiari et al., 2015) based on the geochemistry of inferred syn-depositional basalts (Spaggiari and Smithies, 2015), and the presence of the oldest (ca. 1455

Figure 2. (facing page) Time–space plot of ca. 3000–1000 Ma regional geology for tectonic elements of the Musgrave–Albany–Fraser–Wilkes Orogen. Adapted from Spaggiari et al. (2015). Terranes denoted as comprising the west, central and east MAFWO (see also Table 2) are indicated.

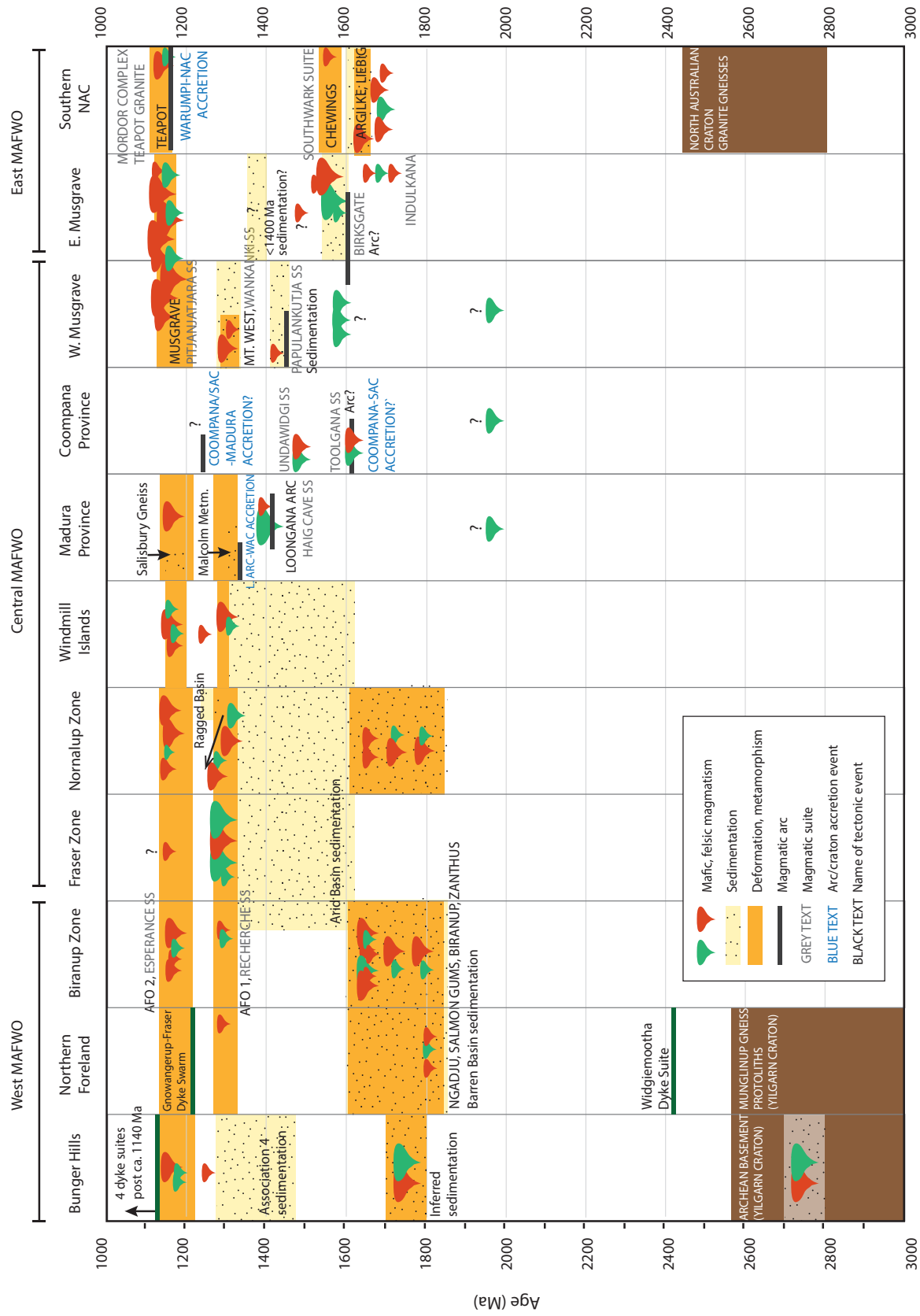
West MAFWO
Central MAFWO
East MAFWO
Bunger Hills
Northern Foreland
Biranup Zone
Fraser Zone
Nornalup Zone
Windmill Islands
Madura Province
Coompana Province
W. Musgrave
E. Musgrave
Southern NAC
Age (Ma)
1000
1200
1400
1600
1800
2000
2200
2400
2600
2800
3000
4 dyke suites post ca. 1140 Ma
Gnowangerup-Fraser Dyke Swarm
AFO 2, ESPERANCE SS
AFO 1, RECHERCHE SS
Association 4 sedimentation
Ragged Basin
Arid Basin sedimentation
Inferred sedimentation
NGADJU, SALMON GUMS, BIRANUP, ZANTHUS
Barren Basin sedimentation
Widgiemootha Dyke Suite
ARCHEAN BASEMENT (YILGARN CRATON)
MUNGLINUP GNEISS PROTOLITHS (YILGARN CRATON)
Salisbury Gneiss
Malcolm Metm.
ARC-WAC ACCRETION
LOONGANA ARC
HAIG CAVE SS
COOMPANA/SAC -MADURA ACCRETION?
UNDAWIDGI SS
TOOLGANA SS
Arc?
COOMPANA-SAC ACCRETION?
PAPULANKUTJA SS
Sedimentation
MT. WEST,WANKANKI SS
<1400 Ma sedimentation?
BIRKSGATE Arc?
MUSGRAVE
PITJANJATJARA SS
SOUTHWARK SUITE
CHEWINGS
ARGILKE, LIEBIG
INDULKANA
MORDOR COMPLEX
TEAPOT GRANITE
TEAPOT
WARUMPI-NAC ACCRETION
NORTH AUSTRALIAN CRATON GRANITE GNEISSES
Mafic, felsic magmatism
Sedimentation
Deformation, metamorphism
Magmatic arc
Magmatic suite
Arc/craton accretion event
Name of tectonic event
GREY TEXT
BLUE TEXT
BLACK TEXT

Ma; Adams, 2012) arc-derived age components in this part of the Arid Basin. Spaggiari et al. (2015) propose subsequent closure of the passive margin following accretion of the Loongana Arc onto the east Nornalup Zone by ca. 1330 Ma, where detritus was then shed into an evolving foreland basin (Snowys Dam Formation).

Pre-Mesoproterozoic basement to the Windmill Islands is unexposed. However, the relatively juvenile isotope signatures of Mesoproterozoic igneous rocks allow inferences to be made that the basement to the Windmill Islands region contains little evolved material (Morrissey et al., 2017b). The oldest ages from the Windmill Islands come from pelitic gneiss that was deposited between ca. 1350–1315 Ma, immediately prior to D_1/M_1 (Morrissey et al., 2017b; Post, 2000; Zhang et al., 2012). The age of sediment deposition, detrital zircon provenance and Hf-isotopes from the detrital zircon indicate that the Windmill Islands metasedimentary rocks are equivalent to the Arid Basin (Morrissey et al., 2017b). This interpretation is consistent with previous geophysical correlations between these two regions (e.g. Aitken et al., 2016; Aitken et al., 2014). However, in addition to the primary source of sediment being the ca. 1410 Ma Loongana Arc, the Windmill Islands metasedimentary rocks also suggest possible contributions from recycled Barren Basin sediments, the Biranup Zone and the Yilgarn Craton (Morrissey et al., 2017b). This combination of sources and the short interval between deposition and high temperature D_1/M_1 metamorphism and magmatism (initiating at ca. 1315 Ma) led Morrissey et al. (2017a,b) to infer a back-arc setting for sediment deposition.

Drill holes intersecting basement in the Madura Province and the Forrest Zone of the west Coompana Province reveal four early–mid-Mesoproterozoic domains (Kirkland et al., 2017; Spaggiari and Smithies, 2015). From east to west, these are the ca. 1610 Ma Toolgana Supersuite, ca. 1490 Ma Undawidgi Supersuite, ca. 1478 Ma Sleeper Camp Formation and 1415–1389 Ma Haig Cave Supersuite (Kirkland et al., 2017; Spaggiari and Smithies, 2015). The extent and understanding of these suites is limited due to few drillholes that have intersected basement over a region of 200,000 km^2. One drill hole intersects ca. 1500 Ma isotopically-juvenile granite gneiss in the east Coompana Province, supporting an eastern continuation of these basement rocks, towards the SAC (Wade et al., 2007).

The Madura–Forrest–Coompana rocks contain magmatic zircon with ca. 2400–1700 Ma Lu–Hf depleted mantle model ages. As a result, these rocks are interpreted to have formed by repeated and variable reworking/melting of Paleoproterozoic oceanic (juvenile) crust that was periodically re-fertilised by new mantle melts (Kirkland et al., 2017; Spaggiari and Smithies, 2015). Hyper-extension of Archean (Yilgarn) crustal fragments may have provided a minor evolved contribution to the parent magmas (e.g. Sleeper Camp Fm; Kirkland et al., 2017). Similarites in the age and geochemistry of the Toolgana Supersuite with the arc-related St. Peter Suite in the SW Gawler Craton suggests the two may be corelatives (Dutch et al., 2015a). The Coompana Province is inferred to have been thrust over the west SAC (west Gawler Craton) at ca. 1600 Ma due to seismic imagery indicating a west-dipping structure, differences in Nd-model ages between these two regions, and a lack of evidence for < ca. 1500 Ma deformation and metamorphism in the Gawler Craton (Dutch et al., 2015a).

4.3 Musgrave Inlier

Precise details on the basement to the Musgrave Inlier are limited, particularly in the central Inlier, due to the remote and inaccessible nature of this region. As a result, the specific number, age and nature of basement components remains unclear. Aitken et al. (2016) characterise the Musgrave Inlier into north, west, central and east domains, on the basis of inferred differences in mid-Mesoproterozoic crustal evolution.

The eastern domain contains the oldest recognised ages in the Musgrave Inlier with ca. 2900–2800 Ma inherited zircon with ca. 1700 Ma magmatic overgrowths in felsic orthogneiss (Smits et al., 2014). This Archean age peak is not observed in the NAC nor SAC, both of which are dominated by ca. 2600–2440 Ma ages, but it is observed in the Yilgarn Craton, suggesting an exotic origin for this Archean inheritance (Smits et al., 2014). Mafic and felsic orthogneiss, pelite gneiss, calc-silicate and quartzite of the Birksgate Complex (ca. 1600–1550 Ma; Camacho and Fanning, 1995; Dutch et al., 2013b; Edgoose et al., 2004; Gray, 1978; Wade et al., 2008), are exposed in the north, central and east Musgrave Inlier. Subduction-like geochemistry and juvenile Nd isotope signatures

suggest that the Birksgate Complex is a felsic intrusive and volcano-sedimentary sequence with protoliths that were deposited and emplaced in a ca. 1600 Ma magmatic arc (Edgoose et al., 2004; Glikson et al., 1996; Wade et al., 2006; Wade et al., 2008). This arc has been interpreted to be situated outboard of the SAC (Aitken and Betts, 2009; Aitken et al., 2016; Betts and Giles, 2006; Wade et al., 2006). Similarly-aged, arc-related magmatism is documented in the Forrest Zone of the Coompana Province (Kirkland et al., 2017; Spaggiari and Smithies, 2015). A lack of information from the central and east Musgrave Inlier, relative to the west, makes the nature of basement to these regions difficult to assess further at this stage.

Equivalent-aged magmatism and sedimentation is rare in the west and central Musgrave Inlier (Howard et al., 2015). The oldest exposed rocks in the west Musgrave Inlier comprise the localised ca. 1575 Ma Warlawuraa Supersuite (~20 km^2 outcrop), the ca. 1400 Ma metagranitic and metavolcanic Papulanktja Supersuite, and the equivalent-aged volcano-sedimentary successions that they intrude (Howard et al., 2015). However, considerably older, inferred exotic, Paleoproterozoic (ca. 1820–1700 Ma) and rare Archean (ca. 3100 Ma) age components are documented in the detrital zircon age spectra of the Wirku Metamorphics in the Latitude Hills area (Howard et al., 2015). The majority of detritus in the Wirku Metamorphics is Mesoproterozoic (ages predominantly ca. 1570–1320 Ma) and shows a spatial trend in younging provenance from NE to SW (Evins et al., 2012). The abundance of > ca. 1410 Ma detritus in the NE with no exposed rocks of this age suggests that the zircon are from an exotic source (e.g. Yilgarn Craton, Gawler Craton, Rudall Province) or were sourced from an unexposed basement terrane (Evins et al., 2012). The abundance of < ca. 1410 Ma detritus in the SW is considered locally-sourced, largely from coeval ca. 1345–1280 Ma felsic intrusives (Wankanki Supersuite, Section 5.2; Evins et al., 2012; Howard et al., 2015). Deposition occurred at ca. 1340–1300 Ma and is interpreted to have occurred in a continental arc setting or an intracontinental basin above N-dipping subduction (Evins et al., 2012). While the Wirku Metamorphics (senso stricto) are unrecognised in the east Musgrave Inlier, Wade et al. (2006) note that some metavolcano-sedimentary rocks assigned to the Birksgate Complex yield inferred depositional ages < ca. 1400 Ma, with a significant proportion of detrital zircon aged ca. 1540–1420 Ma (Wade et al., 2005; Wade et al., 2008). Howard et al. (2015) also note that the detrital zircon spectra of paragneiss assigned to the Wirku Metamorphics from the Latitude Hills region (described above) is very similar to the interpreted magmatic and xenocrystic zircon ages of the Indulkana orthogneiss from the east Musgrave Inlier. This observation suggests that re-examination of the inferred Indulkana protolith may be required, with potential implications for the interpreted timing of magmatism and/or the extent of Wirku Metamorphic sedimentation, and therefore the geodynamic evolution of the east Musgrave Inlier.

Whole rock Sm–Nd and zircon Lu–Hf isotope model ages suggest that basement to the west Musgrave Inlier formed in two stages, involving juvenile crustal addition at ca. 1950–1900 Ma and ca. 1600–1550 Ma (Kirkland et al., 2015a; Kirkland et al., 2013a). Basement to the west Musgrave Inlier is therefore considerably younger and more juvenile than the Albany–Fraser Orogen, despite being within the same orogenic system. Possible links are instead invoked between basement to the west Musgrave Inlier, parts of the Gawler Craton, and the Madura and Coompana Provinces (Kirkland et al., 2017, 2015a, 2013a; Reid et al., 2014; Spaggiari and Smithies, 2015; Wade et al., 2006). These regions are suggested to form a geographically continuous expanse of juvenile Paleo–Mesoproterozoic crust (i.e. relict oceanic crust and new mantle melts; Kirkland et al., 2017).

4.4 Southern NAC

The oldest lithological component of the southern NAC comprises ca. 1690–1610 Ma felsic orthogneiss and metasedimentary rocks that form an inferred volcano-sedimentary sequence (Scrimgeour et al., 2005; Warren and Shaw, 1995; Wong et al., 2015). Protoliths to these rocks were metamorphosed and deformed under amphibolite–granulite facies conditions during the late Paleo–early Mesoproterozoic (Fig. 2; Collins and Shaw, 1995; Scrimgeour et al., 2005; Wong et al., 2015).

The Warumpi Province is separated from the Aileron Province by a series of east–west-trending thrusts at the surface interface and by the lithospheric-scale Central Australian Suture in geophysical imagery (Selway et al., 2009),

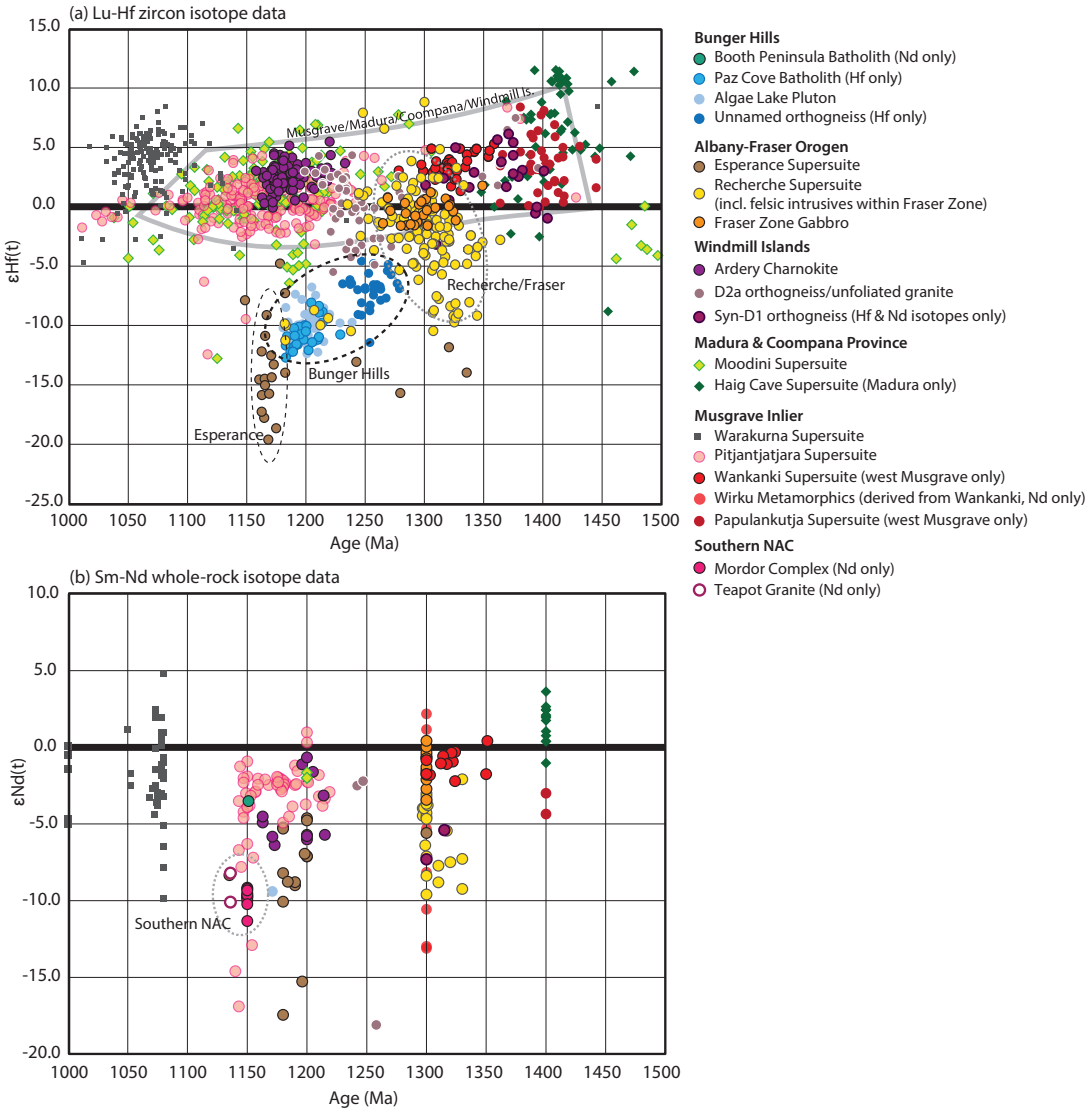
(a) Lu-Hf zircon isotope data
εHf(t)
Age (Ma)
Musgrave/Madura/Coompana/Windmill Is.
Recherche/Fraser
Bunger Hills
Esperance
(b) Sm-Nd whole-rock isotope data
εNd(t)
Age (Ma)
Southern NAC
Bunger Hills
Booth Peninsula Batholith (Nd only)
Paz Cove Batholith (Hf only)
Algae Lake Pluton
Unnamed orthogneiss (Hf only)
Albany-Fraser Orogen
Esperance Supersuite
Recherche Supersuite
(incl. felsic intrusives within Fraser Zone)
Fraser Zone Gabbro
Windmill Islands
Ardery Charnokite
D2a orthogneiss/unfoliated granite
Syn-D1 orthogneiss (Hf & Nd isotopes only)
Madura & Coompana Province
Moodini Supersuite
Haig Cave Supersuite (Madura only)
Musgrave Inlier
Warakurna Supersuite
Pitjantjatjara Supersuite
Wankanki Supersuite (west Musgrave only)
Wirku Metamorphics (derived from Wankanki, Nd only)
Papulankutja Supersuite (west Musgrave only)
Southern NAC
Mordor Complex (Nd only)
Teapot Granite (Nd only)

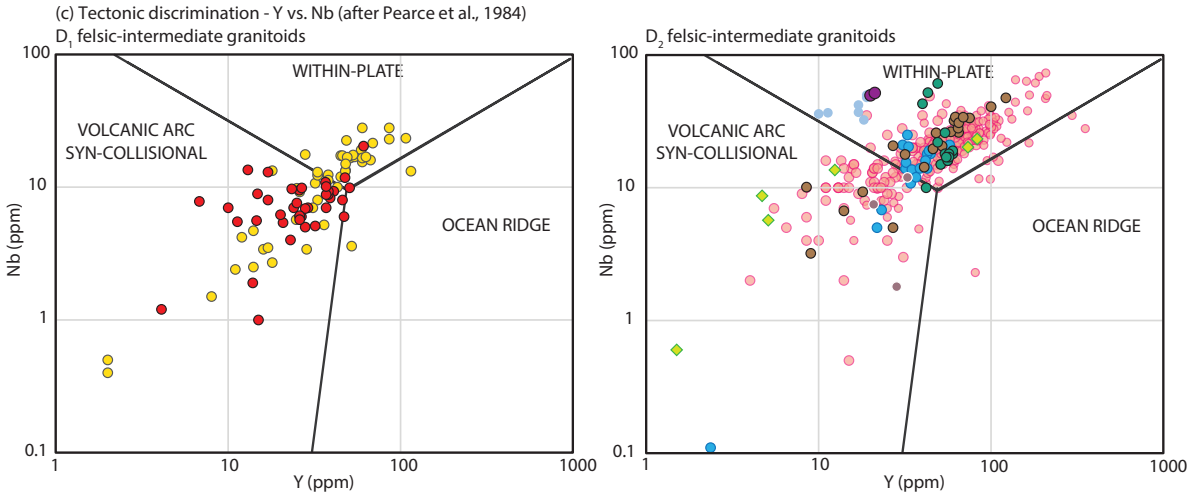
(c) Tectonic discrimination - Y vs. Nb (after Pearce et al., 1984)
D1 felsic-intermediate granitoids
D2 felsic-intermediate granitoids
WITHIN-PLATE
VOLCANIC ARC
SYN-COLLISIONAL
OCEAN RIDGE
Nb (ppm)
Y (ppm)

which extends southwards beneath the Amadeus Basin, towards the Musgrave Inlier. The Warumpi Province was traditionally considered exotic to the NAC (e.g. Scrimgeour et al., 2005). However, recent Hf-isotope data suggests a late Paleoproterozoic (ca. 1690–1670 Ma) connection with at least the west Aileron Province (Kirkland et al., 2013a). Betts et al. (2011) also suggested that the Warumpi Province may represent a fragment of the Aileron Province that was rifted and reattached, as also depicted in recent paleogeographic reconstructions (Aitken et al., 2016). The absence of any major geophysical discontinuities between the northern Musgrave Inlier and the Warumpi Province suggests that a suture does not exist between these two regions (Selway et al., 2011). However, Kirkland et al. (2013a) note that the Warumpi Province does not form basement to the west Musgrave Inlier. Orogenesis in the central Warumpi Province and southern Ailteron Province at ca. 1640 Ma was traditionally inferred to relate to collisional suturing of the Warumpi Province with the NAC along the Central Australian Suture (Scrimgeour et al., 2005). However, more recent work assigns this event to the late Mesoproterozoic, occurring syn- to post-MAFWO orogenesis (ca. 1130–1080 Ma; Morrissey et al., 2011; Wong et al., 2015).

5. MAFWO MAGMATIC FEATURES

A number of pre-established spatial, age and isotopic trends in D_1 and D_2 magmatism are understood from region-specific studies investigating separate terranes of the MAFWO (e.g. Smithies et al., 2015b), but orogen-wide trends have not been evaluated. As such, characteristics of the MAFWO Mesoproterozoic magmatic rocks are discussed below in four sections that reflect their timing of emplacement, rather than their geographical occurrence. Table 3 provides a comprehensive summary of the spatial, age, lithological and geochemical features of MAFWO magmatic rocks. To explore trends in magmatism and metamorphism, and links between crustal growth/reworking and the metamorphic character of D_1–D_2 orogenesis, a series of maps are compiled from published geochronological and isotopic data (Appendix A). Details of the mapping and plotting procedures are also provided in Appendix A. Metadata associated with the compiled datasets are provided in Appendices B–E. Isotopic data ($\varepsilon_{Hf}(t)$ and $\varepsilon_{Nd}(t)$ versus age) and geochemical data for tectonic discrimination are also plotted in Fig. 3. Figure 4 shows zircon saturation thermometry (Tzr) calculated from whole rock analyses for felsic–intermediate granitoids (SiO_2 content >55 wt %) plotted against their relative position (west-to-east) across the MAFWO.

5.1 Pre-D_1 (ca. 1410–1390 Ma) Loongana–Papulankutja arc rocks

Early Mesoproterozoic arc-like rocks are documented in the Madura Province and the West Musgrave Inlier (Smithies et al., 2010; Spaggiari and Smithies, 2015). The Haig Cave Supersuite consists of mafic–ultramafic rocks and plagiogranite that form the ca. 1410 Ma Loongana oceanic arc of the Madura Province (Spaggiari et al., 2015; Spaggiari and Smithies, 2015) that was inferred to have accreted to the east Nornalup Zone by the onset of D_1/M_1 at ca. 1330 Ma (Spaggiari et al., 2015). The Papulankutja Supersuite is spatially isolated in the west Musgrave Inlier (Howard et al., 2015). The tectonic setting in which the Papulankutja Supersuite was emplaced is therefore poorly known, but may reflect continental arc magmatism on the basis of its geochemical and lithological similarities to the D_1 calc-alkaline Wankanki Supersuite that is more definitively linked to an arc setting (but see

Figure 3. (facing page) Geochemical and isotope characteristics of MAFWO Mesoproterozoic magmatism. (a) Lu–Hf zircon isotope data; (b) Sm–Nd whole rock isotope data; (c) Geochemical tectonic discrimination diagram (Y vs Nb, after Pearce *et al.,* 1984). In (a) and (b), deviations in Hf and Nd isotopic composition at the time of magma crystallisation (t) from the chondrite uniform reservoir (CHUR) standard are expressed in epsilon units, εHf(t) and εNd(t), respectively. Symbology used to represent the different magmatic suites is equivalent over (a)–(c). Isotope data from specific tectonic regions are annotated to distinguish main differences. Data from pre-D_1 magmas (Haig Cave Supersuite, Papulankutja Supersuite) and the Warakurna Supersuite (post-D_2) are shown for comparison with D_1 and D_2 magmas. Data are sourced from the publically-available Geological Survey of Western Australia online databases (WACHEM and GeoVIEW.WA), supplemented with additional data from the: Bunger Hills (Sheraton et al., 1992, and unpublished data from N. Tucker; Sheraton et al., 1995; Tucker et al., 2017), Windmill Islands (Möller et al., 2002; Morrissey et al., 2017b; Post, 2000; Zhang et al., 2012), Madura and Coompana Provinces (Kirkland et al., 2017; Kirkland et al., 2015a; Spaggiari and Smithies, 2015), Albany–Fraser Orogen (Fletcher et al., 1983; Kirkland et al., 2015a; Kirkland et al., 2011; Maier et al., 2016b; Nelson et al., 1995; Smithies et al., 2013; Smithies et al., 2015b), Musgrave Inlier (Dutch et al., 2013a; Edgoose et al., 2004; Glikson et al., 1996; Kirkland et al., 2015a; Kirkland et al., 2013a; Smithies et al., 2011; Smits et al., 2014), southern North Australian Craton (Nelson et al., 1989; Sun et al., 1995), and the Giles Complex (Dutch et al., 2013a; Edgoose et al., 2004; Glikson et al., 1996; Smithies et al., 2010b; Zhao and McCulloch, 1993).

Section 5.2; Howard et al., 2015; Kirkland et al., 2013a). The more isotopically-evolved signature of the Papulankutja Supersuite compared with the Haig Cave Supersuite suggests a continental crust component in the arc—either as the hosting crust, or as an underthrust component (Kirkland et al., 2013a). Tectonic reconstructions of Aitken et al. (2016) imply that the Haig Cave Supersuite and the Papulankutja Supersuite are analoguous, with the latter forming along a north-eastern extension of the Loongana Arc.

5.2 D_1 (ca. 1345–1280 Ma) felsic calc-alkaline and mafic magmatism

The spatial representation of U–Pb magmatic age data in Appendix A illustrates that D_1 magmatism is largely confined to the central MAFWO, occurring in the Windmill Islands, along the east margin of the Albany–Fraser Orogen within the Nornalup and Fraser Zones, and in the west Musgrave Inlier (Fig. 1). The magmatic expression of D_1 involved emplacement of three compositionally and lithologically distinct suites: (1) regionally-expansive, calc-alkaline, felsic–intermediate intrusives; (2) relatively localised, weakly peraluminous anatectic melts; and, (3) mafic rocks assigned to the Fraser Gabbro that occur only within the Fraser Zone (Table 3). In general, all D_1 magmas exhibit relatively juvenile zircon and whole-rock isotopic compositions (Figs. 3a and b). Calc-alkaline, felsic–intermediate rocks are represented by the Wankanki Supersuite (1345–1293 Ma) in the west Musgrave Inlier and

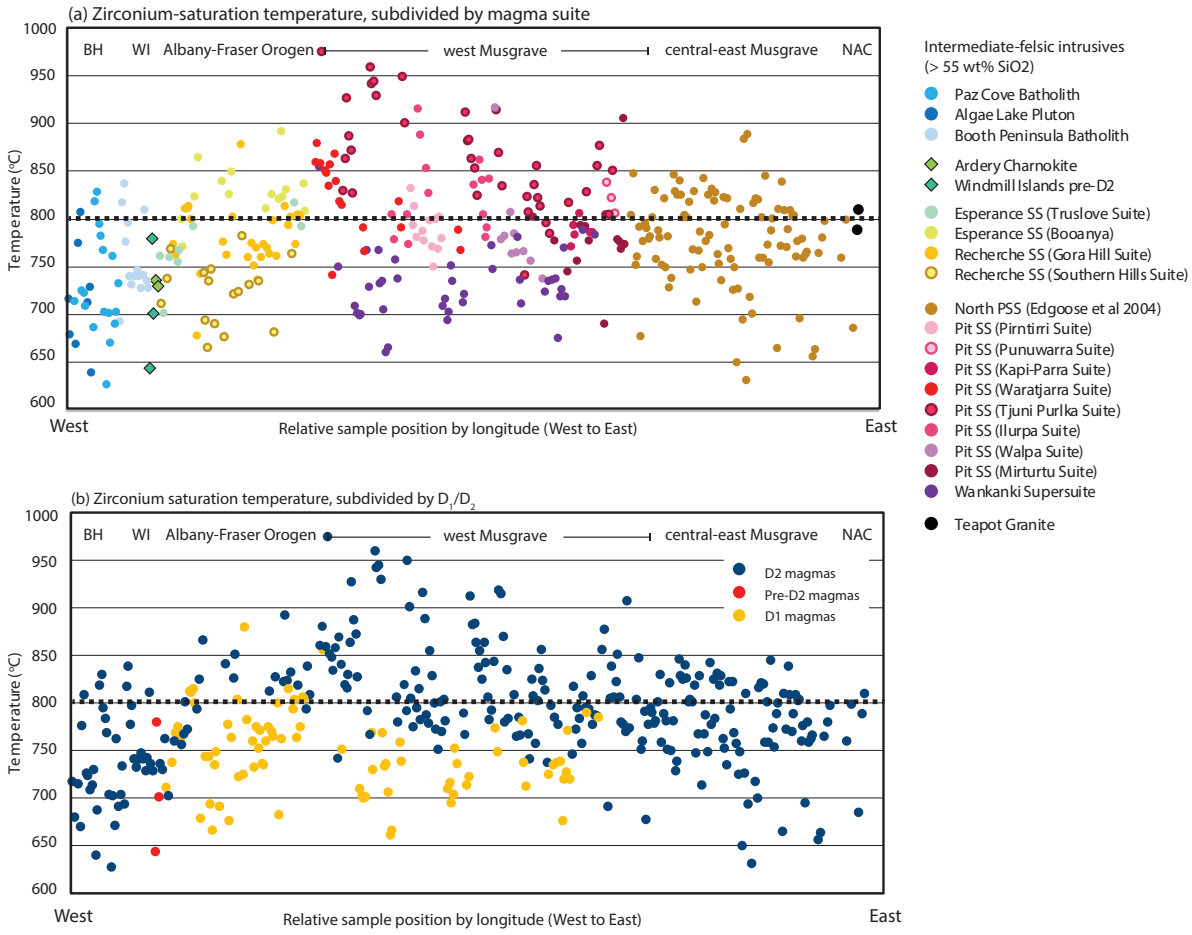

Figure 4. Zirconium saturation temperature (Tzr) of D_1 and D_2 MAFWO magmas. (a) Calculated Tzr categorised by magma suite; (b) Calculated Tzr categorised as D_1 or D_2 magmas (and pre-D_2/post-D_1 magmas from the Windmill Islands). Granitoids are either directly dated, or inferred from field observations and geochemical similarities (by the original data source), as D_1 or D_2 magmas. Data points are ordered relative to one another, from left to right, according to their position by longitude (i.e. west to east across the MAFWO) in order to identify orogen-scale trends. The tectonic regions corresponding to segments of this west-to-east transect are indicated. Tzr are calculated from whole-rock XRF and LA–ICP–MS geochemical data (references as per the caption to Fig. 3). D_1 magmas typically yield Tzr below ~800 °C (dotted line); Tzr for D_2 magmas are more variable, exhibiting a broadly concave trend from west to east.

the Gora Hill Suite of the Recherche Supersuite (typically 1305–1283 Ma) in the Albany–Fraser Orogen. The oldest D_1 magmas come from the Wankanki Supersuite, and Gora Hill Suite intrusives that are located closest to the Albany–Fraser Orogen–Madura Province boundary (Appendix A and B). The abundance of Wankanki Supersuite magmatism decreases from SW to NE across the west Musgrave Inlier (Smithies et al., 2011; Smithies et al., 2010). Unlike the Gora Hill Suite however, no geochemical or age trends are observed. The Wankanki Supersuite shows relatively juvenile $\varepsilon_{Hf}(t)$ and $\varepsilon_{Nd}(t)$ values and are, for the most part, slightly more isotopically-evolved than the Recherche Supersuite magmas (Fig. 3a and b).

The Gora Hill Suite exhibits a systematic spatial transition in geochemistry, isotopic composition and age across the regional structural trend of the Albany–Fraser Orogen, towards the Yilgarn Craton (Smithies et al., 2015b). From SE (east Nornalup Zone) to NW (Fraser Zone) the Gora Hill Suite exhibits a lithological transition from syenogranite to granodiorite (i.e. decreasing silica content), a decrease in the interpreted magma crystallisation age (from ca. 1330–1314 Ma in the SE to ca. 1310–1283 Ma in the NW), and an increasingly juvenile isotope composition, reflecting an increase in the proportion of mafic versus crustal material over time (Smithies et al., 2015b). Trends in the Nd-isotope compositions and incompatible element concentration of the Gora Hill Suite and Fraser Gabbro suggest that these rocks form a transitional magmatic series (Smithies et al., 2015b). Overlapping whole-rock Nd-isotope signatures with the pre-existing Biranup Zone igneous rocks suggest that parent magmas to the Gora Hill Suite involved variable and incomplete mixing of Biranup crust (or partial melts of) with juvenile material of Fraser Zone gabbro affinity (Smithies et al., 2015b). As highlighted by Kirkland et al. (2015a), although sharing a calc-alkaline affinity, the Gora Hill Suite has more evolved crustal-like isotopic signatures (Fig. 3a and b) than the Wankanki Supersuite, suggesting reworking of an older crustal source component.

D_1 magmas that formed via partial melting of Arid Basin metasedimentary rocks comprise the Southern Hills Suite of the Recherche Supersuite and syn-D_1 orthogneiss in the north Windmill Islands (Table 3). The Southern Hills Suite (ca. 1320–1287 Ma) is restricted largely to the Fraser Zone and is interlayered with the Fraser Gabbro and the Snowys Dam Formation, from which these magmas were derived (Smithies et al., 2015b; Spaggiari et al., 2014). A crustal anatectic origin for protoliths to D_1 Windmill Islands orthogneiss (ca. 1320–1315 Ma; Morrissey et al., 2017b; Post, 2000) is supported by metasedimentary enclaves that are hosted within the igneous rocks, Arid Basin inherited zircon, and similarities in the isotope composition of the D_1 magmatic zircon and Arid Basin detritus (Morrissey et al., 2017b; Paul et al., 1995; Post, 2000).

Mafic and ultramafic rocks within the Fraser Zone (ca. 1305–1280 Ma) comprise the Fraser Gabbro, and are interlayered with granodioritic Gora Hills Suite rocks, the anatectic Southern Hills Suite and metasedimentary rocks of the Arid Basin into which the magmas intruded (Maier et al., 2016a; Smithies et al., 2013; Spaggiari et al., 2015). Field relationhips indicate mafic–felsic magma mingling and geochemical data suggest variable interaction of the gabbro with the surrounding metasedimentary rocks and coeval felsic–intermediate granitoids (Maier et al., 2016a; Smithies et al., 2013, 2015b). Minor (<10%) contamination of the mafic magmas by assimilation of Archean crust, Biranup Zone rocks and/or contemporaneous Recherche Supersuite magmas is inferred (Maier et al., 2016a; Smithies et al., 2013, 2015b). Mafic magmatism is interpreted to have been long-lived and/or episodic with geophysical imagery showing deformed gabbro and metasedimentary rocks cross-cut by younger intrusions (Maier et al., 2016a).

Spaggiari et al. (2014) propose that the Gora Hill Suite formed at the margin of the Madura Province and east Nornalup Zone. The Gora Hill Suite and Fraser Zone Gabbro are inferred to have been emplaced in a regional, lower crustal hot zone that subsequently migrated NW-wards between 1330–1283 Ma (Maier et al., 2016a; Smithies et al., 2013, 2015b). Maier et al. (2016a) and Smithies et al. (2015b) propose that this hot zone formed via orogenic collapse and lithospheric delamination following accretion and thrusting of the Loongana Arc and west Madura Province over the east Nornalup Zone that resulted in crustal thickening. This interpretation is based on the restricted, linear occurrence of D_1 magmatism (and absence of any subduction-related D_1 magmatism in the Madura Province) and is a modification of the initial

model of Smithies et al. (2013) and Spaggiari et al. (2015) who suggested that D_1 magmatism occurred within a back-arc environment. Geochemical data from D_1 Windmill Islands orthogneiss is lacking. However, Morrissey et al. (2017b) used detrital zircon provenance and *P–T*–t constraints on M_1 metamorphism to argue that a back-arc setting and west-dipping subduction was appropriate for this timeline (discussed further in Section 9.2.2).

In contrast to the Recherche Supersuite that is interpreted to have formed in a within-plate to syn–post accretionary tectonic setting (Smithies et al., 2015b), the Wankanki Supersuite is characterised by distinctly volcanic-arc geochemistry (Fig. 3; Evins et al., 2012). The Wankanki Supersuite is interpreted to reflect either continental arc magmatism (Andean-style) or alternatively post-(arc) accretion partial melting (i.e. reworking) of an isotopically-juvenile basement to the west Musgrave Inlier (ca. 1950–1550 Ma, see also Section 4; Evins et al., 2012; Kirkland et al., 2015a, 2013a; Smithies et al., 2010; Wade et al., 2008). Smithies et al. (2010) note that the arc-like geochemical characteristics of the Wankanki Supersuite could be obtained in a non-subduction setting if existing crust, produced in an earlier subduction environment, was crustally-reworked and/or assimilated into the parent magmas. Slight differences in the geochemistry of the Recherche Supersuite and the Wankanki Supersuite magmas (Table 2) may support their formation via non-identical processes. Additionally, a back-arc setting for D_1 Wankanki Supersuite magmatism has also not been excluded (Evins et al., 2012; Gorczyk et al., 2015; Smithies et al., 2010).

The Recherche Supersuite and Wankanki Supersuite yield Tzr values that are consistently <800 ºC (Fig. 4) and these granitoids are documented to contain variable amounts of Archean–Mesoproterozoic inherited zircon across a number of samples (see Geological Survey of Western Australia online database: <https://geoview.dmp.wa.gov.au/GeoViews/?Viewer=GeoVIEW>). Therefore, the calculated Tzr values likely provide an upper constraint on the crystallisation temperatures of D_1 parental magmas. Geochemical analyses are not documented for syn-D_1 orthogneiss from the Windmill Islands; however, such rocks also contain locally-derived, inherited zircon (1487–1350 Ma; Morrissey et al., 2017b; Post, 2000).

5.3 Localised pre-D_2/post-D_1 (ca. 1260–1215 Ma) felsic magmatism

Minor emplacement of granitic–tonalitic magmatic rocks occurred between D_1 and D_2 within the Antarctic components of the MAFWO (Table 3; Morrissey et al., 2017b; Post, 2000; Tucker et al., 2017; Zhang et al., 2012). Magmatism of this age is not recognised in the Australian components of the MAFWO suggesting that this event was localised, or that the generalised time periods assigned to D_1 and D_2 differ across the orogen (see Section 8). Magmatism of this age is therefore largely tectonically-ambiguous. Hf and Nd isotope signatures suggest that these magmas reflect partial melting of Arid Basin metasedimentary rocks (Möller et al., 2002; Morrissey et al., 2017b; Zhang et al., 2012) and Yilgarn/Biranup crust (Tucker et al., 2017) with some minor mantle-derived magma addition, in the Windmill Islands and Bunger Hills, respectively. Morrissey et al. (2017b) note that ca. 1250–1215 Ma granitoids in the Windmill Islands are foliated and deformed by upright folds. In contrast, D_2 charnockites are largely undeformed (Morrissey et al., 2017b; Paul et al., 1995; Post, 2000; Sheraton et al., 1995; Tucker et al., 2017), suggesting that crustal melting and emplacement of the ca. 1260–1215 Ma rocks could have been associated with a phase of compressional orogenesis (Morrissey et al., 2017b).

5.4 D_2 (ca. 1220–1130 Ma) felsic–charnockitic magmatism

In constrast to the spatially confined nature of D_1 magmatism, D_2 magmatism was widespread, and is documented across all regions of the MAFWO (Appendix A). D_2/M_2 involved the emplacement of almost exclusively voluminous, felsic–intermediate to charnockitic intrusives with a general lack of physical evidence for mafic magmatism (Table 3). However, field evidence for bimodal mafic and felsic magmatism (e.g. Bunger Hills, southern NAC (Collins and Shaw, 1995; Sheraton et al., 1995) and minor, late–post D_2 mafic dyke emplacement, is documented for parts of the MAFWO (Dawson et al., 2003; Paul et al., 1995; Sheraton et al., 1995; Smithies et al., 2011, 2010). Zircon Hf isotope compositions and whole-rock Nd isotopes from D_2 felsic rocks also suggest variable incorporation of a mantle end member source into the parent magmas (Howard et al., 2015; Kirkland et al., 2017; Morrissey et al.,

2017b; Smithies et al., 2011, 2015b; Tucker et al., 2017).

Compiling the age of D_2 magmas from across the MAFWO (Fig. 5, Appendix B) indicates a broadly bimodal age of crystallisation with major peaks at ca. 1200–1170 Ma and ca. 1160–1140 Ma. Smithies et al. (2011) note that some rocks comprising the Pitjantjatjara Supersuite from the west Musgrave Inlier also define an older age group (ca. 1220–1200 Ma, not distinguishable in Fig. 5). The youngest D_2 magmas (ca. 1140–1130 Ma) occur in the east Musgrave Inlier (also classed as Pitjantjatjara Supersuite) and along the southern margin of the NAC (Teapot Granite Complex), but in general, there are no regionally systematic orogen-wide trends for the age of D_2 magmatism (Appendix A). However, within the individual tectonic regions of the MAFWO, spatial–age trends are observed (e.g. west Musgrave Inlier and Madura Province, Table 3; Smithies et al., 2011; Spaggiari and Smithies, 2015), reflecting a shift in the locus of partial melting and/or emplacement (discussed below). As can be expected from the broad age range of D_2 magmatism (Appendix A, Fig. 6, Table 3), D_2 magmas show complex lithological field relationships (e.g. locally-derived anatectic melts to externally-derived composite plutonic bodies) and variable timing of emplacement relative to deformation and metamorphism (Table 3; Howard et al., 2015; Sheraton et al., 1995; Smithies et al., 2010; Spaggiari et al., 2011).

The range of calculated Tzr for D_2 granitoids (Fig. 4) is more variable than for D_1 and, in general, is lowest at the western and eastern ends of the orogen (i.e. Bunger Hills, Windmill Islands, east Musgrave Inlier, NAC margin). The most elevated Tzr come from D_2 granitoids within the west Musgrave Inlier (>800 °C), and in particular, the Tjuni Pulka Zone. In general, studies report that D_2 plutonic granitoids do not contain xenocrystic zircon. Few exceptions include the Teapot Granite (Black and Shaw, 1995), three samples from the east Musgrave Inlier (Dutch et al., 2013b), and minor inheritance preserved within the Esperance Supersuite at some localities (e.g. GSWA 193839, Appendix B). In many of these instances, the proportion of inherited zircon ages is generally minor, and the samples are typically interpreted to represent anatectic melts of their surrounding host rock. D_2 plutonic granitoids are therefore considered largely inheritance-poor to absent and their Tzr deemed representative of a minimum estimate on magma crystallisation temperature. Smithies et al. (2011) previously calculated Tzr for Pitjantjatjara Supersuite granites from the west Musgrave Inlier and determined an average value of 868 ºC and a maximum of 993 ºC. A paucity of zircon inheritance also led Smithies et al. (2011) to conclude that the temperature of these magmas is underestimated by Tzr. Combined with UHT *P–T* constraints from surrounding metamorphic rocks (Walsh et al., 2015), calculated Tzr in the west Musgrave Inlier suggests that regional, upper granulite facies to UHT conditions were attained at the level of magma emplacement (Smithies et al., 2011).

Since D_2 magma Tzr are considered minimum estimates, significance cannot be given to the trends observed in Fig. 4. It is possible that the seemingly low Tzr for D_2 magmas from the Antarctic regions of the MAFWO are a reflection on their more intermediate than felsic composition, and therefore lower Zr contents, but not necessarily lower crystallisation temperatures. This interpretation is supported by conventional thermobarometry that yielded crystallisation temperatures up to ~910 ºC at mid-crustal pressures (~5–8 kbar; Sheraton et al., 1995) in the Bunger Hills, and 960–1100 ºC at 3–4 kbar for the Ardery Charnockite in the Windmill Islands (Kilpatrick and Ellis, 1992). Given the lithological similarities of D_2 magmas across the Musgrave Inlier, the slightly lower Tzr of the central and east Musgrave Inlier relative to the west might reflect their emplacement at a higher structural level. This possibility is supported by differences in *P–T* conditions of the exposed metamorphic rocks (Section 6). Alternatively, it may suggest that this region underwent less thermal priming during D_1/M_1 (Section 9.3).

Increasingly younger Pitjantjatjara Supersuite granites in the west Musgrave Inlier show a shift in geographical location (NE to SW), a change from Yb-depleted to enriched trace element compositions, and a transition towards more juvenile Nd-isotope compositions (Table 3; Howard et al., 2015; Smithies et al., 2011, 2015a). These observations are interpreted to reflect that younger melting and/or magma emplacement in the west Musgrave Inlier occurred at shallower depths, (i.e. low pressures, thin crust), and that mantle input into the parental magmas was progressively increasing (Howard et al., 2015; Smithies et al., 2015a). However, it is also plausible that a shift

Table 3. The age, distribution and character of pre-D_1, D_1 and D_2 MAFWO Mesoproterozoic magmatism (ca. 1410–1130 Ma)*

Region	Magma suite	Age (Ma)	Distribution	Lithological character	Key geochemical features	$\varepsilon_{Hf}(t)$	$\varepsilon_{Nd}(t)$	Tectonic interpretation(s)
Southern NAC	Mordor Complex	1133 ± 5	Localised, SE Aileron	Mafic–ultramafic, undeformed.	Alkaline	-	-10.6 to -9.5	Within-plate magmatism; Sourced from metasomatised mantle.
	Teapot Granite	1136 ± 6	West Warumpi	Granite, deformed.	High-K	-	-10.1 to -8.2	Anatectic, partial melting of Paleoproterozoic crust.
Musgrave Inlier (MI)	Papulankutja Supersuite	ca. 1400	West MI	Foliated granodiorite and monzogranite.	Calc-alkaline	-	-	Possible arc-magmatism (Loongana Arc equivalent?).
	Wankanki Supersuite	1345–1293	West MI; increasing NE to SW	Foliated granodiorite and monzogranite. Interlayered with metasedimentary rocks (Wirku Metamorphics).	Calcic to calc-alkaline, I-type, metaluminous, magnesian, volcanic-arc geochemistry	+1 to +5	-2.4 to -0.6	Continental arc magmatism (Andean-style) or Re-melting of juvenile Proterozoic basement (post-arc accretion).
	Pitjantjatjara Supersuite	**East MI:** ca. 1155–1143 **Central MI:** ca. 1190–1140 **West MI:** ca. 1220–1150 Two groups: (1) 1220–1200; (2) 1190–1150 Broad NE to SW age decrease	Regional, voluminous	Near-exclusively felsic–charnockitic, intrusive and extrusive. Variably deformed (unfoliated to gneissic). **West MI:** (1) bi–opx-bearing leucogranite veins and sheets (restricted occurrence); (2) Granodiorite–syenogranite plutons (heterogeneous, clustered intrusions); (3) Granite sheets and veins (anatectic). **East and central MI:** (1) Anatectic granites (early); (2) Porphyritic granite plutons; (3) Microgranitic–aplitic dykes (late).	Ferroan, alkali-calcic, high-K, Th, U, A-type, low-H_2O **West MI:** Nine geochemical suites identified. Transition from Yb-depleted to enriched geochemistry with decreasing age.	**West MI:** -2.5 to +4 **East MI:** -3 to +4	**West MI:** -2.2 to -3.6 increasingly juvenile over time **East MI:** -2 to -16.9	Within-plate magmatism; Significant mantle component within felsic magmas (up to 50 %); Magma mixing within a lower crustal hot zone/MASH zone; Emplacement associated with crustal thinning; Episodic crustal extension (thus episodic magmatism); Migration in the locus of melting/emplacement; High-*T* magma crystallisation (>900 °C). *(NB: interpretations based largely on west MI)*
SAC margin	Haig Cave Supersuite	1415–1389	Drill hole (Madura only)	Mafic–ultramafic (basalt, gabbro, peridotite). Leucogranite (inferred late, intrudes gabbro).	**(1) Mafic rocks:** Low–medium-K, tholeiitic, negative Nb anomalies, high Th/Yb and La/Nb, HFSE akin N-MORB; **(2) Leucogranite:** sodic plagiogranites, adakitic.	-8.8 to +13	-4 to +3	Comprises the Loongana Oceanic Arc. Mafic rocks indicate melting of modified N-MORB source during subduction (metasomatised mantle and minor assimilation of crustal material likely derived from the Arid Basin).
	Moodini Supersuite	**Madura:** 1181–1125 NW to SE age decrease **Coompana:** 1192–1140	Drill hole (Madura & Coompana)	**(1) Leucogranite** (inferred anatectic; 1192–1150 Ma, Coompana). **(2) Monzogabbro–granite**, opx- and pigeonite-bearing (charnockitic; 1181–1125 Ma, largely Madura); **(3) Mafic–felsic shoshonite** (Bottle Corner Shoshonite, 1192–1180 Ma, West Coompana).	**Leucogranites:** high-K, alkali-calcic, magnesian, peraluminous; **High-KFe magmas and shoshonite series:** High-KFe, A-type (charnockitic), metaluminous, ferroan, LILE-enriched. Rich in TiO_2 and P_2O_5 (in felsic lithologies).	**Madura:** -4.4 to +5.1 **Coompana:** -12.8 to +9.9 (suites undivided)	**Madura:** -4.8 to -1.9 Inc. juvenile NW to SE **Coompana:** -4.6 to -3.3 (leucogranite) -2 to +1 (shoshonite)	Within-plate magmatism. Anatectic melts reflect *in situ*, intraplate, low-*P* melting of mafic crust. High-KFe magmatic rocks suggest mixing of mafic lower crustal melts and asthenosphere melts at the base of thinned crust. Increasing mantle contribution with decreasing age.

Table 3. (continued)

Region	Magma suite	Age (Ma)	Distribution	Lithological character	Key geochemical features	$\varepsilon_{Hf}(t)$	$\varepsilon_{Nd}(t)$	Tectonic interpretation(s)
Albany–Fraser Orogen	Fraser Zone Gabbro	1310–1283	Localised, Fraser Zone	Metagabbro sheets interlayered with felsic Recherche Supersuite and metasedimentary rocks (Snowys Dam Fm., Arid Basin); Mafic–felsic magma mingling (with Recherche Supersuite).	Ferroan, low to medium-K, tholeiitic, negative Nb anomalies. Metagabbro subdivided into two groups: **(1) Main gabbro**: no interaction with surrounding country rock; **(2) Hybrid gabbro**: variable interaction with country rock (further subdivided according to degree of mixing).	-1.5 to +1.9	-3.8 to -0.8	Repeat mafic intrusion into a lower-crustal hot zone. Extending crust due to orogenic collapse and delamination (previously interpreted back-arc setting). Possible mantle melt underplate. Minor (<10 %) crustal contamination (Biranup crust). Magma mingling/hybridization between gabbro and felsic melts (Recherche Supersuite). Magmatism pre–syn M_1 metamorphism.
	Recherche Supersuite	**Southern Hills:** 1320–1287 **Gora Hill:** 1305–1283 (main) SE to NW age decrease	**Southern Hills:** Localised; Fraser Zone (mostly) **Gora Hill:** Largely east Nornalup, SE Biranup	**Southern Hills Suite (anatectic):** Leucocratic, syenogranitic, garnet-bearing **Gora Hill Suite:** Granodiorite, monzogranite and syenogranite; compositional trend across AFO (syenogranite in SE to granodiorite in NW); Granodiorite restricted to the Fraser Zone. Hosts xenoliths of Fraser Zone gabbro. Mafic–felsic magma mingling (field obs.). Typically gneissic; deformed and metamorphosed to amphibolite–granulite facies.	**Southern Hills Suite:** Weakly peraluminous, high SiO_2 content (>72–78 wt %), depleted in incompatible elements. **Gora Hill Suite:** Weakly ferroan, calc-alkaline; Increasing SiO_2 content NW to SE.	-10 to +5 (main, suites undivided)	**SH:** -3.0 to -7.8 **GH:** -3.5 to -9.4 Increasingly juvenile SE to NW. Juvenile also at Madura margin.	Geochemically syn-collisional/volcanic arc to within-plate magmas. **Southern Hills Suite:** Local partial melts of predominantly (but not exclusively) interlayered Arid Basin sediments within the Fraser Zone. **Gora Hill Suite:** Sourced from a regional lower crustal hot zone (hot zone initiated via orogenic collapse and delamination). Magma mixing between Biranup crust and mantle input. Contemporaneous with and forms a transitional geochemical series with the Fraser Gabbro. Migration of the hot zone from SE to NW over 1330–1283 Ma.
	Esperance Supersuite	1196–1135 (suites undivided)	Regional, excl. Fraser Zone **Truslove Suite:** Biranup–Nornalup sheared boundary **Booyanya Suite:** East Nornalup (mostly)	Near-exclusively felsic. Leucogranitic–aplite veins, pegmatites and dykes, porphyritic monzogranite–granite. Lower grade of deformation/metamorphism than Recherche Supersuite (typically greenschist–amphibolite facies). Locally magmatic fabrics are observed. **Truslove Suite (anatectic):** Partial melting of surrounding lithologies (from field obs.), locally garnet-bearing. **Booyanya Suite (plutonic):** Charnockitic mineralogy and composition.	**Truslove Suite:** Depleted in incompatible REE, weakly peraluminous, sodic. Trace element chemistry transitions towards anatectic Southern Hills Suite at high SiO_2. **Booyanya Suite:** Distinctly within-plate, ferroan, alkali-calcic to alkali, A-type, metaluminous, enriched in incompatible elements (particularly LREE). Rich in K_2O, TiO_2 and P_2O_5.	-20 to -10 (1 sample, suite unspecified, East Nornalup)	**TS:** -6.9 (1 analysis) **BS:** -4.9 to -7.3	**Truslove Suite:** Partial melts of Biranup crust/Barren Basin sediments (i.e. recycled Biranup) with minor juvenile input. Partial melting occurred at variable depths along major shear zones. **Booyanya Suite:** Higher-*T*, lower-*P* melting than Truslove Suite and Recherche Supersuite. Two alternative interpretations: (1) Partial melts of anhydrous lower crust (largely Biranup Zone) with significant juvenile input; (2) Magma sourced from lower crustal equivalents to the Gora Hill Suite that is remobilised into a new MASH chamber with renewed mantle input. Magmatism likely associated with extension.

Table 3. (continued)

Region	Magma suite	Age (Ma)	Distribution	Lithological character	Key geochemical features	$\varepsilon_{Hf}(t)$	$\varepsilon_{Nd}(t)$	Tectonic interpretation(s)
Bunger Hills region	Unnamed orthogneiss	1256 ± 4	Unknown, (1 sample, SW Bunger Hills)	bi–opx-bearing tonalite orthogneiss	Within-plate, ferroan (predominantly), sub-alkaline, tholeiitic, metaluminous, LREE-enriched.	-11.4 to -4.6	-	Geochemically within-plate magmas. Significance of unnamed orthogneiss unclear. Paz Cove and Algae Lake magmas inferred late D_2; Booth Peninsula magmas inferred post-D_2. Paz Cove Batholith and Algae Lake Pluton derived from reworked Archean/Paleoproterozoic crust with possible lesser juvenile (mantle) input. Episodic magma emplacement. Mid-crustal emplacement (~20 km). High-*T* magma crystallisation, followed by relatively slow cooling.
	D_2 granitoids	**Paz Cove Batholith** **Algae Lake Pluton** ca. 1200–1170	Regional, Bunger Hills	Lithologically heterogeneous - gabbro, quartz monzogabbro–diorite, opx ± gt-bearing granitoids. Commonly opx–pigeonite-bearing (charnockitic mineralogy). Composite plutonic bodies (clustered intrusions with varied mineralogy and lithology), locally migmatitic. Weak (inferred) magmatic fabrics observed. Paz Cove Batholith is interlayered with metasedimentary rocks at its margin.		-12.7 to -6.8	-9.4 and -3.5	
		Booth Peninsula Batholith 1151 ± 4	Regional, Highjump Archipelago	Lithologically heterogeneous (gabbro, quartz gabbro, granite). Includes minor, late, felsic (monzonite–granite) dykes. Felsic rocks locally post-date mafic rocks but gradational contacts are observed.		-	-	
Windmill Islands	Syn-D_1 orthogneiss	ca. 1315	North Windmill Is.	K-feldspar augen (granite) gneiss, weakly foliated. Contains rafts of metasedimentary rocks.	Unspecified	-3 to +6	-5.4	Inferred partial melting of metasedimentary rocks (Arid Basin equivalents). Inferred back-arc setting.
	D_{2a} granitoids	ca. 1250–1210	North–central Windmill Is.	bi-bearing and gt-bearing granite (variably-foliated) and gt-bearing gneiss. Intrudes metasedimentary rocks. Deformed by upright folds.	Silica-rich, moderate Rb, Th, K, LREE-enrichment, Nb, Ta, Sr, P and Ti depletion	-5 to +4	-5.7 to -2.2	Tectonic significance unclear due to local occurrence. Multiple, distinct intrusive phases. Likely reflects reworking of Windmill Islands metasedimentary rocks with some juvenile input. Inferred short-lived compressional phase in overall extensional setting.
	D_{2b} granitoids	**Ardery Charnockite:** ca. 1200–1160	South Windmill Is.	opx–hbl–bi-bearing, felsic–intermediate (charnockitic mineralogy), weakly-foliated. Comprises clustered intrusions of varied mineralogy and lithology. Hosts metasedimentary xenoliths.	Silica-poor, depletion in Th, U, Nb, Ta, Sr, P and Ti. Enrichment in LREE, Rb, Ba, K.	0 to +5 (1178 Ma)	-4.9 to -4.5 (1170 Ma) -1.6 to -1.1 (1200 Ma)	Inferred syn–post tectonic. Geochemically within-plate magmas. Episodic magma emplacement. High-*T* melting of anhydrous, mafic lower crust. Associated with mafic magma underplating and/or post-collisional extension. Minor crustal component (Arid Basin).
		Ford Granite: 1173 ± 9	Localised, South Windmill Is.	gt-bearing granite, texturally-heterogeneous (cross-cutting relationships observed). Weakly-foliated. Contains xenoliths of metasedimentary rocks.	High Th, peraluminous	-	-	

*Syn-D_2 mafic dyke suites are recognised in the MAFWO but are not included in the above summary.
Mineral abbreviations: bi, biotite; gt, garnet; opx, orthopyroxene.

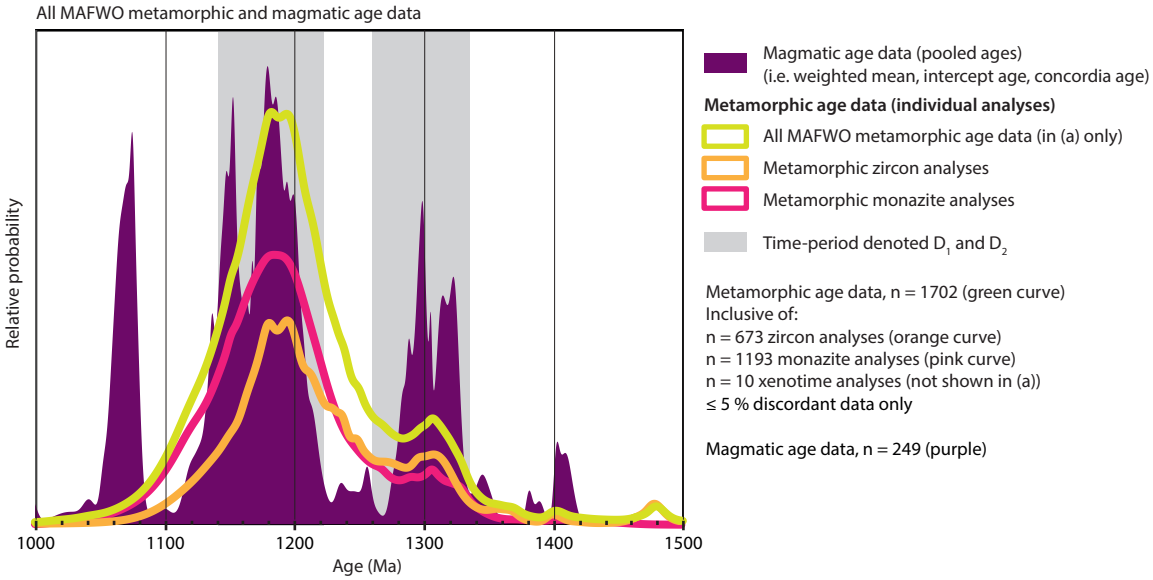

Figure 5. Orogen-wide comparison of MAFWO metamorphic and magmatic age data. Probability density curves are shown for all MAFWO magmatic age data (pooled analyses) and metamorphic age data (invidual analyses) in purple and green, respectively, over the time–period 1500–1000 Ma. Metamorphic age data are segregated further as originating from zircon (orange) or monazite (pink) to investigate potential differences in the metamorphic age record according to different mineral chronometers. Analyses are interpreted as being of metamorphic origin from the original data source. Data were compiled from published datasets (including State Survey Publications and online databases, refer to Appendicies B and C). The time-periods assigned to D_1/M_1 and D_2/M_2 across the MAFWO (Section 2, Table 1) are shaded grey.

to Yb-enrichment may reflect a decrease in the abundance of garnet in the source(s) of the parent magmas. Similarly, the Nd whole-rock composition of Moodini Supersuite magmas also reflects an increasing mantle contribution in the parent melts over time, with younger magmas also emplaced NW to SE, away from the Yilgarn Craton margin (Spaggiari and Smithies, 2015). The tectonic interpretation for D_2 magmatism is broadly considered to be intracratonic (Table 3), supported by their within-plate geochemistry (Fig. 3c). Specifically, D_2 magmatism is associated with melting of thinned, anhydrous lower crust, possibly within a migrating/remobilised MASH (melting, assimilation, storage, homogenization) zone, and/or post-collision crustal extension (Table 3; Kirkland et al., 2017; Morrissey et al., 2017b; Smithies et al., 2011, 2015a; Spaggiari and Smithies, 2015; Zhang et al., 2012).

As D_2 magmas across the entire MAFWO are interpreted to reflect partial melting of existing crust with variable degrees of juvenile input (Morrissey et al., 2017b; Smithies et al., 2010, 2015b; Spaggiari and Smithies, 2015; Tucker et al., 2017), the isotopic composition of D_2 magmas can be at least partly considered to reflect the composition of the crust they are derived from. The most juvenile D_2 magmas come from the central MAFWO (west Musgrave Inlier, east Nornalup Zone, Madura and Coompana Provinces) and the east Musgrave Inlier (Appendix A). This is likely a reflection of the pre-existing (pre-D_1 to D_1) tectonic environment where little to no old, isotopically-evolved lower crust existed beneath these regions (Kirkland et al., 2017; Maier et al., 2016b; Morrissey et al., 2017b; Smithies et al., 2015a; Spaggiari et al., 2015). Therefore, there is little evolved material available to contaminate the isotope signature of any new (D_2) juvenile melts. In the case that D_2 magmas were derived via the reworking (partial melting) of pre-existing crust, this must have involved recycling of isotopically-juvenile (mafic) basement. The most evolved isotope signatures from D_2 magmas come from the far east (e.g. southern NAC) and west MAFWO (e.g. Bunger Hills, west Albany–Fraser Orogen), in regions with a known pre-D_1/M_1 crustal history that involves the reworking of existing craton margins rather than predominantly new, juvenile crustal growth (Section 4).

6. MAFWO METAMORPHIC FEATURES

An orogen-wide investigation into variation in the M_1 and M_2 metamorphic character has not previously been undertaken for the MAFWO. Accordingly, a spatial representation of the geographical occurrence of M_1 and M_2 is presented in Appendix A. Table 3 provides a comprehensive

summary of the deformational character and *P–T* constraints of MAFWO metamorphic rocks. A comparison of metamorphic and magmatic age data at the orogen-scale (Fig. 5) and by tectonic region (Fig. 6) is also shown. Figure 7 presents a visual comparison of *P–T* conditions documented from conventional thermobarometry and mineral equilibria modelling. Some broad generalisations can be made regarding the metamorphic characteristics of M_1 and M_2 that unifies and builds upon pre-existing interpretations from the individual tectonic regions of the MAFWO.

6.1 M_1 metamorphism

M_1 metamorphic ages are restricted largely to the central MAFWO within the Windmill Islands, Fraser Zone, east Nornalup Zone, and the west Musgrave Inlier (Appendix A). The geographical occurrence of M_1 metamorphic age data is the same as the documented occurrence of D_1 magmatism, suggesting a similar tectonic driver for both magmatism and metamorphism and/or a causal relationship between the two. Rare M_1 ages are recorded by inferred metamorphic zircon in the Bunger Hills (Tucker et al., 2017) and from monazite in the east Musgrave Inlier (Appendix A; Walsh et al., 2015). However, ages older than ca. 1220 Ma obtained from the Bunger Hills were subsequently interpreted as reflecting the incomplete recrystallisation of older detrital zircon (Tucker et al., 2018), in which case, these M_1 ages may be mixed ages and are not geologically meaningful. The oldest inferred metamorphic monazite from from the east Musgrave Inlier are ca. 1265 Ma which post-date D_1/M_1 in this region of the MAFWO (Mount West Orogeny; ca. 1345–1293 Ma), and therefore does not provide clear evidence for M_1 in this region.

P–T constraints for M_1 come from the Snowys Dam Formation (Fraser Zone), the Malcolm Metamorphics (Madura Province), and the Windmill Islands. All three localities occur within the central MAFWO, and all are from inferred Arid Basin (or equivalent) metasedimentary sequences (Fig. 7, Table 3). Although the west Musgrave Inlier records evidence for D_1 magmatism, M_1 metamorphic zircon ages, and D_1 deformation from field observations, there are no M_1 *P–T* constraints documented. This may be a result of pervasive, high-temperature overprinting by D_2/M_2 (Howard et al., 2015) such that M_1 metamorphic mineral assemblages formed but are no longer preserved.

A shared metamorphic evolution across the central MAFWO is supported by the observation that peak M_1 metamorphism was accompanied by the development of horizontal, gneissic to migmatitic fabrics (Blight and Oliver, 1977; Clark et al., 2014; Clark et al., 2000; Clark et al., 1999; Howard et al., 2015; Morrissey et al., 2017a; Paul et al., 1995; Post, 2000). However, apparent thermal gradients from the Windmill Islands (>150 °C/kbar; Fig. 7; Morrissey et al., 2017a) are considerably more elevated than those from the Fraser Zone (95–120 °C/kbar; Fig. 7; Clark et al., 2014). Approximate *P–T* estimates from the Malcolm Metamorphics are based on field observations of inferred high-temperature garnet-bearing assemblages and leucosomes that were interpreted as evidence for partial melting (Adams, 2012; Clark et al., 2000). The timing of high-temperature metamorphism is constrained by structural and lithological relationships and ca. 1310 Ma monazite from pelite gneiss (Adams, 2012; Clark et al., 2000). However, the age data are not directly linked to the development of the inferred peak mineral assemblage by *in situ* geochronology and *P–T* modelling, and the same samples also record dominant ca. 1180 Ma (M_2) age populations (Adams, 2012). Therefore the possibility that the high temperature conditions relate to M_2 rather than M_1 is not entirely precluded.

The post-peak *P–T* evolution of M_1 is unclear due to a paucity of quantitative constraints. Clark et al. (2014) suggest that peak metamorphism in the Fraser Zone was followed by slow, isobaric cooling at moderately high pressures (~9 kbar). However, this interpretation was based on earlier observations of microstructural mineral reaction textures (Clark et al., 1999) and come from different samples to those specifically used for *P–T* modelling by Clark et al. (2014). Specifically, Clark et al. (2014) state that there is no evidence for isobaric cooling.

In essence, M_1 metamorphism and associated deformation was preferentially recorded by the Arid Basin (east Albany–Fraser Orogen and Windmill Islands) and the Wirku Metamorphics (west Musgrave Inlier). M_1 was associated with the development of flat-lying fabrics, pre- to syn-metamorphic sedimentation (Evins et al., 2012; Spaggiari et al., 2015), and *P–T* conditions were high thermal gradient. Limited and variable *P–T* constraints means it is difficult, from a metamorphic-only standpoint, to assign regional

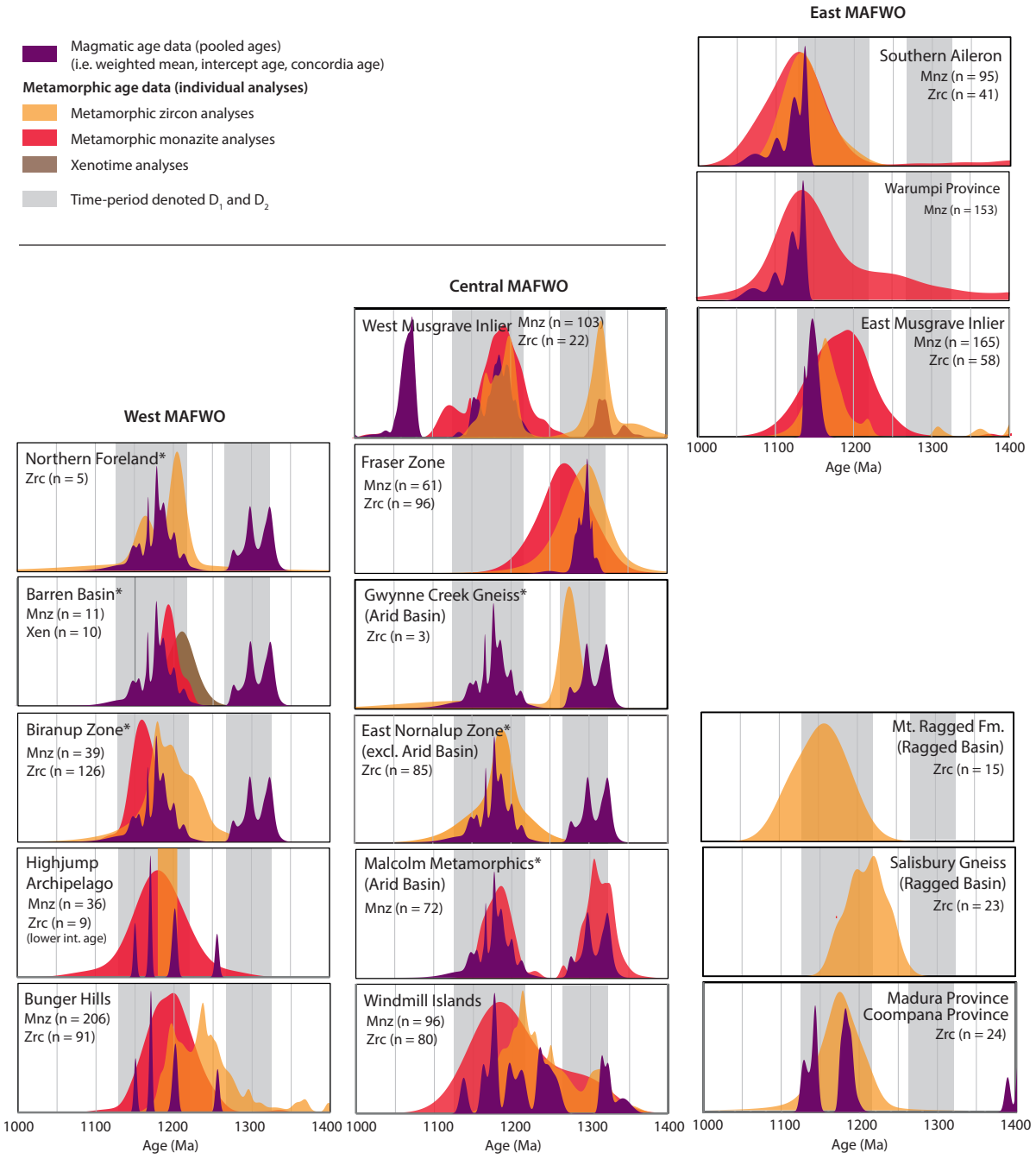

Figure 6. Terrane-scale comparison of MAFWO metamorphic and magmatic age data. Probability density curves are shown for MAFWO metamorphic and magmatic age data, subdivided by tectonic region/unit. The probability density curves are overlain to assess variation and offset between magmatic age data (purple) and metamorphic age data (pink, monazite; orange, zircon; brown, xenotime). Magmatic age data are pooled analyses (i.e. weighted mean, intercept age, concordia age); metamorphic age data are invidual zircon, monazite and xenotime analyses, excluding metamorphic zircon ages from the Highjump Archipelago (lower intercept age). The number of analyses comprising the metamorphic probability density curves are indicated. Data are compiled from published datasets (including State Survey Publications and online databases; refer to Appendices B and C). The time-periods assigned to D_1/M_1 and D_2/M_2 across the MAFWO (Section 2, Table 1) are shaded grey. Magmatic age probability density curves in plots marked with an asterisk encompass all data from across the Albany–Fraser Orogen, except for the Fraser Zone. Magmatic age data specifically from the Fraser Zone are shown separately (in the Fraser Zone plot).

Table 4. The age, distribution and character of MAFWO M_1 and M_2 metamorphism^

Tectonic region	Age of peak metamorphism*	Deformation	Peak *P–T* conditions	*P–T* path	Tectonic interpretation(s)
Southern NAC *S. Aileron Province* *Warumpi Province*	ca. 1160–1130 Ma	Development of regional flat-lying fabrics (syn-D_2). Subsequent late–post-D_2 deformation involved E–W-trending upright–isoclinal folding, development of NE-trending mineral lineations, NNE-directed thrusting and south-side-up shear systems. Overprinting migmatitic–ultramylonitic fabrics.	**Eastern Warumpi**: 3.5 kbar, 570 °C **Southern Aileron & Northern Warumpi:** 5–5.5 kbar, 775–820 °C	**East Warumpi**: Clockwise	Regional low-angle fabrics and peak metamorphism associated with extension. Coeval with syn–late D_2/M_2 bimodal magmatism. Subsequent NNE-directed compression (between ca. 1140–1080 Ma), associated with suturing of Warumpi Province to NAC.
Musgrave Inlier	ca. 1315–1300 Ma	Development of a layer-parallel gneissosity. Subsequent kilometre-scale folding (NE-trending axial planes) prior to ca. 1217 Ma.	-	-	Specific tectonic setting of D_1 deformation unclear. Inferred SE–NW compression post D_1, pre-D_2 (west MI only). Deformation undocumented in the east MI.
	ca. 1220–1140 Ma	Regionally pervasive gneissic fabrics and migmatitic layering. Overprinting W–NW-striking fabrics, including strong mylonitic fabrics. Tight to isoclinal folding (variable degree and orientation).	**East MI:** 5–6 kbar, 650–850 °C (thermobarometry) 6.0–6.5 kbar, 900 °C (*P–T* modelling) **Central–North MI:** Mid–amphibolite facies (andalusite-bearing assemblages, field obs.) **West MI:** 5–6 kbar, 750–850 °C (thermobarometry) 7–8 kbar, >950 °C (*P–T* modelling)	**East MI:** Isobaric to slightly up-pressure cooling (local constraint) **West MI:** Clockwise (regional constraint)	Inferred intraplate reworking and anatexis. Spatially-confined delamination of mantle lithosphere/lower crust (at the join of NAC–WAC–SAC cratons). Possible regional back-arc or ultra-hot orogen. Voluminous juvenile magmatism maintains high heat flow in thinned crust. East MI records evidence for contact metamorphism resulting from transient syn-metamorphic Pitjantjatjara Supersuite magmatism (within the broader mantle-driven system).
Coompana Province	1179–1150 Ma	Gneissic fabrics, local anatexis.	Low amphibolite facies (field obs.)	-	Coeval with Moodini Supersuite magmatism.
Madura Province *Salisbury Gneiss*	1214–1183 Ma	Gneissic fabric development and isoclinal folding Subsequent NW–SE open folding and shear development	> 5 kbar, 800 °C (metamorphic zircon, field obs.)	Inferred down-pressure	High-temperature exhumation along ductile thrusts. Constraints on D_1 and D_2 not obtained at present from Madura Province drill core.
Ragged Basin	>1154 Ma ± 15 Ma	NW–SE and NE–SW open folding, layer-parallel shearing	4–5 kbar, 550 °C (metamorphic rutile, field obs.)	-	Crustal thickening (due to over thrusting of Salisbury Gneiss).
Northern Foreland *Munglinup Gneiss*	1195 ± 17 Ma (1 sample)	Macroscale folding (at least 1 phase), localised shearing and boudinage (late). Metamorphic grade and deformation intensity increases away from the Yilgarn Craton.	Amphibolite–granulite (field obs.)	-	Unclear; NW–SE compression inferred from dextral shears that cross-cut macroscale folds. Boudinage during subsequent NE–SW extension.
Fraser Zone	ca. 1305–1290 Ma	Gneissic–migmatitic fabrics Subsequent localised, dextral shearing	7–9 kbar, 850 °C (*P–T* modelling)	Unclear; prior thermobarometry suggests possible isobaric cooling	Contact metamorphism from coeval mafic and felsic magmatism. Associated extension (by orogenic collapse and delamination). Exhumation of the Fraser Zone to mid-crustal depths by D_2. Cooling at mid-crustal depths.

Table 4. (continued)

Tectonic region	Age of peak metamorphism*	Deformation	Peak *P–T* conditions	*P–T* path	Tectonic interpretation(s)
Biranup Zone *Coramup Gneiss*	D_2**	Layer-parallel gneissosity. Subsequent shear zone development, tight asymmetric folding and NW-directed thrusting.	5–7 kbar, 800–850 °C** (thermobarometry)	Anticlockwise (through 10 kbar, 800–850 °C) to 7–8 kbar, 700–800 °C**	Extension, subsequent burial and recrystallization.
Biranup Zone *Dalyup Gneiss*	ca. 1225–1150 Ma	Gneissic fabric development. Repeat open–isoclinal, recumbent–upright folding (oblique compression) and NE–NW-trending boudinage. Ductile shearing (late).	5–6 kbar, 750–850 °C (thermobarometry)	Down-pressure	Alternating extension and NNW-directed compression. Exhumation along shear zones (late).
Barren Basin *Mt. Barren Group*	1205 ± 10 Ma	-	7–12 kbar, 560–675 °C (thermobarometry)	-	Inferred contact metamorphism. (ca. 1200 Ma Gnowangerup–Fraser Dyke Suite).
Barren Basin *Fly Dam Formation*	ca. 1200–1150 Ma	-	6.5–8.5 kbar, 675–725 °C (*P–T* modelling)	-	Unclear; presumed regional metamorphism.
West Nornalup Zone *(near Albany)*	1314 ± 5 Ma 1304 ± 3 Ma	Layer-parallel gneissic fabrics and recumbent folding. Subsequent NW-directed shortening involving thrusting, transposition of fabrics to steep NE-trending orientations, and dextral transpression.	Amphibolite–granulite (field obs.)	-	-
Arid Basin *Malcolm Metamorphics*	ca. 1330–1304 Ma	Layer parallel gneissosity Subsequent isoclinal folding and open–tight folding (NW-directed compression).	4 kbar, 750 °C (field obs.)	-	-
	ca. 1215–1140 Ma	NE-trending ductile thrusting and strike-slip reactivation.	-		
Windmill Islands	ca. 1340–1300 Ma	Development of horizontal fabrics, isoclinal folding.	3.7–4.2 kbar, 710–740 °C (thermobarometry, *P–T* modelling)	-	Extension, possible back-arc setting.
	ca. 1240–1140 Ma	Two deformational phases: D_{2a}: Upright–inclined isoclinal folding. D_{2b}: Open–tight (SE-plunging) folding, partial melting (in axial planes of F2b folds, and structurally discordant leucosomes).	4 kbar, >850 °C (thermobarometry, *P–T* modelling)	Down-pressure to isobaric	Contact metamorphism.
Bunger Hills region	ca. 1300–1170 Ma Minor >1300 Ma	Layer parallel gneissic fabric transposed by tight–isoclinal mesoscale folding. Subsequent regional, open, upright NW–SE folding. Localised shear zone development.	5.5–7.1 kbar, 800–960 °C (HJA) 6–9 kbar, 850–950 °C (BH) (*P–T* modelling)	Down-pressure to isobaric	Extension of thickened crust.

*The age of peak metamorphism, quoted as individual ages or weighted mean ages by the original data source.

***P–T* conditions subsequently reinterpreted by Spaggiari et al. (2009) to represent Stage-2 Albany–Fraser Orogen (initially interpreted as ca. 1300 Ma Stage-1 by Bordorkos and Clark (2004a)).

^Refer to Appendix F for references to the literature.

Constraints on peak *P–T* conditions are denoted as being from interpretations on the growth of mineral chronometers (e.g. rutile and zircon), field observations, thermobarometry or forward phase equilibria modelling (*P–T* modelling).

versus local significance to the *P–T* conditions experienced during D_1/M_1.

6.2 M_2 metamorphism

Similarly to D_2 magmatism, M_2 metamorphism was widespread and occurred within most tectonic regions of MAFWO, as well as the Madura and Coompana Provinces and southern NAC (Appendix A, Table 4). The only region in which M_2 metamorphic age data and *P–T* constraints are not recorded is the Fraser Zone, which is inferred to have been exhumed to mid-crustal levels by D_2/M_2, supported by biotite Rb–Sr and Ar–Ar, and hornblende Ar–Ar cooling ages (Fletcher et al., 1991; Scibiorski et al., 2016). However , the Fraser Zone is interpreted to have attained mid–upper amphibolite facies conditions based on D_2/M_2 reset titanite ages (Kirkland et al., 2016).

Based on the available geochronological data, and excluding the Windmill Islands, spatial trends in the age of M_2 across the MAFWO are not observed (Fig. 6, Table 4). Within the Windmill Islands, the intensity and pervasiveness of D_2/M_2 increases from north to south, where it is spatially-linked to the syn-D_2 Ardery Charnockite (Blight and Oliver, 1977; Morrissey et al., 2017b; Paul et al., 1995; Post, 2000; Post et al., 1997). In general, the youngest M_2 ages come from the southern NAC (Table 4).

One of the most intriguing features of M_2 is the remarkable consistency in apparent thermal gradients recorded by the metamorphic rocks (generally ~150 °C/kbar), despite clear differences in absolute *P–T* values across the orogen (Fig. 7). This observation is significant in that it is directly indicative of a regional geodynamic control on M_2 metamorphism. The specific *P–T* estimates determined at each locality are related to the depth from which the rocks were exhumed and are therefore of second-order significance in determining the geodynamics associated with metamorphism. In saying this, given how high and consistent apparent geothermal gradients were during M_2, it is intriguing that there are only few large temperature differences, suggesting that there was little differential exhumation syn–post M_2. This observation implies that the orogenic thickness was relatively uniform over a very large length scale.

Mineral equilibria forward modelling indicates that the lowest M_2 metamorphic grades occurred in the east Warumpi Province (Morrissey et al., 2011). Similar *P–T* conditions are inferred from the Ragged Basin that was deposited between D_1/M_1 and D_2/M_2 (Waddell et al., 2015), although this is based soley on the presence of metamorphic rutile (Clark et al., 2000), and from the Mulga Park region of the east Musgrave Inlier where andalusite-bearing schists are recorded, suggesting that low-pressure, mid-amphibolite facies conditions prevailed (Edgoose et al., 2004) . The highest temperatures, and the only clear occurrence of UHT conditions , are documented in the west Musgrave Inlier (7–8 kbar, 930–1000 °C; Walsh et al., 2015). However, the highest apparent thermal gradients come from the south Windmill Islands (>150 °C/kbar; Fig. 7; Morrissey et al., 2017a) where metamorphic temperatures increase with proximity to the Ardery Charnockite, yet pressures associated with peak metamorphism remain constant (Morrissey et al., 2017b). This observation suggests that differences in absolute *P–T* conditions within the Windmill Islands are not due to differential exhumation, but instead result from advective heating (Morrissey et al., 2017a). This interpretation from the Windmill Islands suggests that there may be other regions of the MAFWO in which M_2 is predominantly driven by the emplacement of syn-D_2 magmas. As D_2 magmatism was voluminous in many parts of the orogen, metamorphism resulting from its emplacement may therefore also be considered regionally significant, despite being a seemingly under-represented heat source in the *P–T* constraints obtained to date.

The interpreted post-peak metamorphic *P–T* path was associated with constant to slightly decreasing pressure (Clark et al., 2000; Morrissey et al., 2011; Tucker and Hand, 2016; Tucker et al., 2018; Walsh et al., 2015) and is therefore considered of regional significance. In some instances (e.g. west Musgrave Inlier; Walsh et al., 2015), decompression is inferred to have been slow (Clarke and Powell, 1991; Edgoose et al., 2004). In contrast however, the post-peak *P–T* path in the east Musgrave Inlier is interpreted to have been slightly up-pressure and relatively rapid, relating to short-lived, localised heating by structurally overlying syn-metamorphic magmas (Tucker et al., 2015). Interpretations on the thermal driver for M_2 metamorphism in the Windmill Islands and east Musgrave Inlier are therefore similar. Similarities in the longevity of

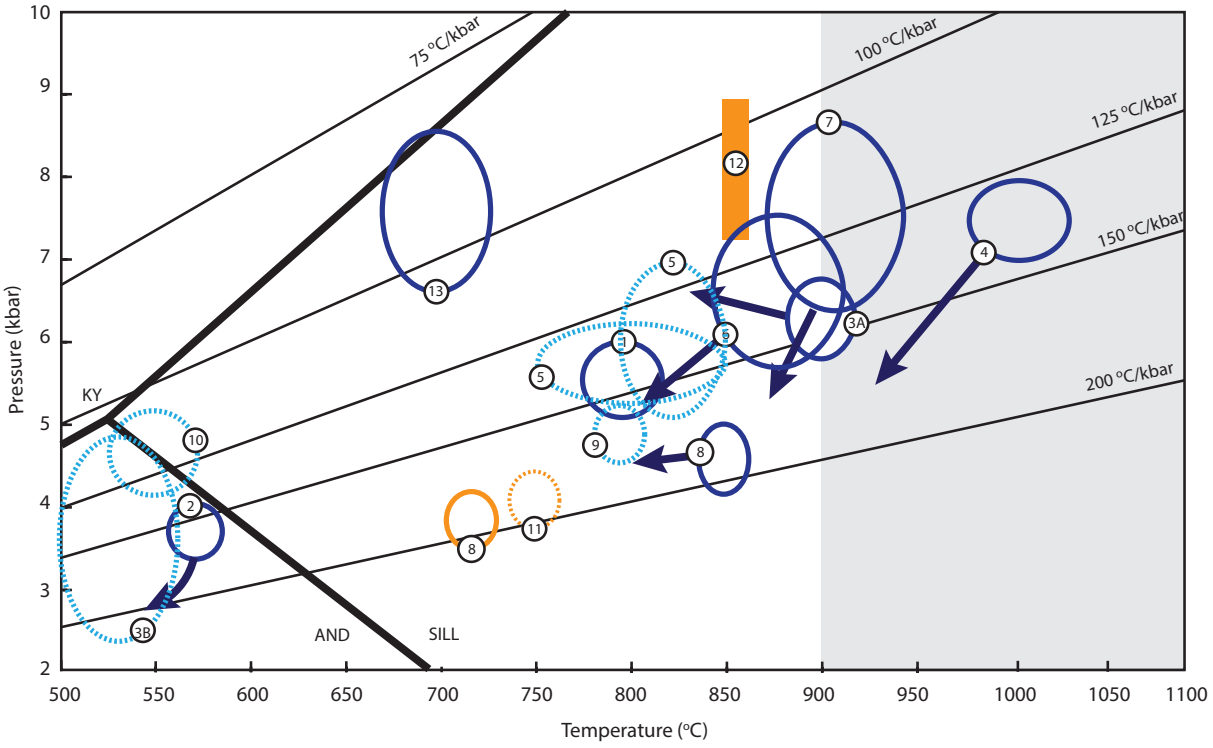

Figure 7. Summary *P–T* diagram of M_1 and M_2 metamorphic conditions. Quantitative *P–T* constraints and interpreted post-peak metamorphic *P–T* paths are indicated in orange (M_1) and blue (M_2). *P–T* constraints are numbered, corresponding to the following localities: (1) southern Aileron Province/North Warumpi Province (Wong et al., 2015); (2) East Warumpi Province (Morrissey et al., 2011); (3A) east Musgrave Inlier (Tucker et al., 2015); (3B) east Musgrave Inlier (andalusite-bearing rocks; Edgoose et al., 2004); (4) west Musgrave Inlier (Walsh et al., 2015); (5) Biranup Zone (Bodorkos and Clark, 2004a); (6) Bunger Hills (Tucker et al., 2017); (7) Highjump Archipelago (Tucker and Hand, 2016); (8) Windmill Islands (Morrissey et al., 2017a); (9) Salisbury Gneiss (Madura Province; Clark et al., 2000); (10) Ragged Basin (Clark et al., 2000); (11) Malcolm Metamorphics (Arid Basin; Clark et al., 2000); (12) Snowys Dam Formation (Arid Basin; Clark et al., 2014); and (13) Barren Basin (Fly Dam Fm.; Kirkland et al., 2016). Dashed lines in lighter shades of orange or blue indicate that *P–T* constraints are calculated by conventional thermobarometry or estimated from field observations. All other constraints are based on forward phase equilibria modelling. The *P–T* region corresponding to ultrahigh temperature metamorphism (>900 °C, definition based on temperature only) is shaded light grey.

metamorphism (discussed below), the extreme apparent geothermal gradients and (in general), the *P–T* paths suggest a regional mechanism. However, it is plausible that slight variations in the apparent thermal gradients and *P–T* paths from different localities across the MAFWO (Fig. 7) might be indicative of local-scale processes such as contact metamorphism from the emplacement of syn-metamorphic magmas within this more regional-scale system.

7. D_2/M_2 STRESS REGIME

A number of regions within the MAFWO record evidence for inferred D_2/M_2 thrusting and/or shearing (Table 4). Field observations commonly suggest that fabric transposition involved NNE-directed shortening along the NAC margin, and NW-directed shortening in the Albany–Fraser Orogen, towards the Yilgarn Craton. A D_2/M_2 compressional regime conflicts with observations from *P–T* modelling that identify low–moderate peak M_2 pressures, a post-peak evolution evolving along constant to slightly decreasing pressure, and in some instances, evidence for slow cooling (Section 6). These *P–T* observations, combined with high–ultrahigh thermal gradients associated with peak M_2, are suggestive of extending crust and high heat flow, rather than tectonic thickening (see also Section 9.3). The relative timing of D_2 structure development versus peak M_2 metamorphism therefore requires some consideration.

The timing of contractional deformation in the Warumpi Province and southern Aileron Province is directly constrained by *in situ* geochronology of migmatitic to ultramylonitic fabrics within south-side-up shear systems (ca. 1140–1080 Ma (Wong et al., 2015). However, structural observations also indicate that an earlier, flat-lying metamorphic fabric in the east Warumpi Province formed at

ca. 1140–1110 Ma, and was associated with the development of peak M_2 mineral assemblages (Morrissey et al., 2011), and the emplacement of the Teapot Granite Complex (ca. 1130 Ma; Black and Shaw, 1995; Wong et al., 2015). Wong et al. (2015) and Morrissey et al. (2011) accordingly propose that the formation of early, regional low-angle fabrics, high to ultrahigh thermal gradients and associated clockwise (down-pressure) *P–T* evolution, occurred in an extensional setting associated with D_2/M_2. NNE-directed shortening occurred post-D_2 extension, and is interpreted to relate to late- to post-D_2 north-directed reattachment of the Warumpi Province to the NAC (Wong et al., 2015).

Studies from the Albany–Fraser Orogen document evidence for NW-directed thrusting, dextral shearing, and NW-vergent folding (Table 4; Adams, 2012; Barquero-Molina, 2009; Beeson et al., 1988; Bodorkos and Clark, 2004b; Clark et al., 2000; Duebendorfer, 2002; Spaggiari et al., 2011; Wetherley, 1998). Fast cooling of the Albany–Fraser Orogen is considered to have occurred via exhumation along these thrusts (Scibiorski et al., 2015). The east Biranup Zone cooled to ~550 °C (hornblende Ar–Ar) by ca. 1190 Ma. In contrast, the west Biranup and Nornalup Zones cooled more slowly to ~550 °C (by ca. 1170 Ma; Scibiorski et al., 2015). The entire Albany–Fraser Orogen is interpreted to have reached ~350 °C at a similar time (ca. 1170–1150 Ma; Scibiorski et al., 2015). Variation in exhumation rate is interpreted as a consequence of transpressional deformation in an obliquely compressional setting (Scibiorski et al., 2015). These observations suggest that cooling and exhumation in a compressional setting was occurring during ongoing D_2 magmatism and high-temperature M_2 metamorphism (e.g. Tables 3 and 4).

However, in a number of instances, there are no direct temporal links between peak M_2 *P–T* conditions and the development of shear fabrics associated with NW–SE compression, specifically within the same metamorphic sample (i.e. as per Wong et al., 2015). The inference that high-temperature M_2 metamorphism was associated with NW-directed structures is based on independent observations of M_2 metamorphic ages in the surrounding pelitic rocks, D_2 crystallisation ages of inferred syn-kinematic igneous rocks, and cross-cutting and structural relationships. M_2 mineral assemblages are also commonly inferred as being high-temperature from field observations and seldom conventional thermobarometry (e.g. Bodorkos and Clark, 2004a,b; Clark et al., 2000; Spaggiari et al., 2011). Therefore, while NW-directed thrusting may have been associated with D_2, the specific timing of compressional deformation in relation to growth of the peak M_2 metamorphic mineral assemblage, and whether the two are in fact linked, remains unclear in many cases.

8. DISTINGUISHING TWO-STAGE VERSUS SINGLE-STAGE METAMORPHISM

By definition, the MAFWO is characterised by two-stage tectonism (Table 1), that is broadly attributed to the convergence of the three Australian–East Antarctic cratons. However, it is important to distinguish that some parts of the MAFWO (i.e. regions other than central MAFWO) do not record geochronological evidence for D_1/M_1; the tectonic event that unites all regions of the MAFWO is D_2/M_2. With this clarified, there are two outstanding problems in adequately characterising and interpreting age data from the MAFWO. Firstly, it is difficult to distinguish whether different parts of the MAFWO experienced a single- or two-stage metamorphic evolution due to a continuum of metamorphic age data that encompass a much broader interval (up to ~200 Myr) than the seemingly discrete denoted D_1/M_1 and D_2/M_2 time periods would imply (e.g. Figs. 5 and 6). Distinguishing between these two possibilities is often difficult with the available geochronology. The spread in MAFWO metamorphic age data contrasts with the record of magmatic age data that reveals distinct age populations (Figs. 5 and 6). Some petrochronologic studies from the Bunger Hills and central Windmill Islands provide support for discrete metamorphic events (despite the large metamorphic age record), distinguished by differences in age, zircon and monazite morphology, and REE concentration (Morrissey et al., 2017a; Tucker and Hand, 2016; Tucker et al., 2018). In contrast, Morrissey et al. (2017a), Walsh et al. (2015) and Tucker et al. (2015) report large spreads in monazite age data from the south Windmill Islands (ca. 1300–1150 Ma), and the Musgrave Inlier (ca. 1260–1110 Ma), with no subordinate age populations, nor discrete REE domains.

Secondly, there are difficulties in matching segments of the large spreads in M_2 metamorphic

age data to the M_2 *P–T* path. Consequently, petrochronologic interpretations vary between different MAFWO metamorphic studies. For instance, Walsh et al. (2015) interpret ~150 Myr of largely prograde and peak metamorphic monazite growth on the basis that monazite may be resistant to isotopic resetting, even after long-duration UHT conditions (e.g. Korhonen et al., 2013; Yakymchuk and Brown, 2014). Morrissey et al. (2017a) suggest the reverse, interpreting ca. 1300–1150 Ma ages to reflect isotopic resetting (of M_1 ages) during M_2. Further, Tucker et al. (2018) and Tucker et al. (2015) note that the large age spread is likely the combined result of preserved prograde and peak ages, cooling ages and the recrystallisation of older zircon. Accordingly, and importantly, the interpreted metamorphic age data compiled in Figs. 5 and 6, does not necessarily identify the specific timing of peak metamorphism. Rather, it reflects the duration of overall high temperature conditions that are conducive for the growth and recrystallisation of mineral chronometers. Timescales of "long-lived" high thermal gradients that characterise the MAFWO are therefore poorly resolved.

At the terrane-scale, the preservation of discrete metamorphic events versus a continuum of metamorphic age data may be a function of differences in the onset and duration of 'D_1/M_1' and 'D_2/M_2' across the orogen, in turn linked to variation in the longevity of the heat source(s). It is likely that the effects of the same regional metamorphic event at mid–lower crustal depths may record a seemingly longer duration of metamorphism than rocks situated at higher structural levels (e.g. compare Arid Basin units with the Musgrave Inlier and Bunger Hills, Fig. 6). At mid–lower crustal depths, higher temperatures, partial melting, the availability of fluids post-melt crystallisation, and slow cooling, promote the protracted growth and dissolution–recrystallisation of mineral chronometers (Kelsey and Hand, 2015; Taylor et al., 2016; Yakymchuk and Brown, 2014). Offset observed in the age of metamorphism recorded by different geochronometers in some parts of the MAFWO (Fig. 6) is likely a response to differences in the physical and chemical stability of zircon and monazite at high temperatures (Kelsey et al., 2008; Stepanov et al., 2012; Yakymchuk and Brown, 2014). In particular, the greater reactivity of monazite relative to zircon in melt-bearing environments (e.g. Yakymchuk and Brown, 2014) means that monazite may be more likely to dissolve and reprecipitate as melt crystallises, and thus record younger (cooling) ages.

M_1 metamorphism occurred largely syn–post D_1 magmatism (Morrissey et al., 2017a; Paul et al., 1995; Smithies et al., 2013; Spaggiari et al., 2011). In contrast, the timing of magmatism relative to metamorphism during D_2/M_2 was more varied with field relationships, geochronological evidence and interpretations on *P–T* constraints suggesting that D_2 magmatism preceded, was synchronous with, and was emplaced post-peak M_2 metamorphism (Dutch et al., 2013b; Howard et al., 2015; Morrissey et al., 2017a; Sheraton et al., 1995; Smithies et al., 2015a; Spaggiari et al., 2011; Tucker et al., 2018, 2017b). Commonly, temporal offsets in the age of D_2 magmatism and M_2 metamorphism are not observed which may be a reflection of metamorphism being an inherently more continuous process than magma crystallisation (e.g. compare age peaks in Fig. 5). Whilst D_2 magmatism may have provided heat for M_1 metamorphism in some instances (e.g. south Windmill Islands; Morrissey et al., 2017a), this relationship is not systematically observed across the MAFWO. This implies a broader-scale thermal driver for both D_2/M_2 magmatism and metamorphism.

9. TOWARDS A TECTONIC SYNTHESIS

The preceding summary of key MAFWO Mesoproterozoic magmatic and metamorphic features provides the background necessary to address the following three questions:

1. Why was D_2/M_2 magmatism and metamorphism such high temperature?

2. Why did D_2/M_2 high-thermal gradient metamorphism and magmatism seemingly last for such a long duration?

3. What were the geodynamic settings of D_1/M_1 and D_2/M_2?

This section builds upon existing tectonic interpretations for D_1/M_1 and D_2/M_2 to explore the most plausible geodynamic scenarios for the generation of regional, long-lived, high thermal gradients across the MAFWO. A series of tectonic schematics in Fig. 8 present the various current tectonic models for D_1/M_1 and D_2/M_2, and a revised interpretation of these models, for different parts

of the orogen.

9.1 Mantle-heating versus crustal-heating

As established in Section 1, regional, long-lived, high thermal gradient conditions in convergent settings are generated through: (1) the incubation and self-heating of thickened and abnormally radiogenic crust (e.g. Clark et al., 2015), or (2) advective and/or conductive mantle heating (e.g. Sizova et al., 2010). Before discussing in more detail the geodynamic mechanism, it is first important to clarify that the Mesoproterozoic evolution of the MAFWO is indicative of the latter. The burial of high heat producing crust may provide a long-lived, conductive heat source but this requires substantial crustal thickening (i.e. thickening factor of 2–3, e.g. Tibetan–Himalayan collisional system) followed by 40–60 Myr of tectonic stability and low erosion rates, after which time a thermal anomaly in the mid-crust is maintained for as long as the terrane remains buried (Clark et al., 2011, 2015; McKenzie and Priestley, 2008; Sandiford and Hand, 1998; Vilà et al., 2010). Reduced fertility by partial melting and dehydration (by melt removal) of the crust in a prior metamorphic event is also advantageous as it limits further partial melting (Clark et al., 2011; Korhonen et al., 2013; Vielzeuf et al., 1990). Despite a broad association with continental convergence, a model of conductive heating through radioactive decay is not supported as the main thermal driver for the MAFWO. Namely, pre-D_1/M_1 formation (and possible accretion) of the Loongana Arc with the MAFWO does not appear to have resulted in significant deformation or crustal thickening ("soft-collision"; Spaggiari et al., 2015). Similarities in the inferred timing of juvenile crustal addition in the Musgrave Inlier, Gawler Craton and Madura and Coompana Provinces also suggests that they form a geographically continuous expanse of oceanic crust that separates the WAC, NAC and SAC (e.g. Kirkland et al., 2017; Kirkland et al., 2015a). In addition, pressures associated with peak M_1 and M_2 are modest and therefore do not support crustal thickening. High thermal gradients generated by orogenic thickening are typically also associated with small–moderate volume crustal anatexis (Douce and McCarthy, 1998; Faccenda et al., 2008) rather than evidence for voluminous mantle magmatism. This is not the case for the MAFWO with isotopically-juvenile mafic and calc-alkaline felsic magmatism during D_1, and voluminous, A-type felsic magmatism with a significant mantle source component during D_2. Whereas overarching mantle-driven system is endorsed for the MAFWO, this does not preclude that radiogenic heat was still a contributing factor.

9.2 Tectonically-controlled and spatially-confined: a D_1/M_1 synopsis

The geodynamic regime associated with D_1/M_1 must satisfy four key criteria. First, the effects of D_1/M_1 were confined to a linear belt in the central MAFWO. This interpretation assumes that the documented spatial extent of D_1/M_1 as reflected by magmatic and metamorphic ages and M_1 *P–T* constraints is a true reflection of its restricted geographical occurrence. There is very little record of D_1/M_1 at the east and west ends of the orogen within regions of the MAFWO that have pre-D_1/M_1 geological histories involving reworking of isotopically-evolved crust (e.g. Northern Foreland, Biranup Zone, Bunger Hills, southern NAC). This may be a reflection of the inability of these already tectonised terranes to record subsequent metamorphic events (Brown and Korhonen, 2009). However, given they record D_2/M_2, it is more likely that the spatially-restricted record of D_1/M_1 is primarily controlled by the pre-D_1/M_1 tectonic setting of the central MAFWO.

Second, the D_1/M_1 geodynamic regime must account for extensive, isotopically-juvenile, bimodal mafic and felsic calc-alkaline magmatism. The isotopically-juvenile nature of D_1 magmas may be a reflection of the addition of new mantle material, reworking (partial melting) of previously thinned and juvenile crust, or both. Further, spatial–age trends of D_1 magmatism imply a craton-wards shift in the locus of melting and/or magma emplacement in parts of the central MAFWO. Although the Fraser Zone is the only known region with physical evidence for voluminous mafic magmatism, a mantle contribution has been inferred for other regions as a thermal driver for metamorphism (e.g. Windmill Islands) and a source component in parent melts to felsic D_1 magmas on the basis of isotopic data (e.g. Gora Hill Suite).

Third, peak M_1 metamorphic conditions are high-temperature but with seemingly varied thermal gradients (e.g. compare Windmill Islands and Fraser Zone, Fig. 7), with the caveat that unambiguous identification of M_1 *P–T* conditions is difficult due to overprinting by M_2. Regardless,

the *P–T* constraints do not provide clear evidence for significant crustal thickening during D_1/M_1 as peak pressures are modest (<9 kbar in the Fraser Zone, <4 kbar in the Windmill Islands) and there is no robust mineralogical evidence for clockwise *P–T* paths. The development of quasi-horizontal fabrics in M_1 metamorphic rocks is also a common feature, although this observation is scale-dependent, and in high-grade, melt-bearing rocks, horizontal fabrics can be equivocal.

Fourth, in all regions that experienced D_1/M_1, D_1 magmatism was immediately preceded by basin formation. The interval between basin sediment deposition and high thermal gradient metamorphism during D_1/M_1 was short in parts of the central MAFWO (e.g. <25 Myr in the Fraser Zone, <30 Myr in the Windmill Islands). A mechanism for the generation of high thermal gradients during D_1/M_1 must therefore account for the relatively short geological time interval between sedimentation, magmatism and metamorphism. Detrital zircon provenance is dominated by Mesoproterozoic sources, but major contributions from Archean and Paleo–Mesoproterozoic crust also occur and must be accounted for in any tectonic model.

Two alternative hypotheses are currently proposed for the D_1/M_1 tectonic setting of the east Albany–Fraser Orogen and formerly contiguous Windmill Islands (Model A and B; Fig. 8). An additional, separate tectonic scenario (Model C), is proposed in Fig. 8 for the D_1/M_1 evolution of the west Musgrave Inlier. In essence, all three models endorse extensional–accretionary orogenesis for D_1/M_1. However, there are differences between the three models that relate primarily to the timing of arc accretion versus extension, and the specific mechanism of extension. Each model accounts for some, but not all, of the key features of D_1/M_1, and there remains ambiguity surrounding some interpretations on which the models are fundamentally based. The rationale and limitations of each are discussed below.

9.2.1 Model A: subduction inversion, arc accretion and orogenic collapse/delamination

Model A is primarily based on inferences of Arid Basin detrital zircon provenance and the geochemistry of pre-D_1 and D_1 magmas from the east Albany–Fraser Orogen. Initially east-dipping subduction places the Loongana Arc on an oceanic margin and a separate plate from the Yilgarn Craton and therefore limits crustal contamination of the emplaced arc rocks (e.g. Haig Cave Supersuite; Spaggiari et al., 2015). At this time, the eastern-most Arid Basin (Malcolm Metamorphics) is considered as a fore-arc basin, within the overall passive margin setting (Fig. 8; Spaggiari et al., 2015). A fore-arc basin has been proposed on the basis of ca. 1455 Ma Loongana Arc-derived detritus (Adams, 2012) and N-MORB geochemistry of inferred (yet undated) syn-depositional basaltic sills within the Malcolm Metamorphics (Spaggiari and Smithies, 2015). A switch to west-dipping subduction was subsequently required to facilitate transport of the Loongana Arc closer to the Biranup Zone/Yilgarn margin Spaggiari et al. (2015). D_1/M_1 was then initiated at ca. 1330 Ma following closure of the (passive) marginal Arid Basin by soft-collision of the Loongana Oceanic Arc and east Nornalup Zone (Fig. 8). Madura Province crust was subsequently thrust westwards onto the east Nornalup Zone, and predominantly Loongana Arc detritus was shed into an evolving foreland basin (Snowys Dam Formation in the Fraser Zone, Fig. 8). West-dipping subduction commenced under the accreted Loongana arc crust and slab roll back, away from the Yilgarn Craton margin, placed the Fraser Zone into a back-arc setting for D_1/M_1 (Spaggiari et al., 2015). This accounted for the interpretations of Clark et al. (2014) who suggested that heat advection within a back-arc

Figure 8. (ensuing pages) Pre-D_1/M_1 to D_2/M_2 tectonic models for the MAFWO. Separate schematics are shown for different parts of the orogen, based on existing tectonic models and interpretations. Typically, existing tectonic interpretations are presented for either the D_1/M_1 or D_2/M_2 time period, but not both. Model A (east Albany–Fraser Orogen) is based on (Maier et al., 2016b; Spaggiari et al., 2015; Spaggiari and Smithies, 2015); Model B (Windmill Islands) is based on (Morrissey et al., 2017a; Morrissey et al., 2017b); Model C (Musgrave Inlier and southern NAC) is based on (Gorczyk et al., 2015; Howard et al., 2015; Smithies et al., 2011; Smithies et al., 2010b; Walsh et al., 2015; Wong et al., 2015); Model D (west Albany–Fraser Orogen and Bunger Hills) is based on (Tucker et al., 2017). The four schematics highlight the divergent pre-D_1/M_1 crustal architecture of these regions of the MAFWO that translates into differences in their D_1/M_1 tectonic evolution. The D_1/M_1 tectonic interpretation for the west Musgrave Inlier is ambiguous with the currently available data (Section 9.2, main text) and therefore a D_1/M_1 model is not hypothesised for this region. Key features of each tectonic model are annotated. Fig. 1 shows the approximate geographic position of the cross-section transects. Note that Model A and B are considered to reflect the same transect due to the reconstructed position of the Windmill Islands on the east Nornalup Zone.

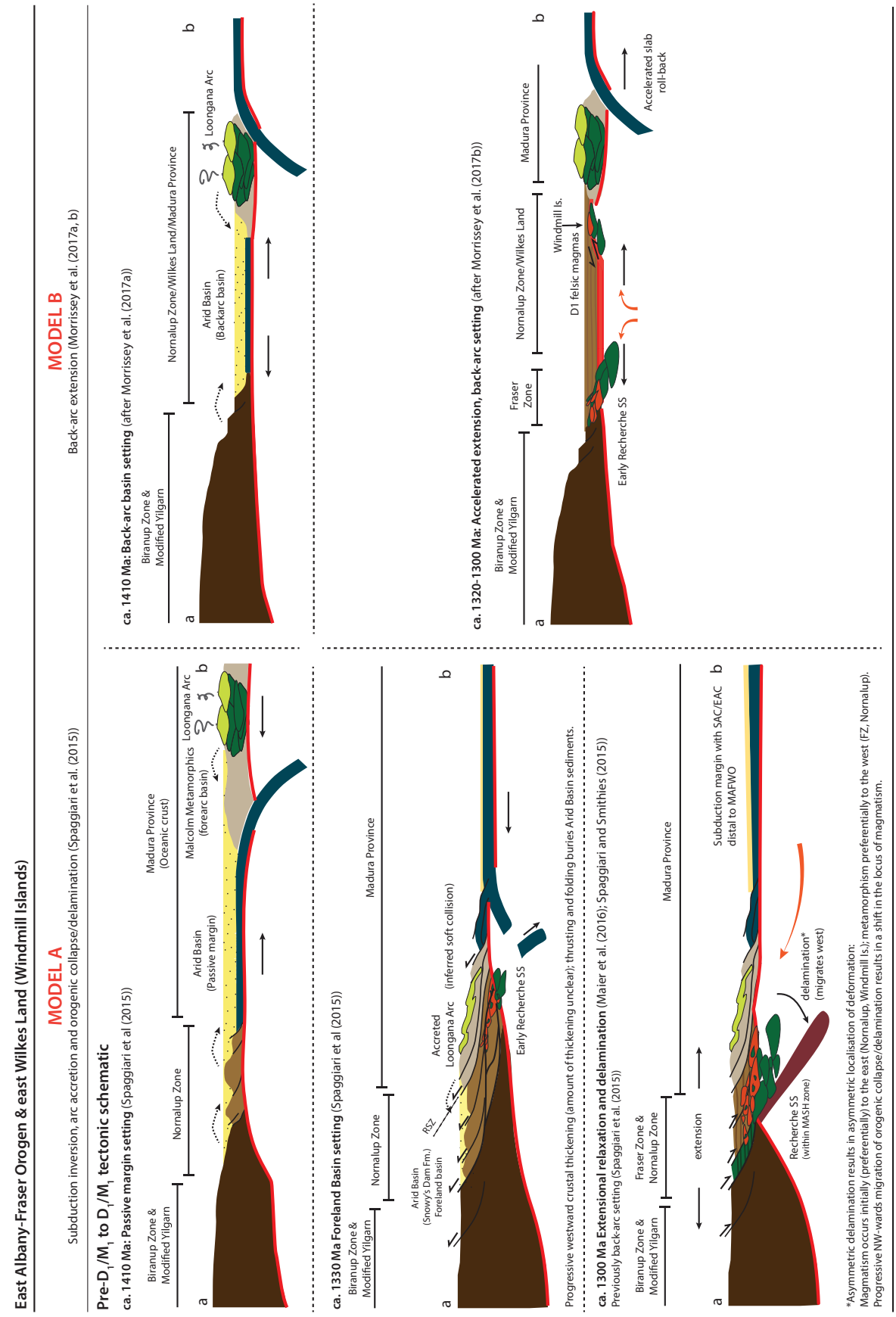

Figure 8. (continued)

Figure 8. (continued)

East Albany-Fraser Orogen & east Wilkes Land (Windmill Islands)

MODEL A (continued)

Extrapolating D_1 accretion/orogenic collapse model of Spaggiari et al. (2015)

Pre-D_2/M_2 tectonic schematic

ca. 1260-1210 Ma: Accretion (Coompana & SAC/EAC), shortening, minor felsic magmatism

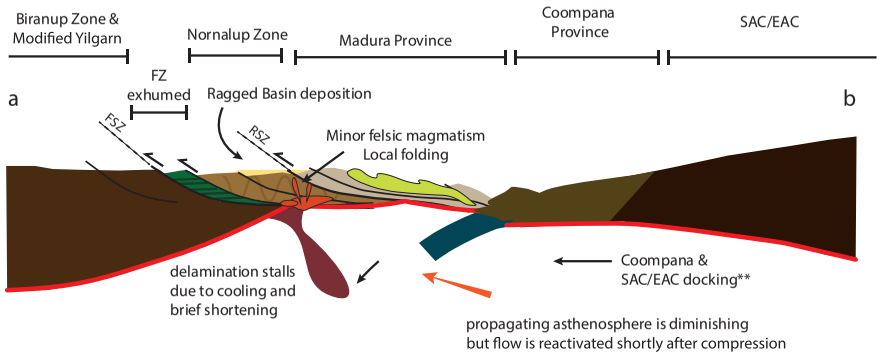

Fraser Zone inferred exhumed due to pre-D_2/M_2 compression

**Model assumes Coompana Province was previously accreted to the SAC (ca. 1600 Ma; Dutch et al. 2015a)

MODEL B (continued)

Adapted back-arc extension model of Morrissey et al. (2017a, b)

ca. 1260-1210 Ma:
Accretion (all MAFWO, Coompana & SAC/EAC), shortening, minor felsic magmatism (after Morrissey et al. (2017b))

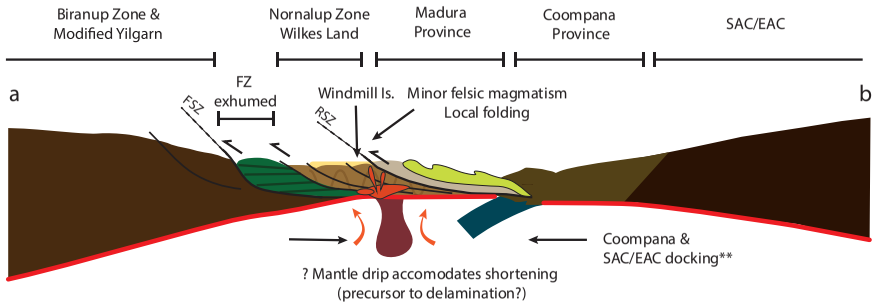

Shortening and thickening of lithosphere during Coompana/SAC-EAC accretion (amount of thickening unclear).
Negative buoyancy of thickened lithosphere results in mantle drip.
Localised magmatism in East Antarctica (response to mantle drip?).

D_2/M_2 tectonic schematic

ca. 1200-1160 Ma: delamination, extension, voluminous felsic magmatism, metamorphism

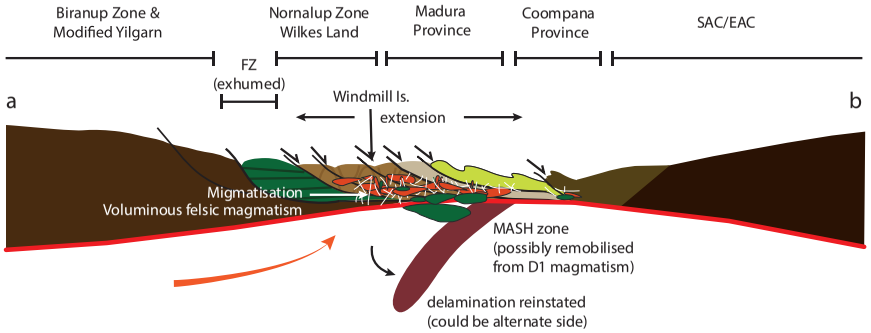

D2/M2 tectonic summary:

1. Lower crust/mantle lithosphere delamination
2. Extensional collapse of thickened (upper-mid) crust
3. High heat flux (upwelling asthenosphere)
4. Voluminous magmatism (felsic surface expression, but significant asthenosphere mantle contribution)
5. Magmatism associated with MASH zone/deep hot zone/mafic underplate
6. Migmatisation/HT-UHT metamorphism (mid-lower crust)
7. Locally crustal anatexis
8. Possible contributions from radiogenic heating
9. ? syn-metamorphic exhumation (upper-mid crust) along thrusts/shears

From scenario 1: Ongoing delamination? Earlier compressional phase renews flow of asthenosphere and facilitates second delamination (concept after Gorzyk et al. (2015))
From scenario 2: Gravitational mantle drip(s) precedes main delamination phase by ~30 Myr (e.g. Chapman et al. (2018))

Musgrave Inlier & NAC margin

MODEL C

D_2/M_2 tectonic schematic

ca. 1200-1160 Ma: post-collision extension, voluminous felsic magmatism, metamorphism

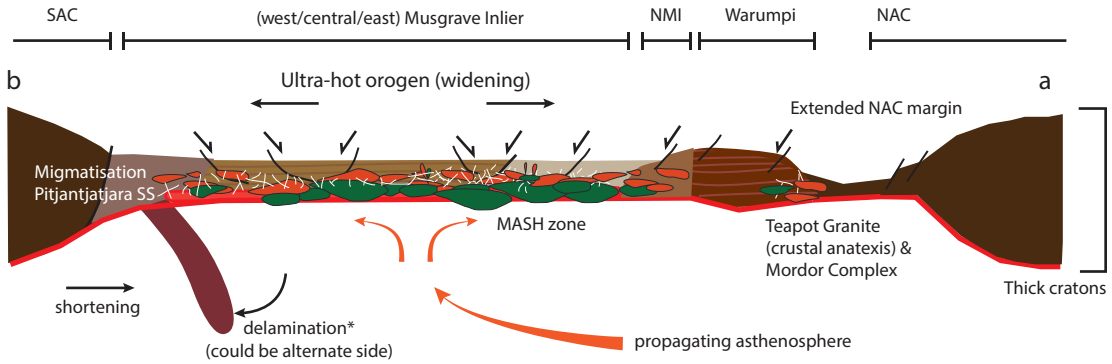

*Imposed shortening results in delamination/sagduction as crust is thin and hot. Converging crust must be thin, juvenile and slow velocity.
Asymmetric delamination results in asymmetric localisation of deformation.
Locus of magmatism (but not heat flux) migrates as the zone of extension widens.
Flanking cratons spatially confine delamination, allowing delamination to persist for long duration.

Late-post D_2/M_2 tectonic schematic

ca. >1130 Ma: Warumpi-NAC reattachment (Aitken et al. (2016), Wong et al. (2015), Selway et al. (2006), Selway et al. (2009)).
Slow-cooling orogen, localised felsic magmatism, NNE-directed deformation

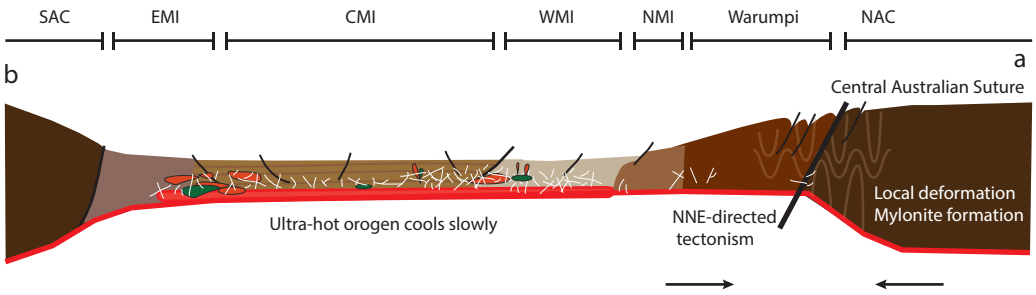

Figure 8. (continued)

West Albany-Fraser Orogen & west Wilkes Land (Bunger Hills)

MODEL D

Pre-D_1/M_1 tectonic schematic

> ca. 1410 Ma: Passive margin setting (after Tucker et al. (2017))

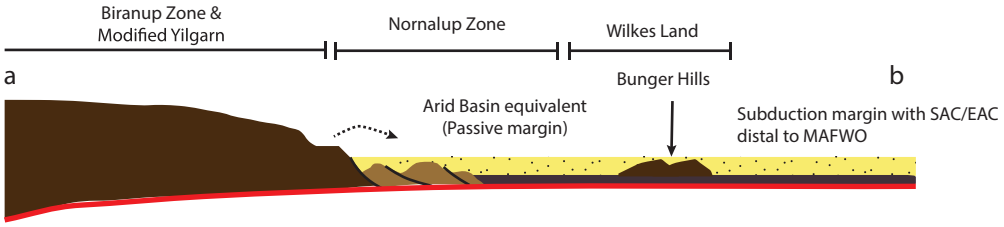

West MAFWO does not ovserve Loongana Arc accretion.
Bunger Hills inferred located in a passive margin setting outboard of Yilgarn Craton at ca. 1490 Ma.

D_1/M_1 tectonic schematic

ca. 1300 Ma: Limited tectonism
West Albany-Fraser Orogen and Bunger Hills (largely) do not observe D_1/M_1

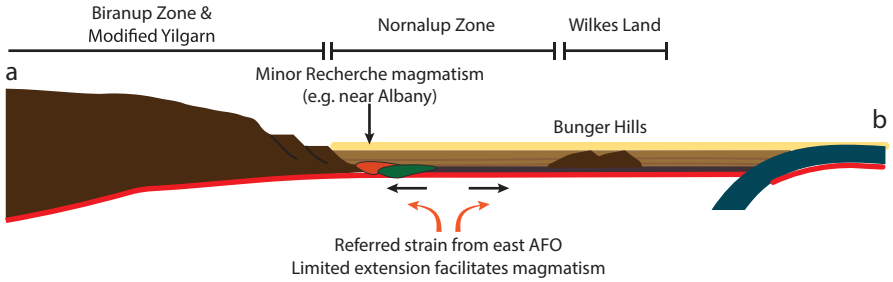

Schematic follows the D_1 back-arc extension model of Morrissey et al. (2017a).
Alternatively, accretion of the west Nornalup Zone and Bunger Hills region to the Biranup Zone/WAC may have already occurred prior to D1 (following D_1 model of Spaggiari et al. (2015)). In which case, minor magmatism (pictured) may also result from extensional collapse and delamination.

D_2/M_2 tectonic schematic

ca. 1200-1160 Ma: post-collision extension, voluminous felsic magmatism, metamorphism

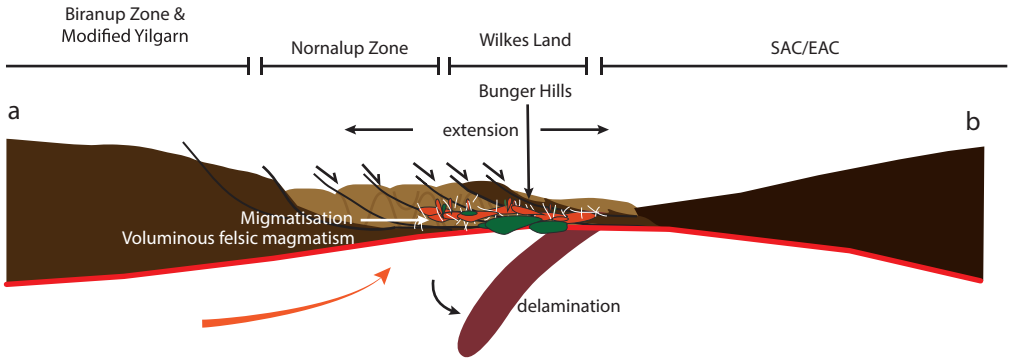

Equivalent model to the eastern Albany-Fraser Orogen and Windmill Islands during D_2/M_2.

Figure 8. (continued)

setting was required to drive high temperature metamorphism and synchronous magmatism in the Fraser Zone.

Maier et al. (2016b) and Spaggiari and Smithies (2015) subsequently re-evaluated this back-arc interpretation due to a lack of evidence for subduction-related D_1 magmatism and the absence of D_1 tectonism and magmatism in the Madura Province (at this time accreted and thrust on the Nornalup margin). Instead, they proposed that following arc-accretion and crustal thickening, subduction did not reinitiate (as per Spaggiari et al. (2015)) but extensional relaxation by orogenic collapse occurred, possibly combined with lithosphere mantle delamination. The decreasing age of felsic–intermediate magmas in the Nornalup Zone from SE to NW is interpreted to reflect the migration of a lower crustal hot zone initiated through orogenic collapse (Smithies et al., 2015b). The Yilgarn Craton is interpreted to have acted as a primary tectonic control, terminating this migrating extensional system (Maier et al., 2016b).

Model A accounts for the crustally uncontaminated geochemistry of the Loongana Arc (pre-D_1) magmas, and non-subduction related D_1 magmatism, as well as providing one explanation for the detrital zircon provenance of the Arid Basin. Manlte lithosphere delamination conceivably also explains the progressive NW-migration of D_1 magmatism in the Albany–Fraser Orogen, and their increasingly juvenile isotope composition over time. As delamination is typically asymmetric, the locus of deformation and magmatism would have migrated and widened with progressive delamination (e.g. Wang and Currie, 2015), and over time, the existing lower crust would have been increasingly removed and replaced with juvenile asthenosphere melts (e.g. Gorczyk et al., 2015). However, several aspects of Model A fail to account for some key features of D_1/M_1, and there is ambiguity surrounding some interpretations on which Model A is fundamentally based. Firstly, despite the fore-arc interpretation for the Malcolm Metamorphics, Spaggiari and Smithies (2015) also note that N-MORB basalt geochemistry does not preclude a back-arc setting. Therefore the tectonic setting prior to D_1/M_1 may be different to that depicted in Model A.

It is also important to clarify that orogenic collapse, its associated pressure decrease, and increase in thermal gradients over time (Spear, 1993), are a response to asthenospheric upwelling during mantle lithosphere delamination (coherent "peeling-off"; Gray and Pysklywec, 2012). Primary uncertainties with Model A regard the mechanism and extent of crustal thickening, and the lag time required between crustal thickening (instability initiation) and delamination. In Model A, crustal thickening is triggered by "soft-collision" (Spaggiari et al., 2015). Soft-collision (compare hard-collision: e.g. Tibetan-Himalayan, Kohistan Arc–Eurasia/India, Western Alps; Faccenda et al., 2008; Gibbons et al., 2015) typically occurs when the arc is situated on an oceanic rather than continental substrate, the velocity of convergence is low, or the duration of active collision is short. It seems unlikely, unless Loongana Arc convergence was high-velocity, that significant crustal thickening in the central MAFWO would have ensued. Where associated with crustal thickening, delamination is typically driven by the gravitational instability of high-density lithosphere (eclogitised due to the collision process) in less dense, underlying asthenosphere (Krystopowicz and Currie, 2013; Leech, 2001). Logically, if crustal thickening was appreciable in the MAFWO, metamorphic rocks should exhibit relatively high pressures (e.g. >9 kbar; O'Brien and Rotzler, 2002) and clockwise *P–T* paths (England and Thompson, 1984), of which there is currently no evidence.

Evidence for crustal thickening might be provided by seismic and gravity anomaly data from the Albany–Fraser Orogen (depth to MOHO: 35–52 km) that are interpreted to reflect underthrusting of a magmatic underplate (Sippl et al., 2017). In this instance, magmatic underplating is considered akin to tectonic wedging of an exotic, subducting lower crustal terrane (Snyder and Goleby, 2016) beneath the Yilgarn Craton during D_1–D_2 convergence. However, a lack of time constraints on thrust-related structures in the Albany–Fraser Orogen means that, if related to convergence, it is unclear in which event this occurred (Sippl et al., 2017). Given the long-lived deformational history associated with the Paleoproterozoic Biranup Orogeny (pre-D_1/M_1; see Section 4), the possibility that at least some of these structures are Paleoproterozoic and were subsequently reactivated, cannot be dismissed. Further, the lack of subduction-related magma geochemistry, and no indication of ongoing subduction after D_1, also makes tectonic underthrusting as a result of subduction difficult to justify. Magmatic

underplating is also typically considered as an *in situ* process involving ponding of mantle magas at the base of the MOHO (e.g. Thybo and Artemieva, 2013).

As a final consideration for Model A, collisional orogens commonly develop much earlier than the onset of delamination and upper–mid crustal extensional collapse (e.g. up to 30-40 Myr time lag; Chapman et al., 2018; Gray and Pysklywec, 2012; Krystopowicz and Currie, 2013; Sobolev and Babeyko, 2005). A relatively short time period occurred between basin deposition and onset of D_1/M_1 in parts of the central MAFWO such as the Fraser Zone (Snowys Dam Formation: 1335–1305 Ma; D_1: ca. 1305–1290 Ma) and the Windmill Islands (ca. 1350–1315 Ma; D_1: ca. 1320–1315 Ma). It is unclear whether the rapid attainment of high thermal gradients could therefore be explained by crustal thickening and delamination.

9.2.2 Model B: accelerated back-arc extension

Morrissey et al. (2017b) present an alternative scenario (Model B) that is based on the detrital zircon provenance and *P–T* conditions of metasedimentary rocks from the Windmill Islands. A fundamental difference between Model A and B is the pre-D_1 subduction polarity that subsequently influenced D_1/M_1 tectonic interpretations. Model B suggests ongoing D_1 west-dipping subduction, placing the eastern margin of the Albany–Fraser Orogen and Windmill Islands into a back-arc setting.

Evidence for sustained, high thermal gradients but limited thickening is commonly linked to extension (e.g. Currie and Hyndman, 2006; Hyndman et al., 2005; Sizova et al., 2014; Wickham and Oxburgh, 1985). Back-arcs are generally regions of thinned lithosphere (approx. half normal crustal thickness), high surface heat flow due to upwelling asthenosphere and heat advection from voluminous mafic magmatism (Currie and Hyndman, 2006; Hyndman et al., 2005; Sizova et al., 2014; Sizova et al., 2010). Back-arcs are also characterised by relatively short geological time periods between basin deposition, and magmatism and metamorphism (~5–20 Myr; Collins, 2002; Harley, 2016).

Model B accounts for a number of D_1/M_1 features including the short time between sediment deposition and the onset of D_1/M_1, the elevated thermal gradients associated with M_1 metamorphism, and the development of horizontal fabrics during peak metamorphism. Provided that the back-arc was distal to the Yilgarn Craton margin, Model B also explains the dominance of Mesoproterozoic Loongana Arc detritus in the basin sediments as well as variably minor age components from the Yilgarn Craton and Paleoproterozoic Biranup Zone that suggest a spatial linkage (i.e. detritus cannot jump subduction trench). If the back-arc system were comprised of multiple, variably-linked or localised depocentres along strike (e.g. Collins and Richards, 2008), this may govern differences in the age of sediment deposition and provenance. M_1 *P–T* constraints from Arid Basin metasedimentary rocks supports that this was the region of active extension. Model B also satisfies the isotopically-juvenile nature of D_1 magmas which may reflect the addition of voluminous mantle magmatism in the actively extending zone (e.g. Fraser Zone) and/or the partial melting of pre-existing, extended, juvenile basement (e.g. Windmill Islands). In an extensional regime, thinned crust is too volumetrically minor in comparison to added mantle melts and existing juvenile basement to dominate the isotope signature of the D_1 melts. With increasing extension, there may be an increased juvenile source component in the emplaced magmas simply by virtue of less crust availability in the magmatic system.

In Model B, the Fraser Zone was the focus for mafic magmatism and deformation; the Windmill Islands are interpreted to have been located in the footwall of the extending basin system, at shallower depths than the Fraser Zone (Morrissey et al., 2017b). This explains the variation in *P–T* conditions between these two regions, but also provides justification that the Madura Province may not necessarily record D_1/M_1 if it was situated at the rift shoulder (one of the reasons for switch in the interpretation of Model A).

The main reservations with Model B relate firstly to explaining trends in magmatic age and geochemistry, and secondly in uncertainty about the mechanism for back-arc generation and maintenance. Spaggiari et al. (2015) note that crustal contamination of juvenile arc magmas (in a west-dipping scenario) may not have occurred if the arc was a substantial distance from the craton margin. However, if the D_1 magmas were generated in a back-arc setting they may exhibit subduction-like geochemical signatures, which are

not documented. It is also unclear whether a back-arc setting could have accounted for migration in the locus of melting/magma emplacement. Examples of asymmetric and episodic back-arc extension, and migrating back-arc magmatism are documented (e.g. Barker and Hill, 1980; Davey et al., 1995; Faccenna et al., 1997; Magni et al., 2014). Within the MAFWO, if magma migration was related to ongoing slab roll-back in a west-dipping subduction system, younger magmas should be emplaced further eastwards. Instead, the reverse trend is observed within the Albany–Fraser Orogen, with a decrease in crystallisation age and increasing juvenile isotope composition towards the Yilgarn Craton. Therefore, slab roll-back alone is not a viable mechanism. However, migrating lithosphere mantle delamination within a back-arc setting, may offer a plausible explanation (e.g. Collins, 1994; Göğüş, 2015).

Morrissey et al. (2017b) proposed accelerated slab-roll back induces back-arc extension in the MAFWO, but the exact mechanism is speculative. Typically, slab roll back causes thinning of the overriding plate due to slab pull (e.g. Husson, 2006; Sizova et al., 2010). However, back arc tectonics may be more complex, involving a coupled response of mantle lithosphere removal and slab retreat/roll-back (e.g. Aegean Sea–west Anatolia back-arc; Göğüş, 2015). Subduction retreat and back-arc thinning commonly occur after crustal thickening, although this interpretation is not compatible with Model B. In contrast, Currie et al. (2008) propose thinning of normal thickness mantle lithosphere due to subduction related flow. Mantle flow perturbs mantle density and causes localised instability which leads to lithosphere "dripping". However, dripping only involves the lower lithosphere, and not the entire mantle lithosphere (as per delamination, "peeling off"), and therefore the magmatic expression is likely to be more localised (Beall et al., 2017; Göğüş and Pysklywec, 2008b). The majority of thinning via mantle-flow induced lithosphere dripping is also suggested to occur within 30 Myr of subduction initiation (Currie et al., 2008), which may not be compatible with the Model B timeline. A further limitation of a back-arc setting is also highlighted by numerical modelling (e.g. Sizova et al., 2014) that suggests high temperatures may dissipate too quickly and thus granulite formation may be short-lived (e.g. Pownall et al., 2014). Therefore back-arcs may not be effective in forming long durations of high thermal gradient conditions.

9.2.3 Model C: back-arc extension? (west Musgrave Inlier)

A D_1/M_1 tectonic interpretation for the west Musgrave Inlier cannot be confidently proposed. This is due to limited exposure of the pre-D_1 Papulankutja Supersuite and D_1 Wankanki Supersuite, their ambiguous geochemical characteristics, and a conspicuous lack of M_1 *P–T* metamorphic constraints despite evidence for D_1 magmatism and M_1 metamorphic ages. In addition, limited data means that our understanding of the Musgrave Inlier as a single entity (i.e. same plate), occurring on different plates (e.g. NAC, WAC, SAC) or as exotic, microcontinent fragments is not completely clear. As a result, Model C in Fig. 8 does not speculate on the D_1/M_1 tectonic setting.

Pre-D_1 arc-like magmatism in the west Musgrave Inlier (Papulankutja), but not the east Musgrave Inlier is suggestive of a west-dipping subduction system at ca. 1400 Ma (e.g. Aitken et al., 2016). During D_1/M_1, the Wankanki Supersuite is interpreted to reflect additional (or ongoing) continental arc magmatism or post-(Papulankutja) arc accretion melting of isotopically-juvenile basement rocks (Evins et al., 2012; Kirkland et al., 2015a; Kirkland et al., 2013a; Smithies et al., 2010; Wade et al., 2008). This arc setting may have been associated with pre-D_1 to D_1 (Loongana) arc accretion along the eastern Albany–Fraser Orogen, but at present, this interpretation is geochemically ambiguous (Smithies et al., 2010). A back-arc setting for pre-D_1 to D_1 basin sedimentation (Wirku Metamorphics) and coeval D_1 magmatism has also been suggested (Evins et al., 2012; Gorczyk et al., 2015; Smithies et al., 2010). In this scenario, it is logical that parts of the Musgrave Inlier (i.e. central and east Musgrave Inlier) that are not within the actively extending back-arc region, would not experience D_1/M_1. If a back-arc setting in Model C also holds true, this is consistent with the interpreted setting of the Windmill Islands from Model B. This would potentially place the west Musgrave Inlier on the eastern WAC margin at this time, as part of a linked arc–back-arc system associated with extension along the eastern WAC.

In summary, the spatially-confined nature of D_1/M_1, its arc association and evidence for subsequent extensional tectonics reflects that it is a direct response to pre-D_1/M_1 tectonic control on the central MAFWO. It is therefore logical that other parts of the MAFWO do not observe D_2/M_2. It is

also important to highlight that D_1/M_1 is not the defining feature of the MAFWO that is epitomised by regional, long-lived and high thermal gradient conditions.

9.3 Long, hot and regional: a D_2/M_2 synopsis

The geodynamic regime for D_2/M_2 must account for five key observations. Firstly, D_2/M_2 magmatism and metamorphism was pervasive across the entire MAFWO, and independent of the spatial extent of D_1/M_1. This suggests that the thermal driver for D_2/M_2 was dissimilar to D_1/M_1 and considerably more regional.

Second, M_2 metamorphism in all locations was characterised by remarkably similar high–ultrahigh apparent thermal gradients (~150 °C/kbar), suggesting an orogen-wide thermal driver. Differences in absolute *P–T* reflect different mid- to lower-crustal expressions of M_2 within the same orogenic system. Peak pressures associated with M_2 are low to moderate, and differences in metamorphic pressures across the orogen are smaller in magnitude than variations in temperature. This suggests that metamorphism was associated with thinning rather than thickening. Moreover, post-peak M_2 *P–T* paths are associated with constant to decreasing pressure. This is also consistent with an extensional rather than compressional regime. Parts of the MAFWO (e.g. west Musgrave Inlier) also preserve metamorphic evidence for relatively slow cooling.

Third, the duration of supra-solidus temperatures during D_2/M_2, but not necessarily peak metamorphic conditions, was long-lived (>80 Myr). This is supported by a spread in metamorphic age data, a range in crystallisation ages of syn-D_2 crustally-derived magmas, and their variable degrees of deformation (i.e. gneissic to undeformed).

Fourth, D_2 magmatism was voluminous and dominantly felsic. All regions except the Warumpi Province were intruded by high-KFe charnockitic magmas that have within-plate geochemistry (Table 3) and show isotopic evidence for a significant mantle contribution. The isotopic signature of D_2 magmas reflects the pre-existing geological architecture of the crust that they intrude, as well as new mantle input, with the most evolved D_2 magmas occurring in regions that are interpreted to be reworked cratonic margins (e.g. Biranup Zone, Bunger Hills). The ubiquitous nature of D_2 magmatism suggests that the thermal driver was also independent of pre-existing crustal character. A thermal mechanism for D_2/M_2 must also explain the spatial, age and isotope trends that are observed within parts of the MAFWO, where magmatism becomes increasingly juvenile with decreasing age and the locus of magmatism appears to migrate (e.g. Madura Province and west Musgrave Inlier). Yb-enrichment in progressively younger granites from the west Musgrave Inlier, combined with an increasingly juvenile isotope signature, suggests that the crust was thinning.

Finally, a geodynamic mechanism for D_2/M_2 must also account for observations of regional, inferred syn-D_2 craton-vergent folding, thrusting and shearing within the Albany–Fraser Orogen that suggests tectonic thickening. Interpretations of D_2/M_2 compression, based on structural geology, are at odds with interpretations of mid–lower crustal extension, which are based on *P–T* constraints and the character of D_2 magmatism.

9.3.1 A case for mantle lithosphere delamination in the MAFWO

Regional, long-lived, and anomalously-high thermal gradients at the orogen-scale, evidence for thin crust, and large-volume crustal melting with a significant mantle source contribution requires unusually high heat flow. These characteristics suggest that D_2/M_2 occurred in response to mantle lithosphere removal (e.g. Göğüş and Pysklywec, 2008b; Wang and Currie, 2015). Removal of the lithosphere induces upwelling of hot asthenospheric mantle, resulting in voluminous magmatism via decompression mantle melting coupled with partial melting by heat advection into the residual lithosphere/crust (Chung et al., 2003; Kay and Kay, 1993; Kay et al., 2011; Wang and Currie, 2015). Smithies et al., (2010) suggest that D_2 magmatism in the west Musgrave Inlier was sourced within a lower crustal hot zone/MASH (melting, assimilation, storage, homogenization) zone. Given lithological and geochemical similarities between D_2 magmas from all regions of the MAFWO, it is reasonable to assume that this interpretation is applicable orogen-wide. The development of deep crustal hot zones and MASH domains are intrinsically related to magma underplating and lithosphere removal, and specifically lithosphere delamination, and involve the hybridisation of locally-derived crustal melts with periodically replentished juvenile input

from asthenospheric mantle (Annen et al., 2006; Huppert and Sparks, 1988; Solano et al., 2012; Voshage et al., 1990). Progressively younger magmatism therefore records increasingly isotopically-juvenile compositions (Annen et al., 2006). D_2 magmas in the west Musgrave Inlier and Madura Province show increasingly juvenile isotopic signatures with decreasing age (Table 3), consistent with the above characteristics of lithosphere delamination. Compositional heterogeneity in the emplaced magmas (Smithies et al., 2010) could also be explained by varied degrees of mantle input and assimilation of existing crust within different parts of the MASH zone. Hot zones may also create a physical barrier to mantle magmatism reaching higher crustal levels (Annen et al., 2006), which may explain the apparent lack of exposed D_2 mafic magmatism within the MAFWO. In addition, delamination is typically characterised by a narrow (Bajolet et al., 2012; Göğüş and Pysklywec, 2008a) and asymmetric surface expression of magmatism (Wang and Currie, 2015) that widens and migrates with mantle lithosphere–crust decoupling (akin to subduction roll-back; e.g. Bajolet et al., 2012; Collins, 1994; Gorczyk et al., 2015; Krystopowicz and Currie, 2013; Wang and Currie, 2015). This process may explain the spatial–age trends in D_2 magmatism from parts of the MAFWO. Furthermore, charnockite and high-K felsic magmas are commonly interpreted as a magmatic expression of high-temperature, anhydrous, partial melting of mafic lower crust (Kilpatrick and Ellis, 1992) in association with lithosphere delamination (Farmer et al., 2002). Delamination has also been associated with low-pressure, high-temperature metamorphism and decompression (Collins, 1994; Göğüş and Pysklywec, 2008b; Loosveld and Etheridge, 1990), consistent with *P–T* constraints and down-pressure *P–T* paths from the MAFWO. Hot zones/MASH domains may remain hot for long timescales (Annen et al., 2006), explaining slow cooling interpreted for some parts of the MAFWO.

Both extension and shortening during lithosphere delamination appears to be a relatively common feature (Bajolet et al., 2012; Chapman et al., 2018; Göğüş and Pysklywec, 2008a; Wells and Hoisch, 2008). This may be due to decoupling of the crust and mantle lithosphere during delamination, facilitating upper crustal shortening (e.g. thrusting and folding) above a mid-crust decollement (e.g. Collins, 1994). Göğüş and Pysklywec, (2008a; b) also note that the surface expression of delamination may show distinct zones of contraction and thickening above the migrating delamination hinge, as well as extension and thinning away from the hinge, within the orogen core. Therefore, delamination may also account for interpretations from both *P–T*–t constraints and structural observations from the MAFWO that suggest synchronously extending mid–lower crust and contractional deformation in the upper–mid crust.

9.3.2 Pre-requisites for D_2/M_2 lithosphere removal

As outlined above, the key characteristics of D_2/M_2 can be explained by lithosphere removal, yet the specific mechanism is unclear. The mantle lithosphere (with or without the lower crust) may be removed via delamination (i.e. "peeling-off"; Bird, 1979), lithospheric "dripping" (i.e. Rayleigh-Taylor instability; Houseman et al., 1981), or convective erosion (Houseman and McKenzie, 1982; Morency et al., 2002). The first two mechanisms are top-down processes, driven by the gravitational instability of high-density lithosphere with respect to less dense, underlying asthenosphere. Top-down processes are typically triggered by external geological process such as convergence during subduction (e.g. Gray and Pysklywec, 2012) or the migration and localisation of strain (e.g. Jones et al., 2004). Shortening may lead to crustal thickening and eclogitisation of the lower crust, hence its negative buoyancy (Kay and Kay, 1993; Krystopowicz and Currie, 2013; Leech, 2001; Li et al., 2016; Sobolev and Babeyko, 2005). Lithosphere dripping may also initiate without dynamic weakening if there are existing rheological (density) instabilities in the lower crust that are gravitationally unstable with respect to the asthenosphere (Beall et al., 2017; Elkins-Tanton and Hager, 2000; Gorczyk et al., 2012; Morency et al., 2002).

In contrast, convective erosion of the lithosphere by the asthenosphere is a bottom-up process and may occur, for example, due to edge-driven convection at the interface of a transition in lithosphere thickness (e.g. Currie et al., 2008; Stern et al., 2013; Van Wijk et al., 2010). Alternatively, bottom-up processes may be driven by adiabatic upwelling of mantle asthenosphere that generates buoyant partial melts, and the ponding and crystallisation of these melts at the base of the

lithosphere, causing destabilisation and thus lithosphere removal (Levander et al., 2011).

Numerical modelling suggests that delamination may take up to ca. 40 Myr to initiate after crustal thickening but once commenced, the rate of lithosphere removal is generally rapid (<10 Myr) (Beall et al., 2017; Krystopowicz and Currie, 2013; Wang and Currie, 2015). In addition to more rapid onset, elevated temperatures will persist for longer during and after delamination than dripping (Göğüş and Pysklywec, 2008b). In contrast to delamination, dripping is a localised process, occurring at a small perturbation, and might therefore be evidenced by short-lived magmatic events and the spatially restricted and symmetric surface appearance of magmatism at the point of instability (Ducea, 2011; Gogus, 2017; Göğüş and Pysklywec, 2008b; Wang and Currie, 2015). Similarly, bottom-up convective removal appears to be a relatively small-scale process with a localised magmatic surface expression (e.g. Levander et al., 2011; Van Wijk et al., 2010). Lithosphere removal may occur continuously, or episodically (e.g. Gorczyk et al., 2015), and the mechanism may switch (Beall et al., 2017). For example, if delamination is too slow to outpace cooling of the upwelling asthenosphere then delamination may stall and revert to dripping (Beall et al., 2017). In contrast, Chapman et al. (2018) propose a model for the Central Pamir Terrane involving lithosphere dripping as a precursor to delamination, induced by the collision between India and Asia.

Many features of D_2/M_2 appear consistent with lithosphere delamination (as opposed to dripping or convective erosion), however, there is limited evidence for significant crustal thickening in the MAFWO, making it difficult to argue for delamination as a result of eclogitisation of the lower crust and mantle lithosphere. The timing of final convergence between the WAC and SAC is ambiguous but is considered to have occurred between D_1/M_1 and D_2/M_2. This interpretation is based on the accretionary and extensional character of D_1/M_1 rather than continental collision, a lack of evidence for ongoing subduction or back-arc extension (e.g. Morrissey et al., 2017b; Spaggiari et al., 2015) such as the within-plate, rather than arc-related, chemistry of D_2 magmas (e.g. Fig. 3; Smithies et al., 2015b). Post-D_1/M_1 (ca. 1260 Ma) exhumation of the Fraser Zone to mid-crustal depths (Section 6) and upright folding in the Windmill Islands recorded in ca. 1250–1215 Ma (pre-D_2) granites, but not D_2 (<1200 Ma) charnockite (Section 5.3) may record shortening related to WAC–SAC convergence. Howard et al. (2011) also observe NW–SE folding post D_1 gneissic fabric development but prior to D_2 magmatism in the west Musgrave Inlier. Poorly age-constrained thrusting and folding within the Albany–Fraser Orogen also suggests a period of compression, although the relationship between compressional deformation and peak M_2 metamorphism is unclear, and it is possible that these are re-activated structures (e.g. Sippl et al., 2017; Spaggiari et al., 2015). The WAC and SAC are separated by a vast tract of poorly exposed juvenile crust, meaning that the nature and timing of collision or docking of the WAC and SAC remains speculative. However, in a delamination model, shortening between D_1 and D_2 at ca. 1260–1240 Ma would be consistent with a ca. 40 Myr time lag between crustal thickening and delamination. The timing of convergence of the Musgrave Inlier and Warumpi Province with the NAC is also uncertain. In general, D_2/M_2 in the Musgrave Inlier is considered intracratonic (Gorczyk et al., 2015; Smithies et al., 2011; Wade et al., 2008), implying that craton convergence also occurred prior to D_2. However, more recent interpretations from the Warumpi Province suggest reattachment of the combined Warumpi–Musgrave with the NAC occurred at ca. 1130–1080 Ma (Wong et al., 2015), which is late–post D_2/M_2.

In essence, if lithosphere removal was the thermal driver for D_2/M_2, the trigger is not overtly clear. Mantle lithosphere delamination (peeling-off) explains many D_2/M_2 features, however, the amount of thickening in the MAFWO to promote delamination is unknown. Without clear evidence for significant crustal thickening, regional scale delamination (i.e. top-down processes) driven by gravitational instability cannot be confidenty evoked. Nonetheless, Fig. 8 presents a series of schematics for the D_2/M_2 evolution of the MAFWO that are extrapolated from D_1/M_1 tectonic models and interpretations (Models A to C; Section 9.2). An additional model (Model D) is presented for the west MAFWO that does not observe D_1/M_1. The tectonic models in Fig. 8 hypothesise the effects of crustal shortening on delamination due to craton convergence between D_1 and D_2. However, lithosphere erosion via asthenospheric upwelling (bottom-up process) is also a possible mechanism.

Regardless of the mechanism, the metamorphic and magmatic expression of lithosphere removal illustrated in the presented models does not significantly change.

9.3.3 Spatial controls on delamination

As an extension on the concept of lithosphere delamination, Gorczyk et al. (2015) propose that the seemingly more thermally extreme D_2/M_2 conditions in the Musgrave Inlier (e.g. peak UHT conditions, higher magma crystallisation temperatures, high-volume magmatism) can be explained by specifically considering this region as an ultra-hot orogen (UHO; Fig. 8). Gorczyk et al. (2015) and Smithies et al. (2011) suggest that the tectonic position of the Musgrave Inlier at this time, assumed locked between the NAC, SAC and WAC (but see Wong et al., (2015)), played a vital role in maintaining high thermal gradients and providing a foci for upwelling asthenosphere (e.g. Begg et al., 2009). As a result, mantle lithosphere delamination is proposed to have occurred over a much longer timeframe (>50 Myr) than would be the case if it were not spatially confined (e.g. Li et al., 2016). A period of short-lived compression is suggested to have initiated lithosphere delamination. The pre-D_2/M_2 crust is interpreted to have been thin, rheologically weak and hot and therefore the crustal response to shortening was removal of the mantle lithosphere via sagduction or gravitational dripping, rather than increased crustal thickness and topography (Gorczyk et al., 2015). With increasing delamination, the UHO spread laterally and self-propagated (on the order of 100 km/Myr; Gorczyk et al., 2015; Perchuk et al., 2016). Phases of short-lived compression after delamination commenced may have reinitiated further delamination (Gorczyk et al., 2015; Gorczyk and Vogt, 2015). Perchuk et al. (2016) identify that the development of an UHO (i.e. crustal thinning and delamination), rather than continental collision (i.e. crustal thickening), is strongly dependent on the converging crust being thin, warm and slowly converging. The wide region of juvenile crust that is inferred to presently separate the SAC from the WAC and NAC (e.g. Kirkland et al., 2017) supports the first criteria, but constraints on the rate of convergence are unknown. Further, although the model of Gorczyk et al. (2015) and Model C in Fig. 8 explore the thermal consequences of D_2/M_2 with hot and thin crust, a clear explanation is not provided for how hot and thin crustal conditions were already initiated prior to D_2/M_2. A back-arc setting has been tentatively suggested for the west Musgrave Inlier prior to D_2/M_2 (Evins et al., 2012; Gorczyk et al., 2015; Smithies et al., 2011), but this does not provide justification for D_2/M_2 then occurring in other regions of the Musgrave Inlier. In essence, it is unclear why the crust was able to retain elevated thermal conditions into D_2/M_2 to allow the Musgrave Inlier to remain more reactive to reworking that the bounding cratons, so that delamination could occur.

9.3.4 Bottom-up processes at the supercontinent scale

The Giles Event (ca. 1080–1040 Ma) occurred post-D_2/M_2 in central Australia, involved voluminous mafic magmatism, and is suggested to be a continuum of the D_2/M_2 evolution of the west Musgrave Inlier (Smithies et al., 2015a). Tectonic interpretations on the Giles Event may provide further clarity on the D_2/M_2 MAFWO evolution.

Smithies et al. (2010) postulate that D_2/M_2 in the Musgrave Inlier may have been associated with a mantle superswell given its position at the triple point of the converging cratons, analogous to failed supercontinent breakup, but at a time when the cratons were converging, not dismantling. Recent interpretations propose that the Giles Event specifically represents the magmatic expression of a failed rift system (Evins et al., 2010; Smithies et al., 2015a), which aligns with the earlier interpretations of Smithies et al. (2010). Theoretically, mantle superswells could be considered as a continental scale expansion on the bottom-up mechanisms (discussed above) for lithosphere removal as they involve the passive upwelling of asthenosphere mantle (Davaille, 1999; McNutt, 1998). Convective upwelling, expansion and decompression melting of the mantle is largely considered to result from a stagnant-lid regime where supercontinents thermally insulate the underlying mantle (Hoffman, 1989; Sears et al., 2005). Associated magmatism is anorogenic and occurs at a triple-point (Sears et al., 2005), as is the case for the MAFWO.

As discussed previously, the primary limitation with invoking a top-down delamination mechanism for the MAFWO is a lack of convincing evidence for significant crustal thickening prior to D_2/M_2 and therefore uncertainty surrounding the trigger to initiate lithosphere instability. Therefore,

a mantle superswell hypothesis presents an interesting alternative to a top-down mechanism for lithosphere removal, although it is unclear whether such a process could apply to the entire orogen.

Van Kranendonk and Kirkland (2013) propose that the rate of continental drift between ca. 1200–1100 Ma, immediately prior to final Rodinia assembly, was an order of magnitude larger than any time in Earth history due to a hotter and more rapidly convecting mantle, and potentially greater slab-pull of oceanic crust. This supposition implies that there was increased potential for bottom-up mechanisms of lithosphere removal at this time. Therefore, processes similar to those responsible for present-day rifting in the East African rift (Corti, 2009), or Laurentia or Gondwana breakup (Hoffman, 1989; Sears et al., 2005), cannot be dismissed as a possible broader-scale thermal driver for D_2/M_2. Van Kranendonk and Kirkland (2013) also identify that the Grenville Orogen (ca. 1300–1100 Ma) in North America records evidence for the significant addition of juvenile crust in arc and back-arc settings marginal to the converging cratons, prior to large-scale back-arc inversion and crustal collision (marking Grenville orogenesis itself). Although the scale of the MAFWO is significantly less than the Grenville Orogen, these two regions share similar characteristics of juvenile crust formation, potentially in a back-arc setting, prior to the main phase of orogenesis.

9.3.5 Other factors in the attainment of high-temperatures in D_2/M_2

Although conductive heating from the mantle was almost certainly the dominant thermal driver for D_2/M_2, preconditioning of the crust and crustal heat production may have also played a role in the attainment of high temperatures. Partial melting is an endothermic process that consumes heat and buffers temperature increase (Brown and Korhonen, 2009; Stüwe, 1995; Vielzeuf et al., 1990). Partial melting and melt loss also makes the crust less fertile to subsequent melt generation without significant increases in temperature or the addition of fluids. Modelling by Clark et al. (2011) shows that UHT conditions are attained more readily if rocks are dehydrated in a previous metamorphic event. The high metamorphic temperatures attained during D_2/M_2 may reflect, in part, that each of the regions of the MAFWO had experienced prior metamorphism, either during D_1/M_1 (central MAFWO terranes) or during the Paleoproterozoic (west and east MAFWO terranes; Fig. 2). The prolongued metamorphic evolution during D_2/M_2 in some parts of the MAFWO would have also facilitated the attainment of high temperatures by dehydration during prograde partial melting (e.g. Brown and Korhonen, 2009). Crustal preconditioning also means that juvenile mantle input was required to refertilise the crust for the generation of voluminous felsic magmatism during D_2/M_2 (Smithies et al., 2010).

The MAFWO does not preserve evidence for substantial thickening nor tectonic stability at the required scale for radiogenic heat production to facilitate regional long-lived high-temperatures (e.g. Clark et al., 2011, 2015), but the possible contribution of radiogenic heating to the heat source should still be appraised. Figure 9 shows heat production values in the Australian tectonic components of the MAFWO back-calculated to ca. 1150 Ma. It is evident that heat production from parts of the MAFWO significantly exceeds typical global heat production values (0.1–3 Wm-3; Vilà et al., 2010). The majority of data presented in Fig. 9 come from syn-D_2 magmatic rocks as they comprise the bulk of exposed rocks in the MAFWO. However, given that the volume of felsic magmatism at the surface exposure is up to 80 % (west Musgrave Inlier; (Smithies et al., 2010), the heat producing element (HPE) content of the D_2 magmas may be a reflection of the HPE budget of majority of the pre-existing crust from which they were sourced. High HPE crust may therefore have contributed in part to the attainment of high temperatures during D_2/M_2, and slow cooling at mid–lower crustal depths post-D_2/M_2.

10. CONCLUDING REMARKS

The MAFWO is a high-grade metamorphic belt that extends over 2000 km, separating the WAC, NAC and SAC, and continuing into East Antarctica. MAFWO tectonism occurred during the Mesoproterozoic (ca. 1345–1130 Ma) and was related to convergence of the Australian and East Antarctic cratons. Within this period, the MAFWO records evidence for a two-stage magmatic and metamorphic history with D_1/M_1 occurring at ca. 1345–1260 Ma and D_2/M_2 occurring at ca. 1220–1130 Ma. The defining feature of the MAFWO is the D_2/M_2 evolution that was characterised by prolongued duration of high–ultrahigh thermal gradient conditions,

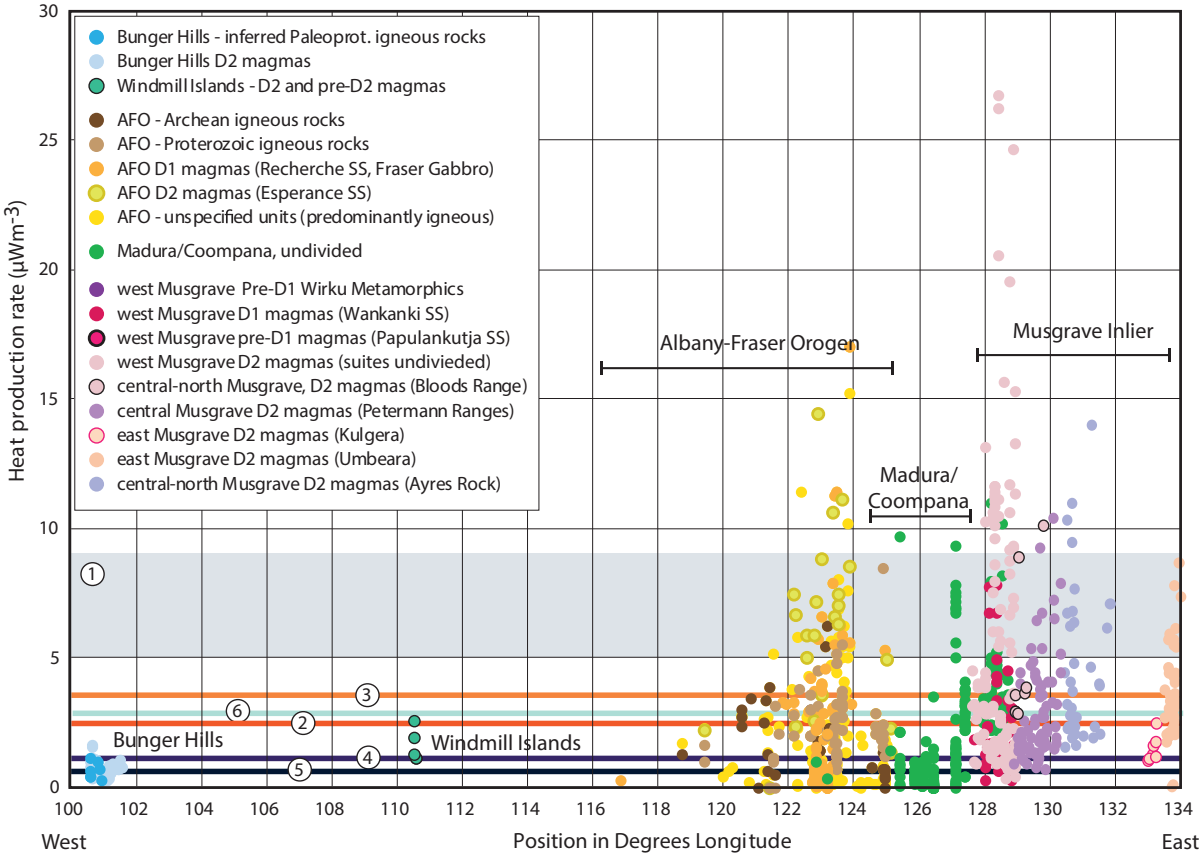

Figure 9. MAFWO crustal heat production from Archean–Mesoproterozoic rocks, back-calculated to 1150 Ma. Data are from predominantly D_1 and D_2 felsic–intermediate igneous rocks that dominate the MAFWO outcrop. Geochemical data cover the majority of the exposed MAFWO geographical extent and are sourced from the publically-available Geological Survey of Western Australia online geochemical database (WACHEM), with additional data (Edgoose et al., 2004; Sheraton et al., 1992; Sheraton et al., 1995; Smithies et al., 2010b; Smithies et al., 2015b; Sun et al., 1995; Zhang et al., 2012, and unpublished data from N. Tucker). Data points are positioned according to longitude. For comparison, heat production values are shown for the Grenville Orogen (Mareschal and Jaupart, 2013) and the South Austraian Heat Flow Anomaly (Neumann et al., 2000). Median heat production values for Australian granites (ca. 1300–900 Ma), and global Archean, Proterozoic (Rodinian) and Phanerozoic granites are also shown and come from an updated version (manuscript in preparation) of datasets presented in Hasterok et al. (2017) and Hasterok and Webb (2017).

evidence for voluminous mantle and crustal melting, metamorphic *P–T* paths that evolved on shallowly decompressive to quasi-isobaric post-peak evolutions, and limited evidence for crustal thickening. These characteristics challenge a simple view of continental amalgamation.

This review provides a compilation of magmatic and metamorphic data from across the MAFWO. It seeks to provide clarity on the spatial, temporal and thermal character of Mesoproterozoic orogenesis, and the likely thermal drivers for regional, long-lived, high thermal gradient conditions. Several conclusions can be drawn:

1. The thermal character of the MAFWO reflects mantle-driven heating, not crustal-heating, as the overall geodynamic driver;

2. D_1/M_1 was spatially confined, characterised by isotopically-juvenile bimodal mafic and calc-alkaline felsic magmatism, involved variably high-temperature metamorphism, the development of horizontal fabrics, and was associated with basin formation;

3. The pre-D_1/M_1 geological architecture (arc accretion) significantly influenced the crustal expression of metamorphism and magmatism during D_1/M_1;

4. D_1/M_1 exhibits characteristics consistent with an extensional accretionary orogen, although the specific mechanism for extension and the timing of extension relative to arc accretion is unclear. Delamination followed by orogenic collapse, and back-arc extension, are two viable alternatives for D_1/M_1. The majority of D_1 magmatic features are explained by the former, and metamorphic features by the latter;

5. The isotopic composition of the D_2 magmas is a reflection of the pre-existing crust that they intrude;

6. D_2/M_2 was long-lived, regionally pervasive, and was characterised by consistently high thermal gradients (~150 kbar/°C) and post-peak M_2 isobaric to down-pressure *P–T* paths. D_2/M_2 involved the emplacement of voluminous, high-temperature, near-exclusively felsic–charnockitic magmatism, and these magmas also reflect a significant **mantle source contribution;**

7. D_2/M_2 appears to qualify for a model of mantle lithosphere and lower crustal removal although the specific mechanism (i.e. top-down versus bottom-up processes) is not overtly clear. That said, D_2/M_2 can be explained by a number of characteristics of mantle lithosphere delamination (coherent "peeling off");

8. The geodynamic trigger for D_2/M_2 lithosphere removal is presently ambiguous, but is inferred related to tectonism between D_1/M_1 and D_2/M_1. This period is interpreted to reflect final craton amalgamation with the MAFWO as all regions are unitied in their D_2/M_2 evolution. The anatomy of convergence is therefore central to the unusual thermal character of D_2/M_2. However, the precise timing and nature of events are unclear, largely due to reservations about the position of the SAC and NAC relative to the WAC at this time. This uncertainty leads to ambiguity in the thermal mechanism for D_2/M_2.

9. Historically, tectonic components of the MAFWO are interpreted to record a two-stage evolution for the amalgamation of the Australian and East Antarctic cratons. It is important to distinguish that D_2/M_2 is the event that links these three cratons. Therefore the MAFWO may be better considered as a single-stage event (ca. 1220–1130 Ma), excluding D_1/M_1 from its definition.

This review presents some critical observations of the metamorphic and magmatic character of the MAFWO and a number of plausible tectonic scenarios for its Mesoproterozoic evolution are appraised. However, at this stage, there is not enough data of the right kind in the right places to come to definitive conclusions about the geodynamic driver for thermally extreme conditions within the MAFWO.

ACKNOWLEDGEMENTS

The Geological Survey of Western Australia (H. Smithies) is acknowledged for providing some Sm–Nd analyses for the regional comparison (reproduced in figures and tables with permission). NMT acknowledges the support of a Australian Government Research Training Program Scholarship.

REFERENCES

Adams M. 2012. Structural and geochronological evolution of the Malcolm Gneiss, Nornalup Zone, Albany–Fraser Orogen, Western Australia: Geological Survey of Western Australia, Record 2012/4, 132p.

Aitken A. R. A. & Betts P. G. 2008. High-resolution aeromagnetic data over central Australia assist Grenville-era (1300–1100 Ma) Rodinia reconstructions. Geophysical Research Letters 35, L01306.

Aitken A. R. A. & Betts P. G. 2009. Constraints on the Proterozoic supercontinent cycle from the structural evolution of the south-central Musgrave Province, central Australia. *Precambrian Research* 168, 284–300.

Aitken A. R. A., Betts P. G., Young D. A., Blankenship D. D., Roberts J. L. & Siegert M. J. 2016. The Australo–Antarctic Columbia to Gondwana transition. *Gondwana Research* 29, 136–152.

Aitken A. R. A., Young D. A., Ferraccioli F., Betts P. G., Greenbaum J. S., Richter T. G., Roberts J. L., Blankenship D. D. & Siegert M. J. 2014. The subglacial geology of Wilkes Land, East Antarctica. *Geophysical Research Letters* 41, 2014GL059405.

Annen C., Blundy J. & Sparks R. 2006. The genesis of intermediate and silicic magmas in deep crustal hot zones. *Journal of Petrology* 47, 505–539.

Bajolet F., Galeano J., Funiciello F., Moroni M., Negredo A. & Faccenna C. 2012. Continental delamination: insights from laboratory models. *Geochemistry, Geophysics, Geosystems* 13, 22p.

Barker P. F. & Hill I. A. 1980. Asymmetric spreading in back-arc basins. *Nature* 285, 652.

Barquero-Molina M. 2009. Kinematics of bidirectional extension and coeval NW-directed contraction in orthogneisses of the Biranup Complex, Albany–Fraser Orogen, southwestern Australia. PhD thesis. The University of Texas, Austin.

Bea F. 2012. The sources of energy for crustal melting and the geochemistry of heat-producing elements. *Lithos* 153,

278–291.

Beall A. P., Moresi L. & Stern T. 2017. Dripping or delamination? A range of mechanisms for removing the lower crust or lithosphere. *Geophysical Journal International* 210, 671–692.

Beaumont C., Jamieson R. & Nguyen M. 2010. Models of large, hot orogens containing a collage of reworked and accreted terranes This article is one of a series of papers published in this Special Issue on the theme Lithoprobe—parameters, processes, and the evolution of a continent. *Canadian Journal of Earth Sciences* 47, 485–515.

Beaumont C., Nguyen M., Jamieson R. A. & Ellis S. 2006. Crustal flow modes in large hot orogens. *Geological Society, London, Special Publications* 268, 91–145.

Beeson J., Delor C. P. & Harris L. B. 1988. A structural and metamorphic traverse across the Albany Mobile Belt, Western Australia. *Precambrian Research* 40, 117–136.

Begg G. C., Griffin W. L., Natapov L. M., Suzanne Y., O'reilly S. Y., Grand S. P., O'neill C. J., Hronsky J. M. A., Poudjom Djomani Y., Swain C. J., Deen T. & Bowden P. 2009. The lithospheric architecture of Africa: seismic tomography, mantle petrology, and tectonic evolution. *Geosphere* 5.

Betts P. G. & Giles D. 2006. The 1800–1100 Ma tectonic evolution of Australia. *Precambrian Research* 144, 92–125.

Betts P. G., Giles D. & Aitken A. 2011. Palaeoproterozoic accretion processes of Australia and comparisons with Laurentia. *International Geology Review* 53, 1357–1376.

Bird P. 1979. Continental delamination and the Colorado Plateau. *Journal of Geophysical Research: Solid Earth* 84.

Black L. P. & Shaw R. D. 1995. An assessment, based on U–Pb zircon data, of Rb–Sr dating in the Arunta Inlier, central Australia. *Precambrian Research* 71, 3–15.

Blight D. & Oliver R. 1977. The metamorphic geology of the Windmill Islands, Antarctica: a preliminary account. *Journal of the Geological Society of Australia* 24, 239–262.

Bodorkos S. & Clark D. J. 2004a. Evolution of a crustal-scale transpressive shear zone in the Albany–Fraser Orogen, SW Australia: 1. *P–T* conditions of Mesoproterozoic metamorphism in the Coramup Gneiss. *Journal of Metamorphic Geology* 22, 691–711.

Bodorkos S. & Clark D. J. 2004b. Evolution of a crustal-scale transpressive shear zone in the Albany–Fraser Orogen, SW Australia: 2. Tectonic history of the Coramup Gneiss and a kinematic framework for Mesoproterozoic collision of the West Australian and Mawson cratons. *Journal of Metamorphic Geology* 22, 713–731.

Brown M. & Korhonen F. J. 2009. Some remarks on melting and extreme metamorphism of crustal rocks. *In: Gupta A. K. & Dasgupta S. eds. Physics and Chemistry of the Earth's Interior,* pp. 67–87, Springer, New York.

Camacho A. & Fanning C. M. 1995. Some isotopic constraints on the evolution of the granulite and upper amphibolite facies terranes in the eastern Musgrave Block, central Australia. *Precambrian Research* 71, 155–181.

Chamberlain C. P. & Sonder L. J. 1990. Heat-producing elements and the thermal and baric patterns of metamorphic belts. *Science* 250, 763–769.

Champion D. 2013. Neodymium depleted mantle model age map of Australia: explanatory notes and user guide. Geoscience Australia, Canberra.

Chapman J. B., Scoggin S. H., Kapp P., Carrapa B., Ducea M. N., Worthington J., Oimahmadov I. & Gadoev M. 2018. Mesozoic to Cenozoic magmatic history of the Pamir. *Earth and Planetary Science Letters* 482, 181–192.

Chardon D., Gapais D. & Cagnard F. 2009. Flow of ultra-hot orogens: a view from the Precambrian, clues for the Phanerozoic. *Tectonophysics* 477, 105–118.

Chung S. L., Liu D., Jianqing J., Chu M.-F., H.-Y. L., Wen D.-J. & Lo C.-H. 2003. Adakites from continental collision zones: melting of thickened lower crust beneath southern Tibet. *Geology* 31, 1021–1024.

Clark C., Fitzsimons I. C. W., Healy D. & Harley S. L. 2011. How does the continental crust get really hot? *Elements* 7, 235–240.

Clark C., Healy D., Johnson T., Collins A. S., Taylor R. J., Santosh M. & Timms N. E. 2015. Hot orogens and supercontinent amalgamation: A Gondwanan example from southern India. *Gondwana Research* 28, 1310–1328.

Clark C., Kirkland C. L., Spaggiari C. V., Oorschot C., Wingate M. T. D. & Taylor R. J. 2014. Proterozoic granulite formation driven by mafic magmatism: An example from the Fraser Range Metamorphics, Western Australia. *Precambrian Research* 240, 1–21.

Clark D. J., Hensen B. J. & Kinny P. D. 2000. Geochronological constraints for a two-stage history of the Albany–Fraser Orogen, Western Australia. *Precambrian Research* 102, 155–183.

Clark D. J., Kinny P. D., Post N. J. & Hensen B. J. 1999. Relationships between magmatism, metamorphism and deformation in the Fraser Complex, Western Australia: Constraints from new SHRIMP U–Pb zircon geochronology. *Australian Journal of Earth Sciences* 46, 923–932.

Clarke G. L. & Powell R. 1991. Decompressional coronas and symplectites in granulites of the Musgrave Complex, central Australia. *Journal of Metamorphic Geology* 9, 441–450.

Collins W. J. 1994. Upper and middle crustal response to delamination: An example from the Lachlan fold belt, eastern Australia. *Geology* 22, 143–146.

Collins W. J. 2002. Hot orogens, tectonic switching, and creation of continental crust. *Geology* 30, 535–538.

Collins W. J. & Richards S. W. 2008. Geodynamic significance of S-type granites in circum-Pacific orogens. *Geology* 36, 559–562.

Collins W. J. & Shaw R. D. 1995. Geochronological constraints on orogenic events in the Arunta Inlier: a review. *Precambrian Research* 71, 315–346.

Corti G. 2009. Continental rift evolution: from rift initiation to incipient break-up in the Main Ethiopian Rift, East Africa. *Earth Science Reviews* 96, 1–53.

Currie C. A., Huismans R. S. & Beaumont C. 2008. Thinning of continental backarc lithosphere by flow-induced gravitational instability. *Earth and Planetary Science Letters* 269, 436–447.

Currie C. A. & Hyndman R. D. 2006. The thermal structure of subduction zone back arcs. *Journal of Geophysical Research: Solid Earth* 111, B08404.

Davaille A. 1999. Simultaneous generation of hotspots and superswells by convection in a heterogeneous planetary mantle. *Nature* 402, 756.

Davey F. J., Henrys S. A. & Lodolo E. 1995. Asymmetric rifting in continental back-arc environment, North Island, New Zealand. *Journal of Volcanology and Geothermal Research* 68.

Dawson G. C., Krapež B., Fletcher I. R., Mcnaughton N. J. & Rasmussen B. 2003. 1.2 Ga thermal metamorphism in the

Albany–Fraser Orogen of Western Australia: consequence of collision or regional heating by dyke swarms? *Journal of the Geological Society* 160, 29–37.

Douce A. E. P. & Mccarthy T. C. 1998. Melting of crustal rocks during continental collision and subduction. *In: Hacker B. R. & Liou J. G. eds. Geodynamics and Geochemistry of Ultrahigh-Pressure rocks. Petrology and Structural Geology,* pp. 27–55, Springer, Dordrecht.

Drüppel K., Elsäßer L., Brandt S. & Gerdes A. 2013. Sveconorwegian Mid-crustal Ultrahigh-temperature Metamorphism in Rogaland, Norway: U–Pb LA–ICP–MS Geochronology and Pseudosections of Sapphirine Granulites and Associated Paragneisses. *Journal of Petrology* 54, 305–350.

Ducea M. N. 2011. Fingerprinting orogenic delamination. *Geology* 39, 191–192.

Duebendorfer E. M. 2002. Regional correlation of Mesoproterozoic structures and deformational events in the Albany–Fraser orogen, Western Australia. *Precambrian Research* 116, 129–154.

Dutch R. A., Doublier M. P., Pawley M. J., Wise T. W., Reid A. J., Clark D., Kennett B. L. N., Fraser G., Thiel S. & Van Der Wielen S. 2015a. Geological and geodynamic implications of the western Gawler Craton section of seismic line 13GA-EG1. *In: Dutch, R. A., Pawley, M. J. and Wise, T. W., (eds.) What lies beneath the western Gawler Craton? 13-GA-EG1E Seismic and Magnetotelluric Workshop 2015, Report Book 2015/00029.* Department of State Development, South Australia, Adelaide.

Dutch R. A., Pawley M. J. & Wise T. W. 2015b. What lies beneath the western Gawler Craton? 13GA-EG1E Seismic and Magnetotelluric Workshop 2015, Report Book 2015/00029. Department of State Development, South Australia, Adelaide.

Dutch R. A., Pawley M. J., Wise T. W., Tylkowski L., Lockheed A., Mcalpine S. R. B. & Heath P. 2017. PACE Copper Coompana Drilling Project: Drillhole CDP001 preliminary field-data report, Report Book 2017/00022. Department of the Premier and Cabinet, South Australia, Adelaide.

Dutch R. A., Payne J. L. & Woodhouse A. 2013a. Sm–Nd and Hf isotopic data of the Tieyon (5645) 1:100 000 mapsheet, Report Book 2013/00010. Department for Manufacturing, Innovation, Trade, Resources and Energy, South Australia, Adelaide.

Dutch R. A., Werner M. X., Krapf C. B. E. & Rusak T. 2013b. Geology of the Tieyon 1:100 000 map sheet (5645), Report Book 2013/00011. Geological Survey of South Australia. Department for Mamufacturing, Innovation, Trade, Resources and Energy, South Australia, Adelaide.

Edgoose C. J., Scrimgeour I. R. & Close D. F. 2004. Geology of the Musgrave Block, Northern Territory. Northern Territory Geological Survey, Report 15.

Elkins-Tanton L. T. & Hager B. H. 2000. Melt intrusion as a trigger for lithospheric foundering and the eruption of the Siberian flood basalts. *Geophysical Research Letters* 27.

England P. C. & Thompson A. B. 1984. Pressure—Temperature—Time Paths of Regional Metamorphism I. Heat Transfer during the Evolution of Regions of Thickened Continental Crust. *Journal of Petrology* 25, 894–928.

Evins P., Kirkland C. L., Wingate M. T. D., Smithies R. H., Howard H. M. & Bodorkos S. 2012. Provenance of the 1340–1270 Ma Ramarama Basin in the west Musgrave Province, central Australia. Geological Survey of Western Australia, Report 116.

Evins P. M., Smithies R. H., Howard H. M., Kirkland C. L., Wingate M. T. D. & Bodorkos S. 2010. Devil in the detail; The 1150–1000 Ma magmatic and structural evolution of the Ngaanyatjarra Rift, west Musgrave Province, Central Australia. *Precambrian Research* 183, 572–588.

Faccenda M., Gerya T. V. & Chakraborty S. 2008. Styles of post-subduction collisional orogeny: influence of convergence velocity, crustal rheology and radiogenic heat production. *Lithos* 103, 257–287.

Faccenna C., Mattei M., Funiciello F. & Jolivet L. 1997. Styles of back-arc extension in the Central Mediterranean. *Terra Nova* 9, 126–130.

Farmer G. L., Glazner A. F. & Manley C. R. 2002. Did lithospheric delamination trigger late Cenozoic potassic volcanism in the southern Sierra Nevada, California? *Geological Society of America Bulletin* 114, 754–768.

Fitzsimons I. 2003. Proterozoic basement provinces of southern and southwestern Australia, and their correlation with Antarctica. *Journal of the Geological Society, London* 206, 93–130.

Fletcher I., Wilde S., Libby W. & Rosman K. 1983. Sm-Nd model ages across the margins of the Archaean Yilgarn Block, Western Australia—II; southwest transect into the Proterozoic Albany-Fraser Province. *Journal of the Geological Society of Australia* 30, 333–340.

Fletcher I. R., Myers J. S. & Ahmat A. I. 1991. Isotopic evidence on the age and origin of the Fraser Complex Western Australia – a sample of Midproterozoic Lower Crust. *Chemical Geology* 87, 197–216.

Gibbons A., Zahirovic S., Müller R., Whittaker J. & Yatheesh V. 2015. A tectonic model reconciling evidence for the collisions between India, Eurasia and intra-oceanic arcs of the central-eastern Tethys. *Gondwana Research* 28, 451–492.

Glikson A. Y., Stewart A. J., Ballhaus C. G., Clarke G. L., Feeken E. H. J., Leven J. H., Sheraton J. W. & Sun S. S. 1996. Geology of the western Musgrave Block, central Australia, with particular reference to the mafic–ultramafic Giles Complex. *Australian Geological Survey Organisation, Bulletin* 239.

Gogus O. H. 2017. Drip tectonics and the enigmatic uplift of the Central Anatolian Plateau. *Nature Communications* 8, 1538.

Göğüş O. H. 2015. Rifting and subsidence following lithospheric removal in continental back arcs. *Geology* 43, 3–6.

Göğüş O. H. & Pysklywec R. N. 2008a. Mantle lithosphere delamination driving plateau uplift and synconvergent extension in eastern Anatolia. *Geology* 36, 723–726.

Göğüş O. H. & Pysklywec R. N. 2008b. Near-surface diagnostics of dripping or delaminating lithosphere. *Journal of Geophysical Research: Solid Earth* 113.

Gorczyk W., Hobbs B. & Gerya T. 2012. Initiation of Rayleigh-Taylor instabilities in intra-cratonic settings. *Tectonophysics* 514–517, 146–155.

Gorczyk W., Smithies H., Korhonen F., Howard H. & Quentin De Gromard R. 2015. Ultra-hot Mesoproterozoic evolution of intracontinental central Australia. *Geoscience Frontiers* 6, 23–37.

Gorczyk W. & Vogt K. 2015. Tectonics and melting in intra-continental settings. *Gondwana Research* 27.

Gray C. M. 1978. Geochronology of granulite-facies gneisses in the western Musgrave Block, central Australia. *Journal of the Geological Society of Australia* 25, 403–414.

Gray R. & Pysklywec R. N. 2012. Geodynamic models of mature continental collision: evolution of an orogen

from lithospheric subduction to continental retreat/ delamination. *Journal of Geophysical Research: Solid Earth* 117, B03408, 14p.

Harley S. L. 2016. A matter of time: The importance of the duration of UHT metamorphism. *Journal of Mineralogical and Petrological Sciences* 111, 50–72.

Hasterok D., Gard M. & Webb J. 2017. On the radiogenic heat production of metamorphic, igneous, and sedimentary rocks. *Geoscience Frontiers*, in press, doi: 10.1016/j.gsf.2017.10.012.

Hasterok D. & Webb J. 2017. On the radiogenic heat production of igneous rocks. *Geoscience Frontiers* 8, 919–940.

Hoffman P. F. 1989. Speculations on Laurentia's first gigayear (2.0 to 1.0 Ga). *Geology* 17, 135–138.

Houseman G. & Mckenzie D. P. 1982. Numerical experiments on the onset of convective instability in the Earth's mantle. *Geophysical Journal International* 68.

Houseman G. A., Mckenzie D. P. & Molnar P. 1981. Convective instability of a thickened boundary layer and its relevance for the thermal evolution of continental convergent belts. *Journal of Geophysical Research: Solid Earth* 86.

Howard H., Werner M., Smithies R. H., Kirkland C. L., Kelsey D., Hand M., Collins A., Pirajno F., Wingate M. T. D., Maier W. D. & Raimondo T. 2011. The geology of the west Musgrave Province and the Bentley Supergroup - a field guide. Geological Survey of Western Australia Record 2011/4, p. 119.

Howard H. M., Smithies R. H., Kirkland C. L., Kelsey D. E., Aitken A., Wingate M. T. D., Quentin De Gromard R., Spaggiari C. V. & Maier W. D. 2015. The burning heart — The Proterozoic geology and geological evolution of the west Musgrave Region, central Australia. *Gondwana Research* 27, 64–94.

Huerta A. D., Royden L. H. & Hodges K. V. 1998. The thermal structure of collisional orogens as a response to accretion, erosion, and radiogenic heating. *Journal of Geophysical Research: Solid Earth* 103, 15287–15302.

Huppert H. E. & Sparks R. 1988. The generation of granitic magmas by intrusion of basalt into continental crust. *Journal of Petrology* 29, 599–624.

Husson L. 2006. Dynamic topography above retreating subduction zones. *Geology* 34.

Hyndman R. D., Currie C. A. & Mazzotti S. P. 2005. Subduction zone backarcs, mobile belts, and orogenic heat. *GSA Today* 15, 4–10.

Jamieson R. A. & Beaumont C. 2013. On the origin of orogens. *Geological Society of America Bulletin* 125, 1671–1702.

Jamieson R. A., Beaumont C., Nguyen M. H. & Lee B. 2002. Interaction of metamorphism, deformation and exhumation in large convergent orogens. *Journal of Metamorphic Geology* 20, 9–24.

Jones C. H., Farmer G. L. & Unruh J. 2004. Tectonics of Pliocene removal of lithosphere of the Sierra Nevada, California. *GSA Bulletin* 116, 1408–1422.

Kay R. W. & Kay M. 1993. Delamination and delamination magmatism. *Tectonophysics* 219, 177–189.

Kay S. M., Coira B., Worner G., Kay R. W. & Singer B. S. 2011. Geochemical, isotopic and single crystal 40Ar/39Ar age constraints on the evolution of the Cerro Galan ignimbrites. *Bulletin of Volcanology* 73, 1487–1511.

Kelsey D. E., Clark C. & Hand M. 2008. Thermobarometric modelling of zircon and monazite growth in melt-bearing systems: examples using model metapelitic and metapsammitic granulites. *Journal of Metamorphic Geology* 26, 199–212.

Kelsey D. E. & Hand M. 2015. On ultrahigh temperature crustal metamorphism: Phase equilibria, trace element thermometry, bulk composition, heat sources, timescales and tectonic settings. *Geoscience Frontiers* 6, 311–356.

Kilpatrick J. A. & Ellis D. J. 1992. C-type magmas: igneous charnockites and their extrusive equivalents. *Geological Society of America Special Papers* 272, 155–164.

Kirkland C., Smithies R., Spaggiari C., Wingate M., De Gromard R. Q., Clark C., Gardiner N. & Belousova E. 2017. Proterozoic crustal evolution of the Eucla basement, Australia: Implications for destruction of oceanic crust during emergence of Nuna. *Lithos* 278, 427–444.

Kirkland C. L., Smithies R. H. & Spaggiari C. V. 2015a. Foreign contemporaries – Unravelling disparate isotopic signatures from Mesoproterozoic Central and Western Australia. *Precambrian Research* 265, 218–231.

Kirkland C. L., Smithies R. H., Woodhouse A. J., Howard H. M., Wingate M. T. D., Belousova E. A., Cliff J. B., Murphy R. C. & Spaggiari C. V. 2013a. Constraints and deception in the isotopic record; The crustal evolution of the west Musgrave Province, central Australia. *Gondwana Research* 23, 759–781.

Kirkland C. L., Smithies R. H., Woodhouse A. J., Howard H. M., Wingate M. T. D., Belousova E. A., Cliff J. B., Murphy R. C. & Spaggiari C. V. 2013b. Constraints and deception in the isotopic record; the crustal evolution of the west Musgrave Province, central Australia. *Gondwana Research* 23, 759–781.

Kirkland C. L., Spaggiari C. V., Johnson T. E., Smithies R. H., Danišík M., Evans N., Wingate M. T. D., Clark C., Spencer C., Mikucki E. & Mcdonald B. J. 2016. Grain size matters: Implications for element and isotopic mobility in titanite. *Precambrian Research* 278, 283–302.

Kirkland C. L., Spaggiari C. V., Pawley M. J., Wingate M. T. D., Smithies R. H., Howard H. M., Tyler I. M., Belousova E. A. & Poujol M. 2011. On the edge: U–Pb, Lu–Hf, and Sm–Nd data suggests reworking of the Yilgarn craton margin during formation of the Albany–Fraser Orogen. *Precambrian Research* 187, 223–247.

Kirkland C. L., Spaggiari C. V., Smithies R. H., Wingate M. T. D., Belousova E. A., Gréau Y., Sweetapple M. T., Watkins R., Tessalina S. & Creaser R. 2015b. The affinity of Archean crust on the Yilgarn—Albany–Fraser Orogen boundary: Implications for gold mineralisation in the Tropicana Zone. *Precambrian Research* 266, 260–281.

Korhonen F. J., Clark C., Brown M., Bhattacharya S. & Taylor R. 2013. How long-lived is ultrahigh temperature (UHT) metamorphism? Constraints from zircon and monazite geochronology in the Eastern Ghats orogenic belt, India. *Precambrian Research* 234, 322–350.

Krystopowicz N. J. & Currie C. A. 2013. Crustal eclogitisation and lithosphere delamination in orogens. *Earth and Planetary Science Letters* 361, 195–207.

Leech M. L. 2001. Arrested orogenic development: eclogitisation, delamination, and tectonic collapse. *Earth and Planetary Science Letters* 185, 149–159.

Levander A., Schmandt B., Miller M. S., Liu K., Karlstron K. E., Crow R. S., Lee C.-T. A. & Humphreys E. D. 2011. Continuing Colorado plateau uplift by delamination-style convective lithospheric downwelling. *Nature* 472, 461–466.

Li Z.-H., Liu M. & Gerya T. 2016. Lithosphere delamination in continental collision orogens: a systematic numerical

study. Journal of Geophysical Research: Solid Earth 121.

Li Z. X., Bogdanova S. V., Collins A. S., Davidson A., De Waele B., Ernst R. E., Fitzsimons I. C. W., Fuck R. A., Gladkochub D. P., Jacobs J., Karlstrom K. E., Lu S., Natapov L. M., Pease V., Pisarevsky S. A., Thrane K. & Vernikovsky V. 2008. Assembly, configuration, and break-up history of Rodinia: A synthesis. *Precambrian Research* 160, 179–210.

Loosveld R. J. H. & Etheridge M. A. 1990. A model for low-pressure facies metamorphism during crustal thickening. *Journal of Metamorphic Geology* 8.

Love G. J. 1999. A study of wall-rock contamination in a tonalitic gneiss from King Point, near Albany, Western Australia. BSc. (Honours) Thesis. Curtin University of Technology, Perth.

Magni V., Faccenna C., Van Hunen J. & Funiciello F. 2014. How collision triggers backarc extension: insight into Mediterranean style of extension from 3-D numerical models. *Geology* 42.

Maier W. D., Smithies R. H., Spaggiari C. V., Barnes S. J., Kirkland C. L., Kiddie O. & Roberts M. P. 2016a. The evolution of the mafic and ultramafic rocks of the Mesoproterozoic Fraser Zone, Albany-Fraser Orogen, and implications for Ni-Cu sulfide potential of the region: Geological Survey of Western Australia, Record 2016/8, 49p.

Maier W. D., Smithies R. H., Spaggiari C. V., Barnes S. J., Kirkland C. L., Yang S., Lahaye Y., Kiddie O. & Macrae C. 2016b. Petrogenesis and Ni–Cu sulphide potential of mafic–ultramafic rocks in the Mesoproterozoic Fraser Zone within the Albany–Fraser Orogen, Western Australia. *Precambrian Research* 281, 27–46.

Mareschal J.-C. & Jaupart C. 2013. Radiogenic heat production, thermal regime and evolution of continental crust. *Tectonophysics* 609, 524–534.

Mckenzie D. & Priestley K. 2008. The influence of lithospheric thickness variations on continental evolution. *Lithos* 102, 1–11.

Mcnutt M. K. 1998. Superswells. *Reviews of Geophysics* 36, 211–244.

Möller A., Post N. J. & Hensen B. J. 2002. Crustal residence history and garnet Sm–Nd ages of high-grade metamorphic rocks from the Windmill Islands area, East Antarctica. *International Journal of Earth Sciences* 91, 993–1004.

Morency C., Doin M. & Dumoulin C. 2002. Convective destabilization of a thickened continental lithosphere. *Earth and Planetary Science Letters* 202, 303–320.

Morrissey L., Payne J. L., Kelsey D. E. & Hand M. 2011. Grenvillian-aged reworking in the North Australian Craton, central Australia: constraints from geochronology and modelled phase equilibria. *Precambrian Research* 191, 141–165.

Morrissey L. J., Hand M. & Kelsey D. E. 2017a. A curious case of agreement between conventional thermobarometry and phase equilibria modelling in granulites: new constraints on *P–T* estimates in the Antarctica segment of the Musgrave–Albany–Fraser–Wilkes Orogen. *Journal of Metamorphic Geology* 35: 1023–1050.

Morrissey L. J., Payne J. L., Hand M., Clark C., Taylor R., Kirkland C. L. & Kylander-Clark A. 2017b. Linking the Windmill Islands, east Antarctica and the Albany–Fraser Orogen: Insights from U–Pb zircon geochronology and Hf isotopes. *Precambrian Research* 293, 131–149.

Nelson D. R., Black L. P. & Mcculloch M. T. 1989. Nd-pb isotopic characteristics of the mordor complex, northern territory: Mid-proterozoic potassic magmatism from an enriched mantle source. *Australian Journal of Earth Sciences* 36, 541–551.

Nelson D. R., Myers J. S. & Nutman A. P. 1995. Chronology and evolution of the Middle Proterozoic Albany-Fraser Orogen, Western Australia. *Australian Journal of Earth Sciences* 42, 481–495.

Neumann N., Sandiford M. & Foden J. 2000. Regional geochemistry and continental heat flow: implications for the origin of the South Australian heat flow anomaly. *Earth and Planetary Science Letters* 183, 107–120.

O'brien P. J. & Rotzler J. 2002. High-pressure granulites: formation, recovery of peak conditions and implications for tectonics. Journal of Metamorphic Geology 21, 3–20.

Occhipinti S. A., Tyler I. M., Spaggiari C. V., Korsch R. J., Kirkland C. L., Smithies R. H., Martin K. & Wingate M. T. D. 2017. Tropicana translated: a foreland thrust system imbricate fan setting for 2520 Ma orogenic gold mineralization at the northern margin of the Albany–Fraser Orogen, Western Australia. *Geological Society, London, Special Publications* 453.

Paul E., Stüwe K., Teasdale J. & Worley B. 1995. Structural and metamorphic geology of the Windmill Islands, east Antarctica: field evidence for repeated tectonothermal activity. *Australian Journal of Earth Sciences* 42, 453–469.

Payne J. L., Mcinerney D. J., Barovich K. M., Kirkland C. L., Pearson N. J. & Hand M. 2016. Strengths and limitations of zircon Lu–Hf and O isotopes in modelling crustal growth. *Lithos* 248–251, 175–192.

Pearce J. A., Harris N. B. & Tindle A. G. 1984. Trace element discrimination diagrams for the tectonic interpretation of granitic rocks. *Journal of Petrology* 25, 956–983.

Perchuk A. L., Safonov O. G., Smit C. A., Van Reenen D. D., Zakharov V. S. & Gerya T. V. 2016. Precambrian ultra-hot orogenic factory: Making and reworking of continental crust. *Tectonophysics*, in press, doi: 10.1016/j.tecto.2016.11.041.

Pisarevsky S. A., Wingate M. T., Powell C. M., Johnson S. & Evans D. A. 2003. Models of Rodinia assembly and fragmentation. *Geological Society, London, Special Publications* 206, 35–55.

Post N. J. 2000. Unravelling Gondwana fragments: an integrated structural, isotopic and petrographic investigation of the Windmill Islands, Antarctica. PhD Thesis. University of New South Wales, Sydney.

Post N. J., Hensen B. J. & Kinny P. D. 1997. Two metamorphic episodes during a 1340–1180 Ma convergent tectonic event in the Windmill Islands, East Antarctica. *In: Ricci C. A. (ed.) The Antarctic Region: Geological Evolution and Processes,* pp. 157–161, Terra Antarctica, Siena.

Pownall J. M., Hall R., Armstrong R. A. & Forster M. A. 2014. Earth's youngest known ultrahigh-temperature granulites discovered on Seram, eastern Indonesia. *Geology* 42, 279–282.

Reid A. J., Jagodzinski E. A., Armit R. J., Dutch R. A., Kirkland C. L., Betts P. G. & Schaefer B. F. 2014. U–Pb and Hf isotopic evidence for Neoarchean and Paleoproterozoic basement in the buried northern Gawler Craton, South Australia. *Precambrian Research* 250, 127–142.

Roberts N. M., Slagstad T. & Viola G. 2015. The structural, metamorphic and magmatic evolution of Mesoproterozoic orogens. *Precambrian Research* 265, 1–9.

Sandiford M. & Hand M. 1998. Controls on the locus of intraplate deformation in central Australia. *Earth and Planetary Science Letters* 162, 97–110.

Sandiford M., Hand M. & Mclaren S. 1998. High geothermal

gradient metamorphism during thermal subsidence. *Earth and Planetary Science Letters* 163, 149–165.

Sandiford M., Mclaren S. & Neumann N. 2002. Long-term thermal consequences of the redistribution of heat-producing elements associated with large-scale granitic complexes. *Journal of Metamorphic Geology* 20, 87–98.

Santosh M., Sajeev K., Li J., Liu S. & Itaya T. 2009. Counterclockwise exhumation of a hot orogen: the Paleoproterozoic ultrahigh-temperature granulites in the North China Craton. *Lithos* 110, 140–152.

Scibiorski E., Tohver E. & Jourdan F. 2015. Rapid cooling and exhumation in the western part of the Mesoproterozoic Albany–Fraser Orogen, Western Australia. *Precambrian Research* 265, 232–248.

Scibiorski E., Tohver E., Jourdan F., Kirkland C. L. & Spaggiari C. 2016. Cooling and exhumation along the curved Albany–Fraser orogen, Western Australia. *Lithosphere* 8, 551–563.

Scrimgeour I. R., Kinny P. D., Close D. F. & Edgoose C. J. 2005. High-T granulites and polymetamorphism in the southern Arunta region, central Australia: evidence for a 1.64 Ga accretional event. *Precambrian Research* 142, 1–27.

Sears J. W., George G. M. S. & Winne J. C. 2005. Continental rift systems and anorogenic magmatism. *Lithos* 80, 147–154.

Selway K., Hand M., Heinson G. S. & Payne J. L. 2009. Magnetotelluric constraints on subduction polarity: reversing reconstruction models for Proterozoic Australia. *Geology* 37, 799–802.

Selway K. M., Hand M., Payne J. L., Heinson G. S. & Reid A. 2011. Magnetotelluric constraints on the tectonic setting of Grenville-aged orogenesis in central Australia. *Journal of the Geological Society* 168, 251–264.

Sheraton J. W., Black L. P. & Tindle A. G. 1992. Petrogenesis of plutonic rocks in a Proterozoic granulite-facies terrane — the Bunger Hills, East Antarctica. *Chemical Geology* 97, 163–198.

Sheraton J. W., Tingey R., Oliver R. & Black L. 1995. Geology of the Bunger Hills–Denman Glacier region, East Antarctica. *AGSO Bulletin*, No. 244, 1–136.

Sippl C., Brisbout L., Spaggiari C., Gessner K., Tkalčić H., Kennett B. & Murdie R. 2017. Crustal structure of a Proterozoic craton boundary: East Albany–Fraser Orogen, Western Australia, imaged with passive seismic and gravity anomaly data. *Precambrian Research* 296, 78–92.

Sizova E., Gerya T. & Brown M. 2014. Contrasting styles of Phanerozoic and Precambrian continental collision. *Gondwana Research* 25, 522–545.

Sizova E., Gerya T., Brown M. & Perchuk L. L. 2010. Subduction styles in the Precambrian: insight from numerical experiments. *Lithos* 116, 209–229.

Smithies H. R., Spaggiari C. V., Kirkland C. L., Howard H. & Maier W. D. 2013. Petrogenesis of gabbros of the Mesoproterozoic Fraser Zone: constraints on the tectonic evolution of the Albany–Fraser Orogen. Geological Survey of Western Australia, Record 2013/5, p. 29.

Smithies R. H., Howard H. M., Evins P. M., Kirkland C. L., Kelsey D. E., Hand M., Wingate M. T. D., Collins A. S. & Belousova E. 2011. High-temperature granite magmatism, crust-mantle interaction and the mesoproterozoic intracontinental evolution of the Musgrave Province, central Australia. *Journal of Petrology* 52, 931–958.

Smithies R. H., Howard H. M., Evins P. M., Kirkland C. L., Kelsey D. E., Hand M., Wingate M. T. D., Collins A. S., Belousova E. & Allchurch S. 2010. Geochemistry, geochronology, and petrogenesis of Mesoproterozoic felsic rocks in the western Musgrave Province of central Australia, and implication for the Mesoproterozoic tectonic evolution of the region. Geological Survey of Western Australia, Report 106, 73 pp.

Smithies R. H., Kirkland C. L., Korhonen F. J., Aitken A. R. A., Howard H. M., Maier W. D., Wingate M. T. D., Quentin De Gromard R. & Gessner K. 2015a. The Mesoproterozoic thermal evolution of the Musgrave Province in central Australia — Plume vs. the geological record. *Gondwana Research* 27, 1419–1429.

Smithies R. H., Spaggiari C. V. & Kirkland C. L. 2015b. Building the crust of the Albany–Fraser Orogen: constraints from granite geochemistry. Geological Survey of Western Australia, Report 150, 49p.

Smits R. G., Collins W. J., Hand M., Dutch R. & Payne J. 2014. A Proterozoic Wilson cycle identified by Hf isotopes in central Australia; implications for the assembly of Proterozoic Australia and Rodinia. *Geology* 42, 231–234.

Snyder D. B. & Goleby B. R. 2016. Seismic reflection patterns associated with continental convergent margins through time. *Tectonophysics* 692, 3–13.

Sobolev S. V. & Babeyko A. Y. 2005. What drives orogeny in the Andes? Geology 33.

Solano J., Jackson M., Sparks R., Blundy J. & Annen C. 2012. Melt segregation in deep crustal hot zones: a mechanism for chemical differentiation, crustal assimilation and the formation of evolved magmas. *Journal of Petrology* 53, 1999–2026.

Spaggiari C. V., Bodorkos S., Barquero-Molino M., Tyler I. M. & Wingate M. T. D. 2009. Interpreted bedrock geology of the South Yilgarn and central Albany–Fraser Orogen, Western Australia: Geological Survey of Western Australia, Record 2009/10, 84p.

Spaggiari C. V., Kirkland C. L., Pawley M. J., Smithies R. H., Wingate M. T. D., Doyle M. G., Blenkinsop T. G., Clark C., Oorschot C. W., Fox L. J. & Savage J. 2011. The geology of the east Albany–Fraser Orogen-a field guide: Geological Survey of Western Australia, Record 2011/23, 97p.

Spaggiari C. V., Kirkland C. L., Smithies R. H., Occhipinti S. A. & Wingate M. T. D. 2014. Geological framework of the Albany–Fraser Orogen. *In: Albany–Fraser Orogen seismic and magnetotelluric (MT) workshop 2014: extended abstracts:* Geological Survey of Western Australia, Record 2014/6. p. 44–59.

Spaggiari C. V., Kirkland C. L., Smithies R. H., Wingate M. T. D. & Belousova E. A. 2015. Transformation of an Archean craton margin during Proterozoic basin formation and magmatism: The Albany–Fraser Orogen, Western Australia. *Precambrian Research* 266, 440–466.

Spaggiari C. V. & Smithies R. H. 2015. Eucla basement stratigraphic drilling results release workshop: extended abstracts: Geological Survey of Western Australia, Record 2015/10, 70p.

Spaggiari C. V. & Tyler I. M. 2014. Albany–Fraser Orogen seismic and magnetotelluric (MT) workshop 2014: extended abstracts: Geological Survey of Western Australia, Record 2014/6. 165p.

Spear, F. S., & Spear, F. S. 1993. Metamorphic phase equilibria and pressure-temperature-time paths, Mineralogical Society of America, Washington DC, pp. 799.

Stepanov A. S., Hermann J., Rubatto D. & Rapp R. P. 2012. Experimental study of monazite/melt partitioning with implications for the REE, Th and U geochemistry of crustal rocks. *Chemical Geology* 300, 200–220.

Stern T., Houseman G., Salmon M. & Evans L. 2013. Instability of a lithospheric step beneath western North Island, New Zealand. *Geology* 41.

Stüwe K. 1995. Thermal buffering effects at the solidus. Implications for the equilibration of partially melted metamorphic rocks. *Tectonophysics* 248, 39–51.

Sun S., Warren R. G. & Shaw R. D. 1995. Nd isotope study of granites from the Arunta Inlier, central Australia: constraints on geological models and limitation of the method. *Precambrian Research* 71, 301–314.

Taylor R. J., Kirkland C. L. & Clark C. 2016. Accessories after the facts: Constraining the timing, duration and conditions of high-temperature metamorphic processes. *Lithos* 264, 239–257.

Thybo H. & Artemieva I. M. 2013. Moho and magmatic underplating in continental lithosphere. *Tectonophysics* 609, 605–619.

Tucker N. M. & Hand M. 2016. New constraints on metamorphism in the Highjump Archipelago, East Antarctica. *Antarctic Science* 28, 487–503.

Tucker N. M., Hand M., Kelsey D. E. & Dutch R. A. 2015. A duality of timescales: Short-lived ultrahigh temperature metamorphism preserving a long-lived monazite growth history in the Grenvillian Musgrave–Albany–Fraser Orogen. *Precambrian Research* 264, 204–234.

Tucker N. M., Hand M., Kelsey D. E., Taylor R., Clark C. & Payne J. L. 2018. A tripartite approach to unearthing the duration of high temperature conditions versus peak metamorphism: an example from the Bunger Hills, East Antarctica. *Precambrian Research*, in press.

Tucker N. M., Payne J. L., Clark C., Hand M., Taylor R. J. M., Kylander-Clark A. R. C. & Martin L. 2017. Proterozoic reworking of Archean (Yilgarn) basement in the Bunger Hills, East Antarctica. *Precambrian Research* 298, 16–38.

Van Kranendonk M. J. & Kirkland C. L. 2013. Orogenic climax of Earth: The 1.2–1.1 Ga Grenvillian superevent. *Geology* 41, 735–738.

Van Wijk J. W., Baldridge W. S., Van Hunen J., Goes S., Aster R., Coblentz D. D., Grand S. P. & Ni J. 2010. Small-scale convection at the edge of the Colorado Plateau: implications for topography, magmatism and evolution of Proterozoic lithosphere. *Geology* 38.

Vielzeuf D., Clemens J., Pin C. & Moinet E. 1990. Granites, granulites, and crustal differentiation. *In: Granulites and crustal evolution,* Springer, Dordrecht, pp. 59–85.

Vilà M., Fernández M. & Jiménez-Munt I. 2010. Radiogenic heat production variability of some common lithological groups and its significance to lithospheric thermal modeling. *Tectonophysics* 490, 152–164.

Voshage H., Hofmann A. W., Mazzucchelli M., Rivalenti G., Sinigoi S., Raczek I. & Demarchi G. 1990. Isotope evidence from the Ivrea Zone for a hybrid lower crust formed by magmatic underplating. *Nature* 347, 731–736.

Waddell P.-J. A., Timms N. E., Spaggiari C. V., Kirkland C. L. & Wingate M. T. D. 2015. Analysis of the Ragged Basin, Western Australia: Insights into syn-orogenic basin evolution within the Albany–Fraser Orogen. *Precambrian Research* 261, 166–187.

Wade B. P., Barovich K. & Hand M. 2005. Geochemistry and provenance of a Mesoproterozoic (1.4 Ga) eastern Musgrave Block basin: buddying up to the Belt-Purcell Basin. *In: Pisarevsky, S. (ed.), Supercontinents and Earth Evolution Symposium, 2005.* Geological Society of Australia Inc. Abstracts, p. 43.

Wade B. P., Barovich K. M., Hand M., Scrimgeour I. R. & Close D. F. 2006. Evidence for Early Mesoproterozoic Arc Magmatism in the Musgrave Block, central Australia: Implications for Proterozoic Crustal Growth and Tectonic Reconstructions of Australia. *Journal of Geology* 114, 43–63.

Wade B. P., Kelsey D. E., Hand M. & Barovich K. M. 2008. The Musgrave Province: stitching north, west and south Australia. *Precambrian Research* 166, 370–386.

Wade B. P., Payne J. L., Hand M. & Barovich K. M. 2007. Petrogenesis of ca 1.50 Ga granitic gneiss of the Coompana Block; filling the "magmatic gap" of Mesoproterozoic Australia. *Australian Journal of Earth Sciences* 54, 1089–1102.

Walsh A. K., Kelsey D. E., Kirkland C. L., Hand M., Smithies R. H., Clark C. & Howard H. M. 2015. *P–T–*t evolution of a large, long-lived, ultrahigh-temperature Grenvillian belt in central Australia. *Gondwana Research* 28, 531–564.

Wang H. & Currie C. A. 2015. Magmatic expressions of continental lithosphere removal. *Journal of Geophysical Research: Solid Earth* 120, 7239–7260.

Warren R. G. & Shaw R. D. 1995. Hermansburg, Northern Territory (second ed.) 1:250 000 Geological Map Series Explanatory Notes, Darwin, Northern Territory Geological Survey.

Wells M. L. & Hoisch T. D. 2008. The role of mantle delamination in widespread Late Cretaceous extension and magmatism in the Cordilleran orogen, western United States. *Geological Society of America Bulletin* 120, 515–530.

Wetherley S. 1998. Tectonic evolution of the Mount Barren Group, Albany–Fraser Province, Western Australia. PhD Thesis. University of Western Australia, Perth.

Wickham S. M. & Oxburgh E. R. 1985. Continental rifts as a setting for regional metamorphism. *Nature* 318, 330–333.

Wise T. W., Pawley M. J. & Dutch R. A. 2015. Preliminary interpretations from the 2015 Coompana aeromagnetic survey, *MESA Journal.* 79, 22–30.

Wong B. L., Morrissey L. J., Hand M., Fields C. E. & Kelsey D. E. 2015. Grenvillian-aged reworking of late Paleoproterozoic crust of the southern North Australian Craton, central Australia: Implications for the assembly of Mesoproterozoic Australia. *Precambrian Research* 270, 100–123.

Yakymchuk C. & Brown M. 2014. Behaviour of zircon and monazite during crustal melting. *Journal of the Geological Society, London* 171, 465–479.

Zhang S., Zhao Y., Liu X., Liu Y., Hou K., Li C. & Ye H. 2012. U–Pb geochronology and geochemistry of the bedrocks and moraine sediments from the Windmill Islands: Implications for Proterozoic evolution of East Antarctica. *Precambrian Research* 206–207, 52–71.

Zhao J. & Mcculloch M. T. 1993. Melting of a subduction-modified continental lithospheric, mantle: Evidence from late Proterozoic mafic dike swarms, in central Australia. *Geology* 21, 463–466.

APPENDIX A.

A SPATIAL REPRESENTATION OF D_1–D_2 OROGENESIS

The distribution of Mesoproterozoic magmatism and metamorphism within the MAFWO may be investigated by considering the presence or absence of secular changes in age and isotopic composition in time and space. Accordingly, a series of spatial–age and spatial–isotope maps are presented in Figs. 1–3 below.

Data were compiled from published datasets (including State Survey Publications and online databases). Associated metadata for the compiled data are given in Appendicies B–E. The majority of rock samples have well-constrained and documented sample locations. Where specific sampling coordinates were not provided in published sources, approximate sample locations were estimated using satellite imagery, geological maps, and the described geography.

Data were gridded for magmatic crystallisation age (Fig. 1) and Sm–Nd and Lu–Hf isotope values (Fig. 2) in ArcGis ProTM using the Natural Neighbour Interpolation with interpolation intervals set to reflect natural breaks in the dataset to account for potential non-uniform data distribution (i.e. outlying values). Gridding simplifies the isotopic signature for each output data cell in that the dominant signature is portrayed with outliers and anomalies largely ignored except where data density is low. Extensive Palaeozoic to recent sedimentary cover between regions of exposed bedrock, cultural sensitivities, and remoteness means that data are generally heterogeneously distributed. This is the primary reasoning for use of the ArcGis ProTM Natural Neighbour interpolation technique as it is considered to work well with clustered scatter points. Interpolated values are determined by a weighted-average calculation of the surrounding data, in which data points closest to the output cell have greater influence than data that are further away.

The produced maps should be used as a guide only (i.e. not a quantitative measure) to the overall regional trends in age and geochemistry across the MAFWO, in conjunction with isotopic and other geological data to assess their validity. Antarctic data are not interpolated given uncertainties on the unexposed geology. The Natural Neighbour technique only interpolates as far as the data are distributed and therefore it is also not appropriate to interpolate between the Australian and Antarctic datasets.

The geographical and temporal distribution of sampled mafic and felsic igneous rocks across the MAFWO that yield interpreted magmatic crystallisation ages between ca. 1410–1120 Ma is illustrated in Fig. 1. The specific crystallisation ages from individual samples are interpolated across the geographical range of the sampled localities. Due to overlap in the spatial extent of D_1 and D_2 magmatism, separate age plots are also presented to highlight variation in the age of magmatism within the narrower timeframes that characterise D_1 and D_2 (also Fig. 1). Each magmatic crystallisation age plotted represents a pooled age (e.g. weighted mean age, concordia age) of individual analyses from that sample (see also Appendix B).

Sm–Nd whole-rock and Lu–Hf zircon isotopic data are interpolated in Fig. 2 for samples with an inferred Mesoproterozoic igneous protolith and accompanying age data. Age data are direct geochronological constraints or inferred as D_1 and D_2 ages (by the original data source; Appendicies D and E). D_1 Sm–Nd data points in the west MAFWO that are enclosed by the black box in Fig. 2 have inferred D_1 ages. Sm–Nd whole-rock isotopic data are plotted as epsilon Nd, calculated at the time of magma crystallisation ($\varepsilon_{Nd}(t)$). Each Sm–Nd data point shown in Fig. 2 represents one whole-rock analysis from one sample. Lu–Hf zircon isotopic data are likewise plotted as epsilon Hf, also calculated for the time of magma crystallisation ($\varepsilon_{Hf}(t)$). Each Lu–Hf data point in Fig. 2 represents one sample but comprises multiple εHf(t) zircon analyses (plotted at the same coordinates). Due to limited geographical spread of Lu–Hf data for the D_1 time-period, these analyses have not been extrapolated.

A two-stage depleted mantle model age map of Nd presently exists for Australia using unpublished and published data prior to 2011 for Australian components of the MAFWO (Champion, 2013). Although significantly more Sm–Nd analyses for the MAFWO have since been documented, a revised Nd model age map for the MAFWO is not undertaken in this review. The tacit assumption of Lu–Hf and Sm–Nd model ages is that the parent magma was homogeneous and formed in a single event, without subsequent modification by addition or crustal or mantle components, which is seldom the case (e.g. Payne et al., 2016). The crustal evolution documented for the MAFWO suggests that Mesoproterozoic and Paleoproterozoic magmatism likely involved reworking of multiple crustal sources as well as episodic juvenile (mantle) addition, and assimilated crustal components (Section 4 and 5, main text). This means that depleted mantle model ages for Mesoproterozoic MAFWO magmas are more complex than reflecting the timing of magma extraction from the mantle and are thus not necessarily geologically meaningful.

Metamorphic age data for individual samples commonly yield a large spread and thus a pooled age cannot be calculated, nor is pooling metamorphic age data geologically valid (see Section 8). Therefore, for the purposes of a generalised spatial representation, samples that yield interpreted metamorphic ages are classified according to the age of the individual analyses within that sample (a sample may have more than one classification). Samples that classify as recording evidence for D_1/M_1 and D_2/M_2 metamorphism (as per Section 2, Table 1, not taking uncertainties into consideration) are represented spatially in Fig. 3 as a map of point density to reflect the broad predicted distribution of the age of metamorphism. Metamorphic ages presented are from interpreted metamorphic zircon grains and overgrowths, monazite and xenotime, as inferred by the original data source (see Appendix C). To account (visually) in Fig. 3 for samples containing only few metamorphic ages versus samples that record abundant metamorphic age data, the data points are weighted in the point density calculation based on whether the number of analyses per sample are deemed significant ($n \geq 20$) or minor ($n < 20$).

In Figs. 1–3, data for the D_1 time period is shown in a cream to red colour scale; maps showing D_2 data use a cream to blue colour scheme. Transition from cream to red/blue represents increasing age of magmatic crystallisation (Fig. 1), increasing age of metamorphism (Fig. 3), or increasingly juvenile isotope (Nd whole-rock and Hf zircon) composition (Fig. 2).

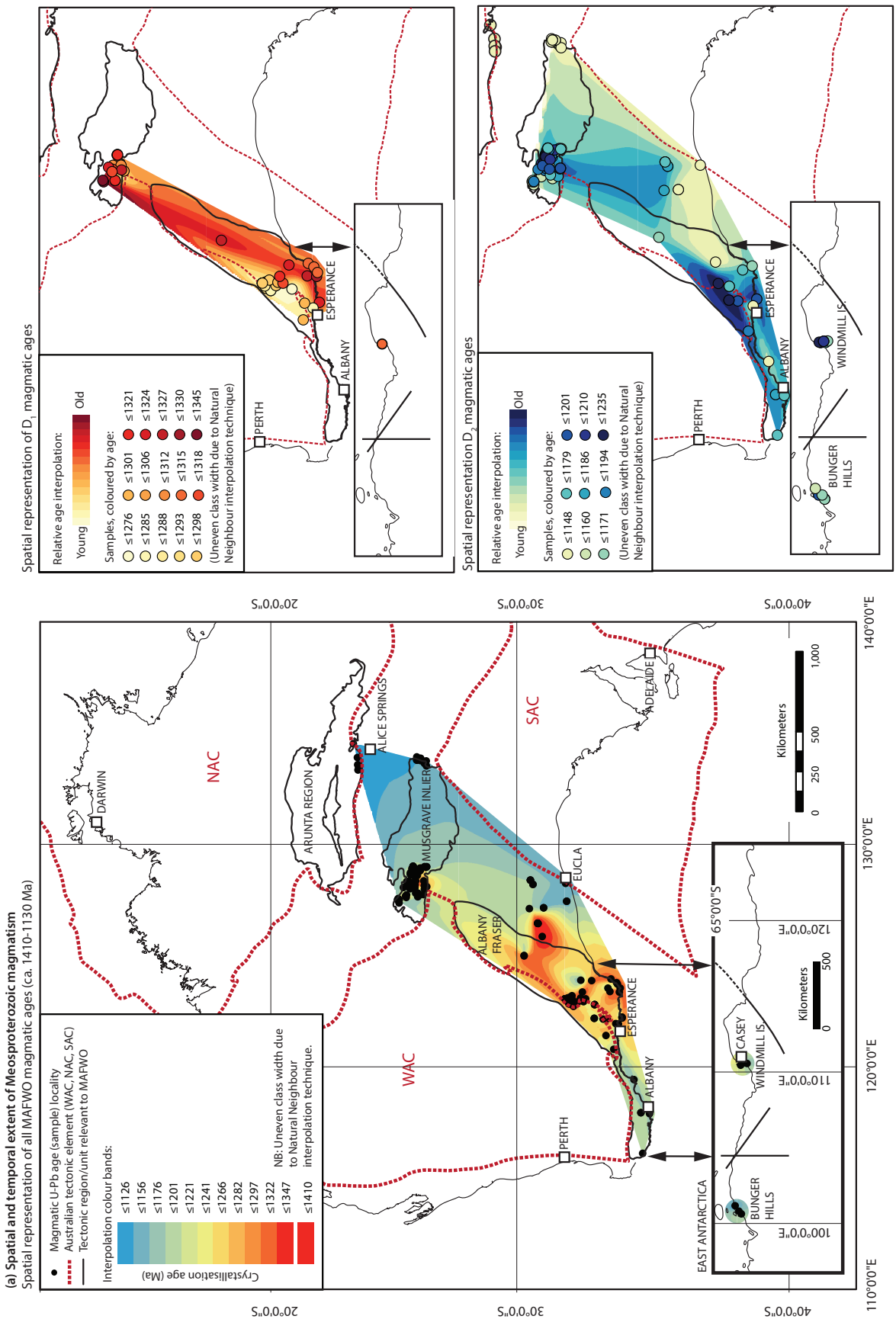
(a) Spatial and temporal extent of Mesoproterozoic magmatism
Spatial representation of all MAFWO magmatic ages (ca. 1410-1130 Ma)
Magmatic U-Pb age (sample) locality
Australian tectonic element (WAC, NAC, SAC)
Tectonic region/unit relevant to MAFWO
Interpolation colour bands:
≤1126
≤1156
≤1176
≤1201
≤1221
≤1241
≤1266
≤1282
≤1297
≤1322
≤1347
≤1410
Crystallisation age (Ma)
NB: Uneven class width due to Natural Neighbour interpolation technique.
NAC
SAC
WAC
DARWIN
ALICE SPRINGS
ARUNTA REGION
MUSGRAVE INLIER
ALBANY FRASER
ADELAIDE
EUCLA
PERTH
ALBANY
ESPERANCE
EAST ANTARCTICA
CASEY
WINDMILL IS.
BUNGER HILLS
Kilometers
0 250 500 1,000
Kilometers
0 500
65°0'0"S
120°0'0"E
110°0'0"E
100°0'0"E
20°0'0"S
30°0'0"S
40°0'0"S
110°0'0"E
120°0'0"E
130°0'0"E
140°0'0"E
Spatial representation of D1 magmatic ages
Relative age interpolation:
Young
Old
Samples, coloured by age:
≤1276 ≤1285 ≤1288 ≤1293 ≤1298
≤1301 ≤1306 ≤1312 ≤1315 ≤1318
≤1321 ≤1324 ≤1327 ≤1330 ≤1345
(Uneven class width due to Natural Neighbour interpolation technique)
PERTH
ALBANY
ESPERANCE
Spatial representation D2 magmatic ages
Relative age interpolation:
Young
Old
Samples, coloured by age:
≤1148 ≤1160 ≤1171
≤1179 ≤1186 ≤1194
≤1201 ≤1210 ≤1235
(Uneven class width due to Natural Neighbour interpolation technique)
PERTH
ALBANY
ESPERANCE
WINDMILL IS.
BUNGER HILLS

Figure 1.

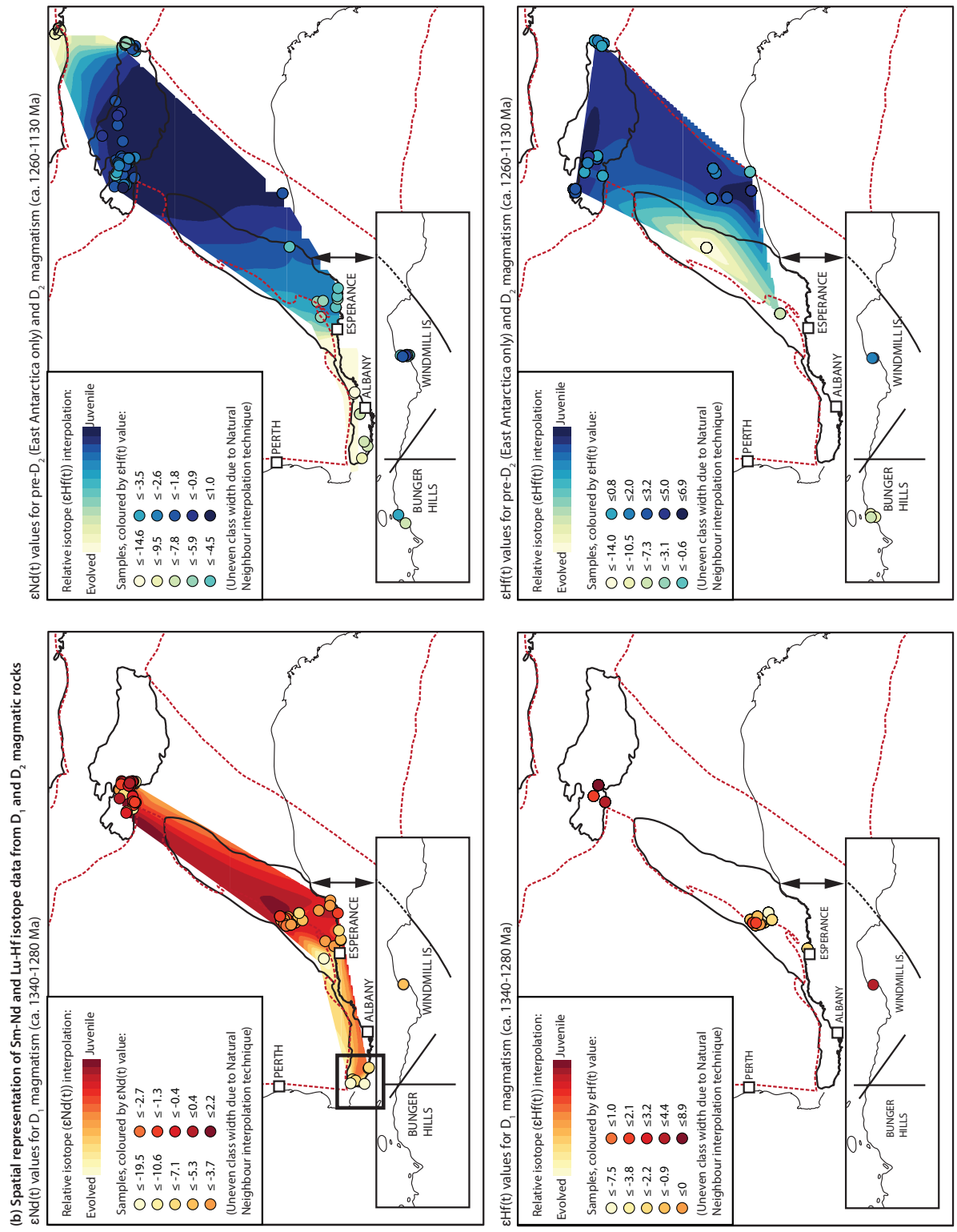
(b) Spatial representation of Sm-Nd and Lu-Hf isotope data from D1 and D2 magmatic rocks
εNd(t) values for D1 magmatism (ca. 1340-1280 Ma)
εNd(t) values for pre-D2 (East Antarctica only) and D2 magmatism (ca. 1260-1130 Ma)
εHf(t) values for D1 magmatism (ca. 1340-1280 Ma)
εHf(t) values for pre-D2 (East Antarctica only) and D2 magmatism (ca. 1260-1130 Ma)
Relative isotope (εNd(t)) interpolation:
Relative isotope (εHf(t)) interpolation:
Evolved
Juvenile
Samples, coloured by εNd(t) value:
≤ -19.5
≤ -10.6
≤ -7.1
≤ -5.3
≤ -3.7
≤ -2.7
≤ -1.3
≤ -0.4
≤0.4
≤2.2
Samples, coloured by εHf(t) value:
≤ -14.6
≤ -9.5
≤ -7.8
≤ -5.9
≤ -4.5
≤ -3.5
≤ -2.6
≤ -1.8
≤ -0.9
≤1.0
Samples, coloured by εHf(t) value:
≤ -7.5
≤ -3.8
≤ -2.2
≤ -0.9
≤0
≤1.0
≤2.1
≤3.2
≤4.4
≤8.9
Samples, coloured by εHf(t) value:
≤ -14.0
≤ -10.5
≤ -7.3
≤ -3.1
≤ -0.6
≤0.8
≤2.0
≤3.2
≤5.0
≤6.9
(Uneven class width due to Natural Neighbour interpolation technique)
PERTH
ALBANY
ESPERANCE
BUNGER HILLS
WINDMILL IS

Figure 2.

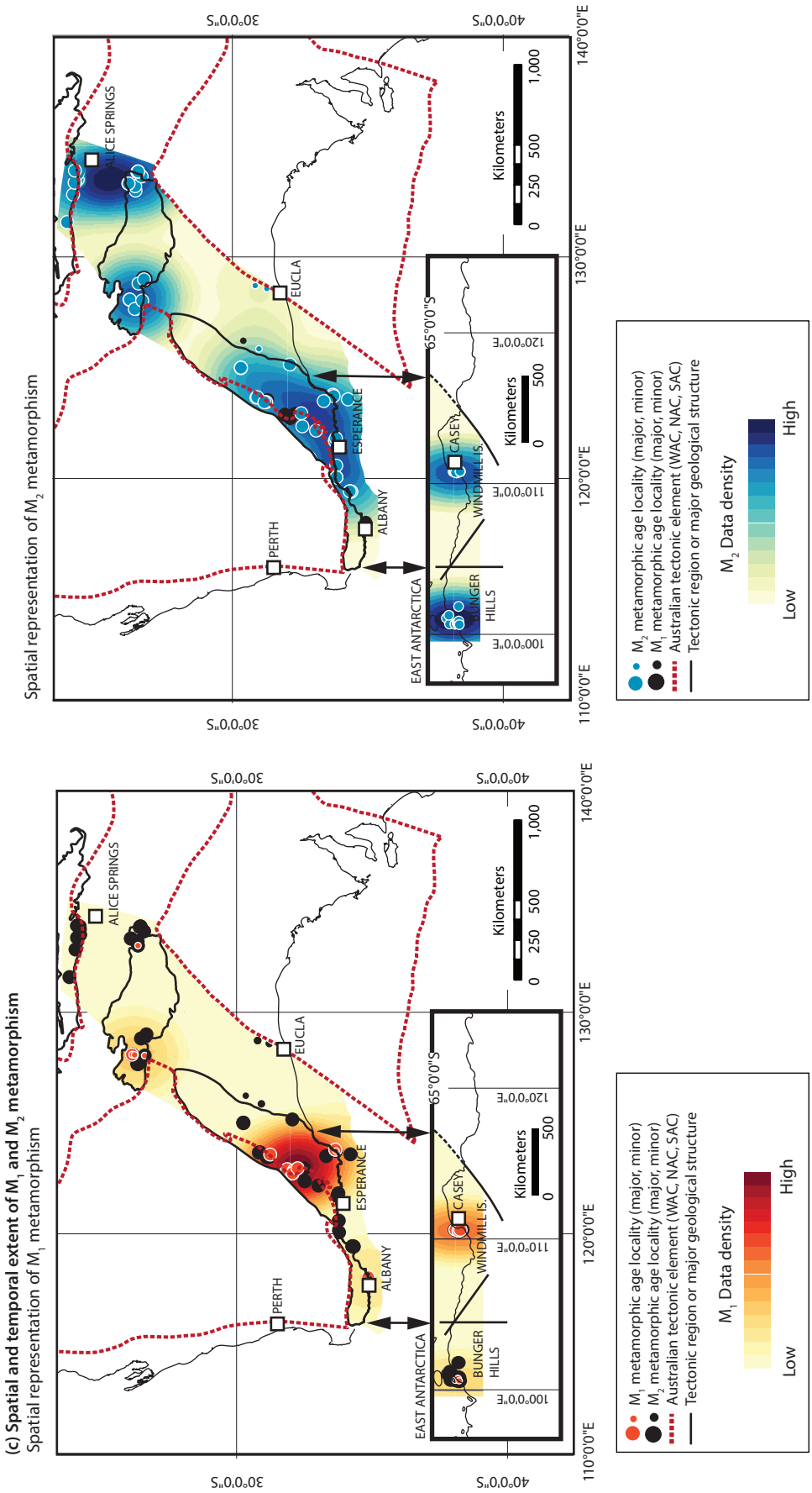
Spatial representation of M2 metamorphism
(c) Spatial and temporal extent of M1 and M2 metamorphism
Spatial representation of M1 metamorphism
ALICE SPRINGS
EUCLA
ESPERANCE
ALBANY
PERTH
EAST ANTARCTICA
BUNGER HILLS
CASEY
WINDMILL IS.
Kilometers
0 250 500 1,000
0 500
65°0'0"S
110°0'0"E
120°0'0"E
130°0'0"E
140°0'0"E
30°0'0"S
40°0'0"S
100°0'0"E
110°0'0"E
120°0'0"E
M2 metamorphic age locality (major, minor)
M1 metamorphic age locality (major, minor)
Australian tectonic element (WAC, NAC, SAC)
Tectonic region or major geological structure
M2 Data density
M1 Data density
Low
High

Figure 3.

Appendix B. Compiled U–Pb age data for MAFWO Mesoproterozoic magmatic rocks (ca. 1410–1130 Ma)[a]

Sample	Latitude	Longitude	Tectonic Region	Geographic/geologic descriptor	Magmatic suite (if assigned)[b]	Lithological description	Age class[c]	Age[d]	Error[e]	Reference
FR12A2	-31.98811	122.89425	Fraser Zone	NW-margin, near Fraser Fault	Fraser gabbro	Two-pyroxene mafic granulite	D1	1299	10	1
FR15A1	-31.95645	122.91741	Fraser Zone	NW-margin, near Fraser Fault	Fraser gabbro	Two-pyroxene mafic granulite	D1	1291	8	1
FR16A1	-31.92470	122.94431	Fraser Zone	NW-margin, near Fraser Fault	Recherche*	gt-bearing metagranite, within mafic granulite	in-between	1250	23	1
FR20A1	-31.87212	123.00889	Fraser Zone	NW-margin, near Fraser Fault	Recherche*	gt-bearing metagranite, within mafic granulite	D1	1282	11	1
FR21B1	-31.85294	123.03174	Fraser Zone	Symons Hill	Recherche*	Melt within boudin neck	D1	1296	4	1
FR21B2	-31.85294	123.03174	Fraser Zone	Symons Hill	Fraser gabbro	Mafic granulite (boudin), within gt-bearing	D1	1283	5	1
FR21B3	-31.85294	123.03174	Fraser Zone	Symons Hill	Recherche*	gt-bearing granite (encloses boudin)	D1	1296	7	1
194780	-32.02889	122.81632	Fraser Zone	Wyralinu Hill, Fraser Range Station	Recherche (Gora Hill)	gt-amphibole-bearing pegmatite	D1	1283	7	2
194787	-32.05082	123.11014	Fraser Zone	Eyre Highway	Recherche (Southern Hills)	Granite pegmatite	D1	1288	3	3
194779	-32.04690	122.79519	Fraser Zone	Wyralinu Hill, Fraser Range Station	Recherche (Gora Hill)	gt-pxn-sill(?) metagranite	D1	1293	8	4
194717	-32.11247	123.02205	Fraser Zone	Eyre Highway	Fraser gabbro	Metagabbro	D1	1299	3	5, 6
194782	-32.11270	123.02729	Fraser Zone	S Eyre Highway, S. Hills Station	Recherche (Southern Hills)	Granite pegmatite	D1	1299	6	7
183653	-32.23312	122.85720	Fraser Zone	Mt. Malcolm	Recherche	Pegmatite	D1	1301	6	5, 8
194776	-32.19809	122.83529	Fraser Zone	Southern Hills Homestead	Recherche (Southern Hills)	Metagranite	D1	1305	2	9
183671	-31.95837	123.07634	Fraser Zone	N Cullinia Rocks, N Eyre Highway	Recherche (Gora Hill)	opx-bearing granitic gneiss	D1	1310	7	10
194781	-32.06096	122.90049	Fraser Zone	N Bullock Hills Dam	Fraser gabbro	Metagabbro (granulite)	D1	1312	8	11
194711	-32.37013	122.92457	Fraser Zone	Kent Dam, SE Mt. Malcolm, Fraser Range	Recherche (Gora Hill)	Metamonzogranite	D1	1297	8	12
194719	-31.85357	123.03266	Fraser Zone	Symons Hill	Recherche (Southern Hills)	Banded orthogneiss with mafic schlieren	D1	1298	5	13, 14
MM-1	-32.22698	122.83288	Fraser Zone	Mt. Malcolm	Recherche*	Charnockite	D1	1301	6	15
GH-1	-32.17292	122.69956	Fraser Zone	Gnamma Hill	Recherche*	Aplite dyke	D1	1288	12	15
FR-1	-32.22698	122.83288	Fraser Zone	N Mt. Malcolm, Fraser Range	Recherche*	Opx-bearing granite	D1	1293	9	15
194718	-31.99575	122.80060	Fraser Zone	American Granulite Quarry	Fraser gabbro*	Mafic granulite	D1	1292	6	15
194715	-32.17291	122.69956	Fraser Zone	Gnamma Hill	Recherche*	Leucosome in psammitic gneiss	D1	1285	7	16
182459	-32.97473	122.76891	Nornalup Zone	Drill core NSD001, Splinter Prospect	Esperance (Truslove)	bi-bearing metatonalite	D2	1156	5	17
182474	-30.27393	124.98043	Nornalup Zone	Drill core BRDDH001, Big Red Prospect	Esperance (Truslove)	Granite	D2	1167	2	18
192586	-33.47327	123.51162	Nornalup Zone	Scott Rocks, near Mt. Ragged	Esperance (Booanya)	Porphyritic monzogranite	D2	1175	12	19
182465	-32.9702	122.77849	Nornalup Zone	Drill core NSD002, Splinter Prospect	Esperance (unspecified)	Metagabbro	D2	1178	6	20
194839	-34.00004	122.20422	Nornalup Zone	Thistle Cove, Cape Le Grand National	Esperance (Truslove)	Metasyenogranite	D2	1186	8	21
184374	-33.29282	122.12083	Nornalup Zone	West of Mt. Ridley	Esperance (Truslove)	Metamonzogranite	D2	1198	11	22
194840	-34.00004	122.20422	Nornalup Zone	Thistle Cove, Cape Le Grand National	Esperance (Truslove)	Weakly-foliated metamonzogranite	D2	1200	11	23
182462	-32.97473	122.76891	Nornalup Zone	Splinter Prospect	Recherche (unspecified)	Garnetiferous metagabbro	D1	1276	6	24
177909	-31.94597	122.9066	Biranup Zone	Yardilla Bore	Recherche (Southern Hills)	gt-bearing augen monzogranitic gneiss	D1	1287	14	25
194783	-32.11414	123.17101	Nornalup Zone	Eyre Highway (Newman Rock)	Recherche (Gora Hill)	Metamonzogranite	D1	1297	12	26
194712	-32.44222	123.0688	Nornalup Zone	W Boingaring Rocks, N old Telegraph	Recherche (Southern Hills)	Leucocratic metasyenogranite	D1	1299	7	27

Appendix B. (continued)

Sample	Latitude	Longitude	Tectonic Region	Geographic/geologic descriptor	Magmatic suite (if assigned)[b]	Lithological description	Age class[c]	Age[d]	Error[e]	Reference
194710	-32.63548	123.03	Nornalup Zone	SW Boingaring Rocks, NE Mt Andrew	Recherche (Gora Hill)	Metagranite	D1	1317	7	28
194786	-32.51091	123.33677	Nornalup Zone	N of Charlina Granite Rock	Recherche (Southern Hills)	bi-bearing monzogranite	D1	1320	8	29
194883	-32.86055	123.84952	Nornalup Zone	Mardarbilla Rock	Recherche (Southern Hills)	Metasyenogranite	D1	1322	12	30
194836	-34.00441	122.16874	Nornalup Zone	Hellfire Bay	Recherche (Gora Hill)	Metamonzogranite	D1	1323	5	31
182476	-30.27426	124.95861	Nornalup Zone	Drill core BRDDH02, Big Red Prospect	Recherche (Gora Hill)	Migmatitic gneiss	D1	1326	6	32
194876	-33.54721	123.35954	Nornalup Zone	Gora Hill	Recherche (Gora Hill)	Metagranite	D1	1327	8	33
83700A	-33.76678	121.91666	Biranup Zone	Coramup Hill Quarry	Recherche*	hbl-bi syenogranite gneiss	D1	1283	13	34
83690	-33.40012	121.38332	Northern	Bald Rock	Recherche (Southern Hills)	Banded granodioritic gneiss	D1	1299	14	35
83697	-33.45011	122.13333	Nornalup Zone	West of Wittenoom Hills	Recherche (Southern Hills)	Monzogranite lens, enclosed by mylonitized	D1	1299	18	36
184326	-34.44328	119.4005	Biranup Zone	Short beach headland, Bremer Bay	Esperance*	Pegmatitic leucogranite	D2	1148	9	37
194703	-32.95905	122.1555	Biranup Zone	SW Double Tank, west Fraser Range	Esperance*	Pegmatitic leucosome in quartzofeldspathic	D2	1201	5	38
194704	-32.95905	122.1555	Biranup Zone	SW Double Tank, west Fraser Range	Esperance*	Quartzofeldspathic gneiss	D2	1213	7	39
194708	-32.55563	122.90361	Biranup Zone	N of Mt. Andrew	Esperance*	Leucosome in metamonzogranite	D2	1217	22	40
83663	-33.58717	123.92266	Nornaup Zone	Isralite Bay	Recherche (Gora Hill)	orthogneiss	D1	1314	21	41
83662	-33.90012	123.33334	Nornaup Zone	Poison Creek	Recherche (Gora Hill)	orthogneiss	D1	1330	14	42
83667	-32.45012	123.86668	Nornaup Zone	Balladonia Rock	Esperance (Truslove)	Porphyritic biotite granite	D2	1135	56	43
83657A	-33.86679	121.89999	Nornaup Zone	Esperance Harbour jetty	Esperance*	Porphyritic biotite monzogranite	D2	1138	38	44
MF2	116°47'	34°50'	Nornaup Zone	Mt. Franklin, 200 km W of Albany	Esperance*	Late-tectonic granite	D2	1189	9	45
AFP9	-34.70006	117.91323	Nornaup Zone	Serena Park, Porongurup Range	Esperance*	Augen orthogneiss	D2	1184	11	45
AFP8	-34.70006	117.91323	Nornaup Zone	Serena Park, Porongurup Range	Esperance*	Aplite dyke, discordant to foliated granite	D2	1184	12	45
W140	-34.764769	116.08666	Nornaup Zone	Mt. Chudalup (western AFO)	Esperance*	Post-tectonic adamellite	D2	1177	4	46
W139	-35.018526	117.86919	Nornaup Zone	Mt. Melville, Albany	Esperance*	Post-tectonic adamellite	D2	1174	12	46
192956	-33.68922	120.76327	N. Foreland		Gnowangerup–Fraser Dyke Suite	Metagabbro	D2	1193	11	47
95091214	-33.797154	123.75862	Arid Basin	Point Malcolm	Recherche	Aplite dyke	D1	1313	16	48
9411112	-33.830578	123.69198	Arid Basin	Little Bellinger	Recherche	Pegmatite dyke	D2	1165	5	48
9509243	-33.932616	123.51242	Arid Basin	Cape Arid	Recherche	Aplite dyke (Recherche SS)	D1	1313	16	48
178072	-30.80171	126.42628	Madura Province	Drill hole LNGD0002	Haig Cave	bi-bearing tonalite gneiss	Pre-D1	1407	7	49
178071	-30.81970	126.41503	Madura Province	Drill hole LNGD0001	Haig Cave	Unfoliated biotite microtonalite	Pre-D1	1408	7	50
178070	-30.80171	126.42628	Madura Province	Drill hole LNGD0001	Haig Cave	Amphibolite	Pre-D1	1415	7	51
192565	-31.91140	127.41624	Madura Province	Drill hole MORC001	Moodini	Metamonzogranite	Post-D2	1127	7	52
192566	-31.91328	127.41632	Madura Province	Drill hole MORC002	Moodini	Metamonzogranite	Post-D2	1132	9	53
206778	-31.02995	127.12321	Madura Province	Drill hole MAD011	Moodini	Leucocratic monzogabbro	D2	1143	5	54
206779	-31.02995	127.12321	Madura Province	Drill hole MAD011	Moodini	Leucocratic monzogabbro	D2	1144	7	55
192595	-30.47861	127.08571	Madura Province	Drill hole MAD014	Moodini	Monzogranite	D2	1182	7	56
206754	-30.97575	125.83145	Madura Province	Drill hole MAD002	Haig Cave	Leucocratic monzogranite	Pre-D1	1389	7	57

Appendix B. (continued)

Sample	Latitude	Longitude	Tectonic Region	Geographic/geologic descriptor	Magmatic suite (if assigned)[b]	Lithological description	Age class[c]	Age[d]	Error[e]	Reference
192558	-30.80029	126.42767	Madura Province	Drill hole LNGD0002	Haig Cave	Granitic gneiss	Pre-D1	1411	6	58
192557	-30.80029	126.42767	Madura Province	Drill hole LNGD0002	Haig Cave	Metagabbro	Pre-D1	1403	6	59
206753	-30.5186	128.36604	Coompana	Drill hole FOR010, NE of Forrest	Moodini	Granite	Stage-2	1192	13	60
213838	-30.61716	128.17583	Coompana	Drill hole FOR011, NNE of Forrest	Moodini	Granitic vein	Stage-2	1189	6	61
206752	-30.5186	128.36604	Coompana	Drill hole FOR010, NE of Forrest	Moodini	Porphyritic granite	Stage-2	1184	8	62
206729	-30.61716	128.17583	Coompana	Drill hole FOR011, NNE of Forrest	Moodini	bi-hbl metagranite	Stage-2	1180	6	63
192593	-30.5186	128.36604	Coompana	Drill hole FOR010, NE of Forrest	Moodini	Hornblende-metagranite	Stage-2	1175	5	64
194773	-31.87084	128.2225	Coompana	Eucla 1, ditch cuttings	Moodini	Granite	Stage-2	1140	8	65
R1842261	-26.32880	133.61582	East Musgrave	Tieyon	Pitjantjatjara (plutonic, porphyritic)	Weakly foliated bi-hbl metasyenogranite	D2	1147	11	66
R1842256	-26.17444	133.74077	East Musgrave	Tieyon	Pitjantjatjara (plutonic, porphyritic)	bi-hbl monzodiorite	D2	1149	10	66
R1842255	-26.40518	133.72359	East Musgrave	Tieyon	Pitjantjatjara (plutonic, porphyritic)	bi-hbl monzodiorite	D2	1147	11	66
R1842268	-26.17935	133.83125	East Musgrave	Tieyon	Pitjantjatjara (early anatectic)	bi-bearing leuco-granitoid	D2	1147	16	66
R1039150	-26.05946	133.84395	East Musgrave	Tieyon	Pitjantjatjara (plutonic, porphyritic)	hb-bi monzodiorite	D2	1152	9	66
R1850807	-26.41185	133.50055	East Musgrave	Tieyon	Pitjantjatjara (early anatectic)	Weakly foliated bi-monzogranite	D2	1143	9	66
R1850797	-26.03811	133.75592	East Musgrave	Tieyon	Pitjantjatjara (late dyke suite)	Monzogranite dyke	D2	1143	9	66
R1039230	-26.05973	133.84420	East Musgrave	Tieyon	Pitjantjatjara (plutonic, porphyritic)	Porphyritic biotite monzogranite	D2	1155	14	66
R1842263	-26.17809	133.84262	East Musgrave	Tieyon	Pitjantjatjara (late dyke suite)	Monzogranite dyke	D2	1143	8	66
R1850772	-26.02344	133.90415	East Musgrave	Tieyon	Pitjantjatjara (early anatectic)	Granite with pegmatite	D2	ca. 1140		66
R1850778	-26.06613	133.85166	East Musgrave	Tieyon	Pitjantjatjara (late dyke suite)	Syenogranite dyke	D2	1154	9	66
R1850740	-26.01425	133.76466	East Musgrave	Tieyon	Pitjantjatjara (early anatectic)	Monzogranite	D2	1147	8	66
R1039232	-26.05946	133.84395	East Musgrave	Tieyon	Pitjantjatjara (late dyke suite)	Aplite/bi-bearing leuco-syenogranite	D2	1136	3	66
180299	-25.87268	128.99045	West Musgrave	SE Mount Gosse	Pitjantjatjara (Mirturtu)	pxn-gt-bearing porphyritic granite	D2	1175	15	67
180256	-25.82743	128.88603	West Musgrave	Hubert Soak	Pitjantjatjara (Mirturtu)	pxn-gt-bearing metagranodiorite	D2	1176	6	68
180262	-25.8449	128.88858	West Musgrave	S Hubert Soak	Pitjantjatjara (Kapi-Parra)	Syenogranite with mylonitic fabric	D2	1180	4	69
180300	-25.87379	128.9904	West Musgrave	SE Mt. Gosse	Pitjantjatjara (Mirturtu)	cpx-gt-bearing porphyritic metamonzogranite	D2	1181	6	70
180270	-25.8729	128.90738	West Musgrave	SW Mt. Gosse	Pitjantjatjara	cpx-gt-bearing metamonzogranite dyke	D2	1183	9	71
191763	-26.07354	127.64909	West Musgrave	Minnie Hill	Pitjantjatjara	Pegmatite dyke	D2	1134	9	72
189522	-26.05799	127.78234	West Musgrave	NE Lightning Rock	Pitjantjatjara	Leucogranitic vein	D2	1149	5	73
189547	-26.3292	127.95955	West Musgrave	E Borrows Hill	Pitjantjatjara	hbl-bearing granodiorite	D2	1152	5	74
190231	-25.71928	128.02708	West Musgrave	SW Prostanthera Hill	Pitjantjatjara (Tjuni Purlka)	Megacrystic granite	D2	1153	5	75
194376	-26.075	127.64802	West Musgrave	Minnie Hill	Pitjantjatjara	Norite dyke	D2	1155	15	76
185591	-26.42202	128.96783	West Musgrave	S Latitude Hill	Pitjantjatjara	gt-rich leucogranite	D2	1157	81	77
208506	-25.30608	127.33892	West Musgrave	Gungangmura Waterhole	Pitjantjatjara	gt-bi-hbl metamonzogranite	D2	1157	9	78
189523	-26.05451	127.78082	West Musgrave	NNE Lightning Rock	Pitjantjatjara (Waratjarra)	hbl-bi-bearing metagranodiorite	D2	1157	9	79
194367	-25.6101	127.70316	West Musgrave	NW Ngaturn, Tjuni Purlka Zone	Pitjantjatjara (Tjuni Purlka)	Syenogranite	D2	1159	7	80

Appendix B. (continued)

Sample	Latitude	Longitude	Tectonic Region	Geographic/geologic descriptor	Magmatic suite (if assigned)[b]	Lithological description	Age class[c]	Age[d]	Error[e]	Reference
180860	-25.92771	128.2119	West Musgrave	Pirrul Bore	Pitjantjatjara (Waratjarra)	pxn-hbl metamonzogranite	D2	1159	13	81
191751	-26.06215	127.61739	West Musgrave	W Red Rock, near Cohn Hill	Pitjantjatjara	migmatitic bi-granite	D2	1160	15	82
208504	-25.23746	127.47957	West Musgrave	N Yulun-Kudara Waterhole	Pitjantjatjara	bi-hbl metamonzogranite	D2	1160	7	83
183509	-26.13865	128.78084	West Musgrave	NNW Mt. West	Pitjantjatjara (Tjuni Purlka)	Leucogranite dyke (pxn-hbl-bearing)	D2	1165	10	84
201320	-25.26713	127.53742	West Musgrave	N Wanarn	Pitjantjatjara	Leucogranite vein	D2	1171	4	85
184147	-26.38339	128.08637	West Musgrave	ESE Borrows Hill	Pitjantjatjara	Undeformed granite dyke cutting syenogranite	D2	1173	10	86
187154	-25.86383	128.85273	West Musgrave	SW Hubert Soak	Pitjantjatjara	Mafic granulite	D2	1185	10	87
184149	-26.38342	128.08547	West Musgrave	ESE Borrows Hill	Within Wirku Metamorphics	opx-rich migmatitic felsic rock (may be	D2	1185	4	88
187171	-25.65496	128.1869	West Musgrave	Prostanthera Hill	Pitjantjatjara (Ilurpa)	Charnockite syenogranite (opx-gt-mt-bearing)	D2	1185	5	89
194421	-26.28479	127.71753	West Musgrave	Mulaggora Hills	Mummawarrawarra Basalt (Bentley	Basalt-andesite	D2	1186	7	90
201305	-25.30609	127.46811	West Musgrave	NW Yulun-Kudara Waterhole	Pitjantjatjara	Pegmatite	D2	1188	6	91
194485	-25.7583	127.98117	West Musgrave	NE Finlay Range	Pitjantjatjara	Pegmatitic leucosome	D2	1188	5	92
187105	-26.04724	128.58068	West Musgrave	Mount Aloysius	Pitjantjatjara (Tjuni Purlka)	Ksp-rich cpx-hbl-bearing granite	D2	1190	7	93
187174	-25.65931	128.19537	West Musgrave		Pitjantjatjara	Granite	D2	1191	14	94
190228	-25.79786	128.0763	West Musgrave	NNE Mount Scott, Tjuni Purlka Zone	Pitjantjatjara (Tjuni Purlka)	bi-hbl granite	D2	1191	14	95
187179	-25.65861	128.20934	West Musgrave	NE Prostanthera Hill	Pitjantjatjara	mt-cpx metamonzogranite	D2	1192	9	96
208500	-25.3064	127.48884	West Musgrave	NNE Yulun-Kudara Waterhole	Pitjantjatjara	Pegmatite	D2	1194	14	97
187113	-26.02395	128.66277	West Musgrave	Mount Aloysius	Pitjantjatjara	Folded pegmatite vein (anatectic)	D2	1194	3	98
185590	-26.3823	128.94514	West Musgrave	S Latitude Hill	Pitjantjatjara	Charnockite (opx-hbl-bearing)	D2	1195	7	99
194766	-25.94023	128.04375	West Musgrave	S Mt. Scott	Pitjantjatjara	Pegmatite vein	D2	1197	4	100, 101
185610	-26.36197	128.05542	West Musgrave	ESE Borrows Hill	Pitjantjatjara	Leucogranite with irregular cpx-hbl aggregates	D2	1199	5	102
184146	-26.38357	128.08562	West Musgrave	ESE Borrows Hill	Pitjantjatjara	Monzogranite-quartz syenite	D2	1201	6	103
187274	-25.61885	128.30472	West Musgrave	NE Murray Range	Pitjantjatjara (Pirntirri)	K-feldspar porphyritic granite	D2	1205	6	104
185593	-26.33578	128.97281	West Musgrave	E Latitude Hill	Pitjantjatjara	Leucogranite	D2	1207	4	105
185339	-26.15409	128.90646	West Musgrave	Hazlett Rocks	Pitjantjatjara (Tjuni Purlka Suite)	Opx-rich mylonitic granite	D2	1210	10	106
187172	-25.65646	128.18628	West Musgrave	Prostanthera Hill, Tjuni Purlka Zone	Pitjantjatjara	gt-bearing pegmatite	D2	1212	56	107
187166	-25.69801	128.31357	West Musgrave	N Pirntirri Mulari	Pitjantjatjara (Pirntirri)	opx-bearing metamonzogranite	D2	1213	11	108
184158	-26.42497	128.07231	West Musgrave	Track N of Kampurarr Pirti	Wankanki	Pxn-bearing metamonzogranite (charnockite)	D1	1303	10	109
194379	-26.07118	127.64628	West Musgrave	Minnie Hill, Mamutjarra Zone	Wankanki	Mylonitic granite (minor gt)	D1	1306	11	110
187151	-25.98039	128.32838	West Musgrave	NE Papulankutja (Blackstone), Tjuni	Wankanki	hbl-bearing metamonzogranite	D1	1312	5	111
185581	-26.30432	128.33336	West Musgrave	W MacDougall Bluff	Wankanki	Foliated biotite granite	D1	1312	7	112
183726	-26.16051	128.81933	West Musgrave	NW Michael Hills	Wankanki	Leucogranitic gneiss	D1	1314	8	113
194804	-25.95578	128.15395	West Musgrave	Mount Clianthus	Wankanki	bi-bearing metamonzogranite	D1	1316	6	114
194765	-25.9416	128.04248	West Musgrave	S Mt. Scott, Tjuni Purlka Zone	Wankanki	Syenogranite	D1	1318	9	100, 115
194381	-26.06473	127.65204	West Musgrave	Minnie Hill	Within Wirku Metamorphics	Granitic gneiss	D1	1319	20	116

Appendix B. (continued)

Sample	Latitude	Longitude	Tectonic Region	Geographic/geologic descriptor	Magmatic suite (if assigned)[b]	Lithological description	Age class[c]	Age[d]	Error[e]	Reference
183492	-26.1451	128.79055	West Musgrave	NNW Mt. West	Wankanki	Porphyritic granite (minor opx)	D1	1322	6	117
180867	-25.79866	128.24322	West Musgrave	SW Pirntirri Mulari	Wankanki	opx-bearing quartz monzonite	D1	1324	7	118
185606	-26.32395	128.11963	West Musgrave	E Borrows Hill	Wankanki	bi-bearing leucogranite	D1	1325	7	119
194333	-25.59694	127.58718	West Musgrave	NW Mt. Finlayson, Tjuni Purlka Zone	Wankanki	Migmatitic gneiss	D1	1341	10	120
194393	-25.56758	127.65356	West Musgrave	NW Ngaturn, Tjuni Purlka Zone	Wankanki	Pyroxene-granitic gneiss	D1	1345	7	121
183587	-26.19088	128.90153	West Musgrave	Michael Hills, Champ de Mars area.	Wankanki	Migmatitic leucogranite (pyroxene-bearing)	Pre-D1	1351	8	122
194764	-25.94153	128.0425	West Musgrave	S Mt. Scott	Papulankutja	hbl-pxn bearing metagranite	Pre-D1	1402	4	100, 123
174538	-25.83923	128.79486	West Musgrave	S Mt. Daisy Bates	Pitjantjatjara (Mirturtu)	Pyroxene-bearing metamonzogranite	D2	1178	8	124
183459	-26.3945	128.94481	West Musgrave	S Latitude Hill	Pitjantjatjara (Punuwarra)	Porphyritic charnockite	D2	1178	12	125
174736	-25.78573	128.60667	West Musgrave	ESE Mt. Fanny	Pitjantjatjara	opx-bearing metasyenogranite	D2	1180	7	126
193850	-25.76625	128.69888	West Musgrave	E Mt. Fanny	Unspecified (intrudes Wirku	Leucogranitic dyke	D2	1181	9	127
174594	-25.91766	128.90576	West Musgrave	Mirturtu Camp	Pitjantjatjara	Meta-leucogabbro	D2	1190	9	128
174747	-25.75855	128.63911	West Musgrave	ENE Mt. Fanny	Pitjantjatjara/Giles Complex (?)	Pxn-gt-bearing metagabbro	D2	1205	24	129
174558	-25.78002	128.66978	West Musgrave	E Mt. Fanny	Pitjantjatjara (Walpa Suite)	Pxn-gt-bearing meta-quartzdiorite	D2	1215	13	130
174737	-25.78596	128.60612	West Musgrave	ESE Mt. Fanny	Pitjantjatjara	gt-hbl-bearing metamonzogranite	D2	1219	12	131
189452	-25.97835	127.78018	West Musgrave	N Lightning Rock	Pitjantjatjara (Waratjarra)	hbl-bearing metagranodiorite	D2	1179	10	132
187199	-25.48075	128.03356	West Musgrave	Walu Rockhole	Pitjantjatjara (Tjuni Purlka Suite)	Dacite	D2	1193	6	133
187196	-25.66124	128.1969	West Musgrave	Prostanthera Hill	Pitjantjatjara	Leucogranite (opx-bearing)	D2	1200	5	134
194802	-25.96641	128.47724	West Musgrave	W Arnold Creek	Pitjantjatjara	Monzogranite	D2	1203	10	135
183496	-26.16352	128.79668	West Musgrave	NW Mt. West	Wankanki	Pyroxene-bearing orthogneiss	D1	1321	7	136
AS2010-66J	-23.60133	133.87729	NAC margin	Southern Aileron	Teapot Granite	Microgranite	Post-D2	1117	10	137
RBN-43	-23.64816	133.50724	NAC margin	Warumpi Province	Teapot Granite	Undeformed pegmatite	Post-D2	1070	26	137
RBN-67	-23.63100	133.51627	NAC margin	Southern Aileron	Teapot Granite	Quartzofeldspathic gneiss	Post-D2	1122	12	137
RBN-71	-23.61459	133.55713	NAC margin	Southern Aileron	Teapot Granite	Granitic gneiss	Post-D2	1126	14	137
RBN-54	-23.62546	133.31737	NAC margin	Warumpi Province	Teapot Granite	Granitic bi-gneiss	Post-D2	1098	12	137
Unspecified	-23.43381	134.49733	NAC margin	Warumpi Province	Teapot Granite	Plagioclase pyroxenite	D2	1133	5	138
84091632			NAC margin	Southern Aileron	Teapot Granite	Granite	D2	1136	6	139
WI43	-66.26012	110.55981	Windmill Islands	Clark Peninsula	Syn-D1 granitoids	Orthogneiss	Pre-D1	1381	5	140
WI43	-66.26012	110.55981	Windmill Islands	Clark Peninsula	Syn-D1 granitoids	Orthogneiss	D1	1323	7	140
WI17	-66.30959	110.51253	Windmill Islands	Mitchell Peninsula	D2a granitoid	Unfoliated bi-bearing granite	D2	1235	7	140
WI84	-66.37493	110.58194	Windmill Islands	South Windmill Islands	Ardery Charnockite	Charnockite (coarse-grained)	D2	1178	7	140
WI85	-66.37463	110.58255	Windmill Islands	Robinson Ridge	Ardery Charnockite	Charnockite (fine-grained)	D2	1178	6	140
54294	-66.24880	110.59813	Windmill Islands	Clark Peninsula	Syn-D1 granitoids	Orthogneiss	D1	1315	6	141
3161193	-66.27789	110.53918	Windmill Islands	Bailey Peninsula	Syn-post D2a granitoids	gt-bearing orthogneiss	D2	1214	10	141
6161293	-66.41124	110.52041	Windmill Islands	Ford Island	Ford Granite	Granite	D2	1173	9	141

Appendix B. (continued)

Sample	Latitude	Longitude	Tectonic Region	Geographic/geologic descriptor	Magmatic suite (if assigned)[b]	Lithological description	Age class[c]	Age[d]	Error[e]	Reference
1011194	-66.45835	110.60322	Windmill Islands	Bosner Island	D2b granitoids*	Charnockite	D2	1163	7	141
6301193	-66.37384	110.58430	Windmill Islands	Robinson Ridge	D2b granitoids*	Aplite dyke	D2	1138	9	141
64294	-66.24880	110.59813	Windmill Islands	Clark Peninsula	Syn-D1 granitoids*	gt-bearing leucosome (in psammitic gneiss)	D1	1342	21	141
33-1	-66.28172	110.51189	Windmill Islands	Bailey Peninsula	D2a granitoids*	gt-bearing granite gneiss	in-between	1247	13	142
33-2	-66.28100	110.51697	Windmill Islands	Near Casey station	D2a granitoids*	gt-bearing granite gneiss	in-between	1258	12	142
34-1	-66.28064	110.51933	Windmill Islands	Near Casey station	D2a granitoids*	gt-bearing granite	in-between	1242	13	142
35-1	-66.37336	110.58625	Windmill Islands	Robinson Ridge	Ardery Charnockite	Charnockite	D2	1196	8	142
35-2	-66.37339	110.58633	Windmill Islands	Robinson Ridge	Ardery Charnockite	Charnockite	D2	1205	13	142
BH100	-66.29787	100.60327	Bunger Hills	SW Bunger Hills	Unnamed	bi-opx tonalite-granite gneiss	in-between	1256	5	143
BH38	-66.17838	100.83523	Bunger Hills	Geologov Island	Paz Cove Batholith	Migmatitic enderbite	D2	1200	6	143
BH98	-66.30894	100.62680	Bunger Hills	SW Bunger Hills	Algae Lake Pluton	Migmatitic enderbite	D2	1203	5	143
86285962	-66.30400	100.61700	Bunger Hills	Central Bunger Hills, Algae Lake	Algae Lake Pluton	Quartz monzogabbro	D2	1171	3	144
86286245	-66.25200	100.83900	Bunger Hills	N Bunger Hills, Paz Cove	Paz Cove Batholith	Quartz monzogabbro	D2	1170	4	144
86285815	-66.10500	101.18800	Bunger Hills	Highjump Archipelago (Booth Peninsula)	Booth Peninsula Batholith	Quartz monzodiorite	D2	1151	4	144

[a]Data are sourced from a combination of geological survey online databases, report books and peer-review publications (complete reference list follows table).
Location coordinates are taken directly from the data source, where provided (and converted to decimal degrees as required). Where not given, approximate coordinates are estimated from geological maps and geographic place names documented in the data source, as well as satellite imagery (approximated coordinates shown in blue).
[b]Where magma suites are inferred, this is indicated with blue text and an asterisk.
[c]Age data are classified according to the D_1/M_1 and D_2/M_2 time periods defined in the main text. The age classification is made on the basis of age value only (i.e. age uncertainties not taken into consideration) for the purposes of visual representation of age data in the main text. Subdivisions: D_1 (ca. 1345–1260 Ma), in-between (ca. 1260–1220 Ma), D_2 (ca. 1220–1130 Ma), Post-D_2 (<ca. 1130 Ma).
[d]Ages are interpreted magma crystallisation ages (interpreted by the original data source) and are pooled ages of individual analyses (generally weighted mean ages; few intercept and concordia ages).
[e]Uncertainties given at a 95 % confidence interval or 2σ level, unless indicated otherwise.
Mineral abbreviations: bi, biotite; gt, garnet; hbl, hornblende; mt, magnetite; opx, orthopyroxene; pxn, pyroxene.

REFERENCES (FOR APPENDIX B)

1. De Waele B. & Pisarevsky S. 2008. Geochronology, paleomagnetism and magnetic fabric of metamorphic rocks in the northeast Fraser Belt, Western Australia. *Australian Journal of Earth Sciences* 55, 605–621.
2. Kirkland, C. L., Wingate, M. T. D. and Spaggiari, CV 2013, 194780: granite pegmatite, Wyralinu Hill; Geochronology Record 1093: Geological Survey of Western Australia, 4p.
3. Kirkland, C. L., Wingate, M. T. D. and Spaggiari, CV 2013, 194787: granite pegmatite, Eyre Highway; Geochronology Record 1095: Geological Survey of Western Australia, 4p.
4. Kirkland et al 2015; Kirkland, C. L., Wingate, M. T. D. and Spaggiari, CV 2013, 194779: metagranite, Wyralinu Hill; Geochronology Record 1092: Geological Survey of Western Australia, 4p.
5. Clark C., Kirkland C. L., Spaggiari C. V., Oorschot C., Wingate M. T. D. & Taylor R. J. 2014. Proterozoic granulite formation driven by mafic magmatism: An example from the Fraser Range Metamorphics, Western Australia. *Precambrian Research* 240, 1–21.
6. Kirkland, C. L., Wingate, M. T. D. and Spaggiari, CV 2013, 194717: metagabbro, Eyre Highway; Geochronology Record 1090: Geological Survey of Western Australia, 5p.
7. Kirkland, C. L., Wingate, M. T. D. and Spaggiari, CV 2013, 194782: granite pegmatite, Eyre Highway; Geochronology Record 1094: Geological Survey of Western Australia, 5p.
8. Kirkland, C. L., Wingate, M. T. D., Howard, HM and Spaggiari, CV 2013, 183653: pegmatite, Mount Malcolm; Geochronology Record 1086: Geological Survey of Western Australia, 4p.
9. Kirkland, C. L., Wingate, M. T. D. and Spaggiari, CV 2013, 194776: metagranite, Southern Hills Homestead; Geochronology Record 1091: Geological Survey of Western Australia, 4p.
10. Kirkland, C. L., Wingate, M. T. D., Spaggiari, CV and Howard, HM 2013, 183671: granitic gneiss, Cullinia Rocks; Geochronology Record 1087: Geological Survey of Western Australia, 4p.
11. Wingate, M. T. D., Lu, Y, Kirkland, C. L. and Spaggiari, CV 2016, 194781: metagabbro, Bullock Hills Dam; Geochronology Record 1320: Geological Survey of Western Australia, 4p.
12. Kirkland et al 2011, 2015; Kirkland, C. L., Wingate, M. T. D. and Spaggiari, CV 2012, 194711: metamonzogranite, Kent Dam; Geochronology Record 1044: Geological Survey of Western Australia, 4p.
13. Kirkland, C. L., Wingate, M. T. D., Spaggiari, CV and Pawley, MJ 2010, 194719: metasyenogranite, Symons Hill; Geochronology Record 848: Geological Survey of Western Australia, 5p.
14. Kirkland C. L., Spaggiari C. V., Pawley M. J., Wingate M. T. D., Smithies R. H., Howard H. M., Tyler I. M., Belousova E. A. & Poujol M. 2011. On the edge: U–Pb, Lu–Hf, and Sm–Nd data suggests reworking of the Yilgarn craton margin during formation of the Albany–Fraser Orogen. *Precambrian Research* 187, 223–247.
15. Clark D. J., Kinny P. D., Post N. J. & Hensen B. J. 1999. Relationships between magmatism, metamorphism and deformation in the Fraser Complex, Western Australia: Constraints from new SHRIMP U–Pb zircon geochronology. *Australian Journal of Earth Sciences* 46, 923–932.
16. Kirkland, C. L., Wingate, M. T. D. and Spaggiari, CV 2011, 194715: leucosome in psammitic gneiss, Gnama Hill; Geochronology Record 1000: Geological Survey of Western Australia, 4p.
17. Wingate, M. T. D., Lu, Y, Kirkland, C. L. and Spaggiari, CV 2016, 182459: equigranular metatonalite, Splinter prospect; Geochronology Record 1301: Geological Survey of Western Australia, 4p.
18. Kirkland, C. L., Wingate, M. T. D. and Spaggiari, CV 2012, 182474: granite vein, Big Red prospect; Geochronology Record 1051: Geological Survey of Western Australia, 4p.
19. Kirkland, C. L., Wingate, M. T. D. and Spaggiari, CV 2014, 192586: monzogranite, Scott Rocks; Geochronology Record 1216: Geological Survey of Western Australia, 4p.
20. Wingate, M. T. D., Lu, Y, Kirkland, C. L. and Spaggiari, CV 2016, 182465: metagabbro, Splinter prospect; Geochronology Record 1304: Geological Survey of Western Australia, 4p.
21. Wingate, M. T. D., Lu, Y, Kirkland, C. L. and Spaggiari, CV 2016, 194839: metamonzogranite, Thistle Cove; Geochronology Record 1326: Geological Survey of Western Australia, 4p.
22. Kirkland, C. L., Wingate, M. T. D., Spaggiari, CV and Pawley, MJ 2012, 184374: monzogranite, Mount Ridley; Geochronology Record 1045: Geological Survey of Western Australia, 4p.
23. Wingate, M. T. D., Lu, Y, Kirkland, C. L. and Spaggiari, CV 2016, 194840: metamonzogranite, Thistle Cove; Geochronology Record 1327: Geological Survey of Western Australia, 4p.
24. Wingate, M. T. D., Lu, Y, Kirkland, C. L. and Spaggiari, CV 2015, 182462: garnetiferous metagabbro, Splinter prospect; Geochronology Record 1302: Geological Survey of Western Australia, 6p.
25. Wingate, M. T. D. and Bodorkos, S 2007, 177909: monzogranite gneiss, Yardilla Bore; Geochronology Record 659: Geological Survey of Western Australia, 4p.
26. Kirkland, C. L., Wingate, M. T. D. and Spaggiari, CV 2012, 194783: metamonzogranite: Newman Rock; Geochronology Record 1027: Geological Survey of Western Australia, 4p.
27. Kirkland, C. L., Wingate, M. T. D. and Spaggiari, CV 2011, 194712: metasyenogranite, west of Boingaring Rocks; Geochronology Record 997: Geological Survey of Western Australia, 4p.
28. Kirkland, C. L., Wingate, M. T. D. and Spaggiari, CV 2011, 194710: metagranite, southwest of Boingaring Rocks; Geochronology Record 996: Geological Survey of Western Australia, 4p.
29. Wingate, M. T. D., Lu, Y, Kirkland, C. L. and Spaggiari, CV 2016, 194786: monzogranite gneiss, Charlina Granite Rock; Geochronology Record 1321: Geological Survey of Western Australia, 4p.
30. Wingate, M. T. D., Lu, Y, Kirkland, C. L. and Spaggiari, CV 2016, 194883: metamonzogranite, Mardarbilla Rock; Geochronology Record 1328: Geological Survey of Western Australia, 4p.
31. Wingate, M. T. D., Lu, Y, Kirkland, C. L. and Spaggiari, CV 2016, 194836: metagranodiorite, Hellfire Bay; Geochronology Record 1325: Geological Survey of Western Australia, 5p.
32. Kirkland, C. L., Wingate, M. T. D. and Spaggiari, CV

2012, 182476: migmatitic gneiss Big Red prospect; Geochronology Record 1053: Geological Survey of Western Australia, 4p.

33. Kirkland, C. L., Wingate, M. T. D. and Spaggiari, CV 2014, 194876: alkali feldspar metagranite, Gora Hill; Geochronology Record 1221: Geological Survey of Western Australia, 5p.
34. Nelson, DR 1995, 83700A: hornblende–biotite syenogranite gneiss, Coramup Hill Quarry; Geochronology Record 82: Geological Survey of Western Australia, 4p.
35. Nelson, DR 1995, 83690: biotite granodiorite gneiss, Bald Rock; Geochronology Record 78: Geological Survey of Western Australia, 4p.
36. Nelson, DR 1995, 83697: biotite monzogranite gneiss, Mount Burdett; Geochronology Record 81: Geological Survey of Western Australia, 4p.
37. Bodorkos, S and Wingate, M. T. D. 2008, 184326: pegmatitic leucogranite, Short Beach headland; Geochronology Record 711: Geological Survey of Western Australia, 6p.
38. Kirkland, C. L., Wingate, M. T. D. and Spaggiari, CV 2011, 194703: pegmatitic leucosome in quartzofeldspathic gneiss, Double Tank; Geochronology Record 984: Geological Survey of Western Australia, 4p.
39. Kirkland, C. L., Wingate, M. T. D. and Spaggiari, CV 2011, 194704: quartzofeldspathic gneiss, Double Tank; Geochronology Record 986: Geological Survey of Western Australia, 5p.
40. Kirkland, C. L., Wingate, MTD and Spaggiari, CV 2011, 194708: leucosome in metamonzogranite, Mount Andrew Track; Geochronology Record 989: Geological Survey of Western Australia, 5p.
41. Nelson, DR 1995, 83663: granodiorite gneiss, Israelite Bay; Geochronology Record 74: Geological Survey of Western Australia, 4p.
42. Nelson, DR 1995, 83662: biotite–hornblende monzogranite gneiss, Poison Creek; Geochronology Record 86: Geological Survey of Western Australia, 4p.
43. Nelson, DR 1995, 83667: porphyritic biotite granite, Balladonia Rock; Geochronology Record 76: Geological Survey of Western Australia, 4p.
44. Nelson, DR 1995, 83657A: porphyritic biotite monzogranite, Esperance Harbour jetty; Geochronology Record 100: Geological Survey of Western Australia, 4p.
45. Black L. P., Harris L. B. & Delor C. P. 1992. Reworking of Archaean and early Proterozoic components during a progressive, middle Proterozoic tectonothermal event in the Albany Mobile Belt, Western Australia. *Precambrian Research* 59, 95–123.
46. Pidgeon, R. T. 1990. Timing of plutonism in the Proterozoic Albany mobile belt, southwestern Australia. *Precambrian Research* 47: 157–167.
47. Lu, Y., Wingate, M. T. D., Kirkland, C. L., Goscombe, B and Wyche, S 2015, 192956: metagabbro, Hanna farm; Geochronology Record 1281: Geological Survey of Western Australia, 4p.
48. Clark D. J., Hensen B. J. & Kinny P. D. 2000. Geochronological constraints for a two-stage history of the Albany–Fraser Orogen, Western Australia. *Precambrian Research* 102, 155–183.
49. Nelson, DR 2005, 178072: tonalitic gneiss, Haig Cave; Geochronology Record 598: Geological Survey of Western Australia, 4p.
50. Nelson, DR 2005, 178071: recrystallized biotite microtonalite, Haig Cave; Geochronology Record 597: Geological Survey of Western Australia, 4p.
51. Nelson, DR 2005, 178070: amphibolite, Haig Cave; Geochronology Record 596: Geological Survey of Western Australia, 4p.
52. Wingate, M. T. D., Lu, Y, Kirkland, C. L. and Spaggiari, CV 2015, 192565: metamonzogranite, Moodini prospect; Geochronology Record 1269: Geological Survey of Western Australia, 4p.
53. Wingate, M. T. D., Lu, Y, Kirkland, C. L. and Spaggiari, CV 2015, 192566: metamonzogranite, Moodini prospect; Geochronology Record 1270: Geological Survey of Western Australia, 4p.
54. Wingate, M. T. D., Lu, Y, Spaggiari, CV and Smithies, R. H. 2016, 206778: coarse-grained monzogabbro, Madura Province; Geochronology Record 1292: Geological Survey of Western Australia, 4p.
55. Wingate, M. T. D., Lu, Y, Spaggiari, CV and Smithies, R. H. 2016, 206779: medium-grained monzogabbro, Madura Province; Geochronology Record 1293: Geological Survey of Western Australia, 4p.
56. Wingate, M. T. D., Lu, Y, Kirkland, C. L., Spaggiari, CV and Smithies, R. H. 2016, 192595: biotite-hornblende granodiorite, Madura Province; Geochronology Record 1290: Geological Survey of Western Australia, 4p.
57. Wingate, M. T. D., Lu, Y, Spaggiari, CV and Smithies, R. H. 2016, 206754: metagranodiorite, Madura Province; Geochronology Record 1291: Geological Survey of Western Australia, 4p.
58. Kirkland, C. L., Wingate, M. T. D. and Spaggiari, CV 2013, 192558: granitic gneiss, Haig Cave; Geochronology Record 1089: Geological Survey of Western Australia, 4p.
59. Kirkland, C. L., Wingate, M. T. D. and Spaggiari, CV 2013, 192557: metagabbro, Haig Cave; Geochronology Record 1140: Geological Survey of Western Australia, 4p.
60. Wingate, M. T. D., Lu, Y, Spaggiari, CV and Smithies, R. H. 2015, 213838: monzogranite vein, Forrest Zone; Geochronology Record 1278: Geological Survey of Western Australia, 4p.
61. Wingate, M. T. D., Lu, Y, Spaggiari, CV and Smithies, R. H. 2015, 206753: equigranular syenogranite, Forrest Zone; Geochronology Record 1277: Geological Survey of Western Australia, 4p.
62. Wingate, M. T. D., Lu, Y, Spaggiari, CV and Smithies, R. H. 2015, 206752: porphyritic syenogranite, Forrest Zone; Geochronology Record 1276: Geological Survey of Western Australia, 4p.
63. Wingate, M. T. D., Lu, Y, Spaggiari, CV and Smithies, R. H. 2015, 206729: biotite–hornblende diorite, Forrest Zone; Geochronology Record 1273: Geological Survey of Western Australia, 4p.
64. Wingate, M. T. D., Lu, Y, Kirkland, C. L. and Spaggiari, C. V. 2015, 192593: hornblende–biotite metagranite, Forrest Zone; Geochronology Record 1272: Geological Survey of Western Australia, 4p.
65. Spaggiari and Smithies 2015; Kirkland C. L., Wingate, M. T. D., Spaggiari, CV and Tyler, IM (2011) 194773: granitic rock, Eucla No.1 drillhole; Geochronology Record 001: Geological Survey of Western Australia, 4p.
66. Dutch R. A., Werner M. X., Krapf C. B. E. & Rusak T. 2013. Geology of the Tieyon 1:100 000 map sheet (5645), Report Book 2013/00011. Geological Survey of South

Australia. Department for Manufacturing, Innovation, Trade, Resources and Energy, South Australia, Adelaide.

67. Bodorkos, S, Love, GJ and Wingate, M. T. D. 2006, 180299: fi ne-grained metagranite, Mount Gosse; Geochronology Record 652: Geological Survey of Western Australia, 5p.
68. Bodorkos, S, Love, GJ and Wingate, M. T. D. 2006, 180256: metagranodiorite, Hubert Soak; Geochronology Record 649: Geological Survey of Western Australia, 5p.
69. Bodorkos, S, Love, GJ and Wingate, M. T. D. 2006, 180262: mylonitic syenogranite, Hubert Soak; Geochronology Record 650: Geological Survey of Western Australia, 4p.
70. Bodorkos, S, Love, GJ and Wingate, M. T. D. 2006, 180300: porphyritic metamonzogranite, Mount Gosse; Geochronology Record 653: Geological Survey of Western Australia, 4p.
71. Bodorkos, S, Love, GJ and Wingate, M. T. D. 2006, 180270: metamonzogranite dyke, Mount Gosse; Geochronology Record 651: Geological Survey of Western Australia, 4p.
72. Sen, A, Kirkland, C. L. and Wingate, M. T. D. 2010, 191763: granitic pegmatite dyke, Minnie Hill; Geochronology Record 919: Geological Survey of Western Australia, 4p.
73. Kirkland, C. L., Wingate, M. T. D. and Smithies, R. H. 2013, 189522: leucogranite, Lightning Rock; Geochronology Record 1133: Geological Survey of Western Australia, 5p.
74. Kirkland, C. L., Wingate, M. T. D. and Smithies, R. H. 2012, 189547: granodiorite, Cooper; Geochronology Record 1064: Geological Survey of Western Australia, 4p.
75. Kirkland, C. L., Wingate, M. T. D. and Evins, P. M. 2010, 190231: granite, southwest of Prostanthera Hill; Geochronology Record 914: Geological Survey of Western Australia, 4p.
76. Kirkland, C. L., Wingate, M. T. D. and Evins, P. M. 2010, 194376: norite dyke, Minnie Hill; Geochronology Record 921: Geological Survey of Western Australia, 4p.
77. Kirkland, C. L., Wingate, M. T. D., Bodorkos, S and Smithies, R. H. 2009, 185591: garnet-rich leucogranite, Latitude Hill; Geochronology Record 761: Geological Survey of Western Australia, 4p.
78. Wingate, M. T. D., Kirkland, C. L., Smithies, R. H., Howard, HM and Quentin De Gromard, R 2015, 208506: foliated metamonzogranite, Gungungmura Waterhole; Geochronology Record 1255: Geological Survey of Western Australia, 4p.
79. Kirkland, C. L., Wingate, M. T. D. and Smithies, R. H. 2009, 189523: metagranodiorite, Lightning Rock; Geochronology Record 826: Geological Survey of Western Australia, 4p.
80. Kirkland, C. L., Wingate, M. T. D. and Evins, ME 2013, 194367: syenogranite, Ngaturn; Geochronology Record 1134: Geological Survey of Western Australia, 5p.
81. Kirkland, C. L., Wingate, M. T. D. and Smithies, R. H. 2012, 180860: metamonzogranite, Pirrul Bore; Geochronology Record 1058: Geological Survey of Western Australia, 4p.
82. Sen, A, Kirkland, C. L., Wingate, M. T. D. and Smithies, R. H. 2010, 191751: migmatitic granite, Red Rock; Geochronology Record 918: Geological Survey of Western Australia, 4p.
83. Wingate, M. T. D., Smithies, R. H., Howard, HM and Quentin De Gromard, R 2015, 208504: foliated metamonzogranite, Yulun-Kudara Waterhole; Geochronology Record 1254: Geological Survey of Western Australia, 4p.
84. Kirkland, C. L., Wingate, M. T. D. and Bodorkos, S 2007, 183509: leucogranite dyke, Mount West; Geochronology Record 724: Geological Survey of Western Australia, 4p.
85. Kirkland, C. L., Wingate, M. T. D., Smithies, R. H., Howard, HM and Quentin De Gromard, R 2014, 201320: leucogranite vein, Wanarn; Geochronology Record 1223: Geological Survey of Western Australia, 4p.
86. Kirkland, C. L., Bodorkos, S Wingate, M. T. D. and Smithies, R. H. 2009, 184147: undeformed granite dyke, Borrows Hill; Geochronology Record 822: Geological Survey of Western Australia, 4p.
87. Kirkland, C. L., Wingate, M. T. D. and Smithies, R. H. 2010, 187154: mafic granulite, Hubert Soak; Geochronology Record 911: Geological Survey of Western Australia, 4p.
88. Kirkland, C. L., Bodorkos, S., Wingate, M. T. D. and Smithies, R. H. 2009, 184149: stromatic migmatite, Borrows Hill; Geochronology Record 824: Geological Survey of Western Australia, 4p.
89. Kirkland, C. L., Wingate, M. T. D. and Smithies, R. H. 2012, 187171: charnockitic syenogranite, Prostanthera Hill; Geochronology Record 1041: Geological Survey of Western Australia, 5p.
90. Kirkland, C. L., Wingate, M. T. D. and Evins, P 2010, 194421: basaltic andesite, Mulaggora Hills; Geochronology Record 837: Geological Survey of Western Australia, 4p.
91. Wingate, M. T. D., Kirkland, C. L., Smithies, R. H., Quentin De Gromard, R and Howard, HM 2015, 201305: granite pegmatite, Yulun-Kudara Waterhole; Geochronology Record 1250: Geological Survey of Western Australia, 4p.
92. Kirkland, C. L., Wingate, M. T. D. and Evins, P 2011, 194485: pegmatitic leucosome, Finlay Range; Geochronology Record 931: Geological Survey of Western Australia, 5p.
93. Kirkland, C. L., Bodorkos, S, Wingate, M. T. D. and Smithies, R. H. 2009, 187105: foliated schlieric leucogranite, Mt Aloysius; Geochronology Record 796: Geological Survey of Western Australia, 6p.
94. Kirkland, C. L., Wingate, M. T. D. and Smithies, R. H. 2011, 187174: metasandstone, Prostanthera Hill; Geochronology Record 933: Geological Survey of Western Australia, 5p.
95. Kirkland, C. L., Wingate, M. T. D. and Evins, P. M. 2011, 190228: biotite–hornblende granite, Mount Scott; Geochronology Record 839: Geological Survey of Western Australia, 4p.
96. Kirkland, C. L., Wingate, M. T. D. and Smithies, R. H. 2012, 187179: metamonzogranite, Prostanthera Hill; Geochronology Record 1063: Geological Survey of Western Australia, 4p.
97. Wingate, M. T. D., Quentin De Gromard, R, Howard, HM and Smithies, R. H. 2015, 208500: granite pegmatite, Yulun-Kudara Waterhole; Geochronology Record 1252: Geological Survey of Western Australia, 5p.
98. Kirkland, C. L., Wingate, M. T. D. and Bodorkos, S 2009, 187113: folded pegmatite vein, Mount Aloysius; Geochronology Record 798: Geological Survey of Western Australia, 4p.

99. Kirkland, C. L., Bodorkos, S, Wingate, M. T. D. and Smithies, R. H. 2009, 185590: charnockite, Latitude Hill; Geochronology Record 764: Geological Survey of Western Australia, 6p.

100. Kirkland C. L., Smithies R. H., Woodhouse A. J., Howard H. M., Wingate M. T. D., Belousova E. A., Cliff J. B., Murphy R. C. & Spaggiari C. V. 2013. Constraints and deception in the isotopic record; the crustal evolution of the west Musgrave Province, central Australia. *Gondwana Research* 23, 759–781.

101. Kirkland, C. L., Wingate, M. T. D. and Smithies, R. H. 2012, 194766: granite pegmatite vein, Mount Scott; Geochronology Record 1039: Geological Survey of Western Australia, 4p.

102. Kirkland, C. L., Bodorkos, S, Wingate, M. T. D. and Smithies, R. H. 2009, 185610: coarse-grained leucogranite, Borrows Hill; Geochronology Record 794: Geological Survey of Western Australia, 4p.

103. Kirkland, C. L., Wingate, M. T. D., Bodorkos, S and Smithies, R. H. 2009, 184146: syenogranite, Borrows Hill; Geochronology Record 823: Geological Survey of Western Australia, 4p.

104. Kirkland, C. L., Wingate, M. T. D., Bodorkos, S and and Howard, HM 2009, 187274: laminated paragneiss, Murray Range; Geochronology Record 825: Geological Survey of Western Australia, 4p.

105. Wingate, M. T. D., Bodorkos, S, Kirkland, C. L. and Smithies, R. H. 2009, 185593: leucogranite, Latitude Hill; Geochronology Record 762: Geological Survey of Western Australia, 5p.

106. Kirkland, C. L., Wingate, M. T. D., Bodorkos, S and Howard, H 2009, 185339: mylonitic granite, Hazlett Rocks; Geochronology Record 768: Geological Survey of Western Australia, 4p.

107. Kirkland, C. L., Wingate, M. T. D. and Smithies, R. H. 2011, 187172: granite pegmatite, Prostanthera Hill; Geochronology Record 991: Geological Survey of Western Australia, 4p.

108. Kirkland, C. L., Wingate, M. T. D. and Smithies, R. H. 2012, 187166: metasyenogranite, Murray Range; Geochronology Record 1062: Geological Survey of Western Australia, 4p.

109. Kirkland, C. L., Wingate, M. T. D. and Bodorkos, S 2012, 184158: metamonzogranite, Kampurarr Pirti; Geochronology record 1060: Geological Survey of Western Australia, 5p.

110. Kirkland, C. L., Wingate, M. T. D. and Evins, P. M. 2011, 194379: biotite granite, Minnie Hill; Geochronology Record 929: Geological Survey of Western Australia, 4p.

111. Kirkland, C. L., Wingate, M. T. D. and Smithies, R. H. 2012, 187151: metamonzogranite, Blackstone; Geochronology Record 1061: Geological Survey of Western Australia, 4p.

112. Kirkland, C. L., Bodorkos, S, Wingate, M. T. D. and Smithies, R. H. 2009, 185581: foliated biotite monzogranite, MacDougall Bluff; Geochronology Record 766: Geological Survey of Western Australia, 4p.

113. Kirkland, C. L., Wingate, M. T. D. and Smithies, R. H. 2012, 183726: leucogranitic gneiss, Michael Hills; Geochronology Record 1046: Geological Survey of Western Australia, 5p.

114. Kirkland, C. L., Wingate, M. T. D. and Smithies, R. H. 2014, 194804: metamonzogranite, Mount Clianthus; Geochronology Record 1197: Geological Survey of Western Australia, 4p.

115. Kirkland, C. L., Wingate, M. T. D. and Smithies, R. H. 2012, 194765: syenogranite, Mount Scott; Geochronology Record 1040: Geological Survey of Western Australia, 4p.

116. Kirkland, C. L., Wingate, M. T. D. and Evins, P. M. 2011, 194381: granitic gneiss, Minnie Hill; Geochronology Record 928: Geological Survey of Western Australia, 5p.

117. Kirkland, C. L., Wingate, M. T. D., Bodorkos, S and Smithies, R. H. 2009, 183492: K-feldspar porphyritic granite, Mount West; Geochronology Record 757: Geological Survey of Western Australia, 4p.

118. Kirkland, C. L., Wingate, M. T. D., Evins, P. M. and Smithies, R. H. 2009, 180867: quartz monzonite, Mount Holt; Geochronology Record 910: Geological Survey of Western Australia, 4p.

119. Kirkland, C. L., Wingate, M. T. D., Bodorkos, S and Smithies, R. H. 2009, 185606: foliated biotite leucogranite, Borrows Hill; Geochronology Record 793: Geological Survey of Western Australia, 4p.

120. Kirkland, C. L., Wingate, M. T. D. and Evins, P. M. 2011, 194333: migmatitic gneiss, Mount Finlayson; Geochronology Record 938: Geological Survey of Western Australia, 5p.

121. Kirkland, C. L., Wingate, M. T. D. and Evins, P. M. 2010, 194393: granitic gneiss, Ngaturn; Geochronology Record 920: Geological Survey of Western Australia, 4p.

122. Kirkland, C. L., Wingate, M. T. D., Bodorkos, S and Smithies, R. H. 2009, 183587: migmatitic leucogranite, Michael Hills; Geochronology Record 759: Geological Survey of Western Australia, 5p.

123. Kirkland, C. L., Wingate, M. T. D. and Smithies, R. H. 2010, 194764: monzogranite, Mount Scott; Geochronology Record 965: Geological Survey of Western Australia, 4p.

124. Bodorkos, S, Wingate, M. T. D. and Kirkland, C. L. 2008, 174538: metamonzogranite, Mount Daisy Bates; Geochronology Record 712: Geological Survey of Western Australia, 4p.

125. Kirkland, C. L., Wingate, M. T. D. and Bodorkos, S. 2008, 183459: charnockite, Latitude Hill; Geochronology Record 722: Geological Survey of Western Australia, 5p.

126. Bodorkos, S., Wingate, M. T. D. and Kirkland, C. L. 2008, 174736: granofelsic metasyenogranite, Mount Fanny; Geochronology Record 717: Geological Survey of Western Australia, 4p.

127. Kirkland, C. L., Wingate, M. T. D. and Bodorkos, S. 2008, 193850: leucogranite dyke, Mount Fanny; Geochronology Record 748: Geological Survey of Western Australia, 4p.

128. Bodorkos, S. and Wingate, M. T. D. 2008, 174594: metamorphosed leucogabbro, Mirturtu Camp; Geochronology Record 716: Geological Survey of Western Australia, 4p.

129. Bodorkos, S. Wingate, M. T. D. and Kirkland, C. L. 2008, 174747: metagabbro, Mount Fanny; Geochronology Record 719: Geological Survey of Western Australia, 4p.

130. Bodorkos, S. Wingate, M. T. D. and Kirkland, C. L. 2008, 174558: metamorphosed quartz diorite, Mount Fanny; Geochronology Record 713: Geological Survey of Western Australia, 4p.

131. Bodorkos, S. Wingate, M. T. D. and Kirkland, C. L.

2008, 174737: foliated metamonzogranite, Mount Fanny; Geochronology Record 718: Geological Survey of Western Australia, 5p.

132. Kirkland, C. L., Wingate, M. T. D. and Smithies, R. H. 2013, 189452: metagranodiorite, Lightning Rock; Geochronology Record 1132: Geological Survey of Western Australia, 4p.
133. Kirkland, C. L., Wingate, M. T. D. and Smithies, R. H. 2013, 187199: dacite, Walu Rockhole; Geochronology Record 1131: Geological Survey of Western Australia, 4p.
134. Kirkland, C. L., Wingate, M. T. D. and Smithies, R. H. 2013, 187196: leucogranite, Prostanthera Hill; Geochronology Record 1130: Geological Survey of Western Australia, 4p.
135. Kirkland, C. L., Wingate, M. T. D., Howard, H. M. and Smithies, R. H., M 2013, 194802: monzogranite, Arnold Creek; Geochronology Record 1145: Geological Survey of Western Australia, 4p.
136. Kirkland, C. L., Wingate, M. T. D. and Bodorkos, S. 2008, 183496: orthogneiss, Mount West; Geochronology Record 747: Geological Survey of Western Australia, 5p.
137. Wong B. L., Morrissey L. J., Hand M., Fields C. E. & Kelsey D. E. 2015. Grenvillian-aged reworking of late Paleoproterozoic crust of the southern North Australian Craton, central Australia: Implications for the assembly of Mesoproterozoic Australia. *Precambrian Research* 270, 100–123.
138. Claoué-Long J. C. & Hoatson D. M. 2005. Proterozoic mafic–ultramafic intrusions in the Arunta Region, central Australia: Part 2: Event chronology and regional correlations. *Precambrian Research* 142, 134–158.
139. Black L. P. & Shaw R. D. 1995. An assessment, based on U–Pb zircon data, of Rb–Sr dating in the Arunta , central Australia. *Precambrian Research* 71, 3–15.
140. Morrissey L. J., Payne J. L., Hand M., Clark C., Taylor R., Kirkland C. L. & Kylander-Clark A. 2017. Linking the Windmill Islands, east Antarctica and the Albany–Fraser Orogen: Insights from U–Pb zircon geochronology and Hf isotopes. *Precambrian Research* 293, 131–149.
141. Post N. J. 2000. Unravelling Gondwana fragments: an integrated structural, isotopic and petrographic investigation of the Windmill Islands, Antarctica. PhD Thesis. University of New South Wales, Sydney.
142. Zhang S., Zhao Y., Liu X., Liu Y., Hou K., Li C. & Ye H. 2012. U–Pb geochronology and geochemistry of the bedrocks and moraine sediments from the Windmill Islands: Implications for Proterozoic evolution of East Antarctica. *Precambrian Research* 206–207, 52–71.
143. Tucker N. M., Payne J. L., Clark C., Hand M., Taylor R. J., Kylander-Clark A. R. C. & Martin L. 2017. Proterozoic reworking of Archean (Yilgarn) basement in the Bunger Hills, East Antarctica. *Precambrian Research* 298, 16–38.
144. Sheraton J. W., Black L. P. & Tindle A. G. 1992. Petrogenesis of plutonic rocks in a Proterozoic granulite-facies terrane — the Bunger Hills, East Antarctica. *Chemical Geology* 97, 163–198.

Appendix C. Compiled U–Pb MAFWO Mesoproterozoic metamorphic age data (ca. 1410–1120 Ma)[a]

Sample No.	Latitude	Longitude	Tectonic region	Geographic descriptor	Lithological unit[b]	Lithological description	Interpreted age (Ma)[c]	Chronometer	Reference
8628-6264	-65.98401	101.067	Highjump Archipelago	North Raketa Island	Association 3[3]	gt–sill–ru gneiss	1188 ± 12*	Monazite	1
8628-5607	-66.067	100.68199	Highjump Archipelago	Geografov Island	Association 3[3]	gt–sill–ru gneiss	1161 ± 18*	Monazite	1
8628-6251	-66.049	101.25198	Highjump Archipelago	Zabyyty Island	Association 3[3]	gt–cd gneiss	1186 ± 11*	Monazite	1
BH20	-66.25148	100.68945	Bunger Hills	Central Bunger Hills	Association 4	gt–cd–sill–bi–mt gneiss	1245–1157^	Monazite	2
BH23	-66.251	100.68997	Bunger Hills	Central Bunger Hills	Association 4	gt–cd–bi–mt–sp gneiss	1195–1153, 1257^	Monazite	2
BH32	-66.21308	100.67292	Bunger Hills	NW Bunger Hills	Association 4	gt–cd–sill gneiss	1220–1144, 1277^	Monazite	2
							1235–1192, 1310, 1473^	Zircon	2
BH44	-66.27483	100.73867	Bunger Hills	Central Bunger Hills	Association 4	gt–cd–mt–sp gneiss, with opx-leucosomes	1260–1122, 1313^	Monazite	2
BH48	-66.27469	100.73612	Bunger Hills	Central Bunger Hills	Association 4	gt–cd–mt–sp gneiss, with opx-leucosomes	1241–1087^	Monazite	2
BH54	-66.27469	100.73612	Bunger Hills	Central Bunger Hills	Association 4	gt–cd–mt–sp ± sill gneiss	1256–1143^	Monazite	2
							1268–1201, 1365^	Zircon	2, 3
BH74	-66.28866	100.78637	Bunger Hills	NE Bunger Hills	Association 3	gt–cd–sill gneiss	1254–1142, 1364, 1324^	Monazite	2
							1295–1186, 1414^	Zircon	2
BH62	-66.31158	100.87607	Bunger Hills	SE Bunger Hills	Association 1	gt–cd–opx ± sa gneiss	1221 ± 37*	Zircon	3
BH67	-66.30621	100.8344	Bunger Hills	SE Bunger Hills	Association 1	opx-bearing tonalitic–granodioritic gneiss	1245 ± 19*	Zircon	3
BH95	-66.32544	100.63867	Bunger Hills	South Bunger Hills	Association 1	gt–cd–sp–opx gneiss	ca. 1300–1200^	Zircon	3
86285628	-66.10100	100.958	Highjump Archipelago	Thomas Island	Association 3[3]	Granodioritic gneiss	1190 ± 15*	Zircon	4
194767	-25.83338	128.05254	West Musgrave	North of Mt. Scott	Papulankutja gneiss	Psammitic enclave within gt-bearing gneiss	1205–1154^ 1313 ± 15*	Zircon	5
194768	-25.84559	128.04451	West Musgrave	North of Mt. Scott	Papulankutja gneiss	Migmatitic paragneiss (diatexite)	1206–1167^ 1311 ± 21*	Zircon	5
187195	-25.84743	128.05779	West Musgrave	North of Mt. Scott	Papulankutja gneiss	gt-bearing leucogranitic gneiss (diatexite)	1196, 1179^ 1298^ (metm/mag?)	Zircon	5
194764	-25.94153	128.0425	West Musgrave	South of Mt. Scott	Papulankutja gneiss	foliated hbl–pxn-bearing monzogranite	1316^	Zircon	5
CHR124	-26.10175	127.63714	West Musgrave	Cohn Hill	Wirku Metamorphics	gt–sill–pl–ksp–ilm–q	1263–1163^	Monazite	6
CHR33	-26.07659	127.62679	West Musgrave	Cohn Hill	Wirku Metamorphics	gt–sill–pl–ksp–ilm	1234–1162^	Monazite	6
CHR17	-26.05002	127.63301	West Musgrave	Cohn Hill	Wirku Metamorphics	gt–sill–pl–ksp–ilm	1246–1155^	Monazite	6
MW4	-26.20247	128.7811	West Musgrave	Mt. West	Wirku Metamorphics	gt–sill–sp–pl–ksp–ilm–q	1219–1116, 1040, 1020^	Monazite	6
195353	-26.34968	128.01083	West Musgrave	Mt. Blythe	Wirku Metamorphics	gt–sill–sp–pl–ksp–ilm–q	1244–1152, 1318^	Monazite	6
LH7	-26.42168	128.96791	West Musgrave	Latitude Hills	Wirku Metamorphics	gt–sill–sp–ksp–ilm–q	1147–1111^	Monazite	6
ETR512	-26.07991	132.97526	East Musgrave	Eateringinna	Birksgate Complex	gt–sill–sp–pl–ksp–ilm–q	1251–1193, >1300^	Monazite	6
R2017275	-26.06521	133.17531	East Musgrave	near Kulgera	Birksgate Complex	gt–sill–cd–mt gneiss	1173 ± 9*	Monazite	7
K9	-25.78906	133.29391	East Musgrave	near Kulgera	Birksgate Complex	gt–sill–cd–mt gneiss	1190 ± 7*	Monazite	7
K6	-25.79746	133.29307	East Musgrave	near Kulgera	Birksgate Complex	sill–cd–mt gneiss	1171 ± 8*	Monazite	7
R1039161	-26.15138	133.80563	East Musgrave	Tieyon	Birksgate Complex	Foliated bi-bearing monzogranite	1158 ± 8*	Zircon	8
R1842262	-26.32798	133.61522	East Musgrave	Tieyon	Birksgate Complex	Foliated bi–hbl-metamonzogranite	ca. 1140^	Zircon	8
R1842265	-26.17809	133.84262	East Musgrave	Tieyon	Birksgate Complex	Migmatitic pelitic gneiss	1168 ± 7*	Zircon	8
R1842269	-26.17906	133.82968	East Musgrave	Tieyon	Birksgate Complex	bi–hbl–pxn-bearing quartzofeldspathic gneiss	1154 ± 19*	Zircon	8
R1039159	-26.18510	133.83375	East Musgrave	Tieyon	Birksgate Complex	Quartzofeldspathic gneiss	1153 ± 8*	Zircon	8
182485	-30.36870	126.19797	Madura Province	Drillcore BKD2, Burkin Prospect	Burkin Gneiss (informal)	Migmatitic gneiss	1478 ± 4*	Zircon	9

Appendix C. (continued)

Sample No.	Latitude	Longitude	Tectonic region	Geographic descriptor	Lithological unit[b]	Lithological description	Interpreted age (Ma)[c]	Chronometer	Reference
177910	-31.95641	122.83252	Fraser Zone (margin)	near Peters Dam, Fraser Range	Fraser Range Metamorphics(?)	Metasandstone	1304 ± 7*	Zircon	10
182477	-30.27426	124.95861	Nornalup Zone	Drillcore BRDDH002, Big Red Prospect	Unspecified	Mafic granulite	1188 ± 4*	Zircon	11
182473	-30.27393	124.98043	Nornalup Zone	Drillcore BRDDH001, Big Red Prospect	Barren Basin or Arid Basin	Migmatitic gneiss	1193 ± 5*	Zircon	12
182475	-30.27393	124.98043	Nornalup Zone	Drillcore BRDDH001, Big Red Prospect	Barren Basin or Arid Basin	Migmatitic gneiss	1176 ± 10*	Zircon	13
182203	-32.16574	125.12543	Nornalup Zone	Drillcore Hannah1, N Eyre Highway	Recherche SS/Fraser gabbro(?)	Metagabbro	1170 ± 4*	Zircon	14
216276	-30.82903	128.68614	Coompana Province	Drillcore FOR008, E of Reid	Toolgana Supersuite	Migmatitic gneiss	1153 ± 9	Zircon	15
213822	-31.28008	128.55396	Coompana Province	Drillcore FOR004, NW of Eucla	Toolgana Supersuite	Schleiric leucogranite	1179 ± 10*	Zircon	16
216261	-30.82903	128.68614	Coompana Province	Drillcore FOR008, E of Reid	Toolgana Supersuite	Migmatitic gneiss	1151 ± 6*	Zircon	17
206730	-30.61716	128.17583	Coompana Province	Drillcore FOR011, Gunnadorrah	Undawidgi Supersuite	Metagranite	1174 ± 12*	Zircon	18
184128	-33.92292	120.55881	Northern Foreland	Powell Point	Munglinup Gneiss	Leucocratic tonalitic gneiss	1195 ± 17*	Zircon	19
184312	-34.44202	119.39927	Biranup Zone	Short Beach	Dalyup Gneiss	Granodioritic gneiss	1154 ± 25*	Zircon	20–22
184307	-34.47911	119.38724	Biranup Zone	Point Henry	Dalyup Gneiss	Pegmatitic granodiorite	1172 ± 16*	Zircon	21–23
184119	-34.48046	119.38624	Biranup Zone	Point Henry	Dalyup Gneiss	Monzogranitic gneiss	1178 ± 4*	Zircon	21, 22, 24
184123	-33.87395	121.67462	Biranup Zone	Plum Pudding Rocks (coastal exposure)	Coramup Gneiss	gt-bearing monzogranitic gneiss	1224 ± 9*	Zircon	25
184122	-33.87395	121.67462	Biranup Zone	Plum Pudding Rocks (coastal exposure)	Coramup Gneiss	Metasandstone	1225 ± 7*	Zircon	26
184125	-33.90813	121.79566	Biranup Zone	Observatory Point (coastal exposure)	Recherche Supersuite	opx-bearing dioritic gneiss	1195 ± 4*	Zircon	27
194705	-32.6428	122.33439	Biranup Zone	Fraser Range Track, W of Cowalinya Pool	Biranup Zone orthogneiss	Metasyenogranite	1161 ± 5*	Monazite	28
184310	-34.42654	119.40249	Biranup Zone	Fisheries Bay headland	Dalyup Gneiss	Leucocratic granodiorite	1178 ± 3*	Zircon	21, 22, 29
194728	-30.87863	123.63144	Biranup Zone	Ponton Creek, NE Zanthus Railway	Biranup Zone orthogneiss	gt-bearing quartzofeldspathic gneiss	1201 ± 15*	Zircon	30
194730	-30.89276	123.65672	Biranup Zone	E Ponton Creek, NE Zanthus (deposit)	Biranup Zone orthogneiss	hbl-bearing migmatitic metamonzogranite	1247^ (discordant)	Zircon	30
194734	-30.91229	123.6474	Biranup Zone	Ponton Creek, NE Zanthus (deposit)	Biranup Zone orthogneiss	gt-bearing migmatitic metagranite	1193 ± 9*	Zircon	30
194701	-33.16172	122.14022	Biranup Zone	Crystal Lake	Biranup Zone orthogneiss	Metagranite	1203 ± 11*	Zircon	30
194725	-31.25871	123.42907	Biranup Zone	S Uraryie Rock	Biranup Zone orthogneiss	gt-rich metagranite	1205 ± 20 (common-Pb reg.)	Zircon	30
194726	-31.18606	123.42232	Biranup Zone	Uraryie Rock, E Udarra Bore	Biranup Zone orthogneiss	gt–hbl-bearing granodiorite gneiss	1162 ± 39*	Zircon	30
194709	-32.60143	122.9241	Biranup Zone	Cave Rock, N Mt. Andrew	Biranup Zone orthogneiss	hbl-bearing syenogranite gneiss	1171 ± 30 (lower int.)	Zircon	30
83676A	-32.53	122.92	Biranup Zone	N Mt. Andrew	Biranup Zone orthogneiss	hbl-bearing syenogranite gneiss	1184 ± 12*	Zircon	31
17 samples (unspecified)	-33.92723	120.03058	Barren Basin	West of Hopetoun	Mt. Barren Group	g–st–ky gneiss and sandstone	1194 ± 8*	Monazite	32
13 samples (unspecified)	-33.92723	120.03058	Barren Basin	West of Hopetoun	Mt. Barren Group	g–st–ky gneiss	1206 ± 8*	Xenotime	32
194718.1	-31.96989	122.88469	Fraser Zone	American Granulite Quarry	Fraser Range Metamorphics	Mafic granulite	1292 ± 6* (also mag age)	Zircon	33
194740	-31.31523	123.54213	Fraser Zone	SW Harris Lake	Fraser Range Metamorphics	Garnet-bearing pelite gneiss	1283 ± 8*	Zircon	34
194714	-32.17291	122.69956	Fraser Zone	Gnamma Hill	Fraser Range Metamorphics	Psammitic gneiss with gt-rich leucosomes	1292 ± 5*	Zircon	35

Appendix C. (continued)

Sample No.	Latitude	Longitude	Tectonic region	Geographic descriptor	Lithological unit[b]	Lithological description	Interpreted age (Ma)[c]	Chronometer	Reference
FR10-011	-32.17292	122.69956	Fraser Zone	Gnamma Hill	Fraser Range Metamorphics	gt–sill gneiss	1279 ± 19* (mnz in gt) 1274 ± 9* (matrix mnz) 1234 ± 17* (mnz rims)	Monazite	35, 36
FR10-007	-32.17292	122.69956	Fraser Zone	Gnamma Hill	Fraser Range Metamorphics	gt–sill gneiss	1285 ± 16*	Monazite	35, 36
182447	-32.22698	122.83287	Fraser Zone	Mt. Malcolm	Fraser Range Metamorphics	sill-bearing gneiss	1268 ± 12*	Monazite	35, 36
GH-2	-32.17292	122.69956	Fraser Zone	Gnamma Hill	Fraser Range Metamorphics	gt–sill–cd–bi gneiss	1305 ± 80*	Zircon	37
194735	-32.37013	122.92457	Arid Basin	Gwynne Creek	Gwynne Creek Gneiss	Migmatitic quartzofeldspathic gneiss	1270 ± 11*, 1193 ± 26*	Zircon	38
Unnamed	-35.03389	117.92056	West Nornalup	Whalehead Rock, near Albany	Arid Basin (unit unspecified)	gt–sill migmatitic gneiss	1314 ± 5	Zircon	39
Unnamed	-35.01956	118.00475	West Nornalup	Ledge Beach, near Albany	Arid Basin (unit unspecified)	gt–sill migmatitic gneiss	1304 ± 3	Zircon	40
PM-11-011	-33.79571	123.76159	Arid Basin	Pt. Malcolm	Malcolm Gneiss	Leucosome (in migmatitic paragneiss)	1313 ± 6*, 1178 ± 10*	Monazite	41
194867	-33.79578	123.76245	Arid Basin	Pt. Malcolm	Malcolm Gneiss	Quartzofeldspathic gneiss	1307 ± 7*, 1168 ± 28*, 1291, 1311^	Monazite	41
194869	-33.82243	123.70085	Arid Basin	SW Pt. Malcolm	Malcolm Gneiss	Schist	1183 ± 7*, 1335 ± 11	Monazite	41
9611201	-34.35929	123.55279	Ragged Basin	Salisbury Island	Salisbury Gneiss	Migmatitic gt–sp–cd–sill gneiss (leucosome)	1214 ± 8* (cores) 1182 ± 13* (rims)	Zircon	42
9510092	-33.45237	123.47287	Ragged Basin	Mt. Ragged	Mt Ragged Formation	and–mica schist	1154 ± 15* (min. metm. age)	Metm. rutile	42
STC-09-04	-23.7113	133.4661	NAC margin	Warumpi Province	Chewings Range Pelites	gt–st–bi–mus schist	1129 ± 11*	Monazite	43
STC-09-8A	-23.71206	133.45539	NAC margin	Warumpi Province	Chewings Range Pelites	gt–st–and–bi–mus schist	1121 ± 8* (lower int.)	Monazite	43
STC-09-10	-23.71092	133.46802	NAC margin	Warumpi Province	Chewings Range Pelites	gt–st–and–bi–mus schist	1139 ± 4*	Monazite	43
Blain-4	-23.70935	133.85311	NAC margin	Warumpi Province	Teppa Hill Metamorphics	gt–st–and–bi–mus schist	1117 ± 11* (lower int.)	Monazite	43
AS-09-14	-23.70122	133.85889	NAC margin	Warumpi Province	Teppa Hill Metamorphics	gt–st–and–bi–mus schist	1109 ± 7*	Monazite	44
AS-2010-13	-23.69956	133.72668	NAC margin	Warumpi Province	Simpsons Gap Metasediments	bi–mus–chl schist	1145 ± 9* (lower int.)	Monazite	44
AS2010-63D	-23.61888	133.83248	NAC margin	Southern Aileron Province	Paleoprot. gneisses	gt–sill–cd-bearing pelitic gneiss	1085 ± 16*	Monazite	44
AS2010-66D	-23.63064	133.85233	NAC margin	Southern Aileron Province	Charles River Gneiss	gt–sill-bearing migmatitic gneiss	1083 ± 17*	Monazite	44
AS2010-67A2	-23.63079	133.85908	NAC margin	Southern Aileron Province	Charles River Gneiss	gt–sill-bearing migmatitic metapelite	1133 ± 17*	Monazite	44
830-18	-23.26694	131.55203	NAC margin	Warumpi Province (Mt. Leibig area)	Yaya Metamorphic Complex	gt–sill-bearing metapelite	1146^	Monazite	44
AS09-01	-23.61267	133.85256	NAC margin	Southern Aileron Province	Charles River Gneiss	gt–sill–cd bearing migmatitic metapelite	1125 ± 11*	Monazite	44
AS2010-65J	-23.60133	133.87729	NAC margin	Southern Aileron Province	Paleoprot. gneisses	gt–sill-bearing migmatitic metapelite	1138 ± 14*	Monazite	44
AS2010-72D	-23.60704	133.88054	NAC margin	Southern Aileron Province	Paleoprot. gneisses	bi–ksp–pl-bearing ultramylonite	1126 ± 8*	Monazite	44
RED2011-01	-23.51832	132.79815	NAC margin	Warumpi Province	Yaya Metamorphic Complex	gt–sill-bearing metapelite	1143 ± 10*	Monazite	44
HAM2011-02	-23.60137	133.3365	NAC margin	Southern Aileron (Wigley Block)	Paleoprot. gneisses	Pegmatite segregation within boudin neck	1136 ± 8*	Zircon	44
HAM2011-08	-23.58344	133.33294	NAC margin	Southern Aileron (Wigley Block)	Paleoprot. gneisses	Migmatitic melt vein	1139 ± 19*	Zircon	44
AS2012-1	-23.55471	133.8677	NAC margin	Southern Aileron Province	Flint Springs Gneiss	Migmatitic granitic gneiss	1115^	Zircon	44
AS2012-2	-23.59694	133.87943	NAC margin	Southern Aileron Province	Paleoprot. gneisses	Migmatitic orthogneiss	1152 ± 34*	Zircon	44
WI07	-66.21728	110.60329	Windmill Islands	Cameron Island	Arid Basin equiv.	g–bi–mt gneiss	1325–1270^	Zircon	45

Appendix C. (continued)

Sample No.	Latitude	Longitude	Tectonic region	Geographic descriptor	Lithological unit[b]	Lithological description	Interpreted age (Ma)[c]	Chronometer	Reference
WI12	-66.21603	110.61068	Windmill Islands	Cameron Island	Arid Basin equiv.	g–cd–mt gneiss	ca. 1300–1150^	Monazite	46
WI29	-66.3124	110.52378	Windmill Islands	Mitchell Peninsula	Arid Basin equiv.	g–cd–mt–opx gneiss	1177 ± 4*	Monazite	46
WI40	-66.31622	110.53449	Windmill Islands	Mitchell Peninsula	Arid Basin equiv.	g–sill–cd–sp–mt gneiss	1305 ± 7* (cores) 1206 ± 19* (rims)	Monazite	46
							1355–1180^	Zircon	45
WI68	-66.40534	110.61428	Windmill Islands	Herring Island	Arid Basin equiv.	opx–cd–mt gneiss	1185 ± 8*	Monazite	46
							1250–1175, 1300^	Zircon	45
WI89	-66.36676	110.59064	Windmill Islands	Robinson Ridge	Arid Basin equiv.	gt–cd–mt gneiss	1325–1170^	Zircon	45
64294	-66.2488	110.59813	Windmill Islands	Clark Peninsula	Arid Basin equiv.	gt-bearing leucosome (in psammitic gneiss)	1171 ± 6*	Monazite	47
54294	-66.2488	110.59813	Windmill Islands	Clark Peninsula	Arid Basin equiv.	orthogneiss	1169 ± 7*	Monazite	47
3161193	-66.27789	110.53918	Windmill Islands	Bailey Peninsula	Arid Basin equiv.	gt-bearing orthogneiss	1171 ± 13*	Monazite	47
12311293	-66.40138	110.62399	Windmill Islands	Herring Island	Arid Basin equiv.	gt–cd–opx–pl diatexite (restite)	1171 ± 9*	Zircon	47
12311293	-66.40138	110.62399	Windmill Islands	Herring Island	Arid Basin equiv.	gt–cd–opx–pl diatexite (restite)	1142 ± 7*	Monazite	47

[a]Data are sourced from a combination of geological survey online databases, report books and peer-review publications (complete reference list follows table).
Location coordinates are taken directly from the data source, where provided (and converted to decimal degrees as required). Where not given, approximate coordinates are estimated from geological maps and geographic place names documented in the data source, as well as satellite imagery (approximated coordinates shown in blue).
[b]Inferred lithological units are indicated by blue text. Superscripts, where shown, refer to literature reference.
[c]Age data are provided for any sample with an interpreted metamorphic age as specified in the original data source. Ages come from inferred metamorphic zircon (cores and rims), monazite, xenotime and rutile (specified in adjacent column). Ages are marked according to whether they are individual analyses^, pooled analyses (weighted mean or concordia age)*, or intercept ages of a regression (noted in brackets). Uncertainties on pooled analyses are given and are at a 95% confidence interval or 2σ level, unless indicated otherwise.
Mineral abbreviations: and, andalusite; bi, biotite; cd, cordierite; gt, garnet; hbl, hornblende; ilm, ilmenite; ky, kyanite; mt, magnetite; mus, muscovite; opx, orthopyroxene; pl, plagioclase; q, quartz; ru, rutile; sa, sapphirine; sill, sillimanite; sp, spinel.

REFERENCES (FOR APPENDIX C)

1. Tucker N. M. & Hand M. 2016. New constraints on metamorphism in the Highjump Archipelago, East Antarctica. *Antarctic Science* 28, 487-503.
2. Tucker, N. M., Hand, M., Kelsey, D. E., Taylor, R. J. M., Clark, C. and Payne, J. L. 2017. A tripartite approach to unearthing the duration of high temperature conditions versus peak metamorphism: an example from the Bunger Hills, East Antarctica. *Precambrian Research*, in review.
3. Tucker N. M., Payne J. L., Clark C., Hand M., Taylor R. J. M., Kylander-Clark A. R. C. & Martin L. 2017. Proterozoic reworking of Archean (Yilgarn) basement in the Bunger Hills, East Antarctica. *Precambrian Research* 298, 16-38.
4. Sheraton J. W., Black L. P. & Tindle A. G. 1992. Petrogenesis of plutonic rocks in a Proterozoic granulite-facies terrane — the Bunger Hills, East Antarctica. *Chemical Geology* 97, 163-198.
5. Kirkland C. L., Smithies R. H., Woodhouse A. J., Howard H. M., Wingate M. T. D., Belousova E. A., Cliff J. B., Murphy R. C. & Spaggiari C. V. 2013. Constraints and deception in the isotopic record; The crustal evolution of the west Musgrave Province, central Australia. *Gondwana Research* 23, 759-781.
6. Walsh A. K., Kelsey D. E., Kirkland C. L., Hand M., Smithies R. H., Clark C. & Howard H. M. 2015. *P–T*–t evolution of a large, long-lived, ultrahigh-temperature Grenvillian belt in central Australia. *Gondwana Research* 28, 531-564.
7. Tucker N. M., Hand M., Kelsey D. E. & Dutch R. A. 2015. A duality of timescales: Short-lived ultrahigh temperature metamorphism preserving a long-lived monazite growth history in the Grenvillian Musgrave–Albany–Fraser Orogen. *Precambrian Research* 264, 204-234.
8. Dutch R. A., Werner M. X., Krapf C. B. E. & Rusak T. 2013. Geology of the Tieyon 1:100 000 map sheet (5645), Report Book 2013/00011. Geological Survey of South Australia. Department for Mamufacturing, Innovation, Trade, Resources and Energy, South Australia, Adelaide.
9. Kirkland, CL, Wingate, MTD and Spaggiari, CV 2012, 182485: migmatitic gneiss, Burkin prospect; Geochronology Record 1054: Geological Survey of Western Australia, 4p.
10. Wingate, MTD and Bodorkos, S 2007, 177910: metamorphosed quartz sandstone, Peters Dam; Geochronology Record 660: Geological Survey of Western Australia, 6p.
11. Kirkland, CL, Wingate, MTD and Spaggiari, CV 2012, 182477: mafic granulite, Big Red prospect; Geochronology Record 1055: Geological Survey of Western Australia, 4p.
12. Kirkland, CL, Wingate, MTD and Spaggiari, CV 2012, 182473: migmatitic gneiss, Big Red prospect; Geochronology Record 1050: Geological Survey of Western Australia, 6p.
13. Kirkland, CL, Wingate, MTD and Spaggiari, CV 2012, 182475: migmatitic gneiss, Big Red prospect; Geochronology Record 1052: Geological Survey of Western Australia, 7p.
14. Kirkland, CL, Wingate, MTD, Hall, CE and Spaggiari, CV 2012, 182203: metagabbro, Hannah prospect; Geochronology Record 1049: Geological Survey of Western Australia, 5p.
15. Wingate, MTD, Lu, Y, Spaggiari, CV and Smithies, RH 2016, 216276: granodiorite gneiss, Forrest Zone; Geochronology Record 1298: Geological Survey of Western Australia, 4p.
16. Wingate, MTD, Lu, Y, Spaggiari, CV and Smithies, RH 2016, 213822: metasyenogranite, Forrest Zone; Geochronology Record 1295: Geological Survey of Western Australia, 5p.
17. Wingate, MTD, Lu, Y, Spaggiari, CV and Smithies, RH 2016, 216261: monzogranite gneiss, Forrest Zone; Geochronology Record 1297: Geological Survey of Western Australia, 4p.
18. Wingate, MTD, Lu, Y, Spaggiari, CV and Smithies, RH 2015, 206730: hornblende-biotite metasyenite, Forrest Zone; Geochronology Record 1274: Geological Survey of Western Australia, 5p.
19. Bodorkos, S and Wingate, MTD 2008, 184128: leucocratic tonalitic gneiss, Powell Point; Geochronology Record 705: Geological Survey of Western Australia, 4p.
20. Bodorkos, S and Wingate, MTD 2008, 184312: granodioritic gneiss, Short Beach headland; Geochronology Record 709: Geological Survey of Western
21. Spaggiari C. V., Bodorkos S., Barquero-Molino M., Tyler I. M. & Wingate M. T. D. 2009. Interpreted bedrock geology of the South Yilgarn and central Albany–Fraser Orogen, Western Australia: Geological Survey of Western Australia, Record 2009/10, 84p.
22. Barquero-Molina M. 2009. Kinematics of bidirectional extension and coeval NW-directed contraction in orthogneisses of the Biranup Complex, Albany–Fraser Orogen, southwestern Australia. PhD thesis. The University of Texas, Austin.
23. Bodorkos, S and Wingate, MTD 2008, 184307: pegmatitic granodiorite, Point Henry; Geochronology Record 706: Geological Survey of Western Australia, 4p.
24. Bodorkos, S and Wingate, MTD 2008, 184119: monzogranitic gneiss, Point Henry; Geochronology Record 699: Geological Survey of Western Australia, 4p.
25. Bodorkos, S and Wingate, MTD 2008, 184123: garnet-bearing monzogranitic gneiss, Plum Pudding Rocks; Geochronology Record 702: Geological Survey of Western Australia, 4p.
26. Bodorkos, S and Wingate, MTD 2008, 184122: metamorphosed quartz sandstone, Plum Pudding Rocks; Geochronology Record 701: Geological Survey of Western Australia, 6p.
27. Bodorkos, S and Wingate, MTD 2008, 184125: orthopyroxene-bearing dioritic gneiss, Observatory Point; Geochronology Record 703: Geological Survey of Western Australia, 4p.
28. Kirkland, CL, Wingate, MTD and Spaggiari, CV 2011, 194705: metasyenogranite, Cowalinya Pool; Geochronology Record 988: Geological Survey of Western Australia, 4p.
29. Bodorkos, S and Wingate, MTD 2008, 184310: leucocratic granodiorite, Fisheries Bay headland; Geochronology Record 707: Geological Survey of Western Australia, 4p.
30. Kirkland C. L., Spaggiari C. V., Pawley M. J., Wingate M. T. D., Smithies R. H., Howard H. M., Tyler I. M., Belousova E. A. & Poujol M. 2011. On the edge: U–Pb, Lu–Hf, and Sm–Nd data suggests reworking of the Yilgarn craton margin during formation of the Albany–Fraser Orogen. *Precambrian Research* 187, 223-247.

31. Nelson D. R. 1995. 83676A: hornblende syenogranite gneiss, Mount Andrew, in. Compilation of geochronology data, 1994: Geological Survey of Western Australia, Record 1995/3, p. 49-52.
32. Dawson G. C., Krapež B., Fletcher I. R., Mcnaughton N. J. & Rasmussen B. 2003. 1.2 Ga thermal metamorphism in the Albany–Fraser Orogen of Western Australia: consequence of collision or regional heating by dyke swarms? *Journal of the Geological Society* 160, 29-37.
33. Clark et al 2014; Kirkland, CL, Wingate, MTD and Spaggiari, CV 2011, 194718: mafic granulite, American Granulite Quarry; Geochronology Record 993: Geological Survey of Western Australia, 4p.
34. Kirkland, CL, Wingate, MTD and Spaggiari, CV 2014, 194740: psammitic gneiss, Harris Lake; Geochronology Record 1217: Geological Survey of Western Australia, 7p.
35. Clark C., Kirkland C. L., Spaggiari C. V., Oorschot C., Wingate M. T. D. & Taylor R. J. 2014. Proterozoic granulite formation driven by mafic magmatism: An example from the Fraser Range Metamorphics, Western Australia. *Precambrian Research* 240, 1–21.
36. Oorschot, CW 2011, *P–T*–t evolution of the Fraser Zone, Albany–Fraser Orogen, Western Australia:Geological Survey of Western Australia, Record 2011/18, 101p.
37. Clark D. J., Kinny P. D., Post N. J. & Hensen B. J. 1999. Relationships between magmatism, metamorphism and deformation in the Fraser Complex, Western Australia: Constraints from new SHRIMP U-Pb zircon geochronology. *Australian Journal of Earth Sciences* 46, 923-932.
38. Kirkland C. L., Spaggiari C. V., Pawley M. J., Wingate M. T. D., Smithies R. H., Howard H. M., Tyler I. M., Belousova E. A. & Poujol M. 2011. On the edge: U–Pb, Lu–Hf, and Sm–Nd data suggests reworking of the Yilgarn craton margin during formation of the Albany–Fraser Orogen. *Precambrian Research* 187, 223–247.
39. Love G. J. 1999. A study of wall-rock contamination in a tonalitic gneiss from King Point, near Albany, Western Australia. BSc. (Honours) Thesis. Curtin University of Technology, Perth.
40. Clark W. C. 1995. Granite petrogenesis, metamorphism and geochronology of the western Albany–Fraser Orogen, Albany, Western Australia. School of Applied Geology, Curtin University of Technology.
41. Adams M. 2012. Structural and geochronological evolution of the Malcolm Gneiss, Nornalup Zone, Albany–Fraser Orogen, Western Australia: Geological Survey of Western Australia, Record 2012/4, 132p.
42. Clark D. J., Hensen B. J. & Kinny P. D. 2000. Geochronological constraints for a two-stage history of the Albany–Fraser Orogen, Western Australia. *Precambrian Research* 102, 155–183.
43. Morrissey L., Payne J. L., Kelsey D. E. & Hand M. 2011. Grenvillian-aged reworking in the North Australian Craton, central Australia: constraints from geochronology and modelled phase equilibria. *Precambrian Research* 191, 141–165.
44. Wong B. L., Morrissey L. J., Hand M., Fields C. E. & Kelsey D. E. 2015. Grenvillian-aged reworking of late Paleoproterozoic crust of the southern North Australian Craton, central Australia: Implications for the assembly of Mesoproterozoic Australia. *Precambrian Research* 270, 100-123.
45. Morrissey L. J., Payne J. L., Hand M., Clark C., Taylor R., Kirkland C. L. & Kylander-Clark A. 2017. Linking the Windmill Islands, east Antarctica and the Albany–Fraser Orogen: Insights from U–Pb zircon geochronology and Hf isotopes. *Precambrian Research* 293, 131-149.
46. Morrissey L. J., Hand M. & Kelsey D. E. 2017a. A curious case of agreement between conventional thermobarometry and phase equilibria modelling in granulites: new constraints on *P–T* estimates in the Antarctica segment of the Musgrave–Albany–Fraser–Wilkes Orogen. *Journal of Metamorphic Geology* 35: 1023–1050.
47. Post N. J. 2000. Unravelling Gondwana fragments: an integrated structural, isotopic and petrographic investigation of the Windmill Islands, Antarctica. PhD Thesis. University of New South Wales, Sydney.

Appendix D. Compiled Sm–Nd whole-rock MAFWO magmatic data and metadata^

Sample	Latitude	Longitude	Region	Lithological unit	Age (Ma)**	$\varepsilon_{Nd}(t)$	Reference
83667	123.86813	-32.44870	Albany–Fraser Orogen	Unspecified, Nornalup Zone	1135	-8.3	Nelson *et al.* (1995)
84091632	132.56375	-23.45801	Warumpi Province	Teapot Granite Complex	1136	-10.1	Sun *et al.* (1995)
84091668	132.29666	-23.45676	Warumpi Province	Teapot Granite Complex	1136	-8.2	Sun *et al.* (1995)
1850772	-26.02344	133.90415	East Musgrave	Pitjantjatjara Supersuite	1140	-14.6	Dutch *et al.* (2013)
1842263	-26.17809	133.84262	East Musgrave	Pitjantjatjara Supersuite	1143	-16.9	Dutch *et al.* (2013)
1850797	-26.03811	133.75592	East Musgrave	Pitjantjatjara Supersuite	1143	-6.7	Dutch *et al.* (2013)
1850807	-26.41185	133.50055	East Musgrave	Pitjantjatjara Supersuite	1143	-3.5	Dutch *et al.* (2013)
P89/433	129.65885	-25.24961	Musgrave Province	Pitjantjatjara Supersuite	1144	-1.3	Edgoose *et al.* (2004)
1842255	-26.40528	133.72361	East Musgrave	Pitjantjatjara Supersuite	1147	-2.0	Dutch *et al.* (2013)
1842261	-26.32889	133.61611	East Musgrave	Pitjantjatjara Supersuite	1147	-2.3	Dutch *et al.* (2013)
1842268	-26.17935	133.83125	East Musgrave	Pitjantjatjara Supersuite	1147	-4.2	Dutch *et al.* (2013)
1850740	-26.01425	133.76466	East Musgrave	Pitjantjatjara Supersuite	1147	-4.6	Dutch *et al.* (2013)
1842256	-26.17444	133.74083	East Musgrave	Pitjantjatjara Supersuite	1149	-3.0	Dutch *et al.* (2013)
3434	-23.30000	134.25000	Warumpi Province	Mordor Complex	1150	-10.2	Nelson *et al.* (1989)
3435	-23.30000	134.25000	Warumpi Province	Mordor Complex	1150	-11.6	Nelson *et al.* (1989)
3438	-23.30000	134.25000	Warumpi Province	Mordor Complex	1150	-10.2	Nelson *et al.* (1989)
3441	-23.30000	134.25000	Warumpi Province	Mordor Complex	1150	-9.9	Nelson *et al.* (1989)
3446	-23.30000	134.25000	Warumpi Province	Mordor Complex	1150	-9.5	Nelson *et al.* (1989)
3450	-23.30000	134.25000	Warumpi Province	Mordor Complex	1150	-9.6	Nelson *et al.* (1989)
3452	-23.30000	134.25000	Warumpi Province	Mordor Complex	1150	-10.2	Nelson *et al.* (1989)
4142	-23.30000	134.25000	Warumpi Province	Mordor Complex	1150	-9.9	Nelson *et al.* (1989)
4202	-23.30000	134.25000	Warumpi Province	Mordor Complex	1150	-9.9	Nelson *et al.* (1989)
4213	-23.30000	134.25000	Warumpi Province	Mordor Complex	1150	-9.7	Nelson *et al.* (1989)
4578	-23.30000	134.25000	Warumpi Province	Mordor Complex	1150	-10.6	Nelson *et al.* (1989)
1039228	-26.04350	133.80895	East Musgrave	Pitjantjatjara Supersuite	1150	-6.3	Dutch *et al.* (2013)
1039237	-26.16841	133.79938	East Musgrave	Pitjantjatjara Supersuite	1150	-3.9	Dutch *et al.* (2013)
1039341	-26.29691	133.57950	East Musgrave	Pitjantjatjara Supersuite	1150	-1.9	Dutch *et al.* (2013)
1850773	-26.03047	133.88207	East Musgrave	Pitjantjatjara Supersuite	1150	-3.9	Dutch *et al.* (2013)
72913434	-23.42833	134.48734	Aileron Province	Mordor Complex	1150	-9.8	Nelson *et al.* (1989)
72913435	-23.44184	134.47652	Aileron Province	Mordor Complex	1150	-11.3	Nelson *et al.* (1989)
72913438	-23.43375	134.48830	Aileron Province	Mordor Complex	1150	-9.8	Nelson *et al.* (1989)
72913441	-23.44729	134.48727	Aileron Province	Mordor Complex	1150	-9.7	Nelson *et al.* (1989)
72913446	-23.45268	134.47648	Aileron Province	Mordor Complex	1150	-9.2	Nelson *et al.* (1989)
72913450	-23.44726	134.47650	Aileron Province	Mordor Complex	1150	-9.2	Nelson *et al.* (1989)
72913452	-23.44184	134.47652	Aileron Province	Mordor Complex	1150	-10.0	Nelson *et al.* (1989)
73914142	-23.43192	134.48145	Aileron Province	Mordor Complex	1150	-9.5	Nelson *et al.* (1989)
73914202	-23.46081	134.47644	Aileron Province	Mordor Complex	1150	-9.6	Nelson *et al.* (1989)
73914213	-23.45535	134.46472	Aileron Province	Mordor Complex	1150	-9.3	Nelson *et al.* (1989)
75914578	-23.49936	134.39696	Aileron Province	Mordor Complex	1150	-10.2	Nelson *et al.* (1989)
A92/10A	-25.85939	130.88638	Musgrave Province	Pitjantjatjara Supersuite	1150	-0.9	Edgoose *et al.* (2004)
86285815	-66.10500	101.18800	Bunger Hills	Booth Peninsula Batholith	1151	-3.5	Sheraton *et al.* (1990)
1842257	-26.05944	127.84389	East Musgrave	Pitjantjatjara Supersuite	1152	-3.8	Dutch *et al.* (2013)
190231	-25.71928	128.02708	West Musgrave	Pitjantjatjara Supersuite	1153	-3.2	Kirkland et al 2015
1850778	-26.06613	133.85165	East Musgrave	Pitjantjatjara Supersuite	1154	-12.9	Dutch *et al.* (2013)
1842272	-26.05972	133.84417	East Musgrave	Pitjantjatjara Supersuite	1155	-7.2	Dutch *et al.* (2013)
189523	-26.05451	127.78082	West Musgrave	Pitjantjatjara Supersuite	1157	-2.9	Kirkland *et al.* (2015)
189523	-26.05451	127.78082	West Musgrave	Pitjantjatjara Supersuite	1157	-2.9	Kirkland *et al.* (2015)
180860	-25.92771	128.21190	West Musgrave	Pitjantjatjara Supersuite	1159	-2.0	Kirkland *et al.* (2015)
194367	-25.61010	127.70316	West Musgrave	Pitjantjatjara Supersuite	1159	-2.4	Kirkland *et al.* (2015)
1011194	-66.45835	110.60322	Windmill Islands	Ardery Charnockite	1163	-4.9	Moller *et al.* (2002)
16294b	-66.45835	110.60322	Windmill Islands	Ardery Charnockite	1163	-4.5	Moller *et al.* (2002)
183509	-26.13865	128.78084	West Musgrave	Pitjantjatjara Supersuite	1165	-2.1	Kirkland *et al.* (2015)
PR96IRS747	-25.73006	130.33211	Musgrave Province	Pitjantjatjara Supersuite	1168	-2.5	Edgoose *et al.* (2004)
12311293	-66.40138	110.62399	Windmill Islands	Syn/post-D_2 orthogneiss	1171	-5.8	Moller *et al.* (2002)
86285962	-66.30400	100.61700	Bunger Hills	Algae Lake Pluton	1171	-9.4	Sheraton *et al.* (1990)
6161293	-66.41124	110.52041	Windmill Islands	Ford Granite	1173	-6.4	Moller *et al.* (2002)
180299	-25.87268	128.99045	West Musgrave	Pitjantjatjara Supersuite	1175	-2.2	Kirkland *et al.* (2015)
183508	-26.13492	128.77571	West Musgrave	Pitjantjatjara Supersuite	1175	-2.4	Kirkland *et al.* (2015)
PR96IRS714	-25.92882	129.64460	Musgrave Province	Pitjantjatjara Supersuite	1175	-1.9	Edgoose *et al.* (2004)
180256	-25.82743	128.88603	West Musgrave	Pitjantjatjara Supersuite	1176	-2.0	Kirkland *et al.* (2015)
91988083	-26.15260	128.91532	Musgrave Province	Unnamed gabbro	1176	-2.3	Glikson *et al.* (1996)
174538	-25.83923	128.79486	West Musgrave	Pitjantjatjara Supersuite	1178	-2.1	Kirkland *et al.* (2015)
183459	-26.39450	128.94481	West Musgrave	Pitjantjatjara Supersuite	1178	-2.7	Kirkland *et al.* (2015)
189452	-25.97835	127.78018	West Musgrave	Pitjantjatjara Supersuite	1179	-2.9	Kirkland *et al.* (2015)
174736	-25.78573	128.60667	West Musgrave	Pitjantjatjara Supersuite	1180	-4.9	Kirkland *et al.* (2015)
174796	-25.87618	128.98868	West Musgrave	Pitjantjatjara Supersuite	1180	-2.3	Kirkland *et al.* (2015)
174800	-25.65397	128.82224	West Musgrave	Pitjantjatjara Supersuite	1180	-2.5	Kirkland *et al.* (2015)
180262	-25.84490	128.88858	West Musgrave	Pitjantjatjara Supersuite	1180	-2.5	Kirkland *et al.* (2015)
180294	-25.88669	128.86510	West Musgrave	Pitjantjatjara Supersuite	1180	-2.2	Kirkland *et al.* (2015)
182479	-32.16574	125.12543	Albany–Fraser Orogen	Esperance Supersuite	1180	-5.2	GSWA*
182483	-32.16574	125.12543	Albany–Fraser Orogen	Esperance Supersuite	1180	-5.3	GSWA*
183408	-26.19201	128.73120	West Musgrave	Pitjantjatjara Supersuite	1180	-2.6	Kirkland *et al.* (2015)
55812B	-34.75417	116.07472	Albany–Fraser Orogen	Esperance Supersuite	1180	-10.1	Fletcher *et al.* (1983)

Appendix D. (continued)

Sample	Latitude	Longitude	Region	Lithological unit	Age (Ma)**	$\varepsilon_{Nd}(t)$	Reference
55815A	-34.95056	116.59556	Albany–Fraser Orogen	Esperance Supersuite	1180	-8.2	Fletcher *et al.* (1983)
87010002A	-34.46544	118.83482	Albany–Fraser Orogen	Unnamed granite	1180	-17.5	Geoscience Australia
180300	-25.87379	128.99040	West Musgrave	Pitjantjatjara Supersuite	1181	-2.4	Kirkland *et al.* (2015)
BJ96/277A	-25.64506	131.36567	Musgrave Province	Pitjantjatjara Supersuite	1182	-2.3	Edgoose *et al.* 2004
87010008	-34.68212	117.96816	Albany–Fraser Orogen	Unnamed aplite	1184	-8.8	Geoscience Australia
187171	-25.65496	128.18690	West Musgrave	Pitjantjatjara Supersuite	1185	-4.5	Kirkland *et al.* (2015)
90984041	-26.15960	128.92332	Musgrave Province	Mount Aloysius Complex	1188	-2.4	Glikson *et al.* (1996)
91988066	-26.14260	128.88732	Musgrave Province	Mount Aloysius Complex	1188	-3.8	Geoscience Australia
91988071	-26.15460	128.92532	Musgrave Province	Unnamed granite	1188	-3.9	Glikson *et al.* (1996)
91988072	-26.15460	128.92532	Musgrave Province	Mount Aloysius Complex	1188	-2.7	Glikson *et al.* (1996)
91988073	-26.14760	128.91832	Musgrave Province	Mount Aloysius Complex	1188	-2.8	Glikson *et al.* (1996)
174594	-25.91766	128.90576	West Musgrave	Pitjantjatjara Supersuite	1190	-2.5	Kirkland *et al.* (2015)
87010009	-34.68212	117.96816	Albany–Fraser Orogen	Esperance (Porongurups granite)	1190	-8.8	Geoscience Australia
87010010	-34.83214	116.78483	Albany–Fraser Orogen	Mount Franklin granite	1190	-9.0	Geoscience Australia
A94/644	-25.72650	130.74286	Musgrave Province	Pitjantjatjara Supersuite	1190	-1.2	Edgoose *et al.* (2004)
187103	-26.02275	128.56844	West Musgrave	Pitjantjatjara Supersuite	1191	-2.4	Kirkland *et al.* (2015)
P88/34	-25.13425	129.87597	Musgrave Province	Pitjantjatjara Supersuite	1192	-1.6	Edgoose *et al.* (2004)
87010001	-34.49878	118.90149	Albany–Fraser Orogen	Unspecified	1196	-15.3	Geoscience Australia
35-1	-66.373361	110.58625	Windmill Islands	Ardery Charnockite	1196	-1.1	Zhang *et al.* (2012)
184374	-33.29282	122.12083	AFO (Nornalup)	Esperance Supersuite	1198	-6.9	GSWA*
185610	-26.36197	128.05542	West Musgrave	Pitjantjatjara Supersuite	1199	-3.7	Kirkland *et al.* (2015)
171293	-66.31274	110.57125	Windmill Islands	Mafic gneiss	1200	-6.0	Moller *et al.* (2002)
174747	-25.75855	128.63911	West Musgrave	Pitjantjatjara Supersuite	1200	1.0	Kirkland *et al.* (2015)
174793	-25.79574	128.58170	West Musgrave	Pitjantjatjara Supersuite	1200	-6.0	Kirkland *et al.* (2015)
183510	-26.13107	128.76842	West Musgrave	Pitjantjatjara Supersuite	1200	-2.2	Kirkland *et al.* (2015)
189494	-25.94044	127.66093	West Musgrave	Pitjantjatjara Supersuite	1200	0.3	Kirkland *et al.* (2015)
194828	-33.16380	122.77444	Albany–Fraser Orogen	Esperance Supersuite	1200	-5.9	Kirkland *et al.* (2015)
194829	-33.37342	122.81259	Albany–Fraser Orogen	Esperance Supersuite	1200	-7.1	Kirkland *et al.* (2015)
194849	-33.82743	122.53963	Albany–Fraser Orogen	Esperance Supersuite	1200	-4.6	Kirkland *et al.* (2015)
194855	-33.89439	122.89488	Albany–Fraser Orogen	Esperance Supersuite	1200	-7.1	Kirkland *et al.* (2015)
194856	-33.88043	123.00535	Albany–Fraser Orogen	Esperance Supersuite	1200	-4.8	Kirkland *et al.* (2015)
194860	-33.90685	123.35203	Albany–Fraser Orogen	Esperance Supersuite	1200	-5.7	Kirkland *et al.* (2015)
201216	-31.91139	127.41623	Madura Province	Moodini Supersuite	1200	-1.6	Kirkland *et al.* (2015)
201220	-31.91139	127.41623	Madura Province	Moodini Supersuite	1200	-2.0	Kirkland *et al.* (2015)
201223	-31.91327	127.41632	Madura Province	Moodini Supersuite	1200	-2.0	Kirkland *et al.* (2015)
612294	-66.27789	110.53918	Windmill Islands	Mafic gneiss	1200	-0.7	Moller *et al.* (2002)
91988016	-26.01560	128.66532	Musgrave Province	Mount Aloysius Complex	1200	-2.3	Glikson *et al.* (1996)
91988017	-26.01560	128.66532	Musgrave Province	Mount Aloysius Complex	1200	-2.0	Geoscience Australia
91988030	-26.02060	128.64532	Musgrave Province	Mount Aloysius Complex	1200	-2.7	Geoscience Australia
91988035	-26.05560	128.60232	Musgrave Province	Mount Aloysius Complex	1200	-2.2	Glikson *et al.* (1996)
91988039	-26.03460	128.58632	Musgrave Province	Unnamed syenite	1200	-2.0	Glikson *et al.* (1996)
91988092	-26.18860	128.90132	Musgrave Province	Mount Aloysius Complex	1200	-2.1	Geoscience Australia
2531293m	-66.31846	110.52965	Windmill Islands	Syn/post-D_{2a} leucosome	1200	-5.8	Moller *et al.* (2002)
dc145	-66.40138	110.62399	Windmill Islands	Unspecified, intermediate gneiss	1200	-6.0	Moller *et al.* (2002)
184146	-26.38357	128.08562	West Musgrave	Pitjantjatjara Supersuite	1201	-2.3	Kirkland *et al.* (2015)
35-2	-66.37339	110.586333	Windmill Islands	Ardery Charnockite	1205	-1.6	Zhang *et al.* (2012)
174726	-25.73909	128.72568	West Musgrave	Pitjantjatjara Supersuite	1210	-1.8	Kirkland *et al.* (2015)
185339	-26.15409	128.90646	West Musgrave	Pitjantjatjara Supersuite	1210	-3.2	Kirkland *et al.* (2015)
187166	-25.69801	128.31357	West Musgrave	Pitjantjatjara Supersuite	1213	-3.8	Kirkland *et al.* (2015)
3161193	-66.27789	110.53918	Windmill Islands	Syn/post-D_{2a} orthogneiss	1214	-3.1	Moller *et al.* (2002)
174558	-25.78002	128.66978	West Musgrave	Pitjantjatjara Supersuite	1215	-3.3	Kirkland et al 2015
20311293	-66.22463	110.58717	Windmill Islands	Syn/post-D_{2a} orthogneiss	1215	-5.7	Moller *et al.* (2002)
174737	-25.78596	128.60612	West Musgrave	Pitjantjatjara Supersuite	1219	-2.9	Kirkland *et al.* (2015)
34-1	-66.28069	110.51933	Windmill Islands	D_{2a} gt-bearing granite	1242	-2.5	Zhang *et al.* (2012)
33-1	-66.28172	110.51189	Windmill Islands	D_{2a} gt-bearing granite gneiss	1247	-2.2	Zhang *et al.* (2012)
33-2	-66.28100	110.51697	Windmill Islands	D_{2a} gt-bearing granite gneiss	1258	-18.1	Zhang *et al.* (2012)
194711	-32.37013	122.92457	Albany–Fraser Orogen	Recherche Supersuite	1297	-4.0	Kirkland *et al.* (2015)
194783	-32.11414	123.17101	Albany–Fraser Orogen	Recherche Supersuite	1297	-4.5	Kirkland *et al.* (2015)
194719	-31.85357	123.03266	Albany–Fraser Orogen	Recherche Supersuite	1298	-4.0	Kirkland *et al.* (2011)
83690	-33.39874	121.38482	Albany–Fraser Orogen	Unspecified, Biranup Zone	1299	-19.5	Nelson *et al.* (1995)
83697	-33.44873	122.13482	Albany–Fraser Orogen	Unspecified, Biranup Zone	1299	-3.9	Nelson *et al.* (1995)
194712	-32.44222	123.06880	Albany–Fraser Orogen	Recherche Supersuite	1299	-6.4	GSWA*
174588	-25.90871	128.94336	West Musgrave	Wirku Metamorphics	1300	-2.7	Kirkland *et al.* (2015)
174748	-25.76067	128.64046	West Musgrave	Wirku Metamorphics	1300	2.2	Kirkland *et al.* (2015)
174797	-25.87743	128.98607	West Musgrave	Wirku Metamorphics	1300	-1.8	Kirkland *et al.* (2015)
174798	-25.91641	128.94675	West Musgrave	Wirku Metamorphics	1300	0.1	Kirkland *et al.* (2015)
183440	-26.11743	128.72462	West Musgrave	Wankanki Supersuite	1300	-0.8	Kirkland *et al.* (2015)
183466	-26.39778	128.96217	West Musgrave	Wirku Metamorphics	1300	-13.0	Kirkland *et al.* (2015)
183572	-26.29127	128.98623	West Musgrave	Wirku Metamorphics	1300	-0.1	Kirkland *et al.* (2015)
183595	-26.42131	128.96710	West Musgrave	Wirku Metamorphics	1300	-13.1	Kirkland *et al.* (2015)
183596	-25.79943	128.60937	West Musgrave	Wirku Metamorphics	1300	-4.0	Kirkland *et al.* (2015)
183626	-32.21711	122.84026	Albany–Fraser Orogen	Fraser Gabbro	1300	-0.6	Kirkland *et al.* (2015)
183628	-32.21711	122.84026	Albany–Fraser Orogen	Recherche Supersuite	1300	-3.0	GSWA*

Appendix D. (continued)

Sample	Latitude	Longitude	Region	Lithological unit	Age (Ma)**	$\varepsilon_{Nd}(t)$	Reference
183642	-32.22581	122.85330	Albany–Fraser Orogen	Recherche Supersuite	1300	-3.2	GSWA*
183643	-32.22599	122.85370	Albany–Fraser Orogen	Fraser Gabbro	1300	-1.7	GSWA*
183652	-32.23312	122.85720	Albany–Fraser Orogen	Fraser Gabbro	1300	0.0	GSWA*
183658	-32.04013	122.79300	Albany–Fraser Orogen	Fraser Gabbro	1300	-2.7	Kirkland *et al.* (2015)
183659	-32.04105	122.79441	Albany–Fraser Orogen	Fraser Gabbro	1300	-1.5	Kirkland *et al.* (2015)
183660	-32.02751	122.81173	Albany–Fraser Orogen	Fraser Gabbro	1300	-2.1	GSWA*
183661	-32.02916	122.81244	Albany–Fraser Orogen	Fraser Gabbro	1300	-0.7	Kirkland *et al.* (2015)
183663	-32.11281	123.02742	Albany–Fraser Orogen	Fraser Gabbro	1300	-0.4	Kirkland *et al.* (2015)
183666	-32.50968	123.34083	Albany–Fraser Orogen	Recherche Supersuite	1300	-7.1	Kirkland *et al.* (2015)
183668	-32.05086	123.11013	Albany–Fraser Orogen	Fraser Gabbro	1300	-1.8	GSWA*
183671	-31.95837	123.07634	Albany–Fraser Orogen	Recherche Supersuite	1300	-3.8	Kirkland *et al.* (2015)
185508	-26.03083	128.71382	West Musgrave	Wirku Metamorphics	1300	-2.0	Kirkland *et al.* (2015)
185593	-26.33578	128.97281	West Musgrave	Wirku Metamorphics	1300	1.2	Kirkland *et al.* (2015)
187113	-26.02395	128.66277	West Musgrave	Wirku Metamorphics	1300	-0.4	Kirkland *et al.* (2015)
187115	-26.02395	128.66277	West Musgrave	Wirku Metamorphics	1300	-1.3	Kirkland *et al.* (2015)
187150	-25.96541	128.42542	West Musgrave	Wirku Metamorphics	1300	-8.2	Kirkland *et al.* (2015)
187154	-25.86383	128.85273	West Musgrave	Wirku Metamorphics	1300	-1.4	Kirkland *et al.* (2015)
189540	-26.31421	127.80341	West Musgrave	Wirku Metamorphics	1300	-10.6	Kirkland *et al.* (2015)
189547	-26.32920	127.95955	West Musgrave	Wankanki Supersuite	1300	-1.7	Kirkland *et al.* (2015)
194376	-26.07500	127.64802	West Musgrave	Wirku Metamorphics	1300	-0.7	Kirkland *et al.* (2015)
194433	-26.07263	127.68581	West Musgrave	Wirku Metamorphics	1300	-5.3	Kirkland *et al.* (2015)
194718	-31.96989	122.88469	Albany–Fraser Orogen	Fraser Gabbro	1300	-3.4	Kirkland *et al.* (2015)
194779	-32.04690	122.79519	Albany–Fraser Orogen	Recherche Supersuite	1300	-3.4	Kirkland *et al.* (2015)
194814	-33.77100	121.92115	Albany–Fraser Orogen	Recherche Supersuite	1300	-4.7	GSWA*
194836	-34.00441	122.16874	Albany–Fraser Orogen	Recherche Supersuite	1300	-9.6	GSWA*
194840	-34.00004	122.20422	Albany–Fraser Orogen	Esperance Supersuite	1300	-5.6	GSWA*
194848	-33.93495	122.59353	Albany–Fraser Orogen	Recherche Supersuite	1300	-8.4	Kirkland *et al.* (2015)
194872	-33.63086	123.87703	Albany–Fraser Orogen	Recherche Supersuite	1300	-4.5	Kirkland *et al.* (2015)
194873	-33.61561	123.65684	Albany–Fraser Orogen	Recherche Supersuite	1300	-4.3	Kirkland *et al.* (2015)
194879	-33.21804	123.44776	Albany–Fraser Orogen	Recherche Supersuite	1300	-3.7	GSWA*
201235	-31.81730	123.19974	Albany–Fraser Orogen	Fraser Gabbro	1300	-0.7	GSWA*
201243	-31.81730	123.19974	Albany–Fraser Orogen	Fraser Gabbro	1300	0.4	GSWA*
201255	-31.81730	123.19974	Albany–Fraser Orogen	Fraser Gabbro	1300	-1.3	GSWA*
9503014	-66.24880	110.59813	Windmill Islands	Post-D_1/pre-D_{2a} leucosome	1300	-7.3	Moller *et al.* (2002)
90984007	-26.18660	128.90032	Musgrave Province	Mount Aloysius Complex	1300	-0.1	Geoscience Australia
90984008	-26.28960	128.96132	Musgrave Province	Mount Aloysius Complex	1300	-0.9	Glikson *et al.* (1996)
90984009	-26.20160	128.81232	Musgrave Province	Mount Aloysius Complex	1300	-0.5	Geoscience Australia
90984010	-26.20660	128.76132	Musgrave Province	Mount Aloysius Complex	1300	-0.9	Glikson *et al.* (1996)
90984011	-26.05661	127.62733	Musgrave Province	Mount Aloysius Complex	1300	-1.0	Geoscience Australia
91988099	-26.20160	128.96632	Musgrave Province	Mount Aloysius Complex	1300	-0.1	Geoscience Australia
194716	-32.21711	122.84026	Albany–Fraser Orogen	Recherche Supersuite	1301	-3.8	GSWA*
184158	-26.42497	128.07231	West Musgrave	Wankanki Supersuite	1303	-1.8	Kirkland *et al.* (2015)
56425	-34.41548	116.21681	Albany–Fraser Orogen	Unnamed orthogneiss	1310	-8.8	Fletcher *et al.* (1983)
55811C	-34.52306	116.16417	Albany–Fraser Orogen	Unnamed orthogneiss	1310	-7.7	Fletcher *et al.* (1983)
185581	-26.30432	128.33336	West Musgrave	Wankanki Supersuite	1312	-1.1	Kirkland *et al.* (2015)
183726	-26.16051	128.81933	West Musgrave	Wankanki Supersuite	1314	-0.6	Kirkland *et al.* (2015)
54294b	-66.24880	110.59813	Windmill Islands	Syn-D1 orthogneiss	1315	-5.4	Moller *et al.* (2002)
184150	-26.38320	128.08575	West Musgrave	Wankanki Supersuite	1317	-1.1	Kirkland *et al.* (2015)
194710	-32.63548	123.03000	Albany–Fraser Orogen	Recherche Supersuite	1317	-5.4	Kirkland *et al.* (2015)
194786	-32.51091	123.33677	Albany–Fraser Orogen	Recherche Supersuite	1320	-7.5	GSWA*
183496	-26.16352	128.79668	West Musgrave	Wankanki Supersuite	1321	-0.4	Kirkland *et al.* (2015)
183492	-26.14510	128.79055	West Musgrave	Wankanki Supersuite	1322	-0.9	Kirkland *et al.* (2015)
180867	-25.79866	128.24322	West Musgrave	Wankanki Supersuite	1324	-0.3	Kirkland *et al.* (2013)
185606	-26.32395	128.11963	West Musgrave	Wankanki Supersuite	1324	-2.2	Kirkland *et al.* (2015)
56426	-34.98056	116.69167	Albany–Fraser Orogen	Unspecified, Nornalup Zone	1330	-9.2	Fletcher *et al.* (1983)
56427	-34.99722	116.72500	Albany–Fraser Orogen	Unspecified, Nornalup Zone	1330	-7.3	Fletcher *et al.* (1983)
66804	-34.35000	116.05000	Albany–Fraser Orogen	Unnamed paragneiss	1330	-20.2	Fletcher *et al.* (1983)
83662	-33.89872	123.33482	Albany–Fraser Orogen	Unspecified, Nornalup Zone	1330	-2.1	Nelson *et al.* (1995)
55813E	-34.84139	116.02472	Albany–Fraser Orogen	Windy Harbour gneiss	1330	-22.4	Fletcher *et al.* (1983)
184149	-26.38342	128.08547	West Musgrave	Wankanki Supersuite	1350	-1.8	Kirkland *et al.* (2013)
183587	-26.19088	128.90153	West Musgrave	Wankanki Supersuite	1351	0.4	Kirkland *et al.* (2015)

^Data are sourced from a combination of peer-review publications (references listed in main text).
Location coordinates are taken directly from the data source, where provided (and converted to decimal degrees as required). Where not given, approximate coordinates are estimated from geological maps and geographic place names documented in the data source, as well as satellite imagery.
*Data provided by the Geological Survey of Western Australia (H. Smithies, personal communication, Dec. 2017).
**Corresponding age data are inferred or directly dated by the original data source.

Appendix E. Metadata for compiled Lu–Hf zircon MAFWO magmatic data^

Sample	Latitude	Longitude	Region	Unit	Reference
174558	-25.78002	128.66978	West Musgrave	Pitjantjatjara Supersuite	Kirkland *et al.* (2013, 2015)
174737	-25.78596	128.60612	West Musgrave	Pitjantjatjara Supersuite	Kirkland *et al.* (2013, 2015)
177909.1	-31.95000	122.91000	Albany–Fraser Orogen	Monzogranite (Recherche?)	GSWA
180256	-25.82743	128.88603	West Musgrave	Pitjantjatjara	Kirkland *et al.* (2013, 2015)
182474	-30.27393	124.98043	AFO	Esperance Supersuite	Kirkland *et al.* (2015)
183496	-26.16352	128.79668	West Musgrave	Wankanki	Kirkland *et al.* (2013)/GSWA
183496	-26.16352	128.79668	West Musgrave	Wankanki	Kirkland *et al.* (2015)
183509	-26.13865	128.78084	West Musgrave	Pitjantjatjara	Kirkland *et al.* (2013, 2015)
183653	-32.23312	122.85720	Albany–Fraser Orogen	Fraser Gabbro	Kirkland *et al.* (2015)/GSWA
184125	-33.90813	121.79566	Albany–Fraser Orogen	Recherche Supersuite	Kirkland *et al.* (2015)
184158	-26.42497	128.07231	West Musgrave	Wankanki Supersuite	Kirkland *et al.* (2013, 2015)
184781	-32.06096	122.90049	Albany–Fraser Orogen	Fraser Gabbro	Kirkland *et al.* (2015)
185339	-26.15409	128.90646	West Musgrave	Pitjantjatjara Supersuite	Kirkland *et al.* (2013, 2015)
185610	-26.36197	128.05542	West Musgrave	Pitjantjatjara Supersuite	Kirkland *et al.* (2013, 2015)
187151	-25.98039	128.32838	West Musgrave	Wankanki Supersuite	Kirkland *et al.* (2013, 2015)
187179	-25.65861	128.20934	West Musgrave	Pitjantjatjara Supersuite	Kirkland *et al.* (2013, 2015)
192565.1	-31.91140	127.41624	Madura Province	Moodini Supersuite	GSWA
192566.1	-31.91328	127.41632	Madura Province	Moodini Supersuite	GSWA
192593.1	-30.51860	128.36604	Coompana Province	Moodini Supersuite	GSWA
192595.1	-30.47861	127.08571	Madura Province	Moodini Supersuite	GSWA
194704.1	-32.96000	122.16000	Albany–Fraser Orogen	Esperance Supersuite	GSWA
194710	-32.63548	123.03000	Albany–Fraser Orogen	Recherche Supersuite	Kirkland *et al.* (2015)
194710.1	-32.64000	123.03000	Albany–Fraser Orogen	Recherche Supersuite	GSWA
194711	-32.37013	122.92457	Albany–Fraser Orogen	Recherche Supersuite	Kirkland *et al.* (2011, 2015)
194712.1	-32.44000	123.07000	Albany–Fraser Orogen	Recherche Supersuite	GSWA
194719.1	-31.85000	123.03000	Albany–Fraser Orogen	Recherche Supersuite	Kirkland et al 2011/GSWA
194773.1	-31.87084	128.22250	Coompana Province	Moodini Supersuite	GSWA
194776.1	-32.20000	122.84000	Albany–Fraser Orogen	Recherche Supersuite	GSWA
194779	-32.0469	122.79519	Albany–Fraser Orogen	Recherche Supersuite	Kirkland *et al.* (2015)/GSWA
194781	-32.06096	122.90049	Albany–Fraser Orogen	Fraser Gabbro	Kirkland *et al.* (2015)/GSWA
194782.1	-32.11000	123.03000	Albany–Fraser Orogen	Fraser Zone Supersuite	GSWA
194783	-32.11414	123.17101	Albany–Fraser Orogen	Recherche Supersuite	Kirkland *et al.* (2015)/GSWA
194786.1	-32.51091	123.33677	Albany–Fraser Orogen	Recherche Supersuite	GSWA
206729.1	-30.61716	128.17583	Coompana Province	Moodini Supersuite	GSWA
206752.1	-30.51860	128.36604	Coompana Province	Moodini Supersuite	GSWA
206753.1	-30.51860	128.36604	Coompana Province	Moodini Supersuite	GSWA
206778.1	-31.02995	127.12321	Madura Province	Moodini Supersuite	GSWA
206779.1	-31.02995	127.12321	Madura Province	Moodini Supersuite	GSWA
208500.1	-25.30640	127.48884	West Musgrave	Pitjantjatjara Supersuite	GSWA
208504.1	-25.23746	127.47957	West Musgrave	Pitjantjatjara Supersuite	GSWA
208506.1	-25.30608	127.33892	West Musgrave	Pitjantjatjara Supersuite	GSWA
213838.1	-30.61716	128.17583	Coompana Province	Moodini Supersuite	GSWA
33-1	-66.281722	110.511889	Windmill Islands	Granite gneiss (unnamed)	Zhang *et al.* (2012)
33-2	-66.28100	110.516972	Windmill Islands	Granite gneiss (unnamed)	Zhang *et al.* (2012)
34-1	-66.280639	110.519333	Windmill Islands	Granite (unnamed)	Zhang *et al.* (2012)
35-1	-66.373361	110.58625	Windmill Islands	Ardery Charnockite	Zhang *et al.* (2012)
35-2	-66.373389	110.586333	Windmill Islands	Ardery Charnockite	Zhang *et al.* (2012)
BH100	-66.29787	100.60327	Bunger Hills	Orthogneiss (pre-D1)	Tucker *et al.* (2017)
BH38	-66.17838	100.83523	Bunger Hills	Paz Cove Batholith	Tucker *et al.* (2017)
BH98	-66.30894	100.62680	Bunger Hills	Algae Lake Pluton	Tucker *et al.* (2017)
R1842255	-26.40518	133.72359	East Musgrave	Pitjantjatjara Supersuite	Dutch *et al.* (2013)
R1842256	-26.17444	133.74077	East Musgrave	Pitjantjatjara Supersuite	Dutch *et al.* (2013)
R1842257	-26.05946	133.84395	East Musgrave	Pitjantjatjara Supersuite	Dutch *et al.* (2013)
R1842261	-26.32880	133.61582	East Musgrave	Pitjantjatjara Supersuite	Dutch *et al.* (2013)
R1842268	-26.17935	133.83125	East Musgrave	Pitjantjatjara Supersuite	Dutch *et al.* (2013)
R1842272	-26.05973	133.84420	East Musgrave	Pitjantjatjara Supersuite	Dutch *et al.* (2013)
WI17	-66.30959	110.51253	Windmill Islands	Granite (unnamed)	Morrissey *et al.* (2017)
WI43	-66.26012	110.55981	Windmill Islands	Syn-D1 orthogneiss	Morrissey *et al.* (2017)
WI84	-66.37493	110.58194	Windmill Islands	Ardery Charnockite	Morrissey *et al.* (2017)
WI85	-66.37463	110.58255	Windmill Islands	Ardery Charnockite	Morrissey *et al.* (2017)

^Compiled Lu–Hf data presented in Figure 3b of the main text comprise individual Lu–Hf analyses and their corresponding U–Pb crystallisation ages. Due to the significant number of Lu–Hf zircon analyses, metadata only are summarised here with references given to the published data. Data are sourced from a combination of publically-available geological survey online databases, report books and peer-review publications (all references are listed in main text).

Location coordinates are taken directly from the data source, where provided (and converted to decimal degrees as required). Where not given, approximate coordinates are estimated from geological maps and geographic place names documented in the data source, as well as satellite imagery.

Appendix F. Referenced literature for magmatic and metamorphic data summarised in Tables 3 & 4 of the main text

Region	Magmatism (subdivided by magmatic suite)*	Metamorphism*
Southern NAC *Southern Aileron Province*	**Mordor Complex** Claoué-Long and Hoatson (2005); Nelson *et al.* (1989).	Claoué-Long and Hoatson (2005); Morrissey *et al.* (2011); Wong *et al.* (2015).
Southern NAC *Warumpi Province*	**Teapot Granite Complex** Black and Shaw (1995); Sun *et al.* (1995); Wong *et al.* (2015).	
West Musgrave Inlier	**Wankanki Supersuite and Papulankutja Supersuite** Evins *et al.* (2012); Gray (1978); Howard *et al.* (2011); Howard *et al.* (2015); Kirkland *et al.* (2013); Smithies *et al.* (2011); Smithies *et al.* (2010); White *et al.* (1999). **Pitjantjatjara Supersuite** Howard *et al.* (2015); Kirkland *et al.* (2013); Smithies *et al.* (2011); Smithies *et al.* (2010).	Clarke *et al.* (1995); Glikson *et al.* (1996); Howard *et al.* (2015); Smithies *et al.* (2011); Smithies *et al.* (2015a); Walsh *et al.* (2015); White *et al.* (1999); White *et al.* (2002).
East & central Musgrave Inlier	**Pitjantjatjara Supersuite** Dutch *et al.* (2013a); Dutch *et al.* (2013b); Edgoose *et al.* (2004).	Camacho and Fanning (1995); Edgoose *et al.* (2004); Tucker *et al.* (2015); Wade *et al.* (2008).
Madura Province	**Haig Cave Supersuite and Moodini Supersuite** Kirkland *et al.* (2017); Spaggiari and Smithies (2015).	Clark *et al.* (2000) (**Salisbury Gneiss**)
Coompana Province	**Moodini Supersuite** Kirkland *et al.* (2017); Spaggiari and Smithies (2015).	Spaggiari and Smithies (2015) (**Moodini Supersuite**)
Albany–Fraser Orogen	**Fraser Gabbro** Clark *et al.* (2014); Kirkland *et al.* (2011b); Maier *et al.* (2016a); Maier *et al.* (2016b); Smithies *et al.* (2013); Smithies *et al.* (2015b); Spaggiari and Tyler (2014). **Recherche Supersuite and Esperance Supersuite** Clark *et al.* (2000); Clark (1995); Nelson *et al.* (1995); Smithies *et al.* (2015b); Spaggiari and Tyler (2014).	**Northern Foreland**: Beeson *et al.* (1988); Bodorkos and Wingate (2008b); Spaggiari *et al.* (2009); Spaggiari *et al.* (2011); Spaggiari *et al.* (2014). **Fraser Zone**: Clark *et al.* (2014); Clark *et al.* (1999); De Waele and Pisarevsky (2008); Kirkland *et al.* (2011a); Kirkland *et al.* (2014b); Scibiorski *et al.* (2016); Spaggiari *et al.* (2009); Spaggiari *et al.* (2014); Wingate and Bodorkos (2007). **Biranup Zone**: Barquero-Molina (2009); Beeson *et al.* (1988); Black *et al.* (1992); Bodorkos and Clark (2004a; b); Bodorkos and Wingate (2008a; b; c; d; e); Kirkland *et al.* (2011b); Kirkland *et al.* (2014a); Kirkland *et al.* (2011c); Nelson (1995); Spaggiari *et al.* (2009); Spaggiari *et al.* (2011); Spaggiari *et al.* (2014). **Barren Basin**: *Mount Barren Group*: Dawson *et al.* (2003); Wetherley (1998); *Fly Dam Formation*: Kirkland *et al.* (2016). **Arid Basin**: *West Nornalup Zone (near Albany)*: Clark (1995); Duebendorfer (2002); Love (1999); Spaggiari *et al.* (2009); *East Nornalup Zone (Malcolm Metamorphics)*: Adams (2012); Clark *et al.* (2000); Fitzsimons and Buchan (2005); Spaggiari *et al.* (2009). **Ragged Basin**: Clark *et al.* (2000); Spaggiari *et al.* (2009); Spaggiari *et al.* (2011); Spaggiari *et al.* (2014).
Bunger Hills region	Sheraton *et al.* (1990); Sheraton *et al.* (1992); Sheraton *et al.* (1995); Tucker *et al.* (2017).	Sheraton *et al.* (1995); Stüwe and Powell (1989); Tucker and Hand (2016); Tucker *et al.* (2018); Tucker *et al.* (2017).
Windmill Islands	Kilpatrick and Ellis (1992); Morrissey *et al.* (2017b); Paul *et al.* (1995); Post (2000); Zhang *et al.* (2012).	Blight and Oliver (1977); Möller *et al.* (2002); Morrissey *et al.* (2017a); Paul *et al.* (1995); Post (2000); Post *et al.* (1997).

*References to the literature also include sample-specific studies that are documented in Appendices B and C (summarised MAFWO magmatic and metamorphic metadata used for the generation of spatial–age and spatial–isotope maps), if not already listed here.

Chapter 6

Summary of key outcomes and future research directions

Summary of key outcomes and future research directions

This thesis endeavours to provide an integrated metamorphic, petrochronologic and isotopic characterisation of long-lived, high thermal gradient metamorphic terranes comprising the Musgrave–Albany–Fraser–Wilkes Orogen (MAFWO). In doing so, this thesis also seeks to further our understanding of the geodynamic impetus for thermally-anomalous conditions during the Proterozoic (Rodinian) amalgamation of components of Australian and East Antarctica. By necessity, the studies in this thesis highlight and investigate the challenges and limitations in providing quantitative geochronological and pressure–temperature constraints on the metamorphic evolution of high-grade terranes, and the ways in which to adequately characterise and interpret such data. Five primary aims, presented in the introduction, are addressed in the preceding chapters through specific investigations from the east Musgrave Inlier, central Australia, and the Bunger Hills region, East Antarctica, and in undertaking a review of the current state of knowledge regarding the metamorphic features of the MAFWO. The following discussion highlights the main outcomes of this thesis in the context of these five specific aims. Potential directions for future research are also outlined to address key, unanswered questions that have arisen from the findings of this thesis.

1. *Investigate the geochronologic and isotopic evolution of under-studied areas of the MAFWO to provide a geodynamic framework in which to understand the Mesoproterozoic metamorphic evolution.*

The Bunger Hills have long been considered the western continuation of the Albany–Fraser Orogen into East Antarctica. However, until recently, this assertion was based upon limited geochronological data that alluded to an approximately similar timing of Mesoproterozoic magmatism and metamorphism. The pre-Mesoproterozoic crustal evolution of the Bunger Hills was largely unknown. The zircon U–Pb, Lu–Hf and oxygen isotope techniques employed in **Chapter 3** show several compelling connections between the Archean–Mesoproterozoic crustal evolution of the Bunger Hills and the Albany–Fraser Orogen.

Igneous and metasedimentary rocks of the Bunger Hills are demonstrated to comprise an Archean basement (ca. 2800–2700 Ma), a Paleo–Mesoproterozoic (ca. 1700–1500 Ma) volcano-clastic sequence and a suite of voluminous late Mesoproterozoic magmatic intrusives (ca. 1260 Ma and ca. 1200–1150 Ma). Specifically, the Archean rocks have age and isotopic affinity to the Yilgarn Craton and are considered to represent a reworked, detached fragment of the Yilgarn margin that was extended during the late Paleoproterozoic (ca. 1815–1600 Ma). The Paleoproterozoic crustal evolution of the Bunger Hills is considered akin to the Biranup Zone of the Albany–Fraser Orogen that involved the *in situ* reworking of this highly-extended Yilgarn crust. The early Mesoproterozoic evolution shares some similarities with the Nornalup Zone of the Albany–Fraser Orogen as it transitioned into a passive margin setting. Late Mesoproterozoic magmatism was synchronous with high-temperature metamorphism and involved crustal recycling of these Paleoproterozoic and Archean rocks. These new findings confirm the initial geochronological interpretations of a direct connection between the Bunger Hills and Albany–Fraser Orogen, and also complement recent geophysical studies that align the Bunger Hills with the truncated end of the west Albany–Fraser Orogen, indicating a direct spatial linkage.

The results of **Chapter 3** highlight a lack of evidence for tectonism within the Bunger Hills between the inferred timing of Mesoproterozoic sediment deposition (ca. 1490 Ma) and the approximate onset of D_2/M_2 MAFWO orogenesis. This tectonic inactivity is significant in that it suggests the Bunger Hills, and by extension the west Albany–Fraser Orogen, did not observe pre-D_1 oceanic arc accretion and subsequent D_1 extension that is the shared tectonic interpretation of regions comprising the central MAFWO. This observation provides support for prior interpretations that D_1/M_1 likely occurred in response to tectonic control along the eastern margin of the central MAFWO. In contrast, evidence for magmatism during D_2/M_2 in the Bunger Hills supports the operation of a broader geodynamic mechanism at this time to facilitate a unified magmatic and metamorphic history between the west MAFWO and other components of the orogen. The findings from **Chapter 3** therefore provide important

geodynamic context in which to understand a lack of metamorphic and magmatic evidence for D_1/M_1, yet widespread evidence for D_2/M_2, as investigated in **Chapters 2** and **4**.

Investigating the age and isotope composition of high-grade terranes is not without its complications. **Chapter 3** highlights the difficulties in interpreting age data, and therefore also age-dependent isotope data, in samples that have undergone ancient-Pb loss as a result of high-temperature metamorphism. Accordingly, there is scope for future studies to further refine the timing of Archean–Paleoprotrozoic magmatism and early Mesoproterozoic sediment deposition in the Bunger Hills with the advent of more precise analytical techniques and/or by targeting samples that do not observe the effects of Pb-loss. The isotopic datasets for igneous rocks presented in **Chapter 3** would also benefit from geochemical appraisal, with the caveat that the open-system behaviour of metamorphism and partial melting may have modified the original rock composition. In which case, mafic rocks may be used preferentially as they are less subject to partial melting and more indicative of mantle conditions.

2. *Place quantitative constraints on the metamorphic architecture through phase equilibria forward modelling to understand the peak conditions, and prograde and retrograde P–T paths associated with high thermal gradient metamorphism within key, under-studied areas of the MAFWO.*

The results of phase equilibria forward modelling in **Chapters 1, 2** and **4** show that the east Musgrave Inlier in central Australia, and the Highjump Archipelago and Bunger Hills in East Antarctica, attained broadly similar P–T conditions despite their location at opposing ends of the MAFWO. Slight differences in absolute pressure and temperature within and between individual tectonic regions of the MAFWO are likely relatable to the depth from which the metamorphic rocks were exhumed. For example, **Chapter 1** indicates that the *P–T* conditions in the east Musgrave Inlier (6.0–6.5 kbar, 900 °C) were slightly lower temperature and pressure than the west Musgrave Inlier (7–8 kbar, 1000 °C). Similarly, slightly elevated pressures are documented in the Highjump Archipelago (6–9 kbar at ~850–950 °C; **Chapter 2**) compared with P–T constraints from the adjacent Bunger Hills (5.5–7.1 kbar at ~800–960 °C; **Chapter 4**).

While absolute *P–T* conditions provide valuable information on the metamorphic character of different crustal levels of the orogen, apparent thermal gradients are useful in that they are often directly relatable to the tectonic setting. Similar apparent thermal gradients associated with the timing of M_2 (~100–150 °C/kbar) from the investigated regions in **Chapters 1, 2** and **4**, along with interpreted similarities in their longevity of metamorphism, suggests that a comparable geodynamic mechanism for the generation of exceptionally high geothermal gradients was operating on a regional scale.

Despite their broad similarities in *P–T* conditions and apparent geothermal gradients, rocks in the east Musgrave Inlier and Bunger Hills region are interpreted to have cooled along slightly different *P–T* paths. The east Musgrave Inlier records evidence for a slightly up-pressure to isobaric post-peak *P–T* path whereas the Bunger Hills and Highjump Archipelago likely tracked down-pressure. The slight increase in pressure along the post-peak *P–T* path in the east Musgrave Inlier is interpreted as the result of local-scale advective processes within a longer-lived, magmatically-driven system. In this scenario, emplacement of syn-metamorphic magmatic rocks into the mid-crust is suggested to have caused the downward displacement of the surrounding country rock. In contrast, the down-pressure *P–T* cooling paths inferred for the Bunger Hills and Highjump Archipelago are interpreted to reflect more regional processes involving decompression and exhumation during extension of thickened crust.

The observations and inferences made on the *P–T* conditions, apparent thermal gradients and *P–T* paths from the metamorphic case studies presented in **Chapters 1, 2** and **4** allow for the synthesis of MAFWO metamorphic features presented in **Chapter 5**. Undertaking case studies from the western and eastern extents of the MAFWO also means that variation in metamorphic features across the orogen can now be fully evaluated.

P–T constraints in **Chapters 1, 2** and **4** were made using the most up-to-date thermodynamic models. However, a major issue identified in the *P–T* modelling of Mg–Al-rich metasedimentary rocks from high-grade terranes is the enhanced stability of some major silicate minerals due to the incorporation of atypical elements (e.g. zinc and fluorine). As these elements are not incorporated

into the activity–composition (*a–x*) models used for phase equilibria modelling, the absolute P–T shift cannot be quantified, and thus confidence assigned to *P–T* constraints diminishes. Investigation into the viability of incorporating such elements into thermodynamic models for phase equilibria modelling would therefore be of significant benefit to understanding (and potentially re-evaluating) metamorphic conditions in high-grade terranes. Further, over the course of this thesis, our understanding of the chemical and physical behaviour of mineral geochronometers such as zircon and monazite has significantly improved. Recent advances in petrochronology, discussed below, now allows increasingly robust links to be made between the trace element composition of major silicate minerals and these accessory phases. Logically, phase equilibria modelling approaches should also now evolve to incorporate trace elements such as yttrium in minerals such as garnet to strengthen ties between the timing of mineral growth and the *P–T* phase relations and mineral stability.

3. *Investigate how the age, timescale and rate of high thermal gradient metamorphism can be adequately characterised and interpreted.*

As presented in **Chapters 1, 2** and **4**, LA–ICP–MS dating of zircon and monazite indicate that peak metamorphism in the east Musgrave Inlier and the Bunger Hills region occurred during D_2/M_2. However, these studies, as well as prior metamorphic work from the MAFWO, typically report large spreads in age data that encompass a significantly greater range than the defined D_1/M_1 and D_2/M_2 time periods. Further, the entire spread of age data from high-grade terranes is rarely though to reflect entirely the duration of peak metamorphism. Therefore, there are two outstanding problems in adequately characterising and interpreting age data from the MAFWO. Firstly, due to the continuum of metamorphic age data, there are challenges in distinguishing between M_1 and M_2 at the terrane- and sample-scale, and hence whether different regions of the MAFWO did experience a two-phase metamorphic history. Secondly, there are difficulties in quantitatively matching segments of the large spreads in age data to the *P–T* path. Metamorphic studies, including those from the MAFWO, indicate that a single rock may preserve a record of the timing of prograde and peak metamorphism, the recrystallization of older (inherited or metamorphic) ages, and/or U–Pb resetting during post-peak cooling. The likelihood that a rock at the outcrop-scale does preserve an age-record of different parts (or all) of the metamorphic evolution at the orogen-scale is reliant on the *P–T–t* path travelled as well as the variable and complex chemical and physical behaviour of mineral chronometers in melt-bearing systems at high temperatures. These issues are ubiquitous to long-lived, high to ultrahigh thermal gradient metamorphic terranes.

Chapters 1, 2 and **4** highlight the value of *in situ* geochronology. Age data obtained *in situ* allows direct links to be investigated between the timing of accessory phase mineral growth and the development of structural fabrics, microstructural mineral textures, and the growth of major silicate minerals such as garnet that are inferred to characterise peak metamorphism. In these chapters, *in situ* timescale information is then used in conjunction with *P–T* modelling to provide constraints on the evolution of the rock through depth with time and thus the tectonic setting. However, as **Chapters 1** and **4** also show, often the age of mineral geochronometers (e.g. zircon and monazite) appears independent of their microstructural location, with no clear age relationship to the growth of different parts of the silicate mineral assemblage. Therefore, while important, the use of *in situ* geochronology and *P–T* modelling alone does not always provide a clear-cut interpretation of what *P–T* segment the age data actually represent.

As a result, **Chapter 4** also investigates the trace element chemistry of zircon, monazite and garnet. The use of trace element chemistry allows in-depth analysis of the equilibrium coexistence, or lack of, of the mineral chronometers and the peak silicate minerals, and therefore provides another robust avenue to obtain information on their absolute timing of growth. Combined with careful interpretation of zircon morphology, *P–T* modelling and *in situ* geochronology, the results of Chapter 4 indicate that peak metamorphism in the Bunger Hills probably only occurred over ca. 40 Myr (ca. 1220–1180 Ma), despite a large spread of metamorphic age data (>150 Myr) spanning across M1 and M2. The concomitant use of two chronometers (zircon and monazite) in Chapter 4, also provides insight into the differences, and thus potential bias, in metamorphic age data that may be obtained from the same sample. Whilst zircon record largely older ages in the Bunger

Hills, interpreted to reflect largely solid-state recrystallization of inherited grains or preserved peak metamorphic ages, monazite is interpreted to record the peak–post peak evolution.

In contrast to the direct petrochronologic approach used in **Chapter 4**, **Chapter 1** supplements interpretations on the timescale and rate of metamorphism indirectly through qualitative measures of garnet REE chemistry. Garnet major element compositions record evidence for high to ultrahigh temperatures yet relict prograde REE zoning imply that such conditions could not have been sustained for as significant a duration. Therefore, while the age data may reflect that high temperatures persisted over a long duration (>70 Myr), an excursion to peak temperatures was likely short-lived.

A single solution, and the same solution, is often not possible to resolve the relationship between age data and the *P–T* evolution across different high-grade terranes. Even with a multi-faceted petrochronologic approach, the relationship between the age data to specific parts of the *P–T* evolution may remain blurred and thus timescales of "long-lived" high temperature metamorphism are often approximate. However, metamorphic geologists are now equipped with a range of efficient petrochronological tools that can, and should, be integrated to provide a standard analytical portfolio for investigations into the age and timescales of high temperature metamorphism. **Chapters 1, 2** and **4** highlight that integrating trace element chemistry of the mineral chronometers and major silicate minerals, *in situ* geochronology and *P–T* modelling appear to provide the most thorough constraints. Over time, analytical methods evolve and improve. The consistent use of a multi-petrochronologic tool-set such as the above-mentioned is encouraged as this will allow new methods to be carried out but importantly, also provides a systematic platform to compare these new data.

4. *Determine whether HT–UHT metamorphic terranes comprising the MAFWO exhibit synchronicity—spatially, temporally and thermally.*

Chapter 5 assesses secular changes in the spatial, temporal and thermal character of MAFWO metamorphism with time. Although the main focus is metamorphism, **Chapter 5** also evaluates variation in the geochemical, age and isotope characteristics of coeval magmatism to provide a holistic understanding of the Mesoproterozoic metamorphic evolution. Some broad generalisations can be made for the MAFWO regarding the metamorphic and magmatic characteristics of its two-stage history.

Firstly, **Chapter 5** confirms that the spatial extent of D_1/M_1 metamorphism and magmatism was restricted, occurring largely within tectonic regions that comprise the central MAFWO. These regions, namely the east Albany–Fraser Orogen, Windmill Islands and Madura Province, have pre-D_1/M_1 geological histories that involved reworking of comparatively young, highly extended and isotopically-juvenile crust. M_1 *P–T* constraints indicate that metamorphism and deformation was preferentially recorded by the Arid Basin (east Albany–Fraser Orogen and Windmill Islands) and Wirku Metamorphics (west Musgrave Inlier) that were deposited immediately prior to D_1/M_1. There is little evidence for D_1/M_1 tectonism in the east and west MAFWO in regions that reflect autochthonous reworking of isotopically-evolved, Archean–Paleoproterozoic crust (e.g. Northern Foreland, Biranup Zone, Bunger Hills, southern North Australian Craton (NAC)). Conversely, D_2/M_2 was widespread, with metamorphism and magmatism occurring across all tectonic regions of the MAFWO, including the Madura and Coompana provinces, and the southern margin of the NAC. Clarification of the D_1/M_1 and D_2/M_2 spatial extent provided by **Chapter 5** unifies preconceived interpretations from region-specific studies across the orogen. The former observation implies strong tectonic control on the development of D_1/M_1 in the central MAFWO; the regionally-extensive nature of D_2/M_2 suggests that a broader geodynamic mechanism is required.

Secondly, **Chapter 5** establishes that the timing of M_1 and M_2 was broadly similar across the central MAFWO, and entire MAFWO, respectively. However, the resolution of metamorphic age data is often blurred by complex mineral growth or Pb-loss, and the interpretation of such data in relation to the *P–T* path is commonly unclear (as discussed above). This means that estimates on the longevity of metamorphism in different parts of the orogen, and age comparisons between the different tectonic regions, are imprecise. If metamorphism was pulsed within the D_1/M_1 and D_2/M_2 time periods in individual tectonic regions of the MAFWO,

as appears to be the case for magmatism, this goes mostly undetected. This may be a reflection of metamorphism being an inherently more continuous process than magmatism.

Unlike the temporal record for metamorphism, clear age trends are observed for D_1 and D_2 magmatism. For example, spatial–age trends are observed for D_1 magmatism in the Albany–Fraser Orogen in which progressively younger and more isotopically-juvenile magmas were emplaced further towards the Yilgarn Craton. Spatial–age trends for D_2 magmas are also observed in the west Musgrave Inlier and the Madura Province. Comparing age data from across the MAFWO also reveals that D_2 magmatism is characterised by a bimodal age distribution with peaks at ca. 1200–1170 Ma and 1160–1140 Ma. Age data compared at the terrane-scale do not necessarily indicate this.

Finally, a comparison of *P–T* constraints reveals that M_1 was high-temperature, but characterised by seemingly variable apparent thermal gradients, with the caveat that data are sparse due to pervasive high-temperature overprinting by M_2. Limited and variable constraints also means that the M_1 post-peak *P–T* path is unclear. With the currently available data, it is difficult to assign regional versus local significance to the *P–T* conditions experienced during D_1/M_1. In contrast to M_1, M_2 was remarkably consistent in its thermal character, with similar apparent thermal gradients (~150 °C/kbar) experienced orogen-wide. This is despite clear differences in absolute *P–T* estimates. M_2 post-peak *P–T* paths were also chiefly down-pressure to isobaric, although the interpreted rate of cooling is interpreted to have varied. Taken together, similarities in the longevity of high temperatures, high apparent thermal gradients and *P–T* paths associated with M_2 across the orogen are suggestive of a regionally-significant geodynamic mechanism. Variation in the specific M_2 *P–T* estimates for different localities across the orogen is interpreted to relate to differential exhumation, and in some instances, also more local-scale processes such as advective heating by the emplacement of syn-D_2 magmas. This recognition provides useful insight into the metamorphic character of different structural levels of the orogen.

Despite the conclusions drawn from **Chapter 5**, the nature and extent of spatial, temporal and thermal similarities for metamorphic rocks across the MAFWO could certainly be better illuminated with further study. For example, the majority of *P–T* constraints from the Albany–Fraser Orogen and central Musgrave Inlier currently rest on field observations of inferred high-temperature mineral assemblages and estimates from conventional thermobarometry. Typically, studies from these regions do not engage different petrochronologic techniques with forward phase equilibria modelling and therefore interpreted metamorphic conditions are not time-constrained. The currently limited and variable *P–T* constraints on M_1 would also benefit from further appraisal with additional metamorphic studies undertaken to provide clarity on the associated thermal conditions and tectonic interpretations. Moving forward, the standardization of petrochronologic methods is also imperative, particularly across the same orogenic system, to create an internally-consistent framework in which to make genuine spatial and temporal comparisons.

5. *Evaluate the available models for the tectonic settings and geodynamic factors that promote long-existing high thermal gradient metamorphic conditions across the MAFWO to ultimately present and integrated framework that characterises the Mesoproterozoic metamorphic features of continental amalgamation in central–southwest Australia, and East Antarctica.*

The generation of regional, long-lived, high thermal gradient conditions requires the thickening, incubation and conductive heating of anomalously radiogenic crust over long timescales, or heat advection and/or conduction from the mantle. The metamorphic and magmatic architecture of the MAFWO appears to be consistent with a mantle-driven thermal regime. Firstly, the spatial extent and volume of D_1 and D_2 magmatism is exceptional and the isotopic signature of emplaced magmas suggests a significant mantle source contribution. Secondly, the metamorphic record does not support significant crustal thickening as absolute pressures are modest (4–9 kbar), temperatures rather than pressures vary across the orogen, and post-peak metamorphic P–T paths are characterised by a constant to slight decrease in pressure.

With overarching mantle-heating established, **Chapter 5** appraises plausible tectonic scenarios

for the generation of regional, long-lived, high thermal gradients across the MAFWO, within the context of continental amalgamation. **Chapter 5** highlights that a number of conditions must be satisfied by the tectonic setting and geodynamic regime to account for the magmatic and metamorphic expression of D_1/M_1 and D_2/M_2. D_1/M_1 was spatially-restricted to the central MAFWO, involved isotopically-juvenile bimodal mafic and calc-alkaline felsic magmatism, high-temperature metamorphism, and the development of horizontal fabrics. Further, magmatism and high-temperature metamorphism were immediately preceded by basin formation, indicating a very short time period between sedimentation and the generation of high thermal gradients. Two models—accelerated back-arc extension, and orogenic collapse associated with lithosphere delamination—are presently proposed to explain these D_1/M_1 criteria. In essence, both models infer that D_1/M_1 is a direct response to the pre-D_1/M_1 geological architecture of the central MAFWO that involved oceanic arc accretion, and D_1/M_1 is indicative of extensional accretionary orogenesis. It is therefore logical that the east and west MAFWO, that were not in the zone of active extension and deformation, did not observe D_1/M_1. However, key differences exist between the two proposed tectonic scenarios that relate to the timing of arc accretion relative to extension, and the specific mechanism of extension. Further, each model can account for some, but not all, of the key D_1/M_1 criteria. For example, back-arc extension may explain the rapid generation of high heat flow shortly after basin deposition, but not necessarily magma geochemistry. Lithosphere delamination and orogenic collapse may account for spatial, temporal and isotopic trends in D_1/M_1 magmatism, but uncertainties surround the mechanism and extent of crustal thickening to initiate instability and the lag time between thickening and the generation of high temperature conditions.

A geodynamic mechanism for D_2/M_2 must satisfy that magmatism and metamorphism were long-lived, hot and regionally-pervasive. **Chapter 5** identifies that D_2/M_2 was spatially-independent of regions that experienced D_1/M_1, occurring across the entire MAFWO. This firstly indicates that the geodynamic driver for D_2/M_2 was different to that for D_1/M_1, and was considerably more regional. Magmatism was high-temperature, voluminous and near-exclusively felsic, but isotope data also suggest significant mantle contribution. Metamorphism was characterised by consistently high–ultrahigh thermal gradients at mid–lower crustal depths (~150 °C/kbar) across the orogen, and post-peak metamorphic *P–T* paths suggest that cooling was associated with decreasing or constant pressure. The metamorphic record combined with magma geochemistry also suggests that the crust was thin. Taken together, these attributes suggest that the D_2/M_2 metamorphic system was dominantly driven by lithosphere removal. Specifically, mantle lithosphere delamination (coherent peeling-off into the asthenosphere), appears to satisfy many D_2/M_2 features. However, the geodynamic state of lithosphere removal involving top-down (e.g. delamination induced by crustal thickening and negative buoyancy) or bottom-up (e.g. convective erosion of the lithosphere by the asthenosphere) remains unresolved. This is primarily due to uncertainties surrounding the trigger for D_2/M_2 lithosphere removal. Without clear evidence for substantial crustal thickening or shortening to initiate regional-scale delamination, this process cannot be confidently assigned. Bottom-up processes that do not require substantial crustal thickening may provide a viable alternative but only if the spatial, temporal and thermal extent of magmatism and metamorphism can be satisfied, and this mechanism can operate at a continental scale.

A key clarification from **Chapter 5** is that, regardless of the currently offered tectonic models, neither D_1/M_1 nor D_2/M_2 appear to represent the event that marks final amalgamation of the Australian–Antarctic cratons. The pervasive metamorphic record of D_2/M_2 indicates that final assembly of the cratons that bound the orogen must have occurred between D_1/M_1 and D_2/M_2. The pre-existing (pre-D_2/M_2) geometry of the craton margins, the way in which the cratons converged, and the timing of convergence was therefore central to the geodynamics that generated unusually high thermal conditions. However, ambiguities in the timing of final convergence particularly between the SAC and the MAFWO still remain. This is largely a result of work on the crustal evolution of the MAFWO to date focussing on the more accessible regions that are closer to the WAC and NAC. These complexities surrounding the timing of SAC convergence may be resolved with further isotopic work from the Coompana Province, South Australia, and the central and east Musgrave Inlier, central Australia. Another significant issue is that the crustal relationship

between the west, central and east Musgrave Inlier is largely ambiguous. Specific questions remain as to whether these regions indeed represent crustally-distinct continental ribbons as is adopted in recent Mesoproterozoic reconstructions of Australia and Antarctica and whether their crustal affinity is to the NAC, SAC or an exotic source. The tectonic setting associated with D_1/M_1 is presently speculative, based on D_1 magma geochemistry, with no *P–T* constraints presently assigned to M_1. This lack of M_1 *P–T* constraints but evidence for M_1 metamorphic ages and D_1 magmatism should be further explored. The in-depth metamorphic study from the east Musgrave Inlier presented in **Chapter 1** covers limited spatial extent. Further metamorphic work in the central and east Musgrave Inlier is thus required to confirm the absence of D_1/M_1 in this region. At present, given the unexplored territory between the east and west Musgrave Inlier, the possibility still remains that the spatial extent of D_1/M_1 is significantly greater than currently hypothesised in **Chapter 5**. Evidence for D_1/M_1 in the east Musgrave Inlier has the potential to radically change interpretations on the Mesoproterozoic geodynamic setting of the east MAFWO.

As discussed in the Appendix, recent recognition of a two-phase Mesoproterozoic metamorphic evolution (ca. 1380 Ma and ca. 1285 Ma) in the Rudall Province has re-evaluated the timing of amalgamation of the NAC and WAC. Similarly-timed convergence of the NAC and WAC to MAFWO orogenesis (i.e. NAC–SAC and WAC–SAC convergence) is a presently under-explored possibility. There is significant motivation for this to become a research priority with specific focus on understanding the relationship between the Rudall Province and MAFWO during the Mesoproterozoic.

Future work might also consider the extensive Warakurna Large Igneous Province (WLIP), central Australia, in models for the amalgamation of Proterozoic Australia involving the MAFWO. Occurring post-craton amalgamation and D_2/M_2, the significance of this event is discussed briefly in **Chapter 5** but warrants further appraisal. Further consideration into the geodynamic drivers for generation of the WLIP may provide additional and useful insight into the D_2/M_2 geodynamic regime, and may provide clarity on the viability of top-down versus bottom-up mechanisms for lithosphere removal.

APPENDIX

This chapter is published as:

Tucker, N. M., Morrissey, L. J., Payne, J. L. & Szpunar, M. 2018. Genesis of the Archean–Paleoproterozoic Tabletop Domain, Rudall Province, and its endemic relationship to the West Australian Craton. *Australian Journal of Earth Science,* in press, doi: 10.1080/08120099.2018.1479307.

Statement of Authorship

Title of paper	Genesis of the Archean–Paleoproterozoic Tabletop Domain, Rudall Province, and its endemic relationship to the West Australian Craton
Pulication status	☒ Published ☐ Accepted for publication ☐ Submitted for publication ☐ Unpublished and unsubmitted work written in manuscript style
Publication details	Tucker, N. M., Morrissey, L. J., Payne, J. L. & Szpunar, M. Genesis of the Archean–Paleoproterozoic Tabletop Domain, Rudall Province, and its endemic relationship to the West Australian Craton. *Australian Journal of Earth Science,* in press, doi: 10.1080/08120099.2018.1479307.

Principal Author

Name of Principal Author	Naomi M. Tucker
Contribution to the paper	Project design; fieldwork; sample selection and preparation; petrography; LA–ICP–MS and SEM data collection; LA–ICP–MS data processing; data interpretation; regional data compilation; manuscript design and composition; creation of all figures.
Overall percentage (%)	60
Certification	This paper reports on original research I conducted during the period of my Higher Degree by Research candidature and is not subject to any obligations or contractual agreements with a third party that would constrain its inclusion in this thesis. I am the primary author of this paper.
Signature	Date 08/02/2018

Co-author contributions

By signing the Statement of Authorship, each author certifies that:

i. the candidate's stated contribution to the publication is accurate (as detailed above);
ii. permission is granted for the candidate to include the publication in the thesis; and,
iii. the sum of all co-authors contributions is equal to 100 % less the candidate's stated contribution.

Name of Co-author	Laura J. Morrissey
Contribution to the paper	Project design; fieldwork; sample selection and preparation; LA–ICP–MS and SEM data collection; LA–ICP–MS data processing; data interpretation; manuscript review.
Signature	Date 08/02/2018

Name of Co-author	Justin L. Payne
Contribution to the paper	Project design; fieldwork; sample selection and preparation; LA–ICP–MS and SEM data collection; LA–ICP–MS data processing; data interpretation; manuscript review.
Signature	Date 08/02/2018

Name of Co-author	Mike Szpunar
Contribution to the paper	Project design; fieldwork and logistical support; discussions/assistance with data interpretation; manuscript review.
Signature	Date 20/02/2018

Genesis of the Archean–Paleoproterozoic Tabletop Domain, Rudall Province, and its endemic relationship to the West Australian Craton

Naomi M. Tucker[a,b], Laura J. Morrissey[b], Justin L. Payne[c,b] and Michael Szpunar[c]

[a]*Department of Earth Science, School of Physical Sciences, The University of Adelaide, Adelaide, South Australia 5005, Australia*

[b]*School of Natural and Built Environments, University of South Australia, Mawson Lakes Campus, South Australia 5095, Australia*

[c]*Fortescue Metals Group Ltd, East Perth, Western Australia 6004, Australia*

ABSTRACT

The Tabletop Domain of the Rudall Province has been long thought an exotic entity to the West Australian Craton. Recent re-evaluation of this interpretation suggests otherwise, but is founded on limited data. This study presents the first comprehensive, integrated U–Pb geochronology and Hf-isotope analysis of igneous and metasedimentary rocks from the Tabletop Domain of the eastern Rudall Province. Field observations, geochronology and isotope results confirm an endemic relationship between the Tabletop Domain and the West Australian Craton (WAC), and show that the Tabletop Domain underwent a similar Archean–Paleoproterozoic history to the western Rudall Province. The central Tabletop Domain comprises Archean–Paleoproterozoic gneissic rocks with three main age components. Paleo–Neoarchean (ca. 3400–2800 Ma) detritus is observed in metasedimentary rocks and was likely sourced from the East Pilbara Craton. Protoliths to mafic gneiss and metasedimentary rocks are interpreted to have been emplaced and deposited during the early Paleoproterozoic (ca. 2400–2300 Ma), and exhibit age and isotopic affinities to the Capricorn Orogen basement (Glenburgh Terrane). Mid–late Paleoproterozoic mafic and felsic magmatism (ca. 1880–1750 Ma) is assigned to the Kalkan Supersuite, which is exposed in the western Rudall Province. The Kalkan Supersuite provided the main source of detritus for mid–late Paleoproterozoic metasedimentary rocks in the Tabletop Domain. Similarities in the age and Hf-isotope compositions of detrital zircon from these metasedimentary rocks and Capricorn Orogeny basin sediments suggests that a regionally extensive, linked basin system may have spanned the northern WAC at this time. The Tabletop Domain records evidence for two metamorphic events. Mid–late Paleoproterozoic deformation (ca. 1770–1750 Ma) was high-grade, regional and involved the development of gneissic fabrics. In contrast, early Mesoproterozoic (ca. 1580 Ma) high-grade deformation was localised and associated with more widespread, late-stage, greenschist facies alteration. These new findings highlight that the Tabletop Domain experienced a much higher grade of deformation than previously assumed, with a Paleoproterozoic metamorphic history similar to that of the western Rudall Province.

1. INTRODUCTION

Two-thirds of the Australian continent comprises Archean–Paleoproterozoic cratons united by Paleo–Mesoproterozoic orogens. These orogens—including the Capricorn Orogen, Paterson Orogen, Musgrave Inlier and Albany–Fraser Orogen (Cawood and Korsch, 2008)—contain the record of the amalgamation of Proterozoic Australia. The Rudall Province forms part of the Paterson Orogen and is situated between the West Australian Craton (WAC) and North Australian Craton (NAC; Fig. 1; Bagas, 2004; Bagas and Smithies, 1997) and is therefore in a unique location to reveal the relationship between these two cratons. However, despite its key position, the Rudall Province remains relatively understudied owing to remoteness and limited outcrop. This has meant that there are relatively few robust geochronological constraints on the timing of magmatism, sedimentation, deformation and metamorphism in the Rudall Province, leading to debate about its origin and relationship to the neighbouring cratons.

Most reconstructions of Proterozoic Australia propose that collision of the WAC and NAC occurred during the Paleoproterozoic Yapungku

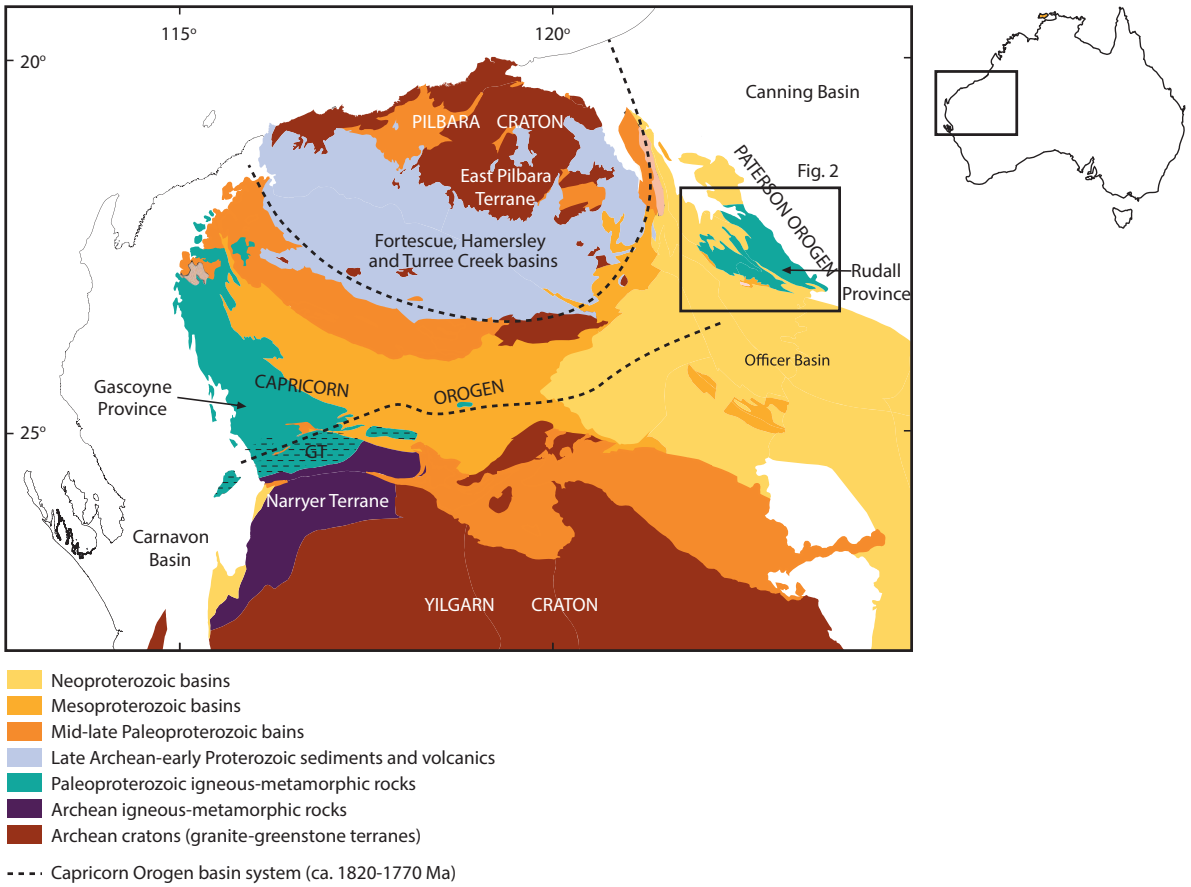

Figure 1. Regional geological map of far northwestern Western Australia showing the Archean Yilgarn and Pilbara cratons, and Neoarchean–Neoproterozoic orogens and basins. The boxed region surrounding the Rudall Province is enlarged in Figure 2. The boxed area on Australia (pictured top right) indicates the geographic location of the map. Abbreviations: GT, Glenburgh Terrane (dashed polygon stippling). Figure modified after Kirkland *et al.* (2013b).

Orogeny at ca. 1800–1765 Ma (e.g. Bagas, 2004; Betts and Giles, 2006; Betts et al., 2016; Cawood and Korsch, 2008; Johnson, 2013; Smithies and Bagas, 1997). The suture zone was long suspected to be in the Rudall Province (e.g. Bagas, 2004; Bagas and Lubieniecki, 1999), supported by the recognition of high-pressure metamorphism (Smithies and Bagas, 1997), as well as differences in the apparent timing of magmatism and the grade of metamorphism between the different domains of the Rudall Province (Bagas, 1999, 2004; Bagas and Smithies, 1998; Smithies and Bagas, 1998), and the suggestion that some parts of the Rudall Province were deformed and metamorphosed at a similar time to the Arunta Orogen, prior to ca. 1765 Ma (Bagas, 2004; Bagas and Smithies, 1997). Accordingly, the Rudall Province was considered a 'suspect' terrane with respect to the WAC. However, recent work utilising U–Pb, Lu–Hf, Sm–Nd and oxygen isotopes suggests that the Rudall Province has more in common with the WAC than the NAC (Kirkland et al., 2013b). Specifically, the western Rudall Province has Hf-isotopic affinity to the East Pilbara Terrane and U–Pb affinities to the Glenburgh Terrane, which occurs as basement to the Capricorn Orogen (Fig. 1; Kirkland et al., 2013b), implying that the proposed exotic origin for the Rudall Province is incorrect. Instead, the Rudall Province is interpreted to be autochthonous, having evolved by thickening and reworking of the WAC margin, with the WAC–NAC suture probably located east of the Rudall Province and beneath the Canning Basin (Kirkland et al., 2013b). Recent geochronological, geochemical and *P–T* data from the Rudall Province (Anderson, 2015; Maidment, 2017) also suggest that the amalgamation of the WAC and NAC may have occurred during the Mesoproterozoic, at a significantly later time than previously considered.

The majority of previous research has focused on the western Rudall Province, with a paucity of geochronological, geochemical and isotopic data for the eastern Rudall Province. The paucity of data from the eastern Rudall Province has created uncertainty about its relationship to the western Rudall Province and, more broadly,

to the WAC or NAC. The lack of geological constraints in the eastern Rudall Province has also significantly hindered the development of well-constrained Proterozoic tectonic reconstruction models involving this region. This study focusses on the Tabletop Domain in the eastern Rudall Province. In this contribution, we present the results of U–Pb geochronology combined with Lu–Hf isotope analyses to constrain the timing of magmatism, sediment provenance, and the isotopic evolution of a previously unrecognised Archean–Paleoproterozoic basement. The findings of this study suggest there are temporal and isotopic similarities between the eastern and western Rudall Province, and confirms affinity of the entire Rudall Province to the WAC.

2. GEOLOGICAL BACKGROUND

2.1 Regional geological framework

The Rudall Province forms part of the Paterson Orogen, which bounds the northeastern margin of the WAC (Fig. 1). The Paterson Orogen comprises a 2000 km-long region of exposed Paleo–Mesoproterozoic meta-igneous and metasedimentary rocks, and unconformably overlying Meso–Neoproterozoic sedimentary rocks (Bagas, 1999, 2004; Bagas and Smithies, 1998; Bagas et al., 2000; Maidment, 2017; Smithies and Bagas, 1998). The Paterson Orogen passes along strike into the Petermann Orogen within the Musgrave Inlier, southeast of the Rudall Province (Camacho and McDougal, 2000; Raimondo et al., 2010; Scrimgeour and Close, 1999; Walsh et al., 2013). These two regions are linked by a pronounced gravity high known as the Anketell Regional Gravity Ridge (Fraser, 1976) that is concealed by the Neoproterozoic–Paleozoic Officer, Yeneena and Canning basins, and recent sand dunes (Bagas et al., 2000; Cawood and Korsch, 2008; Hocking et al., 1994).

The Rudall Province has previously been subdivided into three, fault-bound lithotectonic terranes on the basis of lithology, magmatic protolith ages and variation in metamorphic grade (Fig. 2a; Bagas and Smithies, 1998). However, the term ‘terrane’ is not appropriate to describe these crustal blocks as they do not represent discrete crustal fragments with distinct geological histories (e.g. Kirkland et al., 2013b; Maidment, 2017, and this contribution). We therefore use the term ‘domain’ throughout this contribution, and recommend it for adoption in the wider literature. The Talbot and Connaughton domains occupy the north–northwest and southeast Rudall Province, respectively (Fig. 2). The Tabletop Domain is located in the eastern Rudall Province and is clearly separated from the Talbot and Connaughton domains by the crustal-scale, east-dipping Camel–Tabletop Fault (Fig. 2; Bagas and Smithies, 1998).

The Talbot and Connaughton domains contain similar lithologies, protolith ages and geological timelines (Fig. 3), and although the boundary is taken to be a folded shear zone, the shear zone itself is not a significant structural feature (Fig. 2b; Bagas, 2004; Bagas and Smithies, 1998; Bagas et al., 2000; Hickman and Bagas, 1998, 1999). The Connaughton Domain contains amphibolite, mafic granulite and ultramafic rocks that are, in places, interlayered with banded iron formation, metachert, and metasedimentary rocks (Bagas and Smithies, 1998). The oldest ages from the Connaughton Domain are derived from a sample of quartzite, which has a maximum depositional age of 2833 ± 5 Ma, and detrital zircon spectra ranging between 3579 and 2830 Ma (Maidment, 2017). The age populations in the quartzite are consistent with derivation from volcanic and sedimentary units from the 2775–2629 Ma Fortescue and 2629–2445 Ma Hamersley basins, which unconformably overlie granite–greenstones of the Pilbara Craton (Fig. 1; Maidment, 2017). The Talbot Domain is similar to the Connaughton Domain in that it contains siliciclastic and chemical metasedimentary rocks, voluminous granitic gneiss and minor mafic and ultramafic rocks (Hickman and Bagas, 1998; Maidment, 2017). The Talbot Domain is divided into an older, ‘western’ association of quartzite, mafic–ultramafic rocks and banded iron formation and a ~5 km-thick, younger, ‘eastern’ siliciclastic succession comprising paragneiss, quartzite, schist and chert (Bagas, 2004; Hickman and Bagas, 1998, 1999). The oldest exposed unit in the western Talbot Domain is an intensely layered, inferred granodioritic–syenogranitic orthogneiss that encloses xenoliths of western supracrustal rocks (Hickman and Bagas, 1998). Two samples of the layered quartzo-feldspathic gneiss yielded zircon populations at 2015 ± 26 Ma and 1972 ± 4 Ma (Nelson, 1995a, d), initially inferred as the crystallisation age of a felsic igneous protolith (Hickman and Bagas, 1998). Inferred inherited zircon from the same lithology yielded ages of 2715–2577 Ma (Hickman and Bagas, 1998; Nelson, 1995a). In contrast to previous

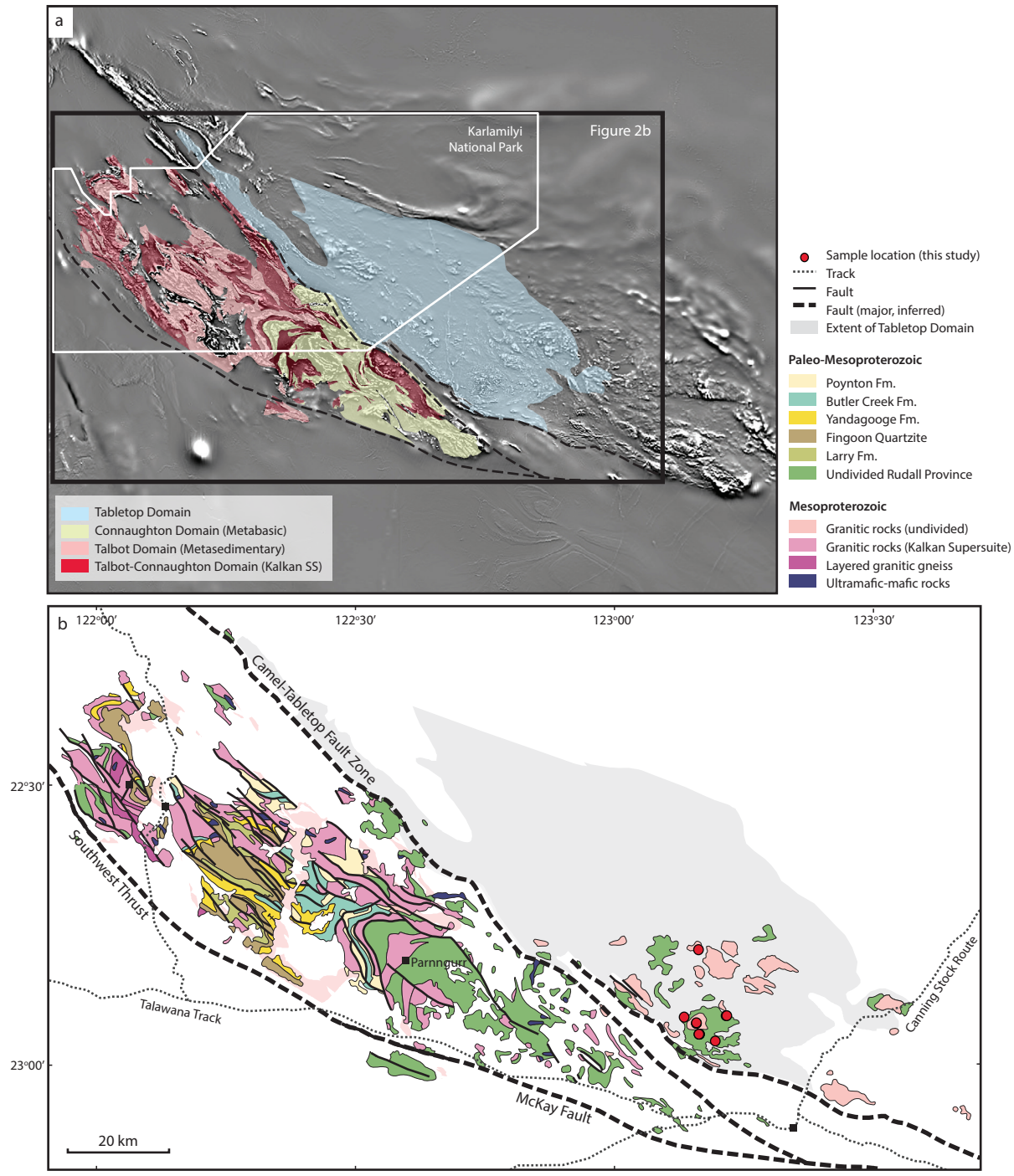

Figure 2. Simplified geology of the Rudall Province. (a) Total magnetic imagery of the Rudall Province overlain by coloured polygons that indicate the spatial extent of the Tabletop Domain (blue), Talbot Domain (pink), Connaughton Domain (yellow) and the Kalkan Supersuite (red; Talbot and Connaughton domains, undivided). The area corresponding to the Karlamilyi National Park is outlined in white. The map extent of Figure 2b is outlined by the black box. (b) Main lithological units and structural features of the Rudall Province (after Maidment, 2017). The approximate areal extent of the Tabletop Domain (as shown in Figure 2a) is shaded grey. Sample localities from this study are indicated as red circles (note that several sample locations overlap in the central Tabletop Domain).

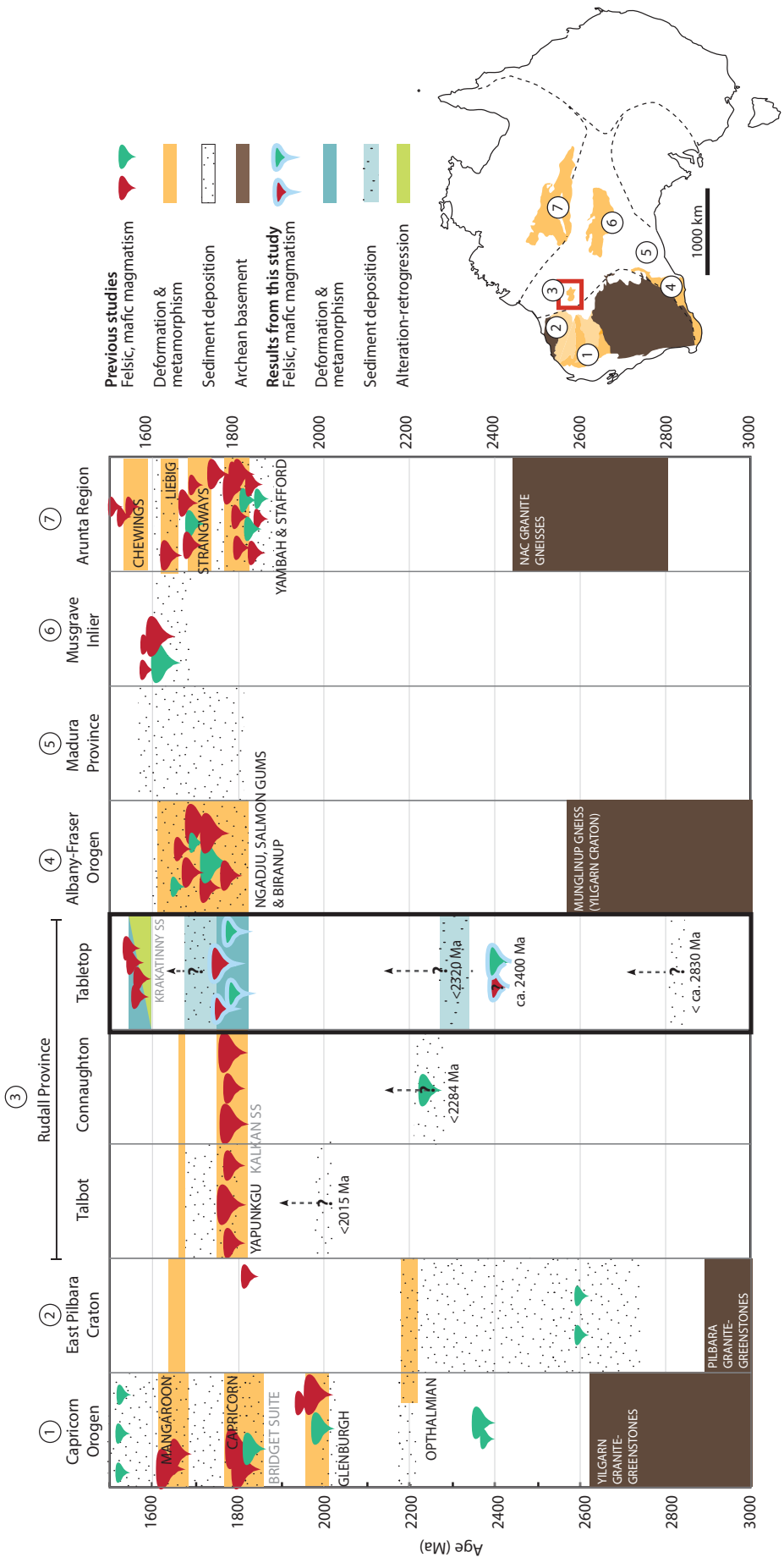
Previous studies
Felsic, mafic magmatism
Deformation & metamorphism
Sediment deposition
Archean basement
Results from this study
Felsic, mafic magmatism
Deformation & metamorphism
Sediment deposition
Alteration-retrogression
1000 km
1 Capricorn Orogen
2 East Pilbara Craton
3 Rudall Province
Talbot
Connaughton
Tabletop
4 Albany-Fraser Orogen
5 Madura Province
6 Musgrave Inlier
7 Arunta Region
MANGAROON
CAPRICORN
BRIDGET SUITE
GLENBURGH
YAPUNKGU
KALKAN SS
KRAKATINNY SS
<2015 Ma
<2284 Ma
<2320 Ma
ca. 2400 Ma
< ca. 2830 Ma
OPTHALMIAN
NGADJU, SALMON GUMS & BIRANUP
MUNGLINUP GNEISS (YILGARN CRATON)
YILGARN GRANITE-GREENSTONES
PILBARA GRANITE-GREENSTONES
CHEWINGS
LIEBIG
STRANGWAYS
YAMBAH & STAFFORD
NAC GRANITE GNEISSES
Age (Ma)
1600
1800
2000
2200
2400
2600
2800
3000

Figure 3. (previous page) Simplified time–space diagram for the Neoarchean to Mesoproterozoic (ca. 1500 Ma) evolution of west and north Australia (after Maidment, 2017). Tectonic regions of interest are ordered (left to right) according to their approximate, present-day geographic location from west to east. These regions are also numbered on the adjacent map of Australia, where they are shown in their present-day configuration. On the map, brown represents Archean cratons; yellow represents Proterozoic orogens; light yellow regions represent Proterozoic basins (also part of the Capricorn Orogen). New results from the Tabletop Domain (this study) are distinguished in blue and green on the time–space plot. The names of orogenic events are denoted in black text; the name of magmatic suites are given in grey. Maximum ages of sediment deposition in the Rudall Province are noted.

interpretations, Maidment (2017) interpreted the protolith to this rock as sedimentary, with a maximum depositional age of ca. 2015 Ma. The 'eastern' siliciclastic succession includes the Fingoon Quartzite and Larry Formation, which were deposited after 1794–1791 Ma and 1760 ± 5 Ma, respectively (Kirkland et al., 2013a; Maidment, 2017; Nelson, 1995c). These units are interpreted to represent a syn- or post-magmatic cover sequence derived from the Kalkan Supersuite (see below; Maidment, 2017).

The Talbot and Connaughton domains share a Paleoproterozoic magmatic history as they both contain sheet-like, felsic–intermediate augen orthogneiss (Kalkan Supersuite) with protoliths emplaced between 1804 and 1762 Ma (Bagas, 2004; Bagas and Smithies, 1998; Hickman and Bagas, 1998, 1999; Maidment, 2017, and references therein; Table 3). Geochemical data suggest that igneous protoliths to the Kalkan Supersuite formed near the crust–mantle interface, beneath extended and thinned crust (Maidment, 2017). Reading, et al. (2012) propose that extended Pilbara Craton crust occurs as basement to the Talbot Domain, based on a series of seismic transects across the Capricorn and Paterson orogens. Kirkland et al. (2013b) subsequently drew similar conclusions, noting that the isotopic signature of magmatic zircon from the Kalkan Supersuite was comparable with the East Pilbara Bridget Suite. Further, similarities are also observed between the isotopic composition and age of inferred xenocrystic (inherited) zircon from the Kalkan Supersuite and detrital zircon in sedimentary rocks from the Capricorn Orogen basement (Glenburgh Terrane of the Gascoyne Province, ca. 2005–1970 Ma; Fig. 1; Kirkland et al., 2013b). This observation suggests that Kalkan Supersuite granitic rocks assimilated the sedimentary successions that they intruded during their emplacement into the upper crust, and that these sedimentary successions were derived from detritus shed off the southern Gascoyne Province, likely into a regionally extensive basin system across the Capricorn and Paterson orogens at this time (Kirkland et al., 2013b).

There is little evidence for magmatism younger than the ca. 1800–1760 Ma Kalkan Supersuite in either the Talbot or Connaughton domains. A monzogranite dated at 1453 ± 10 Ma (Nelson, 1996a) has a zircon Hf-isotope signature that is more juvenile than any analysed samples from the Rudall Province (Kirkland et al., 2013b). This sample, however, has recently been interpreted as a glacigenic clast and comes from a region mapped as Permian glacial deposits where it is surrounded by other boulders of varied lithology (Maidment, 2017). The potential significance of the unique age and Hf-isotope signature of this sample for the Rudall Province is therefore unknown. A pegmatite dyke dated at 1291 ± 10 Ma provides the only evidence of magmatism younger than ca. 1770 Ma in the Connaughton Domain (Nelson, 1995b).

The Tabletop Domain in the eastern Rudall Province is poorly exposed (e.g. Figs 2b and 4a), and is separated from the Talbot and Connaughton domains by the crustal-scale, east-dipping, Camel–Tabletop Fault Zone (Fig. 2; Bagas, 1999; Bagas and Smithies, 1998; Smithies and Bagas, 1998). Limited geochronological data suggest that the Tabletop Domain is dominated by early Mesoproterozoic tonalite that forms part of the calc-alkaline Krackatinny Supersuite (1589–1549 Ma) and leucogranites that form part of the newly defined Camel Suite (1310–1286 Ma). An age of 1476 ± 10 Ma was also obtained for a sample of granodiorite (Bagas, 2004). The Krackatinny Supersuite has geochemical characteristics consistent with A-type magmatism and is suggested to have formed in either a continental arc or as an intraplate rift in thickened crust (Maidment, 2017). Rocks intruded by the Krackatinny Supersuite also have geochemical characteristics consistent with development in an arc-like setting, but their age remains poorly constrained (Maidment, 2017). In contrast to other regions of the Rudall Province, there is an apparent lack of Paleoproterozoic felsic magmatism and sedimentation in the Tabletop Domain (Bagas, 1999; Smithies and Bagas, 1998). Nonetheless, one sample of quartzite yielded a maximum depositional age of 2833 ± 5 Ma, and

Table 1. Paleoproterozoic to Neoproterozoic (Miles Orogeny) tectono-thermal events in the Rudall Province

	Talbot and Connaughton Domains		**Tabletop Domain**		
	Bagas (2004) *Hickman and Bagas (1999)** *Smithies and Bagas (1997)*	*Revised constraints from:* *Maidment (2017)* *Anderson (2015)*	*Bagas (2004)* *Hickman and Bagas (1999)**	*Yeates and Chin (1979)*	*This study*
D_1	Layer-parallel schistosity (S_1); localised preservation			Gneissic layering (S_1)	Gneissic layering (S_1)
	Low-*P*, mid-amphibolite facies			Migmatitic veining; possible (granitic) anatexis	Regional, upper amphibolite facies
	Yapungku Orogeny (early) ≥1802 ± 14 Ma			Age unconstrained; hbl-bearing adamellite, granodiorite, and minor mafic–ultramafic rocks post-date S_1	ca. 1770–1750 Ma
D_2	Regional NE-dipping schistosity (S_2) and lineation; tight to isoclinal F_2 folding (WNW–N-trending, overturned towards SSW)	Regional gneissic fabric (S_2) < ca. 1780 Ma		Schistosity (S_2), isoclinal folding	Transposition of S_1 by NE-plunging folding; development of F_2 axial planar cleavage (S_2)
	Moderate to high-P, high-*T* amphibolite facies (M_2): ~12kbar, 800 °C	Moderate to high-*P*, amphibolite facies (M_2) ca. 1380 Ma: 8–11 kbar, 620–650 °C ca. 1285 Ma: 5.5–8.5 kbar, 600–650 °C		Regional greenschist facies (M_2)	Locally high-grade (geochronology); late, pervasive, greenschist alteration/retrogression
	Yapungku Orogeny (main) ca. 1800–1765 Ma			Pre-Yeneena Basin deposition	*Krackatinny Event* ca. 1600–1550 Ma: locally high-grade ca. 1580 Ma: greenschist alteration
Unassigned ?metamorphic ages		ca. 1680 Ma (geochronology) Significance unclear			ca. 1680 Ma (minor, geochronology) Significance unclear
		ca. 1580 Ma (geochronology) Localised, contact metamorphism			
D_3	Localised faulting and quartz veining along Rudall Province–Yeneena Basin unconformity; localised recumbent folding of Yeneena Basin (F_3)			Folding, NW-trending faulting, and development of a strong cleavage (S_3)	
	No metamorphism documented			Low-grade metamorphism	
	Miles Orogeny (early) Neoproterozoic, post-dates Yeneena Basin formation			Neoproterozoic, post-dates Yeneena Basin formation; pre-dates deposition of Karara Formation	
D_4	Upright, tight to isoclinal, NW-trending folding (F_4); development of steeply NE-dipping (F_4) axial planar cleavage (S_4).	Localised upright NW-trending tight folds		Open to tight W-trending folding; development of spaced fracture cleavage to slaty cleavage	
	Lower greenschist facies (M_4)		Greenschist facies		
	Miles Orogeny (main) ?810-650 Ma		Post-dates Krackatinny Supersuite (<1590–1550 Ma)		

*Summarised after Maidment (2017).

a range of detrital zircon ages between 3579 and 2830 Ma that are consistent with a Pilbara Craton source (Maidment, 2017). Inherited zircon from a sample of ca. 1310 Ma leucogranite yielded ages between 2465 and 1694 Ma, alluding to the presence of unexposed Paleoproterozoic rocks (Maidment, 2017). High Bouguer gravity anomalies also indicate that mafic rocks are potentially more widespread than the outcrop exposures in the Tabletop Domain would suggest (Maidment, 2017).

2.2 Structural evolution of the Rudall Province

The Rudall Province has experienced six deformational phases (Bagas, 2000, 2004; Bagas and Smithies, 1998; Clarke, 1991; Hickman and Bagas, 1999; Maidment, 2017; Smithies and Bagas, 1997), with metamorphism associated with events D_1, D_2 and D_4 (Table 1). This framework, however, has primarily been established from observations in the Talbot and Connaughton domains (Maidment, 2017). Previous studies link D_1 and D_2 to the ca. 1800–1765 Ma Yapungku Orogeny (e.g. Bagas, 2004), and the development of early (S_1) layer-parallel fabrics that are deformed by north–northwest-verging, F_2 tight–isoclinal folds, crosscutting northeast-dipping schistose (S_2) fabrics, and west–southwest-directed thrusts (Bagas, 2000, 2004; Clarke, 1991; Hickman and Bagas, 1999). Deformation was inferred to be synchronous with emplacement of the Kalkan Supersuite (Bagas, 2004; Hickman and Bagas, 1999), with a minimum constraint for D_2 based on an inferred undeformed, cross-cutting 1778 ± 16 Ma aplite dyke (Nelson, 1995e). Re-examination of field relationships by Maidment (2017) indicate that other dykes in the same region are deformed by inferred S_2 fabrics and/or occur subparallel to the S_2 foliation within their host rock, and instead the apparent variable record of deformation is a reflection of the low mica content of the dykes. The age of the deformed felsic dykes and Kalkan granites thus place a maximum, rather than minimum, constraint on the age of D_2 deformation (Maidment, 2017).

Metamorphism associated with the interpreted D_2 event includes garnet–clinopyroxene assemblages that record peak pressures up to 1.2 GPa (Smithies and Bagas, 1997). This event was initially considered to represent Paleoproterozoic (ca. 1780 Ma) collision–accretion of the Pilbara Craton with an exotic terrane, synchronous with deformation in the Arunta Region and Capricorn Orogen (Bagas, 2004; Bagas and Smithies, 1997). More recently, this hypothesis developed to suggest that the ca. 1800–1765 Ma Yapungku Orogeny reflected the amalgamation of the NAC with the WAC, and is now adopted in numerous, current paleo-tectonic reconstructions of Proterozoic Australia (e.g. Aitken et al., 2016; Betts and Giles, 2006; Betts et al., 2002; Cawood and Korsch, 2008; Huston, et al., 2012; Johnson, 2013; Li, 2000; Lindsay, 2002; Payne et al., 2009). In this scenario, the Camel–Tabletop Fault (Fig. 2b) was interpreted to mark the suture zone between the inferred exotic Tabletop Domain (Bagas and Smithies, 1998), and the combined Talbot and Connaughton domains, that were considered part of the WAC. However, phase equilibria modelling and geochronology by Anderson (2015) demonstrated that M_2 reached peak metamorphic conditions of ~0.8–1.1 GPa and ~620–650 °C at ca. 1380 Ma. A sample with modelled *P–T* conditions of 0.55–0.85 GPa and 600–650 °C also yielded a metamorphic age of ca. 1285 Ma (Anderson, 2015). Collectively, these data suggest the identified M_2 (and any hypothesised collision event) was Mesoproterozoic in age. The age of D_1 remains unconstrained in the Talbot and Connaughton domains but Anderson (2015) and Maidment (2017) obtained metamorphic ages of ca. 1790–1740 Ma and ca. 1680 Ma, the former presumably relating to the development of the gneissic fabric (S_1) and a long-lived D_1 event (D_1 of Hickman and Bagas, 1999).

Bagas (2004) and Hickman and Bagas (1999) defined the accepted structural and metamorphic regime of the Tabletop Domain, and did not find evidence for D_1 or D_2 in the Tabletop Domain (Table 1). Pervasive greenschist facies metamorphism was assigned to the D_4 event and intrusive rocks (presumably largely Krackatinny Supersuite) were only considered strongly foliated near the Camel–Tabletop Fault Zone. Conversely, earlier regional mapping summarised in Yeates and Chin (1979) identified paragneiss, banded gneiss, granite gneiss and minor migmatite in addition to various schists and quartzites. The gneissic fabric (S_1) observed in these lithologies is associated with migmatitic veining and possibly anatectic granite formation (Yeates and Chin, 1979). The absolute age of this event was not constrained by Yeates and Chin (1979) but it was considered to pre-date the intrusion of hornblende adamellite, granodiorite, and small bodies of dacite, gabbro and ultramafic rocks. Based upon

Table 2. Summary of samples

Sample	Depth (m)*	Location (Zone 51K)		Lithology	Mineralogy
		Easting (mE)	Northing (mN)		
PMDDH04-14	345.6–346.32	522100	7465150	Mafic gneiss	hbl–pl-q ± pxn (ser–chl)
PMDDH04-12	314.0–315.95	522100	7465150	Foliated hornblende-bearing granite	q–pl–ksp–hbl ± bi (chl-q-ksp veins)
D525128	-	516090	7463607	Hornblende-bearing gneiss	hbl–pl–q–mt–ap (ser–chl)
GAZ7	39.35–40.0	516155	7461440	Granite gneiss	q–pl–ksp ± bi (chl–hem)
D525108	-	516072	7463727	Leucogranite	q–ksp–pl
D525052	-	515695	7478780	Quartzofeldspathic gneiss	q–ksp–pl ± bi
D525121	-	513604	7464866	Foliated muscovite-bearing quartzite	q ± mu
GAZ9	49.3–49.9	516155	7461440	Garnet-biotite gneiss	g–bi–q–pl–ksp ± pxn (ser–chl)
GAZ21	183.6–184.0	516155	7461440	Calc-silicate gneiss	hbl–chl–ep–ser–pl-q ± pxn (calcite veins)
D525013	-	519840	7459454	Calc-silicate/skarn	(ep–chl–pl ± gr–cpy)

Datum WGS84

*Samples from drill core only.

Mineral abbreviations: ap, apatite; bi, biotite; chl, chlorite; cpy, chalcopyrite; ep, epidote; gr, graphite; hem, hematite; hbl, hornblende; ksp, K-feldspar; mt, magnetite; pl, plagioclase; pxn, pyroxene; q, quartz; ser, sericite. Minerals denoted in brackets indicate alteration/retrogression overprint on main mineral assemblage.

their dominance of Tabletop Domain outcrop, it is plausible that these intrusive rocks comprise part of the Krackatinny Supersuite. Yeates and Chin (1979) also identified isoclinal folding of S_1 and the development of a strong schistosity during D_2. This D_2 event was associated with pervasive greenschist facies metamorphism throughout the Tabletop Domain. D_2/M_2 is considered to post-date emplacement of the Krackatinny intrusive rocks but pre-date deposition of the Neoproterozoic Yeneena Group sediments.

The seemingly different metamorphic histories of the Tabletop Domain and Connaughton/Talbot domains as presented in Bagas (2004) was suggested by Maidment (2017) to reflect a paucity of outcrop of units that experienced higher thermal conditions prior to younger, greenschist facies metamorphism. Zircon overgrowths from quartzite within the central Tabletop Domain that have an age of 1790 ± 7 Ma (Maidment, 2017) may support the presence of an older, high-grade metamorphic event. Such an interpretation is potentially consistent with the D_1 and D_2 observations of Yeates and Chin (1979). Maidment (2017) also analysed metamorphic zircon rims from quartzite that yielded an age of ca. 1580 Ma, interpreted to represent contact metamorphism of the host quartzite by nearby Krackatinny Suite intrusions.

The ca. 810–650 Ma D_3–D_4 Miles Orogeny occurred in response to southwest-directed compression and resulted in southeast–northwest-trending, upright to inclined folding, extensive greenschist facies retrogression of Paleo–Neoproterozoic rocks, and re-activation of both the Camel–Tabletop Fault (Czarnota et al., 2009) and the Southwest Thrust–McKay Fault that bounds the southwestern margin of the Rudall Province (Hickman and Bagas, 1998, 1999). The Miles Orogeny has been linked to development of sediment-hosted copper deposits and unconformity-related uranium mineralisation (Huston et al., 2012). The ca. 650–550 Ma D_5 event resulted in localised, northeast-trending open folding in the Talbot Domain (Bagas, 2000, 2004). North–northeast-directed compression during the D_6 Paterson Orogeny (ca. 550 Ma) resulted in strike-slip movement along north–northwest and east–northeast-striking faults, east-southeast-trending open folding and dextral reactivation of D_4 structures (Bagas, 2000, 2004; Hickman and Bagas, 1998). Thrusting and transpressional movement along the Camel–Tabletop Fault during D_4–D_6 also resulted in localised graben development that was infilled by rocks of the ca. 800 Ma Karara Formation (Bagas and Smithies, 1998). The Paterson Orogeny in the Rudall Province was contemporaneous with the Petermann Orogeny in the Musgrave Inlier, which potentially implies the juxtaposition of these two regions by the Neoproterozoic–Cambrian (Bagas, 2004; Raimondo et al., 2008).

3. FIELD OBSERVATIONS AND SAMPLE SELECTION

We present new field observations and photographs (Fig. 4) that confirm the presence of a high-grade tectonic history within the Tabletop Domain. These new observations are similar to Yeates and Chin (1979; Table 1).

The Tabletop Domain can be broadly subdivided


a. Typical outcrop appearance & F1-F2 interference
N
F2
F1
50 cm
b. Leucosomes in quartzofeldspathic gneiss
leucosomes
c. D525128 (mafic gneiss)
d. PMDDH04-14 (mafic granite)
f. GAZ-7 (granite gneiss)
e. PMDDH04-12 (foliated granite)
g. D525108 (leucogranite)
h. D525052 (quartzofeldspathic gneiss)
i. D525121 (foliated quartzite)
j. GAZ-9 (garnet-biotite gneiss)
k. GAZ-21 (calc-silicate)

Figure 4. (facing page) Representative field photographs. (a) Typical outcrop appearance in the Tabletop Domain. A macroscale inferred F_1–F_2 fold interference pattern (outlined by the dashed line) is also pictured; (b) Quartz–feldspar-rich leucosomes occurring layer-parallel to gneissic fabrics in quartzofeldspathic gneiss the Copper Hills region; (c) Retrogressed, hornblende-rich mafic gneiss (sample D525128) exposed in the central Tabletop Domain. Coarse-grained hornblende-bearing leucosomes are shown occurring discordant to gneissic fabrics; (d) Strongly-foliated mafic gneiss intersected in drill core (sample PMDDH04-14); (e) Foliated hornblende-bearing granite (sample PMDDH04-12) intersected within the same drill hole as sample PMDDH04-14. Down-section of the sampled interval, foliated granite similar in appearance to sample PMDDH04-12 hosts centimetre-scale enclaves of strongly-foliated mafic gneiss; (f) Compositionally-banded granite gneiss intersected in drill core (sample GAZ-7); (g) Biotite-poor leucogranite (D525108) from near the location of D525128; (h) Biotite-bearing quartzofeldspathic gneiss (sample D525052); (i) Muscovite-bearing quartzite (D525121). Original sedimentary layering is preserved and dips near-vertically; (j) Garnet–biotite gneiss intersected in drill core (sample GAZ-9); (k) Calc-silicate gneiss (sample GAZ-21) occurring immediately down-section of strongly-deformed mafic gneiss. Where pictured, the scale bar increments represent one centimetre.

into several sub-domains based on geophysical expression and dominant lithology. The central Tabletop Domain comprises strongly deformed and locally homogeneous felsic, intermediate and mafic gneisses, which we interpret to have an igneous protolith. This sub-domain also comprises calc-silicate and garnet-bearing gneisses, interleaved with quartzite and quartzo-feldspathic gneiss that we suggest forms part of a metasedimentary succession. Both the meta-igneous and metasedimentary units have compositional layering (gneissosity), typically defined by alternating biotite- and quartz-rich layers. Biotite forms a well-defined layer-parallel foliation (S_1) with hornblende and quartz defining a linear fabric (L_1) on S_1 surfaces. In the central domain, S_1 is clearly refolded by one, and potentially two generations of folds. At 51K 522242 mE 7464951 mN (Fig. 4a), the outcrop geometry is consistent with a type-2 fold interference pattern. At this locality F_2 fold hinges plunge 45° to the northeast, and S_2 forms an axial planar cleavage (to F_2). Locally, S_2 is defined by the alignment of biotite. All successions in this central subdomain are variably overprinted by a later phase of chlorite-dominated alteration.

Evidence for high-grade deformation and metamorphism is demonstrated by the pervasive gneissic foliation observed in rocks of the central Tabletop Domain and, in some instances, coarse quartzo-feldspathic layers, interpreted as leucosomes that are indicative of partial melting (e.g. Fig. 4b and c). In some instances, leucosomes are deformed and largely parallel the regional gneissic fabric, suggesting syn-D_1 development (e.g. Fig. 4b). In the southwestern part of the central region, undeformed hornblende-bearing leucosomes largely cross-cut the strong gneissic fabric in mafic gneiss (e.g. Fig. 4c), and are accordingly interpreted to post-date D_1. The presence of retrograde chlorite (e.g. sample D525128) replacing hornblende in the leucosomes and paleosomes indicate that melting pre-dates the timing of greenschist retrograde alteration, which is interpreted to be associated with D_2.

The central–northern and northeastern outcrop of the Tabletop Domain is characterised by an abundance of variably deformed to undeformed leucogranites, hornblende–biotite-bearing granitoids, minor quartzo-feldspathic schist, and amphibolite dykes. Based on field observations, these rocks appear to be correlated to the Krackatinny Suite of Maidment (2017). Sparse outcrop in these regions limits inferences on whether the host (country) rock to the Krackatinny intrusive rocks is the mafic and felsic D_1 gneisses exposed within the central sub-region. The southern margin and far eastern region of the Tabletop Domain are characterised by weakly deformed to undeformed granite–granodiorite, quartzo-feldspathic gneiss, augen gneiss and minor mafic rocks. Muscovite-bearing schists and quartzites also crop out in northwestmost part of the southern Tabletop Domain margin (i.e. near the Connaughton Domain) in a region that was previously mapped as unnamed, inferred Mesoproterozoic quartz arenite and schists (Bagas, 1999). The southern Tabletop Domain is juxtaposed against Neoproterozoic sedimentary units of the Officer Basin, and lesser Permian sands, clays and boulder tillite fluvioglacial deposits (Bagas, 1999).

This study focusses on the strongly deformed central region of the Tabletop Domain that in part, comprises a previously unrecognised Archean and Paleoproterozoic succession. Ten representative samples are used for U–Pb geochronology and Lu–Hf isotope analysis to provide robust constraints on the pre-1580 Ma crustal evolution and timing of sedimentation, magmatism and metamorphism of the Tabletop Domain (Fig. 2b; Table 2). Five samples were taken from drill core targeting an elevated magnetic response in the central Tabletop

Domain. Representative field photographs are given in Fig. 4.

4. ANALYTICAL METHODS

4.1 Sample preparation

Zircon grains were separated from crushed rock samples by a combination of hand panning and magnetic separation techniques, and heat treated at 900ºC for 48 h to thermally anneal the internal structural lattice to improve the ablation characteristics and thereby U–Pb age accuracy (e.g. Solari et al., 2015). Approximately 200 zircon grains per sample were hand-picked to obtain a pure separate and mounted in epoxy resin. Zircon grains were imaged using transmitted light, and their internal structure was determined by cathodoluminescence (CL). CL imagery was obtained using an FEI Quanta600 Scanning Electron Microscope equipped with a Gatan CL detector at Adelaide Microscopy, the University of Adelaide.

4.2 U–Pb zircon geochronology

U–Pb zircon geochronology was conducted by Laser–Ablation Inductively Coupled Plasma–Mass Spectrometry (LA–ICP–MS) at Adelaide Microscopy, the University of Adelaide. Analyses were carried out using an ASI M-50 193-nm excimer laser coupled to an Agilent 7700s Quadrupole ICP–MS. Each analysis involved simultaneous measurement on masses ^{202}Hg, ^{204}Pb, ^{206}Pb, ^{207}Pb, ^{208}Pb, ^{232}Th and ^{238}U for dwell times of 20 ms, 20 ms, 30 ms, 60 ms, 20 ms, 20 ms and 30 ms, respectively. Zircon grains were ablated with a frequency of 5 Hz, intensity of approximately 2–3 J cm^{-2} and a spot size of 30 μm. The acquisition time of each analysis was 60 s, inclusive of five pre-ablation laser pulses to remove surficial contamination, 30 s of background measurement and 30 s of ablation.

Data were corrected for mass bias, elemental fractionation and instrument drift based on the measured isotopic ratios of the primary zircon reference material GJ-1 (TIMS normalisation data: ^{207}Pb/^{206}Pb age = 608.3 Ma, ^{206}Pb/^{238}U age = 600.7 Ma, ^{207}Pb/^{235}U age = 602.2 Ma; Jackson et al., 2004), or 91500 (ca. 1065 Ma; Wiedenbeck et al., 1995). GJ-1 and 91500 analyses used as primary standards yielded ^{206}Pb/^{238}U weighted mean ages of 600.3 ± 0.4 Ma (n = 261) and 1062.3 ± 1.0 Ma (n = 116), respectively, over the course of this study providing a measure of the minimum uncertainty that can be expected. Secondary reference standards Plešovice and Temora, as well as GJ-1 and 91500 (when not utilised as primary standards), were analysed concurrently to measure data accuracy by standard–sample bracketing approximately every 15 unknown analyses. Throughout the analytical session, secondary standards Plešovice and Temora yielded respective weighted mean ages of ^{206}Pb/^{238}U = 335.8 ± 0.4 Ma (n = 206, MSWD = 3.8) and ^{206}Pb/^{238}U = 415.7 ± 0.6 Ma (n = 188, MSWD = 2.5), respectively. Where used as secondary standards, GJ-1 and 91500 gave respective ^{206}Pb/^{238}U weighted mean ages of 604.5 ± 0.3 Ma (n = 262, MSWD = 1.0) and 1055.1 ± 1.3 Ma (n = 80, MSWD = 1.02). These measured values for the secondary standards are within analytical uncertainty of the published values (Black et al., 2004; Jackson et al., 2004; Slama et al., 2008; Wiedenbeck et al., 1995).

Data were reduced using Iolite (v. 3.1), including corrections for baseline, instrumental drift, mass bias and down-hole fractionation. Details of the data-reduction methodology are outlined in Paton et al. (2011). Age data were plotted using Isoplot v. 4.15 (Ludwig, 2012). Ages were not corrected for common Pb owing to isobaric interference by ^{204}Hg present in the Ar–He carrier gas; however, analyses were rejected on the basis of elevated levels of ^{204}Pb relative to background concentrations.

The quoted analytical uncertainties on individual analyses are propagated uncertainties that include contributions from the external reproducibility of the primary reference standards GJ-1 and 91500, and are given at the 2σ level. Uncertainties quoted with weighted mean and upper intercept calculations for pooled analyses are given at the 95% confidence level. Calculated weighted mean and upper intercept ages also quote an additional uncertainty (stated in square brackets) that incorporates the systematic uncertainty for the analytical runs (added in quadrature), which is specific to the Adelaide Microscopy facility. This additional uncertainty is derived from the long-term external reproducibility of the secondary reference materials, and amounts to 0.29–0.54%. Both uncertainties are provided in the text to allow for ages and associated uncertainties to be reproduced from the analytical data provided. Analyses that occur outside 2σ uncertainty of concordia are denoted as ‘discordant’.

4.3 Lu–Hf zircon isotope analysis

Lu–Hf isotope analyses by LA–MC–ICP–MS were undertaken at the joint CSIRO–University of Adelaide facility, Waite, South Australia. Analysed grains were selected on the basis of uniform internal structure as visualised in CL, concordance and low ^{204}Pb content. Lu–Hf analysis spots were placed as close as possible to U–Pb analyses and within the same CL zone. For small zircon grains, Lu–Hf analyses were performed directly on top of the U–Pb spots.

Analytical methods for zircon Lu–Hf isotopic determination are detailed in Payne et al. (2013). Analyses were conducted using a New Wave UP–193 Excimer Laser (193 nm) attached to a Thermo-Scientific Neptune Multi Collector ICP–MS equipped with Faraday detectors and 1011 ohm amplifiers. Analyses were carried out under a helium atmosphere mixed upstream of the ablation cell with argon and nitrogen, using a beam diameter of 50 µm, a 5 Hz repetition rate, and an intensity of approximately 6 Jcm^{-2}. Typical ablation times were 60–225 s involving a maximum of 15 measurement cycles, each consisting of ten 0.524 s integrations on ^{171}Yb, ^{173}Yb, ^{175}Lu, ^{176}Hf (+Lu +Yb), ^{177}Hf, ^{178}Hf, ^{179}Hf and ^{180}Hf; one 0.524 s integration on ^{160}Gd, ^{163}Dy, ^{164}Dy, ^{165}Ho, ^{166}Er, ^{167}Er, ^{168}Er, ^{170}Yb and ^{171}Yb, and one 0.524 s integration of Hf oxides with masses ranging from 187 to 196 amu. This ablation time is inclusive of a 1.5 s idle time between subsequent mass changes and an off-peak baseline measurement. Oxide formation rates and REE-oxide interference in high REE zircon were monitored throughout the session. Hf oxide formation rates for all analytical sessions in this study were less than 0.03%.

Data were normalised by an exponential mass bias correction using a natural ^{179}Hf/^{177}Hf ratio of 0.7325. Isobaric interferences of ^{176}Hf by Yb and Lu were corrected using the methods of Woodhead et al. (2004) with direct measurement of ^{171}Yb/^{173}Yb fractionation using the Yb isotopic value of 1.130172 (Segal et al., 2003). Assuming the same mass bias behaviour as Yb, a correction for Lu isotopic interference on ^{176}Hf used a ^{176}Lu/^{175}Lu ratio of 0.02655 (Vervoort et al., 2004).

Instrument performance and stability was monitored by analysis of Plešovice and Mud Tank zircon standards and a JMC475 Hf solution (Payne et al., 2013). Unknown and standard analyses were corrected to a solution JMC ^{176}Hf/^{177}Hf ratio of 0.282160 to account for systematic bias in the measured ^{176}Hf/^{177}Hf of the instrument. This equates to increasing the measured ^{176}Hf/^{177}Hf upwards by approximately 33 ppm (i.e. up by 0.000009). The mean ^{176}Hf/^{177}Hf value for Plešovice over the analytical session was 0.282476 ± 0.000015 (2σ, *n* = 29), which is within uncertainty of the published value of 0.282482 ± 0.000013 (Slama et al., 2008). The mean ^{176}Hf/^{177}Hf value for Mud Tank analyses was 0.282505 ± 0.000014 (2σ, *n* = 46), which is likewise within uncertainty of the published value of 0.282507 ± 0.000006 (Woodhead and Hergt, 2005).

Data were processed using software HfTRAX v. 3.2 (Payne et al., 2013). Depleted mantle crustal model ages ($T_{DMcrustal}$) and epsilon hafnium ($\varepsilon_{Hf}(t)$) values were calculated following the methods of (Griffin et al., 2002). An average crustal composition of ^{176}Lu/^{177}Hf = 0.015, chondritic uniform reservoir (CHUR) values of Bouvier et al. (2008) and a ^{176}Lu decay constant of 1.865 x 10^{-11} yr^{-1} (Scherer et al., 2001) were used.

4.4 U–Pb monazite geochronology

U–Pb monazite geochronology was conducted by LA–ICP–MS at Adelaide Microscopy, the University of Adelaide, using the same methodology and instrumentation as for U–Pb zircon geochronology. Monazite were imaged using a backscatter electron (BSE) detector on a Philips XL30 SEM at Adelaide Microscopy prior to geochronological analysis. Mass bias and elemental fractionation on U–Pb analyses were corrected using the measured isotopic ratios of the primary monazite reference material MAdel (TIMS normalisation data: ^{207}Pb/^{206}Pb = 491.0 ± 2.7 Ma, ^{206}Pb/^{238}U = 518.4 ± 1 Ma and ^{207}Pb/^{235}U = 513.1 ± 0.2 Ma; updated from Payne et al. (2008), with additional TIMS data). During the course of the analyses, MAdel yielded a weighted mean ^{206}Pb/^{238}U age of 518.2 ± 1.5 Ma (MSWD = 0.68, *n* = 11). The accuracy of the collected data was monitored by analysis of the in-house standard 94-222/BrunaNW (450.2 ± 3.4 Ma; Maidment, 2005). The weighted average ^{206}Pb/^{238}U age of 94-222/Bruna NW was 447.7 ± 2.6 (*n* = 8, MSWD = 1.7). Data were reduced using Iolite (v. 3.1) and plotted using Isoplot v. 4.15, consistent with the methods for U–Pb zircon geochronology. Analyses that occur outside 2σ uncertainty of concordia are denoted as being ‘discordant’.

Table 3. Summary of zircon morphology and main isotopic data

Sample	External zircon morphology	Internal CL textures/features	Age (Ma) of CL domains	Age interpretation	$\varepsilon_{Hf}(t)$
PMDDH04-14	Brown; 75–600 μm; subhedral to elongate with sub-rounded crystal face terminations, and minor anhedral grains with internal fracturing; aspect ratios 1:1 to 1:4.	(1) Dark to weakly luminescent oscillatory-zoned cores. Internal zoning sometimes diffuse and/or indistinct, and rarely chaotic and appearing partially recrystallised.	2421 ± 35 Ma†	Crystallisation	−10.2 to −2.5
			1773 ± 51 Ma†	Metamorphism (Pb-loss)	−13.6 to −9.4
		(2) Luminescent rim on dark, zoned core	1675 ± 52 Ma^	-	−13.8 ± 0.8
PMDDH04-12	Colourless–light brown and dark brown–dark pink; 75–400 μm; elongate with sub-rounded to angular crystal face terminations; aspect ratios 1:1 to 1:4.	(1) Dark, weakly oscillatory-zoned cores, often anhedral and partially resorbed.	Early Paleoproterozoic^	Inheritance	−7.5 to −1.9
		(2) Dark, weakly oscillatory-zoned cores.	1882 ± 18 Ma* 1767 ± 20 Ma*	Crystallisation	−17.5 to −8.7
		(3) Dark–weakly luminescent rims on zoned cores.	1538 ± 65 Ma^ 1544 ± 36 Ma^	Metamorphism	−11.2 to −9.0
D525128	Light pink–brown; 100–600 μm; sub-rounded and elongate with sub-rounded crystal faces; minor fracturing; aspect ratios 1:1 to 1:3.	(1) Dark to luminescent, oscillatory-zoned cores. Luminescent cores are typically anhedral.	1821 ± 7*	Crystallisation	−11.9 to −8.8
		(2) Thick dark rims surrounding and/or resorbing zoned cores; two dark, unzoned, homogeneous grains.	1599 ± 9 Ma*	Metamorphism	−12.6 to −10.8
GAZ7	Pink–light brown; 100–500 μm; sub-rounded to elongate with sub-rounded crystal faces; aspect ratios 1:1 to 1:4.	(1) Dark to weakly luminescent oscillatory zoned cores. Minor sector zoning.	1753 ± 8 Ma*	Crystallisation	−14.5 to −10.1
		(2) Minor, thin, dark rims on zoned cores.	ca. 1770–1750 Ma^	Crystallisation	-
D525108	Colourless; 150–400 μm; elongate with sub-rounded crystal faces; aspect ratios 1:2 to 1:3.	(1) Dark, oscillatory-zoned cores.	Neoarchean–early Paleoproterozoic^	Inheritance	-4.4
		(2) Dark to luminescent weakly oscillatory-zoned cores.	Late Paleoproterozoic (ca. 1850–1750 Ma)^	Crystallisation	−11.1 to −7.4 (main), −23.7 and −16.2
		(3) Rare, very thin luminescent rims.	-	-	-
D525052	Light pink–brown; 75–400 μm; Sub-rounded and elongate with euhedral to sub-rounded crystal faces; aspect ratios 1:1.5 to 1:3.	(1) Dark–weakly luminescent, and rarely luminescent, oscillatory-zoned cores. Commonly exhibit dark rims.	Paleoarchean–early Paleoproterozoic^ 2316 ± 18 Ma*	Inheritance Max. dep.	−6.8 to +4.5
		(2) Thick, dark, homogeneous rims on zoned cores.	1722–1576 Ma^	Metamorphism	−14.5 to −13.6 (main), -17.6
D525121	Dark brown–light brown; 50–400 μm; largely prismatic with sub-rounded crystal faces; aspect ratios 1:1 to 1:4.	(1) Dark and luminescent oscillatory-zoned cores. Typically anhedral and overgrown or resorbed by thick, weakly-luminescent rims. Minor fracturing.	Paleoarchean^ (ca. 3360–3250 Ma)	Inheritance	+0.5 to +3.1 (main)
		(2) Thick, weakly-luminescent, unzoned rims on zoned cores; weakly-luminescent unzoned and/or weakly (diffuse) zoned grains.	Late Paleoproterozoic^ (ca. 1810–1775 Ma) 1793 ± 6 Ma*	Inheritance Max. dep.	−28.1 to −11.5
		(3) Thick, weakly-luminescent, featureless rims on dark zoned cores.	1599 ± 14 Ma*	Metamorphism	−16.1 to −13.5

Table 3. (continued)

Sample	External zircon morphology	Internal CL textures/features	Age (Ma) of CL domains	Age interpretation	$\varepsilon_{Hf}(t)$
GAZ9	Pink–light brown to dark brown; 100–600 µm; sub-rounded to elongate; aspect ratios 1:2 to 1:4.	(1) Dark, oscillatory-zoned cores. (2) Weakly-luminescent rims on dark cores. Indistinctly zoned to unzoned. Typically surrounded by a thin, dark rim.	Mesoarchean^ (ca. 3140 Ma, 1 analysis)	Inheritance	
			Early Paleoproterozoic (ca. 2400 Ma)^	Inheritance	–9.3 to –4.4
			Late Paleoproterozoic 1766 ± 7 Ma*	Inheritance Max. dep.	–16.9 to –6.2
GAZ21	Colourless-light pink; 75–350 µm; sub-rounded to elongate with sub-rounded crystal faces; aspect ratios 1:1 to 1:2.	(1) Dark, weakly luminescent and luminescent, oscillatory-zoned cores.	Late Paleoproterozoic^ 1771 ± 7 Ma (unmix)	Inheritance Max. dep.	–15.0 to –8.1 (slightly more evolved with decreasing age)
		(2) Varied CL response. Typically dark and weakly luminescent cores with diffuse and/or indistinct zoning or ghosted-zoning.	1673 ± 9 Ma (unmix)	Metamorphism (Pb-loss)?	
		(3) Dark, unzoned to weakly-zoned grains. Dark and weakly-luminescent rims on resorbed cores.	1587 ± 9 Ma*	Metamorphism	
D525013	Colourless–light pink; 50–200 µm; Sub-rounded or slightly elongate with sub-rounded crystal faces; aspect ratios 1:1 to 1:2.	(1) Sector-zoned cores with varied CL response. In many instances, inner sector zones exhibit a lower CL response (dark) than outer sector zones (weakly–strongly luminescent).	1582 ± 8 Ma*	Alteration, greenschist overprint	–15.3 to –13.1 (main), -9.6

Age calculations: *$^{207}Pb/^{206}Pb$ weighted mean age calculation, ^individual analyses; †$^{207}Pb/^{206}Pb$ upper/lower intercept; (unmix) refers to Isoplot Unmix algorithm.

5. RESULTS

5.1 Sample descriptions and U–Pb zircon geochronology

Representative CL images of zircon grains from all samples are presented in Fig. 5. A summary of zircon morphology, isotope data and interpretation is provided in Table 3. U–Pb zircon age data are presented in Supplementary Table 1 and Figs 6–8. Quoted ages are $^{207}Pb/^{206}Pb$ ages. Samples are discussed below first according to inferred protolith, and second in order of approximate inferred age (oldest to youngest). Sample D525013, discussed last, is analysed to investigate the timing of the greenschist facies retrograde alteration.

5.1.1 Samples with an inferred igneous protolith

Sample PMDDH04-14: A strongly foliated mafic gneiss that is representative of the mafic lithologies that are intercalated with granitic gneiss within drill hole PMDDH04 (Fig. 4d) and exposed in subcrop in the central Tabletop Domain. Twenty-seven analyses were obtained from 25 zircon cores, and one analysis from one strongly luminescent zircon rim. The majority of analyses define an array of ages along a discord with an upper and lower intercept age of 2421 ± 35 [38] Ma and 1773 ± 51 [53] Ma, respectively (MSWD = 2.6, *n* = 28; Fig. 6a). Analyses with $^{207}Pb/^{206}Pb$ ages between ca. 2400 and 1900 Ma can be demonstrated to reflect Pb-loss from the older population using Lu–Hf isotope data (see Section 5.3). As there is clear evidence for ancient Pb-loss, we have calculated a weighted mean age using only the oldest grains that yield a statistically valid age (2402 ± 12 [19] Ma, *n* = 5, MSWD = 0.48). This age is within uncertainty of the upper intercept age and is therefore considered to be an adequate representation of the crystallisation age of the older population within this sample. The four youngest concordant analyses from zircon cores yield ages between ca. 1780 and 1650 Ma. These zircon cores are distinct from those yielding ages older than ca. 2100 Ma in that they are weakly luminescent with convoluted and/or indistinct (i.e. ghosted) internal zoning. One analysis (analysis H04-14-19) from a thick, luminescent rim that truncates a small, dark core gave a concordant age of 1675 ± 52 Ma (Fig. 5a), and is within uncertainty of the four weakly luminescent cores.

The magmatic crystallisation age of the protolith

to this sample is interpreted to be 2402 ± 12 [19]. The spread of discordant analyses to the lower intercept age at ca. 1770 Ma are interpreted to reflect Pb-loss during younger metamorphism. The possibility exists that the older zircon grains represent unimodal inheritance in a younger magmatic rock. This is not considered to be the case, however, as there is no evidence for oscillatory-zoned rims that might otherwise support a younger magmatic age for this sample, and field relationships suggest the mafic gneiss occurs as enclaves in mid–late Paleoproterozoic granite (Fig. 4e, see below).

Sample PMDDH04-12: A weakly foliated, biotite–hornblende-bearing granite that exhibits minor alteration consisting of cross-cutting chlorite veins and interstitial epidote (Fig. 4e). This sample is similar to weakly foliated granite down-hole of the sampled interval that encloses enclaves of mafic gneiss. The mafic enclaves are mineralogically and texturally equivalent to sample PMDDH04-14 (Fig. 4e).

Thirty-seven analyses were obtained from 32 zircon grains; 20 analyses are discordant. The remaining 17 concordant analyses reveal a spread of ages between ca. 2480 and 1540 Ma. The five oldest concordant analyses cluster between ca. 2480 and 2360 Ma and come from oscillatory-zoned cores with a low CL response that are commonly surrounded (or resorbed) by luminescent rims (e.g. Fig. 5b). These zircon cores are interpreted as xenocrystic grains.

The majority of concordant analyses yield ages between ca. 1890 and 1710 Ma and come from dark to weakly luminescent zircon cores with weak internal zoning. Rarely, the dark cores appear resorbed by rims with a higher CL response. These analyses exhibit a bimodal age distribution with weighted mean $^{207}Pb/^{206}Pb$ ages of 1882 ± 18 [21] Ma (MSWD = 0.23, n = 4) and 1767 ± 20 [23] (MSWD = 1.15, n = 3). A single concordant analysis occurs at 1706 ± 47 Ma (analysis PDH04-12-41) and comes from a dark core with metamict appearance. Two concordant rim analyses yield ages of 1538 ± 65 Ma (thick, weakly luminescent rim; PDH04-12-37) and 1544 ± 36 Ma (featureless dark rim; PDH04-12-9). Similar ages were obtained from a dark core with simple oscillatory zoning (analysis PDH04-12-40, 1564 ± 39 Ma) and a dark core with indistinct zoning surrounded by a thick luminescent rim (analysis PDH04-12-31, 1614 ± 34 Ma). Six slightly reversely discordant analyses (Fig. 6b) yield dates between ca. 1600 and 1500 Ma and also come from featureless to weakly zoned, weakly luminescent or dark rims that surround and/or resorb dark cores (Fig. 5b).

The bimodal (ca. 1880 and ca. 1760 Ma) age peaks from dark, weakly zoned zircon cores do not allow for an unambiguous interpretation of the crystallisation age of the felsic magmatic protolith to this sample, but is likely to be late Paleoproterozoic. The ca. 1880 Ma ages are not considered to reflect ancient Pb-loss from the oldest zircon grains in this sample as they yield a range of $Hf_{initial}$ values that are inconsistent with such an interpretation (see below). $Hf_{initial}$ values do, however, suggest that the ca. 1760 Ma group may reflect isotopic resetting from the ca. 1880 Ma group, but the nature of the analysed zircon grains does not allow for an unambiguous interpretation. The ca. 1610–1540 Ma ages are predominantly obtained from zircon rims with CL responses consistent with metamorphic zircon and are therefore interpreted to reflect the approximate timing of a subsequent metamorphic event.

Sample D525128: A strongly foliated, hornblende–plagioclase-rich mafic gneiss with coarse-grained hornblende-bearing leucosomes that are both parallel and discordant to the fabric in the rock (Fig. 4c). This sample has experienced significant alteration of feldspar to clays and sericite, and the partial replacement of hornblende by chlorite and epidote. Thirty-four analyses were obtained from 29 zircon grains; 11 analyses are discordant. The remaining 23 concordant analyses form two age populations. Dark to weakly luminescent cores with weak, broad, simple zoning and anhedral, luminescent cores with indistinct internal features comprise the oldest population and yield a weighted mean $^{207}Pb/^{206}Pb$ age of 1821 ± 7 [21] (MSWD = 1.4, n = 14/15; Fig. 6c). Based on CL imagery and a lack of evidence for younger magmatic crystallisation events, this age is interpreted as the likely magmatic crystallisation age of the mafic magmatic protolith. Two analyses younger than the main population (analysis 128-23, 1712 ± 21 Ma, and analysis 128-12, 1747 ± 21 Ma) are excluded from the weighted mean age calculation. These two younger ages come from thick, dark rims that truncate weakly to strongly luminescent cores (with respective ages 1824 ± 19 Ma and 1848 ± 29 Ma), and are interpreted to represent phases of new zircon growth younger than ca.

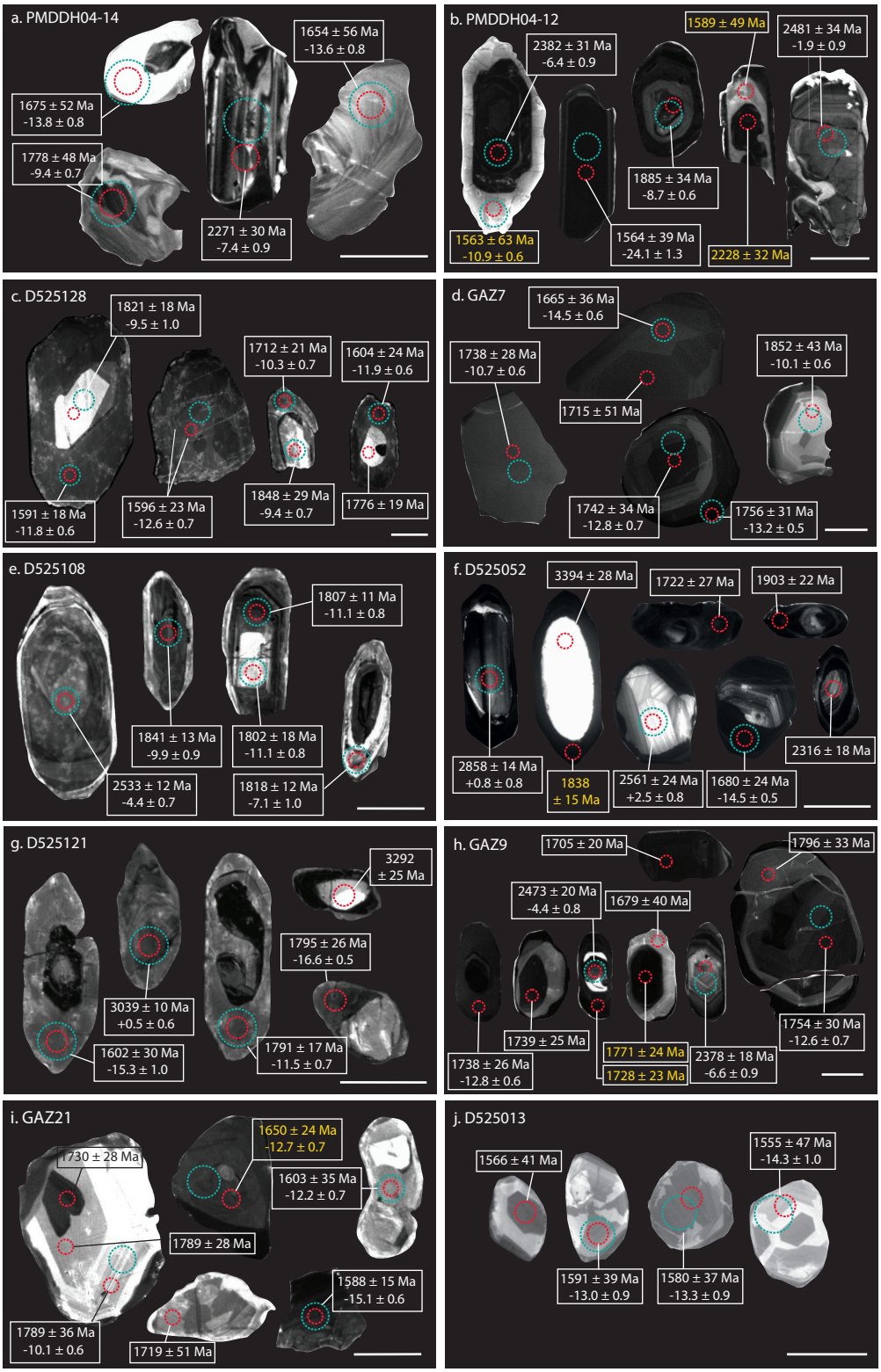

Figure 5. Zircon morphology. Representative cathodoluminescence (CL) imagery of zircon (all samples) are shown. The approximate location and size of U–Pb and Lu–Hf analyses are indicated as red and green circles, respectively, and the corresponding age and isotope data are given. Concordant age data are shown in white; discordant age data are shown in yellow. The scale bar pictured is 100 μm. Zircon morphology and CL appearance is discussed in the main text and summarised in Table 3.

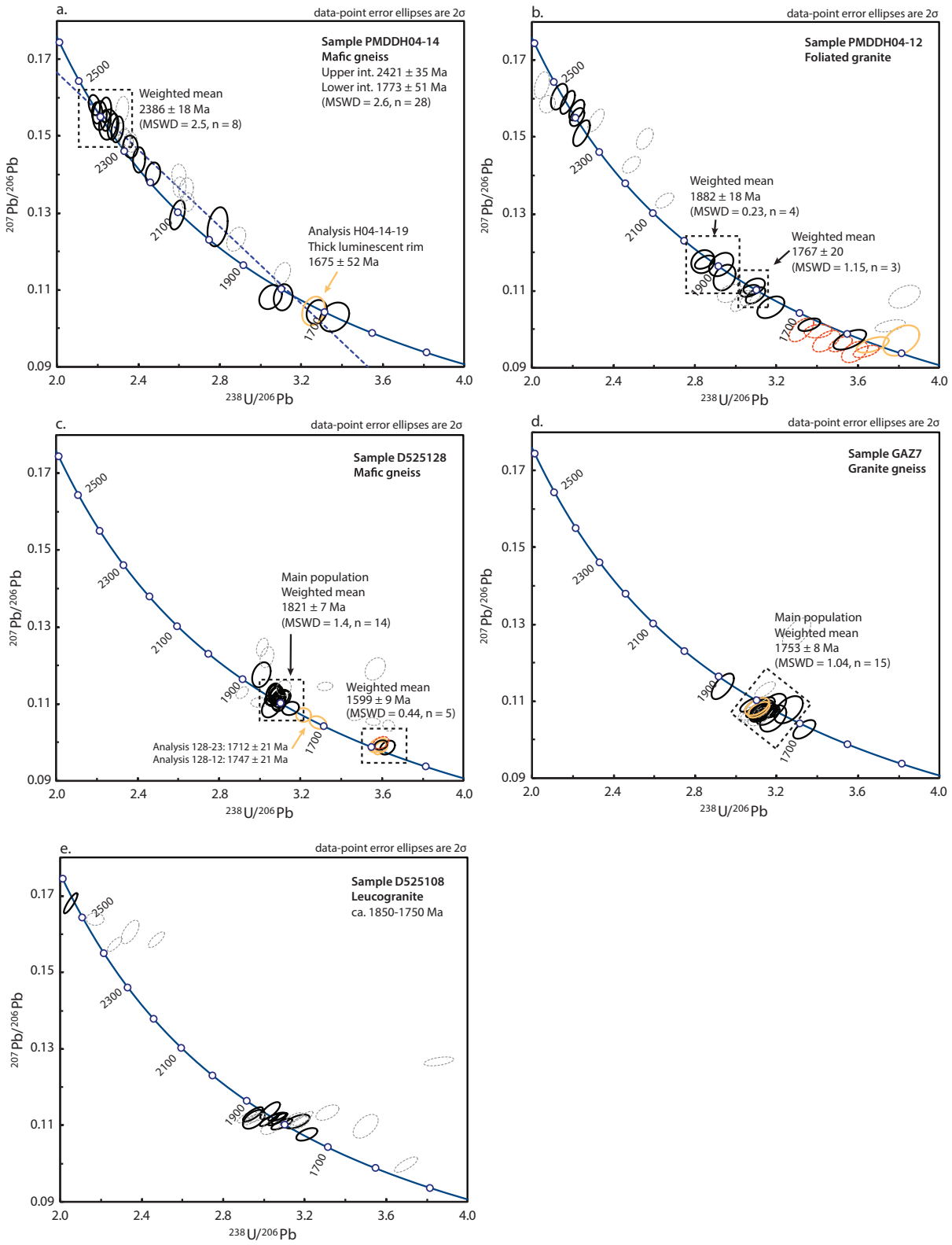

Figure 6. Tera–Wasserburg Concordia diagrams of zircon U–Pb geochronology for samples with an inferred igneous protolith: (a) PMDDH04-14; (b) PMDDH04-12; (c) D525128; (d) GAZ-7 and (e) D525108. Black and yellow ellipses represent analyses from concordant zircon cores and rims, respectively. Grey and red dashed ellipses represent analyses from discordant zircon cores and rims, respectively. Upper and lower U–Pb regression intercept ages (sample PMDDH04-14 only), weighted mean ages of the main age populations and individual analyses noted specifically in the main text are indicated.

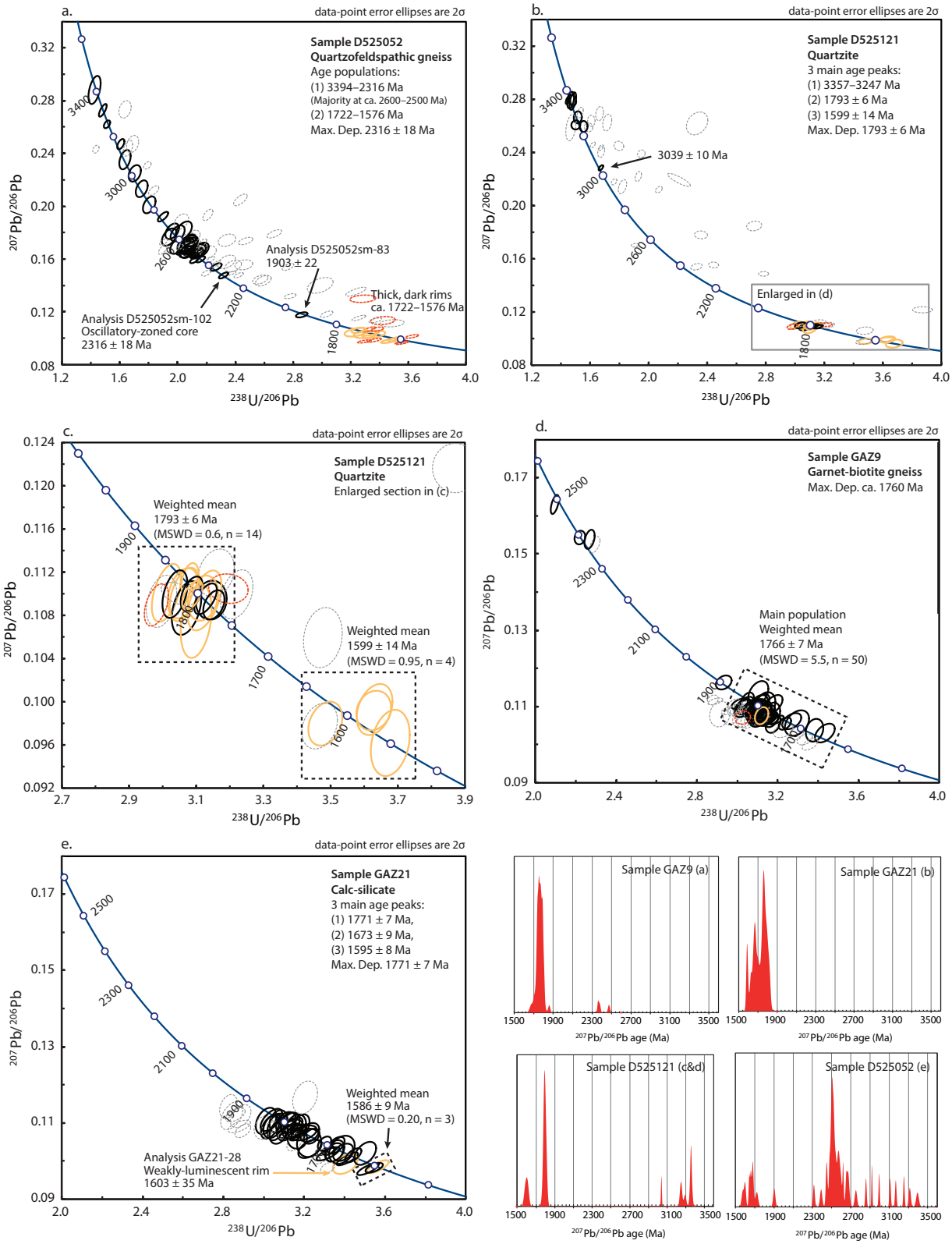

Figure 7. Tera–Wasserburg Concordia diagrams of zircon U–Pb geochronology for inferred metasedimentary samples: (a) D525052; (b) D525121; (c) D525121 (enlarged); (d) GAZ9 and (e) GAZ21. Probability density plots of concordant detrital zircon 207Pb/206Pb ages are also shown for all samples. Black and yellow ellipses represent analyses from concordant zircon cores and rims, respectively. Grey and red dashed ellipses represent analyses from discordant zircon cores and rims, respectively. 207Pb/206Pb weighted mean ages of the main age populations, and individual analyses noted specifically in the main text are indicated.

1820 Ma. It is unclear if these ages represent a distinct, regionally significant metamorphic event.

Three concordant analyses from dark, homogeneous, featureless rims and two analyses from dark grains with a similar internal morphology and CL response form a discrete population with a weighted mean $^{207}Pb/^{206}Pb$ age of 1599 ± 9 Ma [19] (MSWD = 0.44, n = 5; Fig. 6c). The ca. 1600 Ma population has Th/U ratios between 0.9 and 1.27; the Th/U ratios of concordant analyses from the older population are more variable and range between 0.18 and 1.26. The consistent Th/U ratios and homogenous CL response of these analyses suggests that the ca. 1600 Ma age reflects the timing of metamorphism and leucosome formation.

Sample GAZ-7: A strongly foliated, K-feldspar-rich granitic gneiss with moderate chlorite and hematite alteration (Fig. 4f). Twenty-three analyses were obtained from 19 zircon grains; six analyses are discordant. One concordant analysis that is older than the main population comes from a weakly luminescent, sector zoned core and yields an age of 1852 ± 43 Ma (analysis GAZ7-12; Fig. 5d). One concordant analysis that is younger than the main age population also comes from a homogeneous outer region of a broadly sector-zoned, dark core and yields an age of 1665 ± 36 Ma (analysis GAZ7-2, Fig. 5d). The remaining 15 concordant analyses form one population with a weighted mean $^{207}Pb/^{206}Pb$ age of 1753 ± 8 Ma [13] (MSWD = 1.04, Fig. 6d). This age is interpreted as the best estimate for the timing of magmatic crystallisation of the felsic magmatic protolith to this sample. Two analyses included in this age calculation come from thin, dark, homogeneous rims (GAZ7-27, 1776 ± 32 and GAZ7-30, 1756 ± 31 Ma, Fig. 5d) that are equivalent in age to the zoned cores. The significance of the single 1665 ± 36 Ma age is unclear as it does not show unambiguous evidence for being an overgrowth, nor recrystallised zone, and it is within uncertainty of a second core analysis (1715 ± 15 Ma) on the same grain.

Sample D525108: A K-feldspar-rich, biotite-poor leucogranite (Fig. 4g). The paucity of biotite means that it is difficult to identify whether this rock is strongly foliated. Thirty-one analyses were collected from 30 zoned zircon cores; 21 analyses are discordant. One concordant analysis from a dark zoned core gives an age of 2533 ± 12 Ma (analysis 108-28; Fig. 5e) and is similar to four moderately discordant analyses with dates ranging between ca. 2500 and 2400 Ma. These Neoarchean analyses are interpreted as xenocrystic grains. The remaining 10 concordant analyses predominantly cluster between ca. 1850 and 1750 Ma and do not define a single population (Fig. 6e). It is therefore not possible to constrain the magmatic crystallisation age of the protolith to this sample, although the data are nonetheless consistent with a ca. 1800 Ma magmatic event. The ca. 1850–1750 Ma analyses are not considered to reflect inherited zircon owing to their consistent CL response and a lack of oscillatory zoned overgrowths on the analysed cores, which might indicate a subsequent magmatic event.

5.1.2 Samples with an inferred detrital origin

Sample D525052: A quartzo-feldspathic gneiss with a heterogeneous distribution of biotite (Fig. 4h). This rock is strongly deformed and compositionally layered with a strong lineation. It is not possible to conclusively identify a magmatic or sedimentary protolith for this rock but it is interpreted to be sedimentary based upon the observed zircon age spectra and zircon morphology.

Ninety-seven analyses were obtained from 89 grains; 53 analyses are discordant. The majority of concordant analyses produce a continuum of ages between 3394 and 2316 Ma, with a main cluster of analyses at ca. 2600–2500 Ma (Fig. 7a). These analyses come from dark to weakly luminescent, and rarely strongly luminescent, strongly oscillatory-zoned cores, that are consistently surrounded by thick, dark, homogeneous rims (Fig. 5f). These zoned zircon cores are interpreted as detrital grains. The maximum depositional age of this sample is considered to be 2316 ± 18 Ma—the age of the youngest, concordant oscillatory-zoned core (analysis D525052sm-102; Fig. 5f).

A single concordant analysis occurs at 1903 ± 22 (analysis D525052sm-83; Fig. 5f). The significance of this age is uncertain as it is unclear from CL imagery whether this is taken from a dark overgrowth and/or is a mixed analysis that straddles different domains.

Seven analyses from thick, dark, homogenous rims yield ages younger than the main population (ca. 1722–1576 Ma) and are interpreted to reflect

zircon growth during metamorphism (Fig. 7a). The spread of ages and uncertainties on the individual analyses precludes calculation of a statistically valid weighted mean age(s).

Sample D525121: A strongly foliated muscovite-bearing quartzite (Fig. 4i). The quartzite at this locality is moderately clean, with variable abundance and distribution of muscovite, and preserves the original, finely laminated bedding (0.5–2 cm thickness), which dips steeply towards the east. This sample was collected approximately 300 m southeast of muscovite-bearing quartzite (sample GA2006670087) analysed by Maidment (2017) with an inferred maximum depositional age 2833 ± 5 Ma, and a spread of Paleo–Mesoarchean inherited ages.

Sixty-six analyses were obtained from 58 zircon grains; 40 analyses are discordant. The remaining 26 concordant analyses form a group at ca. 3357–3247 Ma (n = 7), and two age peaks at 1793 ± 6 [20] Ma (MSWD = 0.6, n = 14), and 1599 ± 14 [22] Ma (MSWD = 0.95, n = 4; Fig. 7b, c). A single concordant analysis also gave an age of 3039 ± 10 Ma (Figs 5g and 7b).

Archean analyses come from oscillatory-zoned cores that are commonly surrounded and/or resorbed by thick, weakly luminescent rims (Fig. 5g), and are accordingly interpreted as detrital grains. The majority of analyses between ca. 1810 and 1775 Ma come from the thick, weakly luminescent rims that resorb zoned cores, as well as few dark, oscillatory zoned zircon cores (Fig. 5g). The generally sub-rounded appearance of crystal face terminations of grains with ca. 1810–1775 Ma rims suggests that they too are of detrital origin. These ca. 1810–1775 Ma core and rim analyses yield a collective age of 1793 ± 6 [20] Ma (MSWD = 0.60; n = 14; Fig. 7c), which is considered as the maximum depositional age of this sample if the ca. 1810–1775 Ma core and rim analyses are detrital; however, if the ca. 1810–1775 Ma core and rim analyses reflect the timing of *in situ* metamorphism, the maximum depositional age of this sample is 3039 ± 10 Ma.

Four thick, weakly luminescent, featureless rims on dark cores comprise the youngest age population and collectively yield a weighted mean $^{207}Pb/^{206}Pb$ age of 1599 ± 14 [22] Ma (MSWD = 0.95; Fig. 7c). Some grains with ca. 1810–1775 Ma rims exhibit a secondary zircon rim with a higher CL response that is typically similar in appearance to the dated ca. 1600 Ma overgrowths (e.g. Fig. 5g). The shape of the ca. 1600 Ma rims is also typically euhedral and exhibits simple zoning. These observations suggest that the ca. 1600 Ma outer rims formed *in situ* during metamorphism and did not undergo any transport as a detrital phase. These ca. 1600 Ma analyses are therefore interpreted to reflect the timing of metamorphism.

The Archean and Paleoproterozoic detrital populations have variable Th/U ratios of 0.10–1.43 and 0.09–0.57, respectively. The Th/U values for the ca. 1600 Ma population form a coherent group at 0.40–0.53, consistent with metamorphic zircon growth from a single reservoir.

Sample GAZ-9: A strongly layered garnet–biotite gneiss intersected in drill hole Gazza-01 (Fig. 4j). Biotite-rich domains alternate with quartzo-feldspathic layers on a centimetre scale. Coarse garnet grains (individual grains typically 0.5–5 mm, but up to 1 cm) are heterogeneously distributed throughout biotite-rich domains of the rock. This sample exhibits partial to complete alteration of feldspars to fine-grained clay and the partial replacement of biotite by chlorite.

Eighty-nine analyses were obtained from 85 grains; 32 analyses are discordant. Four concordant analyses at 2473 ± 20 Ma, 2378 ± 18 Ma, 2361 ± 15 Ma and 1859 ± 20 Ma (Fig. 5h and 7d) are older than the main population and come from strongly to weakly zoned cores with a low CL response. One near concordant analysis has an age of 3140 ± 19 Ma (analysis GAZ9-39, not visible on Fig. 7d).

The remaining 53 concordant analyses form a dominant age peak at ca. 1800–1730 Ma with a subsidiary spread of ages to ca. 1680 (Fig. 7d). The majority of analyses forming the main population come from dark cores with weak, broad, simple zoning, or weak-luminescent domains that often surround these dark cores (Fig. 5h). Typically, the weakly luminescent domains are indistinctly separated from the internal features of the darker cores that they surround, and exhibit weak ghosted-zoning, sector zoning and/or indistinct and patchy internal textures. Analyses from the dark zoned cores and weakly luminescent domains comprising this main population are equivalent in age. The youngest dark, zoned core yields an age of 1705 ± 20 Ma (analysis GAZ9-88; Fig. 5h). This age is within uncertainty of the two youngest

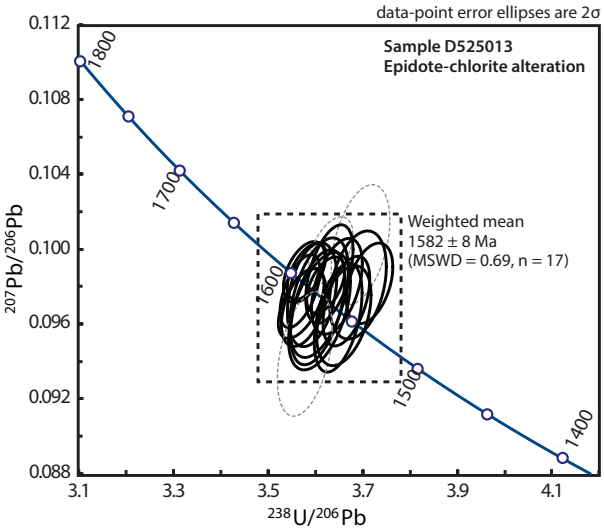

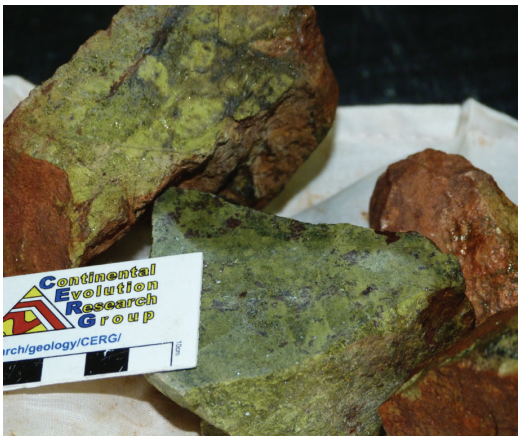

Figure 8. Greenschist facies alteration–retrogression (sample D525013). A Tera–Wasserburg Concordia diagram of zircon U–Pb geochronology from calc-silicate D525013 is shown. Black ellipses represent analyses from concordant zircon cores; grey dashed ellipses represent analyses from discordant zircon cores. The weighted mean age of concordant analyses comprising the main age population is indicated.

concordant analyses from weakly luminescent domains (1677 ± 34 Ma, GAZ9-15 and 1679 ± 40 Ma, GAZ9-5). Many of the dark zoned cores and weakly luminescent domains are in turn surrounded by narrow, featureless, dark rims. The only concordant analysis (GAZ9-10) from a dark rim that surrounds a dark, zoned core has an age of 1738 ± 26 Ma (Fig. 5h). The Mesoarchean–Paleoproterozoic ages are interpreted as detrital. Analyses comprising the main population produce an imprecise weighted mean of 1766 ± 7 [20] Ma (MSWD = 5.5, *n* = 50/53), which is taken to be the conservative maximum depositional age of this sample. The large MSWD indicates significant variation in the age of zircon comprising the main population that is beyond analytical uncertainty. Overlap of uncertainties on individual analyses means that it is not possible to refine the main population for a more precise maximum depositional age calculation.

Sample GAZ-21: Sample GAZ-21 is a strongly foliated calc-silicate rock intersected in drill hole Gazza-01 (Fig. 4k). This sample contains clinopyroxene, hornblende, plagioclase, minor quartz and biotite that are altered to chlorite, sericite and epidote, with minor cross-cutting calcite veins. Fifty-two analyses were obtained from 50 grains; 13 analyses are discordant. The remaining 39 concordant analyses yield a continuum of ages from 1820 ± 20 Ma to 1582 ± 15 Ma (Fig. 7e) with three age peaks at 1771 ± 7 [20] Ma, 1673 ± 9 [20] Ma and 1595 ± 8 [19] Ma (relative misfit = 0.29, respective fractions 0.55, 0.32 and 0.13) using the statistical function 'Unmix' in Isoplot (Ludwig, 2012). The large range of ages and uncertainties on individual analyses means that a statistically valid weighted mean and concordia ages cannot be calculated.

The majority of analyses >1750 Ma come from sub-rounded zircon grains with dark to weakly luminescent cores that are featureless to weakly zoned or sector zoned (Fig. 5i). Analyses that yield ages between ca. 1740 and 1650 Ma are from zircon cores with a varied CL response that cannot be conclusively assigned to metamorphic growth, nor resetting of original detrital ages. Typically, these zircon cores exhibit indistinct and patchy internal features or ghosted zoning.

Two concordant analyses from zircon cores with indistinct to weak zoning and a dark CL response (analyses GAZ21-27 and GAZ21-38) and one dark rim on a dark core (GAZ21-20) gave equivalent ages, and the youngest ages for this sample. Collectively, these three analyses define a weighted mean $^{207}Pb/^{206}Pb$ age of 1586 ± 9 [19] Ma (MSWD = 0.20) that is within uncertainty of the Unmix-calculated 1595 ± 8 [19] Ma age. An additional weakly luminescent rim on a luminescent core (GAZ21-28) gave a slightly older age of 1603 ± 35 Ma (Figs 5i and 7e).

The maximum depositional age of GAZ-21 is conservatively estimated to be 1771 ± 7 [20] Ma based on the age of the oldest age peak composed of weakly zoned zircon cores that are unambiguously interpreted to be detrital. It is unclear from the age data whether analyses comprising the 1673 ± 9 [20] Ma age peak represent an older metamorphic event or whether these ages are a result of ancient

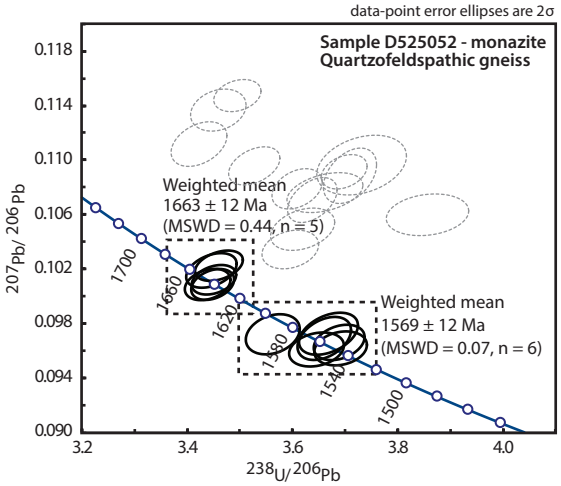

Figure 9. U–Pb monazite geochronology from sample D525052 (quartzofeldspathic gneiss). Black ellipses on the Tera–Wasserburg Concordia diagram represent concordant analyses; grey dashed ellipses represent discordant analyses. The weighted mean ages of the concordant age peaks are indicated.

Pb-loss associated with metamorphism at ca. 1590 Ma. The largely ghosted and indistinct internal features of these grains suggest that these ages may reflect recrystallisation and therefore the effects of ancient Pb-loss.

5.1.3 Calc-silicate altered mafic gneiss (sample D525013)

An epidote–actinolite–plagioclase-rich (calc-silicate) alteration layer with trace graphite and chalcopyrite (Fig. 8). This layer crops out over a ~10 m area adjacent to mafic gneiss, but the precise contact between the two lithologies is not clearly observed. Approximately 100 m east of sample D525013, relatively unaltered mafic gneiss is exposed and appears to grade into calc-silicate altered mafic gneiss that contains minor epidote. This suggests the protolith of the epidote–actinolite–plagioclase altered rock was also a mafic gneiss.

Twenty analyses were obtained from 20 zircon grains with three discordant analyses. The remaining 17 analyses come from sector-zoned zircon cores (Fig. 5j) and comprise a single population with a weighted mean age of 1582 ± 8 [16] Ma (MSWD = 0.69; Fig. 8). This age is interpreted to reflect the timing of the calc-silicate alteration within the rock.

5.2 U–Pb monazite geochronology

Twenty-four analyses were collected from 13 monazite grains mounted in epoxy resin for sample D525052 (quartzo-feldspathic gneiss). U–Pb monazite age data are presented in Supplementary Table 2 and Fig. 9. Monazite grains vary in size between 100 and 300 µm, are typically sub-rounded to round in shape, and unzoned in BSE imagery. Eleven analyses are concordant and form two populations with $^{207}Pb/^{206}Pb$ weighted mean ages of 1663 ± 12 Ma (MSWD = 0.44, *n* = 5) and 1569 ± 12 Ma (MSWD = 0.07, *n* = 6). These populations are taken to be metamorphic ages.

5.3 Lu–Hf zircon isotope analysis

Lu–Hf isotope data are provided in Supplementary Table 3 and presented in Fig. 10a. Lu–Hf analyses were done on zircon grains with CL domains large enough to fit a 50 µm spot either adjacent to, or on top, the U–Pb analysis, and within the same CL domain (e.g. Fig. 5). Where stated, ages given in brackets reflect the inferred crystallisation age or maximum depositional age for igneous and metasedimentary samples, respectively.

Plots of $\varepsilon_{Hf}(t)$ versus $^{207}Pb/^{206}Pb$ age and initial $^{176}Hf/^{177}Hf$ ($Hf_{(i)}$) versus $^{207}Pb/^{206}Pb$ age for individual samples are presented in Supplementary Fig. 1 to assess Pb-loss. In sample PMDDH04-14, progressively younger analyses from the early Paleoproterozoic age population (ca. 2500–2100 Ma) yield noticeably more evolved $\varepsilon_{Hf}(t)$ values resulting in a visually positive correlation between $\varepsilon_{Hf}(t)$ and $^{207}Pb/^{206}Pb$ age and a horizontal trend in $Hf_{(i)}$ versus $^{207}Pb/^{206}Pb$ age (Supplementary Fig. 1). Such trends are an artefact of ancient Pb-loss and are not indicative of the actual crustal processes as U–Pb and Lu–Hf systems become decoupled in zircon during Pb-loss processes (Guitreau and Blichert-Toft, 2014). Minor horizontal trends in $Hf_{(i)}$ versus $^{207}Pb/^{206}Pb$ age are also observed in the late Paleoproterozoic age population of sample PMDDH04-14, and samples PMDDH04-12, D525128, GAZ-7, GAZ-21 and D525013 (Supplementary Fig. 1). However, the shift in $Hf_{(i)}$ and $\varepsilon_{Hf}(t)$ values is not as distinct as the early Paleoproterozoic analyses from PMDDH04-14.

5.3.1 Sample PMDDH04-14 (mafic gneiss, 2402 ± 12 Ma)

Seventeen analyses were done on sample PMDDH04-14 with $\varepsilon_{Hf}(t)$ values ranging between

–13.8 ± 0.8 and –2.5 ± 0.7 Eleven concordant analyses from oscillatory-zoned cores with ages ca. 2400–2100 Ma and one near-concordant analysis (2293 Ma, H04-14-03) yield $\varepsilon_{Hf}(t)$ values between –10.2 ± 0.8 and –2.5 ± 0.7. Five analyses from oscillatory-zoned zircon cores with ages ca. 1780–1650 Ma, and one thick overgrowth (1675 Ma) on a zoned core, gave $\varepsilon_{Hf}(t)$ values between –13.6 ± 0.8 to –9.4 ± 0.7, and –13.8 ± 0.8, respectively. As described above, analyses from the Paleoproterozoic age populations in this sample yield increasingly evolved $\varepsilon_{Hf}(t)$ values that are a result of ancient Pb-loss. $\varepsilon_{Hf}(t)$ values from zircon yielding early Paleoproterozoic ages, for which evidence of ancient Pb-loss is most pronounced (e.g. Supplementary Fig. 1; Fig. 6a), are plotted at their corresponding individual $^{207}Pb/^{206}Pb$ ages in Fig. 10a, but in subsequent figures (Figs 10b and 11), are plotted at the upper intercept age of the U–Pb regression from this sample. $\varepsilon_{Hf}(t)$ values calculated using apparent $^{207}Pb/^{206}Pb$ ages as well as the upper intercept age are both given in Supplementary Table 3).

5.3.2 Sample PMDDH04-12 (foliated granite, late Paleoproterozoic)

Seventeen analyses were done on sample PMDDH04-12 with $\varepsilon_{Hf}(t)$ values ranging between –24.1 ± 1.3 and –1.9 ± 0.9. Analyses from zircon cores with ages ca. 2500–2300 Ma yield the least evolved Hf signature ($\varepsilon_{Hf}(t)$ = –7.5 ± 0.7 to –1.9 ± 0.9, *n* = 5). Analyses from zircon cores yielding ages between ca. 1890 and 1700 Ma gave a spread of $\varepsilon_{Hf}(t)$ values between –17.5 ± 0.8 and –8.7 ± 0.6 (*n* = 7). Analyses from the two dark zircon grains with simple zoning (H04-12-40, 1564 Ma and H04-12-31, 1614 Ma) give the two more evolved values of –24.1 ± 1.3 and –17.6 ± 0.7. These two analyses appear to lie on a horizontal trend in $Hf_{(i)}$ versus $^{207}Pb/^{206}Pb$ age from the ca. 1890–1700 Ma ages, corresponding to a positive correlation between $\varepsilon_{Hf}(t)$ and age, which may indicate that these grains reflect recrystallisation from the older population. The two concordant analyses from a weakly luminescent and dark rim on zoned cores, and one near-concordant analysis from a luminescent rim (ca. 1600–1500 Ma) yield a cluster of $\varepsilon_{Hf}(t)$ values between –11.2 ± 0.7 and –9.0 ± 1.2.

5.3.3 Sample D525128 (mafic gneiss, 1821 ± 7 Ma)

Eighteen analyses were obtained from sample D525128. Fourteen analyses from 1848–1712 Ma oscillatory-zoned zircon cores give $\varepsilon_{Hf}(t)$ values between –11.9 ± 0.9 and –8.8 ± 0.6. A minor horizontal trend observed in $Hf_{(i)}$ versus age may reflect that the youngest Paleoproterozoic analyses were affected by minor ancient Pb-loss. One analysis from a dark, unzoned core (1607 ± 19 Ma) and three analyses from dark zircon overgrowths (1604–1591 Ma) form a discrete population with a slightly more evolved Hf signature ($\varepsilon_{Hf}(t)$ = –12.6 ± 0.7 to –10.8 ± 0.6) than the older, dominant zircon population. The $\varepsilon_{Hf}(t)$ values obtained from these younger analyses are isotopically equivalent to the late Paleoproterozoic–early Mesoproterozoic zircon in other samples.

5.3.4 Sample GAZ7 (granitic gneiss, 1753 ± 8 Ma)

Thirteen analyses from oscillatory-zoned zircon cores in sample GAZ7 yield $\varepsilon_{Hf}(t)$ values that range between –14.5 ± 0.6 and –10.1 ± 0.6. The most evolved analysis corresponds to the youngest analysis from this sample (GAZ7-2, 1665 Ma).

5.3.5 Sample D525108 (leucogranite, ca. 1850–1750 Ma)

Ten analyses from 1851–1752 Ma oscillatory-zoned zircon cores in sample D525108 yield $\varepsilon_{Hf}(t)$ values that range between –23.7 ± 0.7 and –7.4 ± 1.0. One analysis obtained from a significantly older oscillatory-zoned core (2533 Ma, analysis 108-28) gave a much less evolved $\varepsilon_{Hf}(t)$ value of –4.4 ± 0.7 than the main population and is equivalent to $\varepsilon_{Hf}(t)$ values from similarly aged zircon in other samples.

5.3.6 Sample D525052 (quartzo-feldspathic gneiss)

Twenty-seven analyses were obtained from sample D525052. The majority of analyses come from oscillatory-zoned zircon cores with ages of ca. 3300–2480 Ma that comprise the dominant Neoarchean age population in this sample. These analyses yield a spread of relatively juvenile $\varepsilon_{Hf}(t)$ values between –6.8 ± 0.7 and +4.5 ± 1.0. Four analyses from dark, homogeneous rims (ca. 1680–1660 Ma) on oscillatory-zoned cores gave a considerably more evolved Hf-isotope signature than the Archean age population with $\varepsilon_{Hf}(t)$ values of –13.6 ± 0.5, –14.2 ± 0.6 and –14.5 ± 0.5 (analyses 52-03, 52-27 and 52-40) and –17.6 ± 0.6 (ca.

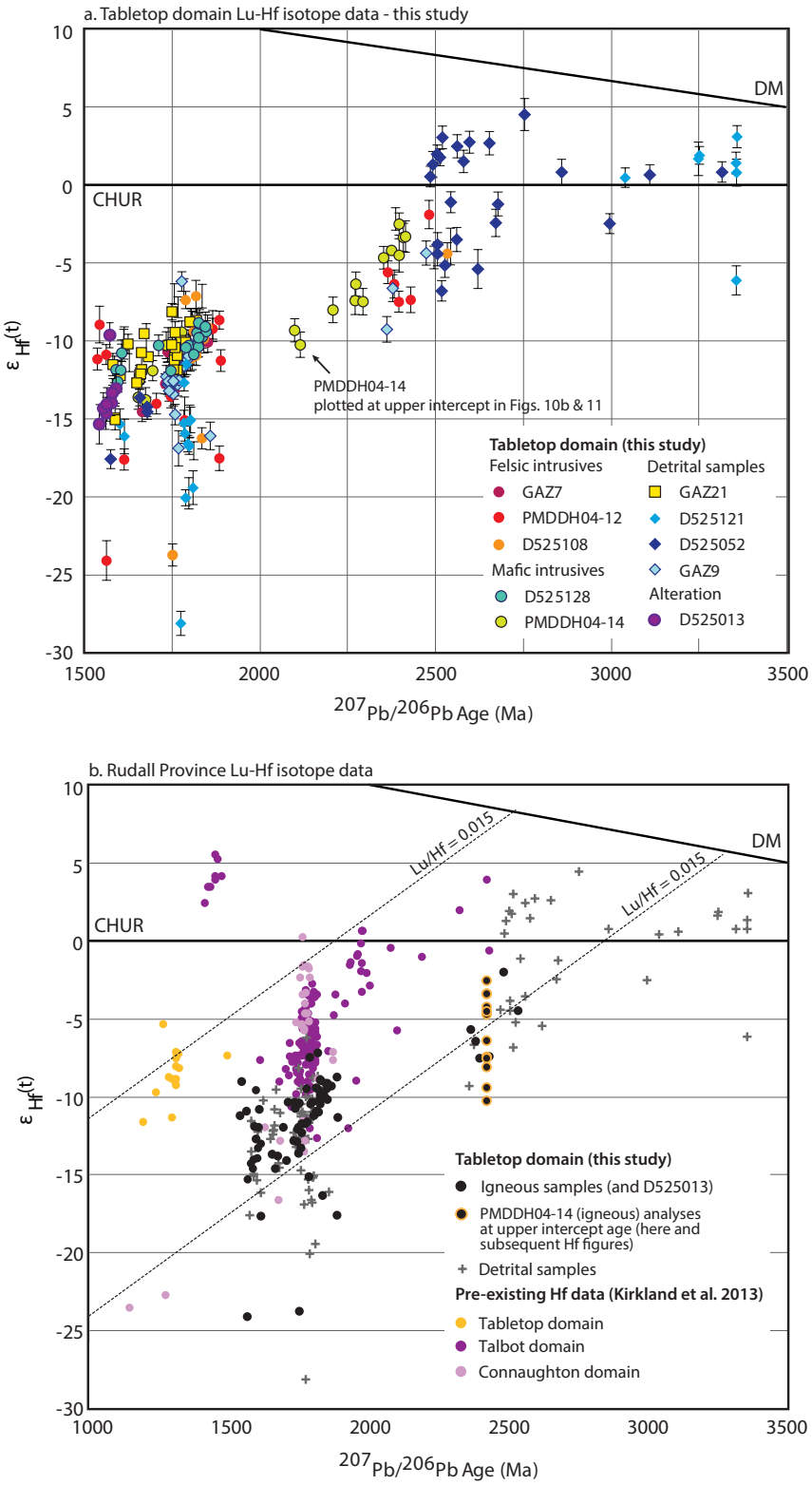

Figure 10. Lu–Hf isotope results from the Rudall Province. (a) Lu–Hf isotope data from the Tabletop Domain (this study). Deviations of Hf ($^{176}Hf/^{177}Hf$) isotopic composition from the chondrite uniform reservoir (CHUR) standard are expressed in epsilon units, $\varepsilon_{Hf}(t)$. Error bars on individual $\varepsilon_{Hf}(t)$ values are shown at the 2σ level. Samples with inferred igneous protolith are shown as circles; detrital samples are shown as diamonds and squares; (b) Lu–Hf isotope data from this study plotted against existing data from the Rudall Province (Kirkland *et al.*, 2013b). Pre-existing data corresponding to the Tabletop, Talbot and Connaughton Domains are shown in yellow, dark purple and light purple, respectively. Data from igneous and metsedimentary samples analysed in this study are shown as black filled circles and grey crosses, respectively. $\varepsilon_{Hf}(t)$ values for early Paleoproterozoic zircon from sample PMDDH04-14 are plotted at their upper intercept age (refer to main text) owing to effects of ancient Pb-loss that mean $\varepsilon_{Hf}(t)$ plotted at apparent $^{207}Pb/^{206}Pb$ ages is not geologically valid (compare Fig. 10a). Crustal growth curves using an average bulk crust value of $^{176}Lu/^{177}Hf = 0.015$ are drawn through the dominant late Paleoproterozoic zircon populations from this study and Kirkland *et al.* (2013b) to provide a visual guide of the Hf-isotope composition of reworked crust, without the addition of juvenile material. Abbreviations: DM, depleted mantle.

1576, analysis 52-12). The Hf-isotope signature of these younger zircon grains approximate the $\varepsilon_{Hf}(t)$ values obtained from similarly aged zircon rims analysed in other samples.

5.3.7 Sample D525121 (quartzite)

Twenty-one analyses obtained from sample D525121 yield a large spread in $\varepsilon_{Hf}(t)$ values [$\varepsilon_{Hf}(t)$ = –28.1 ± 0.8 to +3.1 ± 0.7] that fall into three distinct U–Pb age populations. Analyses from oscillatory-zoned zircon cores with ages >3000 Ma typically exhibit the least evolved Hf-isotope signatures of this sample [$\varepsilon_{Hf}(t)$ = +0.5 ± 0.6 to +3.1 ± 0.7, *n* = 6], excluding one analysis (3355 Ma, analysis 121B-26) with a significantly more evolved $\varepsilon_{Hf}(t)$ value of –6.1 ± 0.9. These older, comparatively juvenile analyses are isotopically similar to the oldest Archean analyses from sample D525052 (Fig. 10a). Oscillatory-zoned zircon cores with ages of ca. 1810–1770 Ma yield $\varepsilon_{Hf}(t)$ values in the range –28.1 ± 0.8 to –11.5 ± 0.7 (*n* = 11), and are typically slightly more evolved than igneous zircon of equivalent age in other samples. Three analyses from weakly luminescent zircon rims on dark, zoned cores (1615 ± 27 Ma, 1602 ± 30 Ma and 1582 ± 29 Ma) gave similarly evolved $\varepsilon_{Hf}(t)$ values that form a discrete cluster between –16.1 ± 1.1 and –13.5 ± 0.6.

5.4.8 Sample GAZ9 (biotite–garnet gneiss)

Twenty-five analyses were done on sample GAZ9. The majority of analyses come from zircon cores yielding ages between ca. 1800 and 1750 Ma, which yield $\varepsilon_{Hf}(t)$ values between –16.9 ± 1.1 and –6.2 ± 0.6. Three older analyses give $\varepsilon_{Hf}(t)$ values of –4.4 ± 0.8 (2473 Ma, analysis GAZ9-02), –6.6 ± 0.9 (2378 Ma, analysis GAZ9-61) and –9.3 ± 0.8 (2361 Ma, analysis GAZ9-25).

5.3.9 Sample GAZ21 (calc-silicate gneiss)

Fifteen analyses from oscillatory-zoned zircon cores (ca. 1820–1580 Ma) in sample GAZ21 yielded $\varepsilon_{Hf}(t)$ values between –15.0 ± 0.6 and –8.1 ± 0.5. The oldest analyses from this sample broadly exhibit the least evolved Hf signatures with progressively younger zircon showing a slight shift to more evolved $\varepsilon_{Hf}(t)$ values (Supplementary Fig. 1). This is consistent with minor ancient Pb-loss resulting in the spread of apparent $^{207}Pb/^{206}Pb$ ages from an original ca. 1800 Ma main population. The CL images support this interpretation, with older zircon displaying clearer zoning whereas younger zircon appears to show partial recrystallisation.

5.3.10 Sample D525013 (calc-silicate altered mafic gneiss, 1582 ± 8 Ma)

Eight analyses were obtained from sample D525013. All analyses come from sector-zoned zircon cores with ages of 1591–1543 Ma. The majority of analyses yield similar Hf-isotope signatures with $\varepsilon_{Hf}(t)$ values clustered between –15.3 ± 1.3 and –13.1 ± 0.9. One analysis gave a slightly more juvenile Hf signature than the main population (–9.6 ± 0.8, analysis 013-16). These $\varepsilon_{Hf}(t)$ values are approximately consistent with the isotopic composition of ca. 1600 Ma zircon of D525128 (mafic gneiss) and GAZ-21 (calc-silicate).

6. DISCUSSION

Previous geochronological and isotopic studies from the Tabletop Domain recognised two magmatic suites and a metasedimentary unit. These are the ca. 1590–1550 Ma Krackatinny Supersuite (Maidment, 2017), the newly named 1310–1286 Ma leucogranitic Camel Suite (Kirkland et al., 2013b; Maidment, 2017; Nelson, 1996b), and a quartzite interpreted to have been deposited in the Archean (Maidment, 2017). The ages of these successions differ from the established geological histories of the Talbot and Connaughton domains, which are dominated by Paleoproterozoic sedimentation and magmatism. This study presents new Lu–Hf and U–Pb data for previously unrecognised Archean–Paleoproterozoic rocks in the Tabletop Domain. The following section: (1) examines the age and isotopic signature of the Tabletop Domain in light of these new findings; (2) reassesses the age and isotopic relationship between the three domains of the Rudall Province; and (3) more broadly considers the geodynamic relationship of the Tabletop Domain to the WAC versus NAC.

6.1 Age and isotope signature of the Tabletop Domain

6.1.1 Archean–Paleoproterozoic crystalline rocks

Five samples with inferred igneous protoliths analysed from the Tabletop Domain provide direct evidence for two phases of magmatism during the Paleoproterozoic (ca. 2400 Ma and

1850–1750 Ma). Oscillatory-zoned zircon cores from mafic gneiss intersected in drill core (sample PMDDH04-14) have concordant ca. 2400 Ma zircon ages, suggesting that crystallisation of mafic magmas occurred at ca. 2400 Ma. An alternative interpretation is that the ca. 2400 Ma zircon in sample PMDDH04-14 are xenocrystic and the crystallisation age is younger (i.e. ca. 1850–1750 Ma). This alternative interpretation requires that the majority of zircon in this sample is inherited. Although not impossible, it seems unlikely that a mafic rock would inherit sufficient crustal material (of a single age) at the intrusive level to contain a significant yield of zircon, but still maintain mafic mineralogy. In addition, enclaves of strongly foliated mafic gneiss similar to sample PMDDH04-14 are observed in foliated granite (Fig. 4e), suggesting that the mafic gneiss is older than the mid–late Paleoproterozoic felsic magmatism in the same drill hole. If inherited, the presence of significant oscillatory zoned early Paleoproterozoic zircon grains in sample PMDDH04-14 would imply that there is a likely magmatic source rock of this age in the Tabletop Domain, albeit unexposed, and the fundamental interpretation for earliest Paleoproterozoic rocks present within the Tabletop Domain remains.

Sample D525128 (mafic gneiss), PMDDH04-12 (foliated granite), GAZ7 (granite gneiss) and D525108 (leucogranite) are dominated by oscillatory-zoned zircon cores that all yield mid–late Paleoproterozoic ages (ca. 1880–1750 Ma). This period is interpreted to reflect the timing of a second phase of magmatism. Two of these samples, PMDDH04-12 and D525128, also contain 2550–2400 Ma zircon with similar $\varepsilon_{Hf}(t)$ values to zircon from the early Paleoproterozoic mafic gneiss, consistent with the apparent intrusive relationship between mafic gneiss and foliated granite observed in drill hole PMDDH04 (Fig. 4e). Further support for a mid–late Paleoproterozoic magmatic event is provided by sample PMDDH04-14, which contains grains with morphologies consistent with recrystallisation (i.e. chaotic internal features and/or are indistinctly zoned; Table 3) that yield concordant ages between ca. 1800 and 1700 Ma. These ages may be associated with minor new growth (e.g. rim analysis, Fig. 4a) but are interpreted to predominantly record the effects of a metamorphic/magmatic event at ca. 1770 Ma resulting in Pb-loss from early Paleoproterozoic zircon. The mid–late Paleoproterozoic oscillatory-zoned zircon have more evolved Hf isotope signatures (typically $\varepsilon_{Hf}(t) = -15$ to -7) than the early Paleoproterozoic zircon. An average crustal isotopic growth curve ($^{176}Lu/^{177}Hf = 0.015$) projected through the mid–late Paleoproterozoic zircon from samples PMDDH04-14, PMDDH04-12 and D525108 (Supplementary Fig. 1) suggests that these zircon may reflect isotopic reworking of the early Paleoproterozoic crust from which the inferred magmatic or xenocrystic zircon in these same samples are derived.

The variable intensity of deformation, limited surficial outcrop in the Tabletop Domain and restricted view in drill core means that the original lithological relationships between the ca. 2400 Ma and ca. 1850–1750 Ma rocks are unclear. If correct, the sample of early Paleoproterozoic mafic gneiss (PMDDH04-14) would now be the oldest recognised magmatic crust identified in the Tabletop Domain, while noting that Neoarchean–early Paleoproterozoic sedimentary sequences have also been identified (Maidment, 2017, and this study, see below).

6.1.2 Archean–Paleoproterozoic sedimentary rocks

Extensive deformation, alteration and weathering across the Tabletop Domain has destroyed primary sedimentary features in exposed metasedimentary rocks and it is therefore difficult to unequivocally assign a sedimentary protolith to some samples. The paucity of outcrop also prevents determination of contact relationships between the metasedimentary and igneous rocks. Despite these limitations, zircon ages obtained from four inferred metasedimentary samples in the Tabletop Domain constrain the timing and provenance of two phases of Paleoproterozoic sedimentation.

A quartzo-feldspathic gneiss (D525052) from the far northwest of the Tabletop Domain is dominated by Paleo–Neoarchean age components (ca. 3300–2500 Ma, predominantly in the range ca. 2600–2500 Ma) with relatively juvenile Hf isotope signatures ($\varepsilon_{Hf}(t) = -7$ to $+4$), and has a complete absence of detrital zircon with ages <2300 Ma. This sample is interpreted to represent a mid-Paleoproterozoic sedimentary succession, deposited after 2316 ± 18 Ma (maximum depositional age) but prior to inferred *in situ* rim growth between ca. 1720 and 1580 Ma. Archean detrital age components (ca. 3580–2830 Ma) have also been noted in a sample of muscovite-bearing

quartzite from the central Tabletop Domain (GA2006670087), interpreted to be derived from the Pilbara Craton (Maidment, 2017). Deposition of the protolith of this sample was interpreted to have occurred between 2833 Ma (maximum depositional age) and the timing of metamorphic zircon rim growth at 1790 ± 7 Ma and/or 1580 ± 34 Ma (Maidment, 2017). Despite their broadly similar depositional interval, the detrital zircon age spectra of GA2006670087 (Supplementary Fig. 2) does not include the prominent ca. 2500 Ma peak seen in sample D525052, and their maximum depositional ages differ by ca. 500 Ma. Therefore, the two samples are unlikely to be direct stratigraphic equivalents, but it is plausible that both were deposited after ca. 2300 Ma, from slightly different detrital zircon provenance.

Sample D525121 is a strongly foliated muscovite-bearing quartzite, taken approximately 300 m from the location of GA2006670087. Sample D525121 yields Paleoarchean detritus (ca. 3100–3400 Ma), a dominant age peak at ca. 1790 Ma and a smaller age peak at ca. 1600 Ma, consistent with the age spectra observed in GA2006670087 (Supplementary Fig. 2). Interpretation of the age spectra for sample D525121 is assisted by the Hf isotope data. Mid–late Paleoproterozoic zircon (ca. 1790 Ma) in D525121 have highly variable $\varepsilon_{Hf}(t)$ with a range of approximately eight epsilon units, plus one outlier at –28. This large variation in Hf isotope composition, combined with the sub-rounded nature of some of the zircon rims and cores comprising this population, suggests the ca. 1790 Ma zircon population is a detrital population and not a single metamorphic population grown *in situ* within the rock. This interpretation implies a maximum depositional age of ca. 1790 Ma. It is possible that metamorphic zircon from a single sample may exhibit a range of Hf isotope compositions due to non-homogeneous partial melting/reworking (Halpin et al., 2013), or recrystallisation of pre-existing zircon and this creates some ambiguity in the interpretation. This ambiguity allows for the alternative interpretation that the ca. 1790 Ma zircon population in D525121 is instead metamorphic, with the maximum depositional age of this sample therefore being 3039 ± 10 Ma, as defined by the next youngest, concordant, oscillatory zoned core. This alternative maximum depositional and metamorphic age aligns more closely with the current interpretation of GA2006670087 (max. dep. 2833 ± 5 Ma; Maidment, 2017). Further field observations and/or geochronology are required to unequivocally resolve the age of this particular sedimentary package.

A garnet–biotite gneiss (GAZ9) and calc-silicate rock (GAZ21) have similar inferred maximum depositional ages to the muscovite-bearing quartzite (D525121), conservatively estimated as ca. 1760 Ma, 1771 ± 7 Ma and 1793 ± 6 Ma, respectively (Fig. 7). All three samples are dominated by detrital ages between ca. 1850 and 1750 Ma. Zircon grains comprising this main age population have variable $\varepsilon_{Hf}(t)$ values (typically between –6 and –17). The age and Hf isotope composition of these zircon grains are approximately equivalent to the mafic and felsic igneous rocks from the Tabletop Domain (see above). The highly deformed and retrogressed nature of rocks in the GAZZA-1 drill hole, the presence of deformed granite in the same drill hole, and the lack of clear "field" relationships between the different lithologies makes it possible that the protoliths to GAZ9 and GAZ21 were igneous. It is plausible that these samples were simply metamorphosed and subsequently altered to provide mineralogical and textural characteristics that are otherwise interpreted to be metasedimentary. However, the range in Hf-isotopic composition for the ca. 1850–1750 Ma zircon in these samples is greater than is commonly observed in a single igneous sample (Fig. 10a). The simplest explanation for the mineralogy and zircon spectra of these samples is that they have a sedimentary origin and late Paleoproterozoic detritus was sourced locally, from exhumed igneous rocks within the Tabletop Domain or broader Rudall Province. Such an interpretation is further supported by the elongate and subhedral morphology of the majority of zircon grains, rather than the euhedral or rounded zircon that may indicate a syn-volcano–sedimentary, or more distal source, respectively. These samples, together with D525121, are therefore interpreted to represent a cover sequence to the early Paleoproterozoic (ca. 2400 Ma) and mid–late Paleoproterozoic (ca. 1850–1750 Ma) crystalline rocks of the Tabletop Domain. A consequence of this interpretation is that this sedimentary cover sequence subsequently underwent metamorphism to at least amphibolite facies, resulting in the development of gneissic fabrics, garnet- and muscovite-bearing assemblages and zircon rim growth during the waning stages of D_1 deformation (ca. 1780 Ma, see Section 2) or during a later ca. 1600–1580

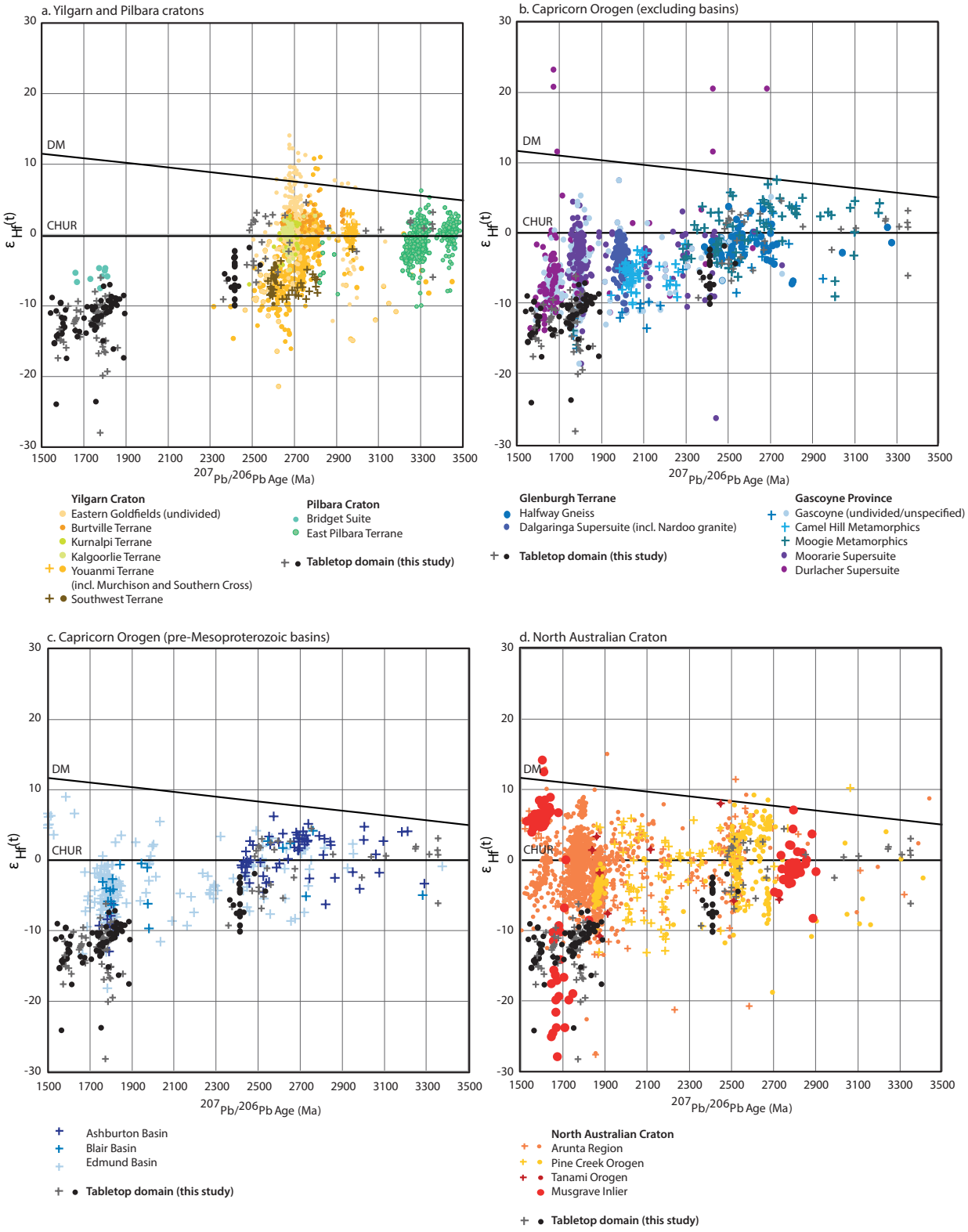

Figure 11. Lu–Hf isotope results from the Tabletop Domain (this study, Fig. 10), plotted against existing data from the West Australian Craton (WAC) and North Australian Craton (NAC). The WAC Hf dataset (shown in Fig. 11a–c) is inclusive of all publically-available data from the Geological Survey of Western Australia online database (GeoVIEW.WA: <https://geoview.dmp.wa.gov.au/GeoViews/?Viewer=GeoVIEW>) with additional published data from the Yilgarn Craton (Ivanic *et al.*, 2012; Wyche *et al.*, 2012), Pilbara Craton (Gardiner *et al.*, 2017), the Capricorn Orogen—incorporating the Gascoyne Province, pre-Mesoproterozoic Ashburton, Blair and Edmund basins, and the Glenburgh Terrane (Johnson *et al.*, 2011a, 2011b, 2017). The NAC dataset is inclusive of analyses from the Arunta Region, Pine Creek Orogen, Tanami Orogen and Musgrave Inlier (Northern Territory Geological Survey online database, STRIKE: <http://strike.nt.gov.au/>) with additional data from Smits *et al.* (2014, and references therein). In all plots, data from rocks with an inferred igneous origin are shown as filled circles; data from rocks with an inferred sedimentary protolith are shown as crosses. Abbreviations: CHUR, chondritic uniform reservoir; DM, depleted mantle.

Ma metamorphic event. This is discussed further below.

6.2 Three domains, not three terranes

Paleoproterozoic magmatism at ca. 1800–1700 Ma was previously thought to be absent from the Tabletop Domain, although it dominates the Talbot and Connaughton domains as the ca. 1800–1765 Ma Kalkan Supersuite (Bagas, 2000, 2004; Bagas and Smithies, 1998; Hickman and Bagas, 1998, 1999; Maidment, 2017). The apparent absence of ca. 1800–1765 Ma magmatism in the Tabletop Domain, in part, formed the basis for the notion that the Tabletop Domain was exotic to the Talbot and Connaughton domains (e.g. Bagas, 2004; Smithies and Bagas, 1998). New results from this study show that this is not the case, and there is a consistent Paleoproterozoic geological record across all three domains of the Rudall Province. Mafic and felsic gneisses from the central Tabletop Domain have similar protolith crystallisation ages (ca. 1820–1750 Ma) to the Kalkan Supersuite (Maidment, 2017, and references therein Table 3), and their zircon Hf-isotope compositions overlap with analyses from the Kalkan Supersuite (Kirkland et al., 2013b). It is therefore reasonable to consider the Kalkan-aged igneous rocks identified in the Tabletop Domain to be an eastern extension of the Kalkan Supersuite. The spread in weighted mean ages across analysed igneous samples in this study (e.g. GAZ7, 1753 ± 8 Ma and D525128, 1821 ± 7 Ma) suggests the previously quoted age range of the Kalkan Supersuite (1804–1762 Ma; Maidment, 2017) can be further expanded to ca. 1820–1750 Ma. Although it is beyond the scope of this study, a ca. 70 Ma duration for the Kalkan Supersuite raises the possibility that the supersuite represents a number of distinct magmatic events.

Inferred metasedimentary rocks of the central Tabletop Domain (D525121, GAZ21 and GAZ9) yield a dominant mid–late Paleoproterozoic detrital age component and inferred maximum depositional ages that align with the age of the Kalkan Supersuite, as outlined above. The Hf isotope compositions of these detrital zircon (Fig. 10) are also comparable with the isotope signature of the Kalkan Supersuite (Kirkland et al., 2013b, and this study). These rocks are interpreted to have been deposited during or after intrusion of the Kalkan Supersuite, but there is a lack of conclusive field relationships in the Tabletop Domain to determine if there is an unconformable relationship between the Kalkan Supersuite and these metasedimentary rocks. Maidment (2017) interpreted the protoliths to the Talbot Domain metasedimentary rocks to have been derived locally from the Kalkan Supersuite and proposed that this occurred either in a synorogenic setting, coeval with granite intrusion overlying a pre-Kalkan succession, or that deposition occurred <1760 Ma on an older Paleoproterozoic succession comprising the exhumed Kalkan Supersuite and their host rocks. The new data in this study suggest a similar tectonic interpretation is likely for the Tabletop Domain during the mid–late Paleoproterozoic.

One unnamed quartzite from the Connaughton Domain dated by Maidment (2017) (sample GA2005670165) yielded a maximum depositional age of 2284 ± 10 Ma and a dominant Paleo–Neoarchean (ca. 3400–2300 Ma) age component that is not observed in the Talbot Domain. The Neoarchean zircon ages form two main age populations at 2721–2610 Ma and 2592–2472 Ma, consistent with the age of detritus from volcano-sedimentary rocks of the Fortescue and Hamersley groups of the Hamersley Basin that overlies the Pilbara Craton (Arndt et al., 1991; Trendall et al., 2004). The minimum depositional age of the quartzite is constrained by Kalkan Supersuite granites that intrude the quartzite (ca. 1780 Ma; Maidment, 2017). Quartzo-feldspathic gneiss dated in this study (sample D525052) yielded a similar dominant ca. 2500 Ma age peak to the dated quartzite in the Connaughton Domain, and has a similar inferred maximum depositional age (2316 ± 18 Ma). A minimum depositional age for sample D525052 is provided by pervasive metamorphic rim growth at ≤ca. 1720 Ma, and is similar to the minimum depositional age of sample GA2005670165. The similar depositional interval and age spectra may indicate that the two metasedimentary rocks formed part of a broader basin system that received detritus from the Neoarchean Fortescue Group. Given the evidence for Kalkan Supersuite magmatism in the Tabletop Domain as early as ca. 1820 Ma (e.g. sample D525128), it is possible that sediment deposition occurred within the slightly narrower age range of ca. 2200–1820 Ma, with sample D525052 (and GA2005670165) representative of the sedimentary country rocks intruded by the Kalkan Supersuite.

The newly highlighted similarities in the geological record of the three domains of the Rudall Province

reflect the inappropriate nature of the 'terrane' nomenclature, which should consequently be discontinued until it can be demonstrated that the Tabletop Domain is not allochthonous. The possibility remains that, although the three domains appear to share a common pre-1590 Ma history, the presence of the ca. 1590–1550 Ma Krackatinny Supersuite within the Tabletop Domain is unique and may hint at a separate evolution until the Mesoproterozoic. Furthermore, although evidence for late Mesoproterozoic tectonism is documented across the entire Rudall Province (ca. 1380–1280 Ma), it has a magmatic expression in the east (e.g. Maidment, 2017) and is characterised by high-grade metamorphism in the west (e.g. Anderson, 2015). This difference does not necessarily negate an overall endemic interpretation, but highlights additional complexity in the post-1590 Ma evolution of the Rudall Province.

6.3 High-grade metamorphism in the Tabletop Domain, and orogenesis in the Rudall Province

Until recently, interpretations within the peer-reviewed literature have focused on the low and variable grade of deformation of the ca. 1590–1550 Ma Krackatinny Suite as a broad indicator that the Tabletop Domain lacks evidence for high-grade metamorphism (e.g. Bagas, 2004; Smithies and Bagas, 1998). Our field observations, and those of Yeates and Chin (1979), show that a significant portion of the outcrop within the Tabletop Domain is in fact gneissic, consistent with observations from the Connaughton and Talbot domains. These exposed lithologies in the Tabletop Domain have now been demonstrated to be pre-Krackatinny Suite in age. Maidment (2017) recently proposed that the Tabletop Domain may have attained a higher grade of metamorphism than previously assumed based on the presence of 1790 ± 7 Ma zircon overgrowths and the assumption that zircon growth requires temperatures to have attained at least amphibolite facies conditions. This is consistent with the presence of ca. 1720–1550 Ma metamorphic zircon rims in a number of samples from this study. The number, nature and exact timing of these high-grade metamorphic events are less clear owing to inconclusive geochronological data, the pervasive greenschist facies overprint and the lack of diagnostic pelitic or mafic mineral assemblages that could be used for quantitative pressure–temperature modelling. However, the available evidence for multiple metamorphic events in the Tabletop Domain are discussed below.

Evidence for high-grade, mid–late Paleoproterozoic deformation and metamorphism is most conclusively provided by metamorphic zircon geochronology and deformation of newly age-constrained granites. Sample GAZ-7 is a granite gneiss, yielding a crystallisation age of 1753 ± 8 Ma. This granite contains an obvious gneissic fabric (Fig. 4f) suggesting that development of the gneissic (S_1) foliation occurred at or after ca. 1750 Ma. Further support for a metamorphic event of this age comes from sample PMDDH04-14, which displays evidence for new zircon growth and/or ancient Pb-loss at 1773 ± 51 Ma (regression lower intercept; Fig. 6a). Notwithstanding the imprecise geochronology on the timing of this event owing to large and overlapping age uncertainties on samples with key lithological relationships, mid–late Paleoproterozoic high-grade metamorphism therefore likely occurred at ca. 1770–1750 Ma. D_1 in the Tabletop Domain, as adopted in this study (D_1 of Yeates and Chin, 1979), is presumably equivalent to D_1/M_1 (as defined for the remainder of the Rudall Province; Table 1). D_2/M_2 in the Connaughton and Talbot domains was recently demonstrated to be younger than previously thought (Anderson, 2015; Maidment, 2017). We suggest that D_1 within the Connaughton and Talbot domains, and D_1 in the Tabletop Domain, be considered a single orogenic event and that the name Yapungku Orogeny is used to refer to this event. The Yapungku Orogeny is proposed to incorporate the Kalkan Supersuite magmatism. The high pressure M_2 event that was initially considered as the Yapungku Orogeny (Bagas, 2004), now postulated to be ca. 1380 Ma (Anderson, 2015), then requires a different term. This M_2 event is proposed as the 'Parnngurr Orogeny' (D. Maidment, personal communication, April 2018).

The second event in the Tabletop Domain for which there is clear metamorphic evidence is an early Mesoproterozoic event that was associated with emplacement of the Krackatinny Supersuite. Four samples in this study reveal evidence for ca. 1600–1550 Ma zircon growth, predominantly as thick, homogeneous and featureless rims with a dark or strongly luminescent CL response (Fig. 5). Monazite data from sample D525052 also reveal a concordant age population at ca. 1570 Ma, supporting the interpretation of a metamorphic event at this time. Further, sample GAZ21 exhibits

the effects of minor, ancient Pb loss to ca. 1550 Ma, evidenced by a large spread in concordant age data (Fig. 7e), zircon having increasingly convoluted and diffuse internal structure with decreasing age (Fig. 5i), and a minor, horizontal trend in $Hf_{(i)}$ versus age (Supplementary Fig. 1). The Hf-isotopic signature of ca. 1600–1550 Ma zircon is consistent within individual samples (< 3 ε_{Hf} unit spread) and falls within the bounds of the expected average crustal growth curve projected from older, Paleoproterozoic and/or Archean zircon in the same samples (Supplementary Fig. 1). This suggests that new ca. 1600–1550 Ma zircon growth probably occurred from a homogenous Hf reservoir released by reworking of the host rock during metamorphism (e.g. Halpin et al., 2013). Field observations of sample D525128 suggest that the mafic gneiss underwent partial melting and geochronology reveal metamorphic zircon rim growth at ca. 1600 Ma. Hornblende-bearing leucosomes and the absence of high-temperature minerals such as orthopyroxene suggest that this rock underwent melting below ~750–850°C (e.g. Green et al., 2016); however, this still indicates that some rocks record at least upper amphibolite facies metamorphism at ca. 1600 Ma. Metamorphism occurring at ca. 1600–1550 Ma at upper amphibolite facies does not seem to be pervasive across the Tabletop Domain and therefore we agree with the suggestion of Maidment (2017) that metamorphism of this style may be driven by contact metamorphism from the Krackatinny Suite (e.g. see GA2006670087; Maidment, 2017). We tentatively assign regional foliations, folding and shear zone development of D_2 to the ca. 1600–1550 Ma event and refer to this as the Krackatinny Event. Alteration assemblages (e.g. chlorite replacement and calcite veins in drill hole GAZZA-1; pervasive alteration of feldspar and hornblende in outcropping rocks) overprint the inferred high-grade gneissic fabrics but themselves do not define a fabric. A possible age for the greenschist facies overprint is provided by the calc-silicate (epidote) alteration in sample D525013 (Fig. 8). This sample suggests that the greenschist facies overprint occurred during the waning stages of D_2 within the Tabletop Domain (ca. 1580 Ma). At present, however, we consider the minimum age of the greenschist facies overprint to be effectively unconstrained, and the possibility remains that it occurred during younger events such as the intrusion of the Camel Suite or the ca. 810–650 Ma Miles Orogeny (Table 1; Hickman and Bagas, 1999).

In addition to the Yapungku Orogeny and Krackatinny Event, geochronology from this study reveal evidence for minor zircon and monazite growth and/or U–Pb resetting at ca. 1680 Ma. However, these age data cannot be linked to deformational fabrics or metamorphic assemblages and thus the geological significance of the ca. 1680 Ma age is unclear. Interestingly, zircon rim analyses from orthogneiss in the Talbot Domain (sample GA2005670080) and a megacrystic granitoid (sample GA2005670162) in the Connaughton Domain also yield inferred (and tentatively assigned) metamorphic ages of 1679 ± 25 Ma and 1688 ± 8 Ma, respectively (Maidment, 2017). Anderson (2015) also document ca. 1665 Ma monazite from staurolite-bearing schist in the far northwestern Talbot Domain. Further investigation is required to clarify whether these ca. 1680–1665 Ma ages are related to an earlier phase of deformation (e.g. partial isotopic resetting of D_1, Yapungku Orogeny), or whether they represent mounting evidence for an additional, discrete instance of deformation and metamorphism.

6.4 Relationship of the Tabletop Domain to the WAC and NAC

Available geochronology suggests that the timing of Proterozoic magmatism and deformation was similar across the Talbot and Connaughton domains of the Rudall Province, the Capricorn Orogen of the WAC, and the Arunta Region of the NAC (Fig. 3; Maidment, 2017). Furthermore, Kirkland et al. (2013b) recently identified that inherited zircon from the Kalkan Supersuite in the Talbot and Connaughton domains were likely derived from detritus shed from the Glenburgh Terrane. The most evolved Paleoproterozoic magmatic zircon from the Kalkan Supersuite are comparable in age and Hf-isotope signature to zircon from lamprophyric dykes and monzogranitic–dioritic rocks of the ca. 1800 Ma Bridget Suite from the East Pilbara Terrane (Bodorkos, Love, Nelson, and Wingate, 2006; Kirkland et al., 2013b). The Hf-isotope signatures of magmatic zircon and whole-rock Nd isotope compositions of the Kalkan Supersuite rocks suggest reworking of a basement component underlying the Rudall Province that is isotopically similar to reworked East Pilbara crust (Kirkland et al., 2013b). Seismic interpretations of Reading et al. (2012) also support interpretations of East Pilbara Terrane basement situated under the Talbot Terrane. These similarities, and the interpretation that ca. 1310 Ma Tabletop Domain

granite may reflect reworked Kalkan Supersuite rocks, led Kirkland et al. (2013b) to propose that at least the western Rudall Province reflects autochthonous reworking of WAC crust and that all three domains appear to be united in their crustal evolution.

A compilation of Lu–Hf isotopic data from tectonic regions of the WAC and NAC with comparable Archean–Paleoproterozoic geochronological histories to the Rudall Province (see also Fig. 3) is presented in Fig. 11. The detrital zircon age spectra of metasedimentary rocks in this study are also compared with select units from the WAC in Supplementary Fig. 2 to discern zircon provenance.

Three main age components identified within the Tabletop Domain rocks are appraised with respect to the WAC and NAC: (1) a ca. 3400–2800 Ma component found as detritus in metasedimentary rocks; (2) a ca. 2500–2300 Ma component found as detritus and minor inheritance in metasedimentary and igneous rocks, and as the age of mafic crystallisation; and (3) ca. 1880–1750 Ma detritus, and magmatic zircon that date the age mafic and felsic magmatism. If the Tabletop Domain were indeed united in its crustal evolution with the WAC, then it is reasonable to expect that geologically related regions of the WAC should exhibit comparable isotopic signatures.

Paleo–early Neoarchean (ca. 3400–2800 Ma) detrital zircon from metasedimentary samples D525121 and D525052 are older than exposed igneous and sedimentary basement rocks of the Capricorn Orogen, Yilgarn Craton and NAC (Fig. 11). However, similarly aged inherited Archean age components are observed in the Glenburgh Terrane of the Capricorn Orogen and are interpreted to have been sourced from an older, unexposed basement (Johnson et al., 2011b, 2017). Granitic gneisses of the Halfway Gneiss (2555–2430 Ma) contain an inherited Archean age component at ca. 3560–2600 Ma (Supplementary Fig. 1), and interleaved calc-silicate, amphibolite and pelitic gneiss of the Moogie Metamorphics contain 3300–2900 Ma ages, also interpreted to have come from Halfway Gneiss basement, as well as the Pilbara Craton (Johnson et al., 2013, 2011a, b, 2013, 2017). The Hf-isotopic composition of >2800 Ma zircon from the Halfway Gneiss, Moogie Metamorphics and Capricorn Orogen basins is similar to the ca. 3400–2800 Ma Tabletop Domain detritus, but a robust comparison is limited by few data points (Fig. 11). The age of the Tabletop Domain Archean zircon also coincides with the age of known magmatism in the Pilbara Craton (Van Kranendonk, Smithies, Hickman, and Champion, 2007). Fig. 11 indicates that the Hf isotope composition of these Archean zircon also correlate approximately with zircon from > ca. 3200 Ma East Pilbara Craton granite–greenstones (Gardiner et al., 2017). In essence, Paleo–Neoarchean zircon from the Tabletop Domain in this study exhibit broad geochronological and isotopic similarities to the East Pilbara Craton, inherited zircon in the Halfway Gneiss, Archean detrital zircon in the Moogie Metamorphics, and abundant Archean detritus (3580–2830 Ma) in another sample of quartzite from the Tabletop Domain (Maidment, 2017, discussed above). These observations indicate that the Pilbara Craton is the likely source of Paleo–early Neoarchean detritus in the Tabletop Domain with possible minor contributions from crust with affinity to the Halfway Gneiss basement.

Figure 11 reveals that the strongest age and isotopic correlation between Neoarchean and early Paleoproterozoic (ca. 2500–2400 Ma) zircon from the Tabletop Domain is with the 2555–2430 Ma Halfway Gneiss and interleaved Moogie Metamorphics. Magmatic zircon from the Halfway Gneiss lies on an average crustal growth curve projected from the isotopic signature of inherited zircon (>2600 Ma) in this same unit that are interpreted to provide evidence of an older basement component, which is now eroded or tectonically removed (Johnson et al., 2011b, 2017). Protoliths to the Halfway Gneiss are thus inferred to have formed via *in situ* crustal reworking of this basement component, without significant juvenile addition (Johnson et al., 2011b, 2017). The distinctly different isotope signature and crystallisation age of the Halfway Gneiss compared with other regions of the WAC is the basis upon which Johnson et al. (2011b) infer that the Glenburgh Terrane is an exotic terrane relative to the Yilgarn and Pilbara cratons. Similarities in the age and isotope signature of inferred magmatic zircon from sample PMDDH04-14 in this study with magmatic zircon from the Halfway Gneiss suggest that the ca. 2400 Ma crystalline rocks of the Tabletop Domain may share a similar Neoarchean crustal evolution to the Glenburgh Terrane.

Protoliths to the Moogie Metamorphics were

deposited in a foreland basin between 2240 and 2145 Ma, immediately post emplacement of the Halfway Gneiss protoliths but prior to collision and amalgamation of the Glenburgh Terrane and Pilbara Craton (Johnson et al., 2011a, 2013). The detrital zircon spectra of the Moogie Metamorphics is dominated by a late Neoarchean (ca. 2850–2700 Ma) and early Paleoproterozoic (ca. 2550–2300 Ma) age component (Johnson et al., 2011a, b). These zircon are interpreted to be recycled from volcano–sedimentary sequences of the Fortescue Group (2775–2630 Ma) and Hamersley Group (2630–2430 Ma) that were deposited in a syn-rift and passive margin setting, respectively, along the south Pilbara Craton (Johnson et al., 2011a, 2013). The detrital zircon age spectra of sample D525052 in this study shares resemblance with the Moogie Metamorphics (Supplementary Fig. 2), and both units yield a similar maximum depositional age, suggestive of a related zircon provenance and depositional history. Specifically, sample D525052 exhibits the dominant ca. 2500 Ma age peak that is common to the Moogie Metamorphics and contemporaneous lower Wyloo Group (2215–2145 Ma; Ashburton Basin), of which the detritus is also inferred sourced from the Hamersley Group (Johnson et al., 2013). The Hf-isotopic composition of detrital zircon of this age from the Ashburton Basin and Moogie Metamorphics is also equivalent to the Tabletop Domain (Fig. 11). However, sample D525052 does not yield ca. 2700 Ma ages that are also common to the Moogie Metamorphics (Supplementary Fig. 2; Johnson et al., 2011b). There is also a conspicuous absence of ca. 2300–2000 Ma zircon in the Tabletop Domain compared with the Capricorn Orogen. This difference may be a reflection of the relatively small sample size of zircon grains analysed in sample D525052 and/or bias in the source regions of detritus that was shed into local depocentres that formed part of a larger early Paleoproterozoic basin system across the Capricorn Orogen.

As previously established, the age and isotope signature of zircon from ca. 1880–1750 Ma igneous rocks and similarly aged detritus in metasedimentary rocks from the Tabletop Domain correspond with the Kalkan Supersuite. The majority of Tabletop Domain ca. 1880–1750 Ma magmatic rocks also fall within the same isotopic space as the most evolved analyses from the Moorarie Supersuite in the Glenburgh Terrane (Fig. 11; Johnson et al., 2017). Although the Tabletop Domain data lack the more juvenile compositions seen in mid–late Paleoproterozoic data from the Capricorn Orogen, the Hf data of Kirkland et al. (2013) for the Talbot and Connaughton domains fill this age–isotope space. The Moorarie Supersuite was emplaced during the intraplate Capricorn Orogeny (Johnson et al., 2013, 2017), after accretion of the Pilbara–Glenburgh Craton and the northern Yilgarn Craton (i.e. inferred final WAC assembly; Johnson et al., 2011a; Occhipinti at al., 2004), and is interpreted to have involved reworking of crust of Halfway Gneiss affinity with some juvenile input (Johnson et al., 2017). The Hf-isotopic evolution of inherited and magmatic zircon within the Kalkan Supersuite in the Talbot and Connaughton domains is interpreted to reflect contributions from a variety of autochthonous source regions, including the sedimentary successions into which they were intruded (Kirkland et al., 2013b). These sedimentary successions are interpreted to include detritus derived from the Halfway Gneiss and continental arc magmas of the 2005–1970 Ma Dalgaringa Supersuite of the Glenburgh Terrane (Kirkland et al., 2013b; Sheppard et al., 2004). The late Paleoproterozoic (ca. 1800–1750 Ma) zircon from the Tabletop Domain lie on a crustal growth curve projected from the isotopic composition of the Neoarchean–early Paleoproterozoic zircon, also suggesting reworking of crust of affinity to the Glenburgh Terrane basement.

The onset of the Capricorn Orogeny (ca. 1820–1770 Ma) was accompanied by deposition of Paleoproterozoic volcano-sedimentary rocks in an extensive foreland basin system (Fig. 1) including the Upper Wyloo Group (Ashburton Basin) and diachronous Capricorn Group (Blair Basin), and protoliths to the Leake Spring Metamorphics of the Gascoyne Province (Evans et al., 2003; Hall et al., 2001; Johnson et al., 2013). Detritus is interpreted to have been shed from the Gascoyne Province, and specifically the Halfway Gneiss, Dalgaringa Supersuite and syn-magmatic Moorarie Supersuite. Kirkland et al. (2013b) previously suggested that the eastern association of the Talbot Domain was also deposited in a series of linked basins that formed part of a regionally extensive basin system along the southern and eastern Pilbara Craton. Specifically, Kirkland et al. (2013b) infers that regional uplift of the southern margin of the Gascoyne Province provided abundant sedimentary detritus into the developing basins. In the Rudall Province, it is likely that detritus was predominantly locally sourced from

the local Kalkan granites, with little detritus from the Capricorn Orogen itself. It is conceivable that a far easterly correlative of the Gascoyne Province may also have provided a local source of detritus in the Rudall Province, although there are no exposures. This does not negate that the Rudall Province and Capricorn Orogen are related. Given similarities between the detrital zircon spectra of Paleoproterozoic Tabletop Domain metasedimentary samples (D525121, GAZ9 and GAZ21) with those from the Talbot Domain and units comprising the Capricorn Orogeny basins, it is likely that they share a similar depositional history. This may have occurred within a series of linked basins that extended towards the eastern Rudall Province.

7. CONCLUSIONS

This study presents the first U–Pb geochronology and Hf-isotope data from rocks in the Tabletop Domain of the eastern Rudall Province. Isotopic results identify a previously unrecognised Archean–Paleoproterozoic gneissic succession in the Tabletop Domain. Magmatism occurred during the early (ca. 2400 Ma) and mid–late Paleoproterozoic (ca. 1880–1750 Ma), and both phases of magmatism were approximately coeval with sedimentation. Early Paleoproterozoic igneous and metasedimentary rocks show age and isotopic similarity to the Glenburgh Terrane that comprises basement to the Capricorn Orogen. Mid–late Paleoproterozoic igneous rocks are assigned to the voluminous Kalkan Supersuite that crops out in the Connaughton and Talbot domains of the Rudall Province. The abundance of mid–late Paleoproterozoic detritus in metasedimentary rocks with similar maximum depositional ages to the Kalkan Supersuite suggests that the sediment was sourced locally from the Kalkan intrusive rocks themselves. Similarities between the detrital zircon age spectra and zircon Hf-isotope composition of the mid–late Paleoproterozoic metasedimentary rocks and Capricorn Orogeny basin units also suggest that a regionally extensive basin system may have existed at this time. This is consistent with prior interpretations from the western Rudall Province. Minor Archean detritus in metasedimentary samples also points to a potential contribution from the East Pilbara Craton.

Two phases of metamorphism are evidenced by zircon and monazite geochronology coupled with field observations that suggest the development of gneissic fabrics at upper amphibolite facies conditions during the mid–late Paleoproterozoic (ca. 1750 Ma), and a subsequent, localised, high-grade event at ca. 1600–1550 Ma. The latter event is also interpreted to have been associated with late, pervasive greenschist facies alteration. Previous interpretations that the Tabletop Domain was an exotic crustal element of the Rudall Province have hinged on the absence of a Paleoproterozoic history akin to the Connaughton and Talbot domains, and the seemingly low grade of metamorphism in the Tabletop Domain compared with the western Rudall Province. Field observations and geochronology from this study indicate that neither of these conditions hold true. The three domains of the Rudall Province share a similar Proterozoic geological evolution and the Tabletop Domain is endemic to the WAC. In light of these new findings, further work is now required to provide clarity on the Mesoproterozoic (< ca. 1590 Ma) crustal evolution of the Tabletop Domain, and the tectonic and metamorphic framework of the Rudall Province.

ACKNOWLEDGEMENTS

The authors gratefully acknowledge the logistical field support of Fortescue Metals Group Ltd. In particular, Chris Van Wijk, Graeme Hardwick and Sarah Jessop are thanked for their assistance and discussions in the field. The Martu people are thanked for access to their land and guidance during fieldwork. D. Maidment and S. Sheppard are thanked for their thorough and constructive comments and suggestions on the manuscript.

This work was funded by a collaborative project between Fortescue Metals Group Ltd. and the University of South Australia. NMT acknowledges the support of an Australian Government Research Training Program Scholarship and Playford Trust PhD Scholarship.

REFERENCES

Aitken A. R. A., Betts P. G., Young D. A., Blankenship D. D., Roberts J. L. & Siegert M. J. 2016. The Australo–Antarctic Columbia to Gondwana transition. *Gondwana Research* 29, 136–152.

Anderson J. A. 2015. Metamorphic and isotopic characterisation of Proterozoic belts at the margins of the North and West Australian Cratons. PhD thesis. University of Adelaide, Adelaide.

Arndt N., Nelson D., Compston W., Trendall A. & Thorne A. 1991. The age of the Fortescue Group, Hamersley Basin, Western Australia, from ion microprobe zircon U-Pb results. *Australian Journal of Earth Sciences* 38, 261–281.

Bagas L. 1999. Geology of the Blanche–Cronin 1:100 000 sheet (part sheets 3551 and 3552): Western Australia

Geological Survey, 1:100 000 Geological Series Explanatory Notes, 16p.

Bagas L. 2000. Geology of the Paterson 1:100 000 sheet: Western Australia Geological Survey, 1:100 000 Geological Series Explanatory Notes, 20p.

Bagas L. 2004. Proterozoic evolution and tectonic setting of the northwest Paterson Orogen, Western Australia. *Precambrian Research* 128, 475–496.

Bagas L. & Lubieniecki Z. 1999. Copper and associated polymetallic mineralization along the Camel–Tabletop Fault Zone in the Paterson Orogen, Western Australia. Geological Survey of Western Australia 2000, 36–41.

Bagas L. & Smithies R. 1997. Palaeoproterozoic tectonic evolution of the Rudall Complex, and comparison with the Arunta Inlier and Capricorn Orogen. Western Australia Geological Survey, 110–115.

Bagas L. & Smithies R. H. 1998. Geology of the Connaughton 1:100 000 sheet: Western Australia Geological Survey, 1: 100 000 Geological Series Explanatory Notes, 38p.

Bagas L., Williams I. & Hickman A. 2000. Rudall, Western Australia . 1: 250,000 Geological Series Explanatory Notes. Western Australia Geological Survey.

Betts P., Armit R., Stewart J., Aitken A., Ailleres L., Donchak P., Hutton L., Withnall I. & Giles D. 2016. Australia and nuna. *Geological Society, London, Special Publications* 424, 47–81.

Betts P. G. & Giles D. 2006. The 1800–1100 Ma tectonic evolution of Australia. *Precambrian Research* 144, 92–125.

Betts P. G., Giles D., Lister G. S. & Frick L. R. 2002. Evolution of the Australian lithosphere. *Australian Journal of Earth Sciences* 49, 661–695.

Black L. P., Kamo S. L., Allen C. M., Davis D. W., Aleinikoff J. N., Valley J. W., Mundil R., Campbell I. H., Korsch R. J., Williams I. S. & Foudoulis C. 2004. Improved 206Pb/238U microprobe geochronology by the monitoring of a trace-element-related matrix effect; SHRIMP, ID–TIMS, ELA–ICP–MS and oxygen isotope documentation for a series of zircon standards. *Chemical Geology* 205, 115–140.

Bodorkos S., Love G. J., Nelson D. R. & Wingate M. T. D. 2006. 178232: trondhjemitic pegmatite vein, Whatsamatta Well; Geochronology Record 654: Geological Survey of Western Australia, 4p.

Bouvier A., Vervoort J. D. & Patchett P. J. 2008. The Lu–Hf and Sm–Nd isotopic composition of CHUR: constraints from unequilibrated chondrites and implications for the bulk composition of terrestrial planets. *Earth and Planetary Science Letters* 273, 48–57.

Camacho A. & Mcdougal I. 2000. Intracratonic, strike-slip partitioned transpression and the formation and exhumation of eclogite facies rocks: An example from the Musgrave Block, central Australia. *Tectonics* 19, 978–996.

Cawood P. A. & Korsch R. 2008. Assembling Australia: Proterozoic building of a continent. *Precambrian Research* 166, 1–35.

Clarke G. 1991. Proterozoic tectonic reworking in the Rudall complex, Western Australia. *Australian Journal of Earth Sciences* 38, 31–44.

Czarnota K., Gerner E., Maidment D., Meixner A. & Bagas L. 2009. Paterson Area 1: 250 000 Scale Solid Geology Interpretation and Depth to Basement Model. Explanatory notes. Geoscience Australia Record 16, pp. 37.

Evans D. A., Sircombe K., Wingate M. T., Doyle M., Mccarthy M., Pidgeon R. T. & Van Niekerk H. S. 2003. Revised geochronology of magmatism in the western Capricorn Orogen at 1805–1785 Ma: diachroneity of the Pilbara–Yilgarn collision. *Australian Journal of Earth Sciences* 50, 853–864.

Fraser A. 1976. Gravity provinces and their nomenclature. *BMR Journal of Australian Geology and Geophysics* 1, 350–352.

Gardiner N. J., Hickman A. H., Kirkland C. L., Lu Y., Johnson T. & Zhao J.-X. 2017. Processes of Crust Formation in the Early Earth Imaged through Hf isotopes from the East Pilbara Terrane. *Precambrian Research* 297: 56–76

Green E., White R., Diener J., Powell R., Holland T. & Palin R. 2016. Activity–composition relations for the calculation of partial melting equilibria in metabasic rocks. *Journal of Metamorphic Geology* 34, 845–869.

Griffin W. L., Wang X., Jackson S. E., Pearson N. J., O'reilly S. Y., Xu X. & Zhou X. 2002. Zircon chemistry and magma mixing, SE China: In-situ analysis of Hf isotopes, Tonglu and Pingtan igneous complexes. *Lithos* 61, 237–269.

Guitreau M. & Blichert-Toft J. 2014. Implications of discordant U–Pb ages on Hf isotope studies of detrital zircons. *Chemical Geology* 385, 17–25.

Hall C., Powell C. M. & Bryant J. 2001. Basin setting and age of the late Palaeoproterozoic Capricorn Formation, Western Australia. *Australian Journal of Earth Sciences* 48, 731–744.

Halpin J. A., Daczko N. R., Clarke G. L. & Murray K. R. 2013. Basin analysis in polymetamorphic terranes: An example from east Antarctica. *Precambrian Research* 231, 78–97.

Hickman A. H. & Bagas L. 1998. Geology of the Rudall 1:100 000 sheet: Western Australia Geological Survey, 1:100 000 Geological Series Explanatory Notes, 30p.

Hickman A. H. & Bagas L. 1999. Geological Evolution of the Palaeoproterozoic Talbot Terrane, and Adjacent Meso-and Neoproterozoic Successions, Paterson Orogen, Western Australia. Geological Survey of Western Australia.

Hocking R., Mory A. & Williams I. Year. An atlas of Neoproterozoic and Phanerozoic basins of Western Australia. The Sedimentary Basins of Western Australia: Proceedings of the Petroleum Exploration Society of Australia Symposium, Perth, pp. 21–43.

Huston D. L., Blewett R. S. & Champion D. C. 2012. Australia through time: a summary of its tectonic and metallogenic evolution. *Episodes* 35, 23–43.

Ivanic T. J., Van Kranendonk M. J., Kirkland C. L., Wyche S., Wingate M. T. D. & Belousova E. A. 2012. Zircon Lu–Hf isotopes and granite geochemistry of the Murchison Domain of the Yilgarn Craton: Evidence for reworking of Eoarchean crust during Meso–Neoarchean plume-driven magmatism. *Lithos* 148, 112–127.

Jackson S. E., Pearson N. J., Griffin W. L. & Belousova E. A. 2004. The application of laser ablation–inductively coupled plasma–mass spectrometry to in situ U–Pb zircon geochronology. *Chemical Geology* 211, 47–69.

Johnson S., Sheppard S., Rasmussen B., Wingate M., Kirkland C., Muhling J., Fletcher I. & Belousova E. 2011a. Two collisions, two sutures: Punctuated pre-1950Ma assembly of the West Australian Craton during the Ophthalmian and Glenburgh Orogenies. *Precambrian Research* 189, 239–262.

Johnson S. P. 2013. The birth of supercontinents and the Proterozoic assembly of Western Australia. Geological Survey of Western Australia, pp. 78.

Johnson S. P., Korhonen F. J., Kirkland C. L., Cliff J. B., Belousova E. A. & Sheppard S. 2017. An isotopic perspective on growth and differentiation of Proterozoic

orogenic crust: From subduction magmatism to cratonization. *Lithos* 268, 76–86.

Johnson S. P., Sheppard S., Wingate M. T. D., Kirkland C. L. & Belousova E. A. 2011b. Temporal and hafnium isotopic evolution of the Glenburgh Terrane basement: an exotic crustal fragment in the Capricorn Orogen: Geological Survey of Western Australia, Report 110, 27p.

Johnson S. P., Thorne A., Tyler I., Korsch R., Kennett B., Cutten H., Goodwin J., Blay O., Blewett R. & Joly A. 2013. Crustal architecture of the Capricorn Orogen, Western Australia and associated metallogeny. *Australian Journal of Earth Sciences* 60, 681–705.

Kirkland C. L., Johnson S. P., Smithies R. H., Hollis J. A., Wingate M. T. D., Tyler I. M., Hickman A. H., Cliff J. B., Belousova E. A., Murphy R. C. & Tessalina S. 2013a. The crustal evolution of the Rudall Province from an isotopic perspective: Geological Survey of Western Australia, Report 122, 30p.

Kirkland C. L., Johnson S. P., Smithies R. H., Hollis J. A., Wingate M. T. D., Tyler I. M., Hickman A. H., Cliff J. B., Tessalina S., Belousova E. A. & Murphy R. C. 2013b. Not-so-suspect terrane: Constraints on the crustal evolution of the Rudall Province. *Precambrian Research* 235, 131–149.

Li Z. 2000. Palaeomagnetic evidence for unification of the North and West Australian cratons by ca. 1.7 Ga: new results from the Kimberley Basin of northwestern Australia. *Geophysical Journal International* 142, 173–180.

Lindsay J. F. 2002. Supersequences, superbasins, supercontinents – evidence from the Neoproterozoic–early Palaeozoic basins of central Australia. *Basin Research* 14, 207–223.

Ludwig K. R. 2012. User's manual for ISOPLOT 3.75, a geochronological toolkit for Microsoft Excel. Berkeley Geochronology Centre Special Publication 5.

Maidment D. W. 2005. Palaeozoic high-grade metamorphism within the Centralian Superbasin, Harts Range region, central Australia. PhD Thesis, Australian National University, Canberra.

Maidment D. W. 2017. Geochronology of the Rudall Province, Western Australia: implications for the amalgamation of the West and North Australian Cratons: Geological Survey of Western Australia, Report 161, 95p.

Nelson D. R. 1995a. 104932: garnet–biotite–muscovite syenogranite gneiss, Sundowner drillhole: Geochronology Record 31: Geological Survey of Western Australia, 4p.

Nelson D. R. 1995b. 104938: pegmatite, Coondegoon; Geochronology Record 35: Geological Survey of Western Australia, 4p.

Nelson D. R. 1995c. 104989: muscovite quartzite, Fingoon Quartzite; Geochronology Record 5: Geological Survey of Western Australia, 4p.

Nelson D. R. 1995d. 112310: granodiorite gneiss, Dunn Creek west; Geochronological Record 471: Geological Survey of Western Australia, 4p.

Nelson D. R. 1995e. 112341: micromonzogranite (meta-aplite) dyke, Rudall airstrip; Geochronology Record 472: Geological Survey of Western Australia, 4p.

Nelson D. R. 1996a. 112102: seriate biotite metamonzogranite, southern part of the Watrara Inlier; Geochronology Record 523: Geological Survey of Western Australia, 3p.

Nelson D. R. 1996b. 118914: foliated granite, north of Harbutt Range; Geochronology Record 485: Geological Survey of Western Australia, 4p.

Occhipinti S. A., Sheppard S., Passchier C., Tyler I. M. & Nelson D. R. 2004. Palaeoproterozoic crustal accretion and collision in the southern Capricorn Orogen: the Glenburgh Orogeny. *Precambrian Research* 128, 237–255.

Paton C., Hellstrom J., Paul B., Woodhead J. & Hergt J. 2011. Iolite: Freeware for the visualisation and processing of mass spectrometric data. *Journal of Analytical Atomic Spectrometry* 26, 2508–2518.

Payne J. L., Hand M., Barovich K. M., Reid A. & Evans D. a. D. 2009. Correlations and reconstruction models for the 2500–1500 Ma evolution of the Mawson Continent. *In: Reddy S. M., Evans D. a. S. & Collins A. S. (eds.) Palaeoproterozoic Supercontinents and Global Evolution,* Geological Society of London, pp. 319–355, UK.

Payne J. L., Hand M., Barovich K. M. & Wade B. P. 2008. Temporal constraints on the timing of high-grade metamorphism in the northern Gawler Craton: implications for assembly of the Australian Proterozoic. *Australian Journal of Earth Sciences* 55, 623–640.

Payne J. L., Pearson N., Grant K. J. & Halverson G. P. 2013. Reassessment of relative oxide formaiton rates and molecular interferences on in-situ Lutetium–Hafnium analysis with Laser Ablation MC–ICP–MS. *Journal of Analytical Atomic Spectrometry* 28, 1068–1079.

Raimondo T., Collins A., Hand M., Walker-Hallam A., Smithies H. & Evins P. 2008. A kinematic, metamorphic and geochronological framework for intracratonic reworking in the western Musgrave Block, central Australia: evidence for lower crustal channel flow? International Geological Congress Abstracts 33, Abstract 1342888.

Raimondo T., Collins A. S., Hand M., Walker-Hallam A., Smithies R. H., Evins P. M. & Howard H. M. 2010. The anatomy of a deep intracontinental orogen. *Tectonics* 29, TC4024.

Reading A. M., Tkalčić H., Kennett B. L., Johnson S. P. & Sheppard S. 2012. Seismic structure of the crust and uppermost mantle of the Capricorn and Paterson Orogens and adjacent cratons, Western Australia, from passive seismic transects. *Precambrian Research* 196, 295–308.

Scherer E., Münker C. & Mezger K. 2001. Calibration of the Lutetium–Hafnium Clock. *Science* 293, 683–687.

Scrimgeour & Close 1999. Regional high-pressure metamorphism during intracratonic deformation: the Petermann Orogeny, central Australia. *Journal of Metamorphic Geology* 17, 557–572.

Segal I., Halicz L. & Platzner I. T. 2003. Accurate isotope ratio measurements of ytterbium by multiple collection inductively coupled plasma mass spectrometry applying erbium and hafnium in an improved double external normalization procedure. *Journal of Analytical Atomic Spectrometry* 18, 1217–1223.

Sheppard S., Occhipinti S. A. & Tyler I. M. 2004. A 2005–1970 Ma Andean-type batholith in the southern Gascoyne Complex, Western Australia. *Precambrian Research* 128, 257–277.

Slama J., Kosler J., Condon D. J., Crowley J. L., Gerdes A., Hanchar J. M., Horstwood M. S. A., Morris G. A., Nasdala L., Norberg N., Schaltegger U., Schoene N., Tubrett M. N. & Whitehouse M. J. 2008. Plesovice zircon - a new natural reference material for U–Pb and Hf isotopic microanalysis. *Chemical Geology* 249, 1–35.

Smithies R. & Bagas L. 1997. High pressure amphibolite–granulite facies metamorphism in the Paleoproterozoic Rudall Complex, central Western Australia. *Precambrian Research* 83, 243–265.

Smithies R. H. & Bagas L. 1998. The Tabletop Terrane of

the Proterozoic Rudall Complex: preliminary notes on the geology, granitoid geochemistry and tectonic implications. *In: Geological Survey of Western Australia Annual Review 1996–97:* Geological Survey of Western Australia, Perth, Western Australia, p. 89–94.

Smits R. G., Collins W. J., Hand M., Dutch R. & Payne J. 2014. A Proterozoic Wilson cycle identified by Hf isotopes in central Australia; implications for the assembly of Proterozoic Australia and Rodinia. *Geology* 42, 231–234.

Thevissen J. 1991. 1990–91 Annual Report, Karara Well Project, E45/841, Rudall River area, W.A.; PNC Exploration (Australia) Pty Ltd: Geological Survey of Western Australia, Statutory mineral exploration report, A33945.

Trendall A., Compston W., Nelson D., De Laeter J. & Bennett V. 2004. SHRIMP zircon ages constraining the depositional chronology of the Hamersley Group, Western Australia. *Australian Journal of Earth Sciences* 51, 621–644.

Van Kranendonk M. J., Hugh Smithies R., Hickman A. H. & Champion D. C. 2007. Review: secular tectonic evolution of Archean continental crust: interplay between horizontal and vertical processes in the formation of the Pilbara Craton, Australia. *Terra Nova* 19, 1–38.

Vervoort J. D., Patchett P. J., Söderlund U. & Baker M. 2004. Isotopic composition of Yb and the determination of Lu concentrations and Lu/Hf ratios by isotope dilution using MC–ICPMS. *Geochemistry, Geophysics, Geosystems* 5, Q11002, doi: 10.1029/2004GC000721.

Walsh A. K., Raimondo T., Kelsey D. E., Hand M., Pfitzner H. L. & Clark C. 2013. Duration of high-pressure metamorphism and cooling during the intraplate Petermann Orogeny. *Gondwana Research* 24, 969–983.

Wiedenbeck M., Alle P., Corfu F., Griffin W., Meier M., Oberli F., Quadt A. V., Roddick J. & Spiegel W. 1995. Three natural zircon standards for U-Th-Pb, Lu-Hf, trace element and REE analyses. *Geostandards Newsletter* 19, 1–23.

Woodhead J., Hergt J., Shelley M., Eggins S. & Kemp R. 2004. Zircon Hf-isotope analysis with an excimer laser, depth profiling, ablation of complex geometries, and concomitant age estimation. *Chemical Geology* 209, 121–135.

Woodhead J. D. & Hergt J. M. 2005. A preliminary appraisal of seven natural zircon reference materials for in-situ Hf-isotope determination. *Geostandards and Geoanalytical Research* 29, 183–195.

Wyche S., Kirkland C. L., Riganti A., Pawley M. J., Belousova E. & Wingate M. T. D. 2012. Isotopic constraints on stratigraphy in the central and eastern Yilgarn Craton, Western Australia. *Australian Journal of Earth Sciences* 59, 657–670.

Yeates A. N. & Chin R. J. 1979. 1:250 000 Geological Series Explanatory Notes, Tabletop, Western Australia, Sheeet SF/51-11, 2nd ed. Bureau of Mineral Resources, Australia & Geological Survey of WA.

Supplementary Figure 1. $\varepsilon_{Hf}(t)$ versus $^{207}Pb/^{206}Pb$ age and initial $^{176}Hf/^{177}Hf$ ($Hf_{initial}$) versus $^{207}Pb/^{206}Pb$ age. Arrows highlight horizontal trends in $Hf_{initial}$ versus age that translate as positive correlation between $\varepsilon_{Hf}(t)$ values and age. Such trends are suggestive of ancient Pb-loss. Analyses corresponding to zircon rims, zoned magmatic zircon cores and inherited grains are highlighted. Dashed lines (with or without grey shading) project average crustal isotopic growth curves (assuming average crust $^{176}Lu/^{177}Hf = 0.015$) through various zircon populations to provide information on the extent of crustal reworking and is discussed in the main text.

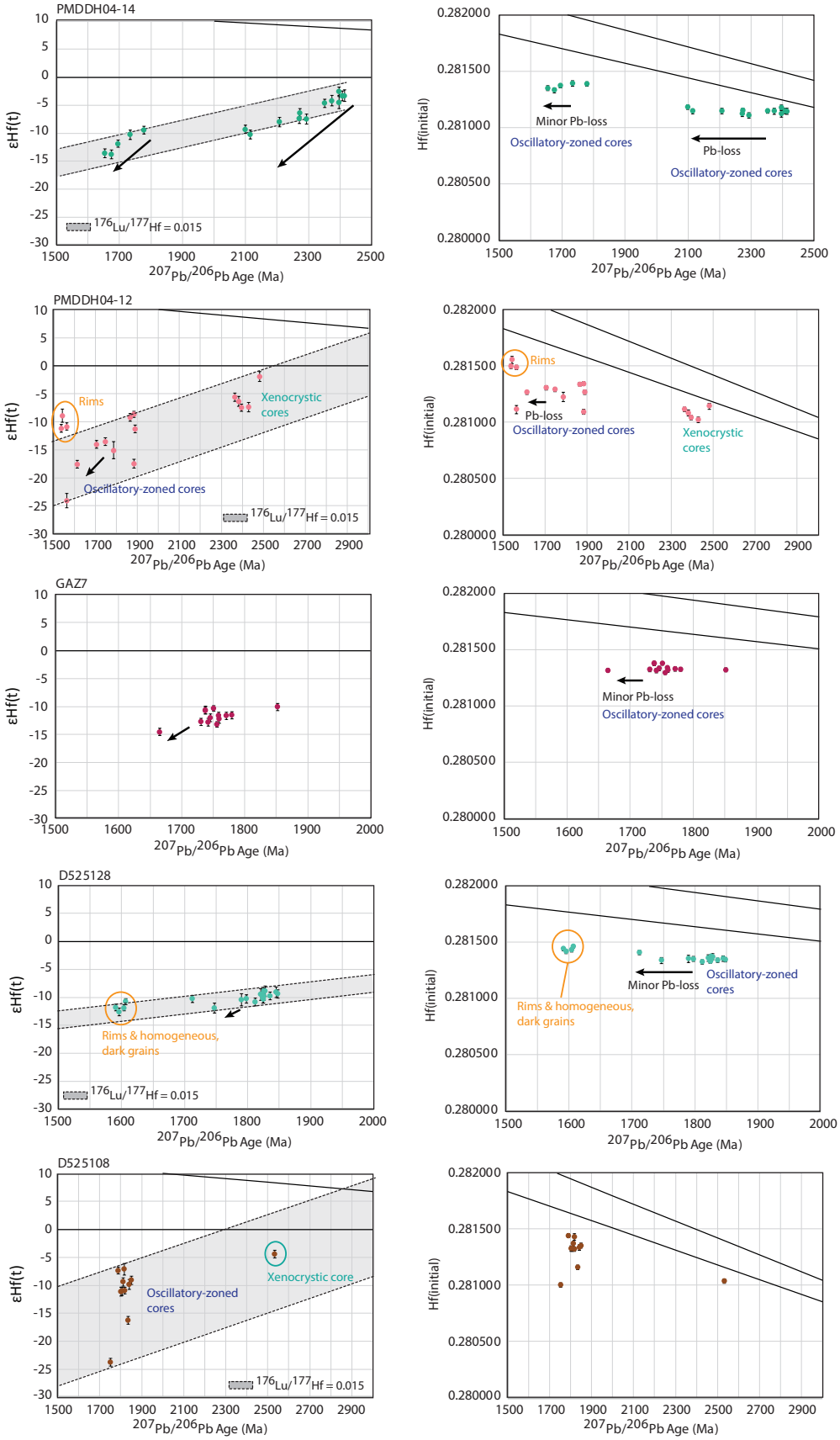

Supplementary Figure 1. (continued)

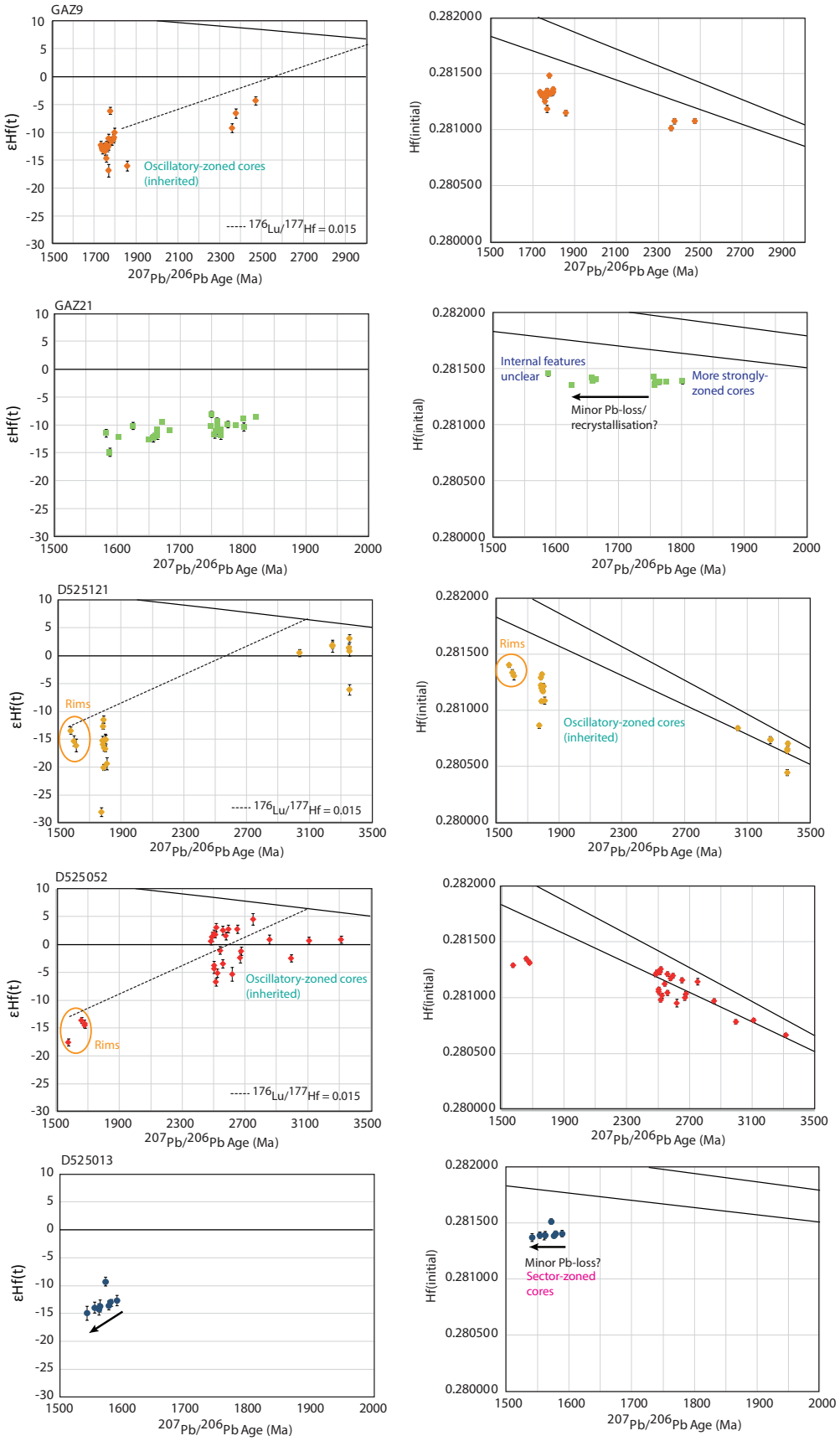

Supplementary Figure 2. Detrital zircon provenance.
Probability density plots of concordant U–Pb age data from Tabletop Domain metasedimentary samples analysed in this study are shown at the top of the figure (in red). Tabletop Domain detrital zircon ages are compared with pre-existing data from the Rudall Province in the left-hand column. Pre-existing data from the Tabletop Domain, Connaughton Domain and Talbot Domain are shown in yellow, light purple and dark pink, respectively. Tabletop Domain data from this study are compared with data from the Capricorn Orogen (in blue) and Pilbara Craton (in green) in the right-hand column. The interpreted provenance (by the original data source) of detrital zircon ages is noted in green text. The shaded grey vertical bars overlain on the probability density plots reect the main age peaks in the Tabletop Domain data obtained from this study, and are shown to aid in comparison with pre-existing Rudall Province, Capricorn Orogen and Pilbara Craton data.

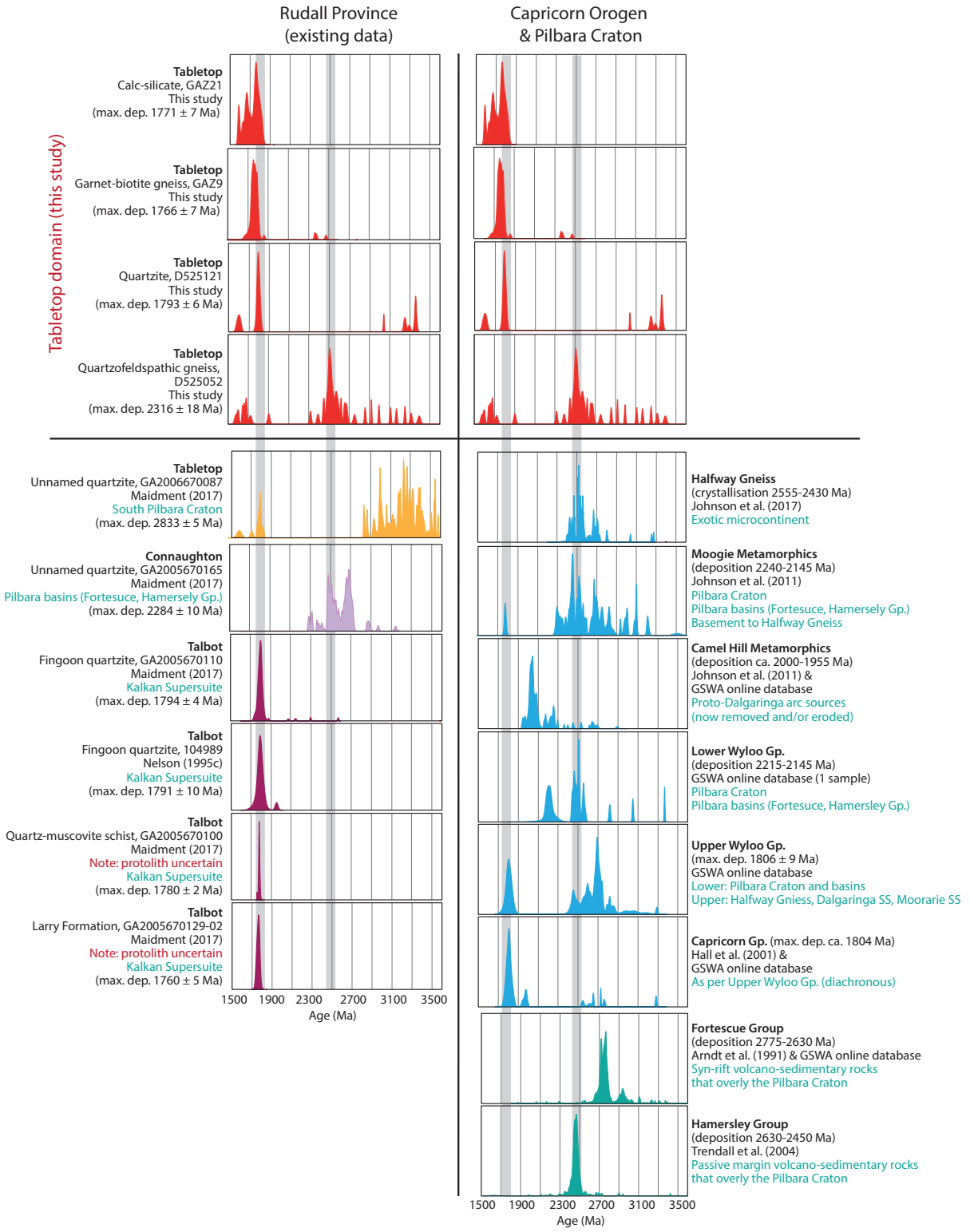

Supplementary Table 1. U–Pb zircon geochronology

Analysis	Analysis location	CL response	U (ppm)	Th (ppm)	Th/U	$^{207}Pb/^{235}U$	2σ	$^{206}Pb/^{238}U$	2σ	$^{207}Pb/^{206}Pb$	2σ	Rho	Age (Ma) $^{207}Pb/^{235}U$	2σ	$^{206}Pb/^{238}U$	2σ	$^{207}Pb/^{206}Pb$	2σ	Conc.**
Sample D525013																			
13-1.d	Core	Dark, zoned	115	188	1.63	3.808	0.047	0.2796	0.0028	0.0979	0.0012	0.28796	1593.2	9.9	1590	15	1589	24	100
13-2.d	Core	Sector-zoned	46	51	1.12	3.74	0.09	0.2706	0.0037	0.0999	0.0026	0.12417	1577	19	1543	19	1622	49	95
13-3.d	Core	Sector-zoned	130	242	1.87	3.794	0.05	0.2753	0.0029	0.0996	0.0014	0.26404	1591	11	1567	15	1619	25	97
13-4.d	Core	Dark, sector-zoned	101	176	1.74	3.736	0.06	0.2797	0.003	0.0974	0.0016	0.19098	1578	13	1589	15	1574	31	101
13-5.d	Core	Dark, sector-zoned	207	386	1.86	3.734	0.041	0.2761	0.0025	0.0985	0.0012	0.23721	1577.8	8.8	1571.7	13	1592	22	99
13-6.d	Core	Luminescent, unzoned	52	154	2.99	3.665	0.085	0.271	0.0036	0.0983	0.0023	0.21887	1570	18	1545	18	1590	45	97
13-7.d	Core	Dark	74	186	2.52	3.744	0.083	0.2783	0.0033	0.0971	0.0022	0.17097	1576	18	1582	17	1566	41	101
13-8.d	Core	Dark	45	86	1.91	3.706	0.084	0.2774	0.0036	0.0971	0.0024	0.018259	1570	18	1578	18	1567	46	101
13-9.d	Core	Weakly-luminescent	84	237	2.83	3.644	0.061	0.2692	0.0029	0.0974	0.0018	0.20945	1557	13	1536	15	1574	34	98
13-10.d	Core	Dark, zoned	261	602	2.31	3.804	0.04	0.2792	0.0026	0.0987	0.0011	0.21079	1592.6	8.4	1586.9	13	1598	22	99
13-11.d	Core	Weakly luminescent, sector-zoned	52	119	2.28	3.641	0.08	0.2741	0.0031	0.0961	0.0024	0.00298	1556	18	1561	16	1543	49	101
13-12.d	Core	Weakly luminescent-dark, sector-zoned	70	140	2.00	3.748	0.071	0.2755	0.0031	0.098	0.0021	0.021946	1582	15	1570	15	1591	39	99
13 - 13.d	Core	Dark, sector-zoned	113	237	2.09	3.778	0.051	0.2803	0.0027	0.0987	0.0015	0.035787	1588	11	1592.7	14	1591	28	100
13 - 14.d	Core	Dark, sector-zoned	84	170	2.01	3.657	0.064	0.2728	0.003	0.0982	0.0019	0.055861	1562	14	1556	15	1580	37	98
13 - 15.d	Core	Dark, sector-zoned	102	237	2.32	3.75	0.049	0.2801	0.0031	0.0974	0.0014	0.16002	1583	10	1592	15	1578	26	101
13 - 16.d	Core	Dark, sector-zoned	60	129	2.14	3.707	0.07	0.2743	0.0033	0.0972	0.002	0.10104	1573	15	1562	17	1573	39	99
13 - 17.d	Core	Weakly luminescent, sector-zoned	39	91	2.34	3.723	0.088	0.2772	0.0039	0.0972	0.0026	0.056768	1574	19	1577	20	1562	53	101
13 - 18.d	Core	Dark, sector-zoned	39	95	2.42	3.638	0.096	0.2795	0.0037	0.095	0.0027	0.059389	1557	20	1588	19	1530	56	104
13 - 19.d	Core	Luminescent-weakly luminescent, sector-zoned	40	93	2.35	3.694	0.085	0.2771	0.0041	0.0959	0.0026	0.066958	1567	19	1576	21	1555	49	101
13 - 20.d	Core	Weakly luminescent, sector-zoned	45	96	2.12	3.633	0.076	0.2732	0.0035	0.0971	0.002	0.16688	1555	17	1556	18	1564	39	99
Sample D525052																			
D525052 - 1.d	Core	Weakly luminescent, zoned	104	71	0.68	7.74	0.15	0.3887	0.0066	0.1443	0.0028	0.44295	2198	17	2116	31	2276	32	93
D525052 - 2.d	Core	Luminescent, convoluted, minor fracturing	217	257	1.19	13.95	0.16	0.5267	0.0081	0.1916	0.0028	0.35465	2745.1	11	2727	34	2753	24	99
D525052 - 3.d	Rim	Dark homogeneous overgrowth on dark zoned core	1070	67	0.06	4.279	0.046	0.2998	0.0044	0.1032	0.0013	0.47792	1688.7	8.8	1690	22	1680	24	101
D525052 - 5.d	Core	Dark, zoned, surrounded by dark overgrowth	138	145	1.05	10.92	0.14	0.475	0.0074	0.1663	0.0026	0.3736	2515.3	12	2507	33	2517	26	100
D525052 - 7.d	Core	Weakly luminescent, weakly-zoned	143	72	0.50	15.93	0.22	0.5452	0.0086	0.2116	0.0031	0.57151	2871	14	2805	36	2914	24	96
D525052 - 8.d	Rim	Dark, surrounds weakly-luminescent core	1920	3400	1.77	4.451	0.068	0.1282	0.0025	0.252	0.0035	0.82029	1721	13	778	14	3195	22	24
D525052 - 9.d	Core	Dark, zoned, surrounded by dark overgrowth	281	162	0.58	11.291	0.13	0.4927	0.0073	0.1657	0.0023	0.4163	2546.6	11	2582	32	2512	23	103
D525052 - 11.d	Core	Dark, zoned	446	632	1.42	10.81	0.14	0.4661	0.0077	0.1674	0.0022	0.79245	2506	12	2466	34	2530	22	97
D525052 - 12.d	Rim	Dark, homogeneous, overgrowth on zoned dark core	858	253	0.30	3.895	0.042	0.2881	0.0042	0.09761	0.0013	0.34881	1612.1	8.7	1631.8	21	1576	25	104
D525052 - 13.d	Rim	Dark, homogeneous, surrounds luminescent core (14)	926	132	0.14	4.847	0.078	0.1907	0.0032	0.1832	0.003	0.52025	1792	14	1125	17	2679	28	42
D525052 - 14.d	Core	Luminescent, weakly zoned	70	37	0.53	7.63	0.16	0.3856	0.0067	0.143	0.0032	0.31392	2183	19	2101	31	2251	40	93
D525052 - 15.d	Core	Dark, homogeneous, weakly sector-zoned	167	155	0.93	10.55	0.13	0.4674	0.0072	0.1632	0.0025	0.2488	2483.6	11	2472	32	2485	26	99

Supplementary Table 1. (continued)

Analysis	Analysis location	CL response	U (ppm)	Th (ppm)	Th/U	$^{207}Pb/^{235}U$	2σ	$^{206}Pb/^{238}U$	2σ	$^{207}Pb/^{206}Pb$	2σ	Rho	Age (Ma) $^{207}Pb/^{235}U$	2σ	$^{206}Pb/^{238}U$	2σ	$^{207}Pb/^{206}Pb$	2σ	Conc.**
D525052 - 16.d	Core	Dark-weakly luminescent, zoned, surrounded by dark overgrowth	451	220	0.49	10.688	0.12	0.4687	0.0072	0.1648	0.0023	0.42246	2495.8	11	2478	32	2504	23	99
D525052 - 17.d	Core	Dark, zoned, surrounded by dark overgrowth	222	88	0.40	25.38	0.27	0.675	0.01	0.2717	0.0037	0.3921	3322.4	10	3329	36	3314	21	100
D525052 - 18.d	Rim	Dark, homogeneous, surrounds dark zoned core (17)	608	104	0.17	5.764	0.076	0.3091	0.0055	0.1352	0.0025	0.152	1940.6	11	1736	27	2163	32	80
D525052 - 20.d	Core	Dark, zoned	381	543	1.43	9.246	0.12	0.3745	0.0059	0.1785	0.0026	0.52229	2361.9	12	2053	26	2637	24	78
D525052 - 22.d	Core	Dark, zoned, surrounded by dark rim	561	671	1.20	9.69	0.14	0.4047	0.0067	0.1732	0.0025	0.6433	2405	13	2190	31	2587	24	85
D525052 - 23.d	Core	Luminescent, weakly zoned, slightly chaotic internal appearance	106	92	0.86	10.59	0.17	0.461	0.0074	0.166	0.0029	0.29344	2485	15	2444	33	2515	31	97
D525052 - 24.d	Core	Luminescent, weakly zoned	117	951	8.14	11.6	0.16	0.4107	0.0065	0.2051	0.0034	0.29919	2573	13	2218	30	2862	27	77
D525052 - 25.d	Rim	Dark, homogeneous, surrounds luminescent core	1283	8980	7.00	5.35	0.064	0.1176	0.002	0.3291	0.0047	0.66006	1876.2	10	716.7	12	3611	22	20
D525052-27.d	Rim	Thick, dark overgrowth on zoned core	1050	223	0.21	4.456	0.11	0.3092	0.0061	0.10317	0.00077	0.35983	1722.3	21	1736.8	30	1679	14	103
D525052-28.d	Core	Dark, zoned, surrounded by dark rim	140	47	0.34	11.58	0.32	0.4799	0.01	0.1724	0.002	0.62249	2569	26	2526	44	2582	19	98
D525052-29.d	Core	Luminescent, zoned	149	429	2.89	5.97	0.19	0.228	0.0052	0.1862	0.0036	0.41007	1969	27	1324	27	2704	32	49
D525052-30.d	Core	Dark, weak sector zoning, surrounded by thick dark rim	207	63	0.30	11.25	0.28	0.4838	0.0096	0.1663	0.0013	0.44963	2543.3	24	2543	42	2519	13	101
D525052-31.d	Core	Dark, appears sector-zoned/heterogeneous zones	768	37	0.05	23.05	0.57	0.6114	0.013	0.2686	0.0017	0.64499	3228.5	24	3075	50	3297	10	93
D525052-32.d	Rim	Dark, surrounds weakly luminescent core (31) (possibly outer core, unclear)	1056	87	0.08	4.294	0.11	0.303	0.006	0.10113	0.00068	0.54508	1691.6	20	1706.1	30	1643	13	104
D525052-33.d	Core	Dark, zoned, surrounded by dark overgrowth (34)	116	136	1.18	11.73	0.3	0.5007	0.01	0.1673	0.002	0.21394	2582	24	2616	44	2526	20	104
D525052-34.d	Rim	Dark overgrowth	803	426	0.53	8.94	0.24	0.2325	0.0052	0.2754	0.0029	0.66395	2331	24	1348	27	3335	16	40
D525052-35.d	Core	Dark, zoned	322	273	0.85	10.702	0.26	0.4662	0.0094	0.1637	0.0013	0.34977	2496.9	23	2467	41	2492	13	99
D525052-37.d	Core	Dark, homogeneous	1001	174	0.17	4.403	0.11	0.287	0.0057	0.10963	0.00086	0.62166	1712.1	21	1626.4	29	1791	14	91
D525052-38.d	Core	Dark, zoned	189	104	0.55	18.21	0.45	0.5872	0.012	0.2223	0.0017	0.50834	2999.9	24	2978	48	2995	12	99
D525052-39.d	Core	Dark, zoned, surrounded by dark rim (40)	399	630	1.58	10.76	0.28	0.4668	0.0094	0.165	0.0013	0.63057	2501.3	24	2469	41	2505	14	99
D525052-40.d	Rim	Dark, homogeneous, surrounds dark zoned core (39)	937	84	0.09	4.226	0.1	0.2978	0.0058	0.10204	0.00073	0.47191	1678.5	20	1680.1	29	1659	13	101
D525052-41.d	Core	Dark, zoned, surrounded by thick dark rim	118	85	0.72	11.08	0.29	0.4828	0.0099	0.1653	0.002	0.30609	2528	25	2539	43	2505	21	101
D525052-42.d	Core	Luminescent, surrounded by thick dark rim (43)	20	12	0.58	27.89	0.79	0.702	0.017	0.2865	0.0051	0.34668	3412	28	3423	65	3394	28	101
D525052-43.d	Rim	Dark, homogeneous, surrounds luminescent core (42)	845	164	0.19	4.567	0.12	0.2922	0.0059	0.11253	0.00095	0.5836	1742.2	22	1652	29	1838	15	90
D525052-45.d	Core	Dark, zoned, surrounded by thick dark rim	385	179	0.47	16.79	0.41	0.571	0.011	0.2121	0.0013	0.39578	2922.5	23	2912	47	2919.7	9.6	100
D525052-46.d	Core	Dark, zoned, surrounded by thick dark rim	142	102	0.72	12.72	0.32	0.5096	0.01	0.1804	0.0016	0.31378	2657.9	24	2655	44	2653	15	100
D525052-47.d	Core	Weakly luminescent-luminescent, zoned, surrounded by thick dark rim	53	40	0.75	11.45	0.32	0.4866	0.011	0.1705	0.0025	0.43591	2558	26	2555	47	2561	24	100
D525052-49.d	Core	Weakly luminescent, zoned to chaotic appearance	182	185	1.01	12.82	0.33	0.4936	0.01	0.1888	0.0019	0.41973	2665.8	24	2586	44	2729	16	95
D525052-51.d	Core	Dark, weakly zoned	168	84	0.50	6.46	0.21	0.3347	0.0082	0.1417	0.0034	0.28373	2038	28	1861	40	2242	41	83
D525052-52.d	Core	Dark, zoned, surrounded by thick dark rim (53)	113	81	0.71	11.22	0.33	0.4842	0.011	0.1702	0.003	0.17951	2543	29	2545	46	2560	32	99
D525052-53.d	Core	Dark, surrounds dark zoned core (52)	687	326	0.47	8.725	0.22	0.4067	0.0083	0.1576	0.0012	0.63797	2308.6	23	2199	38	2427	13	91
D525052-55.d	Core	Dark-weakly luminescent, zoned	840	260	0.31	5.454	0.14	0.3046	0.0068	0.1312	0.0012	0.7419	1892	22	1714	34	2111	16	81
D525052-57.d	Core	Dark, zoned, surrounded by thick dark rim	199	125	0.63	19.84	0.5	0.6115	0.012	0.2385	0.002	0.37991	3082.7	24	3076	49	3109	14	99

Supplementary Table 1. (continued)

Analysis	Analysis location	CL response	U (ppm)	Th (ppm)	Th/U	$^{207}Pb/^{235}U$	2σ	$^{206}Pb/^{238}U$	2σ	$^{207}Pb/^{206}Pb$	2σ	Rho	Age (Ma) $^{207}Pb/^{235}U$	2σ	$^{206}Pb/^{238}U$	2σ	$^{207}Pb/^{206}Pb$	2σ	Conc.**
D525052-58.d	Core	Dark, zoned, surrounded by thick dark rim	251	218	0.87	15.37	0.38	0.5545	0.011	0.2043	0.0017	0.33824	2837.8	24	2843	46	2858	14	99
D525052-59.d	Core	Dark, zoned, surrounded by thick dark rim	136	112	0.82	12.37	0.32	0.5	0.01	0.1825	0.002	0.30142	2632	25	2613	44	2671	19	98
D525052-60.d	Core	Dark grain with thin dark rim	549	200	0.36	11.46	0.29	0.4787	0.01	0.1766	0.0012	0.67594	2560.7	24	2521	44	2620	11	96
D525052-61.d	Core	Dark, zoned, surrounded by thick dark rim	123	103	0.83	11.45	0.3	0.4821	0.0099	0.1745	0.0021	0.17841	2559	24	2536	43	2596	21	98
D525052-62.d	Core	Dark, weakly zoned, surrounded by dark rim	344	255	0.74	8.942	0.22	0.4194	0.0083	0.1567	0.0011	0.4544	2331.4	22	2257	38	2418	12	93
D525052-63.d	Core	Dark, weakly zoned, surrounded by dark rim	282	290	1.03	9.3	0.24	0.4275	0.0093	0.1595	0.002	0.37657	2367	24	2294	42	2447	21	94
D525052-64.d	Core	Dark, weakly zoned, surrounded by dark rim	335	198	0.59	10.3	0.27	0.4519	0.0092	0.1672	0.0015	0.53024	2461	24	2403	41	2527	15	95
D525052-65.d	Core	Weakly luminescent, zoned, surrounded by thick dark rim	100	78	0.78	11.26	0.3	0.4799	0.01	0.1725	0.0022	0.27907	2543	25	2526	43	2579	21	98
D525052-66.d	Core	Dark, zoned, surrounded by thick dark rim	233	208	0.90	10.65	0.27	0.4625	0.0093	0.1688	0.0016	0.3444	2491.6	24	2450	41	2543	15	96
D525052-67.d	Core	Dark, zoned	249	435	1.75	11.56	0.29	0.4753	0.0096	0.178	0.0016	0.39559	2568.4	23	2506	42	2633	15	95
D525052-68.d	Core	Luminescent, surrounded by thick dark rim	62	42	0.68	12.26	0.35	0.4895	0.011	0.1836	0.0032	0.29194	2621	27	2567	47	2677	29	96
D525052-70.d	Core	Dark, zoned	542	292	0.54	10.26	0.26	0.427	0.0091	0.1749	0.0018	0.5808	2458.3	24	2292	41	2603	17	88
D525052-71.d	Core	Weakly luminescent, zoned	203	267	1.32	20.19	0.5	0.5923	0.012	0.2489	0.0018	0.56634	3099.6	24	2998	49	3178	11	94
D525052sm-71.d	Core		128	168	1.31	23.39	0.3	0.6974	0.0087	0.2426	0.0021	0.68895	3241	12	3409	33	3134	14	109
D525052sm-72.d	Core	Dark, internal features unclear	1218	296	0.24	5.373	0.07	0.3298	0.0038	0.1172	0.0012	0.083496	1882	12	1837	19	1911	19	96
D525052sm-73.d	Core	Weakly luminescent, zoned	335	215	0.64	6.541	0.077	0.3598	0.0043	0.1315	0.0014	0.52297	2050	10	1981	21	2117	19	94
D525052sm-74.d	Core	Weakly luminescent, zoned	344	259	0.75	10.604	0.086	0.4726	0.0051	0.1623	0.0012	0.46439	2488.3	7.6	2495	22	2478	13	101
D525052sm-75.d	Core	Weakly luminescent, possible zoning (unclear)	250	379	1.52	7.683	0.093	0.3617	0.0043	0.1549	0.0019	0.30355	2194	11	1990	21	2398	21	83
D525052sm-76.d	Core	Dark, homogeneous	700	861	1.23	4.884	0.047	0.3072	0.0037	0.1158	0.0014	0.099743	1799	8	1726	18	1888	22	91
D525052sm-77.d	Core	Luminescent, anhedral and overgrown by dark rim	24	18	0.74	12.54	0.35	0.515	0.011	0.1774	0.0053	0.26563	2637	26	2675	48	2607	50	103
D525052sm-78.d	Core	Weakly luminescent-dark, weakly-zoned	241	237	0.98	9.36	0.12	0.4411	0.006	0.1543	0.0021	0.33293	2373	11	2355	27	2391	23	98
D525052sm-79.d	Core	Weakly luminescent-dark, diffuse zoning, surrounded by dark rim	256	193	0.75	11.034	0.097	0.4838	0.005	0.1647	0.0015	0.31882	2525	8.1	2543	22	2504	15	102
D525052sm-80.d	Core	Weakly luminescent, zoned	243	196	0.81	10.202	0.097	0.4631	0.0053	0.1595	0.0016	0.37032	2452.2	8.8	2453	24	2447	17	100
D525052sm-82.d	Rim	Thick, dark overgrowth on a small luminescent core	797	261	0.33	4.42	0.043	0.3005	0.0031	0.1061	0.0011	0.017035	1716.2	8.3	1693.7	15	1729	19	98
D525052sm-83.d	Core	Dark, weakly zoned, unclear whether this is an outer section of the core or a rim (possible mixed zones)	783	123	0.16	5.674	0.073	0.3497	0.004	0.1167	0.0015	0.37843	1927	11	1933	19	1903	22	102
D525052sm-84.d	Core	Dark, zoned, surrounded by dark rim	589	415	0.70	10.93	0.12	0.4608	0.0054	0.1729	0.002	0.079139	2517	10	2443	24	2584	19	95
D525052sm-85.d	Core		437	306	0.70	9.871	0.082	0.4486	0.0047	0.1591	0.0013	0.31605	2422.3	7.7	2389	21	2444	14	98
D525052sm-86.d	Core	Luminescent-weakly luminescent, diffuse zoning	143	81	0.57	11.53	0.17	0.4865	0.0059	0.1718	0.0025	0.2769	2568	14	2555	26	2570	24	99
D525052sm-89.d	Core	Luminescent, zoned, surrounded by thin dark rim	135	93	0.69	12.15	0.17	0.5271	0.0066	0.1676	0.0026	0.090968	2614	13	2728	28	2533	25	108
D525052sm-90.d	Core	Dark, weakly zoned, surrounded by thin dark rim	499	177	0.35	9.511	0.079	0.4417	0.0054	0.1566	0.0016	0.21971	2388.1	7.6	2358	24	2417	17	98
D525052sm-92.d	Core	Dark, zoned, surrounded by thick dark rim (93)	664	308	0.46	8.67	0.063	0.421	0.0041	0.1491	0.00096	0.5565	2303.3	6.7	2265	19	2334	11	97
D525052sm-93.d	Rim	Thick, dark overgrowth on dark, zoned core (92)	1052	252	0.24	4.036	0.036	0.2975	0.0035	0.09814	0.00082	0.36192	1640.9	7.3	1679	17	1587	15	106
D525052sm-94.d	Core	Dark, zoned	311	800	2.57	12.53	0.13	0.5255	0.0063	0.1723	0.0017	0.51684	2643.9	9.8	2722	26	2578	17	106
D525052sm-97.d	Core	Dark, internal features unclear	666	427	0.64	4.646	0.051	0.2968	0.0032	0.1136	0.0013	0.33643	1756.7	9.2	1675	16	1854	21	90
D525052sm-98.d	Core	Dark, zoned, surrounded by dark rim	459	307	0.67	21.21	0.26	0.6226	0.0079	0.2476	0.0024	0.46866	3147	12	3120	31	3168	15	98

Supplementary Table 1. (continued)

Analysis	Analysis location	CL response	U (ppm)	Th (ppm)	Th/U	$^{207}Pb/^{235}U$	2σ	$^{206}Pb/^{238}U$	2σ	$^{207}Pb/^{206}Pb$	2σ	Rho	Age (Ma) $^{207}Pb/^{235}U$	2σ	$^{206}Pb/^{238}U$	2σ	$^{207}Pb/^{206}Pb$	2σ	Conc.**
D525052sm-99.d	Core	Dark, zoned, surrounded by dark rim	250	217	0.87	11.11	0.14	0.4817	0.0058	0.1674	0.0016	0.56615	2532	12	2534	25	2529	16	100
D525052sm-100.d	Rim	Dark, thick, on a dark zoned core	949	213	0.22	3.904	0.036	0.2855	0.0028	0.09893	0.00094	0.11417	1613.7	7.5	1619.1	14	1600	18	101
D525052sm-101.d	Core	Dark, internal features unclear	810	297	0.37	8.405	0.076	0.4126	0.0045	0.148	0.0013	0.429	2275	8.2	2226	21	2323	15	96
D525052sm-102.d	Core	Dark, zoned, surrounded by dark rim	311	188	0.60	8.776	0.081	0.4314	0.0049	0.1477	0.0015	0.25956	2314.3	8.4	2311	22	2316	18	100
D525052sm-103.d	Rim	Thick, dark homogeneous rim on a small dark, zoned core	839	588	0.70	3.855	0.034	0.276	0.0028	0.10119	0.00085	0.37054	1603.5	7	1570.9	14	1643	16	96
D525052sm-104.d	Rim	Thick, dark homogeneous rim on dark core	933	282	0.30	4.082	0.038	0.3036	0.0036	0.09727	0.00072	0.62971	1649.9	7.5	1709	18	1570	14	109
D525052sm-105.d	Core	Luminescent, zoned, surrounded by thin dark rim	82	53	0.64	20.32	0.4	0.604	0.0098	0.2424	0.004	0.38858	3104	19	3045	39	3132	26	97
D525052sm-106.d	Core	Dark, zoned, surrounded by dark rim	459	397	0.87	9.36	0.1	0.4551	0.0052	0.1487	0.0015	0.41218	2372.9	9.9	2418	23	2328	17	104
D525052sm-107.d	Rim	Dark, thick, on a dark zoned core	577	268	0.46	4.492	0.066	0.3074	0.0038	0.1057	0.0015	0.38629	1728	12	1728	19	1722	27	100
D525052sm-108.d	Core	Dark, zoned, surrounded by dark rim	380	224	0.59	10.37	0.1	0.4727	0.0054	0.1599	0.0017	0.41028	2469.5	9.8	2495	24	2451	18	102
D525052sm-109.d	Core	Luminescent, zoned, surrounded by thick dark rim	192	180	0.94	23.92	0.26	0.6619	0.0078	0.2614	0.0021	0.67315	3264	11	3274	30	3253	13	101
D525052sm-111.d	Rim	Very thick, dark, homogeneous rim on a small dark core	1256	397	0.32	3.75	0.027	0.2819	0.0027	0.09633	0.00069	0.35464	1581.7	5.8	1601	14	1552	14	103
D525052sm-112.d	Core	Luminescent-weakly luminescent, simple zoning	109	295	2.71	12.07	0.18	0.4526	0.0058	0.1941	0.0032	0.14055	2608	14	2406	26	2771	27	87
D525052sm-113.d	Rim	Very thick, dark, homogeneous rim on a small dark core	683	402	0.59	4.353	0.051	0.2956	0.0031	0.1065	0.0012	0.41505	1702.4	9.6	1669	16	1736	21	96
D525052sm-114.d	Rim	Very thick, dark, homogeneous rim on a small dark core	895	258	0.29	3.746	0.032	0.2813	0.0028	0.09631	0.00072	0.42868	1580.7	6.8	1597.9	14	1551	14	103
D525052sm-116.d	Core	Dark-weakly luminescent, zoned	272	159	0.58	11.57	0.1	0.4965	0.005	0.1687	0.0013	0.42384	2569.2	8.4	2598	22	2544	13	102
D525052sm-117.d	Core	Dark-weakly luminescent, zoned	346	198	0.57	17.79	0.21	0.5586	0.0066	0.2315	0.0021	0.64636	2977	11	2860	27	3060	15	93
Sample GAZ-7																			
GAZ7 - 1.d	Core	Dark, weakly-zoned	71	114	1.60	4.57	0.11	0.3142	0.0052	0.1058	0.0029	0.18232	1741	21	1761	25	1715	51	103
GAZ7 - 2.d	Core	Dark, unzoned, homogeneous, outer core region to (1)	145	212	1.47	4.243	0.067	0.2998	0.004	0.1028	0.002	0.12825	1680	13	1690	20	1665	36	102
GAZ7 - 3.d	Core	Weakly luminescent, unzoned-weakly sector-zoned	63	84	1.35	4.71	0.1	0.3139	0.0049	0.109	0.0027	0.23509	1763	19	1759	24	1771	47	99
GAZ7 - 4.d	Core	Dark, weakly-zoned	562	819	1.46	4.783	0.05	0.3256	0.0042	0.10685	0.0015	0.54984	1782.1	9.1	1817	20	1743	25	104
GAZ7 - 5.d	Core (outer)	Dark, unzoned-weakly-zoned, separated from (4) by narrow weakly luminescent domain	193	309	1.60	4.762	0.06	0.3196	0.0044	0.1081	0.0018	0.24615	1778.1	10	1788	21	1761	31	102
GAZ7 - 6.d	Core	Dark, weakly-zoned	373	357	0.96	4.788	0.049	0.3227	0.0042	0.10785	0.0015	0.29044	1782	8.7	1803	20	1760	26	102
GAZ7 - 7.d	Core	Dark, unzoned-weakly-zoned	511	676	1.32	4.728	0.043	0.3214	0.004	0.10662	0.0014	0.41298	1771.5	7.6	1796.3	20	1740	24	103
GAZ7 - 8.d	Core	Dark, unzoned-weakly sector-zoned	120	145	1.21	4.705	0.07	0.3183	0.0044	0.1076	0.0019	0.2462	1766	12	1781	22	1751	32	102
GAZ7 - 9.d	Core (outer)	Luminescent, unzoned-weakly-zoned	221	309	1.40	4.955	0.057	0.3182	0.0042	0.1131	0.0017	0.25219	1810.8	9.7	1781	21	1845	28	97
GAZ7 - 10.d	Core	Dark grey, unzoned	234	273	1.16	4.689	0.057	0.3187	0.0041	0.1065	0.0017	0.22259	1764	10	1783	20	1738	28	103
GAZ7 - 11.d	Core (outer)	Dark, unzoned, outer domain to (12)	159	267	1.68	4.799	0.07	0.3266	0.0045	0.1069	0.0018	0.38178	1783	12	1821	22	1741	32	105
GAZ7 - 12.d	Core	Weakly luminescent, weak sector zoning	65	93	1.42	5.348	0.1	0.3407	0.0052	0.1142	0.0027	0.01954	1873	16	1889	25	1852	43	102
GAZ7 - 13.d	Core	Luminescent, unzoned-weakly zoned	94	158	1.68	4.646	0.079	0.3167	0.0046	0.1066	0.0022	0.21194	1755	14	1773	23	1731	38	102
GAZ7 - 17.d	Core	Weakly luminescent, weakly-zoned/sector-zoned	123	187	1.52	5.34	0.11	0.3032	0.0052	0.1271	0.003	0.12318	1873	17	1707	25	2056	43	83
GAZ7 - 18.d	Core	Dark, internal features unclear	909	372	0.41	4.659	0.04	0.317	0.0042	0.10639	0.0014	0.4781	1759.3	7.2	1775	21	1738	24	102

Supplementary Table 1. (continued)

Analysis	Analysis location	CL response	U (ppm)	Th (ppm)	Th/U	$^{207}Pb/^{235}U$	2σ	$^{206}Pb/^{238}U$	2σ	$^{207}Pb/^{206}Pb$	2σ	Rho	Age (Ma) $^{207}Pb/^{235}U$	2σ	$^{206}Pb/^{238}U$	2σ	$^{207}Pb/^{206}Pb$	2σ	Conc.**
GAZ7 - 20.d	Core	Dark, fragmented, weakly zoned	211	411	1.95	4.722	0.055	0.3202	0.0044	0.107	0.0016	0.37666	1771.2	9.5	1791	22	1744	28	103
GAZ7 - 21.d	Core	Dark, weakly-zoned	418	416	0.99	4.895	0.053	0.3256	0.0044	0.1091	0.0016	0.37981	1801.6	8.8	1817	21	1780	27	102
GAZ7 - 22.d	Core	Weakly luminescent, weakly zoned	129	148	1.14	4.692	0.078	0.3212	0.0046	0.106	0.002	0.31769	1765	14	1795	22	1727	36	104
GAZ7 - 23.d	Core	Luminescent-weakly luminescent, zoned	85	122	1.43	4.762	0.083	0.3194	0.005	0.1084	0.0024	0.14032	1775	15	1786	24	1759	40	102
GAZ7 - 27.d	Rim	Dark, unzoned	222	47	0.21	4.823	0.078	0.3222	0.005	0.1087	0.002	0.41438	1787	14	1800	24	1776	32	101
GAZ7 - 28.d	Core	Luminescent, zoned	59	70	1.17	4.56	0.11	0.3069	0.0054	0.1076	0.0028	0.20546	1736	19	1724	27	1746	48	99
GAZ7 - 29.d	Core	Dark, weakly-zoned	151	327	2.17	4.729	0.073	0.3205	0.0043	0.1069	0.002	0.20554	1770	13	1792	21	1742	34	103
GAZ7 - 30.d	Rim	Dark, unzoned, outer domain to (29)	212	317	1.50	4.774	0.065	0.3213	0.0045	0.1077	0.0018	0.36966	1779	11	1796	22	1756	31	102
Sample GAZ-9																			
GAZ9 - 1.d	Rim	Dark, unzoned, truncates dark zoned core	324	240	0.74	4.878	0.078	0.3304	0.0034	0.1059	0.0013	0.55975	1796	13	1840	16	1728	23	106
GAZ9 - 2.d	Core	Dark, zoned, resorbed by narrow luminescent domain and thick dark rim (1)	155	127	0.82	10.72	0.11	0.477	0.0037	0.1619	0.0018	0.054025	2498.1	9.5	2514	16	2473	20	102
GAZ9 - 3.d	Core (outer)	Dark, weakly-zoned	326	250	0.77	4.752	0.062	0.324	0.003	0.1055	0.0011	0.5047	1775	11	1809	15	1718	19	105
GAZ9 - 4.d	Core	Dark, unzoned-weakly-zoned, surrounded by weakly luminescent rim (5)	1278	13	0.01	4.811	0.085	0.3269	0.0037	0.1085	0.0014	0.2023	1786	15	1823	18	1771	24	103
GAZ9 - 5.d	Core (outer)	Weakly luminescent, unzoned-weakly-zoned, minor fracturing, surrounds dark core (4)	103	98	0.95	4.23	0.1	0.2957	0.0031	0.1033	0.0021	0.23722	1678	20	1669	15	1679	40	99
GAZ9 - 7.d	Core	Dark, internal features unclear	400	304	0.76	4.796	0.053	0.3231	0.0027	0.10684	0.00099	0.36277	1782.9	9.3	1804	13	1743	17	103
GAZ9 - 8.d	Core (outer)	Dark, zoned	218	176	0.81	4.903	0.078	0.3251	0.0028	0.1087	0.0014	0.2718	1800	14	1814	14	1772	24	102
GAZ9 - 10.d	Rim	Dark, unzoned, truncates dark zoned core	202	118	0.58	4.753	0.08	0.3205	0.0028	0.1064	0.0014	0.23811	1776	14	1792	14	1738	26	103
GAZ9 - 12.d	Core	Dark grey, weakly-zoned	143	182	1.27	4.9	0.083	0.326	0.0033	0.1085	0.0016	0.36402	1799	14	1818	16	1766	27	103
GAZ9 - 13.d	Core	Dark, weakly-zoned	311	218	0.70	4.655	0.065	0.3154	0.0026	0.1063	0.0012	0.42385	1757	12	1767	13	1734	20	102
GAZ9 - 14.d	Core	Dark, weakly-zoned	137	153	1.11	4.579	0.084	0.3148	0.003	0.1053	0.0017	0.20894	1744	15	1764	15	1714	29	103
GAZ9 - 15.d	Core	Dark, weakly-zoned	216	345	1.59	4.914	0.065	0.3202	0.003	0.1094	0.0015	0.28845	1803	11	1790	15	1787	24	100
GAZ9 - 16.d	Core	Dark, unzoned-weakly-zoned	403	293	0.73	4.791	0.049	0.3223	0.0025	0.1064	0.001	0.42756	1782.3	8.6	1801	12	1735	17	104
GAZ9 - 17.d	Core	Dark, unzoned-weakly-zoned	288	664	2.31	4.963	0.059	0.3309	0.003	0.1079	0.0012	0.2116	1812	10	1842	15	1760	20	105
GAZ9 - 18.d	Core	Dark, zoned	398	280	0.70	9.156	0.092	0.4358	0.004	0.152	0.0013	0.28729	2352.6	9.2	2331	18	2366	15	99
GAZ9 - 19.d	Core?	Dark, unzoned-weakly-zoned	1086	124	0.11	4.107	0.045	0.2977	0.0028	0.10034	0.00078	0.2664	1654.9	9	1679	14	1628	14	103
GAZ9 - 20.d	Core	Weakly luminescent, zoned	69	73	1.06	4.85	0.12	0.3186	0.0041	0.1093	0.0025	0.27664	1787	21	1782	20	1769	43	101
GAZ9 - 21.d	Core	Dark, weakly-zoned	521	189	0.36	5.067	0.053	0.332	0.0037	0.1098	0.0011	0.53855	1829.6	8.9	1848	18	1792	19	103
GAZ9 - 22.d	Core	Dark, weakly-zoned	226	144	0.64	4.725	0.073	0.3201	0.0031	0.1067	0.0015	0.22086	1769	13	1790	15	1743	26	103
GAZ9 - 23.d	Core	Dark, zoned	330	165	0.50	4.997	0.073	0.3296	0.0031	0.1091	0.0014	0.2192	1817	12	1836	15	1778	24	103
GAZ9 - 24.d	Core	Dark, weakly-zoned	482	351	0.73	4.822	0.056	0.3212	0.0029	0.1084	0.001	0.26403	1788.8	9.5	1795	14	1769	18	101
GAZ9 - 25.d	Core	Dark, unzoned-weakly-zoned	483	309	0.64	9.58	0.12	0.4503	0.0044	0.1516	0.0013	0.66356	2394	12	2396	20	2361	15	101
GAZ9 - 26.d	Core	Dark, unzoned-weakly-zoned	560	304	0.54	4.845	0.05	0.3243	0.0027	0.10654	0.00095	0.4411	1791.8	8.7	1810	13	1740	17	104
GAZ9 - 27.d	Core (outer)	Grey, unzoned-weakly-zoned	181	146	0.81	5.027	0.085	0.328	0.003	0.1097	0.0019	0.12564	1821	14	1828	15	1789	32	102
GAZ9 - 28.d	Core	Dark, unzoned-weakly-zoned	424	95	0.22	5.467	0.077	0.341	0.0037	0.1137	0.0014	0.4892	1894	12	1891	18	1859	21	102
GAZ9 - 29.d	Core (outer)	Dark, unzoned-weakly-zoned	352	213	0.61	4.81	0.05	0.3213	0.0027	0.1076	0.0012	0.14906	1786.7	9.1	1796	13	1754	21	102
GAZ9 - 30.d	Core (outer)	Dark, zoned	162	175	1.08	4.978	0.076	0.3306	0.0037	0.1081	0.0017	0.31068	1813	13	1841	18	1759	28	105
GAZ9 - 31.d	Core (outer)	Grey, weakly-zoned (outer domain to 32)	207	127	0.61	5.075	0.078	0.3346	0.0035	0.1089	0.0016	0.4196	1832	13	1860	17	1774	26	105
GAZ9 - 33.d	Core	Dark, unzoned-weakly-zoned	458	351	0.77	4.831	0.058	0.3222	0.0029	0.10781	0.00097	0.24855	1789	10	1800	14	1759	17	102

Supplementary Table 1. (continued)

Analysis	Analysis location	CL response	U (ppm)	Th (ppm)	Th/U	$^{207}Pb/^{235}U$	2σ	$^{206}Pb/^{238}U$	2σ	$^{207}Pb/^{206}Pb$	2σ	Rho	Age (Ma) $^{207}Pb/^{235}U$	2σ	$^{206}Pb/^{238}U$	2σ	$^{207}Pb/^{206}Pb$	2σ	Conc.**
GAZ9 - 34.d	Core	Dark, weakly-zoned	436	218	0.50	4.99	0.092	0.3366	0.0038	0.1093	0.0018	0.34352	1816	16	1870	18	1783	31	105
GAZ9 - 36.d	Core (outer)	Grey, weakly-zoned	312	228	0.73	4.911	0.066	0.3272	0.0031	0.1079	0.0014	0.4102	1802	11	1825	15	1761	23	104
GAZ9 - 37.d	Core	Dark grey, weakly-zoned (surrounded by 36)	856	56	0.07	4.813	0.067	0.3214	0.0028	0.1081	0.0011	0.3773	1785	12	1796	14	1768	17	102
GAZ9 - 38.d	Core	Dark grey, weakly-zoned	361	250	0.69	4.835	0.071	0.3232	0.0032	0.1079	0.0013	0.47628	1791	12	1805	16	1760	21	103
GAZ9 - 39.d	Core	Dark grey, weakly-zoned	158	77	0.49	21.3	0.35	0.6195	0.0068	0.2436	0.003	0.63457	3150	16	3107	27	3140	19	99
GAZ9 - 41.d	Core (outer)	Dark grey, weakly-zoned	226	121	0.54	4.796	0.065	0.3223	0.0031	0.1073	0.0015	0.22128	1782	11	1803	15	1746	26	103
GAZ9 - 44.d	Core	Dark grey, weakly-zoned	125	114	0.91	4.774	0.088	0.3208	0.004	0.1076	0.0021	0.069184	1777	16	1793	19	1745	36	103
GAZ9 - 47.d	Core (outer)	Dark grey, weakly-zoned	263	152	0.58	4.828	0.066	0.3195	0.003	0.1086	0.0014	0.34001	1790	11	1787	15	1769	23	101
GAZ9 - 48.d	Core (outer)	Grey, weakly-zoned	232	155	0.67	4.834	0.072	0.3237	0.0039	0.1068	0.0016	0.36355	1789	13	1807	19	1742	27	104
GAZ9 - 50.d	Core	Grey, weakly-zoned	92	80	0.87	4.42	0.11	0.3035	0.0045	0.1073	0.0024	0.23324	1714	20	1708	22	1739	41	98
GAZ9 - 51.d	Core (outer)	Dark grey, weakly-zoned	167	98	0.59	4.861	0.088	0.3221	0.0039	0.1089	0.0019	0.32981	1792	15	1799	19	1770	32	102
GAZ9 - 52.d	Core	Dark grey, weakly-zoned	131	134	1.03	4.851	0.088	0.3292	0.0038	0.1066	0.0019	0.31523	1790	15	1834	18	1735	33	106
GAZ9 - 53.d	Core	Dark, unzoned-weakly-zoned	109	98	0.90	4.991	0.085	0.3295	0.0042	0.1092	0.0021	0.13634	1815	14	1835	20	1773	36	103
GAZ9 - 54.d	Core	Dark, weakly-zoned	241	130	0.54	4.769	0.071	0.322	0.0033	0.107	0.0014	0.32642	1779	12	1799	16	1742	23	103
GAZ9 - 57.d	Core (outer)	Weakly luminescent, zoned	68	84	1.23	5.11	0.14	0.3432	0.0049	0.1074	0.0025	0.39385	1832	23	1901	24	1741	44	109
GAZ9 - 58.d	Core	Dark, unzoned-weakly-zoned	491	346	0.70	4.693	0.057	0.3196	0.0029	0.1058	0.0011	0.46585	1764	10	1787	14	1724	20	104
GAZ9 - 59.d	Core	Dark, unzoned-weakly-zoned	462	242	0.52	4.698	0.053	0.3204	0.003	0.1058	0.001	0.27516	1765.5	9.4	1791	15	1724	18	104
GAZ9 - 61.d	Core	Dark grey, zoned	204	171	0.84	9.35	0.12	0.4408	0.004	0.1533	0.0017	0.3085	2373	12	2353	18	2378	18	99
GAZ9 - 63.d	Core (outer)	Grey, weakly-zoned	149	106	0.71	4.76	0.064	0.3192	0.0028	0.1079	0.0015	0.024003	1776	11	1786	14	1756	26	102
GAZ9 - 65.d	Core	Dark, unzoned-weakly-zoned	450	219	0.49	4.675	0.058	0.3161	0.0024	0.1066	0.0012	0.19812	1761	10	1770	12	1737	20	102
GAZ9 - 66.d	Core	Grey, weakly-zoned	167	211	1.27	4.891	0.097	0.3308	0.0041	0.108	0.0017	0.26302	1797	17	1842	20	1759	29	105
GAZ9 - 67.d	Core	Weakly luminescent-grey, zoned, resorbed by thick dark overgrowth (68)	101	80	0.79	11.6	0.17	0.514	0.0058	0.1618	0.0022	0.35805	2570	13	2673	25	2469	23	108
GAZ9 - 68.d	Core (outer)	Dark, thick, weakly-zoned	515	366	0.71	4.735	0.062	0.3172	0.0028	0.109	0.0012	0.078272	1772	11	1776	14	1779	20	100
GAZ9 - 69.d	Core (outer)	Dark, unzoned-weakly-zoned	451	319	0.71	4.892	0.054	0.3243	0.0029	0.1094	0.0011	0.14547	1799.6	9.4	1811	14	1784	19	102
GAZ9 - 71.d	Core	Dark, weakly-zoned	477	109	0.23	4.944	0.057	0.3257	0.0027	0.1099	0.0012	0.03379	1811.7	8.8	1817	13	1794	19	101
GAZ9 - 72.d	Core	Dark, weakly-zoned	230	141	0.61	4.861	0.087	0.3238	0.0032	0.1085	0.0016	0.20045	1792	15	1808	15	1770	28	102
GAZ9 - 73.d	Core (outer)	Dark, weakly-zoned	109	125	1.15	4.889	0.098	0.3221	0.004	0.1105	0.002	0.18335	1799	16	1799	19	1796	33	100
GAZ9 - 74.d	Core	Dark, unzoned-weakly-zoned	204	146	0.72	4.835	0.084	0.3245	0.0029	0.1079	0.0017	0.078681	1790	14	1811	14	1754	30	103
GAZ9 - 75.d	Core	Dark, unzoned-weakly-zoned	475	323	0.68	4.308	0.059	0.3037	0.0025	0.1026	0.001	0.40429	1693	12	1710	13	1667	19	103
GAZ9 - 76.d	Core	Dark, weakly-zoned	228	135	0.59	4.857	0.066	0.3228	0.0032	0.1088	0.0014	0.29096	1793	12	1803	16	1773	24	102
GAZ9 - 78.d	Core	Dark, weakly-zoned	478	44	0.09	4.426	0.065	0.3099	0.0038	0.1041	0.0014	0.4773	1716	12	1740	19	1695	24	103
GAZ9 - 79.d	Core (outer)	Dark, weakly-zoned	439	351	0.80	4.884	0.064	0.3262	0.0029	0.1079	0.001	0.39956	1798	11	1819	14	1761	18	103
GAZ9 - 80.d	Core	Dark, unzoned-weakly-zoned	249	145	0.58	4.694	0.073	0.3183	0.0034	0.1067	0.0015	0.30544	1764	13	1781	17	1739	25	102
GAZ9 - 81.d	Core	Dark grey, weakly-zoned	252	282	1.12	4.897	0.071	0.3233	0.0028	0.1093	0.0015	0.31999	1800	12	1805	14	1784	25	101
GAZ9 - 82.d	Core	Dark, weakly-zoned	281	161	0.57	4.89	0.065	0.3219	0.0027	0.11	0.0013	0.37048	1800	12	1798	13	1797	20	100
GAZ9 - 83.d	Core	Dark, unzoned-weakly-zoned	99	90	0.91	4.766	0.095	0.3219	0.004	0.1077	0.0021	0.23492	1779	17	1798	19	1748	35	103
GAZ9 - 84.d	Core	Weakly luminescent, zoned, resorbed by dark overgrowth	88	79	0.89	4.69	0.11	0.3156	0.0035	0.1077	0.0022	0.1523	1760	20	1768	17	1755	39	101
GAZ9 - 85.d	Core	Dark grey, weakly-zoned	162	230	1.41	5.04	0.11	0.3222	0.0042	0.1104	0.0025	0.2042	1824	19	1800	21	1798	42	100
GAZ9 - 86.d	Core	Dark, weakly-zoned	702	746	1.06	5.038	0.055	0.335	0.0029	0.10884	0.00091	0.3122	1824.4	9.4	1862	14	1777	15	105

Supplementary Table 1. (continued)

Analysis	Analysis location	CL response	U (ppm)	Th (ppm)	Th/U	$^{207}Pb/^{235}U$	2σ	$^{206}Pb/^{238}U$	2σ	$^{207}Pb/^{206}Pb$	2σ	Rho	Age (Ma) $^{207}Pb/^{235}U$	2σ	$^{206}Pb/^{238}U$	2σ	$^{207}Pb/^{206}Pb$	2σ	Conc.**
GAZ9 - 87.d	Core	Dark, weakly-zoned	1023	31	0.03	5.351	0.055	0.3474	0.0026	0.10962	0.00097	0.49372	1876.2	8.8	1922	13	1790	16	107
GAZ9 - 88.d	Core	Dark, weakly-zoned	505	448	0.89	4.496	0.052	0.3091	0.0024	0.1047	0.0011	0.21205	1729	9.6	1736	12	1705	20	102
GAZ9 - 89.d	Core	Dark, weakly-zoned	368	220	0.60	4.863	0.06	0.3237	0.0028	0.1084	0.0011	0.36434	1796	10	1808	14	1769	19	102
GAZ9 - 90.d	Core	Dark, weakly-zoned	550	201	0.36	4.696	0.056	0.3179	0.0028	0.1069	0.0011	0.29799	1766.9	9.5	1779	14	1742	18	102
GAZ9B - 1.d	Core	Dark, zoned	350	216	0.62	4.86300	0.04000	0.32220	0.00310	0.10968	0.00092	0.35878	1795	7	1800	15	1792	15	100
GAZ9B - 4.d	Core	Dark, zoned	254	191	0.75	5.00000	0.04700	0.33140	0.00350	0.10971	0.00092	0.58583	1819	8	1845	17	1792	15	103
GAZ9B - 5.d	Core	Dark, zoned	589	241	0.41	4.66400	0.03600	0.31640	0.00310	0.10726	0.00060	0.67472	1760	6	1772	15	1752	10	101
GAZ9B - 6.d	Core	Dark, weakly-zoned	48	44	0.91	4.79900	0.09300	0.32010	0.00390	0.10910	0.00220	0.24341	1781	17	1790	19	1772	36	101
GAZ9B - 7.d	Core (outer)	Dark, weakly-zoned	250	144	0.57	4.97700	0.04000	0.33120	0.00350	0.10917	0.00066	0.66757	1815	7	1844	17	1785	11	103
GAZ9B - 8.d	Core	Dark, zoned	77	72	0.94	4.47600	0.06800	0.30590	0.00360	0.10660	0.00160	0.29420	1727	13	1720	18	1735	28	99
GAZ9B - 9.d	Core	Dark, weakly-zoned	516	452	0.88	4.79700	0.03200	0.32590	0.00310	0.10699	0.00061	0.59166	1784	6	1818	15	1747	10	104
GAZ9B - 10.d	Core	Dark, weakly-zoned	731	230	0.31	5.30900	0.04600	0.34590	0.00360	0.11163	0.00060	0.77863	1870	7	1915	17	1824	10	105
GAZ9B - 11.d	Core	Dark, zoned	381	146	0.38	5.03800	0.03500	0.33080	0.00320	0.11062	0.00075	0.38536	1825	6	1842	15	1807	12	102
GAZ9B - 12.d	Core	Dark, zoned	312	138	0.44	4.19200	0.04900	0.30000	0.00280	0.10148	0.00097	0.40959	1671	9	1691	14	1648	17	103
GAZ9B - 13.d	Core	Dark, weakly-zoned	309	275	0.89	5.05700	0.06500	0.33640	0.00480	0.10888	0.00093	0.77468	1830	10	1869	23	1778	16	105
GAZ9B - 14.d	Core	Dark, weakly-zoned	465	154	0.33	4.59600	0.03400	0.31320	0.00290	0.10633	0.00078	0.46283	1748	6	1756	14	1735	13	101
GAZ9B - 15.d	Core (outer)?	Weakly-luminescent, weakly-zoned, surrounds dark core	86	77	0.90	4.13700	0.07200	0.29130	0.00340	0.10340	0.00190	0.14520	1659	14	1648	17	1677	34	98
GAZ9B - 16.d	Core	Dark, zoned	394	284	0.72	4.69500	0.04000	0.31790	0.00350	0.10658	0.00064	0.74181	1766	7	1779	17	1740	11	102
GAZ9B - 17.d	Core	Dark, zoned	670	416	0.62	4.93600	0.03900	0.32530	0.00330	0.10962	0.00053	0.76722	1808	7	1815	16	1792	9	101
GAZ9B - 18.d	Core	Dark, zoned	433	320	0.74	4.71200	0.03100	0.31720	0.00300	0.10737	0.00071	0.40552	1769	6	1776	14	1753	12	101
GAZ9B - 19.d	Core	Weakly luminescent, weakly-zoned, possible minor sector zoning	52	46	0.89	4.79500	0.07600	0.31480	0.00380	0.11040	0.00190	0.13845	1781	13	1764	18	1795	31	98
Sample PMDDH04-12																			
PDH04-12 - 1.d	Core	Dark, unzoned	599	102	0.17	8.073	0.12	0.3915	0.0052	0.1496	0.0028	0.43773	2238	13	2129	24	2341	31	91
PDH04-12 - 2.d	Core	Dark, unzoned	1053	600	0.57	6.939	0.089	0.3771	0.0052	0.1302	0.0024	0.59736	2103	11	2062	24	2098	33	98
PDH04-12 - 3.d	Core	Grey, unzoned-weakly-zoned	154	100	0.65	9.194	0.12	0.432	0.0061	0.1535	0.0031	0.34789	2360	13	2314	27	2380	35	97
PDH04-12 - 4.d	Rim	Dark, unzoned	476	311	0.65	3.77	0.057	0.2845	0.0038	0.0954	0.0019	0.3108	1585	12	1614	19	1534	38	105
PDH04-12 - 5.d	Rim	Grey, unzoned	143	170	1.19	3.619	0.079	0.279	0.0041	0.094	0.0023	0.18896	1554	16	1586	21	1501	45	106
PDH04-12 - 6.d	Core	Dark (generally), complexly zoned and irregularly shaped/resorbed	545	57	0.10	5.31	0.13	0.3395	0.0051	0.1153	0.0023	0.32936	1872	19	1884	25	1885	34	100
PDH04-12 - 7.d	Core (outer)	Dark, weakly-zoned	3060	533	0.17	1.297	0.025	0.1042	0.0021	0.08826	0.0017	0.83648	844	11	639	12	1385	36	46
PDH04-12 - 8.d	Core	Dark, unzoned	476	280	0.59	4.841	0.066	0.3228	0.0041	0.1072	0.0021	0.26995	1790.9	11	1803	20	1747	36	103
PDH04-12 - 9.d	Rim	Dark, unzoned	1500	364	0.24	3.602	0.06	0.2723	0.0048	0.096	0.0019	0.49061	1549	13	1552	24	1544	36	101
PDH04-12 - 10.d	Core	Grey, unzoned-weakly-zoned	128	138	1.07	3.906	0.086	0.2612	0.0043	0.1073	0.0027	0.35261	1611	18	1495	22	1742	47	86
PDH04-12 - 11.d	Rim	Dark, unzoned	1405	409	0.29	3.568	0.048	0.2747	0.0039	0.09425	0.0017	0.51987	1541.8	11	1564	20	1511	35	104
PDH04-12 - 12.d	Core	Dark, weakly-zoned	419	192	0.46	9.28	0.14	0.4457	0.0067	0.1519	0.0031	0.27119	2365	14	2376	30	2364	35	101
PDH04-12 - 14.d	Core	Dark, weakly-zoned	692	415	0.60	9.632	0.13	0.4501	0.0059	0.1535	0.0028	0.56371	2400.3	12	2395	26	2382	31	101
PDH04-12 - 15.d	Rim	Luminescent, unzoned, minor fracturing	85	98	1.16	3.072	0.085	0.2282	0.0043	0.0979	0.0032	0.13254	1422	22	1324	23	1563	63	85
PDH04-12 - 16.d	Core	Grey, unzoned	218	48	0.22	5.71	0.14	0.3522	0.0058	0.1146	0.0028	0.54154	1929	21	1944	28	1866	44	104
PDH04-12 - 17.d	Core	Dark, weakly-zoned	254	237	0.94	10.37	0.18	0.4686	0.0073	0.1627	0.0033	0.46195	2467	16	2477	32	2481	34	100

Supplementary Table 1. (continued)

Analysis	Analysis location	CL response	U (ppm)	Th (ppm)	Th/U	$^{207}Pb/^{235}U$	2σ	$^{206}Pb/^{238}U$	2σ	$^{207}Pb/^{206}Pb$	2σ	Rho	Age (Ma) $^{207}Pb/^{235}U$	2σ	$^{206}Pb/^{238}U$	2σ	$^{207}Pb/^{206}Pb$	2σ	Conc.**
PDH04-12 - 18.d	Core	Dark, unzoned-weakly-zoned	524	471	0.90	4.887	0.079	0.3302	0.0047	0.1088	0.0023	0.074673	1799	14	1839	23	1780	37	103
PDH04-12 - 19.d	Core	Weakly luminescent, weakly-zoned	85	56	0.66	5.5	0.12	0.3414	0.0057	0.1163	0.0028	0.4137	1896	18	1892	27	1889	42	100
PDH04-12 - 21.d	Core	Dark, internal features unclear	688	240	0.35	10.53	0.19	0.4817	0.0074	0.1545	0.0029	0.76783	2481	17	2534	32	2394	32	106
PDH04-12 - 22.d	Core	Dark, weakly-zoned	390	607	1.56	4.956	0.083	0.3235	0.0045	0.1095	0.0022	0.50722	1810	14	1806	22	1786	37	101
PDH04-12 - 23.d	Core	Dark grey, weakly-zoned	112	77	0.68	11	0.2	0.488	0.0072	0.1626	0.0034	0.44822	2523	16	2561	31	2477	35	103
PDH04-12 - 24.d	Core	Dark, weakly-zoned, irregular shape, resorbed by weakly luminescent overgrowth (25)	714	284	0.40	7.912	0.11	0.4019	0.0058	0.1403	0.0026	0.62046	2219.8	12	2177	27	2228	32	98
PDH04-12 - 25.d	Rim	Weakly luminescent, unzoned-weakly-zoned, resorbs (24)	118	68	0.58	4.143	0.087	0.301	0.0045	0.0986	0.0026	0.047813	1659	18	1696	22	1589	49	107
PDH04-12 - 26.d	Core	Dark, weakly-zoned	573	61	0.11	5.687	0.074	0.3512	0.0048	0.11538	0.0021	0.59487	1928.3	11	1940	23	1885	32	103
PDH04-12 - 28.d	Rim	Dark, unzoned	859	285	0.33	4.028	0.08	0.2937	0.0048	0.0987	0.002	0.70592	1638	16	1660	24	1600	39	104
PDH04-12 - 29.d	Core	Dark, weakly-zoned	912	399	0.44	3.701	0.056	0.2661	0.0043	0.09887	0.0019	0.66821	1570	12	1520	22	1599	36	95
PDH04-12 - 31.d	Core	Dark, weakly-zoned	755	108	0.14	4.15	0.057	0.2975	0.0039	0.09961	0.0018	0.51569	1663.1	11	1679	19	1614	34	104
PDH04-12 - 32.d	Rim	Luminescent, unzoned-weakly-zoned, minor fracturing, outer domain to (31)	142	66	0.46	3.878	0.077	0.2903	0.0046	0.096	0.0024	0.15218	1608	16	1643	23	1538	47	107
PDH04-12 - 33.d	Core	Dark, weakly-zoned	329	176	0.53	9.75	0.13	0.4504	0.0062	0.1547	0.003	0.47186	2410	13	2397	28	2395	33	100
PDH04-12 - 34.d	Core (outer)	Dark, internal features unclear	1038	357	0.34	4.94	0.064	0.3258	0.0041	0.10833	0.002	0.59535	1808.1	11	1818	20	1769	33	103
PDH04-12 - 35.d	Core	Dark, unzoned	1128	322	0.29	4.847	0.062	0.3255	0.0043	0.10657	0.002	0.41498	1793.2	10	1818	20	1738	34	105
PDH04-12 - 36.d	Core	Dark, weakly-zoned	385	238	0.62	10.08	0.13	0.4597	0.0062	0.1576	0.003	0.31196	2440.9	13	2437	27	2429	31	100
PDH04-12 - 37.d	Rim	Luminescent-weakly luminescent, unzoned-weakly-zoned, minor fracturing	76	97	1.28	3.51	0.11	0.2623	0.005	0.0968	0.0033	0.19596	1521	25	1501	25	1538	65	98
PDH04-12 - 38.d	Core	Dark, unzoned-weakly-zoned, surrounded by (37)	286	56	0.19	5.071	0.098	0.3365	0.0057	0.1064	0.0024	0.54075	1829	17	1869	28	1732	41	108
PDH04-12 - 39.d	Core (outer)	Dark, unzoned	1548	532	0.34	2.439	0.041	0.1889	0.0037	0.09164	0.0018	0.73499	1253	12	1115	20	1456	37	77
PDH04-12 - 40.d	Core	Dark, unzoned-weakly zoned	989	41	0.04	3.767	0.071	0.2809	0.0052	0.0972	0.002	0.32767	1583	15	1595	26	1564	39	102
PDH04-12 - 41.d	Core	Dark, unzoned, appears metamict	271	161	0.59	4.594	0.097	0.3152	0.0054	0.105	0.0026	0.36324	1744	18	1765	27	1706	47	103
Sample PMDDH04-14																			
H04-14 - 1.d	Core	Dark, zoned (complex)	256	208	0.81	8.25	0.17	0.4161	0.0042	0.1439	0.0025	0.42589	2257	19	2245	20	2271	30	99
H04-14 - 2.d	Core	Dark, zoned	502	749	1.49	7.42	0.15	0.3848	0.0042	0.1374	0.0022	0.56871	2162	18	2098	20	2194	30	96
H04-14 - 3.d	Core	Dark, weakly-zoned	380	96	0.25	8.8	0.19	0.4278	0.0056	0.1456	0.0023	0.76314	2315	20	2295	25	2293	28	100
H04-14 - 4.d	Core	Dark, zoned	339	289	0.85	6.89	0.15	0.3859	0.0045	0.1315	0.0024	0.068641	2096	20	2103	21	2115	32	99
H04-14 - 6.d	Core	Dark, zoned	410	315	0.77	7.126	0.14	0.3796	0.0042	0.1337	0.0023	0.42917	2126	17	2074	20	2143	29	97
H04-14 - 7.d	Core	Dark, zoned	475	591	1.24	9.487	0.16	0.4466	0.004	0.1527	0.0023	0.52043	2385.3	16	2379	18	2374	26	100
H04-14 - 8.d	Core (outer)	Grey, unzoned	363	365	1.01	9.66	0.18	0.4467	0.0046	0.1547	0.0025	0.44518	2401	17	2380	20	2396	27	99
H04-14 - 9.d	Core	Dark-weakly luminescent, zoned	203	107	0.53	6.25	0.2	0.3586	0.0052	0.1304	0.0027	0.1634	2013	25	1975	25	2099	36	94
H04-14 - 10.d	Core	Dark, zoned	671	444	0.66	9.37	0.23	0.4442	0.0071	0.1558	0.0028	0.53358	2373	22	2369	31	2408	31	98
H04-14 - 11.d	Core	Weakly luminescent, zoned	207	200	0.97	9.32	0.18	0.4309	0.0048	0.1546	0.0029	0.39564	2369	18	2309	21	2393	32	96
H04-14 - 12.d	Core	Dark, unzoned-weakly-zoned	741	1118	1.51	8.825	0.16	0.4285	0.004	0.1479	0.0022	0.54044	2318.9	16	2298	18	2320	25	99
H04-14 - 13.d	Core	Dark, zoned	209	121	0.58	5.897	0.12	0.3472	0.0046	0.1248	0.0022	0.29883	1961	19	1920	22	2025	31	95
H04-14 - 14.d	Core	Dark, zoned	601	418	0.70	8.662	0.16	0.4232	0.0046	0.1482	0.0022	0.62594	2302.1	16	2275	21	2323	25	98
H04-14 - 15.d	Core	Dark, zoned	161	123	0.77	9.11	0.17	0.4354	0.0046	0.1509	0.0026	0.32805	2349	17	2329	21	2352	29	99
H04-14 - 16.d	Core	Grey/weakly luminescent, zoned	107	67	0.63	4.388	0.11	0.3053	0.0038	0.1047	0.0025	0.30059	1711	21	1717	19	1695	44	101

Supplementary Table 1. (continued)

Analysis	Analysis location	CL response	U (ppm)	Th (ppm)	Th/U	$^{207}Pb/^{235}U$	2σ	$^{206}Pb/^{238}U$	2σ	$^{207}Pb/^{206}Pb$	2σ	Rho	Age (Ma) $^{207}Pb/^{235}U$	2σ	$^{206}Pb/^{238}U$	2σ	$^{207}Pb/^{206}Pb$	2σ	Conc.**
H04-14 - 17.d	Core	Dark, unzoned-weakly-zoned	810	1129	1.39	9.98	0.19	0.4579	0.0048	0.1563	0.0022	0.71684	2432	17	2432	21	2414	24	101
H04-14 - 18.d	Core	Dark, unzoned-weakly-zoned	779	1110	1.42	9.792	0.17	0.4551	0.0043	0.1546	0.0022	0.54189	2414.2	16	2417	19	2396	24	101
H04-14 - 19.d	Rim	Thick, luminescent overgrowth on small dark zoned core	57	29	0.51	4.42	0.13	0.3068	0.0043	0.104	0.0029	0.24705	1711	24	1724	21	1675	52	103
H04-14 - 20.d	Core	Dark, zoned, fragmented grain	180	202	1.12	5.07	0.1	0.3219	0.0034	0.113	0.0022	0.18602	1829	17	1799	17	1841	35	98
H04-14 - 21.d	Core	Grey, zoned	336	190	0.57	8.6	0.18	0.4236	0.0053	0.144	0.0024	0.64015	2296	19	2276	24	2273	29	100
H04-14 - 22.d	Core (outer)/rim?	Thick, dark, unzoned-weakly-zoned, surrounds a weakly luminescent zoned core	1027	1466	1.43	6.929	0.12	0.3783	0.0036	0.1322	0.002	0.52732	2101.5	16	2068	17	2125	26	97
H04-14 - 24.d	Core	Dark, weakly-zoned	482	572	1.19	7.246	0.13	0.3843	0.0038	0.135	0.0022	0.49592	2141	16	2096	18	2160	28	97
H04-14 - 25.d	Core	Weakly luminescent, zoned, fragmented	85	55	0.64	4.79	0.13	0.3215	0.0039	0.1071	0.0027	0.33188	1777	23	1797	19	1734	47	104
H04-14 - 26.d	Core	Dark, zoned	289	231	0.80	7.82	0.15	0.4046	0.0048	0.1388	0.0024	0.45997	2212	17	2190	22	2208	30	99
H04-14 - 27.d	Core	Dark, zoned	147	139	0.95	9.69	0.22	0.4524	0.0057	0.1529	0.0029	0.49252	2402	21	2405	25	2372	33	101
H04-14 - 28.d	Core	Dark, zoned (complex)	199	187	0.94	4.89	0.12	0.328	0.0049	0.1088	0.0025	0.35912	1798	21	1828	24	1778	44	103
H04-14 - 29.d	Core	Dark, unzoned	478	577	1.21	9.24	0.17	0.4395	0.0042	0.152	0.0023	0.28361	2361	17	2348	19	2368	25	99
H04-14 - 30.d	Core	Weakly luminescent-luminescent, zoned	77	30	0.39	4.22	0.13	0.2974	0.0052	0.1025	0.0029	0.32747	1672	25	1677	26	1654	56	101
Sample D525128																			
128 - 1.d	Core	Dark, unzoned-weakly zoned	88	91	1.03	4.91200	0.08200	0.32330	0.00280	0.11010	0.00140	0.38289	1803	14	1806	14	1798	24	100
128 - 2.d	Core	Dark, unzoned-weakly zoned	271	129	0.48	5.07500	0.07300	0.33350	0.00390	0.11042	0.00086	0.75993	1831	12	1855	19	1804	14	103
128 - 3.d	Core	Dark, unzoned-weakly zoned	116	204	1.76	4.60400	0.09200	0.28040	0.00320	0.11960	0.00220	0.28368	1751	17	1593	16	1943	33	82
128 - 6.d	Core	Dark, zoned	1716	224	0.13	3.96000	0.05400	0.27530	0.00180	0.10425	0.00090	0.57404	1625	11	1568	9	1699	16	92
128 - 7.d	Core	Dark, zoned	722	612	0.85	4.08800	0.04900	0.28130	0.00230	0.10533	0.00056	0.76927	1652	10	1598	12	1719	10	93
128 - 9.d	Core	Luminescent, unzoned-weakly zoned	116	137	1.19	4.98900	0.06200	0.32450	0.00230	0.11150	0.00110	0.00444	1817	10	1811	11	1821	18	99
128 - 10.d	Rim	Thick, dark, featureless to weakly-zoned, surrounds (9)	119	130	1.10	3.78300	0.04900	0.27850	0.00200	0.09844	0.00097	0.12818	1588	10	1584	10	1591	18	100
128 - 11.d	Core	Luminescent, unzoned-weakly zoned	73	106	1.46	4.95600	0.07000	0.32150	0.00280	0.11180	0.00120	0.36420	1811	12	1797	13	1824	19	99
128 - 12.d	Rim	Thick, dark, unzoned, truncates a luminescent core (11)	124	107	0.86	4.59400	0.07600	0.31110	0.00290	0.10710	0.00120	0.56237	1747	14	1746	14	1747	21	100
128 - 15.d	Core	Luminescent-weakly luminescent, broad simple zoning	80	107	1.34	4.95000	0.07100	0.32300	0.00260	0.11120	0.00120	0.25507	1810	12	1804	13	1815	20	99
128 - 16.d	Core	Dark, zoned	457	95	0.21	5.02000	0.05500	0.32800	0.00220	0.11106	0.00058	0.57359	1822	9	1828	11	1815	9	101
128 - 17.d	Core	Dark, unzoned-weakly zoned	976	223	0.23	4.75700	0.05400	0.30120	0.00280	0.11439	0.00065	0.73353	1777	10	1697	14	1869	10	91
128 - 18.d	Core	Luminescent, irregular shape	69	96	1.40	5.02500	0.07300	0.32480	0.00270	0.11200	0.00130	0.12988	1822	12	1813	13	1828	21	99
128 - 20.d	Core	Dark, weak-unzoned	54	56	1.03	5.03700	0.07600	0.32470	0.00280	0.11250	0.00140	0.21682	1824	13	1812	14	1836	23	99
128 - 22.d	Core	Weakly luminescent (surrounded by 23)	44	43	0.98	5.07300	0.08900	0.32590	0.00310	0.11350	0.00180	0.26737	1830	15	1818	15	1848	29	98
128 - 23.d	Rim	Thick, dark, unzoned-weakly zoned (surrounds 22)	129	102	0.79	4.41300	0.08100	0.30440	0.00310	0.10500	0.00120	0.73217	1713	15	1713	15	1712	21	100
128 - 24.d	Core (outer)	Dark, unzoned-weakly zoned	97	103	1.06	4.92700	0.06500	0.32040	0.00250	0.11180	0.00100	0.26687	1806	11	1792	12	1825	17	98
128 - 26.d	Core	Dark, featureless, homogeneous	72	76	1.05	3.75000	0.05400	0.27580	0.00230	0.09880	0.00120	0.21813	1582	11	1570	12	1596	23	98
128 - 27.d	Core	Luminescent	80	102	1.28	5.70900	0.08600	0.33200	0.00260	0.12480	0.00150	0.20090	1931	13	1848	13	2021	22	91

Supplementary Table 1. (continued)

Analysis	Analysis location	CL response	U (ppm)	Th (ppm)	Th/U	$^{207}Pb/^{235}U$	2σ	$^{206}Pb/^{238}U$	2σ	$^{207}Pb/^{206}Pb$	2σ	Rho	Age (Ma) $^{207}Pb/^{235}U$	2σ	$^{206}Pb/^{238}U$	2σ	$^{207}Pb/^{206}Pb$	2σ	Conc.**
128 - 28.d	Rim	Thick, dark, featureless, resorbs/truncates anhedral, luminescent core	128	160	1.25	3.82400	0.05600	0.27940	0.00280	0.09910	0.00130	0.28917	1597	12	1588	14	1604	24	99
128 - 29.d	Core (inner to 28)	Luminescent	86	127	1.48	4.76200	0.07200	0.31740	0.00340	0.10880	0.00110	0.54107	1777	13	1777	17	1776	19	100
128 - 30.d	Core	Dark, unzoned-weakly zoned	66	69	1.04	4.94600	0.07800	0.32370	0.00270	0.11090	0.00150	0.17539	1809	13	1808	13	1812	23	100
128-31 - 1.d	Core	Dark, unzoned-weakly zoned	33	26	0.77	5.39000	0.12000	0.33250	0.00410	0.11770	0.00270	0.25043	1878	19	1850	20	1905	40	97
128-32 - 1.d	Rim (thick)	Dark, homogeneous, resorbs a small anhedral dark core	127	142	1.12	3.79200	0.05000	0.27810	0.00190	0.09890	0.00120	0.36791	1589	11	1582	10	1597	23	99
128-33 - 1.d	Core	Dark, unzoned	247	342	1.39	3.80900	0.04100	0.27820	0.00200	0.09933	0.00099	0.43248	1594	9	1582	10	1607	19	98
128-34 - 1.d	Core	Dark, unzoned-weakly zoned	135	85	0.63	4.98900	0.05100	0.32370	0.00280	0.11170	0.00120	0.36271	1816	9	1807	13	1826	19	99
128-35 - 1.d	Core	Dark, unzoned-weakly zoned	48	41	0.85	5.05000	0.10000	0.32670	0.00270	0.11240	0.00220	0.22860	1824	17	1822	13	1826	35	100
128-36 - 1.d	Core	Luminescent, irregularly-shaped	142	166	1.17	5.34500	0.05800	0.34330	0.00290	0.11310	0.00120	0.36542	1875	9	1902	14	1847	19	103
128-37 - 1.d	Rim (thick)	Thick, dark, featureless, truncates/surrounds a zoned core	122	140	1.14	3.83200	0.05000	0.27820	0.00240	0.09980	0.00120	0.33816	1598	10	1582	12	1622	23	98
128-38 - 1.d	Core	Luminescent	57	71	1.24	5.55000	0.10000	0.32950	0.00300	0.12230	0.00230	0.23293	1904	16	1835	15	1979	33	93
128-39 - 1.d	Core	Weakly luminescent, unzoned (same grain as 40)	124	122	0.98	5.08200	0.06600	0.32560	0.00240	0.11320	0.00150	0.21433	1831	11	1817	12	1845	25	98
128-40 - 1.d	Core	Dark, unzoned (same grain as 39)	67	75	1.12	4.93000	0.10000	0.32700	0.00420	0.11010	0.00250	0.22212	1807	18	1823	20	1790	41	102
128-41 - 1.d	Core	Dark	1563	172	0.11	4.22500	0.03200	0.28800	0.00220	0.10638	0.00060	0.72796	1678	6	1631	11	1737	10	94
128-42 - 1.d	Core	Dark, unzoned-weakly zoned	79	54	0.69	5.04700	0.08200	0.32070	0.00300	0.11430	0.00170	0.47877	1826	14	1792	15	1862	27	96
Sample D525121																			
121 - 4.d	Core (outer)	Dark, weakly-zoned (outer to 5)	497	76	0.15	4.33200	0.09100	0.25830	0.00370	0.12100	0.00200	0.68563	1699	17	1481	19	1970	30	75
121 - 5.d	Core	Dark, weakly-zoned (inner to 4)	861	40	0.05	8.76600	0.15000	0.40920	0.00470	0.15473	0.00210	0.74051	2314	15	2211	21	2398	23	92
121 - 10.d	Rim	Dark, weakly-zoned, surrounds a small dark core	214	133	0.62	3.87700	0.06900	0.28700	0.00340	0.09791	0.00150	0.40356	1608	14	1627	17	1582	29	103
121 - 14.d	Core	Dark, weakly-zoned	310	174	0.56	22.46000	0.42000	0.62900	0.00920	0.25970	0.00370	0.82153	3203	18	3145	36	3244	22	97
121 - 15.d	Outer core	Dark, weakly-zoned	460	121	0.26	4.20100	0.09900	0.28760	0.00390	0.10690	0.00180	0.43622	1665	28	1630	20	1744	30	93
121 - 16.d	Core	Dark, weakly-zoned	503	277	0.55	22.62000	0.42000	0.62180	0.00800	0.26540	0.00390	0.71754	3210	18	3117	32	3278	23	95
121 - 17.d	Core	Luminescent, weakly-zoned, surrounded by thin dark rim	63	70	1.11	24.24000	0.48000	0.65970	0.00980	0.26790	0.00420	0.71702	3277	20	3265	38	3292	25	99
121 - 20.d	Core	Dark, zoned, surrounded by weakly luminescent domain	265	32	0.12	23.01000	0.44000	0.64290	0.00910	0.26080	0.00390	0.73513	3226	19	3199	36	3250	24	98
121 - 22.d	Core	Luminescent, fractured	68	46	0.68	9.36000	0.19000	0.36750	0.00570	0.18510	0.00310	0.62642	2372	19	2017	27	2696	28	75
121 - 24.d	Core	Dark, weakly-zoned	309	61	0.20	10.41000	0.22000	0.42410	0.00650	0.17870	0.00280	0.76929	2471	19	2279	29	2640	26	86
121 - 27.d	Core	Dark, weakly-zoned	453	40	0.09	4.79700	0.08300	0.31800	0.00380	0.10981	0.00160	0.62883	1784	15	1780	19	1795	26	99
121 - 28.d	Rim	Weakly luminescent, unzoned-weakly zoned, surrounds dark core	222	111	0.50	3.60600	0.09400	0.27190	0.00350	0.09870	0.00170	0.24918	1549	23	1550	18	1596	32	97
121 - 29.d	Rim	Weakly luminescent, weakly-zoned	333	174	0.52	3.76900	0.06600	0.27560	0.00320	0.09962	0.00150	0.52444	1587	14	1569	16	1615	27	97
121 - 33.d	Rim	Weakly luminescent, weakly-zoned, surrounds a zoned core	244	82	0.34	5.04100	0.08800	0.33210	0.00390	0.11017	0.00170	0.11530	1826	15	1849	19	1800	29	103
121 - 34.d	Core	Weakly luminescent, weakly-zoned	210	60	0.28	4.87900	0.08700	0.32560	0.00380	0.10870	0.00170	0.24902	1798	15	1817	18	1775	29	102
121 - 36.d	Core	Dark, weakly zoned to complex internal features,	444	252	0.57	1.48900	0.03300	0.06658	0.00110	0.16170	0.00280	0.65584	925	14	416	7	2471	30	17

Supplementary Table 1. (continued)

Analysis	Analysis location	CL response	U (ppm)	Th (ppm)	Th/U	$^{207}Pb/^{235}U$	2σ	$^{206}Pb/^{238}U$	2σ	$^{207}Pb/^{206}Pb$	2σ	Rho	Age (Ma) $^{207}Pb/^{235}U$	2σ	$^{206}Pb/^{238}U$	2σ	$^{207}Pb/^{206}Pb$	2σ	Conc.**
121 - 37.d	Rim	Weakly luminescent, weakly-zoned, surrounds dark core (36)	349	153	0.44	3.39400	0.06700	0.19290	0.00260	0.12790	0.00220	0.31265	1502	16	1137	14	2066	31	55
121 - 39.d	Core	Weakly luminescent zoned core overgrown by a grey, weakly-zoned-unzoned overgrowth (38)	226	382	1.69	26.05000	0.54000	0.67650	0.00990	0.27880	0.00400	0.83705	3348	21	3330	38	3355	23	99
121 - 43.d	Core	Luminescent	91	50	0.55	24.29000	0.75000	0.68100	0.01300	0.26640	0.00430	0.28707	3276	35	3348	49	3283	26	102
121 - 45.d	Core	Dark, zoned	343	56	0.16	16.22000	0.30000	0.54910	0.00710	0.21490	0.00310	0.21486	2889	18	2821	30	2942	24	96
121 - 46.d	Rim	Weakly luminescent, weakly zoned, surrounds zoned core	247	118	0.48	4.95700	0.08700	0.32670	0.00400	0.11033	0.00170	0.37526	1812	15	1822	20	1803	28	101
121 - 48.d	Core	Dark grey, zoned	284	250	0.88	18.80000	0.38000	0.55660	0.00840	0.24530	0.00350	0.81727	3031	20	2852	35	3154	23	90
121 - 50.d	Core	Luminescent, surrounded by (51)	80	47	0.59	22.30000	0.41000	0.60060	0.00780	0.27000	0.00410	0.51932	3196	18	3032	31	3304	24	92
121 - 51.d	Rim	Dark, unzoned-weakly-zoned, surrounds (50)	812	67	0.08	4.82600	0.08700	0.32000	0.00420	0.11030	0.00170	0.14338	1789	15	1789	20	1803	27	99
121 - 54.d	Core	Dark, weakly-zoned	218	120	0.55	3.88700	0.07300	0.28840	0.00360	0.09823	0.00160	0.41627	1610	15	1633	18	1588	30	103
121 - 56.d	Core	Dark, zoned	369	198	0.54	5.32800	0.12000	0.22210	0.00380	0.17410	0.00260	0.88143	1872	19	1292	20	2596	25	50
121 - 57.d	Core	Dark, surrounded by thin weakly luminescent rim	565	425	0.75	2.69300	0.05000	0.11000	0.00150	0.17800	0.00280	0.58416	1326	14	673	9	2632	26	26
121 - 61.d	Core	Resorbed (anhedral), dark, zoned core, surrounded by weakly luminescent, weakly-zoned overgrowth (20B)	955	228	0.24	2.69700	0.05300	0.11482	0.00150	0.17090	0.00270	0.66113	1327	15	701	9	2565	26	27
121 - 62.d	Core	Dark, zoned	536	56	0.10	4.09300	0.11000	0.17140	0.00430	0.17360	0.00260	0.94171	1649	21	1019	24	2591	25	39
121 - 63.d	Core	Dark, zoned (inner region to 62)	417	38	0.09	5.11300	0.09000	0.22240	0.00290	0.16690	0.00270	0.23257	1838	15	1295	15	2525	27	51
121 - 66.d	Rim	Dark, weakly-zoned, surrounds luminescent-weakly luminescent core	294	49	0.17	4.94600	0.08300	0.32630	0.00380	0.11012	0.00160	0.20130	1810	14	1820	18	1799	27	101
121 - 68.d	Core	Dark	290	78	0.27	4.70700	0.08100	0.31050	0.00380	0.11012	0.00170	0.38450	1768	14	1743	19	1799	27	97
121 - 70.d	Rim	Dark, unzoned-weakly-zoned	371	89	0.24	4.78000	0.12000	0.32260	0.00390	0.10958	0.00170	0.17507	1779	25	1802	19	1791	28	101
121 - 72.d	Core	Luminescent, surrounded by weakly luminescent rim (73)	40	35	0.87	26.25000	0.47000	0.68150	0.00880	0.27930	0.00450	0.32330	3355	17	3349	34	3357	25	100
121 - 73.d	Rim	Weakly luminescent, unzoned-weakly-zoned, surrounds luminescent core (72)	722	76	0.11	4.76600	0.09000	0.31290	0.00470	0.11053	0.00160	0.84756	1778	16	1755	23	1807	26	97
121 - 74.d	Core	Dark, zoned	162	51	0.31	19.83000	0.34000	0.59680	0.00690	0.24060	0.00350	0.41875	3083	17	3017	28	3122	23	97
121 - 77.d	Core (outer)	Dark, zoned, surrounds inner luminescent-weakly luminescent core	329	211	0.64	4.88400	0.09300	0.31650	0.00440	0.11191	0.00160	0.55425	1799	16	1772	22	1829	27	97
121 - 78.d	Rim	Dark, unzoned-weakly zoned, appears to truncate inner core	274	82	0.30	4.84300	0.08500	0.32050	0.00380	0.10936	0.00160	0.49553	1792	15	1792	19	1787	27	100
121 - 79.d	Core	Luminescent	11	21	1.86	15.49000	0.49000	0.42900	0.01100	0.26220	0.00700	0.58011	2837	30	2297	49	3248	43	71
121 - 81.d	Core	Dark, zoned	119	84	0.71	25.93000	0.44000	0.67490	0.00840	0.27870	0.00410	0.16307	3344	17	3325	32	3354	23	99
121 - 84.d	Core	Dark	456	92	0.20	13.70000	0.62000	0.45300	0.01300	0.21700	0.00550	0.97777	2722	48	2409	57	2951	46	82
121 - 85.d	Core	Dark, surrounded by thin weakly luminescent rim	1600	50	0.03	4.97700	0.09300	0.32820	0.00450	0.10961	0.00150	0.92586	1814	16	1829	22	1792	26	102
121 - 86.d	Core	Luminescent	18	17	0.95	21.08000	0.44000	0.58240	0.00850	0.26210	0.00480	0.43077	3140	20	2957	34	3254	29	91
121 - 87.d	Rim	Dark, unzoned-weakly-zoned, surrounds small dark core with complex internal CL	202	96	0.47	3.77000	0.07300	0.27540	0.00330	0.09894	0.00160	0.30279	1586	16	1568	17	1602	30	98
121 - 89.d	Core	Dark, zoned	193	129	0.67	23.93000	0.46000	0.66570	0.01100	0.26030	0.00390	0.83250	3265	19	3288	42	3247	23	101
121 - 91.d	Core	Dark, weakly-zoned	308	150	0.49	5.02900	0.09200	0.33370	0.00410	0.10908	0.00170	0.35741	1824	15	1856	20	1782	29	104

Supplementary Table 1. (continued)

Analysis	Analysis location	CL response	U (ppm)	Th (ppm)	Th/U	$^{207}Pb/^{235}U$	2σ	$^{206}Pb/^{238}U$	2σ	$^{207}Pb/^{206}Pb$	2σ	Rho	Age (Ma) $^{207}Pb/^{235}U$	2σ	$^{206}Pb/^{238}U$	2σ	$^{207}Pb/^{206}Pb$	2σ	Conc.**
121B - 1.d	Rim?	Dark, zoned, surrounds a small dark core	215	87	0.41	4.97700	0.05700	0.32450	0.00220	0.11080	0.00120	0.24709	1814	10	1812	11	1810	21	100
121B - 2.d	Core	Dark, zoned	264	44	0.17	20.93000	0.16000	0.61790	0.00540	0.24570	0.00160	0.62481	3135	7	3101	21	3155	10	98
121B - 3.d	Core	Dark, zoned	250	104	0.42	4.76600	0.04900	0.31720	0.00260	0.10910	0.00110	0.41842	1778	9	1776	13	1784	18	100
121B - 4.d	Core	Dark, zoned	295	138	0.47	18.82000	0.12000	0.59740	0.00460	0.22840	0.00140	0.51134	3032	6	3019	19	3039	10	99
121B - 5.d	Core	Dark, zoned	108	53	0.49	4.99300	0.07600	0.32930	0.00330	0.10980	0.00180	0.20897	1816	13	1835	16	1789	30	103
121B - 9.d	Rim?	Dark, resorbs a small anhedral dark core	153	74	0.49	5.03900	0.06800	0.33540	0.00330	0.10880	0.00150	0.24580	1824	11	1864	16	1774	26	105
121B - 11.d	Core	Dark, zoned	310	188	0.61	4.82800	0.04300	0.31970	0.00280	0.10940	0.00110	0.27575	1789	8	1788	14	1785	19	100
121B - 12.d	Core (outer)	Dark, minor fracturing	572	40	0.07	7.36000	0.09900	0.35900	0.00360	0.14890	0.00150	0.70949	2155	12	1977	17	2334	16	85
121B - 14.d	Core	Dark, surrounded by thin weakly luminescent rim	436	248	0.57	16.90000	0.23000	0.51270	0.00550	0.23730	0.00200	0.71082	2928	13	2668	24	3101	13	86
121B - 15.d	Core	Dark, surrounded by thin weakly luminescent rim	419	208	0.50	17.04000	0.16000	0.56700	0.00500	0.21810	0.00180	0.56478	2936	9	2895	20	2964	14	98
121B - 16.d	Core	Dark, surrounded by thin weakly luminescent rim	760	14	0.02	12.32000	0.13000	0.52490	0.00550	0.17030	0.00110	0.82202	2628	10	2719	23	2559	11	106
121B - 17.d	Core	Dark, weakly-zoned	85	65	0.77	15.86000	0.21000	0.51830	0.00480	0.22180	0.00300	0.31383	2866	13	2692	20	2990	22	90
121B - 18.d	Core	Dark, weakly-zoned	202	88	0.44	4.91500	0.05200	0.32400	0.00280	0.11000	0.00120	0.27379	1804	9	1809	14	1795	20	101
121B - 20.d	Rim	Thick, weakly-zoned, surrounds dark zoned core (61)	355	174	0.49	4.90500	0.04200	0.32380	0.00260	0.10970	0.00100	0.28418	1802	7	1808	12	1791	17	101
121B - 22.d	Core	Dark, surrounded by thin weakly luminescent rim	383	45	0.12	9.13000	0.14000	0.42980	0.00590	0.15460	0.00200	0.61477	2350	14	2304	26	2395	21	96
121B - 25.d	Core	Dark, surrounded by thin dark and weakly luminescent rims	45	43	0.95	24.29000	0.30000	0.65250	0.00710	0.27020	0.00330	0.43048	3278	12	3236	28	3303	19	98
121B - 26.d	Core	Dark, surrounded by thin dark and weakly luminescent rims	208	92	0.44	26.62000	0.19000	0.69100	0.00540	0.27900	0.00210	0.35555	3369	7	3386	21	3355	12	101
121B - 27.d	Core	Dark	463	150	0.32	14.13000	0.14000	0.48320	0.00440	0.21250	0.00180	0.53407	2758	10	2541	19	2922	14	87
121B - 28.d	Core	Dark	575	64	0.11	5.55400	0.07600	0.21160	0.00270	0.19070	0.00220	0.59742	1907	12	1237	14	2745	19	45
121B - 29.d	Core	Dark, weakly-zoned	529	171	0.32	20.02000	0.11000	0.59750	0.00430	0.24240	0.00110	0.70505	3092	5	3022	18	3134	7	96
Sample GAZ-21																			
GAZ21 - 1.d	Core (outer)	Dark, featureless to weakly-zoned	77	57	0.73	5.58000	0.12000	0.35410	0.00440	0.11430	0.00310	0.21237	1911	19	1954	21	1862	48	105
GAZ21 - 2.d	Core	Dark, featureless to weakly-zoned	209	101	0.48	4.95300	0.11000	0.32550	0.00380	0.10990	0.00290	0.28769	1810	18	1816	19	1793	47	101
GAZ21 - 3.d	Core	Weakly luminescent, ghosted-zoning, weak internal features	122	87	0.71	4.01600	0.08700	0.28560	0.00360	0.10200	0.00280	0.07412	1637	18	1619	18	1657	53	98
GAZ21 - 4.d	Core	Dark, ghosted-zoning, weak internal features	341	769	2.26	4.22500	0.09000	0.29850	0.00350	0.10230	0.00270	0.18628	1677	17	1684	17	1664	48	101
GAZ21 - 5.d	Core	Dark, weakly-zoned	579			4.75000	0.12000	0.31670	0.00420	0.10860	0.00310	0.23301	1773	21	1773	21	1767	52	100
GAZ21 - 6.d	Core	Dark, weakly-zoned				4.95400	0.10000	0.32990	0.00400	0.10880	0.00290	0.06110	1810	17	1838	19	1776	47	103
GAZ21 - 7.d	Core	Dark, broad weak zoning				4.72900	0.10000	0.31410	0.00340	0.10770	0.00270	0.12348	1771	18	1761	17	1757	45	100
GAZ21 - 8.d	Core	Dark, weakly-zoned to featureless				4.20700	0.08100	0.29850	0.00320	0.10205	0.00250	0.24956	1675	16	1684	16	1658	46	102
GAZ21 - 9.d	Core	Dark, internal features unclear				4.48000	0.14000	0.31020	0.00470	0.10450	0.00350	0.39058	1724	26	1741	23	1695	63	103
GAZ21 - 10.d	Core	Dark, featureless to convoluted internal texture				4.19100	0.12000	0.29530	0.00450	0.10310	0.00330	0.22902	1671	22	1667	23	1666	60	100
GAZ21 - 11.d	Core	Weakly luminescent, weakly-zoned				4.90600	0.12000	0.32670	0.00380	0.10870	0.00320	0.07947	1800	21	1822	19	1765	54	103
GAZ21 - 12.d	Core	Weakly luminescent, weakly-zoned				5.06000	0.12000	0.33210	0.00460	0.11030	0.00330	0.15826	1827	21	1848	22	1793	54	103
GAZ21 - 13.d	Core	Dark, weakly-zoned to sector-zoned, surrounded by thin luminescent rim				4.61200	0.11000	0.31590	0.00390	0.10580	0.00290	0.48925	1748	21	1770	19	1719	51	103
GAZ21 - 14.d	Core	Dark, internal features unclear				4.82600	0.11000	0.32540	0.00390	0.10760	0.00290	0.22171	1787	19	1816	19	1755	48	103
GAZ21 - 15.d	Core	Weakly luminescent, internal features unclear				4.99800	0.12000	0.33330	0.00440	0.10880	0.00300	0.34729	1816	21	1854	21	1770	51	105

Supplementary Table 1. (continued)

Analysis	Analysis location	CL response	U (ppm)	Th (ppm)	Th/U	$^{207}Pb/^{235}U$	2σ	$^{206}Pb/^{238}U$	2σ	$^{207}Pb/^{206}Pb$	2σ	Rho	Age (Ma) $^{207}Pb/^{235}U$	2σ	$^{206}Pb/^{238}U$	2σ	$^{207}Pb/^{206}Pb$	2σ	Conc.**
GAZ21 - 16 - 1.d	Core	Dark	324	279	0.86	4.06200	0.03500	0.29300	0.00370	0.10020	0.00094	0.20750	1646	7	1657	18	1625	17	102
GAZ21 - 17 - 1.d	Core	Dark, weakly-zoned	189	123	0.65	4.93800	0.06400	0.32960	0.00470	0.10840	0.00110	0.56700	1807	11	1836	23	1768	19	104
GAZ21 - 18 - 1.d	Core	Dark grey, weakly-zoned, fragment of zircon	123	58	0.47	4.70000	0.05700	0.31660	0.00430	0.10770	0.00120	0.35296	1766	10	1773	21	1757	21	101
GAZ21 - 19 - 1.d	Core	Dark, weakly-zoned	87	94	1.08	5.40500	0.07000	0.34980	0.00490	0.11240	0.00110	0.54703	1884	11	1933	23	1835	18	105
GAZ21 - 20 - 1.d	Rim?	Dark, possible rim about a darker core	215	147	0.68	3.81000	0.03700	0.28060	0.00350	0.09829	0.00097	0.20948	1594	8	1594	18	1588	19	100
GAZ21 - 21 - 1.d	Core	Dark, weakly-zoned to sector-zoned	105	135	1.29	4.74100	0.06000	0.31960	0.00450	0.10780	0.00140	0.19726	1773	11	1787	22	1759	25	102
GAZ21 - 22 - 1.d	Core	Dark, weakly-zoned	159	165	1.04	5.22400	0.06700	0.34740	0.00550	0.10900	0.00100	0.65523	1856	11	1921	26	1782	18	108
GAZ21 - 23 - 1.d	Core	Weakly luminescent, weakly-zoned	57	60	1.07	5.02900	0.08600	0.32930	0.00470	0.11080	0.00200	0.06905	1821	14	1835	23	1802	33	102
GAZ21 - 24 - 1.d	Core	Dark, zoned	101	94	0.93	4.62700	0.07600	0.31260	0.00500	0.10750	0.00150	0.57711	1751	13	1753	24	1750	25	100
GAZ21 - 25 - 1.d	Core	Dark, internal features unclear	161	128	0.80	4.23300	0.04200	0.30140	0.00420	0.10230	0.00110	0.34733	1679	8	1698	21	1661	20	102
GAZ21 - 27 - 1.d	Core	Dark, internal features unclear	490	1409	2.88	3.83800	0.03200	0.28450	0.00350	0.09791	0.00079	0.26547	1600	7	1614	18	1582	15	102
GAZ21 - 28 - 1.d	Rim?	Weakly luminescent, surrounds resorbed luminescent core, indistinct internal features	80	70	0.87	4.01900	0.08100	0.29390	0.00430	0.09930	0.00190	0.27735	1637	16	1660	21	1603	35	104
GAZ21 - 30 - 1.d	Core	Weakly luminescent, weakly ghost-zoned	81	98	1.21	4.40800	0.07700	0.30980	0.00450	0.10360	0.00180	0.29085	1713	15	1739	22	1683	31	103
GAZ21 - 31 - 1.d	Core	Dark, weakly-zoned	101	73	0.72	4.88800	0.05500	0.31970	0.00330	0.11150	0.00120	0.27351	1799	10	1788	16	1820	20	98
GAZ21 - 32 - 1.d	Core	Dark, weakly zoned to indistinct and patchy internal features	288	126	0.44	3.81800	0.03400	0.28200	0.00280	0.09821	0.00079	0.37867	1596	7	1601	14	1588	15	101
GAZ21 - 33 - 1.d	Core	Luminescent, weak/indistinct internal features	32	17	0.52	4.88000	0.10000	0.32160	0.00420	0.11060	0.00220	0.30831	1797	17	1797	20	1801	36	100
GAZ21 - 34 - 1.d	Core	Weakly luminescent, unzoned-weakly-zoned (outer domain to 41)	62	64	1.03	4.79000	0.06900	0.31790	0.00380	0.10990	0.00170	0.26992	1784	12	1779	19	1789	28	99
GAZ21 - 35 - 1.d	Core	Dark, weakly ghost-zoned	134	51	0.38	4.06500	0.04700	0.29050	0.00280	0.10170	0.00130	0.02012	1646	9	1644	14	1650	24	100
GAZ21 - 36 - 1.d	Core	Weakly luminescent, indistinct features	63	23	0.36	4.15700	0.07200	0.29480	0.00350	0.10250	0.00170	0.27439	1663	14	1667	17	1663	30	100
GAZ21 - 37 - 1.d	Core	Weakly luminescent, indistinct features	74	28	0.38	4.27600	0.06300	0.29790	0.00310	0.10420	0.00160	0.08758	1688	12	1680	15	1696	28	99
GAZ21 - 38 - 1.d	Core	Weakly luminescent, indistinct features	42	22	0.51	4.75600	0.09000	0.31820	0.00420	0.10830	0.00190	0.37197	1778	15	1781	20	1765	32	101
GAZ21 - 39 - 1.d	Core	Weakly luminescent-luminescent, zoned	64	37	0.57	4.79900	0.07000	0.32160	0.00380	0.10810	0.00180	0.17339	1783	12	1797	18	1758	30	102
GAZ21 - 40 - 1.d	Core	Dark, weakly-zoned	99	67	0.68	5.13800	0.06400	0.34530	0.00380	0.10830	0.00140	0.33208	1843	10	1912	18	1766	23	108
GAZ21-41 - 1.d	Core	Dark, unzoned-weakly-zoned, anhedral shape (inner domain to 34 and 42)	202	79	0.39	4.53700	0.06600	0.30900	0.00300	0.10620	0.00160	0.27436	1736	12	1735	15	1730	28	100
GAZ21-42 - 1.d	Core	Weakly-luminescent, ghost-zoned (outer domain to 34)	44	35	0.79	4.85000	0.10000	0.31960	0.00400	0.11020	0.00220	0.39018	1789	18	1787	20	1789	36	100
GAZ21-43 - 1.d	Core	Dark	531	475	0.89	4.75900	0.03700	0.32260	0.00240	0.10688	0.00086	0.36855	1778	6	1802	12	1744	15	103
GAZ21-44 - 1.d	Core	Weakly luminescent, internal features unclear	39	15	0.39	5.34000	0.11000	0.34660	0.00500	0.11190	0.00240	0.24609	1870	18	1917	24	1827	37	105
GAZ21-45 - 1.d	Core	Dark, internal features unclear	461	513	1.11	4.26900	0.03900	0.30130	0.00220	0.10276	0.00093	0.33962	1687	7	1697	11	1671	17	102
GAZ21-46 - 1.d	Core	Dark, weakly-zoned	130	49	0.38	4.36900	0.05700	0.30300	0.00250	0.10470	0.00150	0.15988	1706	11	1706	13	1706	27	100
GAZ21-47 - 1.d	Core	Luminescent, indistinct internal zoning	27	10	0.38	5.43000	0.13000	0.35190	0.00560	0.11240	0.00300	0.13626	1883	21	1942	26	1814	49	107
GAZ21-48 - 1.d	Core	Weakly luminescent, internal features unclear (diffuse, patchy)	108	59	0.55	4.25300	0.06300	0.30490	0.00330	0.10100	0.00150	0.30923	1682	12	1715	16	1639	28	105
GAZ21-49 - 1.d	Core	Dark	113	46	0.40	4.58900	0.07200	0.31730	0.00310	0.10510	0.00190	0.09299	1747	13	1776	15	1705	33	104
GAZ21-50 - 1.d	Core	Luminescent, internal features unclear,	33	16	0.48	5.02000	0.15000	0.31210	0.00490	0.11720	0.00370	0.24727	1820	26	1750	24	1890	55	93

Supplementary Table 1. (continued)

Analysis	Analysis location	CL response	U (ppm)	Th (ppm)	Th/U	$^{207}Pb/^{235}U$	2σ	$^{206}Pb/^{238}U$	2σ	$^{207}Pb/^{206}Pb$	2σ	Rho	Age (Ma) $^{207}Pb/^{235}U$	2σ	$^{206}Pb/^{238}U$	2σ	$^{207}Pb/^{206}Pb$	2σ	Conc.**
GAZ21-51 - 1.d	Core	Luminescent, internal features unclear	39	14	0.35	4.94000	0.11000	0.32840	0.00420	0.10940	0.00250	0.22965	1804	19	1830	20	1777	45	103
GAZ21-53 - 1.d	Core	Dark	160	89	0.56	4.72000	0.05500	0.31730	0.00270	0.10790	0.00130	0.31582	1771	10	1776	13	1759	22	101
GAZ21-54 - 1.d	Core	Weakly luminescent, weakly-zoned, surrounded by thin luminescent overgrowth	55	30	0.53	4.59200	0.08600	0.30990	0.00370	0.10750	0.00200	0.30479	1744	16	1742	19	1749	36	100
GAZ21-55 - 1.d	Core	Dark, internal features unclear	224	93	0.42	4.08200	0.04600	0.30160	0.00260	0.09840	0.00120	0.30410	1650	9	1699	13	1588	22	107
Sample D525108																			
108 - 2.d	Core (outer)	Weakly luminescent-luminescent, weakly-zoned, outer domain to dark, weakly-zoned core	206	98	0.48	2.42400	0.04700	0.16230	0.00310	0.10750	0.00140	0.68404	1250	13	969	17	1756	24	55
108 - 3.d	Core (outer)	Dark, weakly-zoned	179	100	0.56	3.71900	0.04000	0.27050	0.00340	0.09950	0.00110	0.01129	1574	9	1543	17	1610	21	96
108 - 4.d	Core (outer to 9)	Dark, weakly-zoned (outer domain to 9)	584	203	0.35	5.07500	0.03600	0.33060	0.00410	0.11057	0.00069	0.44652	1832	6	1841	20	1807	11	102
108 - 5.d	Core (outer)	Weakly luminescent-luminescent, weakly-zoned, outer domain to dark, weakly-zoned core	263	116	0.44	5.01700	0.03600	0.32600	0.00410	0.11130	0.00077	0.37912	1823	6	1819	20	1818	12	100
108 - 6.d	Core (outer)	Dark, weakly-zoned	225	32	0.14	4.92700	0.04500	0.32390	0.00440	0.10939	0.00071	0.62032	1806	8	1809	22	1789	12	101
108 - 7.d	Core	Dark, zoned	855	96	0.11	8.84400	0.07600	0.40450	0.00530	0.15769	0.00087	0.59715	2321	8	2189	25	2430	9	90
108 - 8.d	Core	Dark, internal features unclear	64	34	0.53	9.45000	0.13000	0.42680	0.00650	0.16020	0.00210	0.42345	2384	13	2291	29	2454	22	93
108 - 9.d	Core	Luminescent (inner domain to 9)	206	42	0.20	4.83900	0.06600	0.31620	0.00500	0.11040	0.00110	0.59925	1792	11	1771	24	1802	18	98
108 - 10.d	Core	Dark, weakly-unzoned	336	140	0.42	4.82800	0.03900	0.31330	0.00390	0.11110	0.00091	0.14672	1789	7	1757	19	1815	15	97
108 - 13.d	Core	Dark, weakly-zoned	1439			4.52900	0.06100	0.25920	0.00400	0.12633	0.00073	0.87349	1736	11	1485	21	2046	10	73
108 - 15.d	Core	Dark, weakly-zoned	767			5.22300	0.03400	0.33910	0.00430	0.11134	0.00062	0.40999	1856	6	1882	21	1822	10	103
108 - 17.d	Core	Dark, zoned	1041			9.56900	0.08100	0.44110	0.00570	0.15641	0.00078	0.66047	2394	8	2355	25	2416	9	97
108 - 19.d	Core	Dark, zoned	528			5.30500	0.04400	0.34300	0.00450	0.11147	0.00071	0.53970	1869	7	1901	22	1822	12	104
108 - 20.d	Core	Dark, weakly-zoned	615			5.28300	0.04900	0.33950	0.00460	0.11233	0.00099	0.32687	1866	8	1884	22	1835	16	103
108 - 21.d	Core	Luminescent-dark (variable CL response), zoned	130			5.21300	0.08500	0.33890	0.00510	0.11080	0.00170	0.34409	1852	14	1881	25	1812	29	104
108 - 23.d	Core	Dark, zoned	282			10.41000	0.19000	0.46050	0.00750	0.16260	0.00160	0.89750	2472	17	2445	35	2483	17	98
108 - 24.d	Core	Dark, weakly-zoned	698			5.17800	0.05900	0.33000	0.00430	0.11310	0.00120	0.11879	1848	10	1838	21	1851	20	99
108 - 26.d	Core	Dark, weakly-zoned	167	141	0.84	4.71900	0.06600	0.30200	0.00420	0.11240	0.00130	0.46055	1769	12	1701	21	1837	21	93
108 - 27.d	Core	Dark, weakly-zoned	199	179	0.90	4.62300	0.05700	0.31150	0.00410	0.10720	0.00110	0.52069	1752	10	1748	20	1752	18	100
108 - 28.d	Core	Dark, weakly-zoned	216	91	0.42	11.30000	0.07700	0.48750	0.00650	0.16770	0.00120	0.31536	2548	6	2559	28	2533	12	101
108 - 29.d	Core	Dark, weakly-zoned	132	68	0.51	4.32500	0.08600	0.28580	0.00410	0.10990	0.00240	0.11763	1696	16	1620	21	1790	39	91
108 - 31 - 1.d	Core (outer)	Dark, weakly-zoned	272	208	0.76	2.49700	0.04200	0.17440	0.00300	0.10310	0.00130	0.74672	1269	12	1036	16	1677	22	62
108 - 32 - 1.d	Core		231	198	0.86	3.70200	0.07200	0.22790	0.00470	0.11770	0.00150	0.81920	1569	16	1322	24	1916	22	69
108 - 33 - 1.d	Core		270	73	0.27	1.64900	0.04200	0.10290	0.00270	0.11710	0.00180	0.79243	987	16	631	16	1907	28	33
108 - 34 - 1.d	Core	Dark, weakly-zoned	125	97	0.78	4.97600	0.06600	0.32980	0.00420	0.10890	0.00130	0.45317	1813	11	1837	20	1779	22	103
108 - 35 - 1.d	Core	Luminescent-weakly luminescent, outer domain to dark, weakly-zoned core	154	48	0.31	3.49000	0.06800	0.24700	0.00390	0.10270	0.00140	0.68611	1523	15	1423	20	1669	26	85
108 - 37 - 1.d	Core	Dark, weakly-zoned	317	382	1.21	5.01400	0.03700	0.32540	0.00300	0.11133	0.00082	0.20686	1821	6	1816	15	1819	13	100
108 - 38 - 1.d	Core	Dark, weakly-zoned	387	239	0.62	5.05000	0.04500	0.32630	0.00380	0.11265	0.00083	0.73025	1827	8	1820	19	1841	13	99
108 - 41 - 1.d	Core	Weakly luminescent, weakly-zoned, partly resorbed (?) by darker outer domain	255	330	1.29	4.80700	0.05400	0.31490	0.00370	0.11040	0.00120	0.48193	1785	10	1764	18	1802	19	98
108 - 42 - 1.d	Core		465	108	0.23	4.90200	0.04100	0.31730	0.00350	0.11242	0.00085	0.57563	1802	7	1776	17	1837	14	97
108 - 43 - 1.d	Core	Dark, weakly-zoned	669	194	0.29	5.21700	0.05400	0.33800	0.00460	0.11225	0.00082	0.77445	1855	9	1876	22	1834	13	102

Analyses denoted in blue text in the table occur outside 2σ uncertainty of concordia and are deemed discordant.
**Concordance value as calculated by ($^{206}Pb/^{238}U$ Age)/($^{207}Pb/^{206}Pb$ Age) x 100.

Supplementary Table 2. U–Pb monazite geochronology from sample D525052

									Age (Ma)					
Analysis	$^{207}Pb/^{235}U$	2σ	$^{206}Pb/^{238}U$	2σ	$^{207}Pb/^{206}Pb$	2σ	Rho	204/206	$^{207}Pb/^{235}U$	2σ	$^{206}Pb/^{238}U$	2σ	$^{207}Pb/^{206}Pb$	2σ
D525052MZ - 1.d	3.65500	0.05100	0.27260	0.00340	0.09709	0.00160	0.52344	0.00008	1560	11	1553	17	1573	33
D525052MZ - 2.d	3.65000	0.05000	0.27320	0.00310	0.09750	0.00170	0.44725	0.00009	1560	11	1556	16	1571	32
D525052MZ - 3.d	4.07700	0.04900	0.29020	0.00330	0.10255	0.00160	0.62229	0.00004	1649	10	1642	16	1668	29
D525052MZ - 5.d	3.59200	0.04900	0.27090	0.00300	0.09695	0.00150	0.65099	0.00004	1547	11	1545	15	1562	30
D525052MZ - 6.d	3.61100	0.04600	0.27110	0.00290	0.09742	0.00160	0.57369	0.00006	1551	10	1546	15	1571	30
D525052MZ - 7.d	3.63400	0.05000	0.27430	0.00320	0.09707	0.00150	0.66262	0.00005	1556	11	1562	16	1567	29
D525052MZ - 11.d	4.04400	0.04700	0.29080	0.00300	0.10174	0.00150	0.64553	0.00002	1642	10	1645	15	1653	28
D525052MZ - 12.d	4.04400	0.04400	0.28980	0.00290	0.10224	0.00150	0.65188	0.00002	1643	9	1640	14	1663	28
D525052MZ - 13.d	4.03300	0.04400	0.29000	0.00280	0.10178	0.00150	0.60760	0.00002	1642	9	1641	14	1654	28
D525052MZ - 14.d	4.07400	0.04500	0.28900	0.00310	0.10274	0.00150	0.66781	0.00002	1648	9	1636	15	1675	28
D525052MZ - 15.d	3.76200	0.05500	0.28070	0.00330	0.09728	0.00160	0.57812	0.00006	1583	12	1594	17	1570	31
D525052MZ - 16.d	3.96600	0.05700	0.27810	0.00340	0.09839	0.00160	0.65541	0.00006	1625	12	1581	17	1589	30
D525052MZ - 17.d	4.28300	0.05100	0.28350	0.00320	0.10337	0.00160	0.59550	0.00004	1689	10	1609	16	1685	28
D525052MZ - 18.d	4.47900	0.06200	0.29220	0.00370	0.10310	0.00170	0.59062	0.00004	1726	12	1652	18	1677	31
D525052MZ - 21.d	3.99700	0.06000	0.27630	0.00380	0.09650	0.00170	0.64971	0.00003	1634	12	1572	19	1553	32
D525052MZ - 22.d	4.05800	0.05000	0.27490	0.00290	0.09705	0.00160	0.40298	0.00003	1645	10	1567	14	1564	31
D525052MZ - 23.d	4.04600	0.06000	0.26960	0.00300	0.09760	0.00180	0.33555	0.00007	1642	12	1539	15	1576	34
D525052MZ - 24.d	4.05100	0.08400	0.26800	0.00500	0.09890	0.00190	0.66043	0.00004	1643	17	1530	26	1599	37
D525052MZ - 25.d	4.53100	0.06600	0.28910	0.00360	0.10076	0.00170	0.67367	0.00004	1735	12	1637	18	1634	31
D525052MZ - 26.d	4.52600	0.05200	0.28610	0.00300	0.10163	0.00150	0.71166	0.00001	1735	10	1622	15	1653	27
D525052MZ - 27.d	4.05200	0.06400	0.27310	0.00440	0.09621	0.00160	0.75727	0.00003	1643	13	1556	22	1549	32
D525052MZ - 28.d	4.06900	0.04500	0.27040	0.00260	0.09693	0.00150	0.59142	0.00002	1647	9	1543	13	1563	29
D525052MZ - 29.d	4.12200	0.05200	0.27710	0.00300	0.09632	0.00160	0.55352	0.00004	1658	10	1577	15	1550	30
D525052MZ - 31.d	3.78900	0.07000	0.25930	0.00430	0.09556	0.00160	0.77922	0.00002	1590	15	1486	22	1537	32

Analyses denoted in blue text in the table occur outside 2σ uncertainty of concordia and are deemed discordant.

Supplementary Table 3. Lu–Hf zircon isotope analyses

Analysis	$^{207}Pb/^{206}Pb$ age (Ma)	$^{176}Hf/^{177}Hf$*	2 S.E.	$^{176}Lu/^{177}Hf$	$^{176}Yb/^{177}Hf$	$^{176}Hf/^{177}Hf_{initial}$	$\varepsilon_{Hf}(t)$	2σ	T(DM)	$T(DM)_{crustal}$
Sample GAZ-7										
GAZ7-2	1665	0.281325	0.000018	0.000307	0.009424	0.281316	-14.5	0.6	2.64	3.22
GAZ7-3	1771	0.281336	0.000019	0.000233	0.007310	0.281328	-11.7	0.7	2.62	3.13
GAZ7-6	1760	0.281345	0.000022	0.000752	0.023686	0.281320	-12.2	0.8	2.65	3.15
GAZ7-8	1751	0.281394	0.000015	0.000452	0.013115	0.281379	-10.3	0.5	2.56	3.03
GAZ7-10	1738	0.281405	0.000018	0.000883	0.025582	0.281376	-10.7	0.6	2.57	3.05
GAZ7-12	1852	0.281330	0.000018	0.000294	0.009283	0.281320	-10.1	0.6	2.64	3.10
GAZ7-13	1731	0.281338	0.000018	0.000452	0.014181	0.281324	-12.7	0.6	2.64	3.16
GAZ7-18	1738	0.281411	0.000020	0.001008	0.031537	0.281378	-10.7	0.7	2.57	3.04
GAZ7-21	1780	0.281351	0.000018	0.000764	0.024139	0.281325	-11.6	0.6	2.64	3.13
GAZ7-23	1759	0.281350	0.000019	0.000403	0.012699	0.281337	-11.6	0.7	2.62	3.12
GAZ7-28	1746	0.281342	0.000020	0.000227	0.006771	0.281334	-12.0	0.7	2.62	3.13
GAZ7-29	1742	0.281330	0.000021	0.000474	0.015261	0.281315	-12.8	0.7	2.65	3.18
GAZ7-30	1756	0.281312	0.000015	0.000537	0.017199	0.281294	-13.2	0.5	2.68	3.21
Sample GAZ-9										
GAZ9-02	2473	0.281103	0.000022	0.000571	0.017504	0.281076	-4.4	0.8	2.96	3.24
GAZ9-10	1738	0.281326	0.000018	0.000248	0.007657	0.281318	-12.8	0.6	2.64	3.17
GAZ9-12	1766	0.281314	0.000021	0.000441	0.013400	0.281299	-12.8	0.7	2.67	3.19
GAZ9-13	1734	0.281341	0.000020	0.000216	0.006736	0.281334	-12.3	0.7	2.62	3.14
GAZ9-15	1787	0.281341	0.000019	0.000650	0.021134	0.281319	-11.6	0.7	2.64	3.14
GAZ9-20	1769	0.281355	0.000021	0.000313	0.009861	0.281345	-11.1	0.7	2.60	3.09
GAZ9-22	1743	0.281322	0.000019	0.000207	0.006334	0.281315	-12.8	0.7	2.64	3.17
GAZ9-23	1778	0.281490	0.000018	0.000350	0.010766	0.281478	-6.2	0.6	2.42	2.81
GAZ9-25	2361	0.281063	0.000023	0.001136	0.034980	0.281012	-9.3	0.8	3.06	3.44
GAZ9-28	1859	0.281174	0.000025	0.000763	0.022791	0.281147	-16.1	0.9	2.88	3.46
GAZ9-29	1754	0.281298	0.000021	0.000252	0.008120	0.281290	-13.4	0.8	2.68	3.22
GAZ9-33	1759	0.281262	0.000019	0.000354	0.010851	0.281250	-14.7	0.7	2.73	3.30
GAZ9-38	1760	0.281334	0.000018	0.000445	0.013839	0.281319	-12.2	0.6	2.64	3.15
GAZ9-47_back	1769	0.281196	0.000032	0.000404	0.011784	0.281183	-16.9	1.1	2.82	3.44
GAZ9-48	1742	0.281329	0.000019	0.000291	0.009074	0.281319	-12.7	0.7	2.64	3.17
GAZ9-50	1739	0.281332	0.000017	0.000265	0.008221	0.281323	-12.6	0.6	2.63	3.16
GAZ9-51	1770	0.281312	0.000020	0.000213	0.006323	0.281305	-12.5	0.7	2.65	3.18
GAZ9-61	2378	0.281099	0.000024	0.000527	0.015561	0.281075	-6.6	0.9	2.96	3.30
GAZ9-63	1756	0.281317	0.000017	0.000181	0.005897	0.281311	-12.6	0.6	2.65	3.18
GAZ9-69	1784	0.281330	0.000021	0.000253	0.007572	0.281322	-11.6	0.7	2.63	3.13
GAZ9-71	1794	0.281339	0.000021	0.000366	0.010689	0.281327	-11.2	0.7	2.63	3.12
GAZ9-74	1754	0.281321	0.000019	0.000221	0.006866	0.281314	-12.6	0.7	2.64	3.17
GAZ9-82	1797	0.281338	0.000018	0.000192	0.006306	0.281331	-11.0	0.6	2.62	3.11
GAZ9-85	1798	0.281368	0.000023	0.000380	0.011363	0.281355	-10.1	0.8	2.59	3.06
GAZ9-90	1742	0.281312	0.000019	0.000238	0.007475	0.281304	-13.2	0.7	2.66	3.20
Sample PMDDH04-12										
H04-12-06	1885	0.281120	0.000023	0.000859	0.025016	0.281089	-17.5	0.8	2.96	3.56
H04-12-08	1747	0.281312	0.000021	0.000655	0.016910	0.281290	-13.6	0.7	2.68	3.22
H04-12-09	1544	0.281620	0.000034	0.002349	0.071223	0.281551	-9.0	1.2	2.37	2.79
H04-12-12	2364	0.281137	0.000021	0.000531	0.014725	0.281113	-5.6	0.7	2.91	3.23
H04-12-14	2382	0.281133	0.000026	0.001171	0.032425	0.281080	-6.4	0.9	2.97	3.28
H04-12-15	1563^	0.281500	0.000018	0.000527	0.015078	0.281485	-10.9	0.6	2.42	2.92
H04-12-16	1866	0.281355	0.000019	0.000564	0.017909	0.281335	-9.2	0.7	2.62	3.06
H04-12-17	2481	0.281185	0.000026	0.000934	0.029582	0.281140	-1.9	0.9	2.88	3.10
H04-12-19	1889	0.281284	0.000020	0.000580	0.017720	0.281263	-11.3	0.7	2.72	3.20
H04-12-22_front	1786	0.281253	0.000042	0.000893	0.031019	0.281222	-15.1	1.5	2.78	3.34
H04-12-26	1885	0.281365	0.000017	0.000724	0.019629	0.281339	-8.7	0.6	2.62	3.04
H04-12-31	1614	0.281288	0.000019	0.000854	0.026843	0.281262	-17.6	0.7	2.73	3.36
H04-12-33	2395	0.281080	0.000019	0.000888	0.026602	0.281040	-7.5	0.7	3.02	3.36
H04-12-36	2429	0.281061	0.000023	0.000869	0.026338	0.281021	-7.4	0.8	3.04	3.38
H04-12-37	1538	0.281507	0.000020	0.000479	0.013976	0.281493	-11.2	0.7	2.41	2.92
H04-12-40_back	1564	0.281135	0.000036	0.000783	0.021388	0.281112	-24.1	1.3	2.93	3.71
H04-12-41	1706	0.281326	0.000019	0.000686	0.019415	0.281304	-14.0	0.7	2.67	3.22

Supplementary Table 3. (continued)

Analysis	$^{207}Pb/^{206}Pb$ age (Ma)	$^{176}Hf/^{177}Hf$*	2 S.E.	$^{176}Lu/^{177}Hf$	$^{176}Yb/^{177}Hf$	$^{176}Hf/^{177}Hf_{initial}$	$\varepsilon_{Hf}(t)$	2σ	T(DM)	$T(DM)_{crustal}$
Sample PMDDH04-14 (Lu–Hf analyses at individual ages)										
H04_14_01	2271*	0.281178	0.000025	0.001271	0.038663	0.281123	-7.4	0.9	2.91	3.26
H04_14_03	2293*^	0.281136	0.000024	0.000671	0.020462	0.281106	-7.5	0.8	2.92	3.28
H04_14_04	2115*	0.281196	0.000023	0.001266	0.039397	0.281145	-10.2	0.8	2.89	3.31
H04_14_07	2374*	0.281199	0.000026	0.001181	0.037328	0.281146	-4.2	0.9	2.88	3.15
H04_14_08	2396*	0.281217	0.000020	0.000834	0.025066	0.281179	-2.5	0.7	2.83	3.07
H04_14_09	2099*	0.281201	0.000021	0.000494	0.013453	0.281181	-9.3	0.7	2.82	3.24
H04_14_10	2408*	0.281203	0.000026	0.001215	0.038725	0.281147	-3.4	0.9	2.87	3.13
H04_14_15	2352*	0.281171	0.000021	0.000540	0.015351	0.281147	-4.7	0.7	2.87	3.16
H04_14_16	1695	0.281379	0.000019	0.000261	0.006904	0.281370	-11.9	0.7	2.57	3.09
H04_14_17	2414*	0.281227	0.000029	0.001783	0.067176	0.281145	-3.3	1.0	2.88	3.13
H04_14_18	2396*	0.281221	0.000031	0.002157	0.081843	0.281122	-4.5	1.1	2.92	3.19
H04_14_19	1675	0.281340	0.000022	0.000296	0.008150	0.281331	-13.8	0.8	2.62	3.18
H04_14_21	2273*	0.281195	0.000022	0.001015	0.030859	0.281151	-6.4	0.8	2.87	3.20
H04_14_25	1734	0.281402	0.000025	0.000322	0.008629	0.281391	-10.3	0.9	2.54	3.02
H04_14_26	2208*	0.281198	0.000023	0.001206	0.035922	0.281147	-8.0	0.8	2.88	3.25
H04_14_28	1778	0.281396	0.000020	0.000286	0.008270	0.281387	-9.4	0.7	2.55	3.00
H04_14_30	1654	0.281355	0.000022	0.000194	0.005205	0.281349	-13.6	0.8	2.60	3.16
Sample PMDDH04-14 (early Paleoproterozoic Lu-Hf analyses at upper intercept age - use these)										
H04_14_01	2421*	0.281177749	2.55E-05	0.001270573	0.03866324	0.281119	-4.1	0.9	2.91	3.18
H04_14_03	2421*^	0.281135809	2.4E-05	0.000670917	0.020461761	0.281105	-4.6	0.8	2.92	3.21
H04_14_04	2421*	0.281195839	2.31E-05	0.001265854	0.039396562	0.281137	-3.4	0.8	2.89	3.14
H04_14_07	2421*	0.281199406	2.61E-05	0.00118092	0.037328287	0.281145	-3.1	0.9	2.88	3.12
H04_14_08	2421*	0.281217016	2.02E-05	0.000834179	0.025065692	0.281178	-1.9	0.7	2.83	3.05
H04_14_09	2421*	0.281200884	2.12E-05	0.000494487	0.013452636	0.281178	-2.0	0.7	2.82	3.05
H04_14_10	2421*	0.281202798	2.59E-05	0.001214594	0.038725009	0.281147	-3.1	0.9	2.87	3.12
H04_14_15	2421*	0.281171282	2.09E-05	0.00053974	0.015350597	0.281146	-3.1	0.7	2.87	3.12
H04_14_16	1695	0.281378824	1.86E-05	0.000261468	0.006903723	0.281370	-11.9	0.7	2.57	3.09
H04_14_17	2421*	0.281226797	2.89E-05	0.001782619	0.067175504	0.281144	-3.2	1.0	2.88	3.13
H04_14_18	2421*	0.281221015	3.06E-05	0.002157015	0.081842648	0.281121	-4.0	1.1	2.92	3.17
H04_14_19	1675	0.281340421	2.21E-05	0.000296055	0.008150182	0.281331	-13.8	0.8	2.62	3.18
H04_14_21	2421*	0.281195195	2.22E-05	0.001015327	0.030858592	0.281148	-3.0	0.8	2.87	3.12
H04_14_25	1734	0.281401692	2.46E-05	0.000322451	0.008629399	0.281391	-10.3	0.9	2.54	3.02
H04_14_26	2421*	0.281197623	2.34E-05	0.001205998	0.035921952	0.281142	-3.2	0.8	2.88	3.13
H04_14_28	1778	0.281396176	2.02E-05	0.000285607	0.008269598	0.281387	-9.4	0.7	2.55	3.00
H04_14_30	1654	0.281354995	2.19E-05	0.000193959	0.005204816	0.281349	-13.6	0.8	2.60	3.16
Sample D525121										
121-10	1582	0.281426	0.000018	0.000885	0.026208	0.281399	-13.5	0.6	2.55	3.09
121-20	3250	0.280771	0.000016	0.000522	0.013429	0.280739	1.9	0.6	3.40	3.48
121-29	1615	0.281364	0.000032	0.001971	0.068864	0.281303	-16.1	1.1	2.71	3.28
121-33	1800	0.281229	0.000030	0.000522	0.013202	0.281211	-15.1	1.0	2.79	3.36
121-34	1775	0.280876	0.000022	0.000402	0.010589	0.280863	-28.1	0.8	3.25	4.10
121-39	3355	0.280754	0.000025	0.001804	0.052761	0.280637	0.8	0.9	3.54	3.63
121-46	1803	0.281234	0.000023	0.000641	0.017680	0.281212	-15.1	0.8	2.79	3.36
121-66	1799	0.281174	0.000015	0.000210	0.006248	0.281167	-16.7	0.5	2.84	3.45
121-72	3357	0.280742	0.000020	0.000637	0.018627	0.280701	3.1	0.7	3.45	3.50
121-78	1787	0.281210	0.000014	0.000357	0.011321	0.281198	-15.9	0.5	2.80	3.40
121-81	3354	0.280714	0.000020	0.000904	0.023657	0.280655	1.4	0.7	3.51	3.60
121-87	1602	0.281380	0.000028	0.001514	0.051558	0.281334	-15.3	1.0	2.65	3.22
121-89	3247	0.280772	0.000031	0.000599	0.018127	0.280734	1.7	1.1	3.40	3.49
121B-01	1810	0.281145	0.000031	0.001764	0.060911	0.281085	-19.4	1.1	3.00	3.62
121B-03	1784	0.281233	0.000023	0.000446	0.014360	0.281218	-15.3	0.8	2.78	3.35
121B-04	3039	0.280882	0.000018	0.000744	0.022389	0.280839	0.5	0.6	3.27	3.40
121B-05	1789	0.281089	0.000015	0.000260	0.007779	0.281080	-20.1	0.5	2.96	3.64
121B-11	1785	0.281307	0.000015	0.000494	0.015312	0.281290	-12.7	0.5	2.68	3.20
121B-18	1795	0.281185	0.000015	0.000334	0.009790	0.281174	-16.6	0.5	2.83	3.44
121B-20	1791	0.281344	0.000019	0.000697	0.022709	0.281320	-11.5	0.7	2.64	3.13
121B-26	3355	0.280536	0.000027	0.001436	0.049989	0.280444	-6.1	0.9	3.80	4.03

Supplementary Table 3. (continued)

Analysis	$^{207}Pb/^{206}Pb$ age (Ma)	$^{176}Hf/^{177}Hf$*	2 S.E.	$^{176}Lu/^{177}Hf$	$^{176}Yb/^{177}Hf$	$^{176}Hf/^{177}Hf_{initial}$	$\varepsilon_{Hf}(t)$	2σ	T(DM)	$T(DM)_{crustal}$
Sample D525128										
128-01	1798	0.281361	0.000022	0.000337	0.008928	0.281349	-10.3	0.8	2.60	3.07
128-09	1821	0.281405	0.000030	0.001388	0.039497	0.281357	-9.5	1.0	2.61	3.04
128-10	1591	0.281454	0.000017	0.000484	0.012483	0.281439	-11.8	0.6	2.48	3.00
128-11	1824	0.281362	0.000024	0.000767	0.022037	0.281335	-10.2	0.8	2.62	3.08
128-12	1747	0.281357	0.000026	0.000605	0.014495	0.281337	-11.9	0.9	2.62	3.13
128-18	1828	0.281399	0.000026	0.000881	0.026144	0.281369	-8.9	0.9	2.58	3.01
128-20	1836	0.281362	0.000020	0.000643	0.017087	0.281340	-9.8	0.7	2.62	3.06
128-22	1848	0.281357	0.000020	0.000434	0.012119	0.281342	-9.4	0.7	2.61	3.05
128-23	1712	0.281418	0.000019	0.000409	0.010955	0.281405	-10.3	0.7	2.52	3.00
128-24	1825	0.281345	0.000018	0.000445	0.010981	0.281330	-10.4	0.6	2.63	3.09
128-26	1596	0.281424	0.000019	0.000332	0.008830	0.281414	-12.6	0.7	2.51	3.05
128-28	1604	0.281444	0.000017	0.000440	0.011837	0.281430	-11.9	0.6	2.49	3.01
128_30	1812	0.281345	0.000020	0.000597	0.017260	0.281324	-10.9	0.7	2.64	3.11
128-33	1607	0.281485	0.000016	0.000853	0.022964	0.281459	-10.8	0.6	2.46	2.95
128-34	1826	0.281380	0.000017	0.000210	0.005618	0.281372	-8.8	0.6	2.56	3.00
128-35	1826	0.281365	0.000022	0.000584	0.015212	0.281345	-9.8	0.8	2.61	3.06
128-39	1845	0.281394	0.000026	0.001170	0.031508	0.281353	-9.1	0.9	2.61	3.03
128-40	1790	0.281394	0.000031	0.001258	0.034056	0.281351	-10.4	1.1	2.62	3.07
Sample GAZ-21										
GAZ21-03	1657^	0.281388	0.000020	0.000227	0.006081	0.281381	-12.4	0.7	2.55	3.09
GAZ21-04	1664^	0.281404	0.000023	0.000365	0.010204	0.281393	-11.8	0.8	2.54	3.06
GAZ21-06	1776	0.281383	0.000017	0.000297	0.008062	0.281373	-10.0	0.6	2.57	3.03
GAZ21-07	1757	0.281366	0.000020	0.000354	0.009957	0.281355	-11.1	0.7	2.59	3.08
GAZ21-08	1658	0.281397	0.000017	0.000307	0.008319	0.281387	-12.2	0.6	2.55	3.07
GAZ21-11	1765	0.281338	0.000022	0.000331	0.009878	0.281327	-11.9	0.8	2.63	3.14
GAZ21-14	1755^	0.281344	0.000017	0.000274	0.008209	0.281335	-11.8	0.6	2.62	3.13
GAZ21-16	1625	0.281472	0.000018	0.000254	0.006933	0.281464	-10.2	0.6	2.44	2.93
GAZ21-18	1757	0.281360	0.000023	0.000311	0.008460	0.281350	-11.2	0.8	2.60	3.09
GAZ21-20	1588	0.281362	0.000022	0.000267	0.007197	0.281354	-14.9	0.8	2.59	3.19
GAZ21-21	1759	0.281413	0.000019	0.000436	0.012763	0.281399	-9.4	0.7	2.53	2.99
GAZ21-23	1802	0.281358	0.000022	0.000419	0.012039	0.281344	-10.4	0.8	2.61	3.08
GAZ21-24	1750	0.281448	0.000015	0.000210	0.005522	0.281441	-8.1	0.5	2.47	2.90
GAZ21-25	1661^	0.281393	0.000014	0.000186	0.005344	0.281387	-12.1	0.5	2.54	3.07
GAZ21-27	1582	0.281474	0.000020	0.000651	0.019333	0.281454	-11.5	0.7	2.47	2.98
GAZ21_28	1603	0.281428	0.000018	0.000221	0.006215	0.281421	-12.2	0.6	2.50	3.03
GAZ21_30	1683^	0.281414	0.000023	0.000322	0.009069	0.281404	-11.0	0.8	2.53	3.02
GAZ21_31	1820	0.281390	0.000018	0.000274	0.007807	0.281381	-8.7	0.6	2.55	2.99
GAZ21_32	1588	0.281363	0.000018	0.000402	0.010882	0.281351	-15.0	0.6	2.60	3.19
GAZ21_33	1801	0.281399	0.000020	0.000264	0.007636	0.281390	-8.8	0.7	2.54	2.98
GAZ21_35	1650^	0.281384	0.000019	0.000198	0.005759	0.281378	-12.7	0.7	2.56	3.10
GAZ21_36	1663^	0.281428	0.000019	0.000133	0.003767	0.281424	-10.7	0.7	2.49	2.99
GAZ21_38	1765^	0.281362	0.000019	0.000269	0.007630	0.281353	-10.9	0.7	2.59	3.08
GAZ21_42	1789^	0.281375	0.000018	0.000394	0.011486	0.281361	-10.1	0.6	2.58	3.05
GAZ21_45	1671	0.281474	0.000025	0.000656	0.019701	0.281453	-9.5	0.9	2.47	2.92
GAZ21_53	1759	0.281382	0.000017	0.000327	0.009221	0.281371	-10.4	0.6	2.57	3.05
GAZ21_54	1749	0.281391	0.000022	0.000259	0.007734	0.281383	-10.2	0.8	2.55	3.03
Sample D525108										
108-37	1819	0.281342	0.000018	0.000717	0.022710	0.281318	-10.9	0.6	2.65	3.12
108-38	1841	0.281379	0.000026	0.001281	0.040163	0.281334	-9.9	0.9	2.64	3.07
108-27	1752	0.281024	0.000020	0.000695	0.021568	0.281001	-23.7	0.7	3.08	3.83
108-28	2533	0.281065	0.000019	0.000599	0.018553	0.281036	-4.4	0.7	3.01	3.29
108-24	1851	0.281384	0.000021	0.000996	0.030706	0.281349	-9.1	0.8	2.61	3.04
108-21	1812	0.281386	0.000021	0.000587	0.017632	0.281366	-9.4	0.8	2.58	3.02
108-20	1835	0.281189	0.000019	0.000894	0.024802	0.281158	-16.2	0.7	2.87	3.45
108-06	1789	0.281460	0.000016	0.000682	0.018693	0.281437	-7.4	0.6	2.49	2.89
108-05_Back	1818	0.281469	0.000029	0.001263	0.036727	0.281425	-7.1	1.0	2.51	2.89
108-09	1802	0.281355	0.000023	0.000938	0.029556	0.281323	-11.1	0.8	2.65	3.12
108-04	1807	0.281351	0.000022	0.000863	0.024717	0.281322	-11.1	0.8	2.65	3.12

Supplementary Table 3. (continued)

Analysis	$^{207}Pb/^{206}Pb$ age (Ma)	$^{176}Hf/^{177}Hf$*	2 S.E.	$^{176}Lu/^{177}Hf$	$^{176}Yb/^{177}Hf$	$^{176}Hf/^{177}Hf_{initial}$	$\varepsilon_{Hf}(t)$	2σ	T(DM)	$T(DM)_{crustal}$
Sample D525013										
013_11	1543	0.281402	0.000036	0.001043	0.027861	0.281372	-15.3	1.3	2.59	3.18
013_12	1591	0.281433	0.000027	0.000906	0.024695	0.281405	-13.0	0.9	2.54	3.07
013_14	1580	0.281440	0.000027	0.001187	0.032563	0.281405	-13.3	0.9	2.55	3.08
013_15	1578	0.281427	0.000023	0.001328	0.037380	0.281388	-14.0	0.8	2.57	3.12
013_16	1573	0.281534	0.000023	0.000683	0.017735	0.281514	-9.6	0.8	2.39	2.86
013_17	1562	0.281399	0.000029	0.000659	0.017963	0.281380	-14.6	1.0	2.57	3.15
013_19	1555	0.281423	0.000028	0.001022	0.027007	0.281393	-14.3	1.0	2.56	3.12
013_20	1564	0.281421	0.000031	0.000900	0.023761	0.281394	-14.1	1.1	2.55	3.11
Sample D525052										
52_02	2753	0.281287	0.000029	0.002763	0.080273	0.281141	4.5	1.0	2.88	2.94
52_03	1680	0.281323	0.000014	0.000547	0.014684	0.281306	-14.5	0.5	2.66	3.23
52_05	2517	0.281014	0.000019	0.000720	0.021941	0.280979	-6.8	0.7	3.09	3.41
52_09	2512	0.281250	0.000015	0.000559	0.015492	0.281223	1.8	0.5	2.76	2.91
52_12	1576	0.281317	0.000017	0.000990	0.027539	0.281288	-17.6	0.6	2.70	3.33
52_15	2485	0.281222	0.000019	0.000337	0.009211	0.281206	0.5	0.7	2.78	2.96
52_16	2504	0.281265	0.000017	0.000649	0.018875	0.281234	2.0	0.6	2.75	2.89
52_17	3314	0.280723	0.000019	0.000894	0.019650	0.280666	0.8	0.7	3.50	3.60
52_27	1679	0.281341	0.000017	0.000800	0.021334	0.281315	-14.2	0.6	2.66	3.21
52_30	2519	0.281277	0.000021	0.000472	0.015222	0.281254	3.0	0.7	2.72	2.84
52_33	2526	0.281065	0.000022	0.000942	0.026507	0.281019	-5.2	0.8	3.04	3.33
52_35	2492	0.281276	0.000024	0.001105	0.030633	0.281223	1.3	0.8	2.77	2.92
52_38	2995	0.280823	0.000018	0.000666	0.019846	0.280785	-2.5	0.6	3.34	3.54
52_39	2505	0.281096	0.000022	0.000882	0.027139	0.281054	-4.4	0.8	2.99	3.27
52_40	1659	0.281353	0.000015	0.000239	0.007361	0.281345	-13.6	0.5	2.60	3.16
52_41	2505	0.281112	0.000022	0.000866	0.028296	0.281071	-3.8	0.8	2.97	3.23
52_46	2653	0.281207	0.000021	0.001019	0.029501	0.281156	2.7	0.7	2.85	2.96
52_47	2561	0.281227	0.000021	0.000322	0.008747	0.281211	2.5	0.7	2.78	2.90
52_52	2560	0.281063	0.000022	0.000408	0.012298	0.281043	-3.5	0.8	3.00	3.26
52_57	3109	0.280838	0.000018	0.000690	0.020034	0.280797	0.6	0.6	3.32	3.44
52_58	2858	0.281045	0.000024	0.001402	0.043223	0.280969	0.8	0.8	3.10	3.24
52_59	2671	0.281058	0.000025	0.001135	0.034726	0.281000	-2.4	0.9	3.06	3.28
52_60	2620	0.281118	0.000035	0.003338	0.119959	0.280951	-5.4	1.2	3.17	3.41
52_61	2596	0.281222	0.000020	0.000547	0.015135	0.281195	2.7	0.7	2.80	2.91
52_65	2579	0.281208	0.000020	0.000729	0.021418	0.281172	1.5	0.7	2.83	2.97
52_66	2543	0.281139	0.000019	0.000353	0.010156	0.281122	-1.1	0.7	2.90	3.10
52_68	2677	0.281101	0.000022	0.001374	0.039362	0.281030	-1.2	0.8	3.03	3.21

*Analyses from sample PMDDH04-14 that should be plotted at upper intercept age of the sample (2421 ± 35 Ma) as they show clear evidence for ancient Pb-loss; analyses from PMDDH04-14 with ages younger than the calculated lower intercept of the regression remain plotted at their individual apparent $^{207}Pb/^{206}Pb$ ages. Data for PMDDH04-14 are given for analyses plotted at their individual ages as well as the upper intercept age of the regression, as applicable (above). Samples D525128, PMDDH04-12, GAZ-21 and D525013 also show possible evidence for minor Pb-loss (Supplementary Figure 1), but is not as distinct as per PMDDH04-14 and thus remain plotted at their individual ages.

^Denotes discordant U–Pb analyses; all other analyses are concordant